Transactions of the ASME®

Technical Editor, LEON M. KEER (1993)

The Technological Institute
Northwestern University
Evanston, IL 60201

APPLIED MECHANICS DIVISION

Chairman, MICHAEL J. FORRESTAL
Secretary, L. B. FREUND
Associate Technical Editors,
R. M. BOWEN (1994)
S. K. DATTA (1993)
G. J. DVORAK (1993)
M. E. FOURNEY (1994)
C. O. HORGAN (1992)
R. L. HUSTON (1994)
D. J. INMAN (1992)
J. T. C. LIU (1993)
R. M. McMEEKING (1994)
A. K. NOOR (1994)
J. W. RUDNICKI (1992)
W. N. SHARPE, JR. (1994)
C. F. SHIH (1993)
J. G. SIMMONDS (1992)
P. D. SPANOS (1992)
K. R. SREENIVASAN (1992)
Z. WARHAFT (1992)

BOARD ON COMMUNICATIONS
Chairman and Vice-President
R. E. NICKELL
Members-at-Large
W. BEGELL, T. F. CONRY, T. DEAR,
R. L. KASTOR, R. MATES,
E. M. PATTON, R. E. REDER,
R. D. ROCKE, A. VAN DER SLUYS,
A. J. WENNERSTROM, W. O. WINER,
B. ZIELS

President, A. E. BERGLES
Exec. Dir.
D. L. BELDEN
Treasurer, ROBERT A. BENNETT

PUBLISHING STAFF
Mng. Dir., Publ.,
CHARLES W. BEARDSLEY
Managing Editor,
CORNELIA MONAHAN
Production Editor, JUDY SIERANT
Prod. Asst., MARISOL ANDINO

Transactions of the ASME, Journal of Applied Mechanics (ISSN 0021-8936) is published quarterly (Mar., June, Sept., Dec.) for $160.00 per year by The American Society of Mechanical Engineers, 345 East 47th Street, New York, NY 10017. Second class postage paid at New York, NY and additional mailing offices. POSTMASTER: Send address changes to Transactions of the ASME, Journal of Applied Mechanics, c/o THE AMERICAN SOCIETY OF MECHANICAL ENGINEERS, 22 Law Drive, Box 2300, Fairfield, NJ 07007-2300.

CHANGES OF ADDRESS must be received at Society headquarters seven weeks before they are to be effective. Please send old label and new address.

PRICES: To members, $29.00, annually: to nonmembers, $160.00. Add $20.00 for postage to countries outside the United States and Canada.

STATEMENT from By-Laws. The Society shall not be responsible for statements or opinions advanced in papers or . . . printed in its publications (B7.1, Par. 3).

COPYRIGHT © 1991 by The American Society of Mechanical Engineers. Reprints from this publication may be made on condition that full credit be given the TRANSACTIONS OF THE ASME, JOURNAL OF APPLIED MECHANICS, and the author, and date of publication be stated.

INDEXED by Applied Mechanics Reviews and Engineering Information, Inc. Canadian Goods & Services Tax Registration #126148048.

Journal of Applied Mechanics

Published Quarterly by The American Society of Mechanical Engineers

VOLUME 58 • NUMBER 2 • JUNE 1991

TECHNICAL PAPERS

305 **Micromechanically Inspired Phenomenological Damage Model** (91-APM-20)
Dusan Krajcinovic, Michal Basista, Dragoslav Sumarac

311 **A Global Damage Theory and the Hyperbolicity of the Wave Problem**
K. C. Valanis

317 **Nonproportional Multiaxial Cyclic Loading: Experiments and Constitutive Modeling** (91-APM-26)
Z. Xia and F. Ellyin

326 **Growth Instability During Nonuniform Directional Solidification of a Pure Metal Plate** (91-APM-15)
Louis G. Hector, Jr., B. Aksel, and Joseph Fridy

334 **Dynamic Cylindrical Cavity-Expansion of Compressible Strain-Hardening Materials** (91-APM-10)
V. K. Luk and D. E. Amos

341 **Prediction of Dynamic Contact Loads in Granular Assemblies**
C. Y. Zhu, A. Shukla, and M. H. Sadd

347 **Elasto-Plastic Finite Element Analysis of Three-Dimensional Pure Rolling Contact Above the Shakedown Limit** (91-APM-23)
S. M. Kulkarni, G. T. Hahn, C. A. Rubin, and V. Bhargava

354 **Convex Models of Vehicle Response to Unknown but Bounded Terrain**
Yakov Ben-Haim and Isaac Elishakoff

362 **The In-Plane Loading of Rigid Disk Inclusion Embedded in an Elastic Half-Space** (91-APM-28)
A. P. Selvadurai, B. M. Singh, and M. C. Au

370 **Torsion of a Rigid Smooth Elliptic Insert in an Infinite Elastic Plane**
Robert S. Gross and James G. Goree

376 **The Nonlinear Elastic Behavior of Open-Cell Foams**
W. E. Warren and A. M. Kraynik

382 **Stress Analysis of Multilayered Anisotropic Elastic Media** (91-APM-21)
Hyung Jip Choi and S. Thangjitham

388 **Elastic Moduli of Thickly Coated Particle and Fiber-Reinforced Composities**
Y. P. Qiu and G. J. Weng

399 **Antiplane Shear Interface Cracks in Anisotropic Bimaterials** (91-APM-35)
Kuang-Chong Wu and Yu Tsung Chiu

404 **Dynamic Stress on a Partially Bonded Fiber** (91-APM-30)
Andrew Norris and Yang Yang

410 **The Crack Problem in Bonded Nonhomogeneous Materials** (91-APM-17)
F. Erdogan, A. C. Kaya, and P. F. Joseph

419 **The Mode III Crack Problem in Bonded Materials With a Nonhomogeneous Interfacial Zone** (91-APM-18)
F. Erdogan, A. C. Kaya, and P. F. Joseph

428 **Interface Crack in a Three-Phase Composite Constitutive Model**
H. A. Luo and U. Chen

435 **Analysis of Embedded and Surface Elliptical Flaws in Transversely Isotropic Bodies by the Finite Element Alternating Method** (91-APM-34)
H. Rajiyah and S. N. Atluri

444 **The Spherical Inclusion With Imperface Interface**
Z. Hashin

450 **Elastic-Plastic Analysis of Cracks on Bimaterial Interfaces: Part III—Large-Scale Yielding** (91-APM-12)
C. F. Shih, R. J. Asaro, and N. P. O'Dowd

464 **Integral Equations Solution for Reinforced Mode I Cracks Opened by Internal Pressure**
Scott W. Fowser and Tsu-Wei Chou

473 **A New Approach to Microbuckling of Fibrous Composites** (91-APM-16)
Dimitris C. Lagoudas, Iradj Tadjbakhsh, and Nabil Fares

480 **Vibration of Circular Plates in Contact With Water** (91-APM-9)
M. K. Kwak

484 **Plate Tenting With a One-Sided Constraint** (91-APM-38)
Richard C. Benson

493 **Extention of the Upper Bound Method to Include Estimation of Stresses** (91-APM-19)
A. Azarkhin and O. Richmond

499 **A Consistent Implicit Formulation for Nonlinear Finite Element Modeling With Contact and Friction: Part I—Theory** (91-APM-1)
M. J. Saran and R. H. Wagoner

507 **A Consistent Implicit Formulation for Nonlinear Finite Element Modeling With Contact and Friction: Part II—Numerical Verification and Results** (91-APM-2)
M. J. Saran and R. H. Wagoner

(Contents continued on Inside Back Cover)

Downloaded 04 May 2010 to 171.66.16.49. Redistribution subject to ASME license or copyright; see http://www.asme.org/terms/Terms_Use.cfm

CONTENTS (CONTINUED)

513 **Systems With Infinitesimal Mobility: Part I—Matrix Analysis and First-Order Infinitesimal Mobility**
E. N. Kuznetsov

520 **Systems With Infinitesimal Mobility: Part II—Compound and Higher-Order Infinitesimal Mechanisms**
E. N. Kuznetsov

527 **On Stability and Stabilization of Mechanical Structures Under Nonlinear Time-Varying Perturbations**
Chun-Liang Lin, Bor-Sen Chen, and Fei-Bin Hsiao

536 **On Energy Rate Theorems for Linear First-Order Nonholonomic Systems**
John G. Papastavridis

545 **Stability and Bifurcation Analysis of Oscillators With Piecewise-Linear Characteristics: A General Approach** (91-APM-22)
Y. B. Kim and S. T. Noah

554 **On the Interaction and Reflection of Shocks in Hyperelastic Strings** (91-APM-29)
J. L. Wegner, L. Jiang, and J. B. Haddow

559 **Chaotic Motions of a Constrained Pipe Conveying Fluid: Comparison Between Simulation, Analysis, and Experiment** (91-APM-36)
M. P. Paidoussis, G. X. Li, and R. H. Rand

566 **Centrifugal Convection due to Mass Transfer Near a Rotating Disk at High Schmidt Number**
M. Toren, M. Ungarish, G. Pinchuk, and A. Solan

572 **On Damping of the Normal Component of Fluctuations in the Wall Region of Turbulent Flow** (91-APM-33)
Włodzimierz Kozlowski

BRIEF NOTES

Flow Across a Stretching Surface **C. Y. Wang** 579

Kinematic Hardening for Nonproportional Loading **C. S. White** 580

Asymptotic Solution for Extrusion of Sintered Power Metals **D. Durban and M. E. Mear** 582

The Branched Crack Problem Revisited **A. Dollar and P. S. Steif** 584

Singularities in *p*-Type Finite Element Computations: Numerical Experiments on the Locality of Pollution Effects **G. Becker, P. Carnevali, B. Chayapathy, W. Imaino, R. B. Morris, Y. Tsuji, and B. Yendler** 586

An Integral Formulation for Dynamic Poroelasticity **J. Dominquez** 588

591 Analysis of the Caustic Method for the Transient Stress Field of Stationary Cracks
C.-C. Ma

593 An Alternative Approach to the Symmetrical Top and Slender Member Analysis
N. Madsen

594 Response of Subsurface Rigid Strips to Plane Harmonic Shear Waves
R. L. Ryan and S. Mall

596 Nonlinear Transient Analysis of Large Rotordynamic Systems
T. N. Shaiu and A. N. Jean

599 On the Response of a Partially Embedded Rod to Axial Load
Ronald Y. S. Pak and J.-D. M. Saphores

BOOK REVIEWS

603 ***Electrodynamics of Continua I: Foundations and Solid Media,*** **by A. C. Eringen and G. A. Maugin . . .** Reviewed by **Y. E. Pak**

603 ***Tribology and Mechanics of Magnetic Storage Devices*****, by Bharat Bhushan . . .** Reviewed by **Y. W. Chung**

ERRATA

565 **Errata on "Rigid Punch on Stressed Orthotropic Half-Plane With Partial Slip" by H. L. Bjarnehed**

ANNOUNCEMENTS AND SPECIAL NOTES

325 Call for Proposals to Host a I.U.T.A.M. Symposium

418 Change of Address Form

434 ECO WORLD '92—Call for Papers

578 18th International Congress of Theoretical and Applied Mechanics—Call for Papers

602 1992 ASME Summer Mechanics and Materials Meeting—Call for Papers

605 Books Received by the Office of the Technical Editor

606 Worldwide Mechanics Meetings List

608 Information for Authors

Downloaded 04 May 2010 to 171.66.16.49. Redistribution subject to ASME license or copyright; see http://www.asme.org/terms/Terms_Use.cfm

Dusan Krajcinovic
Fellow ASME.

Michal Basista[1]
Department of Mechanical and Aerospace Engineering, Arizona State University, Tempe, AZ 85287-6106

Dragoslav Sumarac
Civil Engineering Department, University of Belgrade, Belgrade, Yugoslavia

Micromechanically Inspired Phenomenological Damage Model

The paper suggests a phenomenological damage theory for perfectly brittle response of solids. The theory is based on the micromechanics of brittle deformation processes. The inelastic change of the compliance is identified as the flux and a properly averaged energy release rate as the affinity. The paper identifies conditions under which the damage potential exists. The proposed model is illustrated on the examples of plain concrete specimens subjected to uniaxial tension and compression.

Introduction

Despite their great advantages in modeling physical reality with a minimum of ambiguity and arbitrariness, micromechanical models are computationally inefficient in practical applications. Indeed, in the case of nonuniform fields of stresses and strains the bookkeeping accounting for defects within the representative volume element, mapping on a material point of the continuum, may in itself grow into an overwhelming problem.

Conversely, the ambiguities inherent in macromodeling of microprocesses resulted in emergence of many different, and often contradictory, phenomenological damage models (Krajcinovic, 1984). Since most of these models aspire of being the generalization of the original Kachanov's (1958) model, it seems reasonable to clarify some of the outstanding issues in the light of the recent developments in the field.

The objective of this study is to describe the macrobehavior of the sample containing an ensemble of a large number of microcracks comparable in size to the sources of inhomogeneities within the volume V. The irreversible change in the Gibbs energy of the sample, during a brittle deformation process, can then be written simply as

$$d^i\Psi = \sum_n \int_{L_n} [(G-2\gamma)\delta l]dL \geq 0 \qquad (1)$$

where the sum extends over all n active (propagating) cracks. In equation (1), γ is the fracture energy density; $\delta l(L)$ is an advance of the crack front L in the direction of its normal. The energy release rate G is a function of local stresses $\hat{\sigma}(\mathbf{x})$ which are related to the macrostresses σ by means of an influence tensor $\mathbf{M}(\mathbf{x})$ (Hill, 1967) such that $\hat{\sigma} = \mathbf{M}(\mathbf{x}) : \sigma$.

During semi-brittle and ductile deformation processes other energy dissipating mechanisms exist as well. For example, the frictional losses associated with the sliding of the rough crack surfaces over each other may be of significance when the brittle solids are exposed to compressive tractions. At this point it seems reasonable to start with a simple model for a process during which the energy lost on friction can be neglected in comparison with the energy needed for the propagation of cracks (1).

It has been shown in the past (Krajcinovic and Fanella, 1986; Krajcinovic and Sumarac, 1987, 1989, etc.) that in a simple case of homogeneous stress and strain fields a reasonably simple and accurate but approximate micromechanical model can be formulated, within the context of the self-consistent model whenever analytical expression for G is available. This is true only in the case of isotropic and transversely isotropic materials restricting the direct utilization of micromechanical models to a handful of simple cases. In order to construct a theory of practical utility it is necessary to take advantage of available micromechanical models as building blocks fitted together into a rational phenomenological theory (Ortiz, 1985; Yuazdani and Schreyer, 1988).

Micro-Fluxes

The energy dissipation density rate can always be written in form of a scalar product

$$d^i\Psi = \frac{1}{V}\sum_\alpha f_\alpha d\xi_\alpha \qquad (2)$$

where $d\xi_\alpha$ constitute a set of fluxes defining specific modes of

[1]On leave from the Institute of Fundamental Technological Research, Warsaw, Poland.

Contributed by the Applied Mechanics Division of THE AMERICAN SOCIETY OF MECHANICAL ENGINEERS for presentation at the Joint Applied Mechanics/Bioengineering Conference, Ohio State University, Columbus, Ohio, June 16-19, 1991.

Discussion on this paper should be addressed to the Technical Editor, Prof. Leon M. Keer, The Technological Institute, Northwestern University, Evanston, IL 60208, and will be accepted until two months after final publication of the paper itself in the JOURNAL OF APPLIED MECHANICS. Manuscript received by the ASME Applied Mechanics Division, July 20, 1989; final revision, June 15, 1990.
Paper No. 91-APM-20.

Copyright © 1991 by ASME
Downloaded 03 May 2010 to 171.66.16.248. Redistribution subject to ASME license or copyright; see http://www.asme.org/terms/Terms_Use.cfm

irreversible rearrangements of the material structure, while f_α are their conjugate thermodynamic forces or affinities.

To be of practical utility the set of internal variables must contain as few internal variables as possible. In principle, the selection of internal variables is quite arbitrary even though it is intuitively obvious that the accuracy, simplicity, and tractability can be achieved only if the fluxes reflect the salient aspects of the microstructural rearrangements. A rational choice of fluxes and their affinities is obtained from (1) writing

$$d^i\Psi = \langle (G-2\gamma)dA \rangle \tag{3}$$

where the angular brackets denote the average of bracketed function along the length of the crack front L, while $dA = L\,dl$ is the increment of the crack surface area. Consequently, in view of (2) the thermodynamic force and the corresponding flux are

$$f_\alpha = \frac{L}{2A}\langle G-2\gamma\rangle_\alpha; \qquad d\xi_\alpha = \frac{1}{V}\left\langle \frac{2A\,dA}{L}\right\rangle_\alpha. \tag{4}$$

In (4) f_α is the excess strain energy release rate integrated along the perimeter and averaged over the crack surface area, while $d\xi_\alpha$ is recognizable as the increment of the Budiansky-O'Connell (1976) damage variable. Assuming self-similar growth of penny-shaped cracks, the flux $(4)_2$ is readily integrated into the damage variable promoted in Krajcinovic and Fanella (1986), Krajcinovic and Sumarac (1987, 1989), Sumarac and Krajcinovic (1987), etc.

Macro-Response

Consider an isothermal deformation process of a perfectly brittle solid weakened by a large number of already existing microcracks. Assume the strains to be infinitesimal and neglect residual (plastic) strains. In this case the Gibbs energy density allows decomposition

$$\psi(\sigma,H) = \psi^0(\sigma) + \psi^*(\sigma,H) = (1/2)(\sigma : \mathbf{S}^0 : \sigma) + (1/2)(\sigma : \mathbf{S}^* : \sigma). \tag{5}$$

In (5) H is the history recording parameter, $\mathbf{S}^0$ the compliance of the virgin material, and $\mathbf{S}^*(H)$ the compliance attributable to the presence of cracks. The strain is

$$\epsilon = \frac{\partial\psi}{\partial\sigma} = (\mathbf{S}^0+\mathbf{S}^*) : \sigma = \mathbf{S} : \sigma. \tag{6}$$

In loading (defined as a process during which the history changes, i.e., when at least one of the cracks grows in size $\delta l > 0$), the strain increment is

$$d\epsilon = \mathbf{S} : d\sigma + d\mathbf{S}^* : \sigma = d\epsilon^e + d\epsilon^*. \tag{7}$$

The in-elastic increment in strain $d\epsilon^* = d\mathbf{S}^* : \sigma$ is attributable to the change in compliance; i.e., reduction of the number of atomic bonds (or increase of the total size of the internal surfaces-damage evolution). The term $d\mathbf{S}^*$ and $d\epsilon^*$ are defined as in Rice (1975).

In unloading ($dH = 0$; i.e., all cracks remain of same size) the stress-strain relationship is linear. Consequently, $d\epsilon = \mathbf{S} : d\sigma$ such that the residual strain vanishes when σ is reduced to zero. The total compliance in (6) depends on the already accumulated history. The initial and the unloading segments of the stress-strain curve are not parallel if the history parameter changes during the deformation process. The slope of the initial segment of the loading curve is defined by the compliance of the virgin material $\mathbf{S}^0$, while the slope of the unloading segment of the stress-strain curve is defined by $(\mathbf{S}^0 + \mathbf{S}^*)$.

Macro-Fluxes

The rate at which the energy is dissipated within the representative volume element on the creation of new internal surfaces can be written from (5) and (7) as

$$d^i\psi = \mathbf{Q}\cdot d\mathbf{q} = (1/2)(\sigma : d\mathbf{S} : \sigma) = (1/2)(\sigma : d\epsilon^*) \tag{8}$$

where $\mathbf{Q}$ and $\mathbf{q}$ are macro affinities and internal variables, respectively. As a first option the inelastic strains can be selected as macro fluxes $d\mathbf{q}$. However, there are at least two strong reasons against such a choice. First, in unloading (defined as $\sigma : d\sigma < 0$) the inelastic strains will change and eventually disappear. Secondly, the components of the inelastic changes of the compliance tensor cannot be uniquely determined knowing stresses and inelastic strains. Consequently, this choice of internal variable does not allow for the determination of the overall compliance eliminating it as a viable alternative from further considerations.

Combining (1) and (5) it follows that

$$\sigma : \mathbf{S} : \sigma = \frac{1}{V}\sum_n \int_{L_n}\left[\left(\hat{\sigma} : \frac{\partial^2 G}{\partial\hat{\sigma}\,\partial\hat{\sigma}} : \hat{\sigma} - 4\gamma\right)\delta l\right] dL. \tag{9}$$

In a general case, the expressions for G may not be available. An approximate solution to this problem is frequently sought within the context of the self-consistent model based on the assumption that: (a) the external fields of each crack weakly depend on the exact position of adjacent cracks and (b) the external stress of each crack is equal to the macrostress. The ensuing effective continuum, defined by the compliance $\mathbf{S}$ in (9), recognizes the effect of cracks only through their volume density appropriately weighted by crack orientations. Eliminating from the consideration the distance between the defects the self-consistent model ceases to be applicable to processes such as localization of cracklike defects into a crack band during which the distances between the defects play a dominant role.

Consequently, within the framework of the self-consistent model, and for a homogeneous state of stress from (9)

$$d\mathbf{S} = \frac{1}{V}\sum_n \int_{L_n}\frac{\partial^2 G}{\partial\sigma\,\partial\sigma}\,\delta l\,dL. \tag{10}$$

Thus, selecting the affinities and fluxes in (8) as

$$2\mathbf{Q} = \sigma\otimes\sigma = \{\sigma_{11}^2, \sigma_{22}^2, \ldots\},\ d\mathbf{q} = d\mathbf{S} = \{dS_{1111}, dS_{2222}, \ldots\} \tag{11}$$

seems to be the only rational choice. Anticipating applications the expressions (11) are written in terms of principal stresses. The change of compliance is readily measurable locally, satisfying one of the principal requirements for the selection of internal variables. Moreover, the rate of change of the compliance is related to the rate of loss of primary bonds in the solid. Thus, since the area of cracks is obviously related to a number of ruptured bonds in the material it seems reasonable to measure the increase in the microcrack density by the change in compliance. This is, of course, consistent with the original Kachanov-Rabotnov damage model (Lemaitre and Chaboche 1985). Finally, if ductile deformation is thought of as a material slipping "through" the undisturbed crystalline lattice, brittle deformation can be defined in a complementary manner as a process during which the material is stationary while the lattice is degraded through bond rupturing.

In view of the unilateral constraints placed on the displacement field by the cracks it is only possible to identify the positive change of the compliance as the flux. If in unloading the state of stress changes from tension to compression, the compliance can decrease stepwise without any loss of energy to its original (undamaged) magnitude. Thus, strictly speaking, the compliance itself is not an internal variable even though its positive increment is the flux.

Kinetics of Damage Growth

Consider the change of the Gibbs energy associated with the

Downloaded 03 May 2010 to 171.66.16.248. Redistribution subject to ASME license or copyright; see http://www.asme.org/terms/Terms_Use.cfm

transition from an equilibrium state (σ, H) to the neighboring state $(\sigma + \delta\sigma, H + \delta H)$. With (2)

$$\delta\psi = \mathbf{S} : \delta\mathbf{Q} + \frac{1}{V} f_n \delta\xi_n \tag{12}$$

where $\mathbf{S} : \delta\mathbf{Q} = \epsilon : \delta\sigma$ is the work increment of surface forces. The second term on the right-hand side of (12) embodies the work increments on the internal variables.

If the increase in the surface area of a particular crack depends on the external stress only through its own conjugate force (energy release rate) $\xi_n = F(f_n, H)$, it follows (Rice 1971) that the macropotential

$$\Omega(\mathbf{Q},\xi) = \frac{1}{V} \int_0^{f_n(\mathbf{Q},\xi)} \dot{\xi}_m(f_m, H)\, df_m \tag{13}$$

can be obtained superimposing all micropotentials $F(f_n, H)$. The macrofluxes are then

$$\dot{\mathbf{S}} = \frac{\partial\Omega(\mathbf{Q},\xi)}{\partial\mathbf{Q}}. \tag{14}$$

The derivation of the macropotential (13) is exact within the context of the self-consistent model since the influence of adjacent cracks is introduced indirectly through the parameters of the effective solid. The proposed approximation ceases to be valid in cases when the crack growth is dependent directly on the external stresses or when the direct interaction between the cracks becomes a dominant effect (such as during the final phase of the splitting rocks or concrete; see Horii and Nemat-Hasser, 1986; Kachanov, 1987).

The geometrical representation of the flow potential in the space of the affinities (damage surface) is analogous to the yield surface in conventional plasticity. It may be viewed as a "singular clustering of surfaces of constant flow potential" (Rice, 1971). In other words, the macropotential is an envelope of a polyhedral surface consisting of N planes representing conditions under which a particular crack commences growth. The development of the vortex structure, the normality property, etc., are merely reproductions of the well-known results for the yield surface derived in Rice (1971, 1975). The derivation of fluxes using the normality property is analogous to the determination of plastic strain rates in plasticity. Deviations from normality are associated with frictional sliding losses (Rudnicki and Rice 1975). For obvious reasons the analysis along the proposed lines ceases to be valid in the softening region.

The damage surface is understood herein as a piecewise smooth, simply connected and convex surface enveloping the locus of all points in the space of affinities which can be reached without change in the recorded history. The notion of damage surface has been used before by Dougill (1975), Dragon and Mróz (1979), Krajcinovic and Fonseka (1981) and others. However, in all of these cases the existence of the flow potential is *a priori* postulated, and the fluxes and affinities are selected on the basis of formal arguments.

The existence of the damage surface is not only a matter of conjecture. The damage surface was experimentally identified (Holcomb and Costin, 1986) using the acoustic emission technique. The conventional concepts of loading and unloading (central to the use of the damage surface) were corroborated measuring the so-called Kaiser effect according to which no acoustic emissions will occur during the loading process following unloading until the damage surface is reached.

For the present purposes it is most appropriate to use micromechanical considerations employing cell method as a general guidance. The unilateral nature of the constraints imposed by a crack on the displacement field mandates independent consideration of tension and compression. This is not to say that the decomposition of the general case of stress into positive and negative eigenvalues (as suggested by Ortiz (1985), and Yazdani and Schreyer (1988)) is justified.

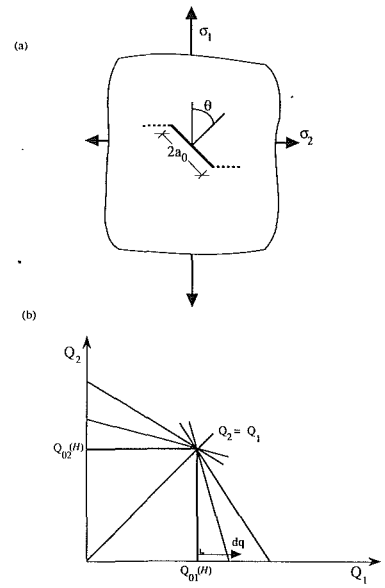

Fig. 1 *(a)* **Cell containing a single microcrack subjected to biaxial tension, *(b)* Griffith criterion (15) in the space of affinities**

(a) Tension. Consider a cell containing a single rectilinear slit of length $2a_0$ embedded in an infinitely extended, homogeneous and isotropic elastic plate, Fig. 1(*a*). The Griffith's criterion following from the inequality (1), assumed to be valid pointwise on L, is

$$\frac{\pi}{E_0}(\sigma_1^2 \cos^2\theta + \sigma_2^2 \sin^2\theta) - 2\gamma \geq 0. \tag{15}$$

The above condition represents a family of straight lines in the space of the affinities ($Q_1 = (1/2)\,\sigma_1^2$, $Q_2 = (1/2)\,\sigma_2^2$) with the angle θ and slit length considered as parameters, Fig. 1(*b*).

For an arbitrary stress path the first crack to become critical is the one being perpendicular to the larger of the two principal stresses. The magnitude of the other principal stress has no influence on the onset of the nonlinear behavior but can, obviously, become important as the external tractions are further increased. The shear stress will play a "corrective role" kinking the slit in the direction normal to the larger of the two tensile stresses (dashed lines in Fig. 1(*a*)).

Thus, in the case when $\sigma_1 > \sigma_2$ it seems justified to assume that, at least in the beginning, only $dS_{1111} > 0$, while all other components of the compliance tensor remain unaltered. The point $Q_1 = Q_2$ in Fig. 1(*b*) corresponds to the isotropic damage evolution since the condition (15) is satisfied for all slits simultaneously.

Consequently, in the case of the biaxial tension it seems reasonable to adopt as a simplest case a damage surface consisting of two perpendicular straight lines intersecting at the isotropic point

$$\Omega_1(Q_1, H) = Q_1 - \overline{Q}_{01}(H) = 0; \quad \Omega_2(Q_2, H) = Q_2 - \overline{Q}_{02}(H) = 0. \tag{16}$$

The initial position of the two lines (16) comprising the damage surface represents the inner envelope of the family of straight lines given by equality (15), Fig. 1(*b*).

In (16), $\overline{Q}_{0i}(H)$ defines the point at which the cracking will commence. It depends on the already recorded history and is path dependent. Owing to the unilateral nature of the constraints, the onset of cracking depends on the sign of the stresses as well.

(b) Compression. The determination of the crack growth in a brittle specimen subjected to a compression-dominated stress field presents a more controversial issue. The most widely accepted model of damage evolution (Horii and Nemat-Nasser,

Downloaded 03 May 2010 to 171.66.16.248. Redistribution subject to ASME license or copyright; see http://www.asme.org/terms/Terms_Use.cfm

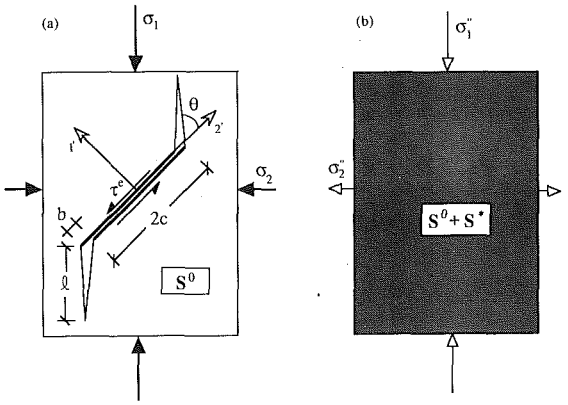

Fig. 2 (*a*) Unit cell containing a single propagating microcrack subject to biaxial compression, (*b*) corresponding effective continuum

1986; Fanella and Krajcinovic, 1988) suggests that the frictional sliding on the pre-existing cracks creates a wedging effect which in turn opens tension cracks kinking in the direction of the maximum compression.

For the present modeling purposes the results of micromechanical analyses of the cracking mechanism shown in Fig. 2(*a*) (Horii and Nemat-Nasser, 1986; Nemat-Nasser and Obata, 1988) will be used only as a guidance. Since these results are not very sensitive for $(\pi/6<\theta<\pi/3)$ it seemed appropriate to select a representative slit at $\theta = \pi/4$ and to assume the kinked part to be straight and parallel to the direction of the larger of two compressive stresses σ_1 (compression is viewed negative).

It is postulated that the inelastic change of the Gibbs energy density rate for a unit cell containing the kinked crack be identical to that of an effective unit cell subjected to axial compression σ_1'' and lateral tension σ_2'' (Fig. 2(*b*))

$$2\dot{\psi}^* = 2\tau^e \dot{\epsilon}_{12}^* = \sigma_1'' \dot{\epsilon}_1^* + \sigma_2'' \dot{\epsilon}_2^* = (\sigma_1'')^2 \dot{S}_{11}^* + (\sigma_2'')^2 \dot{S}_{22}^*. \quad (17)$$

In (17), $2\tau^e = (1-\mu)\sigma_1 - (1+\mu)\sigma_2$ is the effective shear stress acting on the slanted crack while μ denotes the friction coefficient. The shear strain ϵ_{12}^* in the crack coordinate system can be computed after the average slip $b(c, l)$ has been determined (Nemat-Nasser and Obata, 1988). The $\dot{S}_{11}^*$ and $\dot{S}_{22}^*$ are the axial and lateral inelastic changes in compliance of the effective cell.

Assuming τ^e to be the only active stress driving the microcrack growth, the resolved fictitious macrostresses σ_1'' and σ_2'' are

$$\sigma_1'' = (\sin 2\theta)\tau^e, \quad \sigma_2'' = (-\sin 2\theta)\tau^e + \sigma_2. \quad (18)$$

The initial position of the damage surface follows then to be

$$\Omega_c(\mathbf{Q}, H) = Q_1 + Q_2 - \overline{Q}_0(H) = 0 \quad (19)$$

where the affinities and the fluxes are defined as follows:

$$2\mathbf{Q} = \sigma'' \otimes \sigma'' = \{(\sigma_1'')^2, (\sigma_2'')^2, \ldots\},$$
$$d\mathbf{q} = d\mathbf{S} = \{dS_{1111}, dS_{2222}, \ldots\}. \quad (20)$$

It is known that once a Griffith crack in a homogeneous tensile field becomes critical, its growth in a homogeneous elastic material cannot be arrested. However, in the case of real materials and short cracks, the assumption of material homogeneity is not a realistic one. The internal energy barriers (such as grain boundaries, and other inhomogeneities) may arrest a sufficiently short crack. As it grows a microcrack kinks along the path of minimum value of $(G - 2\gamma)$ overcoming a sequence of successively higher energy barriers $\gamma(\mathbf{x})$ randomly distributed in its path. Consequently, $\overline{Q}_{0i}(H)$ must be a monotonically increasing function of stresses (similar to the R-curve) satisfying the following conditions

$$\overline{Q}_0(q=0) = Q_0 = \frac{1}{2}\sigma_0^2; \quad \left.\frac{d\overline{Q}_0}{dq}\right|_{q=q_u} = 0 \quad (21)$$

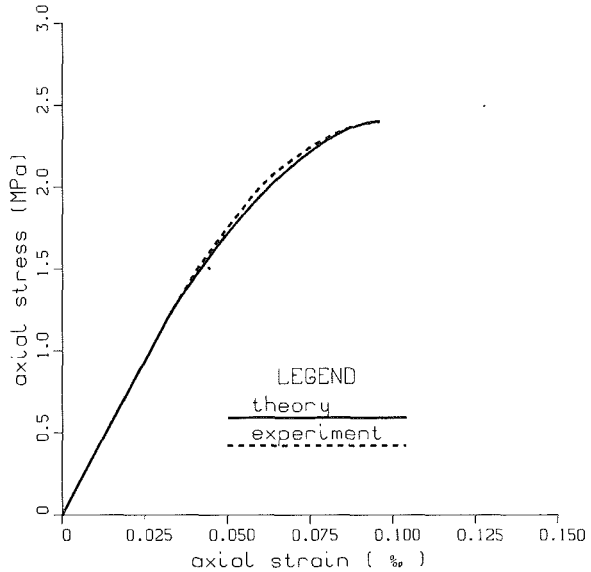

Fig. 3 Uniaxial tension; comparison of analytical (solid line) and experimental (dashed line) results

where σ_0 is the stress level at the onset of nonlinear response. The condition $(21)_2$ reflects the localization of damage (coalescence of neighboring microcracks into a macrocrack) assumed to occur at the apex of the stress-strain curve.

Illustrative Example

(a) Uniaxial Tension. Using the conditions (21) the position of damage surface in the case of tension is

$$\overline{Q}_0(q) = Q_{0t} + (Q_{ut} - Q_{0t})(2q_{ut} - q)q/q_{ut}^2 \quad (22)$$

where $2Q_{ut} = \sigma_{ut}^2$ is the square of the direct tensile strength of the specimen. Once the damage surface (22) is defined, the macroflux is readily determined from the normality property (14) and the final stress-strain relation, for the ascending part of the curve, is

$$\epsilon = \left(\frac{1}{E_0} + q\right)\sigma = \sigma\left\{\frac{1}{E_0} + \left(\frac{\epsilon_{ut}}{\sigma_{ut}} - \frac{1}{E_0}\right)\left(1 - \sqrt{\frac{\sigma_{ut}^2 - \sigma^2}{\sigma_{ut}^2 - \sigma_{0t}^2}}\right)\overline{H}(\sigma - \sigma_{0t})\right\}. \quad (23)$$

In (23), ϵ_{ut} is the strain corresponding to the ultimate stress σ_{ut}, while $\overline{H}$ denotes the Heaviside functional. All other components of the strain tensor and compliance remain unaffected. In biaxial tension the damage evolution in two principal directions is uncoupled and can be computed in form of the expression (23). The stress-strain relation (23) is plotted in Fig. 3 and compared with the experimental results of Brühwiler et al. (1986) for plain concrete specimens in direct tension.

(b) Uniaxial Compression. In uniaxial compression $\sigma_1 = -\sigma < 0$ the fictitious stresses acting on the cell are

$$\sigma_1'' = -\sigma_2'' = \tau^e = -\frac{1}{2}(1-\mu)\sigma. \quad (24)$$

Since the affinities $(20)_1$ are $2Q_1 = 2Q_2 = (\sigma_1'')^2$, the damage surface (19) becomes

$$\Omega_c = Q_1 + Q_2 - \left\{Q_{0c} + \frac{Q_{uc} - Q_{0c}}{2q_{uc}^2}[(2q_{uc} - q_1)q_1 + (2q_{uc} - q_2)q_2]\right\} = 0 \quad (25)$$

Downloaded 03 May 2010 to 171.66.16.248. Redistribution subject to ASME license or copyright; see http://www.asme.org/terms/Terms_Use.cfm

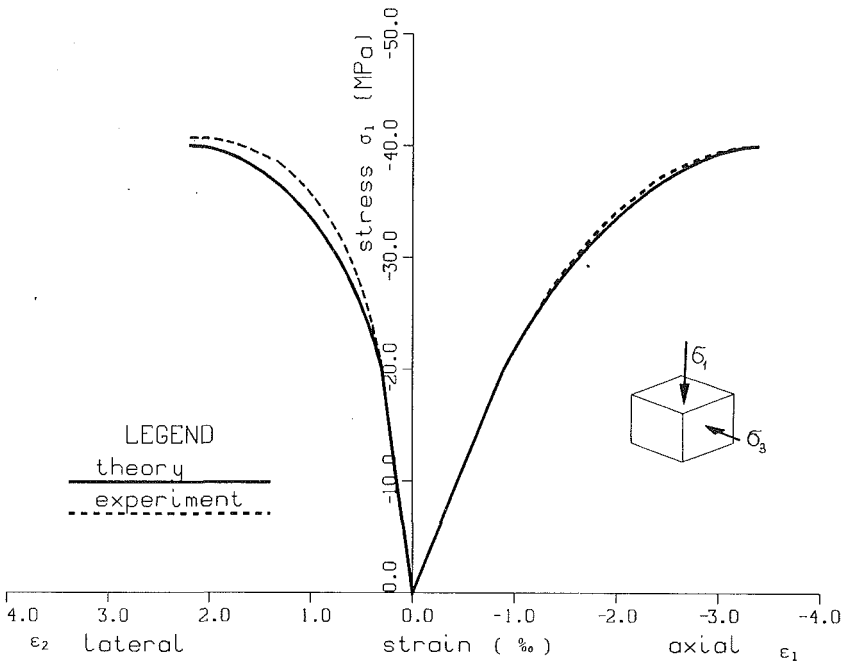

Fig. 4 Uniaxial compression; comparison of analytical (solid lines) and experimental (dashed lines) results

where $\sigma_{0c} = \sqrt{2Q_{0c}}\,(\mu - 1)^{-1}$ is the stress at the onset of kinking, while $\sigma_{uc} = \sqrt{2Q_{uc}}\,(\mu - 1)^{-1}$ stands for compressive strength. Also, q_{uc} is the inelastic component of the compliance at $\sigma = \sigma_{uc}$. The assumed form of the damage surface (25) results in $dq_1 = dq_2$, which seems plausible when compared with the experimental observations.

It is known that the kinked crack in compressive field (Fig. 2(*a*)) can be treated much in the same manner as the tensile crack (Moss and Gupta, 1982; Horii and Nemat-Nasser, 1986). Assume, therefore, that at the onset of kinking ($q = 0$) the thermodynamic forces triggering the microcrack growth are identical as in uniaxial tension case, i.e.,

$$Q_{0c} = Q_{0t}. \tag{26}$$

It is interesting to note that for $\sigma_{0t} = 0.9\ \sigma_{ut}$, $\sigma_{0c} = 0.3\ \sigma_{uc}$, and $\mu = 0.6$, typical of plain concrete, it follows from (25) that $\sigma_{uc}/\sigma_{ut} = 10.6$ in agreement with test results.

The axial and lateral strains are

$$\epsilon_{ax} = -\left(\frac{\sigma}{E_0} - q_1\,\sigma_1''\right) \quad \epsilon_{lat} = \frac{\nu_0}{E_0}\sigma + q_2\,\sigma_2'' \tag{27}$$

where ν_0 is the initial value of the Poisson's ratio. The final expression for the axial strain (27) is identical to that of (23) replacing the parameters ϵ_{ut}, σ_{ut} by ϵ_{uc}, σ_{uc}, respectively. The fluxes q_1 and q_2 are, as before, derived from the normality property.

The comparison between analytical results (27) and experimental curves requires further comments. Implicit in the performed two-dimensional analyses is the assumption that all slits are perpendicular to the third axis. Therefore, the analysis assumes confinement in the direction of the third axis not large enough to cause cracking but sufficient to prevent the kinks in the plane perpendicular to it. Thus, the stress-strain curves computed from expressions (27) plotted in Fig. 4 are compared with the experimental results from Gerstle et al. (1980) for $\sigma_3 = \sigma_1/3$.

(c) General Two-Dimensional State of Stress. Finally, it is necessary to comment briefly on the extension of the presented results on a general case of stresses. On the basis of the experimental evidence it is immediately obvious that the case $\sigma_1 > 0$, $\sigma_2 < 0$ and $\sigma_1 > 0.1\ |\sigma_2|$ can be treated as uniaxial tension (ignoring the compressive stress σ_2) without a significant loss of accuracy.

In the case when all three principal stresses are compressive, the crack growth is arrested soon after the kinking (Horii and Nemat-Nasser, 1986), and the response ceases to be brittle. The determination of the brittle-to-ductile transition is a complex task involving detailed knowledge of material parameters defining both ductile and brittle behaviors.

It is also important to discuss the merits of the decompositions of the general state of stress to positive and negative eigenvalues as suggested by Ortiz (1985) and Yazdani and Schreyer (1988). Quite obviously, the mere existence of the brittle-to-ductile transition represents a clear signal that a decomposition will often lead to erroneous results. Additionally, as shown by Horii and Nemat-Nasser (1986) and Ashby and Hallam (1986), the stability of the kinked crack depends on the sign of the lateral stress. Consequently, separating the influence of the axial (compressive) stress and the lateral (either compressive or tensile) stress might lead to a wrong conclusion.

Summary and Conclusions

The proposed framework for the development of a phenomenological damage model is consistent with the micromechanics of brittle deformation processes in addition to satisfying the requisite requirements of thermodynamics. The flux and its affinity are unambiguously identified as the change in the components of the elastic compliance tensor and the appropriately averaged energy release rate. The choice of the flux is consistent with the original damage model and is derivable from its micromechanical counterpart suggested by Budiansky and O'Connell (1976). Moreover, the suggested flux is readily measurable using methods of nondestructive testing on macrospecimens.

The kinetics of the damage evolution is defined via a process identical to one familiar from the conventional theory of plasticity. The conditions under which the potential exists are clearly identified. In contrast to the plasticity theory, the damage theory is not symmetric with respect to the sign of the stresses.

The analytical solutions are obtained using a total of three

Downloaded 03 May 2010 to 171.66.16.248. Redistribution subject to ASME license or copyright; see http://www.asme.org/terms/Terms_Use.cfm

new parameters (σ_{ut}, ϵ_{ut}, ϵ_{uc}) which are not only sufficient for both tension and compression but are also endowed with well-defined physical meaning. They can easily be determined from the rupture tension and compression tests.

At this stage of development the theory considers primarily the problems dominated by tensile cracks. In other words, it was assumed that the energy dissipated on frictional sliding is negligible compared to the energy needed for creation of new internal surfaces in the material. As a consequence, it was possible to use the normality property of the damage potential and significantly simplify the analyses.

The computations presented in this paper are primarily added as an illustration. Thus, in the future the proposed model must be tested on the three-dimensional case of stress considering interaction of brittle and ductile mechanisms. Current analyses are restricted to the precritical regime. Substantially more attention should be focused on the post-peak behavior in order to enable analyses of a general case of stress and geometry. In that sense this study is but a basis for a more comprehensive effort which will hopefully follow in the future.

Acknowledgment

The authors gratefully acknowledge the financial support in form of a research grant from the U.S. Department of Energy, Office of Basic Energy Sciences, Engineering Research Program which made this work possible.

References

Ashby, M. F., and Hallam, S. D., 1986, "The Failure of Brittle Solids Containing Small Cracks under Compressive Stress States," *Acta Metall.*, Vol. 34, pp. 497–510.

Brühwiler, E., Flückinger, D., and Rösli, H., 1986, "Versuche über den Einfluss hoher Dehngeschwindigkeiten und Vorbelastungsgeschichten auf die Festigkeit und das Verformungsverhalten von Beton," *Versuchsbericht*, Eidgenössiche Technische Hochschule, Zürich.

Dougill, J. W., 1976, "On Stable Progressively Fracturing Solids," *ZAMP*, Vol. 27, pp. 423–437.

Dragon, A., and Mróz, Z., 1979, "A Continuum Model for Plastic-Brittle Behavior of Rock and Concrete," *Int. J. Engng. Sci.*, Vol. 17, pp. 121–137.

Fanella, D., and Krajcinovic, D., 1988, "A Micromechanical Model for Concrete in Compression," *Eng. Fract. Mech.*, Vol. 29, pp. 49–66.

Gerstle, K. H., Aschl, H., Belloti, R., Bertacchi, P., Kotsovos, M. D., Ko, H. Y., Linse, D. H., Newman, J. B., Rossi, P. Schickert, G., Taylor, M. A., Traina, L. A., Winkler, H., and Zimmerman, R. M., 1980, "Behavior of Concrete under Multiaxial Stress States," *J. Engng. Mech. Div. ASCE*, Vol. 106, pp. 1383–1403.

Hill, R., 1967, "The Essential Structure of Constitutive Laws for Metal Composites and Polycrystals," *J. Mech. Phys. Solids*, Vol. 15, pp. 79–95.

Holcomb, D. J., and Costin, L. S., 1986, "Detecting Damage Surfaces in Brittle Materials using Acoustic Emissions," ASME JOURNAL OF APPLIED MECHANICS, Vol. 53, pp. 536–544.

Horii, H., and Nemat-Nasser, S., 1986, "Brittle Failure in Compression: Splitting, Faulting and Brittle-Ductile Transition," *Phil. Trans. Royal Soc. London*, Vol. A319, pp. 337–374.

Kachanov, L. M., 1958, "On the Creep Rupture Time," *Izv. A. N. SSSR*, Otd. Tekhn. Nauk 8, pp. 26–31.

Kachanov, M., 1987, "Elastic Solids with Many Cracks: a Simple Method of Analysis," *Int. J. Solids Struct.*, Vol. 23, pp. 24–43.

Krajcinovic, D., and Fanella, D., 1986, "A Micromechanical Damage Model for Concrete," *Eng. Fract. Mech.*, Vol. 25, pp. 585–596.

Krajcinovic, D., and Sumarac, D., 1987, "Micromechanics of Damage Processes," *Continuum Damage Mechanics: Theory and Application*, D. Krajcinovic and J. Lemaitre, eds., Springer Verlag, Wien, pp. 135–194.

Krajcinovic, D., and Sumarac, D., 1989, "A Mesomechanical Model for Brittle Deformation Processes - Parts 1 and 2," ASME JOURNAL OF APPLIED MECHANICS, Vol. 56, pp. 51–56 and 57–69.

Krajcinovic, D., 1984, "Continuous Damage Mechanics," *Appl. Mech. Rev.* Vol. 37, ASME, New York, pp. 1–5.

Lemaitre, J., and Chaboche, J. L., 1985, *Mëcanique des Materiaux Solides*, Dunod, Paris.

Moss, W. C., and Gupta, Y. M., 1982, "A Constitutive Model Describing Dilatancy and Cracking in Brittle Rocks," *J. Geophys. Res.*, Vol. 87, pp. 2985–2998.

Nemat-Nasser, S., and Obata, M., 1988, "A Microcrack Model of Dilatancy in Brittle Materials," ASME JOURNAL OF APPLIED MECHANICS, Vol. 55, pp. 24–35.

Ortiz, M., 1985, "A Constitutive Theory for the Inelastic Behavior of Concrete," *Mech. Mater.*, Vol. 4, pp. 67–93.

Rice, J. R., 1971, "Inelastic Constitutive Relations for Solids: an Internal Variable Theory and its Applications to Metal Plasticity," *J. Mech. Phys. Solids*, Vol. 19, p. 433–455.

Rice, J. R., 1975, "Continuum Mechanics and Thermodynamics of Plasticity in Relation to Microscale Deformation Mechanisms," *Constitutive Equations in Plasticity*, A. S. Argon, ed., The MIT Press, Cambridge, Mass., pp. 23–79.

Rudnicki, J. W., and Rice, J. R., 1975, "Conditions for the Localization of Deformation in Pressure-Sensitive Dilatant Materials," *J. Mech. Phys. Solids*, Vol. 23, pp. 371–394.

Sumarac, D., and Krajcinovic, D., 1987, "A Self-Consistent Model for Microcrack Weakened Solids," *Mech. Mater.*, Vol. 6, pp. 39–52.

Yazdani, S., and Schreyer, H. L., 1988, "An Anisotropic Damage Model with Application to Concrete," *Mech. Mater.*, Vol. 7, pp. 231–244.

Downloaded 03 May 2010 to 171.66.16.248. Redistribution subject to ASME license or copyright; see http://www.asme.org/terms/Terms_Use.cfm

A Global Damage Theory and the Hyperbolicity of the Wave Problem

K. C. Valanis
Endochronics, Inc.,
Vancouver, WA 98665
Fellow, ASME

It is well known that wave equation in materials that suffer damage in the course of deformation loses it hyperbolicity when the damage process is described by a continuum damage theory of the local type. Here we develop a global (nonlocal) damage theory by (a) *introducing a damage coordinate which is a spatial functional of the strain field in the material domain and* (b) *stipulating that the rate of evolution of damage is with respect to the damage coordinate. We then derive the axial wave equation for a thin rod and thereby demonstrate that, while the rod experiences softening, the wave speed is given in terms of the* secant *modulus and the wave equation retains its hyperbolicity. Various other phenomena, such as the onset of inhomogeneous damage in the presence of homogeneous deformation and the tendency of axial specimens under tension to fracture invariably at the center, are also explained.*

Introduction

The question of propagation of stress waves in materials that suffer damage in the course of deformation has been addressed frequently in recent times. For a thorough review article on the subject of softening, see Read and Hegemier (1984), on the work up to that time. The author addressed this problem (Valanis, 1985) where a representative set of papers in the literature is cited. If a local theory of damage is used, the situation, tacitly stated, is that when the material suffers substantial damage to the point where in one dimension, say, the slope of the stress-strain curve becomes nonpositive in a material neighborhood, the wave equation in that neighborhood loses its hyperbolicity and wave problem is no longer well posed. Because, in reality stress waves do propagate through materials that suffer substantial damage, the loss of hyperbolicity is not to be interpreted as a physical event but a deficiency in the equations that describe the physical process.

There have been attempts in the literature to overcome the difficulty. For instance, Bazant (1984) and Bazant and Belytschko (1987) have proposed nonlocal constitutive equations with *a long-range interaction among material particles.* The difficulty with this approach is that little physical evidence of such interactions has been found in the materials considered when these are in the undamaged state. Since damage causes material separation, it seems doubtful that these long-range forces will become prominent as damage proceeds. In fact, one would expect the opposite to be true, i.e., if such forces were present in the undamaged state, the expectation would be that these would diminish as damage in the materials increased, since the potential interaction between particles decreases with their separation.

The more plausible view is that it is the damage process that is long range rather than the constitutive response. This is in keeping with the philosophy of linear fracture mechanics where it is the gradient of the total energy of a region with respect to the crack length that influences the extension of the crack. Thus, the law of fracture in the aforementioned theory, as originally proposed by Griffith, is of global rather than local character.

This is the view taken by Bazant and Pijaudier-Cabot (1988) in a more recent paper who proposed a theory of *scalar* damage in elastic materials in terms of an evolution equation of a *nonlocal character* but *local* elastic constitutive response. Thus, the idea of an "imbricate" continuum seems to have been supplanted. In the present paper, to overcome the loss of hyperbolicity inherent in local theories we also introduce an evolution equation which has a global (nonlocal) character. However, the two theories are entirely different. To delineate the differences, we give a discussion of the two theories.

The Theory of Bazant and Pijaudier-Cabot. In their paper, Bazant and Pijaudier-Cabot (1988) introduce a local scalar damage, ω, which is related to the strain history by an evolution equation of the *local* type:

$$\dot{\omega} = f(\epsilon, \omega) \tag{i}$$

where the function f is left unspecified, and its form is not subject to any apparent dissipation constraints. They then introduce a scalar nonlocal damage Ω which is related to ω by the spatial linear functional given in equation (*ii*):

$$\Omega(x_i) = \{1/V_r(x_i)\} \int_V \alpha(x_i'-x_i)\ \omega(x_i')\ dV(x_i') \tag{ii}$$

where

$$V_r(x_i) = \int_V \alpha(x_i'-x_i) dV(x_i'). \tag{iii}$$

Contributed by the Applied Mechanics Division of THE AMERICAN SOCIETY OF MECHANICAL ENGINEERS for publication in the JOURNAL OF APPLIED MECHANICS.

Discussion on this paper should be addressed to the Technical Editor, Prof. Leon M. Keer, The Technological Institute, Northwestern University, Evanston, IL 60208, and will be accepted until two months after final publication of the paper itself in the JOURNAL OF APPLIED MECHANICS. Manuscript received by the ASME Applied Mechanics Division, Sept. 1, 1989; final revision, Apr. 18, 1990.

Copyright © 1991 by ASME
Downloaded 03 May 2010 to 171.66.16.248. Redistribution subject to ASME license or copyright; see http://www.asme.org/terms/Terms_Use.cfm

The theory is then developed in a thermodynamic framework. Within an immaterial constant, the free energy per unit volume is defined in terms of Ω in equation (*iv*):

$$\psi = (1/2)(1-\Omega)C_{ijkl}\epsilon_{ij}\epsilon_{kl}. \qquad (iv)$$

Note that in the undamaged state ($\Omega = 0$) ψ has the form:

$$\psi_o = (1/2)C_{ijkl}\epsilon_{ij}\epsilon_{kl}. \qquad (v)$$

The damage driving force is called Y where

$$Y = -\partial\psi/\partial\Omega = \psi_o. \qquad (vi)$$

It is of importance that Y is also the *energy release rate*, which in this case happens to be equal to the strain energy density in the undamaged configuration. The local damage ω is then set equal to $g(Y)$:

$$\omega = g(Y). \qquad (vii)$$

Equation (*vii*) essentially says that the evolution of local damage is governed solely by the evolution of the strain energy density of the *undamaged configuration* and is independent of the current state of damage. *This is difficult to accept physically.*

This characteristic of the theory cannot be modified in a trivial manner. If, to avoid the difficulty, one sets more generally

$$\psi = \psi(\epsilon_{ij}, \Omega), \qquad (viii)$$

and uses equation (*vii*), one finds that

$$\omega = g(-\partial\psi/\partial\Omega) \qquad (ix)$$

which is a *local* relation and in contradiction of equation (*ii*). Thus, it appears that a satisfactory evolution equation is still lacking in the above approach despite the fact that the theory is of *scalar character*. The situation would become more complex in the case of *directed damage*, which is much more realistic for elastic materials.

One other essential characteristic of the above theory is that a uniform strain field will give rise to a uniform damage field. This follows from equations (*i*) and (*ii*). From equation (*i*) it follows that if $\epsilon(x_i)$ is uniform then so is $\omega(x_i)$, while equation (*ii*) gives $\Omega(x_i) = \omega(x_i)$ if $\omega(x_i)$ is uniform. Thus, in the above theory, a uniform strain field cannot give rise to localization of damage.

There remains the question of a uniform stress field. Such a field admits a solution where both ϵ and Ω are uniform by virtue of equation (*x*) which follows from equation (*iv*):

$$\sigma_{ij} = (1-\Omega)C_{ijkl}\epsilon_{kl}. \qquad (x)$$

Either this is the only solution or there are other solutions, *if their existence can be proved*, in which case there is a loss of uniqueness.

Bazant and Pijaudier-Cabot (1988) discuss the problem in a one-dimensional setting, but it is not clear from their discussion whether a solution (other than the uniform one) exists for every (uniform) σ, and for $\dot{\sigma} > 0$ or $\dot{\sigma} < 0$. When unloading takes place, a special "loading function" comes into play and further complicates the mathematical structure of the theory.

At this stage we recognize two possibilities. Either there is a *continuous* loss of uniqueness, i.e., there are two solutions, one uniform and one nonuniform, for every uniform, σ, in which case the problem is ill-posed physically, or loss of uniqueness occurs at a critical stress level σ_c. This is acceptable physically, but the implications are profound. In this case the damage is uniform for all uniform σ, until a critical σ_c is reached when the onset of nonuniform damage occurs as a sudden event. This would imply a sudden discontinuous change in the damage distribution from uniform to nonuniform.

In general, the observed spatial evolution of damage does not follow this pattern. For instance, damage, observed in concrete in tension, is nonuniform for values of stress other than critical, and *localization* is a progressive event. The same is true of metals, in regard to the phenomenon of necking.

The nonlocal theory, which we present here, is more in keeping with the observed physics of damage. A consequence of the theory is that co-existence of uniform stress *and* strain fields is not possible, and damage is always nonuniform in the presence of either a uniform stress *or* strain field. These points will be discussed at length in the text.

The Present Theory. A *local* theory of directed-cum-scalar damage was developed by the author in a series of recent works (Valanis, 1987, 1989), both for elastic and plastic materials. The central elements of the theory are the co-existing tensor and scalar measures of damage and the concept of the *damage coordinate*. This is akin to the intrinsic time in endochronic plasticity and plays a similar role in the evolution equation of damage. Though the theory will be developed at length later in the paper, we illustrate the idea briefly in what follows. Let ϕ be a damage measure and ξ the corresponding damage coordinate. While we used *specific* evolution equations for elastic and plastic materials (cast iron and concrete) in the past, these have the *essential* form:

$$d\phi/d\xi = f(\epsilon, \phi, \xi) \qquad (xi)$$

or,

$$\partial\phi(x_i,t)/\partial t = f(\epsilon,\phi,\xi)\partial\xi(x_i,t)/\partial t \qquad (xii)$$

where, in the local theory, $d\xi$ in a material neighborhood is related to the increment in strain in that neighborhood. The exact form of $d\xi$ is a material property, hence its philosophical proximity to the intrinsic time.

The nonlocal theory is developed through a nonlocal evolution equation for the damage coordinate. Specifically, while in the local theory $\partial\xi/\partial t$ *in a material neighborhood is a function of the strain history of that neighborhood, in the nonlocal theory it is determined by the history of strain of the entire material domain.*

In fact, $\partial\xi/\partial t$ is a *functional* of the strain field with respect to an "influence function" $k(x_i, x_i')$ which is a material property reflecting the physics of interaction of the material particles at x_i and x_i'. We remark that if the range of interaction is infinitesimal then $k(x_i, x_i')$ becomes proportional to the delta function $\delta(x_i - x_i')$ and the evolution equation recovers its local form. We now know that this form is inappropriate. If the material is homogeneous then the influence function attains the simpler form $k(x_i - x_i')$.

To illustrate the theory we derive the wave equation that governs the dynamic axial deformation of an elastic-fracturing solid. The essential result is that while the quasi-static stress response exhibits softening in the usual manner, the wave equation, that governs the dynamic response, is fully hyperbolic. It is of interest that in contrast to the local theory, where the wave speed is governed by the *tangent* modulus (leading to imaginary values of the wave speed in the softening region) in the global theory it is the *secant* modulus which determines the wave speed. Since the secant modulus is always positive, the wave speed, in the global theory, is always real.

We hasten to add that upon unloading the material remains undamaged and behaves elastically in the sense that the stress is related to the strain by the (positive) secant modulus.

Background

To fix ideas consider the wave propagation problem in one dimension in an elastic-fracturing solid whose constitutive response exhibits softening in the sense that under monotonic straining, the stress-strain curve (σ versus ϵ) has a maximum at $\epsilon = \epsilon_c$, while:

$$d\sigma/d\epsilon > 0,\ \epsilon < \epsilon_c;\ d\sigma/d\epsilon < 0,\ \epsilon > \epsilon_c. \qquad (1)$$

Letting x be the axial coordinate, σ the axial stress, t the

Downloaded 03 May 2010 to 171.66.16.248. Redistribution subject to ASME license or copyright; see http://www.asme.org/terms/Terms_Use.cfm

time, and u the displacement (in the x direction), the relevant equations are the equation of motion:

$$\partial\sigma/\partial x = \rho\partial^2 u/\partial t^2 \tag{2}$$

and the constitutive equation:

$$\sigma = E\epsilon \tag{3}$$

where E is the elastic modulus and ϵ the axial strain as in equation (4).

$$\epsilon = \partial u/\partial x \tag{4}$$

In fracturing solids, E is not a constant but decreases with material degradation. When the axial strain at x is a monotonically increasing function of t, current theories lead to an evolution equation for E given, in general form, by equation (5):

$$dE = F\left[\epsilon(x, \overset{t}{\underset{\tau=0}{\tau}})\right]d\epsilon \tag{5}$$

where F at x, is a positive functional of the strain history $\epsilon(t)$ but does not depend on $\partial\epsilon/\partial\tau$ at $\tau = t$.

Substitution of equations (3)–(5) in equation (2) gives the following equation that governs the time-dependent deformation of the solid:

$$(E - \epsilon F)\partial^2 u/\partial x^2 = \rho\partial^2 u/\partial t^2. \tag{6}$$

Equation (6) is hyperbolic in character and the wave propagation problem is well posed, provided that:

$$E - F\epsilon > 0. \tag{7}$$

However, in view of equations (3) and (5):

$$d\sigma/d\epsilon = E - F\epsilon. \tag{8}$$

Thus, equation (6) will retain its hyperbolicity if the tangent modulus is positive, i.e., so long as $d\sigma/d\epsilon > 0$. In view of the $\sigma - \epsilon$ curve, this is possible only if $\epsilon < \epsilon_c$.

It appears, therefore, that damage theories in which the evolution equation is of a local type given in equation (5) will give rise to wave propagation equations that lose their hyperbolicity in the "softening range" of the constitutive response of the material in question. The problem has been discussed in a three-dimensional context and in much detail by the author. Thus, at present, it does not appear feasible to solve problems of wave propagation by means of local damage theories in material domains that suffer *substantial* damage in the process of deformation.

Framework of a Global Fracture Theory

Brief Review of the Local Theory. A *local* theory of damage has been developed by the author (Valanis, 1987, 1989). Experimental data indicate that the local theory gives a good representation of the constitutive behavior of solids, elastic and plastic, in the presence of damage. As discussed previously, the locality of the theory gives rise to difficulties in the solution of the initial value problem. In this section we proceed to give this theory a global character without sacrificing its basic premises that were instrumental in the realistic prediction of observed behavior under quasi-static conditions.

The basic premise of the theory is that directed damage may be represented by a positive semi-definite second-order tensor valued function $\boldsymbol{\phi}$, "the integrity tensor," which appears explicitly in the equation for the free energy, and the constitutive equation. Thermodynamically, $\boldsymbol{\phi}$ is an internal variable. In isotropic linear elastic-fracturing solids, the free energy density is given by equation (9*a*) and the constitutive relation by equation (9*c*). Specifically,

$$\psi = (\lambda/2)\phi_{ij}\phi_{kl}\epsilon_{ij}\epsilon_{kl} + \mu\phi_{ik}\phi_{jl}\epsilon_{ij}\epsilon_{kl} \tag{9a}$$

where λ and μ are the Lame constants. Thus, since:

$$\boldsymbol{\sigma} = \partial\psi/\partial\boldsymbol{\epsilon}, \tag{9b}$$

it follows that:

$$\sigma_{ij} = \lambda\phi_{ij}\phi_{kl}\epsilon_{kl} + 2\mu\phi_{ik}\phi_{jl}\epsilon_{kl}. \tag{9c}$$

Equation (9*a*) is a statement to the fact that:

$$\psi = 1/2 C_{ijkl}\epsilon_{ij}\epsilon_{kl} \tag{9d}$$

where $\mathbf{C}$, the stiffness tensor, is homogeneous and quadratic in $\boldsymbol{\phi}$.

There are two questions regarding $\boldsymbol{\phi}$: (*i*) how it is related to the material damage at some *microscale* and (*ii*) how it evolves with the history of deformation. In regard to question (*i*), it was previously shown (Valanis, 1987) that if in a material element a principal value of $\boldsymbol{\phi}$, say ϕ_r, is zero, and $\mathbf{N}_r$ is the eigenvector of ϕ_r, the traction on a surface normal to $\mathbf{N}_r$ then is zero, and the element cannot support traction on that surface. Thus, ϕ_r represents *damage* on a plane normal to $\mathbf{N}_r$, and as such it is a measure of the effective area in that plane. Hence, when $\phi_r = 0$, an *effective* plane crack has developed across the entire element on a plane normal to $\mathbf{N}_r$. Note that if $\phi_r = 1$ the damage on that plane is zero. In regard to question (*ii*), i.e., the evolution of $\boldsymbol{\phi}$, equation (10) was proposed:

$$d\phi^\alpha = -(Q_n^\alpha)^m d\xi^\alpha \tag{10}$$

in the following notation: $d\phi^\alpha$ is the change in principal component of $\boldsymbol{\phi}$ and n_i^α are the eigenvectors of $d\boldsymbol{\epsilon}$; ξ^α is a damage coordinate and Q_n^α a "damage force" acting in the direction $\mathbf{n}$, i.e.,

$$Q_n^\alpha = n_i^\alpha n_j^\alpha Q_{ij} \ (\alpha, \text{ not summed}). \tag{11}$$

The damage coordinate ξ^α is given by equation (12), i.e.,

$$d\xi^\alpha = \begin{cases} k d\epsilon^\alpha;\ d\epsilon^\alpha > 0,\ \epsilon_n^\alpha \geq 0,\ Q_n^\alpha > 0 \\ 0, \text{ otherwise} \end{cases} \tag{12}$$

where $\epsilon_n^\alpha = \epsilon_{ij} n_i^\alpha n_j^\alpha$ (α, not summed) and k is a positive scalar.

To determine $\mathbf{Q}$, we appealed directly to thermodynamics. Since $\boldsymbol{\phi}$ is an internal variable, the thermodynamic force $\mathbf{Q}$ that drives the damage process is given by the relation

$$\mathbf{Q} = -\partial\psi/\partial\boldsymbol{\phi}. \tag{13}$$

We now reason as follows: The direction of the damage increment $-d\boldsymbol{\phi}$ is dictated by the eigendirections $\mathbf{n}^\alpha$ of the increment of strain $d\boldsymbol{\epsilon}$. In other words, $d\boldsymbol{\phi}$ and $d\boldsymbol{\epsilon}$ are coaxial. The force driving the damage process in the direction $\mathbf{n}^\alpha$ is then Q_n^α, which is $\mathbf{Q}$ projected in direction $\mathbf{n}^\alpha$. Thus,

$$Q_n^\alpha = n_i^\alpha n_j^\alpha Q_{ij} \ (\alpha \text{ not summed}). \tag{14}$$

If one follows the linear thermodynamic principle that the "flux" $d\phi^\alpha/d\xi^\alpha$ is proportional to the conjugate thermodynamic force Q_n^α, then:

$$d\phi^\alpha/d\xi^\alpha = bQ_n^\alpha \tag{15}$$

where b is a material scalar and

$$d\xi^\alpha = \begin{cases} k d\epsilon^\alpha \\ 0 \end{cases},\ d\xi^\alpha \geq 0, \tag{16}$$

k having the significance of a damage propensity parameter. But, the Clausius-Duhem dissipation inequality, i.e.,

$$-\frac{\partial\psi}{\partial\boldsymbol{\phi}} \cdot d\boldsymbol{\phi} > 0,\ \|d\boldsymbol{\phi}\| \neq 0 \tag{17}$$

must be observed. Thus, in view of equations (13) and (15) and the fact that

$$d\phi_{ij} = \sum_\alpha d\phi^\alpha n_i^\alpha n_j^\alpha, \tag{18}$$

$\mathbf{n}^\alpha$ being eigenvectors of $d\boldsymbol{\phi}$, it follows that

$$-\frac{\partial\psi}{\partial\boldsymbol{\phi}} \cdot d\boldsymbol{\phi} = -\sum_\alpha d\phi^\alpha \frac{\partial\psi}{\partial\phi_{ij}} n_i^\alpha n_j^\alpha > 0. \tag{19}$$

Since equation (19) must be true for each α individually, i.e.,

Downloaded 03 May 2010 to 171.66.16.248. Redistribution subject to ASME license or copyright; see http://www.asme.org/terms/Terms_Use.cfm

for each independent fracture mechanism, then the following inequalities must be satisfied for all α:

$$-d\phi^\alpha \frac{\partial \psi}{\partial \phi_{ij}} n_i^\alpha n_j^\alpha > 0; \quad (\partial \psi / \partial \phi_{ij}) n_i^\alpha n_j^\alpha > 0 \tag{20, 21}$$

for all α, whenever $|d\phi^\alpha| \neq 0$, since $d\phi^\alpha$ is negative when nonzero. We now have the full set of conditions that govern the evolution of the damage coordinate $d\xi^\alpha$. Thus,

$$d\xi^\alpha = k d\epsilon^\alpha \tag{22}$$

whenever

$$d\epsilon^\alpha > 0, \ \epsilon_n^\alpha \geq 0, \ \frac{\partial \psi}{\partial \phi_{ij}} n_i^\alpha n_j^\alpha > 0, \tag{23}$$

but $d\xi^\alpha = 0$ otherwise. We write equation (15) in its explicit form given as follows:

$$d\phi^\alpha = -b d\xi^\alpha \{\lambda \epsilon_{ij}(\phi_{kl}\epsilon_{kl}) + 2\mu \phi_{kl}\epsilon_{ik}\epsilon_{jl}\} n_i^\alpha n_j^\alpha. \tag{24}$$

We mention in passing that the theory has been applied to the case of fracture of an elastic plate with a central crack. The fracture stress was determined as a function of the length of the crack, and the analytically determined values were compared with ones obtained experimentally. The agreement was very close (Valanis, 1989).

The Simple Case of One Dimension. We give an illustrative example for a cylindrical material domain under axial stress in the direction x_1. A simple analysis in the light of equations (16), (22), and the constraints (23) shows that:

$$\phi_{11}(=\phi) \neq 0; \ \phi_{ij} = 0 \text{ otherwise.} \tag{25a}$$

$$\sigma_{11}(=\sigma) \neq 0; \ \sigma_{ij} = 0 \text{ otherwise} \tag{25b}$$

$$\epsilon_{11}(=\epsilon) \neq 0; \ \epsilon_{22} = \epsilon_{33} \neq 0; \ \epsilon_{ij} = 0 \text{ otherwise} \tag{25c}$$

The following, then, are the relevant one-dimensional equations where E_o is the Young's modulus in the undamaged configuration and b in equation (15) was set equal to unity:

$$\sigma = E\epsilon; \ E = E_o\phi^2 \tag{26a, b}$$

$$d\phi = -E_o \phi \epsilon^2 d\xi \tag{27}$$

$$d\xi = \begin{cases} = k d\epsilon, \ d\epsilon > 0, \ \epsilon > 0 \\ = 0, \text{ otherwise} \end{cases} \tag{28}$$

$$E = E_o \exp\{-(2/3)kE_o\epsilon^3\}. \tag{29}$$

Equation (26a), in conjunction with equation (29), gives the stress-strain relation:

$$\sigma = E_o \exp\{-(1/3)kE_o\epsilon^3\}\epsilon \tag{30}$$

which exhibits softening, since σ reaches a maximum at $\epsilon = \epsilon_c$ where

$$\epsilon = \epsilon_c = \sqrt[1/3]{1/2kE_o}, \tag{30a}$$

and decreases monotonically thereafter. We note that $\sigma_{\max}$ is given by equation (30a)

$$\sigma_{\max} = E_o\{1/2keE_o\}^{1/3} \tag{30b}$$

where e is the base of the natural logarithm. Thus, k is a fracture propensity constant since $\sigma_{\max}$ decreases monotonically with k.

In view of equations (26)–(29) the wave equation (6) becomes:

$$E(1 - 2kE_o\epsilon^3)\partial^2 u/\partial x^2 = \rho \partial^2 u/\partial t^2. \tag{31}$$

Equation (31) loses its hyperbolicity at the point $\epsilon = \epsilon_c$ which is the point of maximum stress at which $d\sigma/d\epsilon = 0$.

A Global Damage Approach

We shall limit the discussion to directed damage which is of relevance in the case of elastic solids. The simultaneous presence of scalar and directed damage will be taken up in a future work. To remove the difficulty associated with the loss of hyperbolicity, we propose an evolution equation for damage which is of a global character. To this end let D_m denote the material domain, x_i a generic point, and x_i' any other point in D_M. We introduce a *damage influence function* $k(x_i, x_i')$, positive, continuous, and differentiable, whose domain D_K is a proper subset of the material domain. Thus, $D_K \leq D_M$. The essence of the global theory is that:

> the time rate of change of the damage coordinate ξ^α is a linear functional of the strain field $\epsilon_{ij}(x_i, t)$ with respect to the damage influence function k over the domain D_K.

This is a verbal generalization of equation (16). To give a mathematical form to this statement, we proceed as follows. As in the local theory we let n_i^α be the eigenvectors of $\partial \epsilon_{ij}/\partial t$ in a material neighborhood containing x_i. We then introduce the "normal" strain field $\epsilon_n^\alpha(x_i, x_i')$ where

$$\partial \epsilon_n^\alpha(x_i, x_i')/\partial t = n_i^\alpha(x_k) n_j^\alpha(x_k) \partial \epsilon_{ij}^\alpha(x_k')/\partial t \ (\alpha \text{ not summed}), \tag{32}$$

and propose a generalization of equation (16) in the form of equation (33)

$$\partial \xi^\alpha/\partial t = \int\int\int_{D_K} k(x_i, x_i') \partial \epsilon_n^\alpha / \partial t dx_1' dx_2' dx_3' \tag{33}$$

if

$$\partial \epsilon^\alpha/\partial t > 0, \ \epsilon^\alpha > 0: \ \epsilon^\alpha = \epsilon_{ij}(x_k) n_i^\alpha(x_k) n_j^\alpha(x_k) \tag{33a}$$

and

$$\int\int\int_{D_K} k(x_i, x_i')(\partial \epsilon_\alpha^n/\partial t) dx_1' dx_2' dx_3' > 0. \tag{33b}$$

Otherwise,

$$\partial \xi/\partial t = 0.$$

In other words, the entire strain field $\epsilon(x,t)$ will influence the rate of evolution of damage at point x. Inequality (33b) follows from the dissipation inequality (19) and the evolution equation (15) in the light of the fact that $d\phi$ must be negative whenever it is nonzero. Inequality (33b) is also of profound physical significance. It means that even though the local field may be tensile, it may not result in an increase of damage if the outlying strain field is strongly compressive, a conclusion that raises new and interesting questions regarding damage.

Special Forms of the Influence Function. If the material is *initially homogeneous*, the functional form of k must remain invariant with a translation of the coordinate system. Thus,

$$k(x_i, x_i') = k(x_i + a, x_i' + a) \tag{34}$$

for all values of a. In particular, if "a" is infinitesimal, then equation (34) gives

$$\partial k/\partial x_i + \partial k/\partial x_i' = 0, \tag{35}$$

which is a partial differential equation in x_i and x_i' and has the solution

$$k = k(x_i - x_i'). \tag{36}$$

It follows that initially homogeneous materials must obey the form of the (36) and that heterogeneous damage will influence the form of k. However, since brittle materials remain almost damage-free until they are close to failure, one may, in such materials, consider the form of k to be independent of damage as a first approximation.

We also observe that if the domain of influence D_K is localized, the k must be close to a delta function, which will be of the form:

$$k = k_o \delta(x_i - x_i') \tag{37}$$

Downloaded 03 May 2010 to 171.66.16.248. Redistribution subject to ASME license or copyright; see http://www.asme.org/terms/Terms_Use.cfm

since a material is always locally homogeneous. In this case, $k(x-x')$ is a very sharp distribution whose weight is concentrated in the neighborhood of the point x, decaying rapidly away from this point. When equation (37) applies the global equation, (33) reduces to (16), and the local theory is thereby retrieved.

In some materials the domain of k may be a subdomain of the material domain. If such materials are also isotropic, then damage at x_i is influenced by a "sphere," with center at x_i whose radius is a characteristic property determined by the physics of interaction of the particles of the material in question.

Illustration of the Theory

We illustrate the theory by analyzing first a quasi-static problem and then a dynamic problem in one dimension and, in particular, that of a thin rod of height h and radius r under axial stress conditions. The radial strain is approximately uniform so that k is constant in the radial direction, and in view of equation (33), $\partial\xi/\partial t$ is now given by equation (38). Thus,

$$\partial\xi/\partial t=\pi r^2\int_{-h/2}^{h/2}k(x-x')\partial\epsilon(x',t)/\partial t dx' \tag{38}$$

if

$$\partial\epsilon/\partial t>0,\ \epsilon>0 \tag{38a}$$

and

$$\int_{-h/2}^{h/2}h(x-x')\partial\epsilon(x',t)/\partial t dx'>0, \tag{38b}$$

otherwise

$$\partial\xi/\partial t=0. \tag{38c}$$

Let a homogeneous strain field $\epsilon_o(t)$, monotonically increasing with respect to t, be applied in a quasi-static fashion. In the case where the rod is (initially) homogeneous, k is even in its argument by virtue of the symmetry of the geometric configuration of the rod. It now follows from equation (38) that in this case

$$(1/\pi r^2)\partial\xi/\partial t=d\epsilon_o/dt\int_{-h/2}^{h/2}k(x-x')dx'$$

$$=d\epsilon_o/dtK\{x+(h/2)\}+K\{(h/2)-x\} \tag{39}$$

where we have set $D_M=D_K$ and

$$K(x)=\int^x k(x')dx'. \tag{40}$$

If, further, for simplicity the rod is made of amorphous material that has no periodic structure, we may exclude oscillatory behavior in $k(x)$. In keeping with these observations and the fast decaying nature of $k(x)$, we examine the case where $k(x)$ is the normal distribution given by (41). Thus,

$$k(x)=k_o\sqrt{b/\pi}\exp\{-bx^2\} \tag{41}$$

where $(b/\pi)^{1/2}$ is a normalization factor and k_o and b are material parameters. Furthermore, there is no reason at this point to exclude the dependence of influence function k on its domain D_K. Thus, while in general k_o and b may depend on D_K, in the event that they are constant, equations (39)–(41) lead to the following relation:

$$d\xi=d\epsilon(k_o\pi r^2/2)[\mathrm{erf}\{\sqrt{b}((h/2)+x)\}$$

$$+\mathrm{erf}\{\sqrt{b}((h/2)-x)\}] \tag{42}$$

where, in view of the spatial homogeneity, $d\epsilon=d\epsilon_o$. As previously, equation (42) is subject to the constraints $d\epsilon>0$; $\epsilon>0$, otherwise $d\xi=0$.

Discussion of Equation (42). We begin with the observation that equation (42) is the same as the local form (28) with the importance difference that k in equation (28) now depends on the radial dimensions of the specimen as well as the axial coordinate x. Thus, the global theory brings into existence the following:

(*a*) *Softening.* A material will experience softening under homogeneous axial strain conditions in accordance with equation (30) *but the degree of softening will vary along the length of the rod* since now $k=k(x)$.

(*b*) *A Size Effect.* Even if k_o and b are constants and independent of D_K, the damage coordinate is proportional to the square of the radius of the rod and depends on its length through the presence of h in the error function. Thus, thin rods suffer less damage than thick rods.

(*c*) *Heterogeneous Damage.* In view of (*a*), damage is heterogeneous in the presence of uniform strain field.

(*d*) *Nonuniform Stress in the Presence of Uniform Strain.* In the presence of uniform strain, the stress is not uniform in the axial direction in view of equations (28*a*, *b*). Thus, a traction in the axial direction on the curved surface of the rod will be necessary to maintain equilibrium. Conversely, a uniform axial stress will not produce a uniform axial strain.

(*e*) *Maximum Damage at the Center.* The rod will suffer maximum damage at the center. This is immediately apparent from equation (42), the right-hand side of which has a maximum at $x=0$. This is consistent with the observation that uniaxial specimens break at the center under axial strain! We are not aware of another theoretical explanation of this phenomenon.

Impact of the Global Damage Theory on the Wave Problem. At this point we wish to assess the effect of the global theory on the form of the wave equation in degrading materials, specifically with regard to the retention of hyperbolicity irrespective of the degree of damage in the material domain. The simplest case is the uniaxial one-dimensional wave equation in the presence of *monotonically* increasing axial strain with respect to time. In this case use of equation (1) and (26)–(28) in the light of equation (38), which has integrated with respect to time, gives the following wave equation:

$$\partial^2u/\partial x^2-E_o\pi r^2(\partial u/\partial x)^3\int_{-h/2}^{h/2}k^*(x-x')\partial u/\partial x' dx'$$

$$=\frac{1}{c^2}\partial^2u/\partial t^2 \tag{43}$$

where $k^*(x)=dk(x)/dx$ and $c=(\phi^2E_o/\rho)^{1/2}$. In fact, "c" is the wave speed which is determined by the secant modulus ϕ^2E_o. Because of the character of k, k^* is continuous.

Thus, equation (33) is unconditionally hyperbolic since the since term on the left-hand side of equation (33) contains derivatives of u(x,t) *that are of lesser order than the second.*

We remark that in the case of the local theory $k(x)$ is a delta function so that $k^*(x)$ is a dipole. In this event the integral becomes proportional to $\partial^2u/\partial x^2$ and loss of hyperbolicity is possible as shown in equation (30).

A Simple Example. In Figs. 1 and 2, we use equation (41) to give a diagrammatic illustration of the influence function $k(x-x')$ and its derivative $k^*(x-x')$. If the length of the rod is of the same order as the domain of influence of the function $k(x)$, then Fig. 2 suggests an approximate model where:

Downloaded 03 May 2010 to 171.66.16.248. Redistribution subject to ASME license or copyright; see http://www.asme.org/terms/Terms_Use.cfm

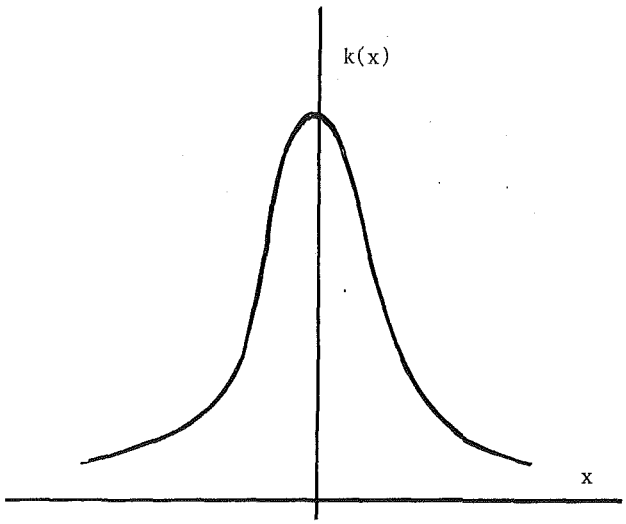

Fig. 1 Diagrammatic illustration of $k(x-x')$

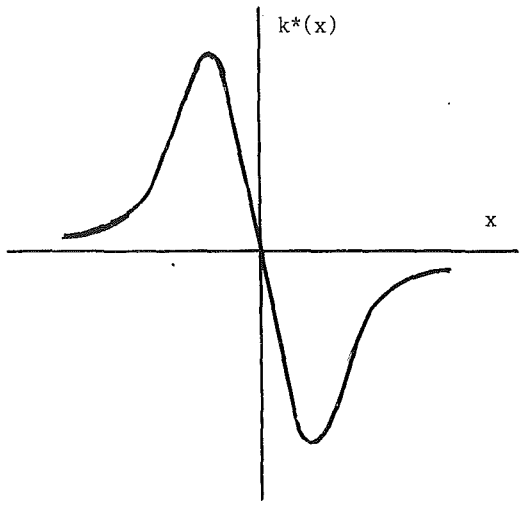

Fig. 2 Diagrammatic illustration of $k^*(x-x')$

$$k^*(x-x') = k_o: \; x-x' < 0$$

$$k^*(x-x') = -k_o: \; x-x' > 0,$$

i.e., k^* is approximated by the signum function. Now,

$$\int_{-h/2}^{h/2} k^*(x-x')\partial u/\partial x'\,dx' = -k_o \int_{-h/2}^{x} \partial u/\partial x'\,dx'$$

$$+ k_o \int_{x}^{h/2} \partial u/\partial x'\,dx' = k_o\{u(-h/2) - 2u(x) + u(h/2)\}. \quad (44)$$

If the rod is rigidly held at $x = h/2$, then $u(h/2) = 0$. Also, $u(-h/2)$ is the boundary displacement, which we denote by $U(t)$. Thus, substitution of equation (44) in equation (43) gives the following analytically explicit form of the wave equation:

$$\partial^2 u/\partial x^2 - E_o k_o \pi r^2 (\partial u/\partial x)^3 \{U(t) - 2u(x)\}$$

$$= (1/c^2)\partial^2 u/\partial t^2, \quad (45)$$

which is quasi-linear and unconditionally hyperbolic.

References

Bazant, Z. P., 1984, "Imbricate Continuum and its Variational Derivation," *J. Eng. Mech. Div., ASCE,* Vol. 110, pp. 1693–1712.

Bazant, Z. P., and Belistschko, T. B., 1987, "Strain-Softening Continuum Damage: Localization and Size Effect," *Proceedings: International Conference on Constitutitve Laws for Engineering Materials,* C. S. Desai, et al., eds., Tucson, Ariz., Elsevier, New York, pp. 11–33.

Bazant, Z. P., and Pijaudier-Cabot, G., 1989, "Nonlocal Continuum Damage, Localization, Instability, and Convergence," ASME JOURNAL OF APPLIED MECHANICS, Vol. 55, pp. 287–293.

Read, H. E., and Hegemier, G. P., 1984, "Strain Softening of Rock, Soil, and Concrete—A Review Article," *Mech. Mat.,* Vol. 3, pp. 271–294.

Valanis, K. C., 1987, "A Continuous Damage Model for Concrete," *Development of Advanced Constitutive Models for Plane and Reinforced Concrete,* by G. A. Hegemier et al., S-CUBED, La Jolla, Calif., Report SSS-R-87-8454.

Valanis, K. C., 1989a, "A Theory of Damage in Brittle Materials," *Eng. Fract. Mech.,* to appear.

Valanis, K. C., 1989b, "Continuum Modeling of Damage due to Sharp Cracks," *Proceedings: PLASTICITY 89: The Second Symposium on Plasticity and its Current Applications,* Mie University, Tsu, Japan.

Valanis, K. C., 1989c, "A Theory of Damage in Brittle and Cementitious Materials," ENDOCHRONICS Inc., Report ENDIC-007-AFOSR-1989.

Valanis, K. C., 1989d, "On the Uniqueness of Solution of the Initial Value Problem in Softening Materials," ASME JOURNAL OF APPLIED MECHANICS, Vol. 52, pp. 649–653.

Downloaded 03 May 2010 to 171.66.16.248. Redistribution subject to ASME license or copyright; see http://www.asme.org/terms/Terms_Use.cfm

Z. Xia

F. Ellyin
Mem. ASME

Department of Mechanical Engineering,
University of Alberta,
Edmonton, AB T6G 2G8, Canada

Nonproportional Multiaxial Cyclic Loading: Experiments and Constitute Modeling

Biaxial tension compression, deformation controlled, out-of-phase cyclic tests were conducted on thin-walled circular cylindrical specimens of a low alloy carbon steel. The influence of strain amplitude and phase angle (a measure of nonproportionality of strain path) on the stress-strain loops have been studied. Material aniostropy and additional cyclic hardening due to the plastic deformation and nonproportional path are clearly observed. A constitutive model is presented which describes the material behavior under complex loading histories including cyclic deformation. The predictions of the model are compared to the experimental results, and the agreement is found to be fairly good.

1 Introduction

A majority of mechanical/structural components of modern industrial installations encounter complex cyclic loading during their service life. In certain instances the loading results in multiaxial out-of-phase stress/strain states. Structures such as pressure vessels, gas turbines, nuclear reactors, aircrafts, ground vehicles, and components such as rotating disks, axles, and crankshafts are some common examples. Experiments indicate that metals have a rather complex response to nonproportional cyclic loading. For example, we observe an extra hardening effect which varies with the extent of nonproportionality, and causes considerably more material damage in comparison to the same equivalent strain magnitude in a proportional path loading. In a biaxial out-of-phase loading, the maximum strain hardening is observed when the phase angle difference is 90 deg.

In attempting to predict damage in such circumstances, a primary prerequisite is a constitutive model capable of simulating the material response to nonproportional cyclic loading, irrespective of the method used to solve the governing field equations.

In particular, extension of damage theories or fatigue failure criteria to nonproportional loadings would have to account for the above-mentioned extra hardening which is a path-dependent phenomena. For example, the cyclic strain energy density has been shown to be an effective criterion for the fatigue failure under multiaxial loading conditions (Ellyin, 1988). The plastic strain energy accounts for the path dependency through the product of stress and strain increment, $\Delta W^p = \int_{\text{cycle}} \sigma d\epsilon_p$. However, experimental results show that hysteresis forms change depending on the nonproportionality of the path, and thus to carry out the integration one would require an accurate constitutive model of the material response.

Out-of-phase loading is one of the simplest forms of the nonproportional cyclic loading. Almost all the experimental data on biaxial out-of-phase loading have been obtained by subjecting thin-walled circular cylindrical specimens to cyclic axial and torsional loading (e.g., see Miller and Brown (1985) where further references are given). In such tests the path of the principal strains varies in a narrow region bounded between the lines with ϵ_2/ϵ_1 ratio of $-\nu$ to -1 (see Fig. 1). However,

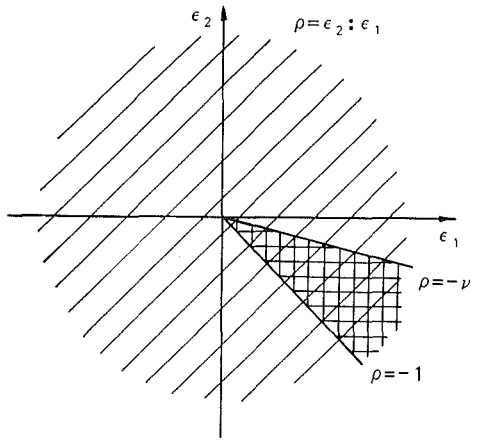

Fig. 1 Comparison between the range of strain ratio covered in the biaxial tension-torsion and the biaxial tension compression, out-of-phase cyclic loading

Contributed by the Applied Mechanics Division of THE AMERICAN SOCIETY OF MECHANICAL ENGINEERS for presentation at the Joint Applied Mechanics/Bioengineering Conference, Ohio State University, Columbus, OH June 16-19, 1991.

Discussion on this paper should be addressed to the Technical Editor, Prof. Leon M. Keer, The Technological Institute, Northwestern University, Evanston, IL 60208, and will be accepted until two months after final publication of the paper itself in the JOURNAL OF APPLIED MECHANICS. Manuscript received by the ASME Applied Mechanics Division, Sept. 1, 1989; final revision, Oct. 18, 1990. Paper No. 91-APM-26.

Copyright © 1991 by ASME
Downloaded 03 May 2010 to 171.66.16.248. Redistribution subject to ASME license or copyright; see http://www.asme.org/terms/Terms_Use.cfm

biaxial fatigue tests show that the most damaging region in Fig. 1 is when the ratio ϵ_2/ϵ_1 is positive.

A more elaborate test facility would be required in order to cover all possible ϵ_2/ϵ_1 ratios; i.e., a biaxial push-pull in both axial and circumferential directions of a circular cylindrical specimen. Through appropriate control, any strain path in the ϵ_1, ϵ_2 space (Fig. 1) can thus be investigated. This would considerably extend the range of tension-torsion experimental data available at present (Fig. 1).

Although test facilities to apply axial force and differential pressure to a thin-walled tubular specimen have been available (see, for instance Rotvel (1970), Ellison and Andrews (1973), Ellyin and Valaire (1982), etc.), they have exclusively been used to generate multiaxial fatigue data for proportional straining paths.

It is the objective of this paper to present experimental data for the biaxial tension compression, out-of-phase cyclic loading, and to study the stress-strain response in axial and circumferential directions and their dependency to the strain amplitude and phase angle. A constitutive model will subsequently be presented which is capable of predicting out-of-phase (nonproportional) biaxial cyclic path, and other types of complex loading histories.

2 Specimen Geometry and Test Setup

Thin-walled circular cylindrical specimens were used in this investigation. The geometry of the specimen was obtained through considerable experimental and theoretical analysis to arrive at a geometry with least amount of undesirable secondary effects (uncontrolled bending strains) (see Ellyin and Valaire, 1982). The specimens were made from a low alloy carbon steel, ASTM designation A-516 Gr. 70, which is extensively used in the manufacturing of modern pressure vessels used in chemical, petrochemical, and electric utility power plants. The procedure for the machining and preparation of the specimen is given elsewhere (Ellyin et al. (1991)).

The tests were carried out on a servo-controlled electro-hydraulic closed-loop system—a modified MTS system. The test rig for loading a thin-walled cylinder was specially designed for this type of experiment. More detailed description regarding the initial and present improved version of the test facility can be found in Ellyin and Valaire (1982), and Ellyin, Golos, and Xia (1991).

3 Experimental Procedure

The tests were performed in a strain-controlled mode, where the input signals were generated numerically by a computer program. The strain wave shapes were sinusoidal which may be represented by:

$$\epsilon_a = A \cos \omega t,$$
$$\epsilon_t = \rho A \cos (\omega t - \phi). \tag{1}$$

In the above, ϵ_a and ϵ_t refer to the axial and tangential strains (in-plane principal strains), A is the amplitude of the axial strain; $\rho = \Delta\epsilon_t/\Delta\epsilon_a$, is the in-plane strain amplitude ratio; ω is the frequency of oscillation, and ϕ is the phase angle between axial and tangential strains. For $\phi = 0$, the strains oscillate in-phase and the strain path is proportional.

The specimen is subjected to a differential pressure and axial loading. The exterior surface is exposed to a constant external pressure of P_e. The interior pressure and axial load fluctuate between certain limits to respond to the controlled strain path. From the instrumentation, voltage readings are available proportional to the applied strains, hydraulic pressures, and axial load. Data were recorded in a real-time mode in four channels (axial strain, tangential strain, internal pressure, and axial load) by a computer—an IBM PC.

To start a test, the strains were set at zero and the external pressure was increased which required an automatic increase in the internal pressure and a compressive axial load to compensate for the pressure effect and to keep axial and tangential strains at zero. After the external pressure reached its preset value of P_e, one of the strains, for example, the axial strain was increased (or decreased), while the other strain was kept at zero until the difference between the two strain values corresponded to the preset value of the phase angle ϕ. The strains were then varied periodically according to equation (1).

The objective of this investigation being the stress-strain

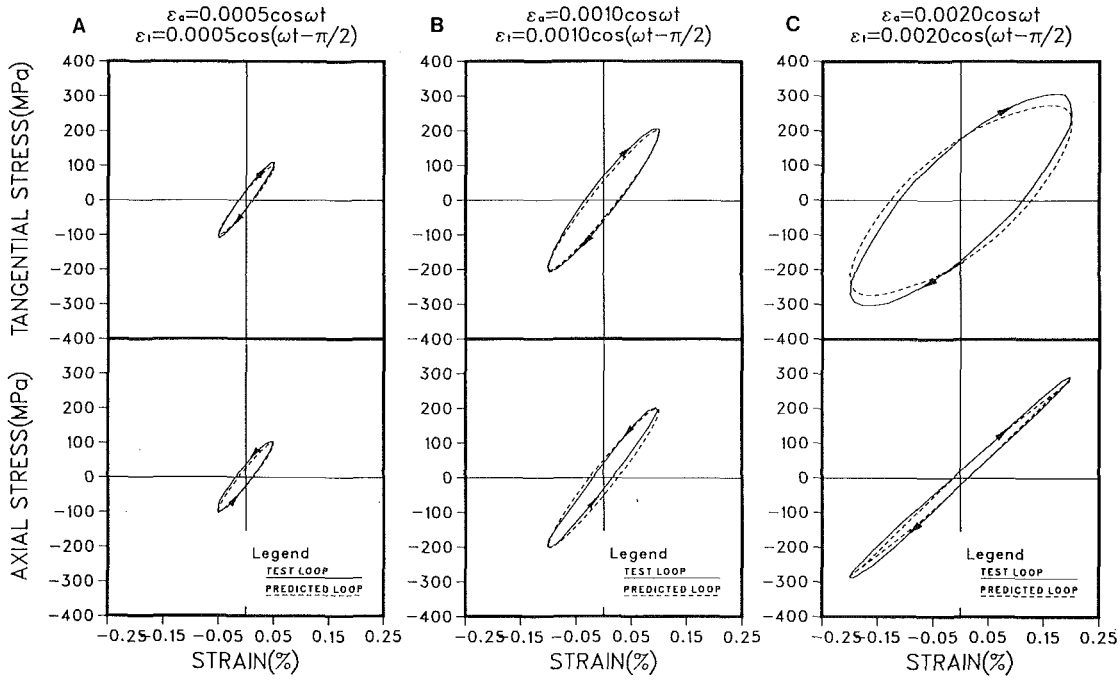

Fig. 2 Hysteresis loops of 90 deg out-of-phase loading with different strain amplitudes: (*a*) $\epsilon_{a,max} = 0.0005$, (*b*) $\epsilon_{a,max} = 0.0010$, (*c*) $\epsilon_{a,max} = 0.0020$

Downloaded 03 May 2010 to 171.66.16.248. Redistribution subject to ASME license or copyright; see http://www.asme.org/terms/Terms_Use.cfm

response rather than fatigue failure, most specimens were loaded up to 100 cycles and data of the first ten cycles and intervals of ten until 50 cycles and intervals of 20 thereafter were collected by the computer. Two specimens, one with $\phi = 0$ (proportional loading) and the other with $\phi = 90$ deg, were cycled until failure. It was noted that the material stabilized during the first few cycles and the shape of the hysteresis loops did not change appreciably during the fatigue life.

4 Experimental Results

The tests were conducted at an oscillatory frequency of 5×10^{-2} Hz and the in-plane strain ratio $\rho = 1$. The strain amplitude varied from 0.0005 to 0.0020 and the phase angles investigated were 0, 30 deg, and 90 deg. Each experiment was repeated at least twice to confirm the results presented herein.

Hysteresis loops for the axial and tangential directions of a 90 deg out-of-phase loading for three different strain amplitudes are shown in Fig. 2. Starting from the smallest strain amplitude, $\epsilon_a = \epsilon_t = 0.0005$ and increasing it each time by a factor of two, we can observe the progression of deformation from the elastic to elastic-plastic response. For the smallest strain amplitude (Fig. 2(*a*)) the material is within the elastic range, and as to be expected, the axial and tangential loops are almost of equal size, but rotate in different directions. The total work done (or the absorbed energy) in each cycle is, therefore, equal to zero, since the algebraic sum of two equal areas is nil. When the strain amplitude is increased to 0.1 percent, a certain amount of irreversible plastic deformation takes place. The loop in the axial direction becomes narrower than that in the tangential direction, although both loops still rotate in opposite directions (Fig. 2(*b*)). Thus, the plastic work done in one cycle is the algebraic sum of the two loop areas.

Upon further increase of the strain amplitude to 0.2 percent, we observe from Fig. 2(*c*) that the direction of rotation of the axial loop has changed and it is now in the same direction as that of the tangential loop. In this case more plastic work is done, since the sum of the two loop areas is now larger. From the above three tests we note that anisotropy in axial and tangential directions is induced by the phase angle (nonproportional path) and plastic deformation. In these tests, the initial loading condition was for the axial strain to reach its minimum value while the tangential strain was kept at zero. Thus, a 90 deg phase angle was produced, and thereafter the strain loading path varied strictly according to equation (1).

To confirm the observed trend, tests were carried out by merely exchanging the input signals of the axial and tangential strains. That is, the phase angle in the axial direction now lagged by 90 deg behind the tangential strain, instead of leading it by 90 deg as in Fig. 2. Figure 3 is an example of the registered response. It is seen that the response is similar to Fig. 2(*c*) except for the axial and tangential directions being interchanged.

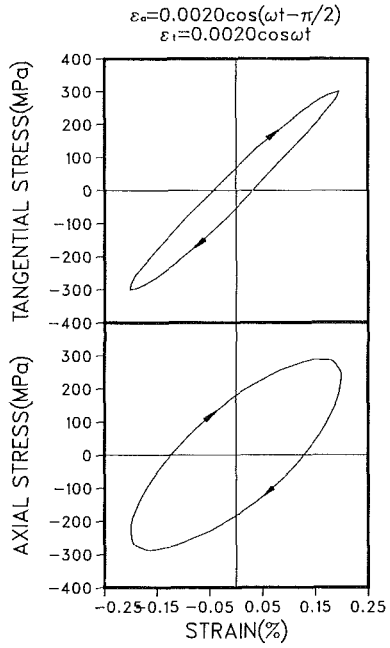

Fig. 3 Hysteresis loops of 90 deg out-of-phase loading after interchanging the input signal channels for axial and tangential strains (lagging versus lead phase angle for the axial strain)

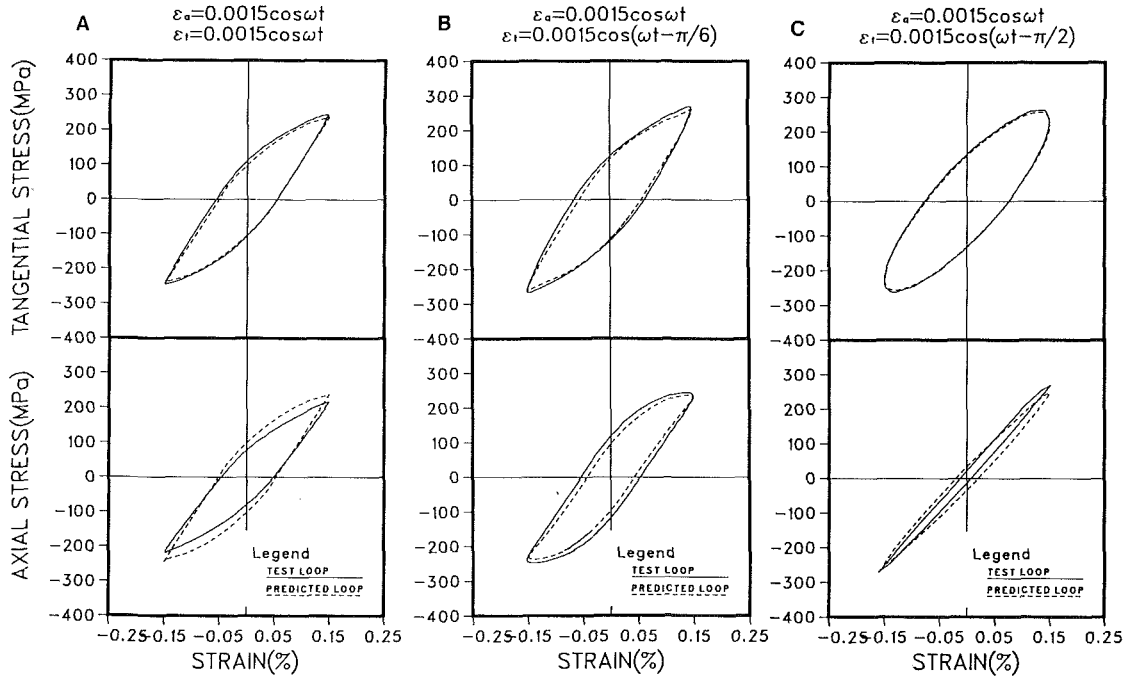

Fig. 4 Hysteresis loops for different phase angles with the same strain amplitude: (*a*) $\phi = 0$ deg, (*b*) $\phi = 30$ deg, (*c*) $\phi = 90$ deg

Downloaded 03 May 2010 to 171.66.16.248. Redistribution subject to ASME license or copyright; see http://www.asme.org/terms/Terms_Use.cfm

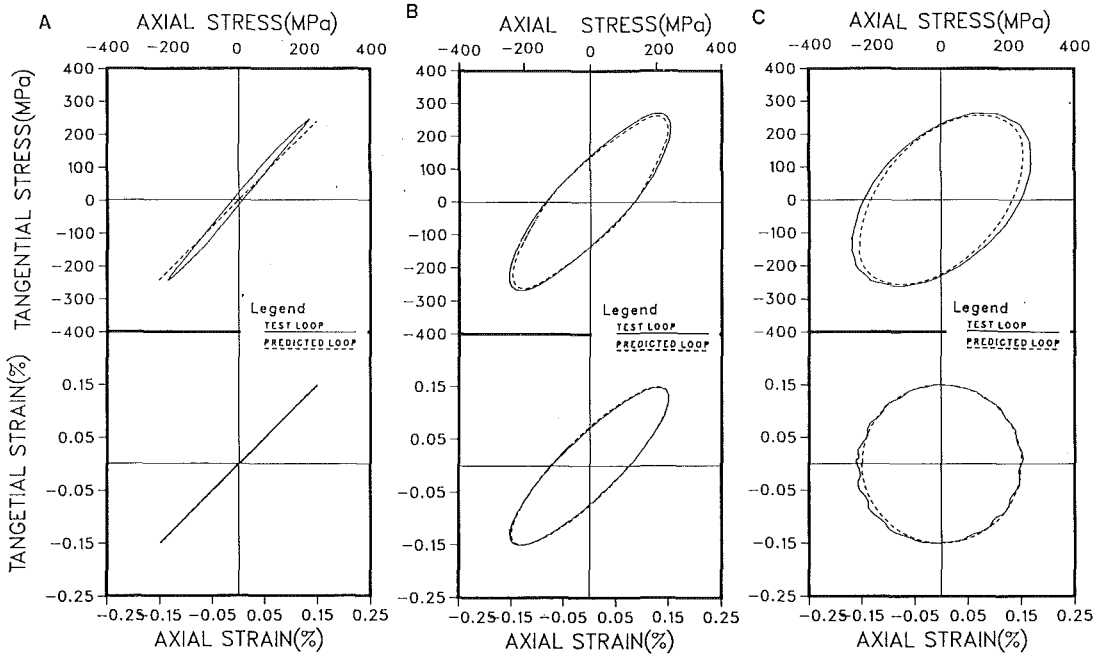

Fig. 5 Controlled strain path and corresponding stress responses for different phase angles with the same strain amplitude: (*a*) $\phi = 0$ deg (*b*) $\phi = 30$ deg (*c*) $\phi = 90$ deg

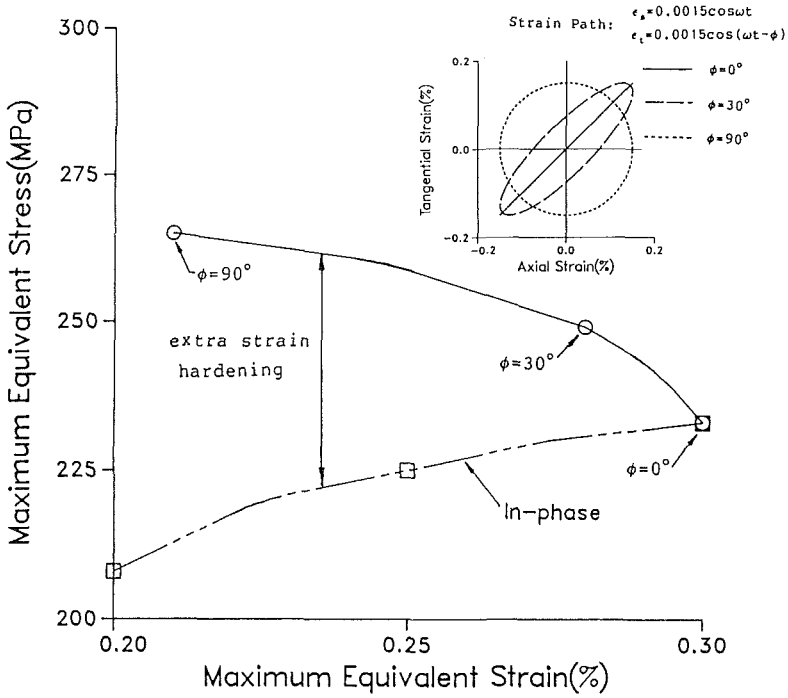

Fig. 6 Extra strain hardening due to nonproportional loading

In the previous tests the phase angle was fixed (i.e., the same nonproportional path), and we investigated the effect of the increasing strain amplitude on the elastic-plastic response. We will now study the effect of the phase angle (i.e., the degree of nonproportionality of path) on the plastic deformation by keeping the strain amplitude constant. Figures 4 and 5 show the effect of three different phase angles, $\phi = 0$ deg, 30 deg, and 90 deg on the material behavior for a constant strain amplitude of $\Delta\epsilon_a/2 = \Delta\epsilon_t/2 = 0.15$ percent. A proportional strain path is obtained when $\phi = 0$, and the corresponding response is shown in Figs. 4(*a*) and 5(*a*). A small amount of anisotropy is observed when comparing the loops in two directions. As the phase angle is increased, the difference in material response in the two principal directions becomes more evident (c.f., Figs. 4(*a*), 4(*b*), 4(*c*) and 5(*a*), 5(*b*), 5(*c*). Note that while Fig. 4 shows the stable (saturated) stress-strain response, Fig. 5 indicates the controlled strain and corresponding stress trajectories. It is worth mentioning that while the maximum equivalent strain[1] decreases with the increase of the phase angle ($\epsilon_{e,\max} = 0.3$ percent, 0.28 percent and 0.21 percent, respectively), the maximum equivalent stress increases with increasing

[1]See the next section and the Appendix for the definition of the equivalent strain and the method of calculating it.

Downloaded 03 May 2010 to 171.66.16.248. Redistribution subject to ASME license or copyright; see http://www.asme.org/terms/Terms_Use.cfm

ϕ ($\sigma_{e,\max}=233$ MPa, 249 MPa, and 265 MPa, respectively), (see Fig. 6).

The above observation indicates an obvious additional hardening due to the nonproportionality of the strain path. In an in-phase ($\phi=0$) test, the strain vector follows a linear path whereas for $\phi=90$ deg, the path is circular (Figs. 5(*a*) and 5(*c*)). The plastic deformation is mainly manifested by dislocation movements along a favorable crystal slip plane. In a proportional path, the direction of the slip plane becomes almost fixed after a few initial cycles. In the case of a circular strain path, there is a tendency to activate all possible crystal slip planes, and as a result additional dislocation barriers are introduced at the intersecting slip planes. Hence, extra stress magnitude is required to overcome these barriers, and in the macro level this process is observed through an additional hardening in comparison to the proportional path (Fig. 6).

In the following section we will discuss a constitutive model capable of simulating all the experimentally observed behavior.

5 Background on Constitutive Modeling

Within the context of the rate-independent elastic-plastic constitutive models, two categories are noted. In the first group are those models which use a single yield surface to delineate the elastic and plastic strains. Examples of this type of constitutive models for cyclic loading are Eisenberg (1976), Chaboche et al. (1979), Drucker and Palgen (1981), and Benallal and Marquis (1987) among others. These models are relatively simple and are more suitable for not too complicated loading histories. The second group of models comprise those which use two or more surfaces to describe plastic deformation (for example, see Mroz (1967), Krieg (1975), Dafalias and Popov (1976), Lamba and Sidebottom (1978), Ohno (1982), Tseng and Lee (1983), and McDowell (1985), where references to similar works are cited). These models generally predict better results than the first group for the nonproportional cyclic loading. More recently, Ellyin (1989) presented a two-surface theory applicable to both quasi-static and stable cyclic loading. However, it could not account for the extra hardening phenomena discussed earlier. The general case of transient nonproportional cyclic loading was treated by Ellyin and Xia (1989). The constitutive model to be developed here considers stable cyclic loading, but incorporates the additional hardening effect without evolving through the transient stage. It includes a simplified evolution rule and expands on certain features of our earlier model.

6 Description of Constitutive Model

Following our previous work, we define two hypersurfaces in the stress space, viz., a yield surface, ϕ_y, and a stress memory surface, ϕ_m^σ, as follows:

$$\phi_y = f_y(\sigma_{ij}-\alpha_{ij}) - q^2 = 0, \tag{2}$$

$$\phi_m^\sigma = f_m^\sigma(\sigma_{ij}) - R^2(\sigma_{e,\max}) = 0. \tag{3}$$

In the above, α_{ij} and q specify the location of the center and the radius of the yield surface. The stress memory surface[2] memorizes the maximum value of the equivalent stress, $\sigma_{e,\max}$, experienced during previous loading history (see Subsection 6.1 for further details). In the case of von Mises yield condition,

$$f_y = \frac{3}{2}(s_{ij}-\alpha_{ij})(s_{ij}-\alpha_{ij}), \tag{4}$$

$$f_m^\sigma = \frac{3}{2} s_{ij}s_{ij}, \tag{5}$$

where s_{ij} is the deviatoric stress tensor.

[2]The term memory surface was used by Ellyin (1983) and independently by Tseng and Lee (1983).

It is assumed that the total strain increment can be decomposed into the elastic and plastic parts, i.e.,

$$d\epsilon_{ij} = d\epsilon_{ij}^e + d\epsilon_{ij}^p. \tag{6}$$

The increment of elastic strain is related to the stress increment through the generalized Hooke's law, and the increment of plastic strain is written as,

$$d\epsilon_{ij}^p = g\frac{\partial f_y}{\partial \sigma_{ij}}\frac{\partial f_y}{\partial \sigma_{k1}} d\sigma_{k1}. \tag{7}$$

The hardening function g in equation (7) can be determined by specializing (7) to the uniaxial case. We thus obtain,

$$g = \frac{1}{4q^2}\left(\frac{1}{E_t}-\frac{1}{E}\right), \tag{8}$$

where E is the elastic modulus and E_t is the instantaneous tangent modulus.

In this model, two types of plastic loading are distinguished by the introduction of the stress memory surface (see Fig. 7(*a*)). The first type is called monotonic loading (ML), in which the stress memory surface expands with the movement of the yield surface, and the two surfaces remain tangent to each other (path AB, Fig. 7(*a*)). The second type is termed reloading (RL). After an elastic unloading (path BC, Fig. 7(*a*)), plastic deformation takes place again. But in this case, the current loading point is inside the stress memory surface and the maximum equivalent stress value experienced is a constant, i.e., the stress memory surface does not change during this loading stage (path CD, Fig. 7(*a*)). When the reloading stress level exceeds the previous maximum equivalent stress, then the current stress point touches the memory surface and moves it through the expansion, we incorporate the latter stage into the ML case.

6.1 Evolution of the Yield and Memory Surfaces. The evolution rule of the yield surface and the calculation of the tangent modulus, E_t, are also different for the two plastic loading cases.

For the ML case, a Ziegler (1959) type of evolution rule is adopted, i.e.,

$$d\alpha_{ij} = d\mu(\sigma_{ij}-\alpha_{ij}). \tag{9}$$

For the RL case it is assumed that the motion of the yield surface is in the direction of the vector connecting the loading point, σ_{ij}^y (D) to a point on the stress memory surface, σ_{ij}^m (E), whose exterior normal is parallel to the outward normal at point σ_{ij}^y (see Fig. 7(*a*)). This is expressed by

$$d\alpha_{ij} = d\mu(\sigma_{ij}^m - \sigma_{ij}^y). \tag{10}$$

By using the consistency condition,

$$d\phi_y = \frac{\partial f_y}{\partial \sigma_{ij}}(d\sigma_{ij}-d\alpha_{ij}) - 2qdq = 0, \tag{11}$$

and one of the equations (9) and (10), the $d\alpha_{ij}$ is completely determined.

Regarding the memory surface, it does not change during the reloading (RL) case, whereas for the ML case it remains tangent to the yield surface. Thus, we have (see Fig. 8)

$$dR = |\alpha_{ij}+d\alpha_{ij}| + q + dq - R,\ dR \geq 0, \tag{12}$$

where $d\alpha_{ij}$ and dq are increments of the vector α_{ij} and the radius of the yield surface, q, respectively.

It is to be noted that for the proportional loading path the current stress point is the common point on the yield and memory surfaces and the value of R is equal to the maximum effective stress magnitude (Fig. 8, point A). For some nonproportional loading path the current stress point may not be on the memory surface (e.g. see Fig. 8, point B), but the point on the memory surface can be reached through an elastic or neutral loading path without plastic deformation; e.g., path BA in Fig. 8. And in this context, we say that the stress memory

Downloaded 03 May 2010 to 171.66.16.248. Redistribution subject to ASME license or copyright; see http://www.asme.org/terms/Terms_Use.cfm

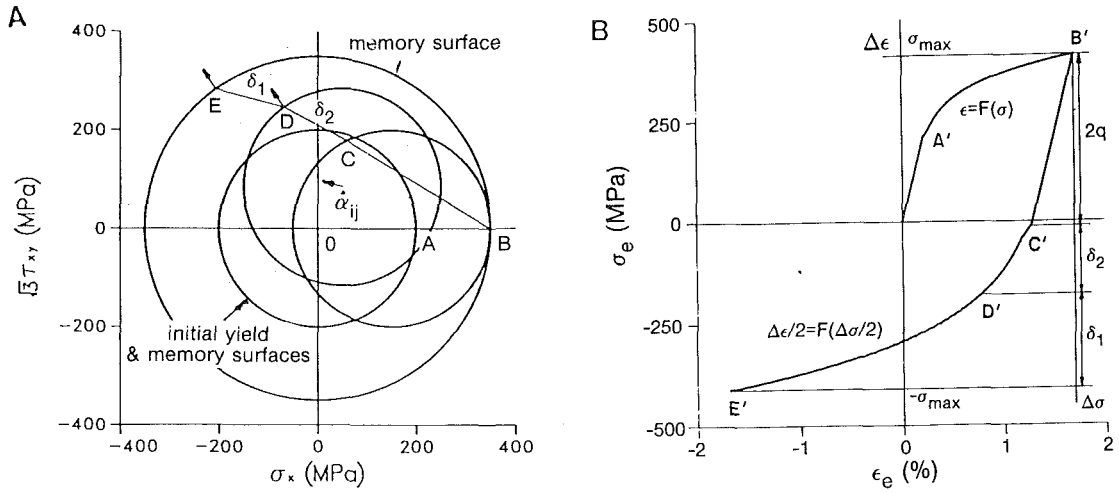

Fig. 7 Evolution rule of yield surface and calculation of tangent modulus for two types of plastic loading

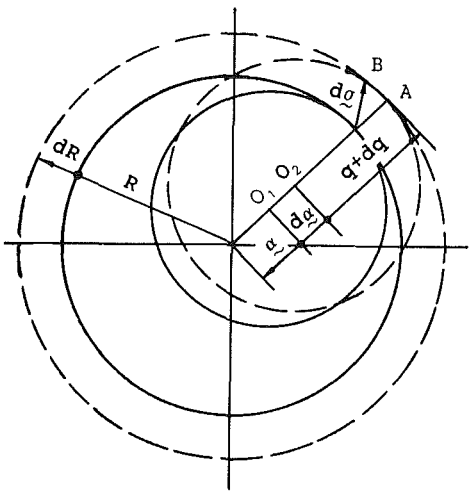

Fig. 8 Evolution of the stress memory surface

surface memorize the maximum value of the equivalent stress, $\sigma_{e,\max}$.

According to the above evolution rules, the yield surface will always be inside the memory surface and no intersection of the two surfaces will occur. The reason why such intersection should be avoided has been discussed by McDowell (1989).

6.2 Determination of Tangent Modulus, E_t. The tangent modulus, E_t, is directly defined as a function of the effective stress, σ_e, in the ML case. The functional relation is obtained from a uniaxial stress-strain curve (Fig. 7(*b*))

$$\epsilon = F(\sigma). \tag{13}$$

In the RL case, for any given loading point in the multiaxial stress space, we can find a ratio $r=\delta_1/\delta_2$, where δ_1 is the distance measured from the current loading point D to a corresponding point on the memory surface, E, as described above, and δ_2 is the distance from the point of the onset of plastic flow C to the point D (Fig. 7(*a*)). It is to be noted that path BC is an elastic unloading and when the reversed loading reaches point C, then the plastic deformation may begin. During the plastic reloading (path CD), the yield surface moves together with the loading point. Having determined r, a corresponding point D′ with the same ratio $r=\delta_1/\delta_2$ (Fig. 7(*b*)) on the reversed curve B′C′E′, is determined. Note that if the uniaxial curve is given by equation (13), then the reversed branch of the stress-strain curve B′C′E′ will be given by

$$\Delta\epsilon/2 = F(\Delta\sigma/2), \tag{14}$$

where the prefix Δ refers to the range of variables. Knowing the coordinate of point C and functional form (13) or (14), the tangent modulus can be determined (for further discussion, see Ellyin and Xia, 1989).

6.3 Simulation of Extra Hardening Due to Nonproportional Path. Experimental observations show that the additional hardening of materials is manifested in two ways. Firstly, there is a change in the elastic regime which is associated with the relative expansion of the yield surface. Secondly, the stress-strain curve of the material varies, thus causing a variation in the tangent modulus. The q and E_t under a stable nonproportional cycling are usually greater than that under a stable proportional cycling. Before establishing a relationship between the proportional and nonproportional loading, we must define a parameter which could describe the extent of the nonproportionality independent of the structure of the constitutive model. Towards this end, we introduced (see Ellyin and Xia, 1989) a strain memory surface,

$$\phi_m^\epsilon = \frac{2}{3} e_{ij}e_{ij} - \epsilon_{e,\max}^2 = 0, \tag{15}$$

where e_{ij} is deviatoric strain tensor and the equivalent strain is defined as $\epsilon_e^2 = 2e_{ij}e_{ij}/3$. The strain memory surface memorizes the maximum equivalent strain value experienced during the previous loading history, and it can be represented by a circle in the strain Π-plane (Fig. 9). For a given strain loading path, we can find a ratio of two areas in the strain Π-plane,

$$F = \frac{A_{sw}^\epsilon}{A_m^\epsilon}, \tag{16}$$

where A_m^ϵ is the projected area of the strain memory surface, and A_{sw}^ϵ is the area of a polygon connecting all vertices of the projection of the strain vector (see Fig. 9). For a strain cycling without abrupt change in the direction of the strain vector, this area is the same as that swept by the strain vector (Fig. 9(*a*)). The value of F is bounded, $0 \le F \le 1$, and $F=0$ indicates a proportional strain path. A strain path with $F=1$, represents a circular path with its radius equal to the maximum equivalent strain. As discussed earlier, such a path will cause activation of slip planes in all possible direction; hence, the maximum resistance to plastic deformation occurs in such a case. Thus, the path-dependent parameter F is used to correlate the yield surface radius, q, and the tangent modulus, E_t between stable (saturated) states in the proportional and nonproportional paths, i.e.,

Downloaded 03 May 2010 to 171.66.16.248. Redistribution subject to ASME license or copyright; see http://www.asme.org/terms/Terms_Use.cfm

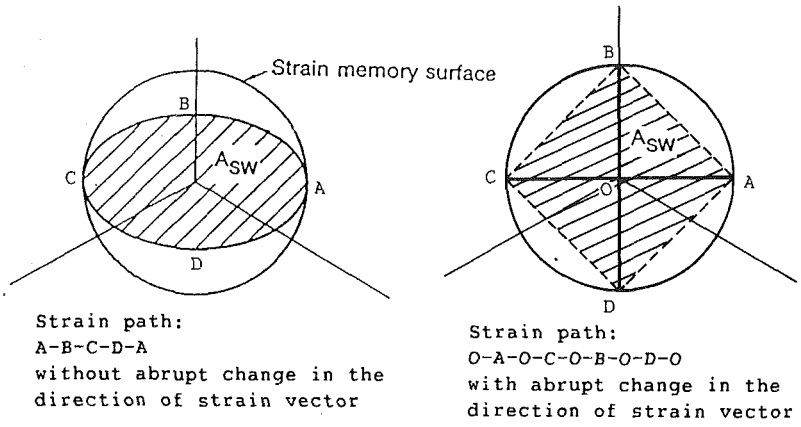

Fig. 9 Projection of the strain memory surface and the area A_{sw} for two kinds of strain loading paths

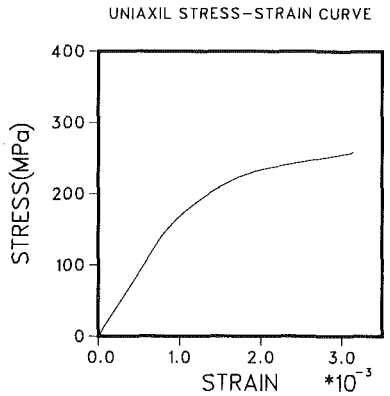

Fig. 10 Uniaxial stress-strain curve used in present calculation

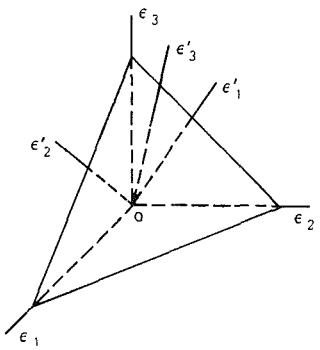

Fig. 11 Principal strain space and Π-plane

$$q = (1 + \eta_1 F) q_0, \tag{17}$$

$$E_t = (1 + \eta_2 F) E_{t,0}, \tag{18}$$

where q_0 and $E_{t,0}$ are the stable values for a proportional path and q and E_t are the corresponding stable values for a nonproportional path defined by F, and η_1, η_2 are material constants. The procedure for calculating F for an out-of-phase strain path is given in the Appendix. Note that when a material reaches its stable state under a nonproportional loading, it will keep the stable values of q and E_t even if the subsequent cycling is proportional. This phenomena was termed "erasure of memory property" by Lamba and Sidebottom (1978).

7 Comparison With Experimental Results

From the description of the constitutive model in the previous section, we note that three material constants, ν (Poisson's ratio), η_1, and η_2, are required in addition to the material's uniaxial stress-strain curve. The elastic modulus, E, and the radius of the yield surface, q_0, and the tangent modulus $E_{t,0}$ as a function of the equivalent stress are all determined from the uniaxial stress-strain curve of the material.

For the material used in this investigation, the uniaxial curve is shown in Fig. 10, and constants $\nu = 0.27$ and $\eta_1 = \eta_2 = 0.371$. An interpolation table of the tangent modulus $E_{t,0}$ obtained from the uniaxial stress-strain curve is given in Table 1. The values of the path-dependent parameter, F, for three phase angles $\phi = 0$, 30 deg, and 90 deg are: 0, 0.155, and 0.577, respectively (see Appendix). Once the value of F is determined, interpolation functions for E_t can be constructed by using (17) and (18) as shown in Tables 2 and 3.

The predicted results using the above material constants and

Table 1 Interpolation table for tangent modulus, $E_{t,0}$ ($\phi = 0$)

σ (MPa)	$\leq$ 140	145	150	160	170	180	190	200
$E_{t,0}$ (MPa)	1.90×10^5	1.50×10^5	1.32×10^5	1.2×10^5	1.04×10^5	9.17×10^4	8.47×10^4	7.69×10^4
σ (MPa)	210	220	225	230	235			
$E_{t,0}$ (MPa)	6.25×10^4	5.71×10^4	4.27×10^4	3.91×10^4	2.54×10^4			

Table 2 Interpolation table for tangent modulus, E_t ($\phi = 30$ deg)

σ (MPa)	$\leq$ 148	153	163	173	183	193	203	213
E_t (MPa)	1.90×10^5	1.58×10^5	1.39×10^5	1.26×10^5	1.10×10^5	9.69×10^4	8.95×10^4	8.13×10^4
σ (MPa)	223	233	238	243	248			
E_t (MPa)	6.61×10^4	6.04×10^4	4.51×10^4	4.12×10^4	2.68×10^4			

Table 3 Interpolation table for tangent modulus, E_t ($\phi = 90$ deg)

σ (MPa)	$\leq$ 170	175	180	190	200	210	220	230
E_t (MPa)	1.90×10^5	1.82×10^5	1.60×10^5	1.46×10^5	1.26×10^5	1.11×10^5	1.03×10^5	9.34×10^4
σ (MPa)	240	250	255	260	265			
E_t (MPa)	7.59×10^4	6.94×10^4	5.19×10^4	4.74×10^4	3.08×10^4			

Downloaded 03 May 2010 to 171.66.16.248. Redistribution subject to ASME license or copyright; see http://www.asme.org/terms/Terms_Use.cfm

function tables are compared to the experimental results in Figs. 2, 4, and 5, and the agreement is found to be very good. It is noted that for $\phi = 0$ and 30 deg, the material experiences elastic unloading and reloading and subsequent plastic deformation at every cycle. However, in the case of $\phi = 90$ deg, there is no elastic unloading and a continuous plastic loading takes place during the cycle.

Conclusions

Experimental results of a deformation controlled, biaxial tension compression out-of-phase loading are presented. By increasing the amplitude of the sine waves, the behavior of the material is investigated as it progresses from a purely elastic to an elastic-plastic response under nonproportional cyclic loading. Two main observations are the induced anisotropy due to the irreversible plastic deformation and an extra hardening phenomenon resulting from the nonproportional cyclic deformation.

A constitutive model is presented which is suitable for complex nonproportional loading paths including cyclic loading. It is relatively simple considering its range of application and requires a knowledge of the uniaxial stress-strain curve of the material and three other material constants. The predicted results are shown to be in good agreement with the experimental data (c.f., Figs. 2, 4, and 5).

Acknowledgment

The work presented here is part of a general investigation into materials behavior under multiaxial states of stress and adverse environments. The research is supported, in part, by the Natural Sciences and Engineering Research Council of Canada (NSERC Grant No. A-3803). The authors would like to express their appreciation to the technical staff, T. Villett, supervisor; B. Faulkner and I. Buttar who diligently assisted in the experimental work. Thanks are also due to the machine shop staff, A. Muir, supervisor, who machined the specimens and built various components of the experimental setup.

References

Benallal, A., and Marquis, D., 1987, "Constitutive Equations Describing Non-Proportional Effects in Cyclic Plasticity," *Constitutive Laws for Engineering Materials—Theory and Applications*, Vol. I, C. S. Desai et al., eds., Elsevier, New York, pp. 505–512.

Chaboche, J. L., et al., 1979, "Moderization of Strain Memory Effect on the Cyclic Hardening of 316 Stainless Steel," Trans. 5th SMiRT, L11/3 Berlin.

Dafalias, Y. F., and Popov, E. P., 1976, "Plastic Internal Variables Formalism of Cyclic Plasticity," ASME JOURNAL OF APPLIED MECHANICS, Vol. 43, pp. 645–651.

Drucker, D. C., and Palgen, L., 1981, "On Stress-Strain Relations Suitable for Cyclic and Other Loading," ASME JOURNAL OF APPLIED MECHANICS, Vol. 48, pp. 479–485.

Eisenberg, M. A., 1976, "A Generalization of Plastic Flow Theory with Application to Cyclic Hardening and Softening Phenomena," *ASME Journal of Engineering Materials and Technology*, Vol. 98, pp. 221–228.

Ellison, E. G., Andrews, J.M.H., 1973, "Biaxial Cyclic High-Strain Fatigue of Aluminum Alloy RR58," *Journal of Strain Analysis*, Vol. 8, pp. 209–219.

Ellyin, F., 1983, "On the Concept of Initial and Subsequent Yield Loci," *Proc. Int. Colloquium on Failure Criteria of Structured Media*, J. P. Boehler, ed., Villard-de-Lans, France.

Ellyin, F., 1988, "Recent Developments in Predicting Multiaxial Fatigue Failure," *Res Mechanica*, Vol. 25, pp. 1–23.

Ellyin, F., Golos, K., and Xia, Z., 1991, "In-Phase and Out-of-Phase Multiaxial Fatigue," *ASME Journal of Engineering Materials and Technology*, Vol. 113, pp. 112–118.

Ellyin F., and Xia, Z., 1989, "A Rate-Independent Constitutive Model for Transient Non-Proportional Loading," *J. Mech. Phys. Solids*, Vol. 37, No. 1, pp. 71–91.

Ellyin, F., and Valaire, B., 1982, "Biaxial High Strain Fatigue Testing Rig," *Procs. Joint SESA-JSME Conference*, Hawaii, May 1982, pp. 136–143.

Krieg, R. D., 1975, "A Practical Two Surface Plasticity Theory," ASME JOURNAL OF APPLIED MECHANICS, Vol. 42, pp. 641–646.

Lamba, H. A., and Sidebottom, O. M., 1978, "Cyclic Plasticity for Nonproportional Path: Part 1—Cyclic Hardening, Erasure of Memory and Subsequent Strain Hardening Experiments; Part 2—Comparison with Predictions of Three Incremental Plasticity Models," *ASME Journal of Engineering Materials and Technology*, Vol. 100, pp. 96–111.

McDowell, D. L., 1985, "A Two Surface Model for Transient Nonproportional Cyclic Plasticity: Part I—Development of Appropriate Equations; Part II—Comparison of Theory with Experiments," ASME JOURNAL OF APPLIED MECHANICS, Vol. 52, pp. 298–308.

McDowell, D. L., 1989, "Evaluation of Intersection Conditions for Two-Surface Plasticity Theory," *Int. J. Plasticity*, Vol. 5, pp. 29–50.

Mroz, Z., 1967, "An Attempt to Describe the Behaviour of Metals Under Cyclic Loads Using a More General Work Hardening Model," *Acta Mechanica*, Vol. 7, pp. 199–212.

Ohno, N., 1982, "A Constitutive Model of Cyclic Plasticity with a Nonhardening Strain Region," ASME JOURNAL OF APPLIED MECHANICS, Vol. 49, pp. 721–727.

Rotvel, F., 1970, "Biaxial Fatigue Tests with Zero Mean Stresses Using Tubular Specimens," *Int. Journal Mech. Sciences*, Vol. 12, pp. 597–613.

Tseng, N. T., and Lee, G. C., 1983, "Simple Plasticity Model of the Two Surface Type," *Journal of Engineering Mechanics*, ASCE, New York, Vol. 109, pp. 795–810.

Ziegler, H., 1959, "A Modification of Prager's Hardening Rule," *Quarterly of Applied Mathematics*, Vol. 17, pp. 55–65.

APPENDIX

Calculation of $F = A_{sw}/A_{mem}$ for Biaxial Out-of-Phase Strain Path

In the principal strain space $0\epsilon_1\epsilon_2\epsilon_3$, we establish a coordinate system $0\epsilon_1'\epsilon_2'\epsilon_3'$, such that the $0\epsilon_1'$ and $0\epsilon_2'$ are parallel to and $0\epsilon_3'$ is perpendicular to the Π-plane (see Fig. 11). It can be shown that the transformation matrix of the two coordinate systems is:

$$\begin{Bmatrix} \epsilon_1' \\ \epsilon_2' \\ \epsilon_3' \end{Bmatrix} = \begin{bmatrix} -\frac{3+\sqrt{3}}{6} & \frac{3-\sqrt{3}}{6} & \frac{\sqrt{3}}{3} \\ \frac{3-\sqrt{3}}{6} & -\frac{3+\sqrt{3}}{6} & \frac{\sqrt{3}}{3} \\ \frac{\sqrt{3}}{3} & \frac{\sqrt{3}}{3} & \frac{\sqrt{3}}{3} \end{bmatrix} \begin{Bmatrix} \epsilon_1 \\ \epsilon_2 \\ \epsilon_3 \end{Bmatrix}. \tag{A1}$$

By using equations (15) and (16), the strain memory surface can be expressed as

$$\varphi_m = \frac{2}{3}(\epsilon_1'^2 + \epsilon_2'^2) - \epsilon_{e,\max}^2 = 0. \tag{A2}$$

From the above, it is seen that the projection of the strain memory surface on the Π-plane is a circle.

For a biaxial out-of-phase path,

$$\begin{cases} \epsilon_1 = A\cos\omega t \\ \epsilon_2 = \rho A\cos(\omega t - \phi). \end{cases} \tag{A3}$$

Using equation (A1) and supposing $\nu = 0.5$, we get

$$\begin{cases} \epsilon_1' = -\frac{1+\sqrt{3}}{2}\epsilon_1 + \frac{1-\sqrt{3}}{2} \\ \epsilon_2' = \frac{1-\sqrt{3}}{2}\epsilon_1 - \frac{1+\sqrt{3}}{2}\epsilon_2 \\ \epsilon_3' = 0 \end{cases}.$$

Then, the areas can be calculated by integrals

$$A_{sw} = \frac{1}{2}\oint(\epsilon_1' d\epsilon_2' - \epsilon_2' d\epsilon_1') = \sqrt{3}\pi\rho A^2 \sin\phi, \text{ and} \tag{A4}$$

Downloaded 03 May 2010 to 171.66.16.248. Redistribution subject to ASME license or copyright; see http://www.asme.org/terms/Terms_Use.cfm

$$A_{\text{mem}} = \pi R_{\max}^2 = \pi(\epsilon_1'^2 + \epsilon_2'^2)_{\max}. \tag{A5}$$

From equations (A2) and (A5) we get

$$\epsilon_{e,\max} = \sqrt{\frac{2}{3}(\epsilon_1'^2 + \epsilon_2'^2)_{\max}} = \sqrt{\frac{2}{3}} R_{\max}.$$

The results for $\rho = 1$ and $\phi = 0$, 30 deg, 90 deg are summarized in Table A1.

Table A1 Calculation of nonproportionality factor, F

ϕ	A_{sw}	$R_{\max}$	$\epsilon_{e,\max} = \sqrt{\frac{2}{3}} R_{\max}$	F
0 deg	0	$\sqrt{6}A$	$2A$	0
30 deg	$\frac{\sqrt{3}}{2}\pi A^2$	$\sqrt{6}A \cos 15$ deg	$2A \cos 15$ deg	0.155
90 deg	$\sqrt{3}\pi A^2$	$\sqrt{6}A \cos 45$ deg	$2A \cos 45$ deg	0.577

Downloaded 03 May 2010 to 171.66.16.248. Redistribution subject to ASME license or copyright; see http://www.asme.org/terms/Terms_Use.cfm

Growth Instability During Nonuniform Directional Solidification of a Pure Metal Plate

Louis G. Hector, Jr.
Staff Scientist,
Aluminum Company of America,
Alcoa Laboratories,
Alcoa Center, PA 15069
Mem. ASME

Bulent Aksel[1]
Research Assistant,
Department of Theoretical and
Applied Mechanics,
Cornell University,
Ithaca, NY 14853

Joseph Fridy
Mathematical Scientist,
Aluminum Company of America,
Alcoa Laboratories,
Alcoa Center, PA 15069

The singly periodic beam theory of freezing front growth instability in pure metal castings due to Richmond et al., (1990) is extended here to the more general case of a doubly periodic plate. The casting is cooled with a doubly periodic heat flux which oscillates along two orthogonal axes of the mold/casting interface. The cooling profile induces nonuniform growth of the freezing front and hence a strain distribution in the casting that leads to contraction of the metal at specific locations along the mold interface. Metal contraction is studied through calculation of the interface pressure. Growth instability occurs when the pressure falls to zero beneath a thickness minimum, thereby signalling the nucleation of an air gap, and simultaneously increases beneath a thickness maximum thereby enhancing the initial nonuniformity of the freezing front. The significant differences between the beam and plate theories for a given pure metal are found in the more extreme stress levels which accumulate within the plate, the magnitude of the admissible uniform cooling term and hence predicted times to air gap nucleation, and casting thickness at air gap nucleation as well as interface pressures beneath thickness maxima. The doubly periodic plate theory permits larger uniform cooling and hence earlier air gap nucleation beneath thickness minima than does the singly periodic beam theory with more severe interface pressures beneath thickness maxima.

Introduction

During solidification of a metal, the freezing front often exhibits nonuniformities known as cellular undulations. These undulations, which are macroscopic (in contrast to the microscopic dendrite morphology), represent a growth instability where certain regions of the freezing front grow preferentially over others. The result is a significant thickness variation in the casting which can have a detrimental effect on the quality of the cast product as well as on the casting process itself. For example, an excessively thin section of a continuously cast shell may be unable to retain the residual molten metal as the casting exits the mold. This can result in a situation known as breakout where the thin section fails thereby releasing molten metal through the shell surface. Nonuniform growth can be accompanied by air gap nucleation which leads to loss of heat transfer or even to surface remelting due to air gap nucleation and separation of metallurgical constituents which promote surface cracking during subsequent metalworking operations. This necessitates a post-casting scalping operation to remove these surface defects which not only increases the mechanical intensity of the ingot processing operation but leads to added production costs. A detailed understanding of cellular undulations in metal casting is thus of significant practical importance.

Experimental studies of growth instability during casting involve decanting residual molten metal after partial casting, and subsequent examination of the residual freezing front. One of the first reported studies of this kind is that of Neymark (1955) who observed growth instabilities in cast metal plates using a vacuum crystallization device. Of particular interest is Neymark's observation that air gaps tended to nucleate beneath minima on the freezing fronts in a variety of metals. Some of the air gaps were found to grow in size and eventually to nucleate cracks on the external surface of the casting. Similar experiments were conducted by Cisse et al. (1971), who studied nonuniform growth in aluminum castings and Singh and Blazek (1974) who observed cellular undulations on continuously cast steel shells. Wray (1977, 1981) used a device similar to that of Neymark to study cellular undulations in lead castings. The external surfaces of the lead castings revealed slight depressions (presumably air gaps) beneath minima on the freezing front which grew deeper as the shell grew thicker.

In a recent model of growth instability during slow solidification of pure aluminum castings, Richmond et al. (1990), assumed that latent heat liberated at the freezing front was

[1]Presently Staff Physicist, Magnet Systems Division, Superconducting Super Collider Laboratory, Dallas, TX 75237.

Contributed by the Applied Mechanics Division of THE AMERICAN SOCIETY OF MECHANICAL ENGINEERS for presentation at the Joint Applied Mechanics/Bioengineering Conference, Ohio State University, Columbus, Ohio, June 16–19, 1991.

Discussion on this paper should be addressed to the Technical Editor, Prof. Leon M. Keer, The Technological Institute, Northwestern University, Evanston, IL 60208, and will be accepted until two months after final publication of the paper itself in the JOURNAL OF APPLIED MECHANICS. Manuscript received by the ASME Applied Mechanics Division, Dec. 12, 1989; final revision, June 5, 1990.
Paper No. 91-APM-15.

Copyright © 1991 by ASME
Downloaded 03 May 2010 to 171.66.16.248. Redistribution subject to ASME license or copyright; see http://www.asme.org/terms/Terms_Use.cfm

extracted through the mold/casting interface with a spatially periodic cooling profile in one direction. This led to initially nonuniform growth of the freezing front. Associated deformation of the casting was assumed to be governed by a hypoelastic constitutive model which accounted for the history dependence of "elastic" behavior. A spatially periodic mold/casting interface pressure, which resulted from the deformation in the casting as it solidified, was calculated by combining the hypoelastic constitutive model with a nonuniform beam model. Air gaps were assumed to nucleate at points along the mold/casting interface where the pressure dropped to zero, after which time the model was no longer valid. These positions of zero pressure, and hence air gap nucleation, were found to occur exactly where the freezing front thickness was already minimal and hence to lead to unstable growth. The theory suggested that this instability can be avoided with increased melt pressure or by application of a cooling profile in which the wavelength of the oscillation is large.

In the present work, the singly periodic cooling profile considered by Richmond et al. (1990), is extended to the more general case of a doubly periodic profile. This necessitates use of plate theory, rather than beam theory. Nonuniform growth of the plate again results from the oscillatory heat extraction through the mold interface. The associated evolution of the mold/casting interface pressure up to air gap nucleation is examined for a pure aluminum casting through combination of a nonuniform plate theory with the hypoelastic constitutive law. This necessarily requires a re-examination of classical thin plate theory (see, for example, Nadai, 1921; Kerr, 1958; Timoshenko and Woinowsky-Kreiger, 1959) in order to account for the time and space varying thickness of the plate. Differences between the beam and plate models are discussed.

Assumptions

The model to be developed is based on the following assumptions:

(1) The molten metal is pure and initially at its fusion temperature T_f.

(2) The molten metal is of finite height H.

(3) Pertinent material properties are temperature independent.

(4) Deformation in the metal casting is governed by a hypoelastic constitutive law.

(5) The heat flux through the casting is due to the liberation of latent heat at the freezing front.

(6) The stress state at the freezing front is isostatic.

(7) The solidified metal at the freezing front is in a state of zero strain.

(8) The variation of the through-thickness stress in the casting σ_{zz} is linear.

(9) The boundary temperature is strictly monotonic prior to air gap nucleation.

(10) The heat conduction and deformation models are thermomechanically uncoupled.

Assumption (6) is an internal boundary condition which asserts that the stress state in the fluid is continuous across the freezing front. This and the other assumptions have been discussed by Richmond et al. (1990).

Heat Conduction Model

Figure 1 illustrates a representative section of the system to be modeled. The theory which follows considers a single cell of solidified metal, with base area $\lambda_x\lambda_y$, as shown at the top of Fig. 1, with contours of the oscillatory cooling profile re-

Nomenclature

c_i^j = i-centroid coordinate of j-face of plate element
$\mathbf{e}_i$ = unit vector
$f_x(t)$ = function of time associated with lateral strain ϵ_{xx}
$f_y(t)$ = function of time associated with lateral strain ϵ_{yy}
g = acceleration due to gravity
$g(t)$ = function of time associated with mold/casting interface pressure P
k = thermal conductivity of metal
$\mathbf{n}$ = normal to freezing front
$s(x,y,t)$ = casting thickness
s_c = casting thickness at air gap nucleation time
t = time
$t^*(x,y,z)$ = layer formation time
t_c = critical time to growth instability
x = lateral spatial variable
y = lateral spatial variable
z = spatial variable through casting thickness
A = amplitude of uniform cooling term
A_m = maximum theoretical value of uniform cooling term
B = amplitude of periodic disturbance in x-direction
C = amplitude of periodic disturbance in y-direction
E = Young's modulus
F_i = net force on plate element
$F(x,y,z,t)$ = equation of the freezing front
H = height of the fluid
L = latent heat of fusion
M = moment per unit length
N = lateral force per unit length
$P(x,y,t)$ = mold/casting interface pressure
$Q(x,y)$ = applied heat flux
R_1 = material property parameter controlling instability
R_2 = process parameter controlling instability
$T(x,y,z,t)$ = temperature distribution in casting
T_f = fusion temperature
V = shear force per unit length

Greek Symbols

α = coefficient of thermal expansion
δ_{ij} = Kronecker's delta
$\epsilon_{ij}(x,y,z,t)$ = total strain tensor
κ = thermal diffusivity
λ_x = wavelength of periodic disturbance in x-direction
λ_y = wavelength of periodic disturbance in y-direction
ν = Poisson's ratio
ϕ_x = uniform lateral strain rate in x-direction
ϕ_y = uniform lateral strain rate in y-direction
ρ = density
$\sigma_{ij}(x,y,z,t)$ = stress tensor
ξ = tolerance

Downloaded 03 May 2010 to 171.66.16.248. Redistribution subject to ASME license or copyright; see http://www.asme.org/terms/Terms_Use.cfm

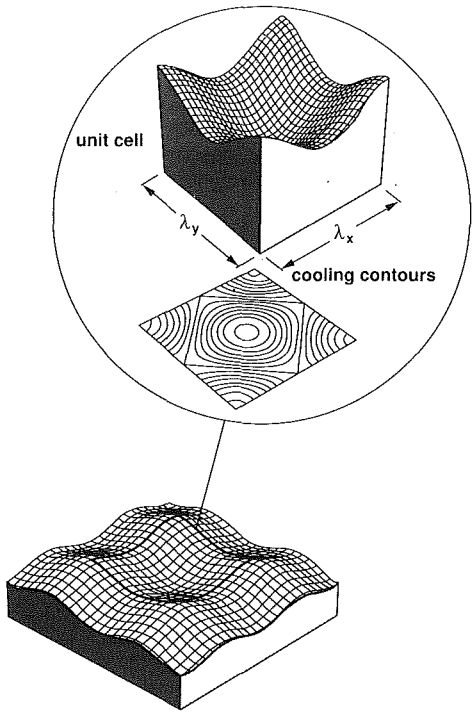

Fig. 1 Freezing front morphology

sponsible for the initial freezing front nonuniformity. The nonuniformity of the cell freezing front is exaggerated for the purpose of illustration. The governing equation for heat transfer in the three-dimensional system shown in Fig. 1 is given by

$$\frac{\partial^2 T}{\partial x^2}+\frac{\partial^2 T}{\partial y^2}+\frac{\partial^2 T}{\partial z^2}=\frac{1}{\kappa}\frac{\partial T}{\partial t} \quad ; t>0, \forall x,y,z. \tag{1}$$

The system is subject to the following conditions:

$$k\frac{\partial T}{\partial z}=Q(x,y); \; z=0 \tag{2}$$

$$T=T_f \qquad ; z=s \tag{3}$$

$$\frac{\partial T}{\partial z}=\frac{\rho L}{k}\frac{\partial s}{\partial t} \quad ; z=s \tag{4}$$

$$s=0 \qquad ; t=0. \tag{5}$$

The temperature distribution in the casting is $T = T(x, y, z, t)$. The thermal diffusivity is denoted by κ and the thermal conductivity by k. Q is the applied heat flux at the mold/casting interface, T_f is the fusion temperature of the metal, L is the latent heat of fusion, and $s = s(x, y, t)$ is the local casting thickness.

Equation (1) is the heat conduction equation and equation (2) indicates that the casting is cooled with a spatially variable heat flux. Equation (3) indicates that the freezing front is isothermal at the fusion temperature. Equation (4) governs the liberation of latent heat at the freezing front (see Patel, 1968), and equation (5) states that there is no solid at initial time.

The quasi-steady approximation for casting temperature distribution due to Chehl (1973) is adopted. The temperature is assumed to vary linearly through the casting and to satisfy the pertinent heat transfer boundary conditions. Further details on this technique may be found in Richmond et al. (1990). The approximate solutions for the casting temperature and growth rate of the solid metal are

$$T=T_f-\frac{Qs}{k}\left(1-\frac{z}{s}\right) \tag{6}$$

$$\frac{\partial s}{\partial t}=\frac{Q}{\rho L}. \tag{7}$$

Equation (7) may be integrated to

$$s=\frac{Qt}{\rho L}. \tag{8}$$

Equation (6) is valid so long as the following condition is satisfied

$$\frac{4Qs}{\kappa\rho L}\ll 1. \tag{9}$$

Equation (6) shows that the approximate temperature distribution in the casting is linear through its thickness. Equation (7) asserts that the approximate growth rate of the solid is proportional to the interface heat flux and equation (9) places a slow-cooling constraint on the theory.

The prescribed mold/casting interface heat flux is

$$Q=A+B\left(1-\cos\left(\frac{2\pi x}{\lambda_x}\right)\right)+C\left(1-\cos\left(\frac{2\pi y}{\lambda_y}\right)\right). \tag{10}$$

The parameter A is the amplitude of the uniform cooling term, the parameters B and C are the amplitudes of the spatial disturbances in the x and y-directions, respectively, and the wavelengths of the disturbances are λ_x and λ_y. The symmetry of the system is such that

$$\frac{\partial T}{\partial x}=0 \quad ; x=\pm\frac{\lambda_x}{2} \tag{11}$$

$$\frac{\partial T}{\partial y}=0 \quad ; y=\pm\frac{\lambda_y}{2}. \tag{12}$$

Equilibrium Relations for a Nonuniform Plate

The plate element which is used to derive the equilibrium relations is shown in Fig. 2 with the usual stress resultants. It is a brick on which the upper surface (adjacent to the molten metal) is slightly inclined with respect to the base (on the mold side) and is actually one-quarter of a less exaggerated version of the encircled cell in Fig. 1. The net fluid force on the cell acts through the centroid of the inclined surface and the net force due to the mold/casting interface pressure P, acts through the centroid of the cell base. The centroids needed for the equilibrium analysis are those of the four vertical faces of the element, the inclined surface, and the base of the element as well as the element itself. These are listed in the Appendix along with derivations of the following equilibrium equations:

$$P-\rho gH-\left(\frac{\partial V_x}{\partial x}+\frac{\partial V_y}{\partial y}\right)=0 \tag{13}$$

$$\frac{\partial N_x}{\partial x}+\frac{\partial N_{yx}}{\partial y}+\rho g(H-s)\frac{\partial s}{\partial x}=0 \tag{14}$$

$$\frac{\partial N_{xy}}{\partial x}+\frac{\partial N_y}{\partial y}+\rho g(H-s)\frac{\partial s}{\partial y}=0 \tag{15}$$

$$V_x+\frac{1}{2}\left[N_{yx}\frac{\partial s}{\partial y}+\{N_x+\rho gs(H-s)\}\frac{\partial s}{\partial x}\right]-\left(\frac{\partial M_x}{\partial x}+\frac{\partial M_{yx}}{\partial y}\right)=0 \tag{16}$$

$$V_y+\frac{1}{2}\left[N_{xy}\frac{\partial s}{\partial x}+\{N_y+\rho gs(H-s)\}\frac{\partial s}{\partial y}\right]-\left(\frac{\partial M_y}{\partial x}+\frac{\partial M_{xy}}{\partial x}\right)=0 \tag{17}$$

$$N_{xy}=N_{yx}. \tag{18}$$

Downloaded 03 May 2010 to 171.66.16.248. Redistribution subject to ASME license or copyright; see http://www.asme.org/terms/Terms_Use.cfm

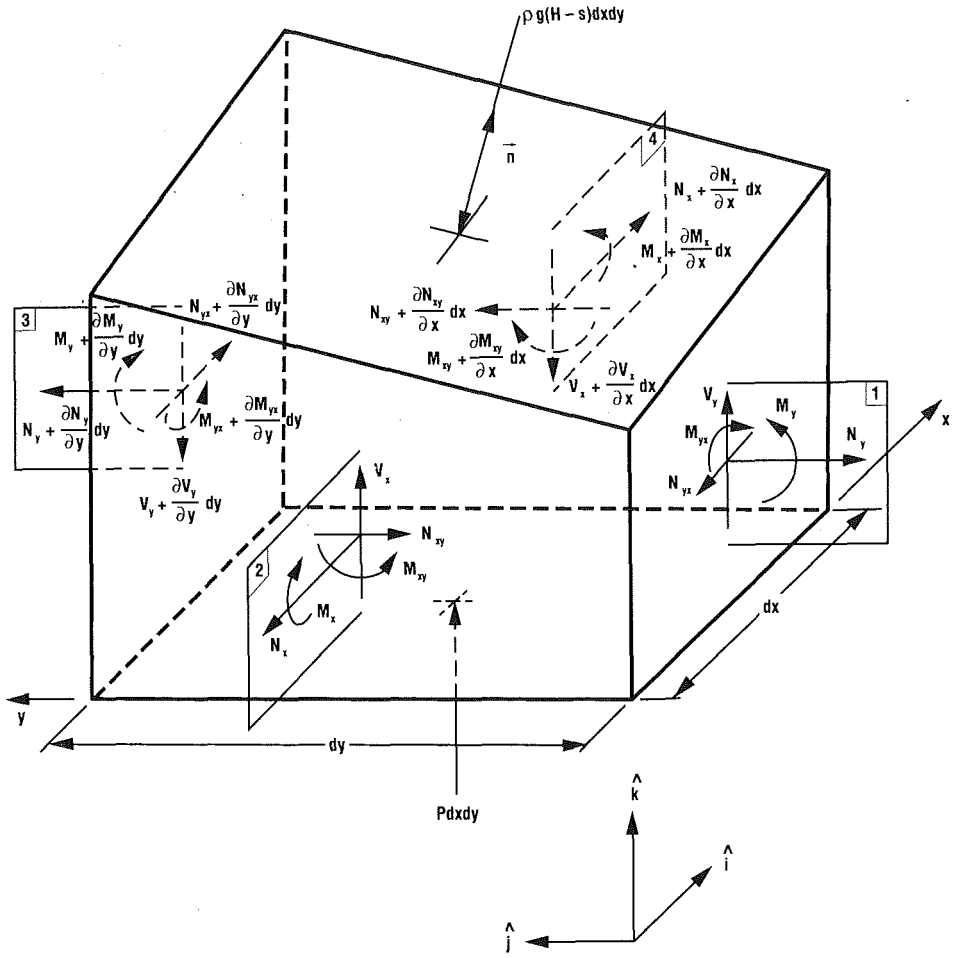

Fig. 2 Nonuniform plate element

When equations (14)–(18) are substituted into equation (13), there results the following expression:

$$P-\rho gH+\frac{1}{2}\left\{(N_x+\rho gs(H-s))\frac{\partial^2 s}{\partial x^2}+(N_y+\rho gs(H-s))\times\frac{\partial^2 s}{\partial y^2}+N_{xy}\frac{\partial^2 s}{\partial y\partial x}+N_{yx}\frac{\partial^2 s}{\partial x\partial y}\right\}-\left(\frac{\partial^2 M_x}{\partial x^2}+\frac{\partial^2 M_y}{\partial y^2}+\frac{\partial^2 M_{yx}}{\partial x\partial y}+\frac{\partial^2 M_{xy}}{\partial y\partial x}\right)=0 \quad (19)$$

where the stress resultants per unit length are N_x, N_y, and N_{xy} (lateral forces), M_x, M_y, and M_{xy} (moments), and V_x and V_y (shear forces). Equation (19) relates the mold/casting interface pressure P, to the stress resultants as well as to the casting thickness, freezing front spatial gradients, and fluid height. The stress resultants are related to the stress distribution in the casting through

$$N_x=\int_o^s \sigma_{xx}dz \quad (20)$$

$$N_y=\int_o^s \sigma_{yy}dz \quad (21)$$

$$N_{xy}=\int_o^s \sigma_{xy}dz \quad (22)$$

$$M_x=-\int_o^s \sigma_{xx}\left(z-\frac{s}{2}\right)dz \quad (23)$$

$$M_y=-\int_o^s \sigma_{yy}\left(z-\frac{s}{2}\right)dz \quad (24)$$

$$M_{xy}=-\int_o^s \sigma_{xy}\left(z-\frac{s}{2}\right)dz \quad (25)$$

where σ_{xx} and σ_{yy} are lateral stresses in the casting and σ_{xy} is the shear stress. For the remainder of the analysis the shear stress distribution is assumed to be negligibly small since the casting will be nearly uniform up to air gap nucleation time. The shear stress will become significant in situations where the casting undergoes large spatial variations in thickness. Using equations (20), (21), (23), (24), and assuming negligible shear stress, the mold/casting interface pressure may be related to the lateral stresses through

$$P-\rho gH+\frac{1}{2}\left[\int_o^s \sigma_{xx}dz+\rho gs(H-s)\right]\left(\frac{\partial^2 s}{\partial x^2}\right)+\frac{1}{2}\left[\int_o^s \sigma_{yy}dz+\rho gs(H-s)\right]\left(\frac{\partial^2 s}{\partial y^2}\right)+\frac{\partial^2}{\partial x^2}\int_o^s \sigma_{xx}\left(z-\frac{s}{2}\right)dz+\frac{\partial^2}{\partial y^2}\int_o^s \sigma_{yy}\left(z-\frac{s}{2}\right)dz=0. \quad (26)$$

Terms 3 through 6 in equation (26) represent spatial variations in the mold/casting interface pressure P, about the initial fluid pressure, ρgH. Equations (14), (15), and (26) must be satisfied by the lateral stress distribution in the casting, i.e., σ_{xx} and σ_{yy}.

Hypoelastic Constitutive Model

Deformation of a solidifying material differs from that of a standard fixed body. Whereas a fixed body, such as a uniformly loaded plate, is usually assumed to deform from an

Downloaded 03 May 2010 to 171.66.16.248. Redistribution subject to ASME license or copyright; see http://www.asme.org/terms/Terms_Use.cfm

initial state which is stress free, a solidifying plate develops residual stresses as it grows and is never in a stress-free state. As a consequence of this attribute, a hypoelastic constitutive model (see Prager, 1961), which is essentially a rate formulation of elastic behavior, is assumed to govern deformation in the casting. The governing equation is given by

$$\frac{\partial \epsilon_{ij}}{\partial t} = \frac{(1+\nu)}{E}\frac{\partial \sigma_{ij}}{\partial t} - \left(\frac{\nu}{E}\frac{\partial \sigma_{kk}}{\partial t} - \alpha\frac{\partial T}{\partial t}\right)\delta_{ij} \tag{27}$$

where ϵ_{ij} is the total strain, σ_{ij} is the stress, ν is Poisson's ratio, E is Young's modulus, α is the coefficient of thermal expansion, and δ_{ij} is Kronecker's delta. An additional strain rate term which accounts for more realistic nonlinear behavior of metals at elevated temperatures could be included in equation (27) although this would considerably increase the complexity of the calculations.

Solidification Stresses and Strains

The solidification problem is a special initial value problem in that the initial conditions of isostatic stress and zero strain at the freezing front (assumptions (6) and (7)) are applied at different times for different positions in the body depending upon when the freezing front reaches those positions. After the start of solidification, it is appropriate to assume that the strain history in each incremental layer of the metal begins with its nucleation from the melt which occurs at a time t^*, necessarily greater than zero. The lateral stresses in the casting are determined through time integration of equations (27) such that the strain accumulates within each added layer of the casting starting with its formation time. Integration for the lateral stresses σ_{xx} and σ_{yy} gives

$$[\sigma_{xx} - \nu(\sigma_{yy}+\sigma_{zz}) - (\sigma_{xx} - \nu\sigma_{yy} - \nu\sigma_{zz})|_{t*} + E\alpha(T-T_f)] - E\int_{t^*}\frac{\partial \epsilon_{xx}}{\partial t}\,dt = 0 \tag{28}$$

$$[\sigma_{yy} - \nu(\sigma_{xx}+\sigma_{zz}) - (\sigma_{yy} - \nu\sigma_{xx} - \nu\sigma_{zz})|_{t*} + E\alpha(T-T_f)] - E\int_{t^*}\frac{\partial \epsilon_{yy}}{\partial t}\,dt = 0 \tag{29}$$

where $\epsilon_{xx} = \epsilon_{xx}(x, y, z, t)$ is the lateral strain in the x-direction, $\epsilon_{yy} = \epsilon_{yy}(x, y, z, t)$ is the lateral strain in the y-direction, and $t^* = t^*(x, y, z)$ is the layer formation time which is given by

$$t^* = \frac{z\rho L}{A + B\left[1-\cos\left(\frac{2\pi x}{\lambda_x}\right)\right] + C\left[1-\cos\left(\frac{2\pi y}{\lambda_y}\right)\right]} \tag{30}$$

and results from the expression for the casting thickness. Assumption (6) asserts that the stress state at the freezing front is isostatic. Therefore,

$$\sigma_{xx} = \sigma_{yy} = \sigma_{zz} = -\rho g(H-s) \quad ; z = s. \tag{31}$$

By assumption (7), no strains accumulate at the time a new layer of solid metal is formed, and thus

$$\epsilon_{xx}(x,y,s,t^*) = 0 \quad ; z = s \tag{32}$$

$$\epsilon_{yy}(x,y,s,t^*) = 0 \quad ; z = s. \tag{33}$$

Substitution of equations (31), (32), and (33) into equations (28) and (29) gives

$$\sigma_{xx} = \nu(\sigma_{yy}+\sigma_{zz}) - \rho g(1-2\nu)(H-z) - E\alpha(T-T_f) + E\epsilon_{xx} \tag{34}$$

$$\sigma_{yy} = \nu(\sigma_{xx}+\sigma_{zz}) - \rho g(1-2\nu)(H-z) - E\alpha(T-T_f) + E\epsilon_{yy} \tag{35}$$

For the early stages of solidification, it may be assumed (by assumption (8)) that σ_{zz} is a linear function of z varying from the isostatic pressure at the freezing front, given by equation (31), to that at the mold/casting interface pressure P, given by equation (26). This leads to

$$\sigma_{zz} = -\left[\left(1-\frac{z}{s}\right)P + \frac{\rho g z}{s}(H-s)\right]. \tag{36}$$

Equation (36) is substituted into equations (34) and (35) which are then solved simultaneously for the following lateral stress distribution in the casting

$$\sigma_{xx} = -\frac{1}{1-\nu}\left[\nu\left(1-\frac{z}{s}\right)P + \rho g\left\{\frac{\nu z}{s}(H-s) + (1-2\nu)(H-z)\right\} + E\alpha(T-T_f) - \frac{E(\epsilon_{xx}+\nu\epsilon_{yy})}{1+\nu}\right] \tag{37}$$

$$\sigma_{yy} = -\frac{1}{1-\nu}\left[\nu\left(1-\frac{z}{s}\right)P + \rho g\left\{\frac{\nu z}{s}(H-s) + (1-2\nu)(H-z)\right\} + E\alpha(T-T_f) - \frac{E(\nu\epsilon_{xx}+\epsilon_{yy})}{1+\nu}\right]. \tag{38}$$

Equations (37) and (38) reveal that a material element of the plate is subjected to a strain field which results in accumulated stresses that are generally more extreme than those of the beam model.

Expressions for the lateral strains in the casting and for the mold/casting interface pressure appropriate for small values of B and C are

$$\epsilon_{xx} = \phi_x\left(t - \frac{z\rho L}{A}\right) + \frac{BH}{kT_f}f_x(t)\left(1-\frac{z}{s}\right)\cos\left(\frac{2\pi x}{\lambda_x}\right) \tag{39}$$

$$\epsilon_{yy} = \phi_y\left(t - \frac{z\rho L}{A}\right) + \frac{CH}{kT_f}f_y(t)\left(1-\frac{z}{s}\right)\cos\left(\frac{2\pi y}{\lambda_y}\right) \tag{40}$$

$$P = \rho g H + \frac{Hg(t)}{kT_f}\left[B\cos\left(\frac{2\pi x}{\lambda_x}\right) + C\cos\left(\frac{2\pi y}{\lambda_y}\right)\right] \tag{41}$$

where $f_x(t)$, $f_y(t)$, and $g(t)$ are unknown functions of time. The first terms in equations (39) and (40) are the lateral strains in the plate in the absence of any oscillatory behavior in the cooling profile. The constants ϕ_x and ϕ_y are lateral strain rates in the referenced directions. These are multiplied by the residence time which is a measure of the amount of time elapsed since the nucleation of a layer of solid metal. The second terms in equations (39) and (40) are first-order perturbations about the uniform strain distribution where the perturbation parameters are B and C, respectively. Equations (39) and (40) incorporate the conditions that the strains vanish at the freezing front and the spatial gradients of strain vanish along the edge of a cell as dictated by symmetry. Similar observations may be made about equation (41).

To determine the three unknown functions of time, equations (39), (40), and (41) are first substituted into equations (37) and (38), which are then substituted into equations (14), (15), and (26). All terms multiplied by B, C, BC, and higher powers of B and C are neglected and the resulting algebraic expressions are solved simultaneously for $f_x(t)$, $f_y(t)$, and $g(t)$. This yields the following desired forms of equations (39), (40), and (41):

$$\epsilon_{xx} = \phi_x\left(t - \frac{z\rho L}{A}\right) + \frac{\alpha AB}{3k\rho^3L^3}\left(\frac{1+\nu}{1-\nu}\right)\left(1-\frac{z}{s}\right) \times\left\{9\rho^2L^2(1-\nu)t - \frac{2\nu\pi^2A^2}{\lambda_x^2}t^3\right\}\cos\left(\frac{2\pi x}{\lambda_x}\right) \quad ; \quad t>0 \tag{42}$$

$$\epsilon_{yy} = \phi_y\left(t - \frac{z\rho L}{A}\right) + \frac{\alpha AC}{3k\rho^3L^3}\left(\frac{1+\nu}{1-\nu}\right)\left(1-\frac{z}{s}\right) \times\left\{9\rho^2L^2(1-\nu)t - \frac{2\nu\pi^2A^2}{\lambda_y^2}t^3\right\}\cos\left(\frac{2\pi y}{\lambda_y}\right) \quad ; \quad t>0 \tag{43}$$

$$P = \rho g H - \frac{2\pi^2\alpha EA^3t^3}{3\rho^3kL^3(1-\nu)}\left[\frac{B}{\lambda_x^2}\cos\left(\frac{2\pi x}{\lambda_x}\right) + \frac{C}{\lambda_y^2}\cos\left(\frac{2\pi y}{\lambda_y}\right)\right]; \quad t \geq 0. \tag{44}$$

Downloaded 03 May 2010 to 171.66.16.248. Redistribution subject to ASME license or copyright; see http://www.asme.org/terms/Terms_Use.cfm

A comparison of equation (44) for the mold/casting interface pressure with the casting thickness

$$s=\left[A+B\left(1-\cos\left(\frac{2\pi x}{\lambda_x}\right)\right)+C\left(1-\cos\left(\frac{2\pi y}{\lambda_y}\right)\right)\right]\frac{t}{\rho L} \tag{45}$$

indicates that the pressure under a thickness minimum on the freezing front decreases from the onset of solidification eventually leading to growth instability. The pressure simultaneously increases under freezing front maxima thereby enhancing the initial nonuniformity. In the limit as $C \rightarrow 0$ and $\phi_y \rightarrow 0$ (i.e., the casting approaches plane strain), equations (42) and (44) reduce to the nonuniform beam results of Richmond et al. (1990). Equation (44) predicts that the mold/casting interface pressure beneath a thickness maximum on a plate of metal will be larger than its beam counterpart given the same process parameters. The thermal stress distribution in the casting may be calculated by substituting equations (6), (42), (43), (44), and (45) into equations (37) and (38).

Instability Condition

The critical time t_c to the onset of unstable growth is determined from equation (44) by setting P, x, and y equal to zero. This gives

$$t_c=0.53(R_1R_2)^{\frac{1}{3}} \tag{46}$$

where

$$R_1=\frac{k\rho^4L^3(1-\nu)}{E\alpha} \tag{47}$$

$$R_2=\frac{g\lambda_x^2\lambda_y^2H}{A^3(\lambda_y^2B+\lambda_x^2C)}. \tag{48}$$

The material property contribution to air gap nucleation time is given by R_1. The parameter R_2 is indicative of the process parameter contribution to air gap nucleation time. In the limit that $C \rightarrow 0$, i.e., uniform cooling in the y-direction, R_2 reduces to

$$R_2=\frac{g\lambda_x^2H}{A^3B} \tag{49}$$

which is the result for the singly periodic case. A comparison of equations (48) and (49) reveals that the time to air gap nucleation for the doubly periodic case is shorter.

The air gap nucleation time t_c, may be eliminated between equations (45) and (46) to give the following expression for the casting thickness:

$$s_c=0.53\left[\frac{k\lambda_x^2\lambda_y^2\rho gH(1-\nu)}{E\alpha(\lambda_y^2B+\lambda_x^2C)}\right]^{\frac{1}{3}} \quad ; t=t_c. \tag{50}$$

If the final casting thickness is less than s_c, then unstable growth of the freezing front will not occur. As expected, the casting thickness at air gap nucleation time predicted for doubly periodic cooling variation is less than that predicted for singly periodic cooling variation.

Equation (9) establishes the validity of the approximation used to derive the temperature distribution in the casting, equation (6). It effectively places the following bound on the choice of uniform cooling term A which may be used in the model:

$$A_m=\frac{\kappa\rho\xi L}{4s_c} \tag{51}$$

where A_m is the maximum theoretically admissible value of the cooling term and $\xi \ll 1$ is a tolerance which must be met to satisfy equation (9). When s_c is eliminated between equations (50) and (51), the following expression, which relates A_m to the casting properties and process parameters, results:

$$A_m=\frac{\kappa\rho^{\frac{2}{3}}\xi L}{2.12}\left[\frac{E\alpha(\lambda_y^2B+\lambda_x^2C)}{gk\lambda_x^2\lambda_y^2H(1-\nu)}\right]^{\frac{1}{3}}. \tag{52}$$

Again, in the limit that $C \rightarrow 0$, equation (52) reduces to its singly periodic counterpart given by

$$A_m=\frac{\kappa\rho^{\frac{2}{3}}\xi L}{2.12}\left[\frac{E\alpha B}{gk\lambda_x^2H(1-\nu)}\right]^{\frac{1}{3}}. \tag{53}$$

A comparison of equations (52) and (53) reveals that the doubly periodic case permits larger values of A_m.

Results and Discussion

The growth stability of a pure aluminum casting is examined using the mold/casting interface pressure, as given by equation (44), and the high temperature material properties listed in Table 1. The following process parameters are prescribed:

$g=9.8\ \text{m/sec}^2$

$A=A_m=9.2\times10^4\ \text{J/m}^2\cdot\text{sec}$

$B=C=0.1\ \text{J/m}^2\cdot\text{sec}$

$H=0.1\ \text{m}$

$\lambda_x=\lambda_y=10^{-5}\text{m}$

$\xi=0.001$

where the case of a square cell of metal, i.e., $\lambda_x = \lambda_y$, with equivalent oscillatory cooling magnitudes, i.e., $B = C$, has been chosen for simplicity. For situations in which $\lambda_x \neq \lambda_y$ and $B = C$, the mold/casting interface pressure and hence the cell itself will elongate in the direction of the larger wavelength. The values chosen for λ_x and λ_y are idealizations of what in reality are typical lengths over which small stochastic variations might occur in the interface heat flux. The value chosen for the uniform cooling term A_m represents relatively slow cooling when compared to more common cooling values in the range of $10^6 - 10^7\ \text{J}\cdot\text{m}^{-2}\cdot\text{sec}^{-1}$ which are typical of many aluminum direct chill casting operations (Liu, 1989). Nevertheless, the value of A_m from the plate theory somewhat exceeds the value of $7.2 \times 10^4\ \text{J}\cdot\text{m}^{-2}\cdot\text{sec}^{-1}$ which was admissible by the beam

Table 1

Properties of Pure Aluminum at the Fusion Temperature after Heinlein, et al. (1986)

Parameter	Symbol	Value at T_f
thermal conductivity	k	229.4 $\frac{\text{J}}{\text{m}\cdot\text{sec}\cdot{}^\circ\text{C}}$
Young's modulus	E	6.0×10^{10} $\frac{\text{N}}{\text{m}^2}$
latent heat of fusion	L	3.9×10^5 $\frac{\text{J}}{\text{kg}}$
fusion temperature	T_f	660.0°C
coefficient of thermal expansion	α	$37.8\times10^{-6}\ ^\circ\text{C}^{-1}$
thermal diffusivity	κ	8.2×10^{-5} $\frac{\text{m}^2}{\text{sec}}$
Poisson's ratio	ν	0.37
density	ρ	2650.0 $\frac{\text{kg}}{\text{m}^3}$

Downloaded 03 May 2010 to 171.66.16.248. Redistribution subject to ASME license or copyright; see http://www.asme.org/terms/Terms_Use.cfm

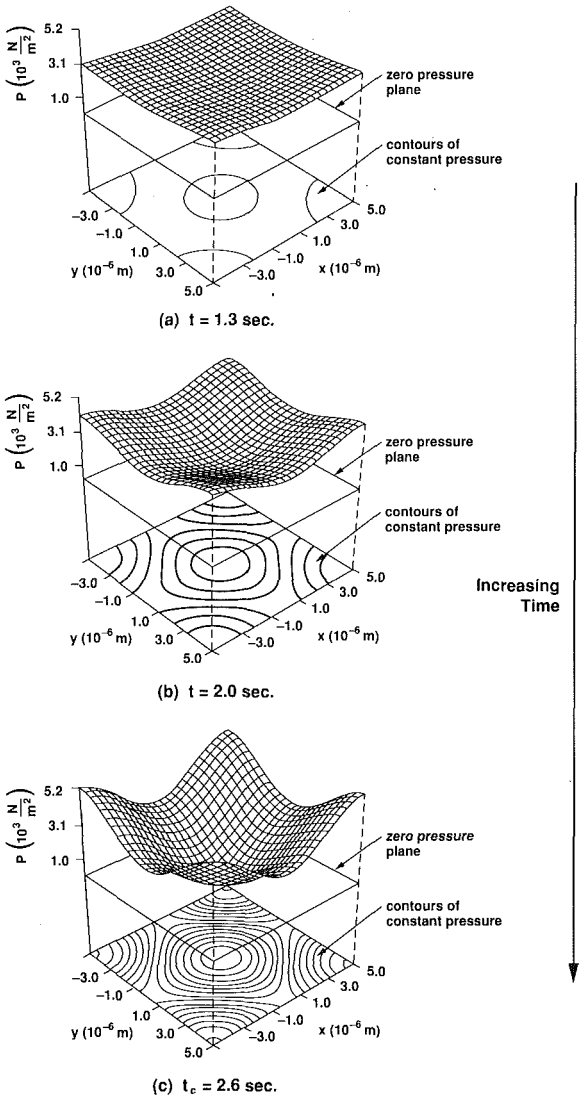

Fig. 3 Evolution of mold/casting interface pressure

theory of Richmond et al. (1990), under identical process parameters. By equation (46) the air gap nucleation time is 2.6 sec.

Figure 3 shows the evolution of the mold/casting interface pressure beneath the cell shown in Fig. 1 at three selected times. At $t = 1.3$ sec, the pressure surface is nearly flat showing only a slight change as evidenced by the contours of constant pressure shown beneath the surface. At $t = 2.0$ sec, the pressure is more highly developed as it is clearly decreasing at the center of the cell and increasing along the cell edges. Finally, at an air gap nucleation time of $t_c = 2.6$ sec, the pressure at the center of the cell drops to zero (i.e., touches the zero pressure plane) signalling the nucleation of an air gap beneath a thickness minimum on the freezing front. In the meantime, the pressure has continued to increase along the edges of the cell which are thickness maxima. An examination of the thermal strain distribution given by equations (42) and (43) along the mold/casting interface at air gap nucleation reveals that the strains are compressive beneath thickness minima (i.e., in the vicinity of an air gap) and tensile beneath thickness maxima, as expected. Changes in the mold/casting interface pressure, which are indicative of changes in the thermal strain distribution through the casting, thus lead to reduced heat extraction beneath freezing front minima and enhanced heat extraction beneath thickness maxima ensuring continued nonuniform growth of the casting at later times. Figure 3 demonstrates that the mold/casting interface pressure is highly sensitive to spatial oscillations in the cooling profile even though the magnitudes of those oscillations are very small. It should also be noted that the integral of the pressure surface (as shown in Fig. 3) over x and y is constant (ρgH) as required by force balance.

Closing Remarks

A first-order, three-dimensional thermomechanical model of growth instability in a pure metal plate has been developed through combination of the hypoelastic constitutive law and a nonuniform plate theory. The theory predicts that air gaps nucleate beneath thickness minima on the freezing front since the mold/casting interface pressure first drops to zero at these locations. On the other hand, the pressure increases beneath thickness maxima thereby enhancing the initial thickness nonuniformity due to periodic heat extraction. The major differences between the singly periodic beam model of Richmond et al. (1990), and the doubly periodic plate model are found in the more extreme stress levels which accumulate in the plate, the magnitude of the admissible uniform cooling term, and term, and hence predicted times to air gap nucleation and casting thickness at air gap nucleation as well as interface pressures beneath thickness maxima. The doubly periodic case permits larger uniform cooling and hence air gaps nucleate beneath thickness minima at earlier times than those predicted by the singly periodic case with larger interface pressures beneath thickness maxima.

Acknowledgments

The authors extend their gratitude to Dr. Owen Richmond of Alcoa Laboratories for suggesting this problem and subsequent critical review of the manuscript. This work was supported by the Process Tribology Program at Alcoa Laboratories. One of the authors (B. Aksel) wishes to thank Alcoa Laboratories for use of its resources and financial support during the summer of 1988. The efforts of the staff of the Alcoa Laboratories Information Center are gratefully acknowledged.

References

Chehl, S. S., 1973, "Multidimensional Heat Conduction Problems with Change-of-Phase," Ph.D. Thesis, North Carolina State University, Raleigh, N.C.

Cisse, J., Cole, G. S., and Bolling, G. F., 1971, "Freezing Front Asymmetry During Ingot Solidification of Aluminum and its Alloys," *AFS Cast Metals Research Journal*, Vol. 7, No. 4, pp. 158–161.

Heinlein, M., Mukherjee, S., and Richmond, O., 1986, "A Boundary Element Method of Analysis of Temperature Fields and Stresses During Solidification," *ACTA Mechanica*, Vol. 59, pp. 59–81.

Kerr, A., 1958, "Uniformly Stretched Plates Loaded by Concentrated Transverse Forces," Ph.D. Thesis, Northwestern University, Evanston, Ill.

Liu, J. C., private communication to L. G. Hector, Alcoa Laboratories, Nov., 1989.

Nadai, A., 1921, "On the Stress Distribution in a Rectangular Plate Loaded by a Single Force," *Der Bauingenieur*, No. 1, pp. 11–16.

Neymark, V. Ye, 1955, "Influence of Inoculants and Crystallization Conditions on the Quality of the Skin of the Ingot," *Transactions of the First All-Union Conference on Continuous Steel Casting*, Moscow, pp. 222–240.

Patel, P. D., 1968, "Interface Conditions in Heat Conduction Problems with Change of Phase," *AIAA J.*, Vol. 6, p. 2454.

Prager, W., 1961, *Introduction to the Mechanics of Continua*, Ginn and Company, New York.

Richmond, O., Hector, L. G., and Fridy, J. M., 1990, "Growth Instability During Nonuniform Directional Solidification of Pure Metals," ASME JOURNAL OF APPLIED MECHANICS, Vol. 57, pp. 529–536.

Singh, S. N., and Blazek, K. E., 1974, "Heat Transfer and Skin Formation in a Continuous-Casting Mold as a Function of Steel Carbon Content," *J. of Metals*, Oct., pp. 17–27.

Timoshenko, S., and Woinowsky-Krieger, S., 1959, *Theory of Plates and Shells*, McGraw-Hill, New York.

Wray, P. J., 1977, "Nonuniform Growth of a Plate Solidifying on a Chilled Surface," presentation notes, Proceedings of AIME Conference, Atlanta, Ga.

Wray, P. J., 1981, "Geometric Features of Chill-Cast Structures," *Metall. Trans.*, Vol. 12B, pp. 167–176.

Downloaded 03 May 2010 to 171.66.16.248. Redistribution subject to ASME license or copyright; see http://www.asme.org/terms/Terms_Use.cfm

APPENDIX

Derivation of Equations (13)–(19)

With reference to Fig. 2, the approximate centroids of faces 1, 2, 3, and 4 are, respectively,

$$c_x^1=\frac{dx}{2},\ c_y^1=0,\quad c_z^1=\frac{1}{2}\left[s-\frac{1}{2}\left(\frac{\partial s}{\partial y}\right)dy\right] \tag{A1}$$

$$c_x^2=0,\quad c_y^2=\frac{dy}{2},\ c_z^2=\frac{1}{2}\left[s-\frac{1}{2}\left(\frac{\partial s}{\partial x}\right)dx\right] \tag{A2}$$

$$c_x^3=\frac{dx}{2},\ c_y^3=dy,\ c_z^3=\frac{1}{2}\left[s+\frac{1}{2}\left(\frac{\partial s}{\partial y}\right)dy\right] \tag{A3}$$

$$c_x^4=dx,\ c_y^4=\frac{dy}{2},\ c_z^4=\frac{1}{2}\left[s+\frac{1}{2}\left(\frac{\partial s}{\partial x}\right)dx\right] \tag{A4}$$

where a face is designated by the number in the plane drawn perpendicular to the face. The centroid of the base is

$$c_x^b=\frac{dx}{2},\ c_y^b=\frac{dy}{2},\ c_z^b=0. \tag{A5}$$

The centroid of the inclined surface is

$$c_x^s=\frac{dx}{2},\ c_y^s=\frac{dy}{2},\ c_z^s=s. \tag{A6}$$

The vertical distance between the base and inclined surface centroids is the local casting thickness $s = s\ (x, y, t)$. The approximate centroid of the element itself is

$$c_x^e=\frac{dx}{2},\ c_y^e=\frac{dy}{2},\ c_z^e=\frac{s}{2}. \tag{A7}$$

The equation of the freezing front is given by $F = F\ (x, y, z, t) = 0$ where

$$F=z-s. \tag{A8}$$

The normal to the inclined surface is

$$\mathbf{n}=-\frac{\partial s}{\partial x}\mathbf{e}_1-\frac{\partial s}{\partial y}\mathbf{e}_2+\mathbf{e}_3 \tag{A9}$$

where $\mathbf{e}_1$, $\mathbf{e}_2$, and $\mathbf{e}_3$ are unit vectors in the i, j, and k directions, respectively, as indicated in Fig. 3, and it is assumed that the following holds true for small spatial gradients of the freezing front:

$$\nabla_s\cdot\nabla_s\approx 1. \tag{A10}$$

The net force due to the fluid pressure is

$$F_{\text{fluid}}=P_{\text{fluid}}dA=-\rho g(H-s)dx\,dy. \tag{A11}$$

With reference to Fig. 2, the equilibrium of forces in the z-direction requires

$$\Sigma F_z=0=\left\{\begin{array}{l} Pdxdy-\rho gsdxdy+V_ydx-\left(V_y+\dfrac{\partial V_y}{\partial y}dy\right)dx+V_xdy-\left(V_x+\dfrac{\partial V_x}{\partial x}dx\right)dy \\ -[\rho g(H-s)dxdy](\mathbf{n}\cdot\mathbf{e}_3)\end{array}\right\}. \tag{A12}$$

Equation (A12) reduces to Equation (13). Equilibrium of forces in the x and y-directions requires, respectively,

$$\Sigma F_x=0=\left\{\left(N_x+\frac{\partial N_x}{\partial x}dx\right)dy-N_xdy+\left(N_{yx}+\frac{\partial N_{yx}}{\partial y}dy\right)\times dx-N_{yx}dx-[\rho g(H-s)dxdy](\mathbf{n}\cdot\mathbf{e}_1)\right\}. \tag{A13}$$

$$\Sigma F_y=0=\left\{\left(N_y+\frac{\partial N_y}{\partial y}dy\right)dx-N_ydx+\left(N_{xy}+\frac{\partial N_{xy}}{\partial x}dx\right)\times dy-N_{xy}dy-[\rho g(H-s)dxdy](\mathbf{n}\cdot\mathbf{e}_2)\right\}. \tag{A14}$$

Equations (A13) and (A14) reduce to equations (14) and (15), respectively.

Equilibrium of moments requires

$$\Sigma M_x=0=\left\{\begin{array}{l} M_xdy-\left(M_x+\dfrac{\partial M_x}{\partial x}dx\right)dy+M_{yx}dx-\left(M_{yx}+\dfrac{\partial M_{yx}}{\partial y}dy\right)dx+V_x\dfrac{dx}{2}dy \\ +\left(V_x+\dfrac{\partial V_x}{\partial x}dx\right)\dfrac{dx}{2}dy+\dfrac{N_x}{4}\dfrac{\partial s}{\partial x}dxdy+\dfrac{1}{4}\left(N_x+\dfrac{\partial N_x}{\partial x}dx\right)\dfrac{\partial s}{\partial x}dxdy+\dfrac{N_{yx}}{4}\dfrac{\partial s}{\partial y}dxdy \\ +\dfrac{1}{4}\left(N_{yx}+\dfrac{\partial N_{yx}}{\partial y}dy\right)\dfrac{\partial s}{\partial y}dxdy-\dfrac{\rho gs(\mathbf{n}\cdot\mathbf{e}_1)dxdy}{2}(H-s)\end{array}\right\} \tag{A15}$$

$$\Sigma M_y=0=\left\{\begin{array}{l} M_ydx-\left(M_y+\dfrac{\partial M_y}{\partial y}dy\right)dx+M_{xy}dy-\left(M_{xy}+\dfrac{\partial M_{xy}}{\partial x}dx\right)dy+V_y\dfrac{dy}{2}dx \\ +\left(V_y+\dfrac{\partial V_y}{\partial y}dy\right)\dfrac{dy}{2}dx+\dfrac{N_y}{4}\dfrac{\partial s}{\partial y}dxdy+\dfrac{1}{4}\left(N_y+\dfrac{\partial N_y}{\partial y}dy\right)\dfrac{\partial s}{\partial y}dxdy+\dfrac{N_{xy}}{4}\dfrac{\partial s}{\partial x}dxdy \\ +\dfrac{1}{4}\left(N_{xy}+\dfrac{\partial N_{xy}}{\partial x}dx\right)\dfrac{\partial s}{\partial x}dxdy-\dfrac{\rho gs(\mathbf{n}\cdot\mathbf{e}_2)dxdy}{2}(H-s)\end{array}\right\} \tag{A16}$$

$$\Sigma M_z=0=\left\{\left(N_{yx}+\frac{\partial N_{yx}}{\partial y}dy\right)dx\frac{dy}{2}+N_{yx}dx\frac{dy}{2}-\left(N_{xy}+\frac{\partial N_{xy}}{\partial x}dx\right)dy\frac{dx}{2}-N_{xy}dy\frac{dx}{2}\right\}. \tag{A17}$$

If products of differentials of order three are neglected, then equations (A15), (A16), and (A17) reduce to equations (16), (17) and (18), respectively. Equations (14), (15), (16), and (17) are substituted into equation (13) which then gives equation (19).

Downloaded 03 May 2010 to 171.66.16.248. Redistribution subject to ASME license or copyright; see http://www.asme.org/terms/Terms_Use.cfm

Dynamic Cylindrical Cavity Expansion of Compressible Strain-Hardening Materials

V. K. Luk
Mem. ASME

D. E. Amos

Sandia National Laboratories,
Albuquerque, NM 87185

We developed models for the dynamic expansion of cylindrical cavities from zero initial radii for compressible, elastic-plastic, rate-independent materials with power-law strain-hardening. Results from cavity-expansion models were used to derive perforation models to predict residual velocities and ballistic limits for rigid, conical-nose projectiles perforating strain-hardening target plates. We compared the numerical results from models for incompressible and compressible materials to show the effect of compressibility. To verify the models, we also compared the model predictions of residual velocities and ballistic limits with the data from terminal-ballistic experiments with tungsten projectiles impacting 5083-H131 aluminum armor plates at normal incidence. Very good agreement was obtained for impact velocities between 200 and 1,200 m/s and 12.7, 50.8, and 76.2-mm thick targets.

Introduction

Bishop, Hill, and Mott (1945) and Hill (1950) derived equations for the quasi-static expansion of spherical and cylindrical cavities and applied these solutions to estimate loads on conical-nose punches. Later, Goodier (1965) developed models to study the penetration of rigid spheres into metal targets. That problem was dynamic, and Goodier approximated the target response by using the spherical cavity-expansion solution for an incompressible, elastic-plastic material derived by Hill (1948). Recently, the spherical and cylindrical cavity-expansion solutions were used to model the penetration and perforation of rock (Forrestal, 1986), concrete (Luk and Forrestal, 1987), and metal targets (Rosenberg and Forrestal, 1988; Forrestal, Okajima, and Luk, 1988).

Kawahara (1986) recently developed a compression test for ductile metals to obtain stress-strain data to 100 percent true strain at rates to $10^2\ s^{-1}$. Figure 1 shows the stress-strain data and the power-law approximation for 5083-H131 aluminum armor plate at a strain rate of $10^0\ s^{-1}$. To improve the penetration and perforation models, we developed solutions for the dynamic expansion of cylindrical cavities from zero initial radii for compressible, elastic-plastic materials with power-law strain hardening. In an earlier study, similar cylindrical cavity-expansion models were developed for incompressible materials (Forrestal, Luk and Brar, 1990). We compared the numerical results from both studies to show the effect of compressibility.

We derived perforation models from the stress solutions of cavity-expansion models to predict residual velocities and ballistic limits for conical-nose projectiles perforating strain-hardening armor plates at normal incidence. The model predictions were compared with the data from terminal-ballistic experiments to verify the models.

Compressible Cylindrical Cavity-Expansion Model

A cylindrically symmetric cavity is expanded from zero initial radius at constant velocity V. As shown in Fig. 2, this

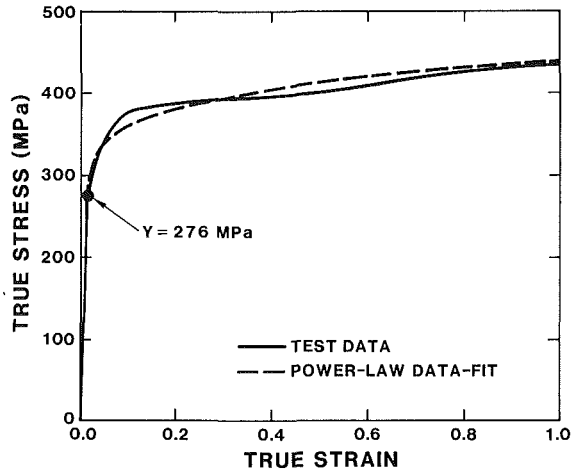

Fig. 1 Stress-strain data for the 5083-H131 aluminum and the power-law data-fit with $E = 70.3$ GPa, $\nu = 1/3$, $Y = 276$ MPa, and $n = 0.084$

Contributed by the Applied Mechanics Division of THE AMERICAN SOCIETY OF MECHANICAL ENGINEERS for presentation at the Joint Applied Mechanics/Bioengineering Conference, Ohio State University, Columbus, Ohio, June 16–19, 1991.

Discussion on this paper should be addressed to the Technical Editor, Leon M. Keer, The Technological Institute, Northwestern University, Evanston, IL 60208, and will be accepted until two months after final publication of the paper itself in the JOURNAL OF APPLIED MECHANICS. Manuscript received by the ASME Applied Mechanics Division, June 13, 1989; final revision, June 20, 1990.

Paper No. 91-APM-10.

Copyright © 1991 by ASME
Downloaded 03 May 2010 to 171.66.16.248. Redistribution subject to ASME license or copyright; see http://www.asme.org/terms/Terms_Use.cfm

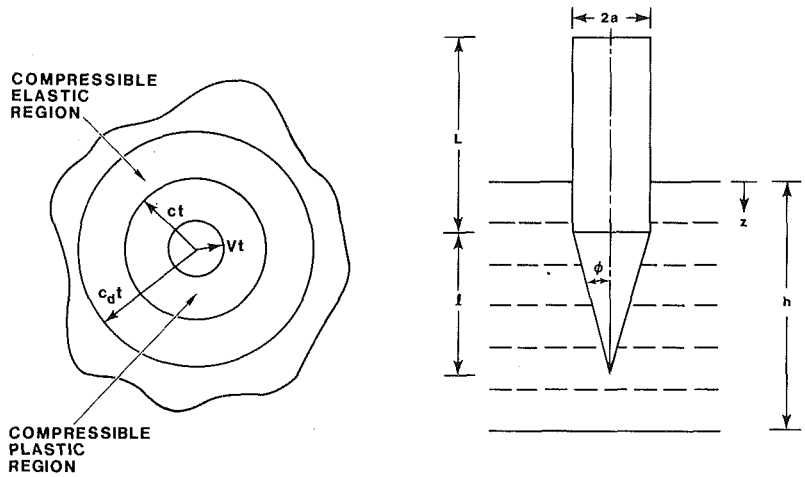

Fig. 2 Response regions and geometry of the problem

expansion produces plastic and elastic response regions. The plastic region is bounded by the radii $r = Vt$ and $r = ct$, where r is the radial Eulerian coordinate, t is time, and c is the elastic-plastic interface velocity. Similarly, the elastic region is bounded by $r = ct$ and $r = c_d t$, where c_d is the elastic, dilatational velocity.

Plastic Region. The equations of momentum and mass conservation in Eulerian coordinates with cylindrical symmetry are

$$\frac{\partial \sigma_r}{\partial r} + \frac{(\sigma_r - \sigma_\theta)}{r} = -\rho\left(\frac{\partial v}{\partial t} + v\frac{\partial v}{\partial r}\right) \tag{1a}$$

$$\rho_t \frac{\partial}{\partial r}[(r-u)^2] = 2\rho r \tag{1b}$$

where σ_r and σ_θ are the radial and circumferential components of Cauchy stress, measured positive in compression; ρ_t and ρ are the densities in the undeformed and deformed states; and u and v are the displacement and particle velocity in the radial direction, with outward motion considered positive.

Particle velocity and displacement are related by

$$v\left(1 - \frac{\partial u}{\partial r}\right) = \frac{\partial u}{\partial t}. \tag{2}$$

In cylindrical cavity-expansion problems, the plane-strain condition is implied, that is, $\epsilon_z = 0$, where ϵ_z is the logarithmic strain component in the axial direction. Following Hill (1949, 1950), we assume that the axial stress is equal to the average of radial and circumferential stresses, or

$$\sigma_z = (\sigma_r + \sigma_\theta)/2. \tag{3}$$

With the plane-strain condition and equation (3), the compressibility relation that incorporates the stress-strain relationship for compressible materials is expressed as

$$\frac{D\epsilon_r}{Dt} + \frac{D\epsilon_\theta}{Dt} = \frac{1}{2K}\left(\frac{D\sigma_r}{Dt} + \frac{D\sigma_\theta}{Dt}\right) \tag{4a}$$

$$\frac{D}{Dt} = \frac{\partial}{\partial t} + v\frac{\partial}{\partial r} \tag{4b}$$

where K is the bulk modulus, and ϵ_r and ϵ_θ are the radial and circumferential components of logarithmic strain. The logarithmic strain-displacement relations are defined as

$$\epsilon_r = \ln(1 - \partial u/\partial r) \tag{5a}$$

$$\epsilon_\theta = \ln(1 - u/r) \tag{5b}$$

where strain is measured positive in contraction.

Plastic flow is introduced by the method presented by Bishop, Hill, and Mott (1945) for the quasi-static problem. We first describe the material behavior from uniaxial compression tests and then generalize for the state of cylindrical symmetry. Figure 1 shows the stress-strain behavior of 5083-H131 aluminum from compression tests at a strain rate of $10^0 s^{-1}$. We use the modified Ludwik equation (Chakrabarty, 1987) as the power-law data-fit to describe the post-yield, uniaxial stress-strain data. Thus,

$$\sigma = E\epsilon \quad , \quad \sigma \le Y \tag{6a}$$

$$\sigma = Y(E\epsilon/Y)^n \quad , \quad \sigma > Y \tag{6b}$$

where σ is Cauchy stress (true stress), ϵ is logarithmic strain (true strain), E is Young's modulus, Y is yield stress, and n is the strain-hardening exponent. Figure 1 shows the power-law data-fit to 5083-H131 aluminum data.

Following the work by Bishop, Hill, and Mott (1945) on incompressible materials, we assume that for compressible materials, the octahedral shear stress τ_n is a definite function of the octahedral plastic shear strain γ_n^p for all strain configurations. For the uniaxial compression test, expressed in terms of material derivative D/Dt,

$$\frac{D\tau_n}{Dt} = ((2)^{1/2}/3)\frac{D\sigma}{Dt} \tag{7a}$$

$$\frac{D\gamma_n^p}{Dt} = (2)^{1/2}\left(\frac{D\epsilon}{Dt} - \frac{1}{E}\frac{D\sigma}{Dt}\right). \tag{7b}$$

The power-law stress-strain relation (6b) is differentiated to obtain

$$\frac{D\epsilon}{Dt} = \frac{1}{E_p(\sigma)}\frac{D\sigma}{Dt} \tag{8a}$$

where

$$E_p(\sigma) = nE(\sigma/Y)^{-(1-n)/n}. \tag{8b}$$

Substitution of equations 7(a), 7(b) into (8a) gives the universal relation between τ_n and γ_n^p

$$\frac{D\gamma_n^p}{Dt} = 3\left[\frac{1}{E_p(\sigma)} - \frac{1}{E}\right]\frac{D\tau_n}{Dt}. \tag{9}$$

For the cylindrical cavity-expansion problem, with the aid of plane-strain condition and equation (3), τ_n and γ_n^p are expressed as

$$\frac{D\tau_n}{Dt} = \left(\frac{D\sigma_r}{Dt} - \frac{D\sigma_\theta}{Dt}\right)/(6)^{1/2} \tag{10a}$$

$$\frac{D\gamma_n^p}{Dt} = 2(2/3)^{1/2}\left[\left(\frac{D\epsilon_r^p}{Dt} + \frac{D\epsilon_z^e}{Dt}\right)^2 - 3\left(\frac{D\epsilon_r^p}{Dt}\right)\left(\frac{D\epsilon_z^e}{Dt}\right)\right]^{1/2} \tag{10b}$$

Downloaded 03 May 2010 to 171.66.16.248. Redistribution subject to ASME license or copyright; see http://www.asme.org/terms/Terms_Use.cfm

where

$$\frac{D\epsilon_z^e}{Dt} = \frac{(1-2\nu)}{2E}\left(\frac{D\sigma_r}{Dt} + \frac{D\sigma_\theta}{Dt}\right) \tag{10c}$$

$$\frac{D\epsilon_r^p}{Dt} = \frac{D\epsilon_r}{Dt} - \frac{1}{2E}\left[(2-\nu)\frac{D\sigma_r}{Dt} - 3\nu\frac{D\sigma_\theta}{Dt}\right]. \tag{10d}$$

The superscripts e and p refer to the elastic and plastic components of physical quantities, respectively.

The plastic flow for the cylindrical cavity-expansion problem is obtained by substituting (10a,b) into (9). Thus,

$$\left[\frac{1}{E_p(\sigma)} - \frac{1}{E}\right]\left(\frac{D\sigma_r}{Dt} - \frac{D\sigma_\theta}{Dt}\right) = \frac{4}{3}\left[\left(\frac{D\epsilon_r^p}{Dt} + \frac{D\epsilon_z^e}{Dt}\right)^2 - 3\left(\frac{D\epsilon_r^p}{Dt}\right)\left(\frac{D\epsilon_z^e}{Dt}\right)\right]^{1/2} \tag{11a}$$

where

$$\sigma = (3)^{1/2}/2\,(\sigma_r - \sigma_\theta). \tag{11b}$$

Equation (11b) is obtained by equating (7a) and (10a). At the elastic-plastic interface, $\sigma = Y$, so from (11b), $(\sigma_r - \sigma_\theta) = 2Y/(3)^{1/2}$, which is the usual Mises yield criterion.

We complete the problem formulation by prescribing the conditions at the cavity surface and the elastic-plastic interface. The boundary condition at the cavity surface is

$$u(r = Vt) = Vt. \tag{12a}$$

The plastic and elastic regions of response at the interface in terms of particle velocity and radial and circumferential stresses are linked through the Hugoniot jump conditions that conserve mass and momentum at the interface. In addition, a boundary condition is obtained by satisfying the mass conservation equation (1b) at the interface. Thus,

$$\rho_t \frac{\partial}{\partial r}[(r-u)^2] - 2\rho_2 r,\ r = ct \tag{12b}$$

where ρ_2 is the density at the interface in the plastic region.

The cylindrical cavity-expansion problem is solved by introducing the similarity transformation

$$\xi = r/ct \tag{13a}$$

and the dimensionless variables

$$S_r = \sigma_r/K,\ S_\theta = \sigma_\theta/K,\ T = Y/K \tag{13b}$$

$$\bar{u} = u/ct,\ U = v/c,\ \gamma = V/c. \tag{13c}$$

After eliminating ρ from (1b) and v from (2), the momentum conservation (1a) in dimensionless form becomes

$$\frac{dS_r}{d\xi} + \frac{(S_r - S_\theta)}{\xi} = -\frac{\lambda^2(\xi - \bar{u})^3}{\xi\left(1 - \frac{d\bar{u}}{d\xi}\right)^2}\cdot\frac{d^2\bar{u}}{d\xi^2} \tag{14}$$

where $\lambda = c/c_p$ and $c_p^2 = K/\rho_t$. This equation can be further simplified by introducing a new variable

$$\omega = \xi - \bar{u} \tag{15}$$

that converts the Eulerian coordinates to the Lagrangian system. Equation (14) then becomes

$$\frac{dS_r}{d\xi} + \frac{(S_r - S_\theta)}{\xi} = \frac{\lambda^2\omega^3}{\xi\left(\frac{d\omega}{d\xi}\right)^2}\cdot\frac{d^2\omega}{d\xi^2}. \tag{16}$$

With the aid of logarithmic strain definitions in equations (5a), (5b), the compressibility relation (4a) can be expressed in dimensionless variables as

$$\frac{d^2\omega}{d\xi^2} - \frac{1}{\xi}\frac{d\omega}{d\xi} + \frac{1}{\omega}\left(\frac{d\omega}{d\xi}\right)^2 = \frac{1}{2}\frac{d\omega}{d\xi}\left(\frac{dS_r}{d\xi} + \frac{dS_\theta}{d\xi}\right). \tag{17}$$

We can convert the plastic flow (11a) to dimensionless form by first introducing an additional dimensionless variable

$$S = \sigma/K. \tag{18a}$$

With (11b) and (13b), S is found to be

$$S = (3)^{1/2}/2\,(S_r - S_\theta). \tag{18b}$$

Then the plastic flow (11a) becomes

$$\left[1 - \frac{1}{\bar{E}_p(S)}\right]\left(\frac{dS_r}{d\xi} - \frac{dS_\theta}{d\xi}\right) = \frac{4}{3}\left\{\left[\frac{3(1-2\nu)}{\frac{d\omega}{d\xi}}\frac{d^2\omega}{d\xi^2} - \frac{(1+\nu)}{(3)^{1/2}}\frac{dS}{d\xi}\right]^2 - 3\frac{d\bar{\epsilon}_z^e}{d\xi}\left[\frac{3(1-2\nu)}{\frac{d\omega}{d\xi}}\frac{d^2\omega}{d\xi^2} - \frac{d\bar{\epsilon}_r^e}{d\xi}\right]\right\}^{1/2} \tag{19a}$$

$$\bar{E}_p(S) = n(S/T)^{-(1-n)/n} \tag{19b}$$

$$\frac{dS}{d\xi} = (3)^{1/2}/2\left(\frac{dS_r}{d\xi} - \frac{dS_\theta}{d\xi}\right) \tag{19c}$$

$$\frac{d\bar{\epsilon}_z^e}{d\xi} = \frac{1}{2}(1-2\nu)\left(\frac{dS_r}{d\xi} + \frac{dS_\theta}{d\xi}\right) \tag{19d}$$

$$\frac{d\bar{\epsilon}_r^e}{d\xi} = \frac{1}{2}\left[(2-\nu)\frac{dS_r}{d\xi} - 3\nu\frac{dS_\theta}{d\xi}\right]. \tag{19e}$$

Now the problem has been formulated in terms of three ordinary differential equations, (16), (17), and (19a). With (13a) and (15), the boundary condition at the cavity surface (12a) transforms to

$$\omega(\xi = \gamma) = 0 \tag{20a}$$

and the boundary condition at the interface (12b) becomes

$$\omega(\xi = 1)\frac{d\omega}{d\xi}(\xi = 1) = \frac{\rho_2}{\rho_t}. \tag{20b}$$

In addition, there are three associated conditions at the interface

$$U(\xi = 1) = U_2 \tag{20c}$$

$$S_r(\xi = 1) = (S_r)_2 \tag{20d}$$

$$S_\theta(\xi = 1) = (S_\theta)_2 \tag{20e}$$

where U_2, $(S_r)_2$, and $(S_\theta)_2$ are particle velocity and radial and circumferential stresses at the interface in the plastic region, respectively. They are linked to their counterparts in the elastic region through the Hugoniot jump conditions. In equation (20c), $U(\xi = 1)$ can be expressed in terms of ω and $\frac{d\omega}{d\xi}$, resulting in the following expression:

$$\omega(\xi = 1) = (1 - U_2)\frac{d\omega}{d\xi}(\xi = 1). \tag{20f}$$

Interface Conditions At the elastic-plastic interface, $\sigma_r - \sigma_\theta = 2Y/(3)^{1/2}$, and the material has not strained to large deformation. Therefore, a linear hydrostat provides a good approximation to describe the material behavior at the interface. Thus,

$$P_2 = K(1 - \rho_t/\rho_2) \tag{21a}$$

$$P_1 = K(1 - \rho_t/\rho_1) \tag{21b}$$

where P is hydrostatic pressure. Subscripts 2 and 1 refer to quantities at the interface in the plastic and elastic regions, respectively.

The Hugoniot jump conditions that conserve mass and mo-

Downloaded 03 May 2010 to 171.66.16.248. Redistribution subject to ASME license or copyright; see http://www.asme.org/terms/Terms_Use.cfm

mentum across the interface link the radial stresses and particle velocities in the plastic and elastic regions. As presented by Forrestal (1986), these physical quantities can be written in dimensionless variables as

$$U_2 = 1 - (\rho_1/\rho_2)(1 - U_1) \tag{22a}$$

$$(S_r)_2 = (S_r)_1 + \lambda^2(\rho_1/\rho_t)(1 - U_1)(U_2 - U_1). \tag{22b}$$

The Mises yield criterion, $\sigma_r - \sigma_\theta = 2Y/(3)^{1/2}$, holds on either side of the interface. However, $P = (\sigma_r + \sigma_\theta)/2$ on the plastic side of the interface, and $P = \nu(\sigma_r + \sigma_\theta)$ on the elastic side. With (21*a*, *b*), the dimensionless radial stresses are expressed as

$$(S_r)_2 = 1 - \rho_t/\rho_2 + T/(3)^{1/2} \tag{22c}$$

$$(S_r)_1 = 1.5(1 - \rho_t/\rho_1)/(1 + \nu) + T/(3)^{1/2}. \tag{22d}$$

After eliminating ρ_1 and ρ_2 from equations (22*a*)-(22*d*) and linearizing, we get

$$U_2 = U_1 + \frac{(1 - 2\nu)[(S_r)_1 - T/(3)^{1/2}]}{3(1 - \lambda^2)} \tag{23a}$$

$$(S_r)_2 = (S_r)_1 + \frac{(1 - 2\nu)\lambda^2[(S_r)_1 - T/(3)^{1/2}]}{3(1 - \lambda^2)}. \tag{23b}$$

With the Mises yield criterion and equation (23*b*), $(S_\theta)_2$ is found to be

$$(S_\theta)_2 = (S_r)_1 - \frac{2T}{(3)^{1/2}} + \frac{(1 - 2\nu)\lambda^2[(S_r)_1 - T/(3)^{1/2}]}{3(1 - \lambda^2)}. \tag{23c}$$

From (22*c*) and (23*b*), we get an expression for ρ_2/ρ_t needed in (20*b*)

$$\frac{\rho_2}{\rho_t} = \frac{3(1 - \lambda^2)}{3(1 - \lambda^2) - [(S_r)_1 - T/(3)^{1/2}][3 - 2(1 + \nu)\lambda^2]}. \tag{23d}$$

Elastic Region. Forrestal (1986) and Crozier and Hunter (1970) derived equations for the response in the elastic region. For the Mises yield criterion,

$$S_r(\xi) = \frac{T\zeta^2}{(3)^{1/2}(1 - 2\nu)(1 - \zeta^2)^{1/2}} \left\{ \frac{(1 - 2\nu)(1 - \zeta^2\xi^2)^{1/2}}{\zeta^2\xi^2} + \ln\left[\frac{1 + (1 - \zeta^2\xi^2)^{1/2}}{\zeta\xi}\right] \right\}, \quad 1 \le \xi < 1/\zeta \tag{24a}$$

where

$$\zeta = c/c_d,\ c_d^2 = E(1 - \nu)/[\rho_t(1 + \nu)(1 - 2\nu)] \tag{24b}$$

and $(S_r)_1 = S_r(\xi = 1)$.
At the elastic-plastic interface,

$$U_1 = \frac{2T(1 + \nu)}{3(3)^{1/2}(1 - 2\nu)} \tag{25a}$$

$$\bar{u}_1 = \frac{T(1 + \nu)}{3(3)^{1/2}(1 - 2\nu)} \times \left\{ 1 - \frac{\zeta^2}{(1 - \zeta^2)^{1/2}} \ln\left[\frac{1 + (1 - \zeta^2)^{1/2}}{\zeta}\right] \right\}. \tag{25b}$$

Response Equations. The interface conditions in (23*a*)-(23*d*) link the elastic solutions in (24*a*) (by setting $\xi = 1$) and (25*a*) to the boundary conditions in (20*a*)-(20*f*). The resulting equations provide the necessary conditions to solve the ordinary differential equations in (16), (17), and (19*a*) numerically. The numerical solution procedures are described in the next subsection.

Numerical Computations. To facilitate numerical computations, (16), (17), and (19*a*) are rewritten into a form suitable for numerical integrations. First, we introduce a new variable

$$y = \frac{d\omega}{d\xi}. \tag{26}$$

Then (17) becomes

$$\frac{dy}{d\xi} = \frac{d^2\omega}{d\xi^2} = R_1 + R_2\frac{dS_r}{d\xi} + R_3\frac{dS_\theta}{d\xi} \tag{27a}$$

where

$$R_1 = y(1/\xi - y/\omega),\ R_2 = R_3 = y/2 \tag{27b}$$

and (16) reduces to

$$\frac{dS_r}{d\xi} = Q_1 + Q_2\frac{dS_\theta}{d\xi} \tag{28a}$$

where

$$Q_1 = \frac{1}{\xi}\left[\frac{\lambda^2\omega^3}{\xi y} - \lambda^2\omega^2 - (S_r - S_\theta)\right] \Bigg/ \left(1 - \frac{\lambda^2\omega^3}{2\xi y}\right) \tag{28b}$$

$$Q_2 = \frac{\lambda^2\omega^2}{2\xi y} \Bigg/ \left(1 - \frac{\lambda^2\omega^3}{2\xi y}\right). \tag{28c}$$

After squaring (19*a*) and using (28*a*), we get the following expression in terms of $dS_\theta/d\xi$

$$\left(W_1 + W_2\frac{dS_\theta}{d\xi}\right)^2 = \left(W_3 + W_4\frac{dS_\theta}{d\xi}\right)^2 - \left(W_5 + W_6\frac{dS_\theta}{d\xi}\right)\left(W_7 + W_8\frac{dS_\theta}{d\xi}\right) \tag{29a}$$

where

$$W_1 = \frac{3}{4}\left[1 - \frac{1}{\bar{E}_p(S)}\right]Q_1$$

$$W_2 = \frac{3}{4}\left[1 - \frac{1}{\bar{E}_p(S)}\right](Q_2 - 1)$$

$$W_3 = 3(1 - 2\nu)\left(\frac{1}{\xi} - \frac{y}{\omega}\right) + \frac{1}{2}(2 - 7\nu)Q_1$$

$$W_4 = \frac{1}{2}(2 - 7\nu)Q_2 + \frac{1}{2}(4 - 5\nu)$$

$$W_5 = \frac{3}{2}(1 - 2\nu)Q_1$$

$$W_6 = \frac{3}{2}(1 - 2\nu)(Q_2 + 1)$$

$$W_7 = 3(1 - 2\nu)\left(\frac{1}{\xi} - \frac{y}{\omega}\right) + \frac{1}{2}(1 - 5\nu)Q_1$$

$$W_8 = \frac{1}{2}(1 - 5\nu)Q_2 + \frac{3}{2}(1 - \nu). \tag{29b}$$

The solution to this quadratic equation that makes the left side of (19*a*) positive is

$$\frac{dS_\theta}{d\xi} = \frac{-H_2 + (H_2^2 - 4H_1H_3)^{1/2}}{2H_1} \tag{30a}$$

where

$$H_1 = W_2^2 - W_4^2 + W_6W_8$$
$$H_2 = 2(W_1W_2 - W_3W_4) + W_6W_7 + W_5W_8$$
$$H_3 = W_1^2 - W_3^2 + W_5W_7. \tag{30b}$$

With the introduction of replacements,

$$y_1(\xi) = S_r(\xi),\ y_2(\xi) = S_\theta(\xi),\ y_3(\xi), = \omega(\xi),$$

$$y_4(\xi) = \frac{d\omega}{d\xi}(\xi) = \omega'(\xi), \tag{31}$$

equations (26), (27*a*), (28*a*), and (30*a*) yield a system of differential equations in a vector form

Downloaded 03 May 2010 to 171.66.16.248. Redistribution subject to ASME license or copyright; see http://www.asme.org/terms/Terms_Use.cfm

$$\frac{dy_1}{d\xi} = Q_1 + Q_2 \frac{dy_2}{d\xi} \tag{32a}$$

$$\frac{dy_2}{d\xi} = \frac{-H_2 + (H_2^2 - 4H_1H_3)^{1/2}}{2H_1} \tag{32b}$$

$$\frac{dy_3}{d\xi} = y_4 \tag{32c}$$

$$\frac{dy_4}{d\xi} = y_4\left[\frac{1}{\xi} - \frac{y_4}{y_3} + \frac{1}{2}\left(\frac{dy_1}{d\xi} + \frac{dy_2}{d\xi}\right)\right]. \tag{32d}$$

To solve (32*a*)–(32*d*) numerically, the boundary conditions discussed in the preceding subsection are revised to incorporate the replacements in (31).

As discussed by Luk, Forrestal, and Amos (1991), the thrust of the numerical procedure is to solve equations (32*a*)–(32*d*) not only for S_r, S_θ, and ω, but also for γ in (20*a*). Thus, we select a value of λ, $0<\lambda<1$ and start a backward integration from $\xi=1$ into the region $0\le\gamma\le\xi\le1$ with the boundary conditions prescribed at $\xi=1$. When $y_3=\omega=0$, γ is known and the expansion velocity $V=\gamma c$ can be computed.

The numerical behavior and difficulties encountered in (32*a*)–(32*d*) are basically the same as those discussed by Luk, Forrestal, and Amos (1991). While the integration proceeds normally for most of the range, the system becomes progressively harder to integrate because ω' becomes very large as $\omega\to0$. It is therefore desirable to use a state-of-the-art integrator that can monitor local error and adjust the integration step size accordingly. The SLATEC library code DEABM (Adams-Bashforth method) developed by Shampine and Watts (1980) is used because of the robust nature of the code. When the requested output step becomes too large (as signaled by DEABM), the problem is restarted at the last successful output point, and the output step is cut by a factor of 10. This process is repeated to refine the value of γ and obtain an estimate of γ with an accuracy on the order of 10^{-5}. The SLATEC library is more fully described by Cowell (1984) and Vandevender (1984).

Incompressible Cylindrical Cavity-Expansion Model

Forrestal, Luk, and Brar (1991) derived the response equations for the incompressible model. We summarize these results in the following. The radial stress in the plastic region is given by

$$\frac{\sigma_r(\xi)}{Y} = \frac{1}{(3)^{1/2}}\left\{1+\left[\frac{E}{(3)^{1/2}Y}\right]^n I(\xi)\right\} + \frac{\rho_t V^2}{2Y}\left\{\frac{1}{(1-\nu)(1-\alpha^2)^{1/2}}\ln\left[\frac{1+(1-\alpha^2)^{1/2}}{\alpha}\right] + \gamma^2 - 2\ln\xi - \frac{\gamma^2}{\xi^2}\right\} \tag{33a}$$

where

$$\gamma = \frac{V}{c} = \left[\frac{2(1+\nu)Y}{(3)^{1/2}E}\right]^{1/2} \tag{33b}$$

$$\alpha = \left[\frac{(3)^{1/2}(1-2\nu)}{2(1-\nu)}\right]^{1/2}[(\rho_t/Y)^{1/2}V] \tag{33c}$$

$$I(\xi) = \int_{1-(\gamma/\xi)^2}^{1-\gamma^2} \frac{(-\ln x)^n}{(1-x)}\,dx. \tag{33d}$$

The perforation model requires the radial stress at the cavity surface. An approximate expression for the quantity is

$$S_i = \frac{\sigma_r(\xi=\gamma)}{Y} = A_i + B_i\left(\frac{\rho_t}{Y}\right)V^2 \tag{34a}$$

where

$$A_i = \frac{1}{(3)^{1/2}}\left\{1+\left[\frac{E}{(3)^{1/2}Y}\right]^n I(\xi=\gamma)\right\} \tag{34b}$$

$$B_i = \frac{1}{2}[(1+\ln 2)/(1-\nu) + \gamma^2 - 2\ln\gamma - 1]. \tag{34c}$$

We need the response equations from the incompressible model to compare with those from the compressible model to show the effect of compressibility.

Perforation Models

A rigid, long-rod projectile with conical nose (Fig. 2) impacts a uniform target at normal incidence with velocity V_i and proceeds to penetrate at rigid-body velocity V_z. As shown in Fig. 2, the cylindrical cavity-expansion approximation idealizes the target as thin, independent layers normal to the penetration direction and simplifies the analysis to one-dimensional radial motion. The conical nose with apical angle 2ϕ radially expands a layer of target material and opens a cavity from zero initial radius at radial velocity V, where $V=V_z\tan\phi$.

Much of the previous work on perforation models of incompressible materials by Forrestal, Luk and Brar (1990) is used in this study. The only exception here is that to obtain the closed-form perforation equation, we have to curve fit the radial stress at the cavity surface with the expression (Forrestal, Okajima, and Luk, 1988)

$$S_c = \frac{\sigma_r(\xi=\gamma)}{Y} = A_c + B_c\left(\frac{\rho_t}{Y}\right)V^2. \tag{35}$$

Here the radial stress is normalized by Y to facilitate comparison of radial stress from incompressible models. In equation (35), A_c refers to the quasi-static expansion of cylindrical cavities from zero initial radii and is the value of S_c for $V\to0$. Therefore, B_c is the only term that needs to be adjusted to fit the cavity-expansion results.

As presented by Forrestal, Luk, and Brar (1990), the axial force on conical nose is

$$F_z = \pi a^2 Y(1+\mu/\tan\phi)\left[A_c + B_c\left(\frac{\rho_t}{Y}\right)\tan^2\phi V_z^2\right] \tag{36}$$

where a and ϕ are defined in Fig. 2 and μ is the sliding-interface friction coefficient. Proceeding with the equation of motion for the projectile, we get the following expressions for the ballistic limit V_{bl} and the residual velocity V_r

$$V_{bl} = \left[\left(\frac{Y}{\rho_t}\right)\left(\frac{A_c}{B_c\tan^2\phi}\right)\right]^{1/2}\left\{\exp\left[2\left(\frac{h}{L+l/3}\right)\cdot\times\left(\frac{\rho_t}{\rho_p}\right)B_c\tan\phi(\tan\phi+\mu)\right]-1\right\}^{1/2} \tag{37a}$$

$$V_r = \left(V_i^2 - V_{bl}^2\right)^{1/2}\exp\left[-\left(\frac{h}{L+l/3}\right)\times\left(\frac{\rho_t}{\rho_p}\right)B_c\tan\phi\,(\tan\phi+\mu)\right] \tag{37b}$$

where h, L, and l are defined in Fig. 2, and ρ_p is the density of projectile material.

Terminal-Ballistic Experiments

A 20-mm, smooth-bore power gun launched the 94 percent tungsten alloy projectiles to incident velocities between 200 and 1,200 m/s. The tungsten alloy has a density $\rho_p=18{,}500$ kg/m^3. The 0.026 kg projectile shown in Fig. 2 has the dimensions: $L=20.70$ mm, $l=14.83$ mm, and $2a=8.31$ mm. Terminal-ballistic experiments were conducted with 12.7, 50.8, and 76.2-mm thick 5083-H131 aluminum armor plates. Experimental data in terms of incident versus residual velocities for each of the three plate thicknesses were reported by Forrestal, Luk, and Brar (1990).

The large-strain compression tests developed by Kawahara (1986) were used to obtain stress-strain data for the 12.7 and

Downloaded 03 May 2010 to 171.66.16.248. Redistribution subject to ASME license or copyright; see http://www.asme.org/terms/Terms_Use.cfm

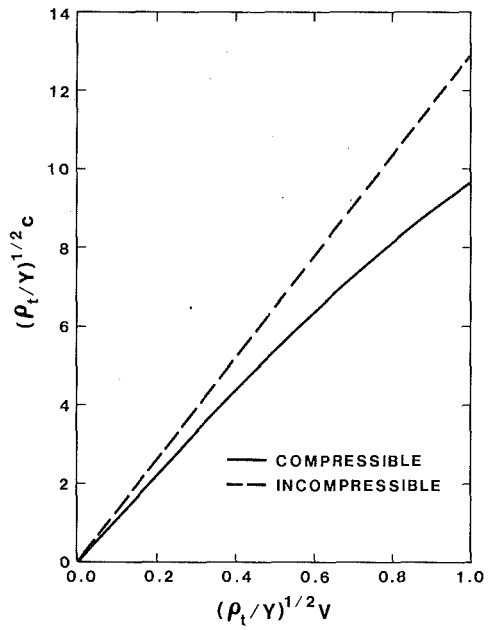

Fig. 3 Elastic-plastic interface velocity versus cavity-expansion velocity

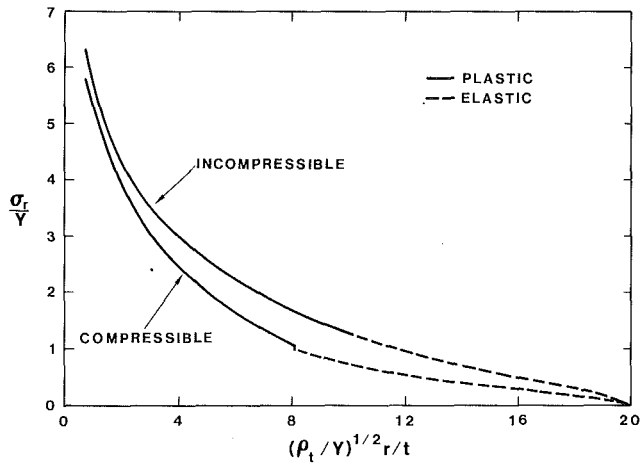

Fig. 4 Radial stress profiles for $(\rho_t/Y)^{1/2}V = 0.79$

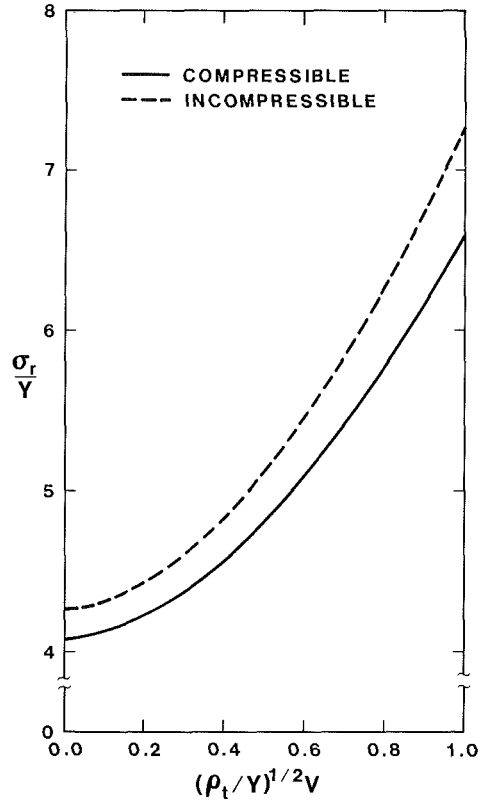

Fig. 5 Comparison of radial stresses on the cavity surface versus cavity-expansion velocity for incompressible and compressible models

50.8-mm thick plates. The compression tests were conducted at strain rates of 10^{-2} and $10^{0}\,s^{-1}$. All stress-strain curves were in close agreement, and Fig. 1 shows a curve for a specimen from the 50.8-mm thick plate at $10^{0}\,s^{-1}$.

Numerical Results and Comparison With Measurements

In Fig. 1, we compare the post-yield, power-law data-fit (equation (6*b*)) and the stress-strain data for 5083-H131 aluminum at a strain rate of $10^{0}\,s^{-1}$. The material parameters for this aluminum are taken as $\rho_t = 2{,}660$ kg/m^3, $E = 70.3$ GPa, $Y = 276$ MPa, and $\nu = 1/3$. By selecting the strain-hardening exponent $n = 0.084$, Fig. 1 shows that the power-law data-fit is in close agreement with the stress-strain data.

Figure 3 shows the elastic-plastic interface velocities c versus the cavity-expansion velocity V. The interface velocity is given by (33*b*) for the incompressible model and computed numerically for the compressible model.

The radial stress profiles from the incompressible and the compressible models are compared in Fig. 4 for $(\rho_t/Y)^{1/2}V = 0.79$ ($V = 254.5$ m/s). As discussed by Forrestal, Luk, and Brar (1990), the radial stress is continuous at the interface ($(\rho_t/Y)^{1/2}r/t = 10.2$) for the incompressible model. However, there is a small jump in radial stress at the interface ($(\rho_t/Y)^{1/2}r/t = 8.0$) for the compressible model. This stress jump is initiated by the assumption on the axial stress in plastic region in (3). It should be mentioned that for the incompressible model, the material is assumed incompressible in the plastic region but compressible in the elastic region. Therefore, both models have continuous radial stress at the elastic wave front at $(\rho_t/Y)^{1/2}r/t = 19.5$. As shown in Fig. 4, the incompressible model predicts higher stresses than the compressible model.

As previously mentioned, the perforation models require the radial stress at the cavity surface versus cavity-expansion velocity. Therefore, we plot the radial stresses at the cavity surface from the incompressible and the compressible models in Fig. 5. As expected, predictions for the two models diverge as cavity-expansion velocity increases.

In the problem formulation, we relate the radial stresses and particle velocities at the interface in plastic and elastic regions, but there is no requirement on particle displacement at the interface. To provide an additional check on the numerical solutions, we calculated particle displacements at the interface to ensure material continuity. The displacements agreed to within the assigned accuracy.

To facilitate computations in the perforation model, we curve fit the radial stress at the interface in Fig. 5 with the expression in equation (35). We found the best fit curve with $A_c = 4.090$ and $B_c = 2.610$. Then the ballistic limit V_{bl} and the residual velocity V_r were calculated from (37*a*), (37*b*) for the projectile defined in Fig. 2 and the three target thicknesses. As discussed for Forrestal, Luk, and Brar (1990), we used the sliding-interface friction coefficient $\mu = 0.02$. Figure 6 compares predicted and measured residual velocity for the 12.7, 50.8, and 76.2-mm thick targets with $\mu = 0.0$ and 0.02. The model predictions are in very good agreement with measurements for all three plate thicknesses. This shows an improvement over the predictions from the incompressible model in Fig. 7. As shown in Fig. 7, the incompressible model provides

Downloaded 03 May 2010 to 171.66.16.248. Redistribution subject to ASME license or copyright; see http://www.asme.org/terms/Terms_Use.cfm

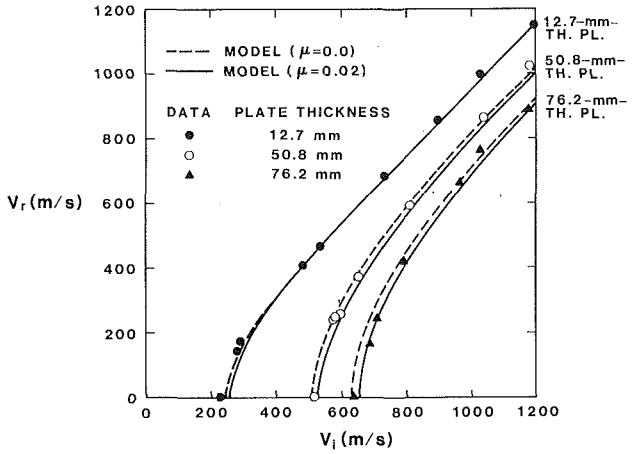

Fig. 6 Comparison of predicted and measured residual velocity for the compressible model

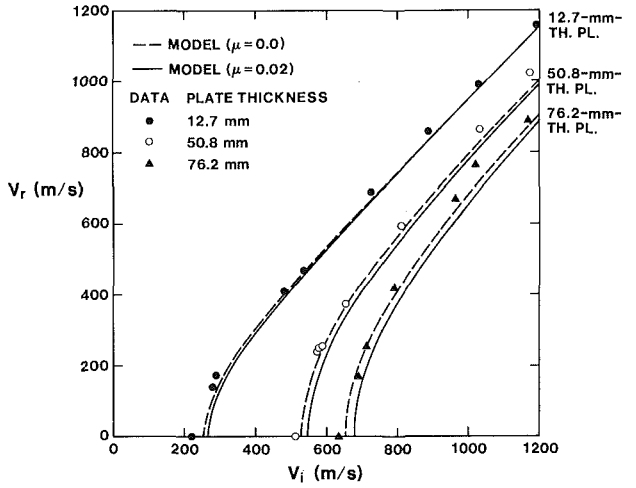

Fig. 7 Comparison of predicted and measured residual velocity for the incompressible model

less accurate predictions for thicker plates and impact velocities much higher than the ballistic-limit velocity.

In Fig. 8, we compare predicted and measured ballistic-limit velocity versus target-plate thickness. As can be seen, very good agreement is achieved.

Summary

We used power-law strain hardening to model the dynamic expansion of cylindrical cavities from zero initial radii for compressible, elastic-plastic, rate-independent materials. Perforation models were also developed to predict residual velocities and ballistic limits for rigid, conical-nose projectiles perforating strain-hardening target plates. Model predictions agreed very closely with measurements from terminal-ballistic experiments with tungsten projectiles and 5083-H131 aluminum armor plates. Comparing the compressible results with those from the incompressible model, we showed that the compressible model provides improved predictions for thicker target plates and impact velocities much higher than the ballistic-limit velocity.

Acknowledgments

This work was supported by the U.S. Department of Energy. The authors thank Dr. M. J. Forrestal for the valuable discussions in model development and Dr. W. A. Kawahara for the data in Fig. 1.

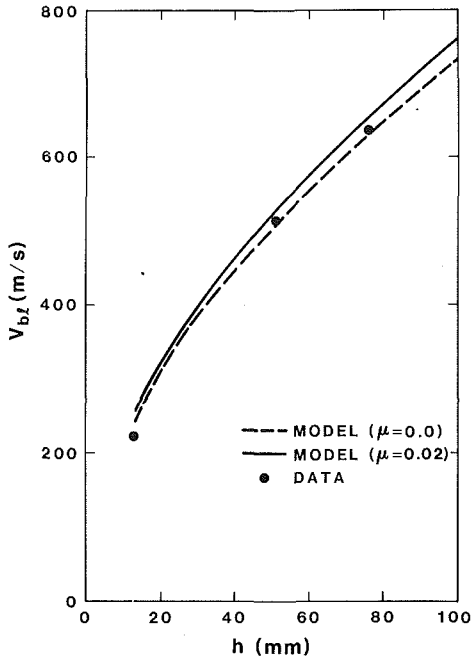

Fig. 8 Comparison of predicted and measured ballistic-limit velocity for the compressible model

References

Bishop, R. F., Hill, R., and Mott, N. F., 1945, "The Theory of Indentation and Hardness Tests," *Proceedings of the Physical Society*, Vol. 57, Part 3, pp. 147–159.

Chakrabarty, J., 1987, *Theory of Plasticity*, McGraw-Hill, New York, p. 12.

Cowell, W. R., 1984, *Sources and Development of Mathematical Software*, Prentice-Hall, New York.

Crozier, R. J. M., and Hunter, S. C., 1970, "Similarity Solution for the Rapid Uniform Expansion of a Cylindrical Cavity in a Compressible Elastic-Plastic Solid," *Quarterly Journal of Mechanics and Applied Mathematics*, Vol. 23, Part 3, pp. 349–363.

Forrestal, M. J., 1986, "Penetration into Dry Porous Rock," *International Journal of Solids and Structures*, Vol. 22, No. 12, pp. 1485–1500.

Forrestal, M. J., Okajima, K., and Luk, V. K., 1988, "Penetration of 6061-T651 Aluminum Targets with Rigid Long Rods," ASME JOURNAL OF APPLIED MECHANICS, Vol. 55, pp. 755–760.

Forrestal, M. J., Luk, V. K., and Brar, N. S., 1990, "Perforation of Aluminum Armor Plates with Conical-Nose Projectiles," *Mechanics of Materials*, Vol. 10, No. 1-2, pp. 97–105.

Goodier, J. N., 1965, "On the Mechanics of Indentation and Cratering in Solid Targets of Strain-Hardening Metal by Impact of Hard and Soft Spheres," *Proceedings of the 7th Symposium on Hypervelocity Impact*, Vol. III, pp. 215–259, AIAA, New York.

Hill, R., 1948, "A Theory of Earth Movement Near a Deep Underground Explosion," Memo No. 12–48, Armament Research Establishment, Fort Halstead, Kent, U.K.

Hill, R., 1949, "General Features of Plastic-Elastic Problems as Exemplified by Some Particular Solutions," ASME JOURNAL OF APPLIED MECHANICS, Vol. 16, pp. 295–300.

Hill, R., 1950, *The Mathematical Theory of Plasticity*, Oxford University Press, London.

Kawahara, W. A., 1986, "Compression Materials Testing at Low to Medium Strain Rates," Paper No. 86-WA/MATS-15, presented at the ASME Winter Annual Meeting, Anaheim, CA, Dec. 7–12, 1986.

Luk, V. K., and Forrestal, M. J., 1987, "Penetration into Semi-Infinite Reinforced-Concrete Targets with Spherical and Ogival Nose Projectiles," *International Journal of Impact Engineering*, Vol. 6, No. 4, pp. 291–301.

Luk, V. K., Forrestal, M. J., and Amos, D. E., 1991, "Dynamic Spherical Cavity Expansion of Strain-Hardening Materials," submitted to ASME JOURNAL OF APPLIED MECHANICS, Vol. 58, pp. 1–6.

Rosenberg, Z., and Forrestal, M. J., 1988, "Perforation of Aluminum Plates with Conical-Nosed Rods—Additional Data and Discussion," ASME JOURNAL OF APPLIED MECHANICS, Vol. 55, No. 1, pp. 236–238.

Shampine, L. F., and Watts, H. A., 1980, "DEPAC—Design of a User Oriented Package of ODE Solvers," SAND 79-2374, Sandia National Laboratories, Albuquerque, N. Mex.

Vandevender, W., 1984, "The SLATEC Mathematical Subprogram Library, Version 2.0," SAND 84-0281, Sandia National Laboratories, Albuquerque, N. Mex.

Downloaded 03 May 2010 to 171.66.16.248. Redistribution subject to ASME license or copyright; see http://www.asme.org/terms/Terms_Use.cfm

C. Y. Zhu
Graduate Research Assistant.

A. Shukla
Professor,
Mem. ASME

M. H. Sadd
Professor,
Mem. ASME

Dynamic Photomechanics Laboratory,
Department of Mechanical Engineering
and Applied Mechanics,
University of Rhode Island,
Kingston, RI 02881

Prediction of Dynamic Contact Loads in Granular Assemblies

An experimental-numerical hybrid technique has been developed to predict the intergranular contact load transfer in granular media subjected to explosive loading. The granular media were simulated by assemblies of circular disks in contact. The peak contact load transfer coefficients (i.e., the ratio of the maximum output contact load to the input contact load as a function of the contact angles) of a given particle were obtained through controlled experimental studies. These coefficients, along with the principle of superposition, were then used to predict the peak contact loads in several regular as well as irregular assemblies of disks. The predicted results compared favorably with the experimental data for several different assemblies.

Introduction

Knowledge of wave propagation in granular materials is important in many branches of engineering. These include powder metallurgy, transducer design, earthquake engineering, and soil mechanics. The study of granular media from a microstructure point of view started many years ago with research modeling granular media as aggregate assemblies of disks or spheres. Early work by Iida (1939), Takahashi and Sato (1949), Hughes and Cross (1952), Gassman (1951), and Brandt (1952) employed a normal granular contact force concept, while Duffy and Mindlin (1957) included tangential forces as well. This initial work investigated wave propagation velocity as a function of confining pressure, particle size, and aggregate geometry. Important new work has been done by Oda (1978) and Nemat-Nasser and Mehrabadi (1983) in the development of so-called fabric tensor theories for granular materials. The development of distributed body theory by Goodman and Cowin (1972) has also proved useful in modeling such materials as demonstrated by Sadd and Hossain (1988). Computational work in modeling large aggregate assemblies of particles has been carried out by using the distinct element method of Cundall and Strack (1979) (see also Sadd et al. (1989)).

With regard to experimental techniques, the method of photoelasticity provides whole field data during an experiment and makes it possible to determine the contact load between neighboring granular particles. Drescher and de Josselin de Jong (1972), and Durelli and Wu (1983) have employed photoelasticity to study granular media behavior under static loading. Shukla et al. (1986, 1987a, 1988) have used photoelasticity combined with high-speed photography to investigate wave propagation phenomena due to explosive loading in an assembly of disks. This experimental method provides sufficient information to determine wave speeds and dynamic contact loads in different kinds of granular packings under various loading conditions.

An experimental-numerical hybrid technique for analyzing the dynamic load transfer in a granular medium is discussed in this paper. In the experiments, dynamic loading was achieved by detonating a small charge of PETN in a specially designed charge holder, which was mounted at the top of the experimental model. High-speed photography and dynamic photoelasticity were used to experimentally determine the peak contact loads between all the particles. The granular medium was simulated by particle assemblies of circular disks in various packing geometries. It has been shown by Shukla et al. (1988) that for these geometries, at most of the contact points the tangential load is less than 15 percent of the normal load. Thus, in this investigation only normal contact loads were considered. A series of calibration experiments of controlled microstructure were conducted in which the locations of contacts between the granules were systematically varied. The data obtained from each experiment was analyzed to calculate the dynamic contact loads and these were then used to determine the load transfer coefficient for a given disk. This coefficient was obtained for several arrangements and number of contacts per disk. With various load transfer coefficients determined, a numerical scheme was developed using the experimental data and based on the principle of superposition. Predictions were made of the intergranular contact loadings for several model assemblies with different microstructures. Numerical predictions were compared with experimental data for these models. The predicted results compared fairly well with the photoelastic experimental data for systematic arrangements, whereas the comparison was marginal for an irregular packing.

Contributed by the Applied Mechanics Division of THE AMERICAN SOCIETY OF MECHANICAL ENGINEERS for publication in the JOURNAL OF APPLIED MECHANICS.

Discussion on this paper should be addressed to the Technical Editor, Prof. Leon M. Keer, The Technological Institute, Northwestern University, Evanston, IL 60208, and will be accepted until two months after final publication of the paper itself in the JOURNAL OF APPLIED MECHANICS. Manuscript received by the ASME Applied Mechanics Division, Nov. 6, 1989; final revision, Feb. 26, 1990.

Copyright © 1991 by ASME
Downloaded 03 May 2010 to 171.66.16.248. Redistribution subject to ASME license or copyright; see http://www.asme.org/terms/Terms_Use.cfm

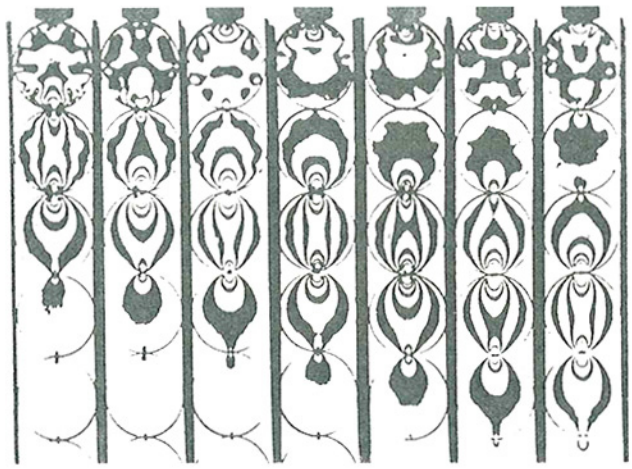

Fig. 1(*a*) Dynamic isochromatic fringes obtained in a single chain arrangement

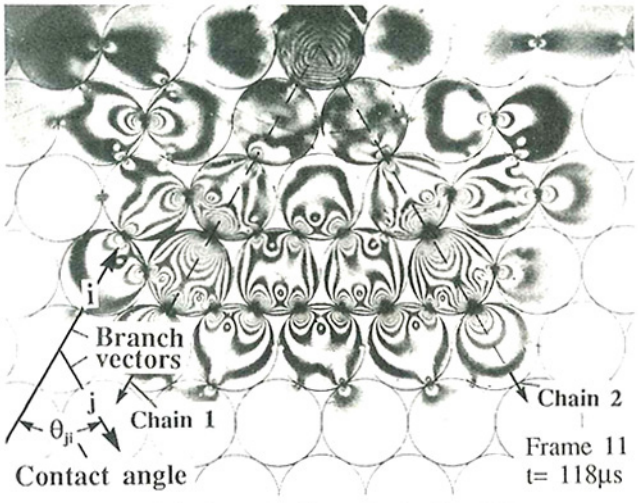

Fig. 1(*b*) Dynamic isochromatic fringes obtained in a HCP arrangement

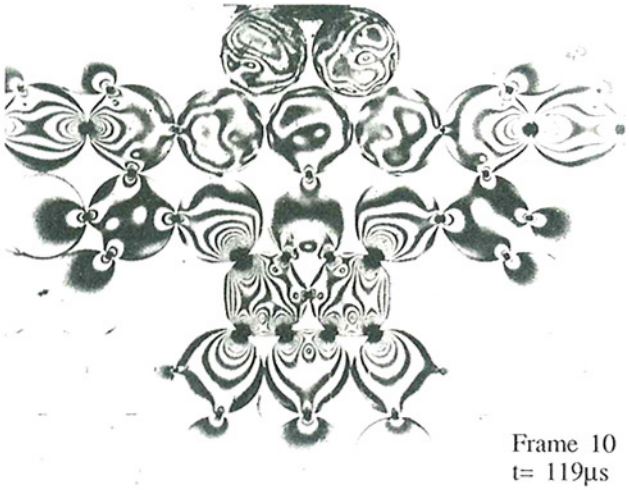

Fig. 1(*c*) Dynamic isochromatic fringes obtained in a HHCP arrangement

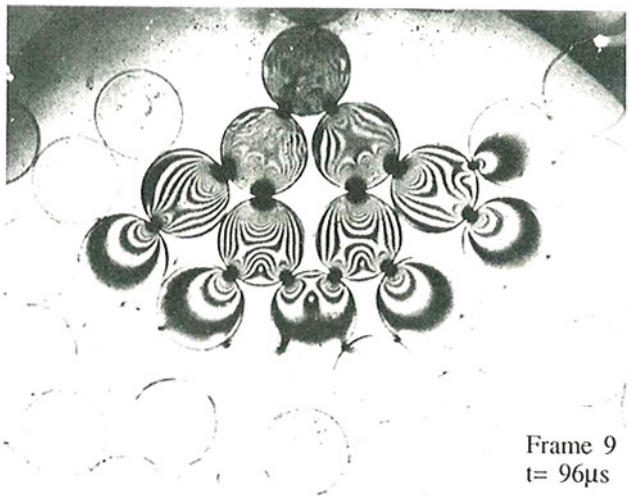

Fig. 1(*d*) Dynamic isochromatic fringes obtained in an irregular arrangement

Load Transfer Formulation

The microstructure of a granular medium can be characterized by branch vectors drawn between the mass centers of adjacent disks as shown in Fig. 1(*b*). The angle θ is that between any two neighboring branch vectors and is denoted as the contact angle. It has been shown by Shukla et al. (1987b) that the dynamic load transfer phenomena in granular media are strongly dependent on the contact angles made by the adjacent branch vectors. Experimental fringe patterns from their work obtained in a hexagonal closed packing (HCP) granular assembly are shown in Fig. 1(*b*). Normal contact load as a function of time of a typical disk in this HCP model are shown in Fig. 2. Wave energy entering at point 1 shows maximum transfer across point 2 which is directly ahead of point 1. Although contact points 3 and 4 make the same angles with the input point 1, the contact load is higher at point 4 than point 3 due to the superposition of loads from the other disks. No load transfer occurs across points 5 and 6 as the contact angles are larger than $(\pi/2)$ for these points. For the dynamic case, inertia becomes significant and the location of the mass centers of the particles will also be important in the load transfer process. For the cases under study with circular disks, the branch vectors defined in Fig. 1(*b*) completely describe the relative location of both the contact points and the particle mass centers. Thus, it seems reasonable to develop a load transfer theory based upon the use of the branch vectors to predict the transmission of dynamic signals from disk to disk. The theory to be proposed is intended to predict the peak intergranular load transfer between disks in model assemblies of granular media.

Referring to Fig. 1(*b*), the peak load transfer through the jth contact of any arbitrary disk may be written in the form,

$$P_j^{(o)} = C_{ji} P_i^{(i)} \tag{1}$$

where $P_j^{(o)}$ is the peak output load at the jth contact, $P_i^{(i)}$ is the peak input load to this disk, and C_{ji} is defined to be the load transfer coefficient matrix which relates these peak intergranular loads. Clearly, this load transfer coefficient depends on various contact angles made by the branch vectors of this disk, in fact $C_{ji} = C_{ji}(\theta_{ji})$, where θ_{ji} is the relative contact angle between any pair of input and output points as shown in Fig. 1(*b*). For disks of equal diameter, the maximum number of possible contacts is limited to six. Furthermore, as mentioned previously, experiments have shown that when the contact angle is greater than or equal to 90 deg, no load transfer will occur and thus C_{ji} will be zero for these cases. Therefore, for equal diameter disks, the range of the index j will be limited from one to three, and the load transfer coefficient will be a function of at most three relative contact angles, i.e., $C_{ji} = C_{ji}(\theta_{1i}, \theta_{2i}, \theta_{3i})$. For brevity, these angles θ_{ji} will be referred to as θ_1, θ_2, θ_3 and are defined in Fig. 4 relative to the input

Downloaded 03 May 2010 to 171.66.16.248. Redistribution subject to ASME license or copyright; see http://www.asme.org/terms/Terms_Use.cfm

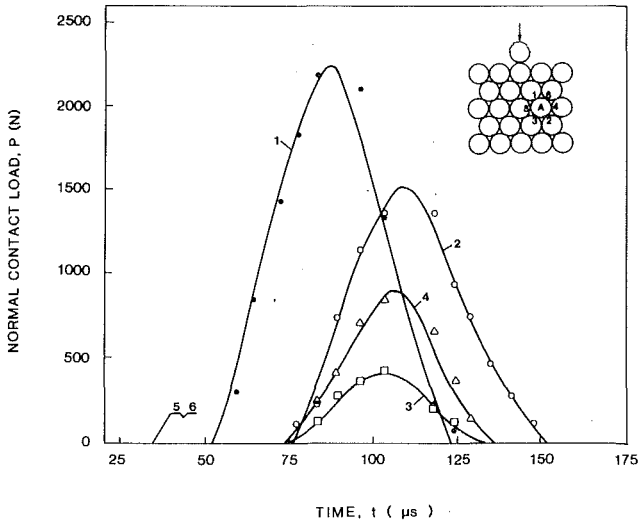

Fig. 2 Normal contact load transfer profiles for disk A in a HCP arrangement for the geometry of Fig. 1(*b*)

direction of the disk. If in any particular assembly one of these angles becomes larger than 90 deg, then this contact is removed from the analysis. Consequently, for a given input point, at most only three output contacts will be able to transmit the dynamic signal to adjacent disks.

Experimental Determination of Load Transfer Coefficients

In order to determine the peak contact load transfer coefficients, $C_{ji}(\theta_1, \theta_2, \theta_3)$, experiments were conducted on the three groups of models, that is, the two, three and four contact point models. In experiments of the two contact point model, contact angles θ_1 and θ_3 were kept at 90 deg. Only contact angle θ_2 was systematically varied from 0 deg to 90 deg. In experiments of the three contact point model, contact angle θ_3 was kept at 90 deg, and both contact angles θ_1 and θ_2 were systematically varied. In experiments of the four contact point model, all three contact angles θ_1, θ_2, and θ_3 were systematically varied. For simplicity the granular materials were simulated by assemblies of 25.4 mm, 6.35 mm thick disks of Homalite 100. The experimental models were placed in the optical bench of a high-speed multiple spark gap camera. The camera was triggered at some prescribed delay time after igniting the explosive. The high-speed photographic system operated as a series of high intensity, extremely short duration pulses of light and provided 20 isochromatic fringe images at discrete times during the dynamic event.

A careful inspection of the photographs obtained from the experiments revealed that the wave length, λ, of the loading pulse was much larger than the disk diameter D, in fact $\lambda \approx 4D$. Furthermore, in most cases the fringe patterns around the contact points are symmetric on either side of the contact points and similar to the fringes obtained under static compression. Both these features indicate that around the contact zone, quasi-static loading was present during the wave propagation event. Thus, Hertz contact stress theory can be used to estimate the stress field in the vicinity of the contact.

The isochromatic fringes photographed during the experiments are lines of constant maximum shear stress, and are related to the stress field by the stress optic law

$$\sigma_1 - \sigma_2 = Nf_\sigma/h \tag{2}$$

where σ_1 and σ_2 are the principal stresses, N is the fringe order, f_σ is the material fringe value, and h is the model thickness.

In equation (2), σ_1 and σ_2 are substituted from Hertz contact

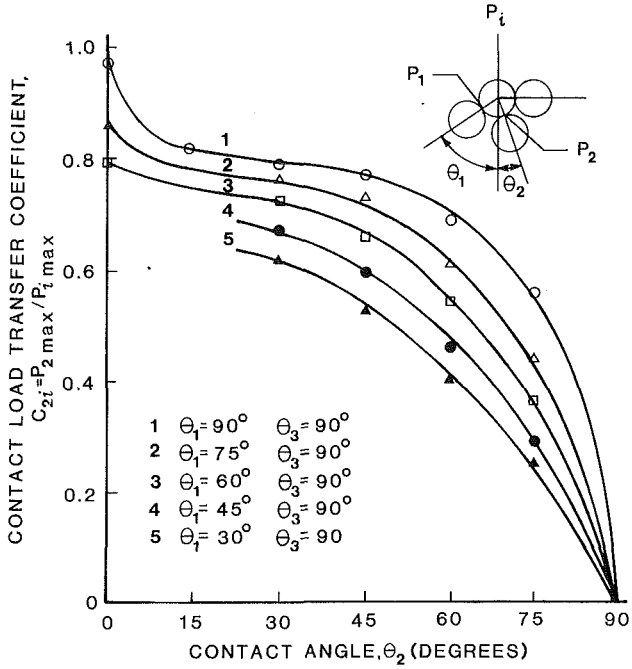

Fig. 3 Contact load transfer coefficient C_{2i} as a function of contact angles

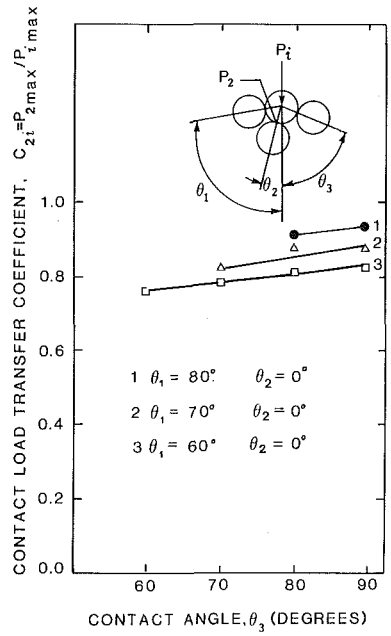

Fig. 4 Contact load transfer coefficient C_{2i} as a function of contact angles

stress field equations, involving unknowns of contact length, b, and friction factor, β. This equation was solved using an overdeterministic method developed by Shukla and Nigam (1985) to determine accurately the contact length and friction factor from the full-field photoelastic fringe patterns. These obtained values were substituted in the Hertz stress field equations and the contact stresses were numerically integrated along the contact length to obtain the normal and tangential contact loads.

For a two contact point model, contact angles θ_1 and θ_3 are 90 deg and C_{1i} and C_{3i} are therefore identically equal to zero. For a three contact point model, θ_3 is taken to be 90 deg and hence C_{3i} is identically zero.

The transfer coefficients C_{ji} thus obtained from the three groups of experiments were plotted as a function of the contact

Downloaded 03 May 2010 to 171.66.16.248. Redistribution subject to ASME license or copyright; see http://www.asme.org/terms/Terms_Use.cfm

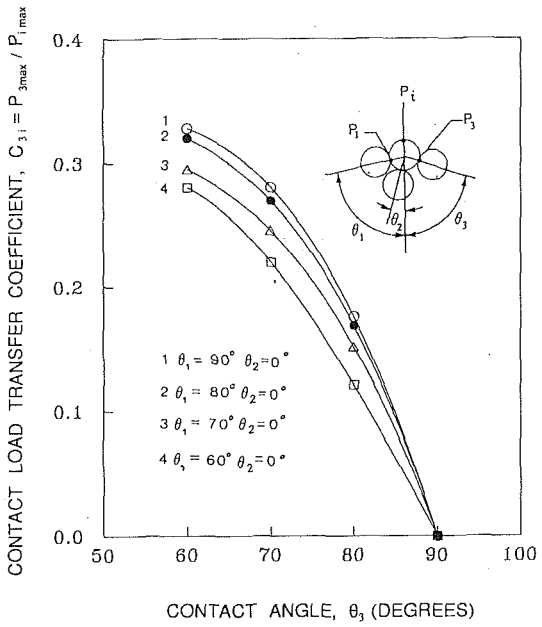

Fig. 5 Contact load transfer coefficient C_{3i} as a function of contact angles

angles θ_1, θ_2 and θ_3, as shown in Figs. 3 to 5. In Fig. 3, curve 1 represents the ratio of $P_2^{(o)}/P_i^{(i)}$ versus contact angle θ_2 when both the contact angles θ_1 and θ_3 are equal to 90 deg. Since both $P_1^{(o)}$ and $P_3^{(o)}$ are zero, it actually represents the transfer coefficient C_{2i} of the two contact point model. The remaining curves in Fig. 3 represent the transfer coefficients C_{2i} versus contact angle θ_2 of the three contact point model when contact angle θ_3 is 90 deg and θ_1 is also a constant but less than 90 deg (it is equal to 30 deg, 45 deg, 60 deg, and 75 deg, respectively). Figure 4 shows the transfer coefficients C_{2i} versus contact angle θ_3 for the four contact point model when the contact angles $\theta_2 = 0$ deg with various values of θ_1, while Fig. 5 shows the transfer coefficient C_{3i} versus contact angle θ_3 for the same four contact point model. The transfer coefficient C_{1i} for the four contact point model can be obtained easily using Figs. 3 and 5 and the property that $C_{1i}(\theta_1, \theta_2, 90 \text{ deg}) = C_{2i}(\theta_2, \theta_1, 90 \text{ deg})$ and $C_{1i}(\theta_1, 0 \text{ deg}, \theta_3) = C_{3i}(\theta_3, 0 \text{ deg}, \theta_1)$.

Numerical Implementation

The experimentally determined peak contact load transfer coefficients were used to construct a numerical scheme capable of predicting dynamic load transfer in granular aggregate assemblies of disks. Several assumptions were used in this numerical method. First, only normal contact loading was considered in this study. The tangential contact loads were assumed to be zero. Next, the speed of propagation of the mechanical signal is assumed to be constant, a fact which has been observed from the experiments. The load transfer coefficients are taken to be independent of the loading amplitude. Finally, simple superposition of loading is used when more than one input contact load occurs on a given disk. Figures 3 to 5 combined with a Lagrangian interpolation method have been used to obtain all the necessary transfer coefficients to predict the peak contact loads in granular media.

Results and Discussion

The experimental-numerical hybrid method was used to predict peak contact loads at every contact point in various models of granular media. Four different microstructural packings were used in this study. Experimental fringe patterns obtained for each of the microstructures are shown in Fig. 1. The comparison of the numerical and experimental results are shown in Figs. 6 to 9.

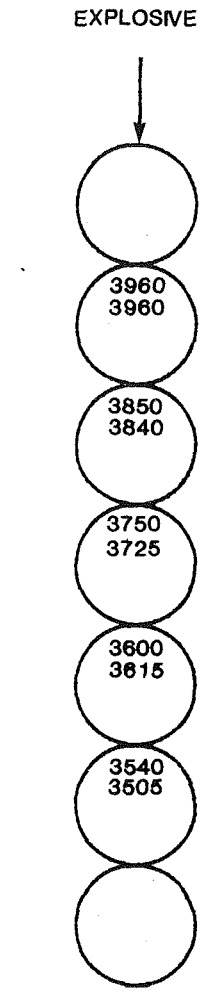

Fig. 6 Comparison of the peak contact loads in a single chain arrangement for the geometry of Fig. 1(*a*) (numerical data at bottom)

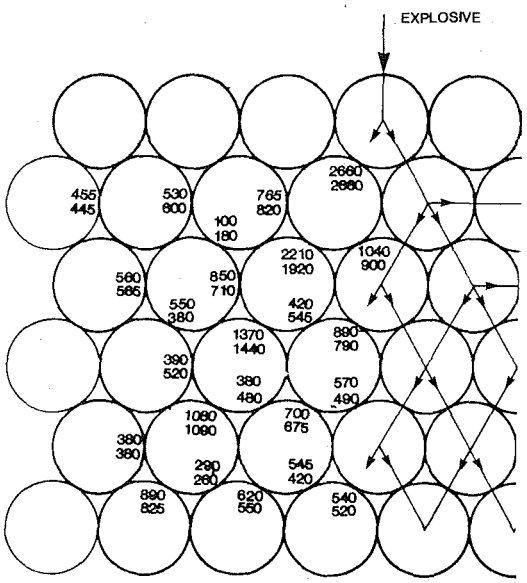

Fig. 7 Comparison of the peak contact loads in a HCP arrangement for the geometry of Fig. 1(*b*); (figure shows the left part of the geometry, numerical data at bottom)

Downloaded 03 May 2010 to 171.66.16.248. Redistribution subject to ASME license or copyright; see http://www.asme.org/terms/Terms_Use.cfm

Figure 1(*a*) shows a sequence of seven photographs obtained as the wave travels in a single chain of granular media. In this geometry each particle has two contact points, hence only one transfer coefficient is needed to model this geometry. This transfer coefficient is obtained from Fig. 3, $C_{2i} = C_{2i}(90 \text{ deg}, 0 \text{ deg}, 90 \text{ deg}) = 0.97$ and this coefficient is the same for all disks in the single chain. Thus, peak contact loads at any contact point n can be determined through successive application of equation (1), i.e.,

$$P_n^{(o)} = C_{21}^{n-1} P_1^{(i)}. \tag{3}$$

The comparison of numerical and experimental peak contact loads in the single chain is shown in Fig. 6. The average peak contact load error, $\{(P_{\text{exp}} - P_{\text{num}})/P_{\text{exp}}{}^{*}100\}$, for this model is computed to be 5 percent. The results are in very good agreement because most of the assumptions made in our numerical model are satisfied.

Figure 1(*b*) shows a photograph obtained as the wave travels in a hexagonal closed packing (HCP) granular medium. In this geometry each particle has six contact points. The major load in this assembly is transferred by two primary chains, 1 and 2, shown in Fig. 1(*b*). Experimental data showed that the tangential contact loads were very close to zero for the primary chains, hence they behaved similar to the single chain assemblies. In the HCP model there are only two independent contact angles, $\theta_1 = \theta_3 = 60$ deg and $\theta_2 = 0$ deg, with respect to the input load. Thus, only two transfer coefficients were needed for the HCP model. From Figs. 3 and 5, we obtain the two transfer coefficients, $C_{1i}(60 \text{ deg}, 0 \text{ deg}, 60 \text{ deg}) = C_{3i}(60 \text{ deg}, 0 \text{ deg}, 60 \text{ deg}) = 0.28$, $C_{2i}(60 \text{ deg}, 0 \text{ deg}, 60 \text{ deg}) = 0.75$. These coefficients were used to determine the peak contact loads throughout the assembly. The comparison of numerical and experimental results of the peak contact loads for the HCP model is shown in Fig. 7. The average error of the peak contact loads for this model is 13 percent, with the average error along the center line of the primary chain being only 6 percent.

Figure 1(*c*) shows a photograph obtained as the wave travels in the so-called half hexagonal closed packing (HHCP) granular medium. In this geometry a particle has either four or five contact points. It is observed that most of the energy was transferred through a vertical column consisting of the HHCP cells under the explosive and several horizontal chains. The peak contact loads were obtained by the same method discussed previously. The comparison of numerical and experimental peak contact loads is shown in Fig. 8. It was found that the average error for this model is 12 percent. However, the average error along the center line of the horizontal chains is only 7.5 percent.

Figure 1(*d*) shows a photograph obtained as the wave travels in an irregular packing granular medium. In this geometry,

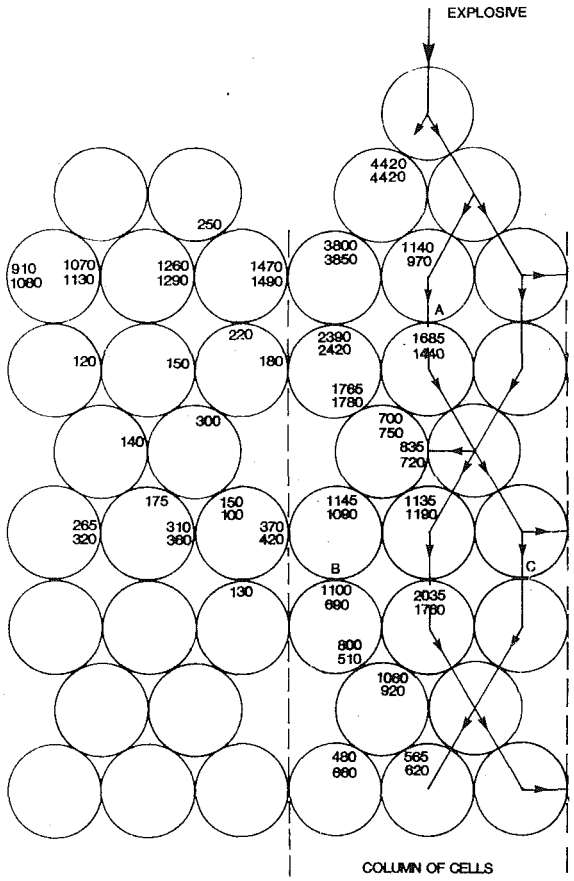

Fig. 8 Comparison of the peak contact loads in a HHCP arrangement for the geometry of Fig. 1(*c*); (figure shows the left part of the geometry, numerical data at bottom)

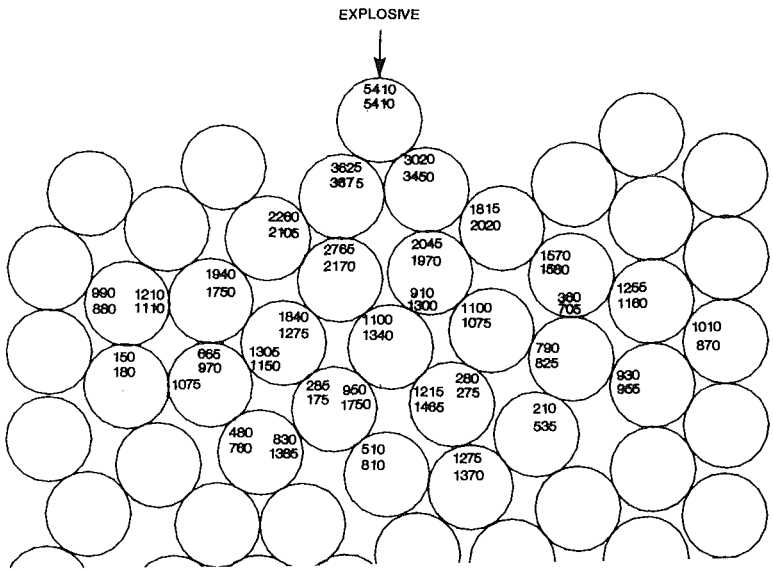

Fig. 9 Comparison of the peak contact loads in an irregular arrangement for the geometry of Fig. 1(*d*) (numerical data at bottom)

Downloaded 03 May 2010 to 171.66.16.248. Redistribution subject to ASME license or copyright; see http://www.asme.org/terms/Terms_Use.cfm

particles have contact points ranging from two to six. The fringes in Fig. 1(*d*) reveal a complex nature of load transfer phenomenon. The energy transfer showed no preferential direction in this model. In the former three models, the tangential contact loads, especially along the main path of the energy transfer, were quite small. However, in this irregular model, at the contacts near the explosive point, the fringes appeared unsymmetrical with respect to the contact points. So it appears that sizable tangential loadings existed in this case. Away from the explosive point, the fringes showed the tendency to become symmetric with respect to the contact points. Again, from Figs. 3 to 5, all the transfer coefficients necessary for the determination of the peak contact loads in the irregular packing granular medium were obtained. The comparison of numerical and experimental peak contact loads is shown in Fig. 9. The tangential contact loads tend to increase the average error in the peak contact loads. This error was computed to be 19.0 percent for this model.

Summary

A hybrid experimental-numerical technique has been developed to predict dynamic intergranular contact loads due to explosive loading in different assemblies of circular disks. For a known geometrical arrangement of disks the technique can predict contact loads at any point in the assembly for a given input loading. The method utilizes experimentally generated load transfer coefficients along with simple linear superposition in space. The results from this scheme are compared with those obtained experimentally using the method of dynamic photoelasticity. In general, the results are in good agreement for regular packings of the disks. However, for an irregular packing the agreement is marginal, and this is primarily due to the fact that the numerical scheme currently does not take into account tangential contact loads which were found to be quite large in an irregular arrangement. Further, the superposition method does not account for any angular dependence of wavelength of the loading pulse, or of the fact that the peak contact loads occur at a different time. It was shown by Shukla et al. (1987b) that the duration of contact loads is dependent on the contact angles. Thus, to obtain better predictions, superpositions must be used both in space as well as time. This work is currently in progress.

Acknowledgments

The authors would like to acknowledge the support of Air Force Office of Scientific Research under contract No. F49620-89-C-0091 and Army Research Office under contract No. DAAL03-86-K-0125.

References

Brandt, H., 1955, "A Study of the Speed in Sound of Porous Granular Media," ASME JOURNAL OF APPLIED MECHANICS, Vol. 22, pp. 479–486.

Cundall, P., and Strack, D. L., 1979, "A Discrete Model for Granular Assemblies," *Geotechnique*, Vol. 29, pp. 47–65.

Drescher, A., and De Josselin De Jong, G., 1972, "Photoelastic Verification of a Mechanical Model for the Flow of a Granular Material," *J. Mech. Phys. Solids*, Vol. 20, pp. 337–351.

Duffy, J., and Mindlin, R. D., 1957, "Stress-Strain Relation and Vibration of a Granular Medium," ASME JOURNAL OF APPLIED MECHANICS, Vol. 24, pp. 585–593.

Durelli, J., and Wu, D., 1983, "Use of Coefficients of Influence to Solve Some Inverse Problems in Plane Elasticity," ASME JOURNAL OF APPLIED MECHANICS, Vol. 50, pp. 288–296.

Gassman, F., 1951, "Elastic Waves Through a Packing of Spheres," *Geophysics*, Vol. 16, pp. 673–685.

Goodman, M. A., and Cowin, S. C., 1972, "A Continuum Theory for Granular Materials," *Arch. Rat. Mech. Anal.*, Vol. 44, pp. 249–266.

Hughes, D. S., and Cross, J. H., 1952, "Elastic Wave Velocities in Rocks at High Pressures and Temperature," *Geophysics*, Vol. 17, pp. 577–593.

Iida, K., 1939, "The Velocity of Elastic Waves in Sand," *Bull. Earthquake Research Inst., Japan*, Vol. 17, pp. 783–807.

Nemat-Nasser, S., and Mehrabadi, M. M., 1983, "Stress and Fabric in Granular Masses," *Mechanics of Granular Materials: New Models and Constitutive Relations*, J. T. Jenkins, and M. Statake, eds., Elsevier, New York, pp. 1–8.

Oda, M., 1978, "Significance of Fabric in Granular Mechanics," *Proc. U.S.-Japan Seminar on Continuum Mechanical and Statistical Approaches in the Mechanics of Granular Materials*, S. C. Cowin and M. Statake, eds., Gaknjutsu Bunken Fukyukai, pp. 7–26.

Sadd, M. H., Shukla, A., and Mei, H., 1989, "Computational and Experimental Modeling of Wave Propagation in Granular Materials," *Computers and Experiments in Stress Analysis*, G. M. Carlomagno and C. A. Brebbia, eds., Capri, Italy.

Sadd, M. H., and Hossain, M., 1988, "Wave Propagation in Distributed Bodies with Applications to Dynamic Soil Behavior," *J. of Wave-Material Interaction*, Vol. 3, pp. 311–326.

Shukla, A., and Nigam, H., 1985, "A Numerical-Experimental Analysis of the Contact Stress Problem," *J. of Strain Analysis*, Vol. 20, pp. 241–245.

Shukla, A., and Rossmanith, H. P., 1986, "Dynamic Photoelastic Investigation of Wave Propagation and Energy Transfer Across Contacts," *J. of Strain Analysis*, Vol. 21, pp. 213–218.

Shukla, A., and Damania, C., 1987a, "Experimental Investigation of Wave Velocity and Dynamic Contact Stress in an Assembly of Discs," *J. Exp. Mech.*, Vol. 27, pp. 268–281.

Shukla, A., Zhu, C. Y., and Sadd, M. H., 1987b, "Angular Dependence of Dynamic Load Transfer Due to Explosive Loading in Granular Aggregate Chains," *J. of Strain Analysis*, Vol. 23, pp. 121–127.

Shukla, A., and Zhu,C. Y., 1988, "Influence of the Microstructure of Granular Media on Wave Propagation and Dynamic Load Transfer," *J. of Wave-Material Interaction*, Vol. 3, pp. 249–265.

Takahashi, T., and Sato, Y., 1949, "On the Theory of Elastic Waves in Granular Substance," *Bull. Earthquake Research Inst. Japan*, Vol. 27, pp. 11–16.

Downloaded 03 May 2010 to 171.66.16.248. Redistribution subject to ASME license or copyright; see http://www.asme.org/terms/Terms_Use.cfm

S. M. Kulkarni[1]
Assoc. Mem. ASME

G. T. Hahn
Professor.

C. A. Rubin
Professor,
Mem. ASME

V. Bhargava[2]

Center for Materials Tribology,
Vanderbilt University,
Nashville, TN 37235

Elasto-Plastic Finite Element Analysis of Three-Dimensional Pure Rolling Contact Above the Shakedown Limit

This paper describes calculations for repeated, frictionless, three-dimensional rolling contact, for a relative peak pressure (p_o/k) of 6.0 (above the shakedown limit) for a circular contact patch. This analysis was carried out for two material responses, elastic-perfectly plastic (EPP) and elastic-linear-kinematic-hardening plastic (ELKP), using the elasto-plastic finite element model developed earlier. The ELKP material parameters are those appropriate for hardened bearing steel. Frictionless three-dimensional rolling contact is simulated by repeatedly translating a Hertzian pressure distribution across the surface of an elasto-plastic half space. The half space is represented by a finite mesh with elastic boundaries. The paper describes the complex stress state existing in the half space and the attending plasticity, as the load translates. The calculations present the distortion of the rim, the residual stress-strain distributions, stress-strain histories, and the cyclic plastic strain increments in the vicinity of the contact. Compared with the analyses at the shakedown limit, higher residual stresses and strains are observed.

Introduction

Physically, the problem being addressed is that of a rigid sphere rolling over a flat surface. A significant amount of literature exists for this three-dimensional rolling contact problem, as reviewed earlier by Kulkarni et al. (1990a), but the bulk of these treatments make questionable simplifying assumptions and offer relatively little information about the residual stresses and cyclic plastic strains in the vicinity of the running track. A three-dimensional elasto-plastic finite element model was developed to simulate this situation (Kulkarni et al., 1990a). The three-dimensional mesh with elastic boundaries was subjected to two frictionless rolling contacts with a semi-ellipsoidal pressure distribution for two different material behaviors, elastic-perfectly plastic (EPP) and elastic-linear-kinematic-hardening plastic (ELKP). The study identified certain important features of the three-dimensional point contact problem, such as the complex system of residual stresses (the three direct components and the three shear components) across the half space, and the presence of ploughing even for a circular contact patch. Residual tensile, axial, and circumferential stresses were observed near the free surface in the vicinity of the applied load. But these calculations were performed at the shakedown limit and no continuing cyclic plasticity was observed, for the EPP as well as the ELKP material, after the first contact cycle.

This paper reports the calculations for repeated, frictionless three-dimensional rolling contact for a relative peak pressure (p_o/k) of 6.0, which is well above the theoretical shakedown limit (4.68) for a circular contact patch. The calculations were performed for EPP and ELKP behavior, the latter using material properties appropriate for hardened bearing steel. Deformations, stress-strain distributions, stress-strain histories, and cyclic plastic strain-range distributions are obtained in the vicinity of the contact and compared with the results at the shakedown limit (Kulkarni et al., 1990a) and appropriate results for two-dimensional contact (Hahn et al., 1987).

Description of the Finite Element Model

The frictionless rolling of a sphere across a flat surface is simulated by repeated translation of a Hertzian pressure distribution over the free surface of a half-space. The half-space is represented by the three-dimensional finite element mesh, with elastically displaced boundaries, developed earlier (Kulkarni et al., 1990a). The mesh (Fig. 1), which was successfully subjected to convergence and model verification tests, has the

[1]Currently Staff Engineer, TRW Safety Systems, Mesa, AZ.

[2]Currently Material Scientist, General Electric Corporation, Research and Development, Schenectady, NY.

Contributed by the Applied Mechanics Division of THE AMERICAN SOCIETY OF MECHANICAL ENGINEERS for presentation at the Joint Applied Mechanics/Bioengineering Conference, Ohio State University, Columbus, Ohio, June 16-19, 1991.

Discussion on this paper should be addressed to the Technical Editor, Leon M. Keer, The Technological Institute, Northwestern University, Evanston, IL 60208, and will be accepted until two months after final publication of the paper itself in the JOURNAL OF APPLIED MECHANICS. Manuscript received by the ASME Applied Mechanics Division, Jan. 29, 1990; final revision, June 8, 1990.

Paper No. 91-APM-23.

Copyright © 1991 by ASME
Downloaded 03 May 2010 to 171.66.16.248. Redistribution subject to ASME license or copyright; see http://www.asme.org/terms/Terms_Use.cfm

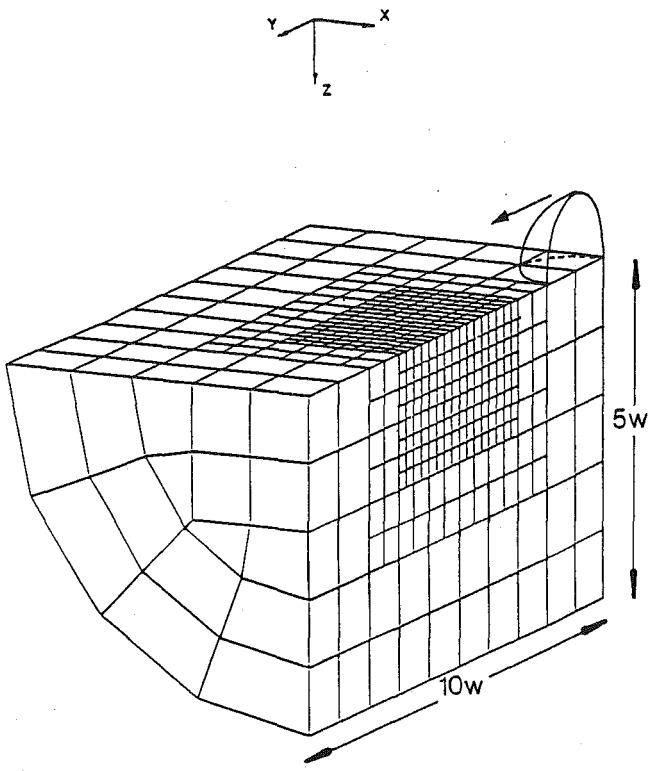

Fig. 1 Three-dimensional finite element mesh

shape of a quadrant of a circle, extended in the third dimension. The mesh is dimensionally finer away from the displaced boundaries and coarser towards them. Also, higher order (20 or 27-noded quadratic brick) elements are employed in the vicinity of the contact and lower order (8-noded linear brick) elements are used away from the contact. This mesh has 1392 elements and 4649 nodes. In this study the coordinate axes are referred to in the following terms: The x-axis is the axial direction, the y-axis or the direction of translation of the contact is the circumferential direction, and the z-axis is the radial direction. The mesh is $10w$ long (in the circumferential direction) and extends to a distance of $5w$ in the axial and radial directions.

The calculations were performed for a peak Hertzian pressure to shear yield strength ratio, $p_o/k = 6.0$ and employ two different material behaviors. One is the elastic-linear kinematic hardening plastic (ELKP) behavior with $k_k = 606$ MPa ($\sigma_k = 1050$ MPa) and $M = 188$ GPa (Hahn et al., 1989), and the other is the elastic-perfectly plastic (EPP) behavior with $k = 227.5$ MPa ($\sigma_o = 393.98$ MPa). Both analyses use the following elastic properties: Young's modulus, $E = 207$ GPa and Poisson's ratio, $\nu = 0.3$. For these calculations, any change in conformity during three-dimensional rolling is neglected (Kapoor and Johnson, 1988). Hence, the pressure distribution is assumed to remain Hertzian throughout the analysis, and is given by

$$p(x, y) = p_o[1 - (x^2 + y^2)/w^2]^{1/2}$$

where the contact patch is assumed to be a circle of constant radius. This radius, w, calculated from the material constants, is 1 mm for the ELKP calculation and 0.38 mm for the EPP case.

The semi-ellipsoidal pressure distribution applied at one end of the mesh, is translated in the circumferential direction through a distance of $8w$ to the other end, and then it is removed. The translation is executed using 22 variable increments. For each translating increment, the boundaries of the mesh are elastically displaced using the solution of Boussinesq's problem of a force acting on the surface of a semi-infinite body. The application of the pressure distribution, followed by the 22 translational increments and the unloading, defines a single contact cycle. Both material types are subjected to three cycles of contact. The multipurpose finite element package ABAQUS is used for the analyses. The calculations, performed on the Cray X-MP super computer, require about 1.5 CPU hours per contact cycle.

Results

The translating three-dimensional Hertzian pressure produces complex stress distributions in the half space. This is shown in Fig. 2 by way of stress contours for the first contact of the ELKP calculations. The contours, drawn for different sections (these sections are indicated in miniature line sketches of the three-dimensional mesh by the side of each plot) of the mesh, are presented for the case when the pressure is halfway through its translation. Figure 2 describes the circumferential, σ_{yy}, stress distributions in the vicinity of the contact. Significant values of stresses extend up to distances between $1.5w$ and $2.0w$ from the surface, and from the YZ plane. It is interesting to note the tensile components occuring at the edge of the contact patch. The repeated application of the Hertzian distribution, with the peak pressure well above the elastic limit, results in plastic deformation of the half-space.

The plasticity may be described in terms of the residual stresses, plastic strains, and distortions accompanying the unloading after each contact cycle, and the stress versus plastic strain history and plastic strain range distributions over each contact. Figure 3 presents residual stress contours after the first contact for ELKP properties. The axial, σ^r_{xx}, and circum-

Nomenclature

x = axial or out-of-plane coordinate, m
y = circumferential or in-plane coordinate, m
z = radial or depth coordinate, m
p_o = peak pressure, MPa
$k = \sigma_o/1.73$ = von Mises shear yield strength, MPa
$k_k = \sigma_k/1.73$ = kinematic shear yield strength, MPa
p_o/k, p_o/k_k = relative peak pressure
$p(x, y)$ = pressure at any point, MPa
w = radius of the contact circle, m
E = Young's modulus, MPa
ν = Poisson's ratio
M = plastic modulus, MPa
G = shear modulus, MPa
EPP = elastic-perfectly plastic
ELKP = elastic-linear-kinematic-hardening plastic
f^r = parameter f for the residual state
σ_{xx} = axial stress, MPa
σ_{yy} = circumferential stress, MPa
σ_{zz} = radial stress, MPa
τ_{xy}, τ_{xz}, τ_{yz} = shear stress, MPa
ϵ_{xx} = axial total strain
ϵ_{yy} = circumferential total strain
ϵ_{zz} = radial total strain
γ_{xy}, γ_{xz}, γ_{yz} = shear total strain
ϵ^p_{xx} = axial plastic strain
ϵ^p_{yy} = circumferential plastic strain
ϵ^p_{zz} = radial plastic strain
γ^p_{xy}, γ^p_{xz}, γ^p_{yz} = shear plastic strain
ϵ_p = equivalent plastic strain
$\Delta\epsilon^p_{zz}$ = radial plastic strain range
$\Delta\gamma^p_{yz}$ = shear plastic strain range
$\Delta eq^p/2$ = half equivalent plastic strain range

Downloaded 03 May 2010 to 171.66.16.248. Redistribution subject to ASME license or copyright; see http://www.asme.org/terms/Terms_Use.cfm

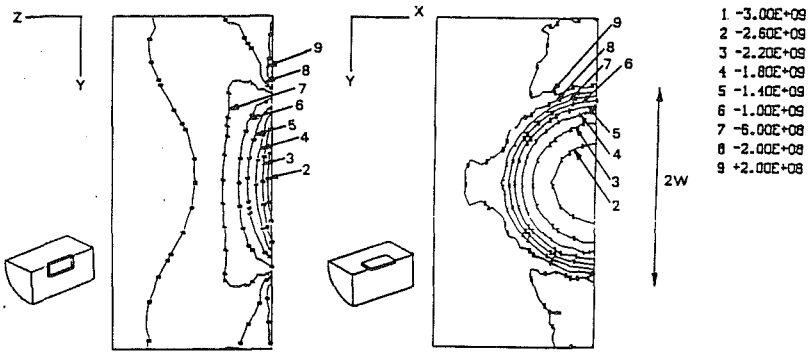

Fig. 2 Circumferential, σ_{yy}, stress contours for sections of the mesh along the rolling direction, during the first pass, for the case when the pressure is halfway through its translation (ELKP) (values in N/m^2 or Pa)

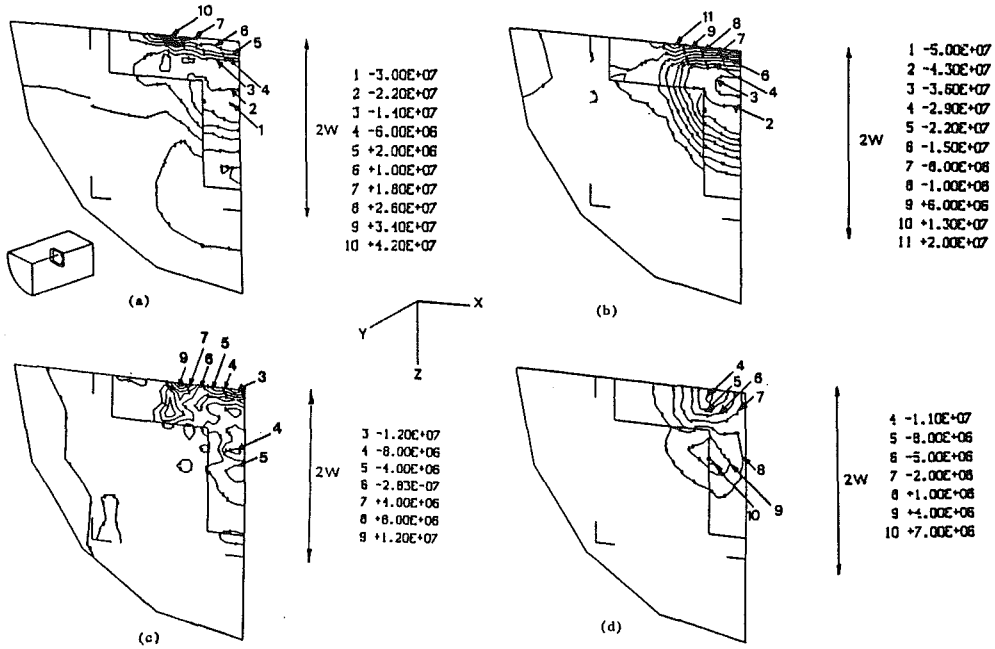

Fig. 3 Contours for a section of mesh perpendicular to the rolling direction after the first pass (ELKP) (*a*) residual axial stress, σ^r_{xx}, (*b*) residual circumferential stress, σ^r_{yy}, (*c*) residual radial stress, σ^r_{zz}, (*d*) residual shear stress, τ^r_{xy} (values in N/m^2 or Pa)

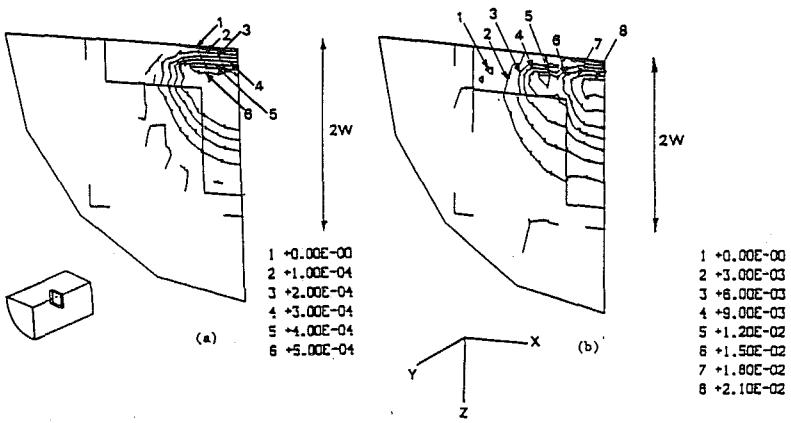

Fig. 4 Residual equivalent plastic strain, ϵ^r_p, contours for a section of the mesh perpendicular to the rolling direction after the first pass; (*a*) ELKP (*b*) EPP

ferential, σ^r_{yy}, stress contours indicate tensile components up to a depth of about $0.1w$ under the surface, extending to a distance of $1.25w$ in the axial or X direction. Peak compressive stresses are located at a depth of about $0.8w$. The radial stress, σ^r_{zz}, attains lower peak compressive values. A tensile component is seen near the surface at a distance of $1.0w$ from the YZ plane. Figure 3(d) describes the distribution of the residual shear stress component, τ^r_{xy}, in the half-space. The highest

Downloaded 03 May 2010 to 171.66.16.248. Redistribution subject to ASME license or copyright; see http://www.asme.org/terms/Terms_Use.cfm

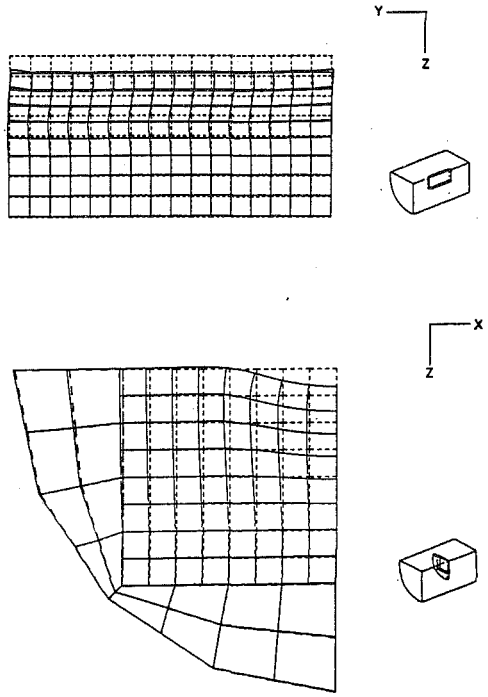

Fig. 5 Residual distortions: sections of the mesh (*a*) along (mag. fac. = 550) and (*b*) perpendicular (mag. fac. = 430) to the rolling direction after the first contact (ELKP)

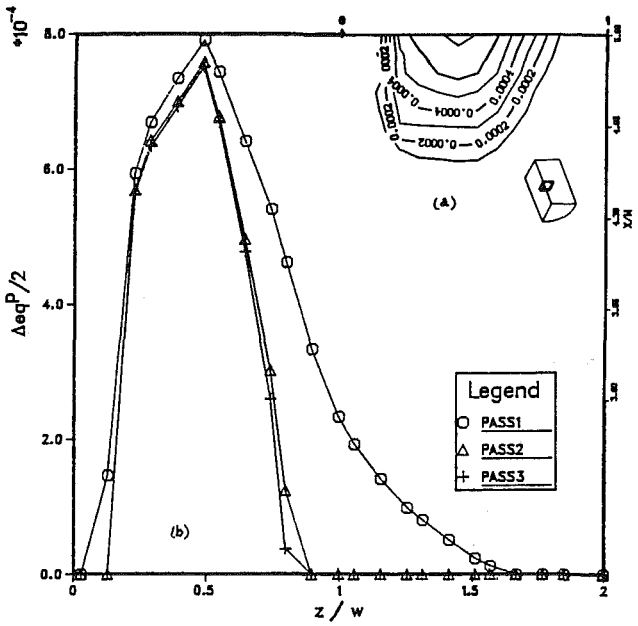

Fig. 6 (*a*) Contours of half-equivalent plastic strain range, $\Delta eq^p/2$, for a section of the mesh perpendicular to the rolling direction during the second contact, and (*b*) variation of half-equivalent plastic strain range, $\Delta eq^p/2$, as a function of normalized depth, *z/w* for one, two, and three successive contacts in the vicinity of the *YZ* plane (ELKP)

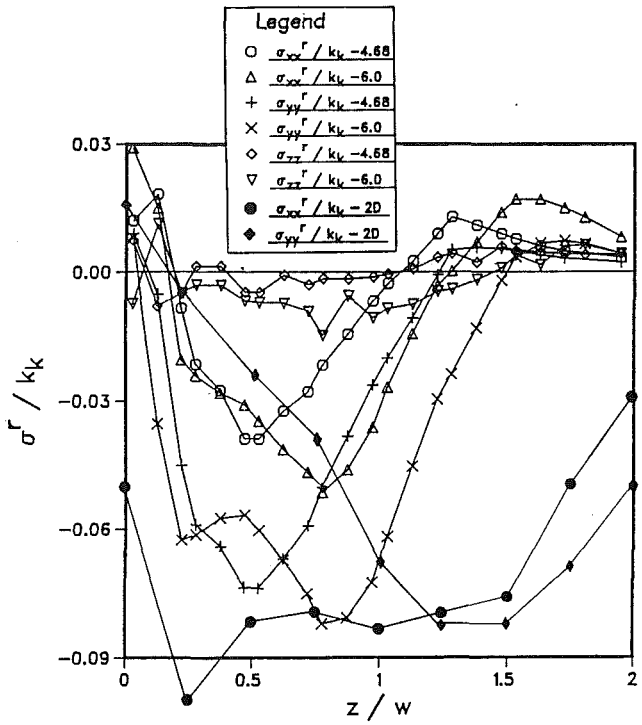

Fig. 7 Comparison of the normalized residual axial, σ^r_{xx}/k_k, circumferential, σ^r_{yy}/k_k, stress as a function of the normalized depth, *z/w*, after one contact, for present study with that at shakedown (Kulkarni et al., 1990a), and two-dimensional analysis (relative load: 6.0) (Hahn, et al., 1987) in the vicinity of the *YZ* plane (ELKP)

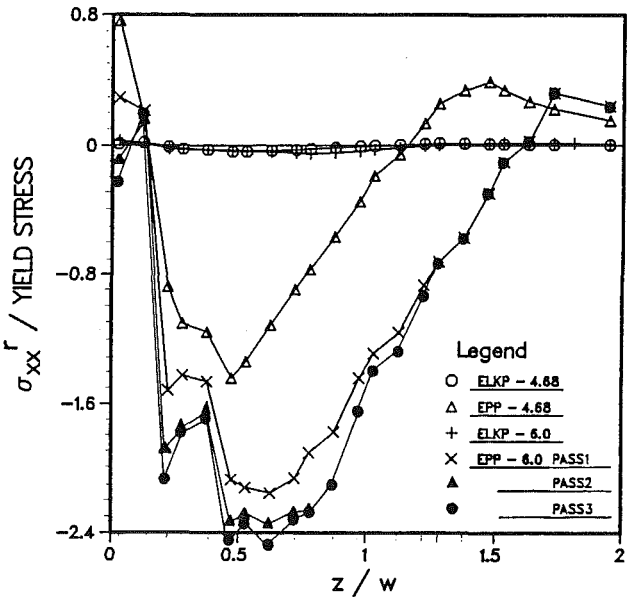

Fig. 8 Comparison of the normalized residual axial stress as a function of the normalized depth, *z/w*, after one contact, for present study (EPP and ELKP) with that at shakedown (Kulkarni et al. 1990a) (EPP and ELKP), and the variation of the (EPP) normalized residual axial stress for the first three contacts, in the vicinity of the *YZ* plane

values are seen at $0.25w$ from the *YZ* plane. The extent and location of the plastic zone is presented in Fig. 4, which describes the equivalent plastic-strain contours after the first contact for both ELKP and EPP material properties.

Figure 5 shows residual displacements for two different sections of the mesh. Figure 5(*a*) portrays forward flow, while Fig. 5(*b*) presents the out-of-plane plasticity occuring in three-dimensional contact. Plasticity in the three-dimensional half-space is also described by way of plastic-strain range distributions; Fig. 6 contains a plot of the half-equivalent plastic-strain range contours, $\Delta eq^p/2$, for the ELKP calculations during the second contact. The variation of $\Delta eq^p/2$ versus the normalized depth, z/w, close to the vicinity of the *YZ* plane for each of the three contacts is also shown in Fig. 6. The plastic activity, as seen from Fig. 4, appears to be subsurface and extends to a radius of about $1.2w$ from the contact center point. The results also describe the variation with depth of the residual stresses. This is to enable comparison of the above ELKP results with earlier work (Kulkarni et al., 1990a) and with the EPP calculations. The residual stresses are normalized with respect to k or k_k, and the depth is normalized with respect

Downloaded 03 May 2010 to 171.66.16.248. Redistribution subject to ASME license or copyright; see http://www.asme.org/terms/Terms_Use.cfm

Table 1 Comparison of two-dimensional and three-dimensional ELKP FE calculations

Analysis	$\Delta\epsilon^p_{zz}$(max)	$\Delta eq^p/2$(max)
three-dimensional p_o/k_k of 6.0	0.48E-3	0.776E-3
three-dimensional p_o/k_k of 4.68	0.4E-3	0.316E.3
two-dimensional p_o/k_k of 6.0	0.64E-3	1.09E-3
two-dimensional p_o/k_k of 5.4	0.48E-3	0.78E-3

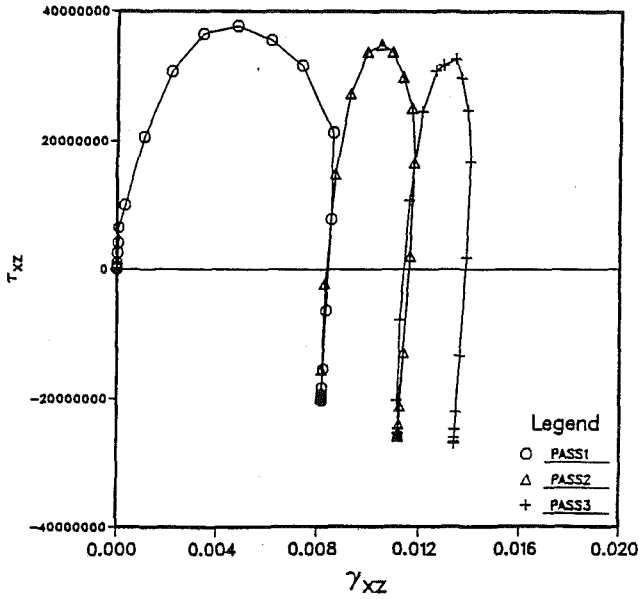

Fig. 9 Stress-strain curve (τ_{xz} versus γ_{xz}) for one, two, and three successive contacts, at a depth of 0.47w at a distance of 0.125w from the YZ plane (EPP)

to w. The residual stresses are presented for integration points located at a distance of 0.125w from the plane of symmetry (the YZ plane). Steady state is attained after the first cycle. Figure 7 compares the residual axial, circumferential, and radial stress distributions for the present ELKP study with those at shakedown (Kulkarni et al., 1990a). The magnitude of the peak compressive stress is about 40 percent higher and the location is 60 percent deeper for the present study. Also, the tensile value close to the surface is greater than that observed at shakedown. In Fig. 8, the variation with depth of the residual axial stress is described (for both ELKP and EPP behavior) after one contact, for four different cases (and at two values of the relative peak pressure): (*a*) at shakedown, $p_o/k = 4.68$ (Kulkarni et al., 1990a) and (*b*) above shakedown, $p_o/k = 6.0$. For the EPP calculations, there is a 50 percent increase in the peak stresses at the higher contact pressure. Also, an order of magnitude difference in the peak residual stress is observed between the EPP and the ELKP results. Another method of comparing ELKP and EPP calculations, is by way of stress-strain histories: Figure 9 shows τ_{xz} versus γ_{xz} plots for three successive contacts. Stress-strain plots are shown for the EPP material in Fig. 9 and for the ELKP material in Fig. 10, for a depth of 0.47w and at a distance of 0.125w from the plane of symmetry (YZ plane). For EPP behavior (Fig. 9), the stress-strain loops at a depth of 0.47w do not reverse at all, although the strain increment per contact cycle decreases with each successive contact. Figure 10 which presents τ_{yz} versus γ_{yz} loops for three successive contacts at a depth of 0.47w for the ELKP calculation, shows that the deformation/cycle is fully reversed after the first contact.

Also presented for the EPP material are plots for the half equivalent plastic strain range, $\Delta eq^p/2$, (Fig. 11) and the normalized residual axial stress, σ'_{xx}/K, (Fig. 10) as a function of normalized depth, z/w. These are for integration points at

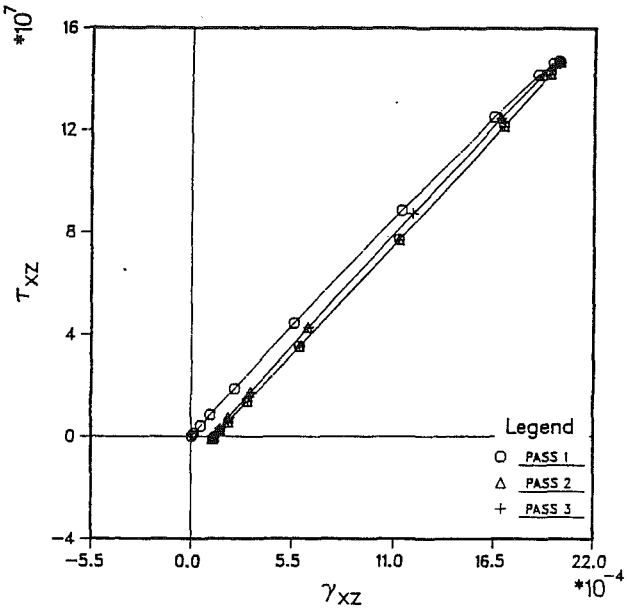

Fig. 10 Stress-strain curve (τ_{xz} versus γ_{xz}) for one, two, and three successive contacts, at a depth of 0.47w at a distance of 0.125w from the YZ plane (ELKP)

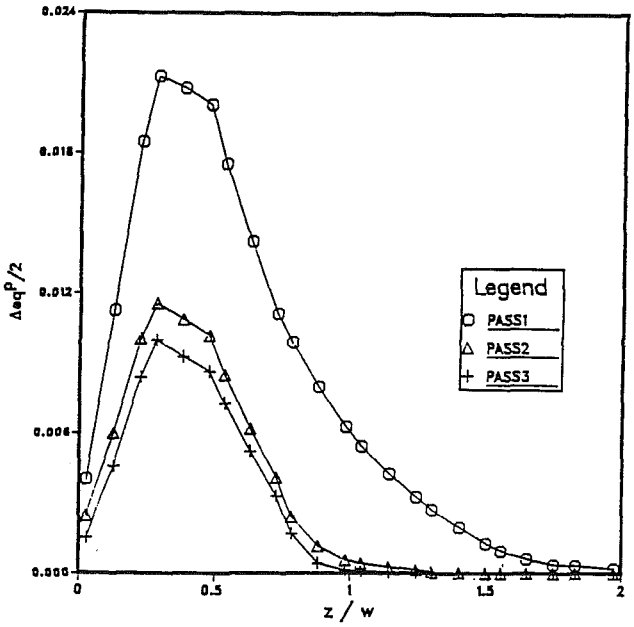

Fig. 11 Variation of half-equivalent plastic strain range, $\Delta eq^p/2$, as a function of normalized depth, z/w for one, two, and three successive contacts in the vicinity of the YZ plane (EPP)

0.125w from the YZ plane and for one, two, and three consecutive passes. Unlike the observations for the ELKP calculations in the present study and those for the calculations at shakedown (Kulkarni et al., 1990a), the plastic zone and hence the plastic activity reaches the surface. Also, there is a substantial drop in the plastic strain increment and the depth of plastic activity between the first and the second contact and very little between the second and the third. The peak value of $\Delta eq^2/2$ for the third pass is 0.01. The residual axial stress also shows a larger increase between the first and second contacts (ten percent) and a marginal change between the second and the third cycles.

Discussion

The present calculations evaluate the effects of plasticity for two constitutive relations: elastic-perfectly plastic (EPP) and

Downloaded 03 May 2010 to 171.66.16.248. Redistribution subject to ASME license or copyright; see http://www.asme.org/terms/Terms_Use.cfm

a bilinear, elastic-linear-kinematic-hardening plastic (ELKP) representation with parameters appropriate for the steady-state behavior of hardened bearing steel. It has been shown that ELKP behavior—an insensitivity to mean stress, the absence of ratchetting and a high rate of strain hardening—is gradually approached by many steels after $N = 10^3$ to 10^4 cycles (Bhargava et al., 1990). Consequently, the present calculations reflect the continuing, steady-state cyclic plasticity produced by rolling contact after an initial, transient period of about $N = 10^3 - 10^4$ contacts. The amounts of plasticity attending the first few contacts, and the resulting residual stresses are expected to be much larger than the values reported here because the plastic slope of the hysteresis loop (the value of m) is initially much lower. This is the case for the two-dimensional rolling problem (Hahn et al., 1987). In the absence of mechanical relaxation, the larger residual stresses produced by the first contact are the ones observed; i.e., $N > 10^4$, while the continuing cyclic strains calculated here with steady-state ELKP-parameters after many contacts are the ones that apply to "many" contacts. Even larger residual stresses are produced after $N = 10^7$ contacts by expansive, cyclic strain-induced phase changes (Voskamp, 1985).

The results for EPP behavior show that this simplification, which provides no strain hardening, i.e., $M = 0$, cannot be relied upon for bearing steels where the plastic modulus, $M = 188$ GPa, is close to the elastic modulus. The kinematic shifting of the yield surface actually reduces the resistance to the onset of yielding, but this does not begin to offset the rapidly increasing resistance to plasticity with strain. Thus, the continuing peak cyclic strain range and axial residual stress for ELKP behavior are 1/16 and 1/40 of the values for EPP behavior. Analogous differences can be expected for softer steels where 40 GPa $< M <$ 180 GPa. Results for a rail steel and rail wheel conditions are reported elsewhere (Kulkarni, 1990b). The present calculations also illustrate that while EPP behavior produces large amounts of ratchetting, ELKP behavior produces no ratchetting (after the initial transient). Work is under way to insert the nonlinear, two surface approximation (McDowell, 1985) of the Mroz law (1967) into the finite element calculations. This is expected to provide even more reliable results for both the initial transient and the steady state.

As opposed to two-dimensional plane-strain rolling contact, two modes of plastic deformation are present in three-dimensional contact: (1) displacement parallel to the motion of the load and (2) groove formation or ploughing (not possible in two-dimensional contact). Comparisons of three-dimensional contact with two-dimensional finite element contact studies are presented in Fig. 9 and Table 1. Figure 9 describes the variations of the normalized residual axial, σ^r_{xx}/k_k, and circumferential, σ^r_{yy}/k_k, stresses for the ELKP material in the present study with the two-dimensional calculations of Hahn et al. (1987), which were done at a p_o/k_k of 6.0. The circumferential stresses are comparable but the axial stresses, σ^r_{xx}/k_k, are lower for the three-dimensional case. Table 1 compares the peak values of the two cyclic plastic strain ranges, the radial, $\Delta\epsilon^p_{zz}$, and the half-equivalent, $\Delta eq^p/2$, for three-dimensional and two dimensional contact at different values of p_o/k_k. It appears that the two-dimensional calculations for a p_o/k_k of 5.4 produce the same amount of plasticity as the three-dimensional study at a p_o/k_k of 6.0. In three-dimensional rolling contact, only part of the free surface touches (along the rolling track) the translating pressure distribution. The material directly below the contact, compressed in the z-direction, is displaced laterally and piles up along the edge of the contact resulting in a groove. Of the alternating shear components, the out-of-plane stress, τ_{xz}, would contribute to this grooving (Figs. 9 and 10). For the ELKP material, in Fig. 10, there is no accumulated out-of-plane plastic deformation after the first cycle (fully reversed stress-strain loops after the first contact). On the other hand, for the EPP material (Fig. 9) there is significant shear deformation during the first contact decreasing with successive contacts. There also exist residual direct strain distributions in the x and y-directions, indicating significant out-of-plane (x) strains. This out-of-plane strain, which contributes to the groove formation, shows increasing magnitudes with increasing p_o/k. Although not considered here, it should be noted that in reality the applied pressure distribution will change from a Hertzian to a lower, more uniform distribution, maintaining conformity with the groove. With successive contacts, the width of the groove will eventually reach a steady-state value.

The variations of the other two shear stress components, τ_{xy} and τ_{yz}, have equal and opposite peaks on opposite sides of the peak pressure. Of the two, τ_{yz} achieves higher values and is the governing factor in the analysis of shakedown and cumulative plastic deformation. The direct stresses do not play a part because the effect of normal compression of the surface can be balanced by the development of residual stresses parallel to the surface. On the other hand, as described by Johnson (1987), yield cannot be inhibited by the addition of a unidirectional residual shear component, τ^r_{yz}. A net residual shear strain, which appears to reach a steady state after two contacts, is identified. The forward displacement for each contact can be obtained by integrating γ^r_{yz} through the depth of the plastically deformed layer. As mentioned earlier, for three-dimensional contact, as compared with two-dimensional plane-strain contact, the in-plane plastic deformation is more constrained by the fact that the translating Hertzian pressure is in contact with part of the rolling surface and the material at the sides of the rolling track remains undeformed and offers resistance to the orthogonal shear.

Another effect of plasticity in the half-space is the plastic work, given by the integral of the product, $\sigma_{ij} \cdot d\epsilon^p_{ij}$, over the history of the loading. This irrecoverable work leads to the exhaustion of ductility, crack initiation, propagation, and eventually fatigue failure. Evidence of noncontinuing plastic activity for calculations at the theoretical shakedown limit have been presented in an earlier work (Kulkarni et al., 1990a). It was observed that the plastic zone was surrounded by an elastic medium for EPP as well as ELKP behavior, though the stresses, strains, etc., differed numerically by an order of magnitude. Figures 3 through 11 describe the plasticity attending rolling contact at $p_o = 6.0$k for EPP as well as ELKP material. Initial yield still occurs at a certain depth below the surface and, for ELKP behavior, all the plastic activity is still subsurface (Figs. 4 and 6), however, for the EPP material the plastic zone reaches the surface (Fig. 11).

The calculations reveal that rolling contact of a bearing steel at a Hertzian pressure of $p_o = 3.64$ GPa ($p_o/k_k = 6$) produces a peak plastic strain range of about $\Delta eq^p/2 = 0.001$. While bearings under these conditions can survive $N = 10^9$ contacts (Voskamp, 1985), laboratory specimens subjected to this cyclic strain range in torsion last only about $N = 10^3$ cycles. This difference is associated with the effects of the high hydrostatic pressure, the rotation of the shear strain direction, and the small stressed volume associated with bearing contact loading and is discussed more fully elsewhere (Bhargava et al., 1990).

The two-dimensional rolling model has been extended to study rolling-sliding (mechanical) (Ham et al., 1988) and rolling-sliding plus heat due to the sliding (thermo-mechanical) (Kulkarni et al., 1990c). Extension of the frictionless three-dimensional model (Kulkarni et al., 1990a) to accomodate rolling sliding and rolling sliding plus heat may provide insights into the contact of rough surfaces (microasperity contact).

Conclusions

1 The elasto-plastic finite element three-dimensional repeated, pure rolling point contact model developed earlier and applied to calculations at the theoretical shakedown limit ($p_o/k = 4.68$) has been used to study repeated contacts at a pressure

Downloaded 03 May 2010 to 171.66.16.248. Redistribution subject to ASME license or copyright; see http://www.asme.org/terms/Terms_Use.cfm

($p_o/k = 6.0$) 30 percent above the shakedown limit, for elastic-perfectly plastic and elastic-linear-kinematic-hardening plastic material behavior.

2 The analysis presents the alternating (translating) as well as the static (residual) stresses, plastic strain distributions, residual distortions, stress-strain histories, and variations of the cyclic plastic strain-range in the vicinity of the contact.

3 For the ELKP calculation the plastic activity is subsurface, whereas the plastic zone for the EPP material reaches the surface. Also, the peak value of the equivalent plastic strain for ELKP is 7E-4 while for EPP it is 1.8E-2.

4 Steady state is achieved after one cycle for ELKP behavior; the stress-strain response after one contact is fully reversed and no net plasticity (ratchetting) is observed after the first cycle.

5 On the other hand, for the EPP material, net plasticity (ratchetting) is observed; in-plane deformation appears to proceed by a constant increment while the out-of-plane plasticity decreases with each successive contact.

6 The peak residual stresses also differ: the peak residual axial stress, $\sigma^r_{xx} = 40$ MPa and $\sigma^r_{xx} = 500$ MPa for ELKP and for EPP behavior, respectively.

7 The out-of-plane plasticity becomes more pronounced with increasing p_o/k, for ELKP as well as EPP behavior.

8 Comparing results with those at shakedown, the peak compressive value of σ^r_{xx} for the present calculation is 40 percent higher and occurs 60 percent deeper.

9 Comparing results for ELKP material with those for the two-dimensional case (Hahn et al., 1989): the peak value of the residual circumferential stress compares but the residual axial stress for the three-dimensional case is lower than for the two-dimensional study. Also, two-dimensional calculations at $p_o/k_k = 5.4$ appear to produce the same amount of cyclic plasticity as the present three-dimensional contact at $p_o/k_k = 6.0$.

10 This study reinforces the absence of a common solution for different materials undergoing rolling contact, and confirms the necessity of selecting appropriate constitutive relations for different materials and loading conditions.

Acknowledgments

This research was supported by the National Science Foundation under Grant No. DMR-8418097. The authors are grateful to Hibbitt, Karlsson, and Sorensen, Inc. for use of their finite element program, ABAQUS and to the San Diego Supercomputer Center for use of their CRAY X-MP/48.

References

Bhargava, V., Hahn, G. T., and Rubin, C. A., 1990, "Rolling Contact Deformation, Etching Effects and Failure of High Strength Bearing Steels," *Met. Tran. A*, Vol. 21, No. 7, pp. 1921–1931.

Hahn, G. T., Bhargava, V., Rubin, C. A., Chen, Q., and Kim, K., 1987, "Analysis of the Rolling Contact Residual Stresses and Cyclic Plastic Deformation of an SAE 52100 Steel Ball Bearing," *Journal of Tribology*, Vol. 109, pp. 618–626.

Ham, G., Rubin, C. A., Hahn, G. T., and Bhargava, V., 1988, "Elasto-Plastic Finite Element Analysis of Repeated, Two-Dimensional Rolling-Sliding Contacts," *Journal of Tribology*, Vol. 110, pp. 44–49.

Johnson, K. L., 1987, *Contact Mechanics*, Cambridge University Press.

Kapoor, A., and Johnson, K. L., 1987, "Shakedown of Rolling Point Contacts Due to Plastic Changes in Conformity," in preparation.

Kulkarni, S., Hahn, G. T., Rubin, C. A., and Bhargava, V., 1990a, "Elasto-Plastic Finite Element Analysis of Three-Dimensional Pure Rolling Contact at the Shakedown Limit," ASME JOURNAL OF APPLIED MECHANICS, Vol. 57, pp. 57–65.

Kulkarni, S., Hahn, G. T., Rubin, C. A., and Bhargava, V., 1990b, Elasto-Plastic Finite Element Analysis of Repeated Three-Dimensional, Elliptical Rolling Contact With Rail Steel Properties," submitted to *Journal of Tribology*.

Kulkarni, S., Rubin, C. A., and Hahn, G. T., 1990c, "Elasto-Plastic Coupled Temperature Displacement Finite Element Analysis of Two-Dimensional Rolling-Sliding Contact with a Translating Heat Source," submitted to *Journal of Tribology*.

McDowell, D. L., 1985, "A Two-Surface Theory for Non-Proportional Cyclic Plasticity, Part 1: Development of Appropriate Equations," ASME JOURNAL OF APPLIED MECHANICS, Vol. 52, pp. 298–302.

Mroz, Z., 1967, "On the Description of Anisotropic Work Hardening," *J. Mech. Phys. Solids*, Vol. 15, pp. 163–175.

Voskamp, A. P., 1985, "Material Response to Rolling Contact Loading," *Journal of Tribology*, Vol. 107.

Downloaded 03 May 2010 to 171.66.16.248. Redistribution subject to ASME license or copyright; see http://www.asme.org/terms/Terms_Use.cfm

Convex Models of Vehicle Response to Unknown but Bounded Terrain

Yakov Ben-Haim
Associate Professor,
Faculty of Mechanical Engineering,
Technion—Israel Institute of Technology,
Haifa 32000, Israel

Isaac Elishakoff
Professor,
Center for Applied Stochastics Research
and Department of Mechanical Engineering,
Florida Atlantic University,
Boca Raton, FL 33431-0991

This study presents a nonprobabilistic set theoretical approach to analyzing uncertainty in vehicle vibrations arising from motion along imperfectly known terrain. The uncertainty in the substrate is described by a set of allowed substrate profile functions. The analysis of the vehicle response consists in determining the range of variation of performance parameters, as the substrate profile varies over the set of allowed functions. This enables characterization of the uncertain but bounded motion of the vehicle as well as optimization of the vehicle design with respect to uncertainty in the substrate. Maximum acceleration during motion on an imperfectly known surface is determined and related to standard design guidelines for limiting exposure to vibrational acceleration. A method is developed for determining the greatest lower bound of the number of sign changes per second of the vibrational acceleration when moving over an irregular and incompletely specified substrate. Motion along uniformly bounded substrates is studied, as well as traversal of barriers.

1 Introduction

Motion of a vehicle over an uneven surface produces stresses and accelerations due to reactions to the substrate. If the substrate profile is known exactly, however complex it might be, then the response of the vehicle can be calculated directly either in closed form or numerically. However, in practice, the substrate irregularities are often known imprecisely, so that conventional deterministic structural analysis is inapplicable. Consequently, many studies have adopted a probabilistic analysis. In particular, spectral analysis has often been used to probabilistically model both the structure of an unknown substrate and its influence on the motion of a vehicle.

Spectral analysis usually postulates vehicle motion with constant horizontal velocity and continuous contact with a weakly homogeneous random substrate. This approach has been initiated by Kozin and Bogdanoff (1960) and by Robson (1984a) and has been successfully pursued by a number of other investigators. The most comprehensive early study, which included a probabilistic description of the road roughness, random vibration analysis of the vehicle and effects of the vibrations on the payload, was conducted by Bogdanoff et al. (1965), Cote et al. (1965, 1966), and Kozin et al. (1966). The current state of the art is discussed in books by Bekker (1969), Nikolaenko (1967), and Robson et al. (1971) and in the reviews by Schiehlen (1986a, 1986b, 1988), Newland (1986), and Robson (1984b). (See also Sobczyk and Macvean (1976) and Sobczyk et al. (1968)).

While spectral analysis is of proven utility, some limitations can be identified. The substrate profile is typically assumed to be described as a stationary Gaussian random process, from which spatial correlation functions are measured. The required data are not always available, and the assumption of stationarity and gaussianity is not always valid.

A nonprobabilistic approach to the analysis of earthquake excitation of civil structures has been pioneered by Drenick (1968, 1970, 1977), Drenick and Yun (1979), and Drenick et al. (1984). Drenick's method has been successfully applied in several applications by Shinozuka (1970), Popplewell and Youssef (1979), and Michelapoulos and Riley (1972).

In this paper a nonprobabilistic, set theoretic methodology—called by the present authors convex modeling—is used for representing uncertainty in the substrate. Substrate uncertainty is specified by a set of allowed substrate profile functions. The formulation of a convex model is based either on limited available information or, alternatively, specifies the substrate design. The analysis of the vehicle response concentrates on evaluating the variation of performance, as the substrate profile varies on the set of allowed functions. Thus, uncertain vehicle motion is characterized and optimization of the vehicle design with respect to uncertainty in the substrate is obtained.

The set theoretical methodology is applicable to a wide range of substrate morphologies, and to the various types of fragmentary information about the substrate. In Sections 3 and 4 the substrate is assumed to be uniformly bounded; in Section 5 uniform bounds on the variation in the slope of the substrate

Contributed by the Applied Mechanics Division of THE AMERICAN SOCIETY OF MECHANICAL ENGINEERS for publication in the ASME JOURNAL OF APPLIED MECHANICS.

Discussion on this paper should be addressed to the Technical Editor, Prof. Leon M. Keer, The Technological Institute, Northwestern University, Evanston, IL 60208, and will be accepted until two months after final publication of the paper itself in the JOURNAL OF APPLIED MECHANICS. Manuscript received by the ASME Applied Mechanics Division, Jan. 19, 1990; final revision, Aug. 2, 1990.

Copyright © 1991 by ASME
Downloaded 03 May 2010 to 171.66.16.248. Redistribution subject to ASME license or copyright; see http://www.asme.org/terms/Terms_Use.cfm

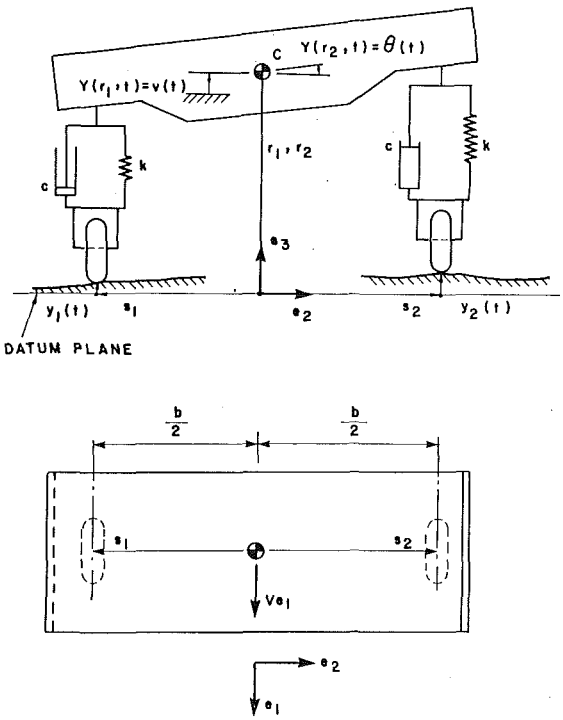

Fig. 1 Two-wheeled trailer (following Newland, 1986)

are employed to represent a barrier or obstacle of uncertain shape. The vehicle model studied here is from Newland (1986), and is described in Section 2.

2 The Vehicle Model

The methodology developed in this paper will be applied to the vertical response of the center of mass of a two-wheeled trailer, as shown in Fig. 1 (from Newland, 1986). The vertical displacement imposed by the substrate on the ith wheel is denoted $y_i(t)$. The forward velocity of the vehicle is constant in time. The equation of motion of the vertical displacement $x(t)$ of the center of mass is

$$M\frac{d^2x}{dt^2}+2c\frac{dx}{dt}+2kx=c\left(\frac{dy_1}{dt}+\frac{dy_2}{dt}\right)+k(y_1+y_2) \tag{1}$$

where the following notation is adopted:

M = mass of the trailer body (mass of wheels and suspension are neglected).

c = damping coefficient of each suspension.

k = stiffness of each suspension.

The initial conditions are

$$x(0)=\frac{dx(0)}{dt}=0. \tag{2}$$

We assume also that $y_i(0)=y_i'(0)=0$, where the prime denotes differentiation with respect to time.

For convenience, let us define the following parameters:

$$\omega_o^2=\frac{2k}{M},\ \zeta\omega_o=\frac{c}{M} \tag{3}$$

$$\beta=\sqrt{1-\zeta^2},\ \omega_o\beta=\omega_d. \tag{4}$$

The values of these parameters, based on the data presented in Newland (1986), are: $\omega_o=8.944\text{s}^{-1}$, $\zeta=0.1118$, $\beta=0.9937$ and $\omega_d=8.888\text{s}^{-1}$.

The general solution of equation (1) for $\zeta<1$ is obtained, after partial integration to remove the derivatives of y_i, as

$$x(t)=\int_0^t[y_1(\tau)+y_2(\tau)]\phi(t-\tau)d\tau \tag{5}$$

where

$$\phi(t)=\frac{\omega_o}{\beta}e^{-\zeta\omega_o t}\left[\left(\frac{1}{2}-\zeta^2\right)\sin\omega_d t+\zeta\beta\cos\omega_d t\right]. \tag{6}$$

Likewise, the vertical velocity $v(t)$ and acceleration $a(t)$ of the center of mass are obtained by differentiation of $x(t)$, for $\zeta<1$, as

$$v(t)=\zeta\omega_o[y_1(t)+y_2(t)]+\int_0^t[y_1(\tau)+y_2(\tau)]\psi(t-\tau)d\tau \tag{7}$$

$$a(t)=\zeta\omega_o\left(\frac{dy_1}{dt}+\frac{dy_2}{dt}\right)+\omega_o^2\left(\frac{1}{2}-2\zeta^2\right)[y_1(t)+y_2(t)]+\int_0^t[y_1(\tau)+y_2(\tau)]\rho(t-\tau)d\tau \tag{8}$$

where

$$\psi(t)=\frac{\omega_o^2}{\beta}e^{-\zeta\omega_o t}\left[\zeta\left(\zeta^2-\beta^2-\frac{1}{2}\right)\sin\omega_d t+\beta\left(\frac{1}{2}-2\zeta^2\right)\cos\omega_d t\right] \tag{9}$$

$$\rho(t)=\frac{\omega_o^3}{\beta}e^{-\zeta\omega_o t}\left[\left(3\beta^2\zeta^2+\frac{1}{2}(\zeta^2-\beta^2)-\zeta^4\right)\sin\omega_d t+\zeta\beta(3\zeta^2-\beta^2-1)\cos\omega_d t\right]. \tag{10}$$

Note that $\psi(t)=\phi'(t)$ and $\rho(t)=\psi'(t)$.

3 Peak Acceleration On Uniformly Bounded Substrates

The response of human passengers to vibration is a critical parameter in the design of vehicles for rough terrain. Experimental data (Harris, (1987)) have been accumulated for assessing the effect of vibration on humans. For instance, data are available which indicate the average peak accelerations at which human subjects first perceive the vibration, then find it unpleasant and finally refuse to tolerate the vibration. Quantitative guidelines for vibration exposure in vehicles have been standardized. These guidelines limit the duration of exposure to vibrational acceleration for preservation of health and safety ("exposure limits"), for preservation of work efficiency ("decreased proficiency boundaries"), and for preservation of comfort ("reduced comfort boundary"). These guidelines are based on experimental measurements with human subjects under idealized conditions of constant frequency and uniform vibrational modes. The guidelines specify approximate limits for safety, work efficiency, and comfort since laboratory tests cannot reproduce the complete range of subject-vehicle-environment interactions combined with the inevitable physiological and psychological variations of the subjects. Nevertheless, the standards provide benchmark data with respect to which vehicle performance on rough terrain can be evaluated.

The peak vertical acceleration of the vehicle described in Section 2 is evaluated in this section for motion on a rough but uniformly bounded substrate. This analysis, combined with standards for vibrational acceleration, serves as the basis for vehicle design to attain satisfactory performance with respect to vibrational acceleration when traversing a rough surface. The following section discusses the duration of acceleration excursions.

A physical substrate is represented by a function which describes the vertical displacement of the substrate above and below the nominal profile, at each point on the plane. The uncertainty in the substrate profile is specified by a set of allowed displacement functions. This set approximates the ensemble of all physically realizable profiles.

The uniform bound model of uncertainty in the substrate profile asserts that an actual substrate can deviate from the

Downloaded 03 May 2010 to 171.66.16.248. Redistribution subject to ASME license or copyright; see http://www.asme.org/terms/Terms_Use.cfm

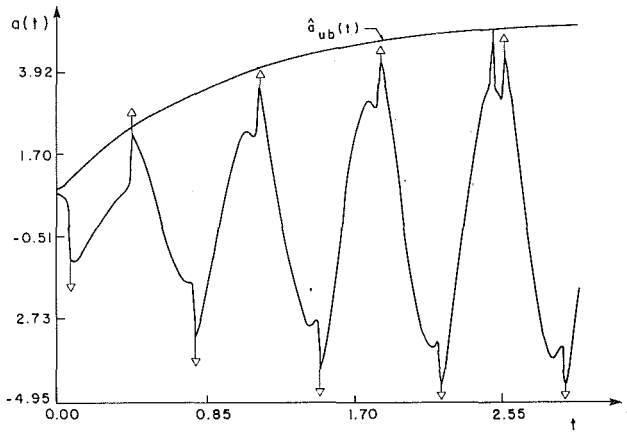

Fig. 2 Envelope of maximum vertical acceleration of center of mass (upper curve) and acceleration history reaching the envelope at several instants (lower curve)

nominal, flat, horizontal profile at any point by no more than a specified amount. This implies that there is no relation between substrate displacements at distinct points of the profile.

Consequently, the vertical displacements imposed on the vehicle ($y_1(t)$ and $y_2(t)$ in equation (1)) each belong to the following set of uniformly bounded functions:

$$Y(\hat{y}) = \{y: |y(t)| \le \hat{y},\ 0 \le t < \infty\}. \tag{11}$$

This means that the actual substrate at any point can deviate from the nominal flat substrate by as much as $\pm\hat{y}$. The value of $\hat{y}$ either represents the only available information about a real substrate or, conversely, is a design parameter to be determined in specifying the substrate.

It will be noticed that $Y(\hat{y})$ is a convex set of functions. That means that, for any functions $u(t)$ and $w(t)$ in $Y(\hat{y})$ and any $0 \le \alpha \le 1$, the function $\alpha u(t) + (1-\alpha)w(t)$ also belongs to the set $Y(\hat{y})$. In other words, any convex combination of allowed substrate profiles is also an allowed profile.

Examination of equation (8) shows that the vertical acceleration of the center of mass of the vehicle at time t attains a maximum if $y_1(\tau)$ and $y_2(\tau)$ are of the same sign as $\rho(t-\tau)$ and equal in magnitude to $\hat{y}$. Thus, in the uniform bound model of substrate uncertainty, the vehicle acceleration is maximized by a "bang-bang" road profile which switches between its extremal values. This results in impulse forces applied to the center of mass at the instants of road profile discontinuity, as indicated by the derivatives on the right-hand side of equation (8). In addition, there act the step loads at these instants, as the last two terms of equation (8) show. Aside from the impulse accelerations, the envelope of maximal vertical acceleration is found from equation (8) to be

$$\hat{a}_{ub}(t) = 2\hat{y}w_o^2 \left|\frac{1}{2} - 2\zeta^2\right| + 2\hat{y}\int_0^t |\rho(\tau)|\, d\tau. \tag{12}$$

The bang-bang characteristic of the road profile which maximizes the acceleration is reminiscent of bang-bang control functions. These frequently arise when linear inequality constraints are placed on the control variables (Bryson and Ho, 1975), or in minimal-time control when the system is "moved from one state to another in the shortest time by all times properly utilizing all available power" (Ogata, 1975).

Figure 2 depicts the envelope of maximum vertical acceleration of the center of mass. The terrain profile which maximizes the acceleration at a preselected instant $t = t^*$ is a periodic bang-bang profile. The phase of the bang-bang profile $y(t)$ which maximizes the acceleration at time t^* is such that $y(0)$ and $\rho(t^*)$ are of the same sign, and such that the first switch in the profile occurs at the smallest non-negative value of τ for which $\rho(t^* - \tau) = 0$. The period of the maximizing profile is $2\pi/\omega_d = 0.707$ sec.

Figure 2 shows the envelope of maximum acceleration, $\hat{a}_{ub}(t)$, with an acceleration history reaching the envelope at $t^* = 2.5$ sec. The uniform bound on the road profile deviation is $\hat{y} = 0.01$ m. Equation (8) reveals that $a(t)$ contains derivatives of the bang-bang profile; i.e., Dirac delta functions, at the instants when the profile discontinuities occur. These impulse accelerations are represented in Fig. 2 by arrows. In addition, the term $\omega_o^2\,(0.5 - 2\zeta^2)(y_1(t) + y_2(t))$ indicates that the acceleration history contains jumps of amplitude 1.52 m/s^2 at the instants when the profile discontinuities occur. This is quite evident in Fig. 2.

4 Duration of Acceleration Excursions on Uniformly Bounded Substrates

Vibrational exposure guidelines limit the exposure to vibrational acceleration at single discrete frequencies. In practice, the vibrational acceleration produced by travel over a rough substrate is composed of a range of frequencies. Nevertheless, the net effect of vertical vibrational acceleration is an up-down motion, regardless of the precise frequency composition of the acceleration waveform. In other words, the acceleration changes sign in a roughly periodic fashion.

A parameter which is derived from the frequency structure of the acceleration is the maximum duration for which the acceleration exceeds a given threshold. A rapidly oscillating vibrational acceleration achieves accelerations above any given value for only a short duration. Conversely, slow oscillation displays long durations of accelerations excursions above a given threshold. Evaluation of the greatest duration of vibrational acceleration above a given threshold enables partial assessment of the typical frequency of the vibrational acceleration. This is relevant since the limits of acceptable vibration vary with the vibration frequency.

In particular, let T_0 be the greatest continuous duration for which the acceleration exceeds zero. From the symmetry of the differential equations describing the oscillation of the vehicle, it is recognized that T_0 is also the greatest duration for which the acceleration is negative. Consequently, the acceleration must change sign at least once in T_0 seconds. In other words, $1/T_0$ is the greatest lower bound for the number of acceleration sign changes per second.

In this section we will evaluate the longest continuous time interval throughout which the vertical acceleration of the center of mass exceeds a given threshold value, given the initial conditions of equation (2). We will study this problem by investigating whether there exists a profile for which the vertical acceleration exceeds the threshold during a given interval. By varying the time interval we will determine the greatest continuous interval for which the acceleration exceeds the threshold.

The acceleration history during a time interval is a function of the road profile during that interval and the state of the system at the onset of the interval. Our task is to determine if there exists a uniformly bounded road profile in the interval $[t_1, t_2]$ such that

$$x(t_1) = x_0 \quad |y(t)| \le \hat{y} \quad y(t_1) = y(t_2) = y'(t_1) = y'(t_2) = 0$$
$$a(t_1) = a(t_2) = a_0 \quad a(t) \ge a_0 \quad t_1 < t < t_2. \tag{13}$$

By varying t_1 and t_2 we can find the longest duration for which the acceleration exceeds a_0, starting from a given initial displacement x_0. The state (x_0, a_0) of the system at t_1 must be consistent with the initial conditions at time $t = 0$ specified in equation (2). At the end of this section we will demonstrate a simple method for determining the set of all values (x_0, a_0) which can be reached at any time t_1.

A comment must be made on the end-point constraints on the acceleration: $a(t_1) = a(t_2) = a_0$. If a road profile exists which satisfies $a(t_1) > a_0$ or $a(t_2) > a_0$ as well as the other constraints in (13), then $[t_1, t_2]$ is certainly not the *longest* interval for

Downloaded 03 May 2010 to 171.66.16.248. Redistribution subject to ASME license or copyright; see http://www.asme.org/terms/Terms_Use.cfm

which such a profile exists. Consequently, since we are seeking the greatest *continuous* duration for which $a(t) \geq a_0$, it is sufficient to require equality constraints rather than inequality constraints at the end points.

We can formulate this task as an optimization problem. Let $L(y, t)$ be a continuous functional of y whose form will be chosen later, and let

$$J = \int_{t_1}^{t_2} L(y, t)dt. \tag{14}$$

Let S be the set of all road profiles for which the road profiles and the response satisfy the constraints in (13). S may be empty or may contain one or more elements. In any case we can ask for the supremum of J on the set S. No such supremum exists if S is empty. $L(y, t)$ is, by definition, a continuous function of y. Also, $Y(\hat{y})$ is a compact set. A theorem of functional analysis states that a continuous function on a compact set achieves a maximum value on that set (Kelly and Weiss, 1979). Hence, if S is not empty, then a supremum exists because S is a subset of all uniformly bounded profiles, $Y(\hat{y})$, and $L(y, t)$ is continuous on the compact set $Y(\hat{y})$. To reiterate, if a road profile exists which satisfies the constraints in (13), then a road profile exists which satisfies (13) and which maximizes J subject to the constraints in (13).

Now, the maximization of J subject to (13) is an optimization problem whose solution can be sought using the technique of Euler-Lagrange. If a solution of the Euler-Lagrange equations exists, then a road profile satisfying (13) exists; if no solution of the Euler-Lagrange equations exists, then no road profile satisfying (13) exists. In the former case, the greatest duration for which the acceleration exceeds a_0 is at least as great $t_2 - t_1$. In the latter case, $t_2 - t_1$ exceeds this greatest duration.

This optimization problem is complicated by the constraints being inequalities. Introduction of additional unknown functions, μ, η, and ξ, converts the constraints to equalities (Vanderplaats, 1984). Consider the maximization of

$$J = \int_{t_1}^{t_2} L(y, \mu, \eta, \xi, t)dt \tag{15}$$

subject to the constraints:

$$f_1(y, \mu, t) \equiv y(t) - \mu^2 + \hat{y} = 0 \tag{16}$$

$$f_2(y, \eta, t) \equiv y(t) + \eta^2 - \hat{y} = 0 \tag{17}$$

$$f_3(y, \xi, t) \equiv a_y(t) - \xi^2 - a_0 = 0. \tag{18}$$

We must find four real functions, $y(t)$, $\mu(t)$, $\eta(t)$, and $\xi(t)$, to maximize J subject to equations (16)–(18). To solve this we employ the calculus of variations (Weinstock, 1974). The constraints are adjoined to the integrand of equation (15) with the introduction of three unspecified multiplier functions $\lambda_1(t)$, $\lambda_2(t)$, and $\lambda_3(t)$. The seven unknown functions must satisfy the three constraint equations and the four Euler-Lagrange equations during the interval $[t_1, t_2]$, to be formulated as follows.

The vertical acceleration of the center of mass, on the road profile $y(t) = y_1(t) = y_2(t)$, given $x(t_1) = x_0$, $a(t_1) = a_0$, $y(t_1) = y'(t_1) = 0$ is written as

$$a_y(t) = \omega_o^2 e^{-\zeta\omega_o t}\left[\left(\frac{\zeta^2}{\beta} - \beta\right)\left(x_0\zeta + \frac{v_0}{\omega_o}\right)\sin \beta\omega_o t + \left(x_0(\beta^2 - \zeta^2) - \frac{2\zeta v_0}{\omega_o}\right)\cos \beta\omega_o t\right] + 2\zeta\omega_o y'(t) + \omega_o^2(1 - 4\zeta^2)y(t) + 2\int_0^t y(\tau)\rho(t-\tau)d\tau \tag{19}$$

where the initial velocity, v_0, is related to the other initial conditions, x_0 and a_0, by

$$v_0 = \frac{x_0\omega_o}{2\zeta}(1 - 2\zeta^2) - \frac{a_0}{2\zeta\omega_o}. \tag{20}$$

Define

$$F(y, y', t) = L + \sum_{m=1}^{3} \lambda_m f_m. \tag{21}$$

Consider the cost function

$$L = \mu^2(t) + \eta^2(t) + \xi^2(t) - y^2(t). \tag{22}$$

The Euler-Lagrange equations are

$$0 = \frac{\partial F}{\partial y} - \frac{d}{dt}\left(\frac{\partial F}{\partial y'}\right) = -2y(t) + \lambda_1(t) + \lambda_2(t) + 2\lambda_3(t)\psi(t) \tag{23}$$

$$0 = \frac{\partial F}{\partial \mu} - \frac{d}{dt}\left(\frac{\partial F}{\partial \mu'}\right) = 2[1 - \lambda_1(t)]\mu(t) \tag{24}$$

$$0 = \frac{\partial F}{\partial \eta} - \frac{d}{dt}\left(\frac{\partial F}{\partial \eta'}\right) = 2[1 + \lambda_2(t)]\eta(t) \tag{25}$$

$$0 = \frac{\partial F}{\partial \xi} - \frac{d}{dt}\left(\frac{\partial F}{\partial \xi'}\right) = 2[1 - \lambda_3(t)]\xi(t). \tag{26}$$

The systematic solution of equations of this type is discussed in Ben-Haim and Elishakoff (1990).

We now consider the determination of the set of values (x, v) which can be reached at time t by the system in equation (1) starting with the conditions in equation (2). Equation (20) relates this set to the set of values (x, a). Let $R(t)$ be the set of displacement and velocity values $(x(t), v(t))$ which can be reached at time t, starting from the initial conditions $x(0) = v(0) = 0$ and traveling over uniformly bounded road profiles $|y(t)| \leq \hat{y}$. That is

$$R(t) = \left\{r : r(t) = \begin{pmatrix} x_y(t) \\ v_y(t) \end{pmatrix} \text{ for all } y \in Y(\hat{y})\right\} \tag{27}$$

where x_y and v_y are given by equations (5) and (7), respectively, with $y = y_1 = y_2$. $R(t)$ is a convex set, so to plot $R(t)$ we need only determine its boundary points. $R(t)$ contains the origin, so the boundary of $R(t)$ is the locus of elements of $R(t)$ which are farthest along rays from the origin. Let $u(\theta) = (\cos \theta, \sin \theta)$ be a unit vector in the (x, v) plane at the angle θ from the x-axis. The line perpendicular to $u(\theta)$ at a distance D from the origin consists of points (x, v) satisfying $x \cos \theta + v \sin \theta = D$. Thus, the distance from the origin of a line perpendicular to $u(\theta)$ and tangent to $R(t)$ is

$$D(\theta) = \max_{y \in Y(\hat{y})} \{x_y(t) \cos \theta + v_y(t) \sin \theta\} \tag{28}$$

$$= 2\hat{y}\zeta\omega_o + 2 \max_{y \in Y(\hat{y})} \int_0^t y(\tau)\{\phi(t-\tau) \cos \theta + \psi(t-\tau) \sin \theta\}\, d\tau. \tag{29}$$

The maximum of the integral in equation (29) is obtained by choosing $y(\tau)$ equal in magnitude to $\hat{y}$ and equal in sign to $\phi(t-\tau) \cos \theta + \psi(t-\tau) \sin \theta$. Let $y_\theta(\tau)$ denote this road profile. That is,

$$y_\theta(\tau) = \hat{y}\, \text{sgn}[\phi(t-\tau) \cos \theta + \psi(t-\tau) \sin \theta]. \tag{30}$$

The line perpendicular to $u(\theta)$ and tangent to $R(t)$ contacts $R(t)$ at the point $(x_{y_\theta}, v_{y_\theta})$. Hence, this point is a boundary point of $R(t)$. Employing equations (5) and (7), the boundary points (x, v) of $R(t)$ are found by varying θ on $[0, 2\pi]$ in the relations

$$x = 2\hat{y}\int_0^t \text{sgn}[\phi(t-\tau) \cos \theta + \psi(t-\tau) \sin \theta]\phi(\tau)d\tau \tag{31}$$

$$v = 2\zeta\omega_o\hat{y}\,\text{sgn}[\phi(0) \cos \theta + \psi(0) \sin \theta] + 2\hat{y}\int_0^t \text{sgn}[\phi(t-\tau) \cos \theta + \psi(t-\tau) \sin \theta]\psi(\tau)d\tau. \tag{32}$$

Further computational details are presented in Ben-Haim and Elishakoff (1990).

A simpler version of this problem occurs if one wishes to determine the greatest continuous duration of acceleration

Downloaded 03 May 2010 to 171.66.16.248. Redistribution subject to ASME license or copyright; see http://www.asme.org/terms/Terms_Use.cfm

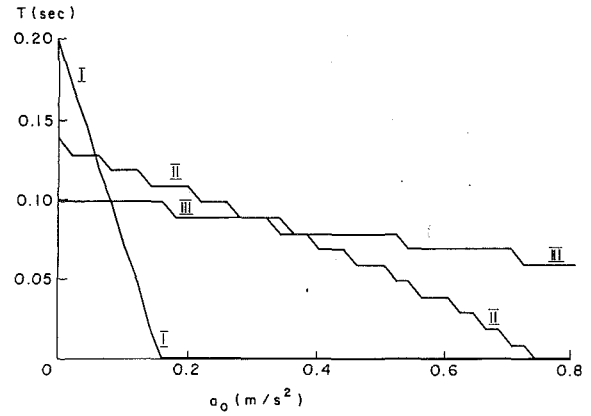

Fig. 3 Maximum duration of excursion from $t=0$ versus the acceleration threshold for three values of the stiffness coefficient

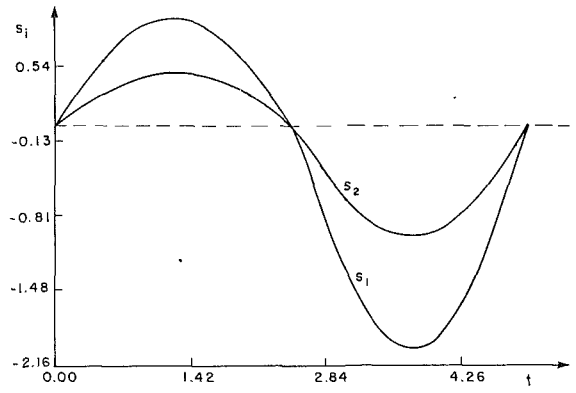

Fig. 4 Envelope functions for a typical unimodal isochronous obstacle

above a given threshold, a_0, starting at time $t=0$. In this case the use of the loop on t_1 is simpler and set $R(t_1)$ contains only a single element: the initial conditions of the vehicle motion.

Figure 3 shows the greatest continuous duration of acceleration excursion versus the acceleration threshold, starting at $t=0$ from the initial conditions in equations (2) and for $\hat{y}=0.01$ m. Results are shown for three different values of the stiffness coefficient k. It is seen that the duration of excursion is very sensitive to the stiffness of the suspension system. In curve II the stiffness coefficient is 4×10^4 N/m, which is the value used in Newland's work (1986) and elsewhere in this paper. This curve shows, for example, that 0.11 s is the greatest continuous duration for which the acceleration can be maintained above 0.2 m/s^2, starting at time $t=0$ from the initial conditions in equation (2). Likewise, the same curve indicates that 0.042 s is the greatest possible duration of acceleration above 0.6 m/s^2. Curve II reaches the axis at $a_0=0.76$ m/s^2, indicating that accelerations greater than this value can not be maintained for a nonzero duration starting from time $t=0$. This agrees with equation (12) and Fig. 2 which indicate that the upper bound of the acceleration at $t=0$ is $\hat{a}_{ub}=2\hat{y}\omega_0^2\left|\frac{1}{2}-2\zeta^2\right|=0.76$ m/s^2 for $\hat{y}=0.01$ m.

When the stiffness is increased to 8×10^4 N/m (curve III) the greatest duration of acceleration excursion above 0.6 m/s^2 is 0.071 s, nearly double the value in curve II. This is due to the fact that the stiffer suspension system is able to attain great accelerations. Conversely, comparison of curves II and III indicates that the stiff suspension system maintains low values of the accelerations for shorter durations than for the suspension of moderate stiffness.

Finally, the results in curve I indicate that a very soft suspension ($k=1\times10^4$ N/m) achieves only comparatively low accelerations, but can maintain these acceleration excursions for longer durations.

As mentioned before, vertical vibrational acceleration resulting from motion on an irregular surface entails roughly periodic changes in the sign of the acceleration. Examination of Fig. 3 for duration of acceleration excursions above $a=0$ indicates that the stiff spring (curve III) tends to oscillate twice as rapidly as the softest spring (curve I). Furthermore, the frequencies involved (for the specific situation examined) are in the range of 5 to 10 sign changes per second. Considerations such as these enable the designer to relate the vehicle performance on an irregular substrate to accepted limits for vibration exposure.

The step-like form of all three curves is due to the fact that bang-bang profiles produce excursions of maximal duration. As the acceleration threshold is reduced, the maximum duration of excursion remains constant until the changing boundary conditions allow an alteration in the bang-bang profile.

5 Isochronous Obstacles

Vehicle dynamics on uniformly bounded substrates, e.g., irregular terrain, was studied in the previous two sections. In this section we employ a different model for uncertainty in the substrate profile, by assuming that the slope rather than the height of the substrate is uniformly bounded. This is a useful and simple representation of rolling terrain and will be used in studying vehicle response to barriers. The aim is to derive the extremal acceleration as the vehicle passes over any barrier from among an ensemble of barriers. The maximum vibrational acceleration is related to the peak acceleration allowed for preservation of safety, work efficiency, or comfort.

The time expended in traversing a barrier depends on the shape and traction properties of the barrier and on the characteristics of the engine in response to a varying load. However, as a simple approximation to these phenomena, we will assume that the duration which the vehicle spends on the obstacle is the same for all allowed obstacles. In addition, in evaluating the vertical response of the center of mass we will assume that both wheels of the trailer follow the same obstacle profile, so $y_1(t)=y_2(t)$ in equation (1). Finally, it is reasonable to define the obstacles in terms of envelope bounds on their slopes. This means that the obstacle profile functions belong to the following set:

$$B(s_1(t),\ s_2(t))=\left\{y:y(0)=0;\ s_1(t)\le\frac{dy}{dt}\le s_2(t)\right\} \qquad (33)$$

where $s_1(t)$ and $s_2(t)$ are specified functions for which $s_1(t)\le s_2(t)$ during $0\le t\le D$, and $s_1(t)=s_2(t)=0$ for $t>D$. D is the duration of passage over the obstacle. The barriers in this ensemble are isochronous in the sense that the duration of passage is the same for all members of the set B.

Figure 4 shows typical slope envelope functions for unimodal isochronous barriers. All the barriers in the ensemble exhibit positive slopes from $t=0$ to $t=2.5$ sec and negative slopes from $t=2.5$ to $t=5$ sec. Thus, all the barriers in the ensemble display a single peak which is reached at $t=2.5$ sec. We have chosen the functions $s_i(t)$ for this case as

$$s_1(t)=a_1\sin\frac{2\pi t}{5}\quad 0\le t\le 2.5$$

$$=a_2\sin\frac{2\pi t}{5}\quad 2.5\le t\le 5$$

$$s_2(t)=\sin\frac{2\pi t}{5}\quad 0\le t\le 5.$$

The slope envelope functions shows in Fig. 5 illustrate that it is not necessary for the barriers to have a fixed number of peaks. The barriers in this ensemble display positive slope during the interval [0, 2] and negative slope during [3, 5]. The intermediate time interval, [2, 3], corresponds to the top region

Downloaded 03 May 2010 to 171.66.16.248. Redistribution subject to ASME license or copyright; see http://www.asme.org/terms/Terms_Use.cfm

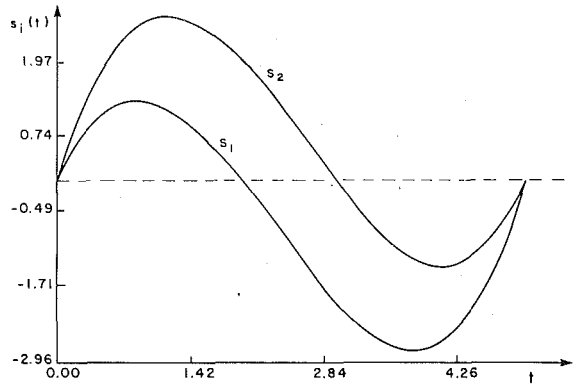

Fig. 5 Envelope functions for a typical multimodal isochronous obstacle

of the barrier, which can be choppy or wavey. Multimodal isochronous barriers are modeled here as

$$s_1(t)=\frac{t}{3}(2-t)(5-t) \tag{34}$$

$$s_2(t)=\frac{t}{3}(3-t)(5-t). \tag{35}$$

Figure 6 illustrates as an example the slope profile of a wavey-topped barrier whose slope is bounded by $s_1(t)$ (equation (34)) and $s_2(t)$ (equation (35)). The slope of this barrier is given by

$$s(t)=s_1(t)\sin^2 2\pi t+s_2(t)\cos^2 2\pi t.$$

The corresponding height profile is shown in Fig. 7.

Equation (8) expresses the vehicle acceleration. However, it should be noted that $y_1(t)=y_2(t)$ in this slope-bounded model, for otherwise the vertical displacement between the two wheels of the trailer could increase without bound. Also, it is convenient to express the vehicle acceleration in terms of the derivatives of the road profile, as follows:

$$a(t)=2\omega_o\zeta y'(t)+2\int_0^t y'(\tau)\psi(t-\tau)d\tau \tag{36}$$

where y' is the time derivative of y and ψ is defined in equation (9).

The maximum acceleration is obtained by defining the instants at which $\psi(\tau)$ changes sign. Specifically, consider the following sets:

$$A_+(t)=\{\tau:0\le\tau\le t,\ \psi(t-\tau)\ge 0\} \tag{37}$$

$$A_-(t)=\{\tau:0\le\tau\le t,\ \psi(t-\tau)<0\}. \tag{38}$$

Thus, $A_+(t)$ is the set of time instants, τ, during $[0, t]$ at which $\psi(t-\tau)$ is non-negative, while $A_-(t)$ is the set of instants at which $\psi(t-\tau)$ is negative.

The maximum acceleration is obtained from equation (36) by choosing the barrier profile whose slope at each instant is either s_1 or s_2, depending on the sign of the rest of the integrand. Explicitly, the maximum vertical acceleration of the center of mass at time $t\ge 0$ is:

$$\hat{a}_{io}(t)=2\omega_o\zeta s_2(t)+2\int_{A_+(t)}s_2(\tau)\psi(t-\tau)d\tau$$

$$+2\int_{A_-(t)}s_1(\tau)\psi(t-\tau)d\tau. \tag{39}$$

It should be noted that this expression describes the maximum possible acceleration at any time t during and after passing the obstacle. The subscript "io" represents "isochronous obstacle."

Figure 8 shows the vertical acceleration of the center of mass in passage over the unimodal isochronous barrier whose envelope functions are shown in Fig. 4. Various values are shown

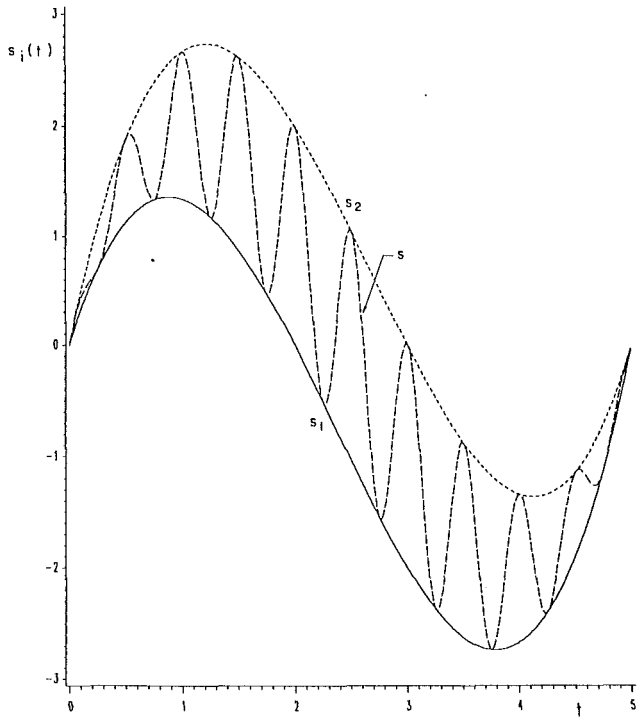

Fig. 6 Slope profile of a wavey-topped isochronous barrier

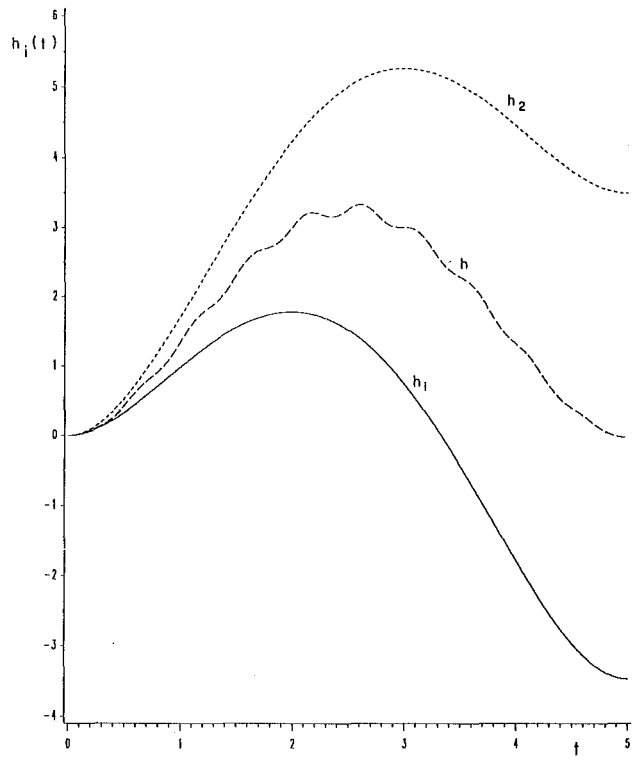

Fig. 7 Height profile of a wavey-topped isochronous barrier

for the coefficients a_1 and a_2. Similarly, Fig. 9 shows the vertical acceleration of the center of mass in passage over a multimodal isochronous barrier whose envelope functions are shown in Fig. 5.

6 Summary and Conclusions

Convex sets of functions, rather than probability densities, are used to describe uncertainty in the profile of irregular

Downloaded 03 May 2010 to 171.66.16.248. Redistribution subject to ASME license or copyright; see http://www.asme.org/terms/Terms_Use.cfm

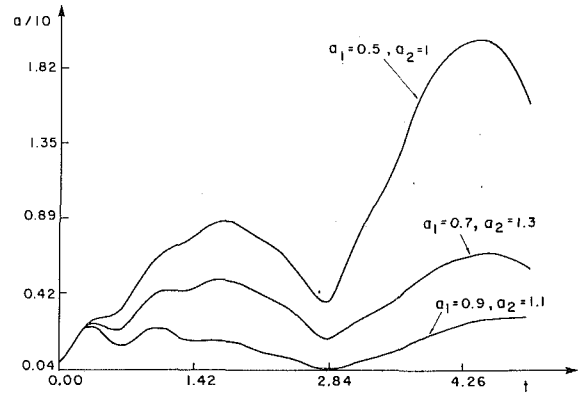

Fig. 8 Vertical acceleration for passage over a unimodal isochronous obstacle

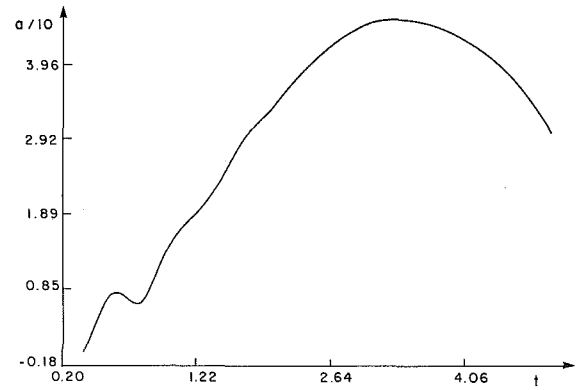

Fig. 9 Vertical acceleration for passage over a multimodal isochronous obstacle

terrain, which distinguishes this paper from traditional probabilistic studies. Two types of convex models have been used. Uniform bounds on the terrain profile represent uneven surfaces with moderate roughness. Slope bounds define rolling terrain and isolated obstacles. The vibrational acceleration produced in a vehicle traversing surfaces such as these is a performance parameter which included in vehicle analysis and design. The vertical acceleration of a two-wheeled trailer has been analyzed in a number of situations, with a linear model of the vibration dynamics. Several conclusions can be made.

(1) The maximum vertical acceleration, for any surface profile in a uniformly bounded set of profiles, can be evaluated without difficulty. The maximum vertical acceleration for the trailer analyzed is no larger that 5.3 m/s^2 on a surface whose height varies within ± 0.01 m. (See Fig. 2.) Industrial standards (Harris, 1987) suggest that this leads to substantial discomfort and reduction of work efficiency in a matter of minutes.

(2) A method has been demonstrated for determining the longest time interval during which the vibrational acceleration exceeds a given threshold. This is useful for relating the complicated vibratory motion on an uneven and incompletely known substrate to the standardized limits of exposure to vibration which are based on single frequency tests. Furthermore, $1/T_0$ is the greatest lower bound of the number of acceleration sign changes per second, if T_0 is the greatest duration for which the acceleration exceeds zero. For the trailer studied here moving on a uniformly bounded substrate, the effect of the spring constant on the maximum duration of acceleration excursions is demonstrated quantitatively. For spring constants from 1×10^4 to 8×10^4 N/m, the maximum duration of positive acceleration varies from 0.2 to 0.1 sec for the situation examined. This corresponds to variation in the minimum number of acceleration sign changes per second from 5 s^{-1} (for the soft spring) to 10 s^{-1} (for the hard spring). (See Fig. 3.)

(3) In practice, the terrain profile may include transient surface irregularities. Dynamic response of a vehicle is quite different in traversing an single obstacle than in passing over moderately uneven but uniformly bounded terrain. This work has demonstrated that uncertainty in barrier profiles can be usefully represented with the set theoretical technique of convex modeling. It is shown that the maximum acceleration can be evaluated for passage over a range of unimodal and multimodal barriers. Large accelerations were obtained in most of the cases examined. (See Figs. 8 and 9.)

Acknowledgments

The authors are indebted to Mr. D. Saddan and Ms. O. Katzanek for assistance in performing the calculations. This research was supported by the Fund for Promotion of Research at the Technion and by the Technion-Niedersachsen (Federal Republic of Germany) Research Cooperation Fund. Some of these results were presented at the ASME-PVP Conference, Hawaii, July 1989. Permission from Prof. D. E. Newland of Cambridge University and Elsevier Science Publishers B. V. to use Fig. 1 is gratefully acknowledged. Some parts of this paper are based on Section 3.2 of Ben-Haim and Elishakoff (1990), by permission of Elsevier, which is acknowledged with thanks.

References

Bekker, M. G., 1969, *Introduction to Terrain-Vehicle Systems*, University of Michigan Press, Ann Arbor, Mich.

Ben-Haim, Y., and Elishakoff, I., 1990, *Convex Models of Uncertainty in Applied Mechanics*, Elsevier Science Publishers, Amsterdam.

Bogdanoff, J. L., Cote, L. J., and Kozin, F., 1965, "Introduction to a Statistical Theory of Land Locomotion—II," *Journal of Terramechanics*, Vol. 2, No. 3, pp. 17-27.

Bryson, A. E., and Ho, Y-C., 1975, *Applied Optimal Control*, John Wiley and Sons, New York, p. 111.

Cote, L. J., Kozin, F., and Bogdanoff, J. L., 1965, "Introduction to a Statistical Theory of Land Locomotion—I," *Journal of Terramechanics*, Vol. 2, No. 2, pp. 17-23.

Cote, L. J., Kozin, F., and Bogdanoff, J. L., 1966, "Introduction to a Statistical Theory of Land Locomotion—IV: Effects of Vibration on the Contents of the Vehicle and Conclusions," *Journal of Terramechanics*, Vol. 3, No. 4, pp. 47-51.

Drenick, R. F., 1968, "Functional Analysis of Effects of Earthquakes," *Second Joint United States—Japan Seminar on Applied Stochastics*, Washington, D.C., Sept. 19-24.

Drenick, R. F., 1970, "Model-free Design of Aseismic Structures," *Journal of Engineering Mechanics Division, Proceedings of the ASCE*, Vol. 96, No. EM4, pp. 483-493.

Drenick, R. F., "On a Class of Non-Robust Problems in Stochastic Dynamics," *Stochastic Problems in Dynamics*, B. L. Clarkson, ed., Pitman, London, pp. 237-255.

Drenick, R. F., Novomestky, F., and Bagchi, G., 1984, "Critical Excitation of Structures," *Wind and Seismic Effects, Proceedings of the 12th Joint UJNR Panel Conference*, U.S. National Bureau of Standards Special Pub., pp. 133-142.

Drenick, R. F., and Yun, C. B., 1979, "Reliability of Seismic Resistence Predictions," *Journal of the Structural Division, Proceedings of the ASCE*, Vol. 105, pp. 1879-1891.

Harris, C. M., ed., 1987, *Shock and Vibration Handbook*, 3rd ed., McGraw-Hill, New York.

Kelly, P. J., and Weiss, M. L., 1979, *Geometry and Convexity*, John Wiley and Sons, New York, p. 50.

Kozin, F., and Bogdanoff, J. L., 1960, "On the Statistical Analysis of the Motion of Some Simple Two-Dimensional Linear Vehicles Moving on a Random Track," *International Journal of Mechanical Sciences*, Vol. 2, pp. 168-178.

Kozin, K., Bogdanoff, J. L., and Cote, J. L., 1966, "Introduction to a Statistical Theory of Land Locomotion—III: Vehicle Dynamics," *Journal of Terramechanics*, Vol. 3, No. 3, pp. 69-81.

Michalopoulos, C. D., and Riley, T. A., 1972, "Response of Discrete Linear Systems to Forcing Functions With Inequality Constraints," *AIAA Journal*, Vol. 10, pp. 1016-1019.

Newland, D. E., 1986, "General Linear Theory of Vehicle Response to Random Road Roughness," *Random Vibrations—Status and Recent Developments*, I. Elishakoff and R. H. Lyon, eds., Elsevier Science Publishers, Amsterdam, pp. 303-326.

Downloaded 03 May 2010 to 171.66.16.248. Redistribution subject to ASME license or copyright; see http://www.asme.org/terms/Terms_Use.cfm

Nikolaenko, N. A., 1967, *Probabilistic Methods of the Dynamic Calculation of the Structures in Mechanical Engineering*, Mashinostroenie Publishing House, Moscow, (in Russian).

Ogata, K., 1970, *Modern Control Engineering*, Prentice-Hall, Englewood Cliffs, N.J., p. 774.

Popplewell, N., and Youssef, N. A. N., 1979, "A Comparison of Maximax Response Estimates," *Journal of Sound and Vibration*, Vol. 62, pp. 339–352.

Robson, J. D., 1984a, *An Introduction to Random Vibrations*, 2nd ed., Edinburgh at the University Press, Elsevier, Amsterdam.

Robson, J. D., 1984, "Researches in Random Vibrations, *Recent Advances in Structural Dynamics*, M. Petyt and H. F. Wolfe, eds., Institute of Sound and Vibration 2nd Intl. Conf., Univ. of Southampton Press, Vol. 2, pp. 621–638.

Robson, J. D., Dodds, C. J., Macvean, D. B., and Paling, V. R., 1971, *Random Vibrations*, (Courses and Lectures No. 115), Springer-Verlag, Vienna.

Schiehlen, W. O., 1986a, "Random Vehicle Vibrations," *Random Vibrations—Status and Recent Developments*, I. Elishakoff and R. H. Lyon, eds., Elsevier Science Publishers, Amsterdam, pp. 379–388.

Schiehlen, W. O., 1986b, "Probabilistic Analysis of Vehicle Vibrations," *Probabilistic Eng. Mechanics*, Vol. 1, pp. 99–104.

Schiehlen, W., 1988, "Modeling, Analysis and Estimation of Vehicle Systems," *Analysis and Estimation of Stochastic Mechanical Systems*, W. Schiehlen and W. Wedig, Springer-Verlag, Vienna, pp. 243–267.

Shinozuka, M., 1970, "Maximum Structural Response to Seismic Excitations," *Journal of the Engineering Mechanics Division, Proceedings of the ASCE*, Vol. 96, No. EM5, pp. 729–738.

Sobczyk, K., and Macvean, D. B., 1976, "Non-stationary Random Vibrations of Systems Travelling With Variable Velocity," *Stochastic Problems in Dynamics*, B. L. Clarkson, ed., Pitman, London, pp. 412–434.

Sobczyk, K., Macvean, D. B., and Robson, J. D., 1977, "Response to Profile-imposed Excitation With Randomly Varying Traversal Velocity," *J. Sound and Vibration*, Vol. 52, pp. 37–49.

Vanderplaats, G. N., 1984, *Numerical Optimization Techniques for Engineering Design*, McGraw-Hill, New York, Section 5-8.2.

Weinstock, R., 1974, *Calculus of Variations*, Dover, New York, Section 4–5.

Downloaded 03 May 2010 to 171.66.16.248. Redistribution subject to ASME license or copyright; see http://www.asme.org/terms/Terms_Use.cfm

A. P. S. Selvadurai
Professor.

B. M. Singh
Research Fellow.

M. C. Au
Research Fellow.

Department of Civil Engineering,
Carleton University,
Ottawa, ON K1S 5B6, Canada

The In-Plane Loading of a Rigid Disk Inclusion Embedded in an Elastic Half-Space

The paper examines the problem of the in-plane loading of a rigid disk inclusion which is embedded in bonded contact with an isotropic elastic half-space region. The governing coupled integral equations, derived via a Hankel transform technique, are evaluated numerically to generate results for the in-plane stiffness of the rigid disk inclusion and the rotation which accompanies the lateral translation.

Introduction

Inclusion problems in classical elasticity theory have a wide range of engineering applications. In the context of mechanics of composite materials, solutions to inclusion problems are used to develop estimates for effective properties of multiphase solids, stress amplification at critical locations of the matrix-inclusion interface, etc. Classical solutions for spheroidal and ellipsoidal inhomogeneities developed by Sadowsky and Sternberg (1949), Dewey (1947), Edwards (1951), Eshelby (1961), Luré (1967), and others have been applied quite extensively in the study of mechanics of composite materials. Extensive accounts of such applications are given by Christensen (1980), Mura (1981), and Hashin and Herakovich (1983). In geomechanical applications, solutions to inclusion problems have been used quite extensively in studies pertaining to ground anchoring mechanisms. Solutions developed for spherical and spheroidal inclusions subjected to axial loads have been used to estimate the stiffness of anchors embedded in isotropic elastic soil media (see, e.g., de Josselin de Jong, 1957; Kanwal and Sharma, 1976; Selvadurai, 1976; Zureick, 1988).

Disk or penny-shaped inclusions are a particular limiting case of the general class of three-dimensional inhomogeneities. Owing to the simplified geometry of the disk inclusion problem it is possible to develop a variety of solutions which are of interest to mechanics of composite materials and geomechanics. Many investigators including Collins (1962), Keer (1965), Kassir and Sih (1968), Selvadurai (1980, 1981, 1982), and Selvadurai and Singh (1982, 1986, 1987) have examined problems related to disk inclusions embedded in elastic media of infinite extent. These studies have been extended to cover disk inclusion problems which deal with the influence of material anisotropy, bimaterial regions, inclusion flexibility, and the interaction of inclusions with cracks. References to these and other studies related to disk inclusion problems are given by Mura (1981, 1988) and Selvadurai (1989, 1992). In a majority of problems dealing with disk inclusions, it is explicitly assumed that the inclusion is contained within a medium of infinite extent. In a generalized treatment of the inclusion problem it is desirable to include the influences of external boundaries. Lawrence (1969) has examined the elastostatic problem of a rigid spherical inclusion which is embedded in an elastic plate. Hunter and Gamblen (1974) have examined the axisymmetric elastostatic problem related to the axial loading of a rigid disk which is embedded in partial bonded contact with an incompressible elastic half-space region. Rajapakse (1988) has examined the problem of the axial loading of a flexible anchor plate embedded in a transversely isotropic elastic half-space by employing a discretization procedure. Wang and Rajapakse (1990) have utilized a discretization procedure to examine a class of inclusion problems related to a transversely isotropic elastic half-space region. References to further work may be found in the works of Mura (1981, 1988).

In this paper we examine the asymmetric elastostatic problem related to the in-plane loading of a rigid disk inclusion which is embedded in bonded contact with an isotropic elastic half-space region. The disk inclusion is embedded at a finite distance from the free surface of the half-space and oriented parallel to the free surface (Fig. 1). The analysis of the problem makes use of a Hankel transform development of the governing equations. The traction-free boundary conditions at the free surface

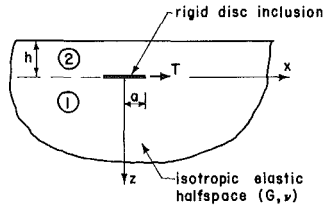

Fig. 1 In-plane loading of a rigid disk inclusion embedded in a half-space

Contributed by the Applied Mechanics Division of THE AMERICAN SOCIETY OF MECHANICAL ENGINEERS for presentation at the Joint Applied Mechanics/Bioengineering Conference, Ohio State University, Columbus, Ohio, June 16-19, 1991.

Discussion on this paper should be addressed to the Technical Editor, Prof. Leon M. Keer, The Technological Institute, Northwestern University, Evanston, IL 60208, and will be accepted until two months after final publication of the paper itself in the JOURNAL OF APPLIED MECHANICS. Manuscript received by the ASME Applied Mechanics Division, Feb. 19, 1990; final revision, July 18, 1990.
Paper No. 91-APM-28.

Copyright © 1991 by ASME
Downloaded 03 May 2010 to 171.66.16.248. Redistribution subject to ASME license or copyright; see http://www.asme.org/terms/Terms_Use.cfm

and the continuity and boundary conditions at the plane of the inclusion yield a system of three coupled integral equations. These integral equations are solved by a quadrature scheme to generate results of engineering interest. Complete numerical results presented in the paper illustrate the manner in which the in-plane stiffness of the disk inclusion and the rotation induced by the lateral force is influenced by the depth of embedment of the inclusion and Poisson's ratio of the elastic medium.

Governing Equations

The asymmetric elastostatic boundary value problem can be analyzed by employing the stress function techniques developed by Muki (1960). The stress functions are governed by the differential equations

$$\nabla^2\nabla^2\Phi(r,\theta,z)=0 \tag{1a}$$

$$\nabla^2\Psi(r,\theta,z)=0 \tag{1b}$$

where

$$\nabla^2=\frac{\partial^2}{\partial r^2}+\frac{1}{r}\frac{\partial}{\partial r}+\frac{1}{r^2}\frac{\partial^2}{\partial\theta^2}+\frac{\partial^2}{\partial z^2} \tag{1c}$$

is Laplace's operator referred to the cylindrical polar coordinate system (r, θ, z). The stresses and displacements in the elastic medium can be uniquely expressed in terms of these stress functions (see, e.g., Muki, 1960; Gurtin, 1972). The expressions for the displacement and stress components in terms of $\Phi(r, \theta, z)$ and $\Psi(r, \theta, z)$ take the forms

$$2Gu_r=-\frac{\partial^2\Phi}{\partial r\partial z}+\frac{2}{r}\frac{\partial\Psi}{\partial\theta} \tag{2}$$

$$2Gu_\theta=-\frac{1}{r}\frac{\partial^2\Phi}{\partial\theta\partial z}-2\frac{\partial\Psi}{\partial r} \tag{3}$$

$$2Gu_z=2(1-\nu)\nabla^2\Phi-\frac{\partial^2\Phi}{\partial z^2} \tag{4}$$

and

$$\sigma_{rr}=\frac{\partial}{\partial z}\left(\nu\nabla^2-\frac{\partial^2}{\partial r^2}\right)\Phi+\frac{\partial}{\partial\theta}\left(\frac{2}{r}\frac{\partial}{\partial r}-\frac{2}{r^2}\right)\Psi \tag{5}$$

$$\sigma_{\theta\theta}=\frac{\partial}{\partial z}\left(\nu\nabla^2-\frac{1}{r}\frac{\partial}{\partial r}-\frac{1}{r^2}\frac{\partial^2}{\partial\theta^2}\right)\Phi-\frac{\partial}{\partial\theta}\left(\frac{2}{r}\frac{\partial}{\partial r}-\frac{2}{r^2}\right)\Psi \tag{6}$$

$$\sigma_{zz}=\frac{\partial}{\partial z}\left[(2-\nu)\nabla^2-\frac{\partial^2}{\partial z^2}\right]\Phi \tag{7}$$

$$\sigma_{\theta z}=\frac{1}{r}\frac{\partial}{\partial\theta}\left[(1-\nu)\nabla^2-\frac{\partial^2}{\partial z^2}\right]\Phi-\frac{\partial^2\Psi}{\partial r\partial z} \tag{8}$$

$$\sigma_{rz}=\frac{\partial}{\partial r}\left[(1-\nu)\nabla^2-\frac{\partial^2}{\partial z^2}\right]\Phi+\frac{1}{r}\frac{\partial^2\Psi}{\partial\theta\partial z} \tag{9}$$

$$\sigma_{r\theta}=\frac{1}{r}\frac{\partial^2}{\partial\theta\partial z}\left(\frac{1}{r}-\frac{\partial}{\partial r}\right)\Phi-\left(2\frac{\partial^2}{\partial r^2}-\frac{\partial^2}{\partial z^2}\right)\Psi \tag{10}$$

where G and ν are the linear elastic modulus and Poisson's ratio, respectively. It may be noted that for axial symmetry $\Phi=\Phi(r, z)$ and $\Psi=0$, and the results (1)–(10) reduce to those given by Love (1944).

Considering a Hankel transform development of the governing equations (1*a*) and (1*b*), we can obtain solutions which are applicable to the regions $0\le z<\infty$ (region 1) and $-h\le z\le 0$ (region 2). For the region 1 $(0\le z<\infty)$ we have

$$\Phi^{(1)}(r,\theta,z)=\cos\theta\int_0^\infty\xi[A(\xi)+zB(\xi)]e^{-\xi z}J_1(\xi r)d\xi \tag{11}$$

$$\Psi^{(1)}(r,\theta,z)=\sin\theta\int_0^\infty\xi C(\xi)e^{-\xi z}J_1(\xi r)d\xi \tag{12}$$

and the corresponding displacement and stress components take the forms

$$2Gu_r^{(1)}(r,\theta,z)=\frac{\cos\theta}{r}\left\{\int_0^\infty[\xi(\xi A(\xi)-(1-\xi z)B(\xi))(\xi rJ_0(\xi r)-J_1(\xi r))+2\xi C(\xi)J_1(\xi r)]e^{-\xi z}d\xi\right\} \tag{13}$$

$$2Gu_\theta^{(1)}(r,\theta,z)=\frac{\sin\theta}{r}\left\{\int_0^\infty[\xi(-\xi A(\xi)+(1-\xi z)B(\xi))J_1(\xi r)-2\xi C(\xi)(r\xi J_0(\xi r)-J_1(\xi r))]e^{-\xi z}d\xi\right\} \tag{14}$$

$$2Gu_z^{(1)}(r,\theta,z)=-\cos\theta\left\{\int_0^\infty\xi^2[\xi A(\xi)+B(\xi)(\xi z+2(1-2\nu))]e^{-\xi z}J_1(\xi r)d\xi\right\} \tag{15}$$

$$\sigma_{zz}^{(1)}(r,\theta,z)=\cos\theta\left\{\int_0^\infty[\xi^4A(\xi)+B(\xi)((1-2\nu)\xi^3+\xi^4z)]e^{-\xi z}J_1(\xi r)d\xi\right\} \tag{16}$$

$$\sigma_{\theta z}^{(1)}(r,\theta,z)=\frac{\sin\theta}{r}\times\left\{\int_0^\infty\xi[\xi^2A(\xi)+B(\xi)(\xi^2z-2\xi\nu)]e^{-\xi z}J_1(\xi r)d\xi+\int_0^\infty\xi^2C(\xi)e^{-\xi z}(\xi rJ_0(\xi r)-J_1(\xi r))d\xi\right\} \tag{17}$$

$$\sigma_{rz}^{(1)}(r,\theta,z)=\frac{\cos\theta}{r}\left\{\int_0^\infty\xi e^{-\xi z}[-\xi^2A(\xi)+(2\xi\nu-\xi^2z)B(\xi)]\cdot(\xi rJ_0(\xi r)-J_1(\xi r))d\xi-\int_0^\infty\xi^2e^{-\xi z}C(\xi)J_1(\xi r)d\xi\right\} \tag{18}$$

where $A(\xi)$, $B(\xi)$, and $C(\xi)$ are arbitrary functions. For the region 2 $(-h\le z\le 0)$,

$$\Phi^{(2)}(r,\theta,z)=\cos\theta\left\{\int_0^\infty\xi[A_1(\xi)+(z+h)B_1(\xi)]\times\frac{\sinh\xi(z+h)}{\sinh(\xi h)}J_1(\xi r)d\xi+\int_0^\infty\xi[C_1(\xi)+(z+h)D_1(\xi)]\frac{\cosh\xi(z+h)}{\sinh(\xi h)}J_1(\xi r)d\xi\right\} \tag{19}$$

$$\Psi^{(2)}(r,\theta,z)=\sin\theta\left\{\int_0^\infty\frac{\xi E_1(\xi)\cosh\xi(z+h)}{\sinh(\xi h)}J_1(\xi r)d\xi\right\} \tag{20}$$

and the corresponding displacement and stress components take the forms

$$2Gu_r^{(2)}=\cos\theta\left\{-\int_0^\infty\xi[\{\xi(A_1(\xi)+(z+h)B_1(\xi))\cosh\xi(z+h)+B_1(\xi)\sinh\xi(z+h)\}\frac{1}{\sinh(\xi h)}+\{\xi(C_1(\xi)+(z+h)D_1(\xi))\sinh\xi(z+h)\right.$$

Downloaded 03 May 2010 to 171.66.16.248. Redistribution subject to ASME license or copyright; see http://www.asme.org/terms/Terms_Use.cfm

$$+D_1(\xi)\cosh\xi(z+h)\}\frac{1}{\sinh(\xi h)}J_1'(\xi r)d\xi + \frac{2}{r}\int_0^\infty \frac{\xi E_1(\xi)\cosh\xi(z+h)J_1(\xi r)d\xi}{\sinh(\xi h)}\Bigg\} \quad (21)$$

$$2Gu_z^{(2)} = \cos\theta\Bigg\{\int_0^\infty [-\xi^3\sinh\xi(z+h)\{A_1(\xi)+(z+h)B_1(\xi)\} + 2(1-2\nu)\xi^2\{\cosh\xi(z+h)B_1(\xi)+\sinh\xi(z+h)D_1(\xi)\} - \xi^3\cosh\xi(z+h)\{C_1(\xi)+(z+h)D_1(\xi)\}]\frac{J_1(\xi r)d\xi}{\sinh(\xi h)}\Bigg\} \quad (22)$$

$$2Gu_\theta^{(2)} = \frac{\sin\theta}{r}\Bigg\{\int_0^\infty \xi[\xi A_1(\xi)\cosh\xi(z+h) + B_1(\xi)\{\sinh\xi(z+h) + \xi(z+h)\cosh\xi(z+h)\} + \xi C_1(\xi)\sinh\xi(z+h) + D_1(\xi)\{\cosh\xi(z+h)+\xi(z+h)\sinh\xi(z+h)\}]\frac{J_1(\xi r)d\xi}{\sinh(\xi h)} - 2r\int_0^\infty \frac{\xi E_1(\xi)\cosh\xi(z+h)}{\sinh(\xi h)}J_1'(\xi r)d\xi\Bigg\} \quad (23)$$

$$\sigma_{zz}^{(2)} = \cos\theta\Bigg\{\int_0^\infty\Bigg[-\frac{\xi^4 A_1(\xi)\cosh\xi(z+h)}{\sinh(\xi h)} + \frac{\xi^3 B_1(\xi)}{\sinh(\xi h)}\{(1-2\nu)\sinh\xi(z+h) - \xi(z+h)\cosh\xi(z+h)\} - \frac{\xi^4 C_1(\xi)\sinh\xi(z+h)}{\sinh(\xi h)} + \frac{\xi^3 D_1(\xi)}{\sinh(\xi h)}\{(1-2\nu)\cosh\xi(z+h) - \xi(z+h)\sinh\xi(z+h)\}\Bigg]J_1(\xi r)d\xi \quad (24)$$

$$\sigma_{rz}^{(2)} = \cos\theta\Bigg\{-(1-\nu)\int_0^\infty \xi^3[A_1(\xi)+(z+h)B_1(\xi)] \times\frac{\sinh\xi(z+h)}{\sinh(\xi h)}J_1'(\xi r)d\xi - \nu\int_0^\infty \{\xi^2[2\cosh\xi(z+h) + \xi(z+h)\sinh\xi(z+h)]B_1(\xi) + \xi^3 A_1(\xi)\sinh\xi(z+h)\}\frac{J_1'(\xi r)d\xi}{\sinh(\xi h)} - (1-\nu)\int_0^\infty \xi^3[C_1(\xi) + (z+h)D_1(\xi)]\frac{\cosh\xi(z+h)}{\sinh(\xi h)}J_1'(\xi r)d\xi - \nu\int_0^\infty \{\xi^2[2\sinh\xi(z+h)+\xi(z+h)\cosh\xi(z+h)]D_1(\xi) + \xi^3 C_1(\xi)\cosh\xi(z+h)\}\frac{J_1'(\xi r)d\xi}{\sinh(\xi h)}\Bigg\} + \frac{\cos\theta}{r}\int_0^\infty \xi^2 E_1(\xi)\frac{\sinh\xi(z+h)}{\sinh(\xi h)}J_1(\xi r)d\xi \quad (25)$$

$$\sigma_{\theta z}^{(2)} = -\frac{\sin\theta}{r}\Bigg\{-(1-\nu)\int_0^\infty \xi^3[A_1(\xi)+(z+h)B_1(\xi)] \times\frac{\sinh\xi(z+h)}{\sinh(\xi h)}J_1(\xi r)d\xi - \nu\int_0^\infty \{\xi^2[2\cosh\xi(z+h) + \xi(z+h)\sinh\xi(z+h)]B_1(\xi) + \xi^3 A_1(\xi)\sinh\xi(z+h)\}\frac{J_1(\xi r)}{\sinh(\xi h)}d\xi - (1-\nu)\int_0^\infty \xi^3[C_1(\xi)+(z+h)D_1(\xi)]\frac{\cosh\xi(z+h)}{\sinh(\xi h)}J_1(\xi r)d\xi - \nu\int_0^\infty \{\xi^2[2\sinh\xi(z+h)+\xi(z+h)\cosh\xi(z+h)]D_1(\xi) + \xi^3 C_1(\xi)\cosh\xi(z+h)\}\frac{J_1(\xi r)d\xi}{\sinh(\xi h)}\Bigg\} - \sin\theta\int_0^\infty \xi^2 E_1(\xi)\frac{\sinh\xi(z+h)}{\sinh(\xi h)}J_1'(\xi r)d\xi, \quad (26)$$

where $(\,)'$ denotes the derivative with respect to r; i.e., $J_1'(\xi r) = d[J_1(\xi r)]/dr$.

The Inclusion Problem

We consider the problem of a rigid penny-shaped inclusion which is embedded in an isotropic elastic half-space and subjected to an in-plane lateral force T. The boundary and continuity conditions associated with the problem are as follows: In the inclusion region we have

$$u_r^{(1)} = \Delta\cos\theta;\ 0\le r\le a;\ z=0 \quad (27a)$$

$$u_r^{(2)} = \Delta\cos\theta;\ 0\le r\le a;\ z=0 \quad (27b)$$

$$u_\theta^{(1)} = -\Delta\sin\theta;\ 0\le r\le a;\ z=0 \quad (27c)$$

$$u_\theta^{(2)} = -\Delta\sin\theta;\ 0\le r\le a;\ z=0 \quad (27d)$$

$$u_z^{(1)} = \Omega r\cos\theta;\ 0\le r\le a;\ z=0 \quad (27e)$$

$$u_z^{(2)} = \Omega r\cos\theta;\ 0\le r\le a;\ z=0. \quad (27f)$$

At the interface between regions (1) and (2), exterior to the inclusion, we have the following continuity conditions

$$u_z^{(1)} = u_z^{(2)};\ a\le r<\infty;\ z=0 \quad (27g)$$

$$u_r^{(1)} = u_r^{(2)};\ a\le r<\infty;\ z=0 \quad (27h)$$

$$u_\theta^{(1)} = u_\theta^{(2)};\ a\le r<\infty;\ z=0 \quad (27i)$$

$$\sigma_{zz}^{(1)} = \sigma_{zz}^{(2)};\ a<r<\infty;\ z=0 \quad (27j)$$

$$\sigma_{rz}^{(1)} = \sigma_{rz}^{(2)};\ a<r<\infty;\ z=0 \quad (27k)$$

$$\sigma_{\theta z}^{(1)} = \sigma_{\theta z}^{(2)};\ a<r<\infty;\ z=0. \quad (27l)$$

At the surface of the half-space region,

$$\sigma_{zz}^{(2)} = 0;\ 0\le r<\infty;\ z=-h \quad (27m)$$

$$\sigma_{\theta z}^{(2)} = 0;\ 0\le r<\infty;\ z=-h \quad (27n)$$

$$\sigma_{rz}^{(2)} = 0;\ 0\le r<\infty;\ z=-h. \quad (27o)$$

In equations (27*a*)–(27*f*) Δ represents the rigid body translation of the disk inclusion due to the in-plane force T and Ω represents the rigid body rotation of the inclusion about the y-axis.

From the boundary conditions (27*m*), (27*n*), and (27*o*) we find that

$$D_1(\xi) = \alpha_1\xi A_1(\xi) \quad (28)$$

$$\xi C_1(\xi) = -\gamma_1 B_1(\xi) \quad (29)$$

where

$$\alpha_1 = \frac{1}{(1-2\nu)};\ \gamma_1 = 2\nu. \quad (30)$$

Considering the continuity conditions (27*a*) to (27*i*) it can be shown that

$$A_1(\xi) = a_1 A(\xi) + a_2 B(\xi) \quad (31)$$

$$B_1(\xi) = a_3 A(\xi) + a_4 B(\xi) \quad (32)$$

$$E_1(\xi) = \tanh(\xi h)C(\xi) \quad (33)$$

where

Downloaded 03 May 2010 to 171.66.16.248. Redistribution subject to ASME license or copyright; see http://www.asme.org/terms/Terms_Use.cfm

$$a_1 = \frac{(b_1 - b_3)}{(b_0 b_3 + b_1 b_2)} \tag{34}$$

$$a_2 = \frac{1}{\xi}\left\{\frac{b_3 + 2(1-2\nu)b_1}{b_0 b_3 + b_1 b_2}\right\} \tag{35}$$

$$a_3 = \frac{-\xi(b_0 + b_2)}{(b_0 b_3 + b_1 b_2)} \tag{36}$$

$$a_4 = \left\{\frac{b_2 - 2(1-2\nu)b_0}{b_0 b_3 + b_1 b_2}\right\} \tag{37}$$

and

$$b_0 = [\alpha_1(\xi h + \coth(\xi h)) + \coth(\xi h)] \tag{38a}$$

$$b_1 = [1 - \gamma_1 + \xi h \coth(\xi h)] \tag{38b}$$

$$b_2 = [1 - 2\alpha_1(1-2\nu) + \alpha_1 h \xi \coth(\xi h)] \tag{39a}$$

$$b_3 = [-\xi h + \gamma_1 \coth(\xi h) + 2(1-2\nu)\coth(\xi h)]. \tag{39b}$$

From (28), (29), and (33) it is evident that

$$D_1(\xi) = [e_1 A(\xi) + f_1 B(\xi)] \tag{40}$$

$$\xi C_1(\xi) = -\gamma_1[a_3 A(\xi) + a_4 B(\xi)] \tag{41}$$

where

$$e_1 = \alpha_1 \xi a_1 \tag{42}$$

$$f_1 = \alpha_1 \xi a_2. \tag{43}$$

Using the results (31)–(43) it is possible to express the integral expressions for $u_r^{(2)}$, $u_\theta^{(2)}$, $u_z^{(2)}$, $\sigma_{zz}^{(2)}$, $\sigma_{\theta z}^{(2)}$ and $\sigma_{rz}^{(2)}$ in terms of only the functions $A(\xi)$, $B(\xi)$, and $C(\xi)$. On the plane $z=0$, the reduced form of these equations are given by

$$2Gu_r^{(2)} = \cos\theta\left\{-\int_0^\infty \xi[\{\xi(a_1 + ha_3)\coth(\xi h) + a_3 + (\xi h e_1 + \gamma_1 a_3) + e_1 \coth(\xi h)\}A(\xi) + \{\xi(a_2 + a_4 h)\coth(\xi h) + a_4 + (\xi h f_1 - \gamma_1 a_4) + f_1 \coth(\xi h)\}B(\xi)]J_1'(\xi r)d\xi + \frac{2}{r}\int_0^\infty \xi J_1(\xi r)C(\xi)d\xi\right\} \tag{44}$$

$$2Gu_z^{(2)} = \cos\theta\left\{\int_0^\infty [\{-\xi^3(a_1 + a_3 h) + 2(1-2\nu)\xi^2[e_1 + a_3 \coth(\xi h)] - \xi^2 \coth(\xi h)(\xi h e_1 - \gamma_1 a_3)\}A(\xi)J_1(\xi r) + \{-\xi^3(a_2 + a_4 h) + 2(1-2\nu)\xi^2[f_1 + a_4 \coth(\xi h)] - \xi^2 \coth(\xi h)(\xi h f_1 - a_4\gamma_1)\}B(\xi)J_1(\xi r)]d\xi\right\} \tag{45}$$

$$2Gu_\theta^{(2)} = \frac{\sin\theta}{r}\left\{\int_0^\infty \xi[A(\xi)\{a_3(1 + \xi h \coth(\xi h)) + \xi a_1 \coth(\xi h) - \gamma_1 a_3 + e_1(\xi h + \coth(\xi h))\}J_1(\xi r) + B(\xi)\{\xi a_2 \coth(\xi h) + a_4(1 + \xi h \coth(\xi h)) - \gamma_1 a_4 + f_1(\xi h + \coth(\xi h))\}J_1(\xi r)]d\xi - 2r\int_0^\infty \xi C(\xi)J_1'(\xi r)d\xi\right\} \tag{46}$$

$$\sigma_{zz}^{(2)} = \cos\theta\left\{\int_0^\infty [A(\xi)\{-a_1\xi^4 \coth(\xi h) + a_3\xi^3(1 - 2\nu - \xi h \coth(\xi h)) + \xi^3\gamma_1 a_3 + e_1\xi^3((1-2\nu)\coth(\xi h) - \xi h)\} + B(\xi)\{-a_2\xi^4 + a_4\xi^3((1-2\nu) - \xi h \coth(\xi h)) + a_4\gamma_1\xi^3 + f_1\xi^3((1-2\nu)\coth(\xi h) - \xi h)\}]J_1(\xi r)d\xi\right\} \tag{47}$$

$$\sigma_{rz}^{(2)} = \cos\theta\left\{\int_0^\infty [A(\xi)\{-(1-\nu)\xi^3(a_1 + a_3 h) - \nu\xi^2[(2\coth(\xi h) + \xi h) + a_3 + \xi a_1] - \xi^2(1-\nu)[e_1\xi h - a_3\gamma_1]\coth(\xi h) - \nu\xi^2[(2 + \xi h \coth(\xi h))e_1 - \gamma_1 a_3]\}J_1'(\xi r) + B(\xi)\{-(1-\nu)\xi^3(a_2 + a_4 h) - \nu\xi^2[(2\coth(\xi h) + \xi h)a_4 + \xi a_2] - (1-\nu)\xi^2[f_1\xi h - \gamma_1 a_4]\coth(\xi h) - \nu\xi^2[(2 + \xi h \coth(\xi h))f_1 - \gamma_1 a_4 \coth(\xi h)]\}J_1'(\xi r)]d\xi\right\} + \frac{\cos\theta}{r}\int_0^\infty \xi^2 \tanh(\xi h)C(\xi)J_1(\xi r)d\xi \tag{48}$$

$$\sigma_{\theta z}^{(2)} = -\frac{\sin\theta}{r}\left\{\int_0^\infty [A(\xi)\{-(1-\nu)\xi^3(a_1 + a_3 h) - \nu\xi^2[(2\coth(\xi h) + \xi h)a_3 + \xi a_1] - \xi^2(1-\nu)[e_1\xi h - \gamma_1 a_3]\coth(\xi h) - \nu\xi^2 \times [(2 + \xi h \coth(\xi h))e_1 - \gamma_1 a_3]\}J_1(\xi r) + B(\xi)\{-(1-\nu)\xi^3(a_2 + a_4 h) - \nu\xi^2[a_4(\xi h + 2\coth(\xi h)) + \xi a_2] - \xi^2(1-\nu)[\xi h f_1 - \gamma_1 a_4]\coth(\xi h) - \nu\xi^2[(2 + \xi h \coth(\xi h))f_1 - \gamma_1 a_4 \coth(\xi h)]\}J_1(\xi r)]d\xi\right\} - \sin\theta\int_0^\infty \xi^2 C(\xi)\tanh(\xi h)J_1'(\xi r)d\xi. \tag{49}$$

Using the results (13) to (18) and (44) to (49), the boundary conditions (27*a*), (27*c*), (27*e*), (27*j*), (27*k*) and (27*l*) become

$$\int_0^\infty \{\xi(\xi A(\xi) - B(\xi))(\xi r J_0(\xi r) - J_1(\xi r)) + 2\xi C(\xi)J_1(\xi r)\}d\xi = 2\Delta G r;\ 0 \le r \le a \tag{50a}$$

$$\int_0^\infty \{\xi(-\xi A(\xi) + B(\xi))J_1(\xi r) - 2\xi C(\xi)(\xi r J_0(\xi r) - J_1(\xi r))\}d\xi = -2\Delta G r;\ 0 \le r \le a \tag{50b}$$

$$\int_0^\infty \xi^2\{\xi A(\xi) + 2(1-2\nu)B(\xi)\}J_1(\xi r)d\xi = -2\Omega G r;\ 0 \le r \le a \tag{50c}$$

$$\int_0^\infty \xi^3\{\xi g_0 A(\xi) + g_1 B(\xi)\}J_1(\xi r)d\xi = 0,\ a < r < \infty \tag{51a}$$

$$\int_0^\infty \xi^2\{g_2\xi A(\xi) + g_3 B(\xi)\}J_1(\xi r)d\xi + \int_0^\infty g_4\xi^2\{\xi r J_0(\xi r) - J_1(\xi r)\}C(\xi)d\xi = 0;\ a < r < \infty \tag{51b}$$

$$\int_0^\infty \xi^2\{g_2\xi A(\xi) + g_3 B(\xi)\}\{\xi r J_0(\xi r) - J_1(\xi r)\}d\xi + \int_0^\infty g_4\xi^2 C(\xi)J_1(\xi r)d\xi = 0;\ a < r < \infty, \tag{51c}$$

Downloaded 03 May 2010 to 171.66.16.248. Redistribution subject to ASME license or copyright; see http://www.asme.org/terms/Terms_Use.cfm

where the functions $g_i(\xi)$ $(i=0,1,\cdots 4)$ are given by

$$g_0 = 1 + a_1 \coth(\xi h) - \frac{a_3}{\xi}\{(1-2\nu) - \xi h \coth(\xi h)\}$$
$$- \frac{\gamma_1 a_3}{\xi} - \frac{e_1}{\xi}\{(1-2\nu)\coth(\xi h) - \xi h\} \quad (52a)$$

$$g_1 = (1-2\nu) + a_2 \xi \coth(\xi h) - a_4\{(1-2\nu) - \xi h \coth(\xi h)\}$$
$$- a_4\gamma_1 - f_1\{(1-2\nu)\coth(\xi h) - \xi h\} \quad (52b)$$

$$g_2 = -1 + (1-\nu)(a_1 + a_3 h) + \frac{\nu}{\xi}\{a_3(\xi h + 2\coth(\xi h)) + a_1 \xi\}$$
$$+ \frac{(1-\nu)}{\xi}\coth(\xi h)\{\xi h e_1 - a_3\gamma_1\}$$
$$+ \frac{\nu}{\xi}\{e_1(2 + \xi h \coth(\xi h)) - \gamma_1 a_3\} \quad (52c)$$

$$g_3 = \xi\left\{\frac{2\nu}{\xi} + (1-\nu)(a_2 + a_4 h) + \frac{\nu}{\xi}\{a_4[\xi h + 2\coth(\xi h)]\right.$$
$$+ \xi a_2\} + \frac{(1-\nu)}{\xi}(\xi h f_1 - \gamma_1 a_4)\coth(\xi h)$$
$$\left. + \frac{\nu}{\xi}\{(2 + \xi h \coth(\xi h))f_1 - \gamma_1 a_4 \coth(\xi h)\}\right\} \quad (52d)$$

$$g_4 = -\frac{2}{(1+e^{-2\xi h})}. \quad (52e)$$

By introducing the substitutions

$$N(\xi) = \xi^2[\xi g_0 A(\xi) + g_1 B(\xi)] \quad (53)$$

$$L(\xi) = \xi^2[\xi g_2 A(\xi) + g_3 B(\xi) + g_4 C(\xi)] \quad (54)$$

$$M(\xi) = \xi^2[\xi g_2 A(\xi) + g_3 B(\xi) - g_4 C(\xi)], \quad (55)$$

the integral equations (50*a*)–(50*c*) and (51*a*)–(51*c*) can be further reduced to the following forms:

$$\int_0^\infty L(\xi)J_0(\xi r)d\xi + \int_0^\infty \left\{\frac{g_4(g_0+g_1)+2p(\xi)}{2g_4 p(\xi)} - 1\right\}$$
$$\times L(\xi)J_0(\xi r)d\xi + \int_0^\infty \left\{\frac{g_4(g_0+g_1)-2p(\xi)}{2g_4 p(\xi)}\right\} M(\xi)J_0(\xi r)d\xi$$
$$- \int_0^\infty \frac{(g_2+g_3)}{p(\xi)} N(\xi)J_0(\xi r)d\xi = 4G\Delta;\ 0 \le r \le a \quad (56)$$

$$\int_0^\infty M(\xi)J_2(\xi r)d\xi + \int_0^\infty \left\{\frac{2p(\xi)+g_4(g_0+g_1)}{2p(\xi)g_4} - 1\right\}$$
$$\times M(\xi)J_2(\xi r)d\xi + \int_0^\infty L(\xi)\left\{\frac{g_4(g_0+g_1)-2p(\xi)}{2p(\xi)g_4}\right\} J_2(\xi r)d\xi$$
$$- \int_0^\infty N(\xi)\frac{(g_2+g_3)}{p(\xi)} J_2(\xi r)d\xi = 0;\ 0 \le r \le a \quad (57)$$

$$\int_0^\infty N(\xi)J_1(\xi r)d\xi + \int_0^\infty \left\{\frac{2(1-2\nu)g_2 - g_3}{p(\xi)} - 1\right\} J_1(\xi r)N(\xi)d\xi$$
$$+ \int_0^\infty \left\{\frac{g_1 - 2(1-2\nu)g_0}{2p(\xi)}\right\} M(\xi)J_1(\xi r)d\xi$$
$$+ \int_0^\infty \left\{\frac{g_1 - 2(1-2\nu)g_0}{2p(\xi)}\right\} L(\xi)J_1(\xi r)d\xi = -2\Omega G r;$$
$$0 \le r \le a \quad (58)$$

$$\int_0^\infty \xi N(\xi)J_1(\xi r)d\xi = 0;\ a < r < \infty \quad (59)$$

$$\int_0^\infty \xi L(\xi)J_0(\xi r)d\xi = 0;\ a < r < \infty \quad (60)$$

$$\int_0^\infty \xi M(\xi)J_2(\xi r)d\xi = 0;\ a < r < \infty \quad (61)$$

where

$$p(\xi) = g_1 g_2 - g_0 g_3. \quad (62)$$

Considering (59), (60), and (61), it it convenient to introduce representations of $L(\xi)$, $N(\xi)$, and $M(\xi)$ in terms of functions $\varphi_1(t)$, $\psi(t)$, and $\varphi_2(t)$ as follows:

$$L(\xi) = \int_0^a \varphi_1(t)\cos(\xi t)dt \quad (63)$$

$$N(\xi) = \int_0^a \psi(t)\sin(\xi t)dt \quad (64)$$

$$M(\xi) = \int_0^a t\varphi_2(t)J_2(\xi t)dt. \quad (65)$$

The representations (63), (64), and (65) identically satisfy (59), (60), and (61), respectively. Using the representations (63) to (65) in (56) to (58), we obtain the following system of coupled integral equations for the functions of $\varphi_1(t)$, $\varphi_2(t)$, and $\psi(t)$; i.e.,

$$\varphi_1(t) + \int_0^a \varphi_1(u)K_1(u,t)du + \int_0^a u\varphi_2(u)K_2(u,t)du$$
$$+ \int_0^a \psi(u)K_3(u,t)du = \frac{8G\Delta}{\pi};\ 0 \le t \le a \quad (66)$$

$$\varphi_2(t) = -\int_0^a u\varphi_2(u)K_5(u,t)du - \int_0^a \varphi_1(u)K_4(u,t)du$$
$$- \int_0^a \psi(u)K_6(u,t)du;\ 0 < t < a \quad (67)$$

$$\psi(t) + \int_0^a \psi(u)K_7(u,t)du + \int_0^a u\varphi_2(u)K_8(u,t)du$$
$$+ \int_0^a \varphi_1(u)K_9(u,t)du = -\frac{8\Omega G t}{\pi};\ 0 \le t \le a \quad (68)$$

where, the kernel functions $K_i(u,t)$, $(i=1,2,\cdots 9)$ are given by

$$K_1(u,t) = \frac{2}{\pi}\int_0^\infty \left\{\frac{g_4(g_0+g_1)+2p(\xi)}{2g_4 p(\xi)} - 1\right\}$$
$$\times \cos(\xi u)\cos(\xi t)d\xi \quad (69)$$

$$K_2(u,t) = \frac{2}{\pi}\int_0^\infty \left\{\frac{g_4(g_0+g_1)-2p(\xi)}{2g_4 p(\xi)}\right\} \cos(\xi t)J_2(\xi u)d\xi \quad (70)$$

$$K_3(u,t) = -\frac{2}{\pi}\int_0^\infty \left\{\frac{g_2+g_3}{p(\xi)}\right\} \cos(\xi t)\sin(\xi u)d\xi \quad (71)$$

$$K_4(u,t) = -\int_0^\infty \cos(\xi u)I(\xi,t)\left\{\frac{g_4(g_0+g_1)-2p(\xi)}{2p(\xi)g_4}\right\} d\xi \quad (72)$$

$$K_5(u,t) = -\int_0^\infty \left\{\frac{g_4(g_0+g_1)+2p(\xi)}{2p(\xi)g_4} - 1\right\}$$
$$\times I(\xi,t)J_2(\xi u)d\xi \quad (73)$$

$$K_6(u,t) = \int_0^\infty \sin(\xi u)\left\{\frac{g_1+g_2}{p(\xi)}\right\} I(\xi,t)d\xi \quad (74)$$

Downloaded 03 May 2010 to 171.66.16.248. Redistribution subject to ASME license or copyright; see http://www.asme.org/terms/Terms_Use.cfm

$$K_7(u,\ t)=\frac{2}{\pi}\int_0^\infty\left\{\frac{2(1-2\nu)g_2-g_3}{p(\xi)}-1\right\}\sin(\xi u)\sin(\xi t)d\xi \quad (75)$$

$$K_8(u,\ t)=\frac{2}{\pi}\int_0^\infty\left\{\frac{g_1-2(1-2\nu)g_0}{2p(\xi)}\right\}\sin(\xi t)J_2(\xi u)d\xi \quad (76)$$

$$K_9(u,\ t)=\frac{2}{\pi}\int_0^\infty\left\{\frac{g_1-2(1-2\nu)g_0}{2p(\xi)}\right\}\sin(\xi t)\cos(\xi u)d\xi \quad (77)$$

where

$$I(\xi,\ t)=\sqrt{\frac{2\xi}{\pi}}\,t\frac{d}{dt}\int_t^a\frac{s^{-1/2}J_{3/2}(\xi s)ds}{(s^2-t^2)^{1/2}}. \quad (78)$$

The coupled system of integral equations defined by (66) to (68) can be solved in a numerical fashion to generate results of engineering interest. The results of primary interest relate to the resultant in plane force (T) acting on the inclusion and the resultant moment (M) acting on the inclusion about the y-axis. Considering the resultant in-plane tractions, we have

$$T=\int_0^{2\pi}\int_0^a r\{(\sigma_{rz}^{(1)}-\sigma_{rz}^{(2)})-(\sigma_{\theta z}^{(1)}-\sigma_{\theta z}^{(2)})\}dr\,d\theta. \quad (79)$$

Using the results presented previously, it can be shown that

$$T=\pi\int_0^a rdr\int_0^\infty\xi M(\xi)J_2(\xi r)d\xi=\pi\int_0^a r\varphi_2(r)dr. \quad (80)$$

Considering the axial stresses $\sigma_{zz}^{(1)}$ and $\sigma_{zz}^{(2)}$ acting on the inclusion, we have

$$M=-\int_0^{2\pi}\int_0^a[\sigma_{zz}^{(1)}(r,\ 0,\ \theta)-\sigma_{zz}^{(2)}(r,\ 0,\ \theta)]r^2\cos\theta d\theta dr\,d\theta. \quad (81)$$

Again, using the results presented earlier, we have

$$M=\pi\int_0^a r^2\left\{\frac{d}{dr}\int_r^a\frac{\psi(t)dt}{\sqrt{t^2-r^2}}\right\}dr=2\pi\int_0^a t\psi(t)dt. \quad (82)$$

By setting $M=0$, we can obtain a relationship between the induced rigid rotation Ω and the rigid translation of the disk inclusion Δ.

Numerical Solution of the Integral Equations

Considering the structure of the kernel functions $K_i(i=1,2,\cdots 9)$ given by (69) to (77), it becomes evident that the coupled integral equations (66), (67), and (68) governing $\varphi_1(t)$, $\varphi_2(t)$, and $\psi(t)$ are not amenable to exact solution. Consequently it is necessary to adopt a numerical technique to generate the relevant results. A variety of techniques have been proposed for the numerical solution of integral equations (see, e.g., Baker, 1978; Delves and Mohammed, 1985). In this paper we present a quadrature scheme for the solution of the coupled system of integral equations.

From (66) to (68) we have

$$\begin{bmatrix}\varphi_1(t)\\ \varphi_2(t)\\ \psi(t)\end{bmatrix}+\int_0^a\begin{bmatrix}K_1(u,\ t) & uK_2(u,\ t) & K_3(u,\ t)\\ K_4(u,\ t) & uK_5(u,\ t) & K_6(u,\ t)\\ K_9(u,\ t) & uK_8(u,\ t) & K_7(u,\ t)\end{bmatrix}\times\begin{bmatrix}\varphi_1(u)\\ \varphi_2(u)\\ \psi(u)\end{bmatrix}du=\frac{8G}{\pi}\begin{bmatrix}\Delta\\ 0\\ -\Omega t\end{bmatrix} \quad (83)$$

where the kernel functions are defined by (69) to (77). Considering the moment free condition on the inclusion we have

$$\int_0^a t\psi(t)dt=0. \quad (84)$$

The result (84) is used as a constraint condition on the solution of the system (83). The function $I(t,\ \xi)$ given by (78) can be expressed in the form

$$\sqrt{\frac{\pi}{2\xi}}I(\xi,\ t)=-\frac{t^2J_{3/2}(\xi a)}{a^{3/2}(a^2-t^2)^{1/2}}-\xi t^2\int_t^a\frac{J_{5/2}(\xi s)ds}{s^{3/2}(s^2-t^2)^{1/2}}. \quad (85)$$

Substituting (85) into (72), (73), and (74) we obtain

$$K_i(u,\ t)=-\frac{t^2K_{i1}(u,\ a)}{a^{3/2}(a^2-t^2)^{1/2}}-t^2\int_t^a\frac{K_{i2}(u,\ s)ds}{s^{3/2}(s^2-t^2)^{1/2}};\ (i=4,5,6) \quad (86)$$

where

$$K_{41}(u,\ a)=-\int_0^\infty\left\{\frac{g_4(g_1+g_0)-2p(\xi)}{2p(\xi)g_4}\right\}\sqrt{\frac{2\xi}{\pi}}J_{3/2}(\xi a)\cos(\xi u)d\xi \quad (87)$$

$$K_{42}(u,\ s)=-\int_0^\infty\left\{\frac{g_4(g_0+g_1)-2p(\xi)}{2p(\xi)g_4}\right\}\sqrt{\frac{2\xi}{\pi}}J_{5/2}(\xi a)\cos(\xi u)d\xi \quad (88)$$

$$K_{51}(u,\ a)=-\int_0^\infty\left\{\frac{g_4(g_1+g_0)+2p(\xi)}{2p(\xi)g_4}-1\right\}\times\sqrt{\frac{2\xi}{\pi}}J_2(\xi u)J_{3/2}(\xi a)d\xi \quad (89)$$

$$K_{52}(u,\ s)=-\int_0^\infty\left\{\frac{g_4(g_0+g_1)2p(\xi)}{2p(\xi)g_4}-1\right\}\times\sqrt{\frac{2\xi^3}{\pi}}J_2(\xi u)J_{5/2}(\xi s)d\xi \quad (90)$$

$$K_{61}(u,\ a)=\int_0^\infty\left\{\frac{(g_1+g_2)}{p(\xi)}\right\}\sqrt{\frac{2\xi}{\pi}}J_{3/2}(\xi a)\sin(\xi u)d\xi \quad (91)$$

$$K_{62}(u,\ s)=\int_0^\infty\left\{\frac{(g_1+g_2)}{p(\xi)}\right\}\sqrt{\frac{2\xi^3}{\pi}}J_{5/2}(\xi s)\sin(\xi u)d\xi. \quad (92)$$

For the numerical solution of the problem, the interval [0, a] is divided into R segments with ends defined by $u_i=(i-1)a/R$; $i=1,2,3,\cdots(R+1)$, and the collocation points are $t_i=(u_i+u_{i+1})/2$; $i=1,2,\cdots R$. Therefore, a matrix equation of order $(3R+1)$ can be obtained with $3R$ equations derived from (83) and a single equation derived from (84). This matrix equation can be written in the form

$$[\mathbf{A}_{ij}]\{\mathbf{X}_j\}=\{\mathbf{B}_i\} \quad (93)$$

where $i,j=1,2,\cdots(3R+1)$. Certain coefficients of $\mathbf{A}_{ij}$ are defined by the kernel functions $K_i(u,\ t)$ and other zero coefficients are as follows:

$$A_{(3\ell-2),(3R+1)}=A_{(3\ell-1),(3R+1)}=A_{(3R+1),(3\ell-2)}=A_{(3R+1),(3\ell-1)}=0 \quad (94)$$

and

$$A_{(3\ell),(3R+1)}=A_{(3R+1),(3\ell)}=-t_\ell \quad (95)$$

where $\ell=1,2,\cdots R$. The coefficients of $\mathbf{A}_{ij}$, other than those given by (94) and (95), are obtained by numerical integrations. The right-hand side vector $\{\mathbf{B}_i\}$ in (93) are given by

$$B_{(3\ell-2)}=1.0;\ B_{(3\ell-1)}=B_{(3\ell)}=B_{(3R+1)}=0 \quad (96)$$

for $\ell=1,2,\cdots R$, and the elements of the unknown vector are:

$$\varphi_1(t_\ell)=\frac{8G\Delta}{\pi}X_{(3\ell-2)};\ \varphi_2(t_\ell)=\frac{8G\Delta}{\pi}X_{(3\ell-1)} \quad (97)$$

Downloaded 03 May 2010 to 171.66.16.248. Redistribution subject to ASME license or copyright; see http://www.asme.org/terms/Terms_Use.cfm

$$\psi(t_\ell) = \frac{8G\Delta}{\pi} X_{(3\ell)};\ \Omega = \Delta X_{(3R+1)}. \tag{98}$$

Upon solution of the matrix equation (93), the load on the inclusion can be obtained from the discretized version of the integral (80). We obtain

$$\overline{T} = \frac{(7-8\nu)T}{64(1-\nu)G\Delta a} = \frac{(7-8\nu)}{8(1-\nu)} \frac{1}{R} \sum_{\ell=1}^{R} t_\ell X_{(3\ell-1)}. \tag{99}$$

The rotation of the rigid inclusion is given by

$$\overline{\Omega} = \frac{\Omega a}{\Delta} = 2aX_{(3R+1)}. \tag{100}$$

Numerical Results

Prior to the presentation of numerical results, it is instructive to record results for certain limiting cases which pertain to inclusions located either within an infinite space region or at the surface of a half-space region.

As the depth of embedment of the inclusion becomes large in comparison with the radius of the inclusion (i.e., $h/a \to \infty$), the problem reduces to that of the in-plane loading of a rigid disk inclusion which is embedded in an isotropic elastic infinite space. The closed-form analytical solution to this problem was obtained, among others, by Keer (1965), Kassir and Sih (1968), and Selvadurai (1980). The load-displacement relationship for the inclusion takes the form

$$\overline{T} = \frac{T(7-8\nu)}{64G\Delta a(1-\nu)}. \tag{101}$$

By virtue of the symmetry of the problem about the plane $z=0$, the rigid rotation of the inclusion embedded in an infinite space is identically equal to zero.

When the depth of embedment $h \to 0$, the problem reduces to that of the in-plane loading of a rigid punch which is bonded to the surface of a half-space region. The solution to this problem was developed by Ufliand (1956) and Gladwell (1969, 1980). The Hilbert-problem approach adopted in these investigations takes into consideration the oscillatory nature of the stress singularity at the boundary of the rigid punch. In this case, the closed-form expression for the load-displacement relationship is given by

$$\overline{T} = \frac{T}{16G\Delta a\{2+\beta+3\omega\alpha\}} \tag{102}$$

where

$$\alpha = \frac{1}{2\pi}\ln(3-4\nu);\ \beta = \frac{(1-2\nu)}{\pi\alpha};\ \omega = \frac{\alpha\beta}{(1+\alpha^2)}. \tag{103}$$

The corresponding rigid rotation is given by

$$\overline{\Omega} = \frac{3\omega T}{16G\Delta a}. \tag{104}$$

It may be noted that integral equation technique adopted in the paper does not take into account the influences such oscillatory singularities which can develop as $(H/a) \to 0$. It has, however, been shown (Selvadurai, 1989) that such oscillatory stress singularities have virtually no influence on the accuracy with which the translational and rotational stiffnesses are computed for a punch bonded to a half-space region. Results developed for the axial loading of an inclusion bonded to a crack (Selvadurai, 1989) indicate that in the extreme case when $\nu = 0$, the discrepancy between the Hankel transform-based integral equation approach and the Hilbert problem approach does not exceed 0.5 percent. This is within the computational efficiency of the numerical procedure adopted in the solution of the system of coupled integral equations, which is presented in the previous section.

Figure 2 illustrates the influence of the depth of embedment

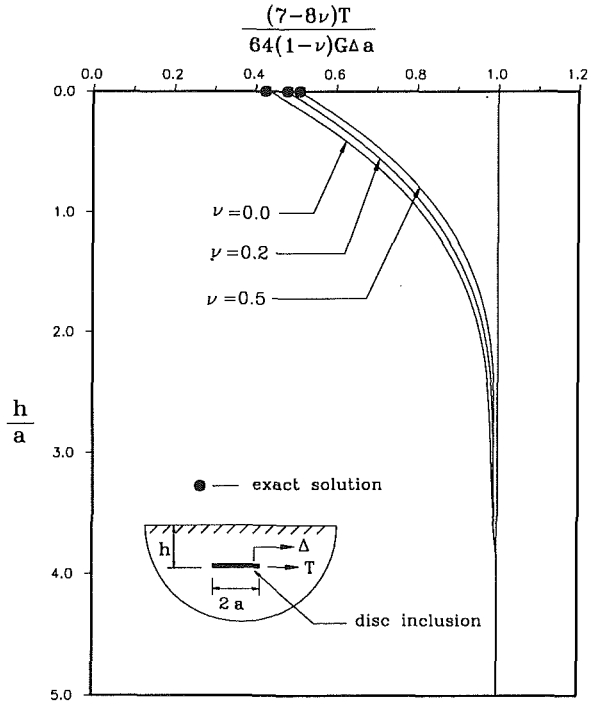

Fig. 2 In-plane stiffness of the rigid disk inclusion embedded in a half-space

of the disk inclusion on the in-plane load-displacement relationship. It is evident that the depth of embedment has a significant influence on the behavior of the in-plane stiffness of the inclusion. The results for the exact closed-form solution for the case $(h/a) = 0$, derived from (102), are also shown in Fig. 2 for purposes of comparison. It is evident that the numerical procedure provides a very accurate result for the in-plane load-displacement response of the rigid punch bonded to a half-space region. Figure 3 illustrates the influence of the depth of embedment on the rigid rotation experienced by the disk inclusion as a result of the in-plane loading. Again, the numerical results for the rotation induced on the laterally loaded punch bonded to a half-space region agree very closely with the exact result given in (104). It is also evident that for the special case when $\nu = 1/2$, the in-plane loading of the inclusion embedded in a half-space region does not induce a corresponding rotation.

Conclusions

An integral equation technique is used to evaluate the load-displacement behavior of a rigid disk inclusion which is embedded in bonded contact with an isotropic elastic half-space region. The mixed boundary value problem associated with the in-plane loading of the rigid inclusion generates a system of three coupled integral equations which are solved numerically by employing a quadrature scheme. The numerical results presented in the paper for the in-plane load-lateral displacement of the inclusion indicate that the influence of the traction-free boundary becomes insignificant as the depth of embedment to inclusion radius ratio exceeds 4. Similar conclusions apply for the results for the rigid rotation of the disk inclusion which is induced as a result of the in-plane loading. As the depth of embedment $h \to 0$, the problem reduces to that of the in-plane loading of a rigid punch which is bonded to the surface of a half-space region. In existing analytical treatments of this problem, the effects of oscillatory stress singularities at the boundary of the rigid punch are incorporated. The integral equation approach, however, does not allow for such provi-

Downloaded 03 May 2010 to 171.66.16.248. Redistribution subject to ASME license or copyright; see http://www.asme.org/terms/Terms_Use.cfm

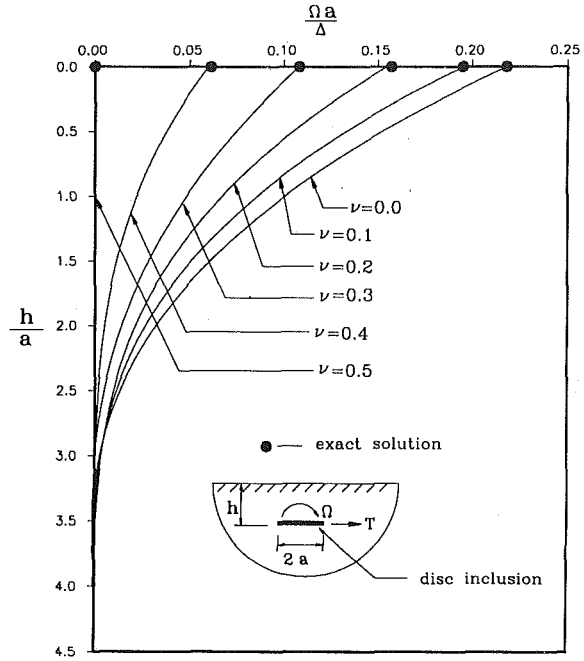

Fig. 3 Rotation of the rigid disk inclusion induced by the in-plane translation

sions. The numerical results derived from the present investigation suggests that such oscillatory phenomena do not influence, to any significant extent, the results for the in-plane displacement and rotation associated with the in-plane loading of the punch.

References

Baker, C. T. H., 1978, *The Numerical Treatment of Integral Equations,* Oxford University Press, Oxford, U. K.

Christensen, R. M., 1980, *Mechanics of Composite Materials,* John Wiley and Sons, New York.

Collins, W. D., 1962, "Some Axially Symmetric Stress Distributions in Elastic Solids Containing Penny-Shaped Cracks. I. Cracks in an Infinite Solid and a Thick Plate," *Proc. Roy. Soc. London,* Vol. A203, pp. 359-386.

de Josselin de Jong, G., 1957, "Application of Stress Functions to Consolidation Problems," *Proc. Fourth Int. Conf. Soil Mech. Fdn. Eng.,* Vol. 3, pp. 320-323.

Delves, L. M., and Mohamed, J. L., 1985, *Computational Methods for Integral Equations,* Cambridge University Press, Cambridge, U. K.

Dewey, J. M., 1947, "Elastic Constants of Materials Loaded with Non-Rigid Fillers," *J. Appl. Phys.,* Vol. 18, pp. 578-584.

Edwards, R. H., 1951, "Stress Concentration Around Spheroidal Inclusions and Cavitities," ASME JOURNAL OF APPLIED MECHANICS, Vol. 18, pp. 19-30.

Eshelby, J. D., 1961, "Elastic Inclusions and Inhomogeneities," *Progress in Solid Mechanics,* I. N. Sneddon and R. Hill, eds., North-Holland, Amsterdam, pp. 89-140.

Gladwell, G. M. L., 1969, "A Contact Problem for a Cylindrical Punch in Adhesive Contact with Elastic Halfspace, the Case of Rocking and Translation Parallel to the Plane," *Int. J. Engng. Sci.,* Vol. 7, pp. 295-307.

Gladwell, G. M. L., 1980, *Contact Problems in the Classical Theory of Elasticity,* Sijthoff and Noordhoff, The Netherlands.

Gurtin, M. E., 1972, "The Linear Theory of Elasticity," *Mechanics of Solids II, Encyclopaedia of Physics,* Vol. VI a/2, S. Flugge, ed., Springer-Verlag, Berlin, pp. 1-295.

Hashin, Z., and Herakovich, C. T., eds., 1983, *Mechanics of Composite Materials, Recent Advances: Proc. IUTAM Symposium,* Pergamon Press, New York.

Hunter, S. C., and Gamblen, D., 1974, "The Theory of a Rigid Circular Disc Anchor Buried in an Elastic Soil Either With or Without Adhesion," *J. Mech. Phys. of Solids,* Vol. 22, pp. 371-399.

Kanwal, R. P., and Sharma, D. L., 1976, "Singularity Methods for Elastostatics," *J. Elasticity,* Vol. 6, pp. 405-418.

Kassir, M. K., and Sih, G. C., 1968, "Some Three-Dimensional Inclusion Problems in Elasticity Theory," *Int. J. Solids Structures,* Vol. 4, pp. 225-241.

Keer, L. M., 1965, "A Note on the Solution of Two Asymmetric Boundary Value Problems," *Int. J. Solids Structures,* Vol. 1, pp. 257-264.

Lawrence, E. G., 1969, "Rigid Inclusions in an Elastic Plate," *Quart. J. Mech. and Applied Math.,* Vol. 12, pp. 291-304.

Love., A. E. H., 1944, *A Treatise on the Mathematical Theory of Elasticity,* 4th ed., Dover Publications, New York.

Luré, A. I., 1967, "Elastostatic Problem for a Triaxial Ellipsoid," *Mech. Tverdogo Tela,* Vol. 1, pp. 80-83.

Muki, R., 1960, "Asymmetric Problems of the Theory of Elasticity for a Semi-Infinite Solid and a Thick Plate," *Progress in Solid Mechanics,* Vol. 1, I. N. Sneddon and R. Hill, eds., North-Holland, Amsterdam, pp. 339-349.

Mura, T., 1981, *Micromechanics of Defects in Solids,* Sijthoff and Noordhoff, The Netherlands.

Mura, T., 1988, "Inclusion Problems," *Applied Mechanics Reviews,* Vol. 41, pp. 15-20.

Rajapakse, R. K. N. D., 1988, "The Interaction Between a Circular Elastic Plate and a Transversely Isotropic Elastic Half-space," *Int. J. Numerical Anal. Meth. in Geomech.,* Vol. 12, pp. 419-436.

Sadowsky, M. A., and Sternberg, E., 1949, "Stress Concentration in a Triaxial Ellipsoidal Cavity," ASME JOURNAL OF APPLIED MECHANICS, Vol. 16, pp. 149-157.

Selvadurai, A. P. S., 1976, "The Load-Deflection Characteristics of a Deep Rigid Anchor in an Elastic Medium," *Geotechnique,* Vol. 26, pp. 603-612.

Selvadurai, A. P. S., 1980, "Asymmetric Displacement of a Rigid Disc Inclusion Embedded in a Transversely Isotropic Elastic Medium of Infinite Extent," *Int. J. Engng. Sci.,* Vol. 18, pp. 979-986.

Selvadurai, A. P. S., 1981, "A Theoretical Estimate of the Tilt of a Surface Foundation due to an Inclined Anchor Load Applied at the Interior of the Soil Medium," *Int. J. Numerical and Anal. Meth. Geomech.,* Vol. 5, pp. 369-378.

Selvadurai, A. P. S., 1982, "On the Interaction Between an Elastically Embedded Rigid Inhomogeneity and a Laterally Placed Concentrated Force," *Jour. Appl. Math. Phys. (ZAMP),* Vol. 33, pp. 241-250.

Selvadurai, A. P. S., and Singh, B. M., 1982, "Some Annular Disc Inclusion Problems in Elasticity," *Int. J. Solids Structures,* Vol. 20, pp. 129-139.

Selvadurai, A. P. S., and Singh, B. M., 1986, "The Axial Displacement of a Disc Inclusion Embedded in a Penny-Shaped Crack," *J. Appl. Math. Phys. (ZAMP),* Vol. 37, pp. 64-77.

Selvadurai, A. P. S., and Singh, B. M., 1987, "Axisymmetric Problems for an Externally Cracked Elastic Solid. II. Effect of a Penny-Shaped Inclusion," *Int. J. Engng. Sci.,* Vol. 25, pp. 1477-1490.

Selvadurai, A. P. S., 1989, "The Influence of a Boundary Fracture on the Elastic Stiffness of a Deeply Embedded Anchor Plate," *Int. J. for Numerical Anal. Meth. Geomech.,* Vol. 13, pp. 159-170.

Selvadurai, A. P. S., 1992, "Disk Inclusion Problems in Classical Elasticity Theory," in preparation.

Ufliand, Ia. S., 1956, "The Contact Problem of the Theory of Elasticity for a Die, Circular in its Own Plane, in the Presence of Adhesion," *Prikl. Math. i Mekh.,* Vol. 20, pp. 578-587.

Wang, Y., and Rajapakse, R. K. N. D., 1990, "Asymmetric Boundary Value Problems for a Transversely Isotropic Elastic Medium," *Int. J. Solids Structures,* Vol. 26, pp. 833-849.

Zureick, A. H., 1988, "Transversely Isotropic Medium With a Rigid Spheroidal Inclusion Under an Axial Pull," ASME JOURNAL OF APPLIED MECHANICS, Vol. 55, pp. 495-497.

Downloaded 03 May 2010 to 171.66.16.248. Redistribution subject to ASME license or copyright; see http://www.asme.org/terms/Terms_Use.cfm

Robert S. Gross
Assistant Professor of Aerospace Engineering, Auburn University, Auburn, AL 36849

James G. Goree
Centennial Professor, Clemson University, Clemson, SC 29634
Mem. ASME

Torsion of a Rigid Smooth Elliptic Insert in an Infinite Elastic Plane

A solution is presented for the non-Hertzian contact stress problem developed during torsion of a smooth rigid elliptic insert in an infinite, linearly elastic plane. The problem is reduced to a singular integro-differential equation which is solved numerically. Results are presented for the contact zones, and for the normal and tangential stresses at the plane-insert interface. The contact region is independent of the magnitude of the applied moment, but depends strongly on the shape of the ellipse, and is weakly dependent on Poisson's ratio of the plane. Results are also given for the reduction in torsional stiffness between a fully bonded insert and the present solution, (i.e., a completely failed bond).

Introduction

A method of evaluating the non-Hertzian contact stresses in an infinite plane with an elliptic hole containing a perfectly smooth rigid elliptic insert under torsion is presented in this paper. The insert exactly fills the hole when the system is unloaded and the plane is taken to be linearly elastic, either in a state of plane stress or plane strain. The loading consists of a pure moment M acting on the insert. Applied stresses and displacements are taken as zero at infinity. This system is illustrated in Fig. 1. The applied moment induces a rotation, ϵ, of the insert resulting in two arcs of plane-insert contact and two arcs of separation. Determination of the contact zones and the normal stress distribution on these zones are sought. Surprisingly, the authors have not been able to locate the solution to this fundamental torsional contact stress problem in the open literature.

The motivation for this study originated during a research program seeking an optimum geometric design for thin-walled composite torque tubes having noncircular end cross-sections. The noncircular end sections were required to provide mechanical torque transfer in the absence of adhesive bonding of the end fitting into the torque tube. The twisting of a rigid elliptic insert in an elastic plane is the simplest shape for an unbonded torsional fitting. Of practical interest is the difference in stiffness between a fully bonded insert and one in which the adhesive completely fails.

The related non-Hertzian contact problems of in-plane loading of both circular and elliptic inserts have been examined in complete detail by several authors. Sheremet'ev (1952) considered the contact problem of an infinite plate loaded in remote tension containing a smooth circular elastic or rigid disk. However, only the formulation was presented and neither the solution nor the results were discussed. This problem was also considered by Szelagowski (1956), but an error was made in determining the contact region. Stippes, Wilson, and Krull (1962) further investigated the problem defined by Sheremet'ev (1952) and were able to develop a complete formulation. In Stippes et al. (1962), the problem was solved in closed form for the contact geometry and stresses under the special condition that the material properties of the plate and disk were identical. For the case of unequal disk-plate material properties or for a rigid disk, only an approximate solution was shown to be possible. Wilson (1964a) later presented an approximate method to solve the governing equations for arbitrary disk and plate material properties. Wilson (1964b) extended this work and formulated the governing equations for the contact problem of an infinite plate loaded in biaxial tension or compression containing a smooth rigid elliptical insert. Goree (1965) then developed an approximate solution for the equations of Wilson (1964b), to complete the solution of the rigid elliptical insert contact problem with in-plane loading.

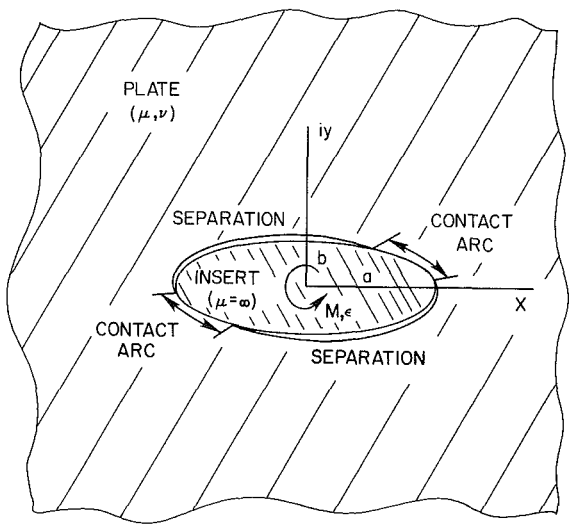

Fig. 1 Infinite elastic plane containing a rigid, smooth, elliptical insert subjected to a moment

Contributed by the Applied Mechanics Division of THE AMERICAN SOCIETY OF MECHANICAL ENGINEERS for publication in the JOURNAL OF APPLIED MECHANICS.

Discussion on this paper should be addressed to the Technical Editor, Prof. Leon M. Keer, The Technological Institute, Northwestern University, Evanston, IL 60208, and will be accepted until two months after final publication of the paper itself in the JOURNAL OF APPLIED MECHANICS. Manuscript received by the ASME Applied Mechanics Division, June 1, 1989; final revision, Mar. 14, 1990.

Copyright © 1991 by ASME
Downloaded 03 May 2010 to 171.66.16.248. Redistribution subject to ASME license or copyright; see http://www.asme.org/terms/Terms_Use.cfm

Much less attention has been given to the related torsion problem. Two special cases are considered by Muskhelishvili (1953) in his classic elasticity text. The first is for a perfectly bonded rigid ellipse (p. 355), and the second solution considers a rigid insert with a frictionless interface, but full plane-insert contact is maintained (p. 563). In this second case, tensile normal stresses are required on parts of the interface to maintain contact.

The present work then extends the solutions presented by Muskhelishvili to the more realistic case of a frictionless rigid insert with plane-insert separation allowed. That is, no shear stresses act anywhere on the insert boundary and only compressive normal stresses act on the contact regions. This solution is not a simple extension of the full contact problem. The determination of the contact region, as in the case of the in-plane loading discussed in the aforementioned papers, adds significantly to the complexity. The contact region, for example, is not just the region of compressive normal stresses found for the case of all-round contact. This error was made by Szelagowski (1956), for the case of in-plane loading with a circular disk.

In the present paper, it is shown that the torsion problem can be reduced to solving a singular integro-differential equation for the contact normal stresses, with the size and location of the contact arcs being determined by auxiliary conditions related to the normal displacements on the contact arc. The form of the development and the solution method has many similarities to the aforementioned papers of Wilson (1964a,b) and Goree (1965), although symmetry of the contact region is changed.

Formulation

The notation used here for the complex stress functions, stress components, and displacements is the same as employed by Muskhelishvili (1953). The region $|\zeta| \geq 1$ is conformally mapped onto the exterior of an elliptic hole in the z-plane by the function

$$z = \omega(\zeta) = R(\zeta + m\zeta^{-1}); \text{ where } z = re^{i\theta},\ \zeta = \rho e^{i\phi}, \qquad R = \frac{a+b}{2},\ m = \frac{a-b}{a+b}. \tag{1}$$

The stresses and displacements in an infinite plane containing a hole (i.e., the mapped plane) depend upon two functions $\phi(\zeta)$ and $\psi(\zeta)$. The general form of these stress functions for an infinite region S mapped onto an infinite region Σ is shown in Muskhelishvili (1953, p. 189), to have the form

$$\phi(\zeta) = -\frac{(X+iY)}{2\pi(1+\kappa)}\ln(\zeta) + R\Gamma\zeta + \phi^0(\zeta), \tag{2}$$

and

$$\psi(\zeta) = \frac{\kappa(X-iY)}{2\pi(1+\kappa)}\ln(\zeta) + R\Gamma'\zeta + \psi^0(\zeta), \tag{3}$$

where X and Y are the components of the resultant force acting on the boundary of the hole and the functions $\phi^0(\zeta)$ and $\psi^0(\zeta)$ are holomorphic in the region $|\zeta| \geq 1$ and are bounded at $\zeta = \infty$. The complex constants Γ and Γ' are functions of the applied stresses and displacements at infinity, and κ depends on Poisson's ratio ν as $\kappa = 3 - 4\nu$ for plane strain or $\kappa = (3-\nu)/(1+\nu)$ for plane stress.

For the case of an out-of-plane moment applied to the insert with the stresses and displacements vanishing at infinity ($\Gamma = \Gamma' = 0$) and zero resultant forces applied to the ellipse ($X = Y = 0$), the stress functions become

$$\phi(\zeta) = \phi^0(\zeta) = \frac{a_1}{\zeta} + \frac{a_2}{\zeta^2} + \ldots\ldots, \tag{4}$$

and

$$\psi(\zeta) = \psi^0(\zeta) = \frac{b_1}{\zeta} + \frac{b_2}{\zeta^2} + \ldots\ldots,\ |\zeta| \geq 1. \tag{5}$$

The stress boundary condition on $|\zeta| \geq 1$ is given in terms of derivatives of the stress functions in Muskhelishvili (1953, p. 536), as

$$\sigma_{\rho\rho} + i\sigma_{\rho\phi} = \Phi(\zeta) + \overline{\Phi(\zeta)} - \frac{\bar{\zeta}^2}{\omega'(\zeta)}[\omega(\zeta)\overline{\Phi'(\zeta)} + \overline{\omega'(\zeta)}\,\overline{\Psi(\zeta)}] \tag{6}$$

where $\Phi(\zeta) = \phi'(\zeta)/\omega'(\zeta)$ and $\Psi(\zeta) = \psi'(\zeta)/\omega'(\zeta)$. The function $\Phi(\zeta)$ can be continued into the region $|\zeta| \leq 1$ by selecting the form of $\Phi(\zeta)$ from Muskhelishvili (1953, p. 536);

$$\omega'(\zeta)\Phi(\zeta) = -\omega'(\zeta)\overline{\Phi}(1/\zeta) + \zeta^{-2}\,\omega(\zeta)\overline{\Phi}'(1/\zeta) + \zeta^{-2}\,\overline{\omega}'(1/\zeta)\overline{\Psi}(1/\zeta). \tag{7}$$

The stress functions on the right-hand side of equation (7) are found by using equations (1), (4), and (5).

The continued function $\Phi(\zeta)$ on the left-hand side of this equation is then

$$\Phi(\zeta) = \alpha_0 + \alpha_1\zeta + \alpha_2\zeta^2 + \alpha_3\zeta^3 + \ldots,\quad |\zeta| \leq 1. \tag{8}$$

Using this continued function, the problem of finding $\Phi(\zeta)$ in both regions may be cast as a Hilbert problem such that the normal stress boundary condition is related to the discontinuity of $\Phi(\zeta)$ across the two contact arcs (L'). That is, equation (6) becomes

$$N(\beta) = \Phi^-(\beta) - \Phi^+(\beta), \quad \text{where } \beta = e^{i\phi} \text{ on the contact arcs } L'. \tag{9}$$

The radial (normal) stress, $\sigma_{\rho\rho}$, in equation (6) has been renamed as $N(\beta)$ on the contact arcs in writing equation (9). Also, the shear stress in equation (6) is zero on the contact arcs for the case of a smooth insert. The + and − signs denote limiting values of $\Phi(\zeta)$ when approaching a point β on L' from inside or outside the circle, respectively. The normal stress $N(\beta)$ is zero for points not on the contact arcs and is symmetric such that $N(\beta) = N(-\beta)$.

The function $\Psi(\zeta)$, which is defined only for $|\zeta| \geq 1$, is expressed in terms of $\Phi(\zeta)$ from Muskhelishvili (1953, p. 537) as

$$\omega'(\zeta)\Psi(\zeta) = \zeta^{-2}\,\overline{\omega}'(1/\zeta)\overline{\Phi}(1/\zeta) - \frac{d}{d\zeta}[\overline{\omega}(1/\zeta)\Phi(\zeta)],\ |\zeta| \geq 1. \tag{10}$$

Recalling the definition of the function $\Phi(\zeta)$ outside the unit circle γ, and the definition of the continued function inside the unit circle γ from equation (8), the behavior of $\Phi(\zeta)$ as $\zeta \to 0$ and $\zeta \to \infty$ is

$$\lim_{\zeta\to 0}\Phi(\zeta) = 0 \text{ and } \lim_{\zeta\to\infty}\Phi(\zeta) = 0. \tag{11}$$

Combining equation (9) with the required behavior of $\Phi(\zeta)$ at $\zeta = 0$ and $\zeta = \infty$, and using the Plemelj formulae, the function $\Phi(\zeta)$ is given as

$$\Phi(\zeta) = -f(\zeta) - \frac{mF}{\zeta^2 - m} \tag{12}$$

where

$$f(\zeta) = \frac{1}{2\pi i}\int_L' \frac{N(t)\,dt}{t-\zeta} \text{ and } F = f(0), \text{ (real constant)}. \tag{13}$$

The term $f(\zeta)$ in equation (12) results directly from the solution to the Hilbert problem posed in equation (9). The second term on the right-hand side of equation (12) is necessary to satisfy the behavior of $\Phi(\zeta)$ at $\zeta = 0$ and $\zeta = \infty$ as given by equation (11). Employing the symmetry properties of $N(t)$ (i.e., $N(t) = N(-t)$), $f(\zeta)$ can be shown to have the following special behavior:

$$f(\zeta) = f(-\zeta) = F - \bar{f}(1/\zeta),\ \overline{f^{\pm}(\beta)} = F - f^{\mp}(\beta) \tag{14}$$

Downloaded 03 May 2010 to 171.66.16.248. Redistribution subject to ASME license or copyright; see http://www.asme.org/terms/Terms_Use.cfm

and

$$\lim_{\zeta\to\infty} f(\zeta) = \lim_{\zeta\to\infty} 0(\zeta^{-2}) = 0. \tag{15}$$

Up to this point the method of solution has been to form the Hilbert problem by writing equation (9). The solution to this problem is given directly by equation (12), and is then complete if the normal contact stresses $N(\beta)$ and the contact arcs L' are known. However, neither $N(\beta)$ nor L' are known, so additional conditions must be employed. Although the normal contact stresses are unknown, the normal displacement on the contact arcs is known in terms of the rotation ϵ of the rigid insert. Additional conditions on $\Phi(\zeta)$ may be constructed to determine $N(\beta)$ and L' by writing the displacement boundary value equation complimentary to equation (9) as

$$2\mu\frac{d}{d\beta}(u+iv) = [\kappa\Phi^-(\beta) + \Phi^+(\beta)]\omega'(\beta) \text{ on } L', \tag{16}$$

where u and v are the cartesian components of displacement at the insert boundary. In equation (16) the derivatives of the displacements on the contact arcs L' are related to the discontinuity of $\Phi(\zeta)$ across L'. By requiring that the normal displacements of the insert and plane be equal for any point β on L', and employing the relationship between the displacement derivatives and $\Phi(\zeta)$ given in equation (16), sufficient conditions are imposed on $\Phi(\zeta)$ such that the normal contact stresses $N(\beta)$ and contact arcs L' may be determined. Equation (16) along with the condition that the normal stress, $N(\beta)$, be zero on the free arcs $(L-L')$ is then the proper statement of this mixed boundary value problem.

The most difficult aspect of contact problems of this type is the determination of the contact zone. The first method described below perhaps gives more physical insight into the behavior while the second technique is more direct computationally, and was the procedure used in determining the present solution.

If the size of the contact arcs are specified, that is, if the insert is somehow attached to the plate over specified arcs L' (still having no shear stress anywhere on the entire interface), then equation (12) and (16) along with $N(\beta)=0$ on $L-L'$ gives a properly stated problem, the solution of which gives $N(\beta)$ on the contact arcs. If this contact region L' is arbitrarily chosen, the normal stress $N(\beta)$ may well be tensile over part of L' and will, in general, be singular at the ends of the contact regions. Conversely, if tensile stresses are not allowed on L', that is, there is no attachment between the insert and the plate, (this is then the desired non-Hertzian contact stress problem), the size of the contact region is just that region such that the normal stress is compressive everywhere on L' and is identically zero at the ends of L'. One could then solve the original problem by using equation (16), with both tensile and singular stresses allowed, and successively adjust the size and location of the contact zone L' until a contact region was found that gave only compressive stresses that also vanished at the ends.

The second method follows a different and more direct approach of requiring the proper form for the contact stress (i.e., zero at the ends and compressive everywhere, and adjusting the contact zone to meet displacement compatibility. In order to include the normal stress directly into the displacement boundary condition, equation (16), an appropriate procedure is to develop the boundary condition such that the derivatives of the displacements u and v are presented in terms of the $\pm$ limiting values of $\Phi^{\pm}(\beta)$ (or $f^+(\beta)$). The rather complicated manipulations given below are required to develop the displacement boundary condition in this form.

The normal displacement u_ρ of the elastic plate as measured in the ζ-plane for any point β on the surface of the unit circle is given by

$$2|\omega'(\beta)|u_\rho = (u+iv)(\beta^{-1}-m\beta) + (u-iv)(\beta-m\beta)^{-1}). \tag{17}$$

The corresponding normal displacement for a given rotation ϵ of the rigid elliptic insert at any point β on the surface of the insert in the ζ-plane is given directly in terms of ϵ as

$$|\omega'(\beta)|u_\rho = -m\epsilon R^2 i(\beta^2-\beta^{-2}). \tag{18}$$

Equation (18) follows from the expression for the normal and tangential components of displacement given in terms of the cartesian component by Muskhelishvili (1953, p. 188) as

$$u_\rho + iv_\phi = \frac{\overline{\zeta\omega'(\zeta)}}{|\omega'(\zeta)|}(u+iv)$$

where u_ρ and v_ϕ are the normal and tangential components of displacement, respectively, and the terms u and v are the cartesian components. For a rigid body rotation ϵ of the elliptical insert, the cartesian components of displacement for any point (x, y) on the ellipse boundary are given by $u=-\epsilon y$ and $v=\epsilon x$. For any point β within the contact region, the normal displacement for the plate and insert as given by equations (17) and (18) must, of course, be equal. This condition is expressible as

$$-2m\epsilon R^2 i(\beta^2-\beta^{-2}) = (u+iv)(\beta^{-1}-m\beta) + (u-iv)(\beta-m\beta^{-1}). \tag{19}$$

As the boundary values of the unknown function $\Phi(\zeta)$ are related to the derivatives of the displacements by equation (16), it is more convenient to also write equation (19) in terms of displacement derivatives. Employing an operator introduced in Stippes, Wilson, and Krull (1964) as

$$L(g) = \frac{d}{d\beta}\left[\beta^3\frac{d}{d\beta}(\beta^{-1}(g))\right], \text{ and from equation (19),} \tag{20}$$

let $g=(u+iv)(\beta^{-1}-m\beta)+(u-iv)(\beta-m\beta^{-1})$,

and also $g=-2m\epsilon R^2 i(\beta^2-\beta^{-2})$,

equation (19) can then be written as

$$-6m\epsilon Ri(\beta^2-\beta^{-2}) = (\beta-m\beta^3)(u''+iv'') + (\beta^3-m\beta)(u''-iv'') - (3m\beta^2+1)(u'+iv') + (3\beta^2+m)(u'-iv'). \tag{21}$$

Using equations (12) and (16), the derivatives of the displacements on the hole can be related to the boundary values of $f(\zeta)$.

After considerable reduction, equation (21) is converted into the following relationship containing only the sums and differences of $f^{\pm}(\beta)$ as

$$\begin{aligned}-12\mu m\epsilon i(\beta^2-\beta^{-2}) &= 3m(1+\kappa)(\beta^2-\beta^{-2})[f^+(\beta)+f^-(\beta)] \\ &+ (1-\kappa)(1-m^2)[f^+(\beta)-f^-(\beta)] \\ &+ (1+\kappa)(m^2+6m\beta^{-2}+1)F - (1+\kappa)\beta[1-m(\beta^{-2}+\beta^2) \\ &+ m^2]\frac{d}{d\beta}[f^-(\beta)-f^+(\beta)].\end{aligned} \tag{22}$$

Employing the Plemelj formulae from Muskhelishvili (1953, p. 268); equation (22) may be written as

$$\begin{aligned}-\frac{12\mu m\epsilon i(\beta^2-\beta^{-2})}{(1+\kappa)} &= 3m(\beta^2-\beta^{-2})\frac{1}{\pi i}\int_L \frac{N(t)dt}{t-\beta} \\ &- [1+m^2-m(\beta^2+\beta^{-2})]\frac{\beta}{\pi i}\int_L \frac{N'(t)dt}{t-\beta} \\ &+ \lambda(1-m^2)N(\beta) + (m^2+6m\beta^{-2}+1)F\end{aligned} \tag{23}$$

where $\lambda=(1-\kappa)/(1+\kappa)$. Equation (23) is a singular integro-differential equation which determines the normal stress distribution on the contact arc.

The integration contour L used in equation (23) is the entire

Downloaded 03 May 2010 to 171.66.16.248. Redistribution subject to ASME license or copyright; see http://www.asme.org/terms/Terms_Use.cfm

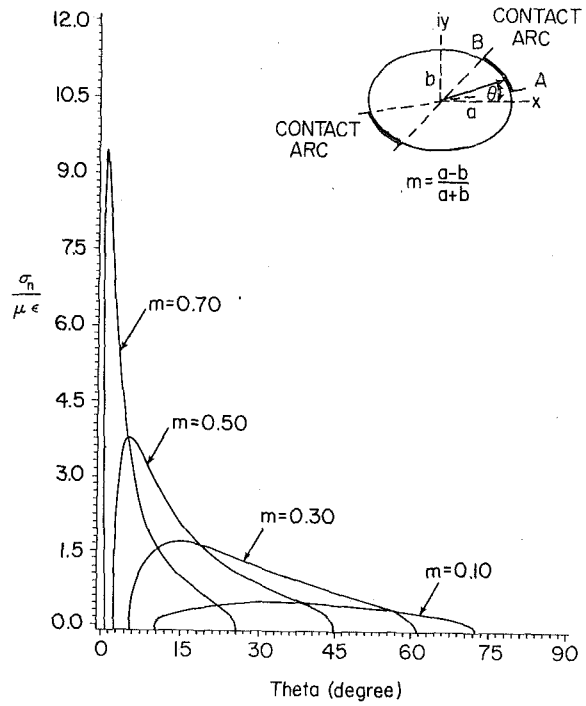

Fig. 2 Normal stress as a function of theta for ellipses with various eccentricities m and with $\kappa = 5/3$

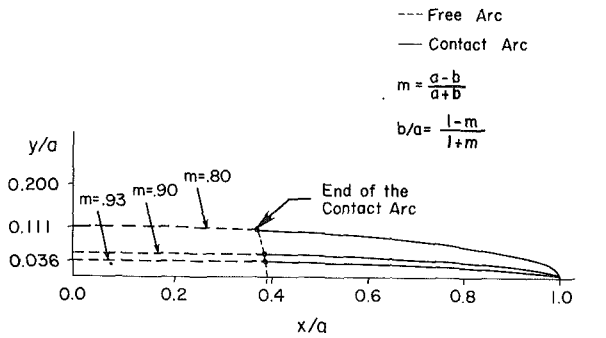

Fig. 3 Contact and separation regions for ellipses with eccentricities of $m = 0.80$, 0.90, and 0.93, $\kappa = 5/3$

circumference of the unit circle. However, $N(t)$ and $N'(t)$ are nonzero only on the contact arc. Consequently, it is sufficient to integrate along the two contact arcs L' defined by the two angles ϕ_1 and ϕ_2 as

$$\phi_1 \le \arg(t) \le \phi_2 \text{ and } (\pi+\phi_1) \le \arg(t) \le (\pi+\phi_2).$$

Solution of the problem involves the determination of $N(t)$, ϕ_1, and ϕ_2. Equation (23) possesses all three of the unknown quantities since ϕ_1 and ϕ_2 appear in the limits of the contour integrals. To complete the solution to the problem, equation (23) must be supplemented by two additional conditions. These additional conditions are found by requiring normal displacement compatability between the plate and insert for any two points within the contact zone. Although these last two conditions may seem redundant in light of equation (19) which requires that the normal displacements of the insert and plate be equal within the contact arcs L', it should be noted that the derivation of the governing singular integral equation (23) is based on equation (21) which involves the first and second derivatives of the displacements, not the actual displacements.

As already mentioned, enforcing normal displacement compatability at any two points within the contact region will provide the final two conditions necessary, and the solution is unique regardless of which two points on the contact region are selected. The compatability equation for any point β in the contact zone is

$$2|\omega'(\beta)|R^{-1}u_\rho(\beta) = (\beta^{-1}-m\beta)[u(\beta)+iv(\beta)] + (\beta-m\beta^{-1})[u(\beta)-iv(\beta)] = -2m\epsilon Ri(\beta^2-\beta^{-2}). \quad (24)$$

The displacements may be defined in terms of the stress functions as

$$2\mu[u(\beta)+iv(\beta)] = \kappa\phi^-(\beta) - \omega(\beta)\overline{\Phi^-(\beta)} - \overline{\psi^-(\beta)}. \quad (25)$$

Using equation (25), the displacement compatability condition, equation (24), becomes

$$-4m\mu R\epsilon i(\beta^2-\beta^{-2}) = [\kappa\phi^-(\beta) - \omega(\beta)\overline{\Phi^-(\beta)} - \overline{\psi^-(\beta)}](\beta^{-1} - m\beta) + [\kappa\overline{\phi^-(\beta)} - \overline{\omega(\beta)}\Phi^-(\beta) - \psi^-(\beta)](\beta - m\beta^{-1}). \quad (26)$$

Employing equations (10) and (12), it follows that for $|\zeta| \ge 1$, the functions $\phi(\zeta)$ and $\psi(\zeta)$ may be written as

$$\phi(\zeta) = -\int_\infty^\zeta \omega'(t)f(t)dt + mFR\zeta^{-1}, \quad (27)$$

and

$$\psi(\zeta) = R\int_\infty^\zeta (t^{-1}+mt)f'(t)dt + RF\zeta^{-1} + RmF\frac{(\zeta^{-1}+m\zeta)}{(\zeta^2-m)}. \quad (28)$$

After substitution of equations (27) and (28) into equation (26), the form of the displacement compatability condition becomes

$$-4m\mu\epsilon i(\beta^2-\beta^{-2}) = [\kappa(\beta^{-1}-m\beta) - m(\beta-m\beta^{-1})]\int_\beta^\infty f(t)dt + [\kappa(\beta-m\beta^{-1}) - m(\beta^{-1}-m\beta)]\overline{\int_\beta^\infty f(t)dt} + [\kappa m(\beta^{-1}-m\beta) - (\beta-m\beta^{-1})]\int_0^{\bar\beta}\bar f(t)dt + [\kappa m(\beta-m\beta^{-1}) - (\beta^{-1}-m\beta)]\overline{\int_0^{\bar\beta}\bar f(t)dt}. \quad (29)$$

The three equations that must be satisfied to determine the correct values of the unknowns $N(t)$ (and therefore $f(\zeta)$ by equation (13)), ϕ_1 and ϕ_2 are equations (23) and (29) evaluated at each of the end points $\beta = e^{i\phi_1}$ and $\beta = e^{i\phi_2}$. The tangential stress at the plane-insert interface is given directly in terms of $N(t)$ as,

$$\sigma_{\phi\phi}(t) = N(t) + \frac{2F(m^2-1)}{1+m^2-2m\cos(2\phi)}. \quad (30)$$

Equation (23) is a first-order singular integrodifferential equation which could not be solved in closed form. In the report by Wilson, Hill, and Goree (1965), an approximate solution was presented for an analogous problem regarding an infinite plate containing a circular elastic insert subject to remote biaxial tractions. The approximate solution used in the present problem is detailed in the Ph.D. thesis by the first author, Gross (1988), and closely parallels the procedure developed by Wilson, Hill, and Goree (1965). In essence, this procedure involves representing the unknown function $f(\zeta)$ as a series of Legendre polynomials with unknown coefficients. The development of the proper form for $f(\zeta)$ is dependent on constructing an appropriate sectionally holomorphic function $\alpha(\zeta)$ that is discontinuous over the contact arcs and is related to the generating function for Legendre polynomials.

Results and Discussion

Employing the approximate solution procedure referenced above, the contact stresses and contact arcs are found for any rigid body rotation, ϵ, of the insert. All results are for plane

Downloaded 03 May 2010 to 171.66.16.248. Redistribution subject to ASME license or copyright; see http://www.asme.org/terms/Terms_Use.cfm

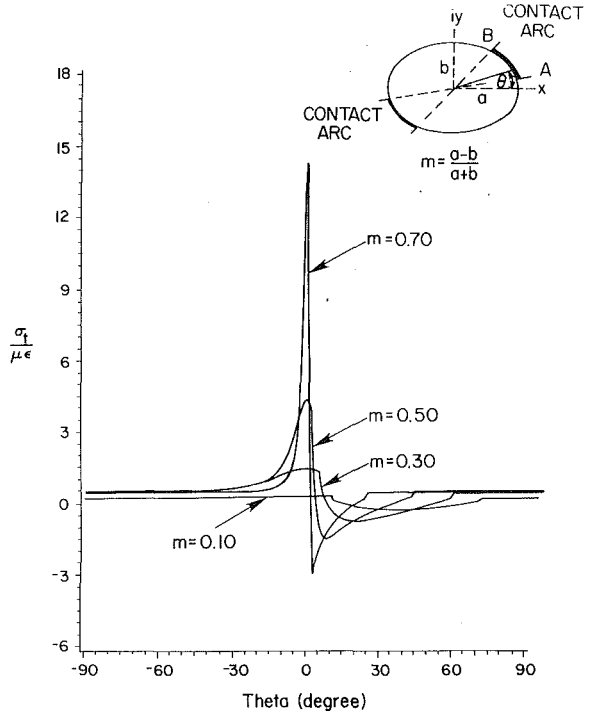

Fig. 4 Tangential (hoop) stress in the plane at the plane-insert interface as a function of theta for ellipses with various eccentricities m and with $\kappa = 5/3$

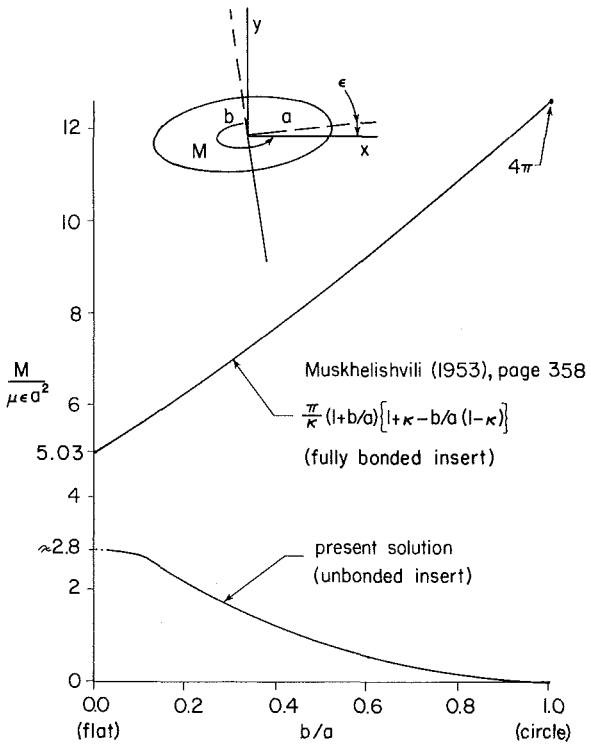

Fig. 5 Comparison of the torsional stiffness between fully bonded and smooth (unbonded) elliptic inserts

strain with $\nu = 0.33$. In the results, note that the stresses on the boundary of the ellipse depend only on m (or, therefore, the ratio b/a) and not on the physical size of the ellipse. The stresses in the plane at a point away from the boundary do, of course, depend on ellipse size, i.e., analogous to a tension plate with a circular hole. In Fig. 2, the normal stress distribution is shown as a function of theta for various ellipse eccentricities. Other cases with different values of ν were examined, and the effect of Poisson's ratio was found to be very small. The ellipse eccentricity m is a much more significant factor with regard to the normal stresses. The contact arcs are given by the end points (A and B) of the normal stress distribution for each different value of m. Note that $\theta_1 > 0$ for all m and $\theta_1 \to 0$ as $m \to 1$.

Although no exact solutions are available to verify the present solution, certain required behavior at the extremes of $m = 0$ (circle) and $m = 1$ (needle) can be checked. For the case of a circular insert ($m = 0$), the normal stresses must be equal to zero and the results given in Fig. 2 show such a trend as $m \to 0$. In the case of a needle-shaped insert ($m = 1$), the contact zone should approach a constant and the normal stress should be square root singular at the end of the needle and smoothly go to zero at the point of separation. Both of these trends are reflected in the curves presented in Fig. 2. In Fig. 3, the contact arc in the first quadrant is shown for values of m near 1.0 and it is apparent that the contact arc does converge to a constant value for $m \to 1$. The limit value of the contact arc cannot be obtained by the current analysis any more closely than that shown in Fig. 3, where it is seen that $x/a \approx 0.39$ as $m \to 1$. The right end of the contact zone was very close to $x/a = 1$ for all m near 1. This behavior is also demonstrated in Fig. 2 where for $m = 0.7$ also $\theta_1 \approx 1$ degree.

The tangential (hoop) stress in the plane at the plane-insert interface is shown as a function of theta in Fig. 4. The maximum tangential stress always occurs at $\theta = 0$, not at the end of the contact zone (point A in Fig. 4). This follows directly from equation (30), and the results that $\phi_1 > 0$ for all $m < 1$, F = real constant given by equation (13) and $N(t)$ is negative and is zero outside the contact arcs. Also note from equation (1) that $\phi = 0$ corresponds to $\theta = 0$. A second (lower) spike in the tangential stress value is observed at the left end of the contact zone (point B), as would be expected by the rotation direction of the insert. As for the case of the normal stress distribution, the influence of Poisson's ratio on the tangential stresses was very small.

Finally, the comparison between a fully bonded insert and a smooth insert is made in Fig. 5. The complete solution for the fully bounded insert is presented in Muskhelishvili (1953, p. 358) as

$$\frac{M}{\mu\epsilon} = \frac{4\pi R^2 (m+\kappa)}{\kappa}. \tag{31}$$

Letting $\xi = b/a$, equation (31) is

$$\frac{M}{\mu\epsilon a^2} = \frac{\pi}{\kappa}(1+\xi)[1+\kappa-\xi(1-\kappa)]. \tag{32}$$

Noting that $0 \le \xi \le 1$, and using the permissible range for κ, it is seen from equation (32) that the maximum moment for a given angle of twist (i.e., the maximum stiffness) for the bonded insert occurs at $\xi = 1$ (circular insert), and the minimum stiffness is for $\xi = 0$ (flat insert). The smooth insert has just the opposite behavior, with no resistance to torque for a circular insert and maximum stiffness for a flat insert. These results are depicted in Fig. 5 for $\nu = 0.33$. The moment is proportional to $\mu\epsilon a^2$ for both cases. It is clear that loss of adhesion gives a very large reduction in stiffness for all ellipse ratios, with the least change being about a factor of 2 as $b \to 0$.

Acknowledgment

The authors discussed this problem at length with Prof. Howard B. Wilson, Jr. of the University of Alabama. We gratefully acknowledge his significant contributions to the study.

Downloaded 03 May 2010 to 171.66.16.248. Redistribution subject to ASME license or copyright; see http://www.asme.org/terms/Terms_Use.cfm

References

Goree, J. G., 1965, "Approximate Determination of Contact Stresses in an Infinite Plate Containing a Smooth Rigid Elliptic Insert," ASME JOURNAL OF APPLIED MECHANICS, Vol. 32, No. 2, (Vol. 87, Series E), pp. 437–439.

Gross, Robert S., "Optimal Design of Composite Torque Tube Ends," Ph.D. Thesis, Clemson University, Clemson, S.C., July 1988.

Muskhelishvili, N. I., 1953, *Some Basic Problems of the Mathematical Theory of Elasticity,* 4th ed., P. Noordhoff Ltd.

Sheremet'ev, M. P., 1952, "The Elastic Equilibrium of an Infinite Plate With an Inserted Absolutely Rigid or Elastic Disk," PMM 16, No. 4, pp. 437–448.

Stippes, M., Wilson, H. B., Jr., and Krull, F. N., 1962, "A Contact Stress Problem for a Smooth Disk in an Infinite Plate," *Proc. of the Fourth U. S. National Congress of Applied Mechanics,* Vol. 2, ASME, New York, pp. 799–806.

Szelagowski, F., 1956, "The Influence of a Bolt Inserted in a Hole of an Infinite Plate Subjected to One-Directional Tension or Compression on the Stresses in the Plate," *Bulletein L'Academie Polonaise Des Sciences,* Cl.IV, Vol. 4, No. 1.

Wilson, H. B., Jr., 1964, "Approximate Determination of Contact Stresses in an Infinite Plate With a Smooth Circular Insert," *Proceedings of the Second Southeastern Conference on Theoretical and Applied Mechanics.*

Wilson, H. B., Jr., 1964, "Contact Stresses in an Infinite Plate Containing a Smooth Rigid Elliptic Insert," ASME JOURNAL OF APPLIED MECHANICS, Vol. 31, (Vol. 86, Series E), p. 703.

Wilson, H. B., Jr., Hill, J. L., and Goree, J. G., 1965, "Mathematical Studies of Composite Materials II," Rohm and Haas Company Special Report No. S-50.

Downloaded 03 May 2010 to 171.66.16.248. Redistribution subject to ASME license or copyright; see http://www.asme.org/terms/Terms_Use.cfm

The Nonlinear Elastic Behavior of Open-Cell Foams[1]

W. E. Warren
Fellow ASME

A. M. Kraynik

Sandia National Laboratories,
Albuquerque, NM 87185

A constitutive model for the nonlinear elastic behavior of isotropic low-density open-cell foams with three-dimensional structure is formulated in terms of a strain energy function. The theory is based on micromechanical analysis of an idealized tetrahedral unit cell of arbitrary orientation that contains four half-struts joining at equal angles. The force-displacement relations for each strut are expressed by compliances for bending and stretching that do not depend on the magnitude of applied force. Contributions to the strain energy from large deformation effects are assumed to depend on strut reorientation and stretching, and are determined by analyzing a pin-jointed structure. The analysis is considered to be valid for finite strains below the onset of yielding associated with strut buckling.

Introduction

Because of their structure, natural and synthetic cellular solids possess unique physical properties, which explains their prevalence in nature and value to man. Examples include wood, bone, bread, and high technology foams manufactured from polymers, ceramics, and metals. Our developing understanding of the mechanics of cellular solids (henceforth referred to as foams) through experiment and theory is well documented (Meinecke and Clark, 1973; Hilyard, 1982; Gibson and Ashby, 1988). The mechanical response of interest is as diverse as the underlying structure and constituent properties of these materials. Like many previous studies, ours is motivated by the practical desire to engineer cellular materials. This requires basic understanding of their constitutive behavior and its origin in structure. Here, we develop a constitutive theory for the nonlinear elastic behavior of isotropic low-density open-cell foams.

This analysis extends our recent model for effective elastic constants (Warren and Kraynik, 1988) to finite deformations, but is restricted to conditions before struts buckle, which can be associated with the onset of yielding. We assume that essential features of mechanical behavior for open-cell foams can be inferred from the deformation response of a representative structural element, the tetrahedral joint shown in Fig. 1. The length of the half-struts is the same, as are the angles between them, and the cross-section of the identical struts can vary along their length. Menges and Knipschild (1975, 1982) considered deformations of a similar structure in less detail. This geometry captures the strut connectivity typical of open-cell foams for which structure is influenced by the tendency to minimize surface area during formation.

The symmetry of the tetrahedral structure, while providing a mathematically tractable mechanical analysis, obviously comprises geometrical features of real materials, such as variable strut length and angles, etc. However, compared to other choices, we view this as an acceptable compromise. For example, early models of foam mechanics (Gent and Thomas, 1959, 1963; Lederman, 1971; Kanakkanatt, 1973) focused on the deformation of individual randomly-oriented struts, which are assumed to stretch according to affine displacement of the network junctions. This assumption suppresses strut bending, which is a dominant mechanism for small distortions of a foam

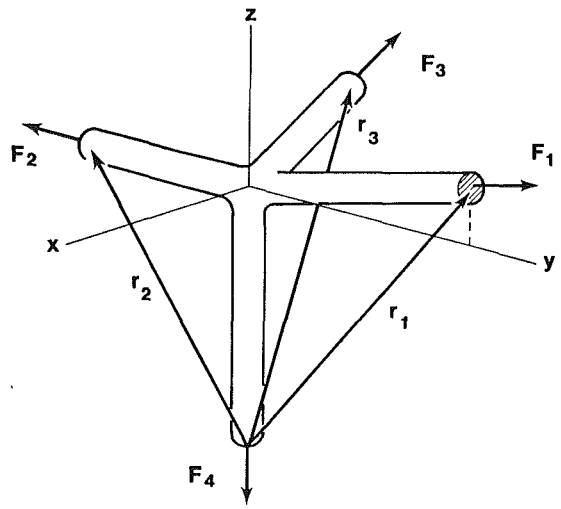

Fig. 1 Schematic of the tetrahedral element, which represents the primary microstructural feature of low-density open-cell foams. Four identical half-struts meet at equal angles. The position vectors r_i represent the relative positions of the strut midpoints and the F_i represent the forces at each strut midpoint.

[1]This work performed at Sandia National Laboratories and supported by the U.S. Department of Energy under contract No. DE-AC04-76DP00789.

Contributed by the Applied Mechanics Division of THE AMERICAN SOCIETY OF MECHANICAL ENGINEERS for publication in the JOURNAL OF APPLIED MECHANICS.

Discussion on this paper should be addressed to the Technical Editor, Prof. Leon M. Keer, The Technological Institute, Northwestern University, Evanston, IL 60208, and will be accepted until two months after final publication of the paper itself in the JOURNAL OF APPLIED MECHANICS. Manuscript received by the ASME Applied Mechanics Division, Apr. 17, 1989; final revision, Jan. 25, 1990.

Copyright © 1991 by ASME
Downloaded 03 May 2010 to 171.66.16.248. Redistribution subject to ASME license or copyright; see http://www.asme.org/terms/Terms_Use.cfm

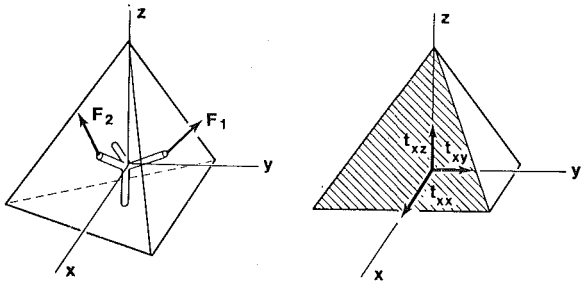

Fig. 2 Schematic of the volume element that contained each tetrahedral element showing the coordinate system used to determine the Piolá-Kirchoff stress. In the undeformed state, the volume element is a regular tetrahedron.

(Ko, 1965; Menges and Knipschild, 1975, 1982; Gibson and Ashby, 1982, 1988; Warren and Kraynik, 1987, 1988). Without bending, the effective Young's modulus E_f for low-density foams varies linearly with the volume fraction of solid Φ. By contrast, with bending, $E_f \sim \Phi^2$, which is supported by experimental data. The cubic model of an open-cell foam proposed by Gibson and Ashby (1982, 1988) also permits bending, but exhibits sharp corners and strut connectivity of three instead of the usual four characteristic of foams. Under the assumption that displacement of strut midpoints is affine, the tetrahedral geometry used here accommodates both bending and stretching mechanisms for strut distortion (Warrent and Kraynik, 1988).

We assume that the undeformed solid structure is contained in the tetrahedral unit cell shown in Fig. 2. This idealization provides a specific relation between the shape of the solid and its volume fraction. The volume of a slender strut (scaled by $\Phi(2L)^3$, where L is the strut half-length) is approximately 0.866. For comparison, the strut volumes for other model cells, such as the regular pentagonal dodecahedron and the tetrakaidecahedron are 0.766 and 0.943, respectively. Changing the volume of the unit cell introduces a new scalar factor, but does not alter the functional dependence between stress and strain. Because tetrahedra do not fill space, our geometric assumptions are not precisely compatible with any three-dimensional network of struts. Although our results cannot be "exact," they do provide useful insight into foam mechanics. We note that in the two-dimensional problem for honeycombs, the unit cell is space filling and specific cellular networks are modeled.

This nonlinear theory for three-dimensional, open-cell foams retains the geometry of our linear theory and builds on that analytical framework. Deformation of struts is related linearly to applied forces through a bending compliance N and a stretching compliance M, which do not depend on the magnitude of applied force. Here, we assume that essential large-deformation effects stem from the geometrical nonlinearity of strut reorientation as they stretch. This is modeled by neglecting strut bending and considering a pin-jointed structure. A similar assumption was adopted by Warren et al. (1989) in developing a large-deformation theory for two-dimensional honeycombs. There, the assumption was supported by results from finite element simulations using Euler-Bernoulli two-dimensional beam elements to model specific foam structures. Simulations for simple shearing deformations indicate that linear elastic response is dominated by film bending as mentioned previously. With increasing macroscopic deformation of the honeycomb, film bending levels off and stretching takes on the dominant role in film distortion. In this situation, one has a structured material whose distortional elastic behavior is dominated by bending of the microstructure for small deformations and stretching for large deformations.

The analysis presented here leads to a strain energy function that retains terms through fourth order in strain. The terms that represent small distortion response follow from our previous linear theory and are dominated by strut bending; the additional terms that provide nonlinear behavior stem from stretching and reorientation of struts. While the strain energy function is determined from homogeneous deformations of the structure, the results presumably hold in a local sense over a neighborhood large with respect to cell size and thus can be used to solve specific boundary value problems in finite elasticity.

When foams are used in compression, buckling of the struts will occur at sufficiently large strains. While this buckling can represent an elastic response, it is not accounted for in this analysis and places a bound on the strain levels for which the strain energy function is valid. This bound is sufficiently small that strain terms of higher order than four will not contribute significantly to the induced stresses.

We use the strain energy function derived here to predict the response of a low-density foam subjected to uniaxial stress. This condition exists in the central region of a tensile or compression test specimen remote from the ends where specific loading constraints can prevail. Response through second order in strain is dominated by strut bending while stretching determines the third-order term, which has the largest coefficient. This analysis provides a micromechanical basis for assessing the relative roles of bending and stretching of the microstructure in foam mechanics.

Micromechanics of the Unit Cell

As in our linear analysis of open-cell foams, we assume that the tetrahedral element shown in Fig. 1 represents essential features of the microstructure. Four half-struts each of length L emanate from a common joint and are initially directed at equal angles to each other. We assume that homogeneous deformations of this element are determined by affine displacement of strut midpoints. For large deformations, strut bending is neglected and the struts deform by stretching through forces which act at each strut midpoint and are directed parallel to the strut. Under these conditions, the deformed tetrahedral element behaves as though pin jointed; struts reorient but remain straight. We also assume a linear force-displacement relation with constant compliance M for each strut. The resulting nonlinearity of this model is geometrical in origin and stems from strut reorientation. It is not necessary to invoke nonlinear behavior of the constituent material to predict large nonlinear behavior for the foam.

We represent strut midpoint forces $\mathbf{F}_i$ in the form

$$\mathbf{F}_i = P_i \mathbf{e}_i \,, \tag{1}$$

where $\mathbf{e}_i$ is a unit vector directed outward along the ith strut. The displacement $\boldsymbol{\Delta}_i$ of each strut midpoint, with respect to the joint, is given by

$$\boldsymbol{\Delta}_i = (L + M P_i)\mathbf{e}_i - L\mathbf{e}_i^o \,, \tag{2}$$

where M is the constant axial compliance and $\mathbf{e}_i^o$ is the initial direction of the ith strut. With reference to Fig. 1, the $\mathbf{e}_i^o$ are given by

$$\begin{aligned} \mathbf{e}_1^o &= (2\sqrt{2}\mathbf{j} + \mathbf{k})/3 \,, \\ \mathbf{e}_2^o &= (\sqrt{6}\mathbf{i} - \sqrt{2}\mathbf{j} + \mathbf{k})/3 \,, \\ \mathbf{e}_3^o &= (-\sqrt{6}\mathbf{i} - \sqrt{2}\mathbf{j} + \mathbf{k})/3 \,, \\ \mathbf{e}_4^o &= -\mathbf{k} \,, \end{aligned} \tag{3}$$

where $\mathbf{i}$, $\mathbf{j}$, $\mathbf{k}$ are unit vectors directed along the x, y, z coordinates. The unit vectors $\mathbf{e}_i^o$, $\mathbf{e}_i$ will be written in the form

$$\mathbf{e}_i^o = \sum_{j=1}^{3} a_i^j \mathbf{g}_j, \quad \mathbf{e}_i = \sum_{j=1}^{3} b_i^j \mathbf{g}_j, \tag{4}$$

where $\mathbf{g}_1 = \mathbf{i}$, $\mathbf{g}_2 = \mathbf{j}$, and $\mathbf{g}_3 = \mathbf{k}$. The a_i^j are obtained from (3) and

$$(b_i^1)^2 + (b_i^2)^2 + (b_i^3)^2 = 1 \,. \tag{5}$$

Downloaded 03 May 2010 to 171.66.16.248. Redistribution subject to ASME license or copyright; see http://www.asme.org/terms/Terms_Use.cfm

Letting

$$M P_i = L \epsilon_i , \tag{6}$$

where ϵ_i represents an average strain in the ith strut, the displacements Δ_i can be put in the form

$$\Delta_i = L \sum_{j=1}^{3} [(1+\epsilon_i) b_i^j - a_i^j] \mathbf{g}_j . \tag{7}$$

The position $\mathbf{r}_i$ of the ith strut midpoint with respect to the midpoint of strut 4 can be written

$$\mathbf{r}_i = \mathbf{r}_i^o + \boldsymbol{\delta}_i , \tag{8}$$

where

$$\boldsymbol{\delta}_i = \Delta_i - \Delta_4 , \tag{9}$$

and $\mathbf{r}_i^o$ are the position vectors in the undeformed structure given by

$$\begin{aligned} \mathbf{r}_1^o &= L(2\sqrt{2}\mathbf{j} + 4\mathbf{k})/3 , \\ \mathbf{r}_2^o &= L(\sqrt{6}\mathbf{i} - \sqrt{2}\mathbf{j} + 4\mathbf{k})/3 , \\ \mathbf{r}_3^o &= L(-\sqrt{6}\mathbf{i} - \sqrt{2}\mathbf{j} + 4\mathbf{k})/3 . \end{aligned} \tag{10}$$

For a given homogeneous deformation, the $\boldsymbol{\delta}_i$ are known. Letting

$$\boldsymbol{\delta}_i = \sum_{j=1}^{3} \delta_i^j \mathbf{g}_j , \tag{11}$$

and using the orthogonality of the $\mathbf{g}_i$, (7), (9), and (11) provide the nine relations,

$$(1+\epsilon_i) b_i^j - (1+\epsilon_4) b_4^j - a_i^j + a_4^j = \frac{1}{L} \delta_i^j . \tag{12}$$

A force balance at the joints requires

$$\sum_{i=1}^{4} \mathbf{F}_i = \mathbf{0}, \tag{13}$$

and with (1), (4), and (6) this provides the three relations

$$\sum_{i=1}^{4} \epsilon_i b_i^j = 0. \tag{14}$$

For given δ_i^j, the system of equations (5), (12), and (14) provide 16 scalar relations to determine the 12 b_i^j and four ϵ_i. With the $\mathbf{b}_i^j$ and ϵ_i determined, the forces $\mathbf{F}_i$ are known and the effective Piolá-Kirchhoff stress tensor can be calculated by considering the representative tetrahedral volume element shown in Fig. 2. The Piolá-Kirchhoff stress t_{ij} represents the current force per unit area of the undeformed structure. Thus, the volume element of Fig. 2 represents the undeformed structure. Cutting this volume element first on the plane $x=0$, then on the phase $y=0$, and finally on the plane $z=-L$, and considering the equilibrium of each section under the action of the induced Piolá-Kirchhoff stress as shown in Fig. 2, we obtain vector equations

$$\begin{aligned} 12\sqrt{2}L^2 (t_{xx}\mathbf{i} + t_{yx}\mathbf{j} + t_{zx}\mathbf{k}) &= \mathbf{F}_2 - \mathbf{F}_3 , \\ 12\sqrt{6}L^2 (t_{xy}\mathbf{i} + t_{yy}\mathbf{j} + t_{zy}\mathbf{k}) &= -3(\mathbf{F}_2 + \mathbf{F}_3) - 2\mathbf{F}_4 , \\ 6\sqrt{3}L^2 (t_{xz}\mathbf{i} + t_{yz}\mathbf{j} + t_{zz}\mathbf{k}) &= -\mathbf{F}_4 , \end{aligned} \tag{15}$$

which provide the nine components of the effective Piolá-Kirchhoff stress tensor. We note that, in general, this stress tensor is not symmetric. We now consider three specific homogeneous deformations.

Uniaxial Strain. We consider a homogeneous uniaxial deformation of the pin-jointed tetrahedral element. The strain magnitude $\epsilon_{z'z'} = \epsilon_o$ refers to the z'-direction of an (x', y', z') coordinate system which is rotated from (x, y, z) through the Euler angles θ, ϕ, φ (Warren and Kraynik, 1988). The affine displacement $\Delta\mathbf{R}$ of any position vector $\mathbf{R}$ satisfies

$$\Delta\mathbf{R} = \epsilon_o (\mathbf{R} \cdot \mathbf{g}_3') \mathbf{g}_3' , \tag{16}$$

where $\mathbf{g}_1'$, $\mathbf{g}_2'$, $\mathbf{g}_3'$ are unit vectors associated with coordinates x', y', z'. In particular, we have

$$\boldsymbol{\delta}_i = \epsilon_o (\mathbf{r}_i^o \cdot \mathbf{g}_3') \mathbf{g}_3' , \tag{17}$$

and the δ_i^j are given by

$$\begin{aligned} \delta_i^1 &= \epsilon_o L \sin\theta \sin\phi \, (\mathbf{r}_i^o \cdot \mathbf{g}_3')/3 , \\ \delta_i^2 &= -\epsilon_o L \sin\theta \cos\phi \, (\mathbf{r}_i^o \cdot \mathbf{g}_3')/3 , \\ \delta_i^3 &= \epsilon_o L \cos\theta \, (\mathbf{r}_i^o \cdot \mathbf{g}_3')/3 , \end{aligned} \tag{18}$$

where

$$\begin{aligned} (\mathbf{r}_1^o \cdot \mathbf{g}_3') &= 2(2\cos\theta - \sqrt{2}\sin\theta\cos\phi) , \\ (\mathbf{r}_2^o \cdot \mathbf{g}_3') + (\mathbf{r}_3^o \cdot \mathbf{g}_3') &= 2(4\cos\theta + \sqrt{2}\sin\theta\cos\phi) , \\ (\mathbf{r}_2^o \cdot \mathbf{g}_3') - (\mathbf{r}_3^o \cdot \mathbf{g}_3') &= 2\sqrt{6}\sin\theta\sin\phi. \end{aligned} \tag{19}$$

We expand the average strut-level strains ϵ_i and the direction cosines b_i^j in power series of ϵ_o of the form

$$\epsilon_i = Q_o \epsilon_o + Q_{i2}\epsilon_o^2 + Q_{i3}\epsilon_o^3, \quad b_i^j = a_i^j + B_{i1}^j \epsilon_o + B_{i2}^j \epsilon_o^2 + B_{i3}^j \epsilon_o^3, \tag{20}$$

where we have made use of known results for the linear (first-order) terms in ϵ_i (Warren and Kraynik, 1988) and the known undeformed geometry. Letting

$$\delta_i^j = \epsilon_o L \, \xi_i^j , \tag{21}$$

substituting these expressions into (5), (12), and (14), and collecting corresponding powers of ϵ_o provides the set of homogeneous relations

$$\begin{aligned} 0 &= \{Q_0(a_i^j - a_4^j) + B_{i1}^j - B_{41}^j - \xi_i^j\}\epsilon_0 \\ &\quad + \{Q_0(B_{i1}^j - B_{41}^j) + Q_{i2}a_i^j - Q_{42}a_4^j + B_{i2}^j - B_{42}^j\}\epsilon_0^2 \\ &\quad + \{Q_0(B_{i2}^j - B_{42}^j) + Q_{i2}B_{i1}^j - Q_{42}B_{41}^j \\ &\qquad + Q_{i3}a_i^j - Q_{43}a_4^j + B_{i3}^j - B_{43}^j\}\epsilon_0^3 , \\ 0 &= 2\{a_i^1 B_{i1}^1 + a_i^2 B_{i1}^2 + a_i^3 B_{i1}^3\}\epsilon_0 \\ &\quad + \{2a_i^1 B_{i2}^1 + 2a_i^2 B_{i2}^2 + 2a_i^3 B_{i2}^3 + (B_{i1}^1)^2 + (B_{i1}^2)^2 + (B_{i1}^3)^2\}\epsilon_0^2 \\ &\quad + 2\{a_i^1 B_{i3}^1 + a_i^2 B_{i3}^2 + a_i^3 B_{i3}^3 + B_{i1}^1 B_{i2}^1 + B_{i1}^2 B_{i2}^2 + B_{i1}^3 B_{i2}^3\}\epsilon_0^3 , \\ 0 &= \{Q_{12}a_1^j + Q_{22}a_2^j + Q_{32}a_3^j + Q_{42}a_4^j + Q_0(B_{11}^j + B_{21}^j + B_{31}^j + B_{41}^j)\}\epsilon_0^2 \\ &\quad + \{Q_{13}a_1^j + Q_{23}a_2^j + Q_{33}a_3^j + Q_{43}a_4^j + Q_0(B_{12}^j + B_{22}^j + B_{32}^j + B_{42}^j) \\ &\qquad + Q_{12}B_{11}^j + Q_{22}B_{21}^j + Q_{32}B_{31}^j + Q_{42}B_{41}^j\}\epsilon_0^3. \end{aligned} \tag{22}$$

Because (22) must hold for all ϵ_o, the individual coefficients of powers of ϵ_o must vanish. This provides a consistent set of linear equations for calculating the coefficients in (20) and determines the forces $\mathbf{F}_i$ to third order in strain. With the strut midpoint forces known for a given homogeneous deformation, the possibility of strut buckling in compression can be investigated to provide a bound on the validity of this analysis. The effective Piolá-Kirchhoff stress is evaluated from (15). These lengthy results will not be presented here, but we note that for this deformation, the forces do not depend on the Euler angle ψ. Also, the Piolá-Kirchhoff stress becomes unsymmetric in the third-order strain terms and depends on all three Euler angles.

At this point, we assume that the foam consists of arbitrarily-oriented tetrahedral elements with all orientations equally probable, as in Warren and Kraynik (1988). We defined the average stress tensor $\mathbf{T}$ as

$$\mathbf{T} = \frac{1}{8\pi^2} \int_0^{2\pi} \int_0^{\pi} \int_0^{2\pi} \mathbf{t}(\phi, \theta, \psi) \sin\theta \, d\phi \, d\theta \, d\psi. \tag{23}$$

Because all orientations are equally probable, the material response of the foam is obviously isotropic. Transforming the

Downloaded 03 May 2010 to 171.66.16.248. Redistribution subject to ASME license or copyright; see http://www.asme.org/terms/Terms_Use.cfm

components of the Piolá-Kirchhoff stress tensor from (x, y, z) to (x', y', z') and averaging over the Euler angles provides

$$T_{x'x'} = T_{y'y'} = \frac{1}{18\sqrt{3}LM}\left[\epsilon_0 - \frac{391}{9(35)}\epsilon_o^3\right],$$

$$T_{z'z'} = \frac{1}{18\sqrt{3}LM}\left[\epsilon_o + \frac{11}{5}\epsilon_o^2 - \frac{382}{9(35)}\epsilon_o^3\right],$$

$$T_{x'y'} = T_{y'x'} = T_{y'z'} = T_{z'y'} = T_{x'z'} = T_{z'x'} = 0 . \quad (24)$$

We will make use of this result later to obtain a strain energy function for the foam.

Biaxial Strain. We now consider biaxial deformations in the (x', y') plane with $\epsilon_{x'x'} = \epsilon_{y'y'} = \epsilon_t$. The affine displacement of any position vector $\mathbf{R}$ satisfies

$$\Delta\mathbf{R} = \epsilon_t[(\mathbf{R}\cdot\mathbf{g}_1')\mathbf{g}_1' + (\mathbf{R}\cdot\mathbf{g}_2')\mathbf{g}_2'] \quad (25)$$

and, in particular,

$$\delta_i = \epsilon_t[(\mathbf{r}_i^o\cdot\mathbf{g}_1')\mathbf{g}_1' + (\mathbf{r}_i^o\cdot\mathbf{g}_2')\mathbf{g}_2'] . \quad (26)$$

Expanding the ϵ_i and b_i^j as power series in ϵ_t of the form

$$\epsilon_i = \hat{Q}_o\epsilon_t + \hat{Q}_{i2}\epsilon_t^2 + \hat{Q}_{i3}\epsilon_t^3 , \quad b_i^j = a_i^j + \hat{B}_{i1}^j\epsilon_t + \hat{B}_{i2}^j\epsilon_t^2 + \hat{B}_{i3}^j\epsilon_t^3 , \quad (27)$$

and using (5), (12), and (14) provides a system of equations similar to (22) for the coefficients of ϵ_i and b_i^j in (27). Following the procedure described for uniaxial deformations, we obtain the components of the averaged Piolá-Kirchhoff stress tensor

$$T_{x'x'} = T_{y'y'} = \frac{1}{18\sqrt{3}LM}\left[2\epsilon_t + \frac{11}{5}\epsilon_t^2 - \frac{1517}{9(35)}\epsilon_t^3\right],$$

$$T_{z'z'} = \frac{1}{18\sqrt{3}LM}\left[2\epsilon_t - \frac{11}{5}\epsilon_t^2 + \frac{544}{9(35)}\epsilon_t^3\right],$$

$$T_{x'y'} = T_{y'x'} = T_{y'z'} = T_{z'y'} = T_{x'z'} = T_{z'x'} = 0 . \quad (28)$$

We now show that this result, together with (24), determines the effective strain energy function for this isotropic foam through terms of fourth order in the strain. We point out that these two results are not sufficient to determine the strut midpoint forces $\mathbf{F}_i$ for arbitrary homogeneous deformations.

Strain Energy Function

To obtain the strain energy function for the foam, we make use of the large deformation theory of elasticity as presented by Green and Zerna (1954) and Green and Adkins (1960). Consider homogeneous deformations of the form

$$X = \lambda_x x, \; Y = \lambda_y y, \; Z = \lambda_z z, \quad (29)$$

where the λ_i are principle stretches, (X, Y, Z) denotes the position of a particle after deformation that was initially located at (x, y, z), and

$$\lambda_x = 1 + \epsilon_{xx}, \; \lambda_y = 1 + \epsilon_{yy}, \; \lambda_z = 1 + \epsilon_{zz} , \quad (30)$$

where the ϵ_{ii} represent homogeneous strains associated with the principle stretches. The nonzero components of the symmetric Green strain tensor γ_{ij} are

$$\gamma_{xx} = \frac{1}{2}(\lambda_x^2 - 1) = \epsilon_{xx} + \frac{1}{2}\epsilon_{xx}^2 ,$$

$$\gamma_{yy} = \frac{1}{2}(\lambda_y^2 - 1) = \epsilon_{yy} + \frac{1}{2}\epsilon_{yy}^2 ,$$

$$\gamma_{zz} = \frac{1}{2}(\lambda_z^2 - 1) = \epsilon_{zz} + \frac{1}{2}\epsilon_{zz}^2 . \quad (31)$$

For a strain energy function $W(\gamma_{xx}, \gamma_{yy}, \gamma_{zz})$, the physical components of the Cauchy stress are given by

$$\sigma_{xx} = \frac{\lambda_x}{\lambda_y\lambda_z}\frac{\partial W}{\partial\gamma_{xx}}, \quad \sigma_{yy} = \frac{\lambda_y}{\lambda_x\lambda_z}\frac{\partial W}{\partial\gamma_{yy}}, \quad \sigma_{zz} = \frac{\lambda_z}{\lambda_x\lambda_y}\frac{\partial W}{\partial\gamma_{zz}}, \quad (32)$$

with the shear stresses vanishing. For an isotropic material, the strain energy function can be written in terms of three strain invariants as

$$W = W(J_1, J_2, J_3) , \quad (33)$$

where J_1, J_2, and J_3 are defined by Green and Adkins (1960). For the deformation field (29) these invariants are given by

$$J_1 = 2(\gamma_{xx} + \gamma_{yy} + \gamma_{zz}) ,$$

$$J_2 = 4(\gamma_{xx}\gamma_{yy} + \gamma_{yy}\gamma_{zz} + \gamma_{zz}\gamma_{xx}) ,$$

$$J_3 = 8\gamma_{xx}\gamma_{yy}\gamma_{zz} , \quad (34)$$

and can be written in the form

$$J_1 = 2(\epsilon_{xx} + \epsilon_{yy} + \epsilon_{zz}) + (\epsilon_{xx}^2 + \epsilon_{yy}^2 + \epsilon_{zz}^2)$$

$$J_2 = 4(\epsilon_{xx}\epsilon_{yy} + \epsilon_{yy}\epsilon_{zz} + \epsilon_{zz}\epsilon_{xx}) + 2[\epsilon_{xx}^2(\epsilon_{yy} + \epsilon_{zz}) + \epsilon_{yy}^2(\epsilon_{xx} + \epsilon_{zz}) + \epsilon_{zz}^2(\epsilon_{xx} + \epsilon_{yy})] + (\epsilon_{xx}^2\epsilon_{yy}^2 + \epsilon_{yy}^2\epsilon_{zz}^2 + \epsilon_{zz}^2\epsilon_{xx}^2)$$

$$J_3 = \epsilon_{xx}\epsilon_{yy}\epsilon_{zz}\{8 + 4(\epsilon_{xx} + \epsilon_{yy} + \epsilon_{zz}) + 2(\epsilon_{xx}\epsilon_{yy} + \epsilon_{yy}\epsilon_{zz} + \epsilon_{zz}\epsilon_{xx}) + \epsilon_{xx}\epsilon_{yy}\epsilon_{zz}\} . \quad (35)$$

We note that

$$J_1 = O(\epsilon) \; , \; J_2 = O(\epsilon^2) \; , \; J_3 = O(\epsilon^3) . \quad (36)$$

The physical components of the Cauchy stress may be written in terms of the invariants J_1, J_2, J_3 and the strains ϵ_{xx}, ϵ_{yy}, and ϵ_{zz} in the form

$$\sigma_{xx} = \frac{2(1+\epsilon_{xx})}{(1+\epsilon_{yy})(1+\epsilon_{zz})}\left\{\frac{\partial W}{\partial J_1} + 2\left[(\epsilon_{yy} + \epsilon_{zz}) + \frac{1}{2}(\epsilon_{yy}^2 + \epsilon_{zz}^2)\right]\frac{\partial W}{\partial J_2} + 4\epsilon_{yy}\epsilon_{zz}\left(1 + \frac{1}{2}\epsilon_{yy}\right)\left(1 + \frac{1}{2}\epsilon_{zz}\right)\frac{\partial W}{\partial J_3}\right\} , \quad (37)$$

and σ_{yy}, σ_{zz} are obtained through permutations of (x, y, z). The off-diagonal stress components are zero. Determining the dependence of stress on strain through third-order terms requires evaluating the strain energy function W through fourth-order terms in strain.

We now define the strain energy function W_s to represent the response of the pin-jointed tetrahedral element averaged over all orientations. The most general polynomial expansion of W_s in terms of the strain invariants (35) is of the form

$$2W_s(J_1, J_2, J_3) = \frac{1}{72\sqrt{3}LM}\{A_2J_1^2 + B_2J_2 + A_3J_1^3 + B_3J_1J_2 + C_3J_3 + A_4J_1^4 + B_4J_1^2J_2 + C_4J_2^2 + D_4J_1J_3\} , \quad (38)$$

where $A_2, B_2, A_3, \ldots$ are constant coefficients with subscripts denoting the lowest order terms in ϵ_{xx}, ϵ_{yy}, ϵ_{zz} in its multiplier. Using (37), the Cauchy stress can be evaluated from the strain energy function (38), and the Piolá-Kirchhoff stress for the deformation field (29) is given by

$$T_{xx} = (1+\epsilon_{yy})(1+\epsilon_{zz})\sigma_{xx} ,$$

$$T_{yy} = (1+\epsilon_{zz})(1+\epsilon_{xx})\sigma_{yy} ,$$

$$T_{zz} = (1+\epsilon_{xx})(1+\epsilon_{yy})\sigma_{zz} . \quad (39)$$

Our results in (24) and (28) for the average Piolá-Kirchoff stress under conditions of specific homogeneous deformations provide a redundant but consistent system of equations for evaluating the coefficients $A_2, B_2, A_3, \ldots$ of W_s.

For uniaxial strain with $\epsilon_{xx} = \epsilon_{yy} = 0$ and $\epsilon_{zz} = \epsilon_o$, the strain invariants become

$$J_1 = 2\epsilon_o + \epsilon_o^2 \; , \; J_2 = J_3 = 0. \quad (40)$$

Downloaded 03 May 2010 to 171.66.16.248. Redistribution subject to ASME license or copyright; see http://www.asme.org/terms/Terms_Use.cfm

Equations (37)-(39) provide the corresponding stress in the form

$$T_{xx}=T_{yy}=\frac{1}{18\sqrt{3}LM}\left\{\frac{1}{2}(2A_2+B_2)\epsilon_o+\frac{1}{4}(2A_2+B_2+12A_3+4B_3)\epsilon_o^2+(3A_3+B_3+8A_4+2B_4)\epsilon_o^3\right\},$$

$$T_{zz}=\frac{1}{18\sqrt{3}LM}\left\{A_2\epsilon_o+\frac{3}{2}(A_2+2A_3)\epsilon_o^2+\frac{1}{2}(A_2+12A_3+16A_4)\epsilon_o^3\right\}. \quad (41)$$

For biaxial strain with $\epsilon_{xx}=\epsilon_{yy}=\epsilon_t$, $\epsilon_{zz}=0$, the strain invariants become

$$J_1=4\epsilon_t+2\epsilon_t^2\ ,\ J_2=J_1^2/4\ ,\ J_3=0, \quad (42)$$

and the induced stresses are

$$T_{xx}=T_{yy}=\frac{1}{18\sqrt{3}LM}\left\{\frac{1}{2}(4A_2+B_2)\epsilon_t+\frac{1}{4}(12A_2+3B_2+48A_3+12B_3)\epsilon_t^2+\frac{1}{4}(4A_2+B_2+96A_3+24B_3+256A_4+64B_4+16C_4)\epsilon_t^3\right\}, \quad (43)$$

$$T_{zz}=\frac{1}{18\sqrt{3}LM}\left\{(2A_2+B_2)\epsilon_t+\frac{1}{2}(2A_2+B_2+24A_3+10B_3+2C_3)\epsilon_t^2+(12A_3+5B_3+C_3+64A_4+24B_4+8C_4+4D_4)\epsilon_t^3\right\}.$$

Equating the stress in (24) with (41) and the stress in (28) with (43) provides the coefficients

$$A_2=1\ ,\ B_2=0\ ,$$

$$A_3=\frac{7}{30}\ ,\ B_3=-\frac{6}{5}\ ,\ C_3=0,$$

$$A_4=-\frac{1961}{9(35)(16)}\ ,\ B_4=\frac{83}{2(35)}\ ,$$

$$C_4=\frac{3}{7}\ ,\ D_4=-\frac{18}{35}\ , \quad (44)$$

and determines W_s to fourth order in strain.

A simple verification of these results can be obtained by considering hydrostatic deformation where $\epsilon_{xx}=\epsilon_{yy}=\epsilon_{zz}=\epsilon_h$. Under these conditions, $b_i^j=a_i^j$; all struts retain their original orientation and deform by stretching only. The average strain in each strut is equal to ϵ_h and the Piolá-Kirchoff stress is given by

$$T_{xx}=T_{yy}=T_{zz}=\frac{\epsilon_h}{6\sqrt{3}LM}. \quad (45)$$

The strain invariants for this deformation field become

$$J_1=6\epsilon_h+3\epsilon_h^2\ ,\ J_2=\frac{1}{3}J_1^2\ ,\ J_3=\frac{1}{27}J_1^3\ , \quad (46)$$

and provide a stress of the form

$$T_{xx}=T_{yy}=T_{zz}=\frac{(1+\epsilon_h)}{72\sqrt{3}LM}\left\{\frac{2}{3}(3A_2+B_2)J_1+\frac{1}{9}(27A_3+9B_3+C_3)J_1^2+\frac{4}{27}(27A_4+9B_4+3C_4+D_4)J_1^3\right\}. \quad (47)$$

Substituting for the coefficients in this equation and retaining terms through third order in ϵ_h substantiates (45).

The strain energy W_s is based on a pin-jointed microstructural element and can only represent the stretching mechanism of strut distortion. We have assumed that the stretching mechanism—as captured by a pin-jointed microstructure—dominates the large deformation elastic response of an open-cell foam. But open-cell foams are not pin jointed, and a pin-jointed microstructure cannot represent essential features of the small deformation response for an open-cell foam. For example, open-cell foams have finite linear shear moduli, but the strain energy function W_s predicts a shear modulus of zero. A finite shear modulus is predicted when the tetrahedral element has elastic joints, and a bending mechanism for strut distortion dominates this response (Warren and Kraynik, 1988). The linear theory for open-cell foams on which the present nonlinear theory is based provides a contribution to the strain energy W_b from bending of the form

$$2W_b=\frac{(11N+4M)}{180\sqrt{3}LN(N+2M)}(J_1^2-3J_2)\ , \quad (48)$$

where N is a compliance for strut bending.

We represent the total strain energy function W_f for an open-cell foam by

$$W_f=W_s+W_b\ . \quad (49)$$

This assumption was adopted in a large deformation theory for honeycombs, where it is supported by finite element simulations for specific structures (Warren et al., 1989).

The total strain energy function of our model open-cell foam is given by

$$2W_f=\frac{1}{72\sqrt{3}LM}\left\{(1+\alpha)J_1^2-3\alpha J_2+\frac{7}{30}J_1^3-\frac{6}{5}J_1J_2-\frac{1961}{9(35)16}J_1^4+\frac{83}{2(35)}J_1^2J_2+\frac{3}{7}J_2^2-\frac{18}{35}J_1J_3\right\} \quad (50)$$

where

$$\alpha=\frac{2M(11N+4M)}{5N(N+2M)} \quad (51)$$

and represents a measure of the relative effects of stretching and bending. Equation (50) represents the principal result of this analysis.

An Open-Cell Foam in Uniaxial Stress

To illustrate our results, we consider the nonlinear elastic response of a low-density foam under conditions of uniaxial stress σ_{zz} with $\sigma_{xx}=\sigma_{yy}=0$. This homogeneous deformation is representative of conditions in a typical tension or compression test in regions of the specimen away from the load bearing ends where surface loading constraints are important. Material isotropy requires $\epsilon_{xx}=\epsilon_{yy}$. We write the transverse strains in the form

$$\epsilon_{xx}=\epsilon_{yy}=H_1\epsilon_{zz}+H_2\epsilon_{zz}^2+H_3\epsilon_{zz}^3\ , \quad (52)$$

and determine the coefficients H_i so that the transverse stresses vanish. This provides

Downloaded 03 May 2010 to 171.66.16.248. Redistribution subject to ASME license or copyright; see http://www.asme.org/terms/Terms_Use.cfm

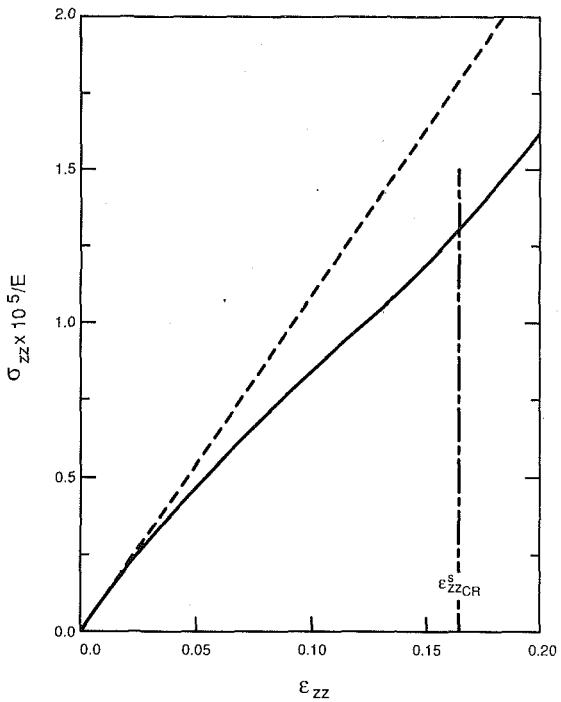

Fig. 3 A representative compression curve for an open-cell foam under conditions of uniaxial stress. The struts have uniform triangular cross-section and $\Phi = 0.01$. Linear elastic behavior and the critical strain for the onset of strut buckling are indicated.

$$H_1 = -\frac{(2-\alpha)}{(4+\alpha)},$$

$$H_2 = -\frac{6(44-17\alpha-10\alpha^2)}{5(4+\alpha)^3},$$

$$(H_3 + H_1 H_2) = -\frac{6}{5(4+\alpha)^5}\left\{\frac{96}{35}(168-460\alpha-157\alpha^2) - 16\alpha^3 + 5\alpha^4\right\}. \quad (53)$$

The last combination occurs in the expression for the stress components $\sigma_{xx} = \sigma_{yy}$ and σ_{zz}. The uniaxial stress σ_{zz} is evaluated from (37). For low-density open-cell foams the bending compliance N is much greater than M and the parameter $\alpha << 1$. Under these conditions, the axial stress is given by

$$\sigma_{zz} = \frac{1}{2\sqrt{3}L}\left\{\frac{11}{10N}\epsilon_{zz} + \frac{187}{50N}\epsilon_{zz}^2 + \frac{6}{175M}\epsilon_{zz}^3\right\}. \quad (54)$$

Note that bending determines the linear response through a coefficient of $O(N^{-1})$, and that stretching first appears at third order with a coefficient of $O(M^{-1})$. For a strut with triangular cross-section that is uniform along its length, the compliances are given by

$$\frac{1}{M} = 2\sqrt{3}EL\Phi, \quad \frac{1}{N} = 2\sqrt{3}EL\Phi^2, \quad (55)$$

where E is Young's modulus of the solid material and Φ is the solid volume fraction, which is small (Warren and Kraynik, 1988). Thus, the coefficients in (54) that stem from bending are $O(\Phi^2)$ and the coefficient that comes from stretching is $O(\Phi)$ and is much larger.

The analysis of uniaxial and biaxial strains provides expressions for the strut midpoint forces $\mathbf{F}_i$ for the deformation field in (52); thus, the onset of strut buckling in foam compression can be investigated. Consider an open-cell foam with uniform triangular struts and $\Phi = 0.01$. With no loss in generality, we consider $\mathbf{F}_4$. For struts of length $2L$ with hinged ends, the Euler critical load is $P_{cr} = \pi EI/4L^2$. Under conditions of uniaxial strain, the critical strain $\epsilon^E_{zz_{cr}}$ for the specific foam structure under consideration is

$$\epsilon^E_{zz_{cr}} = -2.47 \times 10^{-2}. \quad (56)$$

At this strain level, one can neglect the effect on $\mathbf{F}_4$ of higher-order terms that depend on specific strut orientation. Thus, the strut midpoint forces do not depend on orientation and a condition of general buckling of all struts prevails.

For conditions of uniaxial stress with the transverse strains of (52), the $\mathbf{F}_i$ are highly orientation dependent at the strain level necessary to induce buckling. For the specific foam under consideration, buckling initiates when

$$\epsilon^S_{zz_{cr}} = -0.164, \quad (57)$$

which is over six times the corresponding value for the uniaxial strain. At this strain level, which bounds the range of our constitutive theory, only those struts at one specific orientation have begun to buckle.

A representative compression curve for an open-cell foam with $\Phi = 0.01$ is shown in Fig. 3. The model exhibits strain softening well before the onset of strut buckling. This is consistent with experimental curves for elastomeric foams, as shown, for example, in Fig. 5.32 of Gibson and Ashby (1988). Because we assume that the strut material is linearly elastic, the nonlinear behavior can be attributed to geometrical effects associated with large distortions of the struts.

References

Gent, A. N., and Thomas, A. G., 1959, "The Deformation of Foamed Elastic Materials," *J. Appl. Polymer Sci.*, Vol. 1, pp. 107–113.

Gent, A. N., and Thomas, A. G., 1963, "Mechanics of Foamed Elastic Materials," *Rubber Chem. Tech.*, Vol. 36, pp. 597–610.

Gibson, L. J., and Ashby, M. F., 1982, "The Mechanics of Three-Dimensional Cellular Materials," *Proc. Royal Soc. London*, Vol. A382, pp. 43–59.

Gibson, L. J., and Ashby, M. F., 1988, *Cellular Solids*, Pergamon, Oxford, U.K.

Green, A. E., and Adkins, J. E., 1960, *Large Elastic Deformations*, Clarendon, Oxford, U.K.

Green, A. E., and Zerna, W., 1954, *Theoretical Elasticity*, Oxford, U.K.

Hilyard, N. C., ed., 1982, *Mechanics of Cellular Plastics*, Macmillan, New York.

Kanakkanatt, S. V., 1973, "Mechanical Anisotropy of Open-cell Foams," *J. Cellular Plastics*, Vol. 9, pp. 50–53.

Ko, W. L., 1965, "Deformations of Foamed Elastomers," *J. Cellular Plastics*, Vol. 1, pp. 45–50.

Lederman, J. M., 1971, "The Prediction of the Tensile Properties of Flexible Foams," *J. Appl. Polymer Sci.*, Vol. 15, pp. 693–703.

Meinecke, E. A., and Clark, R. C., 1973, *Mechanical Properties of Polymeric Foams*, Technomic, Westport, Conn.

Menges, G., and Knipschild, F., 1975, "Estimation of Mechanical Properties for Rigid Polyurethane Foams," *Polymer Eng. Sci.*, Vol. 15, pp. 623–627.

Menges, G., and Knipschild, F., 1982, "Stiffness and Strength-Rigid Plastic Foams," *Mechanics of Cellular Plastics*, N. C. Hilyard, ed., Macmillan, New York, pp. 27–72.

Warren, W. E., and Kraynik, A. M., 1987, "Foam Mechanics: The Linear Elastic Response of Two-Dimensional Spatially Periodic Cellular Materials," *Mechanics of Materials*, Vol. 6, pp. 27–37.

Warren, W. E., and Kraynik, A. M., 1988, "The Linear Elastic Properties of Open-Cell Foams," ASME JOURNAL OF APPLIED MECHANICS, Vol. 55, pp. 341–347.

Warren, W. E., Kraynik, A. M., and Stone, C. M., 1989, "A Constitutive Model for Two-Dimensional Nonlinear Elastic Foams," *J. Mech. Phys. Solids*, Vol. 37, pp. 717–733.

Downloaded 03 May 2010 to 171.66.16.248. Redistribution subject to ASME license or copyright; see http://www.asme.org/terms/Terms_Use.cfm

Hyung Jip Choi
Graduate Student.

S. Thangjitham
Assistant Professor.

Department of Engineering Science and Mechanics,
Virginia Polytechnic Institute and State University,
Blacksburg, VA 24061

Stress Analysis of Multilayered Anisotropic Elastic Media

The stress analysis of multilayered anisotropic media subjected to applied surface tractions is performed within the framework of linear plane elasticity. The solutions are obtained based on the Fourier transform technique together with the aid of the stiffness matrix approach. A general solution procedure is introduced such that it can be uniformly applied to media with transversely isotropic, orthotropic, and monoclinic layers. As an illustrative example, responses of the semi-infinite media composed of unidirectional and angle-ply layers to a given surface traction are presented.

1 Introduction

The increasing use of composite materials in many engineering applications in recent years has resulted in considerable research activities in the area of stress analysis of a layered medium. Because of the inherent heterogeneous and anisotropic nature of the composites, the analysis of such materials is much more involved than that of homogeneous, isotropic counterparts (Lekhnitskii, 1963). For multilayered composites, the problem becomes more complicated. In this case, solutions to the elasticity problem for all layers are required. These solutions are also to satisfy both the boundary and interface continuity conditions. Consequently, the conventional procedure for stress analysis of multilayered media results in having to solve a system of simultaneous equations for a large number of unknown constants. The complexity of such a procedure can be found in the work of Iyengar and Alwar (1964) as well as Chen (1971) who analyzed the semi-infinite medium composed of isotropic layers and of Pagano (1970) for a problem of anisotropic laminates in cylindrical bending. The stress analysis of an orthotropic semi-space was performed by Aköz and Tauchert (1973) with the use of displacement potentials.

As an alternative efficient approach to the analysis of multilayered media, various solution procedures have been developed. Among them is the transfer matrix approach by Bufler (1971) and independently by Bahar (1972, 1975). This approach is based on the mixed formulation of elasticity proposed by Vlasov and Leontev (1966). In terms of the vectors containing the state variables of the layer, the approach converts the boundary value problem to an equivalent initial value problem. The problem is solved by specifying the initial state vectors for layers with known boundary conditions. The state vector for any given layer is then related to the initial vectors via successive multiplication of the transfer matrices of the intermediate layers. This process amounts to applying the continuity conditions of the state variables at the layer interfaces. By applying the Cayley-Hamilton theorem, Bahar (1972, 1975) and Bufler (1971) derived, respectively, the exact transfer matrices for two and three-dimensional isotropic layers. The transfer matrix of Vlasov and Leontev is, on the other hand, expressed in terms of the infinite series expansion allowing solutions with various orders of approximation to be obtained.

The other forms of matrix approaches are the flexibility and the stiffness matrix methods. In these procedures, a local matrix equation is constructed in terms of the field variables at the upper and lower surfaces of each layer, and the global matrix equation is assembled through the applications of the layer interface continuity conditions. The unknown interfacial variables are then obtained by solving the global matrix equation which also satisfies the surface boundary conditions of the medium. This process results in a significant reduction in the number of simultaneous equations that must be solved when compared to the conventional formulation. On the basis of the stress formulation, Small and Booker (1984) employed the flexibility matrix method for the stress analysis of a layered elastic medium resting on a rigid foundation. Lin and Keer (1989) also utilized the flexibility matrix method in conjunction with the boundary integral formulation to analyze a vertical crack in a layered medium. Choi and Thangjitham (1991) used the stiffness matrix method to investigate, from the micro and macromechanical points of view, the local effects in the regions of high stress gradients. The materials considered in these papers were either isotropic or orthotropic.

In this paper, the stress analysis of multilayered anisotropic media is performed within the framework of linear plane elasticity. For the sake of completeness, media with transversely isotropic, orthotropic, and monoclinic layers are considered. The general solutions to the governing equations of a given layer are obtained by utilizing the Fourier transform technique. The stiffness matrix approach is then applied to obtain the solution of the medium which satisfies the layer interface conditions. As a numerical illustration, the responses of unidi-

Contributed by the Applied Mechanics Division of THE AMERICAN SOCIETY OF MECHANICAL ENGINEERS for presentation at the Joint Applied Mechanics/Bioengineering Conference, Ohio State University, Columbus, OH, June 16–19, 1991.

Discussion on this paper should be addressed to the Technical Editor, Leon M. Keer, The Technological Institute, Northwestern University, Evanston, IL 60208, and will be accepted until two months after final publication of the paper itself in the JOURNAL OF APPLIED MECHANICS. Manuscript received by the ASME Applied Mechanics Division, Aug. 4, 1989; final revision, June 22, 1990.

Paper No. 91-APM-21.

Copyright © 1991 by ASME
Downloaded 03 May 2010 to 171.66.16.248. Redistribution subject to ASME license or copyright; see http://www.asme.org/terms/Terms_Use.cfm

rectional and angle-ply multilayered semi-infinite media to a bell-shape normal surface traction are examined.

2 Methods of Analysis and Solutions

Consider a multilayered medium composed of N layers, each of which possesses its own fiber orientation in the x-y plane (Fig. 1). The fiber angle, θ, is measured from the x-axis in the counterclockwise direction. When the medium is subjected to arbitrary distributions of surface tractions, which do not vary along the y-axis, all the field variables are functions of x and z only. Due to the presence of the off-axis monoclinic layers, the generalized plane-strain state is assumed in distinction to the pure plane-strain state as discussed by Lekhnitski (1963) such that

$$u \equiv u(x,z), \quad v \equiv v(x,z), \quad w \equiv w(x,z) \qquad (1a,b,c)$$

where u, v, and w are the components of displacement in x, y, and z-directions, respectively. It is noted that, for the case of the on-axis transversely isotropic and orthotropic layers, the generalized plane strain and pure plane-strain states are equivalent.

2.1 Layers With Monoclinic Properties. For the case of off-axis monoclinic layers with the plane of elastic symmetry normal to the z-axis, the stress-displacement relations under the generalized plane-strain condition are written as (Lekhnitskii, 1963)

$$\sigma_{xx} = \tilde{C}_{11}\frac{\partial u}{\partial x} + \tilde{C}_{13}\frac{\partial w}{\partial z} + \tilde{C}_{16}\frac{\partial v}{\partial x} \qquad (2a)$$

$$\sigma_{yy} = \tilde{C}_{12}\frac{\partial u}{\partial x} + \tilde{C}_{23}\frac{\partial w}{\partial z} + \tilde{C}_{26}\frac{\partial v}{\partial x} \qquad (2b)$$

$$\sigma_{zz} = \tilde{C}_{13}\frac{\partial u}{\partial x} + \tilde{C}_{33}\frac{\partial w}{\partial z} + \tilde{C}_{36}\frac{\partial v}{\partial x} \qquad (2c)$$

$$\tau_{xy} = \tilde{C}_{16}\frac{\partial u}{\partial x} + \tilde{C}_{36}\frac{\partial w}{\partial z} + \tilde{C}_{66}\frac{\partial v}{\partial x} \qquad (2d)$$

$$\tau_{yz} = \tilde{C}_{44}\frac{\partial v}{\partial z} + \tilde{C}_{45}\left(\frac{\partial u}{\partial z} + \frac{\partial w}{\partial x}\right) \qquad (2e)$$

$$\tau_{xz} = \tilde{C}_{45}\frac{\partial v}{\partial z} + \tilde{C}_{55}\left(\frac{\partial u}{\partial z} + \frac{\partial w}{\partial x}\right) \qquad (2f)$$

where $\sigma_{ii}(x,z)$ and $\tau_{ij}(x,z)$, $ij = x,y,z$, are the normal stress in the i-direction and the shear stress in the i-j plane, respectively, and $\tilde{C}_{ij}$ are the layer elastic stiffness constants in the x-y-z coordinate system and are functions of the fiber angle, θ, and of the stiffness constants, C_{ij}, of the layer in the directions parallel and perpendicular to the fiber (Jones, 1975).

In the absence of body forces, the equations of equilibrium expressed in terms of the displacement components are written as

$$\tilde{C}_{11}\frac{\partial^2 u}{\partial x^2} + \tilde{C}_{55}\frac{\partial^2 u}{\partial z^2} + \tilde{C}_{16}\frac{\partial^2 v}{\partial x^2} + \tilde{C}_{45}\frac{\partial^2 v}{\partial z^2} + (\tilde{C}_{13} + \tilde{C}_{55})\frac{\partial^2 w}{\partial x \partial z} = 0 \qquad (3a)$$

$$\tilde{C}_{16}\frac{\partial^2 u}{\partial x^2} + \tilde{C}_{45}\frac{\partial^2 u}{\partial z^2} + \tilde{C}_{66}\frac{\partial^2 v}{\partial x^2} + \tilde{C}_{44}\frac{\partial^2 v}{\partial z^2} + (\tilde{C}_{36} + \tilde{C}_{45})\frac{\partial^2 w}{\partial x \partial z} = 0 \qquad (3b)$$

$$(\tilde{C}_{13} + \tilde{C}_{55})\frac{\partial^2 u}{\partial x \partial z} + (\tilde{C}_{36} + \tilde{C}_{45})\frac{\partial^2 v}{\partial x \partial z} + \tilde{C}_{55}\frac{\partial^2 w}{\partial x^2} + \tilde{C}_{33}\frac{\partial^2 w}{\partial z^2} = 0 \qquad (3c)$$

where equations (3a)–(3c) constitute a system of coupled partial differential equations.

To solve the system of governing partial differential equations (3a)–(3c), the Fourier transform (Sneddon, 1951) is applied over the variable x. The transform pairs for displacement components are defined as

$$\{\bar{u}(s,z), \bar{v}(s,z), \bar{w}(s,z)\} = \int_{-\infty}^{\infty} \{u(x,z), v(x,z), w(x,z)\} e^{isx} dx \qquad (4a)$$

$$\{u(x,z), v(x,z), w(x,z)\} = \frac{1}{2\pi}\int_{-\infty}^{\infty} \{\bar{u}(s,z), \bar{v}(s,z), \bar{w}(s,z)\} e^{-isx} ds \qquad (4b)$$

where $\bar{u}$, $\bar{v}$, and $\bar{w}$ are the Fourier transform of u, v, and w, respectively, s is the transform variable and $i = \sqrt{-1}$.

Under the conditions that the displacements and their first derivatives with respect to the variable x vanish as $x \to \pm\infty$, the governing equations in the transformed domain are reduced to a system of homogeneous ordinary differential equations which can be written in the form of the following matrix equation

$$M_1 \bar{\mathbf{r}}'' + M_2 \bar{\mathbf{r}}' + M_3 \bar{\mathbf{r}} = \mathbf{0} \qquad (5)$$

where primes denote the differentiation with respect to z, $\bar{\mathbf{r}}(s,z) = [\bar{u}\ \bar{v}\ \bar{w}]^T$, with T indicating the transpose of a row matrix, is the displacement vector of length three, and $M_j(s)$, $j = 1,2,3$ are the 3×3 symmetric matrices defined as

$$M_1 = \begin{bmatrix} \tilde{C}_{55} & \tilde{C}_{45} & 0 \\ \tilde{C}_{45} & \tilde{C}_{44} & 0 \\ 0 & 0 & \tilde{C}_{33} \end{bmatrix},$$

$$M_2 = \begin{bmatrix} 0 & 0 & -is(\tilde{C}_{13} + \tilde{C}_{55}) \\ 0 & 0 & -is(\tilde{C}_{36} + \tilde{C}_{45}) \\ -is(\tilde{C}_{13} + \tilde{C}_{55}) & -is(\tilde{C}_{36} + \tilde{C}_{45}) & 0 \end{bmatrix},$$

$$M_3 = \begin{bmatrix} -s^2\tilde{C}_{11} & -s^2\tilde{C}_{16} & 0 \\ -s^2\tilde{C}_{16} & -s^2\tilde{C}_{66} & 0 \\ 0 & 0 & -s^2\tilde{C}_{55} \end{bmatrix}. \qquad (6a,b,c)$$

Regarding the Fourier variable s as a parameter, the foregoing system of differential equations are solved for the displacements in the transformed domain as

$$\bar{u} = \sum_{j=1}^{3} (A_j \cosh s\lambda_j z + B_j \sinh s\lambda_j z) \qquad (7)$$

$$\bar{v} = \sum_{j=1}^{3} (A_j \cosh s\lambda_j z + B_j \sinh s\lambda_j z) L_j \qquad (8)$$

$$\bar{w} = \sum_{j=1}^{3} i(A_j \sinh s\lambda_j z + B_j \cosh s\lambda_j z) R_j \qquad (9)$$

where $A_j(s)$ and $B_j(s)$, $j = 1,2,3$, are the unknown constants to be evaluated from the boundary and interface conditions and λ_j, $j = 1,2,3$, are the roots of the characteristic equation

$$\det \Delta = 0 \qquad (10)$$

in which Δ is a 3×3 symmetric matrix whose elements, Δ_{ij}, $ij = 1,2,3$, are given as

$$\Delta_{11} = \tilde{C}_{55}\lambda_j^2 - \tilde{C}_{11},\ \Delta_{12} = \Delta_{21} = \tilde{C}_{45}\lambda_j^2 - \tilde{C}_{16},$$
$$\Delta_{13} = \Delta_{31} = -i(\tilde{C}_{13} + \tilde{C}_{55})\lambda_j\ \Delta_{22} = \tilde{C}_{44}\lambda_j^2 - \tilde{C}_{66},$$
$$\Delta_{23} = \Delta_{32} = -i(\tilde{C}_{36} + \tilde{C}_{45})\lambda_j,\ \Delta_{33} = \tilde{C}_{33}\lambda_j^2 - \tilde{C}_{55} \qquad (11)$$

Downloaded 03 May 2010 to 171.66.16.248. Redistribution subject to ASME license or copyright; see http://www.asme.org/terms/Terms_Use.cfm

and the constants L_j and R_j, $j=1,2,3$, for each root λ_j are defined as

$$L_j=\frac{\Delta_{12}\Delta_{13}-\Delta_{11}\Delta_{23}}{\Delta_{12}\Delta_{23}-\Delta_{22}\Delta_{13}},\quad R_j=\frac{i(\Delta_{12}^2-\Delta_{11}\Delta_{22})}{\Delta_{12}\Delta_{23}-\Delta_{22}\Delta_{13}}. \tag{12}$$

It is noted that the quadratic roots λ_j^2, $j=1,2,3$, of equation (10) are positive, real, and distinct (Pagano, 1970).

Taking the Fourier transform of equations (2*a*)-(2*f*) and using the expressions for the displacments, equations (7)-(9), the stresses in the transformed domain (the transform pairs for the stresses are defined in a similar fashion as those for the displacements, equations (4*a*)-(4*b*)) are obtained as

$$\bar{\sigma}_m=\sum_{j=1}^{3} is\,(\tilde{C}_{m3}\lambda_j R_j-\tilde{C}_{1m}-\tilde{C}_{m6}L_j)\,(A_j\cosh s\lambda_j z + B_j\sinh s\lambda_j z),\ m=1,2,3,6 \tag{13}$$

$$\bar{\sigma}_m=\sum_{j=1}^{3} s\,[\tilde{C}_{4m}\lambda_j L_j+\tilde{C}_{m5}(R_j+\lambda_j)]\,(A_j\sinh s\lambda_j z + B_j\cosh s\lambda_j z),\ m=4,5 \tag{14}$$

where $\bar{\sigma}_m(s,z)$, $m=1,2,\ldots,6$, are the contracted notation for $\bar{\sigma}_{xx}$, $\bar{\sigma}_{yy}$, $\bar{\sigma}_{zz}$, $\bar{\tau}_{yz}$, $\bar{\tau}_{xz}$, $\bar{\tau}_{xy}$, respectively.

2.2 Layers With Orthotropic Properties. For the on-axis orthotropic layers with fibers aligned in the x-direction ($\theta=0$ deg), there exist three mutually orthogonal planes of material symmetry. In this case, the elastic stiffness constants $\tilde{C}_{ij}=C_{ij}$ with $\tilde{C}_{m6}=0$, $m=1,2,3$, and $\tilde{C}_{45}=0$. As a result, the displacement v in the governing equations (3*a*)-(3*c*) is decoupled from the remaining components, u and w. Consequently, the expressions for the transformed displacements, equations (7)-(9), and stresses, equations (13)-(14), are no longer valid. By following the similar procedure, the expressions for the transformed displacements of the orthotropic layers become

$$\bar{u}=\sum_{j=1}^{2}(A_j\cosh s\lambda_j z + B_j\sinh s\lambda_j z) \tag{15}$$

$$\bar{w}=\sum_{j=1}^{2} i\,(A_j\sinh s\lambda_j z + B_j\cosh s\lambda_j z)R_j \tag{16}$$

$$\bar{v}=A_3\cosh s\lambda_0 z + B_3\sinh s\lambda_0 z \tag{17}$$

where $\lambda_0=\sqrt{\tilde{C}_{66}/\tilde{C}_{44}}$ and λ_j, $j=1,2$, are the roots of the characteristic equation

$$\tilde{C}_{33}\tilde{C}_{55}\lambda^4+[(\tilde{C}_{13}+\tilde{C}_{55})^2-\tilde{C}_{11}\tilde{C}_{33}-\tilde{C}_{55}^2]\lambda^2+\tilde{C}_{11}\tilde{C}_{55}=0 \tag{18}$$

and the constants R_j, $j=1,2$, are given as

$$R_j=\frac{\tilde{C}_{11}-\tilde{C}_{55}\lambda_j^2}{(\tilde{C}_{13}+\tilde{C}_{55})\lambda_j}. \tag{19}$$

As for the case of the off-axis monoclinic layers, the quadratic roots λ_j^2, $j=1,2$, of equation (18) are positive, real, and distinct.

The transformed stresses for this case are obtained as

$$\bar{\sigma}_m=\sum_{j=1}^{2} is\,(\tilde{C}_{m3}\lambda_j R_j-\tilde{C}_{1m})\,(A_j\cosh s\lambda_j z + B_j\sinh s\lambda_j z),\ m=1,2,3 \tag{20}$$

$$\bar{\tau}_{xz}=\sum_{j=1}^{2} s\tilde{C}_{55}(R_j+\lambda_j)\,(A_j\sinh s\lambda_j z + B_j\cosh s\lambda_j z) \tag{21}$$

$$\bar{\tau}_{yz}=s\lambda_0\tilde{C}_{44}(A_3\sinh s\lambda_0 z + B_3\cosh s\lambda_0 z) \tag{22}$$

$$\bar{\tau}_{xy}=-is\tilde{C}_{66}(A_3\cosh s\lambda_0 z + B_3\sinh s\lambda_0 z) \tag{23}$$

where $\bar{\sigma}_m$, $m=1,2,3$, refer to $\bar{\sigma}_{xx}$, $\bar{\sigma}_{yy}$, $\bar{\sigma}_{zz}$, respectively.

2.3 Layers With Transversely Isotropic Properties. Another case of interest arises when the material properties of the layers are transversely isotropic in the x-z plane. This condition occurs when the material properties in all directions perpendicular to the fibers are the same and the fibers are aligned in the y-direction ($\theta=90$ deg). In addition to $\tilde{C}_{m6}=0$, $m=1,2,3$, and $\tilde{C}_{45}=0$ as for the case of orthotropic layers, the elastic stiffness constants for the transversely isotropic layers are further simplified such that $\tilde{C}_{11}=\tilde{C}_{33}$, $\tilde{C}_{12}=\tilde{C}_{23}$, $\tilde{C}_{44}=\tilde{C}_{66}$, and $\tilde{C}_{55}=(\tilde{C}_{11}-\tilde{C}_{13})/2$. In this case, the quadratic roots of characteristic equation (18) are repeated and equal to unity. Consequently, the expressions for the transformed displacements of the transversely isotropic layers are obtained as

$$\bar{u}=(A_1+A_2z)\cosh sz+(B_1+B_2z)\sinh sz \tag{24}$$

$$\bar{w}=i\left[\left(B_1+B_2z+A_2\frac{R}{s}\right)\cosh sz+\left(A_1+A_2z+B_2\frac{R}{s}\right)\sinh sz\right] \tag{25}$$

$$\bar{v}=A_3\cosh sz+B_3\sinh sz \tag{26}$$

where the constant R is given as

$$R=-\frac{\tilde{C}_{13}+3\tilde{C}_{55}}{\tilde{C}_{13}+\tilde{C}_{55}}. \tag{27}$$

The corresponding transformed stresses are given as

$$\bar{\sigma}_{xx}=i[\tilde{C}_{13}(1+R)B_2-2s\tilde{C}_{55}(A_1+A_2z)]\cosh sz+i[\tilde{C}_{13}(1+R)A_2-2s\tilde{C}_{55}(B_1+B_2z)]\sinh sz \tag{28}$$

$$\bar{\sigma}_{zz}=i[\tilde{C}_{11}(1+R)B_2+2s\tilde{C}_{55}(A_1+A_2z)]\cosh sz+i[\tilde{C}_{11}(1+R)A_2+2s\tilde{C}_{55}(B_1+B_2z)]\sinh sz \tag{29}$$

$$\bar{\tau}_{xz}=\tilde{C}_{55}[(1+R)A_2+2s(B_1+B_2z)]\cosh sz+\tilde{C}_{55}[(1+R)B_2+2s(A_1+A_2z)]\sinh sz \tag{30}$$

$$\bar{\sigma}_{yy}=i\tilde{C}_{12}(1+R)\,(A_2\sinh sz+B_2\cosh sz) \tag{31}$$

$$\bar{\tau}_{xy}=-is\tilde{C}_{44}(A_3\cosh sz+B_3\sinh sz) \tag{32}$$

$$\bar{\tau}_{yz}=s\tilde{C}_{44}(A_3\sinh sz+B_3\cosh sz). \tag{33}$$

The solutions for displacements and stresses of all layers in the medium can now be obtained by solving a specific boundary value problem. For each layer, regardless of the type of layer considered, there are six unknown constants, A_j and B_j, $j=1,2,3$. Consequently, for an N-layer medium, there are a total of $6N$ unknown constants to be evaluated from a set of $6N$ appropriate boundary and interface conditions. This conventional procedure results in a system of $6N$ simultaneous equations.

2.4 Stiffness Matrix Formulation. To utilize the stiffness matrix formulation for a multilayered medium, the following vectors for a typical kth layer are defined as

$$\bar{\mathbf{d}}_k=[-i\ \bar{w}_k\ \bar{u}_k\ \bar{v}_k]^T,\ \bar{\boldsymbol{\sigma}}_k=[-i\bar{\sigma}_{zz}^k\ \bar{\tau}_{xz}^k\ \bar{\tau}_{yz}^k]^T \tag{34a,b}$$

$$\mathbf{a}_k=[A_1^k\ A_2^k\ A_3^k]^T,\ \mathbf{b}_k=[B_1^k\ B_2^k\ B_3^k]^T \tag{34c,d}$$

where $\bar{\mathbf{d}}_k(s,z)$ and $\bar{\boldsymbol{\sigma}}_k(s,z)$ are the vectors for the transformed displacements and tractions, respectively, and $\mathbf{a}_k(s)$ and $\mathbf{b}_k(s)$ are the vectors for the unknown constants.

In terms of $\mathbf{a}_k$ and $\mathbf{b}_k$, the vectors containing values of the transformed displacements $\bar{\mathbf{d}}_k^{\pm}(s)$ and tractions $\bar{\boldsymbol{\sigma}}_k^{\pm}(s)$ at the upper (+) and lower (−) surfaces of the kth layer are expressed as

$$\begin{Bmatrix}\bar{\mathbf{d}}_k^+\\ \hline \bar{\mathbf{d}}_k^-\end{Bmatrix}=\left[\begin{array}{c|c}F_{11}^k & F_{12}^k\\ \hline F_{21}^k & F_{22}^k\end{array}\right]\begin{Bmatrix}\mathbf{a}_k\\ \hline \mathbf{b}_k\end{Bmatrix} \tag{35}$$

Downloaded 03 May 2010 to 171.66.16.248. Redistribution subject to ASME license or copyright; see http://www.asme.org/terms/Terms_Use.cfm

$$\begin{Bmatrix} \bar{\sigma}_k^+ \\ \hline -\bar{\sigma}_k^- \end{Bmatrix} = \left[\begin{array}{c|c} G_{11}^k & G_{12}^k \\ \hline G_{21}^k & G_{22}^k \end{array}\right] \begin{Bmatrix} \mathbf{a}_k \\ \hline \mathbf{b}_k \end{Bmatrix} \tag{36}$$

where $F_{ij}^k(s)$ and $G_{ij}^k(s)$, $i,j=1,2$, are the 3×3 real submatrices.

Upon eliminating the unknown vectors, $\mathbf{a}_k$ and $\mathbf{b}_k$ from equations (35) and (36), the following relations for the surface tractions and displacements for the kth layer are obtained as

$$\begin{Bmatrix} \bar{\sigma}_k^+ \\ \hline -\bar{\sigma}_k^- \end{Bmatrix} = \left[\begin{array}{c|c} K_{11}^k & K_{12}^k \\ \hline K_{21}^k & K_{22}^k \end{array}\right] \begin{Bmatrix} \bar{\mathbf{d}}_k^+ \\ \hline \bar{\mathbf{d}}_k^- \end{Bmatrix} \tag{37}$$

in which $K_{ij}^k(s)$, $ij=1,2$, are the 3×3 real submatrices defined as

$$\left[\begin{array}{c|c} K_{11}^k & K_{12}^k \\ \hline K_{21}^k & K_{22}^k \end{array}\right] = \left[\begin{array}{c|c} G_{11}^k & G_{12}^k \\ \hline G_{21}^k & G_{22}^k \end{array}\right] \left[\begin{array}{c|c} F_{11}^k & F_{12}^k \\ \hline F_{21}^k & F_{22}^k \end{array}\right]^{-1} \tag{38}$$

where the left-hand side of the above equation is the 6×6 real and symmetric local stiffness matrix, K_k, for the kth layer. This matrix is fully populated for the monoclinic layers.

For an N-layer infinite strip subjected to tractions applied on the bounding surfaces, the boundary and interface continuity conditions between any two adjacent layers are imposed such that

$$\bar{\sigma}_1^+ = \bar{\mathbf{p}}^+ \tag{39a}$$

$$\bar{\sigma}_k^- = \bar{\sigma}_{k+1}^+,\ \bar{\mathbf{d}}_k^- = \bar{\mathbf{d}}_{k+1}^+,\ k=1,2,3,\ldots,N-1 \tag{39b,c}$$

$$\bar{\sigma}_N^- = \bar{\mathbf{p}}^- \tag{39d}$$

where $\bar{\mathbf{p}}^{\pm}(s)$ denote the Fourier transform of the applied tractions on the upper $(+)$ and lower $(-)$ bounding surfaces of the medium, respectively.

Defining $\bar{\delta}_1 = \bar{\mathbf{d}}_1^+$ and $\bar{\delta}_{N+1} = \bar{\mathbf{d}}_N^-$ the vectors containing the values of displacements of the upper and lower bounding surfaces of the medium, respectively, and $\bar{\delta}_{k+1} = \bar{\mathbf{d}}_k^- = \bar{\mathbf{d}}_{k+1}^+$, $k=1,2,3,\ldots,N-1$, the vectors containing values of the interfacial displacements common to the kth and $(k+1)$th layers, the following system of equations are obtained through the successive applications of the conditions given in equations (39a)-(39d).

$$K_{11}^1 \bar{\delta}_1 + K_{12}^1 \bar{\delta}_2 = \bar{\mathbf{p}}^+ \tag{40a}$$

$$K_{21}^k \bar{\delta}_k + (K_{22}^k + K_{11}^{k+1})\bar{\delta}_{k+1} + K_{12}^{k+1}\bar{\delta}_{k+2} = \mathbf{0},$$

$$k=1,2,3,\ldots,N-1 \tag{40b}$$

$$K_{21}^N \bar{\delta}_N + K_{22}^N \bar{\delta}_{N+1} = -\bar{\mathbf{p}}^-. \tag{40c}$$

The above system of algebraic equations can be written in matrix notation as

$$K\bar{\delta} = \bar{\mathbf{f}} \tag{41}$$

where $K(s)$ is the $3(N+1)\times 3(N+1)$ banded and symmetric global stiffness matrix, $\bar{\delta}(s)$ is the global vector for the unknown interfacial displacements in the transformed domain, i.e., $[\bar{\delta}_1\ \bar{\delta}_2 \ldots \bar{\delta}_{N+1}]^T$, and $\bar{\mathbf{f}}(s)$ is the vector containing the transformed surface tractions and zero elements. It is noted that the half-bandwidth of K is six. In contrast to the conventional procedure which yields a system of $6N$ simultaneous equations, there is 50 percent reduction in the number of equations in the current solution procedure.

For a semi-infinite layered medium with the Nth layer modeled as a half-space, the regularity conditions are imposed such that the transformed displacements satisfy the followings

$$\bar{u}_N(s,-\infty)=0,\ \bar{v}_N(s,-\infty)=0,\ \bar{w}_N(s,-\infty)=0. \tag{42a,b,c}$$

As a result, the local stiffness matrix equation for the half-space are obtained as

$$\bar{\sigma}_N^+ = K_{11}^N \bar{\mathbf{d}}_N^+ \tag{43}$$

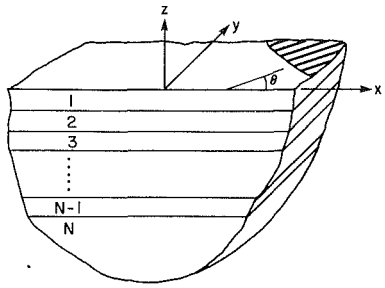

Fig. 1 Configuration of the *N*-layer semi-infinite medium

where $\bar{\mathbf{d}}_N^+$ and $\bar{\sigma}_N^+$ are vectors containing values of the transformed displacements and tractions at the bounding surface of the half-space and $K_{11}^N(s)$ is a 3×3 local stiffness matrix. In the same fashion, the global stiffness matrix equation for the N-layer semi-infinite medium can be assembled. The dimension of the global stiffness matrix, K, in this case is $3N\times 3N$.

The general solution procedure for stress analysis by the stiffness matrix method can be divided into three steps. First, as the main part of the procedure, the global interfacial displacement vector, $\bar{\delta}$, is obtained by solving the global stiffness matrix equation (41). In the second step, the vectors for the unknown constants of the kth layer, $\mathbf{a}_k$ and $\mathbf{b}_k$, are evaluated from equation (35) in terms of the corresponding local interfacial displacements, $\bar{\delta}_k$ and $\bar{\delta}_{k+1}$. As a final step, the inter and intralaminar displacements and stresses within any given layer are calculated by taking the inverse Fourier transform of the appropriate expressions.

3 Numerical Examples and Discussions

As a numerical example, the responses of a semi-infinite medium composed of unidirectional and angle-ply layers to applied surface tractions are investigated. To model the N-layer semi-infinite medium, the Nth layer is regarded as a half-space. The material properties of layers in the far field which constitute the half-space are, therefore, treated on the laminate rather than the lamina level. As a result, the elastic stiffness constants of the half-space, $\tilde{C}_{ij}^N$, are obtained as the homogenized weigthed properties of the N-1 overlying layers such that (Adams, 1989)

$$\tilde{C}_{ij}^N = \frac{\sum_{k=1}^{N-1} \tilde{C}_{ij}^k h_k}{\sum_{k=1}^{N-1} h_k} \tag{44}$$

where h_k is the thickness of the kth layer. For the laminates considered, the resulting weighted constants, $\tilde{C}_{ij}^N$, are orthotropic with respect to the x-y-z coordinates (Fig. 1).

In this study, the following engineering constants in the directions parallel (denoted by subscript 1), transverse (2), and normal (3) to the fibers for a typical graphite/epoxy layer (Tsai and Hahn, 1980) are used.

$$E_{11}=181\text{ GPa},\ E_{22}=E_{33}=10.3\text{ GPa}$$

$$G_{12}=G_{13}=7.17\text{ GPa},\ G_{23}=3.96\text{ GPa}$$

$$\nu_{12}=\nu_{13}=0.28,\ \nu_{23}=0.3$$

where E_{ii}, G_{ij}, and ν_{ij}, $i,j=1,2,3$, are the Young's moduli, shear moduli, and Poisson's ratios, respectively. The thickness of the layer, h, is 0.125 mm.

The corresponding layer elastic stiffness constants, C_{ij}, are obtained (Jones, 1975) as

$$C_{11}=183.3\text{ GPa},\ C_{22}=C_{33}=11.4\text{ GPa},\ C_{12}=C_{13}=4.18\text{ GPa}$$

$$C_{23}=3.49\text{ GPa},\ C_{44}=3.96\text{ GPa},\ C_{55}=C_{66}=7.17\text{ GPa}.$$

Downloaded 03 May 2010 to 171.66.16.248. Redistribution subject to ASME license or copyright; see http://www.asme.org/terms/Terms_Use.cfm

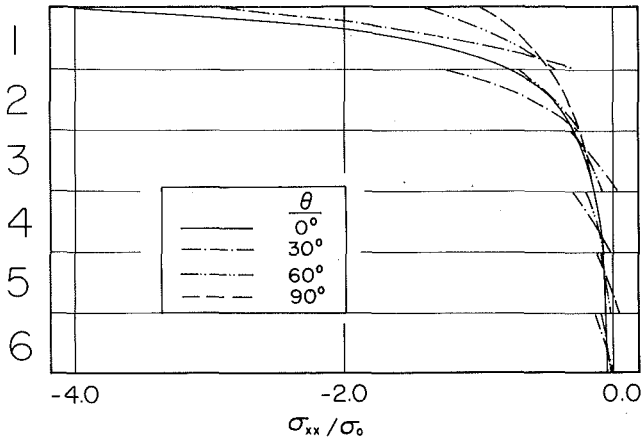

Fig. 2 Distribution of σ_{xx} at $x=0$ for $[\theta/-\theta]_{10}$ laminates on the elastic half-space

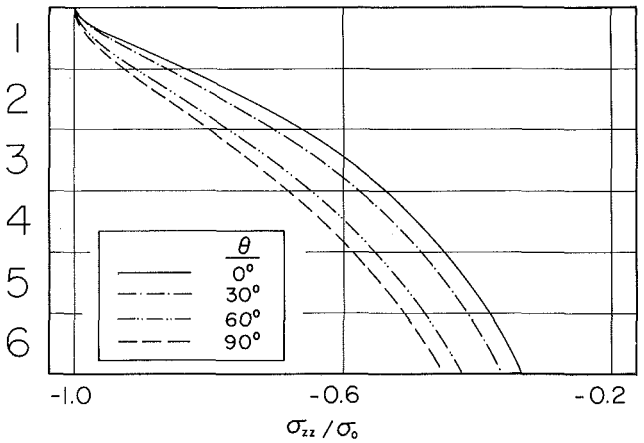

Fig. 3 Distribution of σ_{zz} at $x=0$ for $[\theta/-\theta]_{10}$ laminates on the elastic half-space

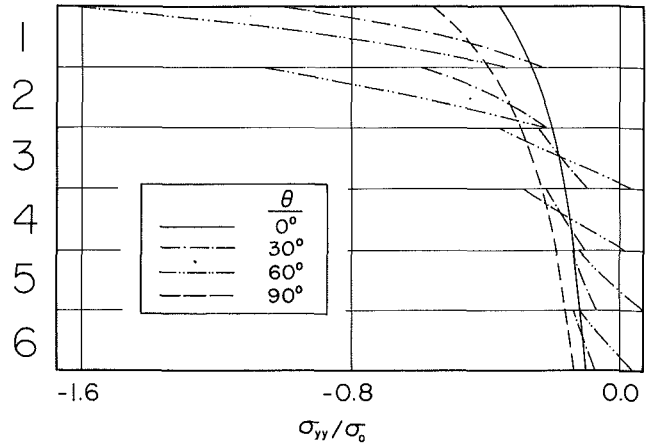

Fig. 4 Distribution of σ_{yy} at $x=0$ for $[\theta/-\theta]_{10}$ laminates on the elastic half-space

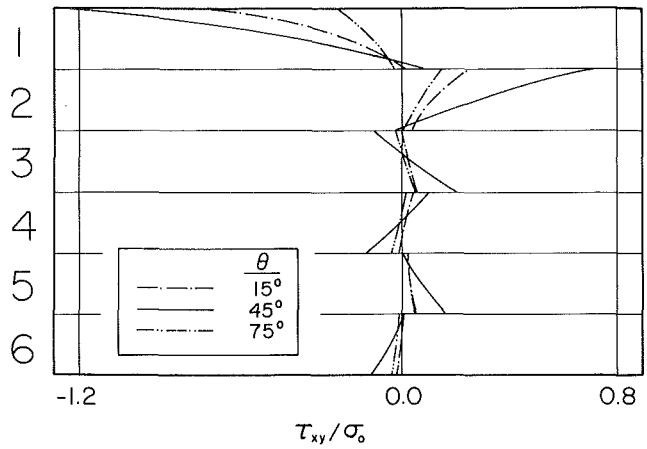

Fig. 5 Distribution of τ_{xy} at $x=0$ for $[\theta/-\theta]_{10}$ laminates on the elastic half-space

To provide the specific loadings, the following applied surface tractions are considered

$$(\sigma_{zz})_1^+ = -\sigma_0 \exp\left[-\frac{1}{2}\left(\frac{x}{c}\right)^2\right], \quad (\tau_{xz})_1^+ = (\tau_{yz})_1^+ = 0 \qquad (45)$$

where σ_0 and c are, respectively, the peak amplitude and shape parameter of the applied normal stress which resembles a bell shape centered at $x=0$. The shape parameter is taken as $c=2h$.

The numerical results are obtained for a 21-layer semi-infinite medium. To evaluate the inverse Fourier transform of the stress responses, the Gauss-Legendre quadrature scheme (David and Rabinowitz, 1984) is employed. Due to the rapid decaying of the induced stresses in the far field, only the responses for the first six layers are presented. The through-the-thickness variations of the normal stress components, σ_{xx}, σ_{zz}, and σ_{yy}, for $x=0$ are shown in Figs. 2–4, respectively, for both the unidirectional ($\theta=0$ deg, 90 deg) and angle-ply ($\theta=30$ deg, 60 deg) laminates.

In Fig. 2, the maximum values (compressive) of σ_{xx} which occur at the bounding surface ($z=0$) are observed to decrease with increasing fiber angle, θ. Due to the material property mismatch which results from the difference in fiber angles between the adjacent layers, the distributions of σ_{xx} across the layer interfaces for the angle-ply laminates are discontinuous. The discontinuities are more pronounced for $\theta=30$ deg than for $\theta=60$ deg. Figure 3 shows the values of σ_{zz} at the bounding surface are invariant with respect to the fiber orientation. Inside the medium, however, the magnitudes (compressive) of σ_{zz} increase with increasing fiber angle. The distributions of σ_{yy} in Fig. 4 are found to have the similar trend as those of σ_{xx} except that the stress discontinuities across the layer interfaces are more severe for $\theta=60$ deg rather than for $\theta=30$ deg.

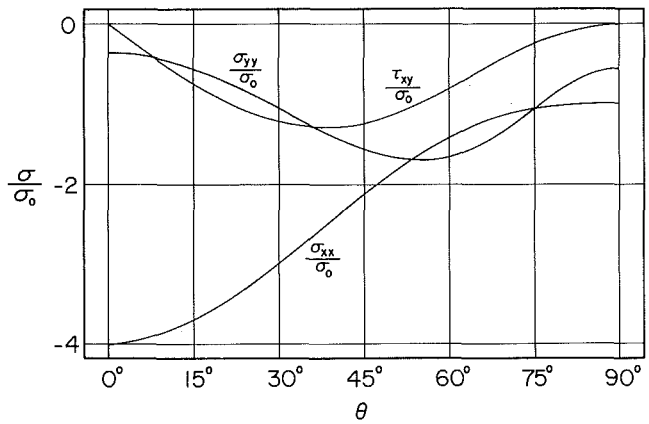

Fig. 6 Stress components versus θ at $x=z=0$ for $[\theta/-\theta]_{10}$ laminates on the elastic half-space

Because the distributions of τ_{xy} component are zero for unidirectional laminates, only those for the angle-ply laminates ($\theta=15$ deg, 45 deg, 75 deg) are shown in Fig. 5. Similarly, the distributions of τ_{xy} exhibit discontinuities at the layer interfaces. For the fiber angles considered, the laminate with $\theta=45$ deg is shown to experience the most severe shear stress, τ_{xy}.

Downloaded 03 May 2010 to 171.66.16.248. Redistribution subject to ASME license or copyright; see http://www.asme.org/terms/Terms_Use.cfm

The other shear stress components, τ_{xz} and τ_{yz}, are identically zero for $x=0$ regardless of the fiber orientations.

The effects of the fiber angles on the values of σ_{xx}, σ_{yy}, and τ_{xy} at $x=z=0$ are plotted in Fig. 6. The maximum and minimum values of σ_{xx} occur at $\theta=0$ deg and $\theta=90$ deg, respectively. The τ_{xy} component is found to have the extreme value at approximately $\theta=38$ deg, an angle which corresponds to the fiber orientation for the maximum shear coupling of the angle-ply laminates. On the other hand, the σ_{yy} component exhibits the extreme value at approximately $\theta=55$ deg.

4 Concluding Remarks

The stiffness matrix method for stress analysis of multilayered anisotropic media is presented. A general formulation is provided such that it can be uniformly applied to media with transversely isotropic, orthotropic, and monoclinic layers. In contrast to the conventional formulation, a significant reduction in the number of simultaneous equations that must be solved is achieved in the present solution procedure. Due to this fact, the matrix formulation is suitable for problems involving media with a large number of layers. Such problems are found, otherwise, becoming intractable in the conventional analysis. As a result, the aforementioned advantages of this formulation may be further extended to the more elaborate problems of stress analysis of laminated composites such as those subjected to the mixed boundary conditions in the presence of contact and cracks.

References

Adams, D. F., 1989, *Micromechanical Analysis of Composite Materials: Applications to Practical Problems* (Seminar Notes), Technomic Publishing Company, Lancaster, Penn.

Aköz, A. Y., and Tauchert, T. R., 1973, "Plane Deformation of an Orthotropic Elastic Semi-space Subjected to Distributed Surface Loads," ASME Journal of Applied Mechanics, Vol. 40, pp. 1135–1136.

Bahar, L. Y., 1972, "Transfer Matrix Approach to Layered Systems," *ASCE Journal of the Engineering Mechanics Division,* Vol. 98, No. EM5, pp. 1159–1172.

Bahar, L. Y., 1975, "A State Space Approach to Elasticity," *Journal of Franklin Institute,* Vol. 299, pp. 33–41.

Bufler, H., 1971, "Theory of Elasticity of a Multilayered Medium," *Journal of Elasticity,* Vol. 1, pp. 125–143.

Chen, W. T., 1971, "Computation of Stresses and Displacements in a Layered Elastic Medium," International Journal of Engineering Science, Vol. 9, pp. 775–800.

Choi, H. J., and Thangjitham, S., 1991, "Micro- and Macromechanical Stress and Failure Analyses of Laminated Composites," *Composites Science and Technology,* Vol. 14, pp. 289–305.

Davis, P. J., and Rabinowitz, P., 1984, *Methods of Numerical Integration,* 2nd ed., Academic Press, Orlando, Fla.

Iyengar, S. R., and Alwar, R. S., 1964, "Stresses in a Layered Half-Plane," *ASCE Journal of the Engineering Mechanics Division,* Vol. 90, No. EM4, pp. 79–96.

Jones, R. M., 1975, *Mechanics of Composite Materials,* Hemisphere Publishing Corporation, New York.

Lekhnitskii, S. G., 1963, *Theory of Elasticity of an Anisotropic Elastic Body,* Holden Day, San Francisco.

Lin, W., and Keer, L. M., 1989, "Analysis of a Vertical Crack in a Multilayered Medium," ASME Journal of Engineering for Industry, Vol. 56, pp. 63–69.

Pagano, N. J., 1970, "Influence of Shear Coupling in Cylindrical Bending of Anisotropic Laminates," *Journal of Composite Materials,* Vol. 4, pp. 330–343.

Small, J. C., and Booker, J. R., 1984, "Finite Layer Analysis of Layered Elastic Materials Using a Flexibility Approach. Part 1-Strip Loadings," *International Journal for Numerical Methods in Engineering,* Vol. 20, pp. 1025–1037.

Sneddon, I. N., 1951, *Fourier Transforms,* McGraw-Hill, New York.

Tsai, S. W., and Hahn, H. T., 1980, *Introduction to Composite Materials,* Technomic Press, Lancaster, Penn.

Vlasov, V. Z., and Leontev, N. N., 1966, *Beams, Plates and Shells on Elastic Foundations,* National Aeronautics and Space Administration TTF-357, TT65-50135.

Downloaded 03 May 2010 to 171.66.16.248. Redistribution subject to ASME license or copyright; see http://www.asme.org/terms/Terms_Use.cfm

Elastic Moduli of Thickly Coated Particle and Fiber-Reinforced Composites

Y. P. Qiu[1]
Graduate Student.

G. J. Weng
Professor,
Mem. ASME

Department of Mechanics and
Materials Science,
Rutgers University,
New Brunswick, NJ 08903

Based on the models of Hashin (1962) and Hashin and Rosen (1964), the effective elastic moduli of thickly coated particle and fiber-reinforced composites are derived. The microgeometry of the composite is that of a progressively filled composite sphere or cylinder element model. The exact solutions of the effective bulk modulus κ of the particle-reinforced composite and those of the plain-strain bulk modulus κ_{23}, axial shear modulus μ_{12}, longitudinal Young's modulus E_{11}, major Poisson ratio ν_{12}, of the fiber-reinforced one are derived by the replacement method. The bounds for the effective shear modulus μ and the effective transverse shear modulus μ_{23} of these two kinds of composite, respectively, are solved with the aid of Christensen and Lo's (1979) formulations. By considering the six possible geometrical arrangements of the three constituent phases, the values of κ, and of κ_{23}, μ_{12}, E_{11}, and ν_{12} are found to always lie within the Hashin-Shtrikman (1963) bounds, and the Hashin (1965), Hill (1964), and Walpole (1969) bounds, respectively, but unlike the two-phase composites, none coincides with their bounds. The bounds of μ and μ_{23} derived here are consistently tighter than their bounds but, as for the two-phase composites, one of the bounds sometimes may fall slightly below or above theirs and therefore it is suggested that these two sets of bounds be used in combination, always choosing the higher for the lower bound and the lower for the upper one.

1 Introduction

Motivated by the recent development in coated-fiber technology, this paper is concerned with the determination of the effective elastic moduli of thickly coated particle and fiber-reinforced composites. Following Hashin (1962) and Hashin and Rosen (1964), the composite element is made up of a three-phase spherically or cylindrically concentric solid, with the inner, intermediate, and outer regions representing the particle or fiber, coating, and matrix in turn. Its size may vary from finite to infinitesimal magnitude so that the composite body can be filled up progressively until no matrix is left between composite elements. The composite as a whole is taken to be macroscopically isotropic in the particle-reinforced case, and transversely isotropic in the fiber-reinforced one. Similar three-phase models have also been considered by Lee and Westmann (1970), and Hashin and Rosen (1964), respectively, in the context of hollow spheres and hollow fibers. Although the methods used here are not new, the results derived are believed to be of some practical usefulness. Other related studies on the coated composites include Walpole (1978), Mikata and Taya (1985a, b; 1986), Sideridis (1988), Pagano and Tandon (1988), and Benveniste et al. (1989), but none addresses this problem.

While the constituents of the particle-reinforced composite will be assumed to be elastically isotropic, those of the fiber-reinforced composite—due to the possible fiber anisotropy—will be treated as transversely isotropic. We shall, throughout the paper, refer to the inclusion (particle or fiber), coating, and matrix as phase 1, 2, and 3, respectively, with the volume fraction of the rth phase denoted by c_r. Referring to the outer radius of the rth phase as a_r, we have the volume fractions:

$$c_1 = (a_1/a_3)^3,\ c_2 = (a_2^3 - a_1^3)/a_3^3,$$

for particle-reinforced composite,

$$c_1 = (a_1/a_3)^2,\ c_2 = (a_2^2 - a_1^2)/a_3^2,$$

for fiber-reinforced composite,

and $c_3 = 1 - (c_1 + c_2)$ for the matrix in both cases.

2 Thickly Coated Particle-Reinforced Composites

The isotropic bulk and shear moduli of the rth phase will be denoted by κ_r and μ_r, and those of the composite by κ and μ, respectively. We shall first consider κ and then μ.

[1]Now at Sonoco Products Co., University of Wisconsin, Research Park, Madison, WI 53711.

Contributed by the Applied Mechanics Division of THE AMERICAN SOCIETY OF MECHANICAL ENGINEERS for publication in the JOURNAL OF APPLIED MECHANICS.

Discussion on this paper should be addressed to the Technical Editor, Prof. Leon M. Keer, The Technological Institute, Northwestern University, Evanston, IL 60208, and will be accepted until two months after final publication of the paper itself in the JOURNAL OF APPLIED MECHANICS. Manuscript received by the ASME Applied Mechanics Division, Aug. 24, 1989; final revision, Mar. 14, 1990.

Copyright © 1991 by ASME
Downloaded 03 May 2010 to 171.66.16.248. Redistribution subject to ASME license or copyright; see http://www.asme.org/terms/Terms_Use.cfm

2.1 Exact Solution of the Effective Bulk Modulus κ. Let us first recall Hashin's (1962) exact solution for a two-phase particle-reinforced composite, given by

$$\kappa = \kappa_m + \frac{c_p}{\dfrac{1}{\kappa_p - \kappa_m} + \dfrac{3c_m}{3\kappa_m + 4\mu_m}}, \tag{1}$$

where the subscripts p and m refer to the particle and matrix, respectively. Since it depends only on κ_p (and not on μ_p) of the particle, we may use the replacement method (see Hill, 1964; Hashin, 1972) and consider the real particle-coating system as the particle here. Replacing κ_p by the effective, exact solution of the particle-coating composite, given similarly by

$$\kappa_p = \kappa_2 + \frac{\dfrac{c_1}{c_1 + c_2}}{\dfrac{1}{\kappa_1 - \kappa_2} + \dfrac{c_2}{c_1 + c_2}\dfrac{3}{3\kappa_2 + 4\mu_2}}, \tag{2}$$

and identifying the matrix in equation (1) as phase 3 and $c_p = c_1 + c_2$, we find the exact solution for the three-phase coated system

$$\begin{aligned}\kappa = \kappa_3 + (3\kappa_3 + 4\mu_3)[&c_1(3\kappa_2 + 4\mu_2)(\kappa_1 - \kappa_3) \\ &+ c_2(3\kappa_1 + 4\mu_2)(\kappa_2 - \kappa_3)]/\{(3\kappa_1 + 4\mu_2)[(3\kappa_2 + 4\mu_3) + 3(c_1 + c_2) \\ &\times(\kappa_3 - \kappa_2)] + 3c_1(\kappa_2 - \kappa_1)[4(\mu_3 - \mu_2)/(c_1 + c_2) + (3\kappa_3 + 4\mu_2)]\}.\end{aligned} \tag{3}$$

2.2 Bounds for the Effective Shear Modulus μ. The shear problem is more complicated, but can be made tractable by using Christensen and Lo's (1979) formulation. For the upper bound we prescribe a boundary displacement giving rise to a uniform deviatoric strain

$$\bar{u}_i = \bar{\epsilon}_{ij} x_j, \text{ with } \bar{\epsilon}_{11} = \bar{e}, \qquad \bar{\epsilon}_{22} = -\bar{e}. \tag{4}$$

In the usual spherical coordinate system with θ measured from the x_3-axis and ϕ measured from the x_1 to the x_2-axis, the solutions of the displacement field can be cast into

$$\begin{aligned} u_r &= U_r(r)\sin^2\theta\cos 2\phi, \\ u_\theta &= U_\theta(r)\sin\theta\cos\theta\cos 2\phi, \\ u_\phi &= -U_\theta(r)\sin\theta\sin 2\phi, \end{aligned} \tag{5}$$

where, in the inclusion

$$U_r = C_1 r - C_2 \frac{6\nu_1}{1 - 2\nu_1}\frac{r^3}{a_1^2}, \qquad U_\theta = C_1 r - C_2 \frac{7 - 4\nu_1}{1 - 2\nu_1}\frac{r^3}{a_1^2}; \tag{6}$$

in the coating

$$U_r = C_3 r - C_4 \frac{6\nu_2}{1 - 2\nu_2}\frac{r^3}{a_2^2} + 3C_5\frac{a_2^5}{r^4} + C_6\frac{5 - 4\nu_2}{1 - 2\nu_2}\frac{a_2^3}{r^2}, \qquad U_\theta = C_3 r - C_4 \frac{7 - 4\nu_2}{1 - 2\nu_2}\frac{r^3}{a_2^2} - 2C_5\frac{a_2^5}{r^4} + 2C_6\frac{a_2^3}{r^2}; \tag{7}$$

and in the matrix

$$U_r = C_7 r - C_8 \frac{6\nu_3}{1 - 2\nu_3}\frac{r^3}{a_2^2} + 3C_9\frac{a_2^5}{r^4} + C_{10}\frac{5 - 4\nu_3}{1 - 2\nu_3}\frac{a_2^3}{r^2}, \qquad U_\theta = C_7 r - C_8 \frac{7 - 4\nu_3}{1 - 2\nu_3}\frac{r^3}{a_2^2} - 2C_9\frac{a_2^5}{r^4} + 2C_{10}\frac{a_2^3}{r^2}, \tag{8}$$

where ν_r is the Poisson ratio of the rth phase. The ten constants $C_1, C_2, \ldots, C_{10}$ are determined from the conditions of displacement (u_r and u_θ) and traction (T_r and T_θ) continuity at $r = a_1$ and a_2, and the displacement boundary condition at $r = a_3$. The results can be written as

$$C_i = b_i^{(\epsilon)}\bar{e}, \qquad i = 1, 2, \ldots, 10, \tag{9}$$

where, in matrix form,

$$[b^{(\epsilon)}]_{10\times 1} = [E^{(\epsilon)}]^{-1}_{10\times 10}[F]_{10\times 1} \tag{10}$$

and $[E^{(\epsilon)}]^{-1}$ is the inverse of $[E^{(\epsilon)}]$, whose components are given in the Appendix. The matrix $[F]$, in its transpose form, has the simple values

$$[F]^T_{10\times 1} = [0, 0, 0, 0, 0, 0, 0, 0, 1, 1]. \tag{11}$$

Although the local strain field in all three phases are triaxial, the volume average of the strain components in the rectangular coordinates—as proved by Luo and Weng (1987)—are purely deviatoric, with an identical structure as in (4). It turns out that only the first two constants in the displacement field will affect such an average. Recognizing that the average shear strain in the rth phase is now represented by $(\bar{\epsilon}_{11}^{(r)} - \bar{\epsilon}_{22}^{(r)})/2$, we find—after some lengthy volume integrations—that the average shear strain concentration factors are:

$$\begin{aligned}\text{For inclusion:}\quad & b_1^{(\epsilon)} - \frac{21}{5(1 - 2\nu_1)}b_2^{(\epsilon)}, \\ \text{coating:}\quad & b_3^{(\epsilon)} - \frac{21}{5(1 - 2\nu_2)}\cdot\frac{(c_1 + c_2)^{5/3} - c_1^{5/3}}{c_2(c_1 + c_2)^{2/3}}b_4^{(\epsilon)}.\end{aligned} \tag{12}$$

The upper bound of μ then follows from the principle of minimum potential energy, as

$$\begin{aligned}\mu \le \mu_3 &+ c_1(\mu_1 - \mu_3)\left[b_1^{(\epsilon)} - \frac{21}{5(1 - 2\nu_1)}b_2^{(\epsilon)}\right] \\ &+ c_2(\mu_2 - \mu_3)\left[b_3^{(\epsilon)} - \frac{21}{5(1 - 2\nu_2)}\cdot\frac{(c_1 + c_2)^{5/3} - c_1^{5/3}}{c_2(c_1 + c_2)^{2/3}}b_4^{(\epsilon)}\right].\end{aligned} \tag{13}$$

To find the lower bound we apply a traction boundary condition which corresponds to the deviatoric stress state

$$T_i = \bar{\sigma}_{ij}n_j, \text{ with } \bar{\sigma}_{11} = \bar{\tau}, \ \bar{\sigma}_{22} = -\bar{\tau}, \text{ others} = 0. \tag{14}$$

The ensuing displacement field under this condition has exactly identical structure as in (5) to (8), but the ten constants $C_1, C_2, \ldots, C_{10}$ now must be determined to satisfy these two traction requirements instead of the two displacement ones. The results can be written as

$$C_i = b_i^{(\sigma)}\frac{\bar{\tau}}{2\mu_3}, \qquad i = 1, 2, \ldots, 10 \tag{15}$$

in parallel to (9), with

$$[b^{(\sigma)}]_{10\times 1} = [E^{(\sigma)}]^{-1}_{10\times 10}[F]_{10\times 1}. \tag{16}$$

Because the first eight continuity conditions at the interfaces $r = a_1$ and a_2 are identical, the components of $[E^{(\sigma)}]$ differ from those of $[E^{(\epsilon)}]$ only in the last two rows, and in fact, only the last three terms in each row. These six components are also given in the Appendix.

Downloaded 03 May 2010 to 171.66.16.248. Redistribution subject to ASME license or copyright; see http://www.asme.org/terms/Terms_Use.cfm

As in the case of average strain, the average stress in the inclusion and the coating are also deviatoric, with the structure of (14). The average deviatoric stress concentration factors are:

$$\text{For inclusion:}\quad \left(b_1^{(\sigma)}-\frac{21}{5(1-2\nu_1)}\,b_2^{(\sigma)}\right)\frac{\mu_1}{\mu_3},$$

$$\text{coating:}\quad \left[b_3^{(\sigma)}-\frac{21}{5(1-2\nu_2)}\cdot\frac{(c_1+c_2)^{5/3}-c_1^{5/3}}{c_2(c_1+c_2)^{2/3}}\,b_4^{(\sigma)}\right]\frac{\mu_2}{\mu_3}\,. \tag{17}$$

Then by way of the principle of minimum complementary energy, we arrive at the lower bound of μ

$$\frac{1}{\mu}\le\frac{1}{\mu_3}+c_1\left(\frac{1}{\mu_1}-\frac{1}{\mu_3}\right)\left[b_1^{(\sigma)}-\frac{21}{5(1-2\nu_1)}\,b_2^{(\sigma)}\right]\frac{\mu_1}{\mu_3}+c_2\left(\frac{1}{\mu_2}-\frac{1}{\mu_3}\right)\times\left[b_3^{(\sigma)}-\frac{21}{5(1-2\nu_2)}\cdot\frac{(c_1+c_2)^{5/3}-c_1^{5/3}}{c_2(c_1+c_2)^{2/3}}\,b_4^{(\sigma)}\right]\frac{\mu_2}{\mu_3}\,. \tag{18}$$

The upper and lower bounds of μ generally do not coincide but, as will be shown later, they are usually tight.

3 Thickly Coated Fiber-Reinforced Composites

Due to the possible transverse isotropy of fibers our consideration will allow each constituent to be transversely isotropic. Special cases involving isotropic constituents can be deduced readily. Taking direction 1 as the symmetrical axis (also the fiber axis) and 2-3 plane as the transverse isotropic plane, we denote the five engineering constants of the rth phase as

$$E_{11}^{(r)},\ \nu_{12}^{(r)},\ \kappa_{23}^{(r)},\ \mu_{12}^{(r)}\ \text{and}\ \mu_{23}^{(r)}, \tag{19}$$

representing the longitudinal Young's modulus, major Poisson's ratio, plane-strain bulk modulus, axial shear modulus, and transverse shear modulus, in turn. The composite as a whole is also transversely isotropic; its five elastic moduli will also be denoted by the same notations, but without the superscript.

We shall first derive the exact solutions of κ_{23}, μ_{12}, E_{11} and ν_{12} by the replacement method, and then find the bounds of μ_{23} by the energy approach.

3.1 Exact Solution of the Plane-Strain Bulk Modulus κ_{23}. For this we recall from Hashin (1979) the exact solution of κ_{23} for a two-phase fiber-reinforced composite

$$\kappa_{23}=\kappa_{23}^m+\frac{c_f}{\dfrac{1}{\kappa_{23}^f-\kappa_{23}^m}+\dfrac{c_m}{\kappa_{23}^m+\mu_{23}^m}}\,, \tag{20}$$

where the superscripts f and m refer to the fiber and matrix, respectively. Since it depends only on κ_{23}^f (and not on μ_{23}^f) of the fiber, we may replace κ_{23}^f by the exact solution of the fiber-coating system, given similarly by

$$\kappa_{23}^f=\kappa_{23}^{(2)}+\frac{\dfrac{c_1}{c_1+c_2}}{\dfrac{1}{\kappa_{23}^{(1)}-\kappa_{23}^{(2)}}+\dfrac{c_2}{c_1+c_2}\dfrac{1}{\kappa_{23}^{(2)}+\mu_{23}^{(2)}}}\,. \tag{21}$$

Substituting it into (20) and identifying the matrix as phase 3 there, we have the exact solution

$$\kappa_{23}=\kappa_{23}^{(3)}+(\kappa_{23}^{(3)}+\mu_{23}^{(3)})[c_1(\kappa_{23}^{(2)}+\mu_{23}^{(2)})(\kappa_{23}^{(1)}-\kappa_{23}^{(3)})+c_2(\kappa_{23}^{(1)}+\mu_{23}^{(2)})(\kappa_{23}^{(2)}-\kappa_{23}^{(3)})/\{(\kappa_{23}^{(1)}+\mu_{23}^{(2)})[(\kappa_{23}^{(2)}+\mu_{23}^{(3)})+(c_1+c_2)(\kappa_{23}^{(3)}-\kappa_{23}^{(2)})]+c_1(\kappa_{23}^{(2)}-\kappa_{23}^{(1)})[(\mu_{23}^{(3)}-\mu_{23}^{(2)})/(c_1+c_2)+(\kappa_{23}^{(3)}+\mu_{23}^{(2)})]\}. \tag{22}$$

3.2 Exact Solution of the Axial Shear Modulus μ_{12}. Also from Hashin (1979), the exact solution for the two-phase system is given by

$$\mu_{12}=\mu_{12}^m+\frac{c_f}{\dfrac{1}{\mu_{12}^f-\mu_{12}^m}+\dfrac{c_m}{2\mu_{12}^m}}\,, \tag{23}$$

where μ_{12}^f of the fiber can be replaced by the exact solution of the true fiber-coating system, similarly given by

$$\mu_{12}^f=\mu_{12}^{(2)}+\frac{\dfrac{c_1}{c_1+c_2}}{\dfrac{1}{\mu_{12}^{(1)}-\mu_{12}^{(2)}}+\dfrac{c_2}{c_1+c_2}\dfrac{1}{2\mu_{12}^{(2)}}}\,. \tag{24}$$

Substituting (24) into (23), and identifying the matrix as phase 3, one arrives at

$$\mu_{12}=\mu_{12}^{(3)}+2\mu_{12}^{(3)}[2c_1\mu_{12}^{(2)}(\mu_{12}^{(1)}-\mu_{12}^{(3)})+c_2(\mu_{12}^{(1)}+\mu_{12}^{(2)})(\mu_{12}^{(2)}-\mu_{12}^{(3)})]/\{(\mu_{12}^{(1)}+\mu_{12}^{(2)})[(\mu_{12}^{(2)}+\mu_{12}^{(3)})+(c_1+c_2)(\mu_{12}^{(3)}-\mu_{12}^{(2)})]+c_1(\mu_{12}^{(2)}-\mu_{12}^{(1)})[(\mu_{12}^{(3)}-\mu_{12}^{(2)})/(c_1+c_2)+(\mu_{12}^{(3)}+\mu_{12}^{(2)})]\}. \tag{25}$$

3.3 Exact Solutions of the Longitudinal Young's Modulus E_{11} and Major Poisson's Ratio ν_{12}. Again from Hashin (1979) for a two-phase system, we have the exact solutions

$$E_{11}=c_fE_{11}^f+c_mE_{11}^m+\frac{4c_fc_m(\nu_{12}^f-\nu_{12}^m)^2}{\dfrac{c_f}{\kappa_{23}^m}+\dfrac{c_m}{\kappa_{23}^f}+\dfrac{1}{\mu_{23}^m}}\,, \tag{26}$$

$$\nu_{12}=c_f\nu_{12}^f+c_m\nu_{12}^m+\frac{c_fc_m(\nu_{12}^f-\nu_{12}^m)\left(\dfrac{1}{\kappa_{23}^m}-\dfrac{1}{\kappa_{23}^f}\right)}{\dfrac{c_f}{\kappa_{23}^m}+\dfrac{c_m}{\kappa_{23}^f}+\dfrac{1}{\mu_{23}^m}}\,, \tag{27}$$

where E_{11}^f and ν_{12}^f of the real fiber-coating system are similarly given by

$$E_{11}^f=\frac{c_1}{c_1+c_2}E_{11}^{(1)}+\frac{c_2}{c_1+c_2}E_{11}^{(2)}+\frac{\dfrac{4c_1c_2}{(c_1+c_2)^2}(\nu_{12}^{(1)}-\nu_{12}^{(2)})^2}{\dfrac{c_1}{c_1+c_2}\dfrac{1}{\kappa_{23}^{(2)}}+\dfrac{c_2}{c_1+c_2}\dfrac{1}{\kappa_{23}^{(1)}}+\dfrac{1}{\mu_{23}^{(2)}}}\,, \tag{28}$$

$$\nu_{12}^f=\frac{c_1}{c_1+c_2}\nu_{12}^{(1)}+\frac{c_2}{c_1+c_2}\nu_{12}^{(2)}+\frac{\dfrac{c_1c_2}{(c_1+c_2)^2}(\nu_{12}^{(1)}-\nu_{12}^{(2)})\left(\dfrac{1}{\kappa_{23}^{(2)}}-\dfrac{1}{\kappa_{23}^{(1)}}\right)}{\dfrac{c_1}{c_1+c_2}\dfrac{1}{\kappa_{23}^{(2)}}+\dfrac{c_2}{c_1+c_2}\dfrac{1}{\kappa_{23}^{(1)}}+\dfrac{1}{\mu_{23}^{(2)}}}\,, \tag{29}$$

Downloaded 03 May 2010 to 171.66.16.248. Redistribution subject to ASME license or copyright; see http://www.asme.org/terms/Terms_Use.cfm

and κ_{23}^f is already given by (21). Substituting these into (26) and (27) and identifying the matrix there as phase 3, we can write the exact solutions as

$$E_{11}=c_1E_{11}^{(1)}+c_2E_{11}^{(2)}+c_3E_{11}^{(3)}+P/R\ , \tag{30}$$

$$\nu_{12}=c_1\nu_{12}^{(1)}+c_2\nu_{12}^{(2)}+c_3\nu_{12}^{(3)}+Q/R\ , \tag{31}$$

where

$$P=4c_1c_2(\nu_{12}^{(1)}-\nu_{12}^{(2)})^2\left[\left(\frac{1}{\mu_{12}^{(3)}}-\frac{1}{\mu_{12}^{(2)}}\right)+(c_1+c_2)\left(\frac{1}{\kappa_{23}^{(3)}}+\frac{1}{\mu_{23}^{(2)}}\right)\right]$$

$$+4c_1c_3(c_1+c_2)(\nu_{12}^{(1)}-\nu_{12}^{(3)})^2\left(\frac{1}{\kappa_{23}^{(2)}}+\frac{1}{\mu_{23}^{(2)}}\right)$$

$$+4c_2c_3(c_1+c_2)(\nu_{12}^{(2)}-\nu_{12}^{(3)})^2\left(\frac{1}{\kappa_{23}^{(1)}}+\frac{1}{\mu_{23}^{(2)}}\right),$$

$$Q=c_1c_2(\nu_{12}^{(1)}-\nu_{12}^{(2)})\left(\frac{1}{\kappa_{23}^{(2)}}-\frac{1}{\kappa_{23}^{(1)}}\right)\left(\frac{1}{\mu_{23}^{(3)}}+\frac{c_1+c_2}{\kappa_{23}^{(3)}}\right)$$

$$+c_1c_3(\nu_{12}^{(1)}-\nu_{12}^{(3)})\left[\frac{c_1+c_2}{\kappa_{23}^{(3)}}\left(\frac{1}{\kappa_{23}^{(2)}}+\frac{1}{\mu_{23}^{(2)}}\right)-\left(\frac{c_1}{\kappa_{23}^{(1)}\mu_{23}^{(2)}}+\frac{c_2}{\kappa_{23}^{(2)}\mu_{23}^{(2)}}+\frac{c_1+c_2}{\kappa_{23}^{(1)}\kappa_{23}^{(2)}}\right)\right]$$

$$+c_2c_3(\nu_{12}^{(2)}-\nu_{23}^{(3)})\left[\frac{c_1+c_2}{\kappa_{23}^{(3)}}\left(\frac{1}{\kappa_{23}^{(1)}}+\frac{1}{\mu_{23}^{(2)}}\right)-\left(\frac{c_1}{\kappa_{23}^{(1)}\mu_{23}^{(2)}}+\frac{c_2}{\kappa_{23}^{(2)}\mu_{23}^{(2)}}+\frac{c_1+c_2}{\kappa_{23}^{(1)}\kappa_{23}^{(2)}}\right)\right].$$

$$R=\left(\frac{1}{\mu_{23}^{(3)}}+\frac{c_1+c_2}{\kappa_{23}^{(3)}}\right)\left(\frac{c_1+c_2}{\mu_{23}^{(2)}}+\frac{c_1}{\kappa_{23}^{(2)}}+\frac{c_2}{\kappa_{23}^{(1)}}\right),$$

$$+c_3\left(\frac{c_1+c_2}{\kappa_{23}^{(1)}\kappa_{23}^{(2)}}+\frac{c_1}{\kappa_{23}^{(1)}\mu_{23}^{(2)}}+\frac{c_2}{\kappa_{23}^{(2)}\mu_{23}^{(2)}}\right). \tag{32}$$

Our numerical calculations show that the contribution by the last term in (30) and (31) is very small and therefore the "rule of mixture" represented by the first three terms is a suitable approximation for these two moduli.

3.4 Bounds for the Transverse Shear Modulus μ_{23}. As of μ in the preceding section, we shall also follow Christensen and Lo's (1979) formulation for determination of μ_{23}.

For the upper bound we prescribe the displacement at $r=a_3$ so that

$$\bar{\epsilon}_{22}=\bar{e},\quad \bar{\epsilon}_{33}=-\bar{e},\ \text{others}=0. \tag{33}$$

In the usual cylindrical coordinate system with θ measured from the x_2 towards the x_3-axis and z-axis coinciding with the x_1-axis, the displacement fields can be written as

$$u_r=U_r(r)\cos 2\theta\ ,$$
$$u_\theta=U_\theta(r)\sin 2\theta\ , \tag{34}$$

where in the fiber

$$U_r=C_1r+C_2(\eta_1-3)\frac{r^3}{a_1^2}\ ,$$
$$U_\theta=-C_1r+C_2(\eta_1+3)\frac{r^3}{a_1^2}\ ; \tag{35}$$

in the coating

$$U_r=C_3r+C_4(\eta_2-3)\frac{r^3}{a_2^2}+C_5\frac{a_2^4}{r^3}+C_6(\eta_2+1)\frac{a_2^2}{r}\ ,$$

$$U_\theta=-C_3r+C_4(\eta_2+3)\frac{r^3}{a_2^2}+C_5\frac{a_2^4}{r^3}-C_6(\eta_2-1)\frac{a_2^2}{r}\ ; \tag{36}$$

and in the matrix

$$U_r=C_7r+C_8(\eta_3-3)\frac{r^3}{a_2^2}+C_9\frac{a_2^4}{r^3}+C_{10}(\eta_3+1)\frac{a_2^2}{r}\ ,$$

$$U_\theta=-C_7r+C_8(\eta_3+3)\frac{r^3}{a_2^2}+C_9\frac{a_2^4}{r^3}-C_{10}(\eta_3-1)\frac{a_2^2}{r}\ , \tag{37}$$

with

$$\eta_r=1+2\mu_{23}^{(r)}/\kappa_{23}^{(r)}\ \text{for the } r\text{th phase.} \tag{38}$$

The ten constants $C_1, C_2, \ldots, C_{10}$ are determined from the continuity conditions of u_r, u_θ, σ_{rr}, $\sigma_{\theta\theta}$ at $r=a_1$ and a_2, and the boundary conditions (33). The results can be written as

$$C_i=d_i^{(\epsilon)}\bar{e},\qquad i=1, 2, \ldots, 10 \tag{39}$$

where, in the matrix form,

$$[d^{(\epsilon)}]_{10\times 1}=[G^{(\epsilon)}]^{-1}_{10\times 10}[H]_{10\times 1}. \tag{40}$$

The components of $[G^{(\epsilon)}]$ are also listed in the Appendix, and the matrix $[H]$, in its transpose, is given by

$$[H]^T_{10\times 1}=[0, 0, 0, 0, 0, 0, 0, 0, 1, 1]. \tag{41}$$

The average strains in all three phases under such a condition have been studied previously by Luo and Weng (1989), who found that, in Cartesian coordinates, they are also purely deviatoric as in (33). The average deviatoric strain $(\bar{\epsilon}_{22}^{(r)}-\bar{\epsilon}_{33}^{(r)})/2$ in the rth phase depends only on the first two constants, with the following average deviatoric strain concentration factors:

$$\text{For fiber:}\quad d_1^{(\epsilon)}-3d_2^{(\epsilon)}\ ,$$
$$\text{coating:}\quad d_3^{(\epsilon)}-3\frac{(c_1+c_2)^2-c_1^2}{c_2(c_1+c_2)}d_4^{(\epsilon)}\ . \tag{42}$$

Then, following the principle of minimum potential energy, the upper bound of μ_{23} is given by

$$\mu_{23}\le\mu_{23}^{(3)}+c_1(\mu_{23}^{(1)}-\mu_{23}^{(3)})(d_1^{(\epsilon)}-3d_2^{(\epsilon)})+c_2(\mu_{23}^{(2)}-\mu_{23}^{(3)})\left[d_3^{(\epsilon)}-3\frac{(c_1+c_2)^2-c_1^2}{c_2(c_1+c_2)}d_4^{(\epsilon)}\right]. \tag{43}$$

For the lower bound we prescribe a surface traction giving rise to a uniform deviatoric stress

$$\bar{\sigma}_{22}=\bar{\tau},\qquad \bar{\sigma}_{33}=-\bar{\tau},\qquad \text{others}=0. \tag{44}$$

The corresponding displacement fields are again given by (34) to (37), with the first eight boundary conditions at $r=a_1$ and a_2 remaining unchanged. The last two at $r=a_3$ now have to meet the prescribed condition (44). The results can be cast into

$$C_i=d_i^{(\sigma)}\frac{\bar{\tau}}{2\mu_{23}^{(3)}}\ ,\ i=1, 2, \ldots, 10 \tag{45}$$

where

$$[d_i^{(\sigma)}]_{10\times 1}=[G^{(\sigma)}]^{-1}_{10\times 10}[H]_{10\times 1}\ . \tag{46}$$

As in the case of $[E^{(\sigma)}]$ versus $[E^{(\epsilon)}]$ for a coated particle, the components of $[G^{(\sigma)}]$ differ from those of $[G^{(\epsilon)}]$ only in the last two rows and only for the last three terms in each row. These components are also listed in the Appendix.

Downloaded 03 May 2010 to 171.66.16.248. Redistribution subject to ASME license or copyright; see http://www.asme.org/terms/Terms_Use.cfm

Table 1 Effective bulk modulus κ for six geometrical arrangements of a thickly coated particle-reinforced composite, and comparison with the Hashin-Shtrikman (1963) bounds

Constituents: $E_a=25$ GPa, $E_b=5$ GPa, $E_c=1$ GPa, and $\nu=0.3$ for all phases

$E_1/E_2/E_3$ (Inclusion/coating/matrix)	$c_a/c_b/c_c=0.7/0.2/0.1$ H-S$^{(+)}=12.24$ GPa H-S$^{(-)}=6.16$ GPa κ, GPa	$c_a/c_b/c_c=0.1/0.2/0.7$ H-S$^{(+)}=2.33$ GPa H-S$^{(-)}=1.25$ GPa κ, GPa
25/5/1	6.47	1.26
25/1/5	6.23	1.38
1/5/25	11.95	2.12
1/25/5	11.01	2.25
5/25/1	7.00	1.28
5/1/25	11.59	1.95

Table 2 Effective plane strain bulk modulus κ_{23} for six geometrical arrangements of a thickly coated fiber-reinforced composite, and comparison with the Hashin (1965) bounds

Constituents: $E_a=25$ GPa, $E_b=5$ GPa, $E_c=1$ GPa, and $\nu=0.3$ for all phases

$E_1/E_2/E_3$ (Fiber/coating/matrix)	$c_a/c_b/c_c=0.7/0.2/0.1$ H$^{(+)}=13.05$ GPa H$^{(-)}=6.68$ GPa κ_{23}, GPa	$c_a/c_b/c_c=0.1/0.2/0.7$ H$^{(+)}=2.43$ GPa H$^{(-)}=1.39928$ GPa κ_{23}, GPa
25/5/1	6.91	1.39936
25/1/5	6.72	1.52
1/5/25	12.56	2.17
1/25/5	11.89	2.31
5/25/1	7.42	1.42
5/1/25	12.11	2.02

Table 3 Effective axial shear modulus μ_{12} for six geometrical arrangements of a thickly coated fiber-reinforced composite, and comparison with the Hashin (1965) bounds

Constituents: $E_a=25$ GPa, $E_b=5$ GPa, $E_c=1$ GPa, and $\nu=0.3$ for all phases

$E_1/E_2/E_3$ (Fiber/coating/matrix)	$c_a/c_b/c_c=0.7/0.2/0.1$ H$^{(+)}=6.07$ GPa H$^{(-)}=3.10$ GPa μ_{12}, GPa	$c_a/c_b/c_c=0.1/0.2/0.7$ H$^{(+)}=1.19$ GPa H$^{(-)}=0.61$ GPa μ_{12}, GPa
25/5/1	3.33	0.62
25/1/5	3.17	0.68
1/5/25	5.99	1.11
1/25/5	5.44	1.17
5/25/1	3.62	0.63
5/1/25	5.85	1.02

The average stress in the constituents are also purely deviatoric, with a structure similar to (44). The average deviatoric stress concentration factors are found to be:

$$\text{For fiber:}\quad (d_1^{(\sigma)}-3d_2^{(\sigma)})\mu_{23}^{(1)}/\mu_{23}^{(3)}\,,$$

$$\text{coating:}\quad \left[d_3^{(\sigma)}-3\,\frac{(c_1+c_2)^2-c_1^2}{c_2(c_1+c_2)}\,d_4^{(\sigma)}\right]\mu_{23}^{(2)}/\mu_{(23)}^{(3)}. \tag{47}$$

The lower bound follows from the principle of minimum complementary energy, as

$$\frac{1}{\mu_{23}}\le\frac{1}{\mu_{23}^{(3)}}+c_1\left(\frac{1}{\mu_{23}^{(1)}}-\frac{1}{\mu_{23}^{(3)}}\right)(d_1^{(\sigma)}-3d_2^{(\sigma)})\,\frac{\mu_{23}^{(1)}}{\mu_{23}^{(3)}}$$
$$+c_2\left(\frac{1}{\mu_{23}^{(2)}}-\frac{1}{\mu_{23}^{(3)}}\right)\left[d_3^{(\sigma)}-3\,\frac{(c_1+c_2)^2-c_1^2}{c_1(c_1+c_2)}\,d_4^{(\sigma)}\right]\frac{\mu_{23}^{(2)}}{\mu_{23}^{(3)}}. \tag{48}$$

These bounds generally do not coincide, but, as will be shown later, are reasonably tight.

The foregoing results are written explicitly in terms of the five engineering constants in (19) of the constituents. The results involving the isotropic phases can be readily deduced by setting, say for the rth phase, $E_{11}^{(r)}=E^{(r)}$, $\nu_{12}^{(r)}=\nu^{(r)}$, $\kappa_{23}^{(r)}=\bar{\kappa}^{(r)}$, and $\mu_{12}^{(r)}=\mu_{23}^{(r)}=\mu^{(r)}$, where $\bar{\kappa}^{(r)}$ is the plane-strain bulk modulus of the rth phase.

4 Comparison With the Bounds of Hashin-Shtrikman, Hashin, Hill, and Walpole

Of considerable theoretical importance is where these exact solutions and bounds stand in light of the bounds of Hashin-Shtrikman (1963), Hashin (1965), and Hill (1964) as extended by Walpole (1969), for a three-phase solid of arbitrary microgeometry. To illustrate their relative positions let us consider the particle-reinforced case first. For simplicity, we choose three constituent materials with the Young's moduli 25 GPa, 5 GPa, and 1 GPa, sharing the same Poisson ratio 0.3, and call them materials **a**, **b**, and **c** (not 1, 2 and 3 which are the reserved notations for the inclusion, coating, and matrix, re-

Downloaded 03 May 2010 to 171.66.16.248. Redistribution subject to ASME license or copyright; see http://www.asme.org/terms/Terms_Use.cfm

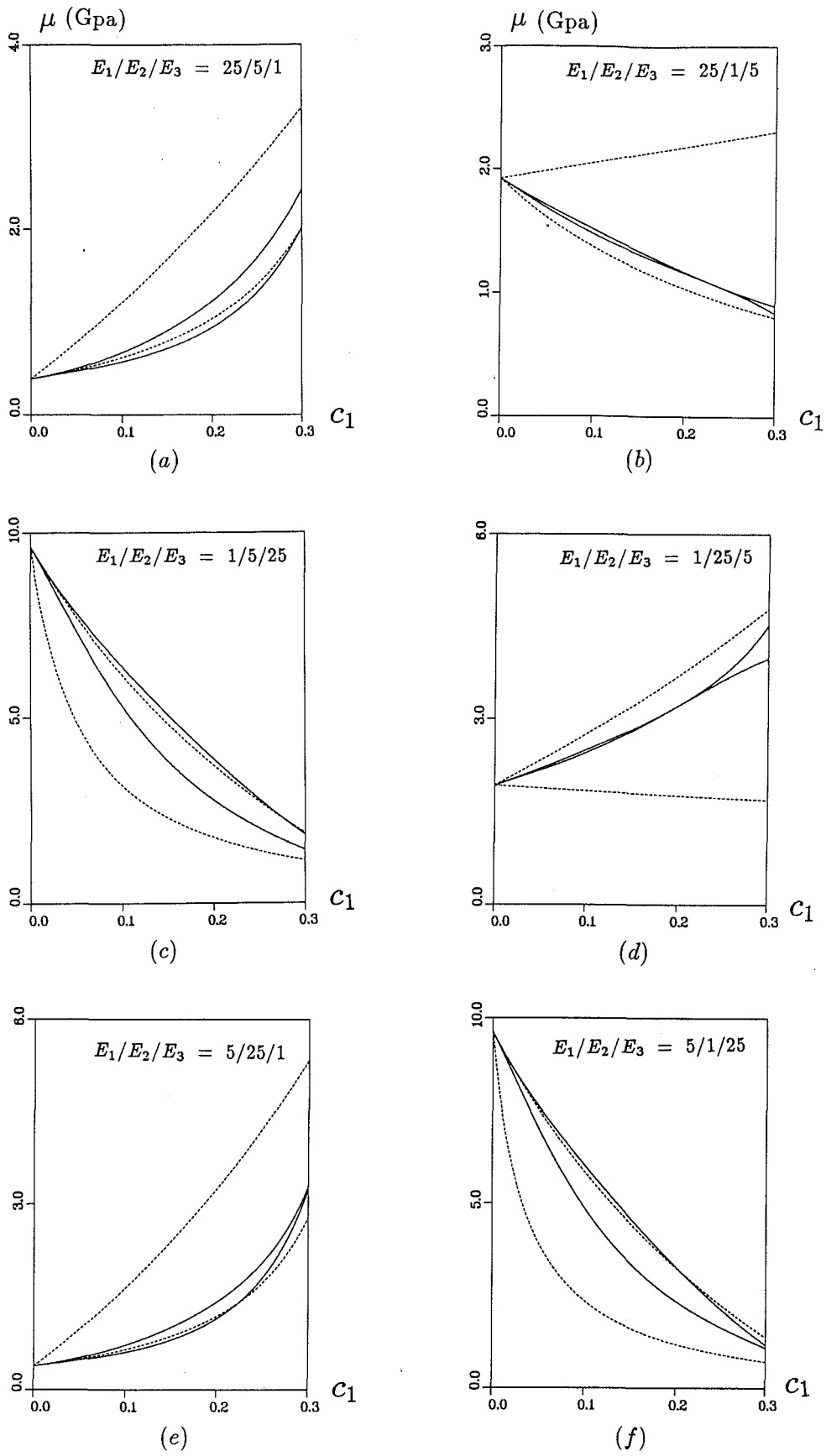

Fig. 1 Comparison between the present bounds (solid lines) and the Hashin-Shtrikman bounds (1963) (dashed lines) for μ of six coated particle-reinforced composites. The Young's moduli of the particle, coating, and matrix are as indicated, with the volume fractions of the coating and particle kept at a constant 2:1 ratio as c_1 increases. The Poisson ratios are set at 0.3 for all phases.

Downloaded 03 May 2010 to 171.66.16.248. Redistribution subject to ASME license or copyright; see http://www.asme.org/terms/Terms_Use.cfm

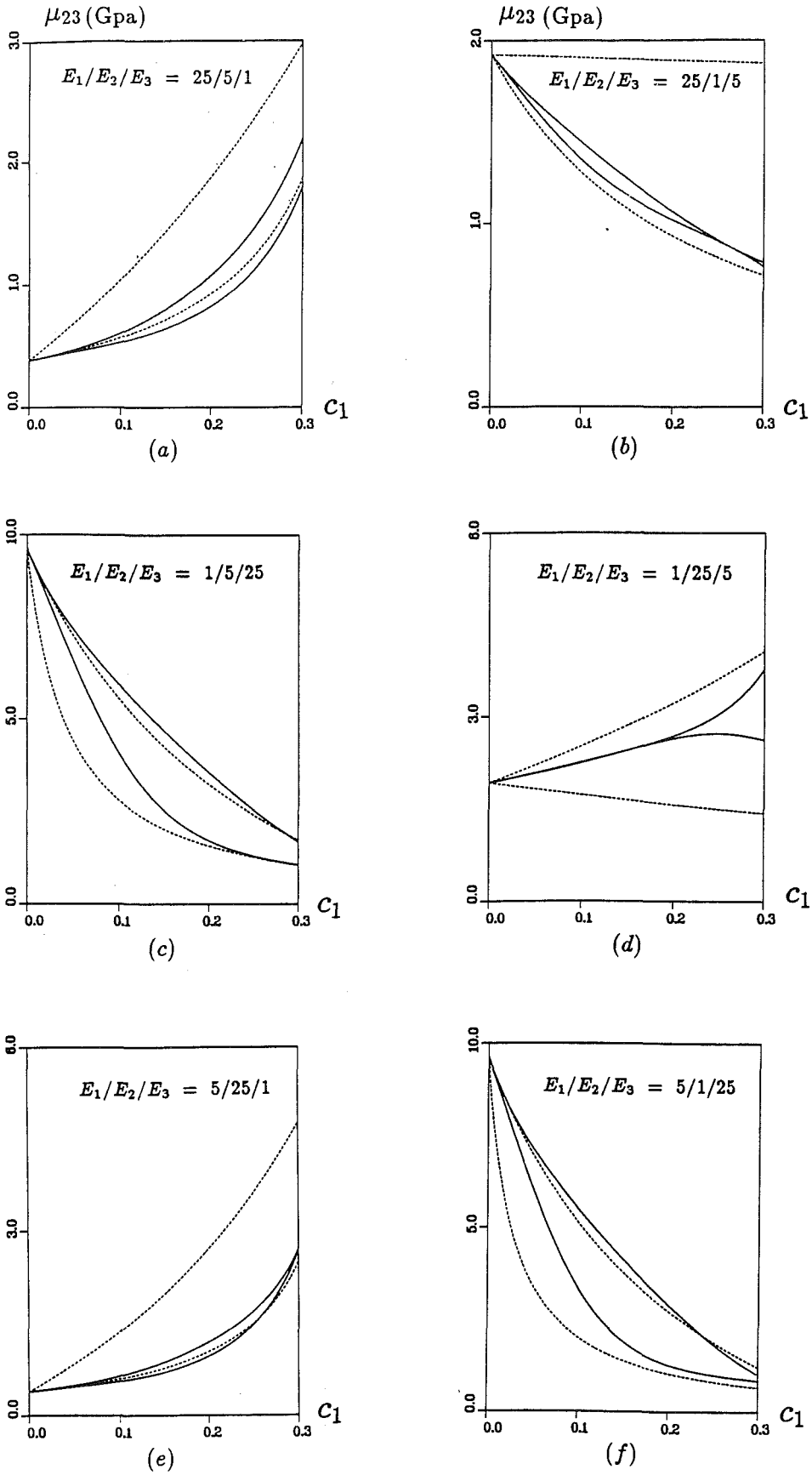

Fig. 2 Comparison between the present bounds (solid lines) and the Hashin bounds (1965) (dashed lines) for μ_{23} of six coated fiber-reinforced composites. The Young's moduli of the fiber, coating and matrix are as indicated, with the volume fractions of the coating and fiber kept at a constant 2:1 ratio as c_1 increases. The Poisson ratios are set at 0.3 for all phases.

Downloaded 03 May 2010 to 171.66.16.248. Redistribution subject to ASME license or copyright; see http://www.asme.org/terms/Terms_Use.cfm

spectively). These three materials are assigned three volume fractions $c_a = 0.7$, $c_b = 0.2$ and $c_c = 0.1$ and with which they can be placed to take the positions of inclusion, coating, and matrix in six possible combinations, leading to six different composite materials. The exact solutions of κ for these six composites are shown in the second column of Table 1, with the corresponding Young's moduli of inclusion/coating/matrix indicated in the first column to their right. For instance, in the first row, the 25/5/1 combination implies that material **a** serves as the inclusion, and materials **b** and **c** as the coating and matrix, respectively; the bulk modulus of the composite is then 6.47 GPa. If we use the softest constituent as the coating and still keep the hardest as the inclusion (the 25/1/5 combination) the effective bulk modulus will become 6.23 GPa. The most effective arrangement here appears to be 1/5/25—placing the softest as the inclusion and the hardest as the matrix—and this gives rise to a bulk modulus of 11.95 GPa. The corresponding Hashin-Shtrikman bounds, denoted by H-$S^{(+)}$ and H-$S^{(-)}$, are given on the top of the second column, with the values of 12.24 GPa and 6.16 GPa, respectively. It is seen that, by whatever combination, the effective bulk modulus of the composite always lies between the H-S bounds, but, unlike the two-phase composite sphere model (Hashin, 1962), none of these coincides with the bounds.

Although the inclusion/coating/matrix combination with an increasing order of stiffness (i.e., the 1/5/25 combination) does give rise to the highest κ here, the combination with a decreasing order of stiffness (i.e., the 25/5/1 combination) is not the one with the weakest response. The former behavior is indeed somewhat anticipated, but the latter one suggests that, in such a three-phase solid, the interactions among the constituents are far more complicated. We therefore decided to do another sample calculation, this time by assigning the volume functions $c_a = 0.1$, $c_b = 0.2$, and $c_c = 0.7$ for materials **a**, **b**, and **c**, respectively. The corresponding results are shown in the third column of Table 1, with the H-S bounds given on the top. The calculated κ for all six combinations again lie within the H-S bounds, but none coinciding with them. It is noted that the inclusion/coating/matrix with a decreasing order of stiffness (25/5/1), now consistent with our intuition, provides the lowest κ, but that the one with an increasing order (1/5/25) does not lead to the stiffest response.

Similar calculations were also performed for κ_{23} and μ_{12}, and the results were compared with the Hashin (1965) bounds. The same three constituents—called materials **a**, **b**, and **c** above—are again used in these calculations. The results for κ_{23}—with the same two types of volume fractions just considered—are given in Table 2, and those for μ_{12} are given in Table 3. In each case the Hashin bounds, denoted by $H^{(+)}$ and $H^{(-)}$, are shown on the top of each column. Similar trends are observed here for these six geometrical arrangements. The calculated κ_{23} and μ_{12} again all lie within the Hashin bounds, and none coincides with them.

For E_{11} and ν_{12}, the Hill (1964) and Walpole (1969) bounds coincide when the constituents share the same Poisson ratio. Other selected calculations with differing Poisson ratios also show that the results derived here consistently lie within their bounds, but none coincides with them.

In the case of μ for the coated-particle composite and μ_{23} for the coated-fiber composite, we also used the same constituents—materials **a**, **b**, and **c**—to calculate the bounds derived in this paper. The results of μ for the six possible geometrical arrangements by keeping the coating to the particle ratio at $c_2/c_1 = 0.2/0.1$ are plotted in Fig. 1 as solid lines, along with the Hashin-Shtrikman bounds (1963) in dashed lines. Those of μ_{23}, at the same ratio, together with the Hashin bounds (1965), are plotted in Fig. 2. The bounds derived here are generally tighter, and in (*b*) and (*d*) of both figures the bounds virtually coincide for some extended volume fraction, only to depart again later. In some cases, however, one of the bounds may fall slightly outside their bounds. This is reminiscent of the particle and fiber-reinforced two-phase composites (see the discussions of Christensen, 1979). Although Hashin and Shtrikman's bounds for μ and Hashin's bounds for μ_{23} have never been proved to be the best possible in terms of the volume fraction of the constituents, they may well be (this was Hashin's own assessment (1983), and the writers agree with this assessment). Thus, in the case of μ and μ_{23} it is suggested that the bounds derived should be used in combination with the bounds of Hashin and Shtrikman (1963) and Hashin (1965), respectively, always choosing the higher for the lower bound and the lower for the upper one.

Acknowledgment

The authors are grateful to the referees for calling to their attention the use of the replacement method. This work was supported by the National Science Foundation, Solid and Geo-Mechanics Program, under Grants MSM-8614151 and MSS-8918235.

References

Benveniste, Y., Dvorak, G. J., and Chen, T., 1989, "Stress Fields in Composites with Coated Inclusions," *Mechanics of Materials*, Vol. 7, pp. 305–317.

Christensen, R. M., 1979, *Mechanics of Composite Materials*, John Wiley and Sons, New York.

Christensen, R. M., and Lo, K. H., 1979, "Solutions for Effective Shear Properties in Three Phase Sphere and Cylinder Models," *Journal of the Mechanics and Physics of Solids*, Vol. 27, pp. 315–330.

Hashin, Z., 1962, "The Elastic Moduli of Heterogeneous Materials," ASME JOURNAL OF APPLIED MECHANICS, Vol. 29, pp. 143–150.

Hashin, Z., 1965, "On Elastic Behavior of Fibre Reinforced Materials of Arbitrary Transverse Phase Geometry," *Journal of the Mechanics and Physics of Solids*, Vol. 13, pp. 119–134.

Hashin, Z., 1972, "Theory of Fiber-Reinforced Materials," NASA CR 1974, pp. 145–147.

Hashin, Z., 1979, "Analysis of Properties of Fiber Composites with Anisotropic Constituents," ASME JOURNAL OF APPLIED MECHANICS, Vol. 46, pp. 543–550.

Hashin, Z., 1983, "Analysis of Composite Materials—A Survey," ASME JOURNAL OF APPLIED MECHANICS, Vol. 50, pp. 481–505.

Hashin, Z., and Rosen, B. W., 1964, "The Elastic Moduli of Fiber-Reinforced Materials," ASME JOURNAL OF APPLIED MECHANICS, Vol. 31, pp. 223–232.

Hashin, Z., and Shtrikman, S., 1963, "A Variational Approach to the Theory of the Elastic Behavior of Multiphase Materials, *Journal of the Mechanics and Physics of Solids*, Vol. 11, pp. 127–140.

Hill, R., 1964, "Theory of Mechanical Properties of Fibre-Strengthened Materials: I. Elastic Behavior," *Journal of the Mechanics and Physics of Solids*, Vol. 12, pp. 199–212.

Lee, K. J., and Westmann, R. A., 1970, "Elastic Properties of Hollow-Sphere-Reinforced Composites," *Journal of Composite Materials*, Vol. 4, pp. 242–253.

Luo, H. A., and Weng, G. J., 1987, "On Eshelby's Inclusion Problem in a Three-Phase Spherically Concentric Solid, and a Modification of Mori-Tanaka's Method," *Mechanics of Materials*, Vol. 6, pp. 347–361.

Luo, H. A., and Weng, G. J., 1989, "On Eshelby's S-Tensor in a Three-Phase Cylindrically Concentric Solid, and the Elastic Moduli of Fiber-Reinforced Composites," *Mechanics of Materials*, Vol. 8, pp. 77–88.

Mikata, Y., and Taya, M., 1985a, "Stress Field in and Around a Coated Short Fiber in Infinite Matrix Subjected to Uniaxial and Biaxial Loadings," ASME JOURNAL OF APPLIED MECHANICS, Vol. 52, pp. 19–24.

Mikata, Y., and Taya, M., 1985b, "Stress Field in a Coated Continuous Fiber Composite Subjected to Thermo-Mechanical Loadings," *Journal of Composite Materials*, Vol. 19, pp. 554–578.

Mikata, Y., and Taya, M., 1986, "Thermal Stress in a Coated Short Fiber Composite," ASME JOURNAL OF APPLIED MECHANICS, Vol. 53, pp. 681–689.

Pagano, N. J., and Tandon, G. P., 1988, "Elastic Response of Multi-Directional Coated-Fiber Composites," *Composites Science and Technology*, Vol. 31, pp. 273–293.

Sideridis,E., 1988, "The In-Plane Shear Modulus of Fiber Reinforced Composites as Defined by the Concept of Interphase," *Composite Science and Technology*, Vol. 31, pp. 35–53.

Walpole, L. J., 1969, "On the Overall Elastic Moduli of Composite Materials," *Journal of the Mechanics and Physics of Solids*, Vol. 17, pp. 235–251.

Walpole, L. J., 1978, "A Coated Inclusion in an Elastic Medium," *Mathematical Proceedings of the Cambridge Philosophical Society*, Vol. 83, pp. 495–506.

Downloaded 03 May 2010 to 171.66.16.248. Redistribution subject to ASME license or copyright; see http://www.asme.org/terms/Terms_Use.cfm

APPENDIX

Components of $[E^{(\epsilon)}]$, $[E^{(\sigma)}]$, $[G^{(\epsilon)}]$ and $[G^{(\sigma)}]$

The components of $[E^{(\epsilon)}]$ for the calculation of the upper bound of μ are (λ_r is the Lamé constant of the rth phase):

$$[E^{(\epsilon)}]_{10\times 10}=\begin{bmatrix}
1 & \frac{-6\nu_1}{1-2\nu_1} & -1 & \frac{6\nu_2}{1-2\nu_2}\left(\frac{c_1}{c_1+c_2}\right)^{2/3} & -3\left(\frac{c_1+c_2}{c_1}\right)^{5/3} \\
1 & -\frac{7-4\nu_1}{1-2\nu_1} & -1 & \frac{7-4\nu_2}{1-2\nu_2}\left(\frac{c_1}{c_1+c_2}\right)^{2/3} & 2\left(\frac{c_1+c_2}{c_1}\right)^{5/3} \\
\frac{\mu_1}{\mu_3} & \frac{21\lambda_1}{\mu_3} & -\frac{\mu_2}{\mu_3} & -\frac{21\lambda_2}{\mu_3}\left(\frac{c_1}{c_1+c_2}\right)^{2/3} & 12\left(\frac{c_1+c_2}{c_1}\right)^{5/3}\frac{\mu_2}{\mu_3} \\
 & -\frac{\mu_1}{\mu_3}\frac{18\nu_1}{1-2\nu_1} & & +\frac{\mu_2}{\mu_3}\frac{18\nu_2}{1-2\nu_2}\left(\frac{c_1}{c_1+c_2}\right)^{2/3} & \\
\frac{\mu_1}{\mu_3} & -\frac{\mu_1}{\mu_3}\frac{7+2\nu_1}{1-2\nu_1} & -\frac{\mu_2}{\mu_3} & \frac{\mu_2}{\mu_3}\frac{(7+2\nu_2)}{(1-2\nu_2)}\left(\frac{c_1}{c_1+c_2}\right)^{2/3} & -8\left(\frac{c_1+c_2}{c_1}\right)^{5/3}\frac{\mu_2}{\mu_3} \\
0 & 0 & 1 & -\frac{6\nu_2}{1-2\nu_2} & 3 \\
0 & 0 & 1 & -\frac{7-4\nu_2}{1-2\nu_2} & -2 \\
0 & 0 & \frac{\mu_2}{\mu_3} & \frac{21\lambda_2}{\mu_3}-\frac{\mu_2}{\mu_3}\frac{18\nu_2}{1-2\nu_2} & -12\frac{\mu_2}{\mu_3} \\
0 & 0 & \frac{\mu_2}{\mu_3} & -\frac{\mu_2}{\mu_3}\frac{7+2\nu_2}{1-2\nu_2} & 8\frac{\mu_2}{\mu_3} \\
0 & 0 & 0 & 0 & 0 \\
0 & 0 & 0 & 0 & 0
\end{bmatrix}$$

$$\begin{bmatrix}
-\frac{5-4\nu_2}{1-2\nu_2}\frac{c_1+c_2}{c_1} & 0 & 0 & 0 & 0 \\
-2\frac{c_1+c_2}{c_1} & 0 & 0 & 0 & 0 \\
3\frac{\lambda_2}{\mu_3}\frac{c_1+c_2}{c_1} & 0 & 0 & 0 & 0 \\
+2\frac{\mu_2}{\mu_3}\frac{5-4\nu_2}{1-2\nu_2}\frac{c_1+c_2}{c_1} & & & & \\
-2\frac{\mu_2}{\mu_3}\frac{(1+\nu_2)}{(1-2\nu_2)}\frac{c_1+c_2}{c_1} & 0 & 0 & 0 & 0 \\
\frac{5-4\nu_2}{1-2\nu_2} & -1 & \frac{6\nu_3}{1-2\nu_3} & -3 & -\frac{5-4\nu_3}{1-2\nu_3} \\
2 & -1 & \frac{7-4\nu_3}{1-2\nu_3} & 2 & -2 \\
-\frac{3\lambda_2}{\mu_3}-2\frac{\mu_2}{\mu_3}\frac{5-4\nu_2}{1-2\nu_2} & -1 & -\frac{21\lambda_3}{\mu_3}+\frac{18\nu_3}{1-2\nu_3} & 12 & \frac{3\lambda_3}{\mu_3}+2\frac{5-4\nu_3}{1-2\nu_3} \\
2\frac{\mu_2}{\mu_3}\frac{1+\nu_2}{1-2\nu_2} & -1 & \frac{7+2\nu_3}{1-2\nu_3} & -8 & -2\frac{1+\nu_3}{1-2\nu_3} \\
0 & 1 & -\frac{6\nu_3}{1-2\nu_3}\left(\frac{1}{c_1+c_2}\right)^{2/3} & 3(c_1+c_2)^{5/3} & \frac{5-4\nu_3}{1-2\nu_3}(c_1+c_2) \\
0 & 1 & -\frac{7-4\nu_3}{1-2\nu_3}\left(\frac{1}{c_1+c_2}\right)^{2/3} & -2(c_1+c_2)^{5/3} & 2(c_1+c_2)
\end{bmatrix}$$

Downloaded 03 May 2010 to 171.66.16.248. Redistribution subject to ASME license or copyright; see http://www.asme.org/terms/Terms_Use.cfm

The components of $[E^{(\sigma)}]$ for the calculation of the lower bound of μ are identical to those of $[E^{(\epsilon)}]$, except for the last three terms in rows 9 and 10, as

$$[E^{(\sigma)}]_{10\times 10}=\begin{bmatrix} \cdots\cdots & \cdots\cdots & \cdots\cdots & \cdots\cdots & \cdots\cdots \\ \cdots\cdots & \text{(same as in } [E^{(\epsilon)}]_{10\times 10}) & & \cdots\cdots & \cdots\cdots \\ \cdots\cdots & \cdots\cdots & \cdots\cdots & \cdots\cdots & \cdots\cdots \\ \cdots\cdots & \cdots\cdots & \dfrac{21\lambda_3}{\mu_3}\left(\dfrac{1}{c_1+c_2}\right)^{2/3} & -12(c_1+c_2)^{5/3} & -\dfrac{3\lambda_3}{\mu_3}(c_1+c_2) \\ & & -\dfrac{18\nu_3}{1-2\nu_3}\left(\dfrac{1}{c_1+c_2}\right)^{2/3} & & -2\dfrac{5-4\nu_3}{1-2\nu_3}(c_1+c_2) \\ \cdots\cdots & \cdots\cdots & -\dfrac{7+2\nu_3}{1-2\nu_3}\left(\dfrac{1}{c_1+c_2}\right)^{2/3} & 8(c_1+c_2)^{5/3} & 2\dfrac{1+\nu_3}{1-2\nu_3}(c_1+c_2) \end{bmatrix}$$

The components of $[G^{(\epsilon)}]$ for the calculation of the upper bound of μ_{23} are:

$$[G^{(\epsilon)}]_{10\times 10}=\begin{bmatrix} 1 & \eta_1-3 & -1 & -(\eta_2-3)\dfrac{c_1}{c_1+c_2} & -\left(\dfrac{c_1+c_2}{c_1}\right)^2 \\ -1 & \eta_1+3 & 1 & -(\eta_1+3)\dfrac{c_1}{c_1+c_2} & -\left(\dfrac{c_1+c_2}{c_1}\right)^2 \\ \dfrac{\mu_{23}^{(1)}}{\mu_{23}^{(3)}} & 3\dfrac{\mu_{23}^{(1)}}{\mu_{23}^{(3)}}(\eta_1-3) & -\dfrac{\mu_{23}^{(2)}}{\mu_{23}^{(3)}} & -3\dfrac{\mu_{23}^{(2)}}{\mu_{23}^{(3)}}(\eta_2-3)\dfrac{c_1}{c_1+c_2} & 3\dfrac{\mu_{23}^{(2)}}{\mu_{23}^{(3)}}\left(\dfrac{c_1+c_2}{c_1}\right)^2 \\ & +3\dfrac{\phi_1}{\eta_{23}^{(3)}}(\eta_1-1) & & -3\dfrac{\phi_2}{\mu_{23}^{(3)}}(\eta_2-1)\dfrac{c_1}{c_1+c_2} & \\ -\dfrac{\mu_{23}^{(1)}}{\mu_{23}^{(3)}} & 6\dfrac{\mu_{23}^{(1)}}{\mu_{23}^{(3)}} & \dfrac{\mu_{23}^{(2)}}{\mu_{23}^{(3)}} & -6\dfrac{\mu_{23}^{(2)}}{\mu_{23}^{(3)}}\dfrac{c_1}{c_1+c_2} & 3\dfrac{\mu_{23}^{(2)}}{\mu_{23}^{(3)}}\left(\dfrac{c_1+c_2}{c_1}\right)^2 \\ 0 & 0 & 1 & \eta_2-3 & 1 \\ 0 & 0 & -1 & \eta_2+3 & 1 \\ 0 & 0 & \dfrac{\mu_{23}^{(2)}}{\mu_{23}^{(3)}} & 3\dfrac{\mu_{23}^{(2)}}{\mu_{23}^{(3)}}(\eta_2-3) & -3\dfrac{\mu_{23}^{(2)}}{\mu_{23}^{(3)}} \\ & & & +3\dfrac{\phi_2}{\mu_{23}^{(3)}}(\eta_2-1) & \\ 0 & 0 & -\dfrac{\mu_{23}^{(2)}}{\mu_{23}^{(3)}} & 6\dfrac{\mu_{23}^{(2)}}{\mu_{23}^{(3)}} & -3\dfrac{\mu_{23}^{(2)}}{\mu_{23}^{(3)}} \\ 0 & 0 & 0 & 0 & 0 \\ 0 & 0 & 0 & 0 & 0 \end{bmatrix}$$

Downloaded 03 May 2010 to 171.66.16.248. Redistribution subject to ASME license or copyright; see http://www.asme.org/terms/Terms_Use.cfm

$$
\begin{bmatrix}
-(\eta_2+1)\dfrac{c_1+c_2}{c_1} & 0 & 0 & 0 & 0 \\
(\eta_2-1)\dfrac{c_1+c_2}{c_1} & 0 & 0 & 0 & 0 \\
\dfrac{\mu_{23}^{(2)}}{\mu_{23}^{(3)}}(\eta_2+1)\dfrac{c_1+c_2}{c_1} & 0 & 0 & 0 & 0 \\
+\dfrac{\phi_2}{\mu_{23}^{(3)}}(\eta_2-1)\dfrac{c_1+c_2}{c_1} & & & & \\
2\dfrac{\mu_{23}^{(2)}}{\mu_{23}^{(3)}}\dfrac{c_1+c_2}{c_1} & 0 & 0 & 0 & 0 \\
\eta_2+1 & -1 & -(\eta_3-3) & -1 & -(\eta_3+1) \\
-(\eta_2-1) & 1 & -(\eta_3+3) & -1 & \eta_3-1 \\
-\dfrac{\mu_{23}^{(2)}}{\mu_{23}^{(3)}}(\eta_2+1) & -1 & -3(\eta_3-3) & 3 & \eta_3+1 \\
-\dfrac{\phi_2}{\mu_{23}^{(3)}}(\eta_2-1) & & -3\dfrac{\phi_3}{\mu_{23}^{(3)}}(\eta_3-1) & & +\dfrac{\phi_3}{\mu_{23}^{(3)}}(\eta_3-1) \\
-2\dfrac{\mu_{23}^{(2)}}{\mu_{23}^{(3)}} & 1 & -6 & 3 & 2 \\
0 & 1 & (\eta_3-3)\dfrac{1}{c_1+c_2} & (c_1+c_2)^2 & (\eta_3+1)(c_1+c_2) \\
0 & 1 & -(\eta_3+3)\dfrac{1}{c_1+c_2} & -(c_1+c_2)^2 & (\eta_3-1)(c_1+c_2)
\end{bmatrix}
$$

where for the rth phase

$$\phi_r = 2\mu_{23}^{(r)}(E_{11}^{(r)}\nu_{23}^{(r)} + E_{22}^{(r)}\nu_{12}^{(r)}\nu_{12}^{(r)})]/[(1 - \nu_{23}^{(r)})E_{11}^{(r)} - 2E_{22}^{(r)}\nu_{12}^{(r)}\nu_{12}^{(r)},\ r=1,\ 2,\ 3$$

and $E_{22}^{(r)}$ is its transverse Young's modulus.

The components of $[G^{(\sigma)}]$ for the calculation of the lower bound of μ_{23} are identical to those of $[G^{(\epsilon)}]$, except for the last three terms in rows 9 and 10, as

$$
[G^{(\sigma)}]_{10\times 10} = \begin{bmatrix}
\cdots\cdots & \cdots\cdots & \cdots\cdots & \cdots\cdots & \cdots\cdots \\
\cdots\cdots & \text{(same as in } [G^{(\epsilon)}]_{10\times 10}) & & \cdots\cdots & \cdots\cdots \\
\cdots\cdots & \cdots\cdots & \cdots\cdots & \cdots\cdots & \cdots\cdots \\
\cdots\cdots & \cdots\cdots & 3\dfrac{\eta_3-3}{c_1+c_2} & -3(c_1+c_2)^2 & -(\eta_3+1)(c_1+c_2) \\
 & & +3\dfrac{\phi_3}{\mu_{23}^{(3)}}\dfrac{\eta_3-1}{c_1+c_2} & & -\dfrac{\phi_3(\eta_3-1)}{\mu_{23}^{(3)}}(c_1+c_2) \\
\cdots\cdots & \cdots\cdots & -6\dfrac{1}{c_1+c_2} & 3(c_1+c_2)^2 & 2(c_1+c_2)
\end{bmatrix}
$$

In the above expressions, it should be noted that in row 3 of $E^{(\epsilon)}$ and $G^{(\epsilon)}$, the second, third, and sixth terms include two lines, and so do the fourth, sixth, eighth, and tenth terms of row 7 in $G^{(\epsilon)}$. This also happens in the eighth and tenth terms in row 9 in $E^{(\sigma)}$ and $G^{(\sigma)}$.

Downloaded 03 May 2010 to 171.66.16.248. Redistribution subject to ASME license or copyright; see http://www.asme.org/terms/Terms_Use.cfm

Antiplane Shear Interface Cracks in Anisotropic Bimaterials

Kuang-Chong Wu
Assoc. Professor.

Yu-Tsung Chiu
Graduate Student

Institute of Applied Mechanics,
National Taiwan University,
Taipei, 10764, Taiwan

An analysis of antiplane shear interface cracks in a finite anisotropic composite body is presented. The analysis is done by a new complex-variable integral equation formulation based on the solutions of a dislocation and body force in an infinite composite body. Numerical results of the stress intensity factors are presented for the composite bodies with finite rectangular cross-sections under uniform shear. The composite bodies are formed by bonding an orthotropic material to an isotropic material. The numerical results show that there exists a lower bound for the stress intensity factor for a fixed crack-length-to-height ratio and that the lower bound is attained in the case of isotropic bimaterial.

1 Introduction

This paper is concerned with a plane interface crack lying between two dissimilar anisotropic cylindrical bodies with finite cross-sections under antiplane shear tractions as shown in Fig. 1. The materials are assumed to possess the material symmetry such that the in-plane deformation and the antiplane deformation are uncoupled. The case in which the upper and the lower materials are identical has been considered by Westmann and Yang (1967) for isotropic materials and by Retting (1986) for orthotropic materials. The problem of interface cracks in general dissimilar anisotropic infinite media has been studied in Willis (1971), Ting (1986), Qu and Bassani (1989), Su (1990), and Wu (1990), among others.

In anisotropic elasticity, Lekhnistskii's formulation (1963) or Stroh's formulation (1958) are the two most widely used methods. The equivalence of these methods has been discussed by Suo (1990). The general complex-variable solution obtained by these methods shows that the present problem can be converted into the one involving isotropic materials by properly changing the geometry of the body of interest and the tractions on the boundary of the body. Attention need, therefore, only be focused on the discussion of interface cracks in isotropic bimaterials.

It has been shown (England, 1965) that the plane-strain interface crack in general is characterized by oscillatory stress singularities if the crack faces are assumed traction-free. Such oscillatory stress singularities lead to a contradiction that the crack faces interpenetrate into each other. In contrast to the plane-strain interface crack, the stress state near the antiplane shear interface crack exhibits the same square root singularity as that for cracks in homogeneous materials and the contradiction of crack face interpenetration does not appear (Suo, 1990). As the antiplane shear interface crack is characterized by the square root singularity, the classical definition of the stress intensity factor applies.

In our analysis, a finite cracked body is considered to be cut out from an infinite body with sources of body forces and dislocations. The body forces and the dislocations are distributed over the contour s that coincides with the noncrack boundary and a distribution of interface dislocations is present on the contour c coinciding with the crack as shown in Fig. 2. The infinite body is divided by s into an interior region D^+ and an exterior region D^-. If the distributions of the sources are assumed to be such that the displacements and the stresses vanish in D^-, an integral representation for the stresses in the finite body in terms of the boundary stresses and the interface dislocation density is obtained. The resulting complex integral equation can be considered as a generalization of Cauchy's

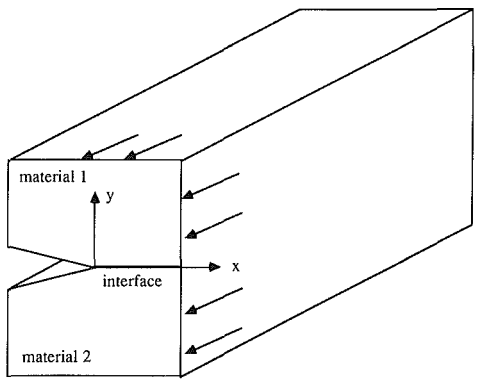

Fig. 1 An antiplane shear interface crack between two dissimilar anisotropic materials

Contributed by the Applied Mechanics Division of THE AMERICAN SOCIETY OF MECHANICAL ENGINEERS for presentation at the Joint Applied Mechanics/Bioengineering Conference, Ohio State University, Columbus, OH, June 16-19, 1991.

Discussion on this paper should be addressed to the Technical Editor, Prof. Leon M. Keer, The Technological Institute, Northwestern University, Evanston, IL 60208, and will be accepted until two months after final publication of the paper itself in the JOURNAL OF APPLIED MECHANICS. Manuscript received by the ASME Applied Mechanics Division, July 24, 1989; final revision, Nov. 19, 1990.

Paper No. 91-APM-35.

Copyright © 1991 by ASME
Downloaded 03 May 2010 to 171.66.16.248. Redistribution subject to ASME license or copyright; see http://www.asme.org/terms/Terms_Use.cfm

integral formula. The integral representation provides boundary integral equations that relate the traction, tangential derivative of the displacement on s and the dislocation density on c. The fundamental solutions for a dislocation and a body force in a general anisotropic composite has been obtained by Suo (1990). The specialized antiplane version of Suo's result is employed here. A special crack-tip element is used so that the stress intensity factors can be obtained directly as the boundary integral equations are numerically solved.

The plan of the paper is as follows: First, a general complex-variable solution is introduced and the correspondence relations between the anisotropy problem and the isotropy problem are discussed. Based on the result given by Suo (1990), the integral equations for solving cracked composite bodies are developed. Finally, a special crack-tip element is introduced to obtain the stress intensity factors as the integral equations are numerically solved for several examples concerning orthotropic-isotropic bimaterials.

2 Antiplane-Strain Problems

In this section, a general complex-variable solution to antiplane-strain problems for homogeneous media is introduced. From the general solution, correspondence between the problems for anisotropic materials and those for isotropic materials is discussed.

Antiplane-strain deformation is characterized by a single displacement component $w=w(x, y)$ in the direction perpendicular to the (x, y) plane. Corresponding to the displacement, there are only two nonzero stress components $\tau_1 \equiv \tau_{xz}$ and $\tau_2 \equiv \tau_{yz}$. The constitutive law is described by given by

$$\tau_\alpha = \mu_{\alpha\beta} w_{,\beta} \tag{1}$$

where $\mu_{\alpha\beta}$ are elastic constants. In equation (1), α, β range from 1 to 2, summation of repeated index is implied and a comma denotes differentiation. The general solution to the antiplane problem can be represented as (Stroh, 1958, Lekhnitskii, 1963)

$$Gw - i\phi = Gf(z) \tag{2}$$

where $i=\sqrt{-1}$, the parameter G is given by

$$G=\sqrt{\mu_{11}\mu_{22}-\mu_{12}^2}, \tag{3}$$

$z=x+py$ with p given by

$$p=\frac{-\mu_{12}+iG}{\mu_{22}}, \tag{4}$$

and ϕ is the stress function defined such that the traction τ_n on a contour s is given by

$$\tau_n = -\frac{d\phi}{ds}. \tag{5}$$

Note that for isotropic materials, the parameter G in equation (2) is simply the shear modulus μ and f is an analytic function of $z=x+iy$. The fact implies that any solution of an anisotropy problem can be obtained by solving a corresponding isotropy problem (Lekhnitskii, 1963). The shear modulus of the isotropy problem μ is given by G. Let the quantities associated with the anisotropy problem be denoted with a hat. The geometry of the corresponding isotropy problem is obtained by

$$x=\hat{x}+\gamma\hat{y} \tag{6}$$

$$y=\beta\hat{y} \tag{7}$$

where

$$\gamma=-\frac{\mu_{12}}{\mu_{22}} \tag{8}$$

$$\beta=\frac{G}{\mu_{22}}. \tag{9}$$

An illustration of the change of the geometry is given in Fig. 3. From equation (5), the traction τ_n on the boundary of the isotropy problem is given by

$$\tau_n=\frac{\hat{\tau}_n}{\beta}[(\beta\cos\theta-\gamma\sin\theta)^2+\sin^2\theta]^{1/2} \tag{10}$$

where θ is the angle between the tangent to the transformed boundary and the x-axis. Let the displacement and the stresses

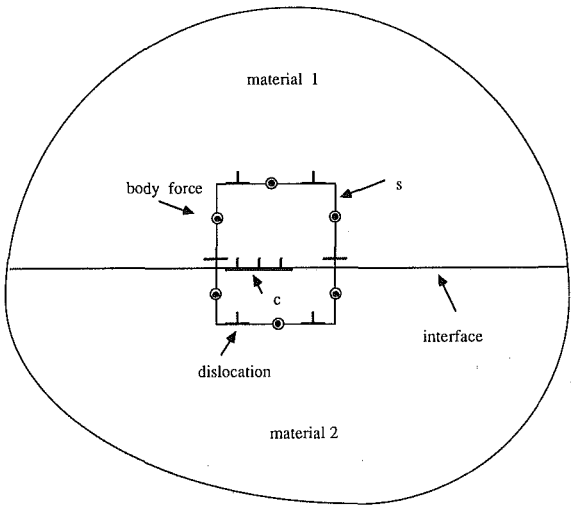

Fig. 2 Body forces and dislocations on the closed contour s and interface dislocations on c

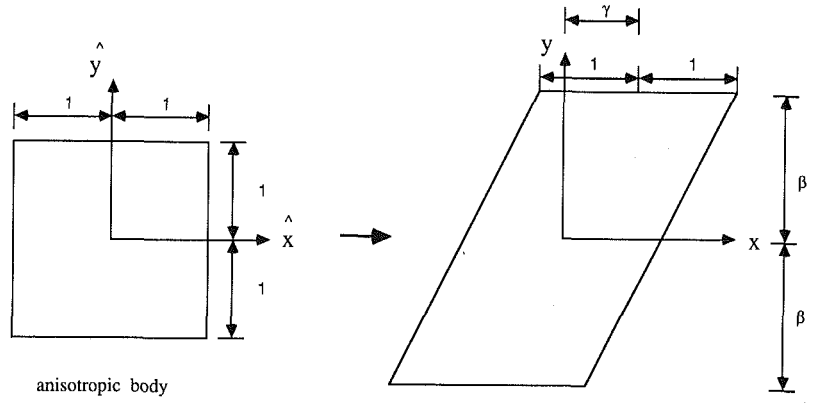

Fig. 3 A geometric representation of the transformation from an anisotropy problem to an isotropy problem

Downloaded 03 May 2010 to 171.66.16.248. Redistribution subject to ASME license or copyright; see http://www.asme.org/terms/Terms_Use.cfm

of the problem for isotropic material be w, τ_1, and τ_2, respectively. From equation (2) the solutions for the actual problem for anisotropic material are given by

$$\hat{w}(\hat{x},\hat{y}) = w(x,y) \tag{11}$$

$$\hat{\tau}_1(\hat{x},\hat{y}) = \beta\tau_1(x,y) - \gamma\tau_2(x,y) \tag{12}$$

$$\hat{\tau}_2(\hat{x},\hat{y}) = \tau_2(x,y). \tag{13}$$

Through the correspondence relations, any antiplane shear problem involving an anisotropic material can be simplified into the one with an isotropic material. In view of this fact, the discussions to be followed will be centered on the isotropic materials. Before closing this section, we note that for isotropic materials, the complex stress $\tau \equiv \tau_1 - i\tau_2$ is related to f by

$$\tau = \mu f'(z). \tag{14}$$

3 Formulation

In this section, a formulation for a finite composite body with an interface crack is derived. 1 and 2 are used to distinguish the two materials.

Consider first a dislocation and body force in an infinite composite material at point (ξ, η) in the lower material 2. The solution for this problem is (Suo, 1990)

$$\mu_1 f^{(1)}(z) = -\frac{1}{\pi(1+\Gamma)}(F + i\mu_2 B)\log(z-\zeta) \tag{15}$$

$$\mu_2 f^{(2)}(z) = -\frac{1}{2\pi}[(F + i\mu_2 B)\log(z-\zeta) - \frac{1-\Gamma}{1+\Gamma}(F - i\mu_2 B)\log(z-\bar{\zeta})] \tag{16}$$

where $\zeta = \xi + i\eta$ and

$$\Gamma = \frac{\mu_2}{\mu_1}. \tag{17}$$

Similarly, for a dislocation and body force in the upper material 1, the result is

$$\mu_1 f^{(1)}(z) = -\frac{1}{2\pi}[(F + i\mu_1 B)\log(z-\zeta) + \frac{1-\Gamma}{1+\Gamma}(F - i\mu_1 B)\log(z-\bar{\zeta})] \tag{18}$$

$$\mu_2 f^{(2)}(z) = -\frac{\Gamma}{\pi(1+\Gamma)}(F + i\mu_1 B)\log(z-\zeta). \tag{19}$$

Now, consider distributions of dislocations and body forces on s and interface dislocations on c as shown in Fig. 2. From equation (14), the stress field produced by such distributions in material 1 is given by

$$\tau^{(1)} = \frac{1}{2\pi}\int_{s_1}\left[\frac{g + i\mu_1\alpha}{\zeta - z} + \left(\frac{1-\Gamma}{1+\Gamma}\right)\frac{g - i\mu_1\alpha}{\bar{\zeta} - z}\right]ds + \frac{1}{\pi(1+\Gamma)}\int_{s_2}\frac{g + i\mu_2\alpha}{\zeta - z}ds + \frac{1}{\pi(1+\Gamma)}\int_c \frac{i\mu_2\alpha}{\xi - z}d\xi \tag{20}$$

where g and α are the body force and the dislocation per unit length along the contour s or c; s_1 and s_2 are the parts of s in material 1 and 2, respectively. Similarly, in material 2, the stress is given by

$$\tau^{(2)} = \frac{1}{2\pi}\int_{s_2}\left[\frac{g + i\mu_2\alpha}{\zeta - z} - \left(\frac{1-\Gamma}{1+\Gamma}\right)\frac{g - i\mu_2\alpha}{\bar{\zeta} - z}\right]ds + \frac{\Gamma}{\pi(1+\Gamma)}\int_{s_1}\frac{g + i\mu_1\alpha}{\zeta - z}ds + \frac{1}{\pi(1+\Gamma)}\int_c \frac{i\mu_2\alpha}{\xi - z}d\xi. \tag{21}$$

Equations (20) and (21) are integrals of Cauchy's type. From the properties of Cauchy's type integrals, it can be shown that the traction and $\tau^{(1)}$ is discontinuous across s_1. In fact,

$$\tau_+^{(1)}(\zeta) - \tau_-^{(1)}(\zeta) = i(g(\zeta) + i\mu_1\alpha(\zeta))e^{-i\theta} \tag{22}$$

where $\tau_\pm^{(1)}(\zeta)$ denotes the limiting value of $\tau^{(1)}$ as $z \to \zeta$ in D^+ and in D^-, respectively, and θ is the angle between the tangent to the contour s and the x-axis. Similarly, for $\tau^{(2)}$,

$$\tau_+^{(2)}(\zeta) - \tau_-^{(2)}(\zeta) = i(g(\zeta) + i\mu_2\alpha(\zeta))e^{-i\theta}. \tag{23}$$

If the distribution of body forces and dislocations at s are chosen such that

$$\tau_-^{(1)} = \tau_-^{(2)} = 0$$

then equation (22) becomes

$$g(\zeta) + i\mu_1\alpha(\zeta) = -i\tau^{(1)}(\zeta)e^{i\theta} \tag{24}$$

and equation (23) gives

$$g(\zeta) + i\mu_2\alpha(\zeta) = -i\tau^{(2)}(\zeta)e^{i\theta}. \tag{25}$$

In equations (24) and (25), subscript + in τ has been omitted for simplicity. Distributions of body forces and dislocations given by equations (24) and (25) will make effectively the exterior region D^- stress free. The stresses $\tau^{(1)}$ and $\tau^{(2)}$ in the interior region D^+ are obtained by substituting equations (24) and (25) into equations (20) and (21). The result is

$$\tau^{(1)}(z) = \frac{1}{2\pi i}\int_{s_1}\left[\frac{\tau^{(1)}(\zeta)}{\zeta - z}d\zeta - \left(\frac{1-\Gamma}{1+\Gamma}\right)\frac{\overline{\tau^{(1)}(\zeta)}}{\bar{\zeta} - z}d\bar{\zeta}\right] + \frac{1}{i\pi(1+\Gamma)}\int_{s_2}\frac{\tau^{(2)}(\zeta)}{\zeta - z}d\zeta - \frac{1}{i\pi(1+\Gamma)}\int_c \frac{\mu_2\alpha}{\xi - z}d\xi \tag{26}$$

and

$$\tau^{(2)}(\zeta) = \frac{1}{2\pi i}\int_{s_2}\left[\frac{\tau^{(2)}(\zeta)}{\zeta - z}d\zeta + \left(\frac{1-\Gamma}{1+\Gamma}\right)\frac{\overline{\tau^{(2)}(\zeta)}}{\bar{\zeta} - z}d\bar{\zeta}\right] + \frac{\Gamma}{i\pi(1+\Gamma)}\int_{s_1}\frac{\tau^{(1)}(\zeta)}{\zeta - z}d\zeta - \frac{1}{i\pi(1+\Gamma)}\int_c \frac{\mu_2\alpha}{\xi - z}d\xi. \tag{27}$$

If $\Gamma = 1$ and $\alpha = 0$, equations (26) and (27) reduce to the well-known Cauchy's integral formula. Equations (26) and (27) can thus be considered as a generalization of the Cauchy's integral formula for a composite body with an interface crack. By taking $z \to \zeta \in s \cup c$, equations (26) and (27) can also be considered as integral equations relating the boundary stresses $\tau^{(1)}$, $\tau^{(2)}$, and the interface dislocation density α. Since in typical boundary value problems either the traction or displacement, or equivalently tangential gradient of the displacement is prescribed on the boundary, it is more convenient to express equations (26) and (27) in terms of these boundary quantities. The tangential shear stress $\tau_t = \mu\partial w/\partial s$ and the traction τ_n along s are related to τ by

$$\alpha^{(\delta)} = \tau_n^{(\delta)} - i\tau_t^{(\delta)} = -i\tau^{(\delta)}e^{i\theta} \tag{28}$$

where $\delta = 1, 2$. The limiting equations of (26) and (27) can be expressed as

$$\sigma^{(1)} = e^{i\theta}\left\{\frac{1}{2\pi i}\int_{s_1}\left[\frac{\sigma^{(1)}}{\zeta - z} + \left(\frac{1-\Gamma}{1+\Gamma}\right)\frac{\bar{\sigma}^{(1)}}{\bar{\zeta} - z}\right]ds + \frac{1}{i\pi(1+\Gamma)}\int_{s_2}\frac{\sigma^{(2)}}{\zeta - z}ds + \frac{1}{\pi(1+\Gamma)}\int_c \frac{\mu_2\alpha}{\xi - z}d\xi\right\} \tag{29}$$

$$\sigma^{(2)} = e^{i\theta}\left\{\frac{1}{2\pi i}\int_{s_2}\left[\frac{\sigma^{(2)}}{\zeta - z} - \left(\frac{1-\Gamma}{1+\Gamma}\right)\frac{\bar{\sigma}^{(2)}}{\bar{\zeta} - z}\right]ds + \frac{\Gamma}{i\pi(1+\Gamma)}\int_{s_1}\frac{\sigma^{(1)}}{\zeta - z}ds + \frac{1}{\pi(1+\Gamma)}\int_c \frac{\mu_2\alpha}{\xi - z}d\xi\right\}. \tag{30}$$

Downloaded 03 May 2010 to 171.66.16.248. Redistribution subject to ASME license or copyright; see http://www.asme.org/terms/Terms_Use.cfm

Equations (29) and (30) are boundary integral equations that relate the traction, the tangential gradient of the displacement on the boundary, and the interface dislocation density. In comparison, conventional real boundary integral equations are expressed in terms of the traction and displacement on the boundary and the crack is represented by displacement discontinuity. One advantage of using the displacement derivative as the primary unknown is that the quantity can be more accurately obtained as no numerical differentiation is required. Another advantage, which is perhaps more relevant to the present problem, is that representation of cracks by interface dislocations results in a weaker singular kernel than that in the conventional boundary integral equations. Similar formulation has been given by Choi and Kwak (1989) for two-dimensional potential problems for homogeneous media. Their formulation contains a multivalued kernel. In the present formulation the kernels are all single-valued.

In the present problem where the traction τ_n is prescribed on the boundary and the crack faces assumed traction-free, equation (29) and equation (30) can be used to solve for $\partial w/\partial s$ at s and the interface dislocation density α. To enforce the traction-free condition for the crack faces, the real part of equation (29) is taken as $z \to c$. As for the traction boundary conditions on s, in principle either the real parts or the imaginary parts of equations (29) and (30) can be used. However, taking the real parts of the equations results in Fredholm equations of the first type while the imaginary parts in Fredholm equations of the second type for the displacement gradient. In general, stability of Fredholm equations of the second type is better than that of the first type. The imaginary parts of the equations are therefore utilized in the present work to solve for the displacement gradient. With the displacement gradient determined, the real parts of the equations are then used to check the accuracy of the numerical solutions.

4 Numerical Results

In this section, stress intensity factors are given for some composite cracked bodies of rectangular cross-section of height $2h$ and width h containing an edge crack of length a. The composite cracked bodies are under a uniform shear τ_0.

Although the formulation presented here is applicable to composite bodies composed of general anisotropic materials, we shall, for simplicity, consider those composite bodies that are formed by bonding an isotropic material for shear modulus μ_1 to an orthotropic material with shear moduli μ_{11} and μ_{22}. As was discussed in Section 2, the orthotropic part of the composite can be transformed into the isotropic material with shear modulus $\mu_2 = \sqrt{\mu_{11}\mu_{22}}$. Since the orthotropic materials $\mu_{12} = 0$, from equation (6) and equation (7), the transformed geometry is obtained by adjusting the height h to βh, where β is given by equation (9). From equation (10), the traction on the transformed boundary does not change. The problem considered is illustrated in Fig. 4.

In the numerical procedure, the boundary of the cross-section as well as the crack line was discretized into a number of line segments. On the boundary, $\partial w/\partial s$ was assumed constant on each element and on the crack line α was assumed linearly varying on each element except the one adjacent to the crack

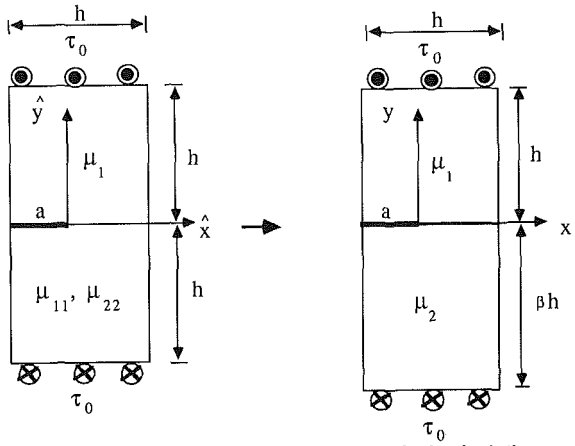

Fig. 4 The problem considered for numerical calculations

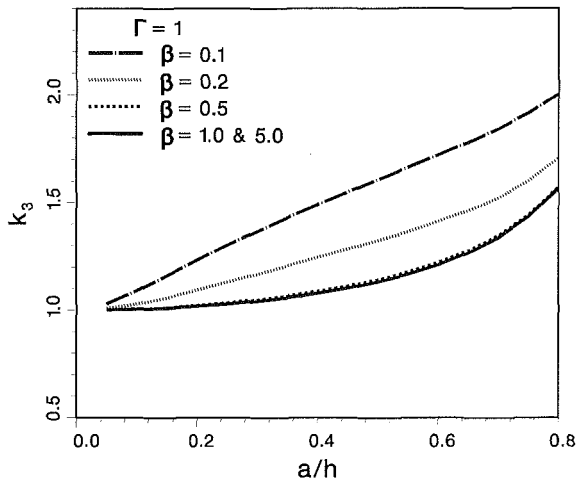

Fig. 6 Stress intensity factors as a function of β and a/h for $\Gamma = 1$

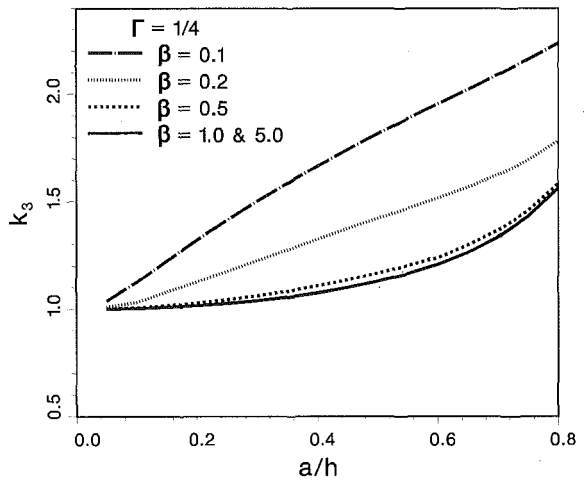

Fig. 5 Stress intensity factors as a function of β and a/h for $\Gamma = 0.25$

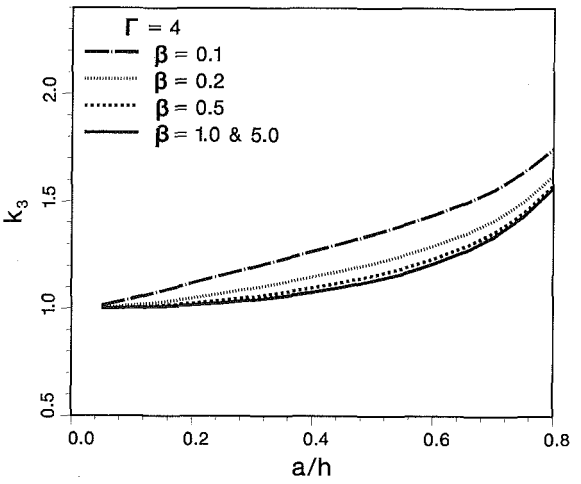

Fig. 7 Stress intensity factors as a function of β and a/h for $\Gamma = 4$

Downloaded 03 May 2010 to 171.66.16.248. Redistribution subject to ASME license or copyright; see http://www.asme.org/terms/Terms_Use.cfm

tip. For this crack-tip element, the asymptotic expression of α (Suo, 1990) given by

$$\alpha = \left(\frac{1}{\mu_1} + \frac{1}{\mu_2}\right)\frac{K_3}{\sqrt{2\pi r}} \tag{31}$$

was incorporated. In equation (31), r is the distance from the crack tip and K_3 is the stress intensity factor. With these assumptions equations (29) and (30) were integrated analytically and a system of algebraic equations for $\partial w/\partial s$, α, and K_3 was obtained by enforcing the boundary conditions and the traction-free condition for the crack by the method of point collocation. The system of equations in conjunction with a auxiliary equation of compatibility:

$$\int_c \alpha dx + \int_s \frac{\partial w}{\partial s} ds = 0$$

was then solved to yield the stress intensity factors directly. Since along the interface τ_2 is given by

$$\tau_2 = \frac{K_3}{\sqrt{2\pi r}} \tag{32}$$

and from equation (13) and equation (6) τ_2 as well as r is not altered by the transformation, the stress intensity factor obtained for the transformed body is the same as that for the original body.

The normalized stress intensity factors $k_3 = K_3/(\tau_0\sqrt{\pi a})$ as a function of Γ defined by equation (17) and β defined by equation (9) for a range of a/h are shown in Figs. 5–7. The values of Γ used are 0.25, 1, and 4. The values of β chosen are 0.1, 0.2, 0.5, 1, 5. The values of a/h range from 0.05 to 0.8. Note that in all cases considered, the stress intensity factors for $\beta > 1$ are indistinguishable from those for $\beta = 1$ which may be considered as the lower bounds.

The case of $\beta = 1$ which corresponds to an isotropic material deserves special attention. For $\beta = 1$ the geometry of the transformed bodies are symmetric with respect to the interface. Let the applied loading be also symmetric with respect to the interface. Assume that $w^{(h)}$, $\tau^{(h)}$ are the displacement and the complex stress as $\Gamma = 1$, corresponding to a homogeneous material. Due to the symmetry conditions, $w^{(h)}$ vanishes along the interface. For arbitrary value of Γ, it can be shown that the displacement and the stress are simply given by $w_1 = w^{(h)}$ and $\tau^{(1)} = \tau^{(h)}$ for $y > 0$ and $w_2 = \Gamma w^{(h)}$ and $\tau^{(2)} = \tau^{(h)}$ for $y < 0$. Thus the stress, and hence the stress intensity factor, is independent of Γ for $\beta = 1$. The fact implies that the lower bound curves in Figs. 5–7 are the same, which is indeed the case.

5 Acknowledgments

The research was supported by National Science Council of the Republic of China under grant NSC-79-0401-E002-22.

References

Choi, J. H., and Kwak, B. M., 1989, "A Boundary Integral Equation Formulation in Derivative Unknowns for Two-Dimensional Potential Problems," ASME Journal of Applied Mechanics, Vol. 56, pp. 617–623.

England, A. H., 1965, "A Crack Between Dissimilar Media," ASME Journal of Applied Mechanics, Vol. 32, pp. 400–402.

Lekhnitskii, S. G., 1963, *Theory of Elasticity of an Anisotropic Body*, Holden-Day, San Francisco, Calif.

Qu, J., and Bassani, J. L., 1989, "Fracture Mechanics of Interfacial Cracks," *J. Mech. Phys. Solids*, Vol. 37, pp. 417–433.

Retting, G., 1986, "Anti-plane Stress Analysis of a Cracked Rectangular Orthotropic Beam," *Engineering Fracture Mechanics*, Vol. 23, pp. 441–454.

Stroh, A. N., 1958, "Dislocations and Cracks in Anisotropic Elasticity," *Philos. Mag.*, Vol. 7, pp. 625–646.

Suo, Z., 1990, "Singularities, Interfaces and Cracks in Dissimilar Anisotropic Media," *Proc. R. Soc. Lond.*, Vol. A427, pp. 331–358.

Ting, T. C. T., 1986, "Explicit Solution and Invariance of the Singularities at an Interface Crack in Anisotropic Composite," *Int. J. Solids Structures*, Vol. 22, No. 9, pp. 965–983.

Westmann, R. A., and Yang, W. H., 1967, "Stress Analysis of Cracked Rectangular Beams," ASME Journal of Applied Mechanics, Vol. 34, pp. 693–701.

Willis, J. R., 1971, "Fracture Mechanics of Interfacial Cracks," *J. Mech. Phys. Solids*, Vol. 19, pp. 353–368.

Wu, K.-C., 1990, "Stress Intensity Factor and Energy Release Rate for Interfacial Cracks Between Dissimilar Anisotropic Materials," ASME Journal of Applied Mechanics, Vol. 57, pp. 882–886.

Downloaded 03 May 2010 to 171.66.16.248. Redistribution subject to ASME license or copyright; see http://www.asme.org/terms/Terms_Use.cfm

Dynamic Stress on a Partially Bonded Fiber

Andrew Norris
Assoc. Mem. ASME

Yang Yang
Department of Mechanics and Materials Science, Rutgers University, Piscataway, NJ 08855-0909

The dynamic stress on a partially bonded fiber is analyzed for shear wave incidence, with particular attention given to the stress intensity factor at the neck joining the fiber to the matrix. The problem is formulated in terms of the unknown stress across the neck and the remainder of the fiber-matrix interface is modeled as a curved interfacial crack. Explicit asymptotic expressions are derived for the near and far-fields that are valid in the frequency range in which the recently discussed resonance phenomenon occurs (Yang and Norris, 1991). This resonance is a rattling effect that is most prominent when the neck becomes very thin, and can occur at arbitrarily small values of the dimensionless frequency ka, *where* a *is the radius of the fiber. The asymptotic results indicate that the dynamic stress intensity factor becomes unbounded as the neck vanishes, in contrast to the prediction of a purely quasi-static analysis that the stress intensity factor vanishes in the same limit.*

1 Introduction

In a recent analysis of the scattering of out-of-plane shear waves from a partially debonded fiber in an otherwise homogeneous matrix, it was demonstrated that the fiber can exhibit a strong resonance at very low frequencies (Yang and Norris, 1991). The reason for this is apparent from Fig. 1: As the size of the debond becomes large, the neck joining the fiber to the matrix becomes correspondingly smaller, allowing the fiber to undergo large relative motion. At the same time the mass of the fiber is unchanged, and thus the fiber acts as a spring-mass system of constant mass and relatively small stiffness. The stiffness goes to zero as the neck vanishes, and so one expects that the frequency of resonance also goes to zero in the same limit. The numerical results of Yang and Norris (1991) clearly show that the resonance can be excited by incident shear waves, and that it can occur at arbitrarily low frequency if the neck is allowed to be sufficiently small.

This type of resonance is clearly related to the Helmholtz resonance of gravity water waves in a harbor with a narrow opening (Miles, 1971; Burrows, 1985), and more generally, with the Helmholtz resonance phenomenon of an acoustical cavity. In the latter case, the compressibility of the acoustic fluid occupying the cavity is volumetric, but the mass of entrained fluid in the cavity opening is independent of the cavity volume, depending instead on the local geometry at the mouth. Thus, the roles of stiffness and inertia are quite different in the fiber and Helmholtz resonances.

One consequence of the fiber resonance is that the scattering cross-section of a *low frequency* shear wave is greatly enhanced, thus providing a possible means of identifying loose fibers using ultrasonic waves. The numerical results of Yang and Norris (1991) also show that the stress intensity factor at the neck is magnified at resonance, which has important implications for the dynamic pullout of fibers and shock-induced debonding and may also be of significance in the vibration of foundation pilings subject to seismic excitation. These increases in response at resonance are analogous to the paradoxical enhancement of the surge in a harbor as the entrance

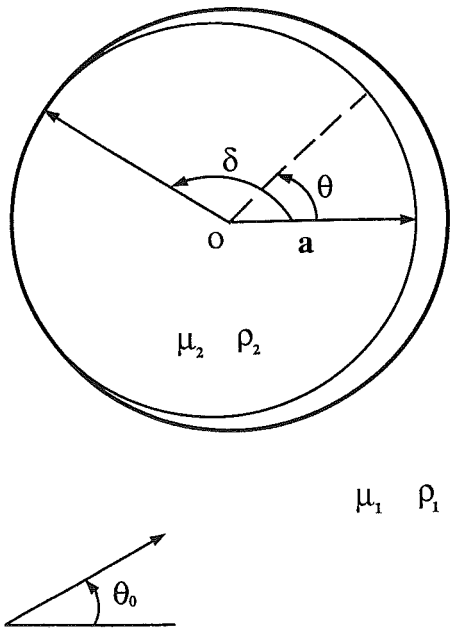

Fig. 1 The partially bonded fiber and the incident wave direction

Contributed by the Applied Mechanics Division of THE AMERICAN SOCIETY OF MECHANICAL ENGINEERS for presentation at the Joint Applied Mechanics/Bioengineering Conference, Ohio State University, Columbus, Ohio, June 16–19, 1991.

Discussion on this paper should be addressed to the Technical Editor, Prof. Leon M. Keer, the Technological Institute, Northwestern University, Evanston, IL 60208, and will be accepted until two months after final publication of the paper itself in the JOURNAL OF APPLIED MECHANICS. Manuscript received by the ASME Applied Mechanics Division, Mar. 20,1990; final revision, July 30, 1990. Paper No. 91-APM-30.

Copyright © 1991 by ASME
Downloaded 03 May 2010 to 171.66.16.248. Redistribution subject to ASME license or copyright; see http://www.asme.org/terms/Terms_Use.cfm

is narrowed, an effect known as the "harbor paradox" (Miles, 1971; Burrows, 1985). In the present paper we focus on the dynamic stress intensity factor using a formulation which leads directly to simple asymptotic expressions for the resonance frequency and the stress intensity factor for small neck size. In the previous analysis (Yang and Norris, 1991) a system of equations was derived for the coefficients in a Chebyshev expansion of the crack opening displacement of the debond. This is the standard approach in attacking scattering problems involving cracks in infinite media (Krenk and Schmidt, 1982; Boström, 1987), and leads to simplifications in the present configuration when the debond is small, but is not suitable for treating the limit in which the neck as very narrow. In this paper we consider the stress on the neck is the unknown to be determined, rather than the COD. This method is similar in spirit to that of Burrows (1985) who considered waves incident on a circular harbor, and some of the asymptotic results reported here are similar to his discussions of the "harbor paradox." One advantage of the present method of solution is that the unperturbed configuration is the fully debonded state (i.e., a void) whereas in the COD method the base state is the perfectly bonded fiber. The dynamic response is simpler for the void and although this simplification is not significant for the SH problem treated here, it is very useful in considering the in-plane problem, the results of which will be published separately.

The formulation and analysis are developed in Sections 2, 3, and 4, and the main discussion regarding the stress intensity factor is in Section 5. Numerical calculations are presented in Section 6.

2 Formulation

The fiber occupies the region $r < a$ (see Fig. 1) with density ρ_2 and shear modulus μ_2, and the matrix $r > a$ has corresponding parameters ρ_1 and μ_1. The motion is out of the plane with time harmonic dependence $\exp(-i\omega t)$ which is omitted in all equations. The debond is of angular width 2δ, or equivalently, the extent of the neck is 2ϵ, where $\epsilon = \pi - \delta$. The total out-of-plane displacement is

$$u^{\text{tot}} = \begin{cases} u^{in} + u_1^{(0)} + u_1^{(1)}, & r > a, \\ u_2^{(1)}, & r < a, \end{cases} \tag{1}$$

where u^{in} is the incident wave and $u_1^{(0)}$ is the scattered field from the void $r < a$, which satisfies the boundary condition

$$\mu_1 \left(\frac{\partial u^{in}}{\partial r} + \frac{\partial u_1^{(0)}}{\partial r} \right) = 0, \quad r = a, \quad -\pi < \theta < \pi, \tag{2}$$

with the appropriate radiation condition at infinity. The total stress must be continuous over the entire interface, implying

$$\mu_1 \frac{\partial u_1^{(1)}}{\partial r} = \mu_2 \frac{\partial u_2^{(1)}}{\partial r} = \begin{cases} 0, & r = a, \quad -\delta < \theta < \delta, \\ \tau(\theta), & r = a, \quad \delta < |\theta| < \pi \end{cases} \tag{3}$$

where $\tau(\theta)$ is the unknown additional stress on the neck.

The displacement continuity condition on the neck $\delta < |\theta| < \pi$ is

$$u^{in} + u_1^{(0)} + u_1^{(1)} = u_2^{(1)}, \quad r = a, \quad \delta < |\theta| < \pi. \tag{4}$$

The incident field is assumed to be a plane wave of amplitude A

$$u^{in} = A e^{ik_1 r \cos(\theta - \theta_0)} = A \sum_{n=0}^{\infty} \epsilon_n i^n J_n(k_1 r) \cos n(\theta - \theta_0), \tag{5}$$

where $\epsilon_0 = 1$, $\epsilon_n = 2$, $n > 0$, and $k_i = \omega/c_i$, $c_i = [\mu_i/\rho_i]^{1/2}$, $i = 1, 2$. The scattered field from the void is then

$$u_1^{(0)} = -A \sum_{n=0}^{\infty} \frac{\epsilon_n i^n J_n'(k_1 a)}{H_n^{(1)\prime}(k_1 a)} H_n^{(1)}(k_1 r) \cos n(\theta - \theta_0). \tag{6}$$

Finally, the additional fields $u_1^{(1)}$ and $u_2^{(1)}$ must satisfy the Helmholtz equations

$$\nabla^2 u_i^{(1)} + k_i^2 u_i^{(1)} = 0, \quad i = 1 \text{ or } 2, \tag{7}$$

in the respective regions, where ∇^2 is the $2D$ Laplacian.

3 The Symmetric Solution

The total field may be separated into parts that are either symmetric or antisymmetric about $\theta = 0$. We concern ourselves here only with the symmetric part since the treatment of the antisymmetric part is very similar (Yang and Norris, 1991). The symmetric part of the additional fields may be expressed, using equation (3), as

$$u_{1s}^{(1)} = \sum_{n=0}^{\infty} E_n^{(s)} H_n^{(1)}(k_1 r) \cos n\theta,$$

$$u_{2s}^{(1)} = \sum_{n=0}^{\infty} \frac{\mu_1 k_1 E_n^{(s)} H_n^{(1)\prime}(k_1 a)}{\mu_2 k_2 J_n'(k_2 a)} J_n(k_2 r) \cos n\theta. \tag{8}$$

Use of (3), (8), and the orthogonality of the cosine functions gives

$$E_n^{(s)} = \frac{\epsilon_n}{\pi \mu_1 k_1 H_n^{(1)\prime}(k_1 a)} \int_{\delta}^{\pi} \tau(\theta) \cos n\theta \, d\theta. \tag{9}$$

Substitution of (5), (6), (8), and (9) into (4), and use of the Wronskian relations (Abramowitz and Stegun, 1965), yields an integral equation for the stress

$$2iA \frac{\mu_2 k_2}{k_1 a} \sum_{n=0}^{\infty} \frac{\epsilon_n i^n \cos n\theta_0}{H_n^{(1)\prime}(k_1 a)} \cos n\theta = \sum_{n=0}^{\infty} \epsilon_n \Lambda_n \cos n\theta \int_{\delta}^{\pi} \tau(\theta') \cos n\theta' d\theta', \tag{10}$$

where

$$\Lambda_n = \frac{J_n(k_2 a)}{J_n'(k_2 a)} - \frac{\mu_2 k_2}{\mu_1 k_1} \frac{H_n^{(1)}(k_1 a)}{H_n^{(1)\prime}(k_1 a)}. \tag{11}$$

The unknown shear stress $\tau(\theta)$ can be expressed using the first kind of Chebyshev polynomials

$$\tau(\theta) = \frac{A i \mu_1 k_1}{\sqrt{1 - \left(\frac{\pi - \theta}{\epsilon} \right)^2}} \sum_{n=0}^{\infty} \beta_n^{(s)} \phi_n^{(s)}(\theta), \tag{12}$$

where (Abramowitz and Stegun, 1965)

$$\phi_n^{(s)}(\theta) = (-1)^n T_{2n}\left(\frac{\pi - \theta}{\epsilon} \right) = (-1)^n \cos\left(2n \arccos \frac{\pi - \theta}{\epsilon} \right). \tag{13}$$

Note that $\tau(\theta)$ has the correct inverse square root singularity at either end of the neck. The Chebyshev functions have the property

$$\int_{\delta}^{\pi} \frac{\phi_n^{(s)}(\theta)}{\sqrt{1 - \left(\frac{\pi - \theta}{\epsilon} \right)^2}} \cos p\theta \, d\theta = (-1)^p \frac{\pi \epsilon}{2} J_{2n}(p\epsilon), \tag{14}$$

and it is therefore possible to reduce (10) to a system of equations for the coefficients $\beta_n^{(s)}$

$$\sum_{n=0}^{\infty} Q_{mn}^{(s)} \beta_n^{(s)} = N_m^{(s)}, \quad m = 0, 1, 2, \ldots, \tag{15}$$

where

$$Q_{mn}^{(s)} = \frac{1}{2} \sum_{p=0}^{\infty} \epsilon_p \Lambda_p J_{2m}(p\epsilon) J_{2n}(p\epsilon),$$

$$N_m^{(s)} = \frac{2}{\pi \epsilon k_1 a} \frac{\mu_2 k_2}{\mu_1 k_1} \sum_{p=0}^{\infty} \epsilon_p \frac{(-i)^p J_{2m}(p\epsilon)}{H_p^{(1)\prime}(k_1 a)} \cos p\theta_0. \tag{16}$$

Downloaded 03 May 2010 to 171.66.16.248. Redistribution subject to ASME license or copyright; see http://www.asme.org/terms/Terms_Use.cfm

In practice, the system of equations (15) is solved by truncation. Also, as we will see below, the term $Q_{00}^{(s)}$ is singular at low frequencies. In order to avoid an ill-conditioned system in the static limit, we eliminate $\beta_0^{(s)}$ using the equation for $m = 0$, and then solve the resulting system.

4 The Scattered Radiation Pattern

The scattered symmetric displacement due to the debond follows from (8), (9), (12), and (14), and the far-field approximation for $u_{1s}^{(1)}$ becomes

$$u_{1s}^{(1)} \sim \left(\frac{8\pi}{k_1 r}\right)^{1/2} F_s^{(1)}(\theta,\theta_0) e^{i\left(k_1 r - \frac{\pi}{4}\right)}, \quad k_1 r \to \infty, \tag{17}$$

where the radiation pattern generated by the debond is

$$F_s^{(1)}(\theta,\theta_0) = \frac{Ai\epsilon}{4\pi}\left(\frac{\beta_0^{(s)}}{H_0^{(1)\prime}(k_1 a)} + 2\sum_{p=1}^{\infty} \frac{i^p \cos p\theta}{H_p^{(1)\prime}(k_1 a)} \sum_{n=1}^{\infty} \beta_n^{(s)} J_{2n}(p\epsilon)\right). \tag{18}$$

At low frequencies such that $k_1 a \ll 1$, $k_2 a \ll 1$, but for fixed $\epsilon = O(1)$, it may be shown that $\beta_0^{(s)} = O(k_2 a)$, and therefore $\beta_0^{(s)} \to 0$ as $k_1 a \to 0$ in agreement with the static condition that the net force acting on the fiber is zero. The net moment on the fiber is automatically zero for the symmetric solution and may be shown to be $O(k_1 a)$ for the antisymmetric solution. The symmetric far-field becomes, in this limit,

$$F_s^{(1)}(\theta,\theta_0) = \frac{Ai}{4}(k_1 a)^2\left(\frac{\rho_2}{2\rho_1} + \epsilon \cos\theta \sum_{n=1}^{\infty} \tilde{\beta}_n^{(s)} J_{2n}(\epsilon)\right) + o(k_1 a)^2. \tag{19}$$

where the $\tilde{\beta}_n^{(s)}$ are real valued and satisfy

$$\sum_{n=1}^{\infty} \tilde{Q}_{mn}^{(s)} \tilde{\beta}_n^{(s)} = \frac{-2\mu_2}{\epsilon(\mu_1+\mu_2)} \cos\theta_0 J_{2m}(\epsilon), \quad m = 1,2,\ldots, \tag{20}$$

and

$$\tilde{Q}_{nm}^{(s)} = \sum_{p=1}^{\infty} \frac{1}{p} J_{2m}(p\epsilon) J_{2n}(p\epsilon). \tag{21}$$

It should be noted that the monopole term in (19), i.e., the term involving the densities, comes from the low frequency limit of $\beta_0^{(s)}$, which is discussed in the next section.

A system of equations very similar to (20) was encountered in the COD formulation of Yang and Norris (1991) for the same problem, but in that case the matrix $\tilde{Q}$ and the right-hand side of the system both depended upon $\delta = \pi - \epsilon$ rather than ϵ. Furthermore, the system corresponding to (20) was previously obtained for the antisymmetric part of the solution. However, based on the analogy with the equations in Yang and Norris (1991) it can be shown that the sum in equation (19) may be simplified, and a similar result is found for the antisymmetric far-field pattern $F_a^{(1)}(\theta, \theta_0)$. Combining these results we find that the total radiation pattern in the low frequency limit is in complete agreement with the quasi-static far-field obtained by Coussy (1982) using the purely static solution discussed below.

5 Stress Intensity Factors and Resonance

The dynamic stress intensity factor at the junction of the neck and debond is defined as

$$KI_d = \lim_{\theta \to \delta^+} [2a(\theta-\delta)]^{\frac{1}{2}} \tau(\theta), \tag{22}$$

and so it follows from (12) and (13) that

$$\frac{KI_d^{(s)}}{\tau_0\sqrt{a}} = \sqrt{\epsilon} \sum_{n=1}^{\infty} (-1)^n \beta_n^{(s)}, \tag{23}$$

where $\tau_0 = i\mu_1 k_1 A$ is the stress applied at infinity in the static limit, and in general, $\beta_n^{(s)}$ are frequency dependent and determined from (15). The shear stress $\tau_s(\theta)$ along the bonded interface for the corresponding static problem may be expressed in closed form using the solution obtained by Tamate and Yamada (1969).

$$\tau_s(\theta) = \frac{\tau_0\mu_2}{\mu_1+\mu_2} \frac{\sin\left(\frac{3\theta}{2}-\theta_0\right) - \cos\delta \sin\left(\frac{\theta}{2}-\theta_0\right)}{\sqrt{\sin\frac{\theta+\delta}{2}\sin\frac{\theta+\delta}{2}}} \operatorname{sgn}(\theta), \quad \delta < |\theta| < \pi. \tag{24}$$

The static SIF follows from equation (22) as $KI_s = KI_s^{(a)} + KI_s^{(a)}$, with symmetric and antisymmetric parts

$$\frac{KI_s^{(s)}}{\tau_0\sqrt{a}} = \frac{2\mu_2}{\mu_2+\mu_2}\sqrt{\sin\epsilon}\sin\frac{\epsilon}{2}\cos\theta_0,$$

$$\frac{KI_s^{(a)}}{\tau_0\sqrt{a}} = \frac{2\mu_2}{\mu_1+\mu_2}\sqrt{\sin\epsilon}\cos\frac{\epsilon}{2}\sin\theta_0. \tag{25}$$

We note in particular that for fixed θ_0, $KI_s^{(s)} = O(\epsilon^{3/2})$ and $KI_s^{(a)} = O(\epsilon^{1/2})$ as $\epsilon \to 0$.

5.1 The Short Neck Approximation. As the fiber becomes almost separated from the matrix ($\epsilon \ll 1$), equation (15) can be simplified quite a bit. Considering m or $n > 0$,

$$Q_{mn}^{(s)} = \sum_{p=1}^{\left[\frac{1}{\sqrt{\epsilon}}\right]-1} \Lambda_p J_{2m}(p\epsilon) J_{2n}(p\epsilon) + \sum_{\left[\frac{1}{\sqrt{\epsilon}}\right]}^{\infty} \Lambda_p J_{2m}(p\epsilon) J_{2n}(p\epsilon), \tag{26}$$

where $\left[\frac{1}{\sqrt{\epsilon}}\right]$ is the integer part of $\frac{1}{\sqrt{\epsilon}}$. The first sum is $O(\epsilon^{m+n})$, while the infinite sum simplifies by using asymptotic expansion for large order Bessel and Hankel functions, to give

$$\sum_{\left[\frac{1}{\sqrt{\epsilon}}\right]}^{\infty} \Lambda_p J_{2m}(p\epsilon) J_{2n}(p\epsilon) = k_2 a\left(1+\frac{\mu_2}{\mu_1}\right)\int_0^{\infty} \frac{J_{2m}(\nu)J_{2n}(\nu)}{\nu}\, d\nu + O(\epsilon),$$

and the integral may be found in Abramowitz and Stegun (1965). In summary, we have the asymptotic results for $\epsilon \ll 1$ that

$$Q_{mn}^{(s)} = k_2 a\left(1+\frac{\mu_2}{\mu_1}\right)\frac{\delta_{mn}}{4m} + O(\epsilon),$$

$$N_m^{(s)} = O(\epsilon^{2m-1}), \quad m > 0, \tag{27}$$

and from (15) and (27),

$$\beta_0^{(s)} = \frac{N_0^{(s)}}{Q_{00}^{(s)}} + O(\epsilon), \quad \beta_m^{(s)} = O(\epsilon^{2m-1}), \quad m > 0. \tag{28}$$

Downloaded 03 May 2010 to 171.66.16.248. Redistribution subject to ASME license or copyright; see http://www.asme.org/terms/Terms_Use.cfm

Equation (28) indicates that the response of the fiber when the neck is small is governed principally by the first term in the expansion (12) for the stress $\tau(\theta)$. Since the first Chebyshev function $\phi_0^{(s)}$ is unity, it follows that the approximate stress in this regime is

$$\tau(\theta) = \frac{\tau_0 \beta_0^{(s)}}{\sqrt{1 - \left(\frac{\pi - \theta}{\epsilon}\right)^2}}. \tag{29}$$

The relatively simple form of $\beta_0^{(s)}$ in (28) means that the resonance reported by Yang and Norris (1991) and illustrated in the numerical examples below is governed by this expression only, rather than the full system of equations (15). It is also clear, if not *a priori* then certainly *a posteriori*, that the resonance must occur at asymptotically small values of $k_1 a$. Therefore, in order to further understand the resonance, we further approximate $\beta_0^{(s)}$ as a doubly asymptotic expansion in both ϵ and $k_1 a$. Expansion of the numerator and denominator in (28) for low frequencies yields

$$\beta_0^{(s)} \sim \frac{ik_2 a}{\epsilon} \frac{\mu_2 k_2}{\mu_1 k_1} f(k_1 a, \epsilon, \theta_0), \tag{30}$$

where

$$f(k_1 a, \epsilon, \theta_0) = \frac{1 - 2ik_1 a \cos\theta_0}{1 - \frac{\mu_2}{\mu_1}(k_2 a)^2 \left[\left(1 + \frac{\mu_1}{\mu_2}\right) S(\epsilon) + \frac{\mu_1}{8\mu_2} - \frac{\gamma}{2} - \frac{1}{2}\log\frac{k_1 a}{2} + i\frac{\pi}{4}\right]}, \tag{31}$$

$$S(\epsilon) = \sum_{p=1}^{\infty} \frac{J_0^2(p\epsilon)}{p}, \tag{32}$$

and γ is Euler's constant. We note that f is asymptotic to unity for $\epsilon = O(1)$, in which case (30) reproduces the low-frequency behavior of $\beta_0^{(s)}$ discussed in Section 4. However, in the doubly asymptotic regime of $\epsilon \ll 1$, $k_1 a \ll 1$, f depends upon ϵ through $S(\epsilon)$ which can be simplified by first using the identity $J_0(x) = \pi^{-1} \int_0^{\pi} \cos(x \sin t) dt$. The sum over p then follows from equation (27.8.6) of Abramowitz and Stegun (1965) to give

$$S(\epsilon) = \frac{-1}{2\pi^2} \int_0^{\pi} \int_0^{\pi} \left\{ \log\left[2 \sin\frac{\epsilon}{2} |\sin t - \sin s|\right] + \log\left[2 \sin\frac{\epsilon}{2}(\sin t + \sin s)\right] \right\} ds dt.$$

Expanding the integrand in ϵ and using equation (4.226.1) of Gradshteyn and Ryzhik (1980) yields

$$S(\epsilon) = \log\left(\frac{2}{\epsilon}\right) + \frac{\epsilon^2}{6} + O(\epsilon^4). \tag{33}$$

The term $S(\epsilon)$ is asymptotically large and therefore f may vary considerably from unity *even as the frequency goes to zero*, in stark contrast to the quasi-static behavior based on the static solution.

This low-frequency effect is manifested as the resonance discussed in the Introduction. To a first approximation, the resonance occurs when the real part of the denominator in (31) vanishes, i.e., at frequency $k_1 a$ which satisfies

$$\left(1 + \frac{\mu_2}{\mu_1}\right) \log\frac{2}{\epsilon} = \frac{1}{(k_2 a)^2} - \frac{1}{8} + \frac{\mu_2}{2\mu_1}\left[\gamma + \log\left(\frac{k_1 a}{2}\right)\right]. \tag{34}$$

This reduces to equation (20) of Burrows (1985) when the material parameters are equal on either side of the neck ($\mu_1 = \mu_2$, $\rho_1 = \rho_2$). The leading-order approximation for $\epsilon \ll 1$ is

$$k_2 a = \beta^{-1}\left[\log\left(\frac{2}{\epsilon}\right)\right]^{-\frac{1}{2}}, \quad \beta = \sqrt{1 + \frac{\mu_2}{\mu_1}}, \tag{35}$$

and so the resonant frequency thus goes to zero very slowly as $\epsilon \to 0$. Yang and Norris (1991) proposed a heuristic spring-mass model of the low-frequency resonance which predicted the resonant frequency in the same form as (35), but the simplicity of the model did not permit the explicit evaluation of β in (35), which was originally cast as an unknown constant. However, it is clear that the model does give the correct leading-order behavior. Furthermore, the precise form of β means that the resonant frequency can be simply modeled as the frequency of a spring-mass system with mass $m = 2\rho_2 \pi a^2$, which is twice the mass of a unit length of the fiber. This is not surprising when one considers that as the fiber oscillates, an equivalent inertial mass of matrix oscillates out of phase. The effective stiffness K of the oscillator follows from Yang and Norris (1991) as the ratio F/w, where F is a uniformly applied axial force over an *isolated* fiber of shear modulus equal to the harmonic mean of the matrix and fiber moduli, i.e., $\mu^{-1} = \frac{1}{2}(\mu_1^{-1} + \mu_2^{-1})$. An equal but opposite force is distributed across the portion of the boundary corresponding to the neck such that the applied shear has the correct inverse square root singularity, and w is the resultant average static displacement of the fiber in the direction of the axial force. The resonant frequency predicted by this model is the frequency of equation (35). It is interesting to note that simple, equivalent-circuit models for the harbor resonance phenomenon have been proposed and discussed at length by Miles (1971). The present phenomenon is, however, probably better understood in terms of mechanical lumped-parameter models.

6 Numerical Results and Discussion

The stress and stress intensity factor have been computed for the matrix/fiber combination of epoxy and glass: $\mu_1 = 1.28$ GPa, $\rho_1 = 1.25$ gm/cc, and $\mu_2 = 29.9$ GPa, $\rho_2 = 2.55$ gm/cc. The calculations were performed by truncating the infinite system of equations (15), and were checked by (*i*) requiring that the optical theorem was satisfied to a given degree of tolerance, and (*ii*) by comparing the results with those obtained using the COD method of Yang and Norris (1991). The latter method was found to be numerically fast for small crack sizes, but required larger and larger truncation limits as δ approached 180 deg. For reasons mentioned previously, the system (15) is in a sense the dual of that obtained by Yang and Norris (1991), and not surprisingly, we found the system required only a small truncation limit for small necks but became unwieldy for small cracks.

The ratio of the dynamic stress intensity factor to the static SIF is plotted in Figs. 2 and 3 for different neck widths. The corresponding quasi-static theory would predict a constant SIF at such low frequencies as those considered in the figures, and normally one would not expect any appreciable change until the dimensionless frequency $k_1 a$ is of order unity. However, the dynamic SIFs in Figs. 2 and 3 clearly exhibit a resonance behavior at a frequency that decreases with ϵ. Note in particular the enormous magnification of the dynamic SIF at resonance, as compared with the static prediction.

The predictions based upon the doubly asymptotic theory of Section 5 are compared with the exact computations in Figs. 4 and 5. It should be noted that the asymptotic theory contains no free parameters. The agreement between the full, numerically intensive computations, and the simple asymptotic theory is excellent, and appears to be reasonable even when both ϵ and $k_1 a$ are of order unity. In fact, the leading-order approximation of equation (35) turns out to be a very good indicator of the resonance frequency. We note that the magnitude of the dynamic SIF becomes unbounded as the neck width vanishes, in stark contrast to the static prediction that the static SIF goes to zero as $\epsilon^{1/2}$ if the applied stress has an antisymmetric

Downloaded 03 May 2010 to 171.66.16.248. Redistribution subject to ASME license or copyright; see http://www.asme.org/terms/Terms_Use.cfm

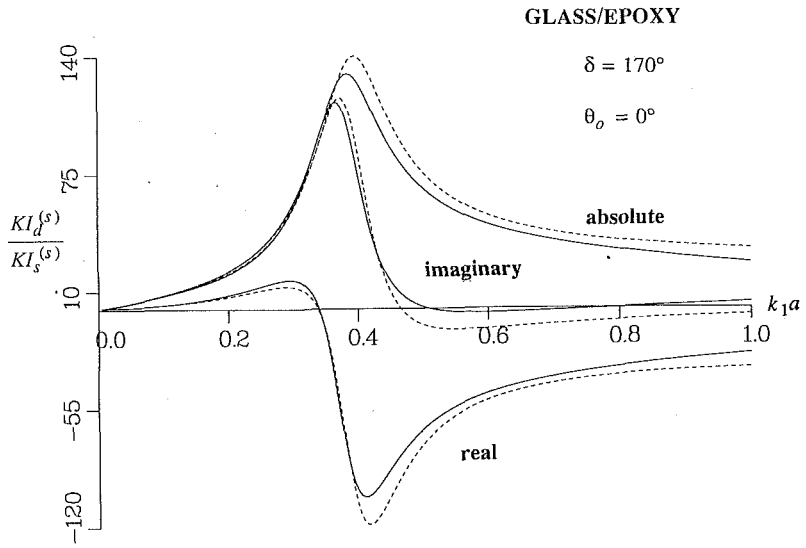

Fig. 2 The complex-valued ratio of the dynamic stress intensity factor to the static SIF versus nondimensional frequency k_1a for glass/epoxy, δ = 170 deg (ϵ = 10 deg) and θ_0 = 0. The solid curves are the results of the "exact" numerical calculations, and the dashed curves follow from the asymptotic approximation of equation (37).

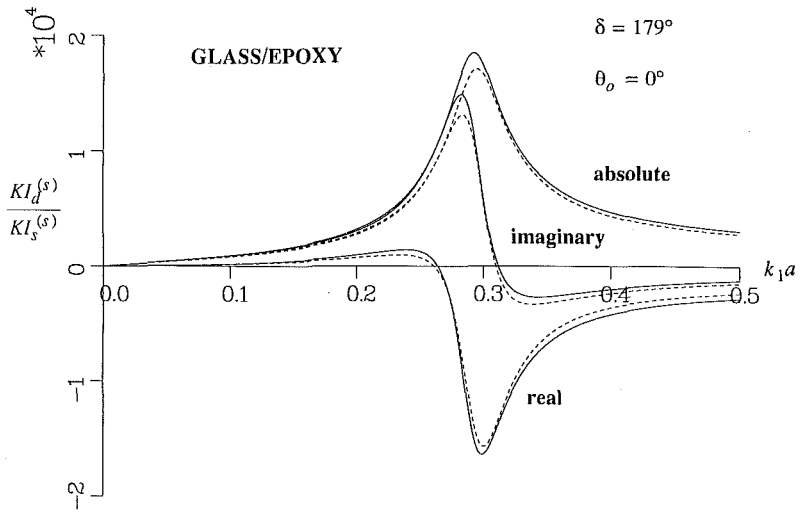

Fig. 3 The same as Fig. 2, but for δ = 179 deg (ϵ = 1 deg)

component and as $\epsilon^{3/2}$ if not. Also, the real part of the SIF at resonance achieves a large but negative value, i.e. it is 180 deg out of phase with the static SIF.

The accuracy of the asymptotic approximation supports the conclusion that stress field $\tau(\theta)$ on the neck is governed mainly by the first term in the expansion (12) when $\epsilon \ll 1$ *and* $k_1a \ll 1$. For fixed ϵ but $k_1a \to 0$, the exact theory reproduces the static stress $\tau_s(\theta)$ of equation (24), and as discussed in Section 4, the term $\beta_0^{(s)} \to 0$, while the remaining $\beta_n^{(s)}$, $n \geq 1$, are of order unity. Therefore, the purely static and the doubly asymptotic limits are in a sense complementary, and we are justified in combining both to form a new approximation uniformly valid in both asymptotic regimes. We call this the *quasi-dynamic* approximation, since it goes beyond the quasi-static approximation based on the static solution, but is not a fully dynamic solution. When the relevant terms are combined, we obtain for the quasi-dynamic stress

$$\tau_{qd}(\theta) = \tau_s(\theta) + \frac{\tau_0 i k_2 a}{\sqrt{\epsilon^2 - (\pi - \theta)^2}} \frac{\mu_2 k_2}{\mu_1 k_1} f(k_1a, \epsilon, \theta_0), \quad (36)$$

where f is defined in (31) and (33). The quasi-dynamic stress intensity factor KI_{qd} is thus

$$KI_{qd} = KI_s + \tau_0 i k_2 a \left(\frac{a}{\epsilon}\right)^{1/2} \frac{\mu_2 k_2}{\mu_1 k_1} f(k_1a, \epsilon, \theta_0). \quad (37)$$

These expressions are uniformly valid for both small ϵ and k_1a, and obviously contain the resonance features of Figs. 2–5. The associated scattered field may be easily computed and it turns out that the far-field pattern is changed only in the monopole term.

In conclusion, we have obtained simple but accurate expressions that fully describe the low-frequency resonant behavior. The numerical and analytical results demonstrate that the stress intensity factor at the neck of the fiber can be greatly magnified in comparison with the static prediction. Thus, for instance, failure predictions based solely upon a static analysis could be quite erroneous.

Acknowledgment

We are grateful to a reviewer for the asymptotic approximation of equation (33).

Downloaded 03 May 2010 to 171.66.16.248. Redistribution subject to ASME license or copyright; see http://www.asme.org/terms/Terms_Use.cfm

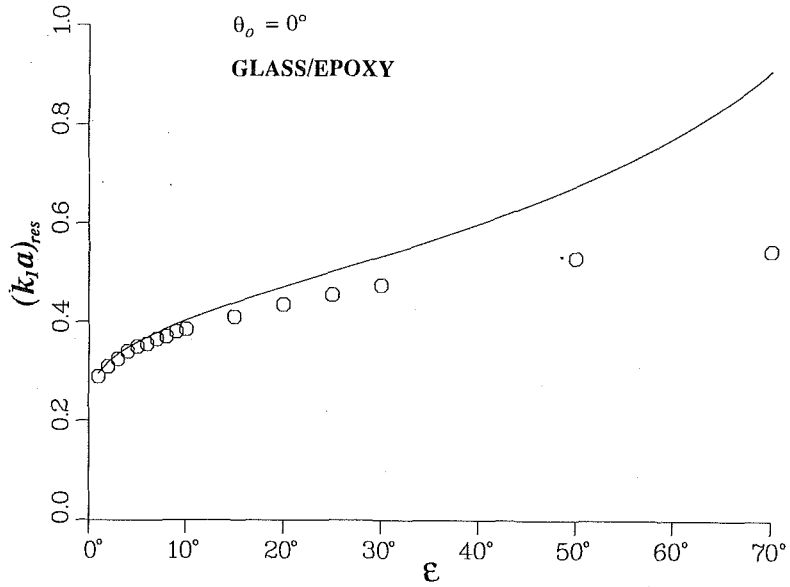

Fig. 4 The dimensionless resonant frequency according to the approximate theory, equation (34), compared with the frequency at which the magnitude of the dynamic SIF achieves a maximum in the exact calculations

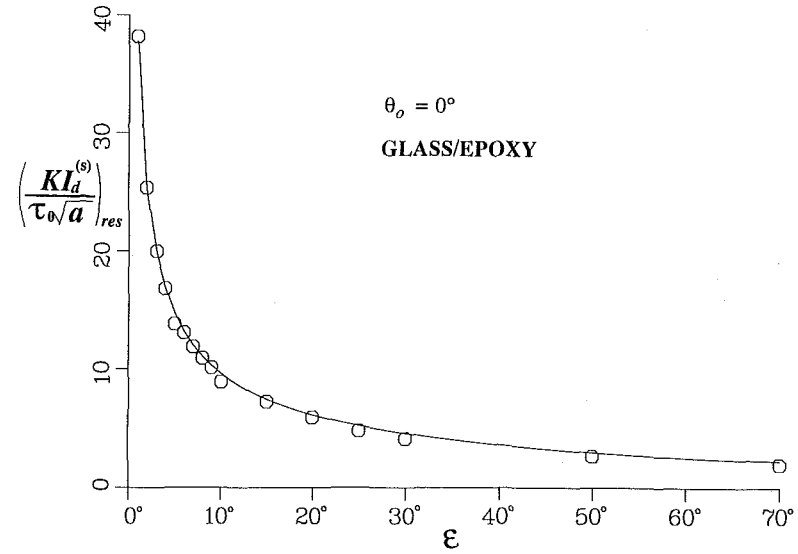

Fig. 5 A comparison of the magnitude of the dimensionless dynamic stress intensity factor at resonance versus the neck angular width ϵ. The solid curve is calculated using the asymptotic expansion of the stress on the neck, equations (12) and (30)–(34). The circles are the numerical computations of the exact solution, equation (15).

References

Abramowitz, M., and Stegun, I. A., 1965, *Handbook of Mathematical Functions*, Dover Publications, New York.

Boström, A., 1987, "Elastic Wave Scattering from an Interface Crack: Antiplane Strain," ASME JOURNAL OF APPLIED MECHANICS, Vol. 55, pp. 503–508.

Burrows, A., 1985, "Waves Incident on a Circular Harbour," *Proceeding of the Royal Society of London*, Vol. A401, pp. 349–371.

Coussy, O., 1982, "Scattering of SH-Waves by a Cylindrical Inclusion Presenting an Interfacial Crack," *C. R. Acad Sc. Paris*, Vol. 295, pp. 1043–1046.

Gradshteyn, I. S., and Ryzhik, I. B., 1980, *Tables of Integrals, Series, and Products*, Academic Press, New York.

Krenk, S., and Schmidt, H., 1982, "Elastic Wave Scattering by a Circular Crack," *Philosophical Transactions of the Royal Society of London*, Vol. A308, pp. 167–198.

Miles, J. W., 1971, "Resonant Response of Harbors: An Equivalent-Circuit Analysis," *Journal of Fluid Mechanics*, Vol. 46, pp. 241–265.

Tamate, O., and Yamada, T., 1969, "Stress in an Infinite Body with a Partially Bonded Circular Cylindrical Inclusion under Longitudinal Shear," *Technology Reports, Tohoku University*, Vol. 34, pp. 161–171.

Yang, Y., and Norris, A. N., 1991, "Shear Wave Scattering from a Debonded Fibre," *Journal of the Mechanics and Physics of Solids*, Vol. 39, pp. 273–294.

Downloaded 03 May 2010 to 171.66.16.248. Redistribution subject to ASME license or copyright; see http://www.asme.org/terms/Terms_Use.cfm

F. Erdogan
Department of Mechanical Engineering and Mechanics,
Lehigh University,
Bethlehem, PA 18015
Fellow ASME

A. C. Kaya[1]
Associate Professor,
Department of Mechanical Engineering,
Middle East Technical University,
Ankara, Turkey

P. F. Joseph
Department of Mechanical Engineering and Mechanics,
Lehigh University,
Bethlehem, PA 18015

The Crack Problem in Bonded Nonhomogeneous Materials

In this paper the plane elasticity problem for two bonded half-planes containing a crack perpendicular to the interface is considered. The primary objective of the paper is to study the effect of very steep variations in the material properties near the diffusion plane on the singular behavior of the stresses and stress intensity factors. The two materials are, thus, assumed to have the shear moduli μ_0 and $\mu_0 exp(\beta x)$, $x = 0$ being the diffusion plane. Of particular interest is the examination of the nature of stress singularity near a crack tip terminating at the interface where the shear modulus has a discontinuous derivative. The results show that, unlike the crack problem in piecewise homogeneous materials for which the singularity is of the form $r^{-\alpha}$, $0<\alpha<1$, in this problem the stresses have a standard square root singularity regardless of the location of the crack tip. The nonhomogeneity constant β has, however, considerable influence on the stress intensity factors.

1 Introduction

From the viewpoint of mechanical failure in diffusion bonded materials and other adhesively bonded structures one of the most important problems is, along with the fracture characterization of the interfacial zones, a proper mechanical modeling of these zones and the development of suitable techniques for solving the related crack problems. The significance of the problem lies in the fact that (*i*) regardless of the mechanism of binding at the atomic level, in many cases there is always a thermodynamically stable and readily distinguishable region between the two homogeneous materials, (*ii*) the interfacial regions are generally locations of higher concentration of stresses and microflaws, and (*iii*) in most material pairs the fracture toughness and the subcritical crack growth resistance of the interfacial zone tend to be lower than that of adjacent homogeneous materials. The standard continuum solid mechanics model for bonded materials has been the usual piecewise homogeneous medium with an ideal interface across which the physical properties of the medium exhibit a jump discontinuity. For many applications this model is quite adequate. However, there are two groups of fracture related problems in which the model leads to some physically anomalous results and may require modifications. The first is the complex power singularity at the tip of an interface crack giving oscillations in stresses and crack opening displacements very near the crack tip (e.g., Muskhelishvili, 1953a; Erdogan, 1965; England, 1965; Rice and Sih, 1965). A crack-tip contact model has been proposed to eliminate these oscillations within the context of the linear elastic theory (Comninou, 1977; Atkinson, 1977).

The second problem deals with a crack intersecting the interface. In this case it is known that the stress state has a power singularity of the form $r^{-\alpha}$ with $\alpha \neq 1/2$ and $0<\alpha<1$ (Cook and Erdogan, 1972; Erdogan and Cook, 1974; Erdogan and Biricikoglu, 1973). The physically objectionable feature of this result is that because of the nonsquare-root singularity the propagating crack would not remain self-similar, and consequently, the standard energy balance-based fracture mechanics techniques would not be applicable to the problems in bonded materials that involve cracks intersecting the interfaces.

The ideal interface model may be improved by considering the interdiffusion nature of the bonding process. In some cases the resulting reaction zone may be very thin and in others it may consist of intermediate phases or intermetallics with mechanical properties substantially different than the adjacent materials. In either case the microprobe line scans seem to indicate that in the interfacial region the percent distribution of atoms from one phase to the next is very steep but, nevertheless, continuous. Thus, in diffusion bonded materials one could replace the ideal interface requiring a jump discontinuity in physical properties across the boundary by a thin nonhomogeneous layer with highly steep variations in the mechanical properties. One may further assume that the elastic parameters of the composite medium are continuous functions of the space coordinates throughout the medium having discontinuous derivatives along the boundaries of the interfacial region. The analytical questions raised by this material model concern the effect of the material nonhomogeneity, particularly of the "kinks" in the distribution of the elastic parameters on the nature of the crack-tip singularities. The crack problem for an

[1]Presently at the General Electric Company, Corporate R&D, Schenectady, NY 12301.

Contributed by the Applied Mechanics Division of THE AMERICAN SOCIETY OF MECHANICAL ENGINEERS for presentation at the Joint Applied Mechanics/Bioengineering Conference, Ohio State University, Columbus, Ohio, June 16-19, 1991.

Discussion on this paper should be addressed to the Technical Editor, Prof. Leon M. Keer, The Technological Institute, Northwestern University, Evanston, IL 60208, and will be accepted until two months after final publication of the paper itself in the JOURNAL OF APPLIED MECHANICS. Manuscript received by the ASME Applied Mechanics Division, Nov. 22, 1988; final revision, Feb. 12, 1990.

Paper No. 91-APM-17.

Copyright © 1991 by ASME
Downloaded 03 May 2010 to 171.66.16.248. Redistribution subject to ASME license or copyright; see http://www.asme.org/terms/Terms_Use.cfm

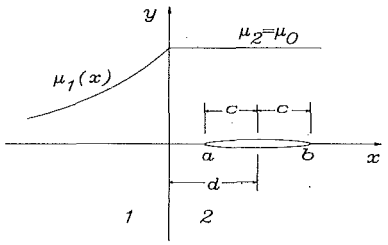

Fig. 1 The crack geometry in bonded materials

infinite nonhomogeneous medium was considered by Delale and Erdogan (1983) who showed that, as expected, the standard square root singularity at the crack tips is maintained if the material parameters are continuous and differentiable functions.

Regarding the physical anomalies that follow from the piecewise homogeneous material model, the first question deals with the nature of singularities for cracks lying along the kink lines of the elastic property distribution. This question was recently considered by Delale and Erdogan (1988a) who showed that for these "interface" cracks not only the square root behavior of singularity but also the angular distribution of stresses very near the crack tips turn out to be identical to that found for the homogeneous materials. Further results for a crack in a nonhomogeneous interfacial zone are given by Delale and Erdogan (1988b). The second basic question in introducing the nonhomogeneous interfacial zone model is concerned with a crack intersecting the interface, specifically with the nature of stress singularity for a crack terminating at the kink line of the elastic property distribution. The problem under antiplane shear loading was considered by Erdogan (1985) who showed that the square root nature of stress singularity remains unaffected by the material nonhomogeneity provided the shear modulus is a continuous but not necessarily a differentiable function near and at the crack tip. The behavior of stress singularity in the corresponding plane-strain problem is one of the remaining unresolved questions that will be considered in this paper.

2 Formulation of the Crack Problem

Consider the plane elasticity problem shown in Fig. 1 where a homogeneous half-plane containing a crack perpendicular to the boundary is bonded to a nonhomogeneous half-plane. For the purpose of examining the nature of crack-tip singularity, and for studying the effect of material nonhomogeneity on the stress intensity factors, it will be assumed that the elastic properties of the two materials are given by

$$\mu_1(x)=\mu_0 e^{\beta x},\ \mu_2=\mu_0,\ \kappa_1=\kappa_2=\kappa \tag{1}$$

where μ is the shear modulus, $\kappa=3-4\nu$ for plane strain, and $\kappa=(3-\nu)/(1+\nu)$ for generalized plane stress, ν being the Poisson's ratio. With equation (1) the Navier's equations may be expressed as

$$\nabla^2 u_i+\frac{2}{\kappa-1}\left(\frac{\partial^2 u_i}{\partial x^2}+\frac{\partial^2 v_i}{\partial x\partial y}\right)+2\beta\frac{\partial u_i}{\partial x}+\beta\left(\frac{3-\kappa}{\kappa-1}\right)\left(\frac{\partial u_i}{\partial x}+\frac{\partial v_i}{\partial y}\right)=0,$$

$$\nabla^2 v_i+\frac{2}{\kappa-1}\left(\frac{\partial^2 v_i}{\partial y^2}+\frac{\partial^2 u_i}{\partial x\partial y}\right)+\beta\left(\frac{\partial u_i}{\partial y}+\frac{\partial v_i}{\partial x}\right)=0,\ (i=1,2) \tag{2a,b}$$

where u_i and v_i, $(i=1,2)$ are the x and y components of the displacement and $\beta\neq 0$ for $i=1$ or $x<0$ and $\beta=0$ for $i=2$ or $x>0$ (Fig. 1). Referring to Fig. 1, it will be assumed that $y=0$ plane is a plane of symmetry for the external loads as well as the geometry. It will also be assumed that the problem in the absence of the crack under the actual loading conditions has been solved and $\sigma^0_{2yy}(x,0)$ has been determined. Thus, the important results concerning the crack problem may be obtained by considering only the perturbation problem for $y>0$ in which the normal traction $p(x)=-\sigma^0_{2yy}(x,0)$ is the only external load. Equation (2) must then be solved under the following conditions:

$$u_1(0,y)=u_2(0,y),\ v_1(0,y)=v_2(0,y),\ 0<y<\infty, \tag{3a,b}$$

$$\sigma_{1xx}(0,y)=\sigma_{2xx}(0,y),\ \sigma_{1xy}(0,y)=\sigma_{2xy}(0,y),\ 0<y<\infty, \tag{4a,b}$$

$$v_1(x,0)=0,\ \sigma_{1xy}(x,0)=0,\ -\infty<x<0, \tag{5a,b}$$

$$\sigma_{2xy}(x,0)=0,\ 0<x<\infty, \tag{6}$$

$$v_2(x,0)=0,\ 0<x<a,\ b<x<\infty,$$

$$\sigma_{2yy}(x,+0)=p(x),\ a<x<b. \tag{7a,b}$$

The solution of equation (2) may now be written as

$$u_1(x,y)=\frac{2}{\pi}\int_0^\infty f(x,\alpha)\cos\alpha y d\alpha,$$

$$v_1(x,y)=\frac{2}{\pi}\int_0^\infty g(x,\alpha)\sin\alpha y d\alpha,\quad -\infty<x<0,\ 0<y<\infty, \tag{8a,b}$$

$$u_2(x,y)=\frac{2}{\pi}\int_0^\infty f_1(x,\alpha)\cos\alpha y d\alpha+\frac{1}{2\pi}\int_{-\infty}^\infty f_2(y,\alpha)e^{-i\alpha x}d\alpha,$$

$$v_2(x,y)=\frac{2}{\pi}\int_0^\infty g_1(x,\alpha)\sin\alpha y d\alpha+\frac{1}{2\pi}\int_{-\infty}^\infty g_2(y,\alpha)e^{-i\alpha x}d\alpha,\ 0<x<\infty,\ 0<y<\infty. \tag{9a,b}$$

By substituting from (8) into (2) it can be shown that

$$f(x,\alpha)=\sum_{j=1}^4 m_j D_j(\alpha)e^{n_j x},\ g(x,\alpha)=\sum_{j=1}^4 D_j(\alpha)e^{n_j x}, \tag{10a,b}$$

where $D_1,\ldots,D_4$ are unknown, $n_1,\ldots,n_4$ are the roots of the characteristic equation

$$n^4+2\beta n^3+(\beta^2-2\alpha^2)n^2-2\beta\alpha^2 n+\left(\frac{3-\kappa}{1+\kappa}\right)\beta^2\alpha^2+\alpha^4=0, \tag{11}$$

and $m_1,\ldots m_4$ are given by

$$m_j=\frac{n_j^2+\beta n_j-(1+d_0)\alpha^2}{(d_0 n_j+\beta)\alpha},\ d_0=\frac{2}{\kappa-1},\ j=1,\ldots,4. \tag{12}$$

By rewriting (11) in the following form

$$(n^2+\beta n-\alpha^2)^2+\left(\frac{3-\kappa}{1+\kappa}\right)\beta^2\alpha^2=0, \tag{13}$$

the roots may be obtained as

$$n_1=\frac{1}{2}(-\beta+R\cos\gamma)+\frac{i}{2}R\sin\gamma,\ n_2=\bar{n}_1, \tag{14a,b}$$

$$n_3=\frac{1}{2}(-\beta-R\cos\gamma)+\frac{i}{2}R\sin\gamma,\ n_4=\bar{n}_3, \tag{15a,b}$$

$$R=\left[(\beta^2+4\alpha^2)^2+16\beta^2\alpha^2\left(\frac{3-\kappa}{1+\kappa}\right)\right]^{1/4},$$

$$\tan 2\gamma=\frac{4\beta\alpha\left(\frac{3-\kappa}{1+\kappa}\right)^{1/2}}{\beta^2+4\alpha^2}, \tag{16a,b}$$

where we note that R is always positive and

$$\mathrm{Re}(n_1,n_2)>0,\ \mathrm{Re}(n_3,n_4)<0. \tag{17}$$

Observing that for the material 1 $x<0$, by using the regularity conditions at infinity we obtain

Downloaded 03 May 2010 to 171.66.16.248. Redistribution subject to ASME license or copyright; see http://www.asme.org/terms/Terms_Use.cfm

$$u_1(x,y)=\frac{2}{\pi}\int_0^\infty \sum_1^2 m_j(\alpha)D_j(\alpha)e^{n_j(\alpha)x}\cos\alpha y d\alpha,$$

$$v_1(x,y)=\frac{2}{\pi}\int_0^\infty \sum_1^2 D_j(\alpha)e^{n_j(\alpha)x}\sin\alpha y d\alpha,$$

$$-\infty<x<0,\ 0<y<\infty, \quad (18a,b)$$

$$\sigma_{1xx}(x,y)=\frac{\mu_0 e^{\beta x}}{\kappa-1}\frac{2}{\pi}\int_0^\infty \sum_1^2 [(1+\kappa)m_j n_j + (3-\kappa)\alpha]D_j e^{n_j x}\cos\alpha y d\alpha,$$

$$\sigma_{1yy}(x,y)=\frac{\mu_0 e^{\beta x}}{\kappa-1}\frac{2}{\pi}\int_0^\infty \sum_1^2 [(1+\kappa)\alpha + (3-\kappa)m_j n_j]D_j e^{n_j x}\cos\alpha y d\alpha,$$

$$\sigma_{1xy}(x,y)=\mu_0 e^{\beta x}\frac{2}{\pi}\int_0^\infty \sum_1^2 (n_j-\alpha m_j)D_j e^{n_j x}\sin\alpha y d\alpha,$$

$$-\infty<x<0,\ 0<y<\infty. \quad (19a\text{–}c)$$

Similarly, substituting from (9) into (2) and letting $\beta=0$, we find

$$u_2(x,y)=\frac{2}{\pi}\int_0^\infty [A_1+\left(x+\frac{\kappa}{\alpha}\right)A_2]e^{-\alpha x}\cos\alpha y d\alpha + \frac{1}{2\pi}\int_{-\infty}^\infty \left(\frac{1-\kappa}{2|\alpha|}+y\right)A_3 e^{-|\alpha|y-i\alpha x}d\alpha,$$

$$v_2(x,y)=\frac{2}{\pi}\int_0^\infty (A_1+A_2 x)e^{-\alpha x}\sin\alpha y d\alpha - \frac{i}{2\pi}\int_{-\infty}^\infty \left(\frac{1+\kappa}{2|\alpha|}+y\right)\frac{|\alpha|}{\alpha}A_3 e^{-|\alpha|y-i\alpha x}d\alpha,$$

$$0<x<\infty,\ 0<y<\infty, \quad (20a,b)$$

$$\frac{1}{2\mu_0}\sigma_{2xx}(x,y)=-\frac{2}{\pi}\int_0^\infty \left[\alpha A_1+\left(\alpha x+\frac{\kappa+1}{2}\right)A_2\right]e^{-\alpha x}\cos\alpha y d\alpha + \frac{i}{2\pi}\int_{-\infty}^\infty \left(\frac{|\alpha|}{\alpha}-\alpha y\right)A_3 e^{-|\alpha|y-i\alpha x}d\alpha,$$

$$\frac{1}{2\mu_0}\sigma_{2yy}(x,y)=\frac{2}{\pi}\int_0^\infty \left[\alpha A_1+\left(\alpha x+\frac{\kappa-3}{2}\right)A_2\right]e^{-\alpha x}\cos\alpha y d\alpha + \frac{i}{2\pi}\int_{-\infty}^\infty \left(\frac{|\alpha|}{\alpha}+\alpha y\right)A_3 e^{-|\alpha|y-i\alpha x}d\alpha,$$

$$\frac{1}{2\mu_0}\sigma_{2xy}(x,y)=-\frac{2}{\pi}\int_0^\infty \left[\alpha A_1+\left(\alpha x+\frac{\kappa-1}{2}\right)A_2\right]e^{-\alpha x}\sin\alpha y d\alpha - \frac{1}{2\pi}\int_{-\infty}^\infty |\alpha| y A_3 e^{-|\alpha|y-i\alpha x}d\alpha,\ 0<x<\infty,\ 0<y<\infty, \quad (21a\text{–}c)$$

where A_1, A_2, A_3 are unknown functions.

It may be seen that because of the assumed symmetry in (8) and (9), the conditions (5) and (6) are identically satisfied. The remaining five conditions (3), (4), and (7) may then be used to determine the unknowns D_1, D_2, A_1, A_2, and A_3.

3 Derivation of the Integral Equation

To reduce the problem to an integral equation we first introduce

$$\phi(x)=\frac{\partial}{\partial x}v_2(x,0),\ a<x<b. \quad (22)$$

From (22) and (20*b*) it then follows that

$$A_3(\alpha)=-\frac{2}{\kappa+1}\int_a^b \phi(t)e^{i\alpha t}dt. \quad (23)$$

The four homogeneous conditions (3) and (4) may now be used to express D_1, D_2, A_1, and A_2 in terms of ϕ, which may then be determined by using (7*b*). The expressions of D_1, D_2, A_1, and A_2 are given in Appendix A.

In considering the boundary condition (7*b*), from (21*b*) and (23) the contribution of the second term on the right-hand side of (21*b*) may easily be evaluated as follows:

$$\lim_{y\to+0}\frac{2\mu_0 i}{2\pi}\int_{-\infty}^\infty \left(\frac{|\alpha|}{\alpha}+\alpha y\right)A_3(\alpha)e^{-|\alpha|y-i\alpha x}d\alpha = \frac{4\mu_0}{\pi(\kappa+1)}\lim_{y\to+0}\int_a^b \left[\frac{t-x}{(t-x)^2+y^2}+\frac{2(t-x)y^2}{[(t-x)^2+y^2]^2}\right]\phi(t)dt = \frac{4\mu_0}{\pi(\kappa+1)}\int_a^b \frac{\phi(t)dt}{t-x}. \quad (24)$$

Evaluating the contribution coming from the first term on the right-hand side of (21*b*) by making use of the results given in Appendix A, the condition (7*b*) may now be expressed as

$$\frac{1}{\pi}\int_a^b \left[\frac{1}{t-x}+K(x,t)\right]\phi(t)dt=\frac{\kappa+1}{4\mu_0}p(x),\ a<x<b, \quad (25)$$

where the kernel K is given by

$$K(x,t)=\int_0^\infty h(\alpha,x,t)e^{-\alpha(t+x)}d\alpha, \quad (26)$$

$$h(\alpha,x,t)=h_1(\alpha)+xh_2(\alpha)+th_3(\alpha)+txh_4(\alpha), \quad (27)$$

$$h_1(\alpha)=(\kappa+1)\left[\alpha p_3(\alpha)+\frac{\kappa-3}{2}p_4(\alpha)\right],$$

$$h_2(\alpha)=(\kappa+1)\alpha p_4(\alpha),$$

$$h_3(\alpha)=(\kappa+1)\left[\alpha q_3(\alpha)+\frac{\kappa-3}{2}q_4(\alpha)\right],$$

$$h_4(\alpha)=(\kappa+1)\alpha q_4(\alpha). \quad (28a\text{–}d)$$

The functions p_3, p_4, q_3, and q_4 may also be found in Appendix A.

Before proceeding with the examination of the asymptotic behavior of the kernel $K(x,t)$, two special cases may be considered. The first is the case of $\beta=0$ for which the problem is one of a homogeneous infinite plane containing a single crack. For $\beta\to0$ it may easily be shown that $A\to\alpha$, $B\to0$, $C\to-1$, $D\to0$ (see Appendix A) and, consequently, $K(x,t)$ vanishes giving

$$\frac{1}{\pi}\int_a^b \frac{\phi(t)}{t-x}dt=\frac{1+\kappa}{4\mu_0}p(x),\ a<x<b \quad (29)$$

which is the expected result. In the second special case we let $\beta=\infty$ which, from Fig. 1 and $\mu_1(x)=\mu_0\exp(\beta x)$, $(x<0)$, is seen to correspond to $\mu_1=0$. The problem would then be one of a homogeneous half-plane having a crack perpendicular to the boundary. From (16) and (A25)–(A28) it can be shown that, for $\beta\to\infty$,

$$A\to0,\ B\to\alpha\left(\frac{3-\kappa}{1+\kappa}\right)^{1/2},\ C\to0,\ D\to\left(\frac{3-\kappa}{1+\kappa}\right)^{1/2}. \quad (30)$$

Thus, by substituting from Appendix A and (30) into (28) and (27) we obtain

$$h(\alpha,x,t)\to(2-\alpha x-3\alpha t+2\alpha^2 tx). \quad (31)$$

From (26) and (31) it then follows that

$$K(x,t)=-\frac{1}{t+x}+\frac{6x}{(t+x)^2}-\frac{4x^2}{(t+x)^3} \quad (32)$$

which is the expected half-plane result (Cook and Erdogan, 1972).

In piecewise homogeneous materials having the same crack geometry the kernel K has a form quite similar to (32), namely (Erdogan and Biricikoglu, 1973)

Downloaded 03 May 2010 to 171.66.16.248. Redistribution subject to ASME license or copyright; see http://www.asme.org/terms/Terms_Use.cfm

$$K(x,t)=\frac{b_1}{t+x}+\frac{b_2x}{(t+x)^2}+\frac{b_3x^2}{(t+x)^3} \tag{33}$$

where b_1, b_2, and b_3 are material property dependent constants. Note that if the crack tip touches the interface, i.e., for $a=0$, K would become unbounded as x and t approach zero and hence would contribute to the singular behavior of the solution. It is then clear that in order to examine the singular nature of the solution of (25), the asymptotic behavior of K must be investigated. Since the function h in (26) is integrable at $\alpha=0$ and bounded elsewhere, any possible divergence in K must be due to the asymptotic behavior of h as $\alpha\to\infty$. Referring now to Appendix B, for $\alpha\to\infty$ we obtain

$$h(\alpha,x,t)\to h_\infty(\alpha,x,t)=\frac{d_1}{\alpha}+\left(d_2+\frac{d_3}{\alpha}\right)t + \left(d_4\alpha+d_5+\frac{d_6}{\alpha}\right)tx, \tag{34}$$

where

$$d_1=\frac{\beta}{4},\ d_2=-d_4=-\frac{\beta}{1+\kappa},\ d_3=-d_5=\frac{(1-\kappa)\beta^2}{2(1+\kappa)^2},\ d_6=-\frac{\kappa(3-\kappa)\beta^3}{4(1+\kappa)^3}. \tag{35}$$

By subtracting and adding h_∞ from and to h in (26) and by evaluating the integrals, it may easily be shown that

$$K(x,t)=k_1(x,t)+k_2(x,t)+k_3(x,t), \tag{36}$$

$$k_1(x,t)=\int_0^\infty (d_2t+d_5tx+d_4\alpha tx)e^{-\alpha(t+x)}d\alpha = d_2\frac{t}{t+x}+d_5\frac{tx}{t+x}+d_4\frac{tx}{(t+x)^2}, \tag{37}$$

$$k_2(x,t)=-(d_1+d_3t+d_6tx)Ei[-\alpha_0(t+x)],$$

$$k_3(x,t)=\int_0^{\alpha_0}[h(\alpha,x,t)-(d_2t+d_5tx+d_4tx\alpha)]e^{-\alpha(t+x)}d\alpha + \int_{\alpha_0}^\infty [h(\alpha,x,t)-h_\infty(\alpha,x,t)]e^{-\alpha(t+x)}d\alpha, \tag{38}$$

where α_0 is any positive constant[2] and the exponential integral is defined by

$$Ei[-\alpha_0(t+x)]=-\int_{\alpha_0}^\infty\frac{1}{\alpha}e^{-\alpha(t+x)}d\alpha = C_0+\log\alpha_0+\log(t+x)+\sum_{k=1}^\infty\frac{(-1)^k(t+x)^k{\alpha_0}^k}{k(k!)}, \quad \alpha_0>0,\ t+x>0, \tag{39}$$

and $C_0=0.5772156649$ is the Euler's constant.

By substituting from (36)-(38) into (25) we obtain

$$\frac{1}{\pi}\int_a^b\left[\frac{1}{t-x}+(d_4-d_2)\frac{x}{t+x}-d_5\frac{x^2}{t+x}-d_4\frac{x^2}{(t+x)^2}\right]\phi(t)dt + \frac{1}{\pi}\int_a^b[d_2+d_5x+k_2(x,t)+k_3(x,t)]\phi(t)dt = \frac{\kappa+1}{4\mu_0}p(x),\ (a<x<b). \tag{40}$$

For $a>0$, equation (40) is an ordinary singular integral equation the dominant part of which has a simple Cauchy singularity. Its solution may, therefore, be expressed as (Muskhelishvili, 1953b)

$$\phi(t)=\frac{F(t)}{\sqrt{(t-a)(b-t)}},\ a<t<b, \tag{41}$$

where F is a bounded unknown function. For $a=0$, the kernel of the second term in the left-hand side of (40) can still be treated as a Fredholm kernel and would not have any contribution to the singular behavior of $\phi(t)$. To examine the first term we let

$$\phi(t)=\frac{F(t)}{t^\omega(b-t)^\eta},\ 0<t<b,\ 0<\mathrm{Re}(\omega,\eta)<1, \tag{42}$$

where F again is a bounded function. Defining the sectionally holomorphic function

$$\psi(z)=\frac{1}{\pi}\int_0^b\frac{\phi(t)}{t-z}dt, \tag{43}$$

it can be shown that (Muskhelishvili, 1953b)

$$\psi(z)=\frac{F(0)e^{i\pi\omega}}{b^\eta\sin\pi\omega}\frac{1}{z^\omega}-\frac{F(b)}{b^\omega\sin\pi\eta}\frac{1}{(z-b)^\eta}+\psi_0(z), \tag{44}$$

where $\psi_0(z)$ may have at most weaker singularities than $z^{-\omega}$ and $(z-b)^{-\eta}$ at $z=0$ and $z=b$, respectively. By using the Plemelj formulas, from (43) and (44) it can be shown that (Muskhelishvili, 1953)

$$\frac{1}{\pi}\int_0^b\frac{\phi(t)}{t-x}dt=\frac{F(0)\cot\pi\omega}{b^\eta}\frac{1}{x^\omega}-\frac{F(b)\cot\pi\eta}{b^\omega}\frac{1}{(b-x)^\eta}+\psi_1(x), \quad 0<x<b, \tag{45}$$

where at the end points the behavior of ψ_1 is the same as that of ψ_0. From (43) and (44) it can also be shown that near $x=0$ we have

$$\frac{1}{\pi}\int_0^b\frac{\phi(t)}{t+x}dt=\psi(-x)=\frac{F(0)}{b^\eta\sin\pi\omega}\frac{1}{x^\omega}+\psi_2(x),\ 0<x<b, \tag{46}$$

where at $x=0$ ψ_2 again may have at most a weaker singularity than $x^{-\omega}$. From (46) it follows that

$$\frac{1}{\pi}\int_0^b\frac{x^k\phi(t)}{t+x}dt=\frac{F(0)}{b^\eta\sin\pi\omega}x^{k-\omega}+x^k\psi_2(x),\ k=1,2,\ldots,\ 0<x<b, \tag{47}$$

$$\frac{1}{\pi}\int_0^b\frac{x^2\phi(t)}{(t+x)^2}dt=\frac{\omega F(0)}{b^\eta\sin\pi\omega}x^{1-\omega}-x^2\frac{d}{dx}\psi_2(x),\ 0<x<b. \tag{48}$$

If we now substitute from (45), (47) and (48) into (40), first multiply both sides by $(b-x)^\eta$ and let $x=b$ then by x^ω and let $x=0$, and observe that $F(0)\neq0$, $F(b)\neq0$, we find

$$\cot\pi\omega=0,\ \cot\pi\eta=0, \tag{49a,b}$$

giving $\omega=\eta=1/2$. This is an important result indicating that the solution of the problem has a square root singularity regardless of the location of the crack tip and the solution has the form as given by (41) for $a=0$ as well as $a>0$.

4 The Stress Intensity Factors

Note that equation (25) gives the expression for $\sigma_{2yy}(x,0)$ outside as well as inside the crack (where $\sigma_{2yy}(x,0)=p(x)$, $a<x<b$). Thus, by substituting from (41) into (25) a simple asymptotic analysis would show that near the crack tips we have (see, for example, Erdogan, 1985)

$$\sigma_{2yy}(x,0)=-\frac{4\mu_0}{1+\kappa}\frac{F(b)}{\sqrt{(x-b)(b-a)}}+\sigma_1(x),\ (x>b),$$

$$\sigma_{2yy}(x,0)=\frac{4\mu_0}{1+\kappa}\frac{F(a)}{\sqrt{(a-x)(b-a)}}+\sigma_2(x),\ (0<x<a), \tag{50a,b}$$

where σ_1 and σ_2 represent the part of the solution that is bounded at $x=b$ and $x=a$, respectively. Defining now the mode I stress intensity factors by

$$k_1(b)=\lim_{x\to b}\sqrt{2(x-b)}\,\sigma_{2yy}(x,0),$$

$$k_1(a)=\lim_{x\to a}\sqrt{2(a-x)}\,\sigma_{2yy}(x,0), \tag{51a,b}$$

[2] In numerical analysis rapid convergence is obtained by selecting $0<\alpha_0<1$.

Downloaded 03 May 2010 to 171.66.16.248. Redistribution subject to ASME license or copyright; see http://www.asme.org/terms/Terms_Use.cfm

from (50) it follows that

$$k_1(b) = -\frac{4\mu_0}{1+\kappa}\frac{F(b)}{\sqrt{(b-a)/2}},$$

$$k_1(a) = \frac{4\mu_0}{1+\kappa}\frac{F(a)}{\sqrt{(b-a)/2}}. \quad (52a,b)$$

For $a=0$ the stress intensity factor is defined in terms of the cleavage stress in material 1, namely

$$k_1(0) = \lim_{x\to -0}\sqrt{-2x}\,\sigma_{1yy}(x,0). \quad (53)$$

Therefore, to determine $k_1(0)$ the asymptotic behavior of σ_{1yy} near the crack tip $x=0$ needs to be examined. From (19*b*) and the expressions given for D_1 and D_2 in Appendix A, it may be seen that

$$\sigma_{1yy}(x,y) = \frac{\mu_0 e^{\beta x}}{\kappa-1}\frac{4}{\pi}\int_0^b H(x,y,t)\phi(t)dt,\ (x<0,\ y>0), \quad (54)$$

where

$$H(x,y,t) = \int_0^\infty [F_1(t,\alpha)\cos Bx + F_2(t,\alpha)\sin Bx]e^{Ax-t\alpha}\cos y\alpha d\alpha,$$

$$F_1(t,\alpha) = (1+\kappa)\alpha c_1 + (3-\kappa)[c_1(AC-BD) - c_2(AD+BC)],$$

$$F_2(t,\alpha) = -(1+\kappa)\alpha c_2 - (3-\kappa)[c_1(AD + BC) + c_2(AC-BD)], \quad (55a\text{–}c)$$

and c_1, c_2, A, B, C, and D are defined in Appendix A. Again, at $y=0$, $x\to -0$ the singular behavior of σ_{1yy} will be defined in terms of the asymptotic nature of its kernel H for $\alpha\to\infty$. First, we express the kernel given by (55*a*) as follows:

$$H(x,y,t) = \int_0^\infty L(x,t,\alpha)\cos y\alpha d\alpha$$

$$= \int_0^\infty [L(x,t,\alpha) - L_\infty(x,t,\alpha)]\cos y\alpha d\alpha + \int_0^\infty L_\infty(x,t,\alpha)\cos y\alpha d\alpha \quad (56)$$

where L is defined by (55*a*) and (56) and L_∞ is the asymptotic representation of L for $\alpha\to\infty$. Next we note that by using the asymptotic expansions given in Appendix B and the definitions given in Appendix A, for $\alpha\to\infty$ the functions F_1 and F_2 may be expressed as

$$F_1(t,\alpha) = \frac{\kappa-1}{1+\kappa}\left[-t\alpha + 2 - \frac{\beta t}{1+\kappa} + \frac{\beta}{4\alpha} + 0\left(\frac{t}{\alpha}\right) + 0\left(\frac{1}{\alpha^2}\right)\right],$$

$$F_2(t,\alpha) = \frac{\kappa-1}{1+\kappa}\sqrt{\frac{1+\kappa}{3-\kappa}}\left[\frac{2\alpha}{\beta} + \frac{\kappa-1}{1+\kappa}t\alpha + 1 + 0(t) + 0\left(\frac{1}{\alpha}\right)\right]. \quad (57a,b)$$

From (55)–(57) and Appendix B it may be shown that

$$L_\infty(x,t,\alpha) = \frac{\kappa-1}{\kappa+1}e^{-\frac{\beta x}{2}}e^{-\alpha(t-x)}\left[-\alpha(t-x) + 2 - \beta\left\{\frac{1}{2}\left(\frac{1-\kappa}{1+\kappa}\right)xt\alpha + \frac{t}{1+\kappa} - \frac{x}{2} - \frac{1}{4\alpha}\right\}\right]. \quad (58)$$

The remaining terms in the expansion of L are of the order $x^3\alpha$, $x^2t\alpha$, xt, x^2, t/α, x/α and $1/\alpha^2$ that would give only a bounded kernel. From (54), (56), and (58) we now have

$$\sigma_{1yy}(x,0) = \lim_{y\to 0}\frac{4\mu_0}{\kappa-1}\frac{e^{\beta x}}{\pi}\int_0^b \phi(t)dt\left[\int_0^\infty L_\infty\cos y\alpha d\alpha + \int_0^\infty (L-L_\infty)\cos y\alpha d\alpha\right]. \quad (59)$$

Evaluating the integrals involving L_∞ and defining the Fredholm kernel

$$k_f(x,t) = \frac{4\mu_0}{\kappa-1}\frac{e^{\beta x}}{\pi}\int_0^\infty [L(x,t,\alpha) - L_\infty(x,t,\alpha)]d\alpha, \quad (60)$$

from (59) we find

$$\sigma_{1yy}(x,0) = \frac{1}{\pi}\frac{4\mu_0}{1+\kappa}e^{\frac{\beta x}{2}}\int_0^b \phi(t)\left[\frac{1}{t-x} - \beta\left\{\left(\frac{1-\kappa}{1+\kappa}\right)\left(\frac{x}{t-x} + \frac{1}{2}\frac{x^2}{(t-x)^2}\right) + \frac{1}{4}\log(t-x) + \frac{1}{1+\kappa}\right\}\right]dt + \int_0^b k_f(x,t)\phi(t)dt,\ (x<0). \quad (61)$$

By observing that for $a=0$ we have

$$\phi(t) = \frac{F(t)}{\sqrt{t(b-t)}},\ 0<t<b, \quad (62)$$

and that at $z=x<0$, $\psi(z)$ defined by (43) is holomorphic, from (43), (44), and (61) it can be shown that

$$\sigma_{1yy}(x,0) = \frac{4\mu_0}{1+\kappa}e^{\frac{\beta x}{2}}\frac{F(0)}{\sqrt{b/2}\sqrt{-2x}} + 0(\sqrt{-x}). \quad (63)$$

Thus, from (53) and (63) the stress intensity factor at $x=0$ is found to be

$$k_1(0) = \frac{4\mu_0}{1+\kappa}\frac{F(0)}{\sqrt{b/2}}. \quad (64)$$

Note that for $a=0$, equation (64) is identical to (52*b*).

5 The Solution and Results

To solve the integral equation (25) we make a change in variable and define the following normalized quantities:

$$t = \left(\frac{b-a}{2}\right)r + \frac{b+a}{2},\ x = \left(\frac{b-a}{2}\right)s + \frac{b+a}{2}, \quad (65)$$

$$\phi(t) = \frac{F(t)}{\sqrt{(t-a)(b-t)}} = \frac{G(r)}{\sqrt{1-r^2}},\ a<t<b,\ -1<r<1, \quad (66)$$

$$\left(\frac{b-a}{2}\right)K(x,t) = k(s,r), \quad (67)$$

$$\frac{1+\kappa}{4\mu_0}p(x) = Q(s). \quad (68)$$

Equation (25) then becomes

$$\frac{1}{\pi}\int_{-1}^1\left[\frac{1}{r-s} + k(s,r)\right]\frac{G(r)}{\sqrt{1-r^2}}dr = Q(s),\ -1<s<1. \quad (69)$$

From (7*a*), (22), and (23) it is clear that the integral equation must be solved under the following single-valuedness condition:

$$\int_a^b \phi(t)dt = 0 \quad (70)$$

or

$$\int_{-1}^1 \frac{G(r)}{\sqrt{1-r^2}}dr = 0. \quad (71)$$

Equation (69) is solved by substituting

$$G(r) = \sum_0^\infty a_n T_n(r) \quad (72)$$

and by using a simple collocation scheme to reduce the resulting

Downloaded 03 May 2010 to 171.66.16.248. Redistribution subject to ASME license or copyright; see http://www.asme.org/terms/Terms_Use.cfm

Table 1 Normalized mode I stress intensity factors for a crack of length $2c$ subjected to constant crack surface pressure σ, $\nu = 0.3$, the case of plane strain

βc	$k_1(a)/\sigma\sqrt{c}$	$k_1(b)/\sigma\sqrt{c}$	$k_1(a)/\sigma\sqrt{c}$	$k_1(b)/\sigma\sqrt{c}$	$k_1(a)/\sigma\sqrt{c}$	$k_1(b)/\sigma\sqrt{c}$
	d/c=1.0		d/c=1.1		d/c=1.25	
0.1	1.0172	1.0087	1.0138	1.0079	1.0112	1.0070
0.5	1.0820	1.0377	1.0638	1.0337	1.0499	1.0291
1.0	1.1546	1.0653	1.1163	1.0572	1.0880	1.0482
2.0	1.2791	1.1042	1.1980	1.0884	1.1426	1.0721
5.0	1.5586	1.1665	1.3472	1.1334	1.2286	1.1033
10.0	1.8785	1.2138	1.4692	1.1620	1.2870	1.1211
20.0	2.3105	1.2562	1.5745	1.1825	1.3298	1.1327
50.0	3.103	1.3029	1.6699	1.1983	1.3625	1.1407
$\to\infty$	∞	1.5861	1.7585	1.2108	1.3875	1.1464
	d/c=1.5		d/c=2.0		d/c=5.0	
0.1	1.0086	1.0059	1.0059	1.0044	1.0019	1.0017
0.5	1.0367	1.0235	1.0234	1.0167	1.0057	1.0049
1.0	1.0621	1.0378	1.0372	1.0255	1.0076	1.0064
2.0	1.0950	1.0543	1.0530	1.0347	1.0091	1.0076
5.0	1.1399	1.0738	1.0711	1.0443	1.0103	1.0085
10.0	1.1662	1.0839	1.0802	1.0488	1.0108	1.0088
20.0	1.1833	1.0900	1.0855	1.0513	1.0110	1.0090
50.0	1.1952	1.0940	1.0890	1.0528	1.0111	1.0091
$\to\infty$	1.2035	1.0967	1.0913	1.0539	1.0112	1.0092
	d/c=1.0		d/c=1.1		d/c=1.25	
-0.1	0.9835	0.9918	0.9867	0.9925	0.9893	0.9933
-0.5	0.9291	0.9676	0.9440	0.9707	0.9557	0.9745
-1.0	0.8778	0.9484	0.9052	0.9537	0.9264	0.9601
-2.0	0.8057	0.9264	0.8529	0.9345	0.8888	0.9443
-5.0	0.6880	0.9008	0.7750	0.9127	0.8374	0.9269
-10.0	0.5963	0.8879	0.7228	0.9019	0.8066	0.9184
-20.0	0.5122	0.8801	0.6840	0.8955	0.7860	0.9135
-50.0	0.4181	0.8749	0.6534	0.8913	0.7712	0.9103
$\to-\infty$	0.	0.8710	0.6283	0.8883	0.7601	0.9081
	d/c=1.5		d/c=2.0		d/c=5.0	
-0.1	0.9918	0.9944	0.9944	0.9958	0.9982	0.9984
-0.5	0.9671	0.9791	0.9789	0.9850	0.9949	0.9956
-1.0	0.9469	0.9680	0.9675	0.9779	0.9933	0.9944
-2.0	0.9227	0.9563	0.9553	0.9710	0.9921	0.9934
-5.0	0.8929	0.9440	0.9422	0.9642	0.9912	0.9927
-10.0	0.8768	0.9382	0.9360	0.9613	0.9908	0.9924
-20.0	0.8669	0.9349	0.9324	0.9596	0.9906	0.9923
-50.0	0.8601	0.9328	0.9300	0.9585	0.9905	0.9922
$\to-\infty$	0.8553	0.9313	0.9284	0.9578	0.9904	0.9922

functional equation to an infinite system. First, from (71) and the orthogonality condition of Chebyshev polynomials, T_n, it may be seen that

$$a_0 = 0. \tag{73}$$

Thus, from (69), (72), and (73) by truncating the series and by using

$$\frac{1}{\pi}\int_{-1}^{1}\frac{T_n(r)dr}{(r-s)\sqrt{1-r^2}} = \begin{cases} 0, & n=0 \\ U_{n-1}(s), & n=1,2,\ldots, \end{cases} \quad -1<s<1, \tag{74}$$

we obtain

$$\sum_{1}^{N} a_n\left[U_{n-1}(s_j)+\frac{1}{\pi}\int_{-1}^{1}\frac{T_n(r)k(s_j,r)}{\sqrt{1-r^2}}\,dr\right] = Q(s_j),\ j=1,\ldots,N, \tag{75}$$

where U_n is the Chebyshev polynomial of the second kind. The collocation points s_j may be selected as follows:

$$T_N(s_j)=0,\ s_j=\cos\left[(2j-1)\frac{\pi}{2N}\right],\ j=1,\ldots,N. \tag{76}$$

The main results obtained in this study regarding the stress intensity factors are shown in Table 1, where it is assumed that

$$\frac{b-a}{2}=c,\ \frac{b+a}{2}=d,\ p(x)=-\sigma. \tag{77}$$

The uniform crack surface pressure σ used in the example is realistic if the composite medium is subjected to a constant displacement loading in the y-direction away from the crack region. In the examples considered it is further assumed that $\nu=0.3$ and the plane-strain conditions prevail. By examining

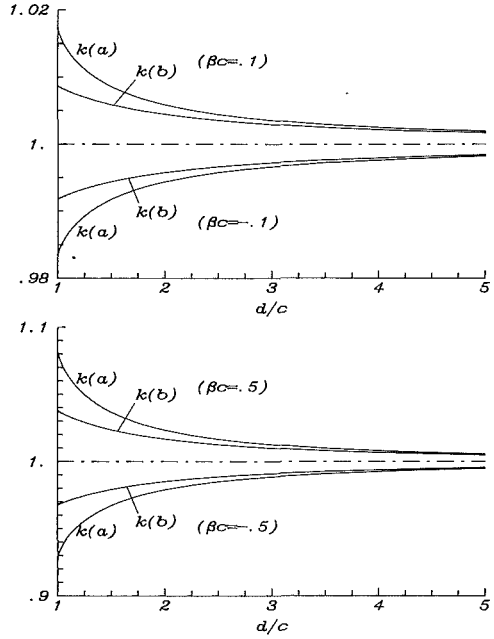

Fig. 2 The variation of the normalized stress intensity factors with the crack distance, $d=(b+a)/2$, $c=(b-a)/2$, $k(a)=k_1(a)/\sigma\sqrt{c}$, $k(b)=k_1(b)/\sigma\sqrt{c}$, the case of plane strain, $\nu=0.3$, $\beta c=\mp 0.1$ and $\beta c=\mp 0.5$

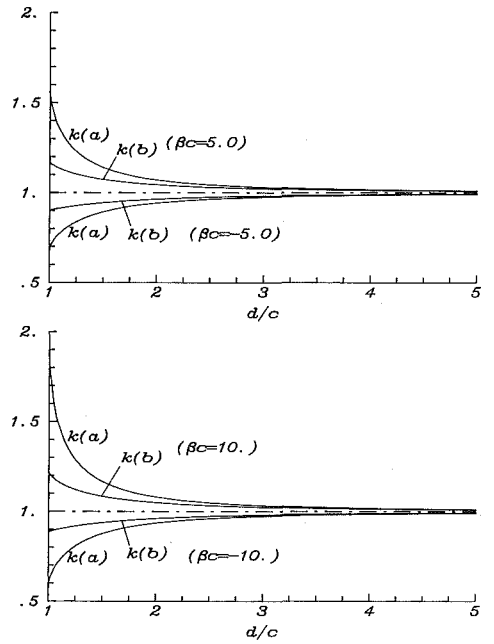

Fig. 3 The variation of the normalized stress intensity factors with the crack distance, $d=(b+a)/2$, $c=(b-a)/2$, $k(a)=k_1(a)/\sigma\sqrt{c}$, $k(b)=k_1(b)/\sigma\sqrt{c}$, the case of plane strain, $\nu=0.3$, $\beta c=\mp 1$ and $\beta c=\mp 2$

the results given in the table a number of observations may be made. First, from Fig. 1 and $\mu_1(x)=\mu_0\exp(\beta x)$ we note that for $\beta>0$ medium 2 is stiffer than medium 1, hence the stress intensity factors would be expected and are seen to be greater than $\sigma\sqrt{c}$, the value for the corresponding homogeneous material having the same crack. For $\beta<0$ material 1 is the stiffer medium and, consequently, the stress intensity factors, as expected, turn out to be less than $\sigma\sqrt{c}$. These trends are also observed for varying β, that is for any crack geometry as β increases, the stress intensity factors increase. For $\beta\to\infty$ the results shown in the table agree with that of a half-plane containing a uniformly pressurized crack of length $2c$ per-

Downloaded 03 May 2010 to 171.66.16.248. Redistribution subject to ASME license or copyright; see http://www.asme.org/terms/Terms_Use.cfm

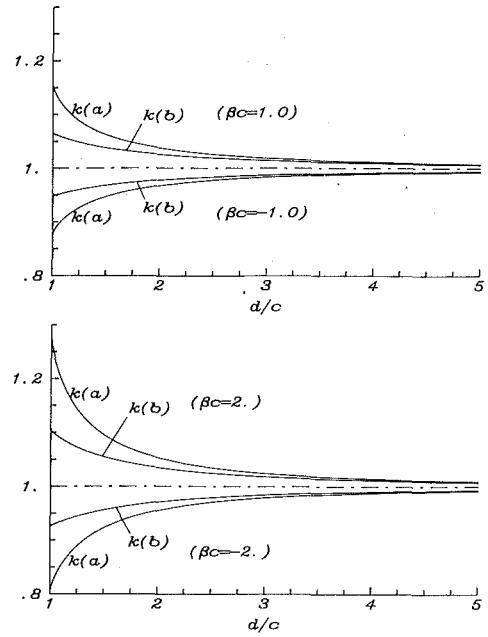

Fig. 4 The variation of the normalized stress intensity factors with the crack distance, $d=(b+a)/2$, $c=(b-a)/2$, $k(a)=k_1/\sigma\sqrt{c}$, $k(b)=k_1(b)/\sigma\sqrt{c}$, the case of plane strain, $\nu=0.3$, $\beta c=\mp 5$ and $\beta c=\mp 10$

pendicular to the boundary. As the distance d increases, the stress intensity factors tend to $\sigma\sqrt{c}$, the homogeneous plane solution.

Figures 2–4 show the variation of the normalized stress intensity factors defined by

$$k(a)=\frac{k_1(a)}{\sigma\sqrt{c}},\quad k(b)=\frac{k_1(b)}{\sigma\sqrt{c}} \tag{78}$$

with the crack distance d and for various values of the nonhomogeneity parameter β. For the specific crack geometry $a=0$, the effect of β on the normalized stress intensity factors are shown in Fig. 5. In this figure the abscissa is selected in such a way that the results include the full range of β, $-\infty<\beta<\infty$. As seen from the figure for $\beta\to\infty$ the stiffness of medium 1 approaches zero, $k(a)\to\infty$ and $k(b)$ goes to the edge crack solution, 1.5861 marked on the figure. Similarly, for $\beta\to-\infty$ medium 1 becomes a rigid half-space, $k(b)$ goes to the corresponding limit 0.8710 shown in the figure, and $k(a)$ tends to zero.

Finally, Fig. 6 shows some examples giving the normalized crack surface displacement for the limiting case of $a=0$ defined by

$$V(x)=\frac{v_2(x,+0)}{(1+\kappa)\sigma c/4\mu_0} \tag{79}$$

and obtained from

$$v_2(x,+0)=\int_0^x \phi(x)dx= -\frac{b}{2}\sum_1^N \frac{1}{n}\,a_n U_{n-1}(s)\sqrt{1-s^2},\quad s=\frac{2x}{b}-1. \tag{80}$$

The dashed line shown corresponds to $\beta=0$ or the homogeneous medium. Again, as expected the displacement is skewed toward or away from the interface depending on the sign of β or the relative stiffnesses of materials 1 and 2.

Acknowledgment

This study was supported by NSF under the grant MSM-8613611, by NASA-Langley under the grant NAG-1-713 and by SRC contract 88-MP-071.

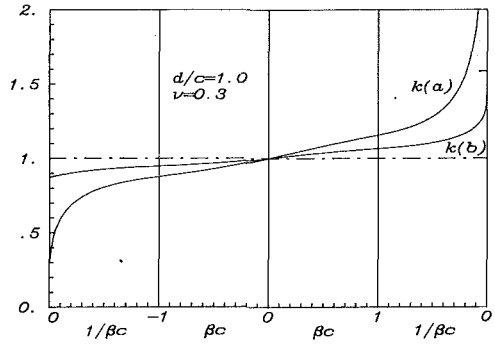

Fig. 5 The variation of the normalized stress intensity factors with the nonhomogeneity constant β for the special crack geometry $a=0$

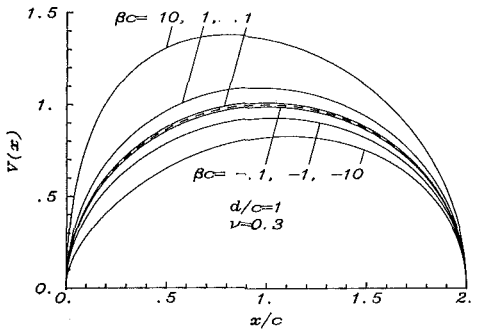

Fig. 6 The normalized crack surface displacement for the special crack geometry $a=0$ and for various values of β, $V(x)=v_2(x,+0)/[(1+\kappa)(\sigma c/4\mu_0)]$.

References

Atkinson, C., 1977, "On Stress Singularities and Interfaces in Linear Elastic Fracture Mechanics," *International Journal of Fracture*, Vol. 13, pp. 807–820.

Comninou, M., 1977, "The Interface Crack," ASME JOURNAL OF APPLIED MECHANICS, Vol. 44, pp. 631–636.

Cook, T. S., and Erdogan, F., 1972, "Stresses in Bonded Materials with a Crack Perpendicular to the Interface," *Int. J. Engng. Sci.*, Vol. 10, pp. 677–697.

Delale, F., and Erdogan, F., 1983, "The Crack Problem for a Nonhomogeneous Plane," ASME JOURNAL OF APPLIED MECHANICS, Vol. 50, pp. 609–614.

Delale, F., and Erdogan, F., 1988a, "Interface Crack in a Nonhomogeneous Medium," *Int. J. Engng. Sci.*, Vol. 26, pp. 559–568.

Delale, F., and Erdogan, F., 1988b, "On the Mechanical Modeling of the Interfacial Region in Bonded Half Planes," ASME JOURNAL OF APPLIED MECHANICS, Vol. 55, pp. 317–324.

England, A. H., 1965, "A Crack Between Dissimilar Media," ASME JOURNAL OF APPLIED MECHANICS, Vol. 32, pp. 400–402.

Erdogan, F., 1965, "Stress Distribution in Bonded Dissimilar Materials with Cracks," ASME JOURNAL OF APPLIED MECHANICS, Vol. 32, pp. 403–410.

Erdogan, F., and Biricikoglu, V., 1973, "Two Bonded Half Planes with a Crack Going Through the Interface," *Int. J. Engng. Sci.*, Vol. 11, pp. 745–766.

Erdogan, F., and Cook, T. S., 1974, "Antiplane Shear Crack Terminating at and Going Through a Bimaterial Interface," *International Journal of Fracture*, Vol. 10, pp. 227–240.

Erdogan, F., 1985, "The Crack Problem for Bonded Nonhomogeneous Materials Under Antiplane Shear Loading," ASME JOURNAL OF APPLIED MECHANICS, Vol. 52, pp. 823–828.

Muskhelishvili, N. I., 1953a, *Some Basic Problems of the Mathematical Theory of Elasticity*, P. Noordhoff, Ltd., Groningen-Holland.

Muskhelishvili, N. I., 1953b, *Singular Integral Equations*, P. Noordhof, Ltd., Groningen-Holland.

Rice, J. R., and Sih, G. C., 1965, "Plane Problems of Cracks in Dissimilar Media," ASME JOURNAL OF APPLIED MECHANICS, Vol. 32, pp. 418–423.

APPENDIX A

The Expressions of the Functions D_1, D_2, A_1, and A_2

By substituting from (18), (19*b*,*c*), (20), (21*b*,*c*), and (23)

Downloaded 03 May 2010 to 171.66.16.248. Redistribution subject to ASME license or copyright; see http://www.asme.org/terms/Terms_Use.cfm

into the homogeneous conditions (3) and (4), and taking the inverse transforms, we obtain

$$\sum_{j=1}^{2} m_j D_j(\alpha) - A_1(\alpha) - \frac{\kappa}{\alpha} A_2(\alpha) = R_1(\alpha),$$

$$\sum_{j=1}^{2} D_j(\alpha) - A_1(\alpha) = R_2(\alpha),$$

$$\sum_{j=1}^{2} \left[-\left(\frac{1+\kappa}{1-\kappa}\right) m_j n_j - \left(\frac{3-\kappa}{1-\kappa}\right)\alpha \right] D_j(\alpha) + 2\alpha A_1(\alpha) + (1+\kappa) A_2(\alpha) = R_3(\alpha),$$

$$\sum_{j=1}^{2} [n_j - \alpha m_j] D_j(\alpha) + 2\alpha A_1(\alpha) - (1-\kappa) A_2(\alpha) = R_4(\alpha), \quad \text{(A1–4)}$$

where the functions R_i, $(i=1,\ldots,4)$ are given by

$$R_1(\alpha) = \frac{1}{(1+\kappa)} \int_a^b \left(-\frac{1-\kappa}{2\alpha} + t \right) e^{-\alpha t} \phi(t)\, dt,$$

$$R_2(\alpha) = \frac{1}{(1+\kappa)} \int_a^b \left(\frac{1+\kappa}{2\alpha} - t \right) e^{-\alpha t} \phi(t)\, dt,$$

$$R_3(\alpha) = \frac{2}{(1+\kappa)} \int_a^b \alpha t e^{-\alpha t} \phi(t)\, dt,$$

$$R_4(\alpha) = \frac{2}{(1+\kappa)} \int_a^b (1-\alpha t) e^{-\alpha t} \phi(t)\, dt. \quad \text{(A5–8)}$$

After rather straightforward algebra, the solution of (A1–4) gives

$$D_1(\alpha) = \int_a^b [c_1(\alpha,t) + i c_2(\alpha,t)] e^{-\alpha t} \phi(t)\, dt,$$

$$D_2(\alpha) = \int_a^b [c_1(\alpha,t) - i c_2(\alpha,t)] e^{-\alpha t} \phi(t)\, dt,$$

$$A_1(\alpha) = \int_a^b c_3(\alpha,t) e^{-\alpha t} \phi(t)\, dt,$$

$$A_2(\alpha) = \int_a^b c_4(\alpha,t) e^{-\alpha t} \phi(t)\, dt, \quad \text{(A9–12)}$$

where

$$c_k(\alpha,t) = p_k(\alpha) + t q_k(\alpha), \ (k=1,2,3,4), \quad \text{(A13)}$$

$$p_1(\alpha) = \frac{1}{Z}\left[-\frac{(\kappa-1)^2}{(\kappa+1)} B + \frac{(\kappa-1)(\kappa+3)}{(\kappa+1)} \alpha D + (\kappa+1)(AD+BC) \right],$$

$$q_1(\alpha) = \frac{2\alpha}{Z}\left[-\left(\frac{\kappa-1}{\kappa+1}\right) B - \left(\frac{\kappa-1}{\kappa+1}\right)\alpha D - AD - BC \right],$$

$$p_2(\alpha) = \frac{1}{Z}\left[(3-\kappa)\alpha - \frac{(\kappa-1)^2}{(\kappa+1)} A + \frac{(\kappa-1)(\kappa+3)}{(\kappa+1)} \alpha C + (\kappa+1)(AC-BD) \right],$$

$$q_2(\alpha) = \frac{2\alpha}{Z}\left[-\alpha - \left(\frac{\kappa-1}{\kappa+1}\right) A - \left(\frac{\kappa-1}{\kappa+1}\right)\alpha C - AC + BD \right],$$

$$p_3(\alpha) = 2p_1(\alpha) - \frac{1}{2\alpha},$$

$$q_3(\alpha) = 2q_1(\alpha) + \frac{1}{(\kappa+1)},$$

$$p_4(\alpha) = \frac{2\alpha}{(\kappa+1)Z}\left[(\kappa-2)B - 3\alpha D - 2AD - 2\kappa BC + (\kappa+2)B(C^2+D^2) + \frac{D}{\alpha}(A^2+B^2) \right],$$

$$q_4(\alpha) = \frac{4\alpha^2}{(\kappa+1)Z}\left[B + \alpha D - B(C^2+D^2) - \frac{D}{\alpha}(A^2+B^2) \right], \quad \text{(A14–21)}$$

$$Z = 2\alpha\left[-B + \kappa\alpha D + 2\kappa AD + 2BC - B(C^2+D^2) + \frac{\kappa D}{\alpha}(A^2+B^2) \right]. \quad \text{(A22)}$$

A, B, C, and D are functions of α and are defined by

$$A + iB = n_1(\alpha), \ C + iD = m_1(\alpha). \quad \text{(A23,24)}$$

By using (12) and (14a), from (A23) and (A24), it can be shown that

$$A = \frac{1}{2}(-\beta + R\cos\gamma),$$

$$B = \frac{1}{2} R\sin\gamma,$$

$$C = \frac{1}{Y}[d_0(A+\beta)(A^2+B^2) - (1+d_0)\alpha^2(d_0 A + \beta) + \beta A(A+\beta) - \beta B^2],$$

$$D = \frac{1}{Y}[d_0 B(A^2+B^2) + d_0(1+d_0)\alpha^2 B + 2\beta AB + \beta^2 B], \quad \text{(A25–28)}$$

$$d_0 = \frac{2}{\kappa-1}, \ Y = \alpha[d_0^2(A^2+B^2) + 2d_0\beta A + \beta^2], \quad \text{(A29,30)}$$

where R and γ are defined by (16a,b).

APPENDIX B

The Asymptotic Expansions Needed to Examine the Singular Behavior of the Kernels

For $\alpha \to \infty$ from Appendix A and equations (12), (14), (16), and (28) it can be shown that

$$R(\alpha) = 2\alpha + \frac{(7-\kappa)\beta^2}{4(1+\kappa)} \frac{1}{\alpha} + 0\left(\frac{1}{\alpha^3}\right), \quad \text{(B1)}$$

$$\gamma = \frac{1}{2}\left(\frac{3-\kappa}{1+\kappa}\right)^{1/2}\left[\frac{\beta}{\alpha} - \frac{(15-\kappa)\beta^3}{12(1+\kappa)} \frac{1}{\alpha^3} + 0\left(\frac{1}{\alpha^5}\right) \right], \quad \text{(B2)}$$

$$A = \alpha - \frac{\beta}{2} + \frac{\beta^2}{2(1+\kappa)} \frac{1}{\alpha} + 0\left(\frac{1}{\alpha^3}\right), \quad \text{(B3)}$$

$$B = \frac{1}{2}\left(\frac{3-\kappa}{1+\kappa}\right)^{1/2}\left[\beta - \frac{\beta^3}{2(1+\kappa)} \frac{1}{\alpha^2} + 0\left(\frac{1}{\alpha^4}\right) \right], \quad \text{(B4)}$$

$$C = -1 - \frac{(2-\kappa)\beta}{2} \frac{1}{\alpha} - \frac{(\kappa^3 - 2\kappa^2 - 3\kappa + 2)\beta^2}{4(1+\kappa)} \frac{1}{\alpha^2} + \frac{(1+\kappa)(2-\kappa)(3-\kappa)\beta^3}{8} \frac{1}{\alpha^3} + 0\left(\frac{1}{\alpha^4}\right), \quad \text{(B5)}$$

$$D = \frac{1}{2}\left(\frac{3-\kappa}{1+\kappa}\right)^{1/2}\left[\kappa\beta \frac{1}{\alpha} + \frac{(1+\kappa)(2-\kappa)\beta^2}{2} \frac{1}{\alpha^2} + \frac{(\kappa^4 - \kappa^3 - 5\kappa^2 - \kappa + 4)\beta^3}{4(1+\kappa)} \frac{1}{\alpha^3} + 0\left(\frac{1}{\alpha^4}\right) \right], \quad \text{(B6)}$$

$$Z = 4\left(\frac{3-\kappa}{1+\kappa}\right)^{1/2}(1-\kappa)(1+\kappa)\left[-\beta\alpha - \frac{(1-\kappa)(2+\kappa)\beta^2}{2(1+\kappa)} + 0\left(\frac{1}{\alpha}\right) \right], \quad \text{(B7)}$$

$$h_1(\alpha) = \frac{\beta}{4\alpha} + 0\left(\frac{1}{\alpha^2}\right), \quad \text{(B8)}$$

$$h_2(\alpha) = 0\left(\frac{1}{\alpha^2}\right), \quad \text{(B9)}$$

Downloaded 03 May 2010 to 171.66.16.248. Redistribution subject to ASME license or copyright; see http://www.asme.org/terms/Terms_Use.cfm

$$h_3(\alpha) = -\frac{\beta}{(1+\kappa)} + \frac{(1-\kappa)\beta^2}{2(1+\kappa)^2}\frac{1}{\alpha} + 0\left(\frac{1}{\alpha^2}\right), \quad \text{(B10)}$$

$$h_4(\alpha) = \frac{\beta}{1+\kappa}\alpha - \frac{(1-\kappa)\beta^2}{2(1+\kappa)^2} - \frac{\kappa(3-\kappa)\beta^3}{4(1+\kappa)^3}\frac{1}{\alpha} + 0\left(\frac{1}{\alpha^2}\right). \quad \text{(B11)}$$

$$\cos Bx \cong 1 - \frac{3-\kappa}{8(1+\kappa)}\beta^2 x^2, \quad \text{(B12)}$$

$$\sin Bx \cong \frac{1}{2}\left(\frac{3-\kappa}{1+\kappa}\right)^{1/2}\left[\beta x - \frac{\beta^3 x}{2(1+\kappa)\alpha^2}\right], \quad \text{(B13)}$$

$$e^{\beta x}e^{Ax-t\alpha} \cong e^{\frac{\beta x}{2}}\, e^{-\alpha(t-x)}, \quad \text{(B14)}$$

$$p_1 = \frac{1}{4\alpha} + \frac{\beta}{8(1+\kappa)}\frac{1}{\alpha^2} + 0\left(\frac{1}{\alpha^3}\right), \quad \text{(B15)}$$

$$q_1 = -\frac{1}{2(1+\kappa)} + \frac{(1-\kappa)\beta}{4(1+\kappa)^2}\frac{1}{\alpha} - \frac{(1-\kappa)^2\beta^2}{8(1+\kappa)^3}\frac{1}{\alpha^2} + 0\left(\frac{1}{\alpha^3}\right), \quad \text{(B16)}$$

$$p_2 = \left(\frac{1+\kappa}{3-\kappa}\right)^{1/2}\left[-\frac{1}{\beta(1+\kappa)} + \frac{(1-\kappa)}{4(1+\kappa)}\frac{1}{\alpha} - \frac{\beta}{8(1+\kappa)}\frac{1}{\alpha^2} + 0\left(\frac{1}{\alpha^3}\right)\right], \quad \text{(B17)}$$

$$q_2 = \frac{1}{2}\left(\frac{1+\kappa}{3-\kappa}\right)^{1/2}\left[\frac{(1-\kappa)}{(1+\kappa)^2} - \frac{(\kappa^3+3)\beta}{2(1+\kappa)^3}\frac{1}{\alpha} - \frac{(\kappa^3-\kappa^2+5\kappa-1)\beta^2}{4(1+\kappa)^4}\frac{1}{\alpha^2} + 0\left(\frac{1}{\alpha^3}\right)\right], \quad \text{(B18)}$$

$$p_3 = \frac{\beta}{4(1+\kappa)}\frac{1}{\alpha^2} + 0\left(\frac{1}{\alpha^3}\right), \quad \text{(B19)}$$

$$q_3 = \frac{(1-\kappa)\beta}{2(1+\kappa)^2}\frac{1}{\alpha} - \frac{(1-\kappa)^2\beta^2}{4(1+\kappa)^3}\frac{1}{\alpha^2} + 0\left(\frac{1}{\alpha^3}\right), \quad \text{(B20)}$$

$$p_4 = 0\left(\frac{1}{\alpha^3}\right), \quad \text{(B21)}$$

$$q_4 = \frac{\beta}{(1+\kappa)^2} - \frac{(1-\kappa)\beta^2}{2(1+\kappa)^3}\frac{1}{\alpha} - \frac{\kappa(3-\kappa)\beta^3}{4(1+\kappa)^4}\frac{1}{\alpha^2} + \left(\frac{1}{\alpha^3}\right). \quad \text{(B22)}$$

Downloaded 03 May 2010 to 171.66.16.248. Redistribution subject to ASME license or copyright; see http://www.asme.org/terms/Terms_Use.cfm

F. Erdogan
Department of Mechanical Engineering
and Mechanics
Lehigh University,
Bethlehem, PA 18015
Fellow ASME

A. C. Kaya[1]
Associate Professor,
Department of Mechanical Engineering,
Middle East Technical University,
Ankara, Turkey

P. F. Joseph
Department of Mechanical Engineering
and Mechanics,
Lehigh University,
Bethlehem, PA 18015

The Mode III Crack Problem in Bonded Materials With a Nonhomogeneous Interfacial Zone

In this paper the mode III crack problem for two bonded homogeneous half planes is considered. The interfacial zone is modeled by a nonhomogeneous strip in such a way that the shear modulus is a continuous function throughout the composite medium and has discontinuous derivatives along the boundaries of the interfacial zone. The problem is formulated for cracks perpendicular to the nominal interface and is solved for various crack locations in and around the interfacial region. The asymptotic stress field near the tip of a crack terminating at an interface is examined and it is shown that, unlike the corresponding stress field in piecewise homogeneous materials, in this case the stresses have the standard square root singularity and their variation is identical to that of a crack in a homogeneous medium. With application to the subcritical crack growth process in mind, the results given include mostly the stress intensity factors for some typical crack geometries and various material combinations.

1 Introduction

In studying the fracture process in bonded materials, there are two groups of problems in which the mechanical modeling of interfacial regions may play a major role. The first is "debonding" and the second, crack penetration. The investigation of the debonding process requires the solution of a crack problem in which the crack is located in the interfacial zone and is parallel to the nominal interface. To study the second problem one may need the solution of a crack which lies in a plane generally perpendicular to the nominal interface and which intersects the interfacial region. Even though there are cases such as certain geophysical problems and some transient thermal stress problems involving materials with heavily temperature-dependent material properties in which the constituent materials under consideration are inherently nonhomogeneous, in many engineering applications the logical assumption has been to treat the bonded materials as piecewise homogeneous media. Within the context of the linear elastic theory the only time such an idealized model of the interfacial regions leads to certain physical anomalies appears to be the presence of a crack in the medium that either lies along or intersects the interface.

As observed, for example, by Muskhelishvili (1953), Erdogan (1963,1965), England (1965), and Rice and Sih (1965), in the case of an interface crack the power of the crack-tip singularity is complex predicting a physically unacceptable result, namely the interference of crack surface displacements (see also Comninou (1977) and Atkinson (1977) for further discussion of the problem based on the crack closure concept). For a crack intersecting the ideal bimaterial interface perpendicularly, the physical difficulty arises from the fact that the analysis gives a singularity that is not the standard square root type. It was shown, for example, by Cook and Erdogan (1972) that for a crack terminating at a bimaterial interface, depending on the relative magnitudes of material constants, the power of stress singularity may be grater or less than 0.5. Similarly, Erdogan and Biricikoglu (1973) showed that for a crack crossing the interface the stress state exhibits a weak power singularity at the point of intersection (see also Bogy (1968, 1971) and Hein and Erdogan (1971) for results in bonded wedges). The consequence of these analytical results is that in such problems, since the stresses and displacements near the crack tip do not remain self-similar as the crack propagates, it is not possible to calculate the strain energy release rate and to apply the techniques of the conventional fracture mechanics.

For a more accurate representation of the actual physical problem in bonded materials involving cracks, it is clear that one needs to reexamine both the material model and the interface model. Maintaining the ideal interface model, Knowles and Sternberg (1975) and Shih and Asaro (1987) studied the interface crack problem for a nonlinear elastic material bonded to a rigid half-space. Even though the anomalous deformation behavior at the tip of an interface crack may perhaps be rectified by a proper choice of the material model, it is highly

[1]Presently at General Electric Company, Corporate R&D, Schenectady, NY 12301.

Contributed by the Applied Mechanics Division of THE AMERICAN SOCIETY OF MECHANICAL ENGINEERS for presentation at the Joint Applied Mechanics/Bioengineering Conference, Ohio State University, Columbus, OH June 16-19, 1991.

Discussion on this paper should be addressed to the Technical Editor, Prof. Leon M. Keer, The Technological Institute, Northwestern University, Evanston, IL 60208, and will be accepted until two months after final publication of the paper itself in the JOURNAL OF APPLIED MECHANICS. Manuscript received by the ASME Applied Mechanics Division, Nov. 22, 1988; final revision, Feb. 12, 1990.

Paper No. 91-APM-18.

Copyright © 1991 by ASME
Downloaded 03 May 2010 to 171.66.16.248. Redistribution subject to ASME license or copyright; see http://www.asme.org/terms/Terms_Use.cfm

unlikely that changes in material model alone will be sufficient to affect the standard square root singularity for a crack terminating at the interface and to eliminate the weaker power singularity for a crack crossing the interface. This is then an important motivation to experiment with the mechanical modeling of interfacial zones. Another reason is, of course, the actual physical nature of interfacial zones. In many cases, regardless of the particular mechanism of the binding process, for thermodynamical consistency the interfacial region needs to be considered as a distinct phase (see, for example, the review article by Good (1967)). There is always some interdiffusion taking place across the interface so that there is usually a gradual change in the volume concentration of certain elements belonging to the adjacent material. Because of this, even in diffusion bonding in which the thickness of the reaction zone may be only a few atomic layers, the actual thickness of the region having very steep variation in material properties may be substantially greater.

The basic assumption made in this study in modeling the interfacial zone, therefore, is that the mechanical properties of the composite medium may exhibit no jump discontinuities. The interfacial zone is thus assumed to be a thin elastic layer between two homogeneous materials with steeply varying mechanical properties. The corresponding plane elasticity problem for a crack lying in the nonhomogeneous interfacial region and parallel to the nominal interface was considered by Delale and Erdogan (1988a). The important special case of the "interface" crack in which the crack is located in the plane where the variation of the Young's modulus forms a kink was studied by Delale and Erdogan (1988b) who showed that by using this model, the oscillatory behavior predicted by the ideal interface model does indeed disappear (see also Atkinson (1977) and Atkinson and List (1978) for related studies). The main interest in this study is in the crack penetration problem. To cover all possible crack configurations it is assumed that the medium contains three collinear cracks, one in each constitutent material oriented perpendicularly to the nominal interface. The medium is assumed to be under antiplane shear loading with displacements specified away from the crack region. The corresponding crack problem for two bonded nonhomogeneous half-planes under mode III loading conditions was studied by Erdogan (1985). The important result found by Erdogan was that for the crack tip terminating at the kink plane of modulus distribution, the stress state has the standard square root singularity. It should perhaps be pointed out that from the viewpoint of applications, mode III crack problems are not of great interest in themselves. However, they often provide a useful analog to the more interesting in-plane fracture problems.

2 Formulation of the Problem

Consider the antiplane shear problem shown in Fig. 1. Assume that the medium is loaded away from the crack region, the problem in the absence of cracks has been solved, and

$$\sigma_{iyz}(x,0)=\tau_i(x)=-\sigma^0_{yz}(x,0),\ a_i<x<b_i,\ i=1,2,3 \tag{1}$$

are the only external forces. We further assume that, compared to the crack lengths and the layer thickness h, the thickness of the homogeneous materials 2 and 3 are large and hence can be treated as being infinite, and the shear modulus of the interfacial layer is given by

$$\mu_1(x)=\mu_2 e^{\beta x},\ 0\le x\le h. \tag{2}$$

From equation (2) and $\mu_1(h)=\mu_3$, it follows that

$$\beta=\frac{1}{h}\log(\mu_3/\mu_2). \tag{3}$$

Noting that $y=0$ is a plane symmetry, the problem shown in Fig. 1 may be formulated as follows:

$$\nabla^2 w_1+\beta\frac{\partial w_1}{\partial x}=0,\ 0<x<h,\ 0\le y\le\infty, \tag{4}$$

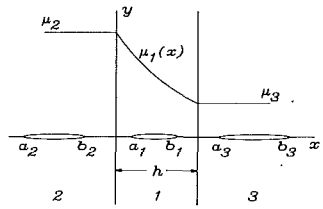

Fig. 1 Geometry of bonded materials containing cracks perpendicular to the nominal interface

$$\nabla^2 w_2=0,\ -\infty<x<0,\ 0\le y<\infty, \tag{5}$$

$$\nabla^2 w_3=0,\ h<x<\infty,\ 0\le y<\infty, \tag{6}$$

$$w_1(0,y)=w_2(0,y),\ \sigma_{1xz}(0,y)=\sigma_{2xz}(0,y),\ 0\le y\le\infty, \tag{7a,b}$$

$$w_1(h,y)=w_3(h,y),\ \sigma_{1xz}(h,y)=\sigma_{3xz}(h,y),\ 0\le y<\infty, \tag{8a,b}$$

$$w_1(x,0)=0,\ 0<x<a_1,\ b_1<x<h,$$

$$\sigma_{1yz}(x,0)=\tau_1(x),\ a_1<x<b_1, \tag{9a,b}$$

$$w_2(x,0)=0,\ -\infty<x<a_2,\ b_2<x<0,$$

$$\sigma_{2yz}(x,0)=\tau_2(x),\ a_2<x<b_2, \tag{10a,b}$$

$$w_3(x,0)=0,\ h<x<a_3,\ b_3<x<\infty$$

$$\sigma_{3yz}(x,0)=\tau_3(x),\ a_3<x<b_3. \tag{11a,b}$$

We now express the solution of (4)–(6) in the following form[1]:

$$w_j(x,y)=\frac{1}{2\pi}\int_{-\infty}^{\infty} f_j(y,\alpha)e^{-i\alpha x}d\alpha + \frac{2}{\pi}\int_0^{\infty} g_j(x,\alpha)\sin(y\alpha)d\alpha+c_j,\ (j=1,2,3). \tag{12}$$

From (4)–(6) and (12) it may be shown that

$$f_1(y,\alpha)=A_1(\alpha)e^{m_1 y},\ y\ge 0, \tag{13}$$

$$g_1(x,\alpha)=B_1(\alpha)e^{n_1 x}+B_2(\alpha)e^{n_2 x},\ 0<x<h, \tag{14}$$

$$f_2(y,\alpha)=A_2(\alpha)e^{-|\alpha| y},\ y\ge 0, \tag{15}$$

$$g_2(x,\alpha)=D(\alpha)e^{\alpha x},\ x<0, \tag{16}$$

$$f_3(y,\alpha)=A_3(\alpha)e^{-|\alpha| y},\ y\ge 0, \tag{17}$$

$$g_3(x,\alpha)=C(\alpha)e^{-\alpha x},\ x>0 \tag{18}$$

where

$$m_1=-|\alpha|\left(1+\frac{i\beta}{\alpha}\right)^{1/2}, \tag{19}$$

$$n_1=-\frac{\beta}{2}+\alpha_1,\ n_2=-\frac{\beta}{2}-\alpha_1,\ \alpha_1=\alpha\left(1+\left(\frac{\beta}{2\alpha}\right)^2\right)^{1/2}. \tag{20}$$

Introducing the unknown functions

$$\phi_j(x)=\frac{\partial}{\partial x}w_j(x,0),\ a_j<x<b_j,\ j=1,2,3, \tag{21}$$

from (12)–(19) and (21), we obtain

$$A_j(\alpha)=\frac{i}{\alpha}\int_{a_j}^{b_j}\phi_j(t)e^{i\alpha t}dt. \tag{22}$$

[1] In equation (12), c_1, c_2, c_3 are included to account for possible rigid body displacements when the cracks cross the interfaces. If, however, in the analysis the continuity conditions (7*a*) and (8*a*) are replaced by

$$\frac{\partial}{\partial y}w_1(0,y)=\frac{\partial}{\partial y}w_2(0,y),\ \frac{\partial}{\partial y}w_1(h,y)=\frac{\partial}{\partial y}w_3(h,y),\ 0\le y<\infty, \tag{A}$$

these constants disappear and conditions (9*a*), (10*a*), and (11*a*) along with (A) insures the single-valuedness and continuity of the displacements.

Downloaded 03 May 2010 to 171.66.16.248. Redistribution subject to ASME license or copyright; see http://www.asme.org/terms/Terms_Use.cfm

It should be observed that at $y = \mp 0$ the solution must satisfy the following conditions (Fig. 1):

$$\lim_{y\to+0} w_2(x,y) = 0,\ x<a_2,$$
$$\lim_{y\to+0} w_2(0,y) = \lim_{y\to+0} w_1(0,y),$$
$$\lim_{y\to+0} w_1(h,y) = \lim_{y\to+0} w_3(h,y),$$
$$\lim_{y\to+0} w_3(x,y) = 0,\ x>b_3. \qquad (23a\text{–}d)$$

By substituting from (12)–(18) and (22) into (23*a*–(*c*), we find

$$c_2 = \frac{1}{2}\int_{a_2}^{b_2} \phi_2(t)dt,$$
$$c_1 - c_2 = \frac{1}{2}\int_{a_1}^{b_1} \phi_1(t)dt + \frac{1}{2}\int_{a_2}^{b_2} \phi_2(t)dt,$$
$$c_3 - c_1 = \frac{1}{2}\int_{a_1}^{b_1} \phi_1(t)dt + \frac{1}{2}\int_{a_3}^{b_3} \phi_3(t)dt, \qquad (24a\text{–}c)$$

which determine the constants, c_1, c_2, and c_3. The fourth condition in (23) gives

$$c_3 = -\frac{1}{2}\int_{a_3}^{b_3} \phi_3(t)dt \qquad (25)$$

which, with (24), implies that

$$\sum_{j=1}^{3}\int_{a_j}^{b_j} \phi_j(t)dt = 0. \qquad (26)$$

Note that if the cracks are disconnected, (9*a*), (10*a*), and (11*a*) require ϕ_j defined by (21) to satisfy the following conditions:

$$\int_{a_j}^{b_j} \phi_j(t)dt = 0,\ j = 1,2,3. \qquad (27)$$

From (24) and (27) it is seen that in this case the constants c_j would be zero. However, if two or all three cracks are connected, then the appropriate combination of (26) and (27) provide the single-valuedness conditions, and (24) gives c_1, c_2, and c_3.

If we now substitute from (12)–(18) into the homogeneous conditions (7) and (8), observe that

$$\sigma_{jxz} = \mu_j \frac{\partial w_j}{\partial x},\ \sigma_{jyz} = \mu_j \frac{\partial w_j}{\partial y},\ j = 1,2,3, \qquad (28)$$

and invert the sine transforms, we obtain

$$B_1(\alpha) + B_2(\alpha) - D(\alpha) = R_1(\alpha),$$
$$n_1 B_1(\alpha) + n_2 B_2(\alpha) - \alpha D(\alpha) = R_2(\alpha),$$
$$e^{n_1 h} B_1(\alpha) + e^{n_2 h} B_2(\alpha) - e^{-\alpha h} C(\alpha) = R_3(\alpha),$$
$$n_1 e^{n_1 h} B_1(\alpha) + n_2 e^{n_2 h} B_2(\alpha) + \alpha e^{-\alpha h} C(\alpha) = R_4(\alpha), \qquad (29a\text{–}d)$$

where the functions R_i, $(i = 1,\ldots,4)$ are given in Appendix A. Thus, from (29) and (A6) it follows that

$$B_1(\alpha) = \frac{1}{\Delta}\left\{\frac{\alpha(\alpha+n_2)}{2\alpha_1}\int_{a_1}^{b_1}\left[-\frac{(\alpha-n_1)}{n_1}e^{-2\alpha_1 h}e^{-n_1 t} + \frac{(\alpha-n_2)}{n_2}e^{-n_1 h}e^{n_2(h-t)}\right]\phi_1(t)dt - (\alpha+n_2)\int_{a_2}^{b_2} e^{-2\alpha_1 h}e^{\alpha t}\phi_2(t)dt - (\alpha-n_2)\int_{a_3}^{b_3} e^{-n_1 h}e^{-\alpha(t-h)}\phi_3(t)dt\right\},$$

$$B_2(\alpha) = \frac{1}{\Delta}\left\{\frac{\alpha(\alpha-n_1)}{2\alpha_1}\int_{a_1}^{b_1}\left[\frac{(\alpha+n_1)}{n_1}e^{-n_1 t} - \frac{(\alpha+n_2)}{n_2}e^{-n_1 h}e^{n_2(h-t)}\right]\phi_1(t)dt + (\alpha+n_1)\int_{a_2}^{b_2} e^{\alpha t}\phi_2(t)dt + (\alpha-n_1)\int_{a_3}^{b_3} e^{-n_1 h}e^{-\alpha(t-h)}\phi_3(t)dt\right\},$$

$$C(\alpha) = \frac{e^{\alpha h}}{\Delta}\left\{\int_{a_1}^{b_1}\left[\frac{\alpha(\alpha-n_1)}{n_1}e^{n_2 h}e^{-n_1 t} - \frac{\alpha(\alpha-n_2)}{n_2}e^{n_2(h-t)}\right]\phi_1(t)dt + 2\alpha_1\int_{a_2}^{b_2} e^{n_2 h}e^{\alpha t}\phi_2(t)dt - \frac{\beta}{2}\int_{a_3}^{b_3}(1-e^{-2\alpha_1 h})e^{-\alpha(t-h)}\phi_3(t)dt\right\},$$

$$D(\alpha) = \frac{1}{\Delta}\left\{\int_{a_1}^{b_1}\left[-\frac{\alpha(\alpha+n_1)}{n_1}e^{-n_1 t} + \frac{\alpha(\alpha+n_2)}{n_2}e^{-n_1 h}e^{n_2(h-t)}\right]\phi_1(t)dt - \frac{\beta}{2}\int_{a_2}^{b_2}(1-e^{-2\alpha_1 h})e^{\alpha t}\phi_2(t)dt - 2\alpha_1\int_{a_3}^{b_3} e^{-n_1 h}e^{-\alpha(t-h)}\phi_3(t)dt\right\}, \qquad (30a\text{–}d)$$

where

$$\Delta = (\alpha-n_1)(\alpha+n_2)e^{-2\alpha_1 h} - (\alpha+n_1)(\alpha-n_2). \qquad (31)$$

3 The Integral Equations

In the previous section the problem has been formulated in terms of three unknown functions ϕ_1, ϕ_2, and ϕ_3. These functions are determined by using (9*b*), (10*b*), and (11*b*) which are the only conditions that have not yet been satisfied. Thus, by substituting (12)–(18) and (28) into (9*b*), (10*b*), and (11*b*), we obtain

$$\lim_{y\to+0}\sigma_{1yz}(x,y) = \frac{\mu_1(x)}{2\pi}\lim_{y\to+0}\int_{-\infty}^{\infty} m_1 A_1(\alpha)e^{m_1 y - i\alpha x}d\alpha + \frac{2\mu_1(x)}{\pi}\int_0^{\infty}[B_1(\alpha)e^{n_1 x} + B_2(\alpha)e^{n_2 x}]\alpha d\alpha = \tau_1(x),\ a_1<x<b_1,$$

$$\lim_{y\to+0}\sigma_{2yz}(x,y) = \frac{\mu_2}{2\pi}\lim_{y\to+0}\int_{-\infty}^{\infty} -|\alpha|A_2(\alpha)e^{-|\alpha|y - i\alpha x}d\alpha + \frac{2\mu_2}{\pi}\int_0^{\infty}\alpha D(\alpha)e^{\alpha x}d\alpha = \tau_2(x),\ a_2<x<b_2,$$

$$\lim_{y\to+0}\sigma_{3yz}(x,y) = \frac{\mu_3}{2\pi}\lim_{y\to+0}\int_{-\infty}^{\infty} -|\alpha|A_3(\alpha)e^{-|\alpha|y - i\alpha x}d\alpha + \frac{2\mu_3}{\pi}\int_0^{\infty}\alpha C(\alpha)e^{-\alpha x}d\alpha = \tau_3(x),\ a_3<x<b_3. \qquad (32a\text{–}c)$$

By substituting from (22) and (30) into (32), we obtain a system of integral equations for ϕ_j, $(j = 1,2,3)$ of the following form:

$$\lim_{y\to+0}\sum_{j=1}^{3}\int_{a_j}^{b_j} h_{ij}(x,y,t)\phi_j(t)dt = \frac{\pi}{\mu_i(x)}\tau_i(x),\ a_i<x<b_i,\ i = 1,2,3, \qquad (33)$$

where the kernels h_{ij} are given in terms of infinite integrals.

The singular parts of the kernels in (33) can be separated after performing the appropriate asymptotic analysis. The leading terms in the asymptotic expansions of the infinite integrals of these kernels are identical to those given by Erdogan (1985). Therefore, the details of the analysis will not be given in this paper. Thus, by following the procedure described by Erdogan (1985), equation (33) may be reduced to

$$\sum_{j=1}^{3}\int_{a_j}^{b_j}\left[\frac{\delta_{ij}}{t-x} + k_{ij}(x,t)\right]\phi_j(t)dt = \frac{\pi}{\mu_i(x)}\tau_i(x),\ a_i<x<b_i,\ i = 1,2,3, \qquad (34)$$

Downloaded 03 May 2010 to 171.66.16.248. Redistribution subject to ASME license or copyright; see http://www.asme.org/terms/Terms_Use.cfm

where the kernels k_{ij}, (i,j=1,2,3) are given in Appendix B.

In examining the asymptotic behavior of the kernels for cracks fully embedded in the three materials shown in Fig. 1, that is for $b_2<0$, $a_1>0$, $b_1<h$, and $a_3>h$, it is sufficient to separate the singular parts of the kernels that become unbounded for $x=t$ only. However, if one or two crack tips touch one of the interfaces $x=0$ or $x=h$, then it is necessary to separate, in addition to the parts that are singular at $x=t$, the terms that become unbounded at $x=t=0$, $(a_2<(t,x)<b_1)$ and at $x=t=h$, $(a_1<(t,x)<b_3)$. The inspection of the kernels given in (34) and Appendix B shows that for embedded cracks as expected, the only unbounded terms in the kernels that may influence the nature of the crack tip singularity are $(t-x)^{-1}$. The remaining unbounded terms are logarithmic (i.e., $\log|t-x|$) which are square integrable and may be treated as Fredholm kernels. It is also seen that the terms that become unbounded for $x=t=0$ and $x=t=h$ are $\log|t+x|$ and $\log|2h-x-t|$. Again, these terms would have no influence on the crack-tip singularity. One may, therefore, conclude that in this problem for all crack geometries the displacement derivative at the crack tip would have the standard square root singularity. Also, as in the case of piecewise homogeneous materials considered by Erdogan and Cook (1974), there would be no singularity at the point of intersection of the crack and the interface.

4 Stress Distribution Near the Crack Tips and Stress Intensity Factors

The stress distribution near the crack tips may be obtained by examining the asymptotic behavior of the corresponding expressions found by substituting from (12)–(18) and (30) into (28) for small values of r, where r is the radial distance from the crack tips. Consider, for example, the distribution of σ_{1yz} around an embedded crack in material 1. From (32a) and (22) the leading term for σ_{1yz} may be expressed as

$$\sigma_{1yz}(x,y)\cong\frac{\mu_1(x)}{2\pi}\int_{a_1}^{b_1}\phi_1(t)dt\int_{-\infty}^{\infty}\frac{\text{im}_1}{\alpha}e^{m_1y}e^{i\alpha(t-x)}d\alpha. \quad (35)$$

Also, from (34) it is clear that the solution of the singular integral equations is of the form

$$\phi_j(t)=\frac{G_j(t)}{\sqrt{(t-a_j)(b_j-t)}},\ a_j<t<b_j. \quad (36)$$

Thus, observing that for $|\alpha|\to\infty$ $m_1\cong-|\alpha|$ and defining

$$t=\frac{b_1-a_1}{2}\tau+\frac{b_1+a_1}{2},\ x=\frac{b_1-a_1}{2}\xi+\frac{b_1+a_1}{2},\ y=\frac{b_1-a_1}{2}\eta,$$

$$\alpha=\frac{2}{b_1-a_1}s,\ G_1(t)=F_1(\tau), \quad (37)$$

equation (35) becomes

$$\sigma_{1yz}(x,y)\cong\frac{-i\mu_1(x)}{\pi(b_1-a_1)}\int_{-\infty}^{\infty}\frac{|s|}{s}e^{-|s|\eta-is\xi}ds\int_{-1}^{1}\frac{F_1(\tau)}{\sqrt{1-\tau^2}}e^{is\tau}d\tau. \quad (38)$$

Again, since the possible unbounded terms in (38) are determined by the leading terms in the integrand for $s\to\infty$, by using (see, for example, Gradshteyn and Ryzhik, (1965))

$$\int_{-1}^{1}\frac{F_1(\tau)}{\sqrt{1-\tau^2}}e^{is\tau}d\tau=\sqrt{\frac{\pi}{2|s|}}\left[F_1(1)e^{i\left(s-\frac{\pi|s|}{4s}\right)}+F_1(-1)e^{-i\left(s-\frac{\pi|s|}{4s}\right)}\right]+0\left(\frac{1}{s}\right), \quad (39)$$

we find

$$\sigma_{1yz}(x,y)\cong\frac{2\mu_1(x)}{\pi(b_1-a_1)}\sqrt{\frac{\pi}{2}}\int_0^{\infty}\frac{e^{-\eta s}}{\sqrt{s}}\left\{-F_1(1)\sin\left[(\xi-1)s+\frac{\pi}{4}\right]-F_1(-1)\sin\left[(\xi+1)s-\frac{\pi}{4}\right]\right\}ds. \quad (40)$$

Similarly, from (see Gradshteyn and Ryzhik, (1965))

$$\int_0^{\infty}s^{\mu-1}e^{-\eta s}\begin{Bmatrix}\sin cs\\ \cos cs\end{Bmatrix}ds=\frac{\Gamma(\mu)}{(\eta^2+c^2)^{\mu/2}}\begin{Bmatrix}\sin\\ \cos\end{Bmatrix}\left(\mu\tan^{-1}\frac{c}{\eta}\right) \quad (41)$$

and (40) it may easily be shown that

$$\sigma_{1yz}(x,y)\cong\frac{-\mu_1(x)}{(b_1-a_1)/2}\frac{F_1(1)}{\sqrt{2\rho}}\cos\frac{\theta}{2}+\frac{\mu_1(x)}{(b_1-a_1)/2}\frac{F_1(-1)}{\sqrt{2\rho}}\sin\frac{\theta}{2}, \quad (42)$$

where

$$\rho\cos\theta=\xi-1,\ \rho\sin\theta=\eta\ \text{and}\ \rho\cos\theta=\xi+1,\ \rho\sin\theta=\eta \quad (43)$$

near $\xi=1$ and $\xi=-1$, respectively. If we now use (37), from (42) we obtain

$$\sigma_{1yz}(x,y)\cong\frac{-\mu_1(b_1)}{\sqrt{(b_1-a_1)/2}}\frac{G_1(b_1)}{\sqrt{2r}}e^{\beta r\cos\theta}\cos\frac{\theta}{2},\quad r\cos\theta=x-b_1,\ r\sin\theta=y \quad (44)$$

near $x=b_1$, $y=0$ and

$$\sigma_{1yz}(x,y)\cong\frac{\mu_1(a_1)}{\sqrt{(b_1-a_1)/2}}\frac{G_1(a_1)}{\sqrt{2r}}e^{\beta r\cos\theta}\sin\frac{\theta}{2},\quad r\cos\theta=x-a_1,\ r\sin\theta=y, \quad (45)$$

near $x=a_1$, $y=0$.

Based on the asymptotic results expressed in (44) and (45) one may observe that:

(a) if we define the mode III stress intensity factors

$$k_3(a_1)=\lim_{x\to a_1}\sqrt{2(a_1-x)}\,\sigma_{1yz}(x,0),$$

$$k_3(b_1)=\lim_{x\to b_1}\sqrt{2(x-b_1)}\,\sigma_{1yz}(x,0), \quad (46)$$

from (44) and (45) it is seen that

$$k_3(a_1)=\frac{\mu_1(a_1)}{\sqrt{(b_1-a_1)/2}}G_1(a_1),$$

$$k_3(b_1)=\frac{-\mu_1(b_1)}{\sqrt{(b_1-a_1)/2}}G_1(b_1). \quad (47a,b)$$

These results are identical to that found for homogeneous materials.

(b) note that since expression (32a) for σ_{1yz} is valid for $0<x<h$ and since the form of the solution given by equation (36) for $\phi_1(t)$ remains unchanged for $a_1=0$ and $b_1=h$, the expressions giving the stress distribution around the crack tips would remain valid for the limiting cases $a_1=0$ and $b_1=h$ provided θ is restricted to $0<\theta<\pi/2$ for $a_1=0$ in (45) and $\pi/2<\theta<\pi$ for $b_1=h$ in (44).

(c) expressions similar to (44) and (45) can easily be developed for $\sigma_{1xz}(x,y)$ near the crack tips. It can indeed be shown that the expressions for σ_{1xz} are identical to (44) and (45) provided $\cos(\theta/2)$ is replaced by $\sin(\theta/2)$ in (44) and $\sin(\theta/2)$ by $\cos(\theta/2)$ in (45).

(d) aside from the factor $e^{\beta r\cos\theta}$, the stress distributions (44) and (45) are identical to that found for homogeneous materials. However, note that the expressions are valid only for "small" values of r for which $e^{\beta r\cos\theta}$ is nearly unity.

(e) from the foregoing result it does not automatically follow that for the limiting cases $a_1=0$ and $b_1=h$ (Fig. 1) (47) is

Downloaded 03 May 2010 to 171.66.16.248. Redistribution subject to ASME license or copyright; see http://www.asme.org/terms/Terms_Use.cfm

still valid and the validity of the expressions (44) and (45) can be extended into materials 3 and 2, respectively. To examine this problem we now consider the distribution of $\sigma_{2yz}(x,y)$ near the crack tip $(a_1,0)$ for the limiting case of $a_1=0$ $b_2<0$. Following Erdogan (1985), the leading term for σ_{2yz} may be expressed as[2]

$$\sigma_{2yz}(x,y)\cong\frac{\mu_2 e^{\gamma x}}{\pi}\int_0^{b_1}\phi_1(t)e^{(\beta t-\gamma x)/2}dt\int_0^{\infty}e^{-\alpha(t-x)}\cos\alpha y d\alpha. \tag{48}$$

By using the definitions (37) (with $F_1(\tau)=G_1(t)e^{\beta t/2}$) from (48) we find

$$\sigma_{2yz}(x,y)\cong\frac{2\mu_2 e^{\gamma x/2}}{\pi b_1}\int_0^{\infty}e^{s\xi}\cos\eta s\,ds\int_{-1}^{1}\frac{F_1(\tau)}{\sqrt{1-\tau^2}}e^{-s\tau}d\tau. \tag{49}$$

If we define

$$F_1(\tau)=\sum_{n=0}^{\infty}A_nT_n(\tau),\ (T_n(\tau)=\cos n\theta_0,\ \tau=\cos\theta_0) \tag{50}$$

and use (see Erdelyi, 1953)

$$\int_0^{\pi}e^{-s\cos\theta_0}\cos n\theta_0 d\theta_0=(-1)^n\,\pi\,I_n(s), \tag{51}$$

(49) becomes

$$\sigma_{2yz}(x,y)\cong\frac{2\mu_2 e^{\gamma x/2}}{b_1}\sum_{n=0}^{\infty}(-1)^nA_n\int_0^{\infty}e^{s\xi}I_n(s)\cos\eta s ds \tag{52}$$

where T_n is the Chebyshev polynomial and I_n is the modified Bessel function. Now, by observing that

$$I_n(s)\cong\frac{e^s}{\sqrt{2\pi s}}\ \text{for}\ s\to\infty\ \text{and}\ \sum_{n=0}^{\infty}(-1)^nA_n=F_1(-1), \tag{53}$$

from (37), (52), and (53) we find

$$\sigma_{2yz}(x,y)\cong\frac{\mu_2}{\sqrt{\pi b_1}}e^{\gamma x/2}F_1(-1)\int_0^{\infty}\frac{1}{\sqrt{\alpha}}e^{\alpha x}\cos\alpha y d\alpha. \tag{54}$$

In material 2 near the crack tip $(a_1=0,\ y=0)$ we have

$$x<0,\ -x=r\cos\theta_1,\ y=r\sin\theta_1, \tag{55}$$

where θ_1 is measured from the negative x-axis. Thus from (54), (41), (55), and $F_1(-1)=G_1(0)$ it may be shown that

$$\sigma_{2yz}(x,y)\cong\frac{\mu_2 e^{-\frac{1}{2}\gamma r\cos\theta_1}}{\sqrt{b_1/2}}\frac{G_1(r\cos\theta_1)e^{\frac{1}{2}\beta r\cos\theta_1}}{\sqrt{2r}}\cos\frac{\theta_1}{2}. \tag{56}$$

If we define the stress intensity factor at the crack tip $(a_1=0,\ y=0)$ by

$$k_3(0)=\lim_{x\to-0}\sqrt{-2x}\,\sigma_{2yz}(x,0) \tag{57}$$

from (56) and (55) it is seen that

$$k_3(0)=\frac{\mu_2}{\sqrt{b_1/2}}G_1(0), \tag{58}$$

which is identical to (47a) with $a_1=0$. Since $\theta_1=\pi-\theta$, also note that aside from the factors $\exp(\beta r\cos\theta)$, $\exp\left(\frac{1}{2}\beta r\cos\theta_1\right)$, and $\exp\left(-\frac{1}{2}\gamma r\cos\theta_1\right)$ the stress distributions (45) and (56) are identical. From a practical viewpoint since all asymptotic expressions such as (56) are valid only for $r\to0$, in (44), (45), and (56) all factors involving e^r should be ignored. This leads to a very simple and important conclusion, namely that the behavior of the singular field near the crack tip in nonhomogeneous materials is identical to that in homogeneous materials provided $\mu(x,y)$ is a continuous (but not necessarily a differentiable) function.

5 The Solution and Results

By defining the normalized quantities

$$t=\frac{b_j-a_j}{2}r+\frac{b_j+a_j}{2},\ x=\frac{b_j-a_j}{2}s+\frac{b_j+a_j}{2},\ \phi_j(t)=f_j(r),$$

$$\frac{b_j-a_j}{2}k_{ij}(x,t)=K_{ij}(s,r),\ \frac{\pi}{\mu_i(x)}\tau_i(x)=g_i(s),\ (i,j=1,2,3), \tag{59}$$

for disconnected cracks the integral equations (34) and conditions (27) may be expressed as

$$\sum_{j=1}^{3}\int_{-1}^{1}\left[\frac{\delta_{ij}}{r-s}+K_{ij}(s,r)\right]f_j(r)dr=g_i(s),$$

$$-1<s<1,\ (i=1,2,3), \tag{60}$$

$$\int_{-1}^{1}f_j(r)dr=0,\ (j=1,2,3). \tag{61}$$

Equations (60) are solved by letting

$$f_j(r)=\frac{F_j(r)}{\sqrt{1-r^2}},\ F_j(r)=\sum_{n=0}^{N_j}c_{jn}T_n(r) \tag{62}$$

and by using

$$\int_{-1}^{1}\frac{T_n(r)dr}{(r-s)\sqrt{1-r^2}}=\pi U_{n-1}(s),\ (n\geq1),\ |s|<1, \tag{63}$$

$$\int_{-1}^{1}\frac{T_n(r)}{\sqrt{1-r^2}}\log|r-s|dr=-\frac{\pi}{n}T_n(s),\ (n\geq1),\ |s|<1 \tag{64}$$

to regularize the system. From (62), (61), and the orthogonality of $T_n(r)$, it may be shown that $c_{jo}=0$, $(j=1,2,3)$. The functional equations resulting from (60) and (62)–(64) may be solved by "collocation." Thus, by specifying s, (60) and (61) may be reduced to an algebraic system of the following form:

$$\sum_{j=1}^{3}\sum_{n=1}^{N_j}c_{jn}H_{ijn}(s_{im})=g_i(s_{im}),\ (i=1,2,3;\ m=1,2,\ldots,N_i). \tag{65}$$

In equation (65) rapidly converging results are obtained by selecting s_{im} as the roots of the Chebyshev polynomials $T_{N_i}(s)$ as follows:

$$s_{im}=\cos\left(\frac{2m-1}{2_{N_i}}\pi\right),\ (i=1,2,3;\ m=1,\ldots,N_i). \tag{66}$$

After solving the integral equations, the stress intensity factors defined by (46) and (47) may be obtained as

$$k_3(a_j)=\lim_{x\to a_j}\mu_j(x)\sqrt{2(x-a_j)}\,\phi_j(x)=\mu_j(a_j)\sqrt{\frac{b_j-a_j}{2}}F_j(-1),$$

$$k_3(b_j)=-\lim_{x\to b_j}\mu_j(x)\sqrt{2(b_j-x)}\,\phi_j(x)=$$

$$-\mu_j(b_j)\sqrt{\frac{b_j-a_j}{2}}F_j(1),\ (j=1,2,3). \tag{67a,b}$$

Also, from (21), (59), and (62) the crack surface displacement are found to be

[2]In Erdogan (1985) μ_2 as well as μ_1 is a function of x ($\mu_2e^{\gamma x}$ and $\mu_2e^{\beta x}$, respectively). Thus, by assuming that both β and γ are nonzero, the asymptotic results given here cover all limiting crack geometries that may arise from Fig. 1.

Downloaded 03 May 2010 to 171.66.16.248. Redistribution subject to ASME license or copyright; see http://www.asme.org/terms/Terms_Use.cfm

Table 1 Normalized mode III stress intensity factors for a crack of length $2a$ located in either material 2 or in material 3 with the inner crack tip touching its respective interface: $\mu_2/\mu_3 = 4, 100$, $k = k_3/\tau_0\sqrt{a}$, $\tau_0 = \gamma_0\mu_2$, γ_0 is uniform shear strain at $y \to \infty$

	$\mu_2/\mu_3 = 4$			
	crack in mat. 2		crack in mat. 3	
2a/h	k(-2a)	k(0)	k(h)	k(2a+h)
0.2	1.0070	1.017	.246	.2483
0.5	1.0153	1.039	.241	.2464
1.0	1.0254	1.071	.234	.2441
2.0	1.0385	1.125	.223	.2415
3.0	1.0471	1.169	.215	.2400
4.0	1.0532	1.206	.209	.2389
5.0	1.0579	1.239	.203	.2382
10.0	1.0716	1.364	.186	.2363
20.0	1.0831	1.524	.167	.2351
50.0	1.0945	1.79	.143	.2341
100.0	1.1005	2.04	.126	.2338
200.0	1.1049	2.34	.110	.2336
2000.0	1.112	4.	.06	.2334
$\to\infty$	1.1144	∞	0	.2333

	$\mu_2/\mu_3 = 100$			
	crack in mat. 2		crack in mat. 3	
2a/h	k(-2a)	k(0)	k(h)	k(2a+h)
.2	1.021	1.053	.00951	.00980
.5	1.042	1.120	.00896	.00963
1.0	1.065	1.214	.00831	.00947
2.0	1.092	1.362	.00747	.00932
4.0	1.121	1.584	.00651	.00920
10.0	1.156	2.021	.00521	.00910
100.0	1.221	4.3	.00256	.00903
$\to\infty$	1.331	∞	0	.00902

Table 2 Normalized mode III stress intensity factors for a crack of length $2a$ with the right crack tip touching the 1-3 interface and the left crack tip either in the material 1 ($2a/h \le 1$) or in material 2 ($2a/h > 1$): $\mu_2/\mu_3 = 4, 100$, $k = k_3/\tau_0\sqrt{a}$, $\tau_0 = \gamma_0\mu_2$, γ_0 is uniform shear strain at $y \to \infty$

	$\mu_2/\mu_3 = 4$		$\mu_2/\mu_3 = 100$	
2a/h	k(h-2a)	k(h)	k(h-2a)	k(h)
.2	.316	.254	.0216	.0105
.4	.399	.258	.0469	.0108
.6	.506	.262	.1034	.0110
.8	.647	.267	.234	.0112
1.0	.859	.275	.590	.0116
1.2	.963	.288	.816	.0131
1.5	1.028	.310	.966	.0158
2.0	1.077	.343	1.092	.0202
3.0	1.115	.395	1.202	.0279
5.0	1.135	.466	1.282	.0397
10.0	1.141	.568	1.336	.0598
20.0	1.138	.679	1.361	.0866

$$w_j(x,+0) = \int_{a_j}^{x} \phi_j(x)dx = -\frac{b_j - a_j}{2} \sum_{n=1}^{N_j} \frac{1}{n} c_{jn}\, U_{n-1}(s)\sqrt{1-s^2}\,,$$

$$s = \frac{2}{b_j - a_j}\left(x - \frac{b_j + a_j}{2}\right),\ (j = 1,2,3). \quad (68)$$

The results given by (59)–(68) are valid for all disconnected crack geometries, including the cracks terminating at "interfaces" $x = 0$ and $x = h$. For cracks crossing the interfaces, since the intersection point of the crack and the interface is not a singular point, the problem can be solved by treating the connected crack as a single crack. For example, if the medium contains a single crack along $y = 0$, $a_2 < x < b_1$ (34) and (27) may be replaced by

$$\int_{a_2}^{b_1} k(x,t)\phi(t)dt = \pi\tau(x),\ a_2 < x < b_1, \quad (69)$$

$$\int_{a_2}^{b_2} \phi(t)dt = 0, \quad (70)$$

where

$$\phi(t) = \begin{cases} \phi_2(t), & a_2 < t \le 0, \\ \phi_1(t), & 0 \le t < b_1 \end{cases} \quad (71)$$

$$\tau(x) = \begin{cases} \tau_2(x)/\mu_2, & a_2 < x < 0, \\ \tau_1(x)/\mu_1(x), & 0 < x < b_1, \end{cases} \quad (72)$$

Table 3 Normalized mode III stress intensity factors for a crack of length $2a$ with the left crack tip touching the 2-1 interface and the right crack tip either in material 1 ($2a/h \le 1$) or in material 3 ($2a/h > 1$): $\mu_2/\mu_3 = 4, 100$, $k = k_3/\tau_0\sqrt{a}$, $\tau_0 = \gamma_0\mu_2$, γ_0 is uniform shear strain at $y \to \infty$

	$\mu_2/\mu_3 = 4$		$\mu_2/\mu_3 = 100$	
2a/h	k(0)	k(2a)	k(0)	k(2a)
.2	.980	.788	.919	.445
.4	.955	.617	.820	.188
.6	.926	.480	.728	.0774
.8	.894	.369	.651	.0312
1.0	.859	.275	.590	.01163
1.2	.821	.246	.541	.00865
1.5	.773	.233	.486	.00792
2.0	.712	.227	.423	.00783
3.0	.635	.225	.347	.00806
5.0	.551	.226	.271	.00838
10.0	.460	.229	.194	.00868
20.0	0	.233	0	.00901

Table 4 Normalized mode III stress intensity factors for a crack of length $2a$ centered at $h/2$ in material 1. Crack is either entirely in material 1 ($2a/h \le 1$) or crosses both interfaces ($2a/h > 1$): $\mu_2/\mu_3 = 4, 100$, $k = k_3/\tau_0\sqrt{a}$, $\tau_0 = \gamma_0\mu_2$, γ_0 is uniform shear strain at $y \to \infty$

	$\mu_2/\mu_3 = 4$		$\mu_2/\mu_3 = 100$	
2a/h	k(h/2-a)	k(h/2+a)	k(h/2-a)	k(h/2+a)
.2	.553	.449	.138	.0685
.4	.611	.401	.189	.0454
.6	.676	.357	.263	.0296
.8	.753	.316	.379	.0190
1.0	.859	.275	.590	.01163
1.4	.927	.255	.758	.00938
2.0	.956	.2493	.842	.00913
3.0	.973	.2477	.899	.00926
5.0	.985	.2478	.941	.00950
9.0	.992	.2485	.968	.00970
20.0	.996	.2492	.985	.00986
200.0	.9997	.2499	.999	.00999
$\to\infty$	1.0000	.2500	1.000	.01000

$$k(x,t) = \frac{1}{t-x} + k_{22}(x,t),\ a_2 < x < 0,\ a_2 < t < 0,$$
$$k(x,t) = k_{21}(x,t),\ a_2 < x < 0,\ 0 < t < b_1,$$
$$k(x,t) = k_{12}(x,t),\ 0 < x < b_1,\ a_2 < t < 0, \quad (73)$$
$$k(x,t) = \frac{1}{t-x} + k_{11}(x,t),\ 0 < x < b_1,\ 0 < t < b_1.$$

The problem may then be solved by following the numerical technique described by(59)–(68). Specifically, by selecting $\phi(t) = f(r)$, $a_2 < t < b_1$, $-1 < r < 1$, as in (62), the stress intensity factors and the crack opening displacement may be obtained from (67) and (68).

Some calculated results are shown in Tables 1–5 and Figs. 2 and 3. From the geometry of the medium it is clear that an external load giving rise to only σ_{xz} in the crack region would have no effect on the crack problem; that is, for this case the relative crack surface displacements and the stress intensity factors would be zero. In the problem under consideration, from a practical viewpoint, perhaps the most important external load would, therefore, be a uniform shear strain $\gamma_{yz} = \gamma_0$ applied to the composite medium away from the crack region. Thus, the perturbation problem will be solved under the following crack surface tractions:

$$\tau_i(x) = -\sigma_{yz}^0(x,0) = -\gamma_0\mu_i(x),\ a_i < x < b_i,\ (i = 1,2,3). \quad (74)$$

Table 1 shows the stress intensity factors for two different material pairs containing a single crack in either material 2 or material 3. In both cases one crack tip is assumed to touch the interface $x = 0$ or $x = h$. The table shows the normalized stress intensity factor defined by

$$k(d_i) = k_3(d_i)/\tau_0\sqrt{a},\ \tau_0 = \mu_2\gamma_0 \quad (75)$$

where $2a$ is the crack length and d_i designates the crack tip.

Downloaded 03 May 2010 to 171.66.16.248. Redistribution subject to ASME license or copyright; see http://www.asme.org/terms/Terms_Use.cfm

Table 5 Normalized mode III stress intensity factors for a crack of length $2a$ located in either material 2 or in material 3. The crack orientation with respect to its respective interface is constant and the position of the other interface is varied by changing $2a/h$: $\mu_2/\mu_3 = 23.08$, $k = k_3/\pi_0\sqrt{a}$, $\tau_0 = \gamma_0\mu_2$, is uniform shear strain at $y \to \infty$

	Crack in material 2					
$\frac{-(b_2+a_2)}{b_2-a_2}$	1.00		1.15		2.00	
2a/h	$k(a_2)$	$k(b_2)$	$k(a_2)$	$k(b_2)$	$k(a_2)$	$k(b_2)$
1.	1.0505	1.154	1.0390	1.0869	1.0159	1.0244
2.	1.0742	1.267	1.0541	1.0869	1.0196	1.0314
5.	1.1081	1.507	1.0717	1.2023	1.0228	1.0379
10.	1.1324	1.777	1.0810	1.2470	1.0241	1.0406
20.	1.1539	2.143	1.0868	1.2791	1.0248	1.0422
50.	1.177	2.81	1.0909	1.3034	1.0253	1.0432
100.	1.192	3.5	1.0923	1.3125	1.0254	1.0435
1000.			1.0937	1.3213	1.0255	1.0438
$\to\infty$	1.2558	∞	1.0938	1.3223	1.0256	1.0438
	Crack in material 3					
$\frac{b_3+a_3-2h}{b_3-a_3}$	1.00		1.15		2.00	
2a/h	$k(a_3)$	$k(b_3)$	$k(a_3)$	$k(b_3)$	$k(a_3)$	$k(b_3)$
1.	0.0377	.04146	.03997	.04182	.04231	.04266
2.	0.0346	.04080	.03843	.04133	.04203	.04252
5.	0.0295	.04009	.03640	.04084	.04178	.04239
10.	0.0253	.03975	.03520	.04061	.04167	.04235
20.	0.0213	.03953	.03439	.04047	.04161	.04232
50.	0.0165	.03939	.03380	.04039	.04158	.04230
100.	0.0134	.03934	.03359	.04036	.04156	.04230
1000.		.03929	.03338	.04033	.04155	.04229
$\to\infty$	0	.03929	.03336	.04033	.04155	.04229

For $a/h \to 0$, as expected, the stress intensity factors approach the corresponding homogeneous results, namely

$$k_3(a_i) \to k_3(b_i) \to \mu_i\gamma_0\sqrt{a}, \ (i=2,3), \tag{76}$$

where $a_2 = -2a$, $b_2 = 0$, $a_3 = h$, $b_3 = h+2a$. For $h/a \to 0$ one would expect to recover the solution of the corresponding crack problem in a piecewise homogeneous material (see Erdogan and Cook, 1974). In this case, near the crack tip terminating at the interface, the stress state has the behavior $\sigma_{iz} \sim r^{-\alpha}$, $(i=x,y)$, where r is the distance from the crack tip. Since $\mu_2 > \mu_3$, $\alpha > 0.5$ for the crack in material 2 and $\alpha < 0.5$ for the crack in material 3. In the limit as $h/a \to 0$, therefore, $k(0) \to \infty$ and $k(h) \to 0$. The stress intensity factors at the far ends of the cracks shown in the table are obtained by using the solution given by Erdogan and Cook (1974). For $\mu_2 = 4\mu_3$ results showing the trends for small values of h/a are also displayed in Fig. 2.

For the crack tip at $b_1 = h$ and the crack length $2a < h$ or $2a > h$, the stress intensity factors are given in Table 2. The results for the similar problem with a crack tip at $x = 0$ are shown in Table 3. Again, it is expected that for $a/h \to 0$, $k_3(d_i) \to \mu_i(d_i)\gamma_0\sqrt{a}$. Observing that k_3 is normalized with respect to $\mu_2\gamma_0\sqrt{a}$, that is seen to be the trend in Tables 2 and 3. For $h/a \to 0$ the stress intensity factors are seen to approach the limiting values given in Table 1 for the piecewise homogeneous material.

In application the results given in Table 1 would correspond to a subcritically propagating crack one end of which is arrested by a relatively tough interfacial zone. If the interfacial zone is less resistant to crack growth than the adjacent materials, then the crack is more likely to initiate in the interfacial zone, propagate through, become arrested by the tougher of the two materials, and grow into the other. Such a process may be studied by using the results similar to that given by Tables 2 and 3.

The stress intensity factors for a crack of length $2a$ centered at $x = h/2$ with $2a/h$ are given in Table 4. Note that for $a/h \to 0$, as expected, we have

$$k_3(a_1) \to k_3(b_1) \to \mu_1(h/2)\gamma_0\sqrt{a}, \tag{77}$$

that is, $k \to 0.5$ for $\mu_2/\mu_3 = 4$ and $k \to 0.1$ for $\mu_2/\mu_3 = 100$. Similarly, for $a/h \to \infty$ the stress intensity factors at the crack tips approach the corresponding homogeneous half-plane solutions[3]. For a crack embedded in material 2 or material 3 some results are given in Table 5. In order to compare the results found in this paper with the limiting results obtained by Erdogan and Cook (1974) and by Kaya and Erdogan (1987), in Table 5 μ_2/μ_3 is assumed to be 23.08 (roughly corresponding to an aluminum–epoxy pair).

Finally, Fig. 3 shows some sample results for the crack opening displacement $w(s) = w(x,0)$ where s is the normalized coordinate defined by (59) with $s = \mp 1$ corresponding to the crack tips. Three examples shown correspond to $h/a = 0$, 0.25, and 1, $2a$ being the crack length. In each case the centerline of the interfacial zone coincides with the quarter point of the crack, and the boundaries of the interfacial zone are indicated by solid vertical lines. For $h = 0$ as shown by Erdogan and Cook (1974), the function $\phi(x) = (\partial/\partial x)w(x,0)$ is discontinuous

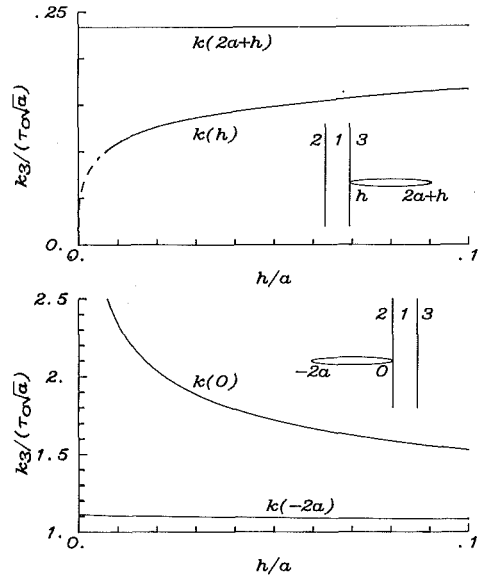

Fig. 2 Normalized stress intensity factors for the crack terminating at the interfacial zone in bonded materials; $\mu_2 = 4\mu_3$, $\tau_0 = \mu_2\gamma_0$, where γ_0 is the uniform shear strain γ_{yz}^{∞} away from the crack region

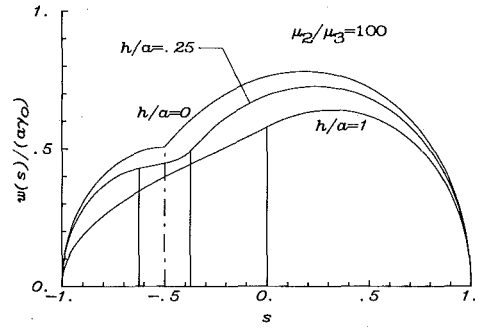

Fig. 3 Normalized crack surface displacement in bonded materials with a nonhomogeneous interfacial zone. In each case shown the crack goes through the zone and the centerline of the zone coincides with the quarter-point of the crack, $s = -0.5$, where s is the normalized coordinate defined by $x = s(b_3 - a_2)/2 + (b_3 + a_2)/2$ (Fig. 1).

[3]Note that for a homogeneous half-plane with a stress-free boundary containing an edge crack of length a perpendicular to the boundary and subjected to uniform antiplane shear traction τ_0 on the crack surfaces, the stress intensity factor is $\tau_0\sqrt{a}$. In a piecewise homogeneous medium (i.e., for $h = 0$) under uniform antiplane shear strain $\gamma_{yz} = \gamma_0$ away from the crack region, since for a symmetrically located crack $(-a < x < a)$ $\sigma_{xz}(0,y)$ along the y-axis is zero, the solution would be identical to that of two half planes with stress-free boundaries having edge cracks of length a (see Edrogan and Cook, 1974).

Downloaded 03 May 2010 to 171.66.16.248. Redistribution subject to ASME license or copyright; see http://www.asme.org/terms/Terms_Use.cfm

at the interface. This may also be seen in Fig. 3. $w(x)$, however, becomes progressively smoother for increasing values of h/a.

Acknowledgment

This study was supported by NSF under grant MSM-8613611, by NASA-Langley under grant NAG-1-713 and by SRC Contract 88-MP-071.

References

Atkinson, C., 1977, "On Stress Singularities and Interfaces in Linear Elastic Fracture Mechanics," *International Journal of Fracture*, Vol. 13, pp. 807–820.

Atkinson, C., and List, R. D., 1978, "Steady State Crack Propagation into Media with Spacially Varying Elastic Properties," *Int. J. Engng. Sci.*, Vol. 16, pp. 717–730.

Bogy, D. B., 1968, "Edge-Bonded Dissimilar Orthogonal Elastic Wedges Under Normal and Shear Loading," ASME JOURNAL OF APPLIED MECHANICS, Vol. 35, pp. 460–466.

Bogy, D. B., 1971, "Two Edge-Bonded Elastic Wedges of Different Materials and Wedge Angles under Surface Tractions," ASME JOURNAL OF APPLIED MECHANICS, Vol. 38, pp. 377–386.

Comninou, M., 1977, "The Interface Crack," ASME JOURNAL OF APPLIED MECHANICS, Vol. 44, pp. 631–636.

Cook, T. S., and Erdogan, F., 1972, "Stresses in Bonded Materials with a Crack Perpendicular to the Interface," *Int. J. Engng. Sci.*, Vol. 10, pp. 677–697.

Delale, F., and Erdogan, F., 1988a, "On the Mechanical Modeling of the Interfacial Region in Bonded Half Planes," ASME JOURNAL OF APPLIED MECHANICS, Vol. 55, pp. 317–324.

Delale, F., and Erdogan, F., 1988b, "Interface Crack in a Nonhomogeneous Elastic Medium," *Int. J. Engng. Sci.*, Vol. 26, pp. 559–568.

England, A. H., 1965, "A Crack Between Dissimilar Media," ASME JOURNAL OF APPLIED MECHANICS, Vol. 32, pp. 400–402.

Erdelyi, A., ed., 1953, *Higher Transcendental Functions*, Vol. II, McGraw-Hill, New York.

Erdogan, F., 1963, "Stress Distribution in a Nonhomogeneous Plane with Cracks," ASME JOURNAL OF APPLIED MECHANICS, Vol. 3, pp. 232–236.

Erdogan, F., 1965, "Stress Distribution in Bonded Dissimilar Materials with Cracks," ASME JOURNAL OF APPLIED MECHANICS, Vol. 32, pp. 403–410.

Erdogan, F., and Biricikoglu, V., 1973, "Two Bonded Half Planes with a Crack Going Through the Interface," *Int. J. Engng. Sci.*, Vol. 11, pp. 745–766.

Erdogan, F., and Cook, T. S., 1974, "Antiplane Shear Crack Terminating at and Going Through A Bimaterial Interface," *International Journal of Fracture*, Vol. 10, pp. 227–240.

Erdogan, F., 1985, "The Crack Problem for Bonded Nonhomogeneous Materials Under Antiplane Shear Loading," ASME JOURNAL OF APPLIED MECHANICS, Vol. 52, pp.823–828.

Gradshteyn, I. S., and Ryzhik, 1965, *Tables of Integrals, Series and Products*, Academic Press, New York.

Hein, V. L., and Erdogan, F., 1971, "Stress Singularities in a Two-Material Wedge," *International Journal of Fracture*, Vol. 7, pp. 317–330.

Kaya, A. C., and Erdogan, F., 1987, "On the Solution of Integral Equations with a Generalized Cauchy Kernel," *Quarterly of Applied Mathematics*, Vol. 45, No. 3, pp. 455–469.

Knowles, J. K., and Sternberg, E., 1975, "On the Singularity Induced by Certain Mixed Boundary Conditions in Linearized and Nonlinear Elastostatics," *Int. J. Solids Structures*, Vol. 11, pp. 1173–1201.

Muskhelishvili, N. I., 1953, *Some Basic Problem of the Mathematical Theory of Elasticity*, P. Noordhoff, Groningen, The Netherlands.

Rice, J. R., and Sih, G. C., 1965, "Plane Problems of Cracks in Dissimilar Media," ASME JOURNAL OF APPLIED MECHANICS, Vol. 32, pp. 418–423.

Shih, C. F., and Asaro, R. J., 1987, "Elastic-Plastic Analysis of Cracks on Bimaterial Interfaces, Part I: Small Scale Yielding," Brown University Report ONR-NOOO14-86K-0235/2.

APPENDIX A

Derivation of $R_1(\alpha),\ldots,R_4(\alpha)$ That Appear in Equation (29)

Substituting from equation (12)–(18) and (28) into (7) and (8), inverting the sine transforms, changing the order of integrations, and evaluating the inner integrals, $R_1,\ldots,R_4$ defined by (29) may be expressed as

$$R_1(\alpha)=-\frac{1}{2\pi}\int_{-\infty}^{\infty}\frac{\alpha A_1(\theta)d\theta}{\alpha^2+\theta^2+i\beta\theta}+\frac{1}{2\pi}\int_{-\infty}^{\infty}\frac{\alpha A_2(\theta)d\theta}{\alpha^2+\theta^2}+(c_2-c_1)\frac{1}{\alpha},$$

$$R_2(\alpha)=\frac{i}{2\pi}\int_{-\infty}^{\infty}\frac{\alpha\theta A_1(\theta)d\theta}{\alpha^2+\theta^2+i\beta\theta}-\frac{i}{2\pi}\int_{-\infty}^{\infty}\frac{\alpha\theta A_2(\theta)d\theta}{\alpha^2+\theta^2},$$

$$R_3(\alpha)=-\frac{1}{2\pi}\int_{-\infty}^{\infty}\frac{\alpha A_1(\theta)e^{-i\theta h}d\theta}{\alpha^2+\theta^2+i\beta\theta}+\frac{1}{2\pi}\int_{-\infty}^{\infty}\frac{\alpha A_3(\theta)e^{i\theta h}d\theta}{\alpha^2+\theta^2}+(c_3-c_1)\frac{1}{\alpha},$$

$$R_4(\alpha)=\frac{i}{2\pi}\int_{-\infty}^{\infty}\frac{\alpha\theta A_1(\theta)e^{-i\theta h}d\theta}{\alpha^2+\theta^2+i\beta\theta}-\frac{i}{2\pi}\int_{-\infty}^{\infty}\frac{\alpha\theta A_3(\theta)e^{-i\theta h}d\theta}{\alpha^2+\theta^2}. \quad \text{(A1–4)}$$

We now substitute from (22) into (A1–4), change the order of integrations, and evaluate the inner integrals by using the following results:

$$\int_{-\infty}^{\infty}\frac{e^{i\theta t}}{\alpha^2+\theta^2}d\theta=\frac{\pi}{\alpha}e^{\alpha t},\ t<0,$$

$$\int_{-\infty}^{\infty}\theta\frac{e^{i\theta t}}{(\alpha^2+\theta^2)}d\theta=\frac{i\pi}{\alpha^2}(e^{\alpha t}-1),\ t<0,$$

$$\int_{-\infty}^{\infty}\frac{e^{i\theta t}}{\alpha^2+\theta^2+i\beta\theta}d\theta=\frac{\pi}{\alpha_1}e^{-n_1 t},\ t>0,$$

$$\int_{-\infty}^{\infty}\frac{e^{i\theta t}}{\theta(\alpha^2+\theta^2+i\beta\theta)}d\theta=i\pi\left[\frac{1}{\alpha^2}-\frac{e^{-n_1 t}}{\alpha_1 n_1}\right],\ t>0,$$

$$\int_{-\infty}^{\infty}\frac{e^{i\theta(t-h)}}{\alpha^2+\theta^2+i\beta t}d\theta=\frac{\pi}{\alpha_1}e^{n_2(h-t)},\ t<h,$$

$$\int_{-\infty}^{\infty}\frac{e^{i\theta(t-h)}}{\theta(\alpha^2+\theta^2+i\beta\theta)}d\theta=-i\pi\left[\frac{e^{n_2(h-t)}}{\alpha_1 n_2}+\frac{1}{\alpha^2}\right],\ t<h,$$

$$\int_{-\infty}^{\infty}\frac{e^{i\theta(t-h)}}{\alpha^2+\theta^2}d\theta=\frac{\pi}{\alpha}e^{-\alpha(t-h)},\ t>h,$$

$$\int_{-\infty}^{\infty}\frac{e^{i\theta(t-h)}}{\theta(\alpha^2+\theta^2)}d\theta=i\pi\left[\frac{1}{\alpha^2}-\frac{e^{-\alpha(t-h)}}{\alpha^2}\right],\ t>h. \quad \text{(A5)}$$

Thus, by also using (24b,c), equations (A1–4) may easily be shown to reduce to

$$R_1(\alpha)=-\frac{\alpha}{2\alpha_1 n_1}\int_{a_1}^{b_1}e^{-n_1 t}\phi_1(t)dt-\frac{1}{2\alpha}\int_{a_2}^{b_2}e^{\alpha t}\phi_2(t)dt,$$

$$R_2(\alpha)=-\frac{\alpha}{2\alpha_1}\int_{a_1}^{b_1}e^{-n_1 t}\phi_1(t)dt+\frac{1}{2}\int_{a_2}^{b_2}e^{\alpha t}\phi_2(t)dt,$$

$$R_3(\alpha)=-\frac{\alpha}{2\alpha_1 n_2}\int_{a_1}^{b_1}e^{n_2(h-t)}\phi_1(t)dt+\frac{1}{2\alpha}\int_{a_3}^{b_3}e^{-\alpha(t-h)}\phi_3(t)dt,$$

$$R_4(\alpha)=-\frac{\alpha}{2\alpha_1}\int_{a_1}^{b_1}e^{n_2(h-t)}\phi_1(t)dt+\frac{1}{2}\int_{a_3}^{b_3}e^{-\alpha(t-h)}\phi_3(t)dt. \quad \text{(A6}a\text{–}d\text{)}$$

APPENDIX B

Expressions of the Kernels k_{ij}, $(i,j=1,2,3)$ That Appear in Equation (34)

To examine the asymptotic behavior of the kernels defined by (32) and (33) we observe that for $|\alpha|\to\infty$

$$m_1=-|\alpha|\left(1+\frac{i\beta}{\alpha}\right)^{1/2}\to-|\alpha|,\ \alpha_1=\alpha\left[1+\left(\frac{\beta}{2\alpha}\right)^2\right]^{1/2}\to\alpha,$$

$$n_1\to\alpha-\frac{\beta}{2},\ n_2\to-\alpha-\frac{\beta}{2},\ \Delta\to-4\alpha^2. \quad \text{(B1)}$$

Thus, after separating the terms that become unbounded at $x=t$, $x=0=t$, and $x=h=t$, the kernels may be expressed as follows:

Downloaded 03 May 2010 to 171.66.16.248. Redistribution subject to ASME license or copyright; see http://www.asme.org/terms/Terms_Use.cfm

$$\lim_{y\to+0} h_{ij}(x,y,t)=\frac{\delta_{ij}}{t-x}+k_{ij}(x,t) \tag{B2}$$

$$k_{11}(x,t)=-\frac{\beta}{2}\log|t-x|+h(x,t)+g(x,t), \tag{B3}$$

$$h(x,t)=-\frac{\beta}{2}\left[C_0+\log A+\sum_{k=1}^{\infty}(-1)^k\frac{A^{2k}}{2k(2k)!}(t-x)^{2k}\right]+\int_0^{\infty}\left[\left(1+\frac{\beta^2}{\alpha^2}\right)^{1/4}\cos\frac{\theta}{2}-1\right]\sin\alpha(t-x)d\alpha+\int_0^{A}\left(1+\frac{\beta^2}{\alpha^2}\right)^{1/4}\sin\frac{\theta}{2}\cos\alpha(t-x)d\alpha+\int_A^{\infty}\left[\left(1+\frac{\beta^2}{\alpha^2}\right)^{1/4}\sin\frac{\theta}{2}-\frac{\beta}{2\alpha}\right]\cos\alpha(t-x)d\alpha, \tag{B4}$$

$$\theta=\tan^{-1}\left(\frac{\beta}{\alpha}\right), \tag{B5}$$

$$g(x,t)=e^{\frac{\beta}{2}(t-x)}\left\{\int_0^{\infty}\frac{\alpha^2}{\alpha_1\Delta}(\alpha-n_1)(\alpha+n_2)\left[-\frac{1}{n_1}e^{-\alpha_1(2h+t-x)}-\frac{1}{n_2}e^{-\alpha_1(2h-t+x)}\right]d\alpha+\int_0^{A}\frac{\alpha^2\beta}{\alpha_1\Delta}[e^{-\alpha_1(t+x)}+e^{-\alpha_1(2h-t-x)}]d\alpha+\int_A^{\infty}\left[\frac{\alpha^2\beta}{\alpha_1\Delta}e^{-\alpha_1(t+x)}+\frac{\beta}{4\alpha}e^{-\alpha(t+x)}\right]d\alpha+\int_A^{\infty}\frac{\alpha^2\beta}{\alpha_1\Delta}e^{-\alpha_1(2h-t-x)}+\frac{\beta}{4\alpha}e^{-\alpha(2h-t-x)}\Big]d\alpha+\frac{\beta}{4}\mathrm{Ei}[-A(t+x)]+\frac{\beta}{4}\mathrm{Ei}[-A(2h-t-x)]\right\}, \tag{B6}$$

$$k_{12}(x,t)=\frac{1}{t-x}+\int_0^{A}\left\{\frac{2\alpha}{\Delta}[-(\alpha+n_2)e^{-2\alpha_1 h}e^{\alpha t}e^{n_1 x}+(\alpha+n_1)e^{\alpha t}e^{n_2 x}]+e^{-\alpha(x-t)}\right\}d\alpha+\int_A^{\infty}\left\{\frac{2\alpha}{\Delta}[-(\alpha+n_2)e^{-2\alpha_1 h}e^{\alpha t}e^{n_1 x}+(\alpha+n_1)e^{\alpha t}e^{n_2 x}]+e^{-\alpha(x-t)}-\frac{\beta}{4\alpha}e^{-\alpha(x-t)}\right\}d\alpha-\frac{\beta}{4}\mathrm{Ei}[-A(x-t)], \tag{B7}$$

$$k_{13}(x,t)=\frac{1}{t-x}+\int_0^{A}\left\{\frac{2\alpha}{\Delta}[-(\alpha-n_2)e^{-n_1(h-x)}e^{-\alpha(t-h)}+(\alpha-n_1)e^{-2\alpha_1 h}e^{-\alpha(t-h)}e^{-n_2(h-x)}]-e^{-\alpha(t-x)}\right\}d\alpha+\int_A^{\infty}\left\{\frac{2\alpha}{\Delta}[-(\alpha-n_2)e^{-n_1(h-x)}e^{-\alpha(t-h)}+(\alpha-n_1)e^{-2\alpha_1 h}e^{-\alpha(t-h)}e^{-n_2(h-x)}]-e^{-\alpha(t-x)}-\frac{\beta}{4\alpha}e^{-\alpha(t-x)}\right\}d\alpha-\frac{\beta}{4}\mathrm{Ei}[-A(t-x)], \tag{B8}$$

$$k_{21}(x,t)=\frac{1}{t-x}+\int_0^{A}\left\{\frac{2\alpha^2}{\Delta}\left[-\frac{(\alpha+n_1)}{n_1}e^{-n_1 t}e^{\alpha x}+\frac{(\alpha+n_2)}{n_2}e^{-n_1 h}e^{n_2(h-t)}e^{\alpha x}\right]-e^{-\alpha(t-x)}\right\}d\alpha+\int_A^{\infty}\left\{\frac{2\alpha^2}{\Delta}\left[-\frac{(\alpha+n_1)}{n_1}e^{-n_1 t}e^{\alpha x}+\frac{(\alpha+n_2)}{n_2}e^{-n_1 h}e^{n_2(h-t)}e^{\alpha x}\right]-e^{-\alpha(t-x)}-\frac{\beta}{4\alpha}e^{-\alpha(t-x)}\right\}d\alpha-\frac{\beta}{4}\mathrm{Ei}[-A(t-x)], \tag{B9}$$

$$k_{22}(x,t)=\int_0^{A}\left[-\frac{\alpha\beta}{\Delta}(1-e^{-2\alpha_1 h})\right]e^{\alpha(t+x)}d\alpha+\int_A^{\infty}\left[-\frac{\alpha\beta}{\Delta}(1-e^{-2\alpha_1 h})-\frac{\beta}{4\alpha}\right]e^{\alpha(t+x)}d\alpha-\frac{\beta}{4}\mathrm{Ei}[A(t+x)], \tag{B10}$$

$$k_{23}(x,t)=\frac{1}{t-x}+\int_0^{\infty}\left[-\frac{4\alpha\alpha_1}{\Delta}e^{-n_1 h}e^{-\alpha(t-h)}e^{\alpha x}-e^{-\alpha(t-x)}\right]d\alpha, \tag{B11}$$

$$k_{31}(x,t)=\frac{1}{t-x}+\int_0^{A}\left\{\frac{2\alpha^2}{\Delta}\left[\frac{(\alpha-n_1)}{n_1}e^{n_2 h}e^{-n_1 t}e^{-\alpha(x-h)}-\frac{(\alpha-n_2}{n_2}e^{n_2(h-t)}e^{-\alpha(x-h)}\right]+e^{-\alpha(x-t)}\right\}d\alpha+\int_A^{\infty}\left\{\frac{2\alpha^2}{\Delta}\left[\frac{(\alpha-n_1)}{n_1}e^{n_2 h}e^{-n_1 t}e^{-\alpha(x-h)}-\frac{(\alpha-n_2)}{n_2}e^{n_2(h-t)}e^{-\alpha(x-h)}\right]+e^{-\alpha(x-t)}-\frac{\beta}{4\alpha}e^{-\alpha(x-t)}\right\}d\alpha-\frac{\beta}{4}\mathrm{Ei}[-A(x-t)], \tag{B12}$$

$$k_{32}(x,t)=\frac{1}{t-x}+\int_0^{\infty}\left[\frac{4\alpha\alpha_1}{\Delta}e^{n_2 h}e^{\alpha t}e^{-\alpha(x-h)}+e^{-\alpha(x-t)}\right]d\alpha, \tag{B13}$$

$$k_{33}(x,t)=\int_0^{A}\left[-\frac{\alpha\beta}{\Delta}(1-e^{-2\alpha_1 h})\right]e^{-\alpha(t+x-2h)}d\alpha+\int_A^{\infty}\left[-\frac{\alpha\beta}{\Delta}(1-e^{-2\alpha_1 h})-\frac{\beta}{4\alpha}\right]e^{-\alpha(t+x-2h)}d\alpha-\frac{\beta}{4}\mathrm{Ei}[-A(t+x-2h)]. \tag{B14}$$

In equations (B4)–(B14), $C_0=0.5772156649$ is the Euler's constant, A is any positive constant, and the exponential integral $\mathrm{Ei}[-Az]$ is defined by $(A>0, z>0)$

$$\mathrm{Ei}[-Az]=-\int_A^{\infty}\frac{1}{\alpha}e^{-\alpha z}d\alpha=C_0+\log A+\log z+\int_0^{Az}\frac{e^{-\alpha}-1}{\alpha}d\alpha=C_0+\log A+\log z+\sum_{k=1}^{\infty}\frac{(-1)^k A^k z^k}{k(k!)} \tag{B15}$$

where rapid convergence is insured by selecting $0<A<1$.

Downloaded 03 May 2010 to 171.66.16.248. Redistribution subject to ASME license or copyright; see http://www.asme.org/terms/Terms_Use.cfm

H. A. Luo
Postdoctoral Research Associate,
Department of Civil Engineering,
Case Western Reserve University,
Cleveland, OH 44106

Y. Chen
Department of Mechanics and
Materials Science,
Rutgers–The State University of New Jersey,
Piscataway, NJ 08854
Fellow ASME

Interface Crack in a Three-Phase Composite Constitutive Model

An arc-shaped crack in fiber-reinforced composite material is the subject of this paper. A three-phase composite cylinder is taken as the material model to take into account the effect of surrounding fibers. Using Muskhelishvili's complex variable method, an exact elastic solution is derived based on the conventional crack opening assumption. The complex stress intensity factors for the interface crack, in the sense defined by Hutchinson, Mear, and Rice, are determined. Some numerical examples are given. It is shown that, as the volume concentration of the fiber is increased, the magnitude of the complex stress intensity factors varies considerably.

1 Introduction

Interface cracking is an important mode of failure in composite materials and has received much attention in the past. The earliest work can be traced back to 1959 when Williams (1959) determined the stress distribution around a semi-infinite interface crack between dissimilar media. Williams (1959) also noticed the stress oscillating singularities near the crack tip. Later, Erdogan (1963, 1965), England (1965), and Rice and Sih (1965) derived a series of elastic solutions for finite interface cracks. However, since England (1965) and Malyshev and Salganik (1965) proved that all these elastic solutions lead to wrinkling of the two crack faces, no serious attention was paid to it until Comninou (1977) reconsidered the problem. She showed that the interface crack between two dissimilar media is not completely open as observed in homogeneous materials, near the crack tip there exists a contact zone. Comninou formulated the problems in terms of a pair of coupled singular integral equations of the first kind and solved them numerically. However, since the contact zones are usually extremely narrow, some numerical difficulties were encountered. Recently, Gautesen and Dundurs (1987) gave an exact solution for a straight interface crack in a tension field.

Meanwhile, being disregarded for two decades, the elastic solution of the interface crack problem based on the conventional crack opening assumption has rekindled researchers' interest again in recent years (Hutchinson, Mear, and Rice, 1987; Shih and Asaro, 1988; Rice, 1988). In particular, Rice (1988) reexamined the elastic fracture concept for the interface crack problem and showed that the conventional elastic solution of the problems is compatible with the complete Williams expansion which contains both positive and negative exponents. In other words, the elastic solution is still valid in the annular region surrounding the crack tip, provided that the contact zone near the tip is sufficiently small. Then, in this case the actual material behavior inside the contact zone is governed by the elastic field of the surrounding annular region. In fracture mechanics, this kind of region is known as K-dominant region where K is the stress intensity factor. For interface crack problem, Hutchinson, Mear, and Rice (1987) introduced a new type of complex stress intensity factor which can uniquely define the singular field. Thus, under the small-scale contact zone approximation the growth condition of interface crack can be expressed in terms of whether the calculated complex stress intensity factor attains its critical locus in a complex plane for the pair of materials being considered. Evidently, such a treatment simplifies the problem considerably. Moreover, as examined by Rice (1988), the condition of small contact zone is satisfied in most practice where there is a certain amount of tensile loading relative to the interface crack.

In this field, most work was concerned with the straight interface crack; less attention has been paid to the arc-shaped interface crack. The interface crack between an isolated circular inclusion and infinitely extended matrix has been studied

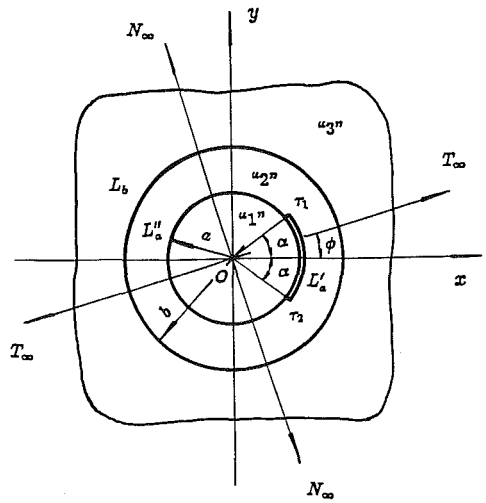

Fig. 1 Interface crack in the three-phase composite cylinder model

Contributed by the Applied Mechanics Division of THE AMERICAN SOCIETY OF MECHANICAL ENGINEERS for publication in the JOURNAL OF APPLIED MECHANICS.

Discussion on this paper should be addressed to the Technical Editor, Prof. Leon M. Keer, The Technological Institute, Northwestern University, Evanston, IL 60208, and will be accepted until two months after final publication of the paper itself in the JOURNAL OF APPLIED MECHANICS. Manuscript received by the ASME Applied Mechanics Division, May 9, 1989; final revision, Jan. 15, 1990.

Copyright © 1991 by ASME
Downloaded 03 May 2010 to 171.66.16.248. Redistribution subject to ASME license or copyright; see http://www.asme.org/terms/Terms_Use.cfm

by England (1966), Perlman and Sih (1967), and Toya (1974). Following Willis (1971), Toya also applied Griffith's virtual work argument to obtain a criterion of crack extension.

As indicated by Luo and Chen (1989), except in the case when the volume concentration of inclusion is very dilute, in two-phase composites there always exists notable interaction among the inclusions. That is, the stress and strain field will considerably depend on its microstructure which, however, usually is too complicated to be taken into account in details. Fortunately, when an imperfectly bonded inclusion is considered in a real composite, a reasonable simplified model is so-called three-phase model (Christensen and Lo, 1979). Unlike the two-phase model where the inclusion is embedded in the infinitely extended pure matrix, the three-phase model considers that in the immediate neighborhood of the inclusion there is a layer of matrix material in action, but at certain distance the average influence of the heterogeneous medium can be represented by the smeared property of the composite. Thus, for the problems of which the interest is in the field near the inclusion, it can reasonably be accepted as a good model. The two-dimensional version of the three-phase model consists of three concentric cylindrical layers with the outer one being extended to infinity and the internal and external radii of the intermediate matrix-phase a and b being related to each other by $(a/b)^2=c$, where c is the volume concentration of the fiber in composite. In this paper, the effective moduli of composite, namely the elastic constants of the outer-phase medium, are calculated by means of modified Mori-Tanaka method suggested by Luo and Weng (1989).

By use of the complex variable approach, the interface crack problem of the three-phase model is reduced to two inhomogeneous Hilbert problems in Section 2. After solving these problems, the stress distribution and the relative crack opening displacement at the interface are found. The complex stress intensity factors, based on the definition of Hutchinson, Mear, and Rice (1987), are formulated in Section 3. In Section 4 several numerical examples are illustrated.

2 Basic Equations

In two-dimensional elasticity, in terms of the well-known Muskhelishvili's complex potentials the stress and displacement fields in a circular region bounded by $r=c$ can be expressed as

$$\sigma_{rr}+\sigma_{\theta\theta}=2[\Phi(z)+\overline{\Phi(z)}]$$

$$\sigma_{rr}+i\sigma_{r\theta}=\Phi(z)-\Phi\left(\frac{c^2}{\bar{z}}\right)+\bar{z}\left(\frac{\bar{z}}{c^2}-\frac{1}{z}\right)\overline{\Psi(z)} \tag{1}$$

and

$$2\mu(u'+v')=iz[\kappa\Phi(z)+\Phi\left(\frac{c^2}{\bar{z}}\right)-\bar{z}\left(\frac{\bar{z}}{c^2}-\frac{1}{z}\right)\overline{\Psi(z)}]. \tag{2}$$

where in polar coordinates, where $z=x+iy$, $\bar{z}=x-iy$, $u'=\partial u_x/\partial\theta$, $v'=\partial u_y/\partial\theta$, μ is the in-plane shear modulus, namely, μ_{12}, and κ is the Muskhelishvili constant. For the plane deformation of isotropic materials, $\kappa=3-4\nu$ where ν is the Poisson's ratio; for the plane deformation of transversely isotropic materials

$$\kappa=1+2\frac{\mu_{12}}{K_{12}} \tag{3}$$

where K_{12} is the plane-strain bulk modulus. Besides, in equations (1) and (2) function $\Psi(z)$ can be further written as

$$\Psi(z)=\frac{c^2}{z^2}\left[\Phi(z)+\overline{\Phi}\left(\frac{c^2}{z}\right)-z\Phi'(z)\right]. \tag{4}$$

As Fig. 1 shows, medium 1, with elastic properties κ_1 and μ_1, occupies the region $r\le a$; medium 2, with elastic properties κ_2 and μ_2, occupies the region $a\le r\le b$; and medium 3, with elastic properties κ_3 and μ_3, occupies the outer region $r\ge b$. The geometric and physical properties of these three phases may be independent of each other; but when the model is used to simulate the fiber-reinforced composite material, the outer-phase will represent a homogeneous transversely isotropic medium which possesses the effective elastic moduli of the composite. In the latter case, μ_3 will be identical to the in-plane shear modulus of the composite μ_{12}, the Muskhelishvili constant κ_3 will be expressed by equation (3), and the relation $(a/b)^2=c$, where c is the volume concentration, is implied.

Denote the circle $r=b$ by L_b, the circle $r=a$ by L_a $(=L_a'+L_a'')$, where L_a' represents the crack surface, L_a'' the rest of L_a. Without loss of generality, the center of the arc L_a' is assumed to be located on the positive x-axis, and the central angle subtended by L_a' is assumed to be 2α. The three-phase system is subjected to remote general biaxial loads T_∞ and N_∞ where $T_\infty\ge N_\infty$ and T_∞ makes an angle ϕ with x-axis.

The boundary conditions and/or the continuity conditions on the interfaces L_a and L_b are

$$\sigma_{rr}^{(1)}(\tau)+i\sigma_{r\theta}^{(1)}(\tau)=0 \quad \text{on } L_a', \tag{5}$$

$$\sigma_{rr}^{(2)}(\tau)+i\sigma_{r\theta}^{(2)}(\tau)=0 \quad \text{on } L_a', \tag{6}$$

$$\sigma_{rr}^{(1)}(\tau)+i\sigma_{r\theta}^{(1)}(\tau)=\alpha_{rr}^{(2)}(\tau)+i\sigma_{r\theta}^{(2)}(\tau) \quad \text{on } L_a'', \tag{7}$$

$$u_x^{(1)}(\tau)+iu_y^{(1)}(\tau)=u_x^{(2)}(\tau)+iu_y^{(2)}(\tau) \quad \text{on } L_a'', \tag{8}$$

$$\sigma_{rr}^{(2)}(\zeta)+i\sigma_{r\theta}^{(2)}(\zeta)=\sigma_{rr}^{(3)}(\zeta)+i\sigma_{r\theta}^{(3)}(\zeta) \quad \text{on } L_b, \tag{9}$$

$$u_x^{(2)}(\zeta)+iu_y^{(2)}(\zeta)=u_x^{(3)}(\zeta)+iu_y^{(3)}(\zeta) \quad \text{on } L_b \tag{10}$$

where $\tau=a\exp(i\theta)$, $\zeta=b\exp(i\theta)$, and the superscripts label the phases under consideration.

By virtue of equation (1), the continuity condition (9) can be expressed in terms of the potential $\Phi(z)$ such that

$$[\Phi_{(2)}(\zeta)+\Phi_{(3)}(\zeta)]^+=[\Phi_{(2)}(\zeta)+\Phi_{(3)}(\zeta)]^- \quad \text{on } L_b \tag{11}$$

where the superscripts "+" and "−" denote the inner and the outer sides of the contour being considered, respectively. As a result, we conclude that the function $\Xi_1(z)=\Phi_{(2)}(z)+\Phi_{(3)}(z)$ is holomorphic in the region $a<|z|<b^2/a$. Thus, we can expand the function $\Xi_1(z)$ as a Laurent series in this annular region:

$$\Xi_1(z)=\Gamma+\overline{\Gamma'}\frac{b^2}{z^2}+\sum_{n=-\infty}^{\infty}A_nz^n \tag{12}$$

where

$$\Gamma=\frac{1}{4}(T_\infty+N_\infty),$$

$$\Gamma'=-\frac{1}{2}(T_\infty-N_\infty)e^{-2i\phi}. \tag{13}$$

Equation (10) together with (2) gives

$$\frac{\kappa_2}{2\mu_2}\Phi_{(2)}^+(\zeta)+\frac{1}{2\mu_2}\Phi_{(2)}^-(\zeta)=\frac{\kappa_3}{2\mu_3}\Phi_{(3)}^-(\zeta)+\frac{1}{2\mu_3}\Phi_{(3)}^+(\zeta). \tag{14}$$

Thus, elimination of $\Phi_{(2)}(\zeta)$ from (14) leads to a Hilbert problem:

$$\Phi_{(3)}^+(\zeta)+\eta_1\Phi_{(3)}^-(\zeta)=f_1(\zeta) \tag{15}$$

where function $\Phi_{(3)}(z)$ is holomorphic in entire plane and

$$\eta_1=\frac{\kappa_3\mu_2+\mu_3}{\kappa_2\mu_3+\mu_2},\quad \beta_1=\frac{\mu_3(\kappa_2+1)}{\kappa_2\mu_3+\mu_2},$$

$$f_1(\zeta)=\beta_1\left(\Gamma+\overline{\Gamma'}\frac{b^2}{\zeta^2}+\sum_{n=-\infty}^{\infty}A_n\zeta^n\right). \tag{16}$$

Its solution is

$$\Phi_{(3)}(z)=(\beta_1-\eta_1)\Gamma+\overline{\Gamma'}\frac{b^2}{z^2}+\beta_1\sum_{n=0}^{\infty}A_nz^n$$

Downloaded 03 May 2010 to 171.66.16.248. Redistribution subject to ASME license or copyright; see http://www.asme.org/terms/Terms_Use.cfm

for $|z|<b$ and

$$\Phi_{(3)}(z)=\Gamma-(1-\beta_1)\frac{\overline{\Gamma'}b^2}{\eta_1}\frac{1}{z^2}+\frac{\beta_1}{\eta_1}\sum_{n=1}^{\infty}A_{-n}z^{-n} \tag{17}$$

for $|z|>b$.

Then, by subtracting $\Phi_{(3)}(z)$ from $\Xi_1(z)$, we get

$$\Phi_{(2)}(z)=(1-\beta_1+\eta_1)\Gamma+\sum_{n=1}^{\infty}A_{-n}z^{-n}+(1-\beta_1)\sum_{n=0}^{\infty}A_nz^n$$

for $a<|z|<b$ and

$$\Phi_{(2)}(z)=\frac{1-\beta_1+\eta_1}{\eta_1}\overline{\Gamma'}\frac{b^2}{z^2}+\left(1-\frac{\beta_1}{\eta_1}\right)\sum_{n=1}^{\infty}A_{-n}z^{-n}+\sum_{n=0}^{\infty}A_nz^n \tag{18}$$

for $b<|z|<b^2/a$. Substitution of equation (18) into (4) yields

$$\begin{aligned}\Psi_{(2)}(z)=&\frac{b^2}{z^2}\{(1-\beta_1+\eta_1)\Gamma+\frac{1-\beta_1+\eta_1}{\eta_1}\Gamma'\left(\frac{z}{b}\right)^2+\overline{A}_0\\&+(1-\beta_1)A_0-(1-\beta_1)\sum_{n=1}^{\infty}A_n(n-1)z^n+\left(1-\frac{\beta_1}{\eta_1}\right)\\&\times\sum_{n=1}^{\infty}\overline{A}_{-n}\left(\frac{z}{b^2}\right)^n+\sum_{n=1}^{\infty}A_{-n}(n+1)z^{-n}\\&+\sum_{n=1}^{\infty}\overline{A}_n\left(\frac{b^2}{z}\right)^n\end{aligned} \tag{19}$$

for $a<|z|<b$.

On the other hand, conditions (5), (6), and (7) together imply that

$$[\Phi_{(1)}(\tau)+\Phi_{(2)}(\tau)]^+=[\Phi_{(1)}(\tau)+\Phi_{(2)}(\tau)]^- \quad \text{on } L_a=L_a'+L_a''. \tag{20}$$

Again, equation (20) suggests that the function $\Xi_2(z)$, which is defined as $\Phi_{(1)}(z)+\Phi_{(2)}(z)$, is holomorphic in the region $a^2/b<|z|<b$. Accordingly, we can expand it as

$$\Xi_2(z)=-\overline{\Phi_{(1)}(0)}+\sum_{n=-\infty}^{\infty}B_nz^n. \tag{21}$$

Meantime, (8) suggests that

$$\frac{\kappa_1}{2\mu_1}\Phi_{(1)}^+(\tau)+\frac{1}{2\mu_1}\Phi_{(1)}^-(\tau)=\frac{\kappa_2}{2\mu_2}\Phi_{(2)}^-(\tau)+\frac{1}{2\mu_2}\Phi_{(2)}^+(\tau) \quad \text{on } L_a''. \tag{22}$$

Eliminating $\Phi_{(2)}(\tau)$ from (22) and combining it with (5), we get another Hilbert problem:

$$\begin{cases}\Phi_{(1)}^+(\tau)+\eta_2\Phi_{(1)}^-(\tau)=f_2(\tau) & \text{on } L_a''\\ \Phi_{(1)}^+-\Phi_{(1)}^-(\tau)=0 & \text{on } L_a'\end{cases} \tag{23}$$

where

$$\eta_2=\frac{\kappa_2\mu_1+\mu_2}{\kappa_1\mu_2+\mu_1},\quad \beta_2=\frac{\mu_1(\kappa_2+1)}{\kappa_1\mu_2+\mu_1},$$

$$f_2(\tau)=\beta_2\{-\overline{\Phi_{(1)}(0)}+\sum_{n=-\infty}^{\infty}B_n\tau^n\}. \tag{24}$$

Following Muskhelishvili (1953), we can readily derive the function $\Phi_{(1)}(z)$ which is holomorphic in entire plane cut along L_a''.

$$\begin{aligned}\Phi_{(1)}(z)=&\frac{\beta_2}{1+\eta_2}\Bigg\{-\overline{\Phi_{(1)}(0)}+\sum_{n=-\infty}^{\infty}B_nz^n\\&-X_0(z)\Bigg[B_{-1}+\sum_{n=0}^{\infty}\sum_{m=0}^{n+1}B_ne_m'\\&\times a^mz^{n-m+1}+ae^{-2\lambda(\pi-\alpha)}\sum_{n=1}^{\infty}\sum_{m=0}^{n-1}B_{-n}e_m'''a^{-n}\left(\frac{a}{z}\right)^{n-m}\Bigg]\Bigg\}\\&-\left(1-\frac{\beta_2}{1+\eta_2}\right)\overline{\Phi_{(1)}(0)}X_0(z)(z+e_1'a)\end{aligned} \tag{25}$$

where $X_0(z)=(z-\tau_1)^{-\gamma}(z-\tau_2)^{\gamma-1}$ with $\tau_1=a\exp(i\alpha)$, $\tau_2=a\exp(-i\alpha)$ and $\gamma=1/2-i\lambda$, $\lambda=\log\eta_2/2\pi$, and

$$e_n'=\sum_{k=0}^{n}c_k'd_{n-k}'e^{-i(n-2k)\alpha}$$

$$e_n'''=\sum_{k=0}^{n}c_k'd_{n-k}'e^{i(n-2k)\alpha} \tag{26}$$

with

$$c_0'=1,\quad d_0'=1,$$

$$c_k'=\frac{-\gamma(1-\gamma)(2-\gamma)\cdots(k-\gamma-1)}{k!}\quad(\text{for } k\geq1) \tag{27}$$

$$d_k'=\frac{(\gamma-1)\gamma(\gamma+1)\cdots(\gamma+k-2)}{k!}\quad(\text{for } k\geq1).$$

Subtracting equation (25) from (21), we find

$$\begin{aligned}\Phi_{(2)}(z)=&\left(1-\frac{\beta_2}{1+\eta_2}\right)[-\overline{\Phi_{(1)}(0)}+\overline{\Phi_{(1)}(0)}e_1'aX_0(z)\\&+\overline{\Phi_{(1)}(0)}zX_0(z)+\sum_{n=-\infty}^{\infty}B_nz^n]\\&+\frac{\beta^2}{1+\eta_2}X_0(z)[B_{-1}+\sum_{n=0}^{\infty}\sum_{m=0}^{n+1}B_ne_m'a^mz^{n-m+1}\\&+ae^{-2\lambda(\pi-\alpha)}\sum_{n=1}^{\infty}\sum_{m=0}^{n-1}B_{-n}e_m'''a^{-n}\left(\frac{a}{z}\right)^{n-m}]\end{aligned} \tag{28}$$

for $a^2/b<|z|<b$. We note that in this region the function $\Phi_{(2)}(z)$ is sectionally holomorphic. We can expand $\Phi_{(2)}(z)$ at $z=\infty$ for $a<|z|<b$ and at $z=0$ for $a^2/b<|z|<a$, respectively. Again, by substituting equation (28) into (4) with $c=a$, we can get $\Psi_{(2)}$.

In order to satisfy the boundary conditions and the continuity conditions on both surfaces $r=a$ and $r=b$ simultaneously, two sets of the complex potentials $\Phi_{(2)}(z)$ and $\Psi_{(2)}(z)$, which are derived from two Hilbert problems, respectively, must be compatible to each other (England, 1971; Luo and Chen, 1989). Comparing their like power of z/a, we obtain the following system of equations:

$$-HA_n^*+(1-G)B_n^*+G\sum_{p=n}^{\infty}\left(\sum_{m=0}^{p-n}e_m'e_{p-m-n}\right)B_p^*=D\Gamma\delta_{n0}$$

$$(\text{for } n=0,1,2,\cdots)$$

$$-A_{-n}^*+Ge_{n-1}B_{-1}^*+(1-G)B_{-n}^*+G\sum_{p=0}^{\infty}\left(\sum_{m=0}^{p+1}e_m'e_{p+n-m}\right)B_p^*$$

$$+\mathrm{Ge}^{-2\lambda(\pi-\alpha)}(1-\delta_{n1})\sum_{p=1}^{\infty}\left(\sum_{m=\max(0,p-n+1)}^{p-1}e_m'''e_{n+m-p-1}\right)B_{-p}^*$$

$$+(1-G)(e_n+e_1'e_{n-1})\overline{\Phi_{(1)}(0)}=0$$

$$(\text{for } n=1,2,\cdots)$$

$$\frac{H}{\delta^2}(n-1)A_n^*-\frac{1}{\delta^2}\delta_{n0}\overline{A_0^*}-\frac{D-1}{D-H}\delta^{2n-2}(1-\delta_{n0})\overline{A_{-n}^*}$$

Downloaded 03 May 2010 to 171.66.16.248. Redistribution subject to ASME license or copyright; see http://www.asme.org/terms/Terms_Use.cfm

$$+Ge^{2\lambda(\pi-\alpha)}\delta_{n0}\overline{B^*_{-1}}-(1-G)(n-1)B^*_n+(1-G)\overline{B^*_{-n}}$$

$$+Ge^{2\lambda(\pi-\alpha)}\delta_{n0}\sum_{p=0}^{\infty}\bar{e}'_{p+1}\overline{B^*_p}-G(n-1)\sum_{p=n}^{\infty}\left(\sum_{m=0}^{p-n}e'_m e_{p-m-n}\right)B^*_p$$

$$+G\sum_{p=\max(n,1)}^{\infty}\left(\sum_{m=0}^{\min(p-n,p-1)}\bar{e}'''_m\bar{e}''_{p-m-n}\right)\overline{B^*_{-p}}+(1-G)$$

$$\times[\bar{e}'_1e^{2\lambda(\pi-\alpha)}-1]\Phi_{(1)}(0)\delta_{n0}=\frac{D\Gamma}{\delta^2}\delta_{n0}+\frac{D}{D-H}\Gamma'\delta_{n2}$$

$$(\text{for } n=0,1,2,\cdots)$$

and

$$-\frac{n+1}{\delta^2}A^*_{-n}-\delta^{-2(n+1)}\overline{A^*_n}+Ge^{2\lambda(\pi-\alpha)}\bar{e}''_n\overline{B^*_{-1}}$$

$$+G(n+1)e_{n-1}B^*_{-1}+(1-G)\overline{B^*_n}+(1-G)(n+1)B^*_{-n}$$

$$+G\sum_{p=1}^{\infty}\left(\sum_{m=0}^{p-1}\bar{e}'''_m\bar{e}''_{p+n-m}\right)\overline{B^*_{-p}}+Ge^{-2\lambda(\pi-\alpha)}(n+1)(1-\delta_{n1})$$

$$\times\sum_{p=1}^{\infty}\left(\sum_{m=\max(0,p-n+1)}^{p-1}e'''_m e_{n+m-p-1}\right)B^*_{-p}+G(n+1)$$

$$\times\sum_{p=0}^{\infty}\left(\sum_{m=0}^{p+1}e'_m e_{p+n-m}\right)B^*_p+Ge^{2\lambda(\pi-\alpha)}\sum_{p=0}^{\infty}\left(\sum_{m=\max(0,p-n+1)}^{p+1}\bar{e}'_m\right)$$

$$\times\bar{e}''_{n+m-p-1}\quad\overline{B^*_p}+(1-G)(n+1)(e'_1e_{n-1}+e_n)\overline{\Phi_{(1)}(0)}$$

$$+(1-G)\times e^{2\lambda(\pi-\alpha)}(\bar{e}'_1\bar{e}''_n+\bar{e}''_{n-1})\overline{\Phi_{(1)}(0)}=0$$

$$(\text{for } n=0,1,2,\cdots)\qquad(29)$$

where δ_{ij} is the Kronecker delta and

$$A^*_n=A_na^n,\quad B^*_n=B_na^n,$$

$$D=1-\beta_1+\eta_1,\quad H=1-\beta_1,$$

$$G=\frac{\beta_2}{1+\eta_2},\quad \delta=\frac{a}{b},$$

$$e_n=\sum_{k=0}^{n}c_kd_{n-k}e^{-i(n-2k)\alpha}$$

$$e''_n=\sum_{k=0}^{n}c_kd_{n-k}e^{i(n-2k)\alpha}$$

$$c_0=1,\quad d_0=1,$$

$$c_k=\frac{\gamma(\gamma+1)(\gamma+2)\cdots(\gamma+k-1)}{k!}\quad(\text{for } k\geq 1)$$

$$d_k=\frac{(1-\gamma)(2-\gamma)\cdots(k-\gamma)}{k!}\quad(\text{for } k\geq 1).\qquad(30)$$

In addition, the condition

$$\lim_{z\to 0}\Phi_{(1)}(z)=\Phi_{(1)}(0)\qquad(31)$$

provides a supplementary equation:

$$GB^*_0-Ge^{2\lambda(\pi-\alpha)}\overline{B^*_{-1}}-Ge^{2\lambda(\pi-\alpha)}\sum_{n=0}^{\infty}B^*_ne'_{n+1}+G\sum_{n=1}^{\infty}B^*_{-n}e'''_n$$

$$-\Phi_{(1)}(0)-[G+(1-G)e'_1e^{2\lambda(\pi-\alpha)}]\overline{\Phi_{(1)}(0)}=0.\qquad(32)$$

Truncate the infinite series at finite terms. The system of equations (29) and (32) together with their conjugates adds up to $8N+6$ equations for total $8N+6$ unknowns: A^*_n, $\overline{A^*_n}$, B^*_n, $\overline{B^*_n}$, $\Phi_{(1)}(0)$, and $\overline{\Phi_{(1)}(0)}$ where the integer n is taken the values from $-N$ to N. After solving this system of linear simultaneous equations, all the complex potentials will be determined.

Especially, if phase 2 and phase 3 are of the same elastic properties, i.e., $\kappa_2=\kappa_3$ and $\mu_2=\mu_3$, we have $\beta_1=\eta_1=1$, or $D=1$, $H=0$, which implies

$$B^*_0=\Gamma,\quad G^*_{-2}=\Gamma',$$
$$B^*_n=0\quad(n<-2,\ n=-1,\ n>0)\qquad(33)$$

The result will be reduced to that obtained by Toya (1974).

3 Complex Stress Intensity Factors

By means of equation (2), we have, for $\tau=ae^{i\theta}$,

$$\frac{d}{d\tau}(\Delta u_x+i\Delta u_y)=\frac{1}{2\mu_2}[\kappa_2\Phi^-_{(2)}(\tau)+\Phi^+_{(2)}(\tau)]$$

$$-\frac{1}{2\mu_1}[\kappa_1\Phi^+_{(1)}(\tau)+\Phi^-_{(1)}(\tau)]\qquad(34)$$

where $\Delta u_x=u^{(2)}_x-u^{(1)}_x$ and $\Delta u_y=u^{(2)}_y-u^{(1)}_y$ are the relative displacement on the interface. Substituting equations (25) and (28) into (34), we obtain

$$\frac{d}{d\tau}(\Delta u_x+i\Delta u_y)=\left(\frac{\kappa_1+1}{2\mu_1}+\frac{\kappa_2+1}{2\mu_2}\right)aQ(\tau)X_0(\tau)\qquad(35)$$

for $\tau\in L'_a$ with

$$Q(\tau)=G\{B^*_{-1}+\sum_{n=0}^{\infty}\sum_{m=0}^{n+1}B^*_n e'_m\left(\frac{\tau}{a}\right)^{n-m+1}+e^{-2\lambda(\pi-\alpha)}$$

$$\times\sum_{n=1}^{\infty}\sum_{m=0}^{n-1}B^*_{-n}e'''_m\left(\frac{a}{\tau}\right)^{n-m}\}+(1-G)\overline{\Phi_{(1)}(0)}\left(\frac{\tau}{a}+e'_1\right).\qquad(36)$$

Since at the crack tips the relative displacement must vanish, we have

$$\Delta u_x+i\Delta u_y=\left(\frac{\kappa_1+1}{2\mu_1}+\frac{\kappa_2+1}{2\mu_2}\right)a\int_{\tau_1\text{ or }\tau_2}^{\tau}Q(t)X_0(t)dt\qquad(37)$$

for $\tau\in L'_a$. And in polar coordinates $\Delta u_r+i\Delta u_\theta=e^{-i\theta}(\Delta u_x+i\Delta u_y)$. In equation (37) the function $X_0(t)$ undergoes violent oscillation near the crack tips. Thus, if very small value of $|t-\tau_1|$ is considered, all regular terms about t or θ in the integrand of equation (37) can be approximately viewed as constants, and then

$$\Delta u_r+i\Delta u_\theta$$

$$=\left(\frac{\kappa_1+1}{\mu_1}+\frac{\kappa_2+1}{\mu_2}\right)ae^{\lambda(\pi-\alpha)}Q(\tau_1)e^{-i(\pi-\alpha)/2}\frac{1}{1+2i\lambda}\left(\frac{\xi}{L}\right)^{1/2+i\lambda}$$

$$(\text{for } \xi/L\ll 1)\qquad(38)$$

where $\xi=|\tau-\tau_1|$, $L=|\tau_1-\tau_2|$ and $(\xi/L)^{i\lambda}=e^{i\lambda\log(\xi/L)}$. The similar relation can be derived for the other tip $\tau=\tau_2$.

Expression (38) indicates that the relative displacement between two crack faces is subjected to an infinite number of reversal of sign at distances very close to the crack tips. That is, as in all other interface crack problems, the linear elastic theory predicts interpenetration of the crack faces near the tips. However, as Rice (1988) showed, provided the contact zone is small enough, the complex intensity factor K derived from the elastic solution uniquely characterizes the real field within the zone and hence determines the onset of crack growth.

Now, in the present case, according to equation (38) near the crack tip $t=\tau_1$, the opening gap vanishes when

$$\text{Re}\{e^{i[\lambda\log(\xi/L)+\delta]}\}=0\qquad(39)$$

where

$$\delta=\arg[Q(\tau_1)]-\frac{\pi}{2}+\frac{\alpha}{2}-\tan^{-1}(2\lambda).\qquad(40)$$

Downloaded 03 May 2010 to 171.66.16.248. Redistribution subject to ASME license or copyright; see http://www.asme.org/terms/Terms_Use.cfm

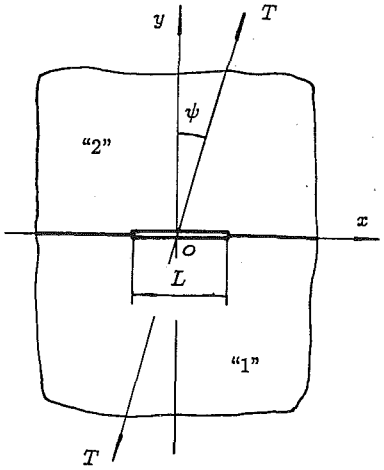

Fig. 2 A simple specimen for toughness of interface crack

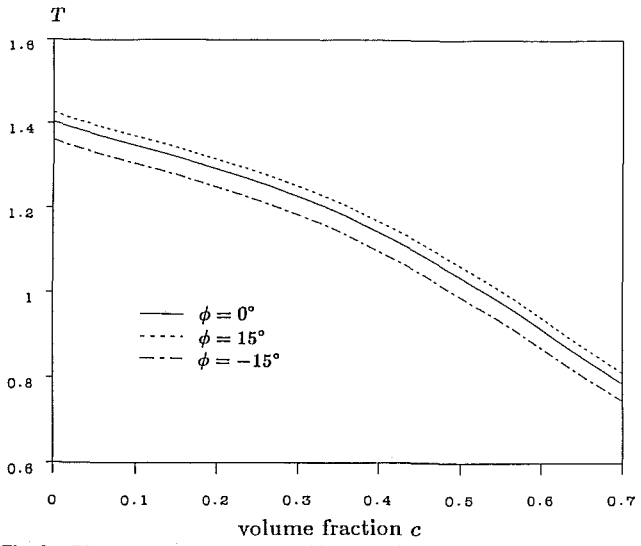

Fig. 3 Effect of volume fraction of fiber on the magnitude of equivalent load

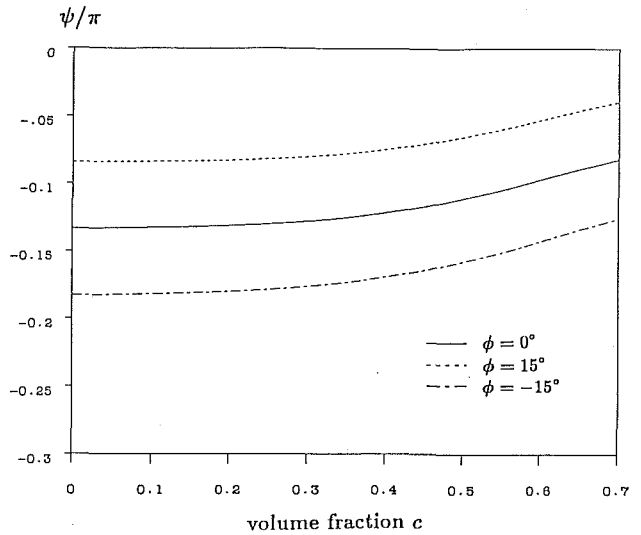

Fig. 4 Effect of volume fraction of fiber on the phase angle of equivalent load

Assume that $\lambda > 0$, then, since $\xi/L \ll 1$, the largest ξ for which equation (39) is satisfied is

$$\xi^*/L = e^{-(\pi/2+\delta)/\lambda}. \tag{41}$$

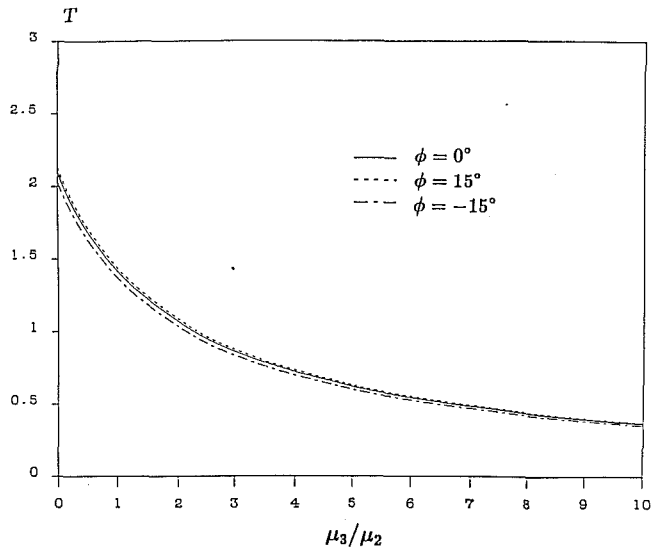

Fig. 5 Effect of μ_3/μ_2 on the magnitude of equivalent load

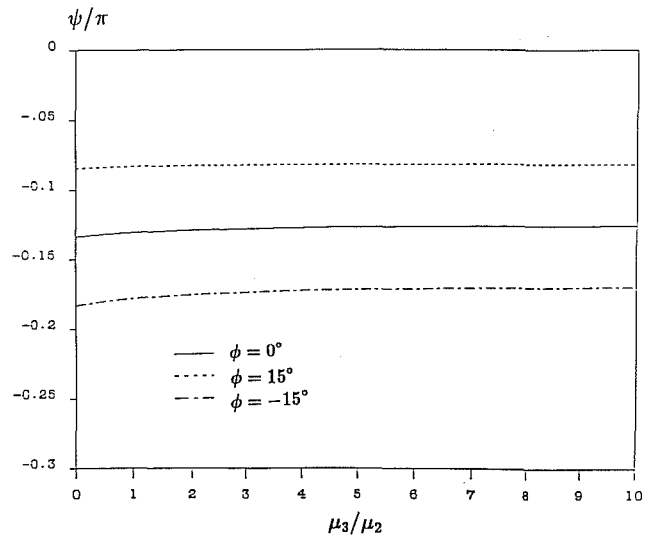

Fig. 6 Effect of μ_3/μ_2 on the phase angle of equivalent load

If λ is negative, the largest ξ for zero gap is

$$\xi^*/L = e^{(\pi/2+\delta)/\lambda}. \tag{42}$$

This is an elementary estimate of the size of contact zone (Rice, 1988; Shih and Asaro, 1988). Since the absolute value of λ is generally small, the condition of small contact zone can be satisfied if $\pi/2+\delta$ for $\lambda>0$ or $\pi/2-\delta$ for $\lambda<0$ is not too small. A suitable restriction on ξ^* adopted by Rice (1988) is $\xi^*/L<0.01$.

Another requirement for the present solution to be applicable is that, except in the vicinity of the crack tip, the radial gap between the two crack faces must be greater than zero (Toya, 1974). In checking this condition, we perform the following numerical integration:

$$\Delta u_r + i\Delta u_\theta = i\left(\frac{\kappa_1+1}{2\mu_1}+\frac{\kappa_2+1}{2\mu_2}\right) \times a^2 e^{-i\theta}\int_{\alpha-\omega}^{\theta} Q(ae^{i\theta})X_0(ae^{i\theta})e^{i\theta}d\theta \tag{43}$$

where $\omega = \xi^*/a$. In equation (43), $(\alpha-\omega)$ instead of α has been used as the lower limit of the integration so as to avoid the oscillating singularity near the crack tip.

Concerning the stress, by virtue of equation (1), we have

$$\sigma_{rr} + i\sigma_{r\theta} = \Phi^-_{(2)}(\tau) - \Phi^+_{(2)}(\tau) = (1+\eta_2)aQ(\tau)X_0^-(\tau) \tag{44}$$

Downloaded 03 May 2010 to 171.66.16.248. Redistribution subject to ASME license or copyright; see http://www.asme.org/terms/Terms_Use.cfm

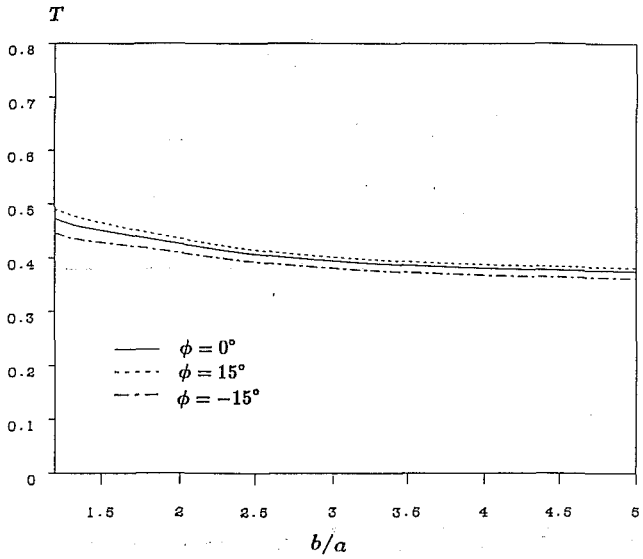

Fig. 7 Effect of *b/a* on the magnitude of equivalent load

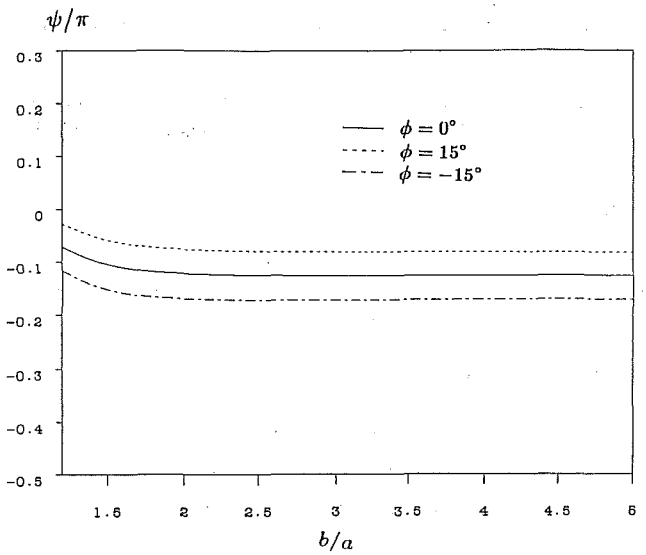

Fig. 8 Effect of *b/a* on the phase angle of equivalent load

on the bonded part of the interface where $\tau = ae^{i\theta}$ and $\alpha < \theta < 2\pi - \alpha$.

As the point τ approaches to τ_1 along the interface, we have

$$\sigma_{rr} + i\sigma_{r\theta} = -i(1+\eta_2)aQ(\tau_1)e^{-\alpha(\lambda+i/2)}\frac{1}{\sqrt{L\xi}}\left(\frac{\xi}{L}\right)^{i\lambda}. \quad (45)$$

Referring to the definition introduced by Hutchinson, Mear, and Rice (1988), the complex stress intensity factor at the tip τ_1 is

$$K = -i(1+\eta_2)aQ(\tau_1)e^{-\alpha(\lambda+i/2)}L^{-i\lambda}\sqrt{2\pi/L}. \quad (46)$$

Recall that the complex stress intensity factor for the right-hand tip of the interface crack of the simple specimen shown in Fig. 2 is (England, 1965)

$$K = Te^{i\psi}(1+2i\lambda)L^{-i\lambda}\sqrt{\pi L/2}. \quad (47)$$

Thus, if we want to duplicate the field condition around the tip $\tau = \tau_1$ of the circular arc-shaped interface crack at the right-hand tip of this specimen, then the specimen must be subjected to the remote loading

$$Te^{i\psi} = \frac{-i}{(1+2i\lambda)\sin\alpha}(1+\eta_2)Q(\tau_1)e^{-\alpha(\lambda+i/2)}. \quad (48)$$

4 Numerical Examples

The following fiber-reinforced composite material is considered:

$$\mu_1/\mu_2 = 23, \quad \nu_1 = 0.3, \quad \nu_2 = 0.35. \quad (49)$$

In the three-phase model the equivalent elastic moduli of the composite phase or the outer phase are calculated based on the modified Mori-Tanaka method suggested by Luo and Weng (1989).

The magnitude T and phase angle ψ/π of the equivalent load which is defined by equation (48) are plotted in Fig. 3 and Fig. 4 versus volume fraction c of the composite for unit uniaxial tension with $\phi = 15$ deg, 0 deg, and 15 deg, respectively. Remarkably, it is observed that the equivalent load which defines the complex stress intensity factor at the crack tip τ_1 through (47) depends on the volume concentration of fiber in composite.

Figures 5 and 6 depict the variation of T and ψ/π with the shear rigidity ratio μ_3/μ_2 for the following material combination:

$$\mu_1/\mu_2 = 20, \quad \nu_1 = \nu_2 = \nu_3 = 0.3, \quad \delta = a/b = 1/8 \quad (50)$$

under the same load condition with $\phi = -15$ deg, 0 deg, and 15 deg, respectively.

In Figs. 7 and 8 the value T and ψ/π are plotted versus $1/\delta(=b/a)$ for the material combination:

$$\mu_1/\mu_2 = 20, \quad \mu_3/\mu_2 = 10, \quad \nu_1 = \nu_2 = \nu_3 = 0.3 \quad (51)$$

under unit uniaxial tension in three different loading directions. It is seen that as the intermediate phase becomes thinner, some interaction exists between the interface crack and the outer-phase medium.

In all the above cases, the size of contact zone near the crack tips has been numerically verified to be small enough ($\xi^*/L < 10^{-6}$) for the application of the theory proposed here.

In the computation, the Laurant series are truncated at $n = \pm 15$. The results indicate satisfactory convergence.

Reference

Christensen, R. M., and Lo, K. H., 1979, "Solutions for Effective Shear Properties in Three Phase Sphere and Cylinder Models," *Journal of Mechanics and Physics of Solids,* Vol. 27, pp. 315–330.

Comninou, M., 1977, "The Interface Crack," ASME JOURNAL OF APPLIED MECHANICS, Vol. 44, pp. 631–636.

England, A. H., 1965, "A Crack between Dissimilar Media," ASME JOURNAL OF APPLIED MECHANICS, Vol. 32, pp. 400–402.

England, A. H., 1966, "An Arc Crack around a Circular Elastic Inclusion," ASME JOURNAL OF APPLIED MECHANICS, Vol. 33, pp. 637–640.

England, A. H., 1971, *Complex Variable Method in Elasticity,* John Wiley and Sons, New York.

Erdogan, F., 1963, "Stress Distribution in a Nonhomogeneous Elastic Plane with Cracks," ASME JOURNAL OF APPLIED MECHANICS, Vol. 30, pp. 232–237.

Erdogan, F., 1965, "Stress Distribution in Bonded Dissimilar Materials with Cracks," ASME JOURNAL OF APPLIED MECHANICS, Vol. 32, pp. 403–410.

Gautesen, A. K., and Dundurs, J., 1987, "The Interface Crack in a Tension Field," ASME JOURNAL OF APPLIED MECHANICS, Vol. 54, pp. 93–98.

Hutchinson, J. W., Mear, M., and Rice, J. R., 1987, "Crack Paralleling an Interface between Dissimilar Materials," ASME JOURNAL OF APPLIED MECHANICS, Vol. 54, pp. 828–823.

Luo, H. A., and Chen, Y., 1989, "An Edge Dislocation in a Three-Phase Composite Cylinder Model," ASME JOURNAL OF APPLIED MECHANICS, Vol. 58, pp. 75–86.

Luo, H. A., and Weng, G. J., 1989, "On Eshelby's S-Tensor in a Three-Phase Cylindrically Concentric Solid, and the Elastic Moduli of Fiber-Reinforced Composites," *Mechanics of Materials,* Vol. 8, pp. 77–88.

Malyshev, B. M., and Salganic, R. L. 1965, "The Strength of Adhesive Joints Using the Theory of Crack," *International Journal of Fracture Mechanics,* Vol. 1, pp. 114–128.

Downloaded 03 May 2010 to 171.66.16.248. Redistribution subject to ASME license or copyright; see http://www.asme.org/terms/Terms_Use.cfm

Muskhelishvili, N. I., 1953, *Some Basic Problems of the Mathematical Theory of Elasticity,* P. Noordhoff, Groningen.

Perlman, A. B., and Sih, G. C., 1967, "Elastostatic Problems of Curvilinear Crack in Bounded Dissimilar Materials," *International Journal of Fracture Mechanics,* Vol. 5, pp. 845-867.

Rice, J. R., 1988, "Elastic Fracture Mechanics Concepts for Interfacial Cracks," ASME JOURNAL OF APPLIED MECHANICS, Vol. 55, pp. 98-103.

Rice, J. R., and Sih, G. C., 1965, "Plane Problem of Crack in Dissimilar Media," ASME JOURNAL OF APPLIED MECHANICS, Vol. 32, pp. 418-432.

Shih, C. F., and Asaro, R., 1988, "Elastic-Plastic Analysis of Cracks on Bimaterial Interfaces; Part 1: Small Scale Yielding," ASME JOURNAL OF APPLIED MECHANICS, Vol. 55, pp. 299-316.

Toya, M., 1974, "A Crack Along the Interface of a Circular Inclusion Embedded in an Infinite Solid," *Journal of Mechanics and Physics of Solids,* Vol. 22, pp. 325-348.

Williams, M. L., 1959, "The Stress around a Fault or Crack in Dissimilar Media," *Bulletin of the Seismological Society of America,* Vol. 49, pp. 199-204.

Wills, J. R., 1971, "Fracture Mechanics of Interfacial Crack," *Journal of Mechanics and Physics of Solids,* Vol. 19, pp. 353-368.

Downloaded 03 May 2010 to 171.66.16.248. Redistribution subject to ASME license or copyright; see http://www.asme.org/terms/Terms_Use.cfm

Analysis of Embedded and Surface Elliptical Flaws in Transversely Isotropic Bodies by the Finite Element Alternating Method

H. Rajiyah
Assoc. Mem. ASME

S. N. Atluri
Fellow ASME

Center for Computational Mechanics,
Georgia Institute of Technology,
Atlanta, GA 30332-0356

The general analytical solution to the problem of a flat elliptical crack embedded in an infinite, transversely isotropic solid, oriented perpendicular to the axis of elastic symmetry, is derived along the lines of Vijayakumar and Atluri's solution procedure for the isotropic case. The prior work of Kassir and Sih on this problem is limited to some constant and linear variations of normal and shear tractions on the crack face. The generalized solution is employed in the Schwarz-Neumann alternating method in conjunction with the finite element method. Such a method of analysis is shown to be an efficient way to evaluate the stress intensity factors along the flaw border.

1 Introduction

The analysis of surface flaws (of a semi-elliptical shape) in laminated composite plates, or even in unidirectionally reinforced composites, is of paramount importance in the integrity and life prediction analysis of such composite structures. A direct computational modeling of such surface flaws is prohibitively expensive. An efficient analysis of elliptical surface flaws in laminates involves the use of the analytical solution for an embedded crack in an infinite solid of transversely isotropic material, subjected to arbitrary crack face loading in conjunction with the Schwarz-Neumann alternating method. In this method a direct analysis of the *uncracked* structure is first performed and the analytical solution for a pressurized embedded elliptical crack in a transversely isotropic solid is then used to erase the stresses in an uncracked solid, at the location of the crack, to create a crack.

The analytical solution, for a flat elliptical crack embedded in an infinite solid of transversely isotropic material, where the axis normal to the ellipse is oriented along the axis of elastic symmetry, and where the crack face is subjected to arbitrary normal as well as shear loads, is considered in detail in this paper. The prior work on this problem (Kassir and Sih, 1968, 1975) is limited to the case of constant and linear variations of normal and shear tractions on the crack face. In the present analysis, the results of an embedded elliptical crack in an infinite isotropic solid subjected to arbitrary crack face loading (Vijayakumar and Atluri, 1981; Nishioka and Atluri 1983) are extended to a transversely isotropic case, wherein the crack axis is perpendicular to the axis of elastic symmetry.

The latter sections of this paper are concerned with the application of the finite element alternating technique to analyze embedded elliptical flaws or part-elliptical flaws in transversely isotropic bodies of finite dimension where the crack axis is perpendicular to the material axis.

As a first attempt, the transversely isotropic material properties are taken to be very close to those of an isotropic body (since the present analytical solution for the transversely isotropic case does not reduce to the isotropic case without an elaborate limiting process) and the stress intensity factors for a finite cracked body are compared with those of the isotropic formulation, as a check for the solution algorithm. The materials considered in the present paper are β-quartz, Zn, and a typical composite laminate (Chirstensen, 1975). The characteristic equation governing material moduli (equation (6)) yields real roots for β-quartz and complex roots for Zn. As for the composite laminate, the ratio of E_L and E_T was taken to be 25. (E_L is the Young's modulus in the fiber direction and E_T is the Young's modulus in the transverse direction.) Both embedded and surface elliptical flaws were considered in the present analysis. Situations where the body is subjected to uniform tensile and bending loads were considered. Comparisons were made with the isotropic case in all situations considered. Convergence studies for certain selected examples are also presented. It is found that there is no appreciable difference in the qualitative nature of the K-factor variation for the case of the embedded flaw, along the flaw border, with changes in material properties. This was not the case for the part elliptical surface flaw.

Contributed by the Applied Mechanics Division of THE AMERICAN SOCIETY OF MECHANICAL ENGINEERS for presentation at the Joint Applied Mechanics/Bioengineering Conference, Ohio State University, Columbus, Ohio, June 16-19, 1991.

Discussion on this paper should be addressed to the Technical Editor, Prof. Leon M. Keer, The Technological Institute, Northwestern University, Evanston, IL 60208, and will be accepted until two months after final publication of the paper itself in the JOURNAL OF APPLIED MECHANICS. Manuscript received by the ASME Applied Mechanics Division, Jan. 29, 1990; final revision, Nov. 19, 1990.
Paper No. 91-APM-34.

Copyright © 1991 by ASME
Downloaded 03 May 2010 to 171.66.16.248. Redistribution subject to ASME license or copyright; see http://www.asme.org/terms/Terms_Use.cfm

2 Potential Function Representation

A material is said to be "transversely isotropic" when it possesses an axis of elastic symmetry such that the material is isotropic in the plane normal to this axis. Such a material can be described by five independent elastic constants (see Lekhnitski, 1981). Let z be in the axis of elastic symmetry. Then the stress-strain relations in the (x, y, z) system could be written as

$$\sigma_{11} = C_{11}\frac{\partial u_1}{\partial x} + C_{12}\frac{\partial u_2}{\partial y} + C_{13}\frac{\partial u_3}{\partial z}$$

$$\sigma_{22} = C_{12}\frac{\partial u_1}{\partial x} + C_{11}\frac{\partial u_2}{\partial y} + C_{13}\frac{\partial u_3}{\partial z}$$

$$\sigma_{33} = C_{13}\left(\frac{\partial u_1}{\partial x} + \frac{\partial u_2}{\partial y}\right) + C_{33}\frac{\partial u_3}{\partial z}$$

$$\sigma_{32} = C_{44}\left(\frac{\partial u_3}{\partial y} + \frac{\partial u_2}{\partial z}\right)$$

$$\sigma_{31} = C_{44}\left(\frac{\partial u_1}{\partial z} + \frac{\partial u_3}{\partial x}\right)$$

$$\sigma_{12} = \frac{1}{2}(C_{11} - C_{12})\left(\frac{\partial u_1}{\partial y} + \frac{\partial u_2}{\partial x}\right). \tag{1}$$

Here, $(\sigma_{ij}, i=1,2,3, j=1,2,3)$ and $(u_i, i=1,2,3)$ are stresses and displacement components in the (x, y, z) system and C_{ij} are elastic constants for transverse isotropy defined in (Lekhnitski, 1981). Equation (1), when substituted into the equilibrium equations, yields a system of three equations for u_j, $(j=1,2,3)$ as:

$$C_{11}\frac{\partial^2 u_1}{\partial x^2} + \frac{1}{2}(C_{11} - C_{12})\frac{\partial^2 u_1}{\partial y^2} + C_{44}\frac{\partial^2 u_1}{\partial z^2} + \frac{\partial}{\partial x}\left[\frac{1}{2}(C_{11} + C_{12})\frac{\partial u_1}{\partial y} + (C_{13} + C_{44})\frac{\partial u_3}{\partial z}\right] = 0$$

$$\frac{1}{2}(C_{11} - C_{12})\frac{\partial^2 u_2}{\partial x^2} + C_{11}\frac{\partial^2 u_2}{\partial y^2} + C_{44}\frac{\partial^2 u_2}{\partial z^2} + \frac{\partial}{\partial y}\left[\frac{1}{2}(C_{11} + C_{12})\frac{\partial u_1}{\partial x} + (C_{13} + C_{44})\frac{\partial u_3}{\partial z}\right] = 0$$

$$C_{44}\left(\frac{\partial^2}{\partial x^2} + \frac{\partial^2}{\partial y^2}\right)u_3 + C_{33}\frac{\partial^2 u_3}{\partial z^2} + (C_{13} + C_{44})\frac{\partial}{\partial z}\left(\frac{\partial u_1}{\partial x} + \frac{\partial u_2}{\partial y}\right) = 0. \tag{2}$$

The displacement field u_1, u_2, and u_3, which satisfies the above equations identically, is represented in terms of potential functions $\phi_j (j=1,2,3)$(see Elliot (1949) and Hu (1952)), as:

$$u_1 = \frac{\partial}{\partial x}(\phi_1 + \phi_2) - \frac{\partial \phi_3}{\partial y}$$

$$u_2 = \frac{\partial}{\partial y}(\phi_1 + \phi_2) - \frac{\partial \phi_3}{\partial x}$$

$$u_3 = \frac{\partial}{\partial z}(m_1\phi_1 + m_2\phi_2) \tag{3}$$

where the potential functions $\phi_j (j=1,2,3)$ satisfy the harmonic equation in the modified[1] coordinates x_j, y_j and z_j $(j=1,2,3)$ as follows:

$$\left(\frac{\partial^2}{\partial x_j^2} + \frac{\partial^2}{\partial y_j^2} + \frac{\partial^2}{\partial z_j^2}\right)\phi_j = 0 \quad (j=1,2,3 \text{ no sum on } j) \tag{4}$$

where

$$x_j = x,\ y_j = y,\ z_j = \frac{z}{\sqrt{n_j}} \quad (j=1,2,3).$$

The constants m_1 and m_2 in equation (3) are defined as

$$m_j = \frac{C_{11}n_j - C_{44}}{C_{13} + C_{44}} = \frac{(C_{13} + C_{44})n_j}{C_{33} - C_{44}n_j} \quad (j=1,2,3). \tag{5}$$

The quantities n_1 and n_2 are the roots of the quadratic equation in n

$$C_{11}C_{44}n^2 + [C_{13}(C_{13} + 2C_{44}) - C_{11}C_{33}]n + C_{33}C_{44} = 0 \tag{6}$$

and n_3 is defined as:

$$n_3 = \frac{2C_{44}}{(C_{11} - C_{12})}. \tag{7}$$

In general, n_1 and n_2 are either real or complex conjugate quantities. The constants m_1 and m_2 behave the same way. When n_1 and n_2 are complex conjugates, care must be taken to take the principal values of $n_1^{1/2}$ and $n_2^{1/2}$. The same applies to m_1 and m_2. In the case of complex n_1 and n_2, the potentials ϕ_1 and ϕ_2 turn out to be complex conjugates and hence, the displacements and stresses turn out to be single valued and real (Elliot, 1949).

The stresses from equation (1) and (3) in the (x, y, z) system take the following form:

$$\sigma_{11} = (C_{11}\partial_x^2 + C_{12}\partial_y^2)(\phi_1 + \phi_2) + C_{13}\partial_z^2(m_1\phi_1 + m_2\phi_2) - (C_{11} - C_{12})\partial_{xy}^2\phi_3$$

$$\sigma_{22} = (C_{12}\partial_x^2 + C_{11}\partial_y^2)(\phi_1 + \phi_2) + C_{13}\partial_z^2(m_1\phi_1 + m_2\phi_2) + (C_{11} - C_{12})\partial_{xy}^2\phi_3$$

$$\sigma_{33} = C_{44}\partial_z^2[(1 + m_1)n_1\phi_1 + (1 + m_2)n_2\phi_2]$$

$$\sigma_{32} = C_{44}\partial_z[\partial_y\{(1 + m_1)\phi_1 + (1 + m_2)\phi_2\} + \partial_x\phi_3]$$

$$\sigma_{31} = C_{44}\partial_z[\partial_x\{(1 + m_1)\phi_1 + (1 + m_2)\phi_2\} + \partial_y\phi_3]$$

$$\sigma_{12} = (C_{11} - C_{22})\partial_{xy}^2(\phi_1 + \phi_2) + \frac{1}{2}(C_{11} - C_{12})(\partial_x^2\phi_3 - \partial_y^2\phi_3). \tag{8}$$

3 Potential Functions for Transverse Isotropy

Let the region of discontinuity in the transversely isotropic material be bounded by an ellipse, which in the (x, y, z) system, takes the following form:

$$\frac{x^2}{a^2} + \frac{y^2}{b^2} = 1 \quad \text{in } z = 0. \tag{9}$$

The axis of elastic symmetry in this case is along the z-axis. The arbitrary loading on the crack face can be decomposed into symmetric and skew symmetric stress distributions. As in Kassir and Sih (1968, 1975) the potential functions for the symmetric case are related to the solution of the equations:

$$\nabla_j^2 f_3(x_j, y_j, z_j) = 0 \quad (j=1,2,3 \text{ no sum on } j) \tag{10}$$

where

$$x_j = x \quad y_j = y \quad \text{and} \quad z_j = \frac{z}{\sqrt{n_j}}$$

and

$$\nabla_j^2 = \frac{\partial^2}{\partial x_j^2} + \frac{\partial^2}{\partial y_j^2} + \frac{\partial^2}{\partial z_j^2}.$$

The potential functions for the skew symmetric case are related to the solutions of the equations:

[1] It should thus be noted that each of the functions $\phi_j (j=1,2,3)$ satisfies the Laplace equation in a different set of coordinates x_j, y_j, and $z_j (j=1,2,3)$.

Downloaded 03 May 2010 to 171.66.16.248. Redistribution subject to ASME license or copyright; see http://www.asme.org/terms/Terms_Use.cfm

$$\nabla_j^2 p_j = 0 \quad \text{and} \quad \nabla_j^2 q_j = 0 \quad (j = 1,2,3 \text{ no sum on } j). \tag{11}$$

Hence, the potentials $\phi_j (j = 1,2,3)$ for arbitrary loading on the crack face can be defined as

$$\phi_1 = \frac{n_1^{1/2}}{1+m_1} f_3(x_1, y_1, z_1) + \frac{1+m_2}{m_1-m_2} F_1(x_1, y_1, z_1)$$

$$\phi_2 = \frac{-n_2^{1/2}}{1+m_2} f_3(x_2, y_2, z_2) + \frac{1+m_1}{m_1-m_2} F_1(x_2, y_2, z_2)$$

$$\phi_3 = F_2(x_3, y_3, z_3) \tag{12}$$

where

$$F_1(x_j, y_j, z_j) = \frac{\partial p_j}{\partial x_j} + \frac{\partial q_j}{\partial y_j} \quad (j = 1,2 \text{ no sum on } j)$$

and

$$F_2(x_3, y_3, z_3) = \frac{\partial p_3}{\partial y_3} - \frac{\partial q_3}{\partial x_3}. \tag{13}$$

Substituting the above-mentioned expressions for $\phi_j (j = 1,2,3)$ in equation (8), we have

$$\sigma_{11} = \left(C_{11} \frac{\partial^2}{\partial x_j^2} + C_{12} \frac{\partial^2}{\partial y_j^2} \right) \left[(-1)^{j-1} \frac{n_j^{1/2}}{1+m_j} f_3(x_j, y_j, z_j) \right.$$
$$\left. + (-1)^{j-1} \frac{(1+m_1)(1+m_2)}{(m_1-m_2)} \left\{ \frac{F_1(x_j, y_j, z_j)}{1+m_j} \right\} \right]$$
$$+ C_{13} \frac{\partial^2}{\partial z_j^2} \left[\frac{(-1)^{j-1} m_j n_j^{1/2}}{1+m_j} f_3(x_j, y_j, z_j) \right.$$
$$\left. + (-1)^{j-1} \frac{(1+m_1)(1+m_2)}{(m_1-m_2)} \left\{ \frac{m_j F_1(x_j, y_j, z_j)}{(1+m_j) n_j} \right\} \right]$$
$$- (C_{11} - C_{12}) \frac{\partial^2 F_2(x_3, y_3, z_3)}{\partial x_3 \partial y_3} \quad (j = 1,2)$$

$$\sigma_{22} = \left(C_{12} \frac{\partial^2}{\partial x_j^2} + C_{11} \frac{\partial^2}{\partial y_j^2} \right) \left[(-1)^{j-1} \frac{n_j^{1/2}}{1+m_j} f_3(x_j, y_j, z_j) \right.$$
$$\left. + (-1)^{j-1} \frac{(1+m_1)(1+m_2)}{(m_1-m_2)} \left\{ \frac{F_1(x_j, y_j, z_j)}{1+m_j} \right\} \right]$$
$$+ C_{13} \frac{\partial^2}{\partial z_j^2} \left[\frac{(-1)^{j-1} m_j n_j^{1/2}}{1+m_j} f_3(x_j, y_j, z_j) \right.$$
$$\left. + (-1)^{j-1} \frac{(1+m_1)(1+m_2)}{(m_1-m_2)} \left\{ \frac{m_j F_1(x_j, y_j, z_j)}{(1+m_j) n_j} \right\} \right]$$
$$- (C_{11} - C_{12}) \frac{\partial^2 F_2(x_3, y_3, z_3)}{\partial x_3 \partial y_3} \quad (j = 1,2)$$

$$\sigma_{33} = C_{44} \frac{\partial^2}{\partial z_j^2} \left[(-1)^{j-1} n_j^{1/2} f_3(x_j, y_j, z_j) \right.$$
$$\left. + (-1)^{j-1} \frac{(1+m_1)(1+m_2)}{(m_1-m_2)} F_1(x_j, y_j, z_j) \right] \quad (j = 1,2)$$

$$\sigma_{23} = C_{44} \frac{\partial^2}{\partial y_j \partial z_j} \left[(-1)^{j-1} f_3(x_j, y_j, z_j) \right.$$
$$\left. + (-1)^{j-1} \frac{(1+m_1)(1+m_2)}{(m_1-m_2) n_j^{1/2}} F_1(x_j, y_j, z_j) \right]$$
$$+ \frac{C_{44}}{n_3^{1/2}} \frac{\partial^2 F_2(x_3, y_3, z_3)}{\partial x_3 \partial z_3} \quad (j = 1,2)$$

$$\sigma_{13} = C_{44} \frac{\partial^2}{\partial x_j \partial z_j} \left[(-1)^{j-1} f_3(x_j, y_j, z_j) \right.$$
$$\left. + (-1)^{j-1} \frac{(1+m_1)(1+m_2)}{(m_1-m_2) n_j^{1/2}} F_1(x_j, y_j, z_j) \right]$$
$$+ \frac{C_{44}}{n_3^{1/2}} \frac{\partial^2 F_2(x_3, y_3, z_3)}{\partial y_3 \partial z_3} \quad (j = 1,2)$$

$$\sigma_{12} = (C_{11} - C_{12}) \frac{\partial^2}{\partial x_j \partial y_j} \left[(-1)^{j-1} \frac{n_j^{1/2}}{1+m_j} f_3(x_j, y_j, z_j) \right.$$
$$\left. + (-1)^{j-1} \frac{(1+m_1)(1+m_2)}{(m_1-m_2)} \frac{F_1(x_j, y_j, z_j)}{(1+m_j)} \right]$$
$$+ \frac{1}{2} (C_{11} - C_{12}) \left(\frac{\partial^2}{\partial x_3^2} - \frac{\partial^2}{\partial y_3^2} \right) F_2(x_3, y_3, z_3) \quad (j = 1,2). \tag{14}$$

The stress boundary conditions to be satisfied on the crack face in the plane $z = 0$ (i.e., $z_j = 0 (j = 1,2,3)$) takes much simpler forms

$$\sigma_{33}^{(0)} = C_{44} (n_1^{1/2} - n_2^{1/2}) \left[\frac{\partial^2 f_3(x, y, z)}{\partial z^2} \right]_{z=0}$$

$$\sigma_{23}^{(0)} = C_{44} \frac{(1+m_1)(1+m_2)}{(m_1-m_2)} \left[\frac{1}{n_1^{1/2}} - \frac{1}{n_2^{1/2}} \right] \left[\frac{\partial^2 F_1}{\partial x \partial z} \right]_{z=0}$$
$$+ \frac{C_{44}}{n_3^{1/2}} \left[\frac{\partial^2 F_2}{\partial y \partial z} \right]_{z=0}$$

$$\sigma_{13}^{(0)} = C_{44} \frac{(1+m_1)(1+m_2)}{(m_1-m_2)} \left[\frac{1}{n_1^{1/2}} - \frac{1}{n_2^{1/2}} \right] \left[\frac{\partial^2 F_1}{\partial y \partial z} \right]_{z=0}$$
$$+ \frac{C_{44}}{n_3^{1/2}} \left[\frac{\partial^2 F_2}{\partial x \partial z} \right]_{z=0}. \tag{15}$$

Making use of equation (13) and defining $f_j (j = 1,2,3)$ as

$$f_1(x_j, y_j, z_j) = \frac{\partial p_j(x_j, y_j, z_j)}{\partial z_j}$$

$$f_2(x_j, y_j, z_j) = \frac{\partial q_j(x_j, y_j, z_j)}{\partial z_j}, \tag{16}$$

we could transform the boundary conditions in equation (15) as

$$\sigma_{33}^{(0)} = \gamma_1 \left[\frac{\partial^2 f_3(x, y, z)}{\partial z^2} \right]_{z=0}$$

$$\sigma_{31}^{(0)} = \gamma_2 \left[\frac{\partial^2 f_1}{\partial x^2} \right]_{z=0} - \gamma_3 \left[\frac{\partial^2 f_1}{\partial y^2} \right]_{z=0} + (\gamma_2 + \gamma_3) \left[\frac{\partial^2 f_2}{\partial x \partial y} \right]_{z=0}$$

$$\sigma_{32}^{(0)} = \gamma_2 \left[\frac{\partial^2 f_1}{\partial y^2} \right]_{z=0} - \gamma_3 \left[\frac{\partial^2 f_1}{\partial x^2} \right]_{z=0} + (\gamma_2 + \gamma_3) \left[\frac{\partial^2 f_2}{\partial x \partial y} \right]_{z=0} \tag{17}$$

where

$$\gamma_1 = C_{44} (n_1^{1/2} - n_2^{1/2})$$

$$\gamma_2 = C_{44} \frac{(1+m_1)(1+m_2)}{(m_1-m_2)} \left[\frac{1}{n_1^{1/2}} - \frac{1}{n_2^{1/2}} \right]$$

$$\gamma_3 = \frac{C_{44}}{n_3^{1/2}}.$$

Downloaded 03 May 2010 to 171.66.16.248. Redistribution subject to ASME license or copyright; see http://www.asme.org/terms/Terms_Use.cfm

Also, it should be noted that from equation (16), $f_j(j=1,2,3)$ should be harmonic since p_j, $q_j(j=1,2,3)$ are harmonic functions.

4 Embedded Elliptical Crack in an Infinite Transversely Isotropic Solid

Let the region of discontinuity in the transversely isotropic material be bounded by an ellipse, which in the (x, y, z) system takes the following form:

$$\frac{x^2}{a^2}+\frac{y^2}{b^2}=1 \quad \text{in } z=0. \tag{18}$$

The axis of elastic symmetry in this case is along the z-axis. The representation of the ellipse remains unchanged in the modified coordinates $(x_j, y_j, z_j)(j=1,2,3)$. Thus, to solve the problem on hand, appropriate potential functions $\phi_j(j=1,2,3)$ each defined in $(x_j, y_j, z_j)(j=1,2,3)$, respectively, will now be employed. The necessary ellipsoidal coordinates ξ^j_1, ξ^j_2, $\xi^j_3(j=1,2,3)$ for a point in the $(x_j, y_j, z_j)(j=1,2,3)$ coordinate system are given by the roots of the cubic equation

$$\omega_j(\xi^j)=0 \quad (j=1,2,3 \text{ no sum on } j) \tag{19}$$

where

$$\omega_j(\xi^j)=1-\frac{x_j^2}{a^2+\xi^j}-\frac{y_j^2}{b^2+\xi^j}-\frac{z_j^2}{\xi^j}. \tag{20}$$

They are connected to the Cartesian coordinates, by the relations

$$a^2(a^2-b^2)x_j^2=(a^2+\xi^j_1)(a^2+\xi^j_2)(a^2+\xi^j_3)$$

$$b^2(b^2-a^2)y_j^2=(b^2+\xi^j_1)(b^2+\xi^j_2)(b^2+\xi^j_3)$$

$$a^2b^2z_j^2=\xi^j_1\xi^j_2\xi^j_3 \quad (j=1,2,3). \tag{21}$$

The expression for $\omega_j(\xi^j)$ in equation (21) may be written in alternate form

$$\omega_j(\xi^j)=\frac{P_j(\xi^j)}{Q_j(\xi^j)} \quad (j=1,2,3)$$

where

$$P_j(\xi^j)=(\xi^j-\xi^j_1)(\xi^2-\xi^j_2)(\xi^j-\xi^j_3) \quad (j=1,2,3)$$

$$Q_j(\xi^j)=\xi^j(\xi^j+a^2)(\xi^j+b^2) \tag{22}$$

and

$$\infty>\mathrm{Re}(\xi^j_3)\geq 0\geq \mathrm{Re}(\xi^j_2)\geq -b^2\geq \mathrm{Re}(\xi^j_1)\geq -a^2$$

where Re( ) denotes real part of ( ).

The partial derivatives of $\xi^j_\alpha(j=1,2,3;\ \alpha=1,2,3)$ with respect to the corresponding x_j, y_j, or $z_j(j=1,2,3)$ required later, are given by

$$\partial'_{\beta_j}\xi^j_\alpha=-\omega_{j,\beta_j}\frac{Q_j(\xi^j_\alpha)}{P'_j(\xi^j_\alpha)}. \tag{23}$$

Here, β_j corresponds to x_j, y_j and z_j when β takes values 1, 2, and 3 respectively. $\partial^n_{\beta_j}$ corresponds to the nth partial derivative of β_j and P'_j indicates the partial derivative w.r.t. ξ^j. The elliptic boundary in the plane $z=0$ (i.e., $z_j=0$ $(j=1,2,3)$) corresponds to the curves $\xi^j_3=\xi^j_2=0$ $(j=1,2,3$, no sum on $j)$. The crack surface, in the region inside the ellipse in the plane $z=0$ is given by $\xi^j_3=0$ $(j=1,2,3$, no sum on $j)$. The three potential functions f_α $(\alpha=1,2,3)$ which satisfy the stress boundary conditions as suggested by Segedin (1967) can be taken as

$$f_\alpha(x_j, y_j, z_j)=\sum_k\sum_l C_{\alpha,k,l}F^j_{kl} \quad (\alpha=1,2,3) \tag{24}$$

where

$$F^j_{kl}=\frac{\partial^{k+l}}{\partial x_j^k\partial y_j^l}\int_{\xi^j_3}^{\infty}[\omega_j(s)]^{k+l+1}\frac{ds}{\sqrt{Q_j(s)}}. \tag{25}$$

$C_{\alpha,k,l}$ are the undetermined coefficients (in equation (24)) which are to be evaluated through applied tractions on the crack face. The abbreviated version of equation (25) can be represented as:

$$F^j_{kl}=\int_{\xi^j_3}^{\infty}\frac{\partial^{k+l}\omega_j^{k+l+1}(s)}{\partial x_j^k\partial y_j^l}\frac{ds}{\sqrt{Q_j(s)}}=\int_{\xi^j_3}^{\infty}\partial_1^{k_1}\partial_2^{l_1}\partial_3^{m_1}\omega_j^{k+l+1}(s)\frac{ds}{\sqrt{Q_j(s)}} \tag{26}$$

where

$$k_1=k \quad l_1=l \quad \text{and } m_1=0.$$

The notation ∂^α_β was used in the above equation to denote the αth partial derivative with respect to $\beta=1,2,3$ which denotes x_j, y_j, and z_j, respectively[2]. By successive differentiation of equation (26) and using the fact that $\omega_j(\xi^j_3)=0$, one can easily show that

$$F^j_{kl,\beta}=\int_{\xi^j_3}^{\infty}\partial_1^{k_1}\partial_2^{l_1}\partial_3^{m_1}\omega_j^{k+l+1}(s)\frac{ds}{\sqrt{Q_j(s)}}$$

$$k_1=k+\delta_{1\beta} \quad l_1=l+\delta_{2\beta} \quad \text{and} \quad m_1=\delta_{3\beta} \tag{27}$$

where $\delta_{1\beta}$, etc., are defined as Kronecker deltas. Further,

$$F^j_{kl,\beta\gamma}=\int_{\xi^j_3}^{\infty}\partial_1^{k_1}\partial_2^{l_1}\partial_3^{m_1}\omega_j^{k+l+1}(s)\frac{ds}{\sqrt{Q_j(s)}}+F^{(0)j}_{kl\beta\gamma} \tag{28}$$

where

$$F^{(0)j}_{kl\beta\gamma}=(k+l+1)!\,\frac{x_j^{k_1}y_j^{l_1}z_j^{m_1}}{(\xi^j_3-\xi^j_2)(\xi^j_3-\xi^j_1)}\,[\rho_1^{k_1}\rho_2^{l_1}\rho_3^{m_1}\sqrt{Q_j(s)}]_{s=\xi^j_3}$$

$$k_1=k+\delta_{1\beta}+\delta_{1\gamma},\ l_1=l+\delta_{2\beta}+\delta_{2\gamma}, \quad \text{and} \quad m_1=\delta_{3\beta}+\delta_{3\gamma};$$

further,

$$\rho_1=\frac{-2}{(a^2+s)},\ \rho_2=\frac{-2}{(b^2+s)} \quad \text{and} \quad \rho_3=0. \tag{29}$$

Evaluation of the generic integral of the type given in equation (27) and (28) can be derived along the lines of Vijayakumar and Atluri (1981) by expanding $\omega_j^{k+l+1}(s)$.

$$\int_{\xi^j_3}^{\infty}\partial_1^{k_1}\partial_2^{l_1}\partial_3^{m_1}\omega_j^{k+l+1}(s)\frac{ds}{\sqrt{Q_j(s)}}$$

$$=(k+l+1)!\sum_{p=0}^{k+l+1}\sum_{q=0}^{p}\sum_{r=0}^{q}\frac{(-1)^p}{(k+l+1-p)!}\frac{(2p-2q)!}{(p-q)!}$$

$$\times\frac{(2q-2r)!(2r)!}{(q-r)!(r)!}\frac{x_j^{2p-2q-k_1}}{(2p-2q-k_1)!}\frac{y_j^{2q-2r-l_1}}{(2q-2r-l_1)!}$$

$$\times\frac{z_j^{2r-m_1}}{(2r-m_1)!}J_{p-q,q-r,r}(\xi^j_3) \tag{30}$$

where

$$J_{p-q,q-r,r}(\xi^j_3)=\int_{\xi^j_3}^{\infty}\frac{ds}{(s+a^2)^{p-q}(s+b^2)^{q-r}s^r\sqrt{Q_j(s)}}. \tag{31}$$

It should be noted here that the integral in equation (31) becomes singular when $r\geq 1$. As noted by Shah and Kobayashi (1971), the singular portion cancels out when equation (28) is considered as a whole. A systematic procedure for the evaluation of the above-mentioned elliptic integrals can be found in Nishioka and Atluri (1983) for real ξ^j_3. As for complex ξ^j_3, the formulation procedure is similar to that of real ξ^j_3 (Nishioka and Atluri, 1983), except for the fact that the elliptic integrals

[2]Admittedly, this is not a very precise notation; but is used here for the sake of simplicity.

Downloaded 03 May 2010 to 171.66.16.248. Redistribution subject to ASME license or copyright; see http://www.asme.org/terms/Terms_Use.cfm

defined here have complex amplitudes. The procedure for evaluating such elliptic integrals can be found in Bird and Friedman (1971) or in Abramowitz and Stegun (1971).

5 Representation of Crack Face Tractions

The tractions on the crack surface can be expressed in the form

$$\sigma_{3\alpha}^{(0)}=\sum_{i=0}^{1}\sum_{j=0}^{1}\sum_{m=0}^{M}\sum_{n=0}^{m}A_{\alpha,m-n,n}^{(i,j)}x^{2m-2n+i}y^{2n+j}\quad(\alpha=1,2,3) \tag{32}$$

so that the values of (i,j) specify the symmetry of the load with respect to the axes of the ellipse. Here, the (x,y) are the global coordinate system which is aligned along the major and minor axis of the ellipse. $A^{(i,j)}_{\alpha,m-n,n}$, in general, is given or can be determined once the tractions on the crackface is prescribed. Taking symmetry into consideration, the potential functions in the modified coordinates $(x_j, y_j, z_j)(j=1,2,3)$ are assumed as

$$f_\alpha(x_j,y_j,z_j)=\sum_{i=0}^{1}\sum_{m=0}^{1}\sum_{k=0}^{M}\sum_{l=0}^{k}C_{\alpha,k-l,l}^{(i,m)}F_{2k-2l+i,2l+j}^{j}\quad(\alpha=1,2,3). \tag{33}$$

Here, $C^{(i,m)}_{\alpha,k-l,l}$ are undetermined coefficients to be evaluated through the traction boundary conditions on the crack face. Substituting equation (33) into equation (26) the crack face stresses in terms of f_α $(\alpha=1,2,3)$(on the crack face $x_j=x$, $y_j=y$, and $z_j=z=0$) can be expressed

$$\begin{aligned}\sigma_{33}^{(0)}&=-\gamma_1 f_{3,33}=\gamma_1(f_{3,11}+f_{3,22})\\ \sigma_{13}^{(0)}&=-\gamma_2 f_{1,11}+\gamma_3 f_{1,22}-(\gamma_2+\gamma_3)f_{2,12}\\ \sigma_{23}^{(0)}&=-\gamma_2 f_{2,22}+\gamma_3 f_{2,11}-(\gamma_2+\gamma_3)f_{1,12}.\end{aligned} \tag{34}$$

Substituting equation (33) into equation (34) and equating coefficients of like powers of x and y in the resulting expression, with those in equation (32), the coefficients $\{A\}$ for the Mode I problem are obtained.

$$A_{3,m-n,n}^{(i,j)}=\gamma_1\frac{(-1)^{m+i+j+1}}{(2m-2n+1)!(2n+j)!}\sum_{k=m}^{M}\sum_{l=0}^{k}(-1)^k\times[I_1^{(i,j)}J_{L_1+1,L_2,0}^{(0)}+I_2^{(i,j)}J_{L_1,L_2,+1,0}^{(0)}]C_{3,k-l,l}^{(i,j)}$$
$$m=0,1,\ldots,M\quad n=0,1,\ldots,m \tag{35}$$

Owing to the skew symmetric nature of the mode II and III problems, they could be decomposed in the following two problems P_1 and P_2 (Vijayakumar and Atluri, 1981): (i) problem P_1: $\sigma_{3\alpha}^{(0)}$ is symmetric and $\sigma_{3\beta}^{(0)}$ is antisymmetric in both x_1 and x_2; (ii) problem P_2: $\sigma_{3\alpha}^{(0)}$ is symmetric in x_1 and antisymmetric in x_2 $\sigma_{3\beta}^{(0)}$ is antisymmetric in x_1 and symmetric in x_2.

The coefficients for problem P_2 can be shown to be the following

$$\begin{aligned}&A_{\alpha,m-n,n}^{(i,j)}\\ &=\frac{(-1)^{m+i+j+1}}{(2m-2n+i)!(2n+j)!}\sum_{k=m}^{M}\sum_{l=0}^{k}(-1)^k\{[\gamma_3(I_1^{(i,j)}J_{L_1+1,L_2,0}^{(0)}\\ &+I_2^{(i,j)}J_{L_1,L_2+1,0}^{(0)})+(\gamma_2+\gamma_3)I_\alpha^{(i,j)}J_{L_1+\delta_{1\alpha},0}^{(0)}]C_{\alpha,k-l,l}^{(i,j)}\\ &+(\gamma_2+\gamma_3)I_{12}^{(1-i,1-j)}J_{L_1+1-i,L_2+1-j,0}^{(0)}C_{\beta,k-l,l}^{(i,j)}\}\end{aligned} \tag{36}$$
$$m=0,1,2,\ldots,M\quad n=0,1,\ldots,m.$$

Similar expressions could be derived along the same line for the P_1 problem (Vijayakumar and Atluri, 1981). Here,

$$L_1=(m-n+k-l+i),\quad L_2=n+l+j$$
$$I_\alpha^{(i,j)}=\frac{(2k+i+j+1)!}{(k-m)!}\frac{(2L_1+2\delta_{1\alpha})!}{(L_1+\delta_{1\alpha})!}\frac{(2L_2+2\delta_{2\alpha})!}{L_2+\delta_{2\alpha})!}\quad(\alpha=1,2)$$

$$I_{12}^{(i,j)}=\frac{(2k+i+j+1)!}{(k-m+i+j-1)!}\frac{(2L+2-2i)!}{(L_1+1-i)!}\frac{(2L_2+2-2j)!}{(L_2+1-j)!}. \tag{38}$$

It should be noted that all elliptic integrals $J^{(0)}_{L_1,L_2,0}$, etc., are in general nonsingular and a systematic procedure (as in Nishioka and Atluri, 1983) is adopted here. The relationship between the parameters $\{A\}$ and the unknown coefficients $\{C\}$, can be put in matrix form as follows:

$$\{A\}=[B]\{C\}. \tag{39}$$

The coefficients of the square matrix $[B]$ are complete elliptic integrals defined above. By solving the system of equations the unknown coefficients, $\{C\}$ can be determined.

6 Stress Intensity Factors

As shown by Kassir and Sih (1968, 1975), the ellipsoidal coordinates in the vicinity of the periphery of the elliptical crack on the plane $z=0$ becomes

$$\begin{aligned}\xi_1&=-(a^2\sin^2\theta+b^2\cos^2\theta)\\ \xi_2&=0\\ \xi_3&=2abr(a^2\sin^2\theta=b^2\cos^2\theta)^{-1/2}\end{aligned} \tag{40}$$

where r is the radial distance normal to the crack border in the plane $z=0$, and θ is the angle in the parametric equations of the ellipse

$$x=a\cos\theta\quad y=b\sin\theta. \tag{41}$$

The explicit K-factor expressions for the mode I problem take the following form

$$K_I=4\gamma_1\left(\frac{\pi}{ab}\right)^{1/2}A^{1/4}\sum_{i=0}^{1}\sum_{j=0}^{1}\sum_{k=0}^{M}\sum_{l=0}^{k}(-2)^{2k+i+j}(2k+i+j+1)!\times\frac{1}{ab}\left(\frac{\cos\theta}{a}\right)^{2k-2l+i}\left(\frac{\sin\theta}{b}\right)^{2l+j}C_{3,k-l,l}^{(i,j)} \tag{42}$$

and for the mode II and III problems are

$$K_{II}=4\gamma_2\left(\frac{\pi}{ab}\right)^{1/2}A^{-1/4}\frac{1}{ab}[\gamma_1 b\cos\theta+\gamma_2 a\sin\theta]$$
$$K_{III}=4\gamma_3\left(\frac{\pi}{ab}\right)^{1/2}A^{-1/4}\frac{1}{ab}[\lambda_2 b\cos\theta-\lambda_1 a\sin\theta]. \tag{43}$$

Here,

$$\gamma_1=\sum_{i=0}^{1}\sum_{j=0}^{1}\sum_{k=0}^{M}\sum_{l=0}^{k}(-2)^{2k+i+j}(2k+i+j+1)!\times\left(\frac{\cos\theta}{a}\right)^{2k-2l+i}\left(\frac{\sin\theta}{b}\right)^{2l+j}C_{1,k-l,l}^{(i,j)}$$

$$\lambda_2=\sum_{i=0}^{1}\sum_{j=0}^{1}\sum_{k=0}^{M}\sum_{l=0}^{k}(-2)^{2k+2-i-j}(2k+3-i-j)!\times\left(\frac{\cos\theta}{a}\right)^{2k-2l+1-i}\left(\frac{\sin\theta}{b}\right)^{2l+1-j}C_{2,k-l,l}^{(i,j)}. \tag{44}$$

7 Finite Element Alternating Method

By employing the Schwarz-Neumann alternating method (hereinafter called the alternating method), it is possible to obtain the stress intensity factor distribution on the crack front

Downloaded 03 May 2010 to 171.66.16.248. Redistribution subject to ASME license or copyright; see http://www.asme.org/terms/Terms_Use.cfm

Table 1 Elastic constants for transversely isotropic material (consistent with (1))

Material	C11	C12	C13	C33	C44
β-Quartz	11.66	1.67	3.28	11.04	3.61
Zn	16.09	3.35	5.01	6.10	3.83
Composite Laminate[5]x10^6 ($E_L/E_T = 25$)	0.537	0.134	0.335	25.168	0.5
Transverse Isotropy tending to Isotropy ($E = 1.0$, $\nu = 0.3$)	1.342	0.574	0.575	1.34	0.382

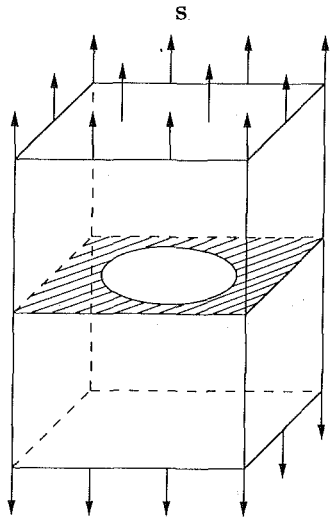

Fig. 1(*a*)

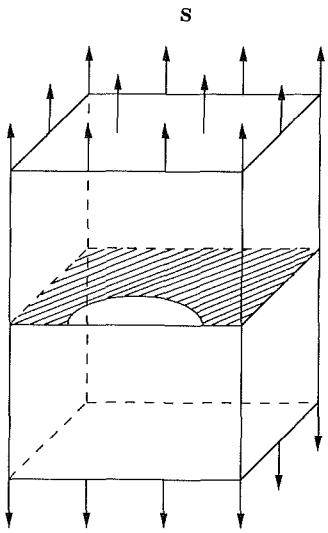

Fig. 1(*b*)

Fig. 1 Cracked configuration analyzed for uniform loading; (*a*) embedded crack, (*b*) surface crack

of an elliptical flaw in a finite transversely isotropic solid. Since no general solution exists for a finite body subjected to arbitrary externally applied tractions, a finite element solution is used to evaluate the stresses at the location of the crack in the transversely isotropic solid. The infinite body with a crack has a closed-form solution which is valid for any degree polynomial applied crack face tractions. Hence, the two main ingredients for the effective implementation of the alternating method for an elliptical crack embedded in a transversely isotropic solid are:

Solution 1: the elliptical crack subjected to arbitrary normal and shear loading on the crack surface in a transversely isotropic infinite solid.

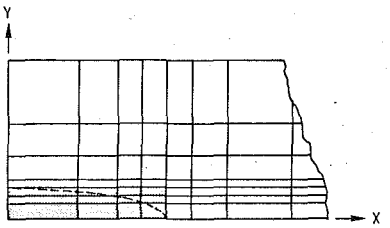

Fig. 2 Crack surface area used in residual pressure fit (rectangular model)

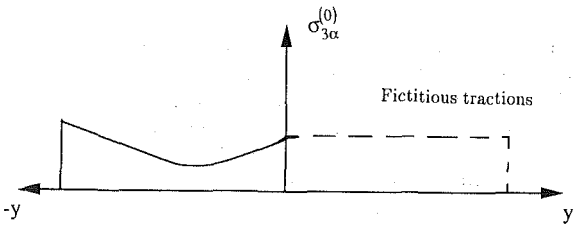

Fig. 3 Fictitious tractions used for the surface flaw problem

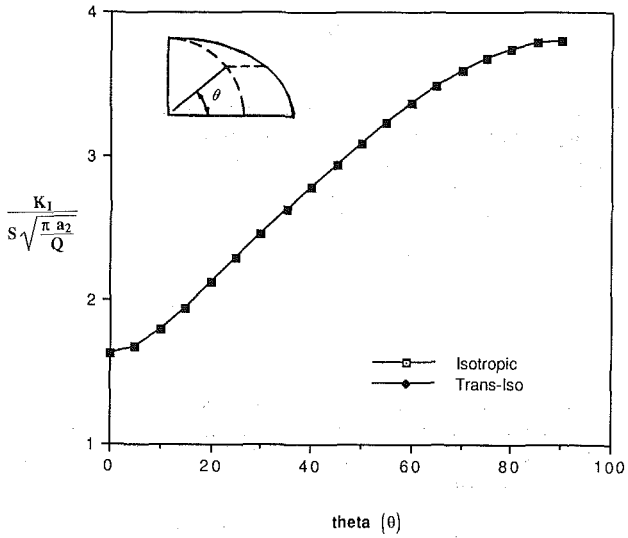

Fig. 4 Comparison of the isotropic situation and transverse isotropy tending to isotropy for the case of embedded flaw

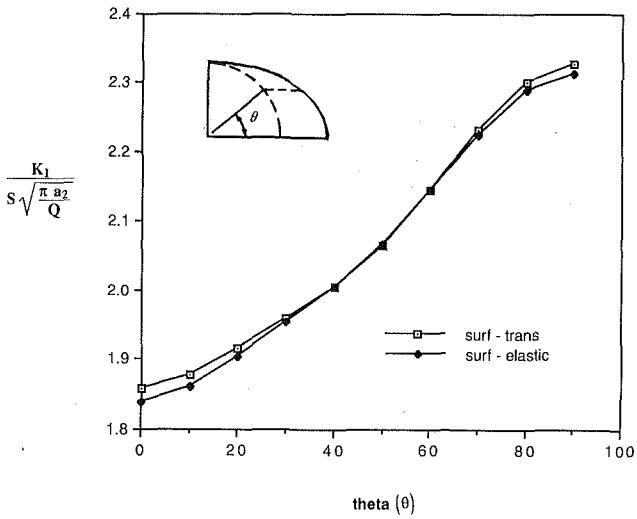

Fig. 5 Comparison of the isotropic situation and transverse isotropy *for the case of surface flaw*

Solution 2: a finite element solution for the uncracked transversely isotropic body: The following iterative solution procedure is adopted for the alternating method.

Downloaded 03 May 2010 to 171.66.16.248. Redistribution subject to ASME license or copyright; see http://www.asme.org/terms/Terms_Use.cfm

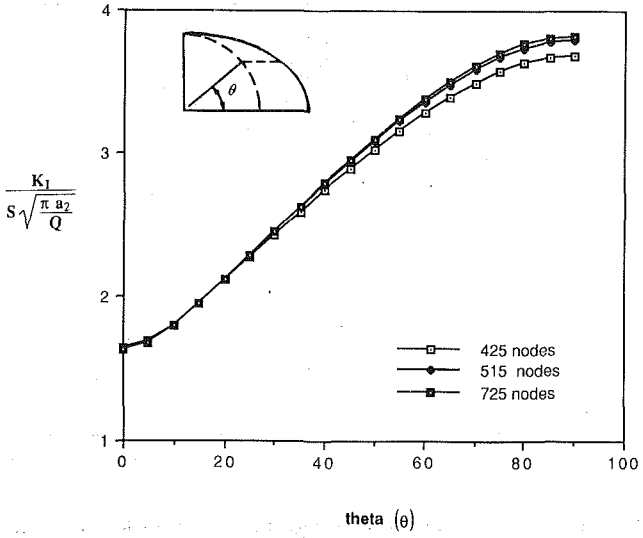

Fig. 6 Stress intensity factor variation for an embedded crack with various mesh discretizations (material: β-quartz)

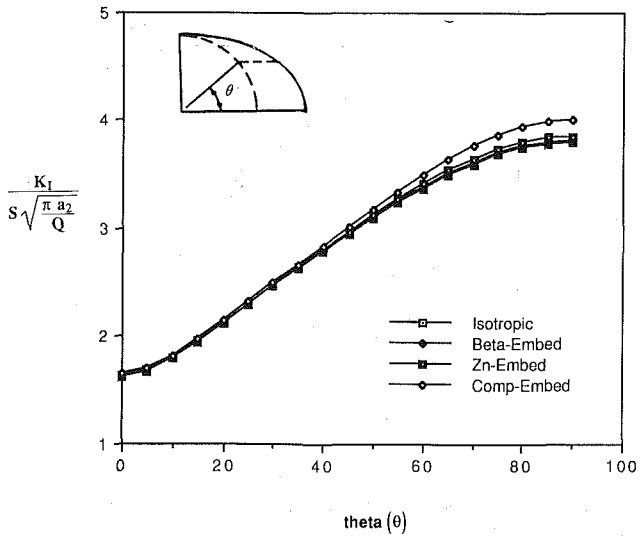

Fig. 7 Stress intensity factor variation for the embedded crack for different material properties

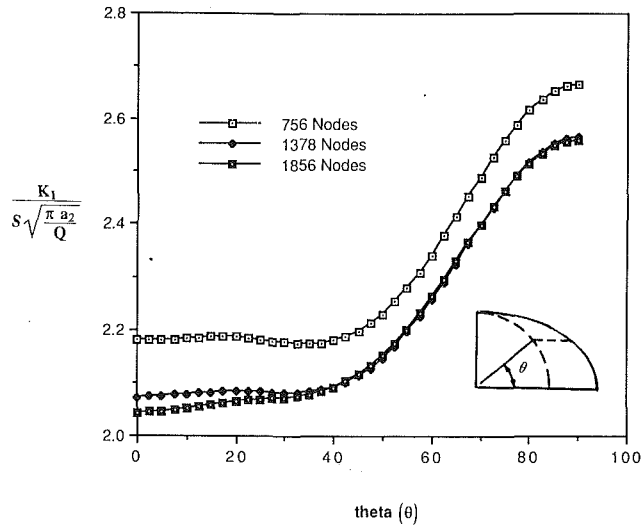

Fig. 8 Stress intensity factor variation for a surface flaw with various mesh discretizations (material: zn)

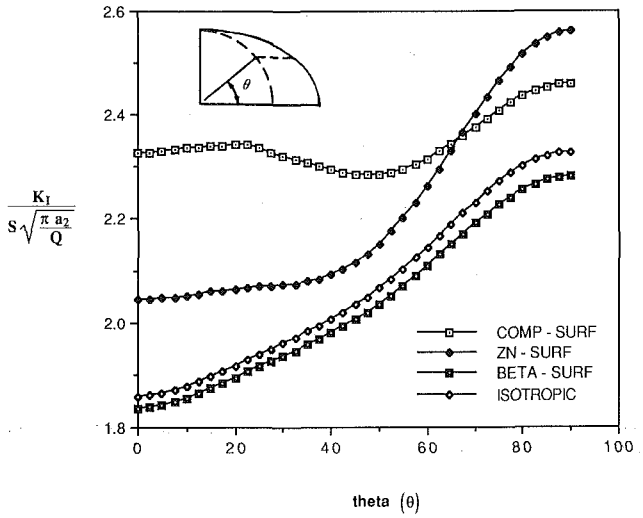

Fig. 9 Stress intensity factor variation for an embedded crack for different material properties

1 Solve the uncracked transversely isotropic body under the given external loads by the finite element method. The uncracked body has the same geometry with the given problem except the crack.
2 The stresses at the location of the original crack in the uncracked structure is computed using the finite element method.
3 Compare the residual stresses calculated in step (2) with a permissible stress magnitude. In the present study one percent of the maximum external applied stress is used for the permissible stress magnitude.
4 To create a crack, reverse the residual stresses at the location of the crack and determine the coefficients $\{A\}$ of equation (39) useful for solution 1 by least squares method.
5 Determine the coefficients $\{C\}$ of equation (39).
6 Compute K-factors for the current iteration by substituting coefficients $\{C\}$ into equations (42)–(44).
7 Calculate the residual stress from equation (14) on external surfaces of the body due to loads in step (4).
8 Reverse the residual surface stresses at the boundary and the solution 2 is made use of to obtain the stresses at the uncracked location as in step (1).

Repeat all steps in the iteration process until the residual stresses on the crack surface become negligible. It should be noted here that the stiffness matrix of solution 2 remains the same during every iteration process and thus needed to be computed only once during the entire solution process. Also, such a solution procedure obviates the need for any singular elements at the crack front, since solution 2 involves the uncracked body only. In the case of the surface flaw, fictitious tractions are introduced to the imaginary portion of the crack (so that the analytical solution for the embedded crack can be employed) before proceeding to step (4) in the solution algorithm. The fictitious tractions could be chosen arbitrarily and will only affect the convergence of the alternating method.

8 Numerical Results

8.1 Isotropic Finite Body Solution. As a check on the correctness of the analytical solution for the transversely isotropic case, embedded as well as surface elliptical flaws in a finite body, subjected to remote uniform tensile loading, were considered. In all the cases, the elastic constants for transverse isotropy were chosen such that they were close to isotropic behavior (Table 1). Is should be noted here that the analytical solution for the isotropic case cannot be recovered from the present transversely isotropic case unless an elaborate limiting process is performed analytically. Hence, as an overall check

Downloaded 03 May 2010 to 171.66.16.248. Redistribution subject to ASME license or copyright; see http://www.asme.org/terms/Terms_Use.cfm

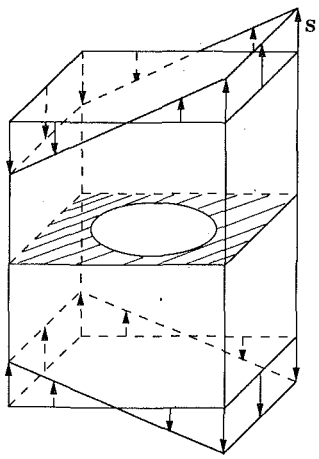

Fig. 10(*a*)

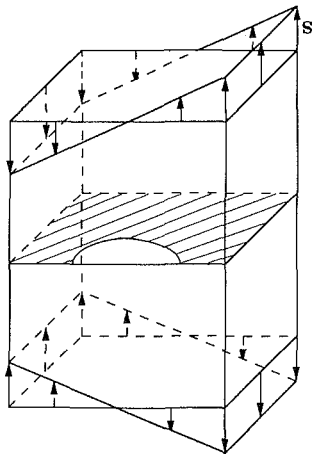

Fig. 10(*b*)

Fig. 10 Cracked configuration analyzed for bending loads; (*a*) embedded crack, (*b*) surface crack

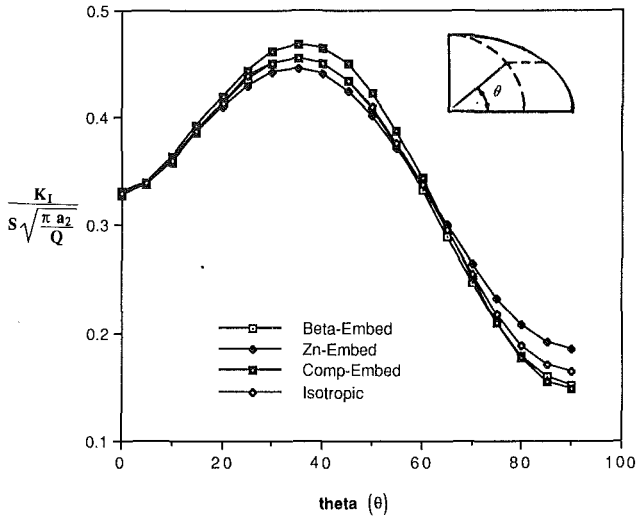

Fig. 11 Stress intensity factor variation for the embedded crack for bending loads with different material properties

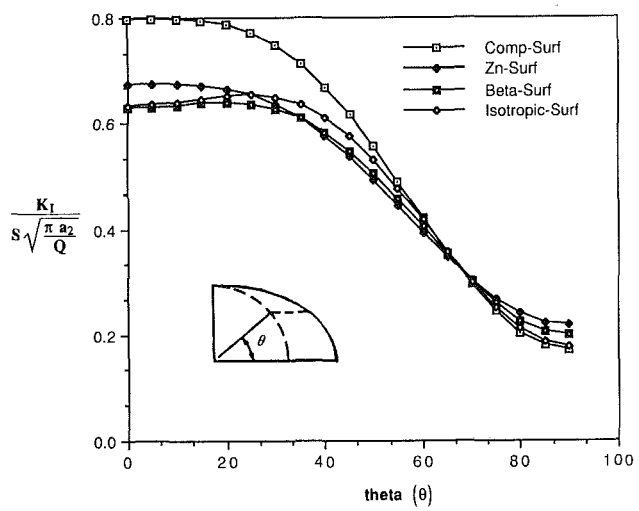

Fig. 12 Stress intensity factor variation for the surface crack for bending loads with different material properties

for the solution algorithm the limiting case for isotropy is taken numerically by taking elastic constants for transverse isotropy to be close to isotropy. The two example problems considered are shown in Fig. 1. The ratio of a_1/a_2 was taken to be 4 for the embedded flaw and 2 for the surface flaw (a_1 and a_2 are the semimajor and semiminor axis of the ellipse, respectively). The specimen and flaw dimensions are the same as in the case of transverse isotropy and will be discussed in the forthcoming section. The highest order polynomial variation (M) in the analytical solution was taken to be 5. Rectangular finite element models were considered (Raju et al., 1988) throughout the present analysis as in Fig. 2. As for the part elliptical surface flaw, the stress distribution in the fictitious region was taken to be a constant, as in Fig. 3. This was found to give the best convergence of all the other variations considered (Nishioka and Atluri, 1983). Twenty noded brick elements were considered throughout the present analysis. As for the embedded elliptical crack, a 756-noded graded mesh with 125 elements was considered. In the case of the part elliptical surface flaw, a 1856 noded graded mesh (with a finer mesh refinement near the region were the crack is supposed to be located) with 343 elements was considered. The above-mentioned meshes are the final mesh discretizations after a systematic convergence study. Such a convergence study would be presented for transversely isotropic materials in the forthcoming section. The nondimensionalized parameter $K_I/S[\pi a_2/Q]^{1/2}$ is plotted against the parametric angle θ. Here, K_I is the mode I stress intensity factor, S is the uniform remote tensile loading of the finite body, a_2 is the semiminor radial distance of the elliptical flaw, and Q is the shape factor of the ellipse (which is the square of the complete integral of the second kind). As seen in Figs. 4 and 5 the agreement between the transversely isotropic algorithm (when the elastic constants were taken to be close to the isotropic situation) and the exact isotropic formulation was good for both the embedded and surface elliptical flaws.

8.2 Embedded Elliptical Crack in a Finite Body. Three different materials were considered in the present paper. They were β-quartz, zinc, and a typical graphite epoxy composite laminate (Christensen, 1979). The properties of the above-mentioned materials are listed in Table 1. The characteristic equation (4) yields real roots for β-quartz and the composite laminate and complex roots for Zn. A convergence study was carried out for the FEM idealization of the uncracked body. An embedded elliptical crack with $a_1 = 1.0$ and $a_2 = 0.25$ in a $8 \times 0.67 \times 8$ solid subjected to a uniaxial load as shown in Fig. 1 was considered. The highest order polynomial considered for a crack face traction variation was $M = 5$. A quarter of the ellipse was modeled due to the symmetry of the problem. A systematic convergence study was undertaken starting with a 425-noded mesh for the uncracked body, for the case of the

Downloaded 03 May 2010 to 171.66.16.248. Redistribution subject to ASME license or copyright; see http://www.asme.org/terms/Terms_Use.cfm

embedded crack for all the materials considered. As shown in Fig. 6, the convergence was excellent for β-quartz with a 725-noded mesh. The mode I K-factor variation was considered for β-quartz, Zinc, and the composite laminate ($E_L/E_T = 25$) with a 725-noded graded mesh. Due to the nature of the symmetry present, the K-factor variation of only quarter of the ellipse was considered (Fig. 7). The results are compared to that of the isotropic material with $E = 1.0$ and $\nu = 0.3$.

8.3 Surface Elliptical Crack. A surface semi-elliptical flaw in a $2.5 \times 2.5 \times 10$ body under uniaxial tension was considered for the present analysis as seen in Fig. 1. The dimensions of the ellipse considered was $a_1 = 1.25$ and $a_2 = 0.625$. Due to the symmetry present, only a half the body was modeled. The highest order polynomial considered for the traction variation was $M = 5$. The extended tractions on the fictitious part of the crack was taken to be a constant as shown in Fig. 3. A systematic convergence study was performed starting from a 725-noded mesh for all the above-mentioned materials considered. The results of such a convergence study are shown for Zinc in Fig. 8. The 1856-noded graded mesh displayed adequate convergence for the present problem. Due to the nature of the symmetry present in the problem, the K-factor variation was presented for half of the elliptical flaw. Figure 9 shows the K-factor variation of β-quartz, Zinc, and the composite laminate (with $E_L/E_T = 25$) after convergence has been established in each case. The results for the above-mentioned materials are compared with those for an isotropic elastic material with $E = 1.0$ and $\nu = 0.3$. The qualitative variation of K-factors for the present problem with the above-mentioned materials was different when compared to that of the embedded crack. The results for the surface flaw in a finite body clearly demonstrate the effect of the degree of transverse isotropy on the K-factors as compared to the case of isotropy.

8.4 Bending Loads. An embedded elliptical flaw in a $8 \times 0.67 \times 8$ solid with $a_1 = 1.0$ and $a_2 = 0.25$ and a semi-elliptical surface flaw in a $2.5 \times 2.5 \times 10$ solid with $a_1 = 1.25$ and $a_2 = 0.625$ were considered when subjected to bending loads as shown in Fig. 10. Due to the nature of the symmetry present in the problem, only quarter of the ellipse was modeled. A convergence study was undertaken for both problems considered. The nondimensionalized parameter $K_I/S[\pi a_2/Q]^{1/2}$ is plotted against the parametric angle of the ellipse. Here, K_I is the mode I stress intensity factor, S is the remote out of fiber loading of the finite body (Fig. 10), a_2 is the semi-minor radial distance of the elliptical flaw, and Q is the shape factor of the ellipse. The materials considered were β-quartz, Zinc, and the composite laminate (Christensen, 1975). Comparisons are made against the isotropic case with $E = 10$ and $\nu = 0.3$. A 725-noded mesh was used for the uncracked solid in the case of the embedded flaw and the results are presented in Fig. 11. As for the semi-elliptical surface flaw a 1856-noded graded mesh was employed for modeling the uncracked body. The K-factor variations are given in the tesile portion of the ellipse in Fig. 12.

9 Conclusions

The solution for an embedded elliptical crack in an infinite transversely isotropic solid (when the crack axis is perpendicular to the axis of elastic symmetry) subjected to arbitrary crack face tractions is derived. This analytical solution, in conjunction with the finite element method, is employed in the Schwarz-Neumann alternating method to solve for K-factors in a finite solid subjected to arbitrary loading. Mode I solutions are obtained for some typical transversely isotropic materials. It was observed that the maximum K-factors for the surface flaw problems were sensitive to material properties of the transversely isotropic body. On the other hand, as is to be expected, the solutions for embedded crack problems in transversely isotropic bodies did not deviate much from the isotropic situation. The ability of the present method to obtain K-factors for arbitrary loading of cracked transversely isotropic bodies using the infinite body solution renders such a technique powerful and versatile.

Acknowledgments

The support of the work by the U.S. Office of Naval Research and the encouragement of Dr. Y. Rajapakse is gratefully acknowledged. It is also a pleasure to thank Mrs. Deanna Bump and Mrs. Linda Large for their assistance in the preparation of this manuscript.

References

Abramowitz, M., and Stegun, A., 1970, *Handbook of Mathematical Functions*, Dover Publications, New York.

Byrd, R. F., and Friedman, M. D., 1971, *Handbook of Elliptic Integrals for Engineers and Scientists*, Springer-Verlag, Berlin.

Christensen, R. M., 1979, *Mechanics of Composite Materials*, John Wiley and Sons, New York.

Elliot, H. A., 1945, "Axial Symmetric Stress Distributions in Hexagonal Aeolotropic Crystals: The Problem of Plane and Related Problems," *Proceedings of the Cambridge Philosophical Society*, Vol. 45, pp. 621–630.

Elliot, H. A., 1949, "Axial Symmetric Stress Distribution in Aeolotropic Hexagonal Crystals," *Proceedings of the Cambridge Philosophical Society*, Vol. 45, pp. 247–268.

Hu, H. C., 1953, "On the 3-D Problems of the Theory of Elasticity of a Transversely Isotropic Body," *Acta Scientifica Sinica*, Vol. 2, pp. 145–151.

Kassir, M. K., and Sih, G. C., 1968, "Three-Dimensional Stresses Around Elliptical Cracks in a Transversely Isotropic Solid," *Journal of Engineering Fracture and Mechanics*, Vol. 1, pp. 327–345.

Kassir, M. K., and Sih, G. C., 1975, "Three-Dimensional Crack Problems," *Mechanics of Fracture*, Vol. 2, G. C. Sih, ed., Noordhoff, The Netherlands.

Lekhnitski, S. C., 1981, *Theory of Elasticity of an Anisotropic Body*, Mir Publishers, Moscow, U.S.S.R.

Nishioka, T., and Atluri, S. N., 1983, "Analytical Solution for Embedded Elliptical Cracks and Finite Element Alternating Method for Elliptical Surface Cracks Subjected to Arbitrary Loading," *Engineering Fracture Mechanics*, Vol. 17, No. 3, pp. 247–268.

Raju, I. S., Atluri, S. N., and Newman, J. C., 1988, "Stress-Intensity Factors for Small Surface and Corner Cracks in Plates, NASA Technical Memorandum 10059.

Segedin, C. M., 1967, "Some Three-Dimensional Mixed Boundary Value Problems in Elasticity," Report 67-3, Dept. of Aeronautics and Astronautics, College of Engineering, University of Washington.

Shah, R. C., and Kobayashi, A. S., 1971, "Stress-Intensity Factors for an Elliptical Crack Under Arbitrary Normal Loading," *Engineering Facture Mechanics*, Vol. 3, pp. 71–96.

Vijayakumar, K., and Atluri, S. N., 1981, "An Embedded Elliptical Crack in an Infinite Solid, Subject to Arbitrary Crack Face Tractions," ASME JOURNAL OF APPLIED MECHANICS, Vol. 103, pp. 88–96.

Downloaded 03 May 2010 to 171.66.16.248. Redistribution subject to ASME license or copyright; see http://www.asme.org/terms/Terms_Use.cfm

The Spherical Inclusion With Imperfect Interface

Z. Hashin[1]
Department of Mechanical Engineering
and Applied Mechanics,
University of Pennsylvania,
Philadelphia, PA 19104-6315
Fellow ASME

A rigorous solution of the spherical inclusion problem with remote uniform strain or stress and imperfect elastic spring-type interface conditions is presented. In the case of thin elastic interphase, the interface spring constants are expressed in terms of interphase elastic properties and thickness. The state of strain/stress in the inclusion is nonhomogeneous for imperfect interface conditions in contrast to the homogeneous state for perfect interface condition. Numerical results are given to demonstrate the significance of imperfect interface effects.

Introduction

Problems of the determination of stress fields in the vicinity of foreign inclusions embedded in a matrix material have been given considerable attention in the mechanics of solids literature, both in the stress concentration context and in relation to composite materials problems. Almost all of the work has been concerned with the classical situation when displacements and tractions are continuous across the inclusion matrix interface. This will here be referred to as perfect interface conditions, and within this context the primary achievement is the well-known Eshelby (1957) solution of the ellipsoidal inclusion problem.

Recently, there has been considerable interest in imperfect interface conditions as may be appropriate in the case of thin coatings on inclusions, produced by design or by chemical interaction, or for interface damage due, for example, to cyclic loading. Walpole (1978) has discussed the coated inclusion problem, in a general sense, on the basis of Hill's (1961, 1972) interface discontinuity theorems.

Mura et al. (1985) have given a solution for the axisymmetric case of a sliding spheroidal inclusion, assuming perfect normal interface bonding and ideally lubricated tangential contact. Ghahremani (1985) gave a solution for the more special case of a spherical inclusion under the same conditions. Mikata and Taya (1985) solved the axisymmetric case of a coated spheroidal inclusion which is embedded in an infinite medium. Using techniques to be described in this paper, this solution could be interpreted to apply for the case of imperfect normal and tangential imperfect interface conditions, thus generalizing the solution of Mura et al. Benveniste (1985) has treated an embedded composite sphere problem with perfect normal interface bonding and imperfect shear bonding for the case of remote shear. For literature on related problems of composite materials with coated reinforcement see, e.g., Hashin (1990).

The present work is concerned with solution of the spherical inclusion problem in the case of imperfect elastic normal and tangential bond between inclusion and matrix.

Formulation

Suppose that two different homogeneous media, which are labeled 1 and 2, are joined by an imperfect interface, S_{12} (Fig. 1). Then the quantitative effect of the imperfection is in the form of displacement discontinuities across the interface while the tractions must remain continuous for reasons of equilibrium. The simplest mathematical description of elastic imperfect interface is based on the assumption that normal and tangential displacement discontinuities are proportional to the respective traction components. Thus,

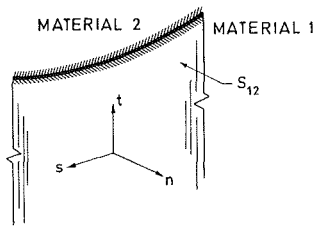

Fig. 1 Interface

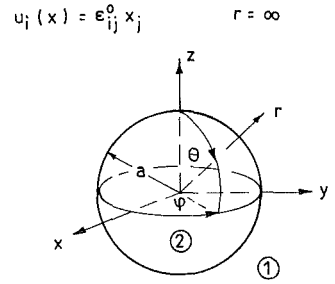

Fig. 2 Spherical inclusion

[1]On leave from Tel Aviv University, Tel Aviv, Israel.

Contributed by the Applied Mechanics Division of THE AMERICAN SOCIETY OF MECHANICAL ENGINEERS for publication in the JOURNAL OF APPLIED MECHANICS.

Discussion on this paper should be addressed to the Technical Editor, Leon M. Keer, The Technological Institute, Northwestern University, Evanston, IL 60208, and will be accepted until two months after final publication of the paper itself in the JOURNAL OF APPLIED MECHANICS. Manuscript received by the ASME Applied Mechanics Division, Oct. 30, 1989; final revision, Feb. 26, 1990.

Copyright © 1991 by ASME
Downloaded 03 May 2010 to 171.66.16.248. Redistribution subject to ASME license or copyright; see http://www.asme.org/terms/Terms_Use.cfm

$$T_n = D_n[u_n] \qquad [u_n] = u_n^{(1)} - u_n^{(2)}$$
$$T_s = D_s[u_s] \qquad [u_s] = u_s^{(1)} - u_s^{(2)} \tag{1}$$
$$T_t = D_t[u_t] \qquad [u_t] = u_t^{(1)} - u_t^{(2)}$$

where D_n, D_s, and D_t are spring constant-type material parameters which will be called interface parameters. It is seen that infinite values of these parameters imply vanishing of the displacement jumps and therefore perfect interface conditions. At the other extremity, zero values of the parameters imply vanishing of interface tractions and therefore disbond of the two adjoining media. Any finite positive values of the interface parameters define an imperfect interface.

The problem of the spherical inclusion with imperfect interface conditions is now formulated as follows: A spherical inclusion of radius, a, consisting of homogeneous isotropic elastic material, 2, is embedded in unbounded elastic isotropic matrix, 1, (Fig. 2). The remote displacement field is

$$u_i^{(1)}(x) = \epsilon_{ij}^o x_j \qquad r \to \infty \tag{2}$$

which implies uniform strain, ϵ_{ij}^o. At the interface $r = a$, we must satisfy the six conditions

$$\sigma_{rr}^{(1)}(a,\theta,\phi) = \sigma_{rr}^{(2)}(a,\theta,\phi) = \eta[u_r]$$
$$\sigma_{r\theta}^{(1)}(a,\theta,\phi) = \sigma_{r\theta}^{(2)}(a,\theta,\phi) = \mu[u_\theta] \tag{3}$$
$$\sigma_{r\phi}^{(1)}(a,\theta,\phi) = \sigma_{r\phi}^{(2)}(a,\theta,\phi) = \mu[u_\phi]$$

where $\eta = D_n$, $\mu = D_s = D_t$.

It will be convenient for our purposes to split the displacement equation (2) as follows:

$$u_i^{(1)} = \epsilon^o x_i + e_{ij}^o x_j, \tag{4}$$

where ϵ^o and e_{ij}^o are the isotropic and deviatoric parts, respectively, of ϵ_{ij}^o. We shall now proceed to construct solutions of the problem for spherical symmetry, axial symmetry, and pure shear.

Spherical Symmetry

The first part of equation (4) is imposed separately. In spherical coordinates this is equivalent to

$$u_r^{(1)} = \epsilon^o r$$
$$r \to \infty \tag{5}$$
$$u_\theta^{(1)} = u_\phi^{(1)} = 0.$$

This defines an elementary spherically symmetric problem with displacements and stresses in the form

$$u_r = Ar + B/r^2$$
$$u_\theta = u_\phi = 0$$
$$\sigma_{rr} = 3KA - 4GB/r^3 \tag{6}$$
$$\sigma_{\theta\theta} = \sigma_{\phi\phi} = 3KA + 2GB/r^3$$
$$\sigma_{r\theta} = \sigma_{\theta\phi} = \sigma_{r\phi} = 0.$$

Inserting into equations (3) and (5) we find

$$A_1 = \epsilon^o$$
$$B_1 a^3 = \frac{3[K_2(1+3p) - K_2]}{3K_2 + 4G_1(1+3p)}\,\epsilon^o$$
$$A_2 = \frac{3K_1 + 4G_1}{3K_2 + 4G(1+3p)}\,\epsilon^o \tag{7}$$
$$B_2 = 0$$
$$p = K_2/a\eta.$$

Consider now the special case where the interface imperfection is due to a thin flexible elastic interphase coating of thickness t and elastic properties K_i and G_i where

$$t \ll a$$
$$K_i,\ G_i \ll K_2. \tag{8}$$

This defines a three-phase spherically symmetric elastic problem with perfect interface conditions. Within the interphase

$$u_r^{(i)} = A_i r + B_i/r^2$$
$$\sigma_{rr}^{(i)} = 3K_i A_i - 4G_i B_i/r^3. \tag{9}$$

It follows that the radial displacement jump is approximated by

$$[u_r] = u_r^{(i)}(a+t) - u_r^{(i)}(a) \cong (A_i - 2B_i/a^3)t. \tag{10}$$

Displacement and traction continuity at $r = a$ requires

$$A_i a + B_i/a^2 = A_2 a$$
$$3K_i A_i - 4G_i B_i/a^3 = 3K_2 A_2. \tag{11}$$

Solving for A_i and B_i from equation (1) and substituting into equation (10) we find

$$\sigma_{rr}^{(2)}(a) = \frac{K_i + 4G_i/3}{t}\,[u_r], \tag{12}$$

and therefore, for thin coating,

$$\eta = (K_i + 4G_i)/3t$$
$$p = \frac{K_2}{K_i + 4G_i/3} \cdot \frac{t}{a}. \tag{13}$$

Note that if only G_i is small and K_i is of the order of K_2, η will become very large, and the interface condition becomes perfect.

Axisymmetry

We consider the case when equation (2) has the form

$$u_x = \epsilon_T x \qquad u_y = \epsilon_T y \qquad u_z = \epsilon_A z \tag{14}$$

Splitting this as in equation (4) we have

$$\epsilon^o = \frac{1}{3}(\epsilon_A + 2\epsilon_T) \qquad (a)$$
$$e_{xx}^o = e_{yy}^o = -\beta \quad e_{zz}^o = 2\beta \qquad (b) \tag{15}$$
$$\beta = \frac{1}{3}(\epsilon_A - \epsilon_T) \qquad (c)$$

The solution for the displacement, associated with equation (15a), has been given above. We thus have to consider only the remote displacement

$$u_x = -\beta x \qquad u_y = -\beta y \qquad u_z = 2\beta z. \tag{16}$$

Converting to spherical coordinates we have

$$u_r = 2\beta r P$$
$$u_\theta = \beta r \dot{P} \tag{17}$$

where

$$P = P_2(\cos\theta) = \frac{1}{2}(3\cos^2\theta - 1)$$
$$\dot{P} = \frac{dP}{d\theta} \tag{18}$$

where P_2 is the Legendre polynomial of order 2.

The axisymmetric elasticity problem for spherical domains can be solved in general fashion in terms of functions of r multiplied by Legendre polynomials. For details see, e.g., Lur'e (1964). In the present case only a solution associated with P_2 is needed. This may be written in the form

Downloaded 03 May 2010 to 171.66.16.248. Redistribution subject to ASME license or copyright; see http://www.asme.org/terms/Terms_Use.cfm

$$u_r=\beta[12\nu A\rho^2+2B+2(5-4\nu)C/\rho^3-3D/\rho^5]rP$$

$$u_\theta=\beta[(7-4\nu)A\rho^2+B+2(1-2\nu)C/\rho^3+D/\rho^5]r\dot{P}$$

$$\sigma_{rr}=2G\beta[-6\nu A\rho^2+2B-4(5-\nu)C/\rho^3+12D/\rho^5]P$$

$$\sigma_{r\theta}=2G\beta[(7+2\nu)A\rho^2+B+2(1+\nu)C/\rho^3-4D/\rho^5]\dot{P} \qquad (19)$$

$$\sigma_{\theta\theta}=2G\beta\left\{3(7+\nu)A\rho^2+2B+(1-2\nu)C/\rho^3+\frac{9}{2}D/\rho^5+\left[-7(2+\nu)A\rho-B+(1-2\nu)C/\rho^3-\frac{11}{2}D/\rho^5\right]3\cos^2\theta\right\}$$

$$\sigma_{\phi\phi}=2G\beta\left\{15\nu A\rho^2-B-5(1-2\nu)\frac{C}{\rho^3}+\frac{3}{2}\frac{D}{\rho^5}+\left[-2(11+2\nu)A\rho^2+3(1-2\nu)C/\rho^3-\frac{5}{2}D/\rho^5\right]3\cos^2\theta\right\}$$

$\rho=r/a$,

where A, B, C, D are unknown constants which will be given index 1 for the matrix solution and index 2 for the inclusion solution.

The displacement equations (19) must reduce to equations (17) for $r\to\infty$ and there can be no singularities at the inclusion center $r=0$. It follows that

$$A_1=A_2=B_2=0 \qquad B_1=1. \qquad (20)$$

The remaining constants are determined from the first two of equations (3) (since $\sigma_{r\phi}$ vanishes identically) which reduce to the linear equations

$$\begin{aligned}
&2(5-\nu_1)C_1-6D_1-&&3\nu_2gA_2+&&gB_2=1\\
&-2(1+\nu_1)C_1+4D_1+&&(7+2\nu_2)gA_2+&&gB_2=1\\
&-2(5-4\nu_1)C_1+3D_1+&&12\nu_2(1-e)A_2+2(1+2e)B_2=2\\
&-2(1-2\nu_1)C_1-D_1+[(7-4\nu_2)+(7+2\nu_2)2m]A_2+(1+2m)B_2=1
\end{aligned} \qquad (21)$$

where

$$e=G_2/a\eta=\frac{3(1-2\nu_2)}{2(1+\nu_2)}p \qquad m=\frac{G_2}{a\mu}$$

$$g=G_2/G_1. \qquad (22)$$

We shall now apply the solution developed to the case of uniaxial stress $\sigma_{zz}=\sigma^o$ at large distance from the inclusion. In this case the strains in equation (14) are

$$\epsilon_A=\frac{\sigma^o}{E_1} \qquad \epsilon_T=-\frac{\nu_1\sigma^o}{E_1} \qquad (23)$$

and, consequently, from equation (15),

$$\epsilon^o=\frac{\sigma^o}{9K_1} \qquad \beta=\frac{\sigma^o}{6G_1}. \qquad (24)$$

This solves the problem for remote uniaxial stress by superposition of a spherically symmetric and an axially symmetric solution. In the following we list some of the resulting stresses

$$\frac{\sigma_{rr}^{(1)}}{\sigma^o}=\frac{K_2(3K_1+4G_1)}{3K_1[3K_2+4G_1(1+3p)]}+\frac{G_2}{3G_1}(-3\nu_2A_2\rho^2+B_2)(3\cos^2\theta-1)$$

$$\frac{\sigma_{r\theta}^{(2)}}{\sigma_o}=-\frac{G_2}{3G_1}[(7+2\nu_2)A_2\rho^2+B_2]\cos\theta\sin\theta$$

$$\frac{\sigma_{\theta\theta}^{(1)}(a,\theta)}{\sigma_o}=\frac{K_2(3K_1-2G_1)+6K_1G_1(1+3p)}{3K_1[3K_2+4G_1(1+3p)]}+\frac{1}{3}\left\{2+(1-2\nu_1)C_1-\frac{5}{2}D_1+\frac{3}{2}[-2+2(1-2\nu_1)C_1+7D_1]\cos^2\theta\right\}$$

$$\frac{\sigma_{\phi\phi}^{(1)}(a,\theta)}{\sigma_o}=\frac{K_2(3K_1-2G_1)+6K_1G_1(1+3p)}{K_1[3K_2+4G_1(1+3p)]}+\frac{1}{3}\left\{1+5(1-2\nu_1)C_1-\frac{3}{2}D_1+\frac{3}{2}[-6(1-2\nu_1)C_1+5D]\cos^2\theta\right\}. \qquad (25)$$

Finally, we consider again the case when the imperfect interface condition is due to thin flexible coating of thickness $t\ll a$ on the inclusion consisting of elastic material with moduli K_i and G_i. It is shown in the Appendix that

$$\mu=\frac{G_i}{t}$$

$$m=\frac{G_2}{G_i}\frac{t}{a}. \qquad (26)$$

Pure Shear

To obtain a solution for remote pure shear we superpose a solution for uniaxial tension on a solution for uniaxial compression, orthogonal to the tension. Since superposition in spherical coordinates is complicated, we shall carry out the out the superposition in cartesian coordinates.

Assume a remote state of stress

$$\sigma_{xx}=\tau^o \qquad \sigma_{yy}-\tau^o. \qquad (27)$$

All others vanish. We first convert the previous solution for uniaxial tension in the z-direction to cartesian coordinates. For this purpose, the displacements in equation (19) are expressed in the form

$$u_r=U_r(r)P \qquad u_\theta=U_\theta(r)\dot{P}. \qquad (28)$$

Converting to cartesian coordinates we have

$$u_x=\frac{1}{2}U_r(3z^2/r^2-1)x/r-3U_\theta xz^2/r^3$$

$$u_y=\frac{1}{2}U_r(3z^2/r^2-1)y/r-3U_\theta yz^2/r^3$$

$$u_z=\frac{1}{2}U_r(3z^2/r^2-1)z/r-3U_\theta(1-z^2/r^2)z/r. \qquad (29)$$

Solutions for uniaxial stress in the x and y-directions are obtained by cyclic interchange of coordinates according to the scheme.

direction of load	coordinates
z	$x\ y\ z$
x	$y\ z\ x$
y	$z\ x\ y$

We recall that a uniaxial stress solution is given by equation (28) or (29) and a spherically symmetric solution. But since we superpose a tension solution on a numerically equal compression solution, the spherically symmetric parts of the solution will cancel. Carrying out the superposition in cartesian coor-

Downloaded 03 May 2010 to 171.66.16.248. Redistribution subject to ASME license or copyright; see http://www.asme.org/terms/Terms_Use.cfm

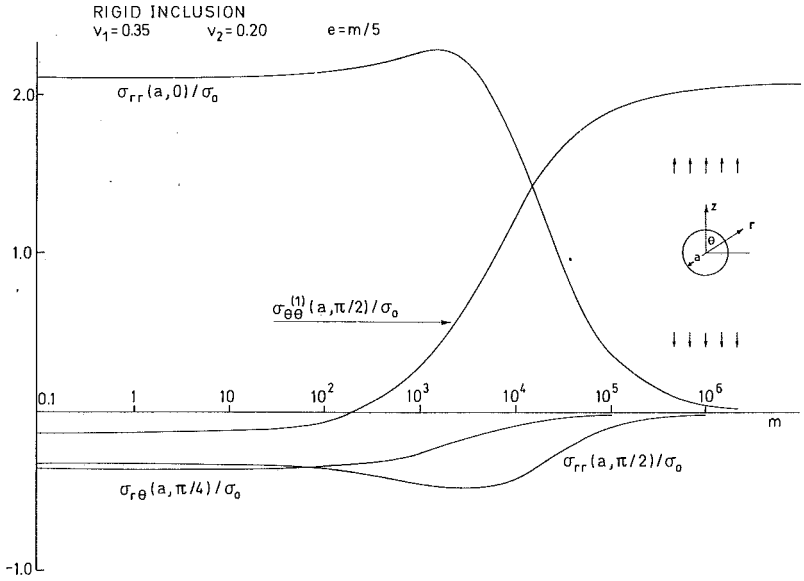

Fig. 3 Remote uniaxial stress, surface stresses on rigid inclusion

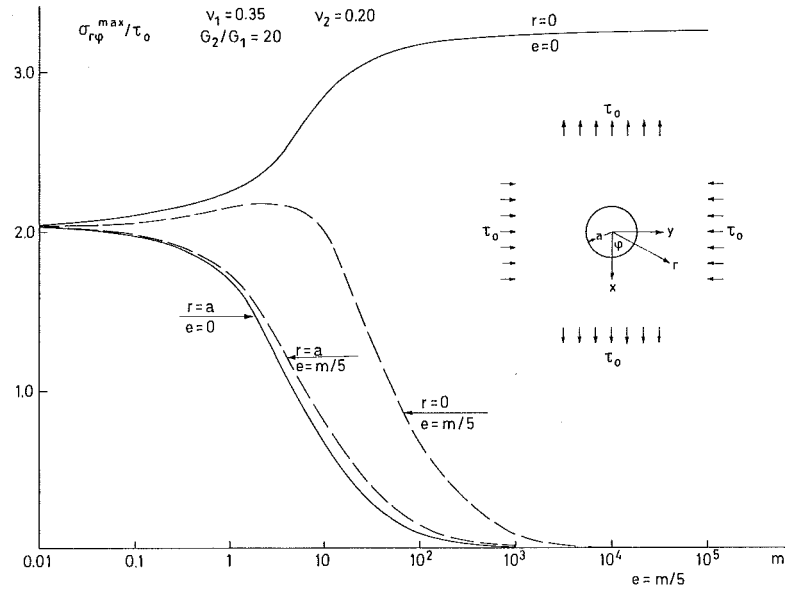

Fig. 4 Remote pure shear, surface shear stresses on elastic inclusion

dinates and converting back to spherical coordinates we find the following displacement field

$$u_r = \frac{3}{2} U_r \cos 2\phi \sin^2\theta$$

$$u_\theta = 3\, U_\theta \cos 2\phi \cos\theta \sin\theta \qquad (30)$$

$$u_\phi = -3\, U_\theta \sin 2\phi \sin\theta$$

where the constants in U_r and U_θ are still defined by equations (20)–(22) and

$$\beta = \frac{\tau^o}{6G_1}. \qquad (31)$$

The stresses may now be computed from equation (30). We give explicit results for the shear stresses $\sigma_{r\theta}$ and $\sigma_{r\phi}$ only

$$\sigma_{r\theta}^{(1)} = \tau_o[1 + 2(1+\nu_1)C_1/\rho^3 - 4D_1/\rho^5]\cos 2\phi \cos\theta \sin\theta$$

$$\sigma_{r\theta}^{(1)} = -\tau_o[1 + 2(1+\nu_1)C_1/\rho^3 - 4D_1/\rho^5]\sin 2\phi \sin\theta$$

$$\sigma_{r\theta}^{(2)} = \tau_o \frac{G_2}{G_1}[(7+2\nu_2)A_2\rho^2 + B_2]\cos 2\phi \cos\theta \sin\theta$$

$$\sigma_{r\phi}^{(2)} = -\tau_o \frac{G_2}{G_1}[(7+2\nu_2)A_2\rho^2 + B_2]\sin 2\phi \sin\theta$$

Results and Discussion

It is well known that in the case of perfect interface conditions, the stress and strain in the spherical inclusion (and also in the ellipsoidal inclusion) are uniform. It is seen that in the present case of imperfect interface conditions this is no longer the case, because of the presence of the ρ^2 term in the inclusion solution, (equations (25) and (32)). However, in the special case $e = m$ it follows from equation (21) that $A_2 = 0$, and in this case the strain and stress in the inclusion are uniform. Then

$$B_2 = \frac{15(1-\nu_1)}{(1+2m)(7-5\nu_1) + 2g(4-5\nu_1)} \qquad (33)$$

Downloaded 03 May 2010 to 171.66.16.248. Redistribution subject to ASME license or copyright; see http://www.asme.org/terms/Terms_Use.cfm

and for remote uniaxial stress the deviatoric part of inclusion stress is

$$\sigma_{xx}=\sigma_{yy}=-s \qquad \sigma_{zz}=2s$$

$$s=\frac{1}{3}\sigma_o B_2. \tag{34}$$

It follows at once that if remote tension σ_o in the x-direction is superposed on remote compression σ_o in the y-direction, the inclusion stress is

$$\sigma_{xx}=3s \quad \sigma_{yy}=-3s \quad \sigma_{zz}=0, \tag{35}$$

thus a pure shear $3s$ at 45 deg to x, y.

In the special case of perfect bond, $m = 0$, and the well-known uniform solution for perfect interface conditions is recovered.

Unfortunately, however, the simple results for $e = m$ are not of practical interest for it follows from equations (13) and (26) that for thin coating,

$$\eta/\mu=K_i/G_i+4/3.$$

Thus, at least for this case, η is substantially larger than μ, and therefore e is substantially smaller than m, and equality of these quantities is impossible.

Numerical results for the case of a rigid inclusion under remote uniaxial tension are shown in Fig. 3. All stresses shown are located at the interface $r = a$. It has been assumed that $e = m/5$, which corresponds to a Poisson's ratio $\nu_i = 0.375$ when the interface imperfection is due to a thin coating of isotropic material. Increase of m implies deterioration of the interface bond, from perfect bond at $m = 0$ to disbond for $m \to \infty$. The maximum and minimum radial stresses are the polar tensile stress, $\sigma_{rr}(a, 0)$, and the equatorial compressive stress, $\sigma_{rr}(a, \pi/2)$. Both of these increase initially with increasing m, but then decrease until they vanish.

The maximum shear stress $\sigma_{r\theta}$ is located at $\theta = \pi/4, 3\pi/4$ and it decreases monotonically with deterioration of the bond. Also shown is the matrix stress $\sigma_{\theta\theta}^{(1)}(a, \pi/2) = \sigma_{zz}$ on the equator. This stress increases from the compressive value for the rigid inclusion with perfect bond to the tensile magnified stress for a spherical hole, i.e., the disbonded inclusion.

Figure 4 shows results for the shear stress $\sigma_{r\phi}$ near the inclusion center and on the interface. For the case of the biaxial loading considered it assumes a maximum value at points $\phi = \pi/4, 3\pi/4, 5\pi/4, 7\pi/4$ on the xy-plane, indicated by points on the circle. We observe the interesting phenomenon that this shear stress increases with decreasing radial distance from the center. The plots show values on the interface $\rho = 1$ and at the center $\rho = 0$. The condition $e = 0$, $m > 0$, implies perfect normal bond and imperfect shear bond. For a thin coating this is realized when the coating material is incompressible, i.e., $\nu_i = .50$. It is seen that in this case the shear stress at the center increases with deterioration of shear bond while the interface shear stress decreases. For the case $e = m/5$ considered before, the shear stress at the center behaves quite differently as seen in the figure.

It is to be expected that the interface parameter η, and thus also e, may be different in tension and compression. This presents a rather difficult problem, for in that case there will be different interface regions defined by tensile and compressive normal tractions and their boundaries are *a priori* unknown.

As a related matter it should be mentioned that if the elasticity problem with interface conditions (1) is regarded in mathematical fashion, without reference to the physical situation it describes, there arises the following difficulty: The normal displacement continuity in (1) cannot be negative for this would imply penetration of the matrix into the inclusion. The mathematical remedy to this would be to require perfect normal bonding when the normal traction is compressive and imperfect bonding for the case of tension. This would complicate the problem enormously in the manner described previously.

If there is a compliant thin interphase then the normal displacement discontinuities are defined by the normal deformations of this interphase which can take place both outward and inward. The interphase contribution is approximated by an imperfect interface condition and in so doing it is assumed that the matrix/interphase interface can be moved inward by a small distance equal to the interphase thickness. With this interpretation a negative normal displacement continuity becomes permissible.

It seems possible that interphase strains could become so large that they would have to be described by finite measures of strain. The normal interface parameters describing such a situation would have to be different in tension and compression raising again the difficulties described previously.

Closure

A rigorous solution of the problem of the spherical inclusion with remote uniform strain or stress, when the interface conditions are imperfect, has been given. The results demonstrate that interface imperfection can have significant effect on stress fields in and near the inclusion.

It has been shown that a thin, flexible interphase layer is equivalent to the present definition of imperfect interface and the interface parameters have been determined in terms of interphase properties and thickness.

Acknowledgment

This work has been supported by the Air Force Office of Scientific Research, Lt. Col. Haritos, and by the Office of Naval Research, Dr. Rembert Jones, through contract between the National Center for Composites Materials Research, University of Illinois, Urbana, Dr. Su Su Wang, Director, and the University of Pennsylvania. I am indebted to the aforementioned for support and encouragement.

References

Benveniste, Y., 1985, "The Effective Mechanical Behavior of Composite Materials with Imperfect Contact Between the Constituents," *Mechanics of Materials*, Vol. 4, pp. 197–208.

Eshelby, J. D., 1957, "The Determination of the Field of an Ellipsoidal Inclusion and Related Problems," *Proceedings of the Royal Society, London*, Vol. A241, pp. 376–396.

Ghahremani, F., 1985, "Effect of Grain Boundary Sliding on Anelasticity of Polycrystals," *International Journal of Solids and Structures*, Vol. 16, pp. 825–845.

Hashin, Z., 1990, "Thermoelastic Properties of Fiber Composites with Imperfect Interface," *Mechanics of Materials*, Vol. 8, pp. 333–348.

Hill, R., 1961, "Discontinuity Relations in Mechanics of Solids," *Progress in Solid Mechanics*, Vol. 2, North Holland Publishing Co., Chapter 4.

Hill, R., 1972, "An Invariant Treatment of Interfacial Discontinuities in Elastic Composites," *Continuum Mechanics and Related Problems of Analysis*, Moscow, pp. 597–604.

Lur'e, A. I., 1964, *Three Dimensional Problems of the Theory of Elasticity*, John Wiley and Sons, New York.

Mikata, Y., and Taya, M., 1985, "Stress Field in and Around a Coated Short Fiber in an Infinite Matrix Subjected to Uniaxial and Biaxial Loadings," ASME JOURNAL OF APPLIED MECHANICS, Vol. 52, pp. 19–24.

Mura, T., Jasiuk, I., and Tsuchida, B., 1985, "The Stress Field of a Sliding Inclusion," *International Journal of Solids and Structures*, Vol. 21, pp. 1165–1179.

Walpole, L. J., 1978, "A Coated Inclusion in an Elastic Medium," *Mathematics Proceedings of the Cambridge Philosophical Society*, Vol. 83, pp. 495–506.

APPENDIX

Evaluation of the Interface Parameters of Thin Interphase

The method is similar to the one employed for establishment

Downloaded 03 May 2010 to 171.66.16.248. Redistribution subject to ASME license or copyright; see http://www.asme.org/terms/Terms_Use.cfm

of the result equation (13). Consider a three-phase problem with remote uniaxial stress when there is an interphase of thickness t and properties K_i and G_i, obeying the conditions equation (8). Then the displacement jumps due to the interphase are

$$[u_r] = u_r^{(i)}(a+t) - u_r^{(i)}(a) \cong \left(\frac{\partial u_r^{(i)}}{\partial r}\right)_{r=a} t$$
$$[u_\theta] = u_\theta^{(i)}(a+t) - u_\theta^{(i)}(a) \cong \left(\frac{\partial u_r^{(i)}}{\partial r}\right)_{r=a} t. \tag{A1}$$

Introducing displacement equation (19) into equation (A1), we have

$$[u_r] = \beta[36\nu_i A_i + 2B_i - 4(5-4\nu_i)C_i + 12D_i]tP$$
$$[u_\theta] = \beta[3(7-4\nu_i)A_i + B_i - 4(1-2\nu_i)C_i - 4D_i]t\dot{P} \tag{A2}$$

where A_i, B_i, C_i, D_i are unknown constants of the interphase field.

Displacement and traction continuity at $r = a$ lead to the following equations

$$12\nu_i A_i + 2B_i + 2(5-4\nu_i)C_i - 3D_i = 12\nu_2 A_2 + 2B_2$$
$$(7-4\nu_i)A_i + B_i + 2(1-2\nu_i)C_i + D_i = (7-4\nu_2)A_2 + B_2$$
$$-6\nu_i A_i + 2B_i - 4(5-\nu_i)C_i + 12D_i = g_i(-6\nu_2 A_2 + 2B_2)$$
$$(7+2\nu_i)A_i + B_i + 2(1+\nu_i)C_i - 4D_i = g_i[(7+2\nu_2)A_2 + B_2] \tag{A3}$$

where

$$g_i = G_2/G_i \gg 1. \tag{A4}$$

Solving equations (A3) for the interphase constants and inserting the results into equation (A2) and taking into account equation (A4) we find

$$[u_r] = \frac{t}{K_i + 4G_i/3} 2G_2\beta[-6\nu_2 A_2 + 2B_2]P$$
$$[u_\theta] = \frac{t}{G_i} 2G_2\beta[(7+2\nu_2)A_2 + B_2]\dot{P}. \tag{A5}$$

Comparison with equation (19) shows that the extreme right factors are the stresses $\sigma_{rr}^{(2)}(a)$ and $\sigma_{r\theta}^{(2)}(a)$. Thus the first result equation (A5) is consistent with equation (13), while the second provides the result equation (26).

Note that in the case of the pure shear solution the result equation (26) will also be valid because of the nature of the solution. Note also that in order to derive equation (26) it is sufficient to require that $G_i \ll G_2$, independently of the magnitude of K_i.

Downloaded 03 May 2010 to 171.66.16.248. Redistribution subject to ASME license or copyright; see http://www.asme.org/terms/Terms_Use.cfm

Elastic-Plastic Analysis of Cracks on Bimaterial Interfaces: Part III—Large-Scale Yielding

C. F. Shih
Division of Engineering,
Brown University,
Providence, RI 02912
Mem. ASME

R. J. Asaro
Department of AMES,
University of California–San Diego,
La Jolla, CA 92093

N. P. O'Dowd
Division of Engineering,
Brown University,
Providence, RI 02912

In Parts I and II, the structure of small-scale yielding *fields of interface cracks were described in the context of small strain plasticity and* J_2 *deformation theory. These fields are members of a family parameterized by the plastic* phase angle ξ *which also determines the shape or phase of the plastic zone. Through full-field analysis, we showed the resemblance between the plane-strain interface crack-tip fields and mixed-mode HRR fields in homogeneous material. This connection was exploited, to the extent possible, inasmuch as the interface fields do not appear to have a separable form. The present investigation is focused on "opening" dominated load states* ($|\xi| \leq \pi/6$) *and the scope is broadened to include finite ligament plasticity and finite deformation effects on near-tip fields. We adopt a geometrically rigorous formulation of* J_2 *flow theory taking full account of crack-tip blunting. Our results reveal several surprising effects, that have important implications for fracture, associated with finite ligament plasticity and finite strains. For one thing the fields that develop near bimaterial interfaces are more intense than those in homogeneous material when compared at the same value of* J *or remote load. For example, the plastic zones, plastic strains, and the crack-tip openings,* δ_t, *that evolve near bimaterial interfaces are considerably larger than those that develop in homogeneous materials. The stresses within the finite strain zone are also higher. In addition, a localized zone of high hydrostatic stresses develops near the crack tip but then expands rapidly within the weaker material as the plasticity spreads across the ligament. These stresses can be as much as 30 percent higher than those in homogeneous materials. Thus, the weaker material is subjected to large stresses as well as strains—states which promote ductile fracture processes. At the same time, the accompanying high interfacial stresses can promote interfacial fracture.*

1 Introduction

Previous investigations by Shih and Asaro (1988, 1989a,b) have been concerned with the structure of plane-strain interface crack-tip fields within the context of small strain plasticity as described by J_2 *deformation* theory. Specifically, in Parts I and II of this article (Shih and Asaro, 1988, 1989a), the structure of the crack-tip fields that develop under conditions pertaining to small-scale yielding were calculated and described. In Shih and Asaro (1989b), the stress and strain fields that evolve under conditions producing contained yielding and fully plastic conditions were examined through a study of collinear crack geometries. These (primarily) numerical studies led to an understanding of the asymptotic structure of interface crack-tip fields along with a correspondence of these fields to the well characterized small strain (HRR) fields in homogeneous media (e.g., see Hutchinson, 1983; Symington et al., 1988). In the present article the plasticity aspects of interface fracture are studied in more detail by way of plane-strain finite deformation calculations of crack fields under small-scale yielding, contained yielding, and fully yielded conditions. In Part IV, which concludes this series, the fields of cracks lying on interfaces with internal structure, such as leads to properties different than those of either of the two primary materials, are described.

The results of the present study show that much of this correspondence between the structure of the "opening" dominated small strain fields of interface cracks and those of cracks in homogeneous media carries over to the finite strain fields. Nevertheless, there are surprising effects which have important implications on fracture path and the fracture toughness of the material system. For example, when an initially sharp crack blunts, and thus loses the strong constraint at its tip, the maximum stresses are shifted somewhat ahead of its tip. When

Contributed by the Applied Mechanics Division of THE AMERICAN SOCIETY OF MECHANICAL ENGINEERS for presentation at the Joint Applied Mechanics/Bioengineering Conference, Ohio State University, Columbus, OH, June 16–19, 1991.

Discussion on this paper should be addressed to the Technical Editor, Leon M. Keer, The Technological Institute, Northwestern University, Evanston, IL 60208, and will be accepted until two months after final publication of the paper itself in the JOURNAL OF APPLIED MECHANICS. Manuscript received by the ASME Applied Mechanics Division, July 1, 1989; final revision, Apr. 9, 1990.

Paper No. 91-APM-12.

Copyright © 1991 by ASME
Downloaded 03 May 2010 to 171.66.16.248. Redistribution subject to ASME license or copyright; see http://www.asme.org/terms/Terms_Use.cfm

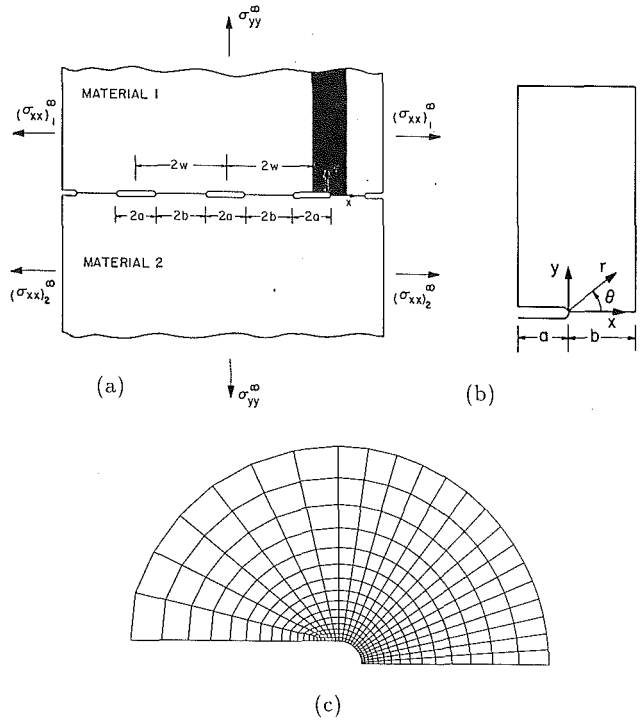

Fig. 1 *(a)* **Infinite row of collinear cracks on a bimaterial interface, (*b*) upper half of strip, (*c*) finite element mesh of upper region near crack tip**

this occurs at an interface crack, for example one lying on the interface of elastic-plastic and elastic materials as detailed below, it is found that the triaxial stresses are somewhat larger than those that develop at the tip of a crack in a homogeneous medium loaded so as to achieve the same value of the J-integral. The plastic zones and the regions of finite strains that evolve near bimaterial interfaces are also considerably larger. Nevertheless, scaling with J is found to be appropriate since at distances larger than, say $r \approx 2\delta_t$ where δ_t is the crack-tip opening, the fields within the weaker elastic-plastic material essentially converge onto those of a crack in the corresponding homogeneous medium of identical material properties. The magnitudes of the stresses in the elastic substrate are limited to those stress levels achieved in the weaker material. Results such as these, as well as the modes of crack-tip blunting, are found to be sensitive to the ratio of the shear stress, parallel to the interface, to the normal stress. Thus, care was taken in our numerical analyses to elucidate the effects of mixed-mode loading in some detail. This was done, not only for cases involving small-scale yielding, but for cases involving contained and fully plastic conditions. Beyond small-scale yielding conditions, the stresses redistribute so as to produce large zones of high hydrostatic stresses in the weaker material—much larger than those typically encountered in homogeneous media. Results for all these cases are presented in what follows.

The plan of the paper is as follows: To provide some background and a perspective for the present study, the pertinent aspects of the linear theory and recent developments in the nonlinear theory are presented in Section 2. Numerical procedures and the constitutive relations are described in Section 3. In Section 4 results for small-scale yielding are given. Sections 5 and 6 are concerned with results for contained and fully plastic behavior. Discussion follows in Section 7.

2 Results From the Linear and Nonlinear Theory

2.1 Some Results From the Linear Theory. We begin with a review of pertinent aspects of the linear theory and restrict attention to plane-strain deformation. With respect to the coordinates shown in Fig. 1(*b*), the in-plane stresses have the singular form (see Cherepanov, 1979; Rice, 1988; Atkinson, 1989; and references to earlier works contained therein),

$$\sigma_{ij}(\theta,r)=\frac{1}{\sqrt{2\pi r}}[\mathrm{Re}\{\mathbf{K}r^{i\varepsilon}\}\tilde{\sigma}^{I}_{ij}(\theta;\varepsilon) + \mathrm{Im}\{\mathbf{K}r^{i\varepsilon}\}\tilde{\sigma}^{II}_{ij}(\theta;\varepsilon)] \text{ for } r \ll L \quad (1)$$

where $\mathbf{K}$ is the complex stress intensity factor and $\tilde{\sigma}^{I}_{ij}(\theta;\varepsilon)$ and $\tilde{\sigma}^{II}_{ij}(\theta;\varepsilon)$ are the universal dimensionless angular functions which depend on the elastic bimaterial constant ε. With the unit normal to the interface defined by $\mathbf{n}$, the angular functions $\tilde{\sigma}^{I}_{ij}n_i$ and $\tilde{\sigma}^{II}_{ij}n_i$ correspond to normal and shear tractions across the interface at $\theta=0$ and are rendered unique by setting $\tilde{\sigma}^{I}_{\theta\theta}$ and $\tilde{\sigma}^{II}_{\theta r}$ at $\theta=0$ equal to unity. Thus, when $\varepsilon=0$, they reduce to the standard mode I and II functions for homogeneous media. The particular form in equation (1) and the above interpretation are due to Rice, Suo, and Wang (1990). L is a characteristic crack dimension which is the shortest of the crack length, uncracked ligament length, film (layer) thickness or the distance between the crack tip and the point of load application. Note that $|r^{i\varepsilon}|=1$. Let φ and K be the phase angle and magnitude of $\mathbf{K}$ as defined by $Ke^{i\varphi}=K_1+iK_2=\mathbf{K}$. Equation (1) predicts overlapping of crack faces at some distance for all values of φ if $\varepsilon\neq 0$. Nevertheless, for a range of φ the predicted zone of interpretation is confined to a distance that is smaller than physically relevant length scales (England, 1965; Rice, 1988).

The phase of complex $\mathbf{K}$ depends on the choice of length units. For example, $\varphi=0$ will not remain 0 if a different physical unit of length, i.e., cm versus μm is chosen. Indeed, this can be anticipated since $\mathbf{K}$ has dimensions of *stress* $\times$ $\sqrt{length} \times length^{-i\varepsilon}$. In any case, a suitable definition of the phase angle is the ratio of the shear to normal tractions directly ahead of the crack. The tractions across the interface

$$\mathbf{t}=te^{i\phi_r}=(\sigma_{yy}+i\sigma_{xy})_{\theta=0}=\frac{\mathbf{K}r^{i\varepsilon}}{\sqrt{2\pi r}} \quad (2)$$

provides a definition of a local phase angle ϕ_r. The subscript r emphasizes that the phase of the traction, i.e., the load state, varies with distance r. It can be verified by inspection that ϕ_r is not affected by changes in length units, and that tension and shear effects are inherently coupled. For example, when the distance is changed from r_1 to r_2, the phase change $\Delta\phi_r \equiv \phi_{r2}-\phi_{r1}$ is $\varepsilon\ln(r_2/r_1)$. Thus, what is primarily tensile traction across the interface at r_1 changes to primarily shear traction at r_2 $(=r_1e^{\pm\pi/2\varepsilon})$. If $r_2/r_1=10$, then $\Delta\phi_r=\varepsilon\ln 10=2.3\,\varepsilon$. This suggests an equivalent bimaterial parameter, or phase index, defined by $\varepsilon^*\equiv(180/\pi)\,\varepsilon\ln 10=132\varepsilon$ which has the interpretation as the phase change in degrees over a decade increase in distance (Suo, 1989; Kim, 1990). For $\varepsilon=0.03$, a value representative of metal/ceramic pairs, $\varepsilon^*=4$ deg/decade. The limiting value of ε is 0.175 and the corresponding value of the phase index ε^* is 23 deg/decade.

It is preferable to work with stress intensity factors which are analogous to classical stress intensity factors. To this end, Shih and Asaro (1988, 1989a,b) considered the *stress intensity vector* $\mathbf{K}L^{i\varepsilon}$, designated by $\mathbf{Q}$, which has dimensions of *stress* $\times$ $\sqrt{length}$. The magnitude is simply K since $|L^{i\varepsilon}|=1$ and the phase of $\mathbf{K}L^{i\varepsilon}$, denoted by ϕ, may be interpreted as the phase of the tractions at $r=L$ if we disregard the asymptotic character of equation (2).

A bimaterial interface is typically subject to normal and shear tractions. Shih (1974) has provided a definition of mode mixity for cracks in homogeneous media. A slight rearrangement leads to a form which is more suited for interface cracks, viz.,

Downloaded 03 May 2010 to 171.66.16.248. Redistribution subject to ASME license or copyright; see http://www.asme.org/terms/Terms_Use.cfm

$$M(r) \overset{\text{def}}{=} \frac{2}{\pi}\tan^{-1}\left(\frac{\sigma_{r\theta}}{\sigma_{\theta\theta}}\right)_{\theta=0},$$

$$M(r) = \frac{2}{\pi}\phi_r = \frac{2}{\pi}(\phi + \varepsilon \ln(L/r)). \quad (3)$$

Thus, the local mixity is related to the overall mixity ϕ with an additional dependence on distance. Liechti and Hanson (1988) and Suo (1989) have introduced a similar local mode mixity or phase angle for interface cracks. Pan and Shih (1990) have employed a similar local mode mixity parameter to describe the phase change with distance of coupled mode I and mode III plastic fields in a homogeneous medium.

The purpose of fracture mechanics is to identify parameters which characterize fully the effects of load and geometry on the crack-tip field. Since the phase of the interfacial tractions varies with distance for material pairs in which $\varepsilon \neq 0$, it is desirable to measure the phase angle or load state at a fixed distance ahead of the crack tip. In rough terms, the fracture process zone can be thought of as a property of the material pair so that a length of that order could serve as a fixed material length. Designating the latter length by $\hat{L}$, the phase of the tractions at $r = \hat{L}$ denoted by $\hat{\phi}$ is related to the intrinsic and overall phase angle by

$$\hat{\phi} \overset{\text{def}}{=} \phi_{r=\hat{L}} = \varphi + \varepsilon \ln \hat{L}, \quad \hat{\phi} = \phi + \varepsilon \ln(\hat{L}/L). \quad (4)$$

In what remains of this section, we discuss how the above characterization of the load state fits within the framework of the overall fracture mechanics approach.

The strong dependence of interfacial fracture toughness on mode mixity has been reported in experimental studies by Cao and Evans (1989), Liechti and Chai (1991), and Wang and Suo (1990). In these investigations, mode mixity is parameterized by $\hat{\psi}$, which is our $\hat{\phi}$ or $\hat{M}$, since $\hat{\psi} = (\pi/2)\hat{M}$ (Liechti and Chai parameterize mode mixity by the overall phase angle ψ). For the purpose of defining, $\hat{\psi}$, $\hat{\phi}$, or $\hat{M}$, Rice (1988) has observed that it does not matter if $\hat{L}$ is chosen to be 1 μm, 1 mm, or 1 m as long as it is fixed for a given material pair and does not change with crack size or other geometric dimensions. Nevertheless, if $\hat{L}$ is of the same order as the relevant microstructural length or the fracture process zone size, then $\hat{\phi} = 0$ corresponds to a tension dominated state over the process zone, while $\hat{\phi} = \pi/2$ corresponds to a shear dominated state. For the purpose stated above, an estimate of the order of $\hat{L}$ is all that is necessary since the phase angle varies slowly with distance for typical values of ε.

For load states defined with respect to a relevant microstructural length, the experimental studies cited above indicate that interfacial toughness increases monotonically with the local phase angle, i.e.,

$$\text{sgn}\hat{\phi}\frac{dK_C(\hat{\phi})}{d\hat{\phi}} > 0 \quad \text{for } -\pi/2 \le \hat{\phi} \le \pi/2. \quad (5)$$

As an example, Cao and Evans' interfacial toughness locus $K_C(\hat{\psi})$ for an epoxy/glass pair, evaluated with respect to $\hat{L} = 25$ μm, is consistent with equation (5). For the above material pair, $\varepsilon = 0.07$ and the phase index $\varepsilon^* = 9$ deg so that if $\hat{L}$ is changed by a factor of 10 the toughness curve is shifted by 9 deg. However, if $\hat{L}$ is taken as 25 mm or 25 nm, the toughness curve is shifted by about ± 28 deg and does not fit the form in equation (5), though the shape of the toughness curve is maintained. Wang and Suo (1990) choose $\hat{L} = 100$ μm to define $\hat{\psi}$; their toughness curves $K_C(\hat{\psi})$ for epoxy/aluminum, epoxy/brass, epoxy/steel and epoxy/plexiglass pairs conform with the form in equation (5). Hutchinson (1989) has suggested an interfacial toughness function which depends on ψ and an "intrinsic" toughness or mode 1 toughness.

By phrasing the mode mixity in terms of $\hat{\phi}$ (or equivalently $\hat{M}$), the interface fracture toughness locus $\mathcal{G}_C(\hat{\phi})$, or equivalently $K_C(\hat{\phi})$, is a property of the material pair, i.e., it does not depend on specimen type and size. The equivalence of K_C and $\mathcal{G}_C$ follows from the relation $\mathcal{G} = C_m K^2$ where C_m is a material parameter involving only the elastic properties of the material pair (e.g., Malyshev and Salganik, 1965; Rice, 1988). Likewise, the applied *stress intensity vector* or the crack extension force $\mathbf{K}L^{i\varepsilon}$ can be phrased in terms of a magnitude $\mathcal{G}$ or equivalently K, and the phase angle $\hat{\phi}$. Then the condition for fracture is

$$\mathcal{G} = \mathcal{G}_C(\hat{\phi}), \text{ or equivalently, } K = K_C(\hat{\phi}), \quad (6)$$

where

$$\hat{\phi} = \phi + \varepsilon \ln(\hat{L}/L) \text{ and } \phi = \text{phase}\{\mathbf{K}L^{i\varepsilon}\}. \quad (7)$$

Here, $\hat{\phi}$ is the loading phase angle defined with respect to $\hat{L}$, the latter being the length used for recording the interfacial toughness locus $\mathcal{G}_C(\hat{\phi})$ of the material pair.

Solutions for several simple crack geometries which are in a form suitable for use with equations (6) and (7) and a procedure for extracting $\mathbf{K}$ from numerical solutions using path-independent integrals are discussed by Shih and Asaro (1988). A handbook containing solutions to a fair number of interface crack geometries is also available (Murakami, 1987).

2.2 Recent Results From the Nonlinear Theory. Several results have emerged from recent studies on the plasticity of bimaterial interface cracks (Shih and Asaro, 1988, 1989a,b). They observed that the small-scale yielding fields of an interface crack are members of a family parameterized by a plastic phase angle, ξ, defined by

$$\xi = \varphi + \varepsilon \ln\left(\frac{K}{\sigma_0}\right)^2 = \hat{\phi} + \varepsilon \ln\left(\frac{K^2}{\sigma_0^2 \hat{L}}\right) = \phi + \varepsilon \ln\left(\frac{K^2}{\sigma_0^2 L}\right) \quad (8)$$

where σ_0 is the yield strength of the weaker material. A similar expression for a phase angle, ζ_0, which differs inconsequentially from ξ by a constant involving ε has been obtained by Zywicz and Parks (1989a,b). Furthermore the plastic zone size r_p, defined by the maximum radial extent from the tip to the elastic/plastic boundary, has the form

$$r_p = \Lambda(\xi)\left(\frac{K}{\sigma_0}\right)^2. \quad (9)$$

The dimensionless factor Λ increases from 0.15 to about 0.7 as $|\xi|$ increases from 0 to $\pi/2$ and is only weakly dependent on elastic and plastic properties of the pair of materials. ξ may be interpreted as the overall phase angle of the plastic zone, and so is analogous to ϕ, the overall phase of the elastic singular field (with respect to L).

The asymptotic fields of an interface crack for "opening" dominated load states bear some resemblance to the well-known HRR fields in homogeneous media (Hutchinson, 1968; Rice and Rosengren, 1968). Within the range, $-\pi/6 \le \xi \le \pi/6$, the fields near the tip can be organized in the form

$$\sigma_{ij} = \sigma_0\left(\frac{J}{\alpha\sigma_0\varepsilon_0 r}\right)^{1/(n+1)} h_{ij}(\theta, \tilde{r}; \xi, n) \quad (10)$$

where J is Rice's J-integral (1968), h_{ij} is a bounded function which is slowly varying with $\tilde{r}$ ($\equiv r/(J/\sigma_0)$), and the material parameters in equation (10) pertain to the weaker material. The variation of the phase of the interfacial tractions at $\theta = 0$ with distance within the plastic zone can be described by a local phase angle ξ_r defined in the manner adopted for the elastic fields as in equation (3*a*). We have explored this to some extent and simply note that for two representative material pairs and for load states within the range $-\pi/6 \le \xi \le \pi/6$,

$$|\xi_{r_2} - \xi_{r_1}| < C|\ln(r_2/r_1)| \quad (11)$$

where C is less than 0.01 when r_1 and r_2 are within the interval $10^{-9}r_p < r < 10^{-1}r_p$, and $|\partial h_{\theta\theta}(\theta = 0)/\partial \ln(r/r_p)| < 0.2$ (Shih and Asaro, 1989a). *Thus, the phase change with distance within*

Downloaded 03 May 2010 to 171.66.16.248. Redistribution subject to ASME license or copyright; see http://www.asme.org/terms/Terms_Use.cfm

the plastic zone is much weaker than that associated with the elastic field. In this respect, plasticity has mitigated the pathological feature of the linear elasticity solution.

A parameter analogous to $\hat{\phi}$ is the local plastic phase angle $\hat{\xi}$ evaluated at a distance $\hat{L}$ within the plastic zone. If $\hat{L}$ is taken to be comparable to the fracture process zone size, then $\hat{\xi}$ defined by

$$\hat{\xi} \overset{\text{def}}{=} \tan^{-1}\left[\frac{\sigma_{r\theta}(\theta=0)}{\sigma_{\theta\theta}(\theta=0)}\right]_{r=\hat{L}}, \tag{12}$$

parameterizes the load state or mode mixity of the tractions near the process zone. For example, the interfacial failure zone is typically some multiple of the reaction/interdiffusion layer. On the other hand, if the interfacial failure zone size scales with the finite strain zone of the surrounding bulk material then $\hat{L}$ should be of the order of the crack-tip opening displacement, δ_t. Our numerical studies show that the value of $\hat{\xi}$, is relatively insensitive to distance when evaluated within the interval $2 \le r/\delta_t \le 5$. Beyond the zone of finite strains, $\hat{\xi}$ evaluated from finite deformation solution differs little from that given by the small-strain solution.

Under conditions of contained yielding, or those leading to fully yielded behavior in the case of highly constrained geometries, the "opening" dominated fields continue to be adequately represented by the form (10) so that the fields are nearly scaled by the value of the J-integral. Under J-dominant conditions, a nonlinear fracture mechanics methodology can be couched along these lines:

$$J = J_C(\hat{\xi}) \tag{13}$$

where

$$\hat{\xi} = F(\text{material pair, geometry, load}) \tag{14}$$

Here, F is a dimensionless function of the remote load state and of dimensionless material combinations and groups of geometric parameters. The value of J and $\hat{\xi}$ must be evaluated at each load level, for the crack geometry and material pair under consideration.

3 Numerical Procedure and Material Relations

3.1 Numerical Procedure. The finite element calculations used the semi-implicit integration scheme developed by Moran et al. (1990). In this scheme, the deformation gradient is taken to be multiplicably decomposable into elastic and plastic parts, via

$$\mathbf{F} = \partial \mathbf{x}/\partial \mathbf{X} = \mathbf{F}^* \cdot \mathbf{F}^p, \tag{15}$$

where $\mathbf{x}$ is the current position of a material particle and $\mathbf{X}$ is its position in a reference state. Here, $\mathbf{F}^p$ is the deformation *solely* due to plastic flow and $\mathbf{F}^*$ is the remaining contribution to $\mathbf{F}$. As described by Moran et al. (1990), stresses are computed directly from a hyperelastic potential, phrased in the so-called intermediate configuration obtained by applying the mapping $\mathbf{F}^p$ to the reference (or undeformed) state. Specifically, an isotropic Neo-Hookean elastic response is assumed wherein

$$\mathbf{S}^* = \lambda \log(F^*)\mathbf{C}^{*-1} + \mu(\mathbf{I} - \mathbf{C}^{*-1}). \tag{16}$$

In equation (16), $\mathbf{S}^*$ is the second Piola-Kirchhoff stress on the intermediate configuration defined in terms of the Kirchhoff stress, τ, as $\mathbf{S}^* = \mathbf{F}^{*-1} \cdot \tau \cdot \mathbf{F}^{*-T}$, $F^* \equiv \det \mathbf{F}^*$, $\mathbf{C}^* = \mathbf{F}^{*T} \cdot \mathbf{F}^*$, $\mathbf{I}$ is the identity tensor and λ and μ are the Lamé constants.

Plastic deformation is described by J_2 flow theory wherein the rate of plastic deformation $\mathbf{D}^{*p} = sym\{\dot{\mathbf{F}}^p \cdot \mathbf{F}^{p-1}\}$ phrased also on the intermediate configuration, is given by

$$\mathbf{D}^{*p} = \dot{\bar{\epsilon}}^p \, \text{sym}\{\mathbf{R}^*\}. \tag{17}$$

Here $\mathbf{R}^*$ is the current direction of the plastic deformation rate, which in J_2 flow theory is given by

$$\mathbf{R}^* = \frac{3}{2\bar{\sigma}} \mathbf{C}^* \cdot \mathbf{S}^{*\prime} \cdot \mathbf{C}^*, \tag{18}$$

$\dot{\bar{\epsilon}}^p$ is the effective plastic strain rate given by a flow law with strain hardening, and $\mathbf{S}^{*\prime}$ is the deviatoric part of $\mathbf{S}^*$ defined by $\mathbf{S}^{*\prime} = \mathbf{S}^* - 1/3(\mathbf{S}^* : \mathbf{C}^*)\mathbf{C}^{*-1}$. The effective stress, $\bar{\sigma}$, is defined as

$$\bar{\sigma}^2 = \frac{3}{2}(\mathbf{S}^{*\prime} \cdot \mathbf{C}^*) : (\mathbf{S}^{*\prime} \cdot \mathbf{C}^*). \tag{19}$$

In the present work, power-law material strain-rate sensitivity and strain hardening are assumed in the form,

$$\begin{aligned} \dot{\bar{\epsilon}}^p &= \dot{\epsilon}_o \left[\left(\frac{\bar{\sigma}}{H(\bar{\epsilon}^p)} \right)^{1/m} - 1 \right], \quad \bar{\sigma} \ge H(\bar{\epsilon}^p) \\ \dot{\bar{\epsilon}}^p &= 0, \qquad\qquad\qquad\quad \bar{\sigma} \le H(\bar{\epsilon}^p) \end{aligned} \tag{20}$$

where

$$H(\bar{\epsilon}^p) = \sigma_o \left(1 + \frac{\bar{\epsilon}^p}{\epsilon_p} \right)^{1/n} \tag{21}$$

is a hardening function with exponent n, σ_0 is a reference yield stress, ϵ_0 and $\dot{\epsilon}_0$ are reference strain and strain rates, respectively, and m is the strain-rate sensitivity exponent. Our present study is restricted to rate-independent material behavior and test calculations with several crack problems show that rate-independent response is reproduced by using m of 0.005. The rate of loading is such that the maximum strain rates is of the order of $\dot{\epsilon}_o$ so that no overstress is generated by rate dependence.

3.2 Two Material Pairs. The first material pair consists of an elastic-plastic material bonded to an elastic substrate. The material in the upper half-plane $y > 0$ (see Fig. 1) is elastic plastic. The Young's modulus is E_1, Poisson's ratio $\nu_1 = 0.33$, yield strength $\sigma_0 = E_1/300$, strain-hardening exponent $n = 10$ and $m = 0.005$. The material in the lower half-plane $y < 0$ is elastic with moduli $E_2 = 5E_1$ and $\nu_2 = 0.2$. These properties are typical of a low strength material (aluminum, copper) bonded to a ceramic material.

The two materials of the second material pair are elastic plastic. Their elastic properties are identical; the Young's modulus is E and Poisson's ratio is 0.3. Material 1 has yield strength $\sigma_{01} = E/300$ and hardening exponent $n_1 = 5$. Material 2 has yield strength $\sigma_{02} = E/150$ and hardening exponent $n_2 = 10$. Both materials are taken to be strain-rate insensitive, with $m = 0.005$. These properties are typical of a high strength steel bonded to a lower strength steel.

In our terminology, the lower yield-strength material is referred to as the weaker material and the lower strain-hardening material is called the plastically more compliant material. Material parameters without subscripts refer to those of material 1.

4 Results for Small-Scale Yielding

In the small-scale yielding formulation, the actual crack problem is replaced by a semi-infinite crack in an infinite bimaterial media with the asymptotic boundary condition that at large r the field approaches that given by equation (1) for the material pair considered. All the results presented in this section are for an elastic-plastic material bonded to an elastic substrate; the properties of the material pair are given in Section 3.2.

The value of the J-integral is extracted from the numerical fields by using the domain integral method (Moran and Shih, 1987). Under small-scale yielding $J = C_m K^2$, and J values obtained for domains within the plastic zone agreed with this relation to an accuracy of better than one percent; only when the domains are wholly within the finite strain zone do the

Downloaded 03 May 2010 to 171.66.16.248. Redistribution subject to ASME license or copyright; see http://www.asme.org/terms/Terms_Use.cfm

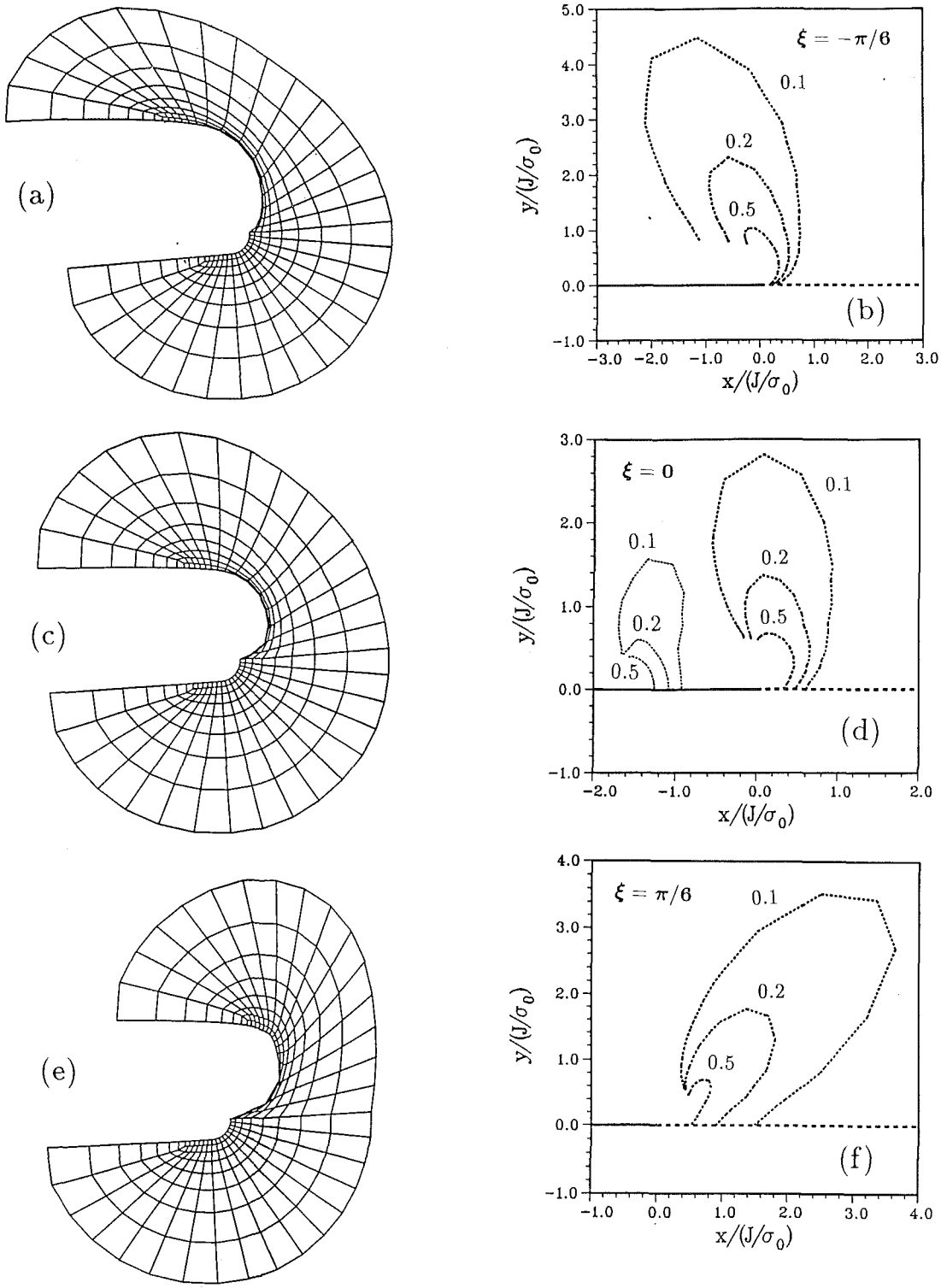

Fig. 2 *(a), (c), and (e)* crack opening profiles for load states $\xi = -\pi/6$, 0 and $\pi/6$ at identical J value; *(b), (d)* and *(f)* contours of $\bar{\epsilon}^p = 0.1$, 0.2 and 0.5 plotted on the deformed geometry; contours for the homogeneous material subject to mode I loading are also shown in *(d)*.

calculated J values deviate substantially from the prescribed remote value.

4.1 Crack Opening Displacement. Crack opening profiles, and plastic strain contours, for the three cases $\xi = -\pi/6$, 0, $\pi/6$ at the identical remote load level are shown in Fig. 2. The notches have opened to more than five times the initial notch width, δ_0, and the profiles and deformation of the surrounding regions are drawn to the same scale. These small-scale yielding solutions were obtained by applying the tractions given by equation (1) at the rate $\dot{K} = \dot{\epsilon}_o E_1 \sqrt{\delta_0}$ at the remote boundary of radial distance R_b. The maximum spatial extent of the plastic zone r_p is less than about a third of R_b. It is evident that moderate amounts of shear parallel to the interface increases the rate of crack-tip opening, and that negative shear has a stronger effect (or positive shear if the materials are interchanged).

Downloaded 03 May 2010 to 171.66.16.248. Redistribution subject to ASME license or copyright; see http://www.asme.org/terms/Terms_Use.cfm

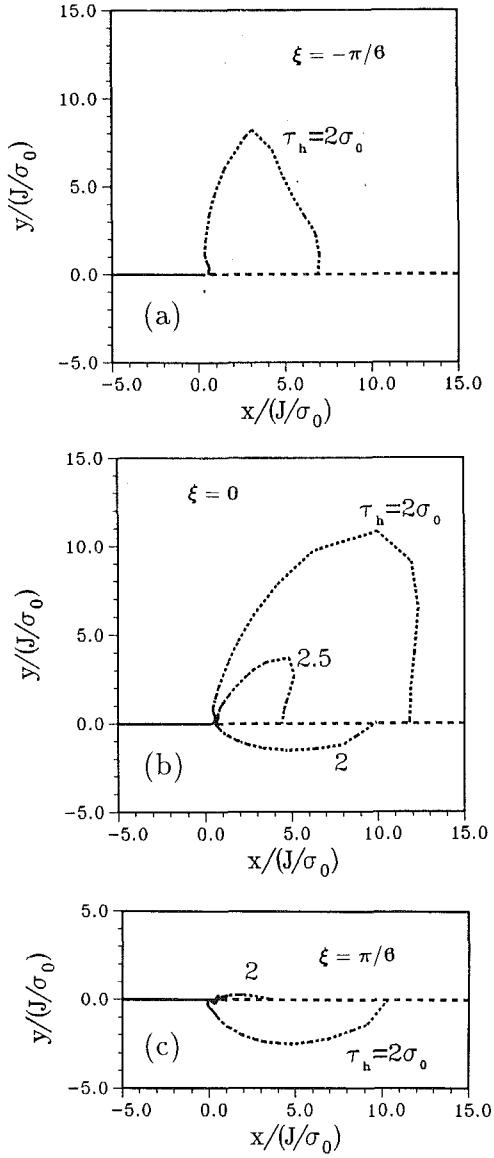

Fig. 3 Hydrostatic stress contours, $\tau_h = 2\sigma_0$ and $2.5\sigma_0$, for load states $\xi = -\pi/6$, 0 and $\pi/6$

In previous studies, a relationship of the form $\delta_t = d(\alpha\epsilon_0, n)J/\sigma_0$ has been shown for homogeneous media in which the normal crack face opening varies with distance like $r^{1/(n+1)}$ (Shih, 1981). The material parameters α, ϵ_0, σ_0, and n are those defined by the Ramberg-Osgood stress-strain relation which takes the form $\sigma/\sigma_0 = \epsilon/\epsilon_0 + \alpha(\sigma/\sigma_0)^n$ in uniaxial tension; δ_t is the opening separation where the 45 deg lines, drawn backwards from the crack tip intercept the deformed crack faces. For $n = 10$ and $\sigma_0/E = 1/300$, d has the value 0.52.

In the present studies, the full-field numerical solutions for "opening" dominated load states, $-\pi/6 \le \xi \le \pi/6$, are nearly separable and additionally the normal crack-face opening varies with distance nearly like $r^{1/(n+1)}$. These features of the interface crack fields suggest the following relation between δ_t and J,

$$\delta_t = d(\alpha\epsilon_0, n, \xi)\frac{J}{\sigma_0} \tag{22}$$

where ξ is the phase angle of the plastic fields. Applying the 45 deg procedure to the notch openings in Fig. 2, we obtain $d = 0.61$, 0.56, 0.67 for $\xi = -\pi/6$, 0, $\pi/6$, respectively. If J is taken as the crack-tip load parameter, these values of d simply mean that crack-tip blunting in a bimaterial system is more severe than that encountered in homogeneous medium. Direct comparisons also show that the openings obtained by the finite deformation analyses can be as much as 30 percent larger than those estimated by small-strain analyses.

Contours of effective plastic strain (plotted on the deformed geometry) for $\bar{\epsilon}^p = 0.1$, 0.2, and 0.5 for load states $\xi = -\pi/6$, 0, $\pi/6$ are shown in Figs. 2(*b*), 2(*d*), and 2(*f*). The relative extent of the plastic strains at the crack tip are broadly consistent with the amounts of crack-tip opening shown in Figs. 2(*a*), 2(*c*), and 2(*e*). As with the crack-tip opening, here the spatial extent of the zone of substantial plasticity is larger than it would be for a crack in a homogeneous medium loaded either with comparable remote stresses or to equivalent values of the J integral. Also shown in Fig. 2(*d*) are contours for $\bar{\epsilon}^p = 0.1$, 0.2, and 0.5 contours (drawn to the same scale) for a crack in the corresponding homogeneous medium (medium with properties identical to material 1), loaded to the same value of J. It can be seen that the spatial extent of the latter plastic strains is significantly less than those for the interface crack.

Figure 3 shows the hydrostatic stress (mean Kirchhoff stress) contours of $\tau_h = 2\sigma_0$ for the three load states, $\xi = -\pi/6$, 0 and $\pi/6$. It can be seen that the highest hydrostatic stress states are encountered for load state $\xi = 0$. Remarkably, it is the weaker material that sustains the higher hydrostatic stresses—recall that the weaker material also suffers large plastic strains. Such stress and strain states promote processes of ductile fracture (void nucleation, growth, and coalescence) in the weaker strength material, assuming that the interfacial toughness and the toughness of material 1 and 2 are comparable. These observations are even more applicable for load state $\xi = -\pi/6$, where it can be seen that the zone of high hydrostatic stresses is confined to the weaker strength material. A different picture emerges for load state $\xi = \pi/6$ where the high hydrostatic stresses develop in the elastic substrate. Under such load states, it is most likely that cracks will propagate in the elastic material.

4.2 Tensile Load State: $\xi \approx 0$. The radial variation of the Kirchhoff stresses, τ_{ij}, and the equivalent plastic strain, $\bar{\epsilon}^p$, near the bond line for predominantly tensile loading at the interface, i.e., $\xi \approx 0$ is shown in Fig. 4. The radial distance defined in the initial (undeformed) configuration has been normalized by J/σ_0, and under small-scale yielding, J is proportional to K^2. The solution in Fig. 4(*a*) corresponds to the state in which the notch tip has opened to approximately five times the initial notch width, δ_0. We have observed that when the notch openings δ_t become larger than about $3\delta_0$, the stress and plastic strain distributions, plotted in the manner shown, change only slightly; in other words, the fields are almost self-similar. As noted in the previous section, $\delta_t \approx 0.56J/\sigma_0$, so that the range of the horizontal axis is effectively $0 \le r/\delta_t \le 9$. Plotted in this form, the stress and strain distribution in Fig. 4(*a*) is fairly representative of the fields of material systems in which the weaker material has properties similar to Material 1. Although not shown here in the interests of space, we note that the fields that develop for a crack on a rigid substrate are very similar to those shown in Fig. 4(*a*). This particular correspondence between the results for cracks on rigid and elastic substrates was noted earlier by Shih and Asaro (1988, 1989a) and can provide a potentially helpful simplification for modeling. Numerical studies of cracks on rigid substrates require considerably smaller numerical models and are thereby computationally more tractable than those that require modeling of the elastic substrate.

In the Figs. 4(*b*) and 4(*d*) the hoop stresses along $\theta = \pi/40$, $\pi/4$ in the bimaterial system and the homogeneous material are compared to the small-strain mode I HRR stresses which are indicated in the plots by circles and triangles. In both cases, the actual fields in the small strain annulus, $1.0 < r/(J/\sigma_0) < 3.0$, are accurately described by the HRR fields for $n = 10$ and

Downloaded 03 May 2010 to 171.66.16.248. Redistribution subject to ASME license or copyright; see http://www.asme.org/terms/Terms_Use.cfm

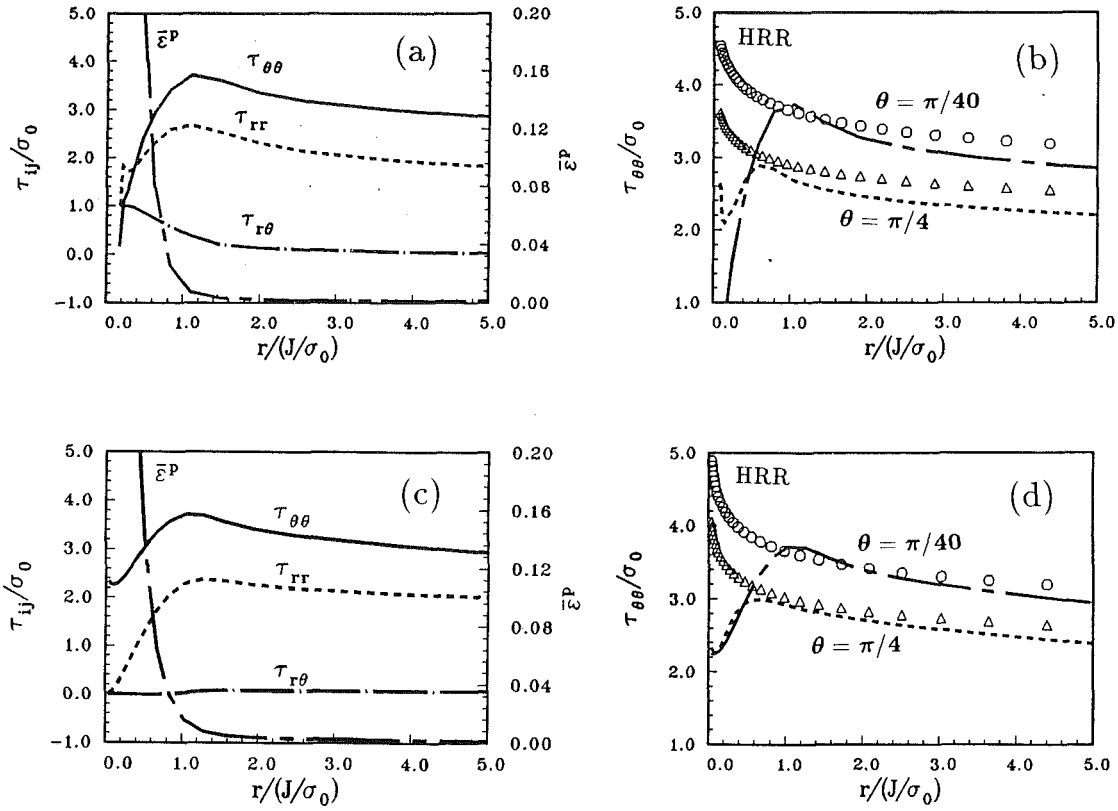

Fig. 4 (*a*) Stress and strain distributions along $\theta = \pi/40$ in material 1 for $\xi = 0$; (*b*) comparison with mode I HRR stresses along $\theta = \pi/40$ and $\pi/4$; (*c*) stress and strain distributions along $\theta = \pi/40$ in the corresponding homogeneous material caused by mode I loading; (*d*) comparison with mode I HRR stresses along $\theta = \pi/40$ and $\pi/4$

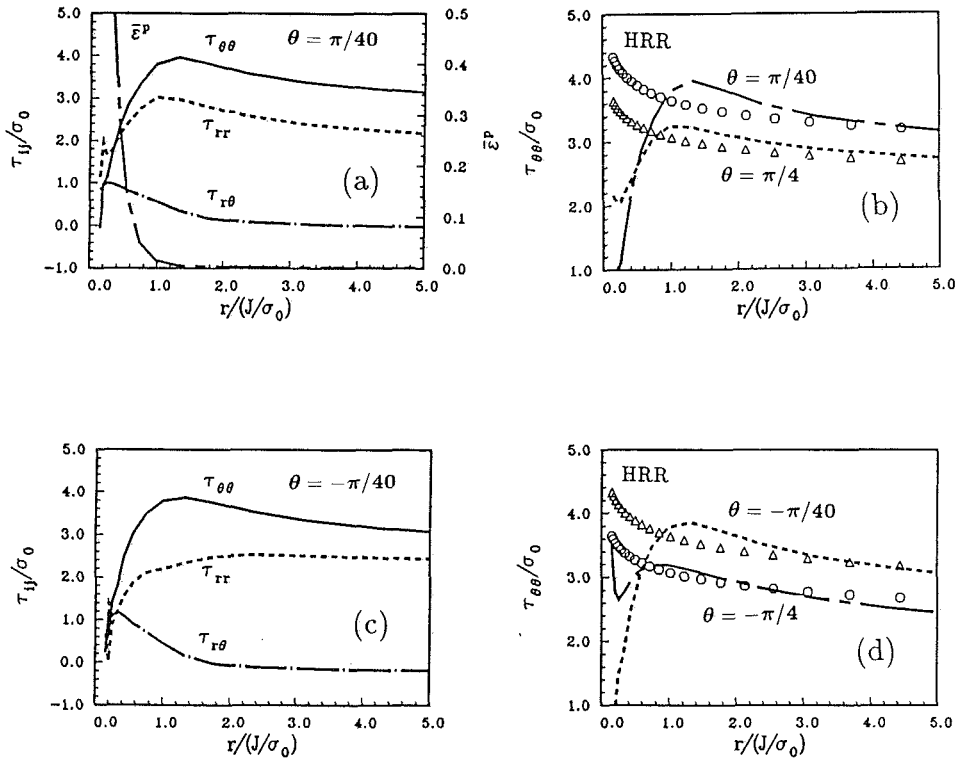

Fig. 5 (*a*) stress and strain distributions along $\theta = \pi/40$ in material 1 for $\xi = -\pi/30$; (*b*) comparison with mode I HRR stresses along $\theta = \pi/40$ and $\pi/4$; (*c*) stress and strain distributions along $\theta = -\pi/40$ in material 2 for $\xi = -\pi/30$; (*d*) comparison with mode I HRR stresses along $\theta = -\pi/40$ and $-\pi/4$

Downloaded 03 May 2010 to 171.66.16.248. Redistribution subject to ASME license or copyright; see http://www.asme.org/terms/Terms_Use.cfm

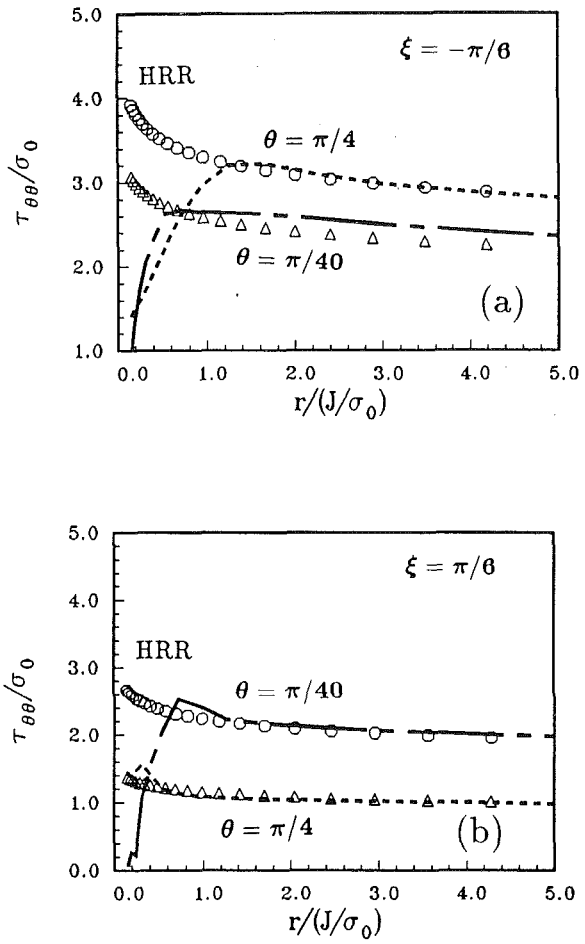

Fig. 6 Comparison of hoop stresses for load states $\xi = -\pi/6$ and $\pi/6$ with HRR stresses for mixities $M^p = -0.05$ and 0.22, respectively ($M^p = -0.95$ and 0.78 in Shih, 1974)

$M^p = 0$—the mixity parameter M^p being defined according to equation (3*a*). (Note that the present mixity differs from the earlier definition given by Shih (1974) where $M^p = 1$ corresponds to the Mode I HRR distribution.) It may also be noted that at a radius equal to five percent of the maximum plastic zone size, the angular variation of the fields determined by the finite deformation analysis is similar to the small-strain solutions given by Shih and Asaro (1989a) for the $\xi \approx 0$ case.

4.3 Slightly Asymmetric Load States. Small departures from the near-tip tensile state deserve attention because they can induce very high stresses near the tip. Such load states are typically caused by small amounts of remote shear superimposed on remote tension normal to the interface. For load state $\xi \approx -\pi/30$, the stress distribution along $\theta = \pi/40$ in material 1, and along $\theta = -\pi/40$ in the elastic substrate, are shown in Figs. 5(*a*) and 5(*c*). A comparison of the hoop stresses in material 1 and in material 2 with the corresponding Mode I HRR stresses is shown in Figs. 5(*b*) and (*d*). It can be seen that within the distances $1 < r/(J/\sigma_0) < 3$, the actual stresses in both materials can be as much as 15 percent higher than those given by the mode I HRR singularity. (We should point out the highest stress levels in a homogeneous medium are those associated with mode I HRR fields.) The high hydrostatic stresses associated with slightly asymmetric load states are detrimental to interfacial fracture toughness. Such effects have also been observed by Parks and Zywicz (1989).

We must point out that though $\pm\xi$ mode mixity of the near-tip fields implies similar ratios of the interfacial tractions, their magnitudes may differ significantly. In the present examples, facial traction magnitudes for $-\pi/30 < \xi < 0$ are larger than those for $0 < \xi < \pi/30$.

4.4 Mixed Mode Loading: $-\pi/6 \le \xi \le \pi/6$. In Parts I and II the similarities between crack-tip fields of interface cracks and mixed-mode HRR fields were discussed. Such similarities persist when finite deformation effects are accounted for. To make this point, Fig. 6 provides a comparison of the hoop stress in the weaker material with the mixed-mode small-strain HRR stress for the corresponding homogeneous material of identical material properties. The interface crack-tip fields for $\xi = -\pi/6$ and $\pi/6$ are compared with the mixed-mode HRR fields of mixities $M^p = -0.05$ and 0.22, respectively (corresponding to $M^p = -0.95$ and 0.78 in Shih (1974) and Symington et al. (1988)). At radial distances beyond $r \approx 2\delta_t$, the actual fields are in good agreement with the HRR fields. The deformed crack face profiles and effective plastic strain contours for those two load states are shown in Fig. 2.

Figure 7 illustrates the angular distribution of stresses for three load states, $\xi = -\pi/6$, 0, and $\pi/6$. The angular variation of the stresses in Figs. 7(*a*), 7(*c*), and 7(*e*) are plotted at $r \approx \delta_t$, which is within the zone where the field is influenced by finite strain effects. The fields in Figs. 7(*b*), 7(*d*), and 7(*f*) are plotted $r \approx 2.5\delta_t$, which is just outside the finite strain zone. Our observation with regard to the size of the finite strain zone is based on Figs. 4 and 6 which show that at radial distances beyond about $2\delta_t$, the field is essentially a small strain field. This observation is also supported by the good agreement between the angular distribution of the stresses in Figs. 7(*b*), 7(*d*), and 7(*f*) and those in Figs. 9(*b*), 9(*d*), and 9(*f*) of Shih and Asaro (1989a) which are based on small-strain solutions for similar mixed-mode load states. The latter fields are normalized differently, but when renormalized using the present form, the magnitudes are also in agreement.

A noteworthy feature of these small-strain stress fields is that the peak stresses for all mixed-mode conditions are roughly comparable, but the angular position of the maximum stress is affected by the mixity, ξ (see Figs. 2(*b*), 2(*d*), and 2(*f*)). In particular, for $\xi = \pi/6$ the peak stress develops at $\theta = -70$ deg (in material 2), whereas the peak stresses occur in material 1 in the other two cases. Within the finite strain zone the magnitudes of the peak stresses are more strongly influenced by mode mixity. For example, when $\xi = \pi/6$ the peak level of $\tau_{\theta\theta}$ is nearly 50 percent larger than it is when $\xi = -\pi/6$ and 40 percent larger when $\xi = 0$.

5 Contained and Fully Yielded Behavior Under Remote Tension

Small-scale yielding is defined such that the plastic zone dimensions are well embedded within the region where the asymptotic elastic field dominates the total stress field; in practical cases this is so if the maximum extent of the plastic zone is less than two percent of the crack length if this is the smallest dimension of the crack geometry (see, e.g., Hutchinson, (1983) for a general discussion pertaining to homogeneous media).

The development of near-tip fields under contained yielding and fully plastic conditions have been studied in the context of an infinite row of collinear cracks on a bimaterial interface in an earlier work based on a small-strain J_2 deformation plasticity theory (Shih and Asaro, 1989b). In that study, the lower region, $y < 0$, was taken to be rigid.

The material system being studied here is identical to that considered in Section 4, namely an elastic/plastic material bonded to an elastic substrate. The crack-length-to-ligament ratio is 1/3, and the vertical boundaries, $x = -a$, $x = b$, are symmetry boundaries which are allowed to displace uniformly but must remain vertical. The normal traction applied to the vertical boundaries of the elastic (stronger) substrate is equal to one third of the normal traction applied to the horizontal

Downloaded 03 May 2010 to 171.66.16.248. Redistribution subject to ASME license or copyright; see http://www.asme.org/terms/Terms_Use.cfm

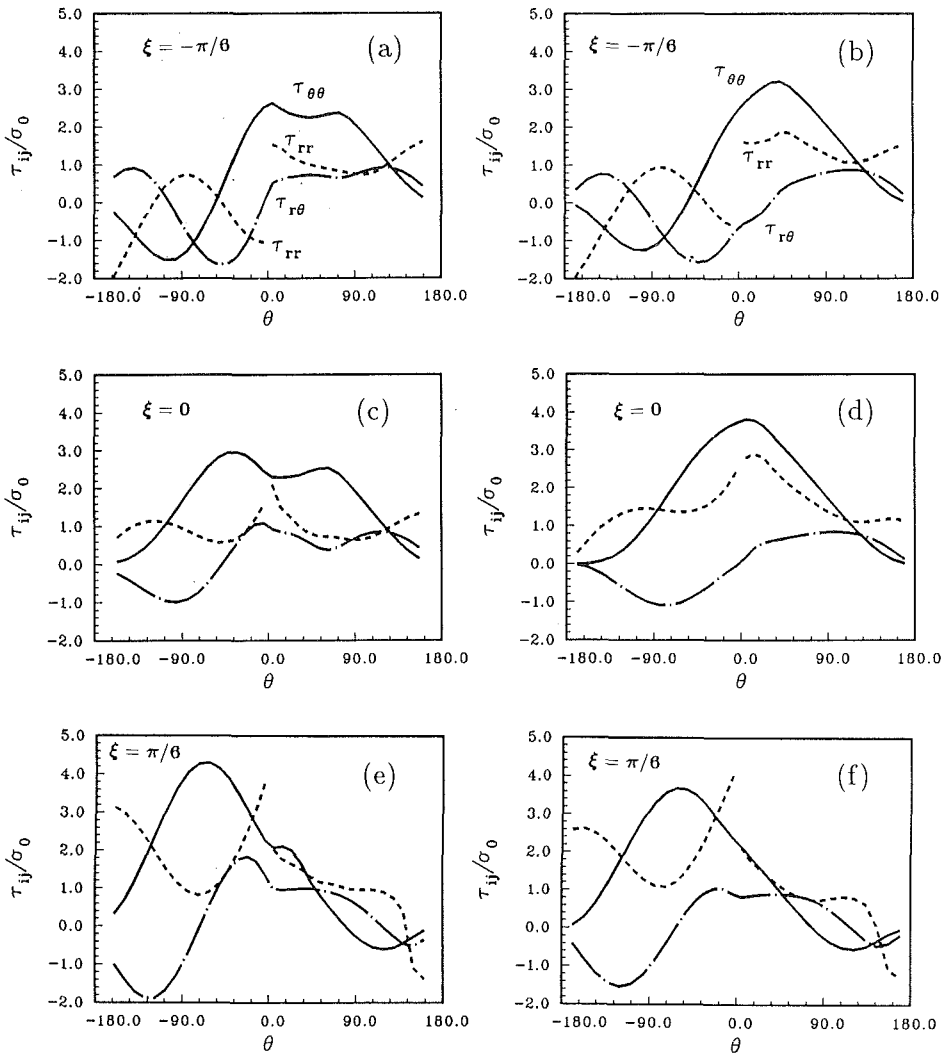

Fig. 7 *(a), (c), and (e)* **angular variation of stresses in elastic substrate (-180 deg $\le \theta \le 0$ deg) and in elastic-plastic material (0 deg $\le \theta \le 180$ deg) at $r \approx \delta_t$ for load states $\xi = -\pi/6$, 0 and $\pi/6$; *(b), (d), and (f)* angular variation of stresses at $r \approx 2.5\delta_t$**

boundaries $y = \pm h$, where $h = 3(a+b)$. The normal traction on the vertical boundaries of material 1 is determined by the condition that the boundary $x = b$ remains vertical. The geometry is depicted in Fig. 1(*a*).

Figure 8 shows the growth of plastic and high hydrostatic stress zones for remote stress levels producing contained and fully yielded states. In the context of the present geometry, fully yielded conditions correspond to plastic zones that spread across the entire ligament. The equivalent plastic strain contours for $\bar{\epsilon}^p = 0.001$ for three remote stress levels of $\sigma^\infty/\sigma_0 = 1.0$, 1.3, and 1.6 are shown in Fig. 8(*a*). Finite strain effects are minimal in the plastic zone development as may be appreciated by comparing these contours with those presented by Shih and Asaro (1989b). In particular, at a remote stress of $\sigma^\infty/\sigma_0 = 1.6$, the plastic zone has spread across the entire ligament in agreement with the small strain results shown in Fig. 4(*c*) of Shih and Asaro (1989b) for the nearly identical crack geometry.

An interesting development is shown in Figs. 8(*b*) and 8(*c*). Here the zone, where the hydrostatic stress exceeds σ_0, spreads rapidly across the ligament of material 1 as the remote load increases, while that in the elastic substrate remains relatively small. The rapid growth of the high hydrostatic zone, $\tau > 2\sigma_0$, within material 1 is shown in Fig. 8(*c*). Note the absence of high hydrostatic stresses in the elastic substrate. The phenomenology of this is quite striking as is evident by the comparison with Fig. 3(*b*) which gives the hydrostatic stress contours under small-scale yielding. In the latter case a small zone of high hydrostatic stress does develop in the elastic material. The rapid growth of the high hydrostatic stress zone in the weaker material as large-scale plasticity takes hold is peculiar to bimaterial pairs where significant mismatch in strengths occurs. By contrast, the hydrostatic stresses in homogeneous media decrease as fully yielded conditions are approached.

Additional insight into this *transitional* behavior can be gained by examining the behavior of the radial component of stress as a function of remote stress level, or as the plasticity extends beyond the small-scale yielding regime to contained and fully yielded state. Figures 9(*a*) and 9(*c*) show distribution of the hoop stress within material 1 and material 2. It can be seen that the magnitude of the hoop stresses near the interface changes only slightly as the remote load increases. The radial stress in material 1 behaves in much the same way—see Fig. 9(*b*). By contrast, Fig. 9(*d*) shows that the radial stress within the elastic substrate undergoes a rapid reduction in magnitude as the extent of plasticity progresses beyond that corresponding to small-scale yielding. This very pronounced stress redistribution gives rise to the effects observed in Figs. 8(*b*) and 8(*c*). In this regard, it deserves mention that the hydrostatic stresses that develop near the tip within the weaker strength material are higher than those that develop for cracks in the corre-

Downloaded 03 May 2010 to 171.66.16.248. Redistribution subject to ASME license or copyright; see http://www.asme.org/terms/Terms_Use.cfm

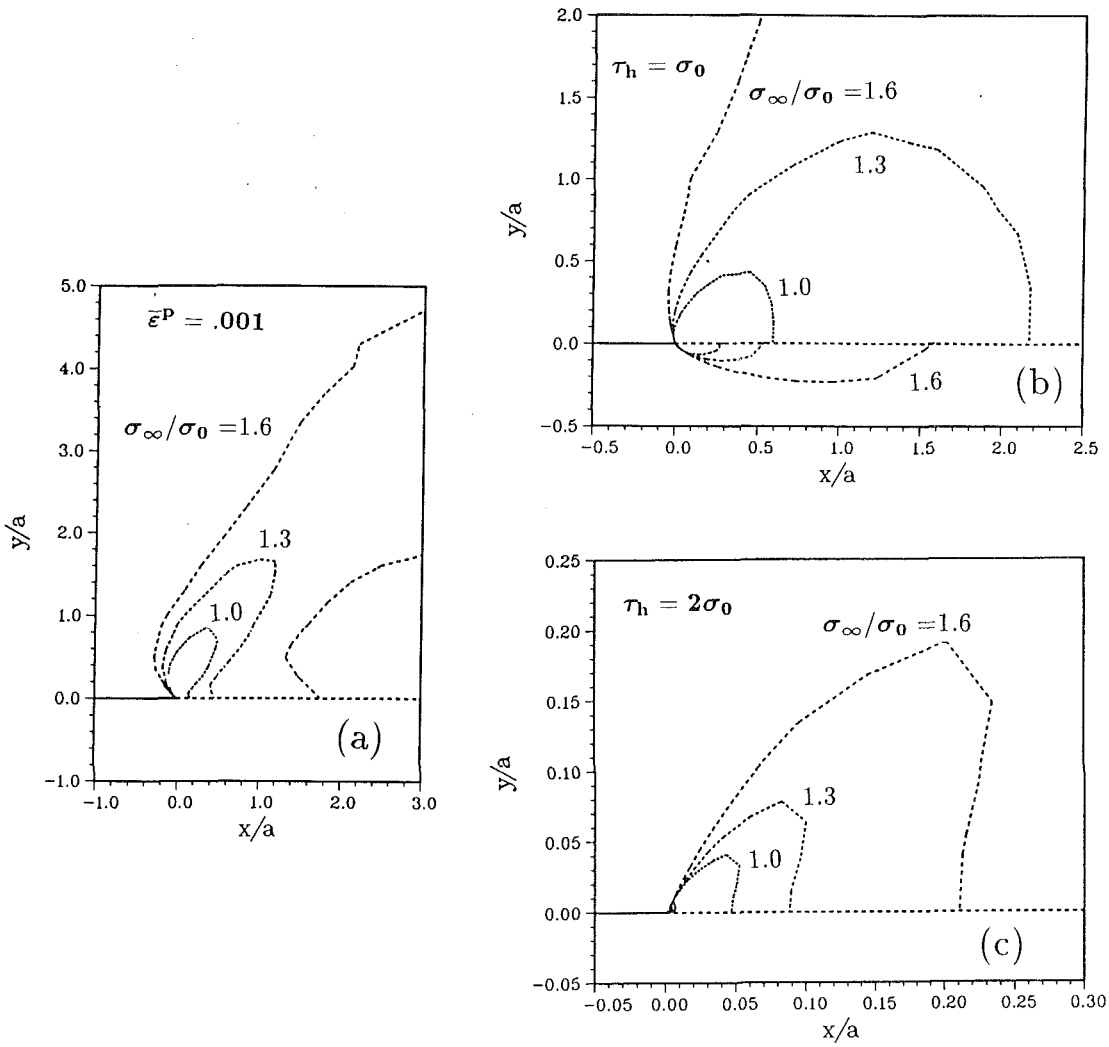

Fig. 8 (*a*) plastic zones at $\sigma^\infty/\sigma_0 = 1.0$, 1.3, and 1.6; (*b*) contours of moderate hydrostatic stress ($\tau_h = \sigma_0$) at same load levels; (*c*) contours of high hydrostatic stress ($\tau_h = 2\sigma_0$) at the same load levels

sponding homogeneous media at all levels of plastic deformation.

6 Two Elastic-Plastic Materials

Calculations were performed for a case of two elastic-plastic materials with the respective properties $\sigma_{02}/\sigma_{01} = 2$, $n_1 = 5$, and $n_2 = 10$; the properties are detailed in Section 3.2. The crack geometry and the applied loads are identical to that described in Section 5. In the following discussion the yield strength of the weaker material will be designated by σ_0. Note that material 1 is the higher strain-hardening material, while material 2 is a moderate hardening material.

Figure 10(*a*) shows contours of plastic strain, $\bar{\varepsilon}^p = 0.001$, for three load levels. Conditions pertaining to contained yielding are clearly established when $\sigma^\infty/\sigma_0 \geq 0.6$, and the fully yielded state is reached at remote stress levels of about $\sigma^\infty/\sigma_0 = 1.0$. At the latter load level, a small plastic zone is detected in the higher strength material. What is particularly interesting, though, is that the respective plastic zone sizes do not scale in any manner close to the ratio of the square of the respective material yield strengths, i.e., $r_{p1}/r_{p2} \neq$ constant $\times (\sigma_{02}/\sigma_{01})^2$. The plastic zone in the weaker strength material, at $\sigma^\infty/\sigma_0 = 1.0$ for example, has extended entirely across the ligament whereas that in the stronger material extends less than five percent of the ligament. A similar nonscalability under small-scale yielding conditions has also been noted by Shih and Asaro (1989a). The extent of the high hydrostatic stress zones, $\tau_h > 2\sigma_0$, for the same three load levels are shown in Fig. 10(*b*). The trends shown here are consistent with those shown in Fig. 8 in that high levels of hydrostatic stress prevail over larger distances in the weaker material.

Figure 11 illustrates the development of the stress fields near the interface as the extent of plastic deformation progresses from a contained to a fully yielded state. The stresses are normalized by the yield stress of the weaker material, σ_0 and distances by J/σ_0. In this case $\delta_t \approx 0.34 J/\sigma_0$ (consistent with δ_t being controlled by the lower strength but higher-hardening material) so that the horizontal axis spans the distances $0 < r/\delta_t < 15$. Apart from a slight drop in level, the distribution of hoop stresses in material 1 and 2 is essentially unchanged as the remote load increases. The peak stress achieved is about $5.5\sigma_0$ which is slightly higher than the peak stress of $5\sigma_0$ that develops in a high strain hardening, $n = 5$, homogeneous material (McMeeking, 1977; Moran et al., 1990). The stress distribution in Figs. 11(*a*) and 11(*c*) is consistent with the observation of Shih and Asaro (1989a) that over size scales somewhat larger than δ_t, the fields are governed by the strength of the weaker material and its strain-hardening exponent n, the latter being equal to 5 for the material pair considered. At large-scale yielding, the radial component of the stress behaves

Downloaded 03 May 2010 to 171.66.16.248. Redistribution subject to ASME license or copyright; see http://www.asme.org/terms/Terms_Use.cfm

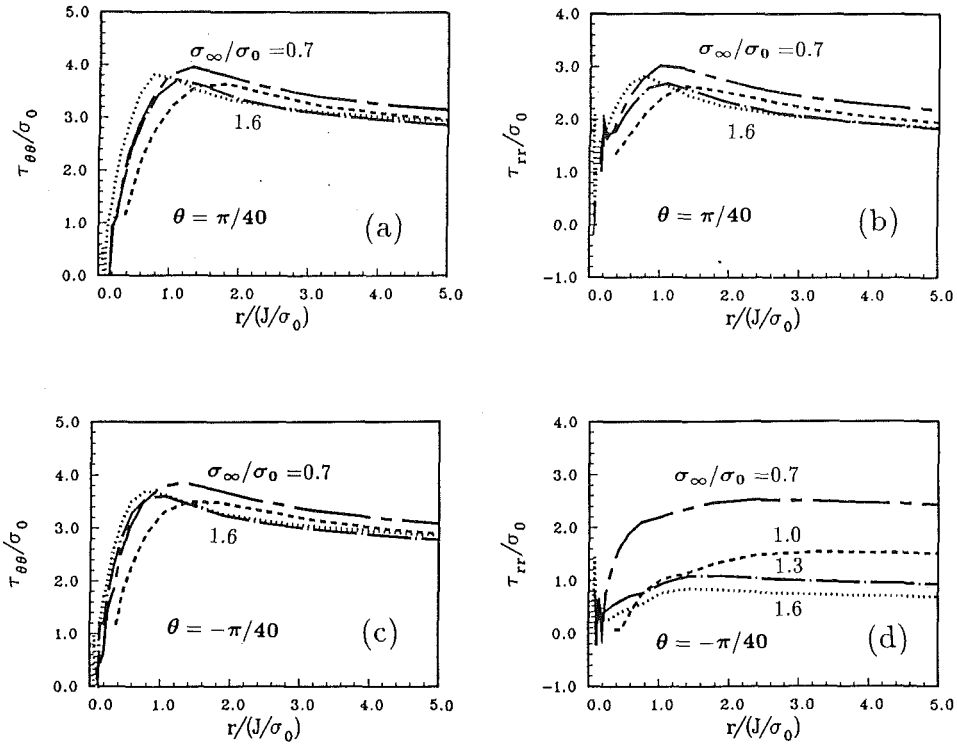

Fig. 9 (*a*) and (*b*) redistribution of $\tau_{\theta\theta}$ and τ_{rr} in elastic-plastic material along $\theta = \pi/40$ for remote loads $\sigma^\infty/\sigma_0 = 0.7$, 1.0, 1.3 and 1.6; (*c*) and (*d*) stress redistribution in elastic substrate along $\theta = -\pi/40$

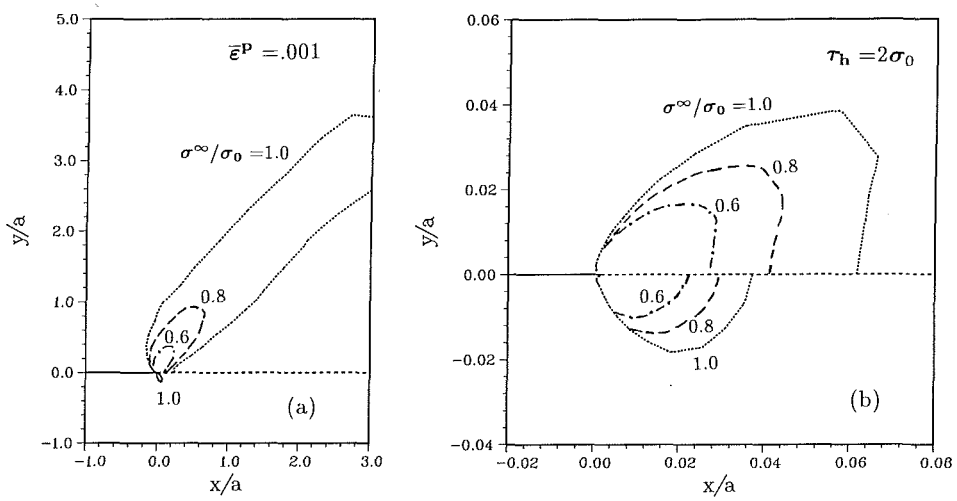

Fig. 10 (*a*) plastic zones at $\sigma^\infty/\sigma_0 = 0.6$, 0.8, and 1.0; (*b*) contours of high hydrostatic stress ($\tau_h = 2\sigma_0$) at the same load levels

quite differently. Figure 11(*b*) shows that the radial stress in material 1 decreases by a moderate amount as the remote load increases beyond the level associated with the beginning of a fully yielded state. The reduction is slightly more pronounced in the higher strength material—this is shown in Fig. 11(*d*). This behavior is less dramatic though consistent with what we have seen for the elastic-plastic material bonded to an elastic substrate which was shown in Fig. 9. The results in Fig. 11 indicate that the hydrostatic stress levels in both material 1 and 2 are reduced as the deformation progresses towards the fully yielded state.

The angular distribution of stresses for the two load levels $\sigma^\infty\sigma_0 = 0.6$ and 1.0, which correspond to contained and fully yielded conditions are shown in Fig. 12. Angular stress distribution at radial distances of about δ_t and $2.5\delta_t$ are shown in Figs. 12(*a*) and 12(*b*), respectively. The stress distribution in Fig. 12(*b*) and the magnitude of $\tau_{\theta\theta}$ are consistent with a *J*-dominated near-tip field. Note that in the finite strain zone $\tau_{\theta\theta}$ peaks at positions away from the interface. At $\sigma^\infty/\sigma_0 = 1.0$, which causes fully plastic response, stress redistribution occurs which results in stress levels which are lower than those given by a *J* dominated field for an $n = 5$ material as can be seen by comparing Fig. 12(*d*) with 12(*b*). In the finite strain zone, the stress distribution is slight (compare Fig. 12(*c*) with 12(*a*)).

7 Discussion and Conclusions

We have carried out plane-strain finite deformation studies

Downloaded 03 May 2010 to 171.66.16.248. Redistribution subject to ASME license or copyright; see http://www.asme.org/terms/Terms_Use.cfm

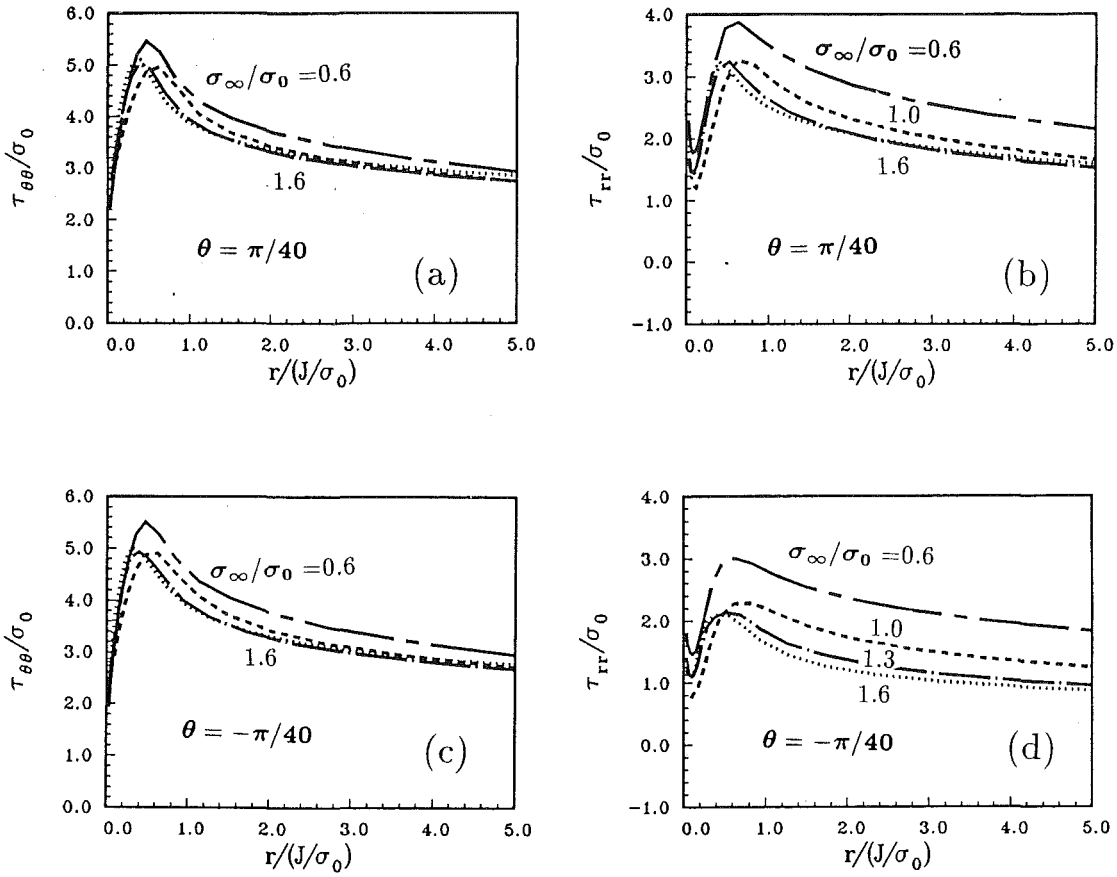

Fig. 11 (*a*) and (*b*) redistribution of $\tau_{\theta\theta}$ and τ_{rr} in lower strength material along $\theta = \pi/40$ for remote loads $\sigma^\infty/\sigma_0 = 0.6$, 1.0, 1.3, and 1.6; (*c*) and (*d*) stress redistribution in higher strength material along $\theta = -\pi/40$

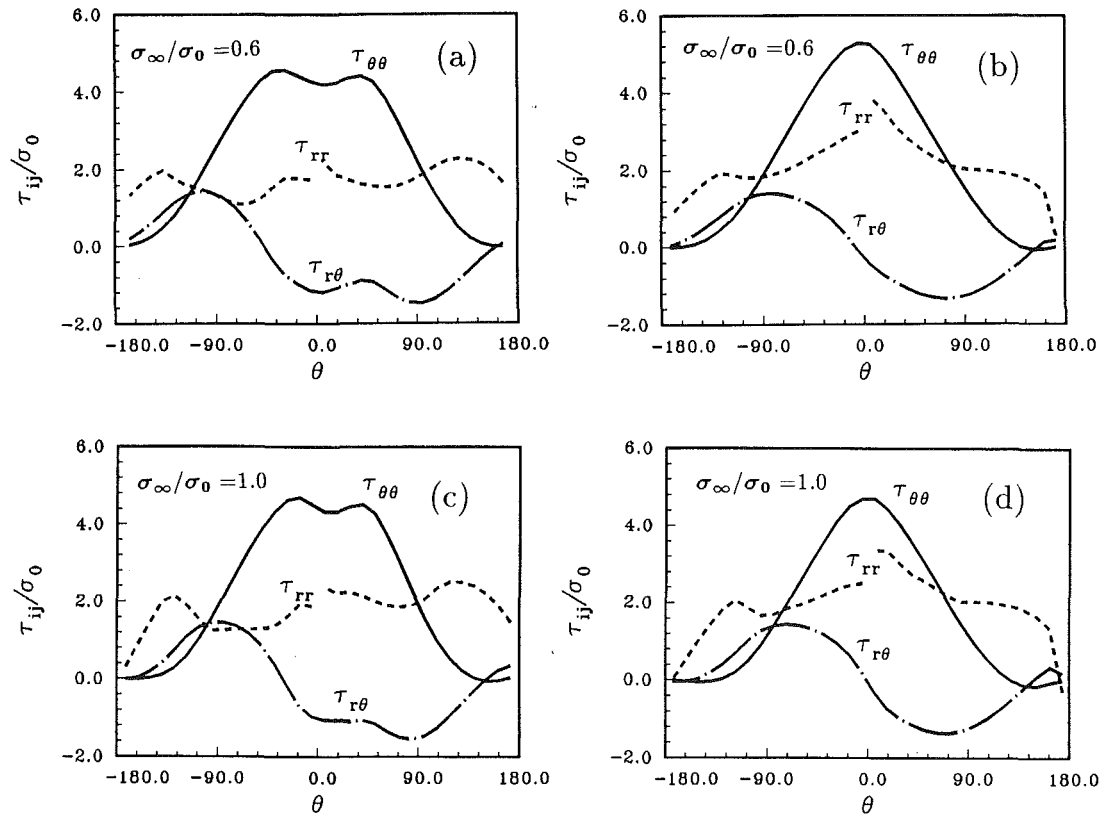

Fig. 12 (*a*) and (*b*) angular variation of stresses at $r \approx \delta_t$ and $2.5\delta_t$ for $\sigma^\infty = 0.6\sigma_0$; (*c*) and (*d*) angular variation of stresses at $r \approx \delta_t$ and $2.5\delta_t$ for $\sigma^\infty = \sigma_0$

Downloaded 03 May 2010 to 171.66.16.248. Redistribution subject to ASME license or copyright; see http://www.asme.org/terms/Terms_Use.cfm

under small-scale yielding and progressing into the contained and fully yielded state for tension dominated load states. The linear dimension of the elements near the tip is about 10^{-5} of the crack length and this is sufficiently small compared to all physical length scales which are of interest in our investigations. In every calculation that we did, there is not the slightest indication of crack faces coming into contact. Instead the crack faces open smoothly as the remote load increases. Indeed, the present studies provide support for our earlier observation that crack-tip plasticity strongly mitigates the pathological behavior, associated with $\varepsilon \neq 0$, at interface crack tips.

While the fields for the interface cracks are similar to those of homogeneous media, they are often more intense than those in homogeneous media when compared at comparable values of the J-integral. For example, openings that develop near the tip under load states, $-\pi/6 \leq \xi \leq \pi/6$, are larger than those that develop in similarly loaded homogeneous material. As a result the zone of finite strain is larger and the plastic strains within the finite strain zone are also larger those that develop in the corresponding homogeneous material.

Under conditions pertaining to small-scale and contained yielding, "opening" dominated load states produce fields within the weaker material which essentially converge onto those of a crack in the corresponding homogeneous material of identical material properties. Maximum normal stress of about $4\sigma_0$ is achieved at a distance of about $2\delta_t$ ahead of the tip in a low-hardening material ($n = 10$) while the peak stress equals $5.5\sigma_0$ in a high-hardening material ($n = 5$). Though these peak stress levels are slightly larger than those that develop in the corresponding homogeneous material, the distributions of the stresses are very similar over a significant fraction of the yielded ligament beyond the peak stress region (McMeeking, 1977; Moran et al., 1990). In other words, in regions beyond the finite strain zone ($r > 2\delta_t$), the fields in the weaker material mildly resemble the small-strain mixed-mode HRR fields of the corresponding homogeneous material. In the elastic substrate (or the higher strength material) the stress magnitudes are limited to those levels attained in the weaker material. Our results for load states, $-\pi/6 \leq \xi \leq \pi/6$, demonstrate the approximate scalability of the interface crack-tip fields by the J-integral.

It is important to note that though $\pm\xi$ mode mixity of the near-tip fields implies similar ratios of the interfacial tractions, their magnitudes may differ significantly. For example, the slightly asymmetric load state, $\xi \approx -\pi/40$, considered in Section 4.3 produce high hydrostatic stresses whose magnitude exceeds those associated with a purely tensile load state. However, the interfacial traction magnitudes associated with $\xi \approx \pi/40$ are much lower than those for $\xi \approx -\pi/40$. Indeed, we have exercised care in detailing such effects of $\pm\xi$ mode mixity on the near-tip stresses and deformation.

A surprising effect of plasticity is the rapid growth of high hydrostatic stress zone, $\tau_h > 2\sigma_0$, in the lower strength material as the plastic deformation progresses beyond small-scale yielding. This effect is most pronounced for tensile and slightly asymmetric load states. The zone of high stresses and the stress magnitude increase till the ligament is fully yielded at which point the stress begins to decrease slightly as the zone of high stress continues to expand. The hydrostatic stress in the stronger material behaves differently. At small-scale yielding the hydrostatic stress is only slightly lower than that in the weaker material. When the plastic zone is about a third of the ligament the hydrostatic stress has decreased by about 20 percent from the level reached under small-scale yielding. As the plastic deformation progresses further, the hydrostatic stress falls by as much as 40 percent, so that the hydrostatic stress never exceeds $2\sigma_0$ anywhere in the elastic substrate when fully yielded state is reached. The large reduction in hydrostatic stress in the elastic substrate (or the stronger material) and the continuous growth of the high stress zone within the weaker material, as large-scale plasticity takes hold, are particular to bimaterial pairs where there are large mismatch in strengths. Such highly stressed near-tip regions are particularly detrimental to interfacial toughness.

Acknowledgments

This investigation is supported by the Office of Naval Research through ONR Grant "Mechanics of Interface Cracks." The computations reported were performed on the CRAY-XMP at the Supercomputer Facility of the U.S. Naval Research Laboratory and on the Alliant Computer at the Computational Mechanics Facility of Brown University. The acquisition of the Alliant was made possible by grants from the U.S. National Science Foundation (Grant DMR-8714665), and the Office of Naval Research (Grant N00014-88-K-0119), DARPA, and matching funds from Brown University. Helpful comments by a reviewer are gratefully acknowledged.

References

Atkinson, C., 1989, "Cracks in Bimaterial Interface—An Overview," *Advances in Fracture Research, Proceedings of ICF7,* Vol. 4, pp. 3053–3061.

Cao, H. C., and Evans, A. G., 1989, "An Experimental Study of the Fracture Resistance of Bimaterial Interface," *Mechanics of Materials,* in press.

Cherepanov, G. P., 1979, *Mechanics of Brittle Fracture,* McGraw-Hill, New York.

England, A. H., 1965, "A Crack Between Dissimilar Media," ASME JOURNAL OF APPLIED MECHANICS, Vol. 32, pp. 400–402.

Hutchinson, J. W., 1968, "Singular Behavior at the End of a Tensile Crack in a Hardening Material," *Journal of the Mechanics and Physics of Solids,* Vol. 16, pp. 13–31.

Hutchinson, J. W., 1983, "Fundamentals of the Phenomenological Theory of Nonlinear Fracture Mechanics," ASME JOURNAL OF APPLIED MECHANICS, Vol. 50, pp. 1042–1051.

Hutchinson, J. W., 1990, "Mixed Mode Fracture Mechanics of Interfaces," *Metal-Ceramic Interfaces, Acta-Scripta Metallurgica Proceedings Series,* Vol. 4, pp. 295–306.

Kim, K. S., 1990, private communication.

Liechti, K. M., and Hanson, E. C., 1988, "Nonlinear Effects in Mixed-Mode Interfacial Delaminations," *International Journal of Fracture,* Vol. 36, pp. 199–217.

Liechti, K. M., and Chai, Y.-S., 1991, "Asymmetric Shielding in Interfacial Fracture Under In-Plane Shear," ASME JOURNAL OF APPLIED MECHANICS, in press.

Malyshev, B. M., and Salganik, R. L., 1965, "The Strength of Adhesive Joints using the Theory of Cracks," *International Journal of Fracture Mechanics,* Vol. 1, pp. 114–128.

McMeeking, R. M., 1977, "Finite Deformation Analysis of Crack-Tip Opening in Elastic-Plastic Materials and Implications for Fracture," *Journal of the Mechanics and Physics of Solids,* Vol. 25, pp. 357–381.

Moran, B., Ortiz, M., and Shih, C. F., 1990, "Formulation of Implicit Finite Elements Methods for Multiplicative Finite Deformation Plasticity," *International Journal for Numerical Methods in Engineering,* Vol. 29, pp. 483–514.

Moran, B., and Shih, C. F., 1987, "Crack Tip and Associated Domain Integrals from Momentum and Energy Balance," *Engineering Fracture Mechanics,* Vol. 27, pp. 615–642.

Murakami, Y., 1987, *Stress Intensity Factors Handbook,* Vols. 1 and 2, Pergamon Press, Oxford, U.K.

Pan, J., and Shih, C. F., 1990, "Elastic-Plastic Analysis of Combined Mode I and III Crack-Tip Fields under Small-Scale Yielding Conditions," *Journal of the Mechanics and Physics of Solids,* Vol. 38, pp. 161–181.

Parks, D. M., and Zywicz, E., 1989, "Elastic/Perfectly-Plastic Small Scale Yielding at Bi-Material Interfaces," *Advances in Fracture Research, Proceedings of ICF7,* Vol. 4, pp. 3081–3088.

Rice, J. R., 1968, "A Path Independent Integral and the Approximate Analysis of Strain Concentration by Notches and Cracks," ASME JOURNAL OF APPLIED MECHANICS, Vol. 35, pp. 379–386.

Rice, J. R., 1988, "Elastic Fracture Mechanics Concepts for Interfacial Cracks, ASME JOURNAL OF APPLIED MECHANICS, Vol. 55, pp. 98–103.

Rice, J. R., and Rosengren, G. F., 1968, "Plane Strain Deformation Near a Crack Tip in a Power Law Hardening Material," *Journal of the Mechanics and Physics of Solids,* Vol. 16, pp. 1–12.

Rice, J. R., Suo, Z., and Wang, J.-S., 1990, "Mechanics and Thermodynamics of Brittle Interfacial Failure in Bimaterial Systems," *Metal-Ceramic Interfaces, Acta-Scripta Metallurgica Proceedings Series,* Vol. 4, pp. 269–294.

Shih, C. F., 1974, "Small-Scale Yielding Analysis of Mixed Mode Plane-Strain Crack Problems," *Fracture Analysis,* ASTM STP 560, pp. 187–210.

Downloaded 03 May 2010 to 171.66.16.248. Redistribution subject to ASME license or copyright; see http://www.asme.org/terms/Terms_Use.cfm

Shih, C. F., 1981, "Relationship between the J-integral and the Crack Opening Displacement for Stationary and Extending Cracks," *Journal of the Mechanics and Physics of Solids,* Vol. 29, pp. 305–326.

Shih, C. F., and Asaro, R. J., 1988, "Elastic-Plastic Analysis of Cracks on Bimaterial Interfaces: Part I—Small Scale Yielding," ASME JOURNAL OF APPLIED MECHANICS, Vol. 55, pp. 299–316.

Shih, C. F., and Asaro, R. J., 1989a, "Elastic-Plastic Analysis of Crack on Bimaterial Interfaces: Part II—Structure of Small Scale Yielding Fields," ASME JOURNAL OF APPLIED MECHANICS, Vol. 56, pp. 763–779.

Shih, C. F., and Asaro, R. J., 1989b, "Elastic-Plastic Analysis of a Collinear Array of Cracks on a Bimaterial Interface," *Materials Science and Engineering,* Vol. A107, pp. 145–157.

Shih, C. F., Asaro, R. J., and O'Dowd, N. P., 1990, "Cracks on Bimaterial Interfaces: Plasticity Aspects," *Metal-Ceramic Interfaces, Acta-Scripta Metallurgica Proceedings Series,* Vol. 4, pp. 313–325.

Suo, Z., 1989, "Mechanics of Interface Fracture," Ph.D. Thesis, Harvard University, Cambridge, Mass. (available through University Microfilms, Ann Arbor, MI).

Symington, M., Shih, C. F., and Ortiz, M., 1988, "Tables of Plane Strain Mixed-Mode Plastic Crack Tip Fields," Brown University Report, MRG/DMR-8714665/1.

Varias, A. G., O'Dowd, N. P., Asaro, R. J., and Shih, C. F., 1990, *Metal-Ceramic Interfaces, Acta-Scripta Metllurgica Proceedings Series,* Vol. 4, pp. 375–382.

Wang, J. S., and Suo, Z., 1990, "Experimental Determination of Interfacial Toughness Curves using Brazil-Nut Sandwiches," *Acta Metall. Mater.*, Vol. 38, pp. 1279–1290.

Zywicz, E., and Parks, D. M., 1989a, "Elastic Yield Zone around an Interfacial Crack Tip," ASME JOURNAL OF APPLIED MECHANICS, Vol. 56, pp. 577–584.

Zywicz, E., and Parks, D. M., 1989b, "Elastic-Plastic Analysis of Fractionless Contact at Interfacial Crack Tips," *International Journal of Fracture,* in press.

Downloaded 03 May 2010 to 171.66.16.248. Redistribution subject to ASME license or copyright; see http://www.asme.org/terms/Terms_Use.cfm

Integral Equations Solution for Reinforced Mode I Cracks Opened by Internal Pressure

Scott W. Fowser

Tsu-Wei Chou
Mem. ASME

Center for Composite Materials and
Department of Mechanical Engineering,
University of Delaware,
Newark, DE 19716

The problem of a series of collinear Mode I cracks loaded by a uniform internal pressure is solved by an integral equations technique. By superimposing the solution for an arbitrarily loaded Mode I crack with the solution for an edge loaded infinite strip, a system of integral equations is developed by making the superposition satisfy the required boundary conditions. Solving the integral equations by a least-squares Ritz method gives boundary values which may then be used with the Green's functions solutions to calculate stress intensity factors for the cracks and the stress and displacement fields in the reinforcement and the cracked regions. By changing the boundary conditions at the reinforcement interface, integral equations modeling other situations such as imperfect bonding may be obtained.

1 Introduction

Integral equations for the problem of a series of uniformly pressurized Mode I cracks in a periodically reinforced plane (Fig. 1) may be formulated by using the Green's functions given by Fowser and Chou (1988 and 1989). Figure 1 shows that the problem consists of two types of infinite strips with different material properties: a cracked strip and a reinforcement strip. By symmetry, one of each of the strips can be modeled to simulate the entire domain. The two types of strips are modeled by using the numerical solution given by Fowser and Chou (1989) for an edge loaded strip. The crack is modeled with the solutions for a crack in an infinite plane (Fowser and Chou, 1988). Superposition of the two strips with the crack plane is used to model the entire domain of the reinforced cracks problem. Integral equations are obtained by satisfying boundary conditions on the crack face and at the reinforcement interface. The boundary conditions on the crack face are such that the superimposed stresses result in a uniform pressure opening the crack, which is normalized to one in this paper. At the reinforcement interface there are conditions of continuity of stress and displacement. The boundary conditions may be altered to model effects such as imperfect bonding at the interface or a different load distribution on the crack faces.

2 Green's Functions for a Mode I Loaded Crack Face

The Green's functions for a Mode I crack opened by unit loads applied to the crack faces (Fowser and Chou, 1988) are used in the formulation of the reinforced crack problem. These Green's functions are obtained by analytical integration of the singular integrals in the double integral expressions of Rudolphi and Ashbaugh (1978), and this reduction simplifies use of these results in numerical calculations. If $-F_{ij}(x,y,\xi)$ and $-F_i(x,y,\xi)$ denote the stress and displacements at the point (x,y) for a crack opened by unit loads as in Fig. 2, the stress and displacement fields around a Mode I crack with a normal

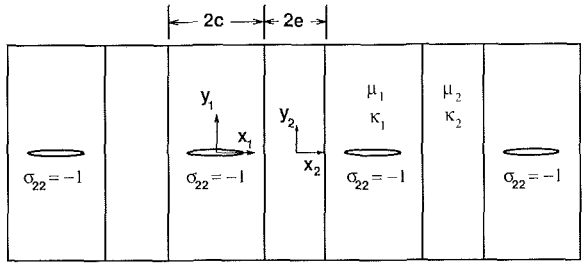

Fig. 1 Uniformly pressurized Mode I cracks in a reinforced plate

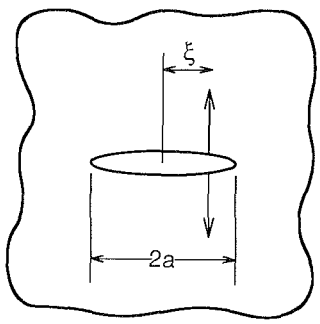

Fig. 2 The negative of the Green's functions for the Mode I crack are the solutions for a crack opened by a pair of concentrated unit forces

Contributed by the Applied Mechanics Division of THE AMERICAN SOCIETY OF MECHANICAL ENGINEERS for publication in the JOURNAL OF APPLIED MECHANICS.

Discussion on this paper should be addressed to the Technical Editor, Prof. Leon M. Keer, The Technological Institute, Northwestern University, Evanston, IL 60208, and will be accepted until two months after final publication of the paper itself in the JOURNAL OF APPLIED MECHANICS. Manuscript received by the ASME Applied Mechanics Division, Apr. 21, 1989; final revision, Jan. 20, 1990.

Copyright © 1991 by ASME
Downloaded 03 May 2010 to 171.66.16.248. Redistribution subject to ASME license or copyright; see http://www.asme.org/terms/Terms_Use.cfm

stress distribution, $\sigma(x)$, applied to the crack faces are given by:

$$\sigma_{ij}(x,y)=\int_{-a}^{+a}\sigma(\xi)F_{ij}(x,y,\xi)d\xi,$$
$$u_i(x,y)=\int_{-a}^{+a}\sigma(\xi)F_i(x,y,\xi)d\xi. \tag{1}$$

The functions $F_{ij}(x,y,\xi)$ and $F_i(x,y,\xi)$ are nonsingular kernels in the above integrals, and are given by:

$$(F_{11},F_{22})=\frac{\sqrt{a^2-\xi^2}}{(x-\xi)^2+y^2}\left\{-\frac{E}{2a\pi\beta}\left[S(2a^2-H^2)+2aD\xi\right]\right.$$
$$\pm\frac{H^2E^3S(2a^2-H^2)}{16a^3\pi\beta[(x-\xi)^2+y^2]}\mp\frac{H^2E\xi}{\pi\beta^3}\left[DS^2r_1r_2-(r_1^3-r_2^3)E^2\right]$$
$$\pm\frac{H^2E^3D\xi}{8a^2\pi\beta[(x-\xi)^2+y^2]}\pm\frac{EH^2}{4a\pi\beta^3}\left[\beta^2S+2E^2(2a^2\right.$$
$$\left.\left.-H^2)(r_1^3+r_2^3)-2r_1r_2D^2S(2a^2-E^2)\right]\right\}, \tag{2}$$

$$F_{12}=\frac{\sqrt{a^2-\xi^2}}{(x-\xi)^2+y^2}\left\{-\frac{H}{2a\pi\beta}\left[D(2a^2+E^2)+2aS\xi\right]\right.$$
$$+\frac{HD}{\pi\beta a}\left[a^2+E^2\right]+\frac{E^2H\xi}{\pi\beta^3}\left[SD^2r_1r_2-(r_1^3+r_2^3)H^2\right]$$
$$+\frac{HS\xi}{\pi\beta}-\frac{E^2H^3D(2a^2+E^2)}{16a^3\pi\beta[(x-\xi)^2+y^2]}-\frac{E^2H^3S\xi}{8a^2\pi\beta[(x-\xi)^2+y^2]}$$
$$-\frac{HE^2}{4a\pi\beta^3}\left[\beta^2D+2H^2(2a^2+E^2)(r_1^3-r_2^3)\right.$$
$$\left.\left.-2r_1r_2DS^2(2a^2+H^3)\right]\right\}, \tag{3}$$

$$F_1=\frac{(1-\kappa)}{4\pi\mu}\tan^{-1}\left[\frac{\sqrt{a^2-\xi^2}(\psi^-(\xi)-\xi E)}{\xi\psi^-(\xi)+E(a^2-\xi^2)}\right]$$
$$+\frac{\sqrt{a^2+\xi^2}}{(x-\xi)^2+y^2}\left[\frac{EH^2S\xi}{8\pi\mu a\beta}+\frac{EH^2D(E^2+2a^2)}{16\pi\mu a^2\beta}\right], \tag{4}$$

$$F_2=\frac{(1+\kappa)}{8\pi\mu}\log\left[\frac{\psi^+(\xi)-H\sqrt{a^2-\xi^2}}{\psi^+(\xi)+H\sqrt{a^2-\xi^2}}\right]$$
$$+\frac{\sqrt{a^2-\xi^2}}{(x-\xi)^2+y^2}\left[\frac{HE^2D\xi}{8\pi\mu a\beta}-\frac{HE^2S(H^2-2a^2)}{16\pi\mu a^2\beta}\right], \tag{5}$$

where the following definitions are used to reduce the size of the equations by making use of a bipolar coordinate system with r_1 and r_2 taken as the distances from the crack tips to the point (x,y):

$$r_1^2=(x-a)^2+y^2,$$
$$r_2^2=(x+a)^2+y^2,$$
$$\beta=4ar_1r_2=a(H^2+E^2),$$
$$S=r_1+r_2,$$
$$D=r_1-r_2,$$
$$E^2=(r_1+r_2)^2-4a^2,$$
$$H^2=4a^2-(r_2-r_1)^2,$$

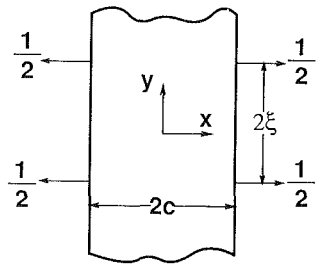

Fig. 3 Physical meaning of kernel $A(x,y,\xi)$

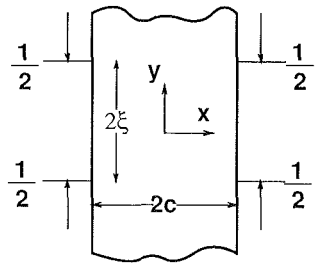

Fig. 4 Physical meaning of kernel $D(x,y,\xi)$

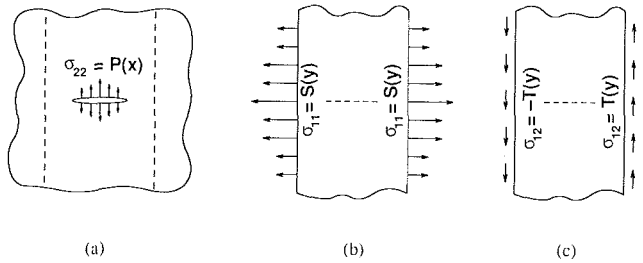

Fig. 5 The four subproblems used in the superposition: (*a*) infinite plate in tension, (*b*) cracked infinite plate, (*c*) infinite strip with edge normal stress, and (*d*) infinite strip with edge shear stress

$$\psi^{\pm}(\xi)=(a+\xi)r_1\pm(a-\xi)r_2,$$
$$H=\begin{cases}+\sqrt{H^2} & y\geq 0,\\ -\sqrt{H^2} & y<0.\end{cases} \tag{6}$$

The material surrounding the crack has a shear modulus of μ, a Poisson's ratio of ν, and κ is given by

$$\kappa=\begin{cases}3-4\nu & \text{plane strain},\\ (3-\nu)/(1+\nu) & \text{plane stress}.\end{cases}$$

3 Green's Functions for an Edge-Loaded Strip

Green's functions for an edge-loaded strip are also used in formulating the problem solved in this paper. The expressions for these Green's functions were first formulated by Filon (1903) and numerical evaluation of the expressions is done with the technique given by Fowser and Chou (1989), where the integral expressions are evaluated by expanding the integrands in a series of integrable terms. If $A_{ij}(x,y,\xi)$ is the stress component at a point, (x,y), in a strip loaded as in Fig. 3, and $D_{ij}(x,y,\xi)$ is the stress in a strip loaded as shown in Fig. 4, these functions may be used to find the stress in a symmetrically edge-loaded strip. If the strip is subjected to the normal stress distribution, $S(y)$, and shear stress distribution, $T(y)$, as depicted in Figs. 5(*b*) and (*c*), the stress and displacement fields within the strip are given by:

Downloaded 03 May 2010 to 171.66.16.248. Redistribution subject to ASME license or copyright; see http://www.asme.org/terms/Terms_Use.cfm

$$\sigma_{ij}(x,y)=2\int_0^\infty S(\xi)A_{ij}(x,y,\xi)-T(\xi)D_{ij}(x,y,\xi)d\xi \quad (i,j=1,2),$$

$$u_i(x,y)=2\int_0^\infty S(\xi)A_i(x,y,\xi)-T(\xi)D_i(x,y,\xi)d\xi \quad (i=1,2). \tag{7}$$

By making the definitions $\bar{x}=x/c$, $\bar{y}=y/c$, and $\bar{\xi}=\xi/c$, the Green's functions, $A_{ij}(x,y,\xi)$ and $D_{ij}(x,y,\xi)$, are given by:

$$A_{11}=\frac{1}{c\pi}\int_0^\infty \frac{\omega\cosh\omega\cosh\omega\bar{x}-\omega\bar{x}\sinh\omega\sinh\omega\bar{x}+\sinh\omega\cosh\omega\bar{x}}{\omega+\cosh\omega\sinh\omega}\cos\omega\bar{y}\cos\omega\bar{\xi}d\omega,$$

$$A_{22}=\frac{1}{c\pi}\int_0^\infty \frac{\omega\bar{x}\sinh\omega\sinh\omega\bar{x}-\omega\cosh\omega\cosh\omega\bar{x}+\sinh\omega\cosh\omega\bar{x}}{\omega+\cosh\omega\sinh\omega}\cos\omega\bar{y}\cos\omega\bar{\xi}d\omega,$$

$$A_{12}=\frac{1}{c\pi}\int_0^\infty \frac{\omega\bar{x}\sinh\omega\cosh\omega\bar{x}-\omega\cosh\omega\sinh\omega\bar{x}}{\omega+\cosh\omega\sinh\omega}\sin\omega\bar{y}\cos\omega\bar{\xi}d\omega,$$

$$A_1=\int_0^\infty \frac{2\omega\cosh\omega\sinh\omega\bar{x}-2\omega\bar{x}\sinh\omega\cosh\omega\bar{x}+(1+\kappa)\sinh\omega\sinh\omega\bar{x}}{4\mu\pi\omega(\omega+\cosh\omega\sinh\omega)}\cos\omega\bar{y}\cos\omega\bar{\xi}d\omega,$$

$$A_2=\int_0^\infty \frac{2\omega\bar{x}\sinh\omega\sinh\omega\bar{x}-2\omega\cosh\omega\cosh\omega\bar{x}-(1-\kappa)\sinh\omega\cosh\omega\bar{x}}{4\mu\pi\omega(\omega+\cosh\omega\sinh\omega)}\sin\omega\bar{y}\cos\omega\bar{\xi}d\omega, \tag{8}$$

$$D_{11}=\frac{1}{c\pi}\int_0^\infty \frac{\omega\bar{x}\cosh\omega\sinh\omega\bar{x}-\omega\sinh\omega\cosh\omega\bar{x}}{\omega+\cosh\omega\sinh\omega}\cos\omega\bar{y}\sin\omega\bar{\xi}d\omega,$$

$$D_{22}=\frac{1}{c\pi}\int_0^\infty \frac{\omega\sinh\omega\cosh\omega\bar{x}-\omega\bar{x}\cosh\omega\sinh\omega\bar{x}-2\cosh\omega\cosh\omega\bar{x}}{\omega+\cosh\omega\sinh\omega}\cos\omega\bar{y}\sin\omega\bar{\xi}d\omega,$$

$$D_{12}=\frac{1}{c\pi}\int_0^\infty \frac{\omega\sinh\omega\sinh\omega\bar{x}-\omega\bar{x}\cosh\omega\cosh\omega\bar{x}-\cosh\omega\sinh\omega\bar{x}}{\omega+\cosh\omega\sinh\omega}\sin\omega\bar{y}\sin\omega\bar{\xi}d\omega,$$

$$D_1=\int_0^\infty \frac{2\omega\bar{x}\cosh\omega\cosh\omega\bar{x}-2\omega\sinh\omega\sinh\omega\bar{x}+(1-\kappa)\cosh\omega\sinh\omega\bar{x}}{4\mu\pi\omega(\omega+\cosh\omega\sinh\omega)}\cos\omega\bar{y}\sin\omega\bar{\xi}d\omega,$$

$$D_2=\int_0^\infty \frac{2\omega\sinh\omega\cosh\omega\bar{x}-2\omega\bar{x}\cosh\omega\sinh\omega\bar{x}-(1+\kappa)\cosh\omega\cosh\omega\bar{x}}{4\mu\pi\omega(\omega+\cosh\omega\sinh\omega)}\sin\omega\bar{y}\sin\omega\bar{\xi}d\omega. \tag{9}$$

4 Formulation for Pressurized Cracks

Since two different material regions are involved in this problem, they will be considered separately but continuity of traction and displacement at the interface between the cracked and reinforcement regions is required. The cracked strips in the problem shown in Fig.1 are modeled by superimposing the three subproblems of Figs. 5(*a*)–5(*c*). In each subproblem the origin of an *x-y* coordinate system is located at the center of the corresponding figure, and the combined stress and displacement fields of the subproblems at the locations marked with dotted lines must result in the desired boundary conditions. The solution to each of these subproblems is written in terms of the functions given by Fowser and Chou (1988 and 1989), and combining these solutions leaves a set of integral equations which must be solved for three unknown functions. The boundary conditions to be satisfied for this problem are:

$$\begin{aligned}
\sigma_{22}^{(1)}(x,0)&=-1 && -a<x<+a,\\
\sigma_{11}^{(1)}(c,y)&=\sigma_{11}^{(2)}(-e,y) && -\infty<y<+\infty,\\
\sigma_{12}^{(1)}(c,y)&=\sigma_{12}^{(2)}(-e,y) && -\infty<y<+\infty,\\
u_1^{(1)}(c,y)&=u_1^{(2)}(-e,y) && -\infty<y<+\infty,\\
u_2^{(1)}(c,y)&=u_2^{(2)}(-e,y) && -\infty<y<+\infty.
\end{aligned} \tag{10}$$

Stresses and displacements with a superscript in parentheses denote values taken in the specified material region. For example, $\sigma_{12}^{(1)}(x_1,y_1)$ is the shear stress at the point with coordinates (x_1,y_1) in material region number 1 (cracked region with material properties μ_1 and κ_1), and $u_1^{(2)}(x_2,y_2)$ is the displacement at (x_2,y_2) in material region number 2 (reinforcement region with material properties μ_2 and κ_2). As shown in Fig. 1, each material region has its own coordinate system. Any point in region 1 uses the x_1-y_1 coordinate system, and points in region 2 use the x_2-y_2 system.

The value of $\sigma_{22}(x,0)$ in Fig. 5(*a*) is denoted by the unknown function, $P(x)$. The solutions for the infinite strip are used to give $\sigma_{22}(x,0)$ for Figs. 5(*b*) and 5(*c*) as $\int_0^\infty 2S(\xi)A_{22}(x,0,\xi)d\xi$ and $-\int_0^\infty 2T(\xi)D_{22}(x,0,\xi)d\xi$, respectively. Here $S(y)$ and $T(y)$ are assumed to have the obvious symmetries. Combining the three subproblems results in the following integral equation which is required in order to satisfy the first boundary condition above:

$$0=\sigma+P(\eta)+\int_0^\infty 2S(\xi)A_{22}(\eta,0,\xi)d\xi - \int_0^\infty 2T(\xi)D_{22}(\eta,0,\xi)d\xi \quad -a<\eta<a. \tag{11}$$

Superposition of the three subproblems leaves the following for displacements at the edges of material region 1:

$$u_i^{(1)}(c,\eta)=\int_0^a P(\xi)[F_i(c,\eta,\xi)+F_i(c,\eta,-\xi)]d\xi \qquad 0\le\eta<\infty + \int_0^\infty 2S(\xi)A_i^{(1)}(c,\eta,\xi)d\xi-\int_0^\infty 2T(\xi)D_i^{(1)}(c,\eta,\xi)d\xi, \tag{12}$$

where the first line above is the contribution from the loaded crack, and the second line represents the effects due the load on the strip's edges. From the conditions of continuity of traction at the interface, it follows that region 2 is a strip with an edge loading of $S(\xi)$ and $T(\xi)$ combined with the effects due to the crack pressurized by $P(\xi)$. Using these edge stresses

Downloaded 03 May 2010 to 171.66.16.248. Redistribution subject to ASME license or copyright; see http://www.asme.org/terms/Terms_Use.cfm

in the solution for the infinite strip leaves the following for the displacement, at the edges of region 2:

$$u_i^{(2)}(-e,\eta)=\int_0^\infty 2\Bigg\{S(\xi)+\int_0^a P(\zeta)[F_{11}(c,\xi,\zeta)+F_{11}(c,\xi,-\zeta)]d\zeta\Bigg\}A_i^{(2)}(-e,\eta,\xi)d\xi+\int_0^\infty 2\Bigg\{T(\xi)+\int_0^a P(\zeta)[F_{12}(c,\xi,\zeta)+F_{12}(c,\xi,-\zeta)]d\zeta\Bigg\}D_i^{(2)}(-e,\eta,\xi)d\xi. \quad (13)$$

Making the definition

$$R_i(\zeta,\eta)=2\int_0^\infty [F_{11}(c,\xi,\zeta)+F_{11}(c,\xi,-\zeta)]A_i^{(2)}(-e,\eta,\xi)d\xi+2\int_0^\infty [F_{12}(c,\xi,\zeta)+F_{12}(c,\xi,-\zeta)]D_i^{(2)}(-e,\eta,\xi)d\xi \quad (14)$$

allows the equation for $u_i^{(2)}(-e,\eta)$ to be written as:

$$u_i^{(2)}(-e,\eta)=\int_0^a P(\zeta)R_i(\zeta,\eta)d\zeta+\int_0^\infty 2S(\xi)A_i^{(2)}(-e,\eta,\xi)d\xi+\int_0^\infty 2T(\xi)D_i^{(2)}(-e,\eta,\xi)d\xi. \quad (15)$$

To satisfy the conditions of displacement continuity at the interface, the difference between the displacements at the edges of the two material regions must be zero:

$$u_i^{(1)}(c,\eta)-u_i^{(2)}(-e,\eta)=0=\int_0^a P(\zeta)[F_i(c,\eta,\zeta)+F_i(c,\eta,-\zeta)-R_i(\zeta,\eta)]d\zeta+\int_0^\infty 2S(\xi)[A_i^{(1)}(c,\eta,\xi)-A_i^{(2)}(-e,\eta,\xi)]d\xi+\int_0^\infty 2T(\xi)[-D_i^{(1)}(c,\eta,\xi)-D_i^{(2)}(-e,\eta,\xi)]d\xi. \quad (16)$$

This equation may be simplified by making the following definitions:

$$W_i(\eta,\xi)=A_i^{(1)}(c,\eta,\xi)-A_i^{(2)}(-e,\eta,\xi),$$
$$Z_i(\eta,\xi)=-D_i^{(1)}(c,\eta,\xi)-D_i^{(2)}(-e,\eta,\xi),$$
$$V_i(\xi,\eta)=F_i(c,\eta,\xi)+F_i(c,\eta,-\xi)-R_i(\xi,\eta), \quad (17)$$

and the conditions of displacement (and stress) continuity, written in terms of the kernels defined above, become

$$0=\int_0^a P(\xi)V_i(\xi,\eta)d\xi+\int_0^\infty 2S(\xi)W_i(\eta,\xi)d\xi+\int_0^\infty 2T(\xi)Z_i(\eta,\xi)d\xi. \quad (18)$$

Writing out the above equation for both displacement components along with the equation for stress on the crack face, results in a system of three integral equations to be solved for $P(\eta)$, $S(\eta)$, and $T(\eta)$:

$$-1=P(\eta)+\int_0^\infty 2S(\xi)A_{22}(\eta,0,\xi)d\xi-\int_0^\infty 2T(\xi)D_{22}(\eta,0,\xi)d\xi \qquad 0\le\eta<a,$$

$$0=\int_0^a P(\xi)V_i(\xi,\eta)d\xi+\int_0^\infty 2S(\xi)W_i(\eta,\xi)d\xi+\int_0^\infty 2T(\xi)Z_1(\eta,\xi)d\xi \qquad 0\le\eta<\infty,$$

$$0=\int_0^a P(\xi)V_2(\xi,\eta)d\xi+\int_0^\infty 2S(\xi)W_2(\eta,\xi)d\xi+\int_0^\infty 2T(\xi)Z_2(\eta,\xi)d\xi \qquad 0\le\eta<\infty. \quad (19)$$

Making the definitions:

$$P_1(\eta)=P(\eta)$$
$$P_2(\eta)=\int_0^a P(\xi)V_1(\xi,\eta)d\xi,$$
$$P_3(\eta)=\int_0^a P(\xi)V_2(\xi,\eta)d\xi,$$
$$S_1(\eta)=\int_0^\infty 2S(\xi)A_{22}(\eta,0,\xi)d\xi,$$
$$S_2(\eta)=\int_0^\infty 2S(\xi)W_1(\eta,\xi)d\xi,$$
$$S_3(\eta)=\int_0^\infty 2S(\xi)W_2(\eta,\xi)d\xi,$$
$$T_1(\eta)=-\int_0^\infty 2T(\xi)D_{22}(\eta,0,\xi)d\xi,$$
$$T_2(\eta)=\int_0^\infty 2T(\xi)Z_1(\eta,\xi)d\xi,$$
$$T_3(\eta)=\int_0^\infty 2T(\xi)Z_2(\eta,\xi)d\xi, \quad (20)$$

allows the integral equations to be expressed as:

$$-1=P_1(\eta)+S_1(\eta)+T_1(\eta) \qquad 0\le\eta<a,$$
$$0=P_2(\eta)+S_2(\eta)+T_2(\eta) \qquad 0\le\eta<\infty,$$
$$0=P_3(\eta)+S_3(\eta)+T_3(\eta) \qquad 0\le\eta<\infty. \quad (21)$$

Instead of satisfying the equations approximately at a finite set of selected locations, they are solved by a least-squares method which best satisfies the equations in an average sense over the entire semi-infinite domain. The following numerical solution of these equations is carried out with $c=1$.

5 Least Squares

The above system of integral equations is solved by a least-squares method. This involves assuming a functional form for the unknown functions, $P(\eta)$, $S(\eta)$, and $T(\eta)$, and finding optimal scaling of the functions which best satisfies the set of integral equations. The residual, R, used for least squares is defined by:

$$R=\int_0^a [1+P_1(\eta)+S_1(\eta)+T_1(\eta)]^2d\eta+\int_0^\infty [P_2(\eta)+S_2(\eta)+T_2(\eta)]^2d\eta+\int_0^\infty [P_3(\eta)+S_3(\eta)+T_3(\eta)]^2d\eta. \quad (22)$$

Downloaded 03 May 2010 to 171.66.16.248. Redistribution subject to ASME license or copyright; see http://www.asme.org/terms/Terms_Use.cfm

The residual is zero for the exact solution, otherwise it has some positive value. A good approximation to the exact solution is obtained by assuming functional forms for $P(\eta)$, $S(\eta)$, and $T(\eta)$ and minimizing the residual by scaling these functions with constants of proportionality. Taking the functional forms to be a linear combination of terms allows minimization of R with little difficulty, thus the following form is assumed:

$$P(\eta)=\sum_{i=1}^{n} a_i^P P^i(\eta),$$

$$S(\eta)=\sum_{i=1}^{m} a_i^S S^i(\eta),$$

$$T(\eta)=\sum_{i=1}^{k} a_i^T T^i(\eta). \tag{23}$$

The selection of the basis functions $P^i(\eta)$, $S^i(\eta)$, and $T^i(\eta)$ should be made so that proper values of the constants, a_i^P, a_i^S, and a_i^T will result in an accurate approximation to the exact solution. A P, S, or T with both a superscript and a subscript denotes the contribution of the basis function (superscript) to one of the functions (subscript) defined in the previous section. For example, the contribution of basis function $S^3(\eta)$ to $S_2(\eta)$ is given by $S_2^3(\eta)$:

$$S_2^3(\eta)=\int_0^\infty 2S^3(\xi)\,W_1(\eta,\xi)d\xi. \tag{24}$$

The equations are considerably shortened by use of the following notation:

$$E_j^i(\eta)=\begin{cases} P_j^i(\eta) & 1\le i\le n,\\ S_j^{i-n}(\eta) & n+1\le i\le n+m,\\ T_j^{i-n-m}(\eta) & n+m+1\le i\le n+m+k,\end{cases}$$

$$\alpha_i=\begin{cases} a_i^P & 1\le i\le n,\\ a_{i-n}^S & n+1\le i\le n+m,\\ a_{i-n-m}^T & n+m+1\le i\le n+m+k.\end{cases} \tag{25}$$

With these definitions the residual becomes:

$$R=\int_0^a\left[1+\sum_{p=1}^{n+m+k}\alpha_p E_1^p(\eta)\right]^2 d\eta + \int_0^\infty\left[\sum_{p=1}^{n+m+k}\alpha_p E_2^p(\eta)\right]^2 d\eta+\int_0^\infty\left[\sum_{p=1}^{n+m+k}\alpha_p E_3^p(\eta)\right]^2 d\eta. \tag{26}$$

A good approximation to the solution of the integral equations is obtained when the constants, α_p, have values which minimize R. The selection of a linear combination of basis functions facilitates the minimization of R, by leaving a system of $n+m+k$ linear equations which is then solved for the constants, α_p. The residual is a minimum when the partial derivative of R with respect to each α_p is zero. Taking these derivatives leaves the following system of linear equations (i ranges from 1 to $n+m+k$):

$$\frac{1}{2}\frac{\partial R}{\partial \alpha_i}=0=-\int_0^a E_1^i(\eta)d\eta+\sum_{p=1}^{n+m+k}\alpha_p\left[\int_0^a E_1^p(\eta)E_1^i(\eta)d\eta + \int_0^\infty E_2^p(\eta)E_2^i(\eta)d\eta+\int_0^\infty E_3^p(\eta)E_3^i(\eta)d\eta\right]. \tag{27}$$

Numerical solution of these linear equations presents little difficulty once the $E_j^i(\eta)$ are evaluated at a number of integration points. The values at the integration points may then be used to evaluate the integrals in the above system of linear equations. Many of the $E_j^i(\eta)$ are independent of the crack size and may be evaluated once and tabulated to greatly speed computation.

Table 1 Stress intensity factors for unreinforced cracks obtained by setting $\mu_2/\mu_1=1$.

a/c	Numerical Solution	Exact	Error
0.2	1.0134	1.0140	−0.0006
0.3	1.0314	1.0325	−0.0011
0.4	1.0589	1.0607	−0.0018
0.5	1.0987	1.1016	−0.0029
0.6	1.1559	1.1606	−0.0047
0.7	1.2398	1.2477	−0.0079
0.8	1.3714	1.3845	−0.0131
0.9	1.6097	1.6279	−0.0182

An important consideration for accurate numerical solution is the selection of basis functions which can accurately represent the solution to the integral equations. By symmetry, $P(\eta)$ is an even function so an even power series is used as an approximation:

$$P(\eta)=\sum_{i=1}^{n} a_i^P\left(\frac{\eta}{a}\right)^{2(i-1)}, \tag{28}$$

thus,

$$P^i(\eta)=\left(\frac{\eta}{a}\right)^{2(i-1)}. \tag{29}$$

This representation has the advantage that once the a_i^P are found, the stress intensity factor follows immediately from the expressions given by Fowser (1988). The stress intensity factor when $P(\eta)$ has the above form is then found to be:

$$\frac{K_I}{\sigma\sqrt{\pi a}}=-a_1^P-\sum_{i=2}^{n}\left[\frac{1\cdot3\cdot5\cdots(2i-3)}{2\cdot4\cdot6\cdots2(i-1)}\right]a_i^P. \tag{30}$$

The behavior of $S(\eta)$ would be expected to be similar to that of normal stress along a vertical line near a uniformly pressurized crack, since $S(\eta)$ is the result of a loaded crack. Examination of the expected behavior shows a function with a sharp, but nonsingular, peak near $\eta=0$ and an asymptotic form for large η. A piecewise linear approximation is used in the intermediate range $0\le\eta\le3$. For this example, ten linear segments are used which result in 11 basis functions for the piecewise linear portion.

$$S^i(\eta)=\begin{cases} 0 & \eta-3(i-2)/10\le 0,\\ \eta-3(i-2)/10 & 0\le\eta-3(i-2)/10\le 3/10,\\ 3/10 & 3/10\le\eta-3(i-2)/10.\end{cases}$$

$$i=1,11 \tag{31}$$

The piecewise linear approximation works well when the variation in $S(\eta)$ is gradual enough that no sharp changes occur within one linear segment. For large η, linear segments are unnecessary since an asymptotic form is sufficient. The asymptotic basis functions also allow accurate integration for large η. From the solutions of Fowser and Chou (1988), it is known that $S(\eta)$ is asymptotic to $-\eta^{-2}$ at infinity, but another basis function of order η^{-3} is also included to improve accuracy:

$$S^{12}(\eta)=\begin{cases}0 & \eta\le3,\\ \eta^{-2} & \eta>3,\end{cases}\qquad S^{13}(\eta)=\begin{cases}0 & \eta\le3,\\ \eta^{-3} & \eta>3.\end{cases} \tag{32}$$

The expected behavior of $S(\eta)$ for η near zero shows a sharp peak which the piecewise approximation would have difficulty representing accurately. Introducing a basis function to model this peak allows an approximation of this effect. Some estimate of the width, δ_s, of this peak is needed to create a basis function. Using the exact solution for unreinforced cracks (Westergard, 1939) as a guide, a value of $\delta_s=0.34\sqrt{1-a^2}$ is use for the

Downloaded 03 May 2010 to 171.66.16.248. Redistribution subject to ASME license or copyright; see http://www.asme.org/terms/Terms_Use.cfm

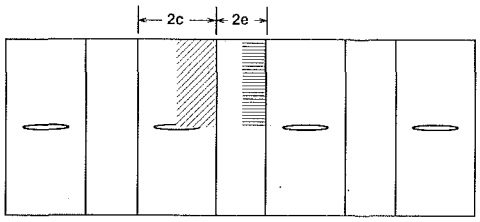

Fig. 6 Cross-hatched area is the region shown in the stress contour plots for the cracked region, and the vertically shaded area is used for contour plots of the reinforcement region

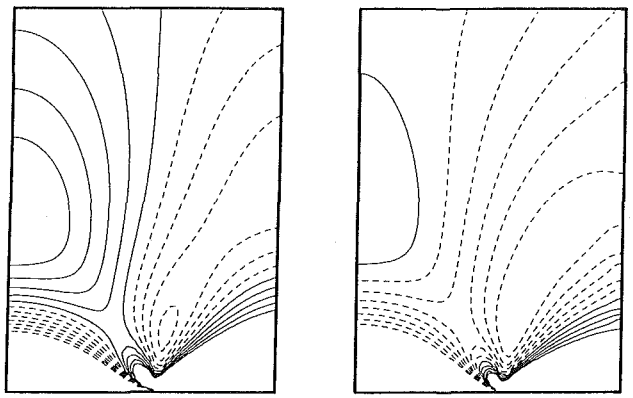

Fig. 7 Comparison of σ_{11} stress fields around the crack for (*a*) $\mu_2/\mu_1 = 1$ and (*b*) $\mu_2/\mu_1 = 1000$ (starting value = -0.21, increment = 0.03)

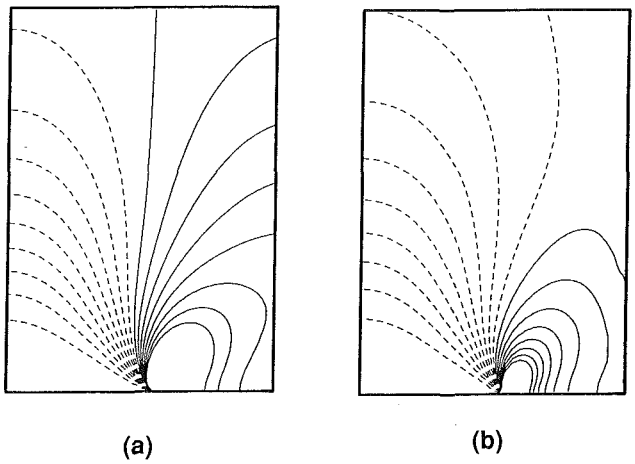

Fig. 8 Comparison of σ_{22} stress fields around the crack for (*a*) $\mu_2/\mu_1 = 1$ and (*b*) $\mu_2/\mu_1 = 1000$ (starting value = -0.9, increment = 0.1)

basis function. A basis function giving this peak with a maximum at $\eta = 0$ is then:

$$S^{14}(\eta) = \begin{cases} \eta^2 - \delta_s^2 & \eta \le \delta_s, \\ 0 & \eta > \delta_s. \end{cases} \tag{33}$$

where $\delta_s = 0.34\sqrt{1-a^2}$.

The basis functions for $T(\eta)$ are similar to those for $S(\eta)$, but only ten segments are needed to model the behavior in $0 \le \eta \le 3$ because it is known from symmetry that $T(0)$ is zero:

$$T^i(\eta) = \begin{cases} 0 & \eta - 3(i-1)/10 \le 0, \\ \eta - 3(i-1)/10 & 0 \le \eta - 3(i-1)/10 \le 3/10, \\ 3/10 & 3/10 \le \eta - 3(i-1)/10. \end{cases}$$

$$i = 1,10 \tag{34}$$

For $T(\eta) > 3$ the asymptotic behavior from Fowser and Chou

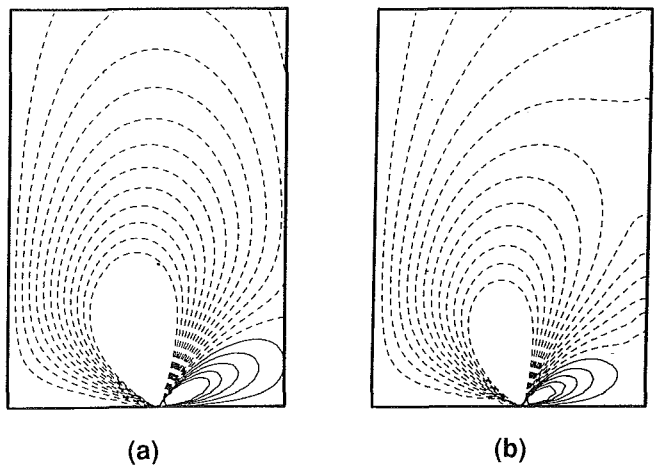

Fig. 9 Comparison of σ_{12} stress fields around the crack for (*a*) $\mu_2/\mu_1 = 1$ and (*b*) $\mu_2/\mu_1 = 1000$ (starting value = -0.36, increment = 0.03)

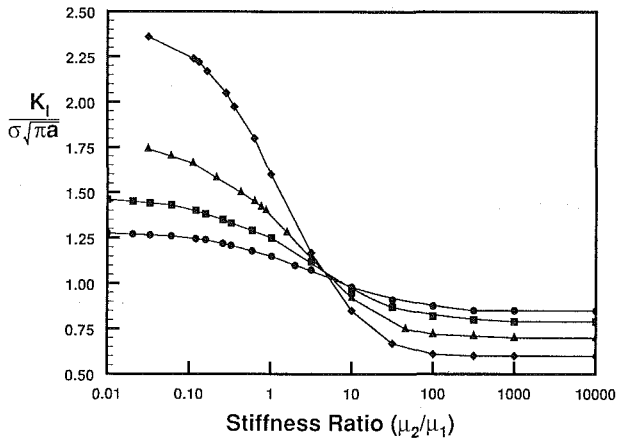

Fig. 10 Effect of stiffness ratio on $K_I/\sigma\sqrt{\pi a}$ for various crack lengths ($e/c = 0.1$)

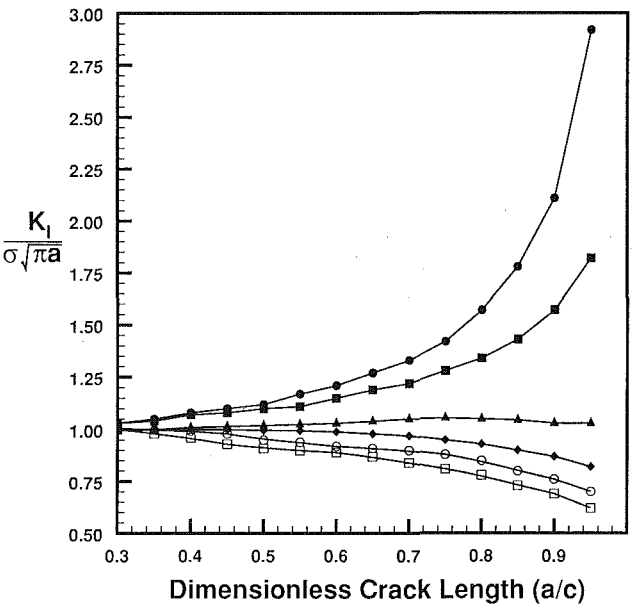

Fig. 11 Effect of crack length on $K_I/\sigma\sqrt{\pi a}$ for various reinforcement thicknesses ($\mu_2/\mu_1 = 10$)

(1988) is used along with a lower order basis function to improve the approximation:

$$T^{11}(\eta) = \begin{cases} 0 & \eta \le 3, \\ \eta^{-3} & \eta > 3, \end{cases} \quad T^{12}(\eta) = \begin{cases} 0 & \eta \le 3, \\ \eta^{-4} & \eta > 3. \end{cases} \tag{35}$$

Downloaded 03 May 2010 to 171.66.16.248. Redistribution subject to ASME license or copyright; see http://www.asme.org/terms/Terms_Use.cfm

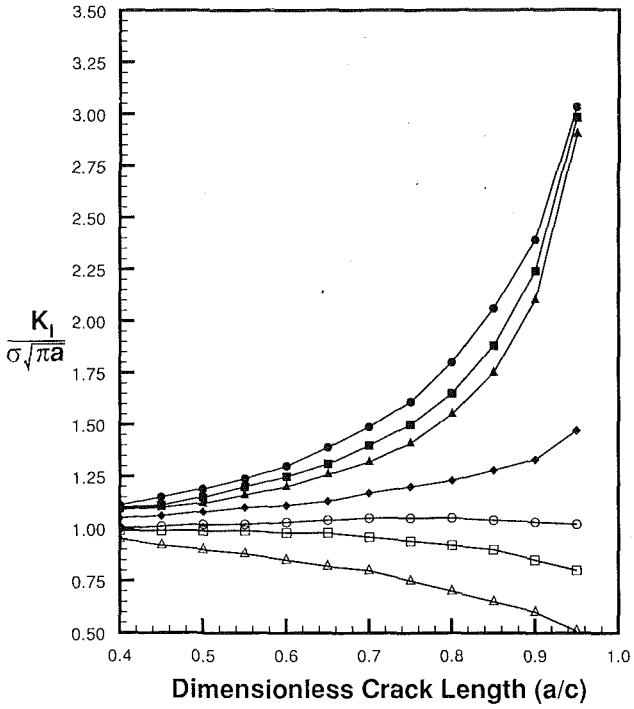

Fig. 12 Effect of crack length on $K_I/\sigma\sqrt{\pi a}$ for various reinforcement stiffness ratios ($e/c = 0.1$)

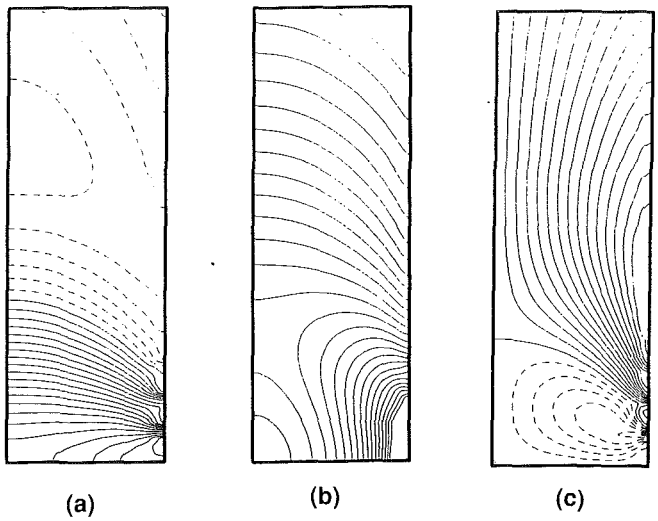

Fig. 13 Contours of the three stress components in the reinforcement region for $a/c = 0.85$, $e/c = 0.5$, and $\mu_2/\mu_1 = 10$: (*a*) σ_{11} (starting value = -0.4, increment = 0.05) (*b*) σ_{22} (starting value = 0.2, increment = 0.05) (*c*) σ_{12} (starting value = -0.3, increment = 0.05)

When the crack approaches the edge, $T(\eta)$ has a sharp peak near $\eta = 0$. This is approximated by a parabola which has zeros at $\eta = 0$ and $\eta = \delta_t$:

$$T^{13}(\eta) = \begin{cases} (\eta - \delta_t/2)^2 - \delta_t^2/4 & \eta \le \delta_t, \\ 0 & \eta > \delta_t. \end{cases} \tag{36}$$

The width of the peak, δ_t, is again approximated from that in unreinforced cracks, which is given analytically by Fowser (1988):

$$\delta_t = \sqrt{\frac{5}{3} - a^2 - \frac{2}{3}\sqrt{4 - 3a^2}}. \tag{37}$$

6 Numerical Results Assuming Perfect Bonding

As a check to the accuracy of this formulation, the properties of the reinforcement strip may be taken as identical to those of the cracked medium. This reduces the problem to that of unreinforced collinear cracks, which has an exact solution (Westergaard, 1939). The accuracy of solution to the collinear cracks problem obtained with this formulation will depend on the assumed size of the reinforcement strip. The identical problem may be solved in an infinite number of forms depending on the choice of the relative sizes of the cracked region and the reinforcement strip. Solution accuracy depends on how closely the assumed form of the boundary stresses approximates the actual stress at the interface. When $e/c = 0.1$, the values for the stress intensity factor shown in Table 1 are obtained for unreinforced collinear cracks.

To show the effects of reinforcement on the stress field, contour plots of stress distribution in the cracked regions are made for different values of reinforcement stiffness. For these plots, $a/c = 0.55$, $e/c = 0.1$, and the region shown in the contour plots is the cross-hatched area shown in Fig. 6. To more clearly show the stress field, dotted lines are used for contours of negative stress, and solid lines denote positive or zero stress. The stress values at the contours are not shown on the figures since they would clutter the diagrams and, for these figures,

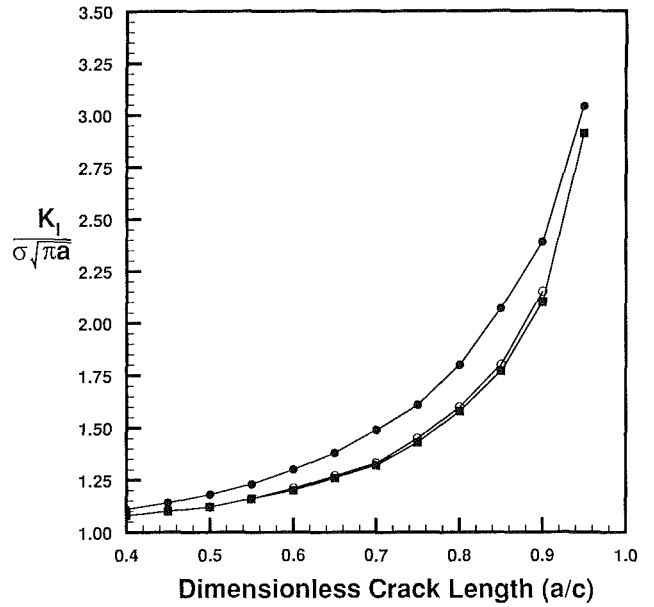

Fig. 14 Effect of crack length on $K_I/\sigma\sqrt{\pi a}$ for various reinforcement stiffness ratios for imperfectly bonded reinforcement ($e/c = 0.1$)

the dotted and solid lines convey the most interesting information. For completeness, the values of the stress contours used in each figure are shown in the figure captions. The starting value is the lowest value for a stress contour appearing on the plot, and the increment is the difference in stress between adjacent contours.

The effects of the reinforcement on the stress distribution are shown in Figs. 7 and 9, where stress contour plots are made for $\mu_2/\mu_1 = 1$ and $\mu_2/\mu_1 = 1000$. These figures show how an increase in reinforcement stiffness decreases the size of the region around the crack which is in tension.

Several plots are also made showing the effects of crack length, reinforcement size, and reinforcement stiffness on the dimensionless stress intensity factor. Figure 10 shows how the stress intensity factor varies with reinforcement stiffness for various crack lengths. For this plot, $e/c = 0.1$, and similar curves would be obtained for different reinforcement volume fractions. A point of interest on this plot is at $\mu_2/\mu_1 \approx 5$. All the curves on the plot pass through this point, which means that for $\mu_2/\mu_1 \approx 5$ the value of the dimensionless stress intensity

Downloaded 03 May 2010 to 171.66.16.248. Redistribution subject to ASME license or copyright; see http://www.asme.org/terms/Terms_Use.cfm

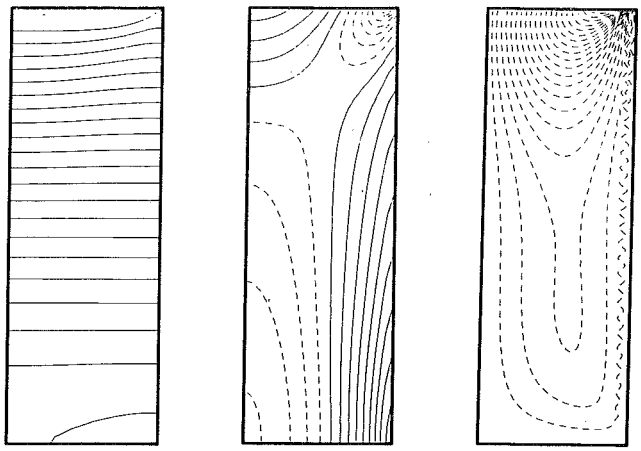

Fig. 15 Contours of the three stress components in an imperfectly bonded reinforcement region for $a/c = 0.85$, $e/c = 0.5$, and $\mu_2/\mu_1 = 10$: (a) σ_{11} (starting value = 0.12, increment = 0.02) (b) σ_{22} (starting value = −0.035, increment = 0.005) (c) σ_{12} (starting value = −0.20, increment = 0.01)

factor is independent of crack length. This is due to the increase in dimensionless stress intensity factor from the periodic cracks approaching each other being exactly canceled by the decrease caused by the crack approaching the reinforcement.

Figure 11 shows how stress intensity factor changes with crack length when the reinforcement stiffness is held at $\mu_2/\mu_1 = 10$, and reinforcement thickness takes on various values. In Fig. 12, a similar plot is made by making a curve for several values of the stiffness ratio while keeping $e/c = 0.1$. Figures 11 and 12 also show the effect discussed above, since they each have a curve where the dimensionless stress intensity factor has a value of one for all crack lengths. These figures also give an indication as to why this situation occurs. For example, in Fig. 12, while e/c is constant, low stiffness ratios result in a monotonically increasing curve for dimensionless stress intensity factor, and higher stiffness ratios cause a monotonic decrease. Since increasing the stiffness ratio should always lower the stress intensity factors, there is a certain stiffness ratio for this value of e/c where the monotonically increasing functions become monotonically decreasing, and this is the curve with a constant value for dimensionless stress intensity factor. As the crack length approaches zero, all the curves must converge to $K_I/\sigma\sqrt{\pi a} = 1$, so the value for the dimensionless stress intensity factor has a value of one when it is independent of crack length.

Figure 13 shows contour plots of the three components of stress in the reinforcement region when $a/c = 0.85$, $e/c = 0.5$, and $\mu_2/\mu_1 = 10$. The region shown in the contour plots represent the area shown shaded with vertical lines in Fig. 6.

7 Formulation for Imperfect Bonding

In the previous solutions it is assumed that there is a perfect bond between the reinforcement and the cracked region, but the effects of imperfect bonding may be modeled by changing the boundary conditions to be satisfied at the interface. A variety of models may be used to simulate the effects of imperfect bonding, but the model used here assumes that the interface cannot support a shear stress but can transmit both tensile and compressive normal stresses. The x-components of displacement are assumed to be continuous across the interface, but the y-components are not. These assumptions allow use of the first two integral equations for the problem with perfect bonding, and a new equation results from the assumption of zero shear stress at the interface. The system of integral equations for this problem is:

$$
\begin{aligned}
-1 &= P(\eta) + \int_0^\infty 2S(\xi)A_{22}(\eta,0,\xi)d\xi \\
&\quad - \int_0^\infty 2T(\xi)D_{22}(\eta,0,\xi)d\xi \qquad 0 \le \eta < a \\
0 &= \int_0^a P(\xi)V_1(\xi,\eta)d\xi + \int_0^\infty 2S(\xi)W_1(\eta,\xi)d\xi \\
&\quad + \int_0^\infty 2T(\xi)Z_1(\eta,\xi)d\xi \qquad 0 \le \eta < \infty, \\
0 &= T(\eta) + \int_0^a P(\xi)[F_{12}(c,\eta,\xi) + F_{12}(c,\eta,-\xi)]d\xi \\
&\quad 0 \le \eta < \infty. \qquad (38)
\end{aligned}
$$

The function used in the integrals above are the same as defined for the problem with perfect bonding.

The last equation may be used to eliminate $T(\xi)$ from the first two integral equations to leave:

$$
\begin{aligned}
-1 &= P(\eta) + \int_0^\infty 2S(\xi)A_{22}(\eta,0,\xi)d\xi \\
&\quad + \int_0^\infty 2D_{22}(\eta,0,\zeta)\int_0^a P(\xi)[F_{12}(c,\zeta,\xi) \\
&\quad + F_{12}(c,\zeta,-\xi)]d\xi d\zeta \qquad 0 \le \eta < a, \\
0 &= \int_0^a P(\xi)V_1(\xi,\eta)d\xi + \int_0^\infty 2S(\xi)W_1(\eta,\xi)d\xi \\
&\quad - \int_0^\infty 2Z_1(\eta,\zeta)\int_0^a P(\xi)[F_{12}(c,\zeta,\xi) \\
&\quad + F_{12}(c,\zeta,-\xi)]d\xi d\zeta \qquad 0 \le \eta < \infty. \qquad (39)
\end{aligned}
$$

Making the definitions:

$$
\begin{aligned}
P_1(\eta) &= P(\eta) + \int_0^\infty 2D_{22}(\eta,0,\zeta)\int_0^a P(\xi)[F_{12}(c,\zeta,\xi) \\
&\quad + F_{12}(c,\zeta,-\xi)]d\xi d\zeta, \\
P_2(\eta) &= \int_0^a P(\xi)X(\eta,\xi)d\xi, \\
S_1(\eta) &= \int_0^\infty 2S(\xi)A_{22}(\eta,0,\xi)d\xi, \\
S_2(\eta) &= \int_0^\infty 2S(\xi)W_1(\eta,\xi)d\xi, \qquad (40)
\end{aligned}
$$

where

$$
\begin{aligned}
X(\eta,\xi) &= V_1(\xi,\eta) - \int_0^\infty 2Z_1(\eta,\zeta)[F_{12}(c,\zeta,\xi) \\
&\quad + F_{12}(c,\zeta,-\xi)]d\zeta, \qquad (41)
\end{aligned}
$$

allows the integral equations to be written as:

$$
\begin{aligned}
-1 &= P_1(\eta) + S_1(\eta) \qquad 0 \le \eta < a, \\
0 &= P_2(\eta) + S_2(\eta) \qquad 0 \le \eta < \infty. \qquad (42)
\end{aligned}
$$

When solved the same way as before, $T(\eta)$ is found from $P(\eta)$ by using the condition of zero shear stress at the interface.

8 Numerical Results With Imperfect Bonding

The stress intensity factors for the imperfect bond problem

Downloaded 03 May 2010 to 171.66.16.248. Redistribution subject to ASME license or copyright; see http://www.asme.org/terms/Terms_Use.cfm

fall between those for a crack in a free strip and for collinear cracks spaced as if there were no reinforcement region. As the reinforcement stiffness goes to infinity or the reinforcement volume fraction goes to zero, the boundary conditions approach those for the collinear cracked plate and results in a lower bound on the stress intensity factor for the problem. An upper bound is the stress intensity for a centrally crack strip since a low stiffness of reinforcement or a large reinforcement volume fraction in conjunction with the zero shear stress condition results in the same boundary conditions as for a cracked strip with free edges. To demonstrate these bounds for the stress intensity factor in this problem, Fig. 14 shows some results for stress intensity factor versus crack length for a reinforcement with $\mu_2/\mu_1 = 10$ and $e/c = 0.1$. A further increase in reinforcement stiffness would move the stress intensity curve closer to the lower bound.

Stress fields are not plotted around the cracked region for this problem since there would be little difference from the plots for the collinear crack problem. As shown in Fig. 15, the stresses in the reinforcement are greatly reduced by the imperfect bond. These plots may be compared to those of Fig. 13 where the bond is assumed perfect. The shapes of the contours are not even similar, and the magnitudes of the stresses have a significant difference. For the imperfect bond problem, any stress in the reinforcement is due to a transfer of normal stress at the interface. The σ_{22} stress contours are similar to those seen in a rectangular beam in bending, indicating that bending of the reinforcement may be the origin of much of the σ_{22} stress. The results demonstrate that the shear stress at the interface is the dominant means of stress transfer for the perfectly bonded reinforcement.

Acknowledgment

This work was supported by the Army Research Office through the University Research Initiative program at the Center for Composite Materials of the University of Delaware.

References

Filon, L. N. G., 1903, "On an Approximate Solution for the Bending of a Beam of Rectangular Cross-Section under any System of Load, with Special Reference to Points of Concentrated or Discontinuous Loading," *Phil. Trans. Roy. Soc.*, Vol. 201, pp. 63–155.

Fowser, S. W., 1988, "Boundary Integral Modeling of Fiber-Crack Interactions," Ph.D. Dissertation, University of Delaware, Newark, Del.

Fowser, S. W., and Chou, Tsu-Wei, 1989, "Simplified Green's Functions for Mode I and II Cracks," *Int. J. Fracture,* Vol. 39, pp. 301–321.

Fowser, S. W., and Chou, Tsu-Wei, 1990, "Numerical Integration of Green's Functions for an Edge-Loaded Infinite Strip," submitted for publication.

Rudolphi, T. J., and Ashbaugh, N. E., "An Integral-Equation Solution for Bounded Elastic Body Containing a Crack: Mode I Deformation," *Int. J. Fracture,* Vol. 49, 1978, pp. 527–541.

Westergaard, H. M., 1939, "Bearing Pressures and Cracks," ASME JOURNAL OF APPLIED MECHANICS, Vol. 61, pp. A49–A53.

Downloaded 03 May 2010 to 171.66.16.248. Redistribution subject to ASME license or copyright; see http://www.asme.org/terms/Terms_Use.cfm

A New Approach to Microbuckling of Fibrous Composites

Dimitris C. Lagoudas
Assistant Professor,
Mem. ASME

Iradj Tadjbakhsh
Professor,
Fellow ASME

Nabil Fares
Research Assistant Professor.

Department of Civil Engineering,
Rensselaer Polytechnic Institute,
Troy, NY 12180

A new approach for the evaluation of the compressive strength of fibrous composites due to microbuckling is considered in this paper. Most of the proposed models, thus far, have tried to improve on the classical analysis by Rosen regarding both phases as separate continua with appropriate interface conditions. In this work the fibrous composite is represented by an inhomogeneous two-dimensional continuum with spatial variation in the axial Young's modulus to account for fibers and matrix. The periodicity of the microstructure is taken into account by expanding the axial Young's modulus in a Fourier series with wavelength the average spacing between fibers. The compressive strength is determined by examining the stability of small perturbations superimposed on a uniform applied compressive strain. It is found that the compressive strength depends on the wavelength of initial imperfections and bound estimates for minimum and maximum imperfection sizes are derived. The upper bound corresponds to perfectly aligned fibers without any imperfections and coincides with Rosen's prediction of the compressive strength, while the lower bound corresponds to the more realistic case of imperfect systems and correlates well with experimental data.

Introduction

Microbuckling of fibers in composites was first observed by Dow and Gruntfest (1960) and later analyzed by Schuerch (1964) and independently by Rosen (1965) with similar results. The well-known Rosen model considers a two-dimensional array of layers of fibers bonded to an elastic matrix. Two possible modes of microbuckling were assumed: a shear mode (all fibers and matrix layers have in-phase deformed shapes) and an extensional mode (every other fiber and every other matrix layer have in-phase deformed shapes). As Fig. 1 also shows, the shear mode involves antisymmetric shapes about the center lines of both fibers and matrix, while in the extensional mode the fibers undergo antisymmetric deformations and the matrix layers undergo symmetric deformations about their center lines. The compressive strength was found by utilizing the energy method and by considering only the strain energy due to bending in the fibers and the strain energy due to shear or extension in the matrix for the shear and extensional modes, respectively. The most important result of Rosen's analysis is that for fiber volume fractions >20 percent the shear buckling mode is predicted and the compressive strength has the simple evaluation $\sigma_c^s = G_m/c_m$, where c_m is the matrix volume fraction. Kulkarni et al. (1975) derive the expression $\sigma_c^s = G_m/(c_m + c_f G_m/G_f)$ and they observe that it is the Reuss estimate of the longitudinal shear modulus of a composite. The same conclusion was derived by Greszczuk (1982) who equated the compressive strength directly with the effective longitudinal shear modulus of the composite.

The experiments that followed Rosen's analysis consistently found compressive strengths much lower than the ones predicted by the model. Many possible explanations were suggested that triggered numerous extensions to the simple analysis of Rosen. Schuerch (1966) conducted experiments on boron/magnesium composite laminates and suggested modifications that accounted for matrix yielding (Schuerch interpreted the matrix shear modulus as the tangent shear modulus of the elastoplastic matrix). Lager and June (1969) suggested a knockdown factor of 0.63 which made Rosen's model predictions fit their experimental data on boron/epoxy laminates.

A more sophisticated modeling of a two-dimensional array of unidirectional equally spaced fibers in an elastic foundation was done by Chung and Testa (1969), Maewal (1981), and Steif (1987), among others. Chung and Testa treated the fibers as beams and the matrix as a two-dimensional elastic medium, whereas Maewal and Steif modeled the fibers as well as the matrix as a two-dimensional medium. A two-dimensional analysis that takes into account the free boundaries was recently done by Waas et al. (1990), predicting lower critical compressive stress values for small fiber volume fractions than Rosen's model. Three-dimensional modeling was independently done by Sadowsky et al. (1967) and Herrmann et al. (1967). Both groups of researchers modeled the fiber as a beam column coupled to a three-dimensional elastic medium.

In this paper we regard the fibrous composite as a two-dimensional inhomogeneous material with periodic spatial var-

Contributed by the Applied Mechanics Division of THE AMERICAN SOCIETY OF MECHANICAL ENGINEERS for presentation at the Joint Applied Mechanics/Bioengineering Conference, Ohio State University, Columbus, Ohio, June 16–19, 1991.

Discussion on this paper should be addressed to the Technical Editor, Prof. Leon M. Keer, The Technological Institute, Northwestern University, Evanston, IL 60208, and will be accepted until two months after final publication of the paper itself in the JOURNAL OF APPLIED MECHANICS. Manuscript received by the ASME Applied Mechanics Division, June 29, 1990; final revision, Nov. 19, 1990.

Paper No. 91-APM-16.

Copyright © 1991 by ASME
Downloaded 03 May 2010 to 171.66.16.248. Redistribution subject to ASME license or copyright; see http://www.asme.org/terms/Terms_Use.cfm

iation of the elastic moduli to represent fibers and the matrix. Buckling strength is determined on the basis of stability of small deformations superimposed on the state of the finitely deformed body due to a uniformly imposed compressive strain. Our results include, as a first approximation, Rosen's (1965) prediction of buckling strength, and to higher order the correlation that exists between strengths and the wavelengths of the imperfections, substantially improving Rosen's analysis.

Two-Dimensional In-Plane Buckling Analysis of Layered Elastic Media

Let X_J, $J=1, 2$ be the cartesian coordinate frame of the reference configuration of a two-dimensional elastic solid. Assume an initially applied linear displacement field $u_1=0$, $u_2=-aX_2$ (a is a constant), which corresponds to uniform strain and for a homogeneous elastic material to uniform stress (Fig. 1). If a small perturbation is superimposed, the total displacement field has the form

$$u_1=\epsilon U_1(X_1,X_2)e^{i\omega t},\ u_2=-aX_2+\epsilon U_2(X_1,X_2)e^{i\omega t}, \quad (1)$$

where ϵ is a small parameter. Based on the above deformation, the Green-Lagrange strain has the explicit evaluation

$$E_{11}=[\epsilon U_{1,1}+\epsilon^2(U_{1,1}^2+U_{2,1}^2)/2]e^{i\omega t},$$

$$E_{22}=-a+a^2/2+[\epsilon(1-a)U_{2,2}+\epsilon^2(U_{1,2}^2+U_{2,2}^2)/2]e^{i\omega t},$$

$$2E_{12}=\{\epsilon[U_{1,2}+(1-a)U_{2,1}]+\epsilon^2(U_{1,1}U_{1,2}+U_{2,1}U_{2,2})\}e^{i\omega t}, \quad (2)$$

where a comma between subscripts denotes partial differentiation. The zeroth-order term of the strain, $E_{22}^0=-a+a^2/2$, determines the loading parameter $b\equiv -E_{22}^0=a-a^2/2$, and for $0\le a<1$ we have $a=1-\sqrt{(1-2b)}$, $0\le b<1/2$.

It is natural to connect the Green-Lagrange strain with the second Piola-Kirchhoff stress tensor through an appropriate constitutive law. For linear finite elastic behavior Hooke's law for an orthotropic two-dimensional elastic medium has the form

$$\sigma_{11}=E_TE_{11}+\nu E_TE_{22},$$

$$\sigma_{22}=\nu E_TE_{11}+E_AE_{22},$$

$$\sigma_{12}=2GE_{12}. \quad (3)$$

In the above, σ_{IJ} denotes the second Piola-Kirchhoff stress tensor, and E_A, E_T, G, and ν are the four independent material parameters for an orthotropic two-dimensional linear elastic solid. E_A represents the axial Young's modulus in X_2-direction, E_T is the transverse Young's modulus measuring the stiffness in X_1-direction, G is the in-plane (longitudinal) shear modulus, and ν is equal to Poisson's ratio ν_{21}, namely $\nu=-E_{11}/E_{22}$ for a uniaxial extension test in the X_2-direction. If we consider E_A, E_T, G, and ν to be the effective overall properties of a fibrous composite, they are all constant and carry no information about the periodic inhomogeneity of the microstructure.

To successfully model microbuckling of a unidirectional fibrous composite with periodically placed fibers, as shown in Fig. 1(*a*), the essential features of the microstructure should be taken into account. An important aspect of the microstructure is the average spacing between fibers, $2h$, which introduces a characteristic length. All material parameters are periodic functions of X_1, of period $2h$. For compressive loads applied in the axial direction, the X_1-dependence of the axial Young's modulus is of particular importance. We therefore assume in the following that *all elastic material moduli are constant and equal to the effective properties, except for the axial Young modulus which is taken to be a periodic function of* X_1, *namely* $E_A(X_1)=E_A(X_1+2h)$. For a unidirectional fibrous composite, therefore, $E_A(X_1)$ represents the exact variation of the axial Young's modulus, E_T is the effective transverse Young's modulus, G is the effective longitudinal shear modulus, and ν the effective axial Poisson's ratio.

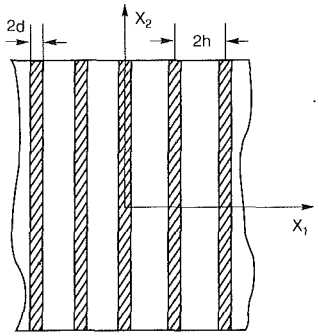

Fig. 1(*a*) A two-dimensional periodic dispersion of fibers

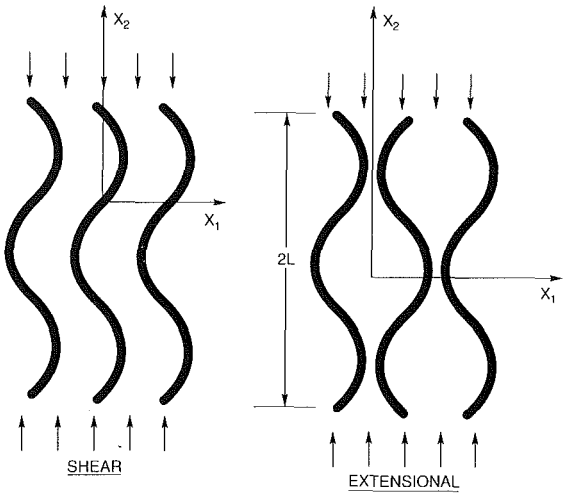

Fig. 1(*b*) In-plane buckling modes

The two-dimensional constitutive description given by (3) represents the idealization of a three-dimensional continuum under plane conditions. To model a thin layered composite under plane stress, we must multiply E_A and E_T by $(1-E_T/E_A\nu^2)^{-1}$, which approaches unity as E_T/E_A goes to zero. To model a thick layered composite under plane-strain conditions, E_T has to be replaced by E_Tf, where

$$f=E_A(1-E_T/E_A\nu^2)/[E_A(1-\nu_T^2)(1-E_T/E_A\nu^2)-E_T\nu^2(1+\nu_T)^2],$$

E_A must be replaced by $E_A(1-\nu_T^2)f/(1-E_T/E_A\nu^2)$ and ν by $\nu(1+\nu_T)/(1-E_T/E_A\nu^2)$. Notice that ν is the axial Poisson's ratio, $\nu=\nu_{21}$, while $\nu_T=\nu_{31}$ is the transverse Poisson's ratio, considering a general transversely isotropic material in three-dimensions. As the ratio E_T/E_A becomes very small, $f\to 1/(1-\nu_T^2)$, E_T is replaced by $E_T/(1-\nu_T^2)$, ν is replaced by $\nu(1+\nu_T)$, and E_A stays the same.

Using the Lagrangian description, in the absence of body forces, the equations of motion can be written as

$$\partial_J\sigma_{JK}(\partial_Ku_i+\delta_{Ki})+\sigma_{Jk}\partial_J\partial_Ku_i=\rho_0\partial_t^2u_i,\ i,J,K=1,2, \quad (4)$$

where the displacement field, u_i, and the second Piola-Kirchhoff stress, σ_{JK}, are functions of the reference space coordinates, X_J, and time, t; $\partial_J\equiv\partial/\partial X_J$, $\partial_t\equiv\partial/\partial t$ denote partial differentiation over the reference spatial configuration and time, respectively; ρ_0 denotes the mass density per unit undeformed volume. The left-hand side terms of the equations of motion derive from expanding the divergence of the first Piola-Kirchhoff stress tensor, namely, $\partial_J(\sigma_{Ji})=\partial_J(\sigma_{JK}\partial_Kx_i)$, where $x_i=u_i+X_K\delta_{Ki}$ is the deformation field (δ_{Ki} is Kronecker's delta). Retaining the nonlinear terms (geometric nonlinearity) in the equations of motion is crucial in obtaining nontrivial in-plane buckling modes. If we use the constitutive equations

Downloaded 03 May 2010 to 171.66.16.248. Redistribution subject to ASME license or copyright; see http://www.asme.org/terms/Terms_Use.cfm

(3) in combination with the expansion for the Green-Lagrange strains given by (2), the equations of motion reduce to ordered polynomials in powers of ϵ. Equating the coefficients of same powers of ϵ, it is easily deduced that the zeroth order equations of motion are identically satisfied, while the first-order equations take the form

$$U_{1,11}(1-\nu b)+U_{1,22}(k-eb)+U_{2,12}\sqrt{1-2b}(k+\nu)=-\eta^2 U_1$$
$$U_{2,11}[k(1-2b)-\nu b]+U_{2,22}e(1-3b)+U_{1,12}\sqrt{1-2b}(k+\nu)=-\eta^2 U_2. \quad (5)$$

The nondimensional quantities appearing in the above equations are the normalized axial Young's modulus, $e(X_1)\equiv E_A(X_1)/E_T$, the normalized shear modulus, $k\equiv G/E_T$, and frequency, $\eta=\omega/\sqrt{(E_T/\rho_0)}$. Notice that the terms that include $e(X_1)$ do not involve derivatives with respect to X_1 and as a result there are no derivatives of e present in the above equations. On the other hand, if ν or k were allowed to depend on X_1, their derivatives would appear in equations (5).

Shear Buckling Mode. The shear buckling mode is associated with predominant shear deformations of material elements in the matrix. We seek a solution of (5) that is harmonic in X_2 with an undetermined wavelength and has a Fourier series representation in X_1-direction. Such a solution is given by

$$U_1=\sum_{m=0}^{\infty}A_m\cos(\alpha_m X_1)\sin(\beta X_2)e^{i\omega t},$$
$$U_2=\sum_{m=1}^{\infty}B_m\sin(\alpha_m X_1)\cos(\beta X_2)e^{i\omega t}. \quad (6)$$

The X_2-direction coincides with the symmetry axis of the fibers (Fig. 1(*b*)), the X_1-direction is transverse to fiber direction and the width of the unit cell is assumed to be equal to $2h$. The symmetry properties of the above equations, namely $U_1(-X_1)=U_1(X_1)$ and $U_2(-X_1)=-U_2(X_1)$, justify naming the above displacements as the shear buckling mode. The spatial wave number α_m is defined by the periodicity of the microstructure, $2h$, and is given by $\alpha_m=m\pi/h$, while β is given by $\beta=\pi/L$, where $2L$ may be interpreted as the wavelength of imperfections in X_2-direction. The parameter L will be allowed to vary arbitrarily in order to determine the stability boundaries of the loading parameter b.

Substituting the modal shapes represented by equations (6) into the equations of motion (5) we derive, after some algebra and using the orthogonality properties of the sin and cos functions, a set of algebraic equations for the unknown coefficients A_0, A_j, and B_j, $j=1, 2, \ldots$. If we define $\gamma\equiv\alpha_1/\beta=L/h$ to be the ratio of the size of imperfections over the fiber spacing, and $\hat{\eta}\equiv\eta/\beta$, these algebraic equations become

$$[(1-\nu b)\gamma^2 j^2+k-\hat{\eta}^2]A_j-\sum_{m=0}^{\infty}b\left(1-\frac{1}{2}\delta_{j0}\right)Q^c_{mj}A_m+(k+\nu)\sqrt{(1-2b)}\gamma jB_j=0,\quad j=0,1,2,\ldots$$
$$[(k-2kb-\nu b)\gamma^2 j^2-\hat{\eta}^2]B_j+\sum_{m=1}^{\infty}(1-3b)Q^s_{mj}B_m+(k+\nu)\sqrt{(1-2b)}\gamma jA_j=0\quad j=1,2,\ldots. \quad (7)$$

The symbol δ_{j0} takes the value 1 whenever $j=0$, and is zero otherwise. The definition of the coefficients Q^c_{mj} and Q^s_{mj} is given in Appendix A by equations (A1) and (A2). If the known function $e(X_1)$ is expanded in a Fourier cosine series, given by equation (A3), the coefficients Q^c_{mj} and Q^s_{mj} can be expressed in terms of the known Fourier coefficients e_k of $e(X_1)$ as shown by equations (A5) and (A7). The homogeneous algebraic system (7) has a nontrivial solution for A_j and B_j provided that its determinant (of infinite dimension) vanishes. The simplest possible case involves only A_0 and the resulting condition is

$$A_0(2k-be_0-\hat{\eta}^2)=0. \quad (8)$$

For the next higher-order approximations, we assume that A_0, A_1, and B_1 are the nonzero coefficients in the Fourier series expansion of the displacement field. Equations (7) reduce to the following algebraic system:

$$\begin{bmatrix} 2k-be_0-\hat{\eta}^2 & -be_1 & 0 \\ -be_1 & (1-\nu b)\gamma^2+k-b(e_0+e_2)/2-\hat{\eta}^2 & (k+\nu)\sqrt{(1-2b)}\gamma \\ 0 & (k+\nu)\sqrt{(1-2b)}\gamma & (k-2kb-\nu b)\gamma^2+(1-3b)(e_0-e_2)/2-\hat{\eta}^2 \end{bmatrix}\begin{bmatrix} A_0 \\ A_1 \\ B_1 \end{bmatrix}=\begin{bmatrix} 0 \\ 0 \\ 0 \end{bmatrix}. \quad (9)$$

Notice that a truncation of the Fourier series implies a Galerkin-type approximation. The selection of the coefficients A_j, B_j is optimized so that equilibrium is best satisfied, within the functional space spanned by the finite number of base functions chosen. For the above case of three coefficients, A_0, A_1, B_1, the basis for the functional space consists of $\sin(\beta X_2)$, $\cos(\alpha_1 X_1)\sin(\beta X_2)$ and $\sin(\alpha_1 X_1)\cos(\beta X_2)$.

Extensional Buckling Mode. The extensional mode is the one associated with relative extension of material elements in the matrix phase and it can be modeled by a perturbation to the displacement field of the form

$$U_1=\sum_{m=1}^{\infty}A_m\sin(\alpha_m X_1)\cos(\beta X_2)e^{i\omega t},$$
$$U_2=\sum_{m=0}^{\infty}B_m\cos(\alpha_m X_1)\sin(\beta X_2)e^{i\omega t}. \quad (10)$$

The symmetry requirements for the extensional mode, namely $U_1(-X_1)=-U_1(X_1)$ and $U_2(-X_1)=U_2(X_1)$, are satisfied by the above selection of the perturbation to the displacement field. The wave number $\alpha_m=m\pi/2h$ is half compared with the similar one for the shear buckling mode, because the unit cell for the extensional mode has twice the size of the unit cell for the shear mode (Fig. 1(*b*)). Following a similar approach used for the analysis of the shear mode, the following results are obtained:

$$[(1-\nu b)\gamma^2 j^2+k-\hat{\eta}^2]A_j-\sum_{m=1}^{\infty}bQ^s_{mj}A_m+(k+\nu)\sqrt{(1-2b)}\gamma jB_j=0,\ j=1,2,\ldots$$
$$[(k-2kb-\nu b)\gamma^2 j^2-\hat{\eta}^2]B_j+\sum_{m=0}^{\infty}(1-3b)Q^c_{mj}B_m+(k+\nu)\sqrt{(1-2b)}\gamma jA_j=0,\ j=0,1,2,\ldots. \quad (11)$$

In the above equations the coefficients Q^c_{mj} and Q^s_{mj} are the same as the ones for the shear buckling mode. As in the shear mode, various levels of approximation can be constructed by selecting the number of coefficients A_j and B_j in the representation for the displacement field. The simplest approximation corresponds to $j=0$, in which case

$$B_0[e_0(1-3b)-\hat{\eta}^2]=0. \quad (12)$$

The next order of approximation involves three nonzero coefficients, A_1, B_0, B_1, which satisfy the following algebraic system

Downloaded 03 May 2010 to 171.66.16.248. Redistribution subject to ASME license or copyright; see http://www.asme.org/terms/Terms_Use.cfm

$$\begin{bmatrix} e_0(1-3b)-\hat{\eta}^2 & e_1(1-3b) & 0 \\ e_1(1-3b) & (k-2b-\nu b)\gamma^2+\frac{1}{2}(e_0+e_2)(1-3b)-\hat{\eta}^2 & (k+\nu)\sqrt{(1-2b)}\gamma \\ 0 & (k+\nu)\sqrt{(1-2b)}\gamma & (1-\nu b)\gamma^2+k\frac{b}{2}(e_0-e_2)/2-\hat{\eta}^2 \end{bmatrix} \begin{bmatrix} B_0 \\ B_1 \\ A_1 \end{bmatrix} = \begin{bmatrix} 0 \\ 0 \\ 0 \end{bmatrix}. \quad (13)$$

Compressive Strength

To proceed with a critical compressive load evaluation, we assume a piecewise constant function $e(X_1)$ representing the normalized axial stiffness of the fiber and matrix. The explicit evaluation of the Fourier coefficients e_k is given in Appendix B for the shear and the extensional modes. The main difference in evaluating e_k for the two modes is the size of the unit cell, which coincides with the periodicity of the displacement field in the X_1-direction. The X_1-wavelength for the extensional mode is twice the X_1-wavelength for the shear mode which is equal to the average distance, $2h$, between fibers. The coefficient $e_0/2$ is the average of $e(X_1)$ for both modes and is given by (B2) or its equivalent (B4). The different higher-order coefficients, given by (B3) and (B4) for the two modes, respectively, are proportional to the difference of the fiber and matrix Young's moduli ($r_f - r_m = (E_f - E_m)/E_T$) and they all vanish for $E_f = E_m$.

Shear Buckling Mode. A nontrivial solution to the algebraic system (7) for the amplitudes A_0, A_j, B_j, j, $n = 1, 2, \ldots$, will allow nonzero perturbations to the homogeneous deformation field. The necessary condition for a nontrivial solution is the vanishing of the determinant of the matrix formed by the coefficients of the unknown amplitudes. For the simple case of only A_0 being nonzero, equation (8) requires that the frequency be determined by $\hat{\eta}^2 = 2k - be_0$ and in order for $\hat{\eta}^2$ to be positive

$$b < b_c^s = \frac{2k}{e_0} = \frac{G}{c_f E_f + c_m E_m} \cong \frac{G_m}{E_f c_f (1-c_f)}, \quad (14)$$

where b_c^s denotes the critical strain for the shear buckling mode to develop. If the imposed strain b remains below b_c^s, small perturbations to the homogeneous solution will remain oscillatory in nature, according to equation (1), because $\hat{\eta}$, and consequently ω, will be real. If the imposed strain increases beyond b_c^s, $\hat{\eta}^2$ becomes negative and, as a result, ω becomes imaginary giving rise to solutions growing with time. Inhomogeneities, fiber waviness or other types of imperfections might then cause small deviations from the homogeneous solution to become unstable. The approximate result in (14) is derived by assuming that $c_f E_f + c_m E_m \cong c_f E_f$, $1/G \cong c_f/G_f + c_m/G_m \simeq c_m/G_m$, $(c_m = 1 - c_f)$. Notice that it coincides with Rosen's result for compressive strength of fibrous composites due to fiber microbuckling in the shear mode (Rosen (1965), Rosen's analysis is also summarized in Jones's (1975) book).

To improve the above simple estimate, the next order approximation will be considered with A_0, A_1, and B_1 being the nonzero coefficients. The resulting algebraic system is given by (9). The requirement that the determinant D of the 3×3 coefficient matrix should vanish results in a quadratic equation for γ^2 with coefficients being cubic polynomials in b. Explicitly the determinant D has the evaluation

$$D = C_1\gamma^4 + C_2\gamma^2 + C_3 + \hat{\eta}^2(-C_4 + C_5\hat{\eta}^2 - \hat{\eta}^4), \quad (15)$$

with $\Delta(\gamma, b) = C_1\gamma^4 + C_2\gamma^2 + C_3$ being the determinant for the static problem ($\hat{\eta}^2 = 0$). The coefficients C_i, $i = 1, \ldots, 5$, are given in Appendix C. The cross-section of the surface $\Delta(\gamma, b)$ with the plane $\Delta = 0$ are the lines shown in Fig. 2 for various fiber volume fractions, c_f, for a fiberglass-epoxy system. Each curve corresponds to the smallest root b of $\Delta(\gamma, b) = 0$ for given γ, partitioning the γ-b plane into two regions, one for which Δ is positive and the other for which Δ is negative. As b crosses the boundary and Δ changes sign, $\hat{\eta}^2$ must also change sign so that the total determinant D remains zero. A change in sign of $\hat{\eta}^2$ will result in a transition from oscillatory to time growing solutions. It is noted that the minimum value of b occurs at $\gamma = 0$ and that b increases monotonically toward an asymptotic value as $\gamma \to \infty$. Thus, the limits of b as $\gamma \to 0$ and $\gamma \to \infty$ yield, respectively, a lower bound and an upper bound for b values for which divergence instability is possible.

To test the accuracy of the 3×3 determinant approximation we evaluated b_c^s for various γ for higher order approximations, namely considering A_0, A_1, A_2, B_1, B_2 to be the nonzero amplitudes (5×5 determinant) and also A_0, A_1, A_2, A_3, A_4, A_5, B_1, B_2, B_3, B_4, B_5 to be the nonzero amplitudes (9×9 determinant). The characteristic equation results in a polynomial of 8th degree in γ for the first case and 20th degree in γ for the second case. The smallest positive root b of the determinant for given γ (which is evaluated using the LU decomposition) is found numerically by the bisection method. Since the difference in b_c^s evaluated by the 3×3, 5×5, and 9×9 systems has been found to be very small, we will concentrate on the 3×3 system (9), for which there is an explicit expression for $\gamma(b)$ (the solution to a quadratic equation for γ^2).

A given characteristic length $2L$ introduced by the spacing of the imperfections determines a critical strain $b_c^s(\gamma)$ for the shear buckling mode as shown in Fig. 2. It is of interest to note that as the number of imperfections increases, the critical strain decreases reaching its minimum value $b_c^s(0)$. There is also an asymptotic value for the critical strain as $\gamma \to \infty$, namely the spacing of the imperfections becomes infinite, which is the maximum critical strain valid for carefully manufactured composites (Fig. 2). The value of the critical strain in the limit $\gamma \to \infty$ can be easily found by vanishing the term multiplying γ^4 in the characteristic equation, $\Delta(\gamma, b) = 0$. It is observed from (C1) and (C2) that $C_1 = (2k - be_0)(1 - \nu b)(k - 2kb - \nu b)$, and the smallest value of b that makes C_1 vanish is $(b_c^s)_{\max} = 2k/e_0$. This is exactly the zeroth-order estimate of the critical strain given by (14). The value of the critical strain in the limit $\gamma \to 0$ can be obtained from the condition $C_3 = 0$. The two limits are given below:

$$(b_c^s)_{\min} \equiv \lim_{\gamma\to 0}(b_c^s) = \frac{2k}{e_0}\frac{2e_0 + e_2 - \sqrt{(e_2^2 + 8e_1^2)}}{2(e_0 + e_2 - 2e_1^2/e_0)} = (b_c^s)_{\max}$$

$$\times \frac{2\pi(c_f E_f + c_m E_m) + (E_f - E_m)\sin(\pi c_f)[\cos(\pi c_f) - \sqrt{(\cos^2(\pi c_f) + 8)}]}{2\pi(c_f E_f + c_m E_m) + (E_f - E_m)\sin(\pi c_f)\left[2\cos(\pi c_f) - \frac{4}{\pi}(E_f - E_m)\sin(\pi c_f)/(c_f E_f + c_m E_m)\right]}$$

$$(b_c^s)_{\max} \equiv \lim_{\gamma\to\infty}(b_c^s) = \frac{2k}{e_0} = \frac{G}{c_f E_f + c_m E_m}. \quad (16)$$

Extensional Buckling Mode. The above procedure that has been developed for the shear mode can be applied in a similar way for the extensional mode. For the simplest estimate, corresponding to only $B_0 \neq 0$, b_c^e turns out to be 1/3 as can be seen

Downloaded 03 May 2010 to 171.66.16.248. Redistribution subject to ASME license or copyright; see http://www.asme.org/terms/Terms_Use.cfm

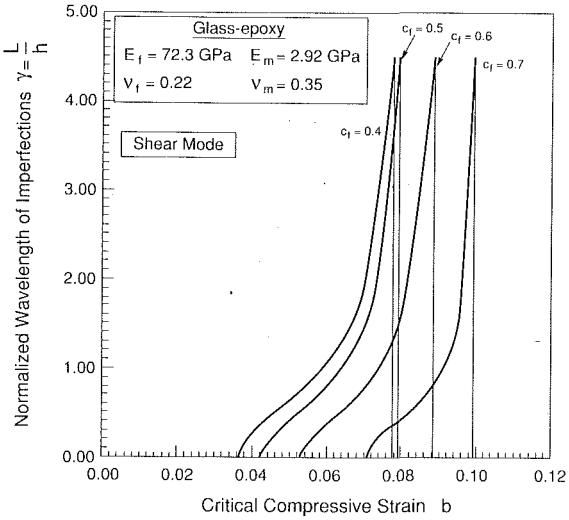

Fig. 2 Critical compressive strains predicted by the shear mode as a function of the wavelength of imperfections for various fiber volume fractions

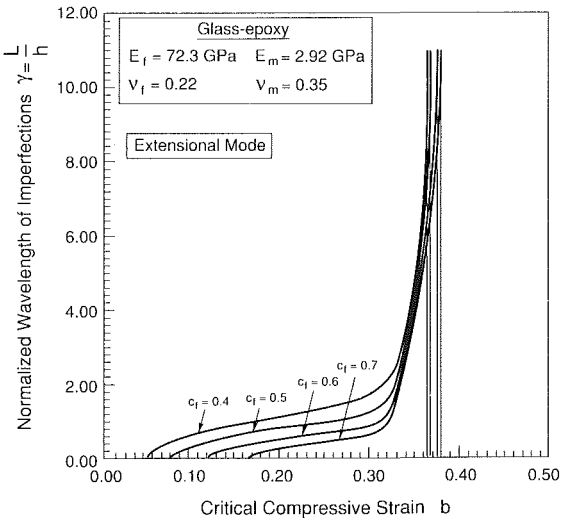

Fig. 3 Critical compressive strains predicted by the extensional mode as a function of the wavelength of imperfections for various fiber volume fractions

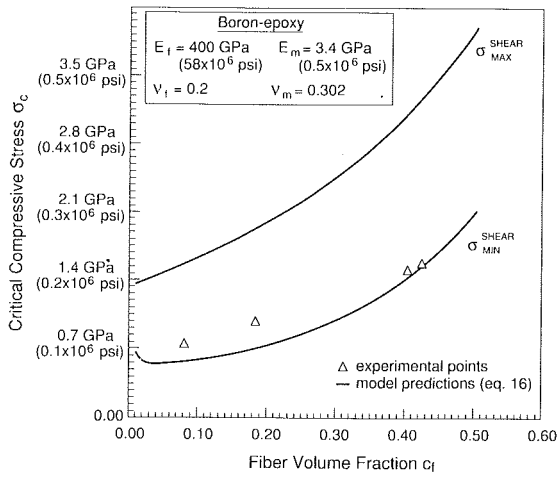

Fig. 4 Critical compressive stress for a boron-epoxy fibrous composite; comparison with the experimental results of Lager and June (1969)

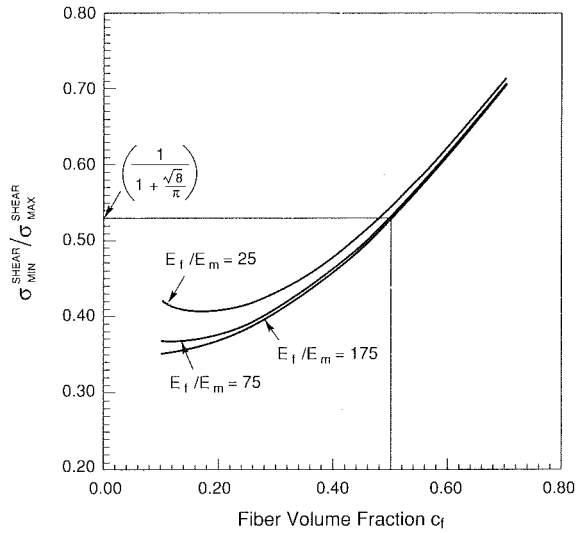

Fig. 5 Ratio of minimum compressive strength over the maximum compressive strength (Rosen's result) as a function of fiber volume fraction for various values of E_f/E_m

from (12). The asymptotic results for $\gamma \to 0$ and $\gamma \to \infty$, which obtain from the 3×3 system (13), are given by

$$(b_c^e)_{\min} \equiv \lim_{\gamma \to \infty} (b_c^e) = \frac{2k}{e_0 - e_2} = \frac{G}{c_f E_f + c_m E_m + (E_f - E_m)\sin(2\pi c_f)/\pi},$$

$$(b_c^e)_{\max} \equiv \lim_{\gamma \to \infty} (b_c^e) = \frac{k}{2k+\nu} = \frac{G}{2G+E_T}, \tag{17}$$

provided that $b < 1/3$. The term $(1-3b)$ factors out in the evaluation of the determinant of the 3×3 system (13) and this makes the value $b = 1/3$ to be the upper limit in the compressive strength evaluation for the extensional mode (from the physical standpoint this is an unacceptable high value of compressive strain for an elastic system).

Selected Results

To be able to calculate the dependence of the volume fraction on the critical strain, the effective properties should be known for different values of c_f, either experimentally measured or theoretically estimated from the phase properties. For the present study the effective properties have been estimated using the Mori-Tanaka averaging scheme (Mori and Tanaka (1973), Weng (1984)). The critical strain is plotted as a function of $\gamma \equiv L/h$ for various values of c_f in Fig. 2 for phase properties given in the figure. For the extensional mode similar results are plotted in Fig. 3 using the 3×3 system and the Mori-Tanaka method for the evaluation of the effective properties (as mentioned earlier, for values of b_c^e larger than 1/3, $b_c^e = 1/3$ should be taken as the compressive strength). A comparison between the compressive strain for the shear and extensional modes can be deduced from Figs. 2 and 3 for the glass-epoxy system as a function of the fiber volume fraction c_f. It is found that the extensional mode requires higher strains to occur and therefore is not the preferable buckling mode for any volume fraction.

Many experiments have been conducted to verify the critical compressive stress predicted by Rosen's analysis. Consistently, it has been observed that it overestimates the experimentally measured results. Experiments on boron-epoxy conducted by Lager and June (1969) showed lower values of the measured compressive strength, and the authors proposed a reduction coefficient of 0.63 by which Rosen's results should be multiplied to fit the experiments. In Fig. 4 we reproduce a set of experimental results and the minimum and maximum compressive strengths predicted by our analysis, namely $(b_c^s)_{\max}$

Downloaded 03 May 2010 to 171.66.16.248. Redistribution subject to ASME license or copyright; see http://www.asme.org/terms/Terms_Use.cfm

and $(b_c^s)_{\min}$ from (16), the maximum also corresponding to Rosen's result. The good agreement with the minimum shear compressive strength indicates that initial imperfections might be important in initiating microbuckling, lowering the compressive strength towards the minimum value. The two curves depicted in Fig. 4 can, therefore, be considered as the lower and upper bounds for the compressive strength under the shear buckling mode.

The two systems studied thus far, with E_f/E_m ratio approximately 25 for the glass-epoxy system and about 100 for the boron-epoxy system, are typical for many fibrous composites. To investigate the influence of the stiffness ratio on the difference between the minimum and maximum compressive strengths in the shear mode, we plot in Fig. 5 the ratio $(\sigma_c^s)_{\min}/(\sigma_c^s)_{\max}$ from (16) as a function of c_f for various values of E_f/E_m. As observed from the figure, the limit $E_f/E_m \to \infty$ could be used as a good estimate for this ratio, especially at high-fiber volume fractions. For the special case of $c_f = 1/2$ and $E_f/E_m \to \infty$ the value of the ratio is $(1+\sqrt{8/\pi})^{-1} = 0.53$ and for values of c_f close to 1/2, we can use the tangent to the curve in Fig. 5 to estimate the ratio. An asymptotic expansion of equation (16), about $c_f = 1/2$, for the case $E_f/E_m \to \infty$, results in the following simple expression:

$$\frac{(b_c^s)_{\min}}{(b_c^s)_{\max}} \cong \left(1+\frac{\sqrt{8}}{\pi}\right)^{-1} + (c_f - 1/2)\left[1 - \frac{16}{\pi^2}\left(1+\frac{\sqrt{8}}{\pi}\right)^{-1}\right]\left(1-\frac{8}{\pi^2}\right)^{-1} = 0.14 + 0.78 c_f. \tag{18}$$

As an example, the approximate value predicted from the above equation for $c_f = 0.6$ is 0.61, while the exact value from equation (16) is 0.63 for the glass-epoxy system (it turns out that the exact value is identical with the experimental knockdown factor used by Lager and June (1969)). Recent direct compression experiments on carbon-thermoplastic composites with $c_f \cong 0.5$, conducted by Yurgartis (1987), suggest a knockdown factor of about 0.5, which also correlates well with (18). Since for most of the advanced composites the ratio E_f/E_m is larger than 25 and the volume fraction is about 0.5, it is reasonable to use the simplified equation (18) instead of (16) for the calculation of the knockdown factor. The asymptotic results, therefore, produce an accurate and simple estimate of the compressive strength, clearly improving Rosen's analysis by supplying the closer to experimental results lower bound for the compressive strength.

References

Chung, W., and Testa, R. B., 1969, "The Elastic Stability of Fibers in a Composite Plate," *J. Comp. Mat.*, Vol. 3, pp. 58–80.

Dow, N. F., and Gruntfest, I. J., 1960, "Determination of Most Needed, Potentially Possible Improvements in Materials for Ballistic and Space Vehicles," General Electric Company, Air Force Contract AF 04(647)-269.

Greszczuk, L. B., 1982, "On Failure Models of Unidirectional Composites under Compressive Loading," *Fracture of Composite Materials,* G. C. Sih and V. P. Tamuzs, eds., Martinus Nijhoff, The Hague, pp. 231–244.

Herrmann, L. R., Mason, W. E., and Chan, S. T. K., 1967, "Response of Reinforcing Wires to Compressive States of Stress," *J. Comp. Mat.*, Vol. 1, pp. 212–226.

Jones, R. M., 1975, *Mechanics of Composite Materials,* Hemisphere, New York.

Kulkarni, S. V., Rice, J. S., and Rosen, B. W., 1975, "An Investigation of the Compressive Strength of Kevlar 49/Epoxy Composites," *Composites,* Vol. 6, pp. 217–225.

Lager, J. R., and June, R. R., 1969, "Compressive Strength of Boron-Epoxy Composites," *J. Comp. Mat.*, Vol. 3, pp. 48–56.

Maewal, A., 1981, "Postbuckling Behavior of a Periodically Laminated Medium in Compression," *Int. J. Solids Structures,* Vol. 17, pp. 335–344.

Mori, T., and Tanaka, K., 1973, "Average Stress in Matrix and Average Energy of Materials with Misfitting Inclusions," *Acta Metall.*, Vol. 21, pp. 571–574.

Rosen, B. W., 1965, "Mechanics of Composite Strengthening," *Fiber Composite Materials,* American Society for Metals, Metals Park, Ohio, pp. 37–75.

Sadowsky, M. A., Pu, S. L., and Hussain, M. A., 1967, "Buckling of Microfibers," ASME JOURNAL OF APPLIED MECHANICS, Vol. 34, pp. 1011–1016.

Schuerch, H., 1964, "Boron Filament Composite Materials for Space Structures, Part I: Compressive Strength of Boron Metal Composites," *Report No. ARC-R-168,* Astro Research Corporation, Santa Barbara, Calif.

Schuerch, H., 1966, "Prediction of Compressive Strength in Uniaxial Boron Fiber-Metal Matrix Composite Materials," *AIAA Journal,* Vol. 4, pp. 102–106.

Steif, P. S., 1987, "An Exact Two-Dimensional Approach to Fiber-Microbuckling," *Int. J. Solids Structures,* Vol. 23, pp. 1235–1246.

Waas, A. M., Babcock, C. D., Jr., and Knauss, W. G., 1990, "A Mechanical Model for Elastic Fiber Microbuckling," ASME JOURNAL OF APPLIED MECHANICS, Vol. 57, pp. 138–149.

Weng, G. J., 1984, "Some Elastic Properties of Reinforced Solids, with Special Reference to Isotropic Ones Containing Spherical Inclusions," *Int. J. Engng. Sci.,* Vol. 22, pp. 845–856.

Yurgartis, S. W., 1987, "The Influence of Matrix Properties and Composite Microstructure on the Longitudinal Compression Strength of High Performance Composites," Ph.D. Thesis, Rensselaer Polytechnic Institute, Troy, N. Y.

APPENDIX A

The coefficients Q_{mj}^c and Q_{mj}^s have been defined by

$$Q_{mj}^c = \frac{2}{h}\int_0^h e(X_1)\cos(\alpha_m X_1)\cos(\alpha_j X_1)dX_1, \tag{A1}$$

$$Q_{mj}^s = \frac{2}{h}\int_0^h e(X_1)\sin(\alpha_m X_1)\sin(\alpha_j X_1)dX_1. \tag{A2}$$

The Fourier cosine series expansion for the symmetric function $e(X_1)$, which represents the variation in the Young's modulus for the two phases, is given by

$$e(X_1) = \frac{1}{2}e_0 + \sum_{k=1}^{\infty} e_k \cos(\alpha_k X_1). \tag{A3}$$

Substituting the above into (A1) and combining cosines to form products of orthogonal functions, we have the following result

$$Q_{mj}^c = \frac{e_0}{2}\delta_{mj} + \sum_{k=1}^{\infty}\frac{e_k}{h}\int_0^h \{\cos[(\alpha_m+\alpha_j)X_1] + \cos[(\alpha_m-\alpha_j)X_1]\}\cos(\alpha_k X_1)dX_1 = \frac{e_0}{2}\delta_{mj} + \sum_{k=1}^{\infty}\frac{e_k}{h}\left[\frac{h}{2}\delta_{(m+j)k} + \frac{h}{2}\delta_{|m-j|k}\right], \tag{A4}$$

where $\delta_{|m-j|k} = \delta_{(m-j)k}$ for $m > j$, $\delta_{|m-j|k} = \delta_{(j-m)k}$ for $m < j$ and $\delta_{|m-j|k} = 0$ for $m = j$. Using the properties of the Kronecker delta we can arrive at the simplified result

$$Q_{mj}^c = \frac{1}{2}(e_{m+j} + e_{|m-j|}),\ m, j = 0,1,2,\ldots. \tag{A5}$$

Similarly, if we start with (A2) and use (A3), we have the following evaluations

$$Q_m^s = \frac{e_0}{2}\delta_{mj} + \sum_{k=1}^{\infty}\frac{e_k}{h}\int_0^h \{\cos[(\alpha_m-\alpha_j)X_1] - \cos[(\alpha_m+\alpha_j)X_1]\}\cos(\alpha_k X_1)dX_1 = \frac{e_0}{2}\delta_{mj} + \sum_{k=1}^{\infty}\frac{e_k}{h}\left[\frac{h}{2}\delta_{k|m-j|} - \frac{h}{2}\delta_{k(m+j)}\right]. \tag{A6}$$

Using the properties of the Kronecker delta we finally get

$$Q_{mj}^s = \frac{1}{2}(e_{|m-j|} - e_{m+j}),\ m, j = 1,2,\ldots. \tag{A7}$$

APPENDIX B

Assume a piecewise constant function $e(X_1)$ representing the normalized stiffness of the fiber and matrix, as shown in

Downloaded 03 May 2010 to 171.66.16.248. Redistribution subject to ASME license or copyright; see http://www.asme.org/terms/Terms_Use.cfm

Fig. 1(*b*) for the shear buckling mode. If $r_f = E_f/E_T$, $r_m = E_m/E_T$, then from the inverse of the Fourier series expansion formula

$$e_k = \frac{2}{h}\int_0^h e(X_1)\cos\left(\frac{k\pi}{h}X_1\right)dX_1,\ k=0,1,2,\ldots, \tag{B1}$$

we can easily find that

$$\frac{e_0}{2} = c_f r_f + (1-c_f)r_m, \tag{B2}$$

$$e_k = \frac{2}{k\pi}(r_f - r_m)\sin(k\pi c_f),\ k=1,2,\ldots, \tag{B3}$$

where the fiber volume fraction is given by $c_f = d/h$. Notice that (B2) is the rule of mixtures estimate for the effective Young's axial modulus. The higher order terms take into account the difference in the stiffness ratio of the two phases, being all equal to zero for $E_f = E_m$.

For the extensional mode the unit cell is twice the size of the unit cell for the shear mode, as shown in Fig. 1(*b*), with the axis being in the middle of the matrix phase. The evaluation of the Fourier coefficients is given by

$$\frac{e_0}{2} = c_f r_f + (1-c_f)r_m, \tag{B4}$$

$$e_k = \frac{2}{k\pi}[(-1)^{k+1}-1](r_f - r_m)\sin(k\pi c_f),\ k=1,2,\ldots. \tag{B5}$$

APPENDIX C

Expanding the determinant of the algebraic system (9), the coefficients C_i, $i=1,\ldots,5$ appearing in equation (15) have the evaluations

$$\begin{aligned}
C_1 &= T_{11}T_{22}T_{33},\\
C_2 &= T_{11}T_{22}T_{33p} + T_{11}T_{22p}T_{33} - T_{11}T_{23}^2 - T_{12}^2 T_{33},\\
C_3 &= T_{11}T_{22p}T_{33p} - T_{12}^2 T_{33p},\\
C_4 &= \gamma^4 T_{22}T_{33} + \gamma^2(T_{11}T_{22} + T_{11}T_{33} + T_{22}T_{33p} + T_{33}T_{22p} - T_{23}^2)\\
&\quad + T_{11}T_{22p} + T_{11}T_{33p} + T_{22p}T_{33p} - T_{12}^2,\\
C_5 &= \gamma^2(T_{22} + T_{33}) + T_{11} + T_{22p} + T_{33p},
\end{aligned} \tag{C1}$$

where

$$\begin{aligned}
&T_{11} = 2k - be_0,\ T_{11} = -be_1,\\
&T_{22} = (1-\nu b),\ T_{22p} = k - b(e_0+e_2)/2,\ T_{23} = (k+\nu)\sqrt{(1-2b)},\\
&T_{33} = k - 2kb - \nu b,\ T_{33p} = (1-3b)(e_0 - e_2)/2.
\end{aligned} \tag{C2}$$

Downloaded 03 May 2010 to 171.66.16.248. Redistribution subject to ASME license or copyright; see http://www.asme.org/terms/Terms_Use.cfm

Vibration of Circular Plates in Contact With Water

M. K. Kwak
Assistant Professor,
Department of Engineering Science and Mechanics,
Virginia Polytechnic Institute and State University,
Blacksburg, VA 24061
Assoc. Mem. ASME

This paper is concerned with the virtual mass effect on vibrating circular plates due to the presence of water. Natural frequencies in water can be estimated from natural frequencies in air by using the approximate formula, which mainly depends upon the so-called added virtual mass incremental factor. The added virtual mass incremental factor is a function of geometry, material properties of the plates and mostly boundary conditions of the plates, and water domain. For practical reasons, the added virtual mass incremental factor is likely to be nondimensionalized. In this paper, the nondimensionalized added virtual mass incremental factors for circular plates having simply-supported, clamped, and free edges are obtained by employing the integral transformation technique in conjunction with the dual integral equation method. It is found that the effect of water on the natural frequencies decreases with order.

Introduction

It is generally known that the natural frequencies of structures which are in contact with water, or immersed in water, decrease significantly compared to the natural frequencies in air. This problem is referred to as the fluid-structure interaction problem. The exact solution for this kind of coupling problem may not exist all the time. However, there are some approximate formulas that have been used for the prediction of changes in natural frequencies in water. To deal with a complex fluid-structure interaction problem, finite element modeling of fluid (FFEM) has been used in conjuntion with finite element modeling of structures. Recently, the boundary element method (BEM) has been developed for the large domain problem, and this method proves its effectiveness in the fluid-structure interaction problem compared to the fluid finite element method (FFEM). However, the use of the FFEM or the BEM requires enormous amounts of time on modeling and computatoin. As a result, it is quite difficult to obtain the qualitative measure of water effect by those methods.

Vibration of structures in contact with water is transferred to the water motion and results in a discernible increase in the kinetic energy of the total system. The ratio between the kinetic energy of the water and the kinetic energy of the structure is often referred to as the added virtual mass incremental (AVMI) factor. To be practically applicable, the nondimensionalized added virtual mass incremental (NAVMI) factor is the constant of interest. But the calculation of the NAVMI factor is not always possible, since the NAVMI factor depends largely on the boundary conditions of the structure and water as well as the geometrical complexity of the structure and water domain.

In this paper, an attempt is made to obtain the NAVMI factors for uniform circular plates having simply-supported, clamped, and free boundary conditions, and vibrating in contact with water. The analytical approach for the addressed problem was initiated by Lord Rayleigh (1877) who calculated the increase of inertia of a rigid disk vibrating in a circular aperture. Lamb (1920) calculated the change in the natural frequencies of a thin circular plate clamped along its boundary and placed in the aperture of an infinitely rigid plane wall in contact with water. Powell and Roberts (1923) experimentally verified the theoretical results of Lamb's work. They observed that the added virtual mass increments in actual experiments were lower than the theoretically predicted values. McLachlan (1932) extended Lamb's work and Peake and Thurston (1954) generalized the work of Lamb and McLachlan. All the work depicted above assumed for the boundry condition that the outside of the circular plates is an infinitely rigid wall. Results from this assumption cannot be applied to circular plates immersed in water or placed on a free surface because outside boundary conditions differ from the rigid wall condition. Kwak and Kim (1991) focused on this problem and solved the mixed boundary problem by using the Hankel transformation technique (Sneddon 1966). They obtained the approximate formula for the circular plates vibrating axisymmetrically in contact with water. This paper extends the analytical approach developed by Kwak and Kim (1991) by taking asymmetrical vibrations into account.

Problem Formulation

Let us consider a circular plate in contact with water (Fig. 1), where a and h represent the radius and the thickness of the

Contributed by the Applied Mechanics Division of THE AMERICAN SOCIETY OF MECHANICAL ENGINEERS for presentation at the Joint Applied Mechanics/Bioengineering Conference, Ohio State University, Columbus, Ohio, June 16–19, 1991.

Discussion on this paper should be addressed to the Technical Editor, Prof. Leon M. Keer, The Technological Institute, Northwestern University, Evanston, IL 60208, and will be accepted until two months after final publication of the paper itself in the JOURNAL OF APPLIED MECHANICS. Manuscript received by the ASME Applied Mechanics Division, Jan. 15, 1990; final revision, Nov. 29, 1990.
Paper No. 91-APM-9.

Copyright © 1991 by ASME
Downloaded 03 May 2010 to 171.66.16.248. Redistribution subject to ASME license or copyright; see http://www.asme.org/terms/Terms_Use.cfm

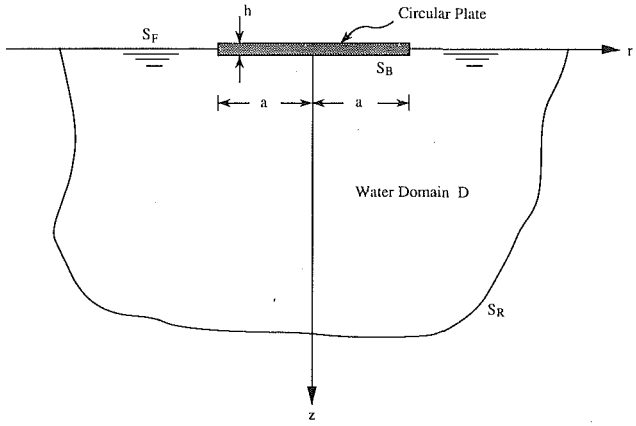

Fig. 1 The circular plate in contact with water

circular plate, respectively, and D denotes a water domain. S_R, S_B, and S_F represent the radiation boundary, the body boundary, and the free surface, respectively.

For simplicity, we assume the following for our analysis:

1 The wavelength is considerably smaller than the diameter of the plate; i.e., motion is small.

2 Water is incompressible, inviscid, and irrotational.

3 The dynamic loading of water has an insignificant effect on mode shapes, so that for the certain mode shape there are little changes in the kinetic and potential energy of the circular plate in contact with water compared to those in air. (Espinosa and Juarez (1984) confirmed experimentally that this hypothesis is a good approximation.)

4 The plate is thin-elastic and has uniform thickness and density, so that the small deflection theory of plates can be applied.

5 There is no internal losses, i.e., the system is conservative.

Rayleigh's quotient is valid only for the fundamental mode. But the third assumption enables us to predict higher natural frequencies of plates in contact with water. Using Rayleigh's quotient, we can write

$$f_a^2 \propto \left(\frac{V_p}{T_p^*}\right)_{\text{air}}, \quad f_w^2 \propto \left(\frac{V_p}{T_p^* + T_w^*}\right)_{\text{water}} \tag{1a,b}$$

where f_a is the natural frequency of plates in air, f_w is the natural frequency of plates in contact with water, T_p^* and V_p represent the reference kinetic energy and the maximum potential energy of the circular plate, respectively, and T_w^* represents the reference kinetic energy of water due to the motion of the circular plate. The relation between the reference and maximum kinetic energy can be written as (Meirovitch, 1975)

$$T_{\max} = T^* \omega^2 \tag{2}$$

where ω is the frequency in radians per second. Based on the third assumption, the following formula can be derived from equation (1)

$$f_w = \frac{f_a}{\sqrt{1+\beta}} \tag{3}$$

where β represents the added virtual mass incremental (AVMI) factor defined by the ratio of the kinetic energy of water due to the motion of the circular plate over the kinetic energy of the circular plate itself, i.e.,

$$\beta = \frac{T_w^*}{T_p^*} = \Gamma \left(\frac{\rho_w}{\rho_p}\right)\left(\frac{a}{h}\right) \tag{4}$$

where ρ_w is the density of water, ρ_p is the mass density of the circular plate, and Γ is the nondimensionalized added virtual mass incremental (NAVMI) factor which is a function of vibrational modes and boundary conditions. The objective of this paper is to compute Γ.

The differential equation of motion for the circular plate shown in Fig. 1 can be written as

$$D_E \nabla^4 w(r,\theta,t) + \rho_p \frac{\partial^2 w(r,\theta,t)}{\partial t^2} = 0 \tag{5}$$

where $w(r, \theta, t)$ is the deflection of the plate, $D_E = Eh^3/12(1 - \nu^2)$ is flexural rigidity, E is Young's modulus, and ν is Poisson's ratio. By separation of variables and assuming harmonic motion, the solution of equation (5) is expressed as;

$$w(r,\theta,t) = \sum_{s=0}^{\infty} \sum_{n=0}^{\infty} W_{sn}(r) \cos s\theta \sin \omega t \tag{6}$$

where ω is a function of the dimensionless parameter λ_{sn} and

$$W_{sn}(r) = A_{sn} J_s\left(\lambda_{sn} \frac{r}{a}\right) + C_{sn} I_s\left(\lambda_{sn} \frac{r}{a}\right) \tag{7}$$

represents the eigenvector corresponding to specified nodal diameter and node circle in which J_s and I_s are the Bessel function of the first kind and the modified Bessel function of the first kind of order s. λ_{sn} (the eigenvalues), A_{sn}, and C_{sn} are determined by applying the boundary conditions. The values are given by Leissa (1961) for the clamped circular plates, by Leissa and Narita (1980) for simply-supported circular plates and by Itao and Crandall (1979) for free-edge circular plates.

Next consider the water domain which the plate rests on. The three-dimensional oscillatory flow in cylindrical coordinates can be described by the velocity potential

$$\Phi(r,\theta,z,t) = \phi(r,z) \cos s\theta \ \omega \cos \omega t \tag{8}$$

where the spatial velocity potential, $\phi(r, z)$, satisfies the Laplace equation.

$$\nabla^2 \phi(r,z) = 0 \quad \text{in} \quad D \tag{9}$$

Since the motions are small, it can be assumed that the resulting free-surface disturbances are small, so that the linearized free-surface boundary condition can be applied.

$$\frac{\partial \phi}{\partial z} - \frac{\omega^2}{g} \phi = 0 \quad \text{on} \quad S_F \tag{10}$$

where g is the gravitational constant. From the above free-surface boundary condition, we can consider two extreme cases. First, the zero-frequency condition implies $\omega = 0$ and therefore

$$\frac{\partial \phi}{\partial z} = 0 \quad \text{on} \quad S_f. \tag{11}$$

This condition was adopted by Lamb (1920) and McLachlan (1932) and is the infinitely rigid wall condition. For the infinite-frequency condition, we have $\omega \to \infty$, and therefore

$$\phi = 0 \quad \text{on} \quad S_f. \tag{12}$$

This condition represents the free surface condition of water when the body vibrates with infinite frequency on the free surface. In this paper, the boundary condition (12) is considered.

Considering the plate to be impermeable, the velocities of water and the plate particle in contact are identical at the water-plate interface.

$$\frac{\partial \phi}{\partial z} = -W_{sn}(r) \quad \text{on} \quad S_B \tag{13}$$

In addition, the radiation condition requires that the disturbance attenuate as the distance from the plate becomes large.

$$\phi, \frac{\partial \phi}{\partial r}, \frac{\partial \phi}{\partial z} \to 0 \quad \text{as} \quad r,z \to \infty \quad \text{on} \quad S_R \tag{14}$$

The dynamic pressure of water acting on the surface of the circular plate is related to the velocity potential by the equation

Downloaded 03 May 2010 to 171.66.16.248. Redistribution subject to ASME license or copyright; see http://www.asme.org/terms/Terms_Use.cfm

$$P_w(r,\theta,t)=\rho_w\left.\frac{\partial\Phi}{\partial t}\right|_{z=0}=\rho_w\phi(r,0)\cos s\theta\ \omega^2\sin\omega t \quad (15)$$

where $P_w(r,\theta,t)$ is the dynamic pressure. The boundary value problem for a circular plate vibrating in contact with water can be written as

$$\frac{\partial^2\phi}{\partial r^2}+\frac{\partial\phi}{r\partial r}+\frac{\partial^2\phi}{\partial z^2}-\frac{s^2}{r^2}\phi=0 \quad \text{in} \quad D \quad (16a)$$

$$\phi=0 \quad \text{on} \quad S_F \quad (16b)$$

$$\frac{\partial\phi}{\partial z}=-W_{sn}(r) \quad \text{on} \quad S_B \quad (16c)$$

$$\phi,\frac{\partial\phi}{\partial r},\frac{\partial\phi}{\partial z}\to 0 \quad \text{as} \quad r,z\to\infty \quad \text{on} \quad S_R. \quad (16d)$$

The mixed boundry value problem consisting of partial differential equation (16a) and boundary conditions (16b,c,d) is conveniently handled by means of an integral transform. Considering the cylindrical coordinate system, the obvious choice is the Hankel transformation (Sneddon, 1951), which is denoted by

$$\overline{\phi_h}(\xi,z)=\int_0^\infty r\phi(r,z)J_s(\xi r)dr. \quad (17)$$

Moreover, we can derive the following relation by integrating by parts yields,

$$\int_0^\infty r\left(\frac{\partial^2\phi}{\partial r^2}+\frac{\partial\phi}{r\partial r}-\frac{s^2}{r^2}\phi\right)J_s(\xi r)dr=-\xi^2\overline{\phi_h}(\xi,z). \quad (18)$$

Multiplying equation (16a) by $rJ_s(\xi r)dr$, integrating over the entire radius, and using equations (17) and (18), the partial differential equation, equation (16a), is reduced to the ordinary differential equation,

$$\frac{d^2\overline{\phi_h}}{dz^2}-\xi^2\overline{\phi_h}=0. \quad (19)$$

From the boundary condition (16d), we conclude that the solution of equation (19) consists of the attenuating part only. Therefore, the solution of equation (19) has the form of

$$\overline{\phi_h}(\xi,z)=B(\xi)e^{-\xi z}. \quad (20)$$

Using the inversion formula of the Hankel transformation and equation (20), we obtain

$$\phi(r,z)=\int_0^\infty\xi\overline{\phi_h}(\xi,z)J_s(\xi r)d\xi=\int_0^\infty\xi B(\xi)e^{-\xi z}J_s(\xi r)d\xi. \quad (21)$$

Inserting equation (21) into the boundary conditions (16b) and (16c), we obtain

$$\int_0^\infty\xi B(\xi)J_s(\xi r)d\xi=0 \quad r>a;$$

$$\int_0^\infty\xi^2B(\xi)J_s(\xi r)d\xi=W_{sn}(r) \quad r\le a. \quad (22a,b)$$

We can nondimensionalize our variables by introducing new variables

$$\rho=\frac{r}{a},\quad \eta=a\xi,\quad A(\eta)=\eta B(\eta),\quad F(\rho)=a^3W_{sn}(\rho). \quad (23a,b,c,d)$$

Hence, the dual integral equations (22) can be cast in the following standard form of dual integral equations

$$\int_0^\infty A(\eta)J_s(\eta\rho)d\eta=0 \quad \rho>1;$$

$$\int_0^\infty\eta A(\eta)J_s(\eta\rho)d\eta=F(\rho) \quad \rho\le 1. \quad (24a,b)$$

If the integral equations (24) are solved for $A(\eta)$, then $B(\eta)$ can be derived using equation (23c) and $\phi(r,z)$ using the inversion formula (21). Based on the results of Titchmarsh (Sneddon, 1966), the solution of the dual integral equations (24) is found to be;

$$A(\eta)=\sqrt{\frac{2\eta}{\pi}}\int_0^1 t^{3/2}J_{s-1}(\eta t)dt\int_0^1\frac{\zeta^{\nu+1}F(t\zeta)d\zeta}{\sqrt{1-\zeta^2}}. \quad (25)$$

Recalling equations (21) and (23c), the potential at $z=0$ can then be written as

$$\phi(\rho,0)=\int_0^\infty\xi B(\xi)J_s(\xi a\rho)d\eta=\frac{1}{a^2}\int_0^1 A(\eta)J_s(\eta\rho)d\eta. \quad (26)$$

Inserting equation (25) into equation (26) and using the result given by Sneddon (1966), equation (26) yields

$$\phi(\rho,0)=\frac{2\rho^s}{a^2\pi}\int_\rho^1\frac{u^{-2s}F^*(u)du}{\sqrt{u^2-\rho^2}} \quad (27)$$

where

$$F^*(u)=\int_0^u\frac{v^{s+1}F(v)dv}{\sqrt{u^2-v^2}}=a^3\int_0^u\frac{v^{s+1}[A_{sn}J_s(\lambda_{sn}v)+C_{sn}I_S(\lambda_{sn}v)]dv}{\sqrt{u^2-v^2}}. \quad (28)$$

Further, using the integral formula (Gradshteyn and Ryzhik, 1980), we obtain

$$F^*(u)=a^3u^{s+1}\sqrt{\frac{\pi}{2\lambda_{sn}u}}\,[A_{sn}J_{s+1/2}(\lambda_{sn}u)+C_{sn}I_{s+1/2}(\lambda_{sn}u)]. \quad (29)$$

Added Virtual Mass Incremental Factor

Using Green's theorem, the reference kinetic energy of the water in an infinite half-space can be expressed by

$$T_w^*=\frac{1}{2}\int_0^{2\pi}\int_0^a\rho_w\phi(r,0)W_{sn}(r)\cos s\theta\ rdrd\theta. \quad (30)$$

Inserting equation (27) into equation (30), recalling equation (23a) and integrating over θ, we obtain

$$T_w^*=\frac{\rho_wD_\theta}{\pi}\int_0^1\int_\rho^1\frac{F^*(u)du\ W_{sn}(\rho)\rho^{s+1}d\rho}{u^{2s}\sqrt{u^2-\rho^2}} \quad (31)$$

where

$$D_\theta=2\pi \text{ for } s=0;\ \pi \text{ for } s\ge 1.$$

Inserting equation (29) into equation (31) and recalling equation (7), and reversing the integration, equation (31) yields

$$T_w^*=\frac{\rho_wa^3D_\theta}{\sqrt{2\pi\lambda_{sn}}}\int_0^1\int_0^u\frac{\rho^{s+1}[A_{sn}J_s(\lambda_{sn}\rho)+C_{sn}I_s(\lambda_{sn}\rho)]d\rho}{\sqrt{u^2-\rho^2}}u^{-s+1/2}[A_{sn}J_{s+1/2}(\lambda_{sn}u)+C_{sn}I_{s+1/2}(\lambda_{sn}u)]du. \quad (32)$$

Considering the result of the integration in equation (29), equation (32) can be written as

$$T_w^*=\frac{\rho_wa^3D_\theta}{2\lambda_{sn}}\int_0^1 u[A_{sn}J_{s+1/2}(\lambda_{sn}u)+C_{sn}I_{s+1/2}(\lambda_{sn}u)]^2du. \quad (33)$$

Using the integral formula (Gradshteyn and Ryzhik, 1980), we obtain

Downloaded 03 May 2010 to 171.66.16.248. Redistribution subject to ASME license or copyright; see http://www.asme.org/terms/Terms_Use.cfm

Table 1 The NAVMI factor for the simply-supported circular plates (ν = 0.3)

n\s	0	1	2	3	4	5
0	0.49458	0.28744	0.20833	0.16513	0.13751	0.11816
1	0.19584	0.15091	0.12429	0.10636	0.09332	0.08335
2	0.12172	0.10246	0.08910	0.07916	0.07143	0.06520
3	0.08818	0.07755	0.06953	0.06320	0.05805	0.05376
4	0.06911	0.06238	0.05703	0.05264	0.04896	0.04582
5	0.05680	0.05217	0.04835	0.04513	0.04236	0.03996

Table 2 The NAVMI factor for the clamped circular plates

n\s	0	1	2	3	4	5
0	0.46674	0.27231	0.19862	0.15829	0.13241	0.11422
1	0.20325	0.15228	0.12399	0.10552	0.09233	0.08235
2	0.12645	0.10450	0.08996	0.07945	0.07142	0.06503
3	0.09121	0.07922	0.07047	0.06372	0.05832	0.05388
4	0.07118	0.06368	0.05786	0.05318		
5	0.05830	0.05319	0.04906	0.04562		

Table 3 The NAVMI factor for the free circular plates (ν = 0.330)

n\s	0	1	2	3	4	5
0	N/A	N/A	0.16091	0.12717	0.10611	0.09921
1	0.21825	0.17281	0.13882	0.11612	0.10012	0.08823
2	0.13700	0.11347	0.09720	0.08530	0.07618	0.06897
3	0.09626	0.08385	0.07451	0.06722	0.06135	0.05650
4	0.07401	0.06641	0.06037	0.05545	0.05135	0.04787
5	0.06008	0.05496	0.05074	0.04719	0.04416	0.04153

$$T_w^* = \frac{\rho_w a^3 D_\theta}{4\lambda_{sn}} [A_{sn}^2 \delta_{w1} + A_{sn} C_{sn} \delta_{w2} + C_{sn}^2 \delta_{w3}] \tag{34}$$

where

$$\delta_{w1} = \{J_{s+1/2}(\lambda_{sn})\}^2 - J_{s-1/2}(\lambda_{sn}) J_{s+3/2}(\lambda_{sn}) \tag{35a}$$

$$\delta_{w2} = \frac{1}{\lambda_{sn}} [J_{s+1/2}(\lambda_{sn}) I_{s-1/2}(\lambda_{sn}) - J_{s-1/2}(\lambda_{sn}) I_{s+1/2}(\lambda_{sn})] \tag{35b}$$

$$\delta_{w3} = \{I_{s+1/2}(\lambda_{sn})\}^2 - I_{s-1/2}(\lambda_{sn}) I_{s+3/2}(\lambda_{sn}). \tag{35c}$$

Note that T_w^* is the reference kinetic energy of water loaded on one side of the circular plate. If the circular plate is loaded on both sides, the expression should be multiplied by 2.

The reference kinetic energy of the circular plate is

$$T_p^* = \frac{1}{2} \rho_p h \int_0^a \int_0^{2\pi} W_{sn}^2(r) \cos^2\theta \, r \, d\theta \, dr = \frac{\rho_p h a^2 D_\theta}{4} [A_{sn}^2 \delta_{p1} + 2A_{sn} C_{sn} \delta_{p2} + C_{sn}^2 \delta_{p3}] \tag{36}$$

where

$$\delta_{p1} = \{J_s(\lambda_{sn})\}^2 - J_{s-1}(\lambda_{sn}) J_{s+1}(\lambda_{sn}) \tag{37a}$$

$$\delta_{p2} = \frac{1}{\lambda_{sn}} [J_s(\lambda_{sn}) I_{s-1}(\lambda_{sn}) - J_{s-1}(\lambda_{sn}) I_s(\lambda_{sn})] \tag{37b}$$

$$\delta_{p3} = \{I_s(\lambda_{sn})\}^2 - I_{s-1}(\lambda_{sn}) I_{s+1}(\lambda_{sn}). \tag{37c}$$

The NAVMI factor, Γ_{sn}, is obtained using equation (34), (36), and (4).

$$\Gamma_{sn} = \left(\frac{T_w^*}{T_p^*}\right)\left(\frac{\rho_p}{\rho_w}\right)\left(\frac{h}{a}\right) = \frac{1}{\lambda_{sn}} \frac{[\delta_{w1} + 2\alpha_{sn}\delta_{w2} + \alpha_{sn}^2 \delta_{w3}]}{[\delta_{p1} + 2\alpha_{sn}\delta_{p2} + \alpha_{sn}^2 \delta_{p3}]} \tag{38}$$

where $\alpha_{sn} = \frac{C_{sn}}{A_{sn}}$.

Using equation (38), the NAVMI factors are computed for the uniform circular plates having various boundary conditions and tabulated in Tables 1 through 3.

Conclusions

Water has a significant effect on the vibration characteristics of structures in contact with water. In general, natural frequencies in water are smaller than those in air because the total kinetic energy increases due to the presence of water. This phenomena is often explained in terms of virtual mass increase. In contrast to natural frequencies, little changes in the mode shapes have been observed experimentally, which enables us to separate the coupled problem into independent boundary value problems. The change of natural frequency subjected to certain mode shape due to the presence of water can be predicted by using the ratio between the kinetic energies of water and the circular plate, often called the added virtual mass incremental (AVMI) factor.

In this paper, the nondimensionalized added virtual mass incremental (NAVMI) factors are obtained in a closed form for the uniform circular plates vibrating in contact with water. The corresponding mixed boundary value problem is solved using methods of integral transform and dual integral equations.

It can be seen from Table 1 that the effect of water is dominant in the simply-supported circular plates and less dominant in the free-edge circular plates. It is generally found that the NAVMI factor decreases as number of nodal diameter and nodal circles increases. For the specified nodal diameter, the NAVMI factor decreases with the number of nodal circles and for the specified nodal circle, the NAVMI factor decreases as the number of nodal diameters increases. It is also found that the presence of water has the most significant effect on the fundamental mode of the circular plate regardless of the boundary condition of the circular plate.

The NAVMI factors given in Tables 1, 2, and 3 can be directly applied to the determination of the natural frequencies of uniform circular plates in contact with water or fully immersed in water. It should be stressed again that the NAVMI factor should be doubled in the case of fully immersed circular plates.

References

Espinosa, F. M., and Gallego-Juarez, J. A., 1984, "On the Resonance Frequencies of Water-Loaded Circular Plates," *Journal of Sound and Vibration*, Vol. 94, No. 2, pp. 217–222.

Gradshteyn, I. S., and Ryzhik, I. M., 1980, *Table of Integrals, Series and Products Corrected and Enlarged Edition*, Academic Press, New York.

Itao, K., and Crandall, S. H., 1979, "Natural Modes and Natural Frequencies of Uniform, Circular Free-Edge Plates," ASME JOURNAL OF APPLIED MECHANICS, Vol. 46, pp. 448–453.

Kwak, M. K., and Kim, K. C., 1991, "Axisymmetric Vibration of Circular Plates in Contact with Fluid," *Journal of Sound and Vibration*, Vol. 145, No. 2, to appear.

Lamb, H., 1920, "On the Vibrations of an Elastic Plate in Contact with Water," *Proc. Roy. Soc., London*, Vol. A98, pp. 205–216.

Leissa, A. W., 1969, "Vibration of Plates," NASA SP-160.

Leissa, A. W., and Narita, Y., 1980, "Natural Frequencies of Simply-Supported Circular Plates," *Journal of Sound and Vibration*, Vol. 70, No. 2, pp. 221–229.

McLachlan, N. W., 1932, "The Accession to Inertia of Flexible Discs Vibrating in a Fluid," *Proc. Phy. Soc., London*, Vol. A44, pp. 546–555.

Meirovitch, L., 1975, *Elements of Vibration Analysis*, McGraw-Hill, New York.

Peake, W. H., and Thurston, E. G., 1954, "The Lowest Resonant Frequency of a Water-Loaded Circular Plate," *Journal of the Acoustical Society of America*, Vol. 26, No. 2, pp. 166–168.

Powell, J. H., and Roberts, J. H. T., 1923, "On the Frequency of Vibration of Circular Diaphragms," *Proc. Phy. Soc., London*, Vol. A35, pp. 170–182.

Lord Rayleigh, 1877, *Theory of Sound*, 2nd ed., Dover Publications, New York (1945 re-issue).

Sneddon, I. N., 1951, *Fourier Transforms*, McGraw-Hill, New York.

Sneddon, I. N., 1966, *Mixed Boundary-Value Problems in Potential Theory*, North-Holland, Amsterdam.

Downloaded 03 May 2010 to 171.66.16.248. Redistribution subject to ASME license or copyright; see http://www.asme.org/terms/Terms_Use.cfm

Plate Tenting With a One-Sided Constraint

Richard C. Benson
Department of Mechanical Engineering,
University of Rochester,
Rochester, NY 14627
Mem. ASME

This paper concerns the loads and deflections of a "tented" plate. A concentrated load pushes the plate transversely away from a rigid surface. Bending rigidity, in-plane tension, foundation stiffness, and weight all act to draw the plate back down to the surface. The deflected region of the tent is assumed to have an ellipsoidal shape, the extent of which is a variable of the problem. Interfacial pressure between the plate and surface is redistributed, after tenting, into a concentrated load at the "tent pole" and a line load along the contour separating contact and noncontact. The problem is analyzed using energy minimization, and approximate, closed-form expressions are obtained for tent dimensions and interfacial loads. Predictions for the tentpole force are compared to experiment and found to be in good agreement.

Introduction

This study is motivated by a problem that arises in magnetic tape recording. In these systems it is common to pull tape around a cylinder in which a read/write head is embedded. The tape either rubs against the cylinder or else is separated by an exceedingly thin layer of lubricating air (Gross et al., 1980). In nominal conditions the tape presses uniformly against the cylindrical foundation. It may happen, however, that debris in the interface acts as a "tentpole," causing the tape to lift away from the foundation. The shape and extent of this "tent" are variables of the problem, and it will be shown later in this paper that the lateral dimensions are many times larger than the transverse displacement at the center.

In magnetic recording it is known that the signal strength reduces dramatically as the read/write head is drawn away from the storage medium. Bogy and Talke (1986) provide an illustration of the "Wallace equation spacing loss" where the signal strength of 1μm separation is less than one percent of what it had been in contact. A combination of tape tenting and spacing loss means that an unwanted asperity in the recording interface may prevent reading or writing over an extensive region of the tape containing many "bits" of data. Also of importance is the load redistribution. What had been a well-distributed pressure becomes a concentrated load at the tentpole, and a line load along the contour where the tape regains contact with the foundation. Calculation of these concentrated loads is important for wear considerations.

In this paper we consider a general model for the described application. The deflection of the tape is governed by classical plate theory, with effects from bending rigidity, in-plane tension, foundation stiffness, and weight. The plate has a prescribed displacement at the center. The contour separating contact and noncontact with the foundation is determined by boundary conditions for zero displacement, slope, and curvature. This aspect of the problem renders the system nonlinear, as the lateral dimensions of the plate become functions of the transverse displacement at the center.

Approximate solution is made through the use of energy minimization, and assumed functions for the tent height and "footprint." This approach gives compact, and quickly evaluated expressions for the geometry of the deflected plate and the reaction loads in the interface. To test the accuracy of the approximate solution a comparison is made to an "exact" solution for a limiting axisymmetric system, and four comparisons are made to force/deflection experiments. Based on these and other checks, it is concluded that the model is useful for deflections of up to about one plate thickness. It is also found that the solution may, with appropriate restrictions, be used as a Green's function (Stakgold, 1969) for plate deflections when the one-sided constraint is not present.

There is a vast literature devoted to point loads on plates and shells. Only a representative number can be cited, and the focus is primarily on works arising from magnetic recording concerns. Additional references may be obtained by consulting these papers and the book by Frýba (1981).

Adams and Bogy (1975) studied moving loads on beams having a one-sided constraint. Their focus was on the complicated beam/foundation contact patterns that develop when the applied load moves rapidly. Papers by Civelek and Erdogan (1975), and Adams (1976) consider through-the-thickness variations. This addition yields better detail of the deflection when the transverse load is small and the deformations are localized. Hobbs (1990) models the axisymmetric buckling of a heavy sheet lying on a rigid surface. There is no tentpole force in Hobbs' problem, rather, the transverse displacement is a buckling response to thermal stress in the midplane of the plate. By assumed symmetries, these studies limit dependence to one

Contributed by the Applied Mechanics Division of THE AMERICAN SOCIETY OF MECHANICAL ENGINEERS for presentation at the Joint Applied Mechanics/Bioengineering Conference, Ohio State University, Columbus, Ohio, June 16-19, 1991.

Discussion on this paper should be addressed to the Technical Editor, Prof. Leon M. Keer, The Technological Institute, Northwestern University, Evanston, IL 60208, and will be accepted until two months after final publication of the paper itself in the JOURNAL OF APPLIED MECHANICS. Manuscript received by the ASME Applied Mechanics Division, Dec. 7, 1989; final revision, Aug. 20, 1990.
Paper No. 91-APM-38.

Copyright © 1991 by ASME
Downloaded 03 May 2010 to 171.66.16.248. Redistribution subject to ASME license or copyright; see http://www.asme.org/terms/Terms_Use.cfm

coordinate in the midplane of the plate (or beam). The present analysis does not make plane-strain or circular-symmetric assumptions, so variation in both spatial dimensions will be considered.

If one removes the one-sided constraint, and the attendant modeling complications, there is then a sizable reference literature for concentrated loads on elastic plates and cylindrical shells. Among them are: Bogy, Greenberg, and Talke (1974), Albrecht, Laenen, and Lin (1977), Greenberg (1979), Ono, Hara, and Murata (1980), Ono and Eibhara (1984), Nishida and Hosaka (1986), and Sundaram and Benson (1989). To varying degrees these papers focus on series solution techniques, speed of convergence, dependence on boundary conditions, resonant phenomena from moving loads, experimental verification, and incorporation of the model into larger physical systems. More will be said about these studies in the body of the paper.

Although the present analysis is for static or steady-state conditions, some readers may be interested in the dynamic response of plates resting on elastic foundations (again without the one-sided constraint). Early studies are provided by Livesley (1953) and Stadler (1971). Stadler also has one of the best summaries of the development of classical plate theory. Sundaram and Benson (1990) modeled transient deflections of a cylindrical shell with the goal of understanding head/tape impact in helical scan recording. For the general treatment of moving loads on elastic structures, the book by Frýba (1981) is very extensive.

Mathematical Formulation

In the context of classical plate theory (Shames and Dym, 1985) the differential equation governing transverse force balance is

$$D\nabla^4 w - T_x\frac{\partial^2 w}{\partial x^2} - T_y\frac{\partial^2 w}{\partial y^2} + kw = F\delta(x)\delta(y) - p, \qquad (1)$$

where $D\nabla^4 w$ is the bending resistance, $T_x(\partial^2 w/\partial x^2)$ and $T_y(\partial^2 w/\partial y^2)$ are loads due to in-plane tension, kw is a foundation stiffness term, $F\delta(x)\delta(y)$ is the concentrated tentpole force, and p is the "weight" per unit area of the plate. (See Fig. 1 and the Nomenclature for further definition of terms.)

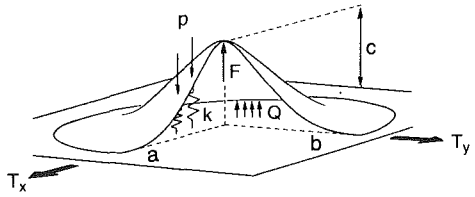

Fig. 1 Geometry

At the center of the tent, $x = y = 0$, the deflection is specified, and the slope in any radial direction, r, is assumed to be zero

$$w = c, \qquad \frac{\partial w}{\partial r} = 0. \qquad (2)$$

The contour separating contact and noncontact is a variable of the problem and may be denoted by a functional constraint $s(x, y) = 1$. On this contour, n is defined to be the direction perpendicular to the contour and into the undeflected portion of the plate. The angle between n and the x-axis is denoted by α.[1] The following boundary conditions supply the information needed to determine $s(x, y) = 1$, and insure that the plate remains flush with the foundation in the region exterior to the tent

$$w = 0, \qquad \frac{\partial w}{\partial n} = 0, \qquad \frac{\partial^2 w}{\partial n^2} = 0. \qquad (3)$$

In physical terms, the deflected tent must have zero slope, displacement, and bending moment as it attaches to the undeflected portion of the plate. It is also presupposed that the plate is not buckled or supporting waves. These related conditions are possible in extreme circumstances, and will be addressed later in the paper. Because the domain of deflection

[1]Explicit forms will soon be given to s, n, and α.

Nomenclature

A = area of the deflected tent
A_i = coefficients in a series solution by Timoshenko
a = footprint radius in the x-direction
B_i = coefficients in a series solution by Timoshenko
b = footprint radius in the y-direction
C_i = constants of integration in a solution by Timoshenko
c = prescribed displacement at the tentpole
D = bending rigidity = $Eh^3/[12(1-\nu^2)]$
E = elastic Young's modulus
F = tentpole force
h = plate thickness
H = spacing function
I_* = an energy integral (subscript denotes kinematic mode)
k = foundation stiffness
K = force/deflection spring rate at tentpole (when linear)
l = distance measured along contact contour
L = a scaling length in a solution by Timoshenko
n = direction normal to the contact contour
p = weight per unit area, or "belt/wrap" pressure
Q = force per unit length along contact contour
Q_{max} = maximum value of Q
Q_{min} = minimum value of Q
Q_{total} = integrated value of Q around contact contour
r = radial coordinate in the plane of the foundation = $(x^2+y^2)^{1/2}$
R = radius of a cylindrical foundation
s = ellipse contour indicator = $(x/a)^2+(y/b)^2$
T_x = in-plane tension in x-direction
T_y = in-plane tension in y-direction
U_* = energy integral (subscript denotes kinematic mode)
V_x = plate/foundation relative velocity in x-direction
V_y = plate/foundation relative velocity in y-direction
w = displacement of plate above foundation
W = total weight of lifted tent
x = Cartesian coordinate in the plane of the foundation = $r\cos(\theta)$
y = Cartesian coordinate in the plane of the foundation = $r\sin(\theta)$
α = angle of normal to contact contour w.r.t. the x-axis
γ = aspect ratio = a/b
δ = Dirac delta function
∇^2 = Laplacian operator = $\frac{\partial^2}{\partial x^2}+\frac{\partial^2}{\partial y^2}$
∇^4 = biharmonic operator = $(\nabla^2)^2$
ν = Poisson's ratio
ρ = mass density of the plate
θ = plate coordinate in the plane of the foundation = arctan (y/x)
$(\bullet)_{ref}$ = a reference value
$(\bar{\bullet})$ = a nondimensional value
$(\bullet)^A$ = an approximate value
$(\bullet)^E$ = an exact value

Downloaded 03 May 2010 to 171.66.16.248. Redistribution subject to ASME license or copyright; see http://www.asme.org/terms/Terms_Use.cfm

changes with penetration, c, the boundary value problem defined by equations (1)–(3) is nonlinear. A similar problem, with nonlinearity entering through the boundary conditions, is described by Timoshenko and Woinowsky-Krieger, (section 70, 1968).

Along the contact contour there is a concentrated force per unit length that balances the transverse shear stress resultant in the plate. This is given by

$$Q = -D\lim_{s\to 1}\left[\cos\alpha\frac{\partial}{\partial x}\nabla^2 w + \sin\alpha\frac{\partial}{\partial y}\nabla^2 w\right], \tag{4}$$

where the limit is approached from below $s = 1$. Similarly, a balance of transverse loads in the limit as $r \to 0$ gives the concentrated tentpole force holding up the center of the plate

$$F = -2\pi D\lim_{r\to 0}\left[r\frac{\partial}{\partial r}\nabla^2 w\right]. \tag{5}$$

Associated with each of the terms on the left-hand side of equation (1) is a stored energy. The following expressions represent the respective contributions from: plate bending, plate stretching, foundation stiffness, lifting of the heavy plate, and the total strain energy.

$$U_b = \frac{D}{2}\int\int_A\left[\frac{\partial^2 w}{\partial x^2}+\frac{\partial^2 w}{\partial y^2}\right]^2 dx\,dy$$

$$U_s = \frac{1}{2}\int\int_A\left[T_x\left(\frac{\partial w}{\partial x}\right)^2 + T_y\left(\frac{\partial w}{\partial x}\right)^2\right] dx\,dy,$$

$$U_f = \frac{k}{2}\int\int_A w^2 dx\,dy, \qquad U_l = p\int\int_A w\,dx\,dy,$$

$$U = U_b + U_s + U_f + U_l. \tag{6}$$

In the preceding integrals, A represents the area of the deflected plate. From Castigliano's first theorem (Shames and Dym, 1985) we may extract the tentpole force as follows[2]

$$F = \frac{\partial U}{\partial c}. \tag{7}$$

Reference Configuration—Circular Tent

When T_x, T_y, and k are all zero, then the system of equations (1)–(3) is easily solved to yield a perfectly circular tent. The radius to the contact contour is

$$r_{\text{ref}} = (64Dc/p)^{1/4}. \tag{8}$$

Here and elsewhere the subscript "ref" denotes a reference value. These quantities will later be used for nondimensionalization, and for use in an approximate solution to the more general problem. The height of the circular tent is given by the function

$$w/c = 1 - \bar{r}^4 + 2\bar{r}^2 ln\bar{r}^2, \qquad \bar{r} = r/r_{\text{ref}}. \tag{9}$$

The tentpole force, and the edge load along $\bar{r} = 1$ have the following values

$$F_{\text{ref}} = 4\pi(Dcp)^{1/2}, \qquad Q_{\text{ref}} = (Dcp^3/4)^{1/4}. \tag{10}$$

The total "weight" of the plate lifted from the foundation is

$$W = \pi r_{\text{ref}}^2 p = 8\pi(Dcp)^{1/2}. \tag{11}$$

Exactly half of this load is absorbed by the tentpole, F_{ref}. The other half is distributed around the tent perimeter.

$$Q_{\text{total}} = 2\pi r_{\text{ref}} Q_{\text{ref}} = 4\pi(Dcp)^{1/2} \tag{12}$$

Similar load redistributions take place in the more general problem, but not so exactly divided as here.

[2]The dependence of the tent area on the penetration at the center does not alter the form of equation (7).

General Solution Using Energy Minimization

Lacking an exact solution to (1)–(3) we seek instead an approximate solution using energy minimization. As a guide we note that the "Reference Configuration" has deflection contours that are concentric circles. For the general problem we assume that the deflection contours will form concentric ellipses with semi-axis lengths of a and b at the contact contour. The contour indicator

$$s = (x/a)^2 + (y/b)^2 \tag{13}$$

ranges from $s = 0$ at the tentpole to $s = 1$ at contact. The height of the tent along a given contour is given by

$$w/c = H(s) \tag{14}$$

where $H(s)$ is a yet unspecified height function consistent with the boundary conditions of the problem

$$H(0) = 1, \quad \lim_{s\to 0} sH'(s) = 0, \quad H(1) = H'(1) = H''(1) = 0. \tag{15}$$

A prime denotes a derivative with respect to s. We next substitute (13)–(15) into the energy integrals (6) and, after some algebra, obtain the following expressions

$$U_b = Dc^2\left[\left(\frac{b}{a^3}+\frac{a}{b^3}\right)I_{b1} + \left(\frac{1}{ab}\right)I_{b2}\right],$$

$$U_s = c^2\left[T_x\left(\frac{b}{a}\right) + T_y\left(\frac{a}{b}\right)\right]I_s,\ U_f = kabc^2 I_f,\ U_l = pabcI_l. \tag{16}$$

The preceding form is such that the entire influence of the spacing function $H(s)$ is contained in the nondimensional integrals

$$I_{b1} = \pi\int_0^1\left\{3[sH''(s)]^2 + 4sH'(s)H''(s) + 2[H'(s)]^2\right\}ds,$$

$$I_{b2} = \pi\int_0^1\left\{2[sH''(s)]^2 + 8sH'(s)H''(s) + 4[H'(s)]^2\right\}ds,$$

$$I_s = \pi\int_0^1 s[H'(s)]^2 ds,\ I_f = \frac{\pi}{2}\int_0^1 [H(s)]^2 ds,$$

$$I_l = \pi\int_0^1 H(s)ds. \tag{17}$$

Solution for the ellipse dimensions a and b is made by substituting (16) and (17) into (6), and minimizing the total stored energy with respect to the unknown parameters

$$\frac{\partial U}{\partial a} = 0, \qquad \frac{\partial U}{\partial b} = 0. \tag{18}$$

Again after some algebra, we arrive at a pair of equations that implicitly determine a and b

$$\gamma^2 = \left(\frac{a}{b}\right)^2 = \left[1 + 2\left(\frac{T_x I_s}{4DI_{b1}}\right)a^2 + \left(\frac{T_y I_s}{4DI_{b1}}\right)^2 a^4\right]^{1/2} - \left(\frac{T_y I_s}{4DI_{b1}}\right)a^2, \tag{19}$$

$$a^4 = \left[1 + \left(\frac{I_{b1}}{I_{b2}}\right)\gamma^2 + \gamma^4\right]\Big/\left[\left(\frac{kI_f}{DI_{b1}}\right) + \left(\frac{pI_l}{cDI_{b1}}\right)\right]. \tag{20}$$

Here, γ is the "aspect ratio" of the ellipsoidal footprint, and a value of $\gamma = 1$ denotes a perfectly circular tent. As an alternative to equations (19) and (20), "a" may be eliminated to yield an eighth-order polynomial for γ. The real root nearest 1.0 is the physically desired solution.

Once the ellipsoidal dimensions have been determined, the tentpole force is found through equation (7)

Downloaded 03 May 2010 to 171.66.16.248. Redistribution subject to ASME license or copyright; see http://www.asme.org/terms/Terms_Use.cfm

$$F=2Dc\left[\left(\frac{b}{a^3}+\frac{a}{b^3}\right)I_{b1}+\left(\frac{1}{ab}\right)I_{b2}\right]+2c\left[T_x\left(\frac{b}{a}\right)+T_y\left(\frac{a}{b}\right)\right]I_s+2kabcI_f+pabI_l, \quad (21)$$

and the edge load is found through equation (4)

$$Q=-8DcH'''(1)\left[\frac{\left(\frac{\cos\theta}{a^2}\right)^2+\left(\frac{\sin\theta}{b^2}\right)^2}{\left(\frac{\cos\theta}{a}\right)^2+\left(\frac{\sin\theta}{b}\right)^2}\right]^{3/2}. \quad (22)$$

In the preceding, the following geometrical relations were used:

$$\tan\alpha=\left(\frac{a}{b}\right)^2\tan\theta, \quad r=s^{1/2}\left[\left(\frac{\cos\theta}{a}\right)^2+\left(\frac{\sin\theta}{b}\right)^2\right]^{-1/2}. \quad (23)$$

As noted earlier, the tenting problem is nonlinear, and the relationships of a, b, F, and Q versus c in equations (19) to (22) reflect this. If, however, the plate is "weightless," $p = 0$, then a and b become independent of the center height, and the loads F and Q fall into a *linear* dependence on c. Of particular interest is the "spring constant" K relating load and deflection at the center of the tent

$$K=\left(\frac{F}{c}\right)_{p=0}=2D\left[\left(\frac{b}{a^3}+\frac{a}{b^3}\right)I_{b1}+\left(\frac{1}{ab}\right)I_{b2}\right]+2\left[T_x\left(\frac{b}{a}\right)+T_y\left(\frac{a}{b}\right)\right]I_s+2kabI_f. \quad (24)$$

The analysis to this point solves the plate tenting problem subject to the specification of a height function $H(s)$ swept around an assumed ellipsoidal footprint. Because the solution will be exact[3] in the limit of the Reference Configuration we choose the function

$$H(s)=1-s^2+2slns. \quad (25)$$

This is the same as equation (9) with $\bar{r}^2$ replaced by s. The height function integrals then take on the values

$$I_{b1}=4\pi,\ I_{b2}=8\pi/3,\ I_s=2\pi/9,\ I_f=43\pi/1080,\ I_l=\pi/6, \quad (26)$$

and we also have $H'''(1) = -2$. These values are substituted into equations (19)–(22) to yield the following nondimensional expressions for the deflection and loading

$$\gamma^2=(\bar{a}/\bar{b})^2=\left[1+2\bar{T}_x\bar{a}^2+(\bar{T}_y\bar{a}^2)^2\right]^{1/2}-\bar{T}_y\bar{a}^2, \quad (27)$$

$$\bar{a}^4=\frac{(3/8)\left[1+(2/3)\gamma^2+\gamma^4\right]}{1+\bar{k}}, \quad (28)$$

$$\bar{F}=\frac{\bar{a}\bar{b}}{3}+\frac{\bar{b}}{4\bar{a}^3}+\frac{\bar{a}}{4\bar{b}^3}+\frac{1}{6\bar{a}\bar{b}}+\frac{\bar{T}_x\bar{b}}{\bar{a}}+\frac{\bar{T}_y\bar{a}}{\bar{b}}+\frac{2\bar{k}\bar{a}\bar{b}}{3}, \quad (29)$$

$$\bar{Q}=\left[\frac{\left(\frac{\cos\theta}{\bar{a}^2}\right)^2+\left(\frac{\sin\theta}{\bar{b}^2}\right)^2}{\left(\frac{\cos\theta}{\bar{a}}\right)^2+\left(\frac{\sin\theta^2}{\bar{b}}\right)}\right]^{3/2}. \quad (30)$$

The independent variables are the same quantities set to zero in the Reference Configuration; i.e., the in-plane tensions and the foundation stiffness. These have been nondimensionalized as follows:

$$\bar{T}_x=T_x/T_{\text{ref}},\quad \bar{T}_y=T_y/T_{\text{ref}},\quad \bar{k}=k/k_{\text{ref}}$$
$$T_{\text{ref}}=9(Dp/c)^{1/2},\quad k_{\text{ref}}=(180p)/(43c). \quad (31)$$

[3]Here and elsewhere exact will always mean in the context of classical plate theory.

The dependent variables have been nondimensionalized with respect to the reference of equations (8) and (10)

$$\bar{a}=a/r_{\text{ref}},\quad \bar{b}=b/r_{\text{ref}},\quad \bar{F}=F/F_{\text{ref}},\quad \bar{Q}=Q/Q_{\text{ref}}. \quad (32)$$

In the limit as $\bar{T}_x = \bar{T}_y = \bar{k} = 0$ the solution limits, as expected, to the reference values of $\bar{a} = \bar{b} = \bar{F} = \bar{Q} = 1$.

Results

Results from equations (27)–(30) are presented in Figs. 2–4. The first of these shows the dependence of the ellipsoidal footprint, $\bar{a}$ and $\bar{b}$, on the foundation stiffness $\bar{k}$ and tension component $\bar{T}_x$. The tension component $\bar{T}_y$ has been set to zero. The point at which the approximate solution by energy minimization becomes exact is marked with a cross. It is seen that an increase in the foundation stiffness $\bar{k}$ causes the footprint to reduce in size. If $\bar{T}_x$ and $\bar{T}_y$ are both equal then the footprint remains perfectly circular. An increase in $\bar{T}_x$ causes the footprint to extend in the x-direction and reduce in the y-direction; that is, it becomes less circular and more ellipsoidal. Compression in the x-direction, $\bar{T}_x < 0$, has a similar effect but with major and minor axes reversed, $\bar{b} > \bar{a}$. At a sufficient level of compression the tentpole force becomes negative, $\bar{F} < 0$, and the graphs end.

To pursue the influence of parameters on $\bar{F}$ we turn to Fig. 3. Once again $\bar{T}_y$ has been set to zero and a cross marks the point of exact solution. As would be expected, an increase in the foundation stiffness or an increase in the tension brings about an increase in the tentpole force. Correspondingly, $\bar{F}$ diminishes when the plate is under compression, and at a critical value becomes zero. This marks a buckled configuration for which the plate can maintain the prescribed displacement without need of any tentpole force.

It should be noted that, even though stretched in tension, a plate may experience an "effective" compression if the plate and foundation slide relative to one another. Steady-state deformation of the plate, measured in a coordinate frame fixed to the tentpole, is governed by equation (1) with the following replacements (e.g., Ono et al., 1980)

$$T_x \to T_x-\rho hV_x^2,\qquad T_y\to T_y-\rho hV_y^2. \quad (33)$$

Here, ρ is the mass density of the plate, V_x and V_y are the relative velocity components, and h is the thickness of the plate.

In Fig. 4 we consider the edge load along the contact contour when $\bar{k} = 0.5$ and $\bar{T}_y = 0$. Graphs are plotted for the quadrant $0 \text{ deg} \le \theta \le 90 \text{ deg}$ as the edge load is symmetric about both the x and y axes. It will be recalled that $\bar{k} = \bar{T}_x = \bar{T}_y = 0$ produces the constant value $\bar{Q} = 1$. When the foundation stiffness is increased to $\bar{k} = 0.5$, then a constant $\bar{Q} = 1.36$ is obtained. When $\bar{T}_x \neq \bar{T}_y$, the edge load varies around the perimeter of the tent. As an example, the graph for $\bar{T}_x = 0.5$ rises to a peak value of $\bar{Q}_{\max} = 1.70$ at $\theta = 90$ deg and drops to a minimum value of $\bar{Q}_{\min} = 1.01$ at $\theta = 0$ deg. Peak loading will always occur at the points of minimum radius in the ellipsoidal footprint, and minimum loading will occur where the radius is greatest. An increase in $\bar{k}$ causes loading to increase at all points.

Tables 1 and 2 present dimensional data in order to make a few points about loads and deflections as a function of penetration, c. These relationships are otherwise obscured by the nondimensionalization. The specifications for Case E are given in Table 1, and are representative of a magnetic recording device with a tape of thickness h pulled under tension T_x around a cylinder of radius R. The tape has elastic modulus E and Poisson's ratio ν. Derived from these specifications are the bending rigidity D, foundation stiffness k, and "belt/wrap" pressure p. (See Timoshenko and Woinowsky-Krieger, Section 121, 1968.)

$$D=\frac{Eh^3}{12(1-\nu^2)},\quad k=\frac{Eh}{R^2(1-\nu^2)},\quad p=\frac{T_x}{R}, \quad (34)$$

Downloaded 03 May 2010 to 171.66.16.248. Redistribution subject to ASME license or copyright; see http://www.asme.org/terms/Terms_Use.cfm

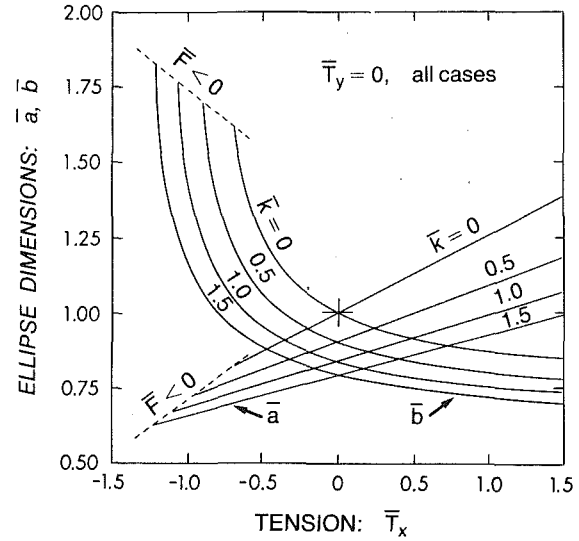

Fig. 2 Ellipse dimensions

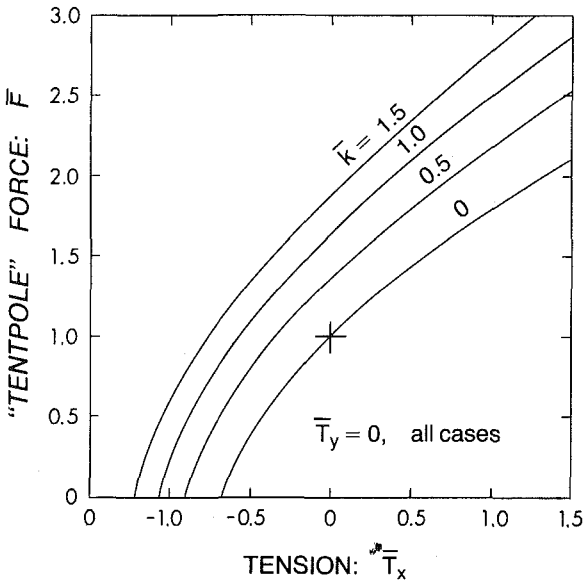

Fig. 3 Tentpole force

Perhaps the most notable feature of Table 2 is the large ratio of the lateral tent dimensions to the traverse displacement at the center, particularly at small penetrations. For example, with $c = 1\mu$m the principal radii of the ellipse are $a = 0.536$mm and b = 0.515mm, approximately 500 times larger. For penetrations of $c = 10\mu$m and 100μm, the "tenting" ratios are roughly 90 and 15, respectively. A second observation is that small penetrations produce roughly circular tents while larger penetrations produce more ellipsoidal tents. Of course, if $T_x = T_y$ then all tents are circular.

There are rapid rates-of-increase in F and Q at the lower penetrations when the deflected area of the tent is growing most rapidly. At higher penetrations the rates-of-increase level off to near constant amounts. It is easily shown that $Q_{max}/Q_{min} = \gamma^3$. Thus, deviations in tent circularity induce larger variations in Q. In Table 2 for example, when $c = 1\mu$m and $\gamma = 1.04$, then $Q_{max}/Q_{min} = 1.12$.

Also listed in Table 2 are the weight of the lifted tent, and the resultant of the edge loading on the contact contour

$$W = pA = \pi abp, \qquad Q_{total} = \oint_{s=1} Q dl. \tag{35}$$

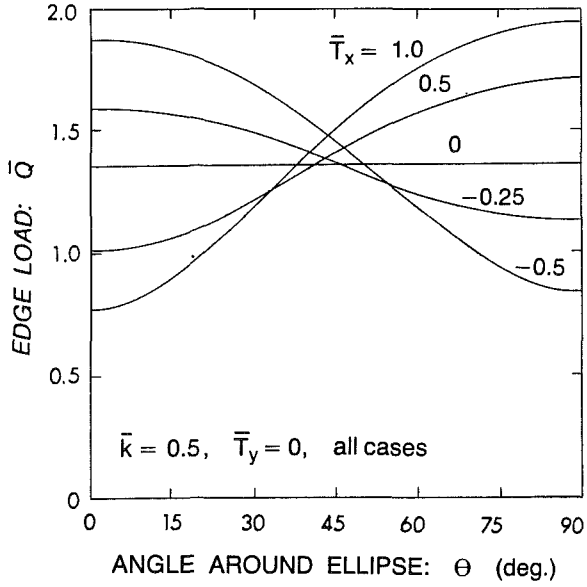

Fig. 4 Edge load

Table 1 Specifications for Cases A-E

		Case A	Case B	Case C	Case D	Case E
E	(GN/m^2)	6.22	4.60	2.4	2.4	3.45
ν		0.3	0.3	0.3	0.3	0.25
h	(μm)	30.	40.	760.	760.	25.0
R	(mm)	50.	50.	1200.	1200.	25.0
T_x	(N/m)	39.2	39.2	676.	939.	100.
T_y	(N/m)	0.	0.	0.	0.	0.
D	(μNm)	15.4	27.0	96000.	96000.	4.79
k	(GN/m^3)	82.0	80.9	1.39	1.39	0.147
p	(N/m^2)	0.	0.	563.	783.	4000.

Table 2 Load/deflection calculations for Case E

c	a	b	γ	Q_{min}	Q_{max}	F	Q_{total}	W
(μm)	(mm)	(mm)		(N/m)	(N/m)	(mN)	(mN)	(mN)
1	0.536	0.515	1.04	0.499	0.560	1.89	1.75	3.47
5	0.813	0.750	1.08	0.713	0.909	4.69	3.99	7.66
10	0.973	0.872	1.12	0.831	1.155	7.17	5.78	10.67
25	1.225	1.048	1.17	1.042	1.666	13.27	9.73	16.13
50	1.437	1.180	1.22	1.293	2.333	22.24	15.04	21.30
100	1.644	1.299	1.27	1.725	3.499	39.19	24.47	26.83

Here, dl is an element of arclength on the curve $s = 1$. After some algebra the integral becomes

$$Q_{total} = -32DcH'''(1) \int_0^{\pi/2} \frac{\left[\left(\frac{\cos\theta}{a^2}\right)^2 + \left(\frac{\sin\theta}{b^2}\right)^2\right]^2}{\left[\left(\frac{\cos\theta}{a}\right)^2 + \left(\frac{\sin\theta}{b}\right)^2\right]^3} d\theta. \tag{36}$$

At 1μm penetration it is seen in Table 2 that F and Q_{total} are roughly equal, and sum to a little bit more than the weight of the lifted tent. In contrast to the Reference Configuration, $F + Q_{total}$ will exceed W due to augmented loading from tension and foundation stiffness. The "overloading" increases as pen-

Downloaded 03 May 2010 to 171.66.16.248. Redistribution subject to ASME license or copyright; see http://www.asme.org/terms/Terms_Use.cfm

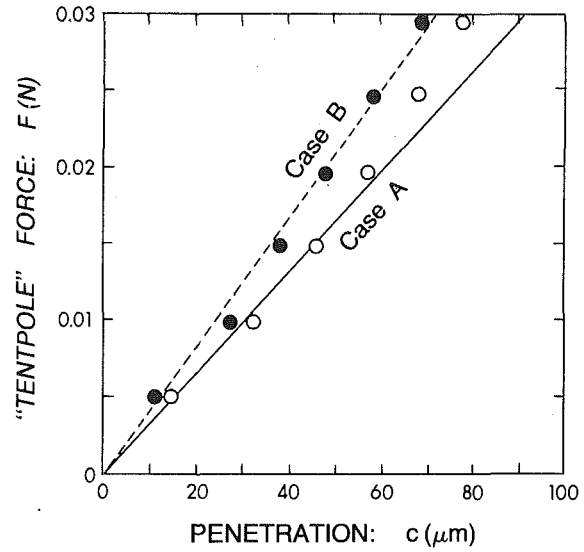

Fig. 5 Force/deflection comparison to experiment, Cases A and B

etration increases. At $c = 100\mu m$ the tentpole is carrying 151 percent of the weight of the lifted tent, and the contact contour absorbs a load equal to 93 percent.

As a general observation stemming from Table 2, the addition of a tentpole imperfection has two deleterious effects on interfacial loading. First, it increases the total load over a given area due to the straining of the deflected plate. Second, it concentrates what had been a well-distributed pressure into a point load at the tentpole and a line load at the contact contour. Of course a point load and a line load are mathematical abstractions. Nevertheless, over whatever small areas these forces act, there will be a substantial increase over nominal interfacial pressure, and an increased problem with wear if the plate slides along the foundation. In addition to the obvious point of concern at the tentpole, there may also be "halo" wear in the region of the contact contour. The halo wear should be greatest at the short sides of the ellipse where $Q = Q_{max}$.

It was observed that the tentpole force could vanish if the plate was compressed to the point of buckling. Alternatively, a critical velocity via equations (33) could induce a similar effect. Adams and Bogy (1975) have made a detailed study of this effect for the case of a beam sliding along a rigid foundation. Similar to the present study they obtained a symmetric tentlike deflection for subcritical velocities (compression). Their analysis then went on to consider numerous supercritical deflection patterns. These patterns can be quite complicated with several transitions from contact to noncontact, and a lack of symmetry about the load point.

An extension of the Adams and Bogy study to independent variation in two spatial variables does not exist. However, if we ignore the one-sided constraint then, as before, a number of comparison studies become available for buckling/resonance on a cylindrical shell. Among them are Bogy et al. (1974), Albrecht et al. (1979), and Nishida and Hosaka (1986). A generally observed feature is that in the supercritical regime the shell deflection pattern changes dramatically. What had been a symmetrical[4] and decaying deflection pattern changes into a nonsymmetrical, nondecaying wave form.

The current model's loss-of-contact phenomenon is a similar manifestation to the onset of resonance seen in other studies with moving loads on cylindrical shells, provides helpful design information in predicting the onset of buckling/resonance. The present model may not be applied to the post-buckled regime as the assumed mode shapes and boundary conditions would be incorrect.

Force-Deflection Experiments

To test the range of validity of the present model several comparisons to experiments have been made. Specifically, the relationship between the tentpole force F and the center penetration c has been measured for four different systems.

The data for cases "A" and "B" are taken from Ono et al. (1980). System specifications are given in Table 1. As with the previous example, the systems are representative of magnetic tape recorders. It is important to note that the tapes of the Ono study were wrapped around a porous cylinder through which pressurized air flowed and lubricated the tape/drum interface. To a high degree of accuracy the "foil bearing" pressure needed to lift the tape from the drum is equal to the belt/wrap pressure T_x/R (Gross et al., 1980). Thus, we set $p = 0$ in Table 1, and recall that this results in a *linear* force-deflection relationship. The spring constants are found from equation (24)

$$K|_A = 343\text{N/m}, \qquad K|_B = 435\text{N/m}. \tag{37}$$

Lines of these slopes are plotted in Fig. 5 along with experimental data extracted from Fig. 12 of the paper by Ono et al. (1980). Before commenting on the match to experiment, it is worth noting that the analytically predicted lines are nearly the same as the lines predicted by Ono's model. From a rather coarse measurement from Ono's Fig. 12, his spring constants are estimated to be $K|_A = 330\text{N/m}$ and $K|_B = 440\text{N/m}$. This is a very close match despite the fact that the present solution technique uses approximate shape functions and boundary conditions not found in Ono's double series solution.[5] As was concluded by Ono et al. (1980) the agreement between experiment and theory is "fairly good" to about $c = 70\mu m$.

A second experiment was designed by the present author to test a system in which the one-sided constraint was important. Specifications for cases "C" and "D" are given in Table 1. These two cases differ only in the tension T_x and hence the belt/wrap pressure $p = T_x/R$. In the experiments a polycarbonate plate was wrapped around an aluminum cylinder. There was no interfacial lubrication, so contact between the plate and foundation *did* occur. Through a small hole in the cylinder a spherically capped penetrator, of diameter 3.2 mm, was pushed into the plate, causing tenting. In the region of the tent the fixture was oriented so that the x-axis aligned with gravity. The tents were sufficiently small so that their perimeters did not extend to the plate edges or to the end of the wrapped region against the cylinder. At the base of the penetrator was a stiff load cell which recorded the tentpole force. Behind the load cell was a micrometer for positioning.

The force/deflection data at the tentpole is graphed in Fig. 6. The data was found to be very repeatable, and the same in loading as in unloading. The greatest source of "noise" occurred in load cell calibration. This error is indicated by the diameter of the dots in Fig. 6. The match between experiment and theory is again judged to be fairly good, say up to the plate thickness, $c \approx h = 0.76\text{mm}$. After that, the experimental data shows larger forces than predicted by the mathematical model. In contrast to Fig. 5, foundation contact is important to the present system. The nonlinear behavior associated with lifting ever larger tent regions up from the foundation is evident in the lower, left side of Fig. 6.

Accuracy of the Approximate Solution

This model relies on two assumed functions for geometry: the ellipsoidal footprint $s(x, y)$, and the height function

[4]We speak of symmetry in the context of the present differential equation. Damping, air pressure, and other external loads can spoil symmetry on a subcritical system. See Albrecht et al. (1979) or Nishida and Hosaka (1986).

[5]See comments about large foundation stiffness in the next section.

Downloaded 03 May 2010 to 171.66.16.248. Redistribution subject to ASME license or copyright; see http://www.asme.org/terms/Terms_Use.cfm

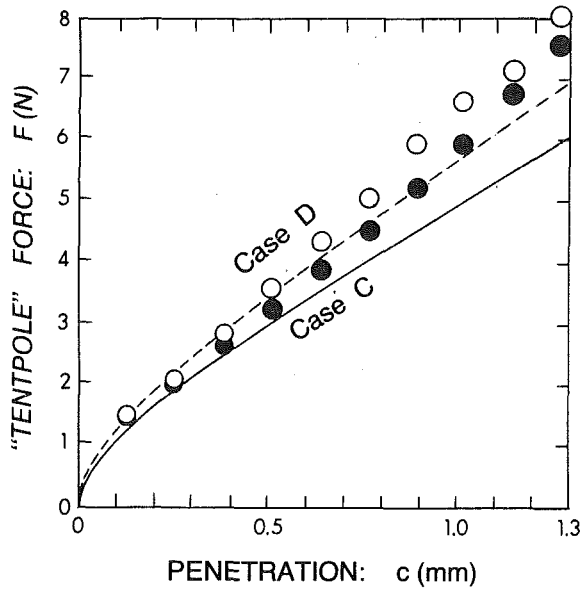

Fig. 6 Force/deflection comparison to experiment, Cases C and D

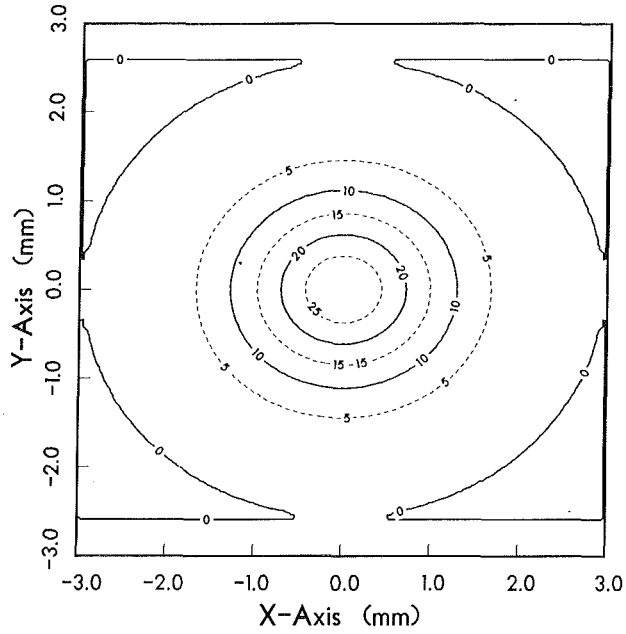

Fig. 7 Deflection contours, present solution, Case A

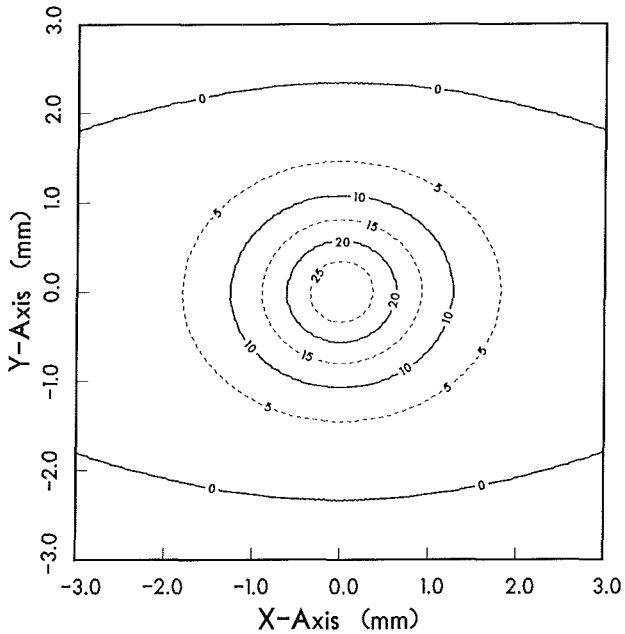

Fig. 8 Deflection contours, comparison solution, Case A

$H(s)$. The solution is exact in the limit upon the Reference Configuration, and experimental verification at the tentpole shows good correlation. To further study the accuracy of the solution technique, three different tests are made in this section.

For the first comparison we recall Case A of Table 1 and set the penetration at the center of $c = 30\mu$m. The numerical technique of Sundaram and Benson (1989) is used to create a "comparison solution," for a plate with simple supports at $x = \pm 43.6$mm, and free edges at $y = \pm 25.4$mm. These are the boundary conditions used originally by Ono et al. (1980). A "present solution" is obtained using the energy minimization and assumed functions of this paper. It will be noted at the onset that the present solution has the one-sided constraint, and the "comparison solution" does not, so the two systems are not identical, and the comparison is only of an approximate nature.

Calculated displacements for the two solutions are shown in Figs. 7 and 8. The respective displacements are very close to each other, especially near-to and far-away-from the load point. The region of greatest difference occurs near the "half height" contour of the present solution where $H(s) = 0.5 \Rightarrow w = 15\mu$m. On this contour, the greatest deviation by the comparison solution is $+1.31\mu$m. At the predicted contact contour of the present solution ($a = 2.94$mm, $b = 2.55$mm) the comparison solution has a maximum deviation of -0.04μm. Of course, the two solutions match exactly at the prescribed value at the tentpole.

Considering the very different boundary conditions between the two models, it may seem surprising that the deflection profiles resemble each other at all. The reason for the similarity is the large stiffness entering into equation (1) through the kw term. Apart from any other equilibrating effect this term resists deviations away from $w = 0$. Thus, despite the absence of a one-sided constraint in the comparison solution, there is, nevertheless, a strong resistance to much "overshoot" below $w = 0$ as the tent decays from the tentpole.

This suggests a (perhaps unanticipated) usage of the present model, in that it may find accurate application to cylindrical shell systems lacking the one-sided constraint. For these systems the behavior is linear and the displacement due to a point load may be used as a Green's function to find deflections due to general distributed loading (e.g., Ono and Ebihara, 1984). The current formulation is *also* linear when $p = 0$, and thus, it too may be used as a Green's function for those cases when a large foundation stiffness localizes deflection. In several studies of this sort observations have been made to the insensitivity on far-field boundary conditions (Ono et al. 1980, 1984; Nishida and Hosaka, 1986; Sundaram and Benson, 1989).

The references cited in the next-to-last paragraph of the Introduction generally utilize series expansions for solution, and can require tens of thousands of terms to converge to a desired accuracy. Speed of convergence is a frequently noted challenge. By contrast, the present model requires only a few function evaluations, and may lead to a great savings in computation time. However, it should again be cautioned that the present and comparison studies have different boundary conditions, make different assumptions about the form of solution, and cannot always be substituted for one another. The most notable exceptions occur near plate edges which this model ignores, and in contact with a rigid surface which the series solutions ignore. It also bears noting that Livesley (1953) and Stadler (1971) use transform methods to obtain solution.

Downloaded 03 May 2010 to 171.66.16.248. Redistribution subject to ASME license or copyright; see http://www.asme.org/terms/Terms_Use.cfm

If "distant" boundary conditions may be ignored, then their asymptotic steady-state solutions may be preferable to series solution for computational efficiency.

In order that a comparison may be made against an exact solution, we next consider Case E in Table 1 with one change: The tension in the x-direction is set to zero. This enables us to use a solution developed in Timoshenko and Woinowski-Krieger, Section 57 (1968). The Timoshenko system includes bending rigidity D and foundation stiffness k, but does not include tensions T_x and T_y, or weight p. It is easy to add a particular solution for the weight contribution, and we will also impose all three of boundary conditions (3) so that the Timoshenko plate will satisfy the one-sided constraint. Because both tensions are zero the tent will obviously be circular symmetric with $\gamma = 1$ and $a = b$. The deflection of the plate, following Timoshenko, is given by

$$w(\hat{r}) = L[C_1 f_1(\hat{r}) + C_2 f_2(\hat{r}) + C_3 f_3(\hat{r})] - (p/k), \quad (38)$$

where

$$\hat{r} = r/L, \qquad L^4 = D/k, \quad (39)$$

C_1, C_2, and C_3 are constants of integration, and f_1, f_2, and f_3 are functions given by the following series

$$f_1(\hat{r}) = \sum_{0,4,8,\ldots} A_n \hat{r}^n, \quad f_2(\hat{r}) = \sum_{2,6,10,\ldots} A_n \hat{r}^n,$$

$$f_3(\hat{r}) = f_2(\hat{r})\ln(\hat{r}) + \sum_{6,10,14,\ldots} B_n \hat{r}^n. \quad (40)$$

The recursions in the coefficients are as follows:

$$A_0 = 1,\ A_2 = 1,\ B_6 = 5/3456,$$

$$A_n = -A_{n-4}/[n^2(n-2)^2];\ n = 4,6,8,\ldots$$

$$B_n = \frac{(-1)^{(n-6)/4}}{n^2(n-2)^2}\left[B_{n-4} + \frac{4n(n-1)(n-2)}{4^2 6^2 \ldots n^2}\right];$$

$$n = 10,\ 14,\ 18,\ldots \quad (41)$$

The boundary condition $w(0) = c$ leads to the requirement[6]

$$C_1 = \frac{c}{L} + \frac{p}{Lk} \quad (42)$$

and the three boundary conditions of (3) require

$$\frac{p}{Lk} = \left(\frac{c}{L} + \frac{p}{Lk}\right) f_1(\hat{R}) + C_2 f_2(\hat{R}) + C_3 f_3(\hat{R}) \quad (43)$$

$$0 = \left(\frac{c}{L} + \frac{p}{Lk}\right) f_1'(\hat{R}) + C_2 f_2'(\hat{R}) + C_3 f_3'(\hat{R}) \quad (44)$$

$$0 = \left(\frac{c}{L} + \frac{p}{Lk}\right) f_1''(\hat{R}) + C_2 f_2''(\hat{R}) + C_3 f_3''(\hat{R}). \quad (45)$$

A prime represents a derivative with respect to $\hat{r}$, and $\hat{R} = a/L$ is the radius of the contact contour. These three equations are solved numerically for C_2, C_3, and $\hat{R}$. Subsequently, from equations (5) and (4), the force at the tentpole and the line load along the contact contour are found

$$F = 8\pi k L^3 C_3 \quad (46)$$

$$Q = (Dk)^{1/2}\left[\left(\frac{c}{L} + \frac{p}{Lk}\right) f_1'''(\hat{R}) + C_2 f_2'''(\hat{R}) + C_3 f_3'''(\hat{R})\right]. \quad (47)$$

The solution obtained in this way is exact in the context of classical plate theory. The approximate solution obtained by the technique of the present paper has the following key results (expressed nondimensionally)

$$\bar{a} = \frac{1}{(1+\bar{k})^{1/4}}, \quad \bar{F} = \frac{1 + \frac{4}{3}\bar{k}}{(1+\bar{k})^{1/2}}, \quad \bar{Q} = (1+\bar{k})^{3/4}. \quad (48)$$

Table 3 shows a comparison of the exact $(\bullet)^E$ and approximate $(\bullet)^A$ values found for tent radius, a, tentpole force F, and total edge load $Q_{\text{total}} = 2\pi a Q$. The system, as noted above, is Case E with no in-plane tension. Values are given for penetrations up to four plate thicknesses.

As would be expected, the approximate and exact solutions match in the limit of $c \to 0$ where both solutions are identical. At a deflection of one plate thickness, $c = h = 25\mu$m, the exact tent radius is 1.4 percent greater than the approximate; the exact tentpole force is 0.7 percent greater than the approximate, and the total edge load is 11.9 percent less than the approximate. Figure 9 plots the two solutions on the same graph. The maximum deviation in displacement is $w^A - w^E = 0.36\mu$m near $r = 0.38$mm.

This would seem to be an acceptable match in light of the fact that classical plate theory employs kinematic assumptions that are generally recognized as valid for deflections of less

Table 3 Exact and approximate values for Case E with $T_x = 0$

c	a^A	a^E	F^A	F^E	Q^A_{total}	Q^E_{total}
(μm)	(mm)	(mm)	(mN)	(mN)	(mN)	(mN)
1	0.525	0.525	1.75	1.75	1.75	1.74
5	0.779	0.781	4.02	4.03	3.97	3.87
10	0.917	0.923	5.87	5.89	5.72	5.46
25	1.123	1.139	10.10	10.17	9.55	8.54
50	1.284	1.317	16.04	16.21	14.62	11.90
100	1.432	1.493	27.06	27.40	23.50	16.31

Table 4 Residual values for Case E, Δ versus s

s	Δ	s	Δ
0.01	0.005810	0.5	−0.000275
0.05	0.001157	0.6	−0.000250
0.1	0.000396	0.7	−0.000204
0.2	−0.000063	0.8	−0.000145
0.3	−0.000218	0.9	−0.000077
0.4	−0.000272	1.0	−0.000002

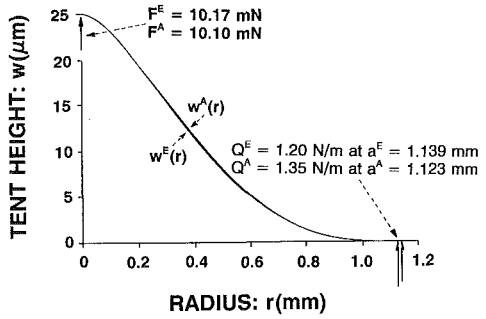

Fig. 9 Exact and approximate results, Case E with $T_x = 0$

[6]There is a fourth independent homogeneous solution $C_4 f_4(\hat{r})$ that can be added to equation (38), but it gives unbounded deflections at the center, and so it is eliminated by setting $C_4 = 0$.

Downloaded 03 May 2010 to 171.66.16.248. Redistribution subject to ASME license or copyright; see http://www.asme.org/terms/Terms_Use.cfm

than one plate thickness (Timoshenko and Woinowsky-Krieger, Section 13, 1986); i.e., even the "exact" solution is approximate at this deflection. Considering also the results of Fig. 5 and 6, solutions for the systems studied in this paper have generally exhibited errors on the order of ten percent at deflections of one plate thickness.

As a third and final check on accuracy, we consider the residual Δ in the differential equation of equilibrium (1)

$$\Delta = \left[D\nabla^4 w - T_x \frac{\partial^2 w}{\partial x^2} - T_y \frac{\partial^2 w}{\partial y^2} + kw + p \right] / p. \tag{49}$$

Accuracy of the approximate solution is measured by the smallness of the residual compared to 1. Table 4 shows the residual for Case E at a penetration of one plate thickness. (The tension $T_x = 100$N/m has been restored to the problem.) The data runs from $s = 0.01$ near the tentpole to $s = 1$ at the contact contour for the ray $\theta = 0$ deg. Residuals were of lower absolute values along other rays. Over most of the domain the residual is less than 10^{-3}, or one tenth of one percent. In the limit as $s \to 0$ the residual approaches infinity; a necessary consequence of resolving the infinite pressure at the tentpole, which was not included in equation (49).

Although point-to-point errors must be accepted with this approximate solution, it is possible to force a weighted average of the error to zero. Because of the energy minimization scheme that is employed, it is easy to demonstrate that, with displacement as the weighting function, the following resultant is identically zero (Shames and Dym, 1985)

$$0 = \int \int_A w \Delta r dr d\theta. \tag{50}$$

Readers wondering whether or not the approximate solution of this paper may be applied to their problem can generate answers and compute Δ. The decision can then be made whether to (1) accept the answer, (2) try to improve the answer through a better choice of $H(s)$, or (3) switch to an entirely different solution scheme.

Summary

The problem of plate tenting with a one-sided constraint has been studied. Solution was obtained through energy minimization and the use of assumed functions for the plate footprint and deflection. Results were obtained in the form of simple algebraic expressions that could be quickly evaluated to provide details of the deflection profile and the interfacial loading. Effects from bending rigidity, in-plane tension, foundation stiffness, and plate weight were considered. If desired, other functions could be substituted for the footprint and deflection choices made here.

Due to the nature in which the plate raises up from the foundation the load/deflection relationship is nonlinear. Initial penetrations create rapidly spreading tents and a rapid build-up of interfacial loads. The growth rates asymptote to constant values as penetrations grow larger. In the absence of in-plane tension all tents would be circular. Differences in T_x and T_y create an ellipsoidal footprint. Increases in tension and bending rigidity increase the area of the deflected plate. Increases in foundation stiffness and weight reduce the area of the deflected plate.

Loads in the plate/foundation interface were studied. As the plate deflects, the plate's weight per unit area is redistributed into a concentrated force at the tentpole and a line load around the perimeter of the tent. These two loads are together greater than the total weight of the lifted tent. The perimeter load is greatest at the short sides of the ellipsoidal tent. Sufficient (effective) compression can buckle the plate and cause a loss of contact between the tentpole and the plate.

When the weight, p, is zero the problem becomes linear, and the present model may be used as an approximate Green's function for the case of a point load on a plate without a one-sided constraint. The accuracy is improved if foundation stiffness effects minimize deflections below $w = 0$. The advantage of the approximate solution is its computational speed relative to series expansions.

Comparison to experiment and to alternative solutions showed accurate results through roughly one plate thickness of deflection.

Acknowledgment

The author wishes to thank Joe Iacona, Roger Leighton, Eric Rosen, and Ken Stack for the experimental data of Fig. 6. Thanks are also extended to Ramesh Sundaram for Figs. 7 and 8. These individuals, as well as Alan Brewen and Kevin Cole, provided the author with many helpful discussions. Funding received from the Eastman Kodak Company is gratefully acknowledged.

References

Adams, G. G., and Bogy, D. B., 1975, "Steady Solutions for Moving Loads on Elastic Beams With One-Sided Constraints," ASME JOURNAL OF APPLIED MECHANICS, Vol. 42, pp. 800–804.

Adams, G. G., 1976, "Moving Loads on Elastic Strips With One-Sided Constraints," *Int. Journal of Engineering Science*, Vol. 14, pp. 1071–1083.

Albrecht, D. M., Laenen, E. G., and Lin, C., 1977, "Experiments on the Dynamic Response of a Flexible Strip to Moving Loads," *IBM Journal of Research and Development*, Vol. 21, No. 7, pp. 379–383.

Bogy, D. B., Greenberg, H. J., and Talke, F. E., 1974, "Steady Solution for Circumferentially Moving Loads on Cylindrical Shells," *IBM Journal of Research and Development*, Vol. 18, No. 5, pp. 395–400.

Bogy, D. B., and Talke, F. E., 1986, "Mechanics Related Problems of Magnetic Recording Technology and Ink-Jet Printing," *ASME Applied Mechanics Reviews*, Vol. 39, pp. 1665–1677.

Civelek, M. B., and Erdogan, F., 1975, "The Frictionless Contact Problem for an Elastic Layer Under Gravity," ASME JOURNAL OF APPLIED MECHANICS, Vol. 42, pp. 136–140.

Frýba, L., 1981, *Vibration of Solids and Structures Under Moving Loads*, Noordhoff International Publishing.

Greenberg, H. J., 1979, "Study of Head-Tape Interaction in High Speed Rotating Head Recording," *IBM Journal of Research and Development*, Vol. 23, No. 2, pp. 197–205.

Gross, W. A., Matsch, L. A., Castelli, V., Eshel, A., Vohr, J. H., and Wildman, M., eds., 1980, *Fluid Film Lubrication*, John Wiley and Sons, New York.

Hobbs, R. E., 1990, "Axisymmetric Upheaval Buckling of a Heavy Sheet," ASME JOURNAL OF APPLIED MECHANICS, Vol. 57, pp. 472–474.

Livesley, R. K., 1953, "Some Notes on the Mathematical Theory of a Loaded Elastic Plate Resting on an Elastic Foundation," *Quarterly Journal of Mechanics and Applied Mathematics*, Vol. 6, pp. 32–44.

Ono, K., Hara, S., and Murata, K., 1980, "Magnetic Tape Deformation Under a Concentrated Load," *Bulletin of the JSME*, Vol. 23, No. 175, pp. 13–19.

Ono, K., and Eibhara, T., 1984, "Improved Green's Function in Tape Deflection and Solutions of Head Contour With Uniform Contact Pressure," *Tribology and Mechanics of Magnetic Storage Systems*, STLE SP-16, pp. 97–102.

Nishida, Y., and Hosaka, H., 1986, "Dynamic Deflection of Magnetic Tape due to Rotating Head Scanning," *Bulletin of the JSME*, Vol. 29, No. 256, pp. 3530–3537.

Shames and Dym, 1985, *Energy Methods and Finite Element Methods in Structural Mechanics*, McGraw-Hill, New York.

Stadler, W., 1971, "The General Solution of the Classical Problem of the Response of a Infinite Plate With an Elastic Foundation and Damping," *Journal of Elasticity*, Vol. 1, No. 1, pp. 37–49.

Stakgold, I., 1969, *Boundary Value Problems of Mathematical Physics*, The MacMillan Co., Toronto.

Sundaram, R., and Benson, R. C., 1989, "A Green's Function With Improved Convergence for Cylindrically Wrapped Tapes," *Tribology and Mechanics of Magnetic Storage Systems*, STLE SP-26, pp. 98–110.

Sundaram, R., and Benson, R. C., 1990, "Tape Dynamics Following an Impact," *IEEE Transactions on Magnetics*, Vol. MAG-26, No. 5, pp. 2211–2213.

Timoshenko, S., and Woinowsky-Krieger, S., 1968, *Theory of Plates and Shells*, McGraw-Hill, New York.

Downloaded 03 May 2010 to 171.66.16.248. Redistribution subject to ASME license or copyright; see http://www.asme.org/terms/Terms_Use.cfm

A. Azarkhin
Mem. ASME

O. Richmond

Product Design and Mechanics Division,
Alcoa Laboratories,
Alcoa Technical Center,
Alcoa Center, PA 15069

Extension of the Upper Bound Method to Include Estimation of Stresses

The upper bound method is a convenient tool for evaluating the rate of work in processes involving predominantly plastic deformation of rigid/perfectly plastic material. Since the rate of work for an incompressible material depends only on the deviator portion of the stress, the hydrostatic portion does not enter the formulation and the stress field is not determined. Here we show that this limitation can be overcome by adding a relatively simple postprocessing procedure. We then apply this technique to examples of rigid asperities penetrating a plastic material undergoing subsurface bulk deformation and compare our results with previous approximate solutions.

1 Introduction

The upper bound method, based on the upper limit load theorem (Gvozdev, 1938; Drucker et al., 1951; Drucker et al., 1952; Drucker, 1954; Prager, 1959; Hill, 1951; Hill, 1952) is a convenient tool for evaluating the rate of work in processes involving predominantly plastic deformation. The upper bound method is attractive for its simplicity, and has been successfully used by researchers in many applications. In view of our interests, we mention a few works where this technique was applied to study friction at metal working tool interfaces due to asperity penetration or flattening (Bowden and Tabor, 1950; Rabinowicz, 1965; Rowe, 1977; Suh, 1986; Abildgaard, 1984; Avitzur et al., 1984; Wanheim, 1978; Oh and Kobayashi, 1975). However, this method has a few drawbacks:

(a) In the case of a single loading force, the rate of work defines the force itself. For combined loading, however, the forces cannot be separated on the basis of the upper bound method alone, and some additional information or assumptions are required. See De Vathire et al. (1981), Satcliffe (1988), and Wilson and Sheu (1988), for example.

(b) The rate of work for a perfectly plastic incompressible material depends only on the deviatoric portion of the stress. Hence, the hydrostatic portion does not enter the formulation and the stress field is not determined.

(c) Strictly speaking, the upper bound method is only applicable to problems with prescribed surface configurations. This restriction was ignored by many researchers who used the upper bound method to find the steady-state shape of the surface. The parameters specifying the surface were used for the minimization of the rate of work. A few examples of this type were mentioned by Azarkhin and Richmond (1989), where it was demonstrated that this procedure could lead to erroneous results.

During the discussion following the presentation of the paper as mentioned above at the ASME/ASCE Summer Conference (San Diego, 1989 July 09–13), the question was posed[1] whether the method could be modified in order to remove these restrictions. In this paper we show that this can be done by adding a relatively simple postprocessing procedure. We then apply this modified technique to examples of rigid asperities penetrating a plastic material subjected to subsurface straining, and compare these results with previous approximate solutions.

2 Upper Bound Method and Euler Equations

The limit load theorem can be written as a problem of minimization of the functional

$$f(\mathbf{u}) = \sqrt{\frac{2}{3}} \int_v \sigma_o \sqrt{\epsilon_{ij}\epsilon_{ij}}\, dv - \int_{s_1} F_i^* \mathrm{u}_i \mathrm{ds} + \frac{1}{\sqrt{3}} \int_{s_2} \mathrm{m}\sigma_o \sqrt{u_i u_i}\, ds. \quad (1)$$

In this expression, $\mathbf{u}$ is the trial vector function of velocities, ϵ_{ij} are the rates of deformation derived from the trial velocities; σ_o is the yield stress; v is the volume of the perfectly plastic body; s_1 is the part of the surface where the traction vector $\mathbf{F}^*$ is specified; and s_2 is the part of the surface with frictional tractions given as some fraction, m, of the yield shear stress. In contrast to the conditions on s_1, the directions of these frictional forces are not known in advance. They are directed

Contributed by the Applied Mechanics Division of THE AMERICAN SOCIETY OF MECHANICAL ENGINEERS for presentation at the Joint Applied Mechanics/Bioengineering Conference, Ohio, June 16–19, 1991.

Discussion on this paper should be addressed to the Technical Editor, Prof. Leon M. Keer, The Technological Institute, Northwestern University, Evanston, IL 60208, and will be accepted until two months after final publication of the paper itself in the JOURNAL OF APPLIED MECHANICS. Manuscript received by the ASME Applied Mechanics Division, May 5, 1990; final revision, Nov. 19, 1990.
Paper No. 91-APM-19.

[1] by K. L. Johnson, Cambridge University, U.K., and A. Drescher, University of Minnesota, Minneapolis, Minn.

Copyright © 1991 by ASME
Downloaded 03 May 2010 to 171.66.16.248. Redistribution subject to ASME license or copyright; see http://www.asme.org/terms/Terms_Use.cfm

against the relative velocities of the plastic medium and the rigid boundary. On the remainder of the surface, s_3, velocities are specified.

The admissible set of velocities should not violate the kinematic boundary conditions, and should satisfy the incompressibility condition

$$\epsilon_{ii}=0. \tag{2}$$

Equation (1) is understood to hold incrementally in time. Therefore, the equivalent yield stress σ_o may be defined by the coordinates and the history of the loading, but does not depend on the trial values of velocities. It is updated, however, after each step to account for inhomogeneity and hardening.

Equation (1) is equivalent to that given by Hill (1985) equation (19) in Chapter III, except for the added friction term. This addition is valid (see Azarkhin and Richmond (1989)), and, as we shall see shortly, leads to appropriate natural boundary conditions.

For numerical implementation, (1) is written in terms of velocities, **u**, and is approximated by a discrete scheme. In most of the papers referenced above, a few planes of velocity discontinuity were passed through the plastic material, and sections of the material between the planes were assumed to move rigidly with the velocity represented by a single vector for the whole block. The rate of work for minimization is then concentrated along these planes. Finite element/difference approaches were used in other works (see Azarkhin and Richmond (1989) and Bin and Luo (1988)). The rate of work and the field of velocities in all of these cases are found as the result of minimization, but the methods do not directly provide the hydrostatic stress, $\sigma_{ii}/3$, and hence stresses remain undefined.

The problem of minimization for (1) can be restated as that of a stationary point for the augmented functional, using Lagrange multipliers

$$\delta L(\mathbf{u},\lambda)=\delta\left[f(\mathbf{u})+\int_v \lambda\epsilon_{ii}ds\right]=0 \tag{3}$$

where $\lambda = \lambda(\mathbf{x})$ is a function of coordinates, **x**. Expanding (3) and rewriting it in terms of stresses, we obtain

$$\begin{aligned}\delta L(\mathbf{u},\lambda)=&\int_v\left[\sqrt{\frac{2}{3}}\,\sigma_o\frac{\epsilon_{ij}\delta\epsilon_{ij}}{\sqrt{\epsilon_{kl}\epsilon_{kl}}}+\lambda\delta\epsilon_{ii}+\epsilon_{ii}\delta\lambda\right]dv\\&-\int_{s_1}F_i^*\delta u_i ds+\int_{s_2}\tau\delta\sqrt{u_iu_i}ds\\=&\int_v[(\sigma_{ij}'+\lambda\delta_{ij})\delta\epsilon_{ij}+\epsilon_{ii}\delta\lambda]dv-\int_{s_i}F_i^*\delta u_i ds\\&+\int_{s_2}\tau\frac{u_i\delta u_i}{\sqrt{u_ju_j}}ds=0.\end{aligned} \tag{4}$$

In this expression, δ_{ij} is the Kronecker delta, subscripts take values 1, 2, 3 unless specified otherwise, and $\tau = m\sigma_o/\sqrt{3}$, where the friction factor, m, takes values between 0 and 1, depending on the surface and lubrication conditions.

Integration by parts yields

$$\begin{aligned}\delta L(\mathbf{u},\lambda)=&-\int_v\frac{\partial}{\partial x_j}[\sigma_{ij}'+\lambda\delta_{ij}]\delta u_i dv+\int_v\epsilon_{ii}\delta\lambda dv\\&+\int_{s=s_1+s_2+s_3}(\sigma_{ij}'+\lambda\delta_{ij})n_i\delta u_j ds\\&-\int_{s_1}F_i^*\delta u_i ds+\int_{s_2}\tau\frac{u_i\delta u_i}{\sqrt{u_ju_j}}ds\end{aligned} \tag{5}$$

where n_i are components of the unit vector normal to the surface. Since δu_i and $\delta\lambda$ are independent in the domain v, the Euler equations are

$$\frac{\partial}{\partial x_j}[\sigma_{ij}'+\lambda\delta_{ij}]=0, \tag{6}$$

and the incompressibility equation (2). Equations (6) are equilibrium equations with λ being identified as the hydrostatic stress. The first integral over the surface, s, in equation (5) should be considered separately for different types of surfaces. The expression

$$F_i\equiv(\sigma_{ij}'+\lambda\delta_{ij})n_j \tag{7}$$

gives components of the traction vector derived from the rates of deformation. On s_1, all virtual velocities are prescribed. Combining these with other terms in the integral over s_1, we obtain the natural boundary condition

$$F_i^*=F_i \tag{8}$$

which states simply that the stresses derived from the rate of deformation are equal to those assigned.

On s_2, not all virtual velocities are known. To simplify considerations for this case, let us assume temporarily that the coordinate system is such that the unit normal vector, n_1, is directed along the Cartesian coordinate, x_1. Then $\delta u_1=0$, and combining terms for the two other components of virtual velocity we obtain

$$\tau_i^*=\tau\frac{u_i}{\sqrt{u_ju_j}};\ i=1,2. \tag{9}$$

This conclusion remains valid for a general orientation of the surface, since the coordinate system can always be transformed to the desired orientation by rotation.

Finally, on s_3 the virtual velocities are zero, and the corresponding portion of the integral vanishes.

3 Numerical Implementation

3.1 Discretization. In most of the papers referenced previously, a few planes of velocity discontinuity are passed through the plastic material. This technique requires little programming and provides fast solutions when a small number of parameters is sufficient to accurately represent the problem. It becomes inefficient for problems requiring descriptions in terms of many parameters. A finite element/difference approach, e.g., Azarkhin and Richmond (1989), Bin and Luo (1988), can then be used. For the examples given below, a version of the finite element/difference method, the balance method (Bin and Luo, 1988; Buhman, 1969; Liszka and Orkisz, 1980), was used. Its idea can be demonstrated as follows. For a sufficiently small element with volume Δv:

$$\frac{\partial u}{\partial x}\Delta v\approx\int_v\frac{\partial u}{\partial x}dv=\int_s u ds_x\approx\sum_{i=1}^{n}\overline{u}\Delta s_{xi}, \tag{10}$$

where n is the number of sides, $\overline{u}$ is the value averaged over the side i, Δs_i is the area of the side, and Δs_{xi} is the projection of this area onto the plane perpendicular to the x-axis. Therefore,

$$\frac{\partial u}{\partial x}\approx\frac{1}{\Delta v}\sum_{i=1}^{n}\overline{u}_i\Delta s_{xi}. \tag{11}$$

This numerical representation, combined with the upper bound method, generates the system of nonlinear algebraic equations with unknown velocities. The technique employed for its solution is described in the following section.

3.2 Numerical Solution. We use the upper bound method to find the field of velocities and the rates of deformations by direct minimization of the functional (1) with constraint (2) and the constraints imposed by the kinematic boundary con-

Downloaded 03 May 2010 to 171.66.16.248. Redistribution subject to ASME license or copyright; see http://www.asme.org/terms/Terms_Use.cfm

ditions. Standard subroutines for minimization with constraints, available in the software for VAX, FPS, and CRAY computers, failed to deliver solutions. The process was too slow and, in certain cases, even divergent. We developed an algorithm based on the method of local variations (Chernoysko, 1965; Cheruault, 1968; Azarkhin and Richmond, 1990a; Elkin, 1968) with modifications as briefly described below.

Suppose an initial approximation for all components of velocities, $\{u_i\}$, is given, where $i = 1, 2, \ldots . 3N$ with N being the number of nodes. We first update the value of u_1 by finding the minimum of functional (1) with respect to this unknown, keeping all other unknowns unchanged. We then repeat the minimization process incrementing u_2 and keeping all other velocities (including the updated u_1) unchanged. The iteration is complete when all unknowns are similarly iterated. We repeat these iterations many times until the convergence to some prescribed tolerance is reached.

There are two advantages of this procedure. First, we minimize the functional with respect to one unknown at a time, which is easy for numerical implementation. Second, by the very nature of the algorithm, the process will always lead in the direction of decrease for the functional. The algorithm is particularly suited for the functional generated by sparsely filled matrices, the situation typical of finite element representations. The relationship of this procedure to the Gauss-Seidel algorithm is apparent (Elkin, 1968).

There is no guarantee, of course, that we find the global minimum. We note, however, that local minima or saddle points are also solutions to the initial problem governed by the Euler equations. Therefore, this is a case of nonuniqueness for the rigid/perfectly plastic model rather than a problem of the algorithm of minimization. In our experience, we have never arrived at a local minimum or a saddle point. This has been verified by starting the iterations from different initial approximations and always arriving at the same results. In the case of nonuniqueness, the algorithm presents one more advantage: It delivers the solution with the minimum rate of work, the only solution of practical interest.

A further modification of the algorithm was used to accelerate convergence. Suppose some changes of velocities are accumulated in a few iterations, giving $\{u_i + du_i\}$, $i = 1, 2, \ldots 3N$. The iterative process is usually monotonic, and probably will continue in the same direction. Thus, the accumulated increments can be used to "project" the trial values $\{u_i + \beta du_i\}$ with β being defined by minimization of (1). Since this requires minimization with respect to a single parameter, β, the same for all increments, it presents no difficulty. In our estimate, this procedure can lead to two or threefold acceleration in solution time.

3.3 Postprocessing. The hydrostatic pressure is found by postprocessing equations (6) and (7), using the velocities found earlier. There is only one unknown hydrostatic pressure at each node, and there are three equations to find it. But this is no contradiction. It follows from the foregoing discussion that the field of velocities is such that all equations are compatible. While this is true for an analytical solution, it can never be achieved for a numerical implementation due to unavoidable inconsistencies in numerical representation of derivatives and due to the fact that iteration is aborted. The problem was resolved by using the least squares method.

3.4 Discussion. The algorithm described here is applied incrementally. We start with given domain configuration and boundary conditions. We then assume that the velocities derived through the minimization process are valid for a short period of time, dt. This permits us to update the configuration of the domain, and to proceed to the next step. Comparing the present algorithm with the full elastic-plastic solution, we note:

1 Each step of the present algorithm is simpler, because all unknowns related to the elastic portion of the problem are excluded from consideration. On the other hand, applications of the algorithm are restricted to problems with predominantly plastic deformations.

2 The increments for each step can be much larger than for the corresponding elastic-plastic problem, since they may be chosen from geometrical considerations alone—updating the boundary with sufficient accuracy.

We shall now compare the present numerical approach with alternative implementations which were under considerations in the course of this work.

We could attempt to find the stationary point of the augmented functional directly. That would provide us with the stresses, $\sigma_{ij} = \sigma_{ij}' + \lambda\delta_{ij}$, without the use of equilibrium equations. This approach faced serious difficulties. For example, the stationary point of the augmented functional is not an extremum point. It can be a saddle point or nothing at all (Washizu, 1950; Abovsky et al., 1978). This makes most of the algorithms for optimization, including the one used here, inapplicable. In the case of nonuniqueness, we would have had a problem to choose the physically meaningful solution.

In the present algorithm, we used the penalty approach to enforce the incompressibility equation and the kinematic boundary conditions. We minimized the functional

$$\phi(\mathbf{u}) = f(\mathbf{u}) + \int_v K_1(\epsilon_{ii})^2 dv + \int_{s_3} K_2(\mathbf{u} - \mathbf{u}^*) ds \qquad (12)$$

where u^* is the prescribed normal velocity on the surface s_3. In a manner similar to that employed in Section 2, it could be shown that the penalty numbers have certain physical meaning. For example, K_1 is the bulk modulus for slightly compressible material, and the hydrostatic pressure could be found as

$$\sigma_{ii} = K_1 \epsilon_{ii}. \qquad (13)$$

This gives stresses without the use of equilibrium equations. Similarly, K_2 is the stiffness of an artificial spring placed between the body and the rigid boundary and resisting interpenetration or separation of both. The contact stress can be computed as

$$\sigma_n = K_2 \Delta u_n. \qquad (14)$$

The problem with this approach is demonstrated on the following example. Suppose that after many iterations we obtained a solution at a point of a rigid boundary which looks like either $0.99999u^*$ or $1.00001u^*$, where u^* is the given velocity. Both results are quite satisfactory for all practical purposes, and it is time to abort the iterations. Normal stresses, however, are different. They are $0.00001\,K_2$ and $-0.00001\,K_2$, respectively. Our experience shows that this is precisely what happens. For high penalty numbers K_1 and K_2,we could not suppress the oscillations in any reasonable number of iterations. The process became more stable for smaller values of K_1 and K_2, but the incompressibility equations yielded unpermissible errors.

The idea of finding stresses in postprocessing, using the field of velocities provided by the upper bound method, was presented by Barata Marques and Martins (1989). The field of velocities was assumed to be compatible with the equilibrium equations. We can see from the foregoing discussion that this assumption was correct. However, the use of the stress function was a substantive portion of the algorithm. This reduced the scope to two-dimensional problems. We also remark that the authors described the configuration of inlet and outlet surfaces by a few free parameters found by the minimization of the rate of work. However, as we mentioned in the introduction, the upper bound method requires the configuration of the surface to be prescribed.

Finally, we mention that in our earlier paper (Azarkhin and Richmond, 1990b) we were not aware that the equilibrium

Downloaded 03 May 2010 to 171.66.16.248. Redistribution subject to ASME license or copyright; see http://www.asme.org/terms/Terms_Use.cfm

equations are fully incorporated in the upper bound method, and so we added equilibrium equations to functional (1) along with the other penalty terms. While there is no error in doing this, it makes convergence of the iterative process much slower.

4 Examples. Influence of Subsurface Straining on Rigid Asperity Penetration

When surfaces are pushed together (under dry conditions or under conditions of boundary lubrication), most of the load is carried by asperities in direct contact (Bowden and Tabor, 1950). The area of direct contact grows with the applied load. The picture is complicated by interaction of asperities and subsurface deformation of the bulk material. Asperity flattening due to subsurface straining was studied experimentally (see Greenwood and Rowe, 1965). The upper bound method was used by Sutcliffe (1988) and by Wilson and Sheu (1988) with a small number of parameters to model the influence of subsurface straining on the growth of the contact area for a regularly distributed array of asperities. In this section, we recompute some of these results for the sake of comparison. We also present some new results, not obtainable by the conventional upper bound method.

4.1 Single Asperity. We start with a single two-dimensional asperity as shown in Fig. 1. The origin is placed in the middle of the contact area with x directed along the interface and y directed inside the plastic material. The angle α in Fig. 1(a) is defined as an angle between the x-axis and the line tangent to the plastic material surface. For a small angle α, the results are valid for either Fig. 1(a) or Fig. 1(b). For a large angle α, the graphs below relate to Fig. 1(b). For all further discussion we will refer to Fig. 1(b). We consider the start of the process in which the penetration of the rigid tool into the asperity with the velocity u_o is accompanied by the remote deformation rates, $\epsilon_x = -\epsilon_y$. Considering the symmetry of the system, half of the domain was taken. The infinite medium was approximated by taking a domain with size considerably larger than the size of the contact. The mesh was condensed in the area of contact, and elements were made progressively larger with increasing distance from the area of contact. We took 126 nodes (256 unknown velocities), and 104 rectangular elements (104 unknown hydrostatic pressures positioned in the middle of the elements). The rate of work for pure tension/compression of a plate of a unit thickness under plain-strain conditions is

$$W = \frac{2\sigma_o}{\sqrt{3}} S|\epsilon_x| \tag{15}$$

where S is the cross-section area of the considered domain. The rate of work increases by some amount ΔW when pure tension/compression is combined with the tool penetration. This amount drops as the subsurface deformation increases (Fig. 2). It can be seen that the curve for the additional rate of work in the case of compression is above that for tension, which is intuitively obvious. Our intuition failed in the problem of ploughing, however, when the two curves turned out to be identical (Azarkhin and Richmond, 1990a). Surprisingly, the two curves in Fig. 2 did not respond to changes in the friction factor, m, at the interface between the asperity, and the half plane. In Fig. 2 and everywhere else in this paper, L denotes the semi-width of the contact area.

The additional rate of work ΔW cannot be identified with the rate of work done by the asperity alone,

$$W_{asp} = F\, u_o \tag{16}$$

since the change ΔW is also due to changes in the bulk straining force. This can be seen from the third curve (denoted by triangles) in Fig. 2 for the force F, plotted for frictionless contact, $m = 0$.

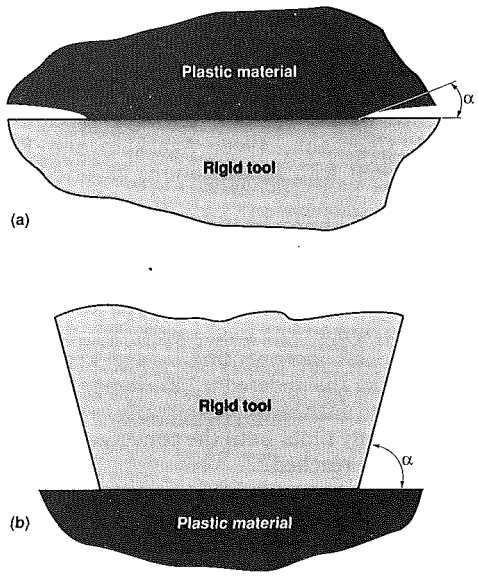

Fig. 1 A model of a single asperity

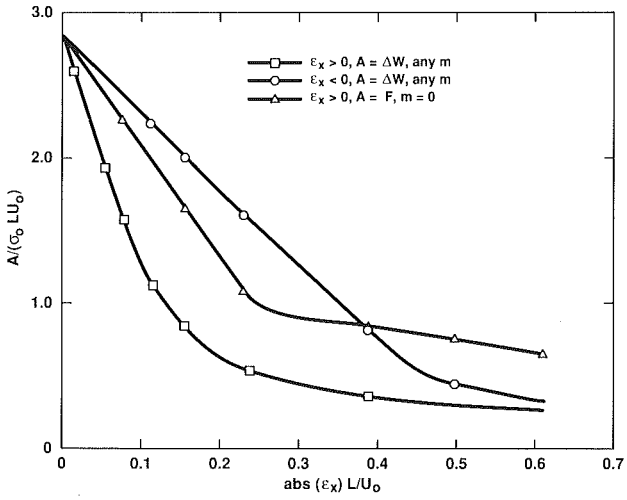

Fig. 2 Influence of subsurface strain on additional rate of work

Figures 3 and 4 show the local normal stress distributions. Strictly speaking, these are stresses σ_y in the middle of the near surface elements which in this case is at the level $L/14$ below the surface. The curves in Fig. 3 demonstrate that the contact stresses drop as the bulk straining rate, ϵ_x, grows. Frictionless contact was assumed here, i.e, $m = 0$. We note good agreement of the curve for $\epsilon_x = 0$ with the average stress $\sigma/\sigma_o = 1 + \pi/2$ obtained by Prandtl (1920) who used the slip line method. The stress is shown in Fig. 3 by the broken line for comparison.

The friction factor, m, influences the local contact stresses. Since the additional rate of work caused by the asperity penetration, ΔW_1, does not depend on the friction factor, one might have expected to see different local contact stress distributions giving the same force F for different friction factors. It can be seen in Fig. 4 that this did not happen; the force F, and the rate of work (16), grow as the friction factor m increases. But since the full rate of work done by the force F and by the prestraining forces is the same, it follows that the forces prestraining the bulk of material decrease as the friction factor grows.

4.2 Array of Asperities. We now consider an array of uniformly distributed asperities as shown in Fig. 5(a). The material is subjected to bulk deformation rate in the z-direction, ϵ_z = const. In view of symmetry, only the area shown

Downloaded 03 May 2010 to 171.66.16.248. Redistribution subject to ASME license or copyright; see http://www.asme.org/terms/Terms_Use.cfm

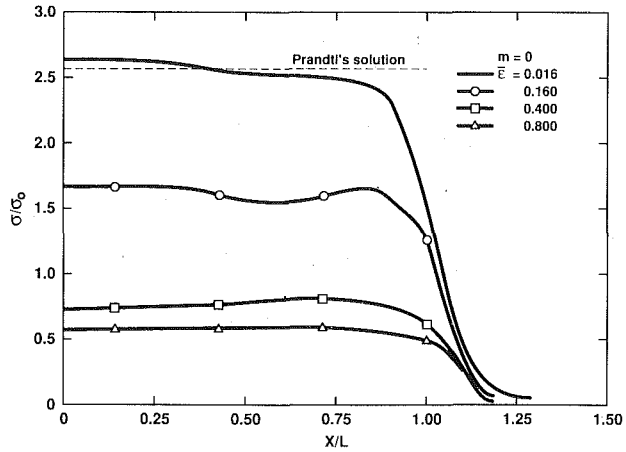

Fig. 3 Influence of the subsurface strain on the contact stresses

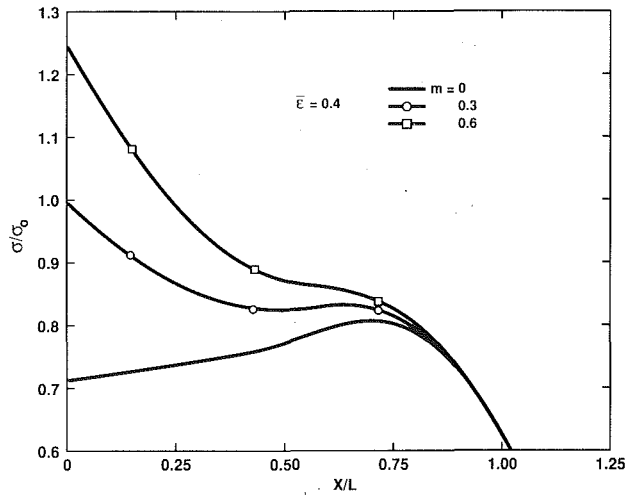

Fig. 4 Influence of the friction factor, m, on the contact stresses

in Fig. 5(b) was considered. The distance h from the surface was taken sufficiently large with respect to the contact width to model an infinite medium. To compensate for the loss of material in the z-direction, we assume the velocity through the bottom of the control volume to be $u_y = e_z h$. Therefore, the surface of the material remains at the same level as for bulk deformation in the absence of asperity penetration. The influence of the bulk deformation on the additional rate of work due to asperity penetration per asperity for $a/b = 1$ is shown in Fig. 6 (line with circles). This problem was solved earlier by Wilson and Sheu (1988) who used only one parameter for minimization. Their result is also shown in Fig. 6 (solid line). The difference is significant, but the results are very reasonable considering the degree of approximation. Those authors assumed that this change in the rate of work can be attributed to the change in the work done by the forces of penetration. In fact, the change in the rate of work is also due to changes in face end forces caused by the penetration. The traditional upper bound method does not permit determination of these forces. Sutcliffe (1988) tried to separate the forces by assigning a value to one of them, average pressure, and calculating the remaining face end forces. The following objection could be raised. The average pressure is already defined by the problem and cannot be assigned arbitrarily. Therefore, the curves are correct at some points but we do not know where. The present technique permits separation of the forces by determining the contact stresses. The results are also shown in Fig. 6 by the curve with squares. We can see that the new curve is located below the two curves discussed before.

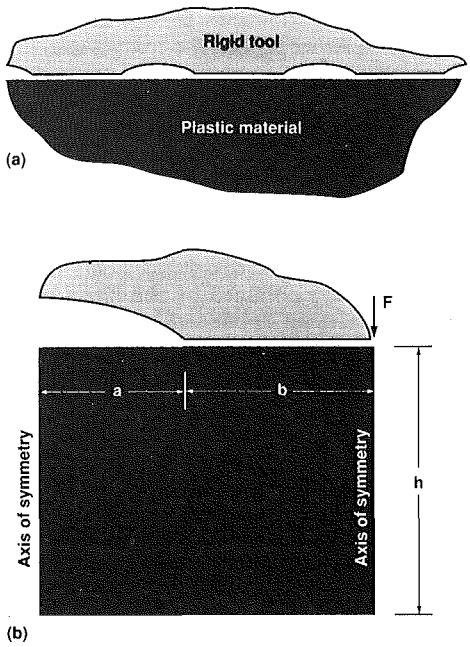

Fig. 5 Array of asperities

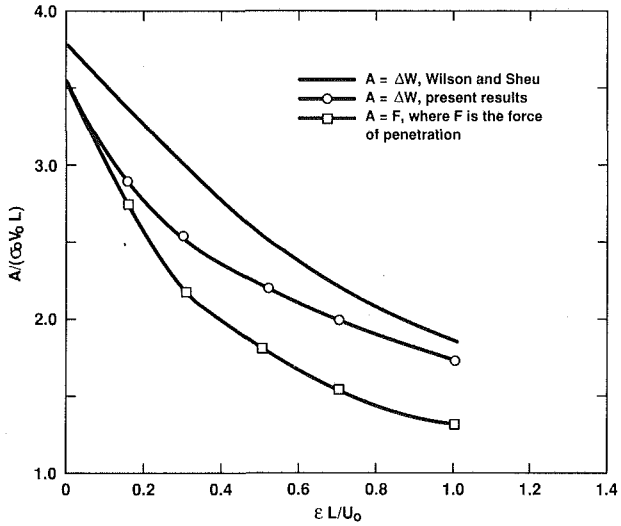

Fig. 6 Influence of the subsurface strain in the longitudinal direction on the work and force of penetration

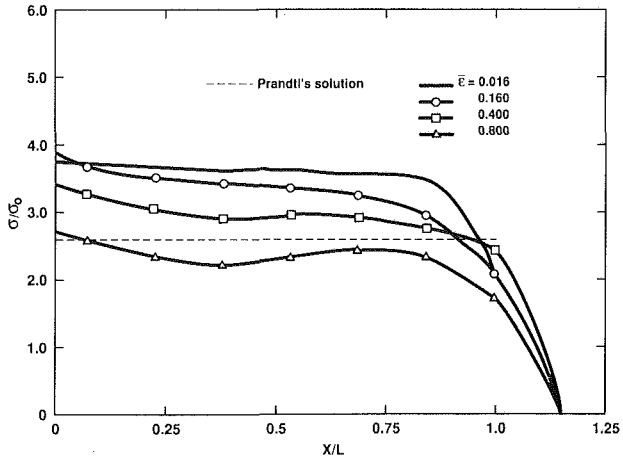

Fig. 7 Contact stress distribution for an array of asperities

Downloaded 03 May 2010 to 171.66.16.248. Redistribution subject to ASME license or copyright; see http://www.asme.org/terms/Terms_Use.cfm

The contact stress distributions for the array of asperities are shown in Fig. 7. As we expect, the contact stresses decrease as the deformation rate ϵ_z increases. The stresses are higher than those for the single asperity, Fig. 3, because the system is now stiffer due to interference of asperities.

5 Conclusion

The present algorithm retains the major feature of the upper bound method in that the field of displacements and evaluation of the rate of work are obtained by the direct minimization of the functional without solving the governing equations. However, the hydrostatic pressure and local stress distribution, which usually are not present in the upper bound method, are recovered from the governing equations through postprocessing. This is a simple task, considering the fact that the equations are linear with respect to hydrostatic pressure. We use a finite element/difference representation which allows us to introduce many parameters in a standard fashion, and which does not require guesses of the planes of velocity discontinuity. Therefore, the technique seems to be a feasible alternative for problems with predominantly plastic flow where higher accuracy is required. We applied this algorithm to a tribological problem, obtained some results and compared them with previous approximate solutions.

References

Abildgaard, T., 1984, "Prediction of the Force Components Acting on a Ploughing Cone by Means of Three-Dimensional Upper Bound Theory," *Advanced Technology of Plasticity*, Vol. 1, pp. 121–126.

Abovsky, N. P., Andreyev, N. P., and Deruga, A. P., 1978, *Variational Principles in Elasticity and Shell Theory*, Nauka, Moscow (in Russian).

Avitzur, B., Huang, C. K., and Zhu, Y. D., 1984, "A Friction Model Based on the Upper Bound Approach to the Ridge and Sublayer Deformation," *Wear*, Vol. 95, pp. 59–77.

Azarkhin, A., and Richmond, O., 1989, "A Generalization of the Upper Bound Method with Particular Reference to the Problem of a Ploughing Indenter," ASME JOURNAL OF APPLIED MECHANICS, Vol. 56, pp. 10–14.

Azarkhin, A., and Richmond, O., 1990a, "On Friction of Ploughing by Rigid Asperities in the Presence of Straining. Upper Bound Method," ASME *Journal of Tribology*, Vol. 112, pp. 324–329.

Azarkhin, A., and Richmond, O., 1990b, "A Simple Algorithm for Predominantly Plastic Flows with Free Surfaces," *Int. J. Mech. Sci.*, Vol. 32, No. 2, pp. 147–157.

Barata Marques, M. J. M., and Martins, P. A. F., 1989, "A Solution to Plane Strain Extrusion by the Upper Bound Approach and the Weighted Residuals Method," *Int. J. Mech. Sci.*, Vol. 31, No. 5, pp. 395–406.

Bin, F., and Luo, Z. J., 1988, "Finite Element Simulation of the Friction Mechanism in Plastic Working Technology," *Wear*, Vol. 121, pp. 41–51.

Bowden, F. P., and Tabor, D., 1950, *The Friction and Lubrication of Solids, Part I*, Clarendon Press, Oxford, U.K.

Buhman, V. E., 1969, "Contour Approximation Method for Finite Difference Equations," *Ob effectivnosti analogovih methodov reshenia kraevih zadach*, Nauka, Moscow (in Russian).

Chernoysko, F. L., 1965, "Method of Local Variations for Numerical Solution of Variational Problems," *Journal of Computational Mathematics and Mathematical Physics* (*Zurnal Vichisl. Mat. i Mat. Fisiki*, in Russian), Vol. 5, No. 4

Cheruault, Y., 1968, "Une Methode Directe de Minimization et Applications," *Rev. Fr. Inform. Rech. Operation*, Vol. 10, pp. 31–52.

De Vathire, M., Delamare, F., and Felder, E., 1981, "An Upper Bound Model of Ploughing by a Pyramidal Indenter," *Wear*, Vol. 66, pp. 51–64.

Drucker, D. C., 1954, "Coulomb Friction, Plasticity, and Limit Loads," ASME JOURNAL OF APPLIED MECHANICS, Vol. 21, pp. 71–74.

Drucker, D. C., Greenberg, H. J., and Prager, W., 1951, "The Safety Factor of an Elastic-Plastic Body in Plane Strain," ASME JOURNAL OF APPLIED MECHANICS, Vol. 18, pp. 371–378.

Drucker, D. C., Prager, W., and Greenberg, H. J., 1952, "Extended Limit Design Theorems for Continuous Media," *Quart. Appl. Math.*, pp. 381–389.

Elkin, R. M., 1968, "Convergence Theorems for Gauss-Seidel and Other Minimization Algorithms," Tech. Rep. 68-59, Univ. of Maryland, Computer Science Center, College Park, Md.

Greenwood, J. A., and Rowe, G. W., 1965, "Deformation of Surface Asperities During Plastic Flow," *J. Appl. Phys.*, Vol. 36, pp. 667–668.

Gvozdev, A. A., 1938, "The Determination of the Value of the Collapse Load for Statically Indeterminate Systems Undergoing Plastic Deformation," *Proceedings of the Conference on Plastic Deformation, Acad. of Sci. USSR*, pp. 19–33 (in Russian); English Translation in *Intern. J. Mech. Sci.*, 1960, Vol. 1, pp. 322–355.

Hill, R., 1951, "On the State of Stress in a Plastic-Rigid Body at the Yield Point," *Phil. Mag.*, Vol. 42, pp. 868–875.

Hill, R., 1952, "A Note on Estimating the Yield-Point Loads in a Plastic-Rigid Body," *Phil. Mag.*, Vol. 43, pp. 353–355.

Hill, R., 1985, *The Mathematical Theory of Plasticity*, Clarendon Press, Oxford, U.K.

Liszka, T., and Orkisz, J., 1980, "The Finite Difference Method at Arbitrary Irregular Grids and its Applications in Applied Mechanics," *Computers and Structures*, Vol. 11, No. 1-2, pp. 83–95.

Oh, S. I., and Kobayashi, S., 1975, "An Approximate Method for a Three-Dimensional Analysis in Rolling," *Intern. J. Mech. Sci.*, Vol. 17, pp. 293–305.

Prager, W., 1959, *An Introduction to Plasticity*, Addison-Wesley, Reading, Mass.

Prandtl, L., 1920, *Über die Härte Plastischer Koerper, Goettinger Nachr., Math Phys. Kl*, pp. 74–78.

Rabinowicz, E., 1965, *Friction and Wear of Materials*, John Wiley and Sons, New York.

Rowe, J. W., 1977, *Principles of Industrial Metal Working Processes*, E. Arnold, Ltd., London.

Suh, N. P., 1986, *Tribophysics*, Prentice-Hall, Englewood Cliffs, N.J.

Sutcliffe, M. P. F., 1988, "Surface Asperity Deformation in Metal Forming Processes," *Int. J. Mech. Sci.*, Vol. 30, pp. 847–868.

Wanheim, T., 1978, "A Model for Friction in Metal Forming Processes," *Ann CIRP*, Vol. 27, pp. 189–196.

Washizu, K., 1950, *Variational Methods in Elasticity and Plasticity*, Pergamon Press, Oxford.

Wilson, W. R. D., and Sheu, S., 1988, "Real Area of Contact and Boundary Friction in Metal Forming," *Int. J. Mech. Sci.*, Vol. 30, pp. 475–489.

Downloaded 03 May 2010 to 171.66.16.248. Redistribution subject to ASME license or copyright; see http://www.asme.org/terms/Terms_Use.cfm

A Consistent Implicit Formulation for Nonlinear Finite Element Modeling With Contact and Friction: Part I—Theory

M. J. Saran
Associate Professor,
Mem. ASME

R. H. Wagoner
Professor,
Mem. ASME

Department of Materials Science and Engineering,
The Ohio State University,
Columbus, OH 43210

A formulation for finite element simulation of highly nonlinear problems including friction and contact with arbitrarily shaped rigid surfaces is proposed (CFS approach), prompted by difficulties in robust and accurate simulations of industrial forming processes. Nonlinearities are caused by large strains, plastic flow, and complex boundary conditions with frictional contact. In Part I the theoretical basis is described and the appropriate numerical algorithm is derived. The complete set of the governing relations, comprising equilibrium and interfacial equations, is appropriately linearized; resulting in a consistent tangent operator of the Newton-Raphson algorithm. In Part II, as a numerical verification, plane-strain sheet-forming processes are analyzed using a rigid-viscoplastic material model. Results are presented and discussed for test problems and for complex simulation of reverse drawing by concave tools.

1 Introduction

During recent years a number of finite element analyses for modeling nonlinear problems including contact and friction have appeared in the literature. A number of problems involving flat contact surfaces, such as classical Herz problem, can now be analyzed numerically with good accuracy. The approaches adopted for such problems are not often successful for the more complex geometries characteristic of many practical applications. The developments presented in this paper were prompted by difficulties encountered in performing robust and accurate analysis of the deep drawing process. The central difficulty, although discovered via sheet metal-forming analysis, is pertinent for all frictional contact applications with the following characteristics: (a) arbitrarily shaped (curvilinear) contact surfaces; (b) large relative movement between material points of the contacting surfaces; (c) changing and unknown set of material points in contact during the deformation process. These characteristics can cause severe nonlinearities in the governing system of equations, thereby inhibiting convergence and robustness. The proposed approach improves solution robustness and accuracy under these severe conditions.

Various models were utilized for description of friction and contact conditions. As physical interpretation of the frictional contact is still under debate (see, for example, Tabor 1975, 1981; Olden, 1981), the simple laws of Coulomb or constant shear condition are usually assumed.

There are a number of procedures proposed for the solution of contact problems. For a mathematical background, works by Duvaut and Lions (1976), Oden and Martins (1985), or Kikuchi and Oden (1986) are recommended. The finite difference approach for large pressures with an explicit algorithm were given by Wilkins (1964) and Maenchen and Sack (1964). On the other hand, Stecher and Johnson (1984) and Belytschko and Lin (1985) used momentum conservation in an eroding surface contact algorithm. A penalty function approach was adapted by Hallquist (1979) as better suited for explosive-metal interaction simulations. It was also used by Oden (1981) and Fellipa (1978), among others. The penalty approach satisfies the contact conditions approximately and the accuracy of the approximate solution depends strongly on the penalty parameter. However, there are no clear rules to choose this parameter; it depends on the particular problems considered.

In metal-forming applications, the direct trial and error approach of enforcing contact by direct application of boundary displacements using separate projection subroutines is often used (see, for example, Nagtegaal and Rebelo, 1986; Germain et al., 1989; or Choudhry and Lee, 1989). In this approach, a consistent linearization procedure cannot be applied, resulting in lower stability and efficiency. An application of a special procedure at the very first step to find close enough trial start-up solution for Newton-Raphson (N-R) solver is necessary (Wang, 1984).

Finally, several algorithms based on variants of the Lagrangian multiplier method have been introduced. The general

Contributed by the Applied Mechanics Division of THE AMERICAN SOCIETY OF MECHANICAL ENGINEERS for presentation at the Joint Applied Mechanics/Bioengineering Conference, Ohio State University, Columbus, OH, June 16-19, 1991.

Discussion on this paper should be addressed to the Technical Editor, Prof. Leon M. Keer, The Technological Institute, Northwestern University, Evanston, IL 60208, and will be accepted until two months after final publication of the paper itself in the JOURNAL OF APPLIED MECHANICS. Manuscript received by the ASME Applied Mechanics Division, July 11, 1990; final revision, Oct. 26, 1990.
Paper No. 91-APM-1.

Copyright © 1991 by ASME
Downloaded 03 May 2010 to 171.66.16.248. Redistribution subject to ASME license or copyright; see http://www.asme.org/terms/Terms_Use.cfm

Lagrangian method raises the dimension of the stiffness matrix, a major drawback in linear applications. However, in nonlinear cases of inelastic models with frictional contact, the size of the linear system is no longer the only decisive factor determining numerical efficiency. The basic advantage of the Lagrangian multiplier approach is that the contact conditions are fulfilled exactly, and the construction of a consistent stiffness matrix is possible. For frictionless contact problems, perturbed and augmented Lagrangian techniques were described by Simo et al. (1985), Luenberger (1984), Landers and Taylor (1985), respectively.

For the most algorithms described in current literature, the contribution of the frictional contact consists only of the linear terms, often derived from the rate equations (see, for example, Hughes et al., 1976; Bathe and Chaudhary, 1985; Mattiasson et al., 1987). Those and other developments, as by Wang (1984), result in nonconsistent stiffness matrices. When highly nonlinear frictional contact problems are considered, this leads to slower convergence and lower stability of the N-R solution. A consistent tangent operator based on the perturbed Lagrangian approach, but for frictionless contact, has been obtained by Wriggers and Simo (1985). Algorithms based on analogy between Coulomb's law of friction with stick-slip model and elastoplasticity were proposed by Ju et al. (1987), Wriggers (1987), and Giannakopoulos (1989). The usefulness of the consistent, with this model, tangent operator was demonstrated on examples with linear contact boundaries between elastic bodies.

In this paper, a consistent linearization of the proposed here governing equations including both contact and friction conditions is developed, resulting in an algorithm exhibiting quadratic rate of convergence and considerably improved robustness.

The proposed approach is quite general, however, the presented applications are aimed primarily at metal forming. Most of the general algorithms described in the literature treat contact as an interaction between deformable bodies. In metal-forming applications, where the tools are practically rigid, a "two pass" algorithm is then necessary, thereby decreasing efficiency. To avoid this, we will assume explicitly in the contact algorithm that the tools are to be rigid relative to the deformable material of the workpiece. For a general review of forming modeling, the reader is referred to the conference proceedings from Numiform (1982, 1986, 1989), or to the review given by Kobayashi (1985) or Kobayashi et al. (1989).

Besides contact and friction, the material model is an important part of the algorithm influencing efficiency and possibly also numerical stability. In metal-forming applications, both rigid and elastoplastic models have been utilized. Rigid-plastic constitutive relations have been used both with the material description of the motion (Kobayashi and Kim, 1978; Oh and Kobayashi, 1980; Wang, 1984; Choudhry and Lee, 1989; Germain et al., 1989; for example), as well as with the flow formulation (Oñate and Zienkiewicz, 1983; Zienkiewicz, 1984; for example). The use of elastic-plastic relations for metal-forming applications was dated from earlier papers by Lee and Kobayashi (1973) and Wang and Budiansky (1978), for example. The use of rate kinematics required very small incremental steps. Since then several improvements have been made (see, for example, Tang, 1981; Wang and Wenner, 1982; Cheng and Kikuchi, 1985; Makinouchi, 1985; Nakamachi, 1986; Massoni et al., 1987; and Saran et al., 1990). It is commonly believed that the elastic-plastic models allowing for analyzing elastic effects are less time efficient than the rigid-plastic because of their generally greater complexity and since smaller step sizes are required. Recent progress in the application for sheet forming of the implicit integration of the constitutive equations and of adaptive remeshing techniques (Saran and Samuelsson, 1990; Saran and Runesson, 1991) should allow for considerably larger steps in the elastic-plastic analysis.

The variety of existing approaches reflects the fact that the highly nonlinear problem with frictional contact is computationally very difficult. It is possible nowadays to simulate, with good accuracy, processes with simple geometries and small changes in contact surfaces, hence predominantly such examples appear in abundance in the literature. Despite this success, there is still a great deal of effort necessary to develop a reliable and cost-effective algorithm for practical analysis of industrial problems which can treat complex, irregularly curved geometries and large material displacements.

The goal of our research was to create an algorithm with considerably increased stability and accuracy for various complex frictional contact conditions, at the same time being cost effective to use for realistic industrial applications.

The fundamental idea for constructing the proposed algorithm (CFS approach) lies in the consistent linearization of the complete set of governing relations comprising kinematic, constitutive, equilibrium, and interfacial equations in order to preserve quadratic rate of asymptotic convergence of the N-R method and to obtain good numerical stability.

In Part I the theory and the numerical method are described. The standard incremental implicit approach, based on displacements as primary unknowns and Lagrangian description of motion was used. The basic governing relations in the notation used in this paper are summarized in Section 2 and interfacial conditions are presented in Section 3. Section 4 deals with the proposed formulation, and with the derivation of the resulting consistent stiffness matrix. The summary of the solution algorithm and the numerical techniques aimed toward further improvement in stability and efficiency are given in Section 5. Finally, the specific formulas for plane-strain sheet-forming problems are derived in Section 6. In Part II numerical evaluation with "section analysis" sheet-forming problems is presented. Simple benchmarks as well as the simulation of redrawing and reverse drawing with two-side draw-in and various drawbead forces are considered. The resulting quadratic rate of asymptotic convergence is documented.

2 Review of the Basic Mechanical Formulation

This section reviews the notation and basic equations for an incremental, implicit finite element approach, following Germain et al. (1989) and Wang (1984). In the present paper the proposed consistent formulation, starting from these equations, will be presented in the next sections. More fundamental details on the derivation of the basic governing equations can be found elsewhere (see, for example, Zienkiewicz, 1977; Bathe, 1982; or Oden and Carey, 1984).

In what follows, we assume a Lagrangian description considering motion of the body from the initial configuration ${}^0C$ (at time $\tau=0$) to configurations ${}^nC$ at time $\tau=t$ and ${}^{n+1}C$ at time $\tau=t+\Delta t$, where Δt is a finite (not infinitesimal) time increment. Further on, in specific applications presented we will assume an updated Lagrangian formulation. The presuperscript is used to denote the time-step number in the time discretization of the mechanical problem.

Denote the position of the typical particle at time $\tau=0$ by ${}^0x$ and at times $\tau=t$ and $\tau=t+\Delta t$ by ${}^nx$ and ${}^{n+1}x$, respectively. Then we introduce the displacement vector $\mathbf{u}$ and the displacement increment vector $\Delta\mathbf{u}$ with the following definitions:

$$ {}^{n+1}\mathbf{x} = {}^n\mathbf{x} + \Delta\mathbf{u} = {}^0\mathbf{x} + \mathbf{u} + \Delta\mathbf{u}. \tag{1} $$

Performing finite element discretization by assuming appropriate shape functions in the standard manner, converting the external surface force distribution into nodal point forces, and denoting for simplicity by $\Delta\mathbf{u}$ the vector of the nodal incremental displacements in further derivations, the equilibrium equation finally becomes

$$ \mathbf{F}_I(\Delta\mathbf{u}) = \mathbf{F}_E(\Delta\mathbf{u}), \tag{2} $$

where $\mathbf{F}_I$ is the internal force vector which is defined later for

Downloaded 03 May 2010 to 171.66.16.248. Redistribution subject to ASME license or copyright; see http://www.asme.org/terms/Terms_Use.cfm

the specific material model used, and $\mathbf{F}_E$ represents the vector of external forces.

To proceed with numerical applications, we must assume a particular constitutive law. A *rigid-viscoplastic model* will be used for numerical calculations of metal forming presented in the paper. This reflects observations from most forming operations that elastic strains can be neglected. The immediate advantage is an increased efficiency over the elastic-plastic model. The main disadvantages concern unloading problems. Local unloading into the elastic region during forming can result in numerical problems when iterating the equilibrium conditions. A numerical algorithm to handle this problem, as proposed by Chung and Wagoner (1987), will be discussed in Section 5.4.

The incremental plastic work associated with the deformation $t \to t+\Delta t$ is

$$\Delta W = \int_V \int_t^{t+\Delta t} \tau^{ij} D_{ij} dt\, dV, \tag{3}$$

where τ^{ij} is Kirchhoff stress tensor, D_{ij} rate of deformation tensor, and integration is over the current volume. Assuming isotropic hardening and the equivalent work principle to hold (Hill, 1950), an alternative form of equation (3) is

$$\Delta W = \int_V \int_t^{t+\Delta t} \sigma_e \dot{\epsilon}_e dt\, dV \tag{4}$$

where σ_e and $\dot{\epsilon}_e$ denote the effective stress and the effective strain rate, respectively.

The incremental effective strain $\Delta\epsilon_e$ is defined as the change of the effective strain rate over the time step

$$\Delta\epsilon_e = \int_t^{t+\Delta t} \dot{\epsilon}_e dt. \tag{5}$$

To avoid the numerical integration of the constitutive equations, a *fixed* strain path throughout the incremental step can be assumed. In this research, following Germain et al. (1989), the minimum plastic work path is adopted. It is guaranteed by the following assumptions: The principal directions of the rate of deformation tensor D_{ij} are parallel to the same material lines, and the ratio of the principal values of D_{ij} remains constant throughout the time step. An error evaluation performed by Germain et al. (1989) showed no error for uniaxial or balanced biaxial state of the deformation. For the simple shear case, at an unrealistically large strain increment of 10 percent, the relative error was less than 0.125 percent, so for usual strain increments (much below 10 percent) the material hardening is integrated very precisely.

With the fixed strain path, for a given displacement increment $\Delta\mathbf{u}$, the increase of the effective strain is no longer path dependent, but is a fixed function of the incremental strain tensor

$$\Delta\epsilon_e = \Delta\epsilon_e(\Delta\epsilon_{ij}). \tag{6}$$

The specific form of equation (6) can be obtained explicitly for most common yield functions, or can be solved numerically for arbitrary yield functions.

After integration over time, the variation of the work increment can be written on the basis of equation (4) as:

$$\delta\Delta W_p = \int \sigma_e \frac{\partial\Delta\epsilon_e}{\partial(\Delta\mathbf{u})} \delta\Delta\mathbf{u} dV, \tag{7}$$

resulting finally in the following expression for internal force vector

$$\mathbf{F}_I = \int \sigma_e \frac{\partial\Delta\epsilon_e}{\partial(\Delta\mathbf{u})} dV. \tag{8}$$

Hill's nonquadratic, normal-anisotropic yield function (Hill, 1979) will be utilized later in this paper when sheet-forming applications are presented. Under the assumed conditions of isotropic hardening (r, M = constants) and the minimum work path (described above), the effective stress σ_e and its associated effective strain increment $\Delta\epsilon_e$ are defined in terms of the principal values as follows:

$$\sigma_e = [2(1+r)]^{\frac{-1}{M}} [|\sigma_1+\sigma_2|^M + [1+2r]\,|\sigma_1-\sigma_2|^M]^{\frac{1}{M}} \tag{9}$$

and

$$\Delta\epsilon_e = B_1[|\Delta\epsilon_1+\Delta\epsilon_2|^{\frac{M}{M-1}} + B_2|\Delta\epsilon_1-\Delta\epsilon_2|^{\frac{M}{M-1}}]^{\frac{M-1}{M}}, \tag{10}$$

where

$$B_1 = \frac{1}{2}[2(1+r)]^{\frac{1}{M}},\quad B_2 = [1+2r]^{\frac{-1}{M-1}}. \tag{11}$$

In equations (9) and (10), σ_i and $\Delta\epsilon_i$ (for $i=1, 2$) are principal values of the Cauchy stress tensor and incremental logarithmic strain tensor, respectively. $\sigma_3 = 0$ for the plane-stress condition, and M and r are indices describing the shape of the yield surface. If $M=2$, equations (9) and (10) reduce to Hill's quadratic theory (Hill, 1950). If $M=2$ and $r=1$, the classical von Mises yield criterion is recovered.

An isotropic hardening law will be used in the following form

$$\sigma_e = K(\epsilon_e + a_0)^n \left(\frac{\dot{\epsilon}_e}{\gamma}\right)^m \tag{12}$$

where σ_e, ϵ_e ($=\int \dot{\epsilon}_e\, dt$), K, n, and m refer to effective stress, effective strain, strength coefficient, work-hardening exponent, and strain-rate sensitivity index, respectively; γ is a base strain rate and a_0 is a prestrain term.

3 Interface Conditions for Contact and Friction

We will consider now conditions for frictional contact at the interface between the contact surfaces of two bodies. One body, referred to later as a tool, is assumed to be rigid, whereas the other one, called a workpiece, is undergoing plastic deformation. The interface condition must satisfy both a force equilibrium requirement as well as geometric constraints at the end of each incremental step.

In order to satisfy the equilibrium (force) condition, we will consider a contact nodal force, $\mathbf{F}_c$, resolved into normal and tangential components (as in Germain et al. (1989) or Wang (1984), for example):

$$\mathbf{F}_C = \mathbf{F}_n + \mathbf{F}_t. \tag{13}$$

Assuming Coulomb's friction law to be valid (although the constant shear model can easily be adopted) and denoting by P the magnitude of the normal force (i.e., $P \equiv |\mathbf{F}_n|$), equation (13) can be rewritten as

$$\mathbf{F}_C = (\mathbf{n} - \mu\mathbf{t})P \tag{14}$$

where $\mathbf{n}$ and $\mathbf{t}$ are the normal and tangential unit vectors and μ is the coefficient of friction. The normal and tangent directions can be defined with respect to the tool or by the current configuration of FEM mesh (as in Keum et al., 1989).

To circumvent the complexities of dealing with stick-slip conditions, Oden and Pires (1983) and Germain et al. (1989) tested ever-slipping friction conditions governed by a piecewise-linear function. A modified version with a smooth transition function will be used in this paper (Fig. 1).

Consider the tangential displacement vector

$$\Delta\mathbf{u}_t = [\Delta\mathbf{u} \times \mathbf{n}] \times \mathbf{n} \tag{15}$$

and the smoothing function

$$\phi(\Delta\mathbf{u}_t) = \tanh\left(\frac{3|\Delta\mathbf{u}_t|}{\delta}\right). \tag{16}$$

The sticking condition is replaced by an ever-slipping condition with smooth transition region, improving numerical sta-

Downloaded 03 May 2010 to 171.66.16.248. Redistribution subject to ASME license or copyright; see http://www.asme.org/terms/Terms_Use.cfm

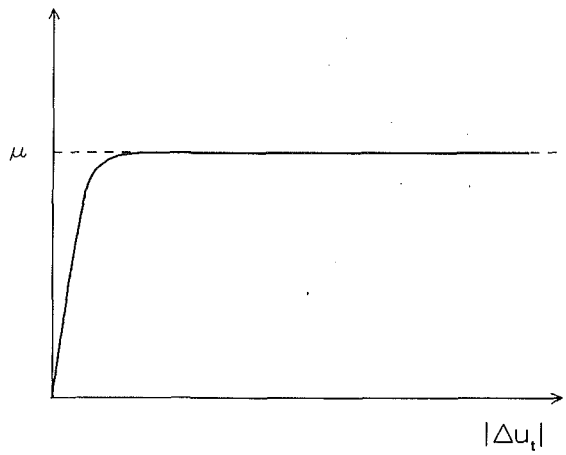

Fig. 1 Modified Coulomb's law of friction

bility of the solution procedure. Thus, the contact force can be written for the node k being in contact as

$$\mathbf{F}_C^k = (\mathbf{n} - \mu\phi(\Delta\mathbf{u}_t)\mathbf{t})P \tag{17}$$

and

$$\mathbf{F}_C^k = 0 \tag{18}$$

for the free node.

Finally, with the assumption of the normal vector pointing outward of the tool surface, the obvious physical condition that the magnitude of the normal force P should be nonnegative must be satisfied. A negative value indicates that the related node should be set free.

Without loss of generality, we assume that the moving tool surface is translated only along the z-direction of a fixed cartesian system (x, y, z). The punch surface at the time $\tau = 0$ can be defined by ${}^0Z_p = {}^0S(x, y)$. Then the current punch surface at the time $\tau = t + \Delta t$ satisfies

$${}^{n+1}Z_p = {}^{n+1}S(x,y,\tau) = {}^0S(x,y) + {}^{n+1}w_p \tag{19}$$

where w_p is the prescribed travel of the rigid tool from $\tau = 0 \rightarrow \tau + \Delta t$ and ${}^0S(x, y)$ is a function describing the punch surface.

For a point in the workpiece in contact with the tool at the time $t + \Delta t$, the following geometric constraint must be satisfied

$${}^{n+1}z = {}^{n+1}Z_p({}^{n+1}x, {}^{n+1}y, t + \Delta t), \tag{20}$$

where x, y, z are coordinates of the material point.

4 Consistent Formulation and Solution Algorithm

The developments presented in this paper were prompted by the difficulties encountered in performing robust and accurate analysis of the deep drawing process. The central difficulty, although discovered via sheet-metal-forming analysis, is pertinent for all frictional contact applications with the following characteristics: (a) arbitrarily shaped (curvilinear) contact surfaces; (b) large relative movement between material points of the contacting surfaces; (c) changing and unknown set of material points in contact during the deformation process, (i.e., different areas of the considered bodies are in contact at various times: new points can come into contact and others can be set free.)

We found that such complex frictional contact conditions manifest themselves in the mathematical description of the problem by significant changes in the normal and tangential vectors and their derivatives at the contact areas during the deformation process. Therefore, all nonlinearities involved at the incremental step are important here.

The key point in the development of the proposed CFS solution algorithm is a consistent linearization of the complete set of governing relations comprising kinematic, constitutive, equilibrium, and interfacial equations where all higher order terms are retained in the resulting stiffness matrix. There are two important aspects of the new procedure which should be mentioned here. First the proper linearization of the complete set of equations results in a *consistent stiffness matrix*. This in turn ensures a quadratic rate of asymptotic convergence of the full Newton-Raphson algorithm, thereby leading to higher efficiency of the computations. Further on, trial simulations confirmed theoretical predictions that this approach considerably increases *numerical stability* of the solution. This is particularly visible in simulations involving generally shaped contact surfaces and when contacting areas undergo large relative movements during the simulation.

With the relations introduced so far, the complete set of governing relations at the time ${}^{n+1}t$ will include general equilibrium relations, equation (14), augmented by geometric constraints, equation (4), for the nodes in contact:

$$\begin{cases} {}^{n+1}\mathbf{F}_I = {}^{n+1}\mathbf{F}_E \\ {}^{n+1}z = {}^{n+1}Z_p\ ({}^{n+1}x, {}^{n+1}y, t + \Delta t). \end{cases} \tag{21}$$

In the boundary value problem considered, it is convenient to split the external force vector into a vector of the contact and friction (nonconservative) forces, $\mathbf{F}_C$, and vector $\mathbf{F}_L$ containing other external forces which we assume to be conservative. The external force vector is then the sum of the two component force vectors:

$$\mathbf{F}_E = \mathbf{F}_L + \mathbf{F}_C \tag{22}$$

where vector $\mathbf{F}_C$ is specified by equations (17) or (18).

By introducing the vector $\mathbf{r}$ of independent unknowns,

$$\mathbf{r} = \begin{bmatrix} \mathbf{u} \\ P \end{bmatrix}, \tag{23}$$

comprising nodal displacements and the magnitude P of the normal contact force $\mathbf{F}_n$, we finally obtain the compact form

$${}^{n+1}\mathbf{R}_I(\Delta\mathbf{r}) = {}^{n+1}\mathbf{R}_E(\Delta\mathbf{r}), \tag{24}$$

where the generalized internal force vector $\mathbf{R}_I$ can be defined as

$$\mathbf{R}_I = \begin{bmatrix} \mathbf{F}_I(\Delta\mathbf{u}) \\ {}^{n+1}z(\Delta\mathbf{u}) \end{bmatrix} \tag{25}$$

and the generalized external force vector becomes

$$\mathbf{R}_E = \mathbf{R}_L + \mathbf{R}_C \tag{26}$$

with the following definitions:

$$\mathbf{R}_L = \begin{bmatrix} {}^{n+1}\mathbf{F}_L \\ {}^{n+1}Z_p \end{bmatrix}; \quad \mathbf{R}_C = \begin{bmatrix} \mathbf{F}_C \\ 0 \end{bmatrix}. \tag{27}$$

The global, highly nonlinear equation (24) must be solved via an iterative scheme. The full Newton-Raphson method is employed here. Equation (24) is linearized by the usual procedure about the known solution. Hence, retaining the first-order terms from Taylor series expansion we obtain

$$\left(\frac{\partial\mathbf{R}_I}{\partial\Delta\mathbf{r}} - \frac{\partial\mathbf{R}_E}{\partial\Delta\mathbf{r}}\right)\Bigg|_{\Delta\mathbf{r}^{i-1}} \delta\mathbf{r}^i = (\mathbf{R}_E - \mathbf{R}_I)\,|_{\Delta\mathbf{r}^{i-1}} \tag{28}$$

where i denotes the current iteration number. (Note that iteration numbers are denoted by post-superscript).

After rearranging the terms in this equation, we arrive at the following compact form:

$${}^{n+1}\mathbf{K}^{i-1}\,\delta\mathbf{r}^i = {}^{n+1}\mathbf{R}_L + {}^{n+1}\mathbf{R}_C^{i-1} - {}^{n+1}\mathbf{R}_I^{i-1}, \tag{29}$$

with the accumulation rules defined as

$$\begin{aligned} \Delta\mathbf{r}^i &= \Delta\mathbf{r}^{i-1} + \delta\mathbf{r}^i \\ {}^{n+1}\mathbf{r}^i &= {}^n\mathbf{r} + \Delta\mathbf{r}^i. \end{aligned} \tag{30}$$

Remark 1. At the first iteration, for all steps after the first one, $\Delta\mathbf{r}^0$ is usually given the converged value of the $\Delta\mathbf{r}$ of the previous step.

Downloaded 03 May 2010 to 171.66.16.248. Redistribution subject to ASME license or copyright; see http://www.asme.org/terms/Terms_Use.cfm

Remark 2. Because of good stability properties of the proposed algorithm, no special procedure (as reported by Wang (1984) and Germain et al. (1989)) is necessary in order to find the "initial guess" at the first step. $\Delta \mathbf{r}^0$ is simply set to zero.

Remark 3. It is worth noting that during accumulation of the generalized vector $\mathbf{r}$, the magnitude of the normal force P is also accumulated.

We will specify now more precisely the terms of the stiffness matrix. Expanding equation (29) in the symbolic matrix form we can obtain

$$\begin{bmatrix} \mathbf{K}_I + \mathbf{K}_C & \mathbf{N} \\ \mathbf{C} & 0 \end{bmatrix} \begin{bmatrix} \delta\ \mathbf{u} \\ \delta\ \mathbf{P} \end{bmatrix} = \begin{bmatrix} {}^{n+1}\mathbf{F}_L \\ {}^{n+1}\mathbf{Z}_p \end{bmatrix} + \begin{bmatrix} {}^{n+1}\mathbf{F}_C \\ 0 \end{bmatrix} - \begin{bmatrix} {}^{n+1}\mathbf{F}_I \\ {}^{n+1}\mathbf{z} \end{bmatrix}, \tag{31}$$

with the following definitions holding

$$\mathbf{K}_C = \frac{\partial \mathbf{F}_C}{\partial \Delta \mathbf{u}} = P\left(\frac{\partial \mathbf{n}}{\partial \Delta \mathbf{u}} - \mu\left(\frac{\partial \mathbf{t}}{\partial \Delta \mathbf{u}}\phi + \frac{\partial \phi}{\partial \Delta \mathbf{u}}\mathbf{t}\right)\right) \tag{32}$$

$$\mathbf{N} = \mathbf{n} - \mu\phi\mathbf{t} \tag{33}$$

$$\mathbf{C} = \mathbf{C}_1 + \mathbf{C}_2 = \left[\frac{\partial S}{\partial x}, \frac{\partial S}{\partial y}, 0\right] + [0,\ 0,\ -1] \tag{34}$$

$$\frac{\partial \phi}{\partial \Delta \mathbf{u}} = \frac{3}{\delta \cosh^2\left(\dfrac{3|\Delta u_t|}{\delta}\right)} \frac{\partial |\Delta u_t|}{\partial \Delta \mathbf{u}}, \tag{35}$$

where $\mathbf{n}$, $\mathbf{t}$ and its derivatives depend upon the geometry of the particular problem. Finally, element forces $\mathbf{F}_I$ and element stiffness matrices $\mathbf{K}_I$ can be derived when the type of finite element and the material model are known (see Section 6 for specific results).

Remark 4. Matrix $\mathbf{K}_C$ and vectors $\mathbf{N}$ and $\mathbf{C}$ represent complete terms resulting from frictional contact. If the higher order term $\mathbf{K}_C$ is dropped, the "linearized theory" is recovered. It is linearized in the sense that only linear terms $\mathbf{N}$ and $\mathbf{C}$ are retained. This procedure is only effective in the case of small (infinitesimal) deformations, although its use is presented in the literature also for large deformations. In Section 7 convergence and stability of this approach is compared with the fully consistent formulation defined by the exact expression given by equation (31).

5 Solution Procedures

A brief description of the solution algorithm and numerical techniques aimed at improved stability and efficiency are presented as follows.

5.1 Initial Solution, Convergence, and Update. For each incremental step the initial value $\Delta \mathbf{r}^0$ is required for the N-R procedure. For the first step this value is set to zero. For subsequent steps the converged result from the previous step is used, usually with a reduction of the number of required iteration steps. Eventual changes in the step size are accounted for by simple linear scaling of the previous converged solution. To determine convergence of the solution, Euclidean norms of the displacement and the residual force vectors are compared with specified tolerances.

5.2 Mechanical Consistency Condition. Before creating the appropriate stiffness matrices, it has to be decided whether particular nodes are in contact or should be treated as free nodes. Generalized equations include interfacial conditions, so the resulting geometry fulfills at the end of the step all geometrical and equilibrium constraints. However, the nodal contact force may not fulfill the mechanical consistency condition, by becoming tensile. A check for this condition is performed and, if necessary, the node is released and the equilibrium iteration is repeated with the new set of active nodes, starting from the latest converged solution. This procedure usually requires very few additional equilibrium iterations.

5.3 Interface Equations Assembly. When frictional contact matrices for a node are created, their contribution must be incorporated into the proper positions of the global stiffness matrix. The direct approach, in which an operation on the global stiffness matrix is necessary, can be cumbersome and creates difficulties whenever the assembly or solver routine must be changed. We use the same assembly routine as for assembly of element stiffness matrices. Nodal frictional contact matrices are treated as "nodal elements" and assembled in the usual way, preserving proper dimensions and connectivity.

5.4 Local Unloading Problem With Rigid-Plasticity. During deformation, the effective stress follows the hardening curve until a material element experiences unloading. Since the rigid-plastic constitutive relations do not allow for unloading, the material becomes rigid and, in consequence, the equilibrium condition cannot be satisfied, resulting in the convergence problems. The simple but effective method of Chung and Wagoner (1987) is adopted to overcome this difficulty.

Linear hardening is introduced between ϵ_e^A and $\sigma_e^{A'}$ as shown in Fig. 2. The dual hardening law can be used for each step; when $\Delta\epsilon_e$ is bigger than the tolerance parameter δ, the standard nonlinear hardening relation is used: when $\Delta\epsilon_e$ is smaller than δ, the effective stress is calculated from the linear segment.

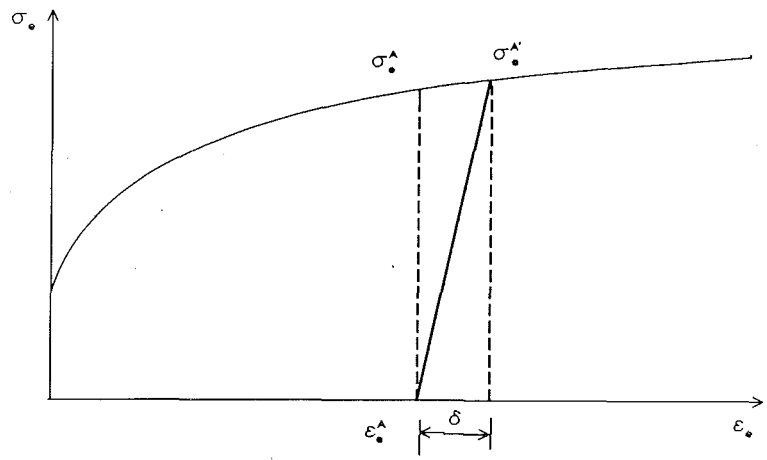

Fig. 2 Unloading process in the rigid-plastic material model (after Chung and Wagoner, 1987)

Downloaded 03 May 2010 to 171.66.16.248. Redistribution subject to ASME license or copyright; see http://www.asme.org/terms/Terms_Use.cfm

Remark. This is not a real unloading behavior, as is possible using an elastic-plastic relation, because the plasticity law is still used to determine the directions of straining. As a consequence, this model can only be used accurately when at least some parts of the body undergo plastic deformation. During one-dimensional unloading, for example, this procedure allows the small strain increments to be in the opposite direction from the elastic unloading results.

5.5 Summary of the Iteration Algorithm. The finite element solution at each incremental step is defined in terms of generalized nodal displacement increments, which are obtained from solution of equation (29). The iterative algorithm at each incremental step can be summarized as follows:

1 A trial set of the contacting nodes is chosen.
2 The iteration steps are performed using the full set of governing equations, equation (29), until convergence is obtained, based on specified tolerances.
3 Mechanical consistency is verified. If not fulfilled, the inconsistent nodes are released and the procedure returns to step 1.
4 The control parameter is incremented and the next time step is processed, beginning at 1.

6 Specification for Plane-Strain Sheet Forming

We will present an application and numerical verification of the proposed algorithm using examples of "section analysis" problems. This approach has a wide application for the simulation of sheet-forming operations when sheet metal is formed by rigid tools. The description of the process must include large strains, plastic flow, and changing frictional contact conditions. Simulation of sheet forming is also known as a very demanding test of the numerical stability of the solution algorithm especially when, for industrial processes with complex tool shapes, a considerable amount of draw-in of the sheet material into the die cavity must be simulated.

Section analysis represents an alternative procedure to the full three-dimensional model for analyzing complex part shapes during sheet forming operations. In this procedure, a vertical plane is passed through the tooling along a direction of interest. The problem is then analyzed in two-dimensions, assuming plane-strain conditions. We assume, for simplicity, that the x-z plane is the plane of interest, with the punch motion occurring in the z-direction.

When the thickness of the sheet is much smaller comparing with the in-plane dimensions, the usual assumption of the plane-stress state ($\sigma_3 = 0$) is justified here. To make a model as simple as possible we will restrict ourselves to the process where the bending effect is insignificant and the membrane model can be used.[1]

With these assumptions at hand, using linear shape functions and considering plane-strain conditions, we derived a finite element with two nodes and two translational degrees-of-freedom at each node (presented by Saran et al., 1989).

It is convenient in this case to operate on the true incremental strain defined as the natural logarithm of the stretch ratio. Having (rigid plasticity) the incompressibility assumption valid, we have only one independent strain increment, as

$$\begin{aligned} \Delta\epsilon_1 &= \ln\left(\frac{{}^{n+1}L}{{}^{n}L}\right) \\ \Delta\epsilon_2 &= 0 \\ \Delta\epsilon_3 &= -\Delta\epsilon_1 \end{aligned} \tag{36}$$

where ${}^{n+1}L$ and ${}^{n}L$ represent lengths of the element at the times ${}^{n+1}t$ and ${}^{n}t$, respectively. The incremental effective strain, equation (10), can be written for the plane-strain conditions as follows:

$$\Delta\epsilon_e = B_{PS}|\Delta\epsilon_1|, \tag{37}$$

where B_{PS} is a constant defined by

$$B_{PS} = B_1(B_2+1)^{\frac{M-1}{M}}. \tag{38}$$

The definitions for B_1 and B_2 are given in equation (11).

We will now specify, for the section analysis, the general relations derived from the previous sections. The general governing equation (21) will read for the plane-strain problem:

$$\begin{cases} \mathbf{F}_I = \mathbf{F}_E \\ {}^{n+1}z = {}^{n+1}Z_p\ ({}^{n+1}x,\ t+\Delta t) \end{cases}, \tag{39}$$

with displacement vector $\mathbf{u}$ having now two components (in x and z-directions) only.

After linearization of equation (39) will obtain the form:

$$\begin{bmatrix} \mathbf{K}_I+\mathbf{K}_C & \mathbf{N} \\ \mathbf{C} & 0 \end{bmatrix} \begin{bmatrix} \delta\ \mathbf{u} \\ \delta\ \mathbf{P} \end{bmatrix} = \begin{bmatrix} {}^{n+1}\mathbf{F}_L \\ {}^{n+1}\mathbf{Z}_p \end{bmatrix} + \begin{bmatrix} {}^{n+1}\mathbf{F}_c \\ 0 \end{bmatrix} + \begin{bmatrix} {}^{n+1}\mathbf{F}_I \\ {}^{n+1}\mathbf{z} \end{bmatrix} \tag{40}$$

where, recalling the incompressibility assumption and denoting original length and thickness by ${}^{0}L$ and ${}^{0}h$, respectively, we arrive at the following definitions of the particular matrices:

$$\mathbf{F}_I = {}^{0}h\,{}^{0}L\sigma_e\frac{\partial\Delta\epsilon_e}{\partial\Delta\mathbf{u}} \tag{41}$$

$$\mathbf{K}_I = \frac{\partial\mathbf{F}_I}{\partial\Delta\mathbf{u}} = {}^{0}h\,{}^{0}L\left\{\sigma_e\frac{\partial^2\Delta\epsilon_e}{\partial\Delta\mathbf{u}\partial\Delta\mathbf{u}} + \left(\frac{\partial\sigma_e}{\partial\epsilon_e}+\frac{1}{\Delta t}\frac{\partial\sigma_e}{\partial\dot{\epsilon}_e}\right)\frac{\partial\Delta\epsilon_e}{\partial\Delta\mathbf{u}}\frac{\partial\Delta\epsilon_e}{\partial\Delta\mathbf{u}}\right\} \tag{42}$$

$$\mathbf{C} = \mathbf{C}_1 + \mathbf{C}_2 = \left[\frac{\partial^0 S}{\partial x},\ 0\right] + [0,\ 0,\ -1], \tag{43}$$

where

$$\frac{\partial\sigma_e}{\partial\epsilon_e},\ \frac{\partial\Delta\epsilon_e}{\partial\Delta\mathbf{u}},\ \frac{\partial^2\Delta\epsilon_e}{\partial\Delta\mathbf{u}\partial\Delta\mathbf{u}}$$

are straightforwardly obtained derivatives when equations (10)–(12) are observed. The explicit forms of $\mathbf{F}_I$ and $\mathbf{K}_I$ are given in Appendix A.

For the plane-strain case, $\mathbf{K}_C$, $\mathbf{C}$, and $\mathbf{N}$ are still given by equations (32), (34), and (33), but the unit normal and tangent vectors and their derivatives can be defined in a simpler way than in the three-dimensional case. The explicit form is given in Appendix B.

Acknowledgments

The authors would like to acknowledge the support of the Center for Net Shape Manufacturing at the Ohio State University, the Chrysler Corporation, and the Ohio Supercomputer Center (PAS 080). The authors also wish to thank J. K. Lee, Y. T. Keum, D. J. Zhou, and C. T. Wang for many useful discussions.

References

Bathe, K.-J., 1982, *Finite Element Procedures in Engineering Analysis,* Prentice-Hall, Englewood Cliffs, N.J.

Bathe, K.-J., and Chaudhary, A., 1985, "A Solution Method for Planar and Axisymmetric Contact Problems," *Int. J. Num. Methods Engng.*, Vol. 21, pp. 65–88.

Belytschko, T., and Lin, J. I., 1985, "A New Interaction Algorithm with Erosion for EPIC-3," U. S. Army Ballistic Research Laboratory, BRL-CR-540.

Cheng, J.-H., and Kikuchi, N., 1985, "An Analysis of Metal Forming Pro-

[1] Note that there is no simple guideline for the actual values of r/t (radius of curvature/sheet thickness) allowable under the membrane assumption. The critical value depends on the local degree of stretching versus bending, that in turn depends on friction and draw-in force. Stoughton (1985), estimated that the r/t values of ~ 6 are sufficiently high while Wang and Wagoner (1990), found good agreement between membrane FEM simulations and experiments for $r/t \sim 6$.

Downloaded 03 May 2010 to 171.66.16.248. Redistribution subject to ASME license or copyright; see http://www.asme.org/terms/Terms_Use.cfm

cesses Using Large Deformation Elastic Plastic Formulations," *Com. Methods in Appl. Mech. and Eng.*, Vol. 49, pp. 71–108.

Choudhry, S., and Lee, J. K., 1989, "Numerical Simulation of Thin Sheet Metal Forming Processes Including Bending Effects," *Proc. Micro. Devel. Cont. Mat. Proc.*, ASME, N.Y.

Chung, K., and Wagoner, R. H., 1987, "Numerical Improvement of Viscoplastic, Nonlinear, Finite Element Analysis," *Int. J. Mech. Sci.*, Vol. 29-1, pp. 45–59.

Duvaut, G., and Lions, J. L., 1976, *Inequalities in Mechanics and Physics*, Springer, Berlin.

Felippa, C. A., 1978, "Iterative Procedures for Improving Penalty Function Solutions of Algebraic Systems," *Int. J. Numer. Methods Eng.*, Vol. 12, pp. 821–836.

Germain, Y., Chung, K., and Wagoner, R. H., 1989, "A Rigid-Viscoplastic Finite Element Program for Sheet Metal Forming Analysis," *Int. J. Mech. Sci.*, Vol. 31, No. 1, pp. 1–24.

Giannokopoulos, A. E., 1989, "The Return Mapping Method for the Integration of Friction Constitutive Relations," *Computers & Structures*, Vol. 32, pp. 157–168.

Hallquist, J. O., 1979, "NIKE2D: an Implicit, Finite-Deformation, Finite-Element Code for Analyzing the Static and Dynamic Response of Two-Dimensional Solids," Rept. UCRL-52678, University of California, Lawrence Livermore National Laboratory.

Hill, R., 1950, *The Mathematical Theory of Plasticity*, Oxford University Press, London.

Hill, R., 1979, "Theoretical Plasticity of Textured Aggregates," *Math. Proc. Camb. Phil. Soc.*, Vol. 85, pp. 179–191.

Hughes, T. R. J., Taylor, R. L., Sackman, J. L., Curnier, A., and Kanoknukulchai, W., 1976, "A Finite Element Method for a Class of Contact-Impact Problems," *Comp. Meth. Appl. Mech. Engn.*, Vol. 8, pp. 249–276.

Ju, J. W., Taylor, R. L., and Cheng, L. Y., 1987, "A Consistent Finite Element Formulation of Nonlinear Frictional Contact Problems," *Proc. of NUMETA 87*, J. Middleton and G. N. Pande, eds., Nijhoff, Dordrecht.

Keum, Y. T., Nakamachi, E., Wagoner, R. H., and Lee, J. K., 1989, "Compatible Description of Tool Surfaces and FEM Meshes for Analyzing Sheet Forming Operations," *Numerical Methods in Industrial Forming Processes*, E. G. Thompson et al., ed., A. A. Balkema, pp. 489–496.

Kikuchi, N., and Oden, J. T., 1986, "Contact Problems in Elasticity: A Study of Variational Inequalities and Finite Element Methods for a Class of Contact Problems in Elasticity," *SIAM Studies*, Vol. 8, SIAM, Philadelphia, Penn.

Kobayashi, S., and Kim, J. H., 1978, "Deformation Analysis of Axisymmetric Sheet Metal Forming Processes by the Rigid-Plastic Finite Element Method," *Mechanics of Sheet Metal Forming*, Koistinen and Wang, eds., Plenum Press, New York, pp. 341–363.

Kobayashi, S., 1985, "Metal Forming and the Finite Element Method—Past and Future," *Proceedings of the 25th Int. Conf. Mach. Tool Des.*, Birmingham, Ala., p. 17.

Kobayashi, S., Oh, S. I., and Altan, T., 1989, *Metal Forming and the Finite Element Method*, Oxford University Press, London.

Landers, J. A., and Taylor, R. L., 1985, "An Augmented Lagrangian Formulation for the Finite Element Solution of Contact Problems," Report No. Ucb/Sesm-85/09, Department of Civil Engineering, University of California, Berkeley, Calif.

Lee, C. H., Kobayashi, S., 1973, "New Solutions to Rigid-Plastic Deformation Problems Using a Matrix Method," *ASME Journal of Engineering for Industry*, Vol. 95, pp. 865–873.

Luenberger, D. G., 1984, *Linear and Nonlinear Programming*, 2nd ed., Addison-Wesley, Reading, Mass.

Maenchen, G., and Sack, S., 1964, "The Tensor Code," *Methods in Computational Physics: Fundamental Methods in Hydrodynamics*, Vol. 3, Berni Alder et al., ed., Academic Press, New York, pp. 181–210.

Makinouchi, A., 1985, "Elastic-Plastic Stress Analysis of Bending and Hemming of Sheet Metal," *Comp. Model Sheet Met. Form. Proc.*, N. M. Wang and S. Tang, eds., pp. 161–176.

Massoni, E., Bellet, M., and Chenot, J. L., 1987, "A Finite Element Model for Deep Drawing of Thin Sheets in the Automotive Industry," *Advanced Technology of Plasticity*, K. Lange, ed., Springer-Verlag, Berlin.

Mattiasson, K., Saran, M., Melander, A., Schedin, E., and Gustafsson, C., 1987, "Finite Element Simulation of Deep-Drawing of Low and High Strength Steel," *Advanced Technology of Plasticity*, Vol. I, K. Lange, ed., Springer-Verlag, Berlin, pp. 657–664.

Nagtegaal, J. C., and Rebelo, N., 1986, "On the Development of a General Purpose Finite Element Program for Analysis of Forming Processes," *Numerical Methods in Industrial Forming Processes,"* K. Mattiasson et al., ed., Balkema, Rotterdam, pp. 41–49.

Nakamachi, E., 1986, "Finite Element Modelling of the Punch Press Forming of Thin Elastic-Plastic Plates," *Numerical Methods in Industrial Forming Processes*, K. Mattiasson et al., ed., Balkema, Rotterdam, pp. 333–338.

Oden, J. T., 1981, "Exterior Penalty Methods for Contact Problems in Elasticity," *Nonlinear Finite Element Analysis in Structural Mechanics*, W. Wunderlich et al., ed., Springer-Verlag, New York.

Oden, J. T., and Martins, J. A. C., 1985, "Models and Computational Methods for Dynamic Friction Phenomena," *Comp. Meth. Appl. Mech. Engng.*, Vol. 52, pp. 527–634.

Oden, J. T., and Carey, G. F., 1984, *Finite Elements Special Problems in Solid Mechanics*, Vol. 5, Prentice-Hall, Englewood Cliffs, N.J.

Oden, J. T., and Pires, E. B., 1983, "Nonlocal and Nonlinear Friction Law and Variational Principles for Contact Problems in Elasticity," ASME JOURNAL OF APPLIED MECHANICS, Vol. 50, pp. 67–76.

Oh, S. I., and Kobayashi, S., 1980, "Finite Element Analysis of Plane Strain Sheet Bending," *Int. J. Mech. Sci.*, Vol. 22, pp. 583–594.

Oñate, E., and Zienkiewicz, O. C., 1983, "A Viscous Formulation for the Analysis of Thin Sheet Metal Forming," *Int. J. Mech. Sci.*, Vol. 25, p. 305.

Proc. of 1st Int. Conf. on Numerical Methods in Industrial Forming Processes, NUMIFORM, 1982, Pittman et al., ed., Pineridge Press, Swansea, U.K.

Proc. of 2nd Int. Conf. on Numerical Methods in Industrial Forming Processes, NUMIFORM, 1986, K. Mattiasson et al., ed., A. A. Balkema, Rotterdam.

Proc. of 3rd Int. Conf. on Numerical Methods in Industrial Forming Processes, NUMIFORM, 1989, E. G. Thompson et al., ed., A. A. Balkema, Rotterdam.

Saran, M. J., Keum, Y. T., and Wagoner, R. H., 1989, "A Rigid-Viscoplastic Line Finite Element for Plane Strain Sheet Forming Simulations," TMS Fall Meeting, Indianapolis, Ind.

Saran, M. J., and Runesson, K., 1991, "A Generalized Closest Point Projection Method for Deformation-Neutralized Formulation in Finite Strain Plasticity," *Engineering Computations I. J.*, in press.

Saran, M. J., and Samuelsson, A., 1990, "Elastic-Viscoplastic Implicit Formulation for Finite Element Simulation of Complex Sheet Forming Processes, *Int. J. Numer. Methods Eng.*, Vol. 30, pp. 1675–1697.

Saran, M. Schedin, E., Samuelson, A., Melander, A., and Gustafsson, C., 1990, "Numerical and Experimental Investigations of Deep Drawing of Metal Sheets," *ASME Journal of Engineering for Industry*, Vol. 112, pp. 272–277.

Simo, J. C., Wriggers, P., and Taylor, R. L., 1985, "A Perturbed Lagrangian Formulation for the Finite Element Solution of Contact Problems," *Comp. Meth. Appl. Mech. Engng.*, Vol. 50, pp. 163–180.

Stecher, F. P., and Johnson, G. C., 1984, "Lagrangian Computations for Projectile Penetration in Thick Plates," *Computers in Engineering*, W. A. Gruver, ed., No. G00240, ASME, New York.

Stoughton, T. B., 1985, "Finite Element Modelling of 1008 AK Sheet Steel Stretched Over a Rectangular Punch with Bending Effects," *Computer Modelling of the Sheet Forming Process, Theory, Verification and Application*, Wang and Tang, eds., TMS, Warrendale, PA, pp. 143–159.

Tabor, D., 1975, *Interaction Between Surfaces: Adhesion and Friction, Surface Physics of Materials*, Vol. II, J. M. Blakely, ed., Academic Press, New York.

Tabor, D., 1981, "Friction: The Present State of Our Understanding," *J. Lubrication Technol.*, pp. 169–179.

Tang, S., 1981, "Large Elasto-Plastic Strain Analysis of Flanged Hole Forming," *Comp. Structures*, Vol. 13, pp. 363–370.

Wang, C. T., and Wagoner, R. H., 1990, "Finite Element Analysis and Experimental Investigation of Square Punch Stretching and Draw-in Processes," Report ERC/NSM-S-90-05.

Wang, N. M., 1984, "A Rigid-Plastic Rate-Sensitive Finite Element Method for Modeling Sheet Forming Processes," *Proc. Numerical Analysis of Forming Processes*, Pittman et al., eds., John Wiley and Sons, New York, pp. 117–164.

Wang, N. M., and Budiansky, B., 1978, "Analysis of Sheet Metal Stamping by a Finite Element Method," ASME JOURNAL OF APPLIED MECHANICS, Vol. 45, pp. 73–82.

Wang, N. M., and Wenner, M. L., 1982, "Effects of Strain Hardening Representation in Sheet Metal Forming Calculations of 2036-T4 Aluminum," *Formability of Metallic Materials*, Neimeier and Newby, ed., ASTM STP = 753, p. 85.

Wilkins, M. L., 1964, "Calculation of Elastic-Plastic Flow," *Methods in Computational Physics: Fundamental Methods in Hydrodynamics*, Vol. 3, Berni Alder et al., ed., Academic Press, New York, pp. 211–263.

Wriggers, P., and Simo, J. C., 1985, "A Note on Tangent Stiffness for Fully Nonlinear Contact Problems," *Commun. Appl. Numer. Meth.*, Vol. 1, pp. 199–203.

Wriggers, P., 1987, "On Consistent Tangent Matrices for Frictional Contact Problems," *Proc. of NUMETA 87*, J. Middleton and G. N. Pande, eds., Nijhoff, Dordrecht.

Zienkiewicz, O. C., 1977, *The Finite Element Method*, McGraw-Hill, Maidenhead, Berkshire, U. K.

Zienkiewicz, O. C., 1984, "Flow Formulation for Numerical Solution of Forming Processes," *Numerical Analysis of Forming Processes*, Pittman et al., ed., John Wiley and Sons, New York, pp. 1–44.

APPENDIX A

Internal Force Vector and Stiffness Matrix for the Plane-Strain Element

For the finite element described in Section 6, the following forms of the $\mathbf{F}_I$ and $\mathbf{K}_I$ are obtained using equations (41)–(42) and equations (10)–(12).

$$\mathbf{F}_I = {}^0h\,{}^0L\sigma_e \frac{\partial \Delta\epsilon_e}{\partial \Delta \mathbf{u}} \tag{A1}$$

Downloaded 03 May 2010 to 171.66.16.248. Redistribution subject to ASME license or copyright; see http://www.asme.org/terms/Terms_Use.cfm

$$\mathbf{K}_I=\frac{\partial \mathbf{F}_I}{\partial \Delta \mathbf{u}}={}^0h^0L\left\{\sigma_e\frac{\partial^2\Delta\epsilon_e}{\partial\Delta\mathbf{u}\partial\Delta\mathbf{u}}+\left(\frac{\partial\sigma_e}{\partial\epsilon_e}+\frac{1}{\Delta t}\frac{\partial\sigma_e}{\partial\dot{\epsilon}_e}\right)\frac{\partial\Delta\epsilon_e}{\partial\Delta\mathbf{u}}\frac{\partial\Delta\epsilon_e}{\partial\Delta\mathbf{u}}\right\} \quad \text{(A2)}$$

with the following definitions:

$$\frac{\partial\Delta\epsilon_e}{\partial\Delta\mathbf{u}}=B_{PS}^{\overline{M}}\frac{1}{L^2}\{-L_x,\ -L_z,\ L_x,\ L_z\} \quad \text{(A3)}$$

$$\frac{\partial^2\Delta\epsilon_e}{\partial\Delta\mathbf{u}\partial\Delta\mathbf{u}}=B_{PS}^{\overline{M}}\frac{1}{L^4}A_{ij}. \quad \text{(A4)}$$

The coefficients of the symmetric matrix A_{ij} are:

$$\begin{aligned} A_{11}&=L^2-2L_x^2 \ ;\ A_{12}=-2L_xL_z \\ A_{13}&=-L^2+2L_x^2;\ A_{14}=2L_xL_z \\ A_{22}&=L^2-2L_z^2 \ ;\ A_{23}=2L_xL_z \\ A_{24}&=-L^2+2L_z^2;\ A_{33}=L^2-2L_x^2 \\ A_{34}&=-2L_xL_z \ ;\ A_{44}=L^2-2L_z^{z2} \end{aligned} \quad \text{(A5)}$$

and

$$L_x=x_j-x_i;\ L_z=z_j-z_i \quad \text{(A6)}$$

where the length and coordinates values of the element nodes i and j are at the current configuration ${}^{n+1}C$.

APPENDIX B

Normal and Tangential Unit Vectors and Their Derivatives

The normal and tangent unit vectors **n** and **t** can be defined with respect to the tool or in the function of the current configuration of the FEM mesh. (The latter was used for the calculations of the examples presented in this paper.)

In the tool normal case, the unit vectors and their derivatives for the considered finite element node l are the functions of coordinates of that node:

$$\mathbf{n}^l=f(\mathbf{x}^l). \quad \text{(B1)}$$

Denoting derivatives of the original punch surface by $S_x=\frac{\partial^0 S}{\partial x}$, and norm $S_n=\sqrt{S_x^2+1}$, we arrive at

$$\mathbf{n}=\frac{1}{S_n}\begin{bmatrix}-S_x\\1\end{bmatrix} \quad \text{(B2)}$$

$$\mathbf{t}=\frac{sn}{S_n}\begin{bmatrix}1\\S_x\end{bmatrix}, \quad \text{(B3)}$$

where sn is a sign of the relative displacement vector.

Denoting further

$$S_{xx}=\frac{\partial S_x}{\partial\Delta\mathbf{u}_x}, \quad \text{(B4)}$$

we can finally obtain:

$$\frac{\partial\mathbf{n}}{\partial\Delta\mathbf{u}}=\frac{1}{S_n^3}\begin{bmatrix}S_{xx}&0\\-S_xS_{xx}&0\end{bmatrix} \quad \text{(B5)}$$

$$\frac{\partial\mathbf{t}}{\partial\Delta\mathbf{u}}=\frac{sn}{S_n^3}\begin{bmatrix}S_xS_{xx}&0\\S_{xx}&0\end{bmatrix}. \quad \text{(B6)}$$

Consider now the case of the normal and tangent vectors based on a finite element mesh. Three adjacent nodes k, l, m situated in the x, z-plane define two line elements between them with the current lengths denoted by L_a and L_b. Unit vectors and their derivatives for node l depend on the coordinates of the considered nodes:

$$\mathbf{n}^l=f(\mathbf{x}^k,\ \mathbf{x}^l,\ \mathbf{x}^m). \quad \text{(B7)}$$

With the assumption that $\mathbf{n}^l$ is a mean value (unweighted) of the normal unit vectors to the neighboring elements a and b and keeping the analogy to the tool normal case we can define again:

$$\mathbf{n}=\frac{1}{S_n}\begin{bmatrix}-S_x\\1\end{bmatrix} \quad \text{(B8)}$$

$$\mathbf{t}=\frac{sn}{S_n}\begin{bmatrix}1\\S_x\end{bmatrix}, \quad \text{(B9)}$$

where S_x is defined now as:

$$S_x=\frac{L_a(z_m-z_l)+L_b(z_l-z_k)}{L_a(x_m-x_l)+L_b(x_l-x_k)}. \quad \text{(B10)}$$

Unit vector derivatives become:

$$\frac{\partial\mathbf{n}^l}{\partial\Delta\mathbf{u}}=\left[\frac{\partial\mathbf{n}^l}{\partial\mathbf{x}^k},\frac{\partial\mathbf{n}^l}{\partial\mathbf{x}^l},\frac{\partial\mathbf{n}^l}{\partial\mathbf{x}^n}\right] \quad \text{(B11)}$$

$$\frac{\partial\mathbf{t}^l}{\partial\Delta\mathbf{u}}=\left[\frac{\partial\mathbf{t}^l}{\partial\mathbf{x}^k},\frac{\partial\mathbf{t}^l}{\partial\mathbf{x}^l},\frac{\partial\mathbf{t}^l}{\partial\mathbf{x}^n}\right], \quad \text{(B12)}$$

where, for example,

$$\frac{\partial\mathbf{n}^l}{\partial\mathbf{x}^k}=\frac{1}{S_n^3}\begin{bmatrix}S_{xx}^{lk}&S_{xz}^{lk}\\-S_x^lS_{xx}^{lk}&S_xS_{xz}^{lk}\end{bmatrix} \quad \text{(B13)}$$

$$\frac{\partial\mathbf{t}^l}{\partial\mathbf{x}^k}=\frac{sn}{S_n^3}\begin{bmatrix}S_x^lS_{xx}^{lk}&S_x^lS_{xz}^{lk}\\S_{xx}^l&S_{xz}^{lk}\end{bmatrix}. \quad \text{(B14)}$$

The derivatives S_{xi}^{lk} are straightforward to obtain using equation (B10) with the following definition:

$$S_{xi}^{lk}=\frac{\partial S_x^l}{\partial x_i^k} \quad \text{(B15)}$$

where i can become x or z in the considered two-dimensional case.

Downloaded 03 May 2010 to 171.66.16.248. Redistribution subject to ASME license or copyright; see http://www.asme.org/terms/Terms_Use.cfm

A Consistent Implicit Formulation for Nonlinear Finite Element Modeling With Contact and Friction: Part II—Numerical Verification and Results

M. J. Saran
Visiting Professor,
Mem. ASME

R. H. Wagoner
Professor,
Mem. ASME

Department of Materials Science and Engineering,
The Ohio State University,
Columbus, OH 43210

Using the method derived in Part I, plane-strain sheet-forming processes are analyzed and discussed. Stretch and deep draw forming by cylindrical and flat-bottom punches are presented and compared to closed-form solutions and existing numerical results. The performance of the new algorithm is successfully tested on a complex set of concave, irregular tools by simulating redrawing and reverse drawing with two-sided draw-in and various drawbead forces. The results demonstrate good robustness, accuracy, and efficiency even in the presence of large relative movements between contact surfaces. A quadratic rate of asymptotic convergence is documented for the consistent algorithm and comparison is made to the "linearized" theory which exhibits only linear rate of convergence and reduced numerical stability.

1 Introduction

In Part I of this study, the theory and numerical algorithm for finite element simulation of complex frictional contact processes were presented. These processes were characterized by curvilinear, irregular contact surfaces and large relative movements between material points of these surfaces.

In this part, numerical verification of section analysis of sheet forming is presented and results are discussed. The behavior of forming processes with complex draw-in conditions is studied with the new technique and the numerical performance is assessed. In order to facilitate a comparison with other formulations, an effort has been made to document in detail the numerical simulations, presented below, by providing the number of iterations by load step and obtained values of residual and energy norms. For this reason, a constant punch travel increment of 1 mm was used throughout all calculations and maximum possible value was not sought. Although the computer code has not been optimized or vectorized in any way, the computing times for all examples presented are in the range of 15 seconds to 2 minutes on a VAX8550 computer, depending on a number of elements assumed and a punch travel distance. This corresponds to approximately 1–10 min on an IBM-PS2/386 personal computer.

Rather tight convergence criteria were employed throughout all presented calculations. The Euclidean norms of displacements and residuals are compared with the tolerance value of 10^{-6}. The convergence in energy (H^1) norm is also monitored and discussed. The examples are chosen to provide comparison with existing analytical or numerical solutions. Finally, a complex tool set with irregular curvilinear tool geometries, demonstrating truly nonlinear frictional contact conditions and rapidly changing solution vectors, is considered. Whenever possible, the approach called here the "linearized theory" (see Part I, Remark 4 in Section 4 and Section 1), containing only linear contact terms of the stiffness matrix, is applied. The convergence and numerical stability properties obtained are compared with the fully consistent model.

2 Benchmark Problem of Out-of-Plane Stretching by Cylindrical Punch

An originally flat blank of metal in plane-strain conditions is subject to the forming operation by tools consisting of cylindrical punch, flat die with cylindrical corner, and flat blankholder. Figure 1 shows the cross-section and the dimensions used. The values of the material constants are as follows:

anisotropy: $r=1.0 \quad M=2.0$
hardening: $\sigma_e=K(\epsilon_e+a_0)^n$
with $K=585$ MPa, $a_0=0.0001$, $n=0.216$
original thickness: 1.0 mm

Contributed by the Applied Mechanics Division of THE AMERICAN SOCIETY OF MECHANICAL ENGINEERS for presentation at the Joint Applied Mechanics/Bioengineering Conference, Ohio State University, Columbus, OH, June 16–19, 1991.

Discussion on this paper should be addressed to the Technical Editor, Prof. Leon M. Keer, The Technological Institute, Northwestern University, Evanston, IL 60208, and will be accepted until two months after final publication of the paper itself in the JOURNAL OF APPLIED MECHANICS. Manuscript received by the ASME Applied Mechanics Division, July 11, 1990; final revision, Oct. 26, 1990.
Paper No. 91-APM-2.

Copyright © 1991 by ASME
Downloaded 03 May 2010 to 171.66.16.248. Redistribution subject to ASME license or copyright; see http://www.asme.org/terms/Terms_Use.cfm

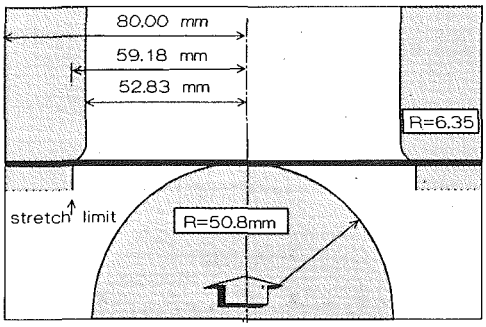

Fig. 1 Cylindrical punch in plane strain; tools and sheet geometry

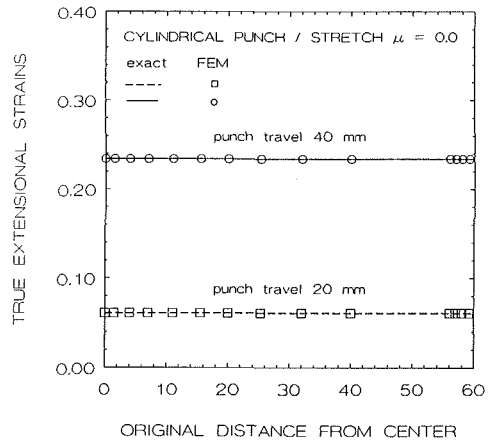

Fig. 2 Stretching by cylindrical punch ($\mu = 0.0$); comparison with closed-form solution

Several simulations were performed with these tools. At first, a comparison with the closed-form solution was performed. An exact solution is immediately available under the assumption that friction is not taken into account. Because of symmetry, only half of the physical specimen was used for the computations, with the appropriate boundary conditions at the symmetry axis. The calculations were performed with the blank clamped at the distance of 59.18 mm from the symmetry axis and with the friction coefficient $\mu = 0$. Numerically obtained results for two punch travel values of 20 mm and 40 mm are given in Fig. 2. These results are in full agreement with the closed-form solution, which in the absence of friction and bending gives uniformly distributed strains represented by the flat lines in Fig. 2.

To assess the performance of the linearized (with respect to the frictional contact contribution) and fully consistent algorithms, a series of calculations was performed with friction coefficients of $\mu = 0.0$ and $\mu = 0.3$.

The trends in number of the full N-R iterations per incremental step are summarized in Table 1.

For the "no friction" case, where the contact nonlinearity is also small, an assumed earlier 40-mm punch depth was achieved by both algorithms. For the linearized approach, the number of the iterations rises gradually for consecutive steps in contrast to the consistent approach where the predominant value of four iterations (with small fluctuations) is flatly preserved throughout the whole simulation process.

The convergence rate for $\mu = 0$ is documented in Table 2, where the values of the energy and residual norms at 10-mm punch travel are presented. The linearized approach reveals linear convergence, while the quadratic rate of the consistent model is clearly seen.

The inclusion of friction considerably increases the nonlinearity of the simulated problem, reflected in the performance

Table 1 Stretching by cylindrical punch. Trends in number of the full Newton iterations per incremental step up to punch travel of 40 mm

$\mu = 0.0$		$\mu = 0.3$	
linearized	consistent	linearized	consistent
5 → 10	4 (predominantly)	6 → 44 (at 13 mm) no convergence at 14 mm	4 (predominantly)

Table 2 Stretching by cylindrical punch, $\mu = 0.0$. Energy and residual norms for step 10 of linearized and consistent algorithms.

it	linearized algorithm		consistent algorithm	
	residual norm	energy norm	residual norm	energy norm
1	0.201E+01	0.362E−02	0.201E+01	0.357E−02
2	0.177E−01	0.429E−06	0.266E−01	0.306E−06
3	0.362E−03	0.115E−09	0.263E−05	0.120E−12
4	0.493E−05	0.280E−13	0.107E−10	0.550E−23
5	0.556E−07	0.366E−17		

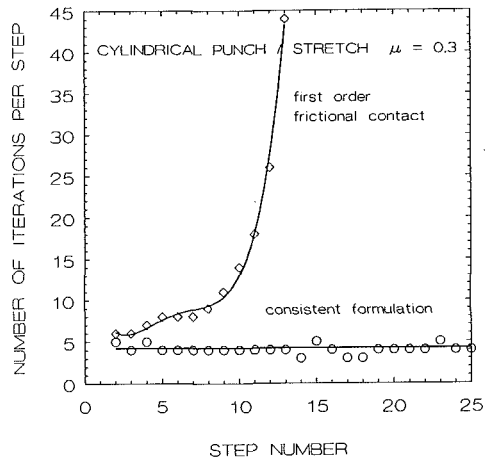

Fig. 3 Stretching by cylindrical punch ($\mu = 0.3$); comparison of the convergence properties during numerical simulation for linearized and consistent algorithms

characteristics obtained for $\mu = 0.3$. The number of iterations for the linearized algorithm rises sharply to 44 at the step 13 (see Fig. 3) and the convergence was not achieved in step 14 after even 300 iterations (although there was still very slow convergence).

In sharp contrast, the consistent algorithm also in this case exhibits constant quadratic convergence independent of the load level. In Table 3 a convergence rate is documented again for step 10, which is typical for the consistent algorithm.

3 Deep Drawing by Cylindrical Punch

A deep drawing process was simulated with tools and material parameters as described in Section 2. The sheet half-length was assumed to be 80 mm in this case. The draw-in into the die cavity was controlled by a drawbead restraining force, F_d. The horizontal drawbead force of $F_d = 300$ kN/m was applied on the edge of the blank to simulate both drawbead and blankholder effects. A friction coefficient of $\mu = 0.3$ was used in this computation.

The calculations were performed with both linearized and fully consistent tangent operators. For the linearized algorithm the number of iterations per step increases gradually from 6

Downloaded 03 May 2010 to 171.66.16.248. Redistribution subject to ASME license or copyright; see http://www.asme.org/terms/Terms_Use.cfm

Table 3 Stretching by cylindrical punch, $\mu = 0.3$. Energy and residual norms for step 10 of linearized and consistent algorithm. ($\mu = 0.3$).

it	linearized algorithm		consistent algorithm	
	residual norm	energy norm	residual norm	energy norm
1	0.150E+01	0.133E−02	0.150E+01	0.117E−02
2	0.338E+00	0.376E−04	0.238E−01	0.199E−06
3	0.105E+00	0.322E−05	0.220E−05	0.105E−12
4	0.342E−01	0.337E−06	0.276E−10	0.157E−20
5	0.113E−01	0.368E−07		
6	0.374E−02	0.405E−08		
7	0.124E−02	0.447E−09		
8	0.412E−03	0.493E−10		
9	0.137E−03	0.544E−11		
10	0.455E−04	0.600E−12		
11	0.151E−04	0.662E−13		
12	0.502E−05	0.732E−14		
13	0.167E−05	0.807E−15		
14	0.554E−06	0.889E−16		

Table 4 Deep drawing by cylindrical punch. Energy and residual norms for step 17 of linearized and consistent algorithms.

it	linearized algorithm		consistent algorithm	
	residual norm	energy norm	residual norm	energy norm
1	0.441E+00	0.238E−03	0.441E+00	0.236E−03
2	0.201E−01	0.533E−06	0.290E−03	0.414E−10
3	0.610E−02	0.456E−07	0.581E−07	0.276E−16
4	0.184E−02	0.399E−08		
5	0.546E−03	0.349E−09		
6	0.162E−03	0.306E−10		
7	0.479E−04	0.268E−11		
8	0.142E−04	0.235E−12		
9	0.419E−05	0.205E−13		
10	0.124E−05	0.180E−14		
11	0.367E−06	0.158E−15		

Table 5 Deep drawing by cylindrical punch. Energy and residual norms for steps 27 and 38 of consistent algorithm.

it	STEP 27		STEP 38	
	residual norm	energy norm	residual norm	energy norm
1	0.654E+01	0.540E−01	0.199E+02	0.333E+00
2	0.123E+01	0.305E−03	0.269E+01	0.113E-01
3	0.270E+00	0.203E−07	0.511E+00	0.573E-05
4	0.999E−04	0.527E−14	0.916E+02	0.245E-02
5	0.250E−07	0.287E−18	0.253E−02	0.114E-09
6			0.654E−06	0.563E-18

to 11. The program diverges at step 18 when the internal force exceeds the value of the drawbead force, and draw-in starts.

On the contrary, the consistent algorithm maintains a nearly constant mean value of five iterations per step with fluctuations unrelated to the increase in the punch travel.

The values of the energy and residual norms during the iterations of three typical incremental steps are given in Tables 4 and 5, respectively.

The quadratic rate of convergence of the proposed consistent algorithm is apparent from these results.

On the other hand, the linearized algorithm exhibits slow

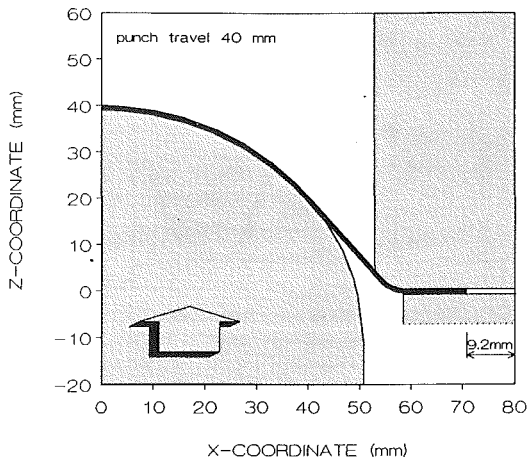

Fig. 4 Deep drawing by cylindrical punch; deformed sheet shape with draw-in of 9.2 mm

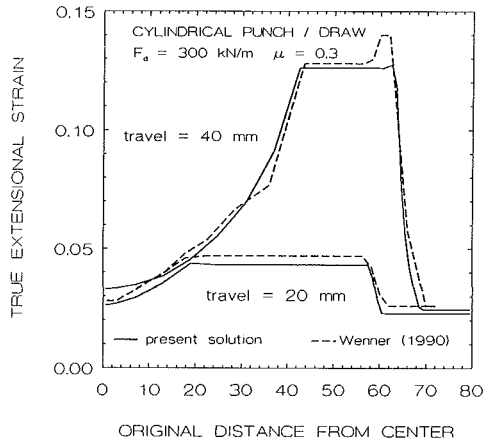

Fig. 5 Deep drawing by cylindrical punch ($\mu = 0.3$); comparison of strain distributions with results from the elastic-plastic code

linear convergence. Moreover, it works only for the first part of the process when, in fact, stretching is predominant and frictional contact nonlinearities are less significant. When the draw-in starts, resulting in large nodal displacements relative to the tools, the linearized algorithm ceases to converge at all.

The presented example was also simulated by Wenner (1990), using an elastic-plastic material law, rate formulation, and contact model based on very small incremental steps (Frey and Wenner, 1987). Figure 4 shows the deformed shape at 40 mm of the punch travel. The 9.2 mm draw-in of the flange is clearly seen and it is in good agreement with 9.3 mm obtained from the Wenner's elastic-plastic code. In Fig. 5, the obtained distributions of the principal true strain along the original position from the symmetry axis are plotted (solid line) for punch travel values of 20 mm, and 40 mm, respectively. The results obtained with the elastic-plastic model, given here for comparison, are represented by the dashed lines. Draw-in starts at a punch travel of 18 mm. The uniformly distributed flat part of the plot corresponds to the region never in contact with the tools.

In the next simulation, the symmetry property was not utilized and the full set of the tools (Fig. 1) was used to test the quality of the solution under more difficult, unsymmetric boundary conditions. For the first test, equal drawbead forces of 307 kN/m were applied to both sides of the sheet resulting in the fully symmetric strain distribution shown in Fig. 6 (dashed line) for the punch travel of 30 mm. These results are also in the full agreement with the results obtained when only half of the blank was simulated. The second strain plot given in Fig. 6 results from the simulation where uneven drawbead forces

Downloaded 03 May 2010 to 171.66.16.248. Redistribution subject to ASME license or copyright; see http://www.asme.org/terms/Terms_Use.cfm

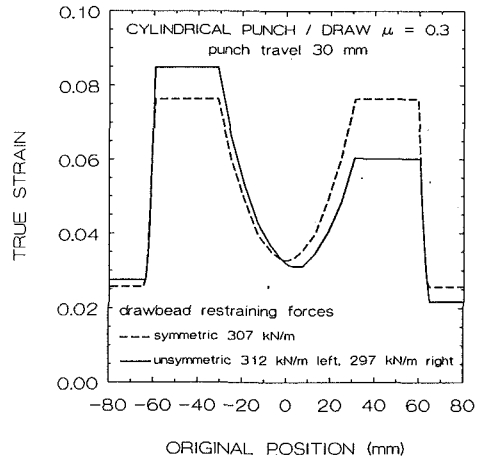

Fig. 6 Deep drawing by cylindrical punch; two-side draw-in test with symmetric and unsymmetric boundary conditions

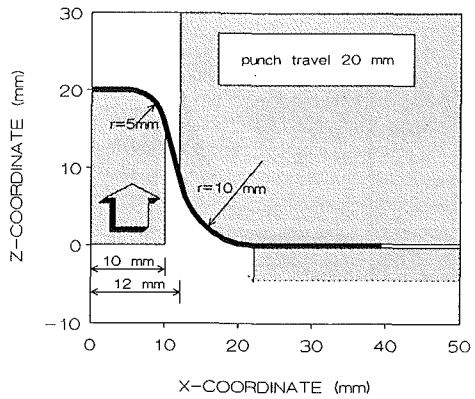

Fig. 7 Deep drawing by flat bottom punch; tools geometry and deformed sheet shape

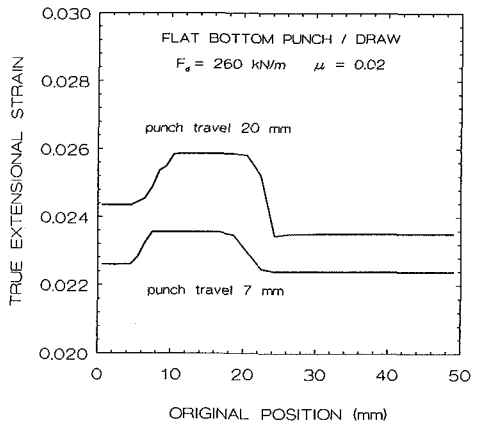

Fig. 8 Deep drawing by flat bottom punch; strain distribution

were applied, namely of 312 kN/m for the left side and 297 kN/m for the right side, documenting the ability to simulate unsymmetric operation. The corresponding asymmetric draw-in (3.8 mm and 5.1 mm) from both sides was obtained.

4 Deep Drawing by Flat Bottom Punch

This example is a test problem which was computed by Wang and Tang (1986) using elastic-plastic finite element code based on the rate formulation. The tool geometry is given in Fig. 7 with the symmetry axis along the z-coordinate. The material parameters follow those used by Wang and Tang: $n=0.2$, $K=482.6$ MPa, $r=1.0$, $M=2.0$, $a_0=0.00001$, $t_0=1.0$ mm, friction coefficient $\mu=0.02$ and drawbead force $=260$ N/mm.

Figure 7 shows that at 20-mm punch travel the flange edge has been drawn 10.6 mm toward the center, which is in good agreement with 10.4 mm given by elastic-plastic solution. The corresponding strain distribution shown in Fig. 8, (maximum value 0.0259) coincides within plotting uncertainties with the elastic-plastic solution. The strain distribution is also given for punch travel of 7 mm when draw starts. Because of the very small value of the friction coefficient, large draw-in is encountered and strains are distributed nearly uniformly at a rather low level.

To demonstrate convergence properties of the consistent algorithm, the values of the energy and residual norms during the iterations of the two incremental steps are given in Table 6.

Table 6 Deep drawing simulation by flat bottom punch. Energy and residual norms for steps 6 and 15 of consistent algorithm.

it	STEP 6		STEP 15	
	residual norm	energy norm	residual norm	energy norm
1	0.115E+02	0.425E+00	0.727E+05	0.150E+04
2	0.395E+01	0.421E−02	0.357E+04	0.341E+02
3	0.105E+00	0.252E−05	0.394E+04	0.947E+01
4	0.601E−04	0.347E−10	0.212E+04	0.771E+00
5	*0.278E−07*	*0.195E−16*	*0.218E+03*	*0.797E−02*
6			0.164E−01	0.500E−08
7			0.737E−05	0.129E−13

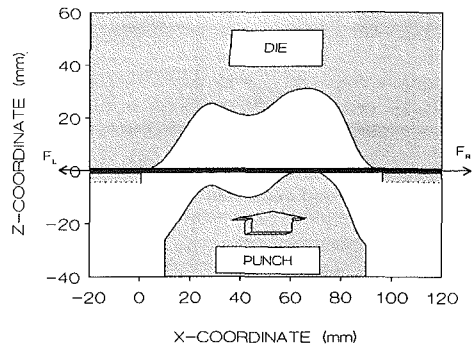

Fig. 9 Reverse drawing simulation with unsymmetric two side draw-in; original tools and sheet geometry

5 Complex Problem of Redrawing and Reverse Drawing Simulation With Irregular Tools and Two-Sided Draw-In

The performance of the consistent approach was successfully tested on a set-up of concave irregular tools given in Fig. 9. Such geometry constitutes a severe test for the numerical algorithm. As the punch progresses, redrawing and reverse drawing with two-side significant draw-in and various drawbead forces are experienced. Reverse drawing is considered to be one of the most challenging problems facing sheet forming FEM. In the early stage of the forming process, a sheet is fixed at the boundaries by the drawbead forces. As simulation proceeds and the value of the internal forces exceeds the drawbead force value, the sheet is allowed to draw into the die cavity. This results in highly nonlinear frictional contact conditions because large relative displacements occur between the tools and the material, and the set of nodes in contact with the tools changes rapidly. Special difficulties are induced by sudden changes in the contact conditions when new areas of the tools

Downloaded 03 May 2010 to 171.66.16.248. Redistribution subject to ASME license or copyright; see http://www.asme.org/terms/Terms_Use.cfm

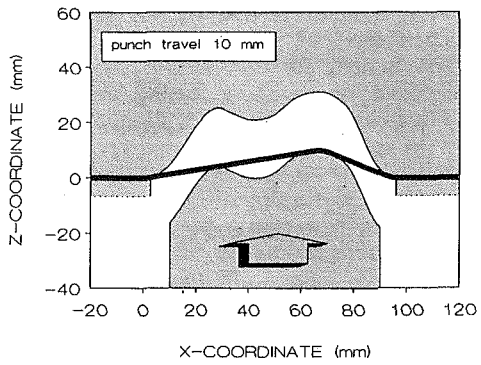

Fig. 10(*a*)

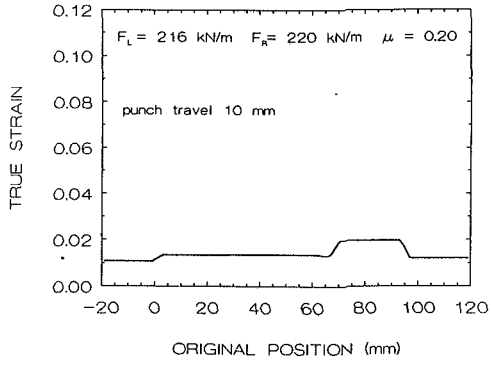

Fig. 10(*b*)

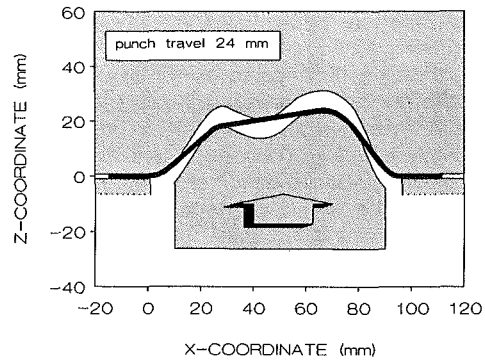

Fig. 10(*c*)

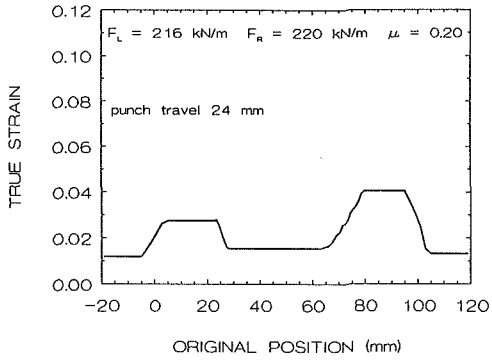

Fig. 10(*d*)

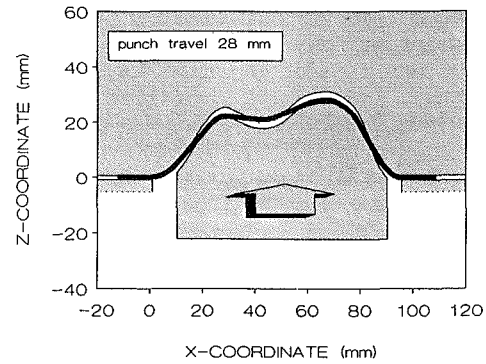

Fig. 10(*e*)

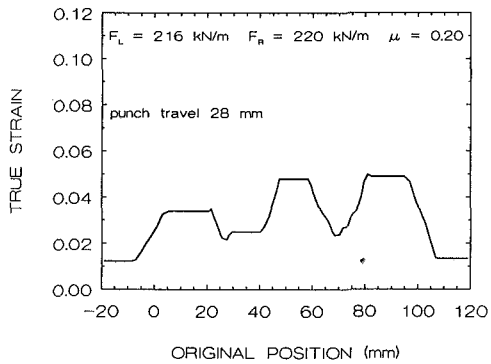

Fig. 10(*f*)

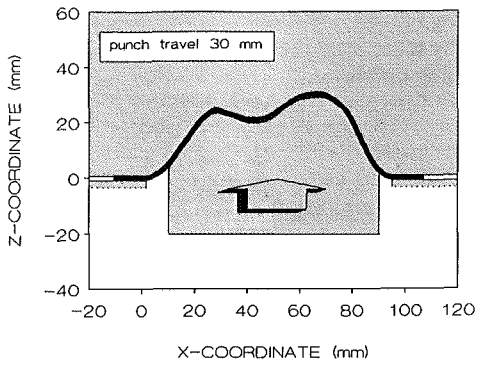

Fig. 10(*g*)

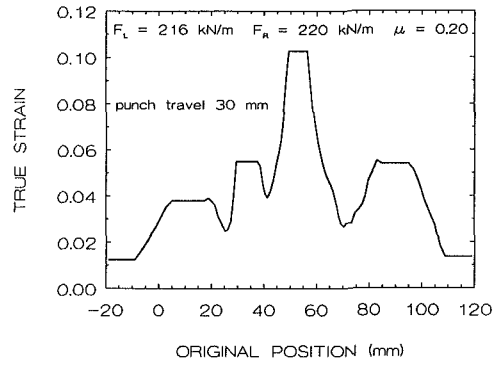

Fig. 10(*h*)

Fig. 10 Reverse drawing simulation; deformed geometries with draw-in and strain distributions at the subsequent stages of the forming process

come into the contact, thereby reversing material flow directions.

The material properties listed below correspond approximately to those of standard AKDQ steel used by automotive industry: $n=0.196$, $K=503.4$, $r=1.46$, $M=2.0$, $a_0=0.0038$, $t_0=0.78$ mm.

Drawbead forces were set to 216 kN/m for the left edge, 220 kN/m for the right edge and the friction coefficient of $\mu=0.20$ was used.

Figure 10 shows the results for various punch travel values. On the left side, subsequent stages of the forming process are

Downloaded 03 May 2010 to 171.66.16.248. Redistribution subject to ASME license or copyright; see http://www.asme.org/terms/Terms_Use.cfm

Table 7 Reverse drawing simulation. Energy and residual norms for steps 17 and 30 of consistent algorithm.

it	STEP 17		STEP 30	
	residual norm	energy norm	residual norm	energy norm
1	0.918E+03	0.287E+00	0.260E+05	0.222E+03
2	0.312E+04	0.547E+01	0.655E+04	0.987E+01
3	0.448E+01	0.288E−03	0.202E+03	0.244E−01
4	0.253E+00	0.156E−04	0.749E+00	0.259E−03
5	0.489E−03	0.483E−09	0.111E+00	0.350E−06
6	0.934E−05	0.698E−15	0.530E−03	0.671E−12
7	0.963E−08	0.214E−18	0.356E−06	0.142E−16

presented, while on the right-hand side, the corresponding principal strain distributions are given.

For a punch travel of 10 mm, the second peak at the punch just touches the sheet, suddenly changing contact conditions and material flow directions. The next critical point is achieved at a punch travel of 24 mm when the sheet touches the middle part of the die, starting reverse drawing and changing the material flow directions again. From this moment new peaks at the strain distribution plot start to build up to achieve the maximum value of about 10 percent for the punch travel of 30 mm at the tools closure. As can be seen from these results, the increase of the friction coefficient value would result in the faster build-up of the strains, the strain localization and subsequent fracture failure on the free surface of the sheet.

Both linearized and consistent models were again tested in this case. The linearized algorithm encountered convergence problems in the early stage of the simulation process. On the contrary, the consistent algorithm simulated the whole forming process, up to the die closure, with the basic mean value of seven iterations per step. To provide an idea of the performance of the Newton iterative solution procedure, the values of the Euclidean norm of the out-of-balance force and the energy norm during two incremental steps are given in Table 7.

A quadratic rate of convergence is clearly exhibited by these results.

6 Summary and Conclusions

A formulation for finite element simulation of highly nonlinear problems including friction and contact with irregularly shaped, curved rigid surfaces has been derived, prompted by difficulties in robust and accurate simulations of industrial forming processes. Nonlinearities are caused by complex frictional contact conditions, large strains, and plastic flow. The goal was to create an algorithm of considerably increased numerical stability and accuracy while retaining cost effectiveness for use with realistic, large-scale industrial applications.

The key point in the development of the proposed algorithm was a consistent linearization of complete set of governing relations including equilibrium and frictional contact equations. The explicit form of the fully consistent tangent operator was derived for large deformations, which was not presented in the literature so far for frictional contact model and material model used in this paper.

Exclusion of nonlinear terms (with respect to frictional contact), from the obtained stiffness matrix, will result in the "linearized" theory efficient only for the case of infinitesimal deformations, although this approach has often been presented in the literature for large deformations. The convergence and stability of the linearized (in the sense defined above) and proposed in this paper fully consistent algorithms have been tested.

It was demonstrated that the consistent model exhibits quadratic rate of asymptotic convergence and good numerical stability independently of severity of the frictional contact nonlinearities. In sharp contrast, the linearized algorithm shows only linear convergence with decreasing rate when friction is included. Moreover, it works only with mild nonlinearities. It was shown on numerical examples that for the problems involving significant movements between material and tools (like, for example, in deep drawing of metal sheets), the linearized algorithm ceases to converge at all.

Several simulations of the sheet-forming processes have been performed to verify numerically the quality of the proposed fully consistent formulation. Stretching and deep drawing by simple tools were favorably compared to the existing analytical or numerical results. In order to facilitate a comparison with other formulations, an effort has been made to document in detail the presented numerical simulations, by providing a number of iterations by load step and obtained values of residual and energy norms.

Finally, the algorithm's performance was successfully tested on a complex set-up of concave, irregular tools with two-sided draw-in and various drawbead forces resembling conditions from real operations in the automotive industry. Here, the ability of the simulation to handle redrawing and reverse drawing operations, considered commonly to be one of the most challenging problems facing sheet forming analysis, was demonstrated.

Several features of the approach are aimed at reducing computation time and although the resulting computer code itself has not been optimized or vectorized in any way, the computing times for examples presented in the paper are less than two minutes on an VAX8550 computer or less than ten minutes on an IBM-PS2/386 personal computer. These preliminary results indicate high efficiency of the proposed formulation and suggest that it should be suitable for realistic industrial applications.

Summarizing, the new approach confers the following benefits:

1 Robustness is improved. Example forming simulations show greater ranges of solution convergence, compared with inconsistent linearization methods.

2 Iteration is reduced relative to inconsistent linearization methods. A quadratic rate of convergence is obtained, improving computation times and accuracies.

3 Special techniques to enforce nonpenetration contact conditions directly are eliminated in the new method.

4 Highly nonlinear frictional contact problems can now be analyzed, in spite of large relative displacements of material points along curved, rigid surfaces. This capability was demonstrated by successfully simulating complex draw and reverse draw-forming operations.

Acknowledgments

The authors would like to acknowledge the support of the Center for Net Shape Manufacturing at the Ohio State University, the Chrysler Corporation, and the Ohio Supercomputer Center (PAS 080). The authors also wish to thank J. K. Lee, Y. T. Keum, D. J. Zhou, and C. T. Wang for many useful discussions.

References

Frey, W. H., and Wenner, M. L., 1987, "Development and Applications of a One-Dimensional Finite Element Code for Sheet Metal Forming Analysis," Proceedings of the ASME Symposium on Interdisciplinary Issues in Materials Processing and Manufacturing, Boston, Mass.

Wang, N.-M., and Tang, S. C, 1986, "Analysis of Bending Effect in Sheet Forming Operations," *Numerical Methods in Industrial Forming Processes*, K. Mattiasson et al., eds., Balkema, Rotterdam, pp. 71–76.

Wenner, M. L., 1990, private communication, General Motors Research Laboratories, Warren, Mich.

Downloaded 03 May 2010 to 171.66.16.248. Redistribution subject to ASME license or copyright; see http://www.asme.org/terms/Terms_Use.cfm

Systems With Infinitesimal Mobility: Part I—Matrix Analysis and First-Order Infinitesimal Mobility

E. N. Kuznetsov
Department of General Engineering,
University of Illinois,
Urbana, IL 61801
Mem. ASME

Structural and mechanical assemblies with infinitesimal mobility are studied by means of analytical statics, elaborating and capitalizing on the conceptual difference between virtual and kinematic displacements. The analysis is based on the resolution of a given load into two mutually orthogonal components, which allows the introduction of a statical-kinematic stiffness matrix. The issue of statical-kinematic duality is explored and extended to second-order analysis. It leads to the complementary exclusion condition between kinematic mobility and statical possibility of stable self-stress, and the ensuing statical criterion of immobility. A computationally efficient matrix method for detecting simple first-order mechanisms is presented and compared to an existing method based on the analysis of a certain reduced quadratic form.

Introduction

For a structural engineer, infinitesimal mobility has traditionally been an obscure side issue. In a typical text on structural analysis, systems with infinitesimal mobility are discussed very briefly, declared geometrically unstable, hence, unsuitable for practical applications, and abandoned from further consideration. For a mechanical engineer, infinitesimal mechanisms have been less interesting as they lack the quintessential feature of mobility. Recently, however, structural and mechanical assemblies with infinitesimal mobility are attracting renewed interest. These systems are unique in that they open a fundamentally different way of obtaining structural stiffness, acquiring it by means of prestress, at the expense of the material strength rather than mass. Advances in materials science, providing an ever-increasing abundance of strength, underlie both the success and the potential of the concept. Moreover, since an increased strength is not necessarily accompanied by a gain in stiffness, prestress may be the only efficient way of capitalizing on the material strength. Among the best known examples are Buckminster Fuller's tensegrity structures, which are multi-freedom infinitesimal mechanisms stiffened by prestress. More recently, the concept attracted the attention of structural, mechanical, and control theory specialists in the area of large, lightweight deployable structures. The issue of infinitesimal mobility has also surfaced in the theory of geometric packing and covering, with applications to materials science ranging from crystallography to the behavior of granular materials.

The first concise description of infinitesimal mechanisms is due to Mobius (1837). When formulating an analytical criterion of a geometrically invariant (stiff) system, he discovered and investigated a singular, degenerate class of systems. Maxwell (1890) was apparently the first to recognize the existence of the opposite exceptional class of systems, those formally possessing a positive number of degrees-of-freedom, yet lacking kinematic mobility. Both Mobius and Maxwell attributed the peculiar nature of their exceptional systems to the presence of maximum or minimum length bars compatible with other structural members. Mohr (1885) found this extremal feature to be a general condition for the statical possibility of self-stress in any structural system.

Kinematic properties of singular systems were studied in more detail by Kotter (1912) and Levi-Civita and Amaldi (1930). The latter developed the most general approach, whereby a structural or mechanical system is modeled as an assembly of material points linked by ideal positional constraints representing the system components. This approach is employed in the present paper as a basis for an investigation in the theory, analysis, and synthesis of systems with infinitesimal mobility.

Infinitesimal mobility in structural and mechanical assemblies is a subject of statical-kinematic analysis (a branch of analytical mechanics). Assuming the system material perfectly rigid, this analysis deals with both general and system-specific relations among external loads, internal forces, equilibrium configurations, and kinematically possible displacements, i.e., all information attainable without invok-

Contributed by the Applied Mechanics Division of THE AMERICAN SOCIETY OF MECHANICAL ENGINEERS for publication in the JOURNAL OF APPLIED MECHANICS.

Discussion on this paper should be addressed to the Technical Editor, Leon M. Keer, The Technological Institute, Northwestern University, Evanston, IL 60208, and will be accepted until two months after final publication of the paper itself in the JOURNAL OF APPLIED MECHANICS. Manuscript received by the ASME Applied Mechanics Division, Sept. 29, 1989; final revision, Jan. 31, 1990.

Copyright © 1991 by ASME
Downloaded 03 May 2010 to 171.66.16.248. Redistribution subject to ASME license or copyright; see http://www.asme.org/terms/Terms_Use.cfm

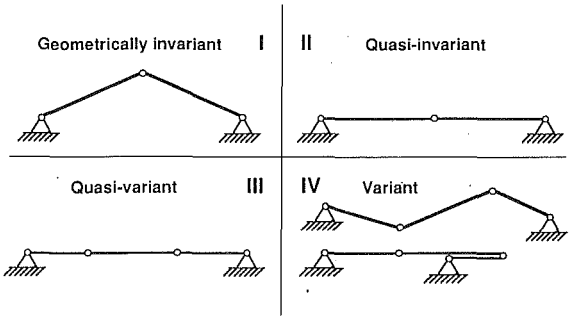

Fig. 1 Four statical-kinematic types of structural systems

ing the constitutive equations. Within the framework of this analysis there exist four and only four statical-kinematic types of systems. Their dual (kinematic and statical) definitions can be found in Kuznetsov (1979) along with the classification Table (Fig. 1) which shows the simplest prototypes of the four types. The main diagonal of the Table (quadrants I and IV) contains the main types of systems—geometrically invariant and variant, and the secondary diagonal—the two degenerate, singular types. Types I, II, and III possess a unique geometric configuration; types II, III, and IV cannot balance an arbitrary load in their original configurations; types II and III are infinitesimal mechanisms: They allow infinitesimal displacements requiring only second or, perhaps, higher-order strains.

The difference between the two types of infinitesimal mechanisms is that of principle and is rooted in structural topology. Type II has a sufficient number of constraints (bars) for being geometrically invariant and is an infinitesimal mechanism only because of its singular, degenerate geometric configuration. There is always a constraint variation (a change in the bar lengths) that would restore the system to the type it generically belongs to, that is, type I. For this reason, systems of type II are called ill-constrained or improperly constrained. In contrast, systems whose structural topology is such that no constraint variation would render them invariant, are referred to as insufficiently constrained or underconstrained. Among them, type III represents a kinematic chain in an exceptional, immobile configuration; here constraint variations can only restore finite mobility thereby reducing the system to its generic type IV.

To emphasize the dissimilar nature and the opposite origins of systems II and III, they are sometimes referred to, respectively, as quasi-invariant and quasi-variant. Further fundamental differences between these two types of infinitesimal mechanisms are revealed in the course of this investigation. For the lack of established terminology, for brevity, and for clarity, the four statical-kinematic types of systems will be identified in this paper by the respective Roman numerals. Adopting the structural engineer's priority, this classification arranges the systems in the order of a step-by-step degradation in stiffness which is also reflected in the successive relaxation of the respective analytical criteria of the four types.

Virtual and Kinematic Displacements Statical-Kinematic Duality

Complete information on the kinematic properties of a structural system is contained in a pertinent set of simultaneous constraint equations

$$F^i(X_1, \ldots, X_n, \ldots, X_N) = 0, \; i = 1, 2, \ldots, C \qquad (1)$$

with at least one known solution $X = X_n{}^0$. The C constraint functions F^i relate the N generalized coordinates X_n to the invariant geometric parameters of the system (member sizes, linear, and angular distances, etc.). For example, constraint equations of a pin-bar assembly are quadratic, of the form

$$\Delta X^2 + \Delta Y^2 + \Delta Z^2 - L^2 = 0 \qquad (2)$$

with Δ denoting the cartesian coordinate difference of the bar ends and L the bar length. Power expansion techniques are systematically utilized throughout the following analysis. It is therefore assumed that F^i can be expanded into power series at the solution point $X = X_n{}^0$ describing the current geometric configuration of the system:

$$f^i = F^i_n x_n + (1/2!) F^i_{mn} x_m x_n + \ldots = 0,$$
$$F^i_n \equiv \partial F^i / \partial X_{n\,,0}, \; m, n = 1, 2, \ldots, N \qquad (3)$$

where x_n are infinitesimal increments of the respective coordinates and f^i are the resulting variations of constraints. Here and below a repeated subscript denotes summation over the indicated range.

Linear forms in equation (3) are linearized constraint functions which appear in the linearized constraint equations

$$F^i_n x_n = f^i = 0. \qquad (4)$$

Infinitesimal coodinate increments satisfying these equations are conventional virtual displacements, which, obviously, are local, i.e., configuration-specific. In contrast, displacements satisfying the original constraint equations (1) are called kinematically possible, or simply *kinematic*; they are system-specific and not necessarily infinitesimal. A subtle, yet crucial distinction of virtual displacements is emphasized in the succinct Webster's definition of the word virtual as "being in effect but not in fact"; this leaves the factual (realization) aspect with kinematic displacements. The relation between virtual and kinematic displacements reflects the fact that the former are tangent to the latter. Inattention to the conceptual difference between virtual and kinematic displacements led in the past to long-standing apparent paradoxes in the membrane shell theory (Kuznetsov, 1989b).

If the rank of the constraint function Jacobian matrix

$$\mathbf{J} = [F^i_n] \qquad (5)$$

is r, equations (4) can be solved in terms of properly selected $(N-r)$ virtual displacements x_s designated as independent:

$$x_p = a_{ps} x_s; \; p = 1, \ldots r; \; s = r+1, \ldots N. \qquad (6)$$

A useful expression of all displacements in terms of the independent ones can be written with the aid of Kronecker's δ:

$$x_n = a_{ns} x_s, \; a_{ns} = \delta_{pn} a_{ps} + \delta_{ns}. \qquad (7)$$

According to the principle of virtual work (which is meaningful only with virtual displacements), a system in a given configuration $X_n = X_n{}^0$ is in equilibrium under an external load $P_n{}^0$ if and only if

$$P^0_n x_n = 0. \qquad (8)$$

Thus, analytically, equilibrium is nothing but the condition of orthogonality between the external loads and the virtual displacements. As shown in analytical statics, equilibrium equations are obtained from equations (4) and (8):

$$F^i_n \Lambda_i = P^0_n. \qquad (9)$$

Here, Λ_i are generalized constraint reactions which depend on the particular form of the constraint functions and, therefore, do not always coincide with the actual member forces.

The fact that the matrices of equations (4) and (9) are mutually transposed underlies an interrelation known as statical-kinematic duality. Accordingly, every pertinent concept, parameter, or relation in kinematics has a statical counterpart and vice versa. The pivotal role in statical-kinematic duality belongs to Jacobian matrix rank, whose

Downloaded 03 May 2010 to 171.66.16.248. Redistribution subject to ASME license or copyright; see http://www.asme.org/terms/Terms_Use.cfm

relation to the number of coordinates, N, and the number of constraints, C, has both kinematic and statical implications.

On the kinematic side, rank r is the number of independent constraints, which is, at the same time, the number of dependent displacements. The rank also determines the number of dependent constraints (degree of statical indeterminacy)

$$S = C - r \tag{10}$$

and the number of independent virtual displacements (virtual degrees-of-freedom)

$$V = N - r. \tag{11}$$

For an underconstrained system, the local parameter V represents the degree of virtual indeterminacy, as opposed to the degree of kinematic indeterminacy, K, which is the number of independent kinematic displacements and is a global parameter. The situation $V > K$ has been referred to as a bifurcation of (constraint) compatibility (Tarnai, 1988).

Changes in a system configuration caused by trivial ($f^i = 0$) or nontrivial constraint variations may lead to a change in the system type, which takes the form of degeneration. The resulting singular configuration is characterized by a drop in the rank r compared to its maximal value, $r_{\max}$, attained at the adjacent ordinary configurations of the system. The drop in the rank, which is the degree of degeneration (or singularity)

$$D = r_{\max} - r \tag{12}$$

is an important local parameter of the system. It establishes the differences between the local and global indeterminacies

$$D = S - S_G = V - K. \tag{13}$$

Here, S_G is the degree of global (topological) statical indeterminacy, present, for example, in a finite mechanism with statically indeterminate components. Note that although both V and S are local, their difference

$$V - S = N - C \tag{14}$$

is a global parameter determined by the system topology.

Rank $r < C$, indicating constraint dependence, means that a set of S-dependent constraints deprives the system of certain degrees-of-freedom more than once (redundancy), while possibly leaving other degrees-of-freedom unconstrained. The statical counterpart of constraint dependence is their potential statical counteraction, which manifests itself in that homogeneous equilibrium equations

$$F_n^i \Lambda_i = 0 \tag{15}$$

admit nontrivial solutions $\Lambda_{ik} \neq 0$ $(k = r+1, \ldots, C)$. Each solution describes a pattern of statically possible initial forces (self-stress). The parameter S in equation (10) is the number of linearly independent self-stress patterns. Thus, constraint dependence makes self-stress statically possible and, conversely, statical possibility of self-stress is a sign of constraint dependence. The opposite is also true: A constraint is independent if and only if it cannot have an initial force.

In any given configuration, a system can balance only loads $P_n{}^0$ that are in the column space of the equilibrium matrix in equation (9). These are called statically possible, or equilibrium loads and are representable as linear combinations of the matrix columns with arbitrary Λ_i. When the rank $r = N$, and only in this case, every load is an equilibrium load. Otherwise, there exist $N - r$ linearly independent loads that cannot be balanced in the original configuration of the system. Such loads belong to the orthogonal complement of the column space of the equilibrium matrix and are of the form (Kuznetsov, 1973)

$$p_n = a_{ns} p_s \tag{16}$$

with arbitrary p_s. Loads (16) are called perturbation loads; if applied, they produce either displacements or infinite constraint reactions. Comparison with equation (7) shows perturbation loads to be related to the virtual displacements of the system: Both span the nullspace of constraint Jacobian matrix and, therefore, are orthogonal to its row space. This confirms the complemental orthogonality between equilibrium and perturbation loads and indicates that the number of arbitrary components p_s, i.e., the number of linearly independent perturbation loads, equals the number of virtual degrees-of-freedom, V.

Statical-kinematic duality is also observed at the right-hand sides of equations (4) and (9). The kinematical counterpart of the concept of equilibrium load is a set of kinematically admissible (compatible) constraint variations. If present in the linearized equations (4), constraint variations f^i are infinitesimally small and local. They represent small changes in the geometric parameters of the system due to thermal, elastic, plastic, rheological and other possible deformations of the structural members. Admissible variations are those for which f^i are in the column space of the constraint Jacobian matrix. When the rank $r = C$, and only in this case, every variation of constraints is admissible. Otherwise, there exist $C - r$ linearly independent incompatible constraint variations.

The observations made so far are summed up in Table 1.

Statical-Kinematic Stiffness Matrix

When a system other than invariant is subjected to a general load, P_n, it must change its geometric configuration in order to balance the load, which makes the problem nonlinear. Furthermore, the problem cannot be linearized in terms of conventional, load incrementing techniques, since the system in a given configuration is incapable of supporting even an arbitrarily small perturbation load component. However, in the presence of forces Λ_i induced either by prestress or by an equilibrium load, the system possesses certain stiffness of statical-kinematic (as opposed to elastic) nature. The required member forces may be induced, in particular, by the equilibrium component, $P_n{}^0$, of the very load P_n if the latter happens to contain one. In this case

$$P_n = P_n{}^0 + p_n \tag{17}$$

and the problem can be linearized and solved, either iteratively or, perhaps, in one step, provided that the perturbation load component p_n is sufficiently small. The required load resolution (17) is facilitated by equations (8) and (16):

$$(P_n - p_n) x_n = (P_n - a_{nt} p_t) a_{ns} x_s = 0, \; s,t = r+1, \ldots, N. \tag{18}$$

Table 1 Summary of statical-kinematic duality relations

Local number	Kinematically is the number of independent	Statically is the number of independent
r	constraints; compatible constraint variations	generalized forces, equilibrium loads
$V = N - r$	virtual displacements (virtual indeterminacy)	perturbation loads
$S = C - r$	incompatible constraint variations	self-stress patterns (statical indeterminacy)

Downloaded 03 May 2010 to 171.66.16.248. Redistribution subject to ASME license or copyright; see http://www.asme.org/terms/Terms_Use.cfm

Since this equation must be satisfied identically with respect to independent displacements x_s, it yields V equations in the unknown components p_t of the perturbation load

$$a_{nt}a_{ns}p_t = a_{ns}P_n. \tag{19}$$

In a computationally more-efficient way, the resolution of a general load into the mutually orthogonal, equilibrium, and perturbation components can be accomplished in a single matrix operation

$$P_n{}^0 = \mathbf{R}P_n, \quad p_n = (\mathbf{I}-\mathbf{R})P_n. \tag{20}$$

Here, $\mathbf{I}$ is the identity matrix and

$$\mathbf{R} = \mathbf{J}_r{}^T(\mathbf{J}_r\mathbf{J}_r{}^T)^{-1}\mathbf{J}_r \tag{21}$$

is an $N\times N$ projection matrix (Strang, 1988) expressed in terms of the constraint Jacobian matrix retaining any r linearly independent rows

$$\mathbf{J}_r = [F^p{}_n] \quad p = 1, 2, \ldots, r. \tag{22}$$

Matrix $\mathbf{R}$ is of rank r, symmetric, and idempotent ($\mathbf{RR}=\mathbf{R}$), which ensures that an equilibrium load is unaffected by the projection, whereas a perturbation load has a zero projection onto the column space of the equilibrium matrix:

$$\mathbf{R}P_n{}^0 = P_n{}^0 \quad \mathbf{R}p_n = 0. \tag{23}$$

With the load resolution carried out, constraint reactions Λ_i corresponding to $P_n{}^0$ are found from the equilibrium equations (9).

To complete the linearized analysis, the system displacements are to be evaluated. This can be done by utilizing the incremented equilibrium equations

$$\delta(F^i{}_n\Lambda_i) = F^i{}_{mn}\Lambda_i x_m + F^i{}_n\lambda_i = \delta P_n \tag{24}$$

where λ_i are increments of the respective constraint reactions Λ_i, and the right-hand side represents the load component increments. The sought displacements x_m must be sufficiently small to justify the incremental linearization.

Equations (24), containing all displacements, are used in conjunction with the linearized constraint equations. The resulting combined system of equations can be presented in a block-matrix form

$$\begin{bmatrix} K_{mn} & F^p_n \\ F^p_m & 0 \end{bmatrix}\begin{bmatrix} x_m \\ \lambda_p \end{bmatrix} = \begin{bmatrix} \delta P_n \\ 0 \end{bmatrix}. \tag{25}$$

The introduced symmetric $N\times N$ matrix

$$K_{mn} = F^i{}_{mn}\Lambda_i \tag{26}$$

is the sum of the constraint function Hessian matrices weighted by the corresponding reactions Λ_i. The Jacobian matrix in equations (57) is again represented by a maximal set (equation (22)) of any r-independent rows. The reason is that a singular Jacobian matrix is a manifestation of statical indeterminacy, and then the problem cannot be solved by purely statical-kinematic means, without constitutive relations. The $(N+r)$ equations (57) form a closed system with N unknown displacements x_m and r unknown increments λ_p of constraint reactions. It is computationally advantageous to separate the equilibrium load component in advance and then to evaluate the corresponding constraint reactions and incorporate them into K_{mn}. This is unavoidable when the load $P_n = \delta P_n$ is the only load applied to the system. As before, solution (6) of the linearized constraint equations (the lower echelon in equation (25)) can be used for eliminating the dependent displacements from the remaining equations:

$$K_{mn}\, a_{ms}\, x_s + F^p{}_n\lambda_p = P_n. \tag{27}$$

As has been demonstrated in the preceding section, the unknown $(N-r)$ independent displacements, x_s and r incremental reactions, λ_p, belong to two orthogonal complement subspaces. Accordingly, the equilibrium component of P_n produces λ_p but no displacements, while the perturbation component gives rise to x_s (and x_n) but no incremental reactions. As a result, the kinematic and statical aspects of the problem (i.e., the evaluation of the system displacements and forces) at each iteration can be uncoupled. To this end, both sides of equations (27) are multiplied by $x_n = a_{nt}x_t$. Since the resulting equation of virtual work must be satisfied identically with respect to the independent virtual displacements x_s, it yields V simultaneous equilibrium equations

$$K_{mn}a_{ms}a_{nt}x_t = a_{ns}P_n. \tag{28}$$

Introducing a $V\times V$ matrix

$$K_{st} = K_{mn}\, a_{ms}\, a_{nt} \tag{29}$$

allows the system of equilibrium equations to be written as

$$K_{st}x_t = a_{ns}P_n \tag{30}$$

where K_{st} is the reduced statical-kinematic stiffness matrix.

The stiffness expressed by matrix K_{st} is peculiar in two ways. First, it is engendered by, and depends on, the internal forces induced by prestress and by the equilibrium component of the applied load. Second, this stiffness is meaningful only in the context of perturbation loads, to which it relates the system displacements. Other than that, the statical-kinematic stiffness matrix is similar to any conventional tangent stiffness matrix used in a linear or iterative analysis. The basic properties of the load resolution underlying the concept of statical-kinematic stiffness matrix can be summed up as follows.

(1) An arbitrary load resolves uniquely into the equilibrium and perturbation components which are mutual orthogonal complements.

(2) An equilibrium load, including its special kind—a self-stress, generates internal forces in the system, but no displacements; a perturbation load produces displacements without changing the member forces.

(3) For equilibrium loads, superposition of the corresponding stress states is valid; for perturbation loads, superposition of displacements holds.

(4) Both the resolution of a general load and the properties of its two components are local, i.e., related to the particular fixed configuration of a system.

The sequence of analytical steps in a procedure utilizing the statical-kinematic stiffness matrix is: forming the projection matrix $\mathbf{R}$ and resolving a given load; evaluating the reactions Λ_i produced by the equilibrium load component and adding them to the prestress; forming the reduced stiffness matrix K_{st}; and, finally, solving for the displacements x_s. In a nonlinear analysis, the next iteration starts with an update of the system configuration.

The described analysis is computationally efficient as well as insightful and helpful in understanding the behavior of underconstrained structural systems. At the same time, it has a "brute force" alternative, utilizing conventional means of solving geometrically nonlinear elastic problems. This is done after formally rendering an underconstrained system invariant by introducing V auxiliary, very flexible constraints. The price is a substantial increase in the problem size, which may be unwarranted or even unacceptable, say, in the case of a real-time shape control of an underconstrained structural system.

First-Order Mobility

If the rank r of the Jacobian matrix is full, that is, equal to the smaller of the matrix sizes, it follows from equations (4) that the system is nonsingular and belongs to one of the two main types, I or IV. Indeed, at $r=N\leq C$, all virtual displacements are zero and the system is of type I, while at

Downloaded 03 May 2010 to 171.66.16.248. Redistribution subject to ASME license or copyright; see http://www.asme.org/terms/Terms_Use.cfm

$r = C < N$, a nonzero solution for x_n exists, so that displacements are possible and the system is of type IV.

The situation is quite different for a singular system, where an analysis based on the linear approximation (4) is inadequate, and higher-order terms of expanded constraint equations (3) must be considered. It can happen that a degenerate system, while allowing virtual dispalcements, nevertheless lacks kinematic mobility. This indicates that even though the system is not geometrically invariant, it possesses a unique configuration. More precisely, such a system allows infinitesimally small displacements requiring only second or, perhaps, higher-order strains in structural members; this property qualifies the system as one with infinitesimal mobility.

Definition. A system with infinitesimal mobility (an infinitesimal mechanism) is a system allowing virtual displacements but no kinematic displacements.

A formal description of a system with infinitesimal mobility is

$$V > K = 0, \tag{31}$$

i.e., such a system possesses virtual degrees-of-freedom but no actual, kinematic, ones and is kinematically immobile.

When $D > 0$, homogeneous equilibrium equations admit at least one nontrivial solution, $\Lambda_i \neq 0$, which can be used to form a linear combination of expanded constraint equations

$$\Lambda_i f^i = \Lambda_i [F^i_r x_n + (1/2!) F^i_{mn} x_m x_n + \ldots] = 0. \tag{32}$$

On multiplying out, the first product vanishes by virtue of equation (4) and the kinematic properties of the system are determined by the remaining higher-order forms. It is convenient to begin the analysis with a simple class of systems satisfying the following assumptions:

(1) degree of degeneracy (singularity) is $D = 1$ and the self-stress is comprehensive, so that all Λ_i are different from zero; (2) the leading (lowest-order) form in equation (32) is quadratic, making the second-order analysis meaningful, if not always conclusive.

By eliminating the dependent displacements in this complete quadratic form with the aid of solution (6), a reduced quadratic form $Q = Q(x_s, x_t, \ldots, x_N)$ in V independent virtual displacements is obtained. If this form is definite, all displacements x_s must be zero. It means that only the linearized equations (4) are compatible and vanish with arbitrary x_s, whereas the quadratic forms in equation (3) can simultaneously turn into zero only in a trivial way. This prevents any nonzero virtual displacement from satisfying the constraint equations (1) and, consequently, prohibits any kinematic displacements. Thus, definiteness of quadratic form Q is a sufficient condition for the system to be an infinitesimal mechanism.

To demonstrate the necessity of this condition, note that the left-hand side of equation (32) is work performed by the initial forces over constraint variations due to virtual displacements. The state of the system does not change if one, say the jth, constraint is cut and the force Λ_j is applied at both sides of the cut. With the rest of the constraints invariant, any set of displacements will produce a discontinuity f^j at the cut (were displacements possible without either a discontinuity or a constraint variation, the system would be kinematically mobile). Eliminating the discontinuity requires the work $\Lambda_j f^j \neq 0$. Since this work equals Q, its being different from zero for any nonzero set of virtual displacements requires the quadratic form Q to be definite.

Thus, definiteness of the reduced quadratic form Q constitutes both a necessary and a sufficient analytical criterion for a system satisfying the above two assumptions, to be an infinitesimal mechanism. It is quasi-invariant (type II) if, upon exiting from the degenerate configuration, the rank restores to $r = N$; according to equation (12), a quasi-invariant system is formally characterized by

$$V = D, \quad K = 0. \tag{33}$$

In contrast, a quasi-variant system (type III)

$$V > D, \quad K = 0. \tag{34}$$

Physically, the existence of a nontrivial solution to homogeneous equilibrium equations indicates statical possibility of initial forces in the system (self-stress). The lowest-order virtual work Q being strictly positive is necessary and sufficient for stability of the self-stress. Moreover, mere definiteness of Q amounts in this case to positive definiteness; if sign reversal is needed for stability, it is achieved by changing the sign of all initial forces. Thus, a definite Q means, in statical terms, that the system allows stable self-stress, and in kinematic terms, that all displacements are zero. In short, a system allowing stable self-stress is kinematically immobile.

Two subtle points are noteworthy in interpreting and implementing this statement. On the kinematic side, the stability in question is of *kinematic* or geometric (as opposed to elastic) nature. The reason is that the system constraints (structural members) were assumed ideal, and the entire development has not involved any notion of elasticity. On the statical side, as is readily seen, it is just the *statical possibility* (as opposed to the actual presence) of stable self-stress, that constitutes the statical criterion of immobility. Indeed, just the formal existence of a solution $\Lambda_i \neq 0$ as a set of numbers producing $Q \neq 0$ for any nonzero x_s, entails immobility; the actual presence or absence of self-stress is irrelevant. At the same time definiteness of Q, indicating stability of the self-stress, makes it physically realizable.

A certain symmetry is now apparent between the concepts of virtual and kinematic displacements on the one hand, and the concepts of statically possible and physically realizable self-stress on the other.

Definition. The pattern of initial forces corresponding to a nontrivial solution of homogeneous equilibrium equations will be called virtual self-stress.

The definition reflects the formal origin of the concept and emphasizes its tentative, effectual, rather than actual, nature.

The concepts of virtual displacement and virtual self-stress have much in common: both are only formal and local effects representing nontrivial solutions of simultaneous homogeneous equations; both are engendered by one and the same constraint Jacobian matrix and belong, respectively, to its nullspace and left nullspace; both may be realizable and become actual; and, finally, the realizability of each depends on certain higher-order conditions. Remarkably, these conditions are mutually exclusive: realizability of self-stress ("prestressability"), which hinges on its stability, requires a definite Q, thus precluding the virtual displacements from becoming kinematic. Conversely, kinematic mobility requires a semidefinite or indefinite Q, thereby prohibiting the realization of virtual self-stress. Note that, in the same way as kinematic mobility is merely the possibility of motion, the feature of prestressability is only a prerequisite for the physical realization of stable prestress.

Mutual Exclusion Condition. In any structural system, kinematic mobility and prestressability are mutually exclusive.

In other words, the presence of one of the two features rules out the other by rendering it unrealizable: either mobility or self-stress remains only virtual. However, the opposite statement does not hold: the absence of one of the two features does not cause the other to be present, so that both of them can be absent at the same time. This is obvious in the case of a

Downloaded 03 May 2010 to 171.66.16.248. Redistribution subject to ASME license or copyright; see http://www.asme.org/terms/Terms_Use.cfm

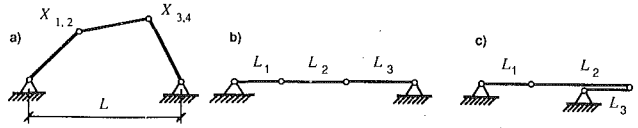

Fig. 2 Ordinary and singular geometric configurations of a three-bar system (*a*) ordinary configuration; (*b*) singular—quasi-variant (type III); (*c*) singular—variant (type IV)

geometrically invariant statically determinate system, which has neither of the features, but not so obvious for systems with infinitesimal mobility. Furthermore, the apparent symmetry of the exclusion condition with respect to mobility and prestressability should not be construed as an indication of equal standing. Actually, the relationship is that of a cause and effect, with the kinematical aspect being primal. Note that the exclusion condition is global and, accordingly, is formulated for a system, and not a configuration.

Statical Criterion of Immobility. A prestressable system is kinematically immobile.

The significance of this corollary criterion is twofold: First, it relates the issue of infinitesimal mobility to the vast knowledge base in stability; and second, stability of a self-stress is in many cases evident, and does not require any analysis. Such is, for example, the case of a comprehensive tensile self-stress, since in this case even the complete quadratic form, as a combination of the squares of coordinate differences with positive Λ_i, is positive. Quite often prestressability is assured by actually prestressing the system.

The kinematical counterpart of the statical criterion is:

Kinematic Criterion of Impossibility of Prestress. Kinematically mobile (variant) system cannot be prestressed.

This criterion seems intuitively obvious; clearly, self-stress in a singular configuration of a variant system is always only virtual, i.e., physically unrealizable (barring friction or other extraneous factors). In any ordinary configuration, a variant system does not possess even a virtual self-stress.

Matrix Method for Detecting an Infinitesimal Mechanism

For a pin-bar assembly, constructing the reduced quadratic form is especially easy since, in this case, the constraint functions are quadratic polynomials. As a result, the quadratic form in all variables is obtained instantly as the sum of constraint functions weighted by the respective constraint reactions, Λ_i. The only remaining step is the elimination of r dependent displacements with the aid of the linearized constraint equations.

Example. The system in Fig. 2 is a conventional probestone when dealing with infinitesimal mechanisms. The constraint equations are

$$X_1^2+X_2^2=L_1^2,\ (X_3-X_1)^2+(X_4-X_2)^2=L_2^2,\ (L-X_3)^2+X_4^2=L_3^2. \quad (35)$$

Upon omitting the factor 2, the constraint Jacobian matrices for an ordinary configuration and the two singular ones are, respectively,

$$\begin{bmatrix} X_1 & X_2 & 0 & 0 \\ X_1-X_3 & X_2-X_4 & X_3-X_1 & X_4-X_2 \\ 0 & 0 & X_3-L & X_4 \end{bmatrix},\ \begin{bmatrix} L_1 & 0 & 0 & 0 \\ -L_2 & 0 & L_2 & 0 \\ 0 & 0 & \mp L_3 & 0 \end{bmatrix} \quad (36)$$

where the double sign corresponds to the two respective singular configurations. Thus, the elements of the Jacobian matrices for a pin-bar assembly are nothing but the coordinate differences of the bar ends. For an ordinary configuaration of the system (Fig. 2(*a*)) the rank is full: $r=r_{\max}=C=3<N=4$. Hence,

$$V=K=1$$

and the linearized constraint equations given by the first matrix (36) allow a nonzero solution; the system is kinematically mobile (variant, type IV).

For the two singular configurations shown, the rank drops to 2 so that $V=N-r=2$. The equilibrium equations for these configurations, given by the second matrix (36), admit the respective nontrivial solutions

$$\Lambda_1=\Lambda/L_1,\ \Lambda_2=\Lambda/L_2,\ \Lambda_3=\pm\Lambda/L_3 \quad (37)$$

differing only in the sign of the third reaction. The complete quadratic form is the sum of the squares of the variables in the constraint functions (35) weighted by the corresonding reactions (37), with displacements x_n replacing the respective coordinates, X_n. The linearized equations given by the second of the matrices (36) serve for the evaluation of dependent displacements: $x_1=x_3=0$. Their elimination from the complete quadratic form yields the reduced one

$$Q=\Lambda[x_2^2/L_1+(x_4-x_2)^2/L_2\pm x_4^2/L_3]. \quad (38)$$

For the configuration in Fig. 2(*b*) the form is definite; hence, $x_2=x_4=0$ and

$$V=2,\ K=0.$$

The system lacks kinematic mobility and is of type III. For the other singular configuration (Fig. 2(*c*)) the form is definite only at $L_3>L_1+L_2$; otherwise it is indefinite, so that

$$V=2,\ K=1$$

and the system is a finite mechanism in a "dead center" position.

However simple, the construction of reduced quadratic form Q and its conversion to matrix format in order to test for sign definiteness involve some "manual" operations. An alternative method, more suited for a computer-aided analysis, is based on a theorem due to Mann (1943). Adapted to the problem in consideration, the theorem states that the complete quadratic form in equation (32) is positive for all nonzero x_n satisfying the linearized constraint equations (4) if and only if

$$(-1)^r det \begin{bmatrix} K_{ss} & J_{sp} \\ J_{ps} & 0 \end{bmatrix} > 0 \quad (39)$$

for each of $s=r+1, \ldots, N$.

This matrix is a familiar one: it is the stiffness matrix (25) obtained by incrementing the equilibrium equations. Accordingly, condition (39) entails positiveness of the reduced stiffness matrix (29) and the reduced quadratic form Q. This implies stability of the reference equilibrium state of the system, which takes place under certain, but not all, equilibrium loads and self-stress patterns. In applications, the matrix test can be implemented with the evaluation of the matrix pivots instead of determinants.

Test (39) is especially attractive for a computer-aided analysis of pin-bar assemblies because of the utter simplicity and immediate availability of the necessary matrices. Indeed, the constraint Jacobian matrices have been shown to involve only the coordinate differences of the bar ends. Quite serendipitously, the Hessian matrices are even more readily available. They are determined solely by the system topology (connectivity), described by the system incidence matrix as seen from the Hessian matrices of constraint functions (35)

Downloaded 03 May 2010 to 171.66.16.248. Redistribution subject to ASME license or copyright; see http://www.asme.org/terms/Terms_Use.cfm

$$F^1_{mn} \quad F^2_{mn} \quad F^3_{mn}$$

$$\begin{bmatrix} 1&0&0&0 \\ 0&1&0&0 \\ 0&0&0&0 \\ 0&0&0&0 \end{bmatrix} \quad \begin{bmatrix} 1&0&-1&0 \\ 0&1&0&-1 \\ -1&0&1&0 \\ 0&-1&0&1 \end{bmatrix} \quad \begin{bmatrix} 0&0&0&0 \\ 0&0&0&0 \\ 0&0&1&0 \\ 0&0&0&1 \end{bmatrix}. \tag{40}$$

Thus, for the analysis of pin-bar systems there is even no need for the constraint equations per se; the required input involves only the set of nodal coordinates and the system connectivity, which is the input of a routine truss analysis. The data contained in equations (36), (37), and (40) suffice for forming the test matrix (39), which is symmetric, with the maximum size 6×6 corresponding to $s=N=4$:

$$\begin{bmatrix} L_1^{-1}+L_2^{-1} & 0 & -L_2^{-1} & 0 & L_1 & 0 \\ & L_1^{-1}+L_2^{-1} & 0 & -L_2^{-1} & 0 & 0 \\ & & L_2^{-1}\pm L_3^{-1} & 0 & 0 & \mp L_3 \\ \vdots & & & L_2^{-1}\pm L_3^{-1} & 0 & 0 \\ & & & & 0 & 0 \\ \cdots & & \cdots & & & 0 \end{bmatrix}.$$

The first four columns represent the sum of the Hessian matrices (40) weighted by the first set of Λ_i from equation (37) with the common scale factor Λ taken as 1. The last two columns are the transposed first and third rows of the Jacobian matrix. Any two of the three rows could be selected, according to the rank $r=2$. As before, the double sign corresponds to the two respective singular configurations.

Two determinants are to be evaluated, D_3 and D_4, with the first one, corresponding to $s=r+1=3$, obtained by deleting from the above matrix the 4th row and 4th column:

$$D_3=(1+L_1/L_2)(\pm L_3)^2,\ D_4=(L_3\pm L_1\pm L_2)L_3/L_2.$$

Since $D_3>0$ for both of the singular configurations, the outcome of the test depends on D_4. For the system in Fig. 2(b), $D_4>0$ and it passes the matrix test as type III. The second degenerate configuration (Fig. 2(c)) is of type III only at $L_3>L_1+L_2$, otherwise it is a system of type IV. For comparison, testing the form (38) for definiteness requires similar means (forming the associated matrix and evaluating its pivots) but somewhat less computational effort due to the smaller matrix size, $V\times V$, as compared to $(N+r)\times(N+r)$.

The terse formalism of the matrix test (39) is quite remarkable. The test first extracts from the constraint functions the necessary information on the system topology and geometry, respectively, in the form of the Hessian and Jacobian matrices, and then arranges it in a matrix format entirely and uniquely suitable for computer treatment (evaluation of the matrix pivots). The described matrix test answers the refined version of Tarnai's (1980) question formulated by Koiter (1984): How can matrix methods be used to decide whether kinematic indeterminancy takes the form of an infinitesimal mechanism of the first or of the higher order? As to the original question, concerning a general infinitesimal mechanism, the conjecture (Kuznetsov, 1989a) on the inadequacy of purely matrix means still stands. The reason is that, in mathematical terms, the problem involves formulating and implementing conditions for a known real solution $X_n=X_n{}^o$ to constraint equations (1) to be isolated; this problem appears to be beyond conventional matrix means.

Summary and Conclusions

(1) The conceptual difference between virtual and kinematic displacements is the key to understanding the behavior of singular underconstrained systems, in particular, systems with infinitesimal mobility.

(2) Linearized or iterative analysis of systems other than invariant is based on resolving an applied load into mutually orthogonal (equilibrium and perturbation) components and the use of the resulting statical-kinematic stiffness matrix, which uncouples the evaluation of the system forces and displacements.

(3) For a pin-bar assembly, the constraint function Jacobian and Hessian matrices, needed for the load resolution and for the matrix test of immobility, are immediately obtained from the set of nodal coordinates and the bar incidence matrix.

(4) The relation between stable self-stress and mobility, culminating in the mutual exclusion condition, is a second-order manifestation of statical-kinematic duality.

(5) The presented matrix method of detecting a system with infinitesimal mobility is a computationally efficient alternative to the currently used procedure of constructing and evaluating the reduced quadratic form.

(6) Prestressable underconstrained systems open an alternative way of obtaining structural stiffness: It is acquired by means of prestress, at the expense of the material strength, rather than mass.

Acknowledgment

The author is grateful to his colleaque, Prof. W. B. Hall, and to Dr. S. Dinkevich from EBASCO, Inc. for discussion and many useful suggestions on this paper.

References

Koiter, W. T., 1984, "On Tarnai's Conjecture with Reference to both Statically and Kinematically Indeterminate Structures," Lab. Report No. 788, Delft University.

Kotter, E., 1912, "Uber die Moglichkeit, n Punkte in der Ebene oder im Raume . . . . ," *Festschrift Heinrich Muller-Breslau*, Kroner, Leipzig, pp. 61–80.

Kuznetsov, E. N., 1973, "Problems in the Statics of Variant Systems," *Mechanics of Solids*, (translation from Russian), Vol. 8, Allerton Press, pp. 90–94.

Kuznetsov, E. N., 1979, "Statical-Kinematic Analysis and Limit Equilibrium of Systems with Unilateral Constraints," *Int. J. Solids Structures*, Vol. 15, pp. 761–767.

Kuznetsov, E. N., 1989a, "On Immobile Kinematic Chains and a Fallacious Matrix Analysis," ASME Journal of Applied Mechanics, Vol. 56, pp. 222–224.

Kuznetsov, E. N., 1989b, "The Membrane Shell as an Underconstrained Structural System," ASME Journal of Applied Mechanics, Vol. 56, pp. 387–390.

Levi-Civita, T., and Amaldi, U., 1930, *Lezioni di Meccanica Razionale*, 2nd ed., (in Italian), Vol. 1, Part 2, Bologna.

Mann, H. B., 1943, "Quadratic Forms with Linear Constraints," *Amer. Math. Monthly*, Vol. 50, pp. 430–433.

Maxwell, J. C., 1890, "On the Calculation of the Equilibrium and Stiffness of Frames," Scientific Papers of J. C. Maxwell. University Press, Cambridge.

Mobius, A. F., 1837, *Lehrbuch der Static*, Vol. 2, Leipzig.

Mohr, O., 1885, "Beitrag zur Theorie des Fachwerkes," *Der Civilingenieur*, Vol. 31, pp. 289–310.

Strang, G., 1988, *Linear algebra and its applications*, 3rd ed., San Diego.

Tarnai, T., 1980, "Problems Concerning Spherical Polyhedra and Structural Rigidity," *Struct. Topology*, Vol. 4, pp. 61–66.

Tarnai, T., 1988, "Bifurcations and Singularities of Compatibility," (abstract), 17th IUTAM Congress, Grenoble, France.

Downloaded 03 May 2010 to 171.66.16.248. Redistribution subject to ASME license or copyright; see http://www.asme.org/terms/Terms_Use.cfm

Systems With Infinitesimal Mobility: Part II—Compound and Higher-Order Infinitesimal Mechanisms

E. N. Kuznetsov
Department of General Engineering,
University of Illinois,
Urbana, IL 61801-2996
Mem. ASME

Building on the analytical results presented in Part I, the issue of multiple singularity is explored. The attained understanding is applied to the analysis and synthesis of compound infinitesimal mechanisms illustrated in several examples. Employing power expansion techniques, higher-order mechanisms are investigated, revealing, in particular, the existence of even-order mechanisms and their peculiar nature. The equivalence condition is established between prestressability and kinematic immobility of underconstrained structural systems with one singularity. A previously unidentified class of systems—unprestressable infinitesimal mechanisms—is revealed. It complements the conventional source of infinitesimally mobile systems associated with a strict constrained extremum and the resulting feature of prestressability.

Multiple Singularity: Compound Systems

The obtained results make further progress possible by lifting, one at a time, the simplifying assumptions of the foregoing analysis. The first of them has restricted the degree of singularity to $D=1$. A structural system may be comprised of several singular subsystems, each involving a set of dependent constraints. Then each subsystem has a virtual self-stress, and together they give rise to D reduced quadratic forms Q_d. Among these, definite and indefinite ones have quite different implications for kinematic mobility. The role of a definite form is straightforward: It immobilizes the subsystem by preventing all of its virtual displacements from becoming kinematic. The effect of an indefinite form is more subtle. It also constrains the kinematic mobility of the subsystem, but only to the extent of mutually relating the virtual displacements figuring in the form. The result is a reduction by 1 in the number of independent displacements, and the corresponding increase in the number of dependent ones.

When considering a system with multiple singularity, two basic and very different cases are encountered, which are, respectively, overlapping and nonoverlapping self-stress patterns. The first one is exemplified by the systems in Fig. 1, where all of the constraints are mutually dependent. In the absence of independent constraints, the situation is similar to that of a simple system ($D=1$) considered earlier. The only difference is that a definite quadratic form Q in all independent displacements is sought as a linear combination of the forms Q_d engendered by the D self-stress patterns. An iterative algorithm for identifying such a linear combination has been recently described by Calladine and Pellegrino (1990).

However, the existence of a definite Q constitutes a necessary and sufficient criterion of infinitesimal mobility only in the absence of independent constraints. In general, this criterion is only sufficient and excessively strong, especially for the second, and more interesting, of the mentioned cases. It represents a compound system, i.e., an assembly of $D>1$ singular subsystems with nonoverlapping self-stress patterns. As before, the question is whether there exists a set of virtual displacements which turns the forms Q_d simultaneously into zero. When there is no such set, the conclusion is unequivocal: The system is kinematically immobile, with first-order infinitesimal mobility. However, the opposite outcome is ambiguous and requires further analysis; it only means that the system constraints are compatible at least to the second order.

Example. The system in Fig. 2(*a*) involves two singular subsystems each comprised of three horizontal bars. Their lengths, shown to scale, are either 1, or 2, except for the bottom

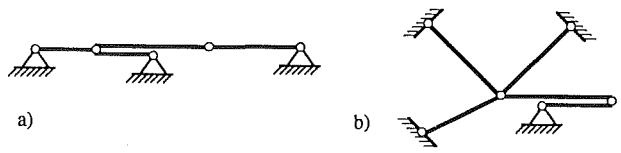

Fig. 1 Examples of multiple singularity with overlapping self-stress

Contributed by the Applied Mechanics Division of THE AMERICAN SOCIETY OF MECHANICAL ENGINEERS for publication in the JOURNAL OF APPLIED MECHANICS.

Discussion on this paper should be addressed to the Technical Editor, Leon M. Keer, The Technological Institute, Northwestern University, Evanston, IL 60208, and will be accepted until two months after final publication of the paper itself in the JOURNAL OF APPLIED MECHANICS. Manuscript received by the ASME Applied Mechanics Division, Sept. 28, 1989; final revision, Jan. 31, 1990.

Copyright © 1991 by ASME
Downloaded 03 May 2010 to 171.66.16.248. Redistribution subject to ASME license or copyright; see http://www.asme.org/terms/Terms_Use.cfm

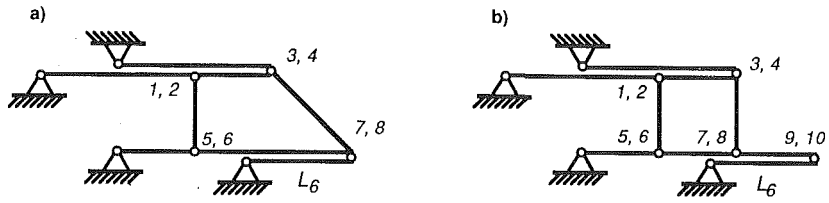

Fig. 2 Compound first-order infinitesimal mechanisms (*a*) quasi-invariant system (type II); (*b*) quasi-variant system (type III)

bar 6 of the length L_6. The constraint equations of the system (with the coordinate origin at the upper left support) are

$$X_1^2+X_2^2=2^2;$$
$$(X_3-1)^2+X_4^2=2^2;\quad (X_5-1)^2+(X_6-1)^2=1^2$$
$$(X_3-X_1)^2+(X_4-X_2)^2=1^2$$
$$(X_7-X_5)^2+(X_8-X_6)^2=2^2;$$
$$(X_7-4+L_6)^2+(X_8-1)^2=L_6^2$$
$$(X_5-X_1)^2+(X_6-X_2)^2=1^2;\quad (X_7-X_3)^2+(X_8-X_4)^2=2. \qquad (a)$$

In the given configuration,

$$X_1=X_5=2,\ X_2=X_4=0,\ X_3=3,\ X_6=X_8=1;\ X_7=4. \qquad (b)$$

Deriving the linearized constraint equations for this configuration, and solving them with virtual displacements x_2 and x_4 as independent, yields

$$x_6=x_2,\ x_8=x_4,\ x_1=x_3=x_5=x_7=0. \qquad (c)$$

The complete quadratic forms for the two subsystems are obtained from the respective two triplets of constraint equations (*a*) by multiplying them by $\Lambda_i=\Lambda/L_i$ as described earlier. Eliminating the dependent displacements leads to the reduced forms which differ from equation (I.38) only in the bar lengths (here the unnecessary factor Λ is omitted):

$$Q_1=x_2^2/2+(x_2-x_4)^2-x_4^2/2 \qquad (1)$$

$$Q_2=x_2^2+(x_2-x_4)^2/2-x_4^2/L_6. \qquad (2)$$

Each form is indefinite and constrains the system in its own way by imposing a certain relation between the displacements involved. Thus, taken separately, each subsystem possesses one actual and two virtual degrees-of-freedom. The utter simplicity of the two forms enables the question of their compatibility to be resolved explicitly. Setting Q_1 to zero gives

$$x_4=(2\pm 1)x_2. \qquad (3)$$

When the two solutions are introduced, one at a time, into the form Q_2, it is found that the latter becomes indefinite, respectively, at $L_6=3$ and $L_6=1$. At any different bar length the form is definite, so that $x_2=0$ leading to $x_4=0$. Accordingly,

$$V=D=2,\ K=0$$

and, by virtue of equation (I.12), the system is quasi-invariant. This conclusion is verified by that the number of constraints, $C=N=8$, is sufficient for invariance and the constraints are dependent only in this particular, degenerate configuration. Upon exiting from it, the Jacobian matrix rank restores to $r=8$.

It appears from the example that this kind of situation should almost always result in infinitesimal mobility, while constraint compatibility and kinematic mobility are exceptional. A geometric interpretation illustrates and confirms this observation. Indefinite form Q_1, expressing the work of initial forces over the corresponding constraint variations, represents in coordinates (x_2, x_4, Q) a hyperbolic paraboloid, with the plane $Q=0$ intersecting it along two linear generators. The latter give the two directions (displacement ratios from (3)) of zero work, hence, zero constraint variations. The same is true for the second form, Q_2. Constraint compatibility takes place only if the two hyperboloids share a generator. Apparently, *incompatibility* is typical and, in fact, so much so, that it can be expected even in cases with more independent virtual displacements, resulting in compound quasi-variant systems.

To explore this eventually, consider a system in Fig. 2(*b*) which cannot be type II since it is underconstrained: $C=9>N=10$ and $V=3>D=2$. While Q_1 given by equation (1) stays unchanged, the modified form Q_2 contains an additional virtual displacement. The linearized constraint equations yield

$$x_6=x_2,\ x_8=x_4,\ x_1=x_3=x_5=x_7=x_9=0 \qquad (d)$$

so that

$$Q_2=x_2^2+(x_2-x_4)^2+(x_4-x_{10})^2-x_{10}^2/L_6. \qquad (4)$$

Replacing x_4 with the solutions (3) leads, respectively, to the forms

$$Q_2=14x_2^2-6x_2x_{10}+(1-1/L_6)x_{10}^2 \qquad (5)$$

$$Q_2=2x_2^2-2x_2x_{10}+(1-1/L_6)x_{10}^2. \qquad (6)$$

The first of them is found to be definite at $L_6>14/5$, the second—at $L_6>3/2$. When both of the inequalities are satisfied, Q_1 and Q_2 are incompatible, i.e., no set of x_s turns them into zero simultaneously. As a result, displacements $x_2=x_6=0$, and the system is quasi-variant. What makes this result remarkable is the fact that at $L_6>3$, which is only slightly greater than 14/5, the outcome would be quite trivial. Indeed, at $L_6>3$, the original Q_2 in equation (4) is definite and the second subsystem alone immobilizes the entire system; in this case Q_1 becomes irrelevant since it does not contain any of the independent displacements absent in Q_2. Interestingly, neither of the systems in Fig. 2 is prestressable, since no positive combinations of forms (1) and (2) or, respectively, (1) and (4), exist. Yet, both of the systems are kinematically immobile and represent a class of systems previously not encountered—unprestressable infinitesimal mechanisms.

In general, the issue of infinitesimal mobility in systems with multiple singularity cannot be resolved without an analysis of either D simultaneous reduced quadratic forms or D complete forms subject to the associate linearized constraint equations. First to notice this was, apparently, Kotter (1912), whose conditions for kinematic immobility was definiteness of one of the reduced forms, say Q_1 subject to $Q_2=Q_3=\ \ldots\ =Q_D=0$.

Geometrically, each of the equations $Q_d=0$ with an indefinite Q_d describes in the coordinate space a convex cone. When all of the cones have just one common point, the apex $x_s=0$, the compound system is kinematically immobile. It is unlikely that a simple matrix approach similar to the test (I.39) can be formulated for determining whether or not the cones intersect, with the exception of one small but notable particular case. When, as in the foregoing example, each of the quadratic forms (except, maybe Q_1) is representable as a product of two linear forms, these can be included, one at a time, into the test matrix instead of the border Jacobian matrices. (The latter are unnecessary since they have been taken into account when eval-

Downloaded 03 May 2010 to 171.66.16.248. Redistribution subject to ASME license or copyright; see http://www.asme.org/terms/Terms_Use.cfm

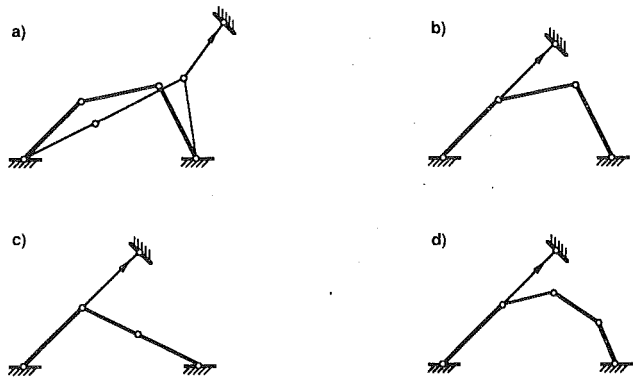

Fig. 3 Formation of infinitesimal mechanism (*a*) comprehensive prestress; (*b*) and (*c*) partial prestress resulting in kinematic immobility; (*d*) immobilized subsystem

uating the reduced forms Q_d.) Then, according to Mann's theorem, Q_1 can be checked for definiteness subject to all of the appropriate combinations of linear forms representing the factored quadratic forms.

An alternative procedure emulates one of the classical methods of structural mechanics. Following it, a system is broken into two or more component subsystems. These are subjected to kinematic analysis evaluating the nodal path prescribed by each subsystem to the node they share. By comparing the paths, the possibility (or otherwise) of compatible displacements of the subsystems is established, leading to a conclusion on the kinematic properties of the assembly as a whole. This analysis requires the r dependent displacements to be presented as power expansions

$$x_p = a_{ps}x_s + (1/2!)a_{pst}x_s x_t + \ldots; \qquad (7)$$

$$p = 1, \ldots r; \quad s,t, \ldots = r+1, \ldots N$$

Example (Continued). In the system of Fig. 2(*a*), bar 6 is disconnected from the assembly and considered as the second subsystem. The nodal path prescribed to the common node by each subsystem is sought in the form (7)

$$x_7 = a_{78}x_8 + (1/2!)a_{788}x_8^2 + \ldots . \qquad (8)$$

In this notation, solution (*c*) of the linearized constraint equations can be rewritten

$$a_{68} = a_{28},\ a_{48} = 1,\ a_{18} = a_{38} = a_{58} = a_{78}^{(1)} = 0. \qquad (e)$$

Evaluating a_{28} requires the second derivatives of the first three constraint equations (*a*)

$$a_{18}^2 + X_1 a_{188} + a_{28}^2 + X_2 a_{288} = 0, \quad a_{38}^2 + X_3 a_{388} + a_{48}^2 + X_4 a_{488} = 0,$$

$$(a_{38} - a_{18})^2 + (X_3 - X_1)(a_{388} - a_{188})$$

$$+ (a_{48} - a_{28})^2 + (X_4 - X_2)(a_{488} - a_{288}) = 0.$$

Taking into account (*b*) and (*e*) these equations yield

$$a_{28} = 1/3(1);\ a_{188} = -1/18(-1/2);\ a_{388} = -1/2.$$

Here, the parenthesized quantities represent the second of the double-valued solutions, reflecting the existence of two different displacement patterns for the first subsystem. Carrying out the second differentiation of the remaining five constraint equations leads (after a few simple calculations) to the coefficients

$$a_{788}^{(1)} = -1/3(1-1); \qquad a_{788}^{(2)} = -1/L_6$$

describing the respective paths imposed on the common node by the subsystems. As expected, the two are found generally compatible to the first order, but at $L_6 = 3$ and $L_6 = 1$ they are compatible to at least the second order.

The presented procedure might seem somewhat cumbersome, but it has one important advantage over the analysis of quadratic forms: it is applicable to systems with higher-order infinitesimal mobility.

Synthesis of First Order Mechanisms

The understanding attained thus far provides some directions for the synthesis of systems with infinitesimal mobility. One method is based on the statical criterion of immobility. Consider an underconstrained system IV, (for example, the familiar three-bar chain) and apply an external force at one of its nodes (Fig. 3). Generally, the system geometry changes before it attains an equilibrium configuration where it balances the force. Assuming the equilibrium stable, introduce an additional link collinear with the force and connecting its point of application to the external frame or foundation. Then, either the entire system (Fig. 3(*a*)) or the prestressed subset of structural members (Figs. 2(*b*), (*c*), and (*d*)), form an infinitesimal mechanism. Indeed, the constraint reactions produced originally by the external force, together with the internal force in the introduced link, constitute a stable self-stress in the resulting system, thus satisfying the statical criterion of immobility. By simultaneously applying several forces or traction loads to a geometrically variant system, a wide variety of configurations can be obtained and then immobilized by introducing the necessary constraints. Note that in this procedure, forces are used only as a convenient means for arriving at prestressable, hence kinematically immobile, configurations; such configurations lack mobility regardless of the actual presence of absence of prestress.

In the case the prestress does not comprise the entire system, the latter, nevertheless, will stick lack mobility, if the stress-free subsystem is immobile (Fig. 3(*b*) and (*c*)). This can be verified by a separate analysis of the stress-free subsystem assuming the nodes, that it shares with the immobile subsystem, fixed. The analysis may indicate prestressability of the subsystem in question (Fig. 3(*c*)) but this must be considered only in the context of higher-order infinitesimal mobility. If the stress-free subsystem is mobile, the system as a whole is geometrically variant (Fig. 3 (*d*)) although it contains an immobile subsystem. This outcome illustrates the relevance of the assumption on a comprehensive self-stress used in the analysis of simple systems in Part I.

A similar method of synthesis involves introducing internal, rather than external constraints. Inserting a variable length bar between two unconnected points of a variant system, and expanding or contracting the bar to the extent possible, will produce a prestressable singular configuration. Moreover, this can be achieved by simply varying the length of one of the existing bars until it attains a maximum or a minimum.

The significance of the statical criterion of immobility goes beyond these elementary examples. Clearly, the best test of prestressability is prestressing: any structural system which is actually in a state of self-stress lacks kinematic mobility. Buckminster Fuller recognized this idea and perpetuated it is his term "*tensegrity*" structure, emphasizing *ten*sion as a means for attaining strutural int*egrity*. His concept of tensegrity structure can be defined as an infinitesimally mobile system with a closed-loop prestress, i.e., with force-free supports (free-standing, in Fuller's terms). The surprisingly diverse class of tensegrity structures includes, among others, various cable-bar systems, wire nets and membranes, exemplified, respectively, by a bicycle wheel, a tennis racket, and a musical drum.

A general analytical approach to synthesis of infinitesimally mobile systems involves generating a singular configuration (by varying the system constraints) and verifying its prestressability. Specifically, retaining one or several geometric parameters of a system unspecified allows them to be disposed of such as to satisfy an analytical criterion of immobility. To illustrate this approach, consider again a symmetric three-bar system. This time the objective is to immobilized it by con-

Downloaded 03 May 2010 to 171.66.16.248. Redistribution subject to ASME license or copyright; see http://www.asme.org/terms/Terms_Use.cfm

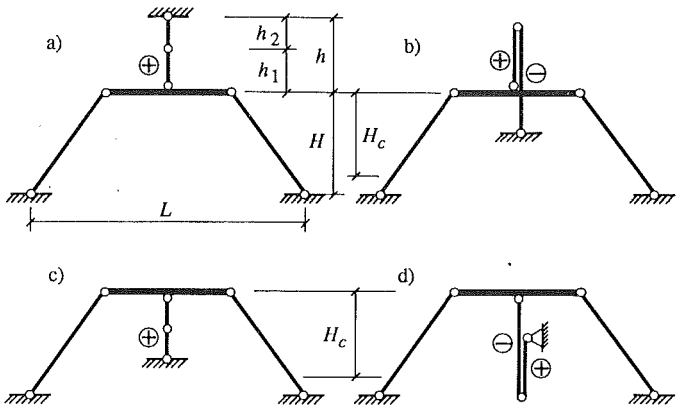

Fig. 4 Quasi-variant mechanisms (type III) corresponding to four combinations of parameters h_1 and h_2 in relation to H_c

necting the midpoint of the second bar to the foundation (frame) with a two-bar chain (Fig. 4(*a*)). This will be done by analyzing the motions of the two subsystems separately and then linking them together. First, the midpoint of the second bar is formally identified as a node is introduced by two linear equations

$$X_1+X_3-2X_5=0, \quad X_2+X_4-2X_6=0 \tag{9}$$

supplementing the three constraint equations (I.35). With displacement x_5 as independent, the nodal path is evaluated as a power expansion (7)

$$x_6=a_{65}x_5+(1/2)a_{655}x_5^2+\ldots \tag{10}$$

Equations for the sought coefficients are obtained by successive differentiation of the five constraint equations.

First derivatives

$$X_1a_{15}+X_2a_{25}=0, \quad -(L-X_3)+X_4a_{45}=0,$$

$$(X_3-X_1)(a_{35}-a_{15})+(X_4-X_s)(a_{45}-a_{25})=0,$$

$$a_{15}+a_{35}=2, \; a_{25}+a_{45}=2a_{65}.$$

Second derivatives

$$a_{15}^2+X_1a_{155}+a_{25}^2+X_2a_{255}=0, \quad a_{155}+a_{355}=0,$$

$$(a_{35}-a_{15})^2+(X_3-X_1)(a_{355}-a_{155})$$
$$+(a_{45}-a_{25})^2+(X_4-X_2)(a_{455}-a_{455})=0,$$

$$a235-(L-X_3)a_{355}+a_{452}+X_4a_{455}=0, \quad a_{255}+a_{455}=2a_{655}$$

The nodal coordinates in the reference configuration are $X_1=L/4$, $X_2=X_4=H$, and $X_3=3L/4$. Denoting $4H/L=c$ the coefficients figuring in equation (10) are found

$$a_{65}=0, \; a_{655}=-(1+2c^2)/H=-1/H_c \tag{a}$$

with a newly introduced parameter

$$H_c=H/(1+2c^2). \tag{b}$$

Next, the two connecting bars are introduced with their respective constraint equations

$$(X_7-X_5)^2+(X_8-X_6)^2=h_1^2,$$

$$(X_7-L/2)^2+(X_8-H+h)^2=h_2^2 \tag{11}$$

where $h=h_1+h_2$. For this two-bar chain, displacements x_5 and x_7 are chosen as independent. Carrying out power expansion yields

$$a_{65}=a_{67}=0, \; a_{655}=-1/h_1,$$

$$a_{657}=a_{675}=1/h_1, \; a_{677}=-h/h_1/h_2. \tag{c}$$

According to (*a*) and (*c*), the two subsystems independently control one and the same displacement, x_6, by prescribing two different nodal paths. The result is a discontinuity which can be expressed as a function of the independent virtual displacements

$$f=x_6^{(1)}-x_6^{(2)}=\Delta x_6=[(1-h_1/H_c)x_5^2-2x_5x_7$$
$$+(h/h_2)x_7^2]/2h_1. \tag{12}$$

The system lacks kinematic mobility if this form is definite, which is the case when

$$h/h_2>0, \; (h/h_2)(1-h_1/H_c)-1>0. \tag{13}$$

Four combinations of parameters satisfy simultaneously both of these inequalities:

(1) $h_1<0$, $h_2<0$ (Fig. 4(*a*))
(2) $h_1<0$, $h_2>0$, $h_2>H_c-h_1$ (Fig. 4(*b*));
(3) $h_1>0$, $h_2>0$, $h_1+h_2<H_c$ (Fig. 4(*c*));
(4) $h_1>0$, $h_2<0$, $h_1>H_c-h_2$ (Fig. 4(*d*)).

The sign of initial forces resulting in stable self-stress patterns is shown in the figures, with plus denoting tension. Note that the retention of only two arbitrary parameters, h_1 and h_2, produced a combinatorial wealth of infinitesimally mobile systems. Also note the critical role of the parameter H_c which is to be studied shortly.

Even more variety is attainable in the synthesis of compound infinitesimal mechanisms. Here it is necessary to compile an assortment of suitable singular components and to assemble them in a meaningful way. The simplest recipe is to choose a system III as a basis and build upon it a desired superstructure. More challenging is the case when none of the component subsystems is of type III. For example, a closer look at the system in Fig. 2(*a*) reveals that each of the two singular subsystems is a simple finite mechanism in a degenerate (dead center) configuration. Each has two vertical virtual displacements, and these are conforming, so that both subsystems might exercise them in concert. However, the respective displacement ratios are, generally, different—hence, unconforming—either accidentally or intentionally. This prevents the displacements from becoming kinematic, and the result is a compound infinitesimal mechanism. Thus, the geometry of a compound system can be manipulated so as to either achieve, or, on the contrary, to prevent the conformity of the virtual displacements.

Higher-Order Mobility

The formal definition of an infinitesimally mobile system introduced in Part I ($V>K=0$) implies that the system possesses mobility but does not provide any information on its order. Moreover, the very concept of the order of infinitesimal mobility has provided elusive and defied several known attempts of a concise definition. A clue for both defining and

Downloaded 03 May 2010 to 171.66.16.248. Redistribution subject to ASME license or copyright; see http://www.asme.org/terms/Terms_Use.cfm

evaluating the order of infinitesimal mobility is found in relation (12). This expression can be viewed as either a constraint discontinuity of a constraint variation necessary to maintain compatibility. It is immediately recognizable as (modulo a constant) the reduced quadratic form of the system, and this, of course, is not an accident.

If the two subsystems are put together but h_1 is not linked (or is cut), the independent displacements produce a gap of the size f in the direction of coordinate x_6. A force Λ, needed to close the gap, induces constraint reactions throughout the system (their pattern corresponds to the system's self-stress), and performs virtual work $Q=\Lambda f$. This work does not depend on the particular distribution of constraint variations: Any bar or a group of bars can move, stretch or contract in order to accommodate to discontinuity. Moreover, since self-stress is determined only as a pattern, the magnitude of the initial forces is just a scale factor which is irrelevant in kinematics and, for this reason, absent in equation (12). Obviously, if displacements are possible without producing any discontinuity, constraints are compatible—no constraint variation ensues and no work is expended. The resolution of this familiar dilemma depends, predictably, on the properties of the quadratic form in (12).

Thus, the entire kinematic analysis (immobility versus infinitesimal or finite mobility, analytical criteria of the four types of systems, analysis, and synthesis of infinitesimally mobile systems, and so on) stems from a single source—the condition of constraint compatibility or incompatability under virtual displacements. In this light, it is only natural to turn to the same source for information on the order of infinitesimal mobility.

In what follows, an expression of type (12) for constraint discontinuity in terms of virtual displacements is considered as a sum of ascending-order forms (linear, quadratic, and so on). Invoked one at a time, they yield information on the kinematic properties of the system, revealing in the process the order of their origin. Infinitesimal displacements turning into zero the linear form are conventional virtual displacements. Those of them which also turn into zero the quadratic form will be called second-order virtual displacements. Proceeding in the same way with higher orders leads to kth order virtual displacements of the system in a given configuration. Not all (if any) of the independent displacements of a given order may make it to the next one. The reason is that, in general, each higher-order form imposes additional relations on the displacements, thereby possibly reducing the number of independent ones among them. For example, a three-bar system in a dead-center position has two independent virtual displacements of the first order but only one of the second order. In a rectilinear configuration, this system has 2 first-order virtual displacements but none of the second order, and same is the case with the compound mechanism in Fig. 2(*a*). Using a prime notation for order designation, this observation can be presented as

$$V^{[k]} \geq V^{[k+1]} \geq K \tag{14}$$

where K and $V^{[k]}$ are, respectively, the degrees of kinematic and kth order virtual indeterminacy (the respective numbers of kinematic and kth order virtual degrees of freedom). Thus, the degree of virtual indeterminacy either stays constant or reduces from order to order. Virtual determinacy of any order entails kinematic determinacy (uniqueness of configuration).

Definition. The order of infinitesimal mobility (the order of an infinitesimal mechanism) is the order of constraint compatibility, that is, the highest order of the constraint discontinuity form vanishing with nontrivial virtual displacements. The order is k if

$$V^{[k]} > V^{[k+1]} = 0. \tag{15}$$

This purely kinematic definition is consistent with the nature of the phenomenon and avoids the conventional notion of the more-sophisticated concept of strain which is extraneous to statical-kinematic analysis.

An analytical procedure for constructing and evaluating the constraint discontinuity form is a continuation of the power expansion analysis employed in the preceeding section. It is convenient to explore higher-order mechanisms starting with a closer look at the parameter H_c (equation (*b*)). At

$$h = H_c = H/(1+2c^2) \tag{16}$$

the quadratic form in equation (12) is no longer definite, leaving the question on kinematic mobility of the system unresolved. However, in the very act of turning into zero, the form yields

$$x_7'' = (h_2/h)x_5''. \tag{17}$$

This relation reduces the number of independent displacements to one, say, x_5. Thus, only one of the two first-order independent virtual displacements passed to the second order, and the respective numbers of virtual degrees-of-freedom of the system are

$$V(\equiv V') = 2,\ V'' = 1.$$

Taking into account relations (16) and (17) and proceeding with higher-order terms in the two parallel power expansions shows that cubic terms are absent in both of them. This indicates the possibility of third-order virtual displacements and constraint compatibility to the third order. However, fourth-order displacements of the two subsystems produce a nonzero discontinuity

$$f = \Delta x_6 = [(1+2c^2)^3 - (1+22c^2+20c^4)]x_5^4/8H^2. \tag{18}$$

Although this is a monomial in x_5, the quantity in the brackets can be of either sign or can equal zero, each of the three eventualities resulting in a different outcome. If the form is positive, the fourth-order virtual displacement x_5^{IV} is zero, constraints are compatible only to the third order, and the system lacks kinematic mobility: This is type III of third order (type III^3). A vanishing discontinuity form leads to an inconclusive outcome, implying merely the possibility of higher-order virtual displacements. Curiously, when the discontinuity form is negative, the system is of type IV, in spite of the form being sign definite. The reason is that the condition of being just definite applies only to forms in all independent variables, while form (18) in its evolution "lost" one of its arguments at a lower order. In this case a stricter requirement of positive definiteness applies since the sign of initial forces cannot be reversed without affecting the stability of self-stress.

The geometric meaning of the analysis is straightforward and illuminating. The origin of parameter H_c shows it to be the local radius of curvature of the nodal path imparted by the first subsystem. Condition (17) indicates that the second subsystem, with its two bars aligned, prescribes a circular path of the same radius. Thus, the two paths share not only the tangent, but the radius of curvature as well, an example suggested by Koiter (1984) in his discussion of higher-order mobility. It is quite possible that the paths have an even closer contact and share several next infinitesimal vicinities. This is determined by the properties of the corresponding higher-order discontinuity forms.

The implication for the ongoing analysis is straightforward. When, at $c^2=2$, the bracketed quantity in (18) becomes zero, further power expansions are needed to refine the paths imposed on the node by the two subsystems, and to evaluate the higher-order discontinuity form. Fifth-order terms are missing in these expansions, but the sixth-order discontinuity form is

$$f = \Delta x_6 = (-0.00317 + 0.00625)x_5^6/H_c^5 > 0. \tag{19}$$

Thus, constraints are compatible up to, and including, the

Downloaded 03 May 2010 to 171.66.16.248. Redistribution subject to ASME license or copyright; see http://www.asme.org/terms/Terms_Use.cfm

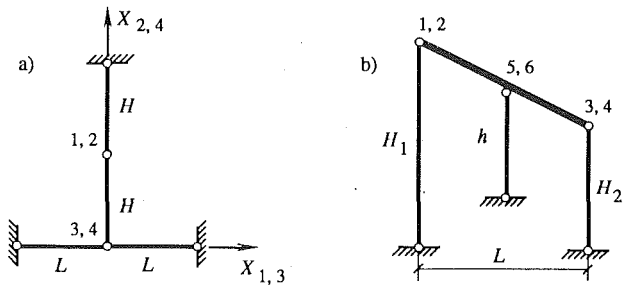

Fig. 5 Complex quasi-invariant mechanisms of third order (*a*) type II^3; (*b*) type II^2

fifth order; hence, the system with $c^2=2$ and $h=H/5$ is of the type III^5.

A somewhat different class of singular systems is represented by a complex infinitesimal mechanism in Fig. 5(*a*). Here the constraint equations are

$$X_1^2+(2H-X_2)^2=H^2,\ (X_1-X_3)^2+(X_2-X_4)^2=H_2^2 \quad (20)$$
$$(X_3+L)^2+X_4^2=L^2,\ (X_3-L)^2+X_4^2=L^2.$$

Let the set of the first three bars be one subsystem and bar 4 the other. With x_1 as an independent displacement in the first subsystem and x_4 in the second, a power expansion analysis yields

$$x_4=x_1^2/H,\ x_3^{(1)}=-x_4^2/2L,\ x_3^{(2)}=x_4^2/2L. \quad (21)$$

The resulting lowest-order nonzero discontinuity form in independent displacements is

$$f=\Delta x_3=x_1^4/LH^2. \quad (22)$$

Since this form is monomial and definite, the system is a third-order infinitesimal mechanism which is quasi-invariant (type II^3) because of $D=V(=1)$. It is not difficult to verify that inserting a pin into one of the vertical bars will result in a definite fourth-order discontinuity form in two independent displacements, and the modified system will be type III^3. On the other hand, inserting a pin into one of the horizontal bars leads to a different outcome. Although the resulting lowest-order discontinuity form in independent virtual displacements is still positive, it is of a mixed order—fourth and second. According to the higher order, the system is again of type III^3.

The obtained results, together with the succession of higher-order mechanisms in the previous example, show that infinitesimal mobility encountered so far is of an odd-numbered order. This prompts a question whether this is a general rule or just the result of symmetry. To elaborate on this, consider again the compound mechanism in Fig. 2(*a*) with $L_6=3$. Power expansion analysis reveals that it is of the third order as well: Disconnecting bar 6 and treating it as the second subsystem produces expansion coefficients coinciding only to the third order, but not to the fourth. The lowest-order nonzero discontinuity form is

$$f=\Delta x_2=(3\ 1/4-3\ 1/8)x_2^4>0. \quad (23)$$

As a result, fourth-order virtual displacement $x_2^{IV}=0$ and the system is type II^3. It seems that the absence of simple infinitesimal mechanisms of an even order is not the consequence of their symmetry.

The reason for skipping the even-order mechanisms transpires in the analysis of the system in Fig. 5(*b*). As before, it is divided into two subsystems, with the middle vertical bar being the second one. The constraint equations for the first subsystem are those of a three-bar system, with a few adjustments in the bar lengths and nodal coordinates. Taking the horizontal displacement x_5 as independent, first-order terms in the power expansions for the two subsystems are found to be identical and, because of $V=D$, the system is type II. The respective second-order coefficients for the two subsystems are

$$a_{655}^{(1)}=-(H_1+H_2)/(2H_1H_2),\ a_{655}^{(2)}=-1/h. \quad (a)$$

They are equal at

$$h=2H_1H_2/(H_1+H_2) \quad (b)$$

in which case the path of the midpoint of the inclined bar in the first subsystem and the path of the same point as the end of the middle vertical bar coincide up to the second order. However, the third-order coefficients are different:

$$a_{6555}^{(1)}=3(H_1-H_2)^3/(4LH_1^2H_2^2),\ a_{6555}^{(2)}=0 \quad (c)$$

so that the lowest-order nonzero discontinuity form is

$$f=\Delta x_5=[(H_1-H_2)^3/(4LH_1^2H_2^2)]x_5^3. \quad (24)$$

The form is cubic, hence indefinite; nevertheless, being a monomial (and barring the case of $H_1=H_2$) the form vanishes only together with x_5. Furthermore, it also satisfies the abovementioned qualifier: It is a form in all independent virtual displacements. The conclusion is that the system in Fig. 5(*b*) is of type II^2. The reason for the absence of even-order mechanisms in each of the previous examples turns out to be the co-symmetry, relative to the common normal, of the paths prescribed by the two subsystems to the node they share. Disrupting this co-symmetry produced the sought second-order mechanism.

Thus, even-order infinitesimal mechanisms, after all, do exist, but not without a surprise: They can only be quasi-invariant, that is, of type II! The reason is that a homogeneous odd-order form in more than one variable can always turn into zero with nonzero values of the variables. For instance, inserting a pin in the middle vertical bar of the system in Fig. 5(*b*) makes it underconstrained but without a chance of becoming a system III. Instead, it becomes a peculiar system IV: Its mobility is finite with $x_5<0$, but only infinitesimal with $x_5>0$. Virtual self-stress of this system, with or without the added pin, is unrealizable; at an attempt of prestressing (say, by a thermal action or a turnbuckle), constraint variation occurs which brings the system out of the degenerate configuration and into the respective generic class (IV with the pin, and I without it). This leads to an interesting conclusion: systems with even-order infinitesimal mobility are unprestressable.

This observation helps to clarify the exclusion condition stated above (finite mobility and prestressability are mutually exclusive) and the resulting formulation of the statical criterion of immobility as only a sufficient one. As has been mentioned, the reason for the criterion not being necessary is that the absence of one of the two mutually exclusive features does not entail the presence of the other. Specifically, even-order infinitesimal mechanisms, as well as some compound first-order mechanisms (Figs. 5(*b*) and 2, respectively), are neither mobile nor prestressable: Their displacements and self-stress are both only virtual.

The exclusion condition holds for any structural system. Indeed, a stable state of self-stress implies that the lowest-order discontinuity form is positive, which entails uniqueness of the configuration. On the other hand, if such a form does not exist or is not positive, stable self-stress is ruled out. These are, respectively, the situations with finite mechanisms, and with even-order and some of the compound infinitesimal mechanisms.

The peculiar character of unprestressable infinitesimal mechanisms, both compound and even-order ones, in a manifestation of a simple analytical fact: Instead of a strict maximum or minimum, one of the constraint functions attains only a stationary value subject to the fixed values of the rest of the functions. Stationarity makes the constraints dependent ($D>0$), which suffices for the system to acquire a virtual self-stress (with no chance of realization) and some mobility. The mobility is virtual when stationarity is local, and actual when it is global. The first case is illustrated in Fig. 6(*a*). The path

Downloaded 03 May 2010 to 171.66.16.248. Redistribution subject to ASME license or copyright; see http://www.asme.org/terms/Terms_Use.cfm

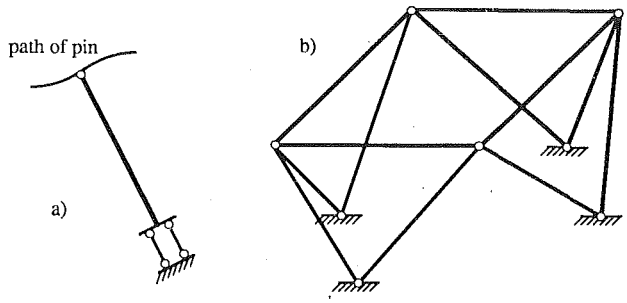

Fig. 6 Systems with constrained stationarity without an extremum

to which the end of the bar is confined by the subsystem not shown has an inflection point (a coupler trajectory can be any algebraic curve (Hilbert and Cohn-Vossen, 1952)). As a result, both the displacement and the self-stress are only virtual, and the system is of type II^{2k}, with k depending on the order of "flatness" of the path at the inflection point. A constraint variation bringing the pin out of the inflection point restores the system to type I.

Thus, constrained local stationarity (without an extremum) of one of the constraint functions is the generic source of unprestressable systems with infinitesimal mobility. It complements the conventional source of infinitesimally mobile systems based on the Mobius-Maxwell-Mohr observation on a strict constrained extremum with the resulting feature of prestressability.

Perhaps, the simplest example of a system with global stationarity is a rigid beam supported at three points by parallel bars of equal length (Kuznetsov, 1988). A distinct feature of this class of systems is that a constraint variation exists which makes the system invariant. An interesting example of this class is a space truss (Tarnai, 1980) where the bars are edges of the Archimedes' antiprism (Fig. 6(*b*)).

Note in conclusion that the order of infinitesimal mobility of a system can be interpreted geometrically as the order of contact of multidimensional surfaces serving as loci prescribed for a given point by the subsystems that share it. In other words, it is the order of flatness of the surface $f(x_s)$ representing the constraint discontinuity form in the coordinate space. Although the order of mobility quantifies the rate of stiffening in relation to the virtual displacements, it may not characterize the actual physical rigidity of the system, which depends mostly on its geometric parameters and material properties. For example, a real finite mechanism with a small interference is formally a first-order infinitesimal mechanism, but actually can be very flexible. On the other hand, an infinitesimal mechanism of an arbitrarily high order can be quite rigid if the lowest-order discontinuity form contains a large parameter.

Summary and Conclusions

(1) The matrix method of detecting infinitesimal mobility is limited to simple and certain compound first-order mechanisms.

(2) Break-up of singular systems followed by the evaluation of the lowest-order discontinuity forms appears to be an effective approach in the analysis and synthesis of both simple and certain compound infinitesimal mechanisms of any order.

(3) Even-order infinitesimal mechanisms exist, are quasi-invariant, and unprestressable.

(4) Constrained local stationarity (without an extremum) of one of the constraint functions is a formal source of a previously unidentified class of structural systems—unprestressable infinitesimal mechanisms. It complements the known source of infinitesimally mobile systems characterized by a strict constrained extremum with the resulting feature of prestressability.

Acknowledgment

The author is grateful to his colleaques, Profs. W. B. Hall and S. A. Burnis, for discussion and many useful suggestions on this paper.

References

Calladine, C. R., and Pellegrino, S., "First-order Infinitesimal Mechanisms," *Int. J. Solids Structures*, to appear.

Hilbert, D., and Cohn-Vossen, S., 1952, *Geometry and the Imagination*, Chelsea Publishing Company, New York.

Koiter, W. T., 1984, "On Tarnai's Conjecture with Reference to both Statically and Kinematically Indeterminate Structures," Lab. Report No. 788, Delft University.

Kotter, E., 1912, "Uber die Moglichkeit, n Punkte in der Ebene oder im Raume....," Festschrift Heinrich Muller-Breslau, Kroner, Leipzig, pp. 61–80.

Kuznetsov, E. N., 1988, "Underconstrained Structural Systems," *Int. J. Solids Structures*, Vol. 24, pp. 153–163.

Kuznetsov, E. N., 1989, "On Immobile Kinematic Chains and a Fallacious Matrix Analysis,"ASME JOURNAL OF APPLIED MECHANICS, Vol. 56, pp. 222–224.

Tarnai, T., 1980a, "Problems Concerning Spherical Polyhedra and Structural Rigidity," *Struct. Topology*, Vol. 4, pp. 61–66.

Tarnai, T., 1980b, "Simultaneous Static and Kinematic Indeterminacy of Space Trusses with Cyclic Symmetry," *Int. J. Solids Structures*, Vol. 16, pp. 347–359.

Downloaded 03 May 2010 to 171.66.16.248. Redistribution subject to ASME license or copyright; see http://www.asme.org/terms/Terms_Use.cfm

Chun-Liang Lin
Institute of Aeronautics and Astronautics,
National Cheng Kung University,
Tainan, Taiwan

Bor-Sen Chen
Department of Electrical Engineering,
National Tsing Hua University,
Hsinchu, Taiwan

Fei-Bin Hsiao
Institute of Aeronautics and Astronautics,
National Cheng Kung University,
Tainan, Taiwan

On Stability and Stabilization of Mechanical Structures Under Nonlinear Time-Varying Perturbations

Asymptotic stability and bounded-input, bounded-output (BIBO) stability of a class of underdamped mechanical structures with nonlinear time-varying perturbations are studied. An upper norm-bound of the state transition matrix of a normal mode system is derived. We provide a sufficient condition which guarantees both asymptotic stability and BIBO stability for the perturbed system. A straightforward extension to a robust modal-space control is also briefly introduced. Finally, simple illustrative examples are presented for demonstrating the applications of our results.

I Introduction

Stability theory of dynamic systems has been developed into a comprehensive, consistent theory over a century, drawing input from various sources (see, for example, Leipholz, 1983; Vidyasagar, 1978). Recently, an important theme in system theory and its applications is the robustness of various system-theoretic properties to variations in the system model. The problem of maintaining stability of a system subject to parameter perturbations and model uncertainties has been of considerable interest to researchers. Some authors (Safonov and Athans, 1977; Doyle and Stein, 1981), based on the frequency domain viewpoint, address the issue on mutlivariable systems, which discuss in broad and simple terms the role of norm or norm-like inequalities in coping with model imprecision in a wide range of engineering problems. In the time-domain approach, Lyapunov theory is widely used to study the robust stability of perturbed systems. Some useful stability conditions have been developed for a class of lumped-parameter systems under linear time-varying perturbations (Chen and Hsu, 1988) or nonlinear time-varying perturbations (Patel et al., 1977). For the Lyapunov approach, stability is inferred from the finding that the Lyapunov function is positive definite and the derivative of the Lyapunov function is negative definite. Although the Lyapunov method is desirable because it bears physical meaning and other various attractive advantages, until recently there has no systematic way to construct appropriate Lyapunov functions. Also, it is inevitable that while examining the key stability inequality, a Lyapunov matrix equation must be solved. In most cases, to solve the Lyapunov matrix equation may lead to a complicated computing procedure.

In this paper, asymptotic stability and bounded-input, bounded-output (BIBO) stability for a class of lumped-parameter systems under nonlinear time-varying perturbations (Lipschitz perturbations) are analyzed. In order to clarify the influence of modal damping ratios and natural frequencies to system stability, the equation of motion of a mechanical structure described in physical coordinates is first transformed into normal coordinates and is later expressed in a state-space form. Since a damping matrix is assumed to be nonproportional, after diagonalizing the mass and stiffness matrices, the induced norm of the remaining nonzero off-diagonal elements of the damping matrix is used as a measure of deviation distance (bounded linear perturbation) to the normal mode case. This approach is similar to Yae and Inman (1987) who addressed the topic on the estimation of response bounds for various linear second-order systems. The concept of the function norm and Gronwall's inequality (Vidyasagar, 1978) will be employed to investigate stability conditions for the system under bounded nonlinear and linear perturbations. By using the defined induced norm, a simple and straightforward procedure is provided to estimate a tightly upper norm-bound of the state transition matrix of the unperturbed (nominal) system.

Because lightly damped structures have only a small stability margin, these structures are sensitive to added plant perturbations. That is, in these systems, even a small perturbation occurred on the original eigenvalues can lead to instability. The classical modal-space control (see Inman, 1989) can be adopted to provide an excess stability margin to the nominal system. However, an improper controller design may not successfully stabilize a perturbed system. We will provide a robust stability criteria for the controller design such that the perturbed system can be stabilized.

Contributed by the Applied Mechanics Division of THE AMERICAN SOCIETY OF MECHANICAL ENGINEERS for publication in the JOURNAL OF APPLIED MECHANICS.

Discussion on this paper should be addressed to the Technical Editor, Prof. Leon M. Keer, The Technological Institute, Northwestern University, Evanston, IL 60208, and will be accepted until two months after final publication of the paper itself in the JOURNAL OF APPLIED MECHANICS. Manuscript received by the ASME Applied Mechanics Division, June 29, 1989; final revision, Dec. 5, 1989.

Copyright © 1991 by ASME
Downloaded 03 May 2010 to 171.66.16.248. Redistribution subject to ASME license or copyright; see http://www.asme.org/terms/Terms_Use.cfm

II System Equations

Before analysis, we first introduce the following notations to clarify our exposition.

The norm of a real vector $x \in R^n$ is defined as

$$\|x\| = \sum_{i=1}^{n} |x_i|$$

where x_i, $i = 1, \ldots, n$ denote the elements of the vector x. The induced matrix norm corresponding to the defined vector norm is given by

$$\|A\| = \max_j \sum_{i=1}^{n} |a_{ij}| \quad \text{(column sum)}$$

where a_{ij}, $i, j = 1, \ldots, n$ denote the entries of the matrix A. And the corresponding matrix measure is defined by (Desoer and Vidyasagar, 1975)

$$\mu(A) = \max_j \left\{ \mathrm{Re}(a_{jj}) + \sum_{\substack{i=1 \\ i \neq j}}^{n} |a_{ij}| \right\}$$

where Re(•) denotes the real part.

In the following, we are concerned with a class of lumped-parameter, in the physical coordinates, finite-dimensional mechanical structures described by the following semilinear matrix-second-order equation:

$$M\ddot{q}(t) + C\dot{q}(t) + Kq(t) + \tilde{f}(\dot{q}(t), q(t), h(t), t) = \tilde{B}h(t),$$
$$q(0) = q_0, \ \dot{q}(0) = \dot{q}_0, \ t \geq 0 \quad (1)$$

where $q(t) \in R^n$ represents the displacements of the n lumped masses of the system, and its time derivatives $\dot{q}(t)$ and $\ddot{q}(t)$ represent the velocity and acceleration, respectively. $M \in R^{n \times n}$, $C \in R^{n \times n}$, and $K \in R^{n \times n}$ are symmetric positive definite and represent, respectively, the nominal mass, damping, and stiffness matrices. $\tilde{B} \in R^{n \times m}$ is an external force influence matrix. $h(t) \in R^m$ represents the external forces acting on the system. The term $\tilde{f}(\dot{q}(t), q(t), h(t), t)$ (for simplicity, it will be expressed as $\tilde{f}(\dot{q}(t), q(t), h(t))$ or further simplified as $\tilde{f}$) represents the class of Lipschitz continuous nonlinearities which $t \to \tilde{f}(\dot{q}(t), q(t), h(t))$ is Lipschitz continuous in t on the semi-infinite interval $[0, \infty)$. That is,

$$\|\tilde{f}(\dot{q}_1(t), q_1(t), h_1(t)) - \tilde{f}(\dot{q}_2(t), q_2(t), h_2(t))\| \leq \tilde{\alpha}_1 \|q_1(t) - q_2(t)\| + \tilde{\alpha}_2 \|\dot{q}_1(t) - \dot{q}_2(t)\| + \tilde{\alpha}_3 \|h_1(t) - h_2(t)\| \quad (2a)$$

and

$$\tilde{f}(0, 0, 0) = 0 \quad (2b)$$

where $\tilde{\alpha}_1$, $\tilde{\alpha}_2$, and $\tilde{\alpha}_3$ are the corresponding Lipschitz constants. This type of the formulation is different from that of Chen and Hsu (1988) who considered a class of lumped-parameter linear structures under linear time-varying uncertainty. The nonlinear case will be treated here via a different way. Equations of the form of (1), the first three terms represent the linearized portion of the equation of motion, the term $\tilde{f}$ can be the modeling error and can be viewed as a nonlinear time-varying perturbation (or, Lipschitz perturbation) to the linear part and $\tilde{\alpha}_1$, $\tilde{\alpha}_2$, $\tilde{\alpha}_3$ in (2a) reflect the size of the perturbation.

In order to clarify the influence of the modal damping ratios and undamped natural frequencies of structural modes on the system stability, it is convenient to discuss the issue in normal coordinates. Modal analysis is now used to transform the dynamic system (1) into a diagonal one and consider the damping matrix (after transformation) as the sum of a diagonal matrix (the normal mode part) and a residual matrix having zero diagonal elements. We assume that the damping matrix C is a linear combination of a diagonalizable part of C_Λ and a residual part $\tilde{C}$ as

$$C = C_\Lambda + \tilde{C} \quad (3)$$

where C_Λ satisfies the modal decoupling condition $M^{-1}C_\Lambda M^{-1}K = M^{-1}KM^{-1}C_\Lambda$ (Caughey and O'Kelly, 1965). While $\tilde{C} = 0$, the system (1), if we neglect $\tilde{f}$, can be directly diagonalized to a normal mode one. If the residual part $\tilde{C}$ exists, it becomes a non-normal mode system. In the latter case, $\tilde{C}$ will be viewed as a linear time-invariant perturbation to the normal mode system. Now let us consider a normalized orthogonal transformation $q(t) = S\eta(t) \in R^n$ where $S = M^{-1/2}P \in R^{n \times n}$, P is a nonzero orthogonally similar transformation matrix, such that

$$S^TMS = I_n, \ S^TKS = \Lambda = \mathrm{diag}[\omega_1^2, \omega_2^2, \ldots, \omega_n^2], \ PP^T = P^TP = I_n \quad (4)$$

where I_n denotes the $n \times n$ identity matrix, and $\omega_i > 0$ ($i = 1, \ldots, n$) is the undamped natural frequency of the ith mode. Pre and post-multiplying (3) by S^T and S, respectively, and from (4) we can obtain

$$S^TCS = 2\xi\Lambda^{1/2} + \hat{C}$$

where $\xi = \mathrm{diag}[\zeta_1, \zeta_2, \ldots, \zeta_n]$ with ζ_i denoting the modal damping ratio of the ith mode, and $\hat{C} = S^T\tilde{C}S = [\hat{c}_{ij}]$ is a symmetric matrix with zero diagonal elements. Throughout this paper, we will restrict our attention to systems with $\zeta_i < 1$, $i = 1, \ldots, n$. That is, the originally unperturbed system is underdamped. Note that by the positive definiteness of C, $\zeta_i > 0$, $i = 1, \ldots, n$. Also note that M, C, and K are all symmetric and positive definite, as $\tilde{f} = 0$, the system is asymptotically stable. Modal damping of the type described above and its effects on linear systems were discussed in details by Chen and Russell (1982), Yae and Inman (1987), and Shahruz and Ma (1988). For mechanical structures with different forms of damping and its related properties, one may refer to Chen and Russell (1982) and Nashif et al. (1985). After applying the coordinate transformation above, the system (1) can be transformed into

$$\ddot{\eta}(t) + (2\xi\Lambda^{1/2} + \hat{C})\dot{\eta}(t) + \Lambda\eta(t) + f(\dot{\eta}(t), \eta(t), h(t)) = S^T\tilde{B}h(t),$$
$$\eta(0) = S^TMq_0, \ \dot{\eta}(0) = S^TM\dot{q}_0, \ t \geq 0 \quad (5)$$

where $f(\dot{\eta}(t), \eta(t), h(t)) = S^T\tilde{f}(S\dot{\eta}(t), S\eta(t), h(t))$.

The system (5) including the initial states $\eta(0)$ and $\dot{\eta}(0)$ can then be put into the following state-space form:

$$\dot{z}(t) = \begin{bmatrix} 0_n & I_n \\ -\Lambda & -2\xi\Lambda^{1/2} \end{bmatrix} z(t) + \begin{bmatrix} 0_n & 0_n \\ 0_n & \hat{C} \end{bmatrix} z(t) + \begin{bmatrix} 0_{n \times 1} \\ f(\dot{\eta}(t), \eta(t), h(t)) \end{bmatrix} + \begin{bmatrix} 0_{n \times m} \\ S^T\tilde{B} \end{bmatrix} h(t), \ z(0) = \begin{bmatrix} \eta(0) \\ \dot{\eta}(0) \end{bmatrix}, \ t \geq 0 \quad (6)$$

where $z(t) = [\eta^T(t) \ \dot{\eta}^T(t)]^T \in R^{2n}$, $0_n = 0_{n \times n}$ is the $n \times n$ zero matrix. For the convenience of analysis, introduce a further coordinate transformation for (6) with $z(t) = Wx(t)$ where

$$W = \begin{bmatrix} I_n & 0_n \\ 0_n & \Lambda^{1/2} \end{bmatrix}$$

and $x(t) = [\eta^T(t) \ v^T(t)]^T \in R^{2n}$ with $v(t) = \Lambda^{-1/2}\dot{\eta}(t) \in R^n$ being the reduced modal velocity vector, then multiplying both sides of (6) by W^{-1}, it carries (6) into

$$\dot{x}(t) = Ax(t) + \hat{A}x(t) + F(x(t), h(t)) + Bh(t), \ t \geq 0$$
$$= \begin{bmatrix} 0_n & \Lambda^{1/2} \\ -\Lambda^{1/2} & -2\xi\Lambda^{1/2} \end{bmatrix} x(t) + \begin{bmatrix} 0_n & 0_n \\ 0_n & \Lambda^{-1/2}\hat{C}\Lambda^{1/2} \end{bmatrix} x(t) + \begin{bmatrix} 0_{n \times 1} \\ \Lambda^{-1/2} f(\Lambda^{1/2}v(t), \eta(t), h(t)) \end{bmatrix} + \begin{bmatrix} 0_{n \times m} \\ \Lambda^{-1/2}S^T\tilde{B} \end{bmatrix} h(t),$$
$$x(0) = W^{-1}z(0) = \begin{bmatrix} \eta(0) \\ v(0) \end{bmatrix}, \ t \geq 0. \quad (7)$$

Downloaded 03 May 2010 to 171.66.16.248. Redistribution subject to ASME license or copyright; see http://www.asme.org/terms/Terms_Use.cfm

It is straightforward to obtain the bound of the nonlinear time-varying perturbation $F(x(t), h(t))$ in (7) as

$$\begin{aligned}
&\|F(x(t), h(t))\| \\
&\quad = \|\Lambda^{-1/2} f(\Lambda^{1/2} v(t), \eta(t), h(t))\| \\
&\quad = \|\Lambda^{-1/2} S^T \tilde{f}(S\Lambda^{1/2} S v(t), S\eta(t), h(t))\| \\
&\quad \le \|\Lambda^{-1/2} S^T\|(\tilde{\alpha}_1 \|S\| \|\eta(t)\| + \tilde{\alpha}_2 \|S\Lambda^{1/2} S\| \|v(t)\| + \tilde{\alpha}_3 \|h(t)\|) \\
&\quad \le \alpha_1 \|x(t)\| + \alpha_2 \|h(t)\| \text{ (using } \|x(t)\| = \|\eta(t)\| + \|v(t)\|) \qquad (8)
\end{aligned}$$

where $\alpha_1 = \max(\tilde{\alpha}_1 \|S\|, \tilde{\alpha}_2 \|S\Lambda^{1/2} S\|) \|\Lambda^{-1/2} S^T\|$ and $\alpha_2 = \tilde{\alpha}_3 \|\Lambda^{-1/2} S^T\|$.

To find the solution of (7), define a state transition matrix of the unperturbed system $\dot{x}(t) = Ax(t) + Bh(t)$ as

$$\Phi(t) = \exp(At).$$

and $\Gamma = -\xi\Lambda^{1/2} + j\Lambda^{1/2}(I_n - \xi^2)^{1/2}$, the notation * denotes the complex conjugate transpose. We have

$$X = \begin{bmatrix} I_n & I_n \\ \Gamma\Lambda^{-1/2} & \Gamma^*\Lambda^{-1/2} \end{bmatrix},$$

$$X^{-1} = \begin{bmatrix} \Gamma^*(\Gamma^* - \Gamma)^{-1} & -\Lambda^{1/2}(\Gamma^* - \Gamma)^{-1} \\ -\Gamma(\Gamma^* - \Gamma)^{-1} & \Lambda^{1/2}(\Gamma^* - \Gamma)^{-1} \end{bmatrix}. \qquad (11)$$

The state transition matrix $\Phi(t)$ can be obtained as:

$$\Phi(t) = \begin{bmatrix} I_n & I_n \\ \Gamma\Lambda^{-1/2} & \Gamma^*\Lambda^{-1/2} \end{bmatrix} \begin{bmatrix} \exp(\Gamma t) & 0_n \\ 0_n & \exp(\Gamma^* t) \end{bmatrix} \begin{bmatrix} \Gamma^*(\Gamma^* - \Gamma)^{-1} & -\Lambda^{1/2}(\Gamma^* - \Gamma)^{-1} \\ -\Gamma(\Gamma^* - \Gamma)^{-1} & \Lambda^{1/2}(\Gamma^* - \Gamma)^{-1} \end{bmatrix}$$

$$= \begin{bmatrix} [\exp(\Gamma t)\Gamma^* - \exp(\Gamma^* t)\Gamma](\Gamma^* - \Gamma)^{-1} & [\exp(\Gamma^* t) - \exp(\Gamma t)]\Lambda^{1/2}(\Gamma^* - \Gamma)^{-1} \\ [\exp(\Gamma t) - \exp(\Gamma^* t)]\Gamma\Lambda^{-1/2}\Gamma^*(\Gamma^* - \Gamma)^{-1} & [\exp(\Gamma^* t)\Gamma^* - \exp(\Gamma t)\Gamma](\Gamma^* - \Gamma)^{-1} \end{bmatrix}.$$

It follows from Pazy (1983) that under the assumption, the nonlinear time-varying perturbation F is continuous in its variable t and uniformly locally Lipschitz continuous in $x(t)$ and $h(t)$ (induced from (2)), then mild solutions of the initial value problem (7) exist. And a unique solution $x(t)$ of (7) on $[0, t]$ is given by

$$x(t) = \Phi(t)x(0) + \int_0^t \Phi(t-\tau)[\hat{A}x(\tau) + F(x(\tau), h(\tau))]d\tau + \int_0^t \Phi(t-\tau)Bh(\tau)d\tau. \qquad (9)$$

It is noted that if the Lipschitz continuous property of F in $x(t)$ and $h(t)$, is dropped, then, as is well known, the existence of $x(t)$ is guaranteed no more. The stability analysis of the system (1) will then be discussed on the basis of the state-space form of (9) in the sequel.

III Stability Analysis

Concerning the stability, first it is necessary to estimate an upper norm-bound for the state transition matrix $\Phi(t) = \exp(At)$. An upper norm-bound for the matrix exponential function $\exp(At)$ induced by the defined vector norm can be directly obtained as

$$\|\exp(At)\| \le k(X)\exp\{\{\max \operatorname{Re}[\lambda(A)]\}t\}, \quad t \ge 0 \qquad (10)$$

where

$$A = X^{-1}\Psi X, \quad \Psi = \operatorname{diag}[\lambda_i(A)], \quad k(X) = \|X\|\|X^{-1}\|$$

with $\lambda(A)$ denoting the eigenvalues of A, $k(X)$ being the condition number of the nonsingular matrix X. In many cases the condition number gives poor bounds (Nicholson, 1987). However, from the observation for the matrix A, it can be anticipated that a better estimate may be obtained by the use of the additional information available in (7). This will be shown as follows.

As in the absence of the nonlinear time-varying perturbation $f(\dot{\eta}(t), \eta(t), h(t))$ and the matrix $\hat{C}$, the vector-second-order system described by (5) is diagonal. This permits us to find eigenvalues and eigenvectors in a straightforward manner. Eigenvalues of the unperturbed system are easily obtained as

$$\lambda_i(A) = -\zeta_i\omega_i \pm j\omega_i\sqrt{1-\zeta_i^2}, \quad 0 < \zeta_i < 1, \quad i = 1, \ldots, n$$

where $j = \sqrt{-1}$. Then, by solving an eigenvalue problem $AX = X\Psi$ with

$$\Psi = \begin{bmatrix} \Gamma & 0_n \\ 0_n & \Gamma^* \end{bmatrix}$$

Using the following easily verified equalities

$$\exp(\Gamma t) + \exp(\Gamma^* t) = 2 \cdot \exp(-\xi\Lambda^{1/2} t)\cos[\Lambda^{1/2}(I_n - \xi^2)^{1/2} t]$$
$$\exp(\Gamma t) - \exp(\Gamma^* t) = 2j \cdot \exp(-\xi\Lambda^{1/2} t)\sin[\Lambda^{1/2}(I_n - \xi^2)^{1/2} t]$$

we have

$$\Phi(t) = \begin{bmatrix} G_1(t) & G_2(t) \\ G_3(t) & G_4(t) \end{bmatrix}$$

where $G_i(t) = \operatorname{diag}[G_i^1(t), \ldots, G_i^n(t)]$, $i = 1, \ldots, 4$ are the $n \times n$ matrices whose n diagonal entries, expressed as $G_i^k(t)$, $k = 1, \ldots, n$, are defined as

$$G_1^k(t) = [\cos(\rho_k t) + \frac{\zeta_k}{\sqrt{1-\zeta_k^2}} \sin(\rho_k t)]\exp(-\zeta_k\omega_k t)$$

$$G_2^k(t) = \frac{1}{\sqrt{1-\zeta_k^2}} \sin(\rho_k t)\exp(-\zeta_k\omega_k t)$$

$$G_3^k(t) = \frac{-1}{\sqrt{1-\zeta_k^2}} \sin(\rho_k t)\exp(-\zeta_k\omega_k t)$$

and

$$G_4^k(t) = [\cos(\rho_k t) - \frac{\zeta_k}{\sqrt{1-\zeta_k^2}} \sin(\rho_k t)]\exp(-\zeta_k\omega_k t), \quad k = 1, \ldots, n \qquad (12)$$

in which $\rho_k = \omega_k(1-\zeta_k^2)^{1/2}$.

From (12), and using the definition of the induced matrix norm, the induced norm of $\Phi(t)$ is given by

$$\begin{aligned}
\|\Phi(t)\| = \max\{&|G_1^1(t)| + |G_3^1(t)|, |G_1^2(t)| \\
&+ |G_3^2(t)|, \ldots, |G_1^n(t)| + |G_3^n(t)|, |G_2^1(t)| + |G_4^1(t)|, |G_2^2(t)| \\
&+ |G_4^2(t)|, \ldots, |G_2^n(t)| + |G_4^n(t)|\}. \qquad (13)
\end{aligned}$$

From (12), we have

$$\begin{aligned}
|G_1^k(t)| + |G_3^k(t)| &= \left[\left|\cos(\rho_k t) + \frac{\zeta_k}{\sqrt{1-\zeta_k^2}} \sin(\rho_k t)\right| \right. \\
&\left. + \frac{1}{\sqrt{1-\zeta_k^2}} |\sin(\rho_k t)| \right] \exp(-\zeta_k\omega_k t) \le \left[|\cos(\rho_k t)| \right. \\
&\left. + \frac{\zeta_k}{\sqrt{1-\zeta_k^2}} |\sin(\rho_k t)| + \frac{1}{\sqrt{1-\zeta_k^2}} |\sin(\rho_k t)| \right] \exp(-\zeta_k\omega_k t) \\
&\le \sqrt{\frac{2}{1-\zeta_k}} \exp(-\zeta_k\omega_k t), \quad \text{for } t \ge 0, \ k = 1, \ldots, n. \qquad (14)
\end{aligned}$$

Downloaded 03 May 2010 to 171.66.16.248. Redistribution subject to ASME license or copyright; see http://www.asme.org/terms/Terms_Use.cfm

Similarly, we can prove that

$$|G_2^k(t)| + |G_4^k(t)| \le \sqrt{\frac{2}{1-\zeta_k}} \exp(-\zeta_k \omega_k t), \quad \text{for } t \ge 0,\ k = 1, \ldots, n. \tag{15}$$

From (13)–(15), we obtain

$$\|\Phi(t)\| \le \max\left\{ \sqrt{\frac{2}{1-\zeta_1}} \exp(-\zeta_1\omega_1 t), \ldots, \sqrt{\frac{2}{1-\zeta_n}} \exp(-\zeta_n\omega_n t) \right\} \le m \cdot \exp(-\beta t), \quad t \ge 0 \tag{16}$$

where $\beta = \min_k(\zeta_k\omega_k) > 0$ indicates the exponentially decaying rate of $\|\Phi(t)\|$ and the multiplier $m = \sqrt{\frac{2}{1-\zeta_{\max}}} > 1$ with $\zeta_{\max} = \max_k(\zeta_k)$, $k = 1, \ldots, n$. It is obvious that for lightly damped structures, $\zeta_k \ll 1$, then $m \simeq \sqrt{2}$.

From (16), we see that the exponentially decaying rate of the induced norm of $\Phi(t)$ is closely related to the dominant eigenvalue of the matrix A.

Remark 1. If we use (10) to estimate the upper bound of $\Phi(t)$, it can be easily found, from (10) and (11), that $m(X) = \sqrt{\frac{4}{1-\zeta_{\max}^2}}$. This leads to $m < m(X)$; i.e., equation (16) gives a less conservative estimate then that of (10).

Remark 2. In practical situations, it is not easy to estimate the modal damping for structural modes. Some similar results extended from the analysis above for alternative system models are discussed in the following:

(*i*) When the damping ratio for each mode is a constant, i.e., $\zeta_k = \zeta$, $k = 1, \ldots, n$, β and m in (16) can then be simplified as

$$\beta = \zeta \cdot \min_k(\omega_k) = -\max \mathrm{Re}[\lambda(A)], \text{ and } m = \sqrt{\frac{2}{1-\zeta}}.$$

That is, the exponentially bounding function is uniquely determined by the damping ratio, ζ, and the real part of the eigenvalue of the lowest structural mode.

(*ii*) The structural damping matrix $2\xi\Lambda^{1/2}$ in (5) is sometimes replaced by γI_n and $\hat{C} = 0$, where the real scalar $\gamma > 0$ is a uniform viscous damping coefficient used to indicate a conservative approximation to the actual structural damping. In this case, β and m become

$$\beta = \frac{\gamma}{2}, \text{ and } m = \sqrt{\frac{2}{1-\nu}} \text{ with } \nu = \frac{\gamma}{2 \cdot \min_k(\omega_k)}$$

if $0 < \nu < 1$.

To prove a stability condition for the perturbed system (7), we need the following lemma.

Lemma 1. (Gronwall's Lemma, Vidyasagar, 1978). Let $a(t)$, $b(t)$, and $c(t)$ be continuous functions of t, and let $b(t) \ge 0$ and $c(t) > 0$ for $t \ge 0$. If

$$a(t) \le c(t) + \int_0^t b(\tau)a(\tau)d\tau, \tag{17}$$

then

$$a(t) \le c(t) + \int_0^t b(s)c(s)\exp\left[\int_s^t b(\tau)d\tau\right]ds. \tag{18}$$

If $b(t) = b = \text{constant}$, equation (18) becomes

$$a(t) \le c(t) + b\int_0^t c(s)\exp[b \cdot (t-s)]ds. \tag{19}$$

If $b(t) = b$ and $c(t) = c$, (17) implies that

$$a(t) \le c \cdot \exp(bt). \tag{20}$$

3.1 Stability of the Unforced System.

Definition 1. (Vidyasagar, 1978; Inman, 1989). A system is said to be asymptotically stable at time t_0, if there exists a positive constant δ such that whenever $\|x(t_0)\| < \delta$, then $\|x(t)\| \to 0$, as $t \to +\infty$.

It is noted that the asymptotic stability definition involves only the initial states and not the force input (i.e., the unforced system). The following theorem gives a sufficient condition for asymptotic stability of the perturbed system (7).

Theorem 1. Consider the perturbed system (7) with $h(t) = 0$. Suppose the nonlinear time-varying perturbation F satisfies (8), and

$$\beta - m(\|\hat{A}\| + \alpha_1) > 0 \tag{21}$$

with $\|\hat{A}\|$ being sufficiently small, then the system is asymptotically stable.

Proof. Taking the norm on both sides of (9) and letting $h(t) = 0$, yields

$$\|x(t)\| \le \|\Phi(t)\|\|x(0)\| + \int_0^t \|\Phi(t-\tau)\|[\|\hat{A}\|\|x(\tau)\| + \|F(x(\tau),0)\|]d\tau$$

where, by the definition of the induced norm and zero diagonal elements of $\hat{C}$,

$$\|\hat{A}\| = \|\Lambda^{-1/2}\hat{C}\Lambda^{1/2}\| = \max_j \sum_{\substack{i=1 \\ i \ne j}}^{n} |\hat{c}_{ij}|\,\omega_j/\omega_i.$$

From (8), we have $\|F(x(t),0)\| \le \alpha_1\|x(t)\|$, then

$$\|x(t)\| \le \|\Phi(t)\|\|x(0)\| + \int_0^t \|\Phi(t-\tau)\|(\|\hat{A}\| + \alpha_1)\|x(\tau)\|d\tau$$

$$\le m \cdot \exp(-\beta t)\|x(0)\| + \int_0^t m(\|\hat{A}\| + \alpha_1)\exp[-\beta(t-\tau)]\|x(\tau)\|d\tau \quad \text{(from (16))}.$$

That is,

$$\|x(t)\|\exp(\beta t) \le m\|x(0)\| + \int_0^t m(\|\hat{A}\| + \alpha_1)\exp[\beta(\tau)]\|x(\tau)\|d\tau.$$

Applying Gronwall's inequality (20), yields

$$\|x(t)\|\exp(\beta t) \le m\|x(0)\|\exp[m(\|\hat{A}\| + \alpha_1)t],$$

or, equivalently,

$$\|x(t)\| \le m\|x(0)\|\exp\{-[\beta - m(\|\hat{A}\| + \alpha_1)]t\}.$$

It is obvious that if $\beta > m(\|\hat{A}\| + \alpha_1)$, then $\|x(t)\| \to 0$, as $t \to +\infty$, and the perturbed system (7) is asymptotically stable.

Remark 3. For the normal mode system $\hat{C} = 0$, the stability condition (21) becomes $\beta - m\alpha_1 > 0$. While in the absence of the nonlinear perturbation $\tilde{f}$, (21) reduces to $\|\hat{A}\| < \beta/m$. As $\tilde{f} = 0$, the system (5) is originally stable, thus the above inequality restricts the system, while neglecting the nonlinearity, that stays near the normal mode case and an upper bound of the deviation distance $\|\hat{A}\|$ from the normal mode system is β/m or, in other words, the matrix $S^T C S$ should be diagonally dominant. In fact, we can show that (21) (when $\alpha_1 = 0$) gives an upper bound for the eigenvalues of $A + \hat{A}$. It is easily found that

$$\mathrm{Re}[\lambda(A + \hat{A})] \le \mu(\Psi + \hat{\Psi}) \le \mu(\Psi) + \mu(\hat{\Psi}) \le -(\beta - m\|\hat{A}\|)$$

where $\mu(\cdot)$ denotes the matrix measure, $\hat{\Psi} = X^{-1}\hat{A}X$, and

Downloaded 03 May 2010 to 171.66.16.248. Redistribution subject to ASME license or copyright; see http://www.asme.org/terms/Terms_Use.cfm

$\mu(\Psi+\hat{\Psi})=\max_j\{-\zeta_i\omega_i+\sum_{\substack{i=1\\ i\neq j}}^{n}|\hat{c}_{ij}|\omega_j/[\omega_i(1-\zeta_i^2)^{1/2}]\}$, which can be found via some trivial calculations. The first left inequality in the above equation is obtained by Gershgorin's disk theorem (Franklin, 1968). The accuracy of this estimate depends on the feature of a diagonal dominant of $\Psi+\hat{\Psi}$ (or S^TCS).

We can define β as the stability margin of the unperturbed system ($\hat{A}=0$, $F=0$), i.e., the real part of the eigenvalue of A which is the nearest one to the imaginary axis on the complex plane. By this setting, the inequality (21) explicitly describes a simple relationship between the stability margin, the largest damping ratio, the nonlinear perturbation bound, and the deviation distance of the nonnormal mode system from the normal mode one in maintaining stability.

3.2 Stability of the Forced System. In the forced system $h(t)\neq 0$ we will discuss BIBO stability for the perturbed system (7). Since BIBO stability concepts involve the force input and not the initial states, thus, in the following, we will assume $x(0)=0$. For the linear or nonlinear structures, the stability of the forced response of a system is defined in terms of the bounds of the response vector $x(t)$. That is, the responses $x(t)$ are referred to as the output of the system. We will show that for the system (1), as the asymptotic stability condition (21) holds, it is BIBO stable as well.

Definition 2. Let us define $\|w(\cdot)\|_\infty=\sup_{t\in[0,\infty)}\|w(t)\|$. Whenever we say a real-vector valued $w(t)\in L_\infty^n$, we shall mean $\|w(t)\|_\infty<\infty$.

Definition 3. (Vidyasagar, 1978; Inman, 1989). A multivariable dynamic system is BIBO stable if there exists some finite positive constants ρ such that

$$\|x(t)\|_\infty\leq\rho\|h(t)\|_\infty$$

for every force input $h(t)\in L_\infty^m$.

Theorem 2. Consider the perturbed system (7). Suppose $h(t)\in L_\infty^m$, the structural nonlinear time-varying perturbation F satisfies (8), and (21) also holds, then the system is BIBO stable in the sense of Definition 3.

Proof. Taking the norm on both sides of (9) and letting $x(0)=0$ yields

$$\|x(t)\|\leq\int_0^t\|\Phi(t-\tau)\|[\|\hat{A}\|\|x(\tau)\|+\|F(x(\tau),\,h(\tau))\|]d\tau+\int_0^t\|\Phi(t-\tau)\|\|B\|\|h(\tau)\|d\tau.$$

From (8) and (16), we have

$$\|x(t)\|\leq\int_0^t m[\|\hat{A}\|\|x(\tau)\|+\alpha_1\|x(\tau)\|+\alpha_2\|h(\tau)\|]\exp[-\beta(t-\tau)]d\tau+\int_0^t m\cdot\exp[-\beta(t-\tau)]\|B\|\|h(\tau)\|d\tau.$$

That is,

$$\|x(t)\|\exp(\beta t)\leq\int_0^t m(\|\hat{A}\|+\alpha_1)\exp(\beta\tau)\|x(\tau)\|d\tau+\int_0^t m\times\exp(\beta\tau)(\alpha_2+\|B\|)\|h(\tau)\|d\tau\leq m(\|\hat{A}\|+\alpha_1)\int_0^t\exp(\beta\tau)\|x(\tau)\|d\tau+[m(\alpha_2+\|B\|)/\beta]\sup_{\tau\in[0,t)}\|h(\tau)\|[\exp(\beta t)-1].$$

By applying Gronwall's inequality (19), we obtain

$$\|x(t)\|\exp(\beta t)\leq[m(\alpha_2+\|B\|)/\beta]\sup_{\tau\in[0,t)}\|h(\tau)\|[\exp(\beta t)-1]+m(\|\hat{A}\|+\alpha_1)\int_0^t[m(\alpha_2+\|B\|)/\beta]\sup_{\tau\in[0,t)}\|h(\tau)\|[\exp(\beta s)-1]\times\exp[m(\|\hat{A}\|+\alpha_1)(t-s)]ds\leq[m(\alpha_2+\|B\|)/\beta]\sup_{\tau\in[0,t)}\|h(\tau)\|\times[\exp(\beta t)-1]+m(\|\hat{A}\|+\alpha_1)[m(\alpha_2+\|B\|)/\beta]\times\sup_{\tau\in[0,t)}\|h(\tau)\|\exp[m(\|\hat{A}\|+\alpha_1)t]\int_0^t[\exp(\beta s)-1]\times\exp[-m(\|\hat{A}\|+\alpha_1)s]ds=[m(\alpha_2+\|B\|)/\beta]\sup_{\tau\in[0,t)}\|h(\tau)\|\times[\exp(\beta t)-1]+\frac{m(\|\hat{A}\|+\alpha_1)[m(\alpha_2+\|B\|)/\beta]}{\beta-m(\|\hat{A}\|+\alpha_1)}\times\sup_{\tau\in[0,t)}\|h(\tau)\|\{\exp(\beta t)-\exp[m(\|\hat{A}\|+\alpha_1)t\}-[m(\alpha_2+\|B\|)/\beta]\times\sup_{\tau\in[0,t)}\|h(\tau)\|\{\exp[m(\|\hat{A}\|+\alpha_1)t]-1\}.$$

That is,

$$\|x(t)\|\leq[m(\alpha_2+\|B\|)/\beta]\sup_{\tau\in0,t)}\|h(\tau)\|[1-\exp(-\beta t)]+\frac{m(\|\hat{A}\|+\alpha_1)[m(\alpha_2+\|B\|)/\beta]}{\beta-m(\|\hat{A}\|+\alpha_1)}\times\sup_{\tau\in[0,t)}\|h(\tau)\|\{1-\exp\{-[\beta-m(\|\hat{A}\|+\alpha_1)]t\}\}+[m(\alpha_2+\|B\|)/\beta]\sup_{\tau\in[0,t)}\|h(\tau)\|\{\exp(-\beta t)-\exp\{-[\beta-m(\|\hat{A}\|+\alpha_1)]t\}\}.$$

Clearly, if $\beta>m(\|\hat{A}\|+\alpha_1)$, i.e., (21) holds then for $t\geq0$, we have

$$\|x(t)\|\leq\rho\sup_{\tau\in[0,\infty)}\|h(\tau)\|,\quad\text{for } t\geq0$$

in which $\rho=\dfrac{m(\|B\|+\alpha_2)}{\beta-m(\|\hat{A}\|+\alpha_1)}>0$. This clearly implies that

$$\|x(t)\|_\infty\leq\rho\|h(t)\|_\infty.$$

Thus, the system is BIBO stable as well.

Asymptotic stability and BIBO stability above bring out an important fact that if the unperturbed system $\dot{x}(t)=Ax(t)+Bh(t)$ is exponentially stable, then it is possible to protect a variety of perturbations, e.g., nonlinearities and additive input. Note that Theorems 1 and 2 provide only sufficient conditions that are by no means necessary. However, they do have the advantage that they are easy to verify and do not require to solve the state transition matrix or other associated equations. According to Theorems 1 and 2, we immediately have the following theorem:

Theorem 3. If a linear lumped-parameter system with bounded nonlinear time-varying and linear time-invariant perturbations and finite initial conditions as described by (7) is asymptotically stable, (i.e., (21) holds), then it is BIBO stable as well. Under the same assumptions, the converse is also true.

Remark 4. The above results can be easily extended to the system under linear time-varying perturbations. If $\tilde{f}(\dot{q}(t),\,q(t),\,h(t),\,t)$ in (1) is linear in $\dot{q}(t)$, $q(t)$, and $h(t)$, it can be written as

$$\tilde{f}(\dot{q}(t),\,q(t),\,h(t))=\Delta C(t)\dot{q}(t)+\Delta K(t)q(t)+\Delta\tilde{B}(t)h(t)$$

where $\Delta C(t)=[\Delta c_{ij}(t)]$, $\Delta K(t)=[\Delta k_{ij}(t)]$ and $\Delta\tilde{B}(t)=[\Delta\tilde{b}_{ij}(t)]$. Furthermore, finite upper bounds of these time-varying perturbations can be estimated as:

$$\|\Delta K(t)\|\leq\max_j\left[\sum_{i=1}^n\sup_{t\in[0,\infty)}|\Delta k_{ij}(t)|\right]=\hat{\alpha}_1$$

$$\|\Delta C(t)\|\leq\max_j\left[\sum_{i=1}^n\sup_{t\in[0,\infty)}|\Delta c_{ij}(t)|\right]=\hat{\alpha}_2$$

$$\|\Delta\tilde{B}(t)\|\leq\max_j\left[\sum_{i=1}^n\sup_{t\in[0,\infty)}|\Delta\tilde{b}_{ij}(t)|\right]=\hat{\alpha}_3.$$

Downloaded 03 May 2010 to 171.66.16.248. Redistribution subject to ASME license or copyright; see http://www.asme.org/terms/Terms_Use.cfm

Based on the proofs on Theorems 1 and 2 if the following inequality holds

$$\beta - m(\|\hat{A}\| + \tilde{\alpha}_1) > 0 \tag{22}$$

where $\tilde{\alpha}_1 = \max(\hat{\alpha}_1 \|S\|, \hat{\alpha}_2 \|S\Lambda^{1/2}S\|)\|\Lambda^{-1/2}S^T\|$, then the system under bounded linear time-varying perturbations above is asymptotically and BIBO stable.

IV Robust Stabilization

As proved in the previous section, lightly damped structures have poor stability margins. Particularly, for undamped structures, those structural poles lie on the imaginary axis and have no stability margin. An active feedback control may effectively increase the stability margin and improve performance of the unperturbed system. However, due to the presence of the nonlinear time-varying perturbation $\tilde{f}(\dot{q}(t), q(t), h(t))$, undesired excitations may also inject into the controlled system via the perturbation $\tilde{f}$ excited by the feedback control signal. Hence, an improper controller design can even lead to instability. It is desirable to have a robust stability criterion, while the chosen control gains satisfy this criterion, the perturbed system is successfully stabilized. This will be discussed in this section.

Suppose $h(t)$ in (1) indicates the control force input, the matrix $\tilde{B}$ denotes the actuator influence matrix, and an external disturbance vector $n(t) \in R^r$ also adds into (1) as follows:

$$M\ddot{q}(t) + C\dot{q}(t) + Kq(t) + \tilde{f}(\dot{q}(t), q(t), h(t)) = \tilde{B}h(t) + \tilde{N}n(t),\ q(0) = q_0,\ \dot{q}(0) = \dot{q}_0,\ t \geq 0 \tag{23}$$

where $\tilde{N} \in R^{n \times r}$ is the disturbance influence matrix. $y(t) \in R^z$ represents the sensor output vector and is defined by

$$y(t) = C_d q(t) + C_v \dot{q}(t)$$

where $C_d \in R^{z \times n}$ and $C_v \in R^{z \times n}$ represent, respectively, the displacement and velocity sensor influence matrices. Without loss of generality, suppose the following necessary and sufficient condition for controllability of the unperturbed system is satisfied

$$\text{rank}[B, AB, A^2B, \ldots, A^{2n-1}B] = 2n \tag{24}$$

where the matrices A and B are defined in (7). It is noted that by judicious use of the additional information available in (7) for lightly damped structures ($\zeta_i \ll 1$) and undamped structures, the rank condition (24) can be further simplified (see Hughes and Skelton, 1980). Also note that if the matrix pair (A, B) is controllable, then the system under bounded linear or nonlinear perturbations is stabilizable by means of a linear feedback control as described by

$$h(t) = -Gy(t) \tag{25}$$

(Quinn, 1987) where $G \in R^{m \times z}$ is a gain matrix.

Now, combining (23) and (25) and introducing the same coordinate transformation $q(t) = S\eta(t)$ used in Section 2, we have the following equation of motion for the closed-loop system

$$\ddot{\eta}(t) + (2\xi\Lambda^{1/2} + \hat{C} + S^T\tilde{B}GC_vS)\dot{\eta}(t) + (\Lambda + S^T\tilde{B}GC_dS)\eta(t) + f_c(\dot{\eta}(t), \eta(t)) = S^T\tilde{N}n(t),\ \eta(0) = S^TMq_0,\ \dot{\eta}(0) = S^TM\dot{q}_0,\ t \geq 0 \tag{26}$$

where $f_c(\dot{\eta}(t), \eta(t)) = S^T\tilde{f}(S\dot{\eta}(t), S\eta(t), -G\{C_dS\eta(t) + C_vS\dot{\eta}(t)\})$. From the observation of (26), an independent control of each mode can be achieved if both $S^T\tilde{B}GC_vS$ and $S^T\tilde{B}GC_dS$ are diagonal. For the case where $\tilde{B}GC_v$ and $\tilde{B}GC_d$ are both symmetric, it can be shown (Inman, 1989) that, if and only if the following equalities hold:

$$\tilde{B}GC_dM^{-1}C_\Lambda = C_\Lambda M^{-1}\tilde{B}GC_d \tag{27a}$$

$$\tilde{B}GC_vM^{-1}C_\Lambda = C_\Lambda M^{-1}\tilde{B}GC_v, \tag{27b}$$

then this requirement can be made to be satisfied. Note that (27) puts some constraints on the location as well as the number of actuators and sensors. If we can choose $\tilde{B}$, G, C_d, and C_v such that (27) holds, we then obtain the following decoupled feedback gain matrices:

$$S^T\tilde{B}GC_dS = \text{diag}[g_{d1}, g_{d2}, \ldots, g_{dn}] \tag{28a}$$

$$S^T\tilde{B}GC_vS = \text{diag}[g_{v1}, g_{v2}, \ldots, g_{vn}]. \tag{28b}$$

Without loss of generality, we let $g_{di} \geq 0$, $g_{vi} \geq 0$ ($i = 1, 2, \ldots, n$), which represent, respectively, the non-negative proportional gain and derivative gain of the kth mode in normal mode coordinates. Note that the choice of non-negative g_{di} and g_{vi} guarantees that the damping ratio, ζ_i, and undamped natural frequency, ω_i, for each mode are effectively increased, and are not to be decreased. Combining (26) and (27) yields

$$\ddot{\eta}(t) + (2\xi_c\Lambda_c^{1/2} + \hat{C})\dot{\eta}(t) + \Lambda_c\eta(t) + f_c(\dot{\eta}(t), \eta(t)) = S^T\tilde{N}n(t) \tag{29}$$

where

$$\xi_c = \text{diag}[\zeta_{c1}, \zeta_{c2}, \ldots, \zeta_{cn}]$$

$$\text{with } \zeta_{ci} = \left(\zeta_i\omega_i + \frac{1}{2}g_{vi}\right)/\sqrt{\omega_i^2 + g_{di}},\ i = 1, \ldots, n$$

$\Lambda_c = \text{diag}[\omega_{c1}^2, \omega_{c2}^2, \ldots, \omega_{cn}^2]$ with $\omega_{ci}^2 = \omega_i^2 + g_{di}$, $i = 1, \ldots, n$.

We will assume $\zeta_i < \zeta_{ci} < 1$, $i = 1, \ldots, n$, i.e., modal dampings for each modes of the compensated system are increased by the feedback control but the system is still underdamped. This assumption is not too restrictive for practical structural controls. In general, from the performance consideration, a second-order system with damping ratio $\zeta \simeq 0.7$ is commonly acceptable. Now, introducing a similar coordinate transformation matrix $\tilde{W} = \text{diag}[I_n, \Lambda_c^{1/2}]$ used in (7), an equivalent state-space form of (29) is given by

$$\dot{x}(t) = A_cx(t) + \hat{A}_cx(t) + F_c(x(t)) + Nn(t),\ t \geq 0 \tag{30}$$

$$= \begin{bmatrix} 0_n & \Lambda_c^{1/2} \\ -\Lambda_c^{1/2} & -2\xi_c\Lambda_c^{1/2} \end{bmatrix}x(t) + \begin{bmatrix} 0_n & 0_n \\ 0_n & \Lambda_c^{-1/2}\hat{C}\Lambda_c^{1/2} \end{bmatrix}x(t) + \begin{bmatrix} 0_{n\times 1} \\ \Lambda_c^{-1/2}f_c(\Lambda_c^{1/2}v(t), \eta(t)) \end{bmatrix} + \begin{bmatrix} 0_{n\times r} \\ \Lambda_c^{-1/2}S^T\tilde{N} \end{bmatrix}n(t),$$

$$x(0) = \begin{bmatrix} \eta(0) \\ \Lambda_c^{-1/2}\dot{\eta}(0) \end{bmatrix} = \begin{bmatrix} \eta(0) \\ v(0) \end{bmatrix},\ t \geq 0.$$

The bound of the nonlinear time-varying perturbation $F_c(x(t))$ in the closed-loop system is given by

$$\begin{aligned} \|F_c(x(t))\| &= \|\Lambda_c^{-1/2}f_c(\Lambda_c^{1/2}v(t), \eta(t))\| \\ &= \|\Lambda_c^{-1/2}S^T\tilde{f}(S\Lambda_c^{1/2}Sv(t), S\eta(t), -G[C_dS\eta(t) + C_vS\Lambda_c^{1/2}Sv(t)])\| \\ &\leq \|\Lambda_c^{-1/2}S^T\|\{\max(\tilde{\alpha}_1\|S\|, \tilde{\alpha}_2\|S\Lambda_c^{1/2}S\|)\|x(t)\| \\ &\quad + \tilde{\alpha}_3\|G[C_dS\ \ C_vS\Lambda_c^{1/2}S]\|\|x(t)\|\} \\ &= \alpha_3\|x(t)\| \end{aligned} \tag{31}$$

where $\alpha_3 = [\max(\tilde{\alpha}_1\|S\|, \tilde{\alpha}_2\|S\Lambda_c^{1/2}S\|) + \tilde{\alpha}_3 \max(\|GC_dS\|, \|GC_vS\Lambda_c^{1/2}S\|)]\|\Lambda_c^{-1/2}S^T\|$. Following the result given in (16), an upper norm-bound of the state transition matrix $\Phi_c(t) = \exp(A_ct)$ for the closed-loop system (30) can be obtained as follows:

$$\|\Phi_c(t)\| \leq m_c\exp(-\beta_ct),\ t \geq 0 \tag{32}$$

where $\beta_c = \min_i(\zeta_{ci}\omega_{ci}) = \min_i\left(\zeta_i\omega_i + \frac{1}{2}g_{vi}\right)$ and $m_c = \sqrt{\frac{2}{1 - \zeta_{c\max}}}$ with $\zeta_{c\max} = \max_i(\zeta_{ci})$.

Downloaded 03 May 2010 to 171.66.16.248. Redistribution subject to ASME license or copyright; see http://www.asme.org/terms/Terms_Use.cfm

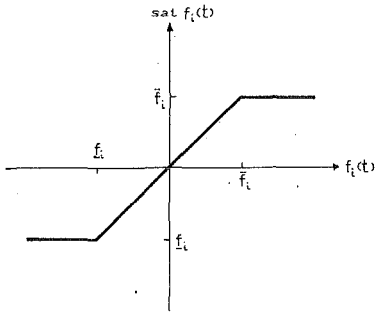

Fig. 1 Nonlinear saturating function

It is now of interest to determine the condition under which the closed-loop system with nonlinear time-varying perturbations and external disturbances is stable.

Theorem 4. Consider the perturbed system (23), which combines with a linear feedback controller as described by (25). The nonlinear perturbation $F_c(x(t))$ resulted by the feedback control satisfies (31). If

$$\beta_c - m_c(\|\hat{A}_c\| + \alpha_3) > 0, \tag{33}$$

then the overall system (30) is asymptotically stable, and if the external disturbances $n(t) \in L_\infty^r$ present, the system is BIBO stable as well.

Proof. The proof directly follows those of Theorems 1 and 2.

If we choose a set of derivative gains g_{vk} for the critical modes to increase the stability margin β_c of the unperturbed closed-loop system, then a suitable choice of proportional gains g_{dk}, $k=1, \ldots, n$ to decrease the multiplier m_c, and robust stability for the perturbed closed-loop system (30) can then be achieved. It should be known, however, that the nonzero controller gains will increase the size α_3 of the closed-loop nonlinear perturbation F_c. This feature imposes a constraint on the control gain selection. A robust modal-space control design is to choose feasible $\tilde{B}$, C_v, C_d, and G such that the stability criterion (33) is satisfied and thus the perturbed system is guaranteed to be stable.

Remark 5. From (32) and (33), it can be found that direct velocity feedback is closely related to the nominal closed-loop stability margin β_c. Since β_c can only be increased by g_{vk}, it follows from (33) that controller designs using only direct position feedback do not contribute to the robust stability.

V Examples

To verify (21), a simple example for a system of the form of (1) is given as follows:

Example 1. A two degree-of-freedom mechanical system contains two nonlinear springs whose dynamics is described by

$$\begin{bmatrix} m_1 & 0 \\ 0 & m_2 \end{bmatrix} \ddot{q}(t) + \left\{ \begin{bmatrix} c_1 & 0 \\ 0 & c_2 \end{bmatrix} + \Delta\delta \begin{bmatrix} 0 & 1 \\ 1 & 0 \end{bmatrix} \right\} \dot{q}(t) + \begin{bmatrix} \text{sat } f_1(t) \\ \text{sat } f_2(t) \end{bmatrix} = \begin{bmatrix} h_1(t) \\ h_2(t) \end{bmatrix}$$

where $q(t) = [q_1(t)\ q_2(t)]^T$. The parameters (m_1, m_2) and (c_1, c_2) are, respectively, the mass and damping coefficients. $\Delta\delta$ is an uncertain parameter controlling the degree of coupling of the modes which is bounded by $|\Delta\delta| \le \epsilon$; the smaller the ϵ is, the closer the system is to a decouplable one. $h_1(t)$ and $h_2(t)$ are the external excitation forces. A graphical illustration of the nonlinear spring forces sat $f_i(t)$ is shown in Fig. 1. In the linear operation region, the terms $f_1(t) = k_1 q_1(t)$ and $f_2(t) = k_2 q_2(t)$ represent the generalized spring forces and k_1 and k_2 are the stiffness coefficients. While the stress and strain exceed the proportionality limit of Hook's law, there exists a saturated characteristic on the nonlinear spring forces. Referring to Fig. 1, the nonlinear function is described by

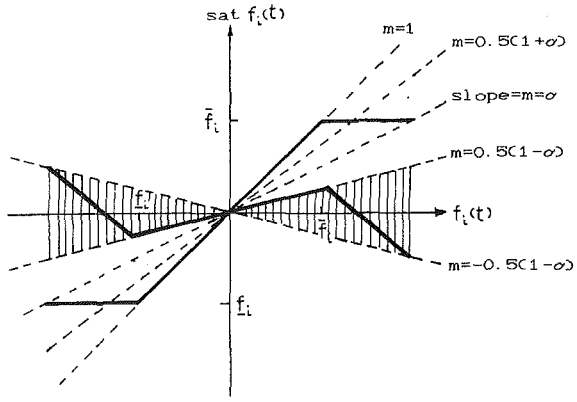

Fig. 2 Nonlinear sector [σ, 1]

$$\text{sat } f_i(t) = \begin{cases} \bar{f}_i, & \text{if } f_i(t) \ge \bar{f}_i \\ f_i(t), & \text{if } \bar{f}_i > f_i(t) > \underline{f}_i \\ \underline{f}_i, & \text{if } f_i(t) \le \underline{f}_i \end{cases} \quad i = 1,2. \tag{34}$$

Suppose the spring forces cannot approach infinity, thus only a finite operation range of the saturation needs to be considered. That is, the spring operation range is only within the sector $[\sigma, 1]$ with $\sigma \in [0, 1]$, as shown in Fig. 2. Referring to Fig. 2, the nonlinear function within the sector can be linearized about a linear line with slope $m = 0.5(1+\sigma)$. Based on this, the system can now be reformulated as follows:

$$\begin{bmatrix} m_1 & 0 \\ 0 & m_2 \end{bmatrix} \ddot{q}(t) + \left\{ \begin{bmatrix} c_1 & 0 \\ 0 & c_2 \end{bmatrix} + \Delta\delta \begin{bmatrix} 0 & 1 \\ 1 & 0 \end{bmatrix} \right\} \dot{q}(t) + \frac{1}{2}(1+\sigma) \begin{bmatrix} k_1 & 0 \\ 0 & k_2 \end{bmatrix} q(t) + \tilde{f}(q(t)) = \begin{bmatrix} h_1(t) \\ h_2(t) \end{bmatrix}$$

where

$$\tilde{f}(q(t)) = \begin{bmatrix} \text{sat } f_1(t) \\ \text{sat } f_2(t) \end{bmatrix} - \frac{1}{2}(1+\sigma) \begin{bmatrix} f_1(t) \\ f_2(t) \end{bmatrix}.$$

In this equation, the third term represents the linearized part of the nonlinear stiffness matrix. The term $\tilde{f}(q(t))$ is now viewed as a nonlinear time-varying perturbation to the linear part which satisfies (see Fig. 2)

$$\|\tilde{f}(q(t))\| \le \frac{1}{2}(1-\sigma) \left\| \begin{bmatrix} f_1(t) \\ f_2(t) \end{bmatrix} \right\| = \frac{1}{2}(1-\sigma) \left\| \begin{bmatrix} k_1 q_1(t) \\ k_2 q_2(t) \end{bmatrix} \right\|$$

$$= \frac{1}{2}(1-\sigma) \left\| \begin{bmatrix} k_1 & 0 \\ 0 & k_2 \end{bmatrix} q(t) \right\| \le \frac{1}{2}(1-\sigma)\max(k_1, k_2)\|q(t)\|.$$

Since σ, k_1, and k_2 are finite positive constants, the nonlinear perturbation is bounded. The system can now be put in a state-space form as described by (7), $(n=2)$, with the following parameters:

$$\zeta_1 = \frac{c_1}{m_1}\sqrt{\frac{m_1}{2(1+\sigma)k_1}},\ \zeta_2 = \frac{c_2}{m_2}\sqrt{\frac{m_2}{2(1+\sigma)k_2}},\ \omega_1 = \sqrt{\frac{(1+\sigma)k_1}{2m_1}},$$

$$\omega_2 = \sqrt{\frac{(1+\sigma)k_2}{2m_2}},\ \|\hat{A}\| \le \epsilon \cdot \max\left(\sqrt{\frac{k_1 m_2}{k_2 m_1}}, \sqrt{\frac{k_2 m_1}{k_1 m_2}}\right),$$

$$\|F(x(t))\| \le \frac{1}{2}(1-\sigma)\max(k_1, k_2)$$

Downloaded 03 May 2010 to 171.66.16.248. Redistribution subject to ASME license or copyright; see http://www.asme.org/terms/Terms_Use.cfm

$$\times \max\left[\sqrt{\frac{2}{(1+\sigma)k_1m_1}}, \sqrt{\frac{2}{(1+\sigma)k_2m_2}}\right]\|x(t)\|.$$

Suppose, as $\sigma=0$, the damping coefficients $\zeta_1 \ll 1$ and $\zeta_2 \ll 1$, i.e., when $\tilde{f}=0$ and $\Delta\delta=0$, the system is lightly damped. If $m_1=m_2$, $c_1 \le c_2$, and $k_1 \le k_2$, a sufficient condition guaranteeing stability can be obtained from (21)

$$\frac{c_1}{2m_1}-\epsilon\sqrt{\frac{2k_2}{k_1}}-\frac{(1-\sigma)k_2}{\sqrt{(1+\sigma)k_1m_1}}>0. \tag{35}$$

Note that for the special cases while $\sigma=0$, the nonlinear spring forces are allowed to be infinite. As $\sigma=1$, this is the case of the system without nonlinearity. From (35) we can find the smallest σ, which indicates the nonlinear sector $[\sigma, 1]$ being the largest operation range of spring saturation. While the nonlinearity lies within the sector $[\sigma, 1]$, the system remains stable.

To show our stabilizing scheme, we give the following example.

Example 2. Consider a practical structure control system with saturated actuators. Its equation of motion is described by

$$\begin{bmatrix} m_1 & 0 \\ 0 & m_2 \end{bmatrix}\ddot{q}(t)+\left\{\begin{bmatrix} c_1 & 0 \\ 0 & c_2 \end{bmatrix}+\Delta\delta\begin{bmatrix} 0 & 1 \\ 1 & 0 \end{bmatrix}\right\}\dot{q}(t)+\begin{bmatrix} k_1 & 0 \\ 0 & k_2 \end{bmatrix}q(t)=\tilde{B}\cdot\text{sat}\, f(t)$$

where $|\Delta\delta| \le \epsilon$, $\text{sat}\, f(t)=[\text{sat}\, f_1(t)\ \text{sat}\, f_2(t)]^T$ in which the saturation functions $\text{sat}\, f_i(t)$ are defined as (34) with the exception $\bar{f}_i=-\underline{f}_i$. A velocity feedback control with $f(t)=-GC_v\dot{q}(t)=-K_v\dot{q}(t)$ is now applied to the system to increase damping. Proceeding with the same procedure as in Example 1, after linearizing the nonlinearity we have

$$\begin{bmatrix} m_1 & 0 \\ 0 & m_2 \end{bmatrix}\ddot{q}(t)+\left\{\begin{bmatrix} c_1 & 0 \\ 0 & c_2 \end{bmatrix}+\Delta\delta\begin{bmatrix} 0 & 1 \\ 1 & 0 \end{bmatrix}+\frac{1}{2}(1+\sigma)\tilde{B}K_v\right\}\dot{q}(t)+\begin{bmatrix} k_1 & 0 \\ 0 & k_2 \end{bmatrix}q(t)+\tilde{B}\tilde{f}(\dot{q}(t))=0$$

where $\tilde{f}(\dot{q}(t))=-\text{sat}\, f(t)+\frac{1}{2}(1+\sigma)f(t)$. The parameter σ and the matrices $\tilde{B}$ and $K_v(=K_v(C_v, G))$ are to be determined such that the controlled system under nonlinear perturbation $\tilde{f}(\dot{q}(t))$ is stable. To obtain an independent control, choose $K_v=\text{diag}[g_1, g_2]$ and $\tilde{B}=\text{diag}[g_3, g_4]$. The system can then be put in a state-space form as (30) with the following parameters:

$$\zeta_{c1}=\frac{(1+\sigma)g_3g_1+2c_1}{4\sqrt{m_1k_1}},\quad \zeta_{c2}=\frac{(1+\sigma)g_4g_2+2c_2}{4\sqrt{m_2k_2}},$$

$$\omega_{c1}=\sqrt{\frac{k_1}{m_1}},\quad \omega_{c2}=\sqrt{\frac{k_2}{m_2}}.$$

From Fig. 2, the nonlinear perturbation is bounded by

$$\|\tilde{f}(\dot{q}(t))\| \le \frac{1}{2}(1-\sigma)\|f(t)\| \le \frac{1}{2}(1-\sigma)\|K_v\Lambda^{1/2}\|\,\|v(t)\|, \quad \text{for } \sigma \in [0, 1] \tag{36}$$

where $\Lambda=\text{diag}[\omega_{c1}, \omega_{c2}]$, $v(t)=\Lambda^{-1/2}\dot{q}(t)$. Note that the permissible range of $f_i(t)$ can be found such that (36) holds. From Fig. 2, we see that the maximum permissible control force $f_i(t)$ occurs at $\bar{f}_i=\sigma f_i(t)$, i.e., the permissible range of $f_i(t)$ is limited by $|f_i(t)| \le \bar{f}_i/\sigma$. Therefore, the inequality (36) holds for

$$|f_i(t)| \le \bar{f}_i/\sigma,\ i=1, 2.$$

Obviously, if $\sigma \to 0$, the control forces allow to be infinite, and the corresponding nonlinear perturbation bound approaches to its upper limit 0.5, whereas the size of the nonlinear perturbation approaches to zero for $\sigma \to 1$. From (36), we can obtain

$$\|F_c(x(t))\| \le \frac{1}{2}(1-\sigma)\left(\frac{g_3}{\sqrt{m_1k_1}}, \frac{g_4}{\sqrt{m_2k_2}}\right)\max\left(g_1\sqrt{\frac{k_1}{m_1}}, g_2\sqrt{\frac{k_2}{m_2}}\right)\|x(t)\|.$$

Letting $\zeta_{ci}<1$ and referring to (33), a stabilizing controller can be found if

$$\min\left[\frac{(1+\sigma)g_3g_1+2c_1}{4m_1}, \frac{(1+\sigma)g_4g_2+2c_2}{4m_2}\right]-\sqrt{\frac{2}{1-\zeta}}\left\{\epsilon\cdot\max\left(\sqrt{\frac{k_1m_2}{k_2m_1}}, \sqrt{\frac{k_2m_1}{k_1m_2}}\right)+\frac{1}{2}(1-\sigma)\max\left(\frac{g_3}{\sqrt{m_1k_1}}, \frac{g_4}{\sqrt{m_2k_2}}\right)\max\left(g_1\sqrt{\frac{k_1}{m_1}}, g_2\sqrt{\frac{k_2}{m_2}}\right)\right\}>0$$

where $\zeta=\max(\zeta_{c1}, \zeta_{c2})$.

A more detailed design procedure without considering plant perturbations for the independent modal-space control was given by Inman (1989).

VI Discussions

(*a*) It should be pointed out that the approach presented restricts our main results which are appropriate for near normal mode systems, i.e., the constraint $\|\hat{A}\|<\beta/m$ described in Remark 3 should be followed. However, the considered dynamic system model is sufficient to describe most of simplified structure models. Specially, some lightly damped cases such as large flexible structures (Ashley, 1984; Alturi and Amos, 1988) are the typical examples. In fact, the actual form of damping in mechanical structures is not always clearly known. The form of modal damping is still an elusive topic of much of the current research (Goldstein and Rosencrans, 1980; Chen and Russel, 1982) and several texts (for instance, Nashif et al., 1985). In practice, modal damping is often estimated by using equivalent viscous proportional damping as an approximation.

(*b*) Since the l_1 vector norm and its corresponding induced matrix norm make the computations quite easy by dispensing with troublesome eigenvalue evaluations, $l_1(0, \infty)$-stability analysis for perturbed mechanical structures is adopted. However, as far as stability is concerned, over a semi-infinite interval $[0, \infty)$, other kinds of function norm are suitable (Chen, 1984). In general, the sharpness of the sufficient conditions (21) and (33) varies with the chosen norm. That is, it is possible that with some norm one can conclude stability, while with others the stability will not hold. The freedom in choosing a suitable norm to improve the conservatism of the stability condition corresponds to that in constructing an appropriate Lyapunov function for the well-documented Lyapunov approaches.

(*c*) Since norms were used to obtain the sufficient conditions (21) and (33), these criteria may be conservative in some cases. However, if the controller gains are selected such that

Downloaded 03 May 2010 to 171.66.16.248. Redistribution subject to ASME license or copyright; see http://www.asme.org/terms/Terms_Use.cfm

(33) holds, the overall system is guaranteed to be asymptotically and BIBO stable.

(*d*) In practice, mechanical structures require a large number of elastic modes to completely describe its dynamic behavior. For control design purposes, this means that a high order controller should be used. However, a reasonable size controller is desirable for actual operations. Further research is needed to address the issue on the reduced-order controller design for large space structures under nonlinear time-varying perturbations.

VII Conclusions

This paper has considered the stability and stabilization for a class of underdamped structures in the presence of nonlinear time-varying perturbations. Based on the induced norm, an upper norm-bound of the state transition matrix for a normal mode system is investigated. Sufficient conditions have been derived for asymptotic stability and BIBO stability of a perturbed structure with and without control. A simple relationship between the dominant eigenvalue of the unperturbed system and perturbation bounds is explicitly established in the derived stability condition. Illustrative examples for a mechanical structure containing nonlinear springs and a practical modal control system with saturated actuators are used to demonstrate the applications of our results.

References

Alturi, S. N., and Amos, A. K., 1988, *Large Space Structures: Dynamics and Control*, Springer-Verlag, New York.

Ashley, M., 1984, "On Passive Damping Mechanisms in Large Space Structures," *AIAA J. Spacecraft*, Vol. 21, pp. 448–455.

Caughey, T. K., and O'Kelly, M. E. J., 1965, "Classical Normal Modes in Damped Linear Dynamic Systems," ASME JOURNAL OF APPLIED MECHANICS, Vol. 32, pp. 583–588.

Chen, C. T., 1984, *Linear System Theory and Design*, Holt, Rinehart and Winston, New York.

Chen, G., and Russell, D. L., 1982, "A Mathematical Model for Linear Elastic Systems with Structural Damping," *Quart. Appl. Math.*, pp. 433–454.

Chen, Y. H., and Hsu, C., 1988, "Structural Decomposition Approach for the Stability of Uncertain Dynamic Systems," ASME JOURNAL OF APPLIED MECHANICS, Vol. 55, pp. 992–994.

Desoer, C. A., and Vidyasagar, M., 1975, *Feedback Systems: Input-Output Properties*, Academic Press, New York.

Doyle, J. C., and Stein, G., 1981, "Multivariable Feedback Design: Concepts for a Classical/Modern Synthesis," *IEEE Trans. Auto. Control*, Vol. AC-26, pp. 4–16.

Franklin, J. N., 1968, *Matrix Theory*, Prentice-Hall, Englewood Cliffs, N. J.

Goldstein, S. J., and Rosencrans, S. I., 1980, "Energy Decay and Partition for Dissipative Wave Equations," *J. Differential Equations*, Vol. 36, pp. 66–73.

Hughes, P. C., and Skelton, R. E., 1980, "Controllability and Observability of Linear Matrix-Second-Order Systems," ASME JOURNAL OF APPLIED MECHANICS, Vol. 47, pp. 415–420.

Inman, D. J., 1989, *Vibration with Control Measurement and Stability*, Prentice-Hall, Englewood Cliffs, N. J.

Leipholz, H. H. E., 1983, "Stability of Dynamic Systems," ASME JOURNAL OF APPLIED MECHANICS, Vol. 50, pp. 1086–1096.

Nashif, A. D., Jones, D. I. G., and Henderson, J. P., 1985, *Vibration Dampings*, John Wiley and Sons, New York.

Nicholson, D. W., 1987, "Response Bounds for Nonclassically Damped Mechanical Systems Under Transient Loads," ASME JOURNAL OF APPLIED MECHANICS, Vol. 54, pp. 430–433.

Patel, R. V., Toda, M., and Sridhar, B., 1977, "Robustness of Linear Quadratic State Feedback Designs in the Presence of System Uncertainty," *IEEE Trans. Auto. Control*, Vol. AC-22, pp. 945–949.

Pazy, A., 1983, *Semigroups of Linear Operators and Applications to Partial Differential Equations*, Springer-Verlag, New York.

Quinn, J. P., 1987, "On Russell's Method of Controllability via Stabilizability," *J. Opt. Theory Applic.*, Vol. 52, pp. 279–290.

Safonov, M. G., and Athans, M., 1977, "Gain and Phase Margins for Multiloop LQG regulators," *IEEE Trans. Auto. Control*, Vol. AC-22, pp. 173–179.

Shahruz, S. M., and Ma, F., 1988, "Approximate Decoupling of the Equations of Motion of Linear Underdamped Systems," ASME JOURNAL OF APPLIED MECHANICS, Vo. 55, pp. 716–720.

Vidyasagar, M., 1978, *Nonlinear Systems Analysis*, Prentice-Hall, Englewood Cliffs, N. J.

Yae, K. H., and Inman, D. J., 1987, "Response Bounds for Linear Underdamped Systems," ASME JOURNAL OF APPLIED MECHANICS, Vol. 54, pp. 419–423.

Downloaded 03 May 2010 to 171.66.16.248. Redistribution subject to ASME license or copyright; see http://www.asme.org/terms/Terms_Use.cfm

On Energy Rate Theorems for Linear First-Order Nonholonomic Systems

John G. Papastavridis
Georgia Institute of Technology,
School of Mechanical Engineering,
Atlanta, GA 30332

Starting with the Boltzmann/Hamel equations of motion of mechanical systems subject to general linear and first-order nonholonomic and rheonomic constraints, and in nonholonomic coordinates, this paper derives the general (reactionless) energy rate, or power, equation for such systems, in a straightforward and physically clear fashion. A power (reaction-containing) equation for these systems, but in holonomic coordinates, is also derived for completeness. An example of a sphere rolling on a uniformly spinning plane serves to illustrate these power theorems. The paper extends and corrects the recent work by Kane and Levinson (1988) on the same topic.

1 Introduction and Overview

The equations of motion of discrete (or discretized) mechanical systems subject to linear and first-order nonholonomic and nonstationary (rheonomic) constraints, in either true (holonomic) or quasi (nonholonomic) coordinates are well known (see, e.g., Prange, 1935; Lur'e, 1968; or Neimark and Fufaev, 1972). Also, the general equation of energy rate, or power, or rate of work, of such systems in true coordinates is relatively well known (see e.g., Lur'e, 1968 (equation (7.2.4)); Bahar and Kwatny, 1986, (pp. 136–137)); a special case of it has been given by Kane and Banerjee (1983). What is less known is the formulation of the power equation, for these systems, in general quasi-coordinates and related quasi/nonholonomic variables. The detailed discussion of this general "nonholonomic coordinate power equation" (NPE) is the subject of this paper. Special cases of NPE have already been discussed by: (1) Neimark/Fufaev (1972, pp. 190–199), for stationary (scleronomic) holonomic and nonholonomic constraints, and (2) Kane/Levinson (1988), hereafter referred to as KL, for a special form of the nonholonomic constraints, in a manner that does not clearly reveal the physical structure of the problem. Also, the main result of KL, their equations (12), (13), (23)–(25), contains an error, which will be corrected, after explaining the reason for its occurrence. The general NPE case has been derived by Papastavridis (1987, equations (26), (27)) as a special result of a very general and simple time-integral, or "virial-like," identity. That discussion covers both linear and nonlinear (first-order) nonholonomic constraints, and several other useful theorems. Another little-known derivation of the general NPE, but in canonical (Hamiltonian) variables via the integral invariants of Poincaré and Cartan, and more, was given by Djukic (1976).

In what follows, this general NPE will be rederived directly from the equations of motion in nonholonomic variables, the Boltzmann/Hamel equations, in a natural and physically motivated fashion, similar in spirit to Neimark and Fufaev's. In the process some new insights, not contained in Papastavridis (1987), will be gained. The theorem will finally be applied to a simple nonholonomic and nonstationary example, in both true and quasi-variables. This exposition is, simultaneously, more general and conceptually clearer than that of KL and, in this process, will remove the earlier-mentioned error of that paper.

2 General Background

Consider a mechanical system S described by n holonomic, or Lagrangean, or true, generalized system positional parameters or coordinates $q = \{q_1, \ldots, q_n\}$, and subject to $m(<n)$ independent, integrable, or nonintegrable (= nonholonomic), velocity (or kinematical, or differential) constraints

$$\sum_{l=1}^{n} a_{dl}\,\dot{q}_l + a_d = 0 \quad [d = 1, \ldots, m(<n)]; \tag{1}$$

$$a_{dl} = a_{dl}(q, t),\ a_d = a_d(a, t)\text{: Given or known functions,} \tag{2}$$

and $\dot{q} = \{\dot{q}_1, \ldots, \dot{q}_n\}$ = holonomic generalized system velocities; $(\ldots)^{\cdot}$ = total time derivative. The kinematically admissible or possible (dq), and virtual (δq) forms of the constraints are given, respectively, by the Pfaffian forms

$$\sum_l a_{dl} dq_l + a_d\,dt = 0,\ \sum_l a_{dl}\,\delta q_l = 0; \tag{3,4}$$

i.e., equation (4) is a special equation (3) when $dt \to \delta t = 0$. The

Contributed by the Applied Mechanics Division of THE AMERICAN SOCIETY OF MECHANICAL ENGINEERS for publication in the JOURNAL OF APPLIED MECHANICS.

Discussion on this paper should be addressed to the Technical Editor, Prof. Leon M. Keer, The Technological Institute, Northwestern University, Evanston, IL 60208, and will be accepted until two months after final publication of the paper itself in the JOURNAL OF APPLIED MECHANICS. Manuscript received by the ASME Applied Mechanics Division, Feb. 20, 1989; final revision, Dec. 13, 1989.

Copyright © 1991 by ASME
Downloaded 03 May 2010 to 171.66.16.248. Redistribution subject to ASME license or copyright; see http://www.asme.org/terms/Terms_Use.cfm

system equations of motion in the q's are the well-known Routh/Voss equations:

$$E_l(T) = Q_l + Q_l^{(r)} \quad (l=1, \ldots, n), \tag{5}$$

where

$$E_l(\bullet\bullet\bullet) \equiv \frac{d}{dt}\left(\frac{\partial \bullet\bullet\bullet}{\partial \dot{q}_l}\right) - \frac{\partial \bullet\bullet\bullet}{\partial q_l} = \text{Euler/Lagrange operator}, \tag{6}$$

T = kinetic energy of S (relative to an inertial frame of reference)
$= T_2 + T_1 + T_0$,

T_α = part of T that is a homogeneous polynomial of degree α in the $\dot{q}$'s $-\alpha = 2, 1, 0$, in general, (7)

Q_l = holonomic generalized system impressed force, corresponding to q_l (or δq_l), (8)

$Q_l^{(r)}$ = same as Q_l but for the constraint (1)–(4)—caused system reaction
$= \sum_d \lambda_d a_{dl}$ ("ideal" reaction postulate), (9)

λ = $\{\lambda_1, \ldots, \lambda_m\}$ = Lagrangean multipliers.

3 The Power Equation in Holonomic Variables (HPE)

Multiplying equation (5) with $\dot{q}_l$ and summing over l (from 1 to n) while observing equation (1) and

$$\sum_l Q_l^{(r)} \dot{q}_l = \sum_l \left(\sum_d \lambda_d a_{dl}\right) \dot{q}_l = \sum_d \lambda_d \left(\sum_l a_{dl} \dot{q}_l\right)$$
$$= \sum_d \lambda_d (-a_d) \quad (d=1, \ldots, m),$$

yields, after some simple differentiations,

$$\frac{d}{dt}\left(\sum_l \frac{\partial T}{\partial \dot{q}_l} \dot{q}_l - T\right) = -\frac{\partial T}{\partial t} + \sum_l Q_l \dot{q}_l - \sum_d \lambda_d a_d. \tag{10}$$

If part of the Q_l (or even the entire Q_l) equals $-\partial V/\partial q_l$, where $V = V(q, t)$ = potential function, then equation (10) reduces to the most general HPE:

$$\frac{dh}{dt} = -\frac{\partial L}{\partial t} + \sum_l Q_l \dot{q}_l - \sum_d \lambda_d a_d, \tag{11}$$

where now

$$h \equiv \sum_l \frac{\partial L}{\partial \dot{q}_l} \dot{q}_l - L = h(t, q, \dot{q})$$

= Generalized Energy [when a function of t, q, and $p_l \equiv \partial T/\partial \dot{q}_l$ = generalized holonomic system momentum, it is called Hamiltonian H: $H = H(t, q, p) = h = h(t, q, \dot{q})$]; the Q_l in equation (11) comprise only the nonpotential parts of the impressed forces.

Application of "Euler's homogeneous function theorem" to h yields

$$h = L_2 - L_0, \text{ or } h = T_2 + (V - T_0), \tag{12}$$

where $L = L(t, q, \dot{q}) = T(t, q, \dot{q}) - V(t, q)$ = Lagrangean function
$= L_2 + L_1 + L_0$(as in T_α);

$$L_2 = T_2, L_1 = T_1, L_0 = T_0 - V^1. \tag{13}$$

Special Cases: (*a*) If the constraints equation (1) are catastatic, i.e., $a_k = 0$ [although there might still be $a_{kl} = a_{kl}(q, t)$], (*b*) If, further, all the nonpotential Q_l's vanish — or if they are "gyroscopic," and (*c*) if, finally, the Lagrangean is time-independent $\partial L/\partial t = 0$ (although neither $\partial T/\partial t$ nor $\partial V/\partial t$ have to be zero individually), then equation (11) results into the following "Jacobi/Painlevé" integral

$$h = T_2 + (V - T_o) = \text{constant}. \tag{14}$$

Of course, circumstances other than (*a*, *b*, *c*) above can nullify the right side of equation (11) and thus reproduce equation (14).

Remark: It is pointed out here that the equality

$$\sum_l E_l(L)\dot{q}_l = \dot{h} + \frac{\partial L}{\partial t}, \tag{15}$$

is a purely analytical result that holds always, independently of any equations of motion and/or constraints.

4 The General Nonholonomic Coordinate, or Boltzmann/Hamel (BH) Equations of Motion

There are two drawbacks in the use of both equations (5) and (11): (1) They contain the multipliers λ; hence, the need for reactionless equations for both motion and power. (2) They do not distinguish whether the constraint equations (1)–(4) are truly nonholonomic, or simply holonomic ones in differential form. The equations of Boltzmann/Hamel, (from 1902–1903) constitute the most general and intellectually satisfying method to overcome these drawbacks, and a lot more; their conceptual simplicity and usefulness is evident in theoretical arguments, such as conservation theorems (i.e., the subject of this paper), differential-geometric/tensorial aspects of dynamics, or group-theoretic properties of the equations of motion; Appell's equations would not be suitable for energy considerations, since they explicitly involve accelerations. On the other hand, the BH equations are not the simplest ones for concrete problems of multibody dynamics, and this may, perhaps, explain their relative unfamiliarity among engineers. However, the general form of the (Heun/Hamel) Central Principle in quasi-variables seems to be the best single equation for both theoretical as well as applied situations (see Hamel, 1949, pp. 480–481, equation (I)). Finally, the presentation of the BH equations in direct/matrix notation does not promote their understanding and usefulness; indicial, and eventually tensorial notation is the ideal tool; in addition, the almost complete absence of any mention of the fundamental transitivity relations (see equation (22)), among English language expositions, contributes to the unjustified perception of the BH equations as being too laborious. The general BH equations are:

$$E_i^*(T^*) - \Gamma_i = \Theta_i \quad (i = m+1, \ldots, n:$$
independent quasi-velocities (see below)). (16)

Here:

$$E_i^*(\bullet\bullet\bullet) \equiv \frac{d}{dt}\left(\frac{\partial \bullet\bullet\bullet}{\partial \omega_i}\right) - \frac{\partial \bullet\bullet\bullet}{\partial \theta_i}$$
$$= \text{nonholonomic Euler/Lagrange operator}, \tag{17}$$

$T^* = T[t, q, \dot{q}(t, q, \omega)] \equiv T^*(t, q, \omega)$
(function of t, q, and all the ω's) $= T_2^* + T_1^* + T_0^*$
(T_α^*: homogeneous of degree α in the ω's), see below;
similarly for any function $f(\bullet\bullet\bullet\dot{q}\bullet\bullet\bullet) \to f^*(\bullet\bullet\bullet\omega\bullet\bullet\bullet)$, (18)

$$-\Gamma_i = \sum_{j=m+1}^{n+1} \sum_{l=1}^{n} \gamma_{ij}^l P_l \omega_j$$
$$= \text{nonholonomic "Corrective Terms"}, \tag{19}$$

[1] Extensions to "generalized (gyroscopic) potentials" $V = V(t, q, \dot{q})$, $Q_l = E_l(V)$, are easily obtainable.

Downloaded 03 May 2010 to 171.66.16.248. Redistribution subject to ASME license or copyright; see http://www.asme.org/terms/Terms_Use.cfm

$$P_l \equiv \frac{\partial T^*}{\partial \omega_l} = \text{nonholonomic generalized system (quasi-)}$$

$$\text{momentum} = P_l(t, q, \omega) \tag{20}$$

$$\frac{\partial(\bullet\bullet\bullet)}{\partial \theta_i} \equiv \sum_{l=1}^{n} \frac{\partial(\bullet\bullet\bullet)}{\partial q_l} \frac{\partial \dot{q}_l(t, q, \omega)}{\partial \omega_i} = \sum_{l=1}^{n} A_{li} \frac{\partial(\bullet\bullet\bullet)}{\partial q_l}$$

= symbolic or "quasi-" chain rule (see equation (36)), (21)

$\gamma^l_{ij} = -\gamma^l_{ji}$ = Ricci/Boltzmann/Hamel "three-index symbols" = Coefficients of $(\bullet\bullet\bullet)\ d\theta \bullet \delta\theta$ in the following transitivity relations (Hamel's "Uebergangsgleichungen"):

$$d(\delta\theta_l) - \delta(d\theta_l) = \sum_{i=m+1}^{n+1} \sum_{j=m+1}^{n+1} \gamma^l_{ij}\, d\theta_j\, \delta\theta_i \quad (l = 1, \ldots, n; n+1), \tag{22}$$

or, equivalently (see equation (54)),

$$(\delta\theta_l)^{\cdot} - \delta\omega_l = \sum_{i,\, i'} \gamma^l_{ii'}\, \omega_{i'} \delta\theta_i + \sum_i \gamma^l_i\, \delta\theta_i \tag{22a}$$

($i, i' = m+1, \ldots, n$: independent quasivelocities index; $l = 1, \ldots, n$) and, finally, the quasi-coordinates $\theta = \{\theta_1, \ldots, \theta_n; \theta_{n+1} = t\}$, and quasi-velocities $\omega = \{\omega_1, \ldots, \omega_n; \omega_{n+1}\}$, with the symbolic derivative[2]

$$\omega \equiv d\theta/dt = \dot{\theta} \tag{23}$$

(since, in general, no θ exists!), are introduced by

$$\begin{cases} \omega_d \equiv \sum_{l=1}^{n} a_{dl}\dot{q}_l + a_d = 0 \quad (d = 1, \ldots, m\text{: dependent } \omega), & (24) \\ \omega_i \equiv \sum_l a_{il}\dot{q}_l + a_i \neq 0 \quad (i = m+1, \ldots, n\text{: independent } \omega), & (25) \\ \omega_{n+1} \equiv \dot{q}_{n+1} \equiv \dot{t} = 1, & (26) \end{cases}$$

or by their kinematically admissible or possible and virtual forms, respectively,

$$\begin{cases} d\theta_d \equiv \sum_l a_{dl}\, dq_l + a_d\, dt = 0, & (27) \\ d\theta_i \equiv \sum_l a_{il}\, dq_l + a_i\, dt \neq 0, \quad d\theta_{n+1} \equiv dq_{n+1} \equiv dt \neq 0, & (28,29) \end{cases}$$

and

$$\begin{cases} \delta\theta_d \equiv \sum_l a_{dl}\, \delta q_l = 0, & (30) \\ \delta\theta_i \equiv \sum_l a_{il}\, \delta q_l \neq 0, \qquad \delta\theta_{n+1} \equiv \delta q_{n+1} \equiv \delta t = 0; & (31,32) \end{cases}$$

for consistency, one could have written

$$a_{l,n+1} \equiv a_l \ (l = 1, \ldots, n);\ a_{n+1,\,l} \equiv \delta_{n+1,\,l} \text{ (Kronecker delta: } l = 1, \ldots, n;\ n+1). \tag{33}$$

The position of the index γ^l does not imply any tensorial properties, but it is used here to stress the skew-symmetry of the γ's in i,j; however, that would be its correct position in a rigorous tensorial treatment. Direct expressions for the γ's appear frequently in the literature (e.g., Whittaker, 1937, pp. 41–44); nevertheless, equation (22) is still their best theoretical and practical definition. Another oft-unnoticed advantage of equation (22), over the direct definition of γ, is this: since the constraint equations (24, 27, 30) can be enforced in equation (22), the latter yields only those γ's that are needed in the reactionless BH equations (16) and no more; the direct definition yields those γ's and additional ones not needed in equation (16); of course, by postponing the satisfaction of the constraints in equation (22) for the final stage, one can obtain all the γ's needed for reaction-containing equations, if so desired (see equations (52)). Accounts of these general nonholonomic and rheonomic equations of motion, equations (16)–(33), are virtually nonexistent in the entire literature in the English language. For the nonholonomic impressed forces Θ_i see equations (44–49) below.

Remarks: (*a*) The vanishing of a particular $\gamma^l \ldots, \ldots$ in a given set of $\omega/d\theta/\delta\theta$, for all values of its two subscripts, in equation (22), is the necessary and sufficient (Frobenius integrability) condition(−s) for θ_l in the Pfaffian forms equations (27)–(28) to be a true, or genuine, or holonomic coordinate, in that set. It also shows that: even though $\dot{\theta}_d \equiv \omega_d = 0$, $d\theta_d = 0$, $\delta\theta_d = 0$ $(d = 1, \ldots, m)$, yet, in general, $d(\delta\theta_d) - \delta(d\theta_d) \neq 0$, $(\delta\theta_d)^{\cdot} - \delta\omega_d \neq 0$! (*b*) The matrix $\mathbf{a} \equiv (a_{kl};\ k, l = 1, \ldots, n$, and $n+1)$ in equation (24)–(34), consists of the original $(m) \times (n+1)$ constraint matrix of equation (1), plus a proper "enlargement"—see equations (36)–(41)—so that it finally becomes a $(n+1) \times (n+1)$ matrix

$$\mathbf{a} = \begin{pmatrix} a_{11} & \bullet\bullet\bullet & a_{1n} & a_1 \\ \vdots & & \vdots & \vdots \\ a_{n1} & \bullet\bullet\bullet & a_{nn} & a_n \\ 0 & \bullet\bullet\bullet & 0 & 1 \end{pmatrix}. \tag{34}$$

(*c*) The constraints are now simply

$$\omega_d = 0, \text{ or } d\theta_d = 0, \text{ or } \delta\theta_d = 0; \tag{35}$$

if $m = 0$, then the above represents the equations of motion of a holonomic system, but in nonholonomic coordinates (e.g., Euler's rigid-body equations). If, however, all the γ's vanish, then equations (1) are really holonomic (integrable) in differential form; then equation (16) reduce to a "holonomic form" of Maggi's reactionless equations (see, e.g., Prange, 1935, pp. 533–535)). (*d*) The constraint equation (35) must be enforced in equation (16), etc. only after all the differentiations have taken place; hence the need for T^* as a function of all the ω's, even if no constraint reactions are sought. In $E^*_i(T^*)$, T^* can be replaced, right from the start with $(T^*)_o \equiv T^*(t, q; \omega_d = 0, \omega_i) = T^*(t, q; \omega_i)$, but not in the $-\Gamma_i$ term; l in equation (19) runs from 1 to n.

Inverting, next, equations (24)–(32) yields, respectively,

$$\dot{q}_l = \sum_i A_{li}\, \omega_i + A_l;\ dq_l = \sum_i A_{li}\, d\theta_i + A_l dt;\ \delta q_l = \sum_i A_{li}\, \delta\theta_i, \tag{36,37,38}$$

where the matrices $\mathbf{a}$ and $\mathbf{A}$

$$\mathbf{A} = \begin{pmatrix} A_{11} & \bullet\bullet\bullet & A_{1n} & A_1 \\ \vdots & & \vdots & \vdots \\ A_{n1} & \bullet\bullet\bullet & A_{nn} & A_n \\ 0 & \bullet\bullet\bullet & 0 & 1 \end{pmatrix} \tag{39}$$

are inverse. For consistency, one could have also written

$$A_{l,n+1} \equiv A_l \ (l = 1, \ldots, n);$$

$$A_{n+1,l} \equiv \delta_{n+1,l} \ (l = 1, \ldots, n;\ n+1). \tag{40,41}$$

Equations (25), (28), (31) are arbitrary, except that when these ω, $d\theta$, $\delta\theta$ values are inserted back into equations (36)–(38), respectively, they satisfy them identically; one thus has a certain "$(n-m)$-freedom" in choosing convenient ω_i, $d\theta_i$, $\delta\theta_i$. Next, some relations among holonomic and nonholonomic variable quantities are in order: (*a*) the chain rule and equations (36)–(38) produce the following vector-like transformations:

$$P_l \equiv \frac{\partial T^*}{\partial \omega_l} = \sum_{k=1}^{n} \frac{\partial T}{\partial \dot{q}_k} \frac{\partial \dot{q}_k}{\partial \omega_l} = \sum_{k=1}^{n} A_{kl}\, p_k, \tag{42}$$

and its inverse

[2]Other authors use $\overset{*}{\theta}$ or $\overset{\circ}{\theta}$, instead of $\dot{\theta}$

Downloaded 03 May 2010 to 171.66.16.248. Redistribution subject to ASME license or copyright; see http://www.asme.org/terms/Terms_Use.cfm

$$p_k = \sum_{l=1}^{n} a_{lk} P_l, \ (k, l = 1, \ldots, n). \tag{43}$$

(b) The invariance of the virtual impressed work, $\delta' W$, between δq and $\delta\theta$ yields

$$\delta' W \equiv \sum_{l=1}^{n} Q_l \delta q_l = \sum_{l} Q_l \left(\sum_{i=m+1}^{n} A_{li} \delta\theta_i \right) \equiv \sum_{i} \Theta_i \, \delta\theta_i, \tag{44}$$

where

$$\Theta_i \equiv \sum_{l} A_{li} \, Q_l \quad (i = 1, \ldots, m; \ m+1, \ldots, n) \tag{45}$$

= nonholonomic generalized system impressed forced corresponding to $\delta\theta_i$, and, inversely, as if the constraints equation (35) did not exist,

$$Q_l = \sum_{k=1}^{n} a_{kl} \, \Theta_k, \tag{46}$$

while, (c), the invariance of the (zero) virtual constraint reaction work, $\delta' W^{(r)}$, between δq and $\delta\theta$, similarly produces

$$0 = \delta' W^{(r)} \equiv \sum_{l=1}^{n} Q_l^{(r)} \, \delta q_l = \ldots = \sum_{l=1}^{n} \Theta_l^{(r)} \, \delta\theta_l, \tag{47}$$

again as if no constraints existed, from which

$$\Theta_l^{(r)} = \sum_{k=1}^{n} A_{kl} \, Q_k^{(r)} \begin{cases} = \lambda_d \neq 0 \ (\delta\theta_d = 0) \ d = 1, \ldots, m; \\ = \lambda_i = 0 \ (\delta\theta_i \neq 0) \ i = m+1, \ldots, n \end{cases} \tag{48}$$

= nonholonomic generalized system reaction corresponding to $\delta\theta_l$ = (multipliers of equations (9)–(11)); inversely

$$Q_l^{(r)} = \sum_{k=1}^{n} a_{kl} \, \Theta_k^{(r)} = \sum_{d} a_{dl} \, \lambda_d \neq 0. \tag{49}$$

(d) Finally, the potential parts of the Θ_l equal $-\partial V/\partial\theta_l$, where again symbolically, as in equation (21),

$$\frac{\partial V}{\partial \theta_l} \equiv \sum_{k=1}^{n} \frac{\partial V}{\partial q_k} \frac{\partial \dot{q}_k}{\partial \omega_l} = \sum_{k=1}^{n} A_{kl} \frac{\partial V(t, q)}{\partial q_k}. \tag{50}$$

Then equation (16) holds with T^* replaced by

$$L^* \equiv T^* - V = L^*(t, q, \omega) = L_2^* + L_1^* + L_0^* = \text{nonholonomic variable Lagrangean} \tag{51}$$
$$(L_2^* = T_2^*, \ L_1^* = T_1^*, \ L_0^* = T_0^* - V).$$

Now, Θ_l stands for only the nonpotential part of the corresponding $\delta\theta_l$ coefficient (equation (44)).

Remark. For $d = 1, \ldots, m$, the BH equations are (see e.g., Lur'e, 1968, pp. 408–410):

$$E_d^*(T^*) - \Gamma_d = \Theta_d + \lambda_d. \tag{52}$$

Since equation (52) does contain reactions, it will not be used for the NPE; it could be used, however, to relate the holonomic equations (10), (11) with the nonholonomic one, to be derived next; such an indirect derivation will not be pursued here. This summary of the BH equations is, unavoidably, incomplete. The reader is thus strongly urged to get familiar with the quoted references.

5 The Power Equation in Nonholonomic Variables (NPE)

First, and recalling equation (26), the BH equations (16) are rewritten as[3]

$$\frac{d}{dt}\left(\frac{\partial L^*}{\partial \omega_i}\right) - \frac{\partial L^*}{\partial \theta_i} + \sum_{j=m+1}^{n} \sum_{l=1}^{n} \gamma_{ij}^{l} \, P_l \omega_j + \sum_{l=1}^{n} \gamma_i^l P_l = \Theta_i, \tag{53}$$

where

$$\gamma_{i,n+1}^{l} = -\gamma_{n+1,i}^{l} \equiv \gamma_i^l \text{ or, sometimes, } \epsilon_i^l \begin{pmatrix} l = 1, \ldots, n; \\ i = m+1, \ldots, n \end{pmatrix}. \tag{53a}$$

The third term (sum) on the left side of equation (53) represents the everpresent stationary/scleronomic nonholonomic coordinate contribution, whereas, the fourth such group represents the nonstationary/rheonomic ones. In what follows, each of the $(n-m)$ equations (53) will be multiplied with ω_i and then summed over i, from $m+1$ to n, and each term of that resulting single equation will be transformed in physically meaningful ways to give rise to the NPE: (a) For the first two terms of equations (53), this yields, successively,

$$\sum_{i} E_i^* \, (L^*) \, \omega_i = \sum_{i} \left\{ \frac{d}{dt}\left(\frac{\partial L^*}{\partial \omega_i}\right) - \frac{\partial L^*}{\partial \theta_i} \right\} \omega_i = \sum_{i} \left\{ \frac{d}{dt}\left(\frac{\partial L^*}{\partial \omega_i}\omega_i\right) - \frac{\partial L^*}{\partial \omega_i}\,\dot{\omega}_i - \frac{\partial L^*}{\partial \theta_i}\omega_i \right\}. \tag{a}$$

But since $L^* = L^*(t, q, \omega)$, and recalling equation (21), the third sum in (a) above transforms successively to

$$-\sum_{i} \frac{\partial L^*}{\partial \theta_i} \omega_i = -\sum_{i}\left(\sum_{l=1}^{n} \frac{\partial L^*}{\partial q_l} \frac{\partial \dot{q}_l}{\partial \omega_i}\right) \omega_i = -\sum_{l} \frac{\partial L^*}{\partial q_l}\left(\sum_{i} A_{li} \, \omega_i\right) \text{ (recalling equation (36))}$$
$$= -\sum_{l} \frac{\partial L^*}{\partial q_l}\left(\dot{q}_l - A_l\right) = -\sum_{l} \frac{\partial L^*}{\partial q_l} \dot{q}_l + \sum_{l} \frac{\partial L^*}{\partial q_l} A_l. \tag{b}$$

And inserting (b) back into (a) yields

$$\sum_{i} E_i^*(L^*)\omega_i = \sum_{i} \frac{d}{dt}\left(\frac{\partial L^*}{\partial \omega_i}\,\omega_i\right) - \sum_{l}\left(\frac{\partial L^*}{\partial q_l}\,\dot{q}_l + \frac{\partial L^*}{\partial \omega_l}\,\dot{\omega}_l\right) + \sum_{l} \frac{\partial L^*}{\partial q_l} A_l. \tag{c}$$

The second right-hand side of the (c) term, however, equals

$$-\left(\frac{dL^*}{dt} - \frac{\partial L^*}{\partial t}\right); \tag{d}$$

therefore, finally, (c) reduces to

$$\sum_{i} E_i^* \, (L^*)\omega_i = \frac{dh^*}{dt} + \frac{\partial L^*}{\partial t} + \sum_{l} \frac{\partial L^*}{\partial q_l} A_l, \tag{54}$$

where, recalling equation (51), h^* is the generalized energy in nonholonomic variables:

$$h^* \equiv \sum_{i} \frac{\partial L^*}{\partial \omega_i} \omega_i - L^* = T_2^* + (V - T_0^*). \tag{55}$$

Equations (54), with equation (55), is a general and purely analytical result that, like equation (15), holds always, independently of equations of motion; of course, when $m = 0$ then i in equations (54), (55) runs from 1 to n. Equations (54) and (15) coincide in form for catastatic constraints—if $a_l = 0$, then $A_l = 0$. (b) The third term of equations (53) multiplied by ω_i and summed over i vanishes due to the skew-symmetry (or gyroscopicity) of the γ_{ij}^l:

$$\sum_{i,j} \gamma_{ij}^{l} \, \omega_j \omega_i = 0. \tag{56}$$

[3]Since not all indices run through the same range, adoption of the well-known summation convention might lead to ambiguities

Downloaded 03 May 2010 to 171.66.16.248. Redistribution subject to ASME license or copyright; see http://www.asme.org/terms/Terms_Use.cfm

Collecting all these results produces the general NPE

$$\frac{dh^*}{dt} = -\frac{\partial L^*}{\partial t} + \sum_i \Theta_i \omega_i + R, \tag{57}$$

where R is the rheonomic nonholonomic power:

$$R \equiv -\sum_{l=1}^{n} \frac{\partial L^*}{\partial q_l} A_l - \sum_{l=1}^{n} \sum_{i=m+1}^{n} \gamma_i^l P_l \omega_i \equiv R_1 + R_2. \tag{58}$$

Contrary to equations (10), (11), this equation does not contain (unknown) multipliers. One notes that all the terms of equation (57), with the exception of R, have holonomic counterparts in equation (11). The R-term, therefore, merits a closer examination: one finds successively

$$(a)\ R_1 \equiv -\sum_l \frac{\partial L^*}{\partial q_l} A_l =$$

$$-\sum_l \frac{\partial L^*}{\partial q_l} \frac{\partial \dot{q}_l}{\partial \omega_{n+1}} \text{ (recalling equations (36), (26))} \equiv -\frac{\partial L^*}{\partial \theta_{n+1}}, \tag{59}$$

thus, extending equation (21), symbolically, to $i = n+1$; generally

$$\frac{\partial(\bullet\bullet\bullet)}{\partial \theta_{n+1}} \equiv \sum_{l=1}^{n} \frac{\partial(\bullet\bullet\bullet)}{\partial q_l} \frac{\partial \dot{q}_l}{\partial \dot{\theta}_{n+1}} = \sum_l A_l \frac{\partial(\bullet\bullet\bullet)}{\partial q_l}. \tag{60}$$

It should be noted that $\theta_{n+1} \equiv q_{n+1} = t$; nevertheless

$$\frac{\partial L^*}{\partial t} \neq \frac{\partial L^*}{\partial \theta_{n+1}}. \tag{61}$$

The reason for this is that the left member of equation (61) is the conventional partial derivative of $L^*(t, q, \omega)$ w.r.t. time t, and persists if, for example, the finite constraints are rheonomic, even if the $\omega \leftrightarrow \dot{q}$ transformation is scleronomic; whereas its right side, as equation (59) makes clear, results almost exclusively from the rheonomicity of equation (36)—specifically, their acatastaticity (A_l). Hopefully, no confusion will arise from these helpful notations.

Remarks. (*i*) Had one defined

$$\frac{d^*L^*}{dt} \equiv \sum_i \left(\frac{\partial L^*}{\partial \theta_i} \omega_i + \frac{\partial L^*}{\partial \omega_i} \dot{\omega}_i \right) + \frac{\partial L^*}{\partial t}, \tag{62}$$

instead of the "orthodox" one made here

$$\frac{dL^*}{dt} = \sum_l \left(\frac{\partial L^*}{\partial q_l} \dot{q}_l + \frac{\partial L^*}{\partial \omega_l} \dot{\omega}_l \right) + \frac{\partial L^*}{\partial t}, \tag{63}$$

then since

$$\frac{dL^*}{dt} - \frac{d^*L^*}{dt} = \bullet\bullet\bullet = \frac{\partial L^*}{\partial \theta_{n+1}} \tag{64}$$

($= 0$, for catastatic $\dot{q} \leftrightarrow \omega$ relations)[4] the power equation would be

$$\frac{dh^*}{dt} = -\frac{\partial L^*}{\partial t} + \sum_i \Theta_i \omega_i + R_2, \tag{65}$$

where now

$$\frac{dh^*}{dt} \equiv \frac{d}{dt}\left(\sum_i \frac{\partial L^*}{\partial \omega_i} \omega_i \right) - \frac{d^*L^*}{dt}. \tag{66}$$

Of course, both equations (57), (58) and (65), (66) are identical and correct, if properly interpreted. To facilitate comparison with KL, from now on equations (57)–(59) shall be considered as the definitive NPE. (*ii*) Other authors, e.g., Novoselov (1966, p. 21) and Johnsen (1941, pp. 34–35) adopt the following related (and perhaps formally better than (60)) definition of the partial "quasi-time" (t) derivative:

$$\frac{\partial(\bullet\bullet\bullet)}{\partial \theta_{n+1}} \equiv \frac{\partial(\bullet\bullet\bullet)}{\partial(t)}$$

$$\equiv \sum_{j=1}^{n+1} \frac{\partial(\bullet\bullet\bullet)}{\partial q_j} \frac{\partial \dot{q}_j}{\partial \omega_{n+1}} = \frac{\partial(\bullet\bullet\bullet)}{\partial t} + \sum_{l=1}^{n} A_l \frac{\partial(\bullet\bullet\bullet)}{\partial q_l}; \tag{67}$$

with definition equation (67) the NPE equation (57) would read simply

$$\dot{h}^* = -\frac{\partial L^*}{\partial(t)} + \sum_i \Theta_i \omega_i + R_2. \tag{67a}$$

Thus, $\partial(\bullet\bullet\bullet)/\partial(t)$ represents, roughly, the sum of holonomic and nonholonomic rheonomic contributions.[5] (*b*) The term R_2: It can be shown (see, e.g., Prange, 1935, p. 525; Lur'e, 1968, p. 24) that equation (22) leads to (recalling that $A_{n+1,s} = \delta_{n+1,s} = 0$, $\omega_{n+1} = 1$)

$$\gamma_i^l = \sum_{r=1}^{n} \sum_{s=1}^{n} \left(\frac{\partial a_{lr}}{\partial q_s} - \frac{\partial a_{ls}}{\partial q_r} \right) A_{ri} A_s + \sum_{r=1}^{n} \left(\frac{\partial a_{lr}}{\partial t} - \frac{\partial a_l}{\partial q_r} \right) A_{ri}$$

$$(l = 1, \ldots, n;\ i = m+1, \ldots, n). \tag{68}$$

This leads to the following conclusions:

(*b*.1) If $a_{l,n+1} \equiv a_l = 0$ (from which $A_{l,n+1} \equiv A_l = 0$), then $R_1 = 0$, and

$$R_2 \equiv -\sum_l \sum_i \gamma_i^l P_l \omega_i =$$

$$-\sum_l \sum_i \sum_r \left(\frac{\partial a_{lr}}{\partial t} A_{ri} \right) \left(\frac{\partial T^*}{\partial \omega_l} \omega_i \right), \text{ or finally}$$

$$R_2 = -\sum_{l,r} \frac{\partial a_{lr}}{\partial t} P_l \dot{q}_r \text{ (recalling equation (36))}. \tag{69}$$

(*b*.2) If, further, $a_{lr} = a_{lr}(q)$, then R_1, $R_2 \to 0$, and NPE reduces to

$$\frac{dh^*}{dt} = -\frac{\partial L^*}{\partial t} + \sum_i \Theta_i \omega_i. \tag{70}$$

(*b*.3) If, in addition, $\partial L^*/\partial t = 0$ (= stationary finite constraints) and $\Theta_i = 0$ (= no nonpotential forces), on if Θ_i = gyroscopic, then equation (70) leads to the nonholonomic-variable "Jacobi/Painlevé" integral (like equation (14))

$$h^* = T_2^* + (V - T_0^*) = \text{constant}. \tag{71}$$

For an alternative derivation of equation (71) via Noether's theorem in quasi-variables, and a lot more see Djukic (1974).

(*b*.4) One notices that R_1 derives from the rheonomic contributions of the differential constraints, whether these constraints are nonholonomic or holonomic; whereas, if all the constraints are holonomic ones in differential, or kinematical form, and since all the γ's will be zero, R_2 will vanish; i.e., R_2 derives from the rheonomicity of the genuinely nonholonomic constraints. For an outline of the extension of equations (57), (58) to nonlinear nonholonomic constraints, see Johnsen (1941, pp. 49–50). It is shown there that the Hamiltonian ($= h^*$, but in canonical nonholonomic variables) remains constant if: (*a*) h^* does not contain the time explicitly, and (*b*) the constraint equations $\dot{q} = \dot{q}(t, q, \omega)$ are homogeneous and linear in the ω's, and also explicitly independent of time; so, in general, no integral like equation (71) seems possible for nonlinear nonholonomic constraints.

[4] For an arbitrary function $f^*(t, q, \omega)$: $\sum_l \dot{q}_l \frac{\partial f^*}{\partial q_l} - \sum_i \omega_i \frac{\partial f^*}{\partial \theta_i} = \sum_l A_l \frac{\partial f^*}{\partial q_l}$

[5] Dobronravov (1976, p. 196) adopts the definition equation (60), and sets further $\frac{\bar{\partial}(\bullet\bullet\bullet)}{\partial t} \equiv \frac{\partial(\bullet\bullet\bullet)}{\partial t} + \frac{\partial(\bullet\bullet\bullet)}{\partial \theta_{n+1}} \left(\equiv \frac{\partial(\bullet\bullet\bullet)}{\partial(t)} \text{ of equation (67)} \right)$. Definition equation (60) keeps the holonomic and nonholonomic rheonomic contributions separate.

Downloaded 03 May 2010 to 171.66.16.248. Redistribution subject to ASME license or copyright; see http://www.asme.org/terms/Terms_Use.cfm

6 The KL Constraint Choice

KL choose the constraints, in the "Voronets-like" form

$$u_d = \sum_i B_{di}\, u_i + B_d \quad \begin{pmatrix} d=1, \ldots, m; \\ i=m+1, \ldots, n \end{pmatrix} \tag{72}$$

where these "intermediate" quasivelocities u (inappropriately referred by them as "generalized speeds") are related to the $\dot{q}$'s by the invertible and generally nonintegrable transformation (although these authors nowhere say anything about integrability or not but, instead, lump all the differential/kinematical, constraints together)

$$\dot{q}_l = \sum_{r=1} W_{lr}\, u_r + W_l = \sum_{r=1}^{m} \cdots + \sum_{r=m+1}^{n} \cdots + W_l = \sum_i C_{li}\, u_i + C_l; \tag{73}$$

$$C_{li} \equiv \sum_d W_{ld}\, B_{di} + W_{li},$$

$$C_l \equiv \sum_d W_{ld}\, B_d + W_l \ (l=1, \ldots, n). \tag{74,75}$$

Here, the $\{B_{di};\ B_d\}$, $\{W_{lr};\ W_l\}$ are given functions of, generally, all the q's and t; this "approximates" the KL notation (1988, equations (7, 8)). The constraint equations (72) are a special case of equation (24)–(26): (*a*) Inverting equations (73) yields

$$u_r = \sum_{l=1}^{n} D_{rl}\, \dot{q}_l + D_r \quad (r=1, \ldots, n), \tag{76}$$

where the matrices **W** and **D**, of equations (73), (76) are inverse. (*b*) Next, equation (72) in the equations (24)–(26) form reads:

$$\omega_d \equiv u_d - \sum_i B_{di}\, u_i - B_d = 0;$$

$$\omega_i \equiv u_i \neq 0;\ \omega_{n+1} \equiv 1; \tag{77,78,79}$$

i.e., the last $(n-m)$ u_i have been chosen as the independent quasivelocities. The inverses of equations (77)–(79) clearly are

$$u_d = \omega_d + \sum_i B_{di}\, u_i + B_d;$$

$$u_i = \omega_i;\ u_{n+1} = 1. \tag{77.1,78.1,79.1}$$

Inserting, next, the u_r from equation (76) into equations (77)–(79) finally yields the equations (24)–(26)-forms of the constraints equation (72):

$$\omega_d \equiv \sum_{l=1}^{n} a_{dl}\, \dot{q}_l + a_d = 0;$$

$$\omega_i \equiv \sum_{l=1}^{n} a_{il}\dot{q}_l + a_i \neq 0 \quad \begin{pmatrix} d=1, \ldots, m; \\ i=m+1, \ldots, n \end{pmatrix} \tag{79.2,79.3}$$

where

$$a_{dl} \equiv D_{dl} - \sum_i B_{di}\, D_{il};$$

$$a_d \equiv D_d - B_d - \sum_i B_{di}\, D_i. \tag{79.4,79.5}$$

Inverting equations (79.2)–(79.5) produces the equation (36)-form of the constraint. However, thanks to equation (78.1) it is clear that here

$$A_{li} \to C_{li},\ A_l \to C_l, \text{ of equation (75).} \tag{79.6}$$

Thus, **a**, **A** and therefore the γ_i^l of equation (68) and $\partial L^*/\partial\theta_{n+1}$ of equation (59) can be directly calculated from equations (72)–(75) and (79.4), (79.6). The equations (24), (27), (30) forms and their inverses are the natural or uncoupled forms of constraint representation, and are thus used in the better works on nonholonomic mechanics (e.g., Hamel, Prange, Dobronravov, Novoselov, Lur'e). Finally, the above immediately show that the KL condition equation (10), in this paper's (slightly different) notation,

$$\frac{\partial V}{\partial t} + \sum_{s=1}^{n} \frac{\partial V}{\partial q_s}\left(W_s + \sum_{d=1}^{m} W_{sd}\, B_d\right) = 0,$$

is (since $C_l \to A_l$) nothing but

$$\frac{\partial V}{\partial t} + \sum_{s=1}^{n} \frac{\partial V}{\partial q_s} A_s = \frac{\partial V}{\partial t} + \frac{\partial V}{\partial \theta_{n+1}}$$

$$\equiv \frac{\partial V}{\partial (t)} = 0 \text{ (recall equation (67)).}$$

7 An Example

A homogeneous sphere S, of mass m and radius r, rolls without slipping on a rough horizontal plane P. This latter spins about an axis perpendicular to it (vertical), OZ, with the constant[6] angular velocity ω. Derive and discuss the HPE and NPE.

If (x, y) are the coordinates of the contact point C, of S with P, measured relative to a space-fixed (or inertial) set of orthodextral axes O-XYZ (and such that O is both space and P-fixed, and P spins about OZ), then the velocity constraint is

$$(\bar{v}_c)_{\text{sphere}} = (\bar{v}_c)_{\text{plane}}, \tag{80}$$

or, with A = center of S, and $\bar{\omega}, \bar{\omega}_p$ = inertial angular velocities of S and P, respectively,

$$\bar{v}_A + \bar{\omega}\times\bar{r}_{c/A} = \bar{\omega}_p\times\bar{r}_{c/o}, \tag{81}$$

or finally in inertial components $\bar{v}_A = (\dot{x}, \dot{y}, 0)$, $\bar{r}_{c/A} = (0, 0, -r)$, $\bar{r}_{c/o} = (x, y, 0)$, $\bar{\omega} = (\omega_x, \omega_y, \omega_z)$, $\bar{\omega}_p = (0, 0, \omega)$,

$$\dot{x} - r\omega_y = -\omega y,\ \dot{y} + r\omega_x = +\omega x. \tag{82,83}$$

In view of equations (82), (83) the following six quasi-velocities ω_l are introduced

$$\begin{cases} \omega_1 \equiv \dot{x} - r\omega_y + \omega y = \dot{x} - r(\sin\phi\ \dot{\theta} - \sin\theta\ \cos\phi\ \dot{\psi}) + \omega y = 0, & (84) \\ \omega_2 \equiv \dot{y} + r\omega_x - \omega x = \dot{y} + r(\cos\phi\ \dot{\theta} + \sin\theta\ \sin\phi\ \dot{\psi}) - \omega x = 0, & (85) \end{cases}$$

$$\begin{cases} \omega_3 = \omega_x = (\cos\phi)\dot{\theta} + (\sin\theta\ \sin\phi)\dot{\psi} \neq 0, & (86) \\ \omega_4 = \omega_y = (\sin\phi)\dot{\theta} + (-\sin\theta\ \cos\phi)\dot{\psi} \neq 0, & (87) \\ \omega_5 = \omega_z = \dot{\phi} + (\cos\theta)\dot{\psi} \neq 0;\ \omega_6 \equiv \dot{q}_6 = \dot{t} = 1; & (88,89) \end{cases}$$

along with their inverses

$$\dot{q}_1 \equiv \dot{x} = \omega_1 + r\omega_4 - \omega y, \tag{90}$$

$$\dot{q}_2 \equiv \dot{y} = \omega_2 - r\omega_3 + \omega x, \tag{91}$$

$$\dot{q}_3 \equiv \dot{\phi} = (-\text{cotg}\theta\ \sin\phi)\ \omega_3 + (-\text{cotg}\theta\ \cos\phi)\ \omega_4 + \omega_5, \tag{92}$$

$$\dot{q}_4 \equiv \dot{\theta} = (\cos\phi)\ \omega_3 + (\sin\phi)\ \omega_4, \tag{93}$$

$$\dot{q}_5 \equiv \dot{\psi} = (\sin\phi/\sin\theta)\ \omega_3 + (-\cos\phi/\sin\theta)\ \omega_4;$$

$$\dot{q}_6 \equiv \dot{t} = \omega_6; \tag{94,95}$$

thus, the system has $n-m = 5-2 = 3$ degrees-of-freedom.[7] Here, ϕ, θ, ψ are the Eulerian angles (precession, nutation, and spin, respectively) defining the angular orientation of S relative to O-XYZ (see, e.g., Rosenberg, 1977, pp. 77–82). Next, the transitivity relations equations (22) or

$$(\delta\theta_l)^{\cdot} - \delta\omega_l = \sum_i \sum_j \gamma_{ij}^l\, \omega_j\, \delta\theta_i \quad (i=3, 4, 5;$$

$$j=3, 4, 5, \text{ and } 6;\ l=1, \ldots, 6), \tag{96}$$

[6]This case was chosen here for its algebraic simplicity. The general case $\omega = \omega(t)$, given function of time, can be discussed without any theoretical difficulty!

[7]The constancy of S's center from P is a holonomic constraint that can be integrated directly, independently of the other constraints and the equations of motion.

Downloaded 03 May 2010 to 171.66.16.248. Redistribution subject to ASME license or copyright; see http://www.asme.org/terms/Terms_Use.cfm

applied to equations (84)–(95) yield after some lengthy but straightforward $\delta(\bullet\bullet\bullet)/(\bullet\bullet\bullet)^{\cdot}$-operations

$$(\delta\theta_1)^{\cdot} - \delta\omega_1 = +r(\omega-\omega_5)\delta\theta_3 + (r\omega_3)\delta\theta_5 + \{(-1)\omega\delta\theta_2\}, \quad (97)$$

$$(\delta\theta_2)^{\cdot} - \delta\omega_2 = +r(\omega-\omega_5)\delta\theta_4 + (r\omega_4)\delta\theta_5 + \{(+1)\omega\delta\theta_1\}, \quad (98)$$

$$(\delta\theta_3)^{\cdot} - \delta\omega_3 = (-\omega_5)\delta\theta_4 + (\omega_4)\delta\theta_5, \quad (99)$$

$$(\delta\theta_4)^{\cdot} - \delta\omega_4 = (\omega_5)\delta\theta_3 + (-\omega_3)\delta\theta_5, \quad (100)$$

$$(\delta\theta_5)^{\cdot} - \delta\omega_5 = (\omega_3)\delta\theta_4 + (-\omega_4)\delta\theta_3, \quad (101)$$

$$(\delta\theta_6)^{\cdot} - \delta\omega_6 = (\delta t)^{\cdot} - \delta(\dot{t}) = 0 \text{ (always)}; \quad (102)$$

the ω-proportional terms in equations (97)–(98) are the (genuinely nonholonomic) rheonomic contributions. Equations (97)–(102) immediately show that the nonvanishing γ's are:

$$\gamma^1_{35} = -\gamma^1_{53} = r,\ \gamma^1_{36} = -\gamma^1_{63} = r\omega\ (=\gamma^1_3),$$

$$\{\gamma^1_{26} = -\gamma^1_{62} = -\omega(=\gamma^1_2)\}; \quad (103,104)$$

$$\gamma^2_{45} = -\gamma^2_{54} = r,\ \gamma^2_{46} = -\gamma^2_{64} = r\omega\ (=\gamma^2_4),$$

$$\{\gamma^2_{16} = -\gamma^2_{61} = +\omega(=\gamma^2_1)\}; \quad (105,106)$$

$$\gamma^3_{54} = -\gamma^3_{45} = 1;\ \gamma^4_{35} = -\gamma^4_{53} = 1;$$

$$\gamma^5_{43} = -\gamma^5_{34} = 1. \quad (107,108,109)$$

The γ's in equations (107)–(109), in effect, equal the "Levi-Civita permutation symbol" ϵ.... Only γ^1_3 and γ^2_4 will be utilized in the NPE. Using the well-known Koenig's theorem, one finds for the kinetic energy of S, relative to O-XYZ,

$$T = \frac{1}{2}m(\dot{x}^2 + \dot{y}^2) + \frac{1}{2}(I_x\,\omega_x^2 + I_y\,\omega_y^2 + I_z\,\omega_z^2), \quad (110)$$

where $I_x = I_y = I_z \equiv I = \frac{2}{5}mr^2$,

from which: (*a*) thanks to equations (86)–(88), in holonomic variables

$$T = \frac{1}{2}m(\dot{x}^2 + \dot{y}^2) + \frac{1}{2}I(\dot{\phi}^2 + \dot{\theta}^2 + \dot{\psi}^2 + 2\cos\theta\,\dot{\phi}\,\dot{\psi}) = T_2, \quad (111)$$

(this should come as no surprise; these q's are inertial), and (*b*) thanks to equations (90)–(94), in quasi-variables

$$T^* = \frac{1}{2}m\left\{(\omega_1 + r\omega_4 - \omega y)^2 + (\omega_2 - r\omega_3 + \omega x)^2\right\} + \frac{1}{2}I\left\{\omega_3^2 + \omega_4^2 + \omega_5^2\right\}, \quad (112)$$

from which, expanding,

$$T_2^* = \frac{1}{2}m\{\omega_1^2 + \omega_2^2 + r^2(\omega_3^2 + \omega_4^2) + 2r(\omega_1\,\omega_4 - \omega_2\,\omega_3)\} + \frac{1}{2}I\{\omega_3^2 + \omega_4^2 + \omega_5^2\}, \quad (113)$$

$$T_1^* = m\{(-y\omega)\,\omega_1 + (-ry\omega)\,\omega_4 + (x\omega)\,\omega_2 + (-rx\omega)\,\omega_3\}, \quad (114)$$

and

$$T_0^* = \frac{1}{2}m\omega^2(x^2 + y^2). \quad (115)$$

T_0^* = "centrifugal" kinetic energy i.e., kinetic energy of sphere when moving, at rest relative to the plane; similarly, T_2^* = kinetic energy of S even in the absence of the plane rotation ω, and T_1^* = kinetic energy of "coupling" of motion of P and S/P. Next: (*a*) V = constant; say, mgr. Therefore,

$\frac{\partial V}{\partial q_l} = 0$, from which and equation (50), $\frac{\partial V}{\partial \theta_l} = 0$; also,

$$\frac{\partial V}{\partial t}, \text{ and } \frac{\partial V}{\partial \theta_{n+1}} \equiv \sum_l \left(\frac{\partial V}{\partial q_l}\right) A_l = 0; \quad (116)$$

similarly, $\Theta_l = 0$, but $\Theta_1^{(r)}$, $\Theta_2^{(r)} \neq 0$ – see below; (117)

$$(b)\ \frac{\partial T^*}{\partial t} = \bullet\bullet\bullet = m\left\{\omega(x^2+y^2) - r(x\omega_x + y\omega_y)\right\}\dot{\omega} = 0$$

(here: ω = constant); (118)

$$(c)\ \frac{\partial T^*}{\partial \theta_{n+1}} \equiv \sum_{l=1}^{5}\frac{\partial T^*}{\partial q_l}A_l \text{ (from equations (110–115))}$$

$$= \left(\frac{\partial T^*}{\partial x}\right)A_1 + \left(\frac{\partial T^*}{\partial y}\right)A_2$$

$$= [(m\omega)(\omega x - r\omega_3)](-\omega y) + [(m\omega)(\omega y - r\omega_4)](\omega x) = mr\omega^2(y\omega_x - x\omega_y),$$

from which

$$R_1 = -\frac{\partial L^*}{\partial \theta_{n+1}} = -\frac{\partial T^*}{\partial \theta_{n+1}} = mr\omega^2(x\omega_y - y\omega_x); \quad (119)$$

$$(d)\ -R_2 \equiv \sum_l \sum_i \gamma^l_{i,6}\left(\frac{\partial T^*}{\partial \omega_l}\right)\omega_i$$

(This is the reason for not enforcing the constraints ω_1, $\omega_2 = 0$ on T^*)

$$= \gamma^1_{36}\omega_3 P_1 + \gamma^2_{46}\omega_4 P_2 + \left\{\gamma^1_{46}\omega_4 P_1 + \gamma^2_{36}\omega_3 P_2\right\}$$

(now the constraints can be enforced)

$$= (r\omega)(\omega_x)\left(\frac{\partial T^*}{\partial \omega_1}\right)_o + (r\omega)(\omega_y)\left(\frac{\partial T^*}{\partial \omega_2}\right)_o$$

$$= (r\omega\omega_x)[m(r\omega_y - \omega y)] + (r\omega\omega_y)[m(-r\omega_x + \omega x)]$$

$$= mr\,\omega^2(x\omega_y - y\omega_x). \quad (120)$$

Equations (119), (120) immediately show that

$$R \equiv R_1 + R_2 = 0, \quad (121)$$

i.e., in this problem, the rheonomic effects of the nonholonomic constraints equations (84), (85) cancel with each other! These results show that here the NPE reduces to the "generalized energy integral"

$$\dot{h}^* = 0 \rightarrow h^* = T_2^* - T_o^* = \text{ constant}, \quad (122)$$

with

$$T_2^* = \frac{1}{2}m\{r^2(\omega_3^2 + \omega_4^2)\} + \frac{1}{2}I(\omega_3^2 + \omega_4^2 + \omega_5^2)$$

$$= \frac{mr^2}{10}7\{\omega_x^2 + \omega_y^2) + 2\omega_z^2\}, \quad (123)$$

$$T_o^* = \frac{1}{2}m\omega^2(x^2 + y^2). \quad (124)$$

Substituting equations (123), (124) into equation (122) yields the nonholonomic Jacobi/Painlevé integral

$$7(\omega_x^2 + \omega_y^2) + 2\omega_z^2 = 5(\omega^2/r^2)(x^2 + y^2) + \text{constant}. \quad (122.1)$$

This was found without recourse to the equations of motion. It is instructive to confirm equation (122.1), or its equivalent

$$\dot{T}_2^* = \dot{T}_o^*, \quad (125)$$

directly from equations (123), (124)[8] and the equations of motion of the system, if the latter are available. This happens to be the case here: as Neimark/Fufaev show (1972, p. 134) these latter are the three reactionless equations ($i = 3, 4, 5, \rightarrow \omega_x, \omega_y, \omega_z$):

[8]Or from equations (113, 115, 116) which amounts to the same, since from $\omega_d = 0$, it follows that $\dot{\omega}_d = 0$, i.e., no "ω-gradient" terms.

Downloaded 03 May 2010 to 171.66.16.248. Redistribution subject to ASME license or copyright; see http://www.asme.org/terms/Terms_Use.cfm

$$\begin{cases} (7/5\ mr^2)\ \dot{\omega}_x - mr\omega(r\omega_y - \omega y) = \Theta_x \to 0, & (126) \\ (7/5\ mr^2)\ \dot{\omega}_y + mr\omega(r\omega_x - \omega x) = \Theta_y \to 0, & (127) \\ (2/5\ mr^2)\ \dot{\omega}_z = \theta_z \to 0, & (128) \end{cases}$$

from which

$$\dot{\omega}_x = (5/7)(\omega/r)(r\omega_y - \omega y);$$

$$\dot{\omega}_y = -(5/7)(\omega/r)(r\omega_x - \omega x);\ \dot{\omega}_z = 0; \quad (129,130,131)$$

also, from equations (84), (85), or (90), (91),

$$\dot{x} = r\omega_y - \omega y,\ \dot{y} = -r\omega_x + \omega x. \quad (132,133)$$

Differentiating now T_2^* from equations (113) or (123), while employing equations (129)–(131), yields:

$$\dot{T}_2^* = \frac{mr^2}{5}\{7(\omega_x\ \dot{\omega}_x + \omega_y\ \dot{\omega}_y) + 2\omega_z\ \dot{\omega}_z\}$$

$$= \bullet\bullet\bullet = mr\omega^2\ (x\omega_y - y\omega_x); \quad (134)$$

similarly, for T_o^*, while employing equations (132), (133):

$$\dot{T}_o^* = \underbrace{m\omega(x^2+y^2)\dot{\omega}}_{=0} + m\omega^2\ (x\dot{x} + y\dot{y})$$

$$= \bullet\bullet\bullet = mr\omega^2\ (x\omega_y - y\omega_x),\ \text{q.e.d.} \quad (135)$$

Therefore, the correctness of equations (122.1, 125) has been checked independently.

It is instructive to find the HPE, equation (11), of this problem: Here, $T = T_2$ is given by equation (111), V = constant, $Q_l = 0$ (no impressed nonpotential forces), and from equations (84)–(89) $a_1 \to a_x = \omega y$, $a_2 \to a_y = -\omega x$, while $\lambda_1 \to \lambda_x \equiv \Theta_1^{(r)}$, $\lambda_2 \to \lambda_y \equiv \Theta_2^{(r)}$ are the OX and OY components of the rolling/no slipping constraint reaction, from the plane P to the sphere S, at the contact point $C(x, y, 0)$. Thus, equation (11) yields here

$$\dot{h} = \dot{T}_2 = -a_1\ \lambda_1 - a_2\ \lambda_2 = -(\omega y)\ \lambda_x - (-\omega x)\ \lambda_y$$

$$= \omega(x\lambda_y - y\lambda_x) = M_o \cdot \omega, \quad (136)$$

$$M_o \equiv x\lambda_y - y\lambda_x$$

$$= \text{moment of rolling contact reaction about } OZ. \quad (137)$$

This is what one would have obtained with "elementary" (Newton/Euler) considerations: The sphere is an open system, and the rate of change of its total (inertial) energy

$$E \equiv T + V(=h) \quad (138)$$

must equal the power of the external forces to the sphere, here the constraint reaction, that is,

$$\dot{E} = M_o\omega. \quad (139)$$

The power of the normal component of the reaction is clearly zero; the externally supplied power $M_o\omega$ is what is needed to keep the plane P spinning with a constant ω. Finally, since by the theorem of linear momentum, applied to the sphere,

$$M_o = x\lambda_y - y\lambda_x = x(m\ddot{y}) - y(m\ddot{x}) = [m(x\dot{y} - y\dot{x})]^{\cdot} = \dot{H}_o, \quad (139.1)$$

where H_o = inertial angular momentum (about O) of a particle of mass m located at the sphere center A, and due to the ω-constancy, equation (139) immediately leads to the conservation equation

$$E - H_o\ \omega = \text{constant, or } T - H_o\ \omega = \text{constant.} \quad (139.2)$$

Remark: The fact that the HPE does not produce a conservation theorem, of the same form as the NPE equation (122) (although a physically equivalent one), should not come as a surprise. It is intimately connected with the choice of holonomic coordinates: if the q's were noninertial then the constraint would be

$$(\bar{v}_c) \text{ relative to plane-fixed axes } O\text{-}xyz = \bar{0},\ (Oz = OZ), \quad (140)$$

instead of equation (80), and therefore, the constraint components would be homogeneous in the noninertial holonomic generalized velocities, or catastatic, i.e., in that description a_1, $a_2 = 0$ — energy conservation is a concept that is both system (bodies + forces + constraints) and frame-of-reference dependent! The right side of equation (11), if everything else stayed the same, would then reduce to zero. But

$$T = T_2 + T_1 + T_0, \quad (141)$$

and therefore equation (11) would result in the "holonomic Jacobi/Painlevé integral"

$$T_2 - T_0 = \text{constant.} \quad (142)$$

If $\omega = \omega(t)$: general function of time, then $-\partial T/\partial t \neq 0$, on the right side of equation (11).

A convenient noninertial set of q's are: the two coordinates of S's center relative to a plane-fixed set of orthodextral axes O-xyz, and the three Eulerian angles that define the orientation of the sphere relative to these moving axes O-xyz: then the constraint equation (140) would lead to two homogeneous equations in the noninertial generalized velocities, identical in form to equations (82), (83), but with the right sides equal to zero; ω would not appear in these constraint equations, but it would appear in T. Only T has to be calculated relative to an inertial frame—here, O-XYZ. The rolling constraint, though, can be expressed relative to any convenient frame, in terms of any convenient set of kinematic parameters, inertial or not. As for the forces, in classical mechanics, they are objective, i.e., frame independent. Thus, analytical mechanics allows great flexibility in setting up constraints, and then obtaining equation of motion and power. On the frame dependence of kinematic constraints, see also Papastavridis (1989).

8 The KL Result: An Extension/Correction

This investigation was inspired by a desire to supply a formulation of the NPE that would, hopefully, be simultaneously simpler, more general and also conceptually more natural and physically motivated than the recent one by KL; a formulation *deriving directly from the general equations of motion* of Analytical Mechanics, just as in the Newton/Euler method. However, it was soon realized that considerably more than this was involved here: The final result of KL, their equations [12], [13], [23]–[25][9], seems to contain a serious theoretical error. Specifically, the entire term

$$R_2 \equiv -\sum_l \sum_i \gamma_i^l\ P_l\ \omega_i \quad (143)$$

is missing from their power equation, and nothing equivalent to it appears anywhere. In the notation of this paper, the KL power equations [24]–[25] would read

$$[T_2^* + (V - T_0^*)]^{\cdot} = -\frac{\partial T^*}{\partial t} - \frac{\partial T^*}{\partial \theta_{n+1}} + \sum_i \Theta_i\ \omega_i, \quad (144)$$

since these authors have assumed that[10]

$$\frac{\partial V}{\partial t} + \frac{\partial V}{\partial \theta_{n+1}} = 0. \quad (145)$$

Clearly, equation (144) is a subcase of equations (57), (58): it occurs when equation (145) and $R_2 = 0$ happen to be true. The KL equation (144) applied to the sphere example (which satisfies all the assumptions of that paper) would have given the incorrect equation

[9] Square brackets denote equations in the KL paper.

[10] A minor point: in their equations [9, 10], KL give the (incorrect) impression that equations (145) (their equation [10]) can always be satisfied. Later, between KL equations [21, 22] they begin to dispell this. Also, it seems that in their equations [24, 25] the summations on the left-hand sides of both these equations should be running from 1 to p, and not from 1 to n.

Downloaded 03 May 2010 to 171.66.16.248. Redistribution subject to ASME license or copyright; see http://www.asme.org/terms/Terms_Use.cfm

$$(T_2^* - T_0^*)^{\cdot} = -\frac{\partial T^*}{\partial \theta_{n+1}}\left(= -\sum_l \frac{\partial T^*}{\partial q_l} A_l = mr\omega^2\right.$$

$$\left.\times (x\omega_y - y\omega_x) = \dot{T}_0^* \neq 0, \text{ even for constant } \omega\right)$$

instead of the correct equations (122), (125).

Finally, the term R_2 should be expected on physical grounds: equations (16), (53), through their γ-terms, do provide for the distinction between holonomic rheonomic constraints disguised in differential, or kinematic, form and genuinely nonholonomic rheonomic constraints; and this provision is carried over into the power equation (57), (58). No matter what kind of reactionless and multiplierless equations of motion one starts with (e.g., equations of Maggi, Appell, BH[11]), the final NPE must contain either R_2 or something equivalent. No such provision appears in the KL formulation. It is when R_2 vanishes that the results of KL and this paper's coincide. All the equations of motion and power discussed in the paper of KL, as well as in their book referenced there (essentially those of Maggi and Appell in their several special forms), are of the kind that hold uniformly for any system under constraints like equation (1), whether these latter are integrable = holonomic, or nonintegrable = nonholonomic. For many problems this doesn't matter and may even be an advantage—not so for the power equation! The more "refined" equations of BH, that do this sort of discriminating, along with the related key concept of integrability versus nonintegrability of the kinematic constraints, are never examined. From a study of their book, this author realized that KL use the terms "kinematic" and "nonholonomic" [constraint (*s*)] synonymously. Such an unorthodox terminology is, at best, at odds with an entire established century-old tradition of dynamics and differential geometry. This tradition, created by such greats as Gibbs, Hertz, Hadamard, Volterra, Poincaré, Klein, Appell, Whittaker, Hamel, Schouten, Struik, Synge, Lur'e, et al., is full of important consequences in the theory and application of dynamics to concrete problems— and power equations.[12]

[11]The equations of Volterra, Chaplygin, Voronets, and Poincaré are all special cases of the BH equations.

[12]Most laymen would agree that there is, indeed, something qualitatively different between skating and walking!

References

Bahar, L. Y., and Kwatny, H. G., 1987, "Extension of Noether's Theorem to Constrained Nonconservative Dynamical Systems," *International Journal of Nonlinear Mechanics*, Vol. 22, pp. 125–138.

Djukic, D. S., 1974, "Conservation Laws in Classical Mechanics for Quasi-Coordinates," *Archive for Rational Mechanics and Analysis*, Vol. 56, pp. 79–98.

Djukic, D. S., 1976, "A Variational Principle Involving a Conditional Extremum for the Hamel-Boltzmann Equations of Motion," *Acta Mechanica*, Vol. 25, pp. 105–110.

Dobronravov, V. V., 1976, *Foundations of Analytical Mechanics* (in Russian), Vischaya Shkola, Moscow, p. 196.

Hamel, G., 1949, *Theoretische Mechanik*, Springer, Berlin, pp. 480–481.

Johnsen, L., 1941, "Dynamique Générale des Systémes Non-Holonomes," *Skrifter Utigitt Av Det Norske Videnskaps Akademi i Oslo, I. Mat. Naturv. Klass*, No. 4, pp. 1–75; pp. 12–14, 49–50.

Kane, T. R., and Banerjee, A. K., 1983, "A Conservation Theorem for Simple Nonholonomic Systems," ASME JOURNAL OF APPLIED MECHANICS, Vol. 50, pp. 647–651.

Kane, T. R., and Levinson, D. A., 1988, "A Method for Testing Numerical Integrations of Equations of Motion of Mechanical Systems," ASME JOURNAL OF APPLIED MECHANICS, Vol. 55, pp. 711–715.

Lur'e, A. I., 1968, *Mécanique Analytique*, Vols. I, II, (original in Russian, 1961), Librairie Universitaire, Louvain, Belgium, pp. 23–26, 408–410.

Neimark, J. I., and Fufaev, N. A., 1972, *Dynamics of Nonholonomic Systems*, (original in Russian, 1967), American Mathematical Society, Providence, R. I., pp. 120–128, 131–135.

Novoselov, V. S., 1966, *Variational Methods in Mechanics*, (in Russian), Leningrad University Press, Leningrad, p. 21.

Papastavridis, J. G., 1987, "Time-integral Theorems for Nonholonomic Systems," *International Journal of Engineering Science*, Vol. 25, No. 7, pp. 833–854.

Papastavridis, J. G., 1989, "On the Structure of Linear, First-Order Nonholonomic Constraints, and the Associated Reaction Forces," *International Journal of Engineering Science*, Vol. 27, No. 5, pp. 469–493.

Prange, G., 1935, "Die algemeinen Integrationsmethoden der analytischen Mechanik," *Encyklopaedie der Mathematischen Wissenschaften*, Vol. 4, Art's. 12 and 13, pp. 505–804; pp. 525, 534.

Rosenberg, R. M., 1977, *Analytical Dynamics of Discrete Systems*, Plenum Publishing, New York, p. 82.

Whittaker, E. T., 1937, *A Treatise on the Analytical Dynamics of Particles and Rigid Bodies* 4th ed., (Latest reprint 1988), Cambridge University Press, Cambridge, U. K., pp. 42–43.

Downloaded 03 May 2010 to 171.66.16.248. Redistribution subject to ASME license or copyright; see http://www.asme.org/terms/Terms_Use.cfm

Stability and Bifurcation Analysis of Oscillators With Piecewise-Linear Characteristics: A General Approach

Y. B. Kim[1]
Graduate Student.

S. T. Noah
Associate Professor,
Mem. ASME

Mechanical Engineering Department,
Texas A&M University,
College Station, TX 77843-3123

A general approach is developed for determining the periodic solutions and their stability of nonlinear oscillators with piecewise-smooth characteristics. A modified harmonic balance/Fourier transform procedure is devised for the analysis. The procedure avoids certain numerical differentiation employed previously in determining the periodic solutions, therefore enhancing the reliability and efficiency of the method. Stability of the solutions is determined via perturbations of their state variables. The method is applied to a forced oscillator interacting with a stop of finite stiffness. Flip and fold bifurcations are found to occur. This led to the identification of parameter ranges in which chaotic response occurred.

Introduction

Many mechanical systems experience intermittent motion of contact and separation due to existing clearances or gaps. Clearance may arise from manufacturing tolerances, wear, or backlash (Hongler et al., 1988), or are incorporated intentionally to accommodate lubrication or thermal expansion (Ko, 1985). Gaps are frequently included in various systems as an essential part of their design (Lee et al., 1982; Masri, 1965; Tung and Shaw, 1988). The complex dynamic responses within such systems, however, can produce adverse conditions of loss of performance and/or proper functioning (Bengisu et al., 1986; Smith et al., 1986). Better understanding of their complex dynamic behavior is vital for their proper design.

The equation of motion describing the motion of such systems includes abrupt variation of stiffness and damping coefficients which can be approximated as piecewise-linear, or more generally, as *piecewise-smooth systems* (Saito, 1985; Bryant, 1985). The systems are, in most cases, strongly nonlinear for which general analytical methods are usually not available.

Periodic Solutions. The intermittent motion of contact/separation in systems with clearances is frequently modeled as a vibro-impact problem (Whiston, 1979). This modeling lends itself to simpler analysis techniques and may produce good results for cases involving very high stiffness at the contact. This approach, however, does not yield information on the contact forces and durations of contact (Rogers and Pick, 1977), which may be relevant for the analysis of wear, fatigue, and deformation history of the components involved. Also, many systems involving intermittent contact can only be realistically modeled with finite stiffness (Kim and Noah, 1989).

An analytical approach to finding the steady-state response of forced piecewise-linear oscillators was proposed by Masri (1978) in which boundary values at the contact points are matched and the resulting nonlinear algebraic equations are then solved using an iterative method. Bapat et al. (1986) improved the solution method of the resulting nonlinear algebraic equations in Masri's approach. They employed a change of the nonlinear simultaneous equations to linear simultaneous equations by setting the duration of contact as a parameter when performing the numerical calculations. Further generalization of this approach was reported by Choi and Noah (1989). Maezawa (1962, 1969) used a Fourier expansion to represent the unknown contact forces as external forces. The forces are determined through enforcing periodicity, and therefore also obtaining the solutions sought. Unfortunately, such solution method based on assumed displacement and contact patterns often suffers restrictions. Unpredicted types of vibration, not included in the assumed response shapes, may be excluded. Furthermore, it is almost impossible to find the exact duration of contact for some parameters ranges because of the severe nonlinear nature of the relations involving the duration of contact.

An alternative approach based on harmonic balance, which is also applicable to the more general case involving piecewise-nonlinearity, was developed by Saito (1985). The method was applied to a modified Jeffcott rotor model with nonlinearly supported bearings with clearances. In that method, *both* the

[1]Presently a Researcher at Samsung Research Center, Giheung, South Korea.

Contributed by the Applied Mechanics Division of THE AMERICAN SOCIETY OF MECHANICAL ENGINEERS for presentation at the Joint Applied Mechanics/Bioengineering Conference, Ohio State University, Columbus, Ohio, June 16-19, 1991.

Discussion on this paper should be addressed to the Technical Editor, Prof. Leon M. Keer, the Technological Institute, Northwestern University, Evanston, IL 60208, and will be accepted until two months after final publication of the paper itself in the JOURNAL OF APPLIED MECHANICS. Manuscript received by the ASME Applied Mechanics Division, Aug. 24, 1989; final revision, Apr. 30, 1990.

Paper No. 91-APM-22.

Copyright © 1991 by ASME
Downloaded 03 May 2010 to 171.66.16.248. Redistribution subject to ASME license or copyright; see http://www.asme.org/terms/Terms_Use.cfm

displacements and support forces were represented by *separate* Fourier series. The physical relationships between the displacements and support forces were used to relate the coefficients of both expansions through discrete Fourier and inverse Fourier transform. This method was also utilized by Choi and Noah (1987) and is modified in the present paper *to eliminate the necessity of utilizing numerical differentiations of the force coefficients as originally suggested by Saito (1985)*. The method is also used to arrive at a perturbation of periodic solutions in order to determine their stability and the type of bifurcations.

It is stressed here that the use of separate Fourier expansions avoids the untractable problem of having to first determine the contact duration with the supports in order to perform a Galerkin's procedure involving integration with respect to time, as employed in the Incremental Harmonic Balance (IHB) approach (Lau et al., 1982). Difficulties would be experienced in calculating the exact contact time duration during iterations. This is the case since multiple contacts can be involved, and also since the incremental form of the equation using the IHB method for piecewise-linear systems involves a Heaviside step function which leads to complicated integration. This was, fortunately, *not* the case with the frictionally damped system treated by Pierre et al. (1985), where only a delta function was involved in the required integration. An alternative procedure based on a collocation approach was developed by Natarj and Nelson (1987). The method was utilized to determine the periodic solution of rotor systems with local nonlinearities.

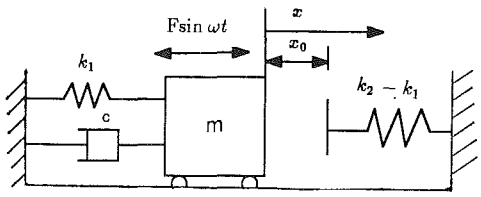

Fig. 1(*a*) The physical model

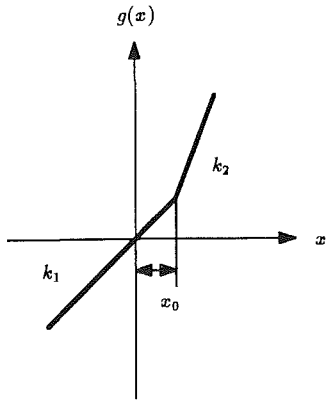

Fig. 1(*b*) Unsymmetric piecewise-linear restoring force

Stability and Bifurcation. Fewer studies were devoted to determining the stability of periodic solutions. Masri and Caughy (1966) performed the stability analysis by examining the propagation of arbitrary perturbations of the starting conditions within successive periodic crossing times between the piecewise-linear regions. Recently, Natsiavas (1989) conducted stability analysis using the aforementioned method of Masri and Caughy together with results from dynamical systems theory to present new results on the behavior of forced oscillators, with trilinear restoring forces. No approximations were made in determining symmetric, double-impact periodic responses and their bifurcations.

A different approach was published in an excellent paper by Shaw and Holmes (1983). The stability and bifurcation of a linear system with a gap were determined by examining the eigenvalues of the Jacobian matrix of a Poincaré map involving time of contact and velocity at each contact. The Poincaré section was taken at the location of contact. The elements of the matrix were obtained using implicit differentiation within the piecewise-linear regions. The approach proved to be exact in case of infinite contact stiffness (impact). However, it is only approximate for finite contact stiffness at the stop, where the time of contact was approximately estimated.

The disadvantages of the above methods in which piecing of the linear responses are employed is that an assumption has to be made *a priori* about the motion patterns in terms of the number of crossing to different regions per one cycle. This could result in very time consuming, error prone, laborious algebra in order to cover all possible cases of contact patterns. More importantly, a generalization to two-dimensional problems (e.g., cylinder motion within a gap) appears to be unfeasible. Needless to say, all the aforementioned approaches do not apply to piecewise-*nonlinear* systems.

The stability approach reported in the present paper is based on a perturbation of state variables and is in general capable of handling piecewise-nonlinear multidimensional systems (say, motion in a plane or three-dimensional space). For a simple illustration a forced linear oscillator interacting through a gap with a stop of a linear stiffness is considered. Both flip and fold bifurcations are determined for given sets of parameters. Period doubling bifurcations and the resulting chaos are shown to occur. The occurrence of chaos in such systems is demonstrated.

The new approach presented herein provides a versatile and systematic means for investigating the periodic solutions and their stability of systems with piecewise smooth stiffness characteristics, including those of two-dimensional and multi-degree-of-freedom systems. An advantage of the present approach is that its formulation is neither problem nor response pattern dependent, except for selecting the least appropriate numbers of harmonics for the Fourier expansions.

Harmonic Balance (Direct Newton-Raphson Procedure)

The governing equation of the example system consists of a mass, a viscous damper, and an unsymmetric piecewise-linear spring, which is excited harmonically, as shown in Fig. 1. As derived by Thompson and Elvey (1984), its nondimensional form is written as

$$\ddot{y}+\alpha\dot{y}+\nu^2 g^*(y)=\frac{\nu^2}{\eta^2}\sin\nu\theta \tag{1a}$$

where

$$g^*(y)=\begin{cases}\beta_1 y+h, & y\geq\delta;\\ \beta_2 y, & y<\delta\end{cases} \tag{1b}$$

in which $y(=xK/F)$ is a nondimensional displacement, $\beta_1\left(=\left(\frac{1+\sqrt{\sigma}}{2\eta}\right)^2\right)$ and $\beta_2\left(=\left(\frac{1+\sqrt{\sigma}}{2\eta\sqrt{\sigma}}\right)^2\right)$ are nondimensional equivalent stiffnesses, α is defined as $\nu\zeta/\eta$ where $\zeta(=c/2m\omega_n)$ is a nondimensional damping, ν is a subharmonic ratio with integer values, $\eta(=\omega/\omega_n)$ is a nondimensional frequency, $\delta(=x_0K/F)$ is a nondimensional gap, $h(=k_1x_0/F\eta^2)$ is a nondimensional constant force, and a dot represents a derivative with respect to the nondimensional time θ. In the above expressions, K is $4k_1k_2/(\sqrt{k_1}+\sqrt{k_2})^2$, ω_n is $\sqrt{K/m}$, ωt is $\nu\theta$, and σ has the value of k_1/k_2. A steady-state periodic solution and the corresponding nonlinear restoring force term may be represented as (Choi and Noah, 1988)

Downloaded 03 May 2010 to 171.66.16.248. Redistribution subject to ASME license or copyright; see http://www.asme.org/terms/Terms_Use.cfm

$$y(\theta)=a_0+\sum_{n=1}^{k}(a_n\cos n\theta-b_n\sin n\theta) \tag{2a}$$

$$g^*(\theta)=c_0+\sum_{n=1}^{k}(c_n\cos n\theta-d_n\sin n\theta) \tag{2b}$$

in which the coefficient a_0, b_0, ... are unknowns to be determined.

Substituting equation (2) into (1) and using the harmonic balance procedure yields:

(i) constant terms

$$\nu^2 c_0=0, \tag{3a}$$

(ii) cosine coefficients

$$-n^2a_n-\alpha n b_n+\nu^2 c_n=0,\quad n=1,\ldots,k \tag{3b}$$

(iii) sine coefficients

$$n^2b_n-\alpha n a_n-\nu^2 d_n=\phi\frac{\nu^2}{\eta^2};\begin{cases}\phi=1, & n=\nu\\ \phi=0, & n\neq\nu\end{cases},\ n=1,\ldots,k. \tag{3c}$$

By combining (i), (ii), and (iii), the following matrix equation may be written

$$[A]\{X\}=\{f\}+\{g\} \tag{4}$$

where

$$[A]=\begin{pmatrix}0&0&0&0&0&0&0&\ldots&0&0\\0&1&\alpha&0&0&0&0&\ldots&0&0\\0&\alpha&-1&0&0&0&0&\ldots&0&0\\0&0&0&4&2\alpha&0&0&\ldots&0&0\\0&0&0&2\alpha&-4&0&0&\ldots&0&0\\0&0&0&0&0&9&3\alpha&\ldots&0&0\\0&0&0&0&0&3\alpha&-9&\ldots&0&0\\\vdots&\vdots&\vdots&\vdots&\vdots&\vdots&\vdots&\ddots&\vdots&\vdots\\0&0&0&0&0&0&0&\ldots&k^2&k\alpha\\0&0&0&0&0&0&0&\ldots&k\alpha&-k^2\end{pmatrix} \tag{5a}$$

$$\{X\}=\{a_0,\ a_1,\ b_1,\ a_2,\ b_2,\ a_3,\ b_3,\ \ldots,\ a_k,\ b_k\}^T \tag{5b}$$

$$\{f\}=\{\nu^2c_0,\ \nu^2c_1,\ -\nu^2d_1,\ \nu^2c_2,\ -\nu^2d_2,\ \nu^2c_3,\ -\nu^2d_3,\ \ldots,\ \nu^2c_k,\ -\nu^2d_k\}^T \tag{5c}$$

$$\{g\}=\left\{0,\ 0,\ -\phi\frac{\nu^2}{\eta^2},\ 0,\ -\phi\frac{\nu^2}{\eta^2},\ \ldots,\ 0,\ -\phi\frac{\nu^2}{\eta^2}\right\}^T;\quad\begin{cases}\phi=1, & \nu=n\\ \phi=0, & \nu\neq n\end{cases},\ n=1,2,\ldots,k \tag{5d}$$

where superscript T stands for transpose.

Equation (4) is implicitly nonlinear, since a_0, a_1, ..., a_k, b_k, c_k, d_k are related through the nonlinear relations of equation (1b). The coefficients of the displacement and force of equations (2a) and (2b) can be related using a DFT (Discrete Fourier Transform) and IDFT (Inverse Discrete Fourier Transform) procedure as follows. For a given harmonic coefficient, the response p_r, which is the discrete value of $y(\theta)$ at the rth discrete time, is calculated using the IDFT as

$$p_r=\text{Real}\left\{\sum_{n=0}^{k}Q_n\left(\cos\frac{2\pi nr}{N}+i\sin\frac{2\pi nr}{N}\right)\right\}\qquad r=0,1,\ldots,N-1 \tag{6}$$

where Q_n is the nth harmonic component, (a_n+ib_n), and $i=\sqrt{-1}$.

According to equation (1b), the nonlinear restoring force s_r, which is the discrete form of $g^*(\theta)$ at the rth discrete time, can be expressed as

$$s_r=\begin{cases}\beta_1 p_r+h, & \text{if } p_r\geq\delta\\ \beta_2 p_r, & \text{if } p_r<\delta.\end{cases} \tag{7}$$

The corresponding discrete value of the force in the frequency domain can be obtained using the DFT as

$$R_n=\frac{\Psi}{N}\sum_{r=0}^{N-1}s_r e^{i\left(-\frac{2\pi nr}{N}\right)} \tag{8}$$

where R_n represents the nth harmonic component, (c_n+id_n) and the value of Ψ is 1 if $n=0$, otherwise is 2.

To find the final value of $\{X\}$ for a given set of system parameters, a Newton-Raphson iterative procedure can be performed as follows:

Assume $\{X\}^{(0)}$ as a starting vector. In order to calculate a better estimate, $\{X\}^{(1)}$, which is the new vector, one can use a Newton-Raphson algorithm, or in general,

$$\{X\}^{(m)}=\{X\}^{(m-1)}-[J]^{-1}\{G\}^{(m-1)} \tag{9}$$

where $[J]^{-1}$ is the inverse of the Jacobian matrix and $\{G\}$ is a column vector of elements

$$\begin{aligned}
g_1&=\nu^2c_0\\
g_2&=a_1+\alpha b_1-\nu^2c_1\\
g_3&=\alpha a_1-b_1+\nu^2d_1+\phi\frac{\nu^2}{\eta^2};\begin{cases}\phi=1, & 1=\nu\\ \phi=0, & 1\neq\nu\end{cases}\\
&\vdots\\
g_{2k}&=k^2a_k+\alpha k b_k-\nu^2c_k\\
g_{2k+1}&=\alpha k a_k-k^2b_k+\nu^2d_k+\phi\frac{\nu^2}{\eta^2};\begin{cases}\phi=1, & k=\nu\\ \phi=0, & k\neq\eta\end{cases}
\end{aligned} \tag{10}$$

The Jacobian matrix J is given by

$$[J]=\begin{pmatrix}\frac{\partial g_1}{\partial a_0}&\frac{\partial g_1}{\partial a_1}&\frac{\partial g_1}{\partial b_1}&\cdots&\frac{\partial g_1}{\partial b_k}\\ \frac{\partial g_2}{\partial a_0}&\frac{\partial g_2}{\partial a_1}&\frac{\partial g_2}{\partial b_1}&\cdots&\frac{\partial g_2}{\partial b_k}\\ \vdots&\vdots&\vdots&\ddots&\vdots\\ \frac{\partial g_{2k+1}}{\partial a_0}&\frac{\partial g_{2k+1}}{\partial a_1}&\frac{\partial g_{2k+1}}{\partial b_1}&\cdots&\frac{\partial g_{2k+1}}{\partial b_k}\end{pmatrix}. \tag{11}$$

To obtain the derivatives in equation (11), using the expressions given in equation (10), equations (6) and (8) are utilized to yield

$$\begin{aligned}
\frac{\partial c_0}{\partial a_0}&=\frac{1}{N}\sum_{r=0}^{N-1}\beta(r)\\
\frac{\partial c_0}{\partial a_1}&=\frac{1}{N}\sum_{r=0}^{N-1}\beta(r)\cos\frac{2\pi r}{N}\\
\frac{\partial c_0}{\partial b_1}&=-\frac{1}{N}\sum_{r=0}^{N-1}\beta(r)\sin\frac{2\pi r}{N}\\
&\vdots\\
\frac{\partial c_1}{\partial a_k}&=\frac{2}{N}\sum_{r=0}^{N-1}\beta(r)\cos\frac{2\pi kr}{N}\cos\frac{2\pi r}{N}\\
\frac{\partial c_1}{\partial b_k}&=-\frac{2}{N}\sum_{r=0}^{N-1}\beta(r)\sin\frac{2\pi kr}{N}\cos\frac{2\pi r}{N}\\
\frac{\partial d_1}{\partial a_k}&=-\frac{2}{N}\sum_{r=0}^{N-1}\beta(r)\cos\frac{2\pi kr}{N}\sin\frac{2\pi r}{N}
\end{aligned}$$

Downloaded 03 May 2010 to 171.66.16.248. Redistribution subject to ASME license or copyright; see http://www.asme.org/terms/Terms_Use.cfm

$$\frac{\partial d_1}{\partial b_k}=\frac{2}{N}\sum_{r=0}^{N-1}\beta(r)\sin\frac{2\pi kr}{N}\sin\frac{2\pi r}{N}$$

$$\vdots$$

$$\frac{\partial c_k}{\partial a_k}=\frac{2}{N}\sum_{r=0}^{N-1}\beta(r)\cos\frac{2\pi kr}{N}\cos\frac{2\pi kr}{N}$$

$$\frac{\partial c_k}{\partial b_k}=-\frac{2}{N}\sum_{r=0}^{N-1}\beta(r)\sin\frac{2\pi kr}{N}\cos\frac{2\pi kr}{N}$$

$$\frac{\partial d_k}{\partial a_k}=-\frac{2}{N}\sum_{r=0}^{N-1}\beta(r)\cos\frac{2\pi kr}{N}\sin\frac{2\pi kr}{N}$$

$$\frac{\partial d_k}{\partial b_k}=\frac{2}{N}\sum_{r=0}^{N-1}\beta(r)\sin\frac{2\pi kr}{N}\sin\frac{2\pi kr}{N} \tag{12}$$

where $\beta(r)$ has the value of either β_1 or β_2. The determination of the $\beta(r)$'s only depends on p_r as expressed in equation (7).

In the formulation utilized by Choi and Noah (1988), an additional set of $2k+1$ equations were obtained by setting (4) in incremental form. The increments Δc_n and Δd_n were then expressed in terms of first-order Taylor expansions involving first-order derivatives of c_n and d_n with respect to a_n and b_n.

In the present approach, a more direct procedure is utilized in which equation (4) is solved iteratively using a closed form for the coefficients of the Jacobian matrix given by equation (11). To calculate a desired periodic solution, the vector $\{X\}$ of the coefficients in equation (2*a*), involving $2k+1$ unknowns, can be determined through an iterative procedure utilizing equation (9) as follows:

(i) With an initial guess $\{X\}^0$, calculate the $[J]^{-1}$ matrix and the $\{G\}$ vector.

(ii) Using equation (9), calculate $\{X\}^{(1)}$.

(iii) Continue the procedure until the iteration converges to a vector $\{X\}$ which is accurate within an allowable error tolerance.

Initial guessed values for subsequent incremental steps are taken as those previously computed. Equations (4) can have multiple solutions. With different initial guesses, or with different subharmonic ratios ν, the periodic response will trace a different path. This is further discussed in a later section.

Advantages of this method in comparison with that used by Saito (1985) and Choi and Noah (1987) are:

(i) Forward numerical differentiation is avoided. This is desirable since it sometimes requires very close initial guesses of the exact solutions. In general, it is very difficult to control the incremental step in numerical differentiation and the related accuracy of the estimated numerical derivatives. This is particularly the case around the response peaks.

(ii) By calculating an accurate estimate of the elements of the Jacobian matrix, the method is readily adapted to analyze the stability of a determined periodic solution, as shown in the following section.

Stability Analysis Using Harmonic Balance

A complete characterization of the dynamic behavior of forced nonlinear systems requires, among other things, determination of stability of their periodic solutions. Delineation of the stable and unstable solutions and the types of bifurcation involved could help in predicting their regular and chaotic motions and transitions to either type of response.

In this section, a stability and bifurcation method is derived, which is particularly effective in the analysis of systems with piecewise-linear and nonlinear characteristics, such as in the system considered herein. The stability method is based on small perturbation of a given periodic solution. The behavior of the perturbed solution reveals whether the periodic solution is stable or not.

The variational equation involving the perturbed value of a given periodic solution can be written as

$$\Delta\ddot{y}+\alpha\Delta\dot{y}+\nu^2\beta(r)\Delta y=0 \tag{13}$$

where $\beta(r)$ is, as before, a discontinuous function whose value depends on the rth discrete time. The same form of the variational equation involving the harmonic coefficients can be arrived at by perturbing p_r and applying the harmonic balance method.

As the $\beta(r)$ is a discontinuous function with a period of 2π and has the value of either β_1 or β_2, an approximate stability analysis can be performed by assuming that $\beta(r)$ is a step function at the rth discrete time. A detailed account of a stability analysis using step functions was performed by Hsu (1973). Since any piecewise-smooth restoring force can be discretized with the present HBM, with DFT/IDFT, the above stability formulation can be directly applied. The stability analysis of the strong nonlinear restoring forces for multi-dimensional problem cases also can readily be performed using this method.

Equation (13) is transformed into a system of first-order equations which can be written in the matrix form

$$\{\dot{z}\}=[u(\nu\theta)]\{z\} \tag{14}$$

where

$$\{z\}=\{\Delta y,\ \Delta\dot{y}\}^T \tag{15a}$$

where superscript T denotes the transpose.

$$[u(\nu\theta)]=\begin{pmatrix}0 & 1\\ -\nu^2\beta(r) & -\alpha\end{pmatrix} \tag{15b}$$

Let $[Z(\nu\theta)]$ be the matrix solution satisfying

$$[\dot{Z}]=[u(\nu\theta)][Z],\quad [Z(0)]=[I] \tag{16}$$

then, the eigenvalues of the monodromy matrix $[Z(\nu\theta)]$, λ_1, λ_2, are the Floquet multipliers and have the following relations

$$\lambda_1\lambda_2=e^{-2\alpha T} \tag{17}$$

where T denotes the period. Clearly, since T and α (damping) are positive scalars, $|\lambda_1\lambda_2|<1$, which excludes bifurcations with complex eigenvalues and $|\lambda|=1$. It is also noted that if absolute value of one multiplier is greater than one, then the other multiplier should be within the unit circle.

As a parameter in the system is varied, a given stable $\nu\theta$-periodic solution may become unstable by having one of its Floquet multipliers leaving the unit circle in one of three possible ways (Guckenheimer and Holmes, 1983):

(i) One of the Floquet multipliers leaves the unit circle at $+1$ while the other remains inside the unit circle. This is called a saddle-node bifurcation corresponding to the merging of two periodic solutions. This was observed with the system considered.

(ii) A complex conjugate pair leaves the unit circle. This case would indicate that the solution is doubly periodic. This case did not happen with any of the cases considered.

(iii) Finally, one of the multipliers leaves the unit circle through -1. This is known as flip bifurcation and an unstable periodic solution will bifurcate into a stable periodic solution of twice the period. This was observed with the system considered.

A numerical integration with discretized $[u(\nu\theta)]$, which is automatically generated with the HBM, is used to construct the monodromy matrix in equation (16) (Noah and Hopkins, 1980).

Numerical Results and Discussion

For illustration, the methods developed in this study are applied to an unsymmetric piecewise-linear system shown in Fig. 1. Figures 2–6 are obtained using the present modified

Downloaded 03 May 2010 to 171.66.16.248. Redistribution subject to ASME license or copyright; see http://www.asme.org/terms/Terms_Use.cfm

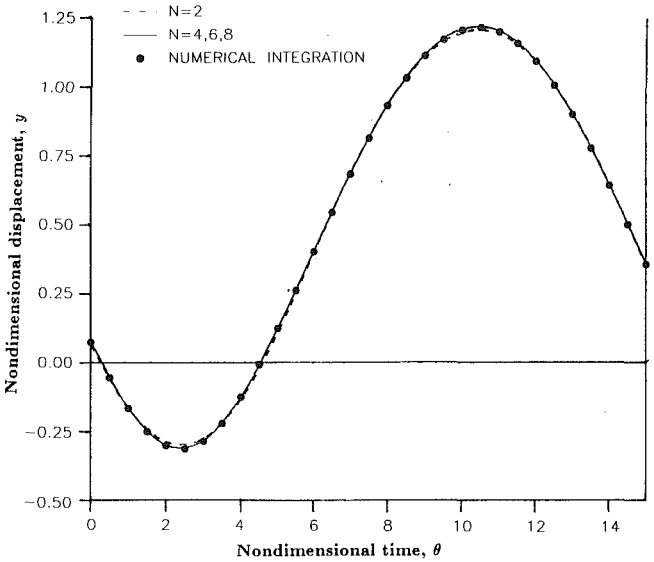

Fig. 2 Effect of retained harmonic terms (period one case); $\nu = 1$, $\zeta = 0.1$, $\eta = 1.5$, $\delta = 0$, $\sigma = 0.1$

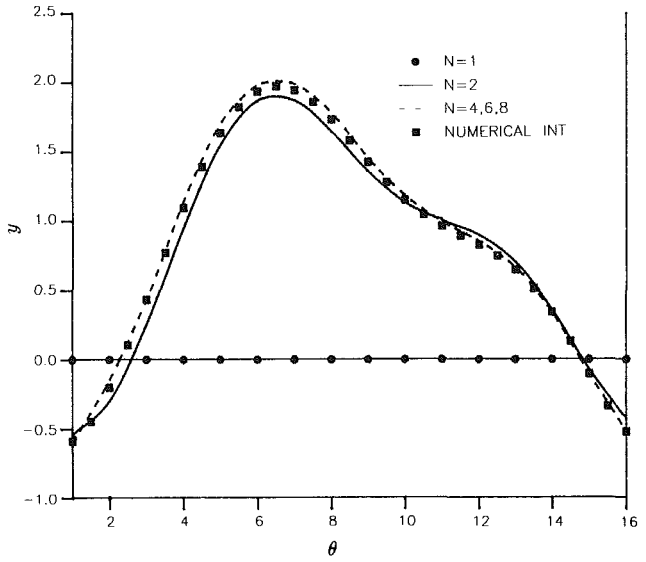

Fig. 3 Effect of retained harmonic terms (subharmonic case); $\nu = 2$, $\zeta = 0.1$, $\eta = 2.0$, $\delta = 0$, $\sigma = 0.1$

harmonic balance method with the nondimensional gap, $\delta = 0$, and the stiffness ratio, $\sigma = 0.1$. A comparison of the accuracy of the method with numerical integration (fourth-order Runge-Kutta) is shown in Fig. 2. The figure shows good agreement for results of a period one response. To find an adequate number of harmonic components in this example, numerical experiments were carried out for 2, 4, 6, and 8 harmonic components. The corresponding results are shown in Fig. 2. The number of discrete data points was taken as four times that of the retained number of harmonic components to avoid aliasing effects. As one might expect, having more retained harmonic components does not influence the accuracy since the period-one response is mostly that of the fundamental harmonic component.

Shown in Fig. 3 is the effect of the retained harmonic terms on the accuracy of the modified harmonic balance method with $\eta = 2$, at which the subharmonic response of order 1/2 is dominant. In this case, increasing the retained harmonic terms yields more accurate response. However, four harmonic terms are sufficient in this case. For 1/3-order and higher subhar-

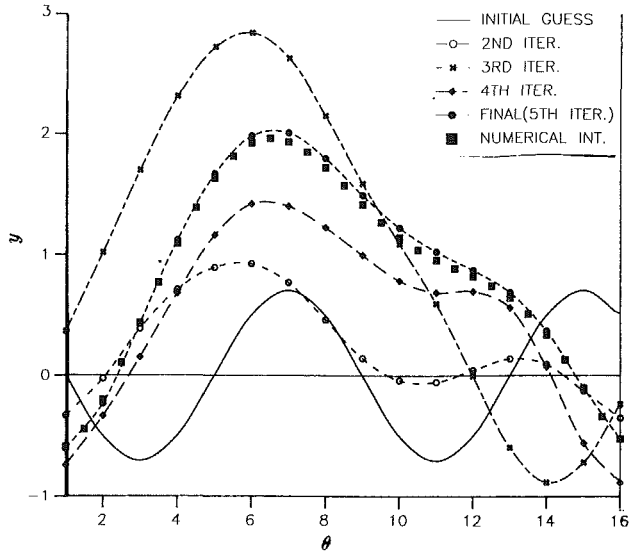

Fig. 4 Convergence of harmonic balance method; $\nu = 2$, $\zeta = 0.1$, $\eta = 2.0$, $\delta = 0$, $\sigma = 0.1$

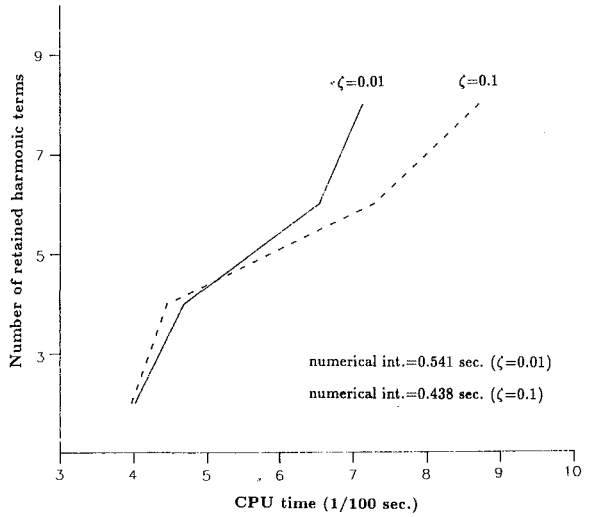

Fig. 5 Effect of retained harmonic terms on CPU time; $\nu = 1$, $\eta = 2.0$, $\delta = 0$, $\sigma = 0.1$

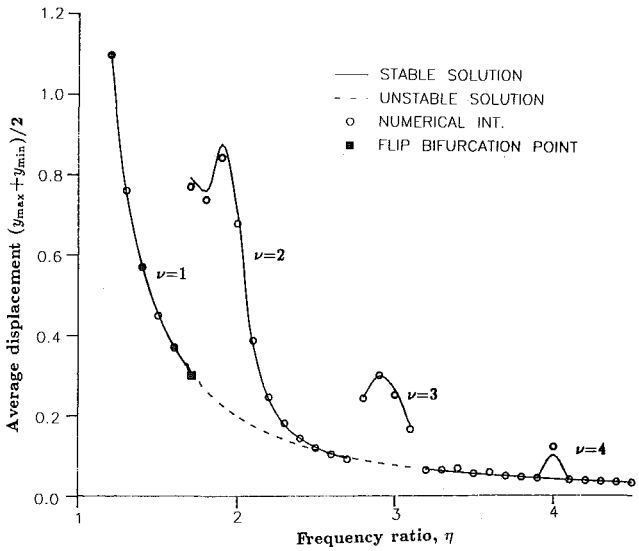

Fig. 6 Comparison between FFT and numerical integration; $\zeta = 0.1$, $\sigma = 0.1$, $\delta = 0$

Downloaded 03 May 2010 to 171.66.16.248. Redistribution subject to ASME license or copyright; see http://www.asme.org/terms/Terms_Use.cfm

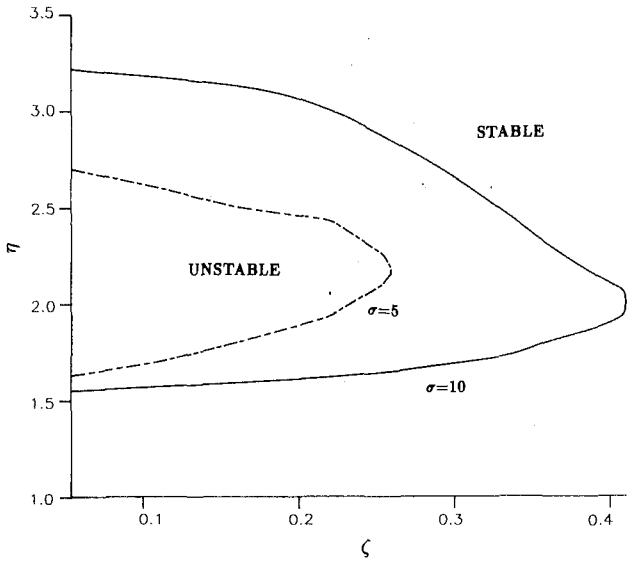

Fig. 7 Flip bifurcation boundary curves; $\nu = 1$, $\delta = 0$, $\sigma = 10$

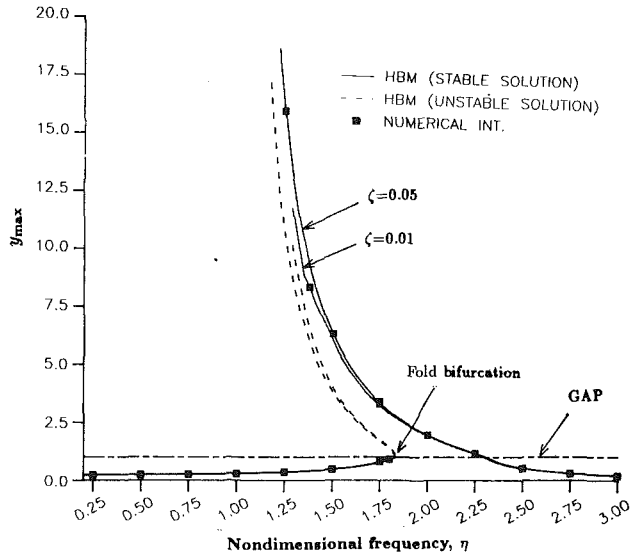

Fig. 8 Response diagram of softening stiffness (system with a gap); $\nu = 1$, $\delta = 1.0$, $\sigma = 0.1$

monic responses, two retained harmonic terms cannot yield converged solutions. To achieve convergence and better accuracy, four or more harmonic terms should be retained for these solutions. The higher order subharmonic response contains more than two harmonic components. For most of the response cases obtained using the harmonic balance method, an error tolerance of 10^{-10} for the Euclidean norm for $\{X\}^{(m)} - \{X\}^{(m-1)}$ in equation (9) was used to obtain satisfactory results. However, a more stringent accuracy requirement and more retained harmonic terms could readily have been used to obtain more accurate results.

Figure 4 shows the convergence development with subsequent iteration of the modified harmonic balance method for the 1/2-order subharmonic case obtained using four harmonic components. The figure shows fast convergence (only five iteration steps needed) to its final subharmonic response even though the initial guess for the response was taken as a single harmonic component. For most simulation cases, only ten or less iterations were needed, although the number of iterations may differ depending on the initial guess and the number of retained harmonic components.

One of the advantages of the harmonic balance method is to get an accurate steady-state response with less computational time as compared to other analytical or integration methods. If the system damping is small, which is usually the case in most engineering systems, the harmonic balance method becomes even more superior (see Fig. 5). Figure 5 shows the effect of the number of retained harmonic components on CPU time (VAX 8300). This figure also reveals that the damping ratio, ζ, does not affect the CPU time much, since the harmonic balance method determines a steady-state solution. The CPU time of numerical integration, which appears at the bottom of this figure, with $\zeta = 0.01$, is almost ten times longer than that of the harmonic balance method with four retained harmonic components. It is expected that if the system had a large number of degrees-of-freedom, the difference of computational time between these two methods could be even greater.

Figure 6 shows close agreement between the results of the average displacements versus dimensionless frequency, η, obtained using the present modified harmonic balance method and those of numerical integration. The results of numerical integration depend on the given initial conditions, making it difficult to find all possible stable solutions. The dotted line in this figure represents the unstable solutions (which a forward numerical integration scheme would not obtain), while the solid line shows the stable solutions. The unstable solutions were detected using equation (16). To obtain further information concerning a possible bifurcation, the Floquet multipliers of the monodromy matrix of equation (16) were investigated. At the initial bifurcation, $\eta \approx 1.6$, one of the Floquet multipliers leaves the unit circle through -1, while the other multiplier remains in the unit circle (flip bifurcation). Figure 7 shows the flip bifurcation regions as determined by the modified harmonic balance method and equation (16). The figure shows the stable boundaries in the plane of the nondimensional frequency, η, and damping ratio, ζ, for two values of the stiffness ratio, σ. Very similar results were obtained by Shaw and Holmes (1983), as shown in Fig. 6 of their paper.

Figure 8 represents the response diagram for $\sigma = 0.1$ (softening spring) and two damping ratios $\zeta = 0.01$ and $\zeta = 0.05$. As would be expected, the piecewise nonlinearity bends the response curve towards the frequency corresponding to the lower slope of the restoring force. In this figure, the coefficients of the previous steady-state solutions were used as the new initial guess to trace the solution curves. The lower curve jumped suddenly to the upper line tracing another stable solution near $\eta = 1.8$, and another jump, from upper to lower, occurred near $\eta = 1.25$. Unstable solutions were obtained using different initial guesses. Stability analysis reveals that two of the solutions are stable while another is unstable (dotted line) between these two jumps. At the junction of the unstable and the lower stable solution, one of the Floquet multipliers left the unit circle via $+1$. Similar results, but for hardening spring system (with $\sigma = 10$), are presented in Fig. 9(*a*). Stable harmonic ($\nu = 1$) or subharmonic ($\nu = 2$) solutions co-exist, while there is a very narrow frequency interval ($\eta = 1.43 - 1.53$) where unstable solutions are also possible. Stability analysis reveals that one of the Floquet multipliers is leaving the unit circle through -1 in this case.

To investigate this flip bifurcation region further, a Poincaré section is used. The section is obtained by stroboscopically looking at the motion synchronous with the periodic impulses and projecting the resulting set of points into the displacement-velocity plane whose coordinates define the Poincaré points $(y_p, \dot{y}_p)$. Figure 9(*b*) shows Poincaré point, y_p, obtained by numerical integration, versus frequency ratio, η. Unstable solutions obtained by the HBM are not included in this figure. The right branch of this figure shows the period 6 orbit, which comes from period 2 orbit through a transition. It bifurcates

Downloaded 03 May 2010 to 171.66.16.248. Redistribution subject to ASME license or copyright; see http://www.asme.org/terms/Terms_Use.cfm

further by decreasing η until a nonperiodic orbit (chaos) occurs. Shaw and Holmes (1983) obtained very similar transition for an oscillator impacting a rigid stop. They referred to such a transition as smooth bifurcation. By further decreasing η, there appears another transition at the left branch where the nonperiodic orbit becomes a period 1 orbit. The authors assume that this transition is very similar to "crisis," which has a sudden response change in this dynamical system. Both transitions play an important role in the dynamics of piecewise-linear systems and further studies need to be done. Figure 13(*c*) shows the chaotic motion at $\eta = 1.436$, which contains 3500 Poincaré points.

The effect of varying stiffness ratio, σ, is shown in Fig. 10 which is obtained by numerical integration, where the dotted marks represent the Poincaré points at each stiffness ratio. A period doubling first occurs near $\sigma = 14$, for which it was determined that one of the Floquet multipliers was negative real leaving the unit circle through -1. Period doubling continues as σ increases, and an irregular or a chaotic motion occurs above $\sigma = 70$. Figure 11 shows some of the orbits in the period doubling sequences. Figure 11(*a*) shows the period-one orbit in the phase plane at $\sigma = 10$. Figure 11(*b*) shows the period 2 orbit at $\sigma = 30$. The period doubling occurs very rapidly with increase of σ, and the period 4, 8, and 16 orbits are shown in Figs. 11(*c*), 11(*d*), and 11(*e*). The period doubling bifurcations can lead to irregular or chaotic motions as shown in Fig. 12 which was constructed using 3500 Poincaré points.

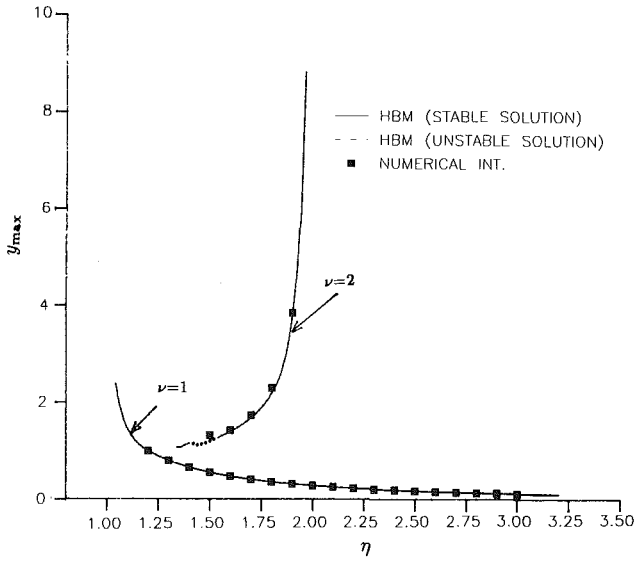

Fig. 9(*a*) Response diagram of hardening stiffness and a gap; $\nu = 1, 2$, $\zeta = 0.01$, $\delta = 1.0$, $\sigma = 10$

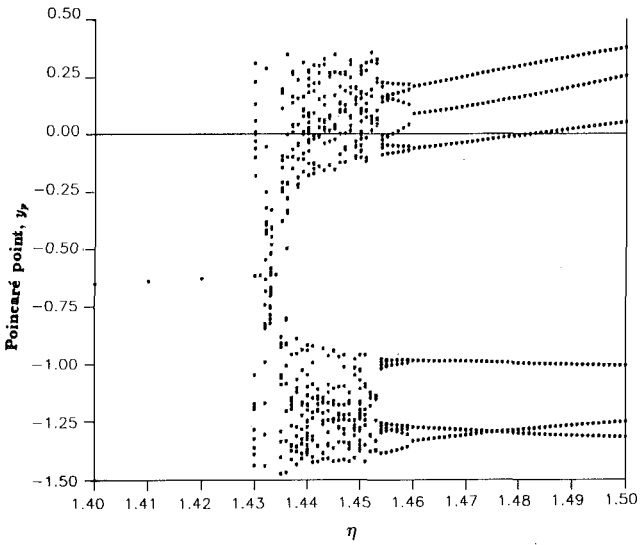

Fig. 9(*b*) Bifurcation plot with hardening stiffness and a gap; $\zeta = 0.01$, $\delta = 1.0$, $\sigma = 10$, $\nu = 1, 2$

Conclusions

A modified harmonic balance method has been developed which provides the exact periodic response of oscillators with piecewise-nonlinear restoring forces under harmonic excitation. The FFT and inverse FFT algorithms are utilized with the harmonic balance formulation to directly provide a closed-form Jacobian matrix of the Newton-Raphson method employed. This leads to a superior approach as compared to the

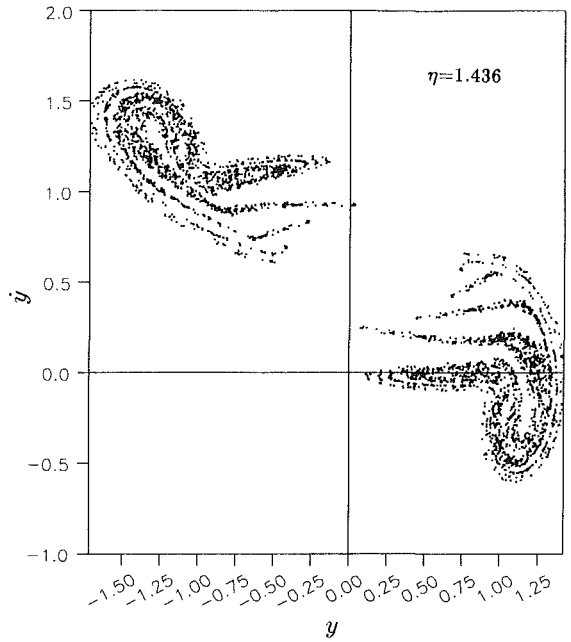

Fig. 9(*c*) Chaotic motion with hardening stiffness and a gap; $\zeta = 0.01$, $\delta = 1.0$, $\sigma = 10$, $\nu = 1, 2$

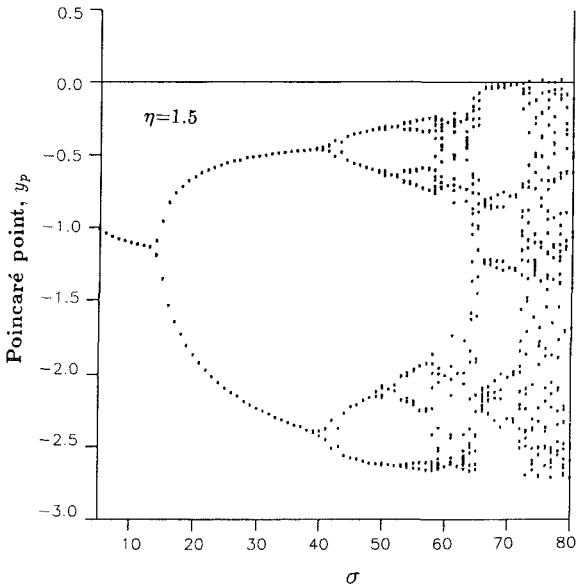

Fig. 10 Bifurcation plot with variation of stiffness ratio, σ; $\nu = 1$, $\zeta = 0.1$, $\delta = 0.05$

Downloaded 03 May 2010 to 171.66.16.248. Redistribution subject to ASME license or copyright; see http://www.asme.org/terms/Terms_Use.cfm

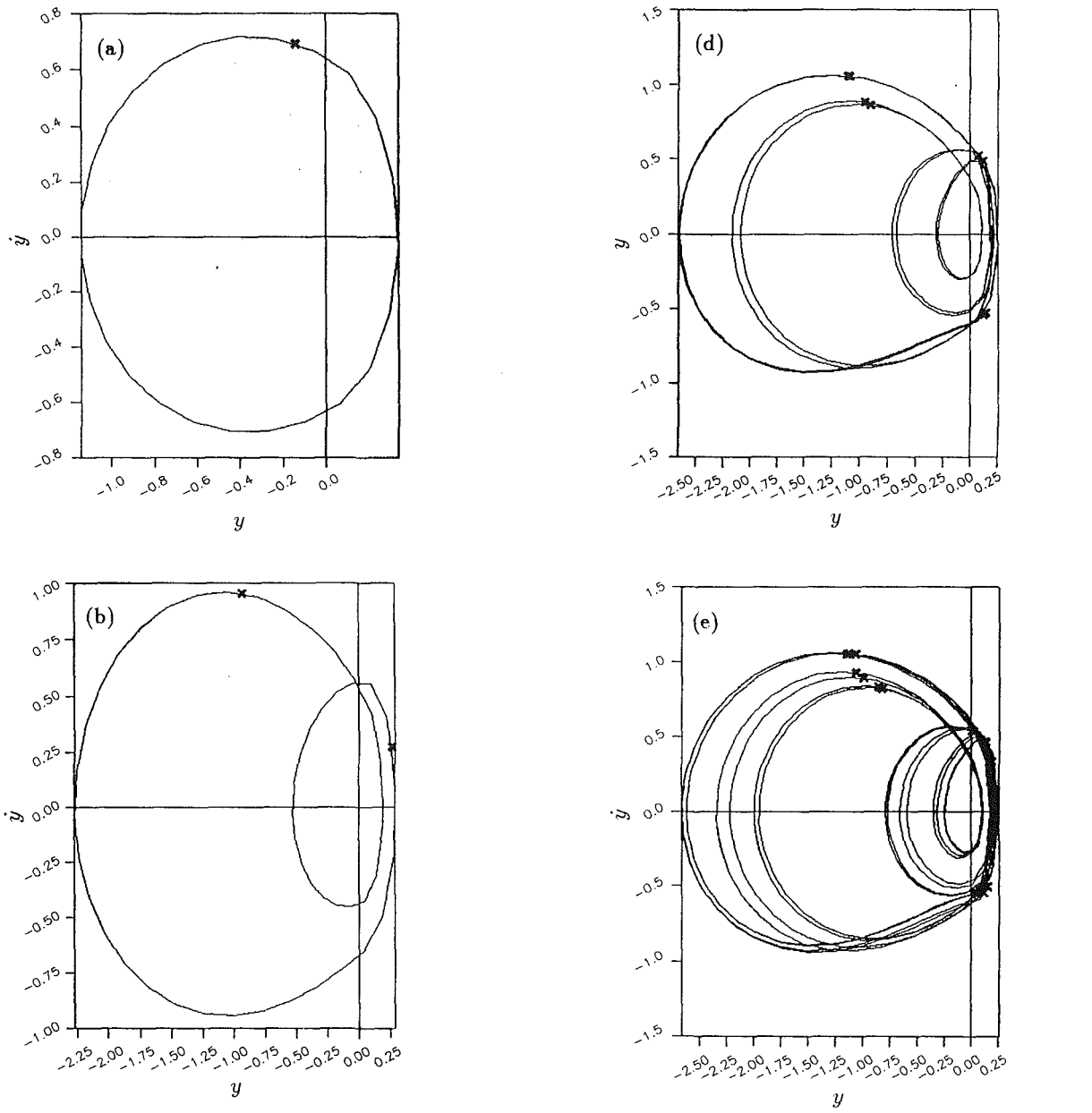

Fig. 11 Period doubling sequence at $\delta = 0.05$, $\zeta = 0.1$ (*a*) period 1 orbit, $\sigma = 10$ (*b*) period 2 orbit, $\sigma = 30$ (*c*) period 4 orbit, $\sigma = 45$ (*d*) period 8 orbit, $\sigma = 49$ (*e*) period 16 orbit, $\sigma = 49.6$;—, Phase plot in (y, $\dot{y}$), and x, Poincaré points

numerical differentiation proposed by Saito (1985).The stability of these solutions is analyzed using a perturbation approach together with results from modern dynamical systems theory. Both period-one and subharmonic oscillations and their stability are considered and the types of bifurcations involved are investigated.

Results on the effects of parameters on an example bilinear system response show that, for some combinations of these parameters, the system response exhibits both flip and fold bifurcation. Chaotic motion was also observed for finite stiffness ratios. The stability analysis, along with the harmonic balance-based method, provide a very powerful tool for better understanding the behavior of systems with clearances. More generally, the method readily offers a useful analytical technique to study multi-degree-of-freedom, multi-dimensional, piecewise nonlinear systems. The method is currently being extended for application to such systems.

Downloaded 03 May 2010 to 171.66.16.248. Redistribution subject to ASME license or copyright; see http://www.asme.org/terms/Terms_Use.cfm

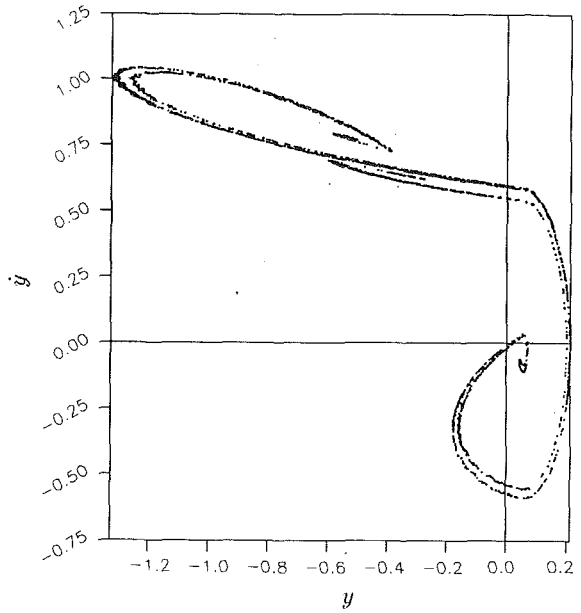

Fig. 12 Chaotic motion at $\eta = 1.5$, $\sigma = 100$, $\delta = 0.05$, $\zeta = 0.1$

Acknowledgment

This work was carried out as part of a research project supported by NASA, Marshall Flight Center under contract No. NAS8-37465. The authors are grateful to Thomas Fox, the technical monitor, for his enthusiastic support and interest. This work was also partially supported by the Offshore Technology Research Center with funds provided by the National Science Foundation Engineering Research Centers program, grant no. CDR-8721512.

References

Bapat, C. N., and Sankar, S., 1986, "Exact Analysis of an Oscillator Hitting a Stop," *ASME Journal of Vibrations, Acoustics, Stress, and Reliability in Design*, Vol. 107, pp. 347–350.

Bengisu, M. T., Hidayetoglu, T., and Akay, A., 1986, "A Theoretical and Experimental Investigation of Contact Loss in the Clearances of a Four-Bar Mechanism," *ASME Journal of Mechanism, Transmission, and Automation in Design*, Vol. 108, pp. 237–244.

Bryant, M. D., 1985, "Nonlinear Forced Oscillation of a Beam Coupled to an Actuator Via Hertzian Contact," *Journal of Sound and Vibration*, Vol. 99, pp. 403–414.

Choi, Y. S., and Noah, S. T., 1987, "Nonlinear Steady-State Response of a Rotor-Support System," *ASME Journal of Vibration, Acoustics, Stress, and Reliability in Design*, Vol. 109, pp. 255–261.

Choi, Y. S., and Noah, S. T., 1988, "Forced Periodic Vibration of Unsymmetric Piecewise-Linear Systems," *Journal of Sound and Vibration*, Vol. 121, pp. 117–126.

Choi, Y. S., and Noah, S. T., 1989, "Periodic Response of a Link Coupling with Clearance," *ASME Dynamic Systems, Measurement and Control*, Vol. 111, pp. 253–259.

Guckenheimer, J., and Holmes, P., 1983, *Nonlinear Oscillations, Dynamical Systems, and Bifurcations of Vector Fields*, Springer-Verlag, New York.

Hongler, M.-O., and Streit, L., 1988, "On the Origin of Chaos in Gearbox Models," *Physica D*, Vol. 29, pp. 402–408.

Hsu, C. S., and Cheng, W. H., 1973, "Applications of the Theory of Impulsive Parametric Excitation and New Treatments of General Parametric Excitation Problems," ASME JOURNAL OF APPLIED MECHANICS, Vol. 40, pp. 78–86.

Kim, Y. B., and Noah, S. T., 1989, "Steady-State Analysis of a Nonlinear Rotor-Housing System," to appear in *ASME Journal of Turbomachinery*.

Ko, P. L., 1985, "Heat Exchanger Tube Fretting Wear: Review and Application to Design," *ASME Journal of Tribology*, Vol. 107, pp. 149–156.

Lau, S. L., Cheung, Y. K., and Wu, S. Y., 1982, "A Variable Parameter Incremental Method for Dynamic Instability of Linear and Nonlinear Elastic Systems," ASME JOURNAL OF APPLIED MECHANICS, Vol. 49, pp. 849–853.

Lee, T. W., and Wang, A. C., 1982, "On the Dynamics of Intermittent-Motion Mechanisms: Part I—Dynamic Model and Response," ASME Paper 82-DET-64.

Maezawa, S., "Perfect Fourier Solution for Subharmonic Vibration of Piecewise-Linear Systems," *Nonlinear Vibration Problems, 5* (2nd Conference on Nonlinear Vibrations), Warsaw, 1962, pp. 156–163.

Maezawa, S., "Superharmonic Resonances in Piecewise-Linear Systems with Unsymmetrical Characteristics," *The 5th Int. Conf. on Nonlinear Oscillation*, Kiev, Aug. 26–Sept. 5, 1969.

Masri, S. F., 1965, "Analytical and Experimental Studies of Impact Dampers," Ph.D. Dissertation, California Institute of Technology.

Masri, S. F., and Caughy, T. K., 1966, "On the Stability of the Impact Damper," ASME JOURNAL OF APPLIED MECHANICS, Vol. 33, pp. 586–592.

Masri, S. F., 1978, "Analytical and Experimental Studies of a Dynamic System with a Gap," *ASME Journal of Mechanical Design*, Vol. 100, pp. 480–486.

Natarj, C., and Nelson, H. D., 1987, "Periodic Solutions in Rotor Dynamic Systems with Nonlinear Supports: A General Approach," ASME Design Conference, Oct. 1987.

Natsiavas, S., 1989, "Periodic Response and Stability of Oscillators with Symmetric Trilinear Restoring Force," accepted for publication in the *Journal of Sound and Vibration*.

Noah, S. T., and Hopkins, G. R., 1980, "Dynamic Stability of Elastically Supported Pipes Conveying Pulsating Fluid," *Journal of Sound and Vibration*, Vol. 71, pp. 103–116.

Pierre, C., Ferri, A. A., and Dowell, E. H., 1985, "Multi-Harmonic Analysis of Dry Friction Damped Systems Using an Incremental Harmonic Balance Method," ASME JOURNAL OF APPLIED MECHANICS, Vol. 52, pp. 958–964.

Rogers, R. J., and Pick, R. J., 1977, "Factors Associated with Support Plate Forces Due to Heat-Exchanger Tube Vibratory Contact," *Nucl. Eng. Design*, Vol. 44, pp. 247–253.

Saito, S., 1985, "Calculation of Nonlinear Unbalance Response of Horizontal Jeffcott Rotors Supported by Ball Bearings with Radial Clearances," ASME Paper No. 85-DET-33.

Shaw, S. W., and Holmes, J. P., 1983, "A Periodically Forced Piecewise-Linear Oscillator," *Journal of Sound and Vibration*, Vol. 108, pp. 129–155.

Smith, C. M., Griffin, R. B., and Noah, S. T., 1986, "Statistical Approach to Modeling the Compound Wear of Steel," presented at the AIME/TMS, ASM Conference on Metal Transfer and Galling in Metallic Systems, Oct. 6–9, Orlando, Fla.

Thompson, J. M. T., and Elvey, J. S. N., 1984, "Elimination of Subharmonic Resonances of Compliant Marine Structures," *International Journal Mechanical Science*, Vol. 26, pp. 419–426.

Tung, P. C., and Shaw, S. W., 1988, "The Dynamic of an Impact Print Hammer," *ASME Journal of Vibration, Acoustics, Stress and Reliability in Design*, Vol. 110, pp. 193–200.

Whiston, G. S., 1979, "Impacting under Harmonic Excitation," *Journal of Sound and Vibration*, Vol. 67, pp. 179–186.

Downloaded 03 May 2010 to 171.66.16.248. Redistribution subject to ASME license or copyright; see http://www.asme.org/terms/Terms_Use.cfm

On the Interaction and Reflection of Shocks in Hyperelastic Strings

J. L. Wegner
Assoc. Mem. ASME

L. Jiang

J. B. Haddow
Mem. ASME

Department of Mechanical Engineering,
University of Victoria,
Victoria, BC V8W 2Y2, Canada

Governing equations for finite amplitude wave propagation in stretched hyperelastic strings are given in recent papers, (Beatty and Haddow, 1985), along with similarity solutions for symmetrically plucked and impacted strings. The similarity solutions are valid until the first reflections at the fixed ends and in this paper we consider symmetrically plucked Mooney-Rivlin strings and investigate the response after reflections. The method of characteristics is applied to extend the results of the similarity solutions and to obtain solutions for the interaction of a reflected longitudinal shock and incident transverse shock and the reflection of an incident transverse shock. A deformed shape, which is not intuitively obvious, is predicted by the solution of the interaction problem and is confirmed by an experimental study. A finite difference scheme is used to obtain numerical solutions, which are valid after multiple wave interactions and reflections occur. Solutions obtained by the method of characteristics are used as a partial check on the numerical results.

1 Introduction

Governing equations for finite amplitude wave propagation in hyperelastic strings are given in recent papers, (Beatty and Haddow, 1985) and (Wegner et al., 1989), henceforth referred to as WHT, along with similarity solutions for symmetrically plucked and impacted strings. These solutions are valid until the first reflections occur at the fixed ends. In the present paper, the response of symmetrically plucked strings of Mooney-Rivlin material is considered, and two of the similarity solutions given in WHT are extended beyond the time of the first reflection.

The similarity solution, which predicts constant state regions separated by a longitudinal shock followed by a transverse shock[1], has been extended by Wegner and Haddow (1990) who considered the reflection of the incident longitudinal shock at the fixed end and obtained a solution which involves a reflected longitudinal shock. We futher extend this solution and obtain a solution, by the method of characteristics, for the interaction of the reflected longitudinal shock and the incident transverse shock. We also extend the similarity solution, which predicts constant state regions separated by a transverse shock followed by a longitudinal shock, by obtaining a solution for the reflection, at a fixed end, of the incident transverse shock.

After multiple wave reflections and interactions have occurred, the application of the method of characteristic becomes extremely complicated; consequently, we then apply a finite difference scheme. The solutions obtained from the method of characteristics are of intrinsic interest and are also used as a partial check on the results obtained from the finite difference scheme.

Experimental results reported in a previous paper (Wegner and Haddow, 1990) are in close agreement with the predictions of the similarity solutions and the results of the finite difference scheme. The deformed shapes predicted by the solution given in this paper, for the interaction of a reflected longitudinal shock and an incident transverse shock, are shown in Fig. 4 for nondimensional time $t<2.05$. These shapes are not intuitively obvious but are confirmed by a further experimental study.

2 Preliminaries

Governing equations and jump relations are given in WHT and are not repeated here. However, we give the preliminaries required for the extension of the similarity solutions. Nondimensional variables are used and quantities with dimension of stress, length, velocity, and time are nondimensionalized by dividing by 3μ, L, $\{3\mu/\rho\}^{1/2}$ and $L\{3\mu/\rho\}^{-1/2}$, respectively, where ρ is the density, $2L$ is the length in the reference configuration, and μ is the infinitesimal shear modulus.

The natural reference configuration of the string occupies the interval $[-1,1]$ of the x_1-axis of a rectangular system $0x_1x_2$. A material particle, whose x_1 coordinate in the reference configuration is $X\in[1,-1]$, is at place $x_\alpha=x_\alpha(X,t)$, $\alpha\in\{1,2\}$ at time t since plane motion is assumed. The ends $X=\pm1$ are fixed at $x_1=\pm\ell$, $x_2=0$.

At time $t=0$ the string is released from the symmetrically deformed configuration indicated in Fig. 1 and given by,

$$x_1(X,0)=\lambda_0 X,\ x_2(X,0)=-\lambda_0(1-X)\tan\theta_1,\ X\in[0,1] \quad (1)$$

[1] A discontinuity in the slope of the string is termed a transverse shock in this paper and WHT, but the terms contact discontinuity is also often used.

Contributed by the Applied Mechanics Division of THE AMERICAN SOCIETY OF MECHANICAL ENGINEERS for presentation at the Joint Applied Mechanics/Bioengineering Conference, Ohio State University, Columbus, Ohio, June 16-19, 1991.

Discussion on this paper should be addressed to the Technical Editor, Prof. Leon M. Keer, The Technological Institute, Northwestern University, Evanston, IL 60208, and will be accepted until two months after final publication of the paper itself in the JOURNAL OF APPLIED MECHANICS. Manuscript received by the ASME Applied Mechanics Division, Mar. 15, 1990; final revision, July 12, 1990.
Paper No. 91-APM-29.

Copyright © 1991 by ASME
Downloaded 03 May 2010 to 171.66.16.248. Redistribution subject to ASME license or copyright; see http://www.asme.org/terms/Terms_Use.cfm

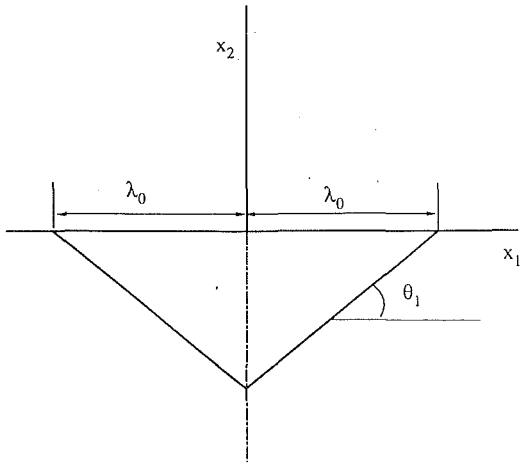

Fig. 1 Deformed configuration before release at $t=0$

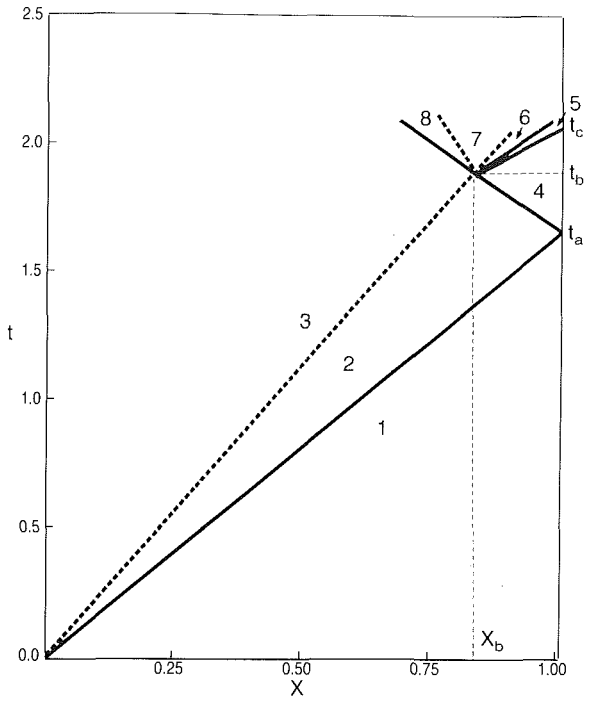

Fig. 2 Characteristic plane for $\lambda_0=1.3$, $\theta_1=45$ deg showing interaction of reflected longitudinal and incident transverse shocks

where $\lambda_0=\ell$, and θ is the angle the tangent to the string makes with the x_1-axis so that $\theta(X,0)=\theta_1$. The total stretch λ_1 at $t=0$ is given by,

$$\lambda_0=\lambda_1\cos\theta_1. \tag{2}$$

If $0<\lambda_0<1$ the string is slack before deformation (1) is applied and λ_0 does not denote the initial stretch unless $\lambda_0\geq 1$. We denote the x_1 and x_2 components of particle velocity by u and v, respectively.

We extend two of the similarity solutions, given in WHT, for a string whose strain energy function is a special case of the Mooney-Rivlin model with the nondimensional nominal stress in simple tension given by,

$$P=(1/3)(0.6+0.4\lambda^{-1})(\lambda-\lambda^{-2}), \tag{3}$$

where λ is the stretch. This relation has been found to be in good agreement with experimental results for certain rubber-like materials with stretches up to about 3.5.

The longitudinal and transverse Lagrangian wave speeds are given by,

$$C_L(\lambda)=\{\partial P/\partial\lambda\}^{1/2},\ C_T(\lambda)=\{P/\lambda\}^{1/2}, \tag{4}$$

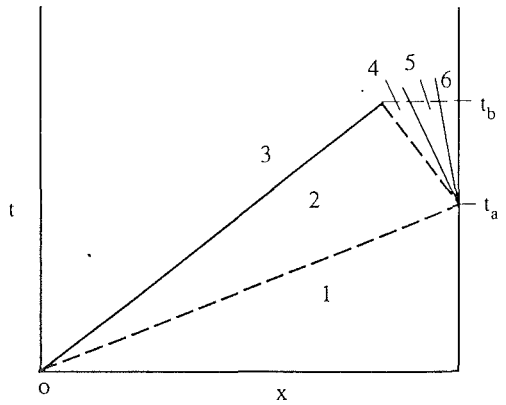

Fig. 3 Characteristic plane (schematic) showing reflected transverse shock

respectively. It follows from (3) and (4) that $C_L(\lambda)=C_T(\lambda)$ when $\lambda=\lambda_c=2.473$. The longitudinal and transverse Lagrangian shock velocities are given by,

$$V_L^{rs}=\pm\left\{\frac{P(\lambda_r^*)-P(\lambda_s^*)}{\lambda_r^*-\lambda_s^*}\right\}^{1/2},$$

$$V_T^{rs}=\pm\left\{\frac{P(\lambda_r^*)}{\lambda_r^*}\right\}^{1/2}=\pm\left\{\frac{P(\lambda_s^*)}{\lambda_s^*}\right\}^{1/2}, \tag{5}$$

respectively, where the superscript rs, $r, s\in\{1,2,3\ldots\}$, indicates the regions in the X, t plane separated by the shock and λ_r^* is the stretch, adjacent to the shock, in region r. Except for the special case when $V_L^{rs}=V_T^{rs}$, $\lambda_r^*=\lambda_s^*$, across the transverse shock. The $+(-)$ sign in (5) is valid for a shock travelling in the $+(-)$ direction.

The similarity solutions that we extend are given in detail in WHT and consist of three constant state regions in the X, t plane separated by a longitudinal shock and a transverse shock. These regions are denoted by 1, 2, and 3 in Figs. 2 and 3, and other numbered regions in these figures are either regions of constant state or simple wave regions. We do not consider reflections or interactions of simple waves or interaction of simple waves and shocks.

A subscript $r\in\{1,2,3\ldots.\}$ attached to a quantity refers to the corresponding region indicated in Fig. 2 or Fig. 3.

3 Characteristic Solution for Shock Interaction

In this section we refer to Fig. 2. A similarity solution is indicated for $t<t_a$, $\forall X$, where $t_a=1/|V_L^{12}|$. This similarity is valid if $\lambda_1<\lambda_c$ or $\lambda_1>\lambda_c$ and $\lambda_2=\lambda_3<\lambda_*$, where $\lambda_*<\lambda_c$ is given by $C_T(\lambda_1)=C_T(\lambda_*)$, so that $|V_L^{12}|>|V_T^{23}|$.

It was shown by Wegner and Haddow (1990) that the incident longitudinal shock with velocity V_L^{12} is reflected as a longitudinal shock, provided λ_0 is large enough for a specific θ_1, otherwise the string buckles, since no compressive stress can be sustained. At point (X_b,t_b) in the characteristic plane, the reflected longitudinal shock meets the incident transverse shock. An extension of the solution up to time t_c is obtained by the method of characteristics, where t_c is the time the result of the shock interaction reaches $X=\pm 1$. The extension of the solution beyond time $t=t_c$ is obtained, numerically, by a finite difference scheme and the characteristic solution is compared with the numerical solution for $t\leq t_c$.

A brief outline of the similarity solution is as follows:

Region 1: $\theta=\theta_1$, $u=v=0$, $\lambda=\lambda_1=\lambda_0/\cos\theta_1$.

Region 2: $\theta=\theta_1$, $u=u_2$, $v=v_2=u_2\tan\theta_1$, $\lambda=\lambda_2$.

Region 3: $\theta=0$, $u=0$, $v=v_3$, $\lambda=\lambda_2=\lambda_3$.

If λ_0 and θ_1 are given, the unknowns are obtained from the jump relations,

Downloaded 03 May 2010 to 171.66.16.248. Redistribution subject to ASME license or copyright; see http://www.asme.org/terms/Terms_Use.cfm

$$(\lambda_2-\lambda_1)V_L^{12}\cos\theta_1=-u_2, \tag{6}$$

$$\lambda_2 V_T^{23}(1-\cos\theta_1)=u_2, \tag{7}$$

$$\lambda_2 V_T^{23}\sin\theta_1=v_3-u_2\tan\theta_1, \tag{8}$$

where V_L^{12} and V_T^{23} are obtained from (5) with the positive sign.

The solution for region 4 is,

$$\theta=\theta_1,\ u=v=0,\ \lambda=\lambda_4,$$

and λ_4 is obtained from the jump relation,

$$V_L^{24}(\lambda_4-\lambda_2)\cos\theta_1=u_2 \tag{9}$$

with u_2 and λ_2 known from the similarity solution.

The values of the dependent variables in regions 3 and 4 are the initial values, at time t_b, of a Riemann problem with origin X_b, and the solution is as follows: Region 5 is a simple wave region and regions 6, 7, and 8 are regions of constant state separated by transverse shocks. A longitudinal shock separates regions 8 and 3 and regions 4 and 6 are separated by centered simple wave region 5.

Region 5:

$$\theta=\theta_1,\ u=u_5=-\int_{\lambda_4}^{\lambda}C_L(\eta)d\eta\cos\theta_1,\ v=v_5=u_5\tan\theta_1,$$

$$(X-X_b)/(t-t_b)=C_L(\lambda). \tag{10}$$

Region 6:

$$\theta=\theta_1,\ u=u_6=-\int_{\lambda_4}^{\lambda_6}C_L(\lambda)d\lambda\cos\theta_1,$$

$$v=v_6=u_6\tan\theta_1,\ \lambda=\lambda_6. \tag{11}$$

Region 7:

$$\theta=\theta_7,\ u=u_7,\ v=v_7,\ \lambda=\lambda_6=\lambda_7. \tag{12}$$

Region 8:

$$\theta=0,\ u=u_8,\ v=v_3=v_8,\ \lambda=\lambda_6=\lambda_8. \tag{13}$$

The jump relations across the shocks give,

$$\lambda_6 V_T^{67}(\cos\theta_7-\cos\theta_1)=-(u_7-u_6), \tag{14}$$

$$\lambda_6 V_T^{67}(\sin\theta_7-\sin\theta_1)=-(v_7-v_6), \tag{15}$$

$$\lambda_6 V_T^{78}(\cos\theta_7-1)=-(u_7-u_8), \tag{16}$$

$$\lambda_6 V_T^{78}\sin\theta_7=-(v_7-v_3), \tag{17}$$

$$V_L^{83}(\lambda_8-\lambda_3)=-u_8, \tag{18}$$

$$V_T^{67}=-V_T^{78},$$

where the jump velocities are obtained from (5) with the appropriate sign. The unknowns in (10)–(13) are θ_7, λ_6, u_6, v_6, u_7, v_7, and u_8 and these are obtained from $(11)_{2,3}$ and (14) to (18).

4 Characteristic Solution for Reflection of Transverse Shock

In this section we refer to Fig. 3. A similarity solution is indicated for $t<t_a$, $\forall X$, where $t_a=1/|V_T^{12}|$. This similarity solution is valid if $\lambda_1>\lambda_c$ and $\lambda_3>\lambda_*$, so that $|V_T^{12}|>|V_L^{23}|$ and a brief outline is as follows:

Region 1:

$$\theta=\theta_1,\ u=v=0,\ \lambda=\lambda_1=\lambda_0/\cos\theta_1. \tag{19}$$

Region 2:

$$\theta=0,\ u=u_2,\ v=v_2,\ \lambda=\lambda_1=\lambda_2. \tag{20}$$

Region 3:

$$\theta=0,\ u=0,\ v=v_2=v_3,\ \lambda=\lambda_3. \tag{21}$$

If λ_0 and θ_1 are given, the unknowns u_2, v_2, and λ_3 in (19)–(20) are obtained from the jump solutions,

$$V_T^{12}\lambda_1(\cos\theta_1-1)=u_2, \tag{22}$$

$$V_T^{12}\lambda_1\sin\theta_1=v_2, \tag{23}$$

$$V_L^{23}(\lambda_2-\lambda_3)=-u_2, \tag{24}$$

where the jump velocities are obtained from (5) with the appropriate sign. The solution for the reflection of the incident transverse shock with velocity V_T^{12} consists of constant state regions 4 and 6 and centered simple wave region 5. A transverse shock with velocity $V_T^{24}=-V_T^{12}$ separates regions 2 and 4. This solution is a similarity solution with similarity variable $(1-X)/(t-t_a)$ and is valid for $t_b>t\geq t_a$, where t_b is the time the reflected transverse shock meets the incident longitudinal shock, and is as follows:

Region 4:

$$\theta=\theta_4,\ u=u_4,\ v=v_4=u_4\tan\theta_4,\ \lambda=\lambda_2=\lambda_4 \tag{25}$$

Region 5:

$$\theta=\theta_4,\ u=u_5=u_4+\int_{\lambda_4}^{\lambda}C_L(\eta)d\eta\cos\theta_4,\ v=v_5=v_4$$

$$+\int_{\lambda_4}^{\lambda}C_L(\eta)d\eta\sin\theta_4\frac{1-X}{t-t_a}=C_L(\lambda) \tag{26}$$

Region 6:

$$\theta=\theta_4,\ u=v=0,\ \int_{\lambda_1}^{\lambda_6}C_L(\lambda)d\lambda\cos\theta_4=-u_4,\ \lambda=\lambda_6. \tag{27}$$

The jump relations across the shocks give,

$$V_T^{24}\lambda_4(\cos\theta_4-1)=-(u_4-u_2), \tag{28}$$

$$V_T^{24}\lambda_4\sin\theta_1=-(v_4-v_2), \tag{29}$$

where the jump velocities are obtained from (5) with the appropriate sign. The unknowns in (25)–(27) are u_4, v_4, θ_4, λ_6 and they are obtained from $(25)_3$, $(27)_3$, (28), and (29).

When a realistic value of λ_1, say $\lambda_c<\lambda_1\leq 3.5$, is considered for the stress-stretch relation given by (3), the difference between $|V_T^{12}|$ and $|V_L^{23}|$ is very small. It follows that it is difficult to show regions 4, 5, and 6 on a diagram which represents an actual case, consequently Fig. 3 is schematic. It is also difficult to compare results from the finite difference scheme with those from the method of characteristics since precise details in the region of the X, t plane in the neighborhood of $(1,t_b)$ are likely to be smeared.

5 Finite Difference Scheme

A modification of the finite difference scheme proposed by Godunov (Holt, 1977) is used to extend the results of the characteristic solutions. In the original Godunov scheme the spatial interval is divided into cells of equal length and each dependent variable is approximated by a sequence of constant values, one for each cell. The discontinuities are resolved by solving a sequence of Riemann problems at each time step.

A second-order scheme based on Godunov's scheme has been proposed by van Leer (1977, 1979). This scheme gives satisfactory results for the present problem, since it has excellent shock capturing capabilities and, where comparisons can be made, the results are in close agreement with those from the method of characteristics. Van Leer's scheme uses piecewise linear approximations at every time step and, in the present application of the scheme, the approximate Riemann solver proposed by Roe (1983) is used.

Downloaded 03 May 2010 to 171.66.16.248. Redistribution subject to ASME license or copyright; see http://www.asme.org/terms/Terms_Use.cfm

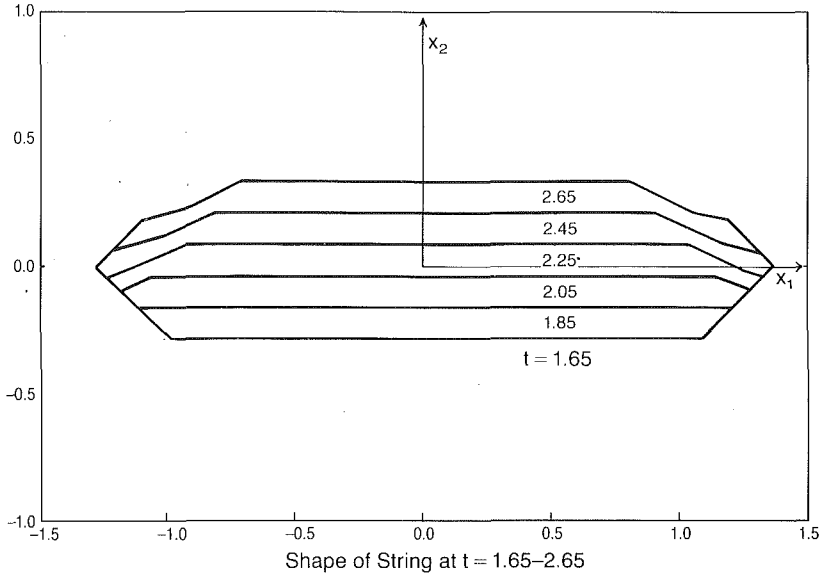

Fig. 4 Shape of string at nondimensional times $t = 1.65$–2.65 for $\lambda_0 = 1.3$, $\theta_1 = 45$ deg

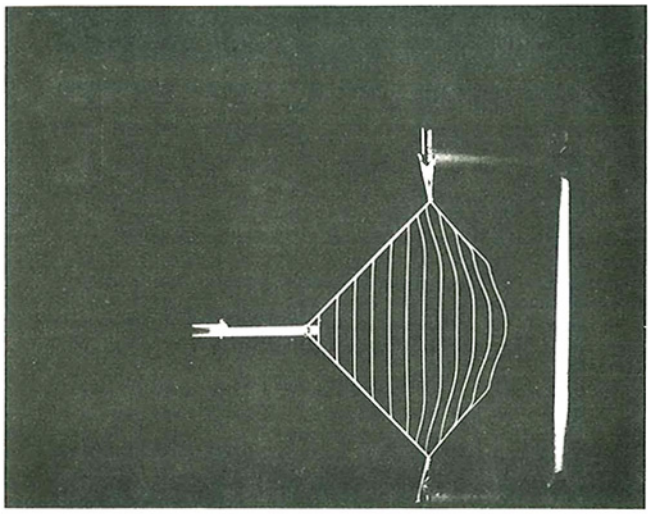

Fig. 5 Experimentally obtained shapes for $\lambda_0 = 1.3$, $\theta_1 = 45$ deg

6 Results

(a) Wave Interaction Problem. We present results for $\lambda_0 = 1.3$ and $\theta_1 = 45$ deg, which give $\lambda_1 = 1.838 < \lambda_c$. This example is considered because there is a significant difference between $|V_L^{12}|$ and $|V_T^{23}|$. Referring to Fig. 2, $t_a = 2.673$, $t_b = 1.898$, $t_c = 2.090$, and results from the method of characteristics are as follows:

$$\lambda_1 = 1.838,\ \lambda_2 = \lambda_3 = 1.412,\ \lambda_4 = 1.080,\ \lambda_6 = \lambda_7 = \lambda_8 = 1.222$$

$$\theta_1 = 45 \text{ deg},\ \theta_3 = \theta_8 = 0,\ \theta_7 = -24.3 \text{ deg},$$

$$u_2 = 0.180,\ u_3 = u_4 = 0,\ u_6 = -0.083,$$

$$u_7 = -0.176,\ u_8 = -0.136,$$

$$v_2 = 0.180,\ v_3 = v_8 = 0.615,\ v_4 = 0,\ v_6 = -0.083,\ v_7 = 0.427,$$

$$V_L^{12} = 0.598,\ V_T^{23} = 0.436,\ V_L^{24} = 0.768$$

$$V_T^{67} = V_T^{78} = 0.374,\ V_L^{38} = -0.716.$$

It is interesting to note that θ_7 is negative. Deformed configurations are shown in Fig. 4 for nondimensional times $t = 1.65$ to $t = 2.65$ at intervals 0.2. The configurations for $t = 1.65$, 1.85, and 2.05 correspond to $t < t_a$, $t_a < t < t_b$, and $t_b < t < t_c$, respectively, and are obtained from both the method of characteristics and the finite difference scheme. Results from two procedures are in excellent agreement and cannot be distinguished in the figure. Configurations for $t > t_c$ shown in Fig. 4 are obtained from the finite difference scheme only.

The centered simple wave of region 5 in Fig. 2 reflects, after the interaction period of the incident and reflected waves, as a simple wave, and the analysis is not difficult. However, when the reflected simple wave interacts with the incident transverse shock with velocity V_T^{67}, preliminary investigations, using relations along characteristics, show that θ varies continuously and a solution by the method of characteristics becomes intractable. The continuously varying slope is evident in the configurations shown in Fig. 4 for $t = 2.25$, 2.45, and 2.65.

An experimental study was undertaken. A rubber string of circular cross-section 1.0-mm diameter, and length 138 mm in the natural reference configuration, was subjected to initial stretch $\lambda_0 = 1.3$ and symmetrically plucked with $\theta_1 = 45$ deg. A high-speed photographic technique was used to obtain Fig. 5 which shows deformed configurations at intervals of 0.5 ms. These configurations are in excellent qualitative agreement and good quantitative agreement with those shown in Fig. 4. In particular, the configuration for $t = 2.05$ with the double kink is confirmed experimentally.

(b) Wave Reflection Problem. We present results for $\lambda_0 = 2.5$ and $\theta_1 = 30$ deg which give $\lambda_1 = 2.887$ and $\lambda* = 2.127$. Referring to Fig. 3, $t_a = 2.059$ and $t_b = 2.075$ and results from the method of characteristics are as follows:

$$\lambda_1 = \lambda_2 = \lambda_4 = 2.887,\ \lambda_6 = 3.609,$$

$$\theta_1 = 30 \text{ deg},\ \theta_2 = \theta_3 = 0,\ \theta_4 = \theta_5 = \theta_6 = -23.794$$

$$u_1 = 0,\ u_2 = -0.188,\ u_3 = 0,\ u_4 = -0.307,\ u_6 = 0,$$

$$v_1 = 0,\ v_2 = v_3 = 0.701,\ v_4 = 0.135,\ v_6 = 0,$$

$$V_T^{12} = -V_T^{24} = 0.486,\ V_L^{23} = 0.478.$$

It is interesting that λ_6 is significantly larger than λ_1.

Deformed configurations are shown in Fig. 6 for nondimensional times $t = 1.674$ to $t = 2.474$ at intervals of 0.2. Deformed configurations for $t < t_b = 2.075$ were obtained from both the method of characteristics and the finite difference

Downloaded 03 May 2010 to 171.66.16.248. Redistribution subject to ASME license or copyright; see http://www.asme.org/terms/Terms_Use.cfm

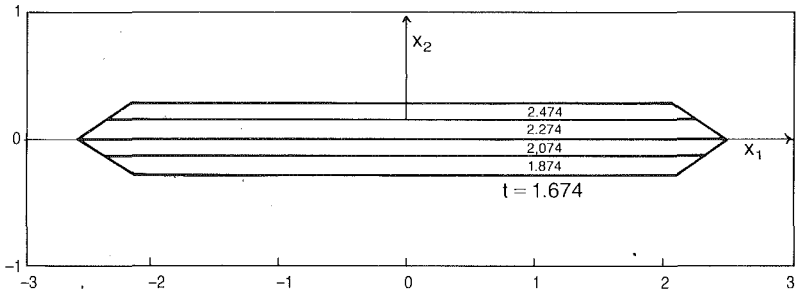

Fig. 6 Shape of string at nondimensional times $t = 1.674$–2.474 for $\lambda_0 = 2.5$, $\theta_1 = 30$ deg

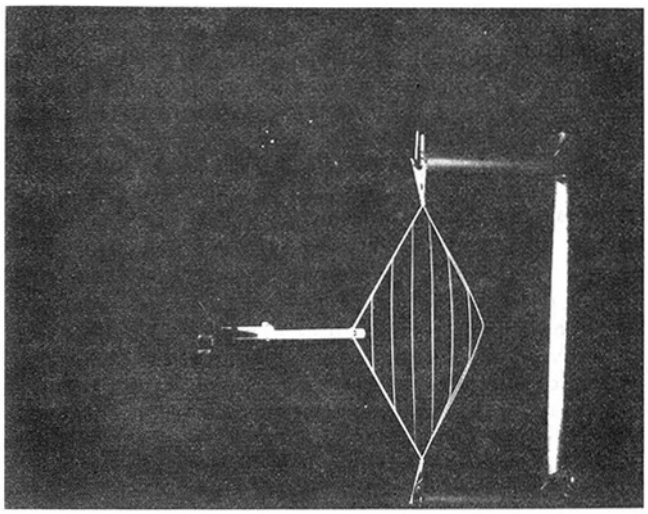

Fig. 7 Experimentally obtained shapes for $\lambda_0 = 2.5$, $\theta_1 = 30$ deg

scheme and results from the two schemes cannot be distinguished in the figure. Configurations for $t > t_b$ were obtained from the finite difference scheme.

It follows from the finite difference scheme that, during the time interval $t_b - t_a$, the deformed configuration for $0 \le X \le 1$ consists of two straight segments with $\theta = 0$ and $\theta = 23.8$ deg, corresponding to regions 2 and 3 and regions 4, 5, and 6, respectively, in Fig. 3. The nondimensional length of the segment with $\theta = 23.8$ deg is much less than one, consequently it is not evident in Fig. 6 because of the scale.

Figure 7 shows the result of the experimental study for $\lambda_0 = 2.5$ and $\theta_1 = 30$ deg. The configurations shown in Fig. 7 are of the same form as those shown in Fig. 6, thus providing experimental support for the theoretical results.

7 Concluding Remarks

Comparison of Figs. 4 and 6 or Figs. 5 and 7 indicate that the shapes of the deformed configurations are qualitatively different, for the two cases considered, after the first reflections at $X = \pm 1$. The configurations shown in Fig. 4 for $t = 2.05$ and 2.25 are not intuitively obvious, but are confirmed by the experimental results shown in Fig. 5.

References

Beatty, M. F., and Haddow, J. B., 1985, "Transverse Impact of a Stretched String," ASME JOURNAL OF APPLIED MECHANICS, Vol. 52, pp. 137–143.

Holt, M., 1977, *Numerical Methods in Fluid Dynamics,* Springer-Verlag, Berlin.

Roe, P. L., 1983, "Approximate Riemann Solvers, Parameter Vectors and Difference Schemes," *J. Comp. Phys.,* Vol. 43, pp. 357–372.

Van Leer, B., 1977, "Towards the Ultimate Conservative Difference Scheme IV: A New Approach to Numerical Convection," *J. Comp. Phys.,* Vol. 23, pp. 276–299.

Van Leer, B., 1979, "Towards the Ultimate Conservative Difference Scheme V: A Second Order Sequel to Godunov's Method," *J. Comp. Phys.,* Vol. 32, pp. 101–136.

Wegner, J. L., Haddow, J. B., and Tait, R. J., 1989, "Unloading Waves in a Plucked Hyperelastic String," ASME JOURNAL OF APPLIED MECHANICS, Vol. 56, pp. 459–465.

Wegner, J. L., and Haddow, J. B., 1990, "An Experimental Study of Unloading Waves in a Plucked Hyperelastic String," ASME JOURNAL OF APPLIED MECHANICS, accepted for publication.

Downloaded 03 May 2010 to 171.66.16.248. Redistribution subject to ASME license or copyright; see http://www.asme.org/terms/Terms_Use.cfm

Chaotic Motions of a Constrained Pipe Conveying Fluid: Comparison Between Simulation, Analysis, and Experiment

M. P. Paidoussis
Fellow ASME

G. X. Li

Department of Mechanical Engineering,
McGill University,
Montreal, QC H3A 2K6, Canada

R. H. Rand
Department of Theoretical and Applied Mechanics,
Cornell University,
Ithaca, NY 14853

A refined analytical model is presented for the dynamics of a cantilevered pipe conveying fluid and constrained by motion limiting restraints. Calculations with the discretized form of this model with a progressively increasing number of degrees of freedom, N, *show that convergence is achieved with* N = *4 or 5, which agrees with previously performed fractal dimension calculations of experimental data. Theory shows that, beyond the Hopf bifurcation, as the flow is increased, a pitchfork bifurcation is followed by a cascade of period doubling bifurcations leading to chaos, which is in qualitative agreement with observation. The numerically computed theoretical critical flow velocities are in excellent quantitative agreement (5–10 percent) with experimental values for the thresholds of the Hopf and period doubling bifurcations and for the onset of chaos. An approximation for the critical flow velocity for the loss of stability of the post-Hopf limit cycle is also obtained by using center manifold concepts and normal form techniques for a simplified version of the analytical model; it is found that the values obtained in this manner are approximately within 10 percent of those computed numerically.*

1 Introduction

The linear and nonlinear dynamics of cantilevered pipes conveying fluid has been studied quite extensively, both theoretically and experimentally. Indeed, this system has become a paradigm in the study of stability nonconservative circulatory systems (Païdoussis, 1987; Païdoussis and Issid, 1974; Holmes, 1977). More recently, variants of this system have been shown to exhibit complex dynamics and chaos, as described below.

Tang and Dowell (1988) have used a pipe with an inset steel strip and equispaced magnets on either side, buckling the pipe into one or the other potential well thus generated. Once the flow velocity is sufficiently above the threshold value for flutter about the buckled state, chaotic oscillations were shown to be possible. This problem was studied theoretically, while its nonautonomous counterpart (forced vibration) was studied both theoretically and experimentally, once again displaying chaos. The theoretical results were in encouragingly good agreement with experimental observations.

Païdoussis and Moon (1988) studied the dynamics of a cantilevered pipe constrained by nonlinear motion restraints. For flow velocities sufficiently higher than the critical for the Hopf bifurcation, the limit cycle motion was large enough for the pipe to impact on the restraints; as the flow was incremented further, a series of period doubling bifurcations led to chaos. The special merit of this study is that it was the first joint experimental/theoretical one involving chaos in an *autonomous mechanical system* (Moon, 1987). This system was studied more fully on the theoretical side by Païdoussis, Li, and Moon (1989).

The analytical model utilized in the foregoing studies was four-dimensional (two degrees-of-freedom), which is the minimum possible for chaos in this autonomous system. Analysis of typical experimental vibration signals yielded a fractal dimension of 3.2 in the chaotic regime (Païdoussis, Cusumano, and Copeland, 1991), suggesting that although four-dimensional modeling may be reasonable, eight or ten-dimensional models may be necessary to capture all essential features of the dynamics. Indeed, although experiment and four-dimensional simulation in that study displayed remarkable qualitative similitude, quantitative agreement, although reasonable, was not good—e.g., for the threshold flow velocities for period doubling or chaos. Moreover, it was not known if the four-dimensional results were representative of those of higher-

Contributed by the Applied Mechanics Division of THE AMERICAN SOCIETY OF MECHANICAL ENGINEERS for presentation at the Joint Applied Mechanics/Bioengineering Conference, Ohio State University, Columbus, OH, June 16–19, 1991.

Discussion on this paper should be addressed to the Technical Editor, Leon M. Keer, The Technological Institute, Northwestern University, Evanston, IL 60208, and will be accepted until two months after final publication of the paper itself in the JOURNAL OF APPLIED MECHANICS. Manuscript received by the ASME Applied Mechanics Division, Nov. 21, 1989; final revision, Oct. 2, 1990.

Paper No. 91-APM-36.

Copyright © 1991 by ASME
Downloaded 03 May 2010 to 171.66.16.248. Redistribution subject to ASME license or copyright; see http://www.asme.org/terms/Terms_Use.cfm

dimensional models in quantitative terms; thus, whether the agreement found was fortuitous or not.

In the present paper, a systematic *quantitative* comparison between experiment and theory is undertaken, considering progressively higher-dimensional models, while at the same time refining the analytical model to bring it closer to experimental reality. Moreover, the first post-Hopf bifurcation in the four-dimensional system is predicted by analytically reducing the problem to a two-dimensional system through center manifold analysis, thus permitting a three-cornered overall comparison between experiment, simulation, and analysis.

In physical terms, this system is an example of a large class of problems involving self-excited oscillations and interactions with motion limiting constraints. An example is the so-called fluid-elastic oscillation of heat exchanger tubes impacting on the generally loosely fitting baffle plates (Axisa et al., 1988), leading to chaotic-looking oscillations and resulting in potentially catastrophic wear rates for the tubes. Hence, understanding and modeling the dynamics of such systems is of both fundamental and practical interest.

2 The Experiments

Although the experimental apparatus, measurements, and data analysis are described fully elsewhere (Païdoussis and Moon, 1988), a few words here will nevertheless be useful. Fig. 1(*a*, *b*) shows the most successful version of the experimental apparatus. It consisted of a vertical cantilevered pipe made of elastomer, containing water flowing downwards. An embedded thin metal-strip-enforced planar motions. The post-Hopf limit cycle amplitude was constrained by motion limiting restraints, typically two polycarbonate bars, Fig. 1(*b*).

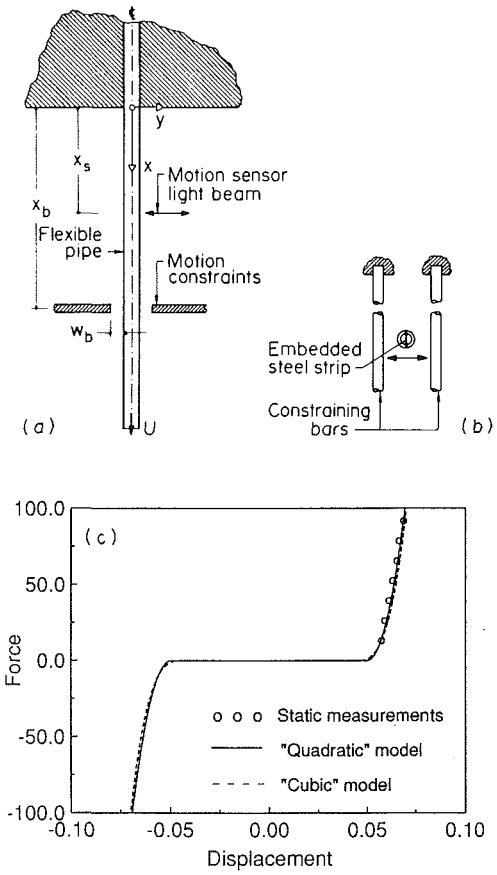

Fig. 1*(a)* Schematic of the experimental system; *(b)* scheme for achieving planar motions with steel strip embedded in the pipe, also showing motion constraining bars; *(c)* modeling of restraint stiffness, also showing static force-displacement measurements

Motion of the system was measured with the aid of a non-contacting optical tracking system. The signal was processed through a FFT Analyzer and a digital storage oscilloscope, yielding power spectra (PSD), phase plane plots, probability density (PDF), and autocorrelation functions, while the flow velocity was incremented.

Typically, experiments showed that as U was increased beyond the Hopf bifurcation, regular motion (involving impacting with one or both constraining bars in each cycle of motion) was succeeded by period-2 motion (with impacting once every two cycles). More irregular motion developed at higher U; with the help of experimental PSD, PDF, and autocorrelation function plots and Poincaré maps, it was conclusively shown that the oscillations, beyond a certain U, became chaotic. Thus, the critical flow velocities for the Hopf and period doubling bifurcations and for the onset of chaos were determined experimentally.

3 The Equation of Motion

3.1 The Basic Model. The equation of motion of a vertical cantilevered pipe conveying fluid (Païdoussis, 1970) was modified to take into account the presence of motion limiting restraints (Païdoussis et al., 1989). For a pipe of flexural rigidity EI, coefficient of Kelvin-Voigt viscoelastic damping a, length L and mass-per-unit-length m, conveying fluid of mass-per-unit-length M with velocity U, subject to planar motions $w(x,t)$ and impacting with nonlinear force $F(w)$ on the restraint, Fig. 1, the nondimensional equation of motion is given by

$$\left(1+\alpha\frac{\partial}{\partial\tau}\right)\frac{\partial^4\eta}{\partial\xi^4}+[u^2-\gamma(1-\xi)]\frac{\partial^2\eta}{\partial\xi^2}+2\beta^{1/2}u\frac{\partial^2\eta}{\partial\xi\partial\tau}+\gamma\frac{\partial\eta}{\partial\xi}+f(\eta)\delta(\xi-\xi_b)+\frac{\partial^2\eta}{\partial\tau^2}=0, \quad (1)$$

where $\eta=w/L$, $\xi=x/L$, $\tau=[EI/(M+m)]^{1/2}t/L^2$, t denoting time, $u=(M/EI)^{1/2}UL$, $\beta=M/(M+m)$, $\gamma=(M+m)gL^3/EI$, $\alpha=[EI/(M+m)]^{1/2}a/L^2$, $f(\eta)=F(w)L^3/EI$, and $\delta(x-x_b)$ is the Dirac delta function. This equation holds for a sufficiently long and slender pipe, where the Euler-Bernoulli beam theory is appropriate, and for small pipe deflections, imposed by the motion restraints, where the motion may adequately be described by a linearized equation (apart from interaction with the nonlinear restraints). It is recalled that the problem is independent of fluid frictional effects (Gregory and Païdoussis, 1966), which are therefore absent from equation (1).

3.2 The Adapted Model. Some aspects of the model, e.g., the stiffness of the restraining bars, Fig. 1(*b*), and the damping characteristics of the pipe, need to be adapted to the particular system being modeled, since direct quantitative comparison to the experimental results will be made. The experimental system, for which the most extensive and reliable set of data was available, was selected (Païdoussis and Moon, 1988; pipe no. 9, Fig. 6). The nondimensional parameters for this system are as follows: $\beta=0.213$, $\gamma=26.76$, $\xi_b=0.65$; the dimensionless gap to the restraints (Fig. 1(*a*)), $\eta_b=w_b/L=0.055$.

The damping characteristics of the empty, silicone rubber vertical pipe were measured with the aid of an FFT Analyzer and Hilbert transform techniques. The logarithmic decrements of the lowest three modes were $\delta_1=0.028$, $\delta_2=0.081$, and $\delta_3=0.144$. This suggests that damping was viscohysteretic, rather than purely viscoelastic. In what follows, it was found convenient to utilize a modal damping representation; thus, for the rth mode, the damping term in equation (1) was modified:

$$\alpha\frac{\partial^5\eta}{\partial\tau\partial\xi^4}\rightarrow c_r\frac{\partial\eta}{\partial\tau}\equiv\frac{\delta_r\omega_r}{\pi}\frac{\partial\eta}{\partial\tau}, \quad (2)$$

Downloaded 03 May 2010 to 171.66.16.248. Redistribution subject to ASME license or copyright; see http://www.asme.org/terms/Terms_Use.cfm

where ω_r are the zero-flow dimensionless eigenfrequencies of the vertical pipe. As the measured δ_r vary almost linearly with r and reliable measurement of δ_r for $r>3$ was found impossible, and higher δ_r were linearly extrapolated when required.

In previous work (e.g., Païdoussis et al., 1989) the restraining force was modeled by a cubic spring, $f(\eta)=\kappa\eta^3$, which represents a compromise: although this form of $f(\eta)$ is mathematically convenient, it does not model the physical situation perfectly, since it does not recognize that in the free gap the constraint is zero, rather than just small. The stiffness of the restraining bars, Fig. 1(*b*), was determined by applying static loads and measuring the resulting deflection; the results are shown in Fig. 1(*c*). The stiffness is slightly hardening, but almost linear, suggesting something close to trilinear modeling (Moon and Li, 1990): $f(\eta)=\kappa\{\eta-1/2(|\eta+\eta_b|-|\eta-\eta_b|)\}$, which yields $\kappa(\eta-\eta_b)$ for $\eta\geq\eta_b$, $\kappa(\eta+\eta_b)$ for $\eta\leq-\eta_b$ and 0 for $|\eta|<|\eta_b|$. However, the appropriateness of a trilinear model for representing dynamical impact (Hunt and Crossley, 1975), especially in view of the pipe itself being flexible, was questioned: in particular, the abrupt application of the total force of the restraint (abrupt change in slope in Fig. 1(*c*)) at $|\eta|=|\eta_b|$. The following three adaptations to the trilinear model were therefore adopted instead:

$$f(\eta)=\kappa_n\left\{\eta-\frac{1}{2}(|\eta+\eta_{bn}|-|\eta-\eta_{bn}|)\right\}^n,\quad n=2,3,5, \tag{3}$$

in which the sharp discontinuity at $|\eta|=|\eta_b|$ is smoothed; least squares fitting gave the following set of values: for $n=2$, $\kappa_2=2.7\times10^5$, $\eta_{b2}=0.050$, for $n=3$, $\kappa_3=5.6\times10^6$, $\eta_{b3}=0.044$; for $n=5$, $\kappa_5=1.0\times10^9$, $\eta_{b5}=0.031$. These models will henceforth be referred to as "quadratic," "cubic," and "quintic" for short; in the quadratic, clearly $(\eta-\eta_b)^2=(\eta-\eta_b)|\eta-\eta_b|$ to preserve functional oddness. The resulting approximations to the dynamical restraint stiffness are shown in Fig. 1(*c*) for $n=2$ and 3; the curve for $n=5$ is very close to those shown but is omitted to preserve clarity. Calculations will be conducted with all three restraint models and the results compared.

4 Low-Dimensional Models and Convergence

In view of the results of fractal dimensional calculations, the infinite dimensional model will be discretized, and the dynamics of the resultant low-dimensional models, represented by a set of ordinary differential equations, will be explored and later compared to experiment.

4.1 The Reduction Procedure. The system is discretized by utilizing the standard Galerkin expansion

$$\eta(\xi,\tau)=\sum_i\phi_i(\xi)q_i(\tau), \tag{4}$$

where the $\phi_i(\xi)$ chosen are the dimensionless orthonormal set of cantilever beam eigenfunctions. Upon substituting (4) into equation (1), with (2) taken into account, multiplying by $\phi_j(\xi)$ and integrating over the domain (0,1), one obtains

$$\{\ddot{q}\}+[C]\{\dot{q}\}+[K]\{q\}+\{f(q)\}=0, \tag{5}$$

where the elements of the matrices are given in Païdoussis et al. (1989). For purposes of numerical simulation, equation (5) should further be reduced to first-order form:

$$\{\dot{q}\}=\{p\},\quad \{\dot{p}\}=-[C]\{p\}-[K]\{q\}-\{f(q)\}, \tag{6}$$

where $\{q\}$ and $\{p\}$ are the generalized displacement and velocity vectors. If the summation in (4) is truncated at $i=N$, an N degree-of-freedom, i.e., a $2N$-dimensional model of the continuous system is generated.

Once $\{p\}$ and $\{q\}$ are determined, the deflection of the pipe and its velocity at any point ξ may be expressed approximately as

$$\eta(\xi,\tau)\simeq\sum_{i=1}^{N}\phi_i(\xi)q_i(\tau),\quad \dot{\eta}(\xi,\tau)\simeq\sum_{i=1}^{N}\phi_i(\xi)p_i(\tau). \tag{7}$$

4.2 The Hopf Bifurcation. All system parameters are fixed as defined in Section 3.2 and the dimensionless flow velocity u is gradually increased. Eventually, for high enough u the hitherto stable equilibrium is lost, giving birth (if nonlinearities are taken into account) to a stable limit cycle. This defines a Hopf bifurcation, which corresponds to single-degree-of-freedom flutter in aeroelastic terminology. The critical value of $u=u_H$ for the Hopf bifurcation may be found by solving the eigenvalue problem of the linearized system (6); it occurs once two complex conjugate eigenvalues with hitherto negative real parts become purely imaginary and then cross to the positive side of the λ-plane.

The main concern here is the number of modes necessary for accurate prediction of the Hopf bifurcation. The results are shown in Fig. 2. It is seen that convergence is effectively achieved with $N=4$ (c.f., Païdoussis, 1970). The $N=2$ model used in the previous studies of this problem underestimates u_H by 14 percent.

4.3 Period Doubling Bifurcations and Chaos. It has been shown previously for an $N=2$ (four-dimensional) system (Païdoussis and Moon, 1988; Païdoussis et al., 1989) that for u sufficiently above u_H, the stability of the limit cycle is destroyed by a transcritical-like pitchfork bifurcation (destroying the symmetry of the limit cycle), followed at higher u by a period doubling bifurcation; as u is increased further, a cascade of period doubling bifurcations leads to chaos. Of interest here is (i) to explore higher-dimensional ($N>2$) model behavior and possible convergence of the results with N, (ii) to do simulations with the refined analytical model for precise values of the parameters applicable to the experimental system. It is important to recall that in all the foregoing simulations with $N=2$ it was possible to conduct calculations only with $\xi_b\geq0.75$, instead of the actual $\xi_b=0.65$; furthermore, diminished values of the stiffness of the cubic spring (used to model restraint stiffness in the earlier studies) had to be used. Both limitations were imposed by failure of the solution to converge otherwise; more specifically, the solution trajectory tended to escape to infinity, no matter how small the integration step size, the reasons for which have not yet been elucidated.

The simulations were done by integrating equations (6) by the standard fourth-order Runge-Kutta algorithm. The parameter varied is u, whilst the output utilized to display bifurcations is the approximate free-tip velocity of the pipe $\dot{\eta}(1,\tau)$, equations (7). The triggering signal is $\eta(1,\tau)$: when $\eta(1,\tau)=0$ and $\dot{\eta}(1,\tau)>0$, the value of $\dot{\eta}(1,\tau)$ is recorded.

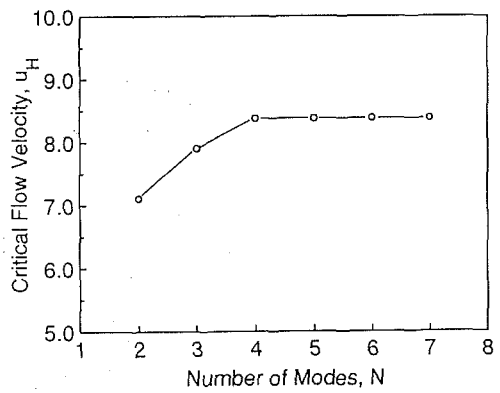

Fig. 2 Convergence of the critical flow velocity for the Hopf bifurcation as a function of the number of modes, *N*, in the Galerkin discretization

Downloaded 03 May 2010 to 171.66.16.248. Redistribution subject to ASME license or copyright; see http://www.asme.org/terms/Terms_Use.cfm

The first thing to remark is that no difficulty was encountered in the simulations for $N>2$ in obtaining convergent solutions for the experimental set of parameters chosen in Section 3.2. Hence, the difficulties referred to in the foregoing must have been related to the inability of the $N=2$ model to properly model the experimental system.

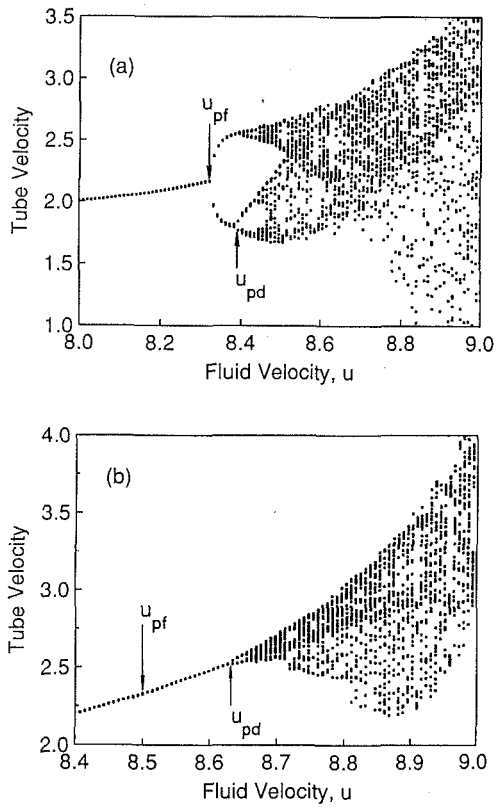

Fig. 3 Bifurcation diagram showing the tube-tip dimensionless velocity amplitude with the dimensionless fluid velocity u as the bifurcation parameter, utilizing the quadratic restraint stiffness representation for *(a)* $N=3$ and *(b)* $N=5$. The subscripts *pf* and *pd*, respectively, refer to pitchfork and period doubling bifurcations

Bifurcation diagrams were constructed for $N=3$ to 7, i.e., six-dimensional to fourteen dimensional systems, for each of three representations of the restraint stiffness, equation (3). Typical results are shown in Fig. 3 for the quadratic model ($n=2$ in equation (3), see also Fig. 1(*b*)) for $N=3$ and $N=5$. Only the portion beyond the Hopf bifurcation is shown in Fig. 3.

In Fig. 3(*a*) it is clearly seen that the first post-Hopf bifurcation occurs at $u=8.325$, followed by another one at $u=8.357$. By referring to Fig. 4(*a*), it is seen that the former is a transcritical-like pitchfork bifurcation, whereby the symmetry of the orbit has been destroyed;[1] the two branches of the pitchfork in Fig. 3(*a*) are obtained with opposite-sign initial conditions. The second bifurcation shown (Fig. 3(*a*), $u=8.357$) is a period doubling one, followed by a cascade of further such bifurcations leading to chaos—a common route to chaos for many continuous systems (Tousi and Bajaj, 1985; Moon, 1988). Figure 4(*b*) shows period-4 motion, while Fig. 4(*c,d*) strongly chaotic motion. In the spectrum of Fig. 4(*d*), the principal frequency peak is only 25 dB approximately above the broadband component of the signal, whereas for weakly chaotic motion at a lower velocity ($u=8.5$, not shown), this peak is prominently above (by 40 dB) the broadband component.

Figure 3(*b*) displays bifurcations for the $N=5$ model, of the same type as for the $N=3$ model of Fig. 3(*a*), but at somewhat different values of u and with some other qualitative differences. Thus, the first period doubling bifurcation occurs at $u=8.630$, as compared to 8.357, which nevertheless are only three percent apart. Also, the pitchfork bifurcation, which is very prominent in Fig. 3(*a*), is just discernible in Fig. 3(*b*).

The bifurcation diagrams with the cubic and quintic representation of the restraint stiffness are quite similar to those of Fig. 3, and are not presented for brevity.

As a measure of convergence of these results, as N is increased and as the model of the restraint stiffness is varied, the first period doubling bifurcation threshold was chosen.

[1] It is recalled that the phase-plane plots are in terms of approximate tip displacement and velocity, equations (7), whereby the $2N$-dimensional space is recomposed into a two-dimensional projection.

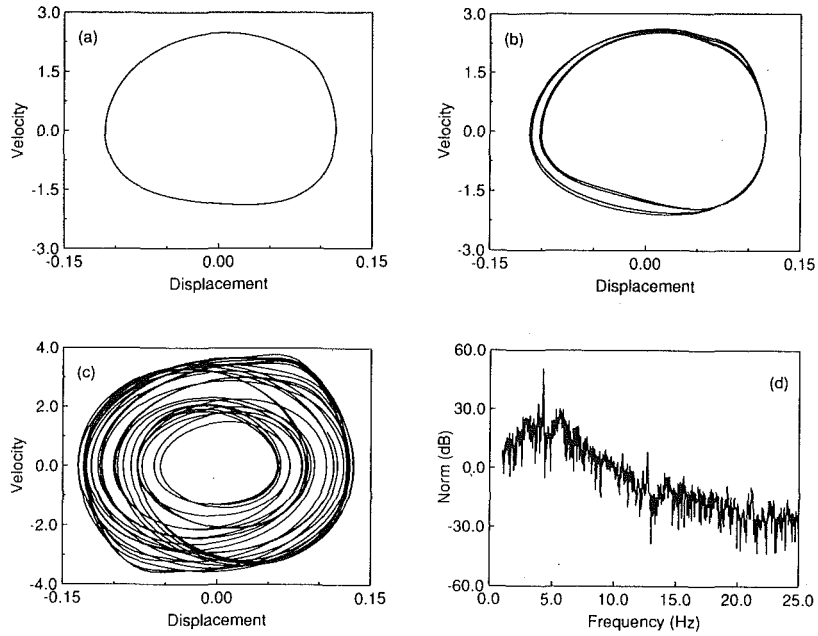

Fig. 4 Phase plane diagrams of tube-tip velocity $\dot{\eta}(1,\tau)$ versus tube-tip displacement, $\eta(1,\tau)$, obtained with $n=2$ and $N=3$; c.f., Fig. 3(*a*), for *(a)* $u=8.35$, *(b)* $u=8.445$, *(c)* $u=9.00$, *(d)* the corresponding power spectrum for $u=9.00$

Downloaded 03 May 2010 to 171.66.16.248. Redistribution subject to ASME license or copyright; see http://www.asme.org/terms/Terms_Use.cfm

The results are shown in Fig. 5. It is seen that for $N=5$ each of the three curves has converged to a steady value. It should be noted that, although looking relatively distant from one another, the three values of the threshold flow velocity for period doubling, u_{pd}, differ by less than 3.5 percent for $N \geq 5$; hence, any one of the three restraint stiffness representations is as good as any of the others, although perhaps the quadratic, which matches closest the data of Fig. 1(*c*)—cf., equation (3), $n=2$—may be considered to be the "best."

Before leaving this section, it should be mentioned that in all simulations, the initial conditions were fixed: $q_1(0) = \pm 0.05$, $q_i(0)=0$ for $i=2, \ldots, N$, and $p_i(0)=0$ for $i=1,2, \ldots, N$, where the $\pm$ values were used to obtain the two branches after the pitchfork bifurcation, Fig. 3. Other initial conditions were tried, but the system was found to be insensitive to the specific choice made, provided that the values were not too large; if they were, then, in some parameter ranges, the numerical solutions "blew up."

5 Comparison of Theoretical to Experimental Results

The results of the analytical model proposed here, encompassing a more realistic representation of the physical system, are qualitatively similar to those of the more idealized versions of the analytical model utilized heretofore (see Païdoussis et al., 1989, 1991), which were already shown to be *qualitatively* similar to those of the experimental system. Accordingly, it is not necessary to undertake a qualitative comparison here. Suffice it to say that the dynamical behavior in terms of the route to chaos and general dynamical character of the motion, as seen in phase plane plots, power spectra, and autocorrelations of the experimental system, is remarkably similar. Nevertheless, it must be stressed that the theoretical results here are the first ever to be presented (and possible) with all system parameters closely matching the experimental system.

In this section the crucial *quantitative* comparison between theory and experiment will be undertaken. In this regard, it is noted that the results of the analytical model have been shown to be convergent (Section 4.3), so that possible agreement with experiment cannot be spurious. The comparison is undertaken in terms of the threshold u for the Hopf and first period-doubling bifurcations, u_H and u_{pd}, and for chaos, u_{ch}. The experimental values have been obtained from Païdoussis and Moon's work (Fig. 6 of that paper).

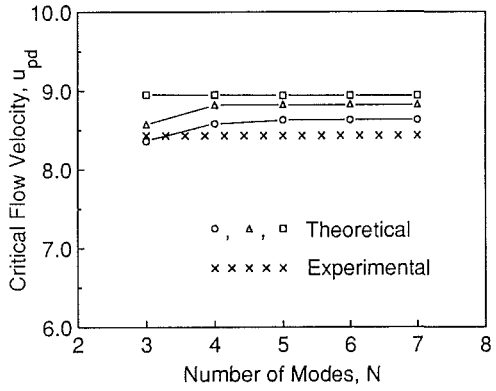

Fig. 5 Convergence of the critical flow velocity for the first period-doubling bifurcation, u_{pd}, with increasing number of modes, N, for the three representations of restraint stiffness: quadratic (○), cubic (△) and quintic (□); also, shown is the experimental result (× ×)

The experimental value of u_{pd} may be compared to theoretical ones in Fig. 5. Numerical values are compared in Table 1. The uncertainty in the experimental results is related to the measurement of the flow velocity and other quantities entering into its nondimensionalization, and also in deciding where exactly the experimental threshold was. The theoretical range arises from the various models for restraint stiffness. The percent discrepancy between theory and experiment is of the order of 5 percent throughout; if possible uncertainties in the experimental results are taken into account, then a maximum possible discrepancy of 8–11 percent is obtained. For this type of system, such agreement between theory and experiment is deemed to be excellent.

6 Stability Analysis

In Section 4 it was seen that the transition to chaos was characterized by a series of bifurcations and associated changes in stability. The first, the Hopf bifurcation, leading to the birth of a limit cycle, has been analyzed through the linearized system. Hence, attention will be focused here on the next bifurcation, which corresponds to loss of stability of the limit cycle itself.

In this section, a stability analysis is undertaken, aimed at calculating u^*, the value of u which corresponds to change of stability of the limit cycle. The approach is based on "center manifold analysis" and follows a strategy described by Rand (1989).

The idea of center manifold analysis is to decrease the dimension of the system being studied by eliminating directions in the phase space which are unimportant for the bifurcation under consideration. This is accomplished by restricting attention to an invariant subspace (the center manifold), containing all essential behavior of the system in the neighborhood of the equilibrium point. Practical considerations dictate that this analysis, feasible in principle for any N, be limited to $N=2$, i.e., a four-dimensional system.

Thus, in system (6), the Hopf bifurcation is characterized by the appearance of two pure imaginary eigenvalues in the equations linearized about the equilibrium point at the origin. Since the other two eigenvalues have negative real parts, the motion of the linearized system will asymptotically approach the space $\mathcal{L}$ spanned by the eigenvectors corresponding to those eigenvalues with zero real parts. In the nonlinear system (6), there exists a curved subspace CM (the center manifold), tangent to the flat subspace $\mathcal{L}$ at the origin, which is invariant under the flow generated by the nonlinear equations.

In order to approximate the critical u^*, the following procedure is followed: (1) an approximation for the CM is obtained; (2) perturbations are used on the resulting two-dimensional problem in order to approximate the limit cycle; (3) the stability of the limit cycle is examined by considering only the two directions normal to the center manifold. The point of the calculation is that, although the original problem was four-dimensional, it is reduced to a two-dimensional problem.

Table 1 Comparison of theoretical to experimental values of the threshold flow velocities for the Hopf and period doubling bifurcations and for chaos. The percent difference is with respect to experiment; "maximum percent differences" represent maximum possible discrepancies, taking into account the five percent experimental uncertainties

Bifurcation	u	Theory	Experiment	|Diff.|	Max. Diff.
Hopf	u_H	8.40	8.04 ± 5 percent	4 percent	9 percent
Period doubling	u_{pd}	8.63–8.94	8.43 ± 5 percent	2–6 percent	11 percent
Chaos	u_{ch}	8.68–8.97	8.72 ± 5 percent	0.5–3 percent	8 percent

Downloaded 03 May 2010 to 171.66.16.248. Redistribution subject to ASME license or copyright; see http://www.asme.org/terms/Terms_Use.cfm

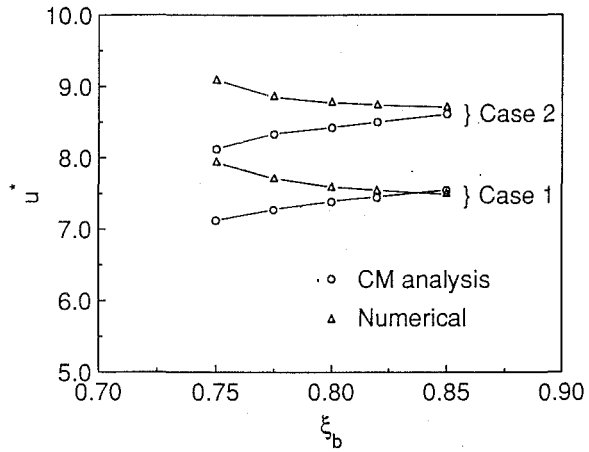

Fig. 6 The critical flow velocity, u^*, for instability of the limit cycle for a cubic spring, $\kappa = 100$, $\alpha = 0.005$ and Case 1: $\beta = 0.2$, $\gamma = 10$; Case 2: $\beta = 0.21$, $\gamma = 26.76$

The calculation was performed by using a MACSYMA computer algebra program (Rand and Armbruster, 1987) which accomplished the foregoing strategy as follows (the step numbers correspond to the numbers in the strategy in the previous paragraph):

1 An eigenanalysis is performed on the linearized equations at $u = u_H$ corresponding to the Hopf bifurcation, and thereafter define $\mu = u - u_H$. The variables in the nonlinear equations are changed, based on the eigencoordinates in the step above. Let y_1, y_2 be the eigencoordinates associated with purely imaginary eigenvalues, while y_3, y_4 correspond to those with negative real parts. The transformed equations are of the form

$$\dot{y}_i = F_i(y_1, y_2, y_3, y_4; \mu), \quad i = 1,2,3,4. \tag{8}$$

A center manifold (CM) is sought in the form of a power series,

$$\begin{aligned} y_3 &= a_1 y_1^3 + a_2 y_1^2 y_2 + a_3 y_1 y_2^2 + a_4 y_2^3 + a_5 \mu y_1 + a_6 \mu y_2, \\ y_4 &= b_1 y_1^3 + b_2 y_1^2 y_2 + b_3 y_1 y_2^2 + b_4 y_2^3 + b_5 \mu y_1 + b_6 \mu y_2. \end{aligned} \tag{9}$$

The actual computation has been automated (Rand and Armbruster, 1987). It consists of substituting (9) into (8) and determining the coefficients a_i and b_i by requiring that the y_3 and y_4 equations be identically satisfied (hence, the CM is an invariant surface).

2 Equations (9) are then substituted into (8) for $i = 1, 2$, giving the flow on the center manifold, in the form $\dot{y}_1 = G_1(y_1, y_2; \mu)$, $\dot{y}_2 = G_2(y_1, y_2; \mu)$. Then a perturbation method, in this case normal forms, is utilized (Rand and Armbruster, 1987) to obtain an approximate solution to the limit cycle in these equations, which will be of the form $y_1 = H_1(t;\mu)$, $y_2 = H_2(t;\mu)$.

3 To study the stability of the limit cycle $y_i = H_i(t;\mu)$, $i = 1,2$, perturbations are introduced away from the limit cycle along the directions y_3 and y_4 by introducing $y_3 = \bar{y}_3 + \zeta_3$, $y_4 = \bar{y}_4 + \zeta_4$, where $\bar{y}_3$ and $\bar{y}_4$ are given by equations (9). The resulting equations for ζ_3 and ζ_4 are

$$\frac{d}{dt}\begin{Bmatrix}\zeta_3\\ \zeta_4\end{Bmatrix} = \begin{bmatrix}\frac{\partial F_3}{\partial y_3} & \frac{\partial F_3}{\partial y_4}\\ \frac{\partial F_4}{\partial y_3} & \frac{\partial F_4}{\partial y_4}\end{bmatrix}\begin{Bmatrix}\zeta_3\\ \zeta_4\end{Bmatrix} \equiv [A(t;\mu)]\begin{Bmatrix}\zeta_3\\ \zeta_4\end{Bmatrix}, \tag{10}$$

where the elements of the $[A(t;\mu)]$ matrix are periodic (which results from the periodicity of the limit cycle). Then, numerical integration of (10) and Floquet theory are used to determine u^*, the smallest value of u for which instability results; from the foregoing sections it is known that this instability is associated with a pitchfork bifurcation.

An important restriction of the foregoing calculation procedure is that the original set of equations, and hence (8), be wholly analytic. In the formulation of equation (3) for the restraint stiffness, however, there is a discontinuity at $\eta = \eta_{bn}$. It is therefore necessary that calculations be confined to those of the earlier analytical model in which an analytic form of restraint stiffness was utilized: $f(\eta) = \kappa\eta^3$; in fact, one of the reasons for introducing this formulation in the earlier studies was so as to allow analysis as well as the computation of Lyapunov exponents.

The results of two sets of calculations are presented in Fig. 6 for systems with parameters as given in the caption. The variable parameter has arbitrarily been chosen to be the restraint location ξ_b. It is seen that with increasing ξ_b agreement between the values of u^* obtained by the center-manifold calculation and by numerical integration improves. The discrepancy between them, however, is in all cases less than 11 percent. This is remarkable, considering that the center manifold calculation involves neglecting terms of order μ^2 and that $\mu(=u-u_H)$, is not so small; e.g., for Case 1, $\xi_b = 0.82$, $u_H = 6.27$, and $u^* = 7.57$, so that $\mu = 1.30$ ($\mu/u_H = 0.21$).

For this analytical model ($f(\eta) = \kappa\eta^3$), the convergence of the critical flow velocities for the pitchfork and period doubling bifurcations and for chaos was also studied with an increasing number of degrees-of-freedom, N; it was found to be quite similar to those in the foregoing sections. The same may be said for the bifurcation diagrams.

7 Conclusion

The main contributions of this paper are three. First, a refined analytical model of the dynamical system was elaborated, to bring it closer to the experimental system than previous attempts, yet retaining its essential simplicity. Furthermore, by utilizing higher-dimensional models than heretofore ($N > 2$), it was for the first time possible to conduct numerical calculations with all parameters matching the experimental ones, without running into any difficulties of convergence of the solution. At the same time, by increasing the number of degrees-of-freedom (N) of the model, it was possible to demonstrate convergence of the results for $N = 4$ or 5 (for all three proposed representations for the restraint stiffness), in terms of the thresholds of pitchfork and period doubling bifurcations. This result agrees well with fractal dimension calculations on the experimental oscillation signal (Païdoussis et al., 1991), giving a fractal dimension of 3.2 in the chaotic regime. This suggests that while two-degree-of-freedom modeling is the bare minimum, as many as four or even five degrees-of-freedom may be necessary for an analytical model to capture the essential dynamics of the system.

The second important contribution of this paper lies in the *quantitative* comparison of theory to experiment. It is not surprising that the dynamical behavior was found to be in good *qualitative* agreement with observation, since simpler, lower-dimensional ($N = 2$) versions of the analytical model achieved as much (Païdoussis and Moon, 1988; Païdoussis et al., 1989, 1991). However, in this paper it has been shown that there is excellent quantitative agreement between theory and experiment as well, in terms of the Hopf and first period doubling bifurcation thresholds and of the onset of chaos: Discrepancies are of the order of five percent (or ten percent when experimental uncertainty margins are included).

The third item of interest in this paper concerns an analytical study of the stability of the limit cycle which emerges via the Hopf bifurcation. This was done by means of center manifold computations, with the aid of symbolic manipulation. Agreement with numerical results for the critical u at which stability is lost was found to be within 11 percent for a range of parameters tested, which is quite reasonable considering that the interval Δu between the Hopf and pitchfork bifurcation (which destroys the stability of the limit cycle) is not very small.

Downloaded 03 May 2010 to 171.66.16.248. Redistribution subject to ASME license or copyright; see http://www.asme.org/terms/Terms_Use.cfm

Acknowledgments

The authors gratefully acknowledge the support to this research by the Natural Sciences and Engineering Research Council of Canada and Le Fonds FCAR of Québec.

References

Axisa, F., Antunes, J., and Villard, B., 1988, "Overview of the Numerical Methods for Predicting Flow-Induced Vibration," ASME *Journal of Pressure Vessel Technology,* Vol. 110, pp. 6–14.

Gregory, R. W., and Païdoussis, M. P., 1966, "Unstable Oscillation of Tubular Cantilevers Conveying Fluid. I. Theory; II. Experiments," *Proceedings of the Royal Society London,* Vol. A293, pp. 512–527 and 528–542.

Holmes, P. J., 1977, "Bifurcations to Divergence and Flutter in Flow-Induced Oscillations: A Finite-Dimensional Analysis," *Journal of Sound and Vibration,* Vol. 53, pp. 471–503.

Hunt, K. H., and Crossley, F. R. E., 1975, "Coefficient of Restitution Interpreted as Damping in Vibroimpact," ASME JOURNAL OF APPLIED MECHANICS, Vol. 42, pp. 440–445.

Moon, F. C., 1987, *Chaotic Vibrations: An Introduction for Applied Scientists and Engineers,* John Wiley and Sons, New York.

Moon, F. C., 1988, "Chaotic Vibrations of a Magnet Near a Superconductor," *Physics Letters A,* Vol. 132, pp. 249–252.

Moon, F. C., and Li, G. X., 1990, "Experimental Study of Chaotic Vibrations in a Pin-Jointed Space Truss Structure," *AIAA Journal,* Vol. 28, pp. 915–921.

Païdoussis, M. P., 1970, "Dynamics of Tubular Cantilevers Conveying Fluid," *Journal of Mechanical Engineering Science,* Vol. 12, pp. 85–103.

Païdoussis, M. P., 1987, "Flow-Induced Instabilities of Cylindrical Structures," *Applied Mechanics Reviews,* Vol. 40, pp. 163–175.

Païdoussis, M. P., Cusumano, J. P., and Copeland, G. S., 1991, "Low-Dimensional Chaos in a Flexible Tube Conveying Fluid," ASME JOURNAL OF APPLIED MECHANICS, accepted for publication.

Païdoussis, M. P., and Issid, N. T., 1974, "Dynamic Stability of Pipes Conveying Fluid," *Journal of Sound and Vibration,* Vol. 33, pp. 267–294.

Païdoussis, M. P., Li, G. X., and Moon, F. C., 1989, "Chaotic Oscillations of the Autonomous System of a Constrained Pipe Conveying Fluid," *Journal of Sound and Vibration,* Vol. 135, pp. 1–19.

Païdoussis, M. P., and Moon, F. C., 1988, "Nonlinear and Chaotic Fluidelastic Vibrations of a Flexible Pipe Conveying Fluid," *Journal of Fluids and Structures,* Vol. 2, pp. 567–591.

Rand, R. H., 1989, "Analytical Approximations for Period-Doubling Following a Hopf Bifurcation," *Mechanics Research Communications,* Vol. 16, pp. 117–123.

Rand, R. H., and Armbruster, D., 1987, *Perturbation Methods, Bifurcation Theory and Computer Algebra,* Springer-Verlag, New York.

Tang, D. M., and Dowell, E. H., 1988, "Chaotic Oscillations of a Cantilevered Pipe Conveying Fluid," *Journal of Fluids and Structures,* Vol. 2, pp. 263–283.

Tousi, S., and Bajaj, A. K., 1985, "Period-Doubling Bifurcations and Modulated Motions in Forced Mechanical Systems," ASME JOURNAL OF APPLIED MECHANICS, Vol. 57, pp. 446–452.

Downloaded 03 May 2010 to 171.66.16.248. Redistribution subject to ASME license or copyright; see http://www.asme.org/terms/Terms_Use.cfm

ERRATA

Errata on "Rigid Punch on Stressed Orthotropic Half-Plane With Partial Slip," by H. L. Bjarnehed and published in the Mar. 1991 issue of the ASME JOURNAL OF APPLIED MECHANICS, Vol. 58, pp. 128–133.

Equations (A15*a*) through (A15c) should read as follows:

$$\sigma_x(x,y)=\frac{\alpha+\beta}{\pi}\int_{-\infty}^{\infty}\frac{[\alpha\beta y\sigma(s)+(x-s)\tau(s)](x-s)^2}{[(\alpha y)^2+(x-s)^2][(\beta y)^2+(x-s)^2]}\,ds, \tag{A15a}$$

$$\sigma_y(x,y)=\frac{\alpha+\beta}{\pi}\,y^2\int_{-\infty}^{\infty}\frac{[\alpha\beta y\sigma(s)+(x-s)\tau(s)]ds}{[(\alpha y)^2+(x-s)^2][(\beta y)^2+(x-s)^2]}, \tag{A15b}$$

$$\tau_{xy}(x,y)=\frac{\alpha+\beta}{\pi}\,y\int_{-\infty}^{\infty}\frac{[\alpha\beta y\sigma(s)+(x-s)\tau(s)](x-s)}{[(\alpha y)^2+(x-s)^2][(\beta y)^2+(x-s)^2]}\,ds. \tag{A15c}$$

Copyright © 1991 by ASME
Downloaded 03 May 2010 to 171.66.16.248. Redistribution subject to ASME license or copyright; see http://www.asme.org/terms/Terms_Use.cfm

M.Toren
Faculty of Mechanical Engineering.

M. Ungarish
Faculty of Computer Science.

G. Pinchuk
Faculty of Mechanical Engineering.

A. Solan
Faculty of Mechanical Engineering, Mem. ASME

Technion—Israel Institute of Technology, Haifa 32000, Israel

Centrifugal Convection due to Mass Transfer Near a Rotating Disk at High Schmidt Number

The centrifugally-driven flow due to a density gradient between the surface of an infinite disk and the ambient fluid in a rotating system with mass transfer is studied for the case of high Schmidt number. Under certain assumptions the velocity and density fields exhibit a similarity like the classical von Karman disk flow, and the governing equations reduce to a nonlinear system of ordinary differential equations. These equations are solved by boundary layer technique or numerically, for high Schmidt number $\sigma = \nu/D$ *and finite or small density difference* $\epsilon_\rho = (\rho_d - \rho_\infty)/\rho_\infty$. *In the latter case it is shown that the major scaling parameter is the product* $\sigma\epsilon_\rho$. *For* $\sigma\epsilon_\rho \gg 1$ *the flow field consists of a constant density* (ρ_∞), *linear Ekman layer driven by a buoyancy sublayer of relative thickness* $(\sigma\epsilon_\rho)^{-1/4}$ *in which* ρ *varies from* ρ_d *to* ρ_∞. *The representative Rossby number of the buoyancy driven flow is* $(\sigma\epsilon_\rho)^{-1/2}$. *The general case* $\epsilon_\rho = O(1)$, $\sigma \gg 1$ *shows similar trends, i.e., a* $\sigma^{-1/4}$ *sublayer. The case of simultaneous driving by density difference and angular velocity difference* $\epsilon_v = (\Omega_d - \Omega_\infty)/\Omega_\infty$ *is also discussed.*

Introduction

Mass transfer between a wall and a fluid in a rotating system occurs in many processes, such as, e.g., rotating electrodes (Levich, 1962) or crystal growth (Riley and Sweet, 1979). The resulting concentration gradient may introduce a density gradient which, in a rotating system, will lead to centrifugal free convection. Under normal gravity conditions, such centrifugal body force will be superimposed on the natural gravity and will be dominant or secondary, depending on the parameters. In particular, in redesigning certain transport processes for space flight, rotation may be considered as a substitute for gravity and may then be the only driving force. Though the detailed analysis of such systems for practical geometries and fluid properties will usually require numerical or approximate solutions, it is of interest to formulate analytically idealized cases as benchmark solutions for the calibration of more general, and less accurate, methods.

In the present paper we discuss the "exact" von Karman disk-type solution for buoyancy-driven convection and mass transfer near an infinite rotating disk in a fluid for a simple binary system and high Schmidt number. The problem is, of course, an analogy of the related heat transfer problem of thermal convection near a rotating disk (Riley, 1964 and 1967, Solan et al., 1983). For the heat transfer case the emphasis is on Prandtl number near unity, and the high Prandtl number case, e.g., oils, is of little practical interest and has not been treated in detail. A numerical solution with only limited asymptotic analysis was given by Hudson (1968). In mass transfer in liquids, in particular, electrochemical processes, high Schmidt numbers, σ, are quite common and relevant (e.g., for the well-known systems of ferro-ferri-cyanide, or copper sulfate in aqueous solution, σ is of the order of 2000–3000) and merit special attention. In this paper we shall focus on high Schmidt number and small or order unity density difference across the boundary layer for problems in which buoyancy is the only driving force for convection or when it is at least of equal importance to the secondary flow driven by an angular velocity difference between wall and fluid.

The major asymptotic scaling parameter will be the high Schmidt number, σ. It may be modified by the density difference $\epsilon_\rho = (\rho_d - \rho_\infty)/\rho_\infty$, which may be asymptotically small or order unity. The subscripts d and ∞ denote the disk and ambient fluid far from the disk, respectively. When a difference in angular velocity is allowed, there shall also appear a velocity difference parameter $\epsilon_v = (\Omega_d - \Omega_\infty)/\Omega_\infty$. In all cases, the solution will admit similarity of the form $rf(z)$. The results will show that when $\sigma \gg 1$ and $\epsilon_\rho \ll 1$, the structure of the boundary layer depends on the product $\sigma\epsilon_\rho$ and will be different as $\sigma\epsilon_\rho$ is small, finite, or large.

Formulation of the Problem

Consider the steady-state, laminar, axisymmetric flow field in a two-component fluid over an infinite disk rotating with angular velocity Ω_d. The fluid far from the disk rotates with angular velocity Ω_∞. Due to mass transfer of the heavier species A at the disk surface, the fluid density at the disk is ρ_d, larger

Contributed by the Applied Mechanics Division of THE AMERICAN SOCIETY OF MECHANICAL ENGINEERS for publication in the JOURNAL OF APPLIED MECHANICS.

Discussion on this paper should be addressed to the Technical Editor, Prof. Leon M. Keer, The Technological Institute, Northwestern University, Evanston, IL 60208, and will be accepted until two months after final publication of the paper itself in the JOURNAL OF APPLIED MECHANICS. Manuscript received by the ASME Applied Mechanics Division, Feb. 20, 1989; final revision, Dec. 20, 1989.

Copyright © 1991 by ASME
Downloaded 03 May 2010 to 171.66.16.248. Redistribution subject to ASME license or copyright; see http://www.asme.org/terms/Terms_Use.cfm

than that at infinity ρ_∞. Assume that the total mass density of the solution ρ is related to the mass concentration of species A in the solution ρ_A (in the parameter range of interest) as

$$\rho = (1 - \rho_B^o/\rho_A^o)\rho_A + \rho_B^o \tag{1}$$

where ρ_A^o, ρ_B^o (constants, $\rho_A^o > \rho_B^o$) are the densities of pure species A and B; i.e., we assume that in this range there is no change of volume upon mixing. We further assume that the density ρ does not depend on pressure, ignore phenomena such as thermal expansion or cross effects, and assume constant viscosity μ and diffusivity D. The governing equations in an inertial cylindrical coordinate system are then:

$$\frac{1}{r}\frac{\partial}{\partial r}(\rho r u) + \frac{\partial}{\partial z}(\rho w) = 0, \tag{2}$$

$$\rho\left(u\frac{\partial u}{\partial r} - \frac{v^2}{r} + w\frac{\partial u}{\partial z}\right) = -\frac{\partial p}{\partial r} + \mu\left\{\frac{1}{r}\frac{\partial}{\partial r}\left[r\left(2\frac{\partial u}{\partial r} - \frac{2}{3}\nabla\cdot\mathbf{v}\right)\right] - \frac{1}{r}\left(2\frac{u}{r} - \frac{2}{3}\nabla\cdot\mathbf{v}\right) + \frac{\partial}{\partial z}\left(\frac{\partial w}{\partial r} + \frac{\partial u}{\partial z}\right)\right\}, \tag{3}$$

$$\rho\left(u\frac{\partial v}{\partial r} + \frac{uv}{r} + w\frac{\partial v}{\partial z}\right) = \mu\left\{\frac{1}{r^2}\frac{\partial}{\partial r}\left(r^2\left[r\frac{\partial}{\partial r}\left(\frac{v}{r}\right)\right]\right) + \frac{\partial}{\partial z}\left(\frac{\partial v}{\partial z}\right)\right\}, \tag{4}$$

$$\rho\left(u\frac{\partial w}{\partial r} + w\frac{\partial w}{\partial z}\right) = -\frac{\partial p}{\partial z} + \mu\left\{\frac{1}{r}\frac{\partial}{\partial r}\left[r\left(\frac{\partial w}{\partial r} + \frac{\partial u}{\partial z}\right)\right] + \frac{\partial}{\partial z}\left(2\frac{\partial w}{\partial z} - \frac{2}{3}\nabla\cdot\mathbf{v}\right)\right\}, \tag{5}$$

$$u\frac{\partial \rho}{\partial r} + w\frac{\partial \rho}{\partial z} = \rho D\left\{\frac{1}{r}\frac{\partial}{\partial r}\left(\frac{r}{\rho}\frac{\partial \rho}{\partial r}\right) + \frac{\partial}{\partial z}\left(\frac{1}{\rho}\frac{\partial \rho}{\partial z}\right)\right\}, \tag{6}$$

$$\nabla\cdot\mathbf{v} = \frac{1}{r}\frac{\partial}{\partial r}(ru) + \frac{\partial w}{\partial z}. \tag{7}$$

Here, all variables have their usual meaning. Note that (6) is the species conservation equation (cf., e.g., Bird et al., 1960, eq. (18.1)-(18.14)) in which the mass concentration ρ_A was eliminated by taking account of the linear dependence of ρ on ρ_A (equation (1)) and the equation of continuity (equation (2)). The boundary conditions at the disk surface and far from it are:

$$z = 0: \quad u = 0, \quad v = \Omega_d r, \quad w = -\frac{D}{\rho_d}\frac{1}{K}\frac{\partial \rho}{\partial z}, \quad \rho = \rho_d;$$
$$z \to \infty: \quad u \to 0, \quad v \to \Omega_\infty r, \quad \rho \to \rho_\infty. \tag{8}$$

Here, $K = 1 - \rho_d/\rho_A^o$. The nonzero axial velocity boundary condition at $z = 0$ emerges from the diffusion-convection mass transfer of species A (cf., e.g., Bird et al., 1960, Table 16.2-1(A)), taking account of the fact that at the disk surface the flux of species B is zero, and of the linear relation in equation (1) at the disk surface which is impermeable to B.

The system of equations is similar to that of the classical von Karman incompressible rotating flow over an infinite plate with the difference that here we allow a variable density, which depends on (and only on) concentration and that at $z = 0$, there is a nonzero axial velocity due to the mass transfer from the wall into the fluid. Two forcing terms are present: (a) the angular velocity difference $\Omega_d - \Omega_\infty$, which has been discussed in detail for the usual one-component fluid, and (b) the density difference $\rho_d - \rho_\infty$, which leads to a centrifugal buoyancy-driven flow. We shall focus on the latter.

Analysis

The system of equations admits a similarity formulation of the von Karman type. In a frame of reference rotating with Ω_∞, we introduce the reduced dimensionless field U, V, W, P, R as follows:

$$u = \Omega_\infty r U(Z), \quad v = \Omega_\infty r(1 + V(Z)),$$
$$w = \Omega_\infty l W(Z), \quad \rho = \rho_\infty R(Z),$$
$$p = \frac{1}{2}\rho_\infty \Omega_\infty^2 r^2 + \rho_\infty \Omega_\infty^2 l^2 P(Z),$$

where

$$z = lZ, \quad l = [\mu/(\rho_\infty \Omega_\infty)]^{1/2}. \tag{9}$$

The governing balances are thus reduced to a system of dimensionless ordinary differential equations

$$2RU + \frac{d}{dZ}(RW) = 0, \tag{10}$$

$$R\left[U^2 - (1+V)^2 + W\frac{dU}{dZ}\right] = -1 + \frac{d^2U}{dZ^2}, \tag{11}$$

$$R\left[2U(1+V) + W\frac{dV}{dZ}\right] = \frac{d^2V}{dZ^2}, \tag{12}$$

$$RW\frac{dW}{dZ} = -\frac{dP}{dZ} + \frac{2}{3}\frac{dU}{dZ} + \frac{4}{3}\frac{d^2W}{dZ^2}, \tag{13}$$

$$W\frac{dR}{dZ} = \frac{1}{\sigma}R\frac{d}{dZ}\left(\frac{1}{R}\frac{dR}{dZ}\right), \tag{14}$$

and boundary conditions

$$Z = 0: \quad U = 0, \quad V = (\Omega_d - \Omega_\infty)/\Omega_\infty = \epsilon_v, \quad W = -\frac{1}{\sigma}\frac{1}{K}\frac{1}{R}\frac{dR}{dZ}, \quad R = \rho_d/\rho_\infty = 1 + (\rho_d - \rho_\infty)/\rho_\infty = 1 + \epsilon_\rho = R_d;$$
$$Z \to \infty: \quad U \to 0, \quad V \to 0, \quad R \to 1. \tag{15}$$

Here, $\sigma = \mu/(\rho_\infty D)$ is the Schmidt number. The axial momentum equation (13) serves to calculate the pressure, and need not be considered in the solution of (10-12), (14).

Numerical solutions of the two point boundary value problem (10)-(15) and those of similar subsequent problems referred to below, were carried out by a finite difference algorithm combined with a modified Newton-Raphson solver. However, valuable information can be obtained by further analysis of particular cases.

Consider the case $\epsilon_v = 0$, i.e., pure buoyancy driving. The driving term is $\epsilon_\rho = (\rho_d - \rho_\infty)/\rho_\infty$ which can be finite $\epsilon_\rho = O(1)$, or small $\epsilon_\rho \ll 1$. The only scaling parameter in the equation is σ, which we assume to be large $\sigma \gg 1$. Since K is $O(1)$, the details of the solution and the results will then depend on σ and ϵ_ρ. Consider $\epsilon_\rho \ll 1$ first:

Small density difference, $\epsilon_\rho \ll 1$.

Bearing in mind that the driving term is small, we rescale using ϵ ($\epsilon \equiv \epsilon_\rho$):

$$U, V, W = \epsilon(\overline{U}, \overline{V}, \overline{W}), \quad R = 1 + \epsilon\overline{R}. \tag{16}$$

Then, to leading order in ϵ, the pertinent system is

$$2\overline{U} + \frac{d\overline{W}}{dZ} = 0,$$
$$-2\overline{V} - \overline{R} = \frac{d^2\overline{U}}{dZ^2},$$
$$2\overline{U} = \frac{d^2\overline{V}}{dZ^2}$$
$$\sigma\epsilon\overline{W}\frac{d\overline{R}}{dZ} = \frac{d^2\overline{R}}{dZ^2};$$

Downloaded 03 May 2010 to 171.66.16.248. Redistribution subject to ASME license or copyright; see http://www.asme.org/terms/Terms_Use.cfm

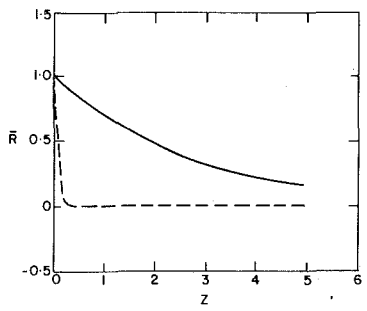

Fig. 1(a)

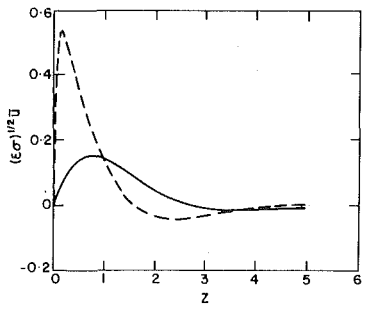

Fig. 1(b)

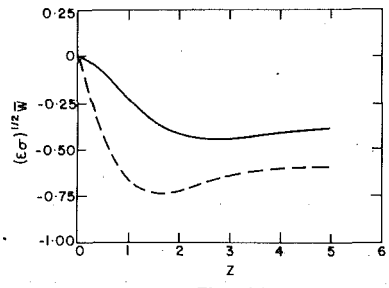

Fig. 1(c)

Fig. 1 Numerical solution of system (17). Density, radial, and axial velocity versus z. ——— $\epsilon\sigma = 1$; - - - - - - $\epsilon\sigma = 10^4$.

$$Z=0: \quad \overline{U}=\overline{V}=\overline{W}=0, \quad \overline{R}=1;$$
$$Z\to\infty: \quad \overline{U}, \overline{V}, \overline{R}\to 0. \tag{17}$$

The only parameter is now the product $\sigma\epsilon$. In general, equations (17) were solved numerically. Representative results are shown in Fig. 1. As expected, the axial density gradient induces a radial flux supported by an axial flow and accompanied by a retrograde angular motion. When $\epsilon\sigma = O(1)$ the density and velocity components display variations on the same axial scale. For a high value of $\sigma\epsilon$ (e.g., 10^4 in Fig. 1), the density gradient is confined to a narrow region near the disk, suggesting an inner density sublayer structure. For $\sigma\epsilon$ small or large, further asymptotic analysis is possible:

$\sigma\epsilon \ll 1$. This is entirely analogous to the problem of thermal convection treated by Riley (1967). The density layer is $O[(\sigma\epsilon)^{-1}]$, i.e., much thicker than the momentum layer which is $O(1)$ on the present scale. The solution is

$$\overline{U}=\frac{1}{2}e^{-Z}\sin Z, \quad \overline{V}=-\frac{1}{2}(1-e^{-Z}\cos Z),$$
$$\overline{W}=\frac{1}{2}[e^{-Z}(\sin Z+\cos Z)-1], \quad \overline{R}=e^{-\frac{1}{2}\sigma\epsilon Z}. \tag{18}$$

$\sigma\epsilon \gg 1$. Here we anticipate an inner density layer, much thinner than the outer momentum layer. In the outer layer, $Z = O(1)$, denoted by the subscript o, the density perturbation vanishes, ($R_o = O$), and the equations reduce to *a linear, Ekman balance:*

$$2\overline{U}_o+\frac{d\overline{W}_o}{dZ}=0,$$
$$-2\overline{V}_o=\frac{d^2\overline{U}_o}{dZ^2},$$
$$2\overline{U}_o=\frac{d^2\overline{V}_o}{dZ^2}; \tag{19}$$

with the outer boundary conditions:

$$Z\to\infty \quad \overline{U}_o, \overline{V}_o\to 0. \tag{20}$$

The solution is

$$\overline{U}_o=-A_oe^{-Z}\cos Z+B_oe^{-Z}\sin Z,$$
$$\overline{V}_o=A_oe^{-Z}\sin Z+B_oe^{-Z}\cos Z,$$
$$\overline{W}_o=(A_o+B_o)e^{-Z}\sin Z+(B_o-A_o)e^{-Z}\cos Z+\overline{W}_\infty. \tag{21}$$

The constants A_o, B_o, $\overline{W}_\infty$ will be found by matching with the inner layer.

The thickness of the inner layer, denoted by the subscript i, is $O[(\sigma\epsilon)^{-1/4}]$. We define rescaled variables:

$$\zeta=(\sigma\epsilon)^{1/4}Z,$$
$$\overline{U}=(\sigma\epsilon)^{-1/2}\overline{U}_i, \quad \overline{V}=(\sigma\epsilon)^{-3/4}\overline{V}_i,$$
$$\overline{W}=(\sigma\epsilon)^{-3/4}\overline{W}_i, \quad \overline{R}=\overline{R}_i, \tag{22}$$

and introduce these into equations (17). The leading order terms are now

$$2\overline{U}_i+\frac{d\overline{W}_i}{d\zeta}=0, \tag{23a}$$
$$-\overline{R}_i=\frac{d^2\overline{U}_i}{d\zeta^2}, \tag{23b}$$
$$0=\frac{d^2\overline{V}_i}{d\zeta^2}, \tag{23c}$$
$$\overline{W}_i\frac{d\overline{R}_i}{d\zeta}=\frac{d^2\overline{R}_i}{d\zeta^2}; \tag{23d}$$

with the inner boundary conditions

$$\zeta=0: \quad \overline{U}_i=\overline{V}_i=\overline{W}_i=0, \quad \overline{R}_i=1. \tag{24}$$

In this case the boundary condition of the axial velocity is reduced to the usual, homogeneous form.

Note that (23) is nonlinear, and must be solved numerically, taking into account matching with (21). The matching between the two layers (at $\zeta\to\infty$, $Z\to 0$) is performed by expanding the outer layer solution (21) in power series for $Z\to 0$ (Appendix). This procedure yields the required constants in equation (21):

$$A_o=\overline{W}_\infty=-(\sigma\epsilon)^{-\frac{1}{2}}\overline{U}_i(\infty), \quad B_o=0 \tag{25}$$

and the outer boundary conditions for the numerical solution of (23):

$$\zeta\to\infty; \quad \frac{d\overline{U}_i}{d\zeta}\to 0, \quad \overline{R}_i\to 0. \tag{26}$$

Consequently, the leading solution for $\overline{V}_i$ is

$$\overline{V}_i=-\overline{U}_i(\infty)\zeta. \tag{27}$$

As a result of the matching, it can be seen that the terms containing B_o in the outer solution are negligible ($O[(\sigma\epsilon)^{-1}]$) as compared with the A_o terms which are $O[(\sigma\epsilon)^{-1/2}]$). Thus, the inner layer equations (23*a*, *b*, *d*) with the boundary conditions (24), (26) are well posed and were solved numerically. The numerical constants characterizing this $\sigma\epsilon \gg 1$ solution are:

$$\overline{U}_i'(0)=0.912, \quad \overline{R}_i'(0)=-0.642, \quad \overline{U}_i(\infty)=0.625. \tag{28}$$

Note that the small density perturbation problem examined here is nonlinear. It should be compared with the related prob-

Downloaded 03 May 2010 to 171.66.16.248. Redistribution subject to ASME license or copyright; see http://www.asme.org/terms/Terms_Use.cfm

lem of velocity-driven flow, with constant density (but variable concentration). In that case the flow field is independent of the concentration field, and the inner (diffusion) layer thickness is $O(\sigma^{-1/3})$ rather than $O[(\sigma\epsilon)^{-1/4}]$ as in the present case. Note also that in the present analysis the representative Rossby number (induced velocity/imposed velocity) is $O[(\sigma\epsilon)^{-1/2}]$.

A uniformly valid solution, obtained by matching the inner and outer layer is then:

$$\overline{U} = (\sigma\epsilon)^{-1/2}\overline{U}_i(\infty)[-f(\zeta) + e^{-Z}\cos Z],$$

$$\overline{V} = -(\sigma\epsilon)^{-1/2}\overline{U}_i(\infty)e^{-Z}\sin Z,$$

$$\overline{W} = (\sigma\epsilon)^{-1/2}\overline{U}_i(\infty)[(\sigma\epsilon)^{-1/4}h(\zeta) - 1 - e^{-Z}(\sin Z - \cos Z)],$$

$$\overline{R} = \overline{R}_i(\zeta). \tag{29}$$

The functions $\overline{R}_i(\zeta)$, $f(\zeta)$, $h(\zeta)$, displayed in Fig. 2, are provided by the numerical solution of the inner layer and the following definitions:

$$f(\zeta) = \frac{1}{\overline{U}_i(\infty)}[\overline{U}_i(\infty) - \overline{U}_i(\zeta)], \quad h(\zeta) = 2\int_0^\zeta f(\zeta)d\zeta.$$

In particular,

$$f(0) = 1, \quad f(\infty) = 0, \quad h(0) = 0, \quad h(\infty) = 1.127. \tag{30}$$

The asymptotic solution (28)–(29) shows good agreement with the fully numerical solution of equations (17), even for a moderately small value of the parameter $(\sigma\epsilon)^{-1/4} = 0.1$, (i.e., $\sigma\epsilon = 10^4$) (see Fig. 3).

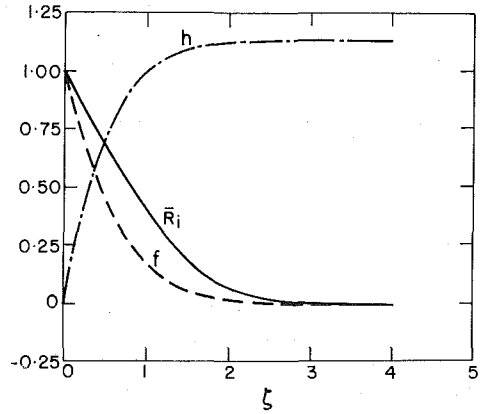

Fig. 2 Inner layer functions R$_i$, *f*, *h* versus stretched coordinate ζ, for the case $\epsilon_\rho \to 0$

Finite Density Difference, $\epsilon_\rho = O(1)$. The case of $\epsilon = \epsilon_\rho = O(1)$ defined by equations (10)–(15) (with $\epsilon_v = 0$), introduces explicitly two additional parameters, ϵ and K. An interesting novel feature of this finite density difference case is the presence of a significant "blowing" velocity at the disk. Nevertheless, the numerical solution of the full system was readily carried out for a wide range of σ, $0.2 \le K \le 0.75$ and $\epsilon \le 1$. Representative results for $\sigma = 10^4$, $\epsilon = 1$ are shown in Fig. 4. The axial velocity W is positive at $Z = 0$ and negative as $Z \to \infty$, illustrating the opposite effects of diffusion (dominant near the disk) and of centrifugally driven axial suction (dominant far from the disk). The phenomenon is more emphasized for low values of K, and its influence is also apparent in U, V, and ρ distributions. Despite this "blowing," the finite density perturbation in Fig. 4 is clearly confined to a thin sublayer, and the velocity field in this region displays similar trends to the $\epsilon \ll 1$ case.

Indeed, the asymptotic analysis shows an inner diffusion layer of thickness $O(\sigma^{-1/4})$ and an outer momentum layer entirely analogous to that of the small density perturbation case discussed previously. As $\sigma \gg 1$, $(\epsilon\sigma)^{-1/2}$ is again the representative Rossby number and the outer region is again a linear Ekman layer. Although ϵ is finite, it is still convenient to include it in the formulation. Consequently, the inner layer variables are scaled again as in (16), (22), and the equations, to leading order in $\sigma^{-1/4}$ (ϵ is now inactive asymptotically), are:

$$2(1+\epsilon\overline{R}_i)\overline{U}_i + \frac{d}{d\zeta}[(1+\epsilon\overline{R}_i)\overline{W}_i] = 0,$$

$$\overline{R}_i = \frac{d^2\overline{U}_i}{d\zeta^2},$$

$$0 = \frac{d^2\overline{V}_i}{d\zeta^2},$$

$$\overline{W}_i\frac{d\overline{R}_i}{d\zeta} = (1+\epsilon\overline{R}_i)\frac{d}{d\zeta}\left[\frac{1}{(1+\epsilon\overline{R}_i)}\frac{d\overline{R}_i}{d\zeta}\right];$$

$$\zeta = 0: \quad \overline{U}_i = \overline{V}_i = 0, \quad \overline{R}_i = 1,$$

$$\overline{W}_i = -\frac{\epsilon}{K}\frac{1}{1+\epsilon}\frac{d\overline{R}_i}{d\zeta};$$

$$\zeta \to \infty: \quad \frac{d\overline{U}_i}{d\zeta} \to 0, \quad \overline{R}_i \to 0. \tag{31}$$

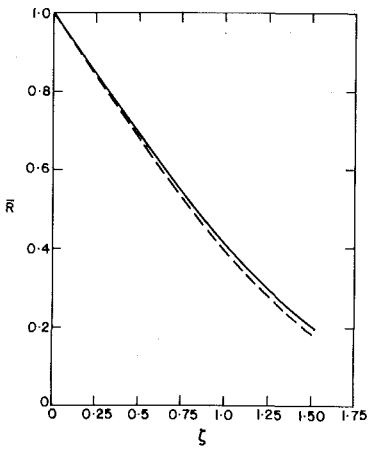

Fig. 3(*a*)

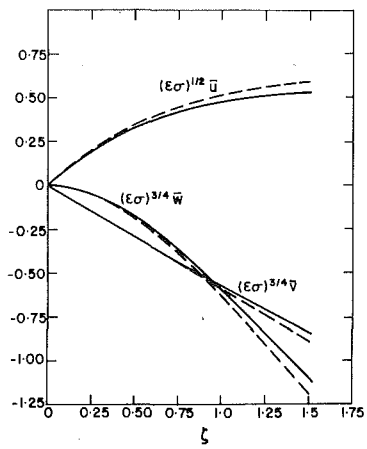

Fig. 3(*b*)

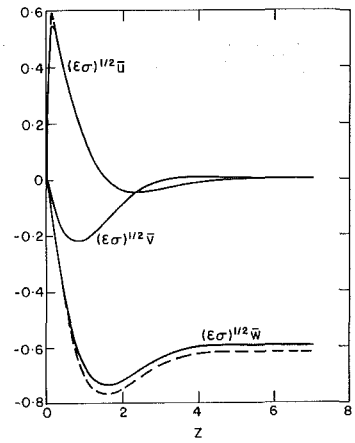

Fig. 3(*c*)

Fig. 3 A comparison between the numerical (——) and matched asymptotic (- - -) solutions of system (17) for $\epsilon\sigma = 10^4$

Downloaded 03 May 2010 to 171.66.16.248. Redistribution subject to ASME license or copyright; see http://www.asme.org/terms/Terms_Use.cfm

Equations (31) are quite similar to equations (23, 24), except for more non-linear coupling, introduced by the explicit dependence on the parameter ϵ and K. In Fig. 5 typical solutions of the sublayer (31) are shown (the extreme $K = \infty$ is physically meaningless, but is useful as a "no blowing" reference result). As K decreases the apparent "blowing" of heavier material increases. This enhances the radial transport in the boundary layer (i.e., $\overline{U}_i(\infty)$ increases) but has little consequences on the profile ρ.

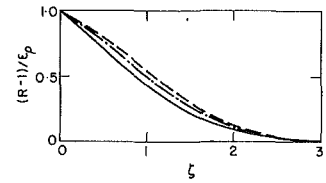

Fig. 4(a)

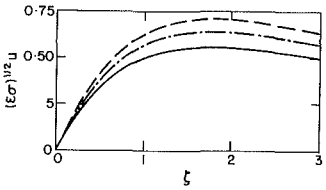

Fig. 4(b)

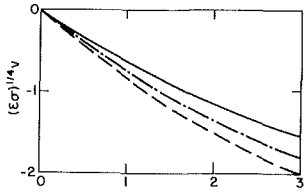

Fig. 4(c)

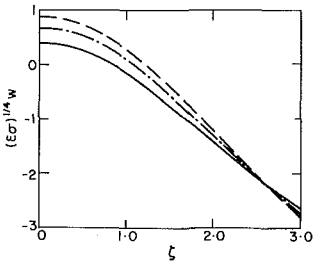

Fig. 4(d)

Fig. 4 Solution of the full similarity equations (10)–(15) for $\epsilon_\rho = 1$, $\epsilon_v = 0$, $\sigma = 10^4$. The sublayer region is plotted for $K = 0.2$ - - -, 0.333 - · - · -, 0.750 ———.

It is emphasized again that outside this sublayer a linear Ekman flow prevails (i.e., equations (21) with $B_o = 0$, $A_o = \overline{W}_\infty = (\sigma\epsilon)^{-1/2}\,\overline{U}_i(\infty)$). Moreover, it is observed that when $\epsilon \leq 1$ and $K \geq 0.2$ the numerical value of $\overline{U}_i(\infty)$ differs from the value obtained for $\epsilon = 0$ by $\pm 30\%$ at most.

Combined Effect of Density and Angular Velocity Driving, $\epsilon_\rho \ll 1$, $e_v \ll 1$. Denote $\epsilon = \epsilon_\rho$, $\beta = \epsilon_v/\epsilon_\rho$, and consider the case $\epsilon \ll 1$, $\sigma\epsilon \gg 1$.

If, in addition $\beta \doteq O[(\sigma\epsilon)^{-1/2}]$, it can be shown that the flow field scales as in the pure density driven case. The inner layer of thickness $O[(\sigma\epsilon)^{-1/4}]$ is unchanged (to leading order in this variable).

The matched solution is a superposition of (29) and the pure velocity-driven field whose radial, azimuthal, and axial components are:

$$\overline{U} = (\sigma\epsilon)^{-1/2}\overline{U}_i(\infty)[-f(\zeta) + e^{-z}\cos z] + \beta e^{-z}\sin z.$$

$$\overline{V} = -(\sigma\epsilon)^{-1/2}\overline{U}_i(\infty)e^{-z}\sin z + \beta e^{-z}\cos z.$$

$$\overline{W} = (\sigma\epsilon)^{-1/2}\overline{U}_i(\infty)[(\sigma\epsilon)^{-1/4}h(\zeta) - 1 - e^{-z}(\sin z - \cos z)] + \beta[e^{-z}(\cos z + \sin z) - 1].$$

However, this superposition is obviously problematic for negative β (i.e., disks rotating slower than the fluid bulk) because it yields a reversal of the axial velocity for $\beta \approx -(\sigma\epsilon)^{-1/2}U_i(\infty)$. Actually, no satisfactory solutions beyond that value have been obtained, which suggests the ill conditioning and instability of the present problem in this parameter range. On the other hand, no difficulties have been encountered for positive β. Significant quantitative discrepancies from the above mentioned superposition show up *in the inner region* when $\beta \geq O[(\sigma\epsilon)^{-1/4}]$: The sublayer shrinks and its driving force decreases. The outer region is dominated by the angular velocity driving in this range of parameters.

Conclusion

The flow due to a density gradient near a rotating infinite disk admits, under certain assumptions, an exact similarity solution of the full equations which reduces the problem to a variation of the classical von Karman rotating disk problem. In general, the resulting system requires numerical treatment. For high Schmidt number σ, the flow field admits asymptotic scaling, and in conjunction with a small density driving term $\epsilon = (\rho_d - \rho_\infty)/\rho_\infty$, even further simplification is possible, which indicates the splitting of the boundary layer into a momentum and a diffusion layer, scaled by $(\sigma\epsilon)^{1/4}$. The relatively simple solution presented here can be used as a limiting case in practical problems for both the improvement of approximate analytical methods and the calibration of less-idealized and more complicated numerical solvers.

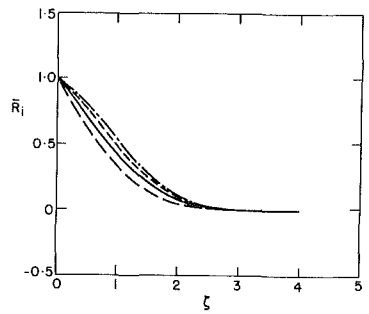

Fig. 5(a)

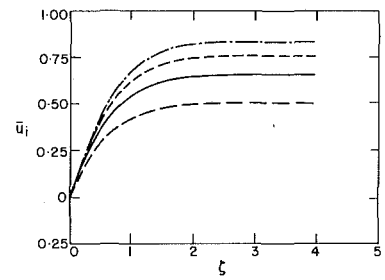

Fig. 5(b)

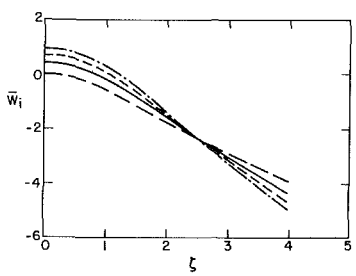

Fig. 5(c)

Fig. 5 Solution of the sublayer equations (31) for $\epsilon_\rho = 1$, $K = 0.200$ - · - ·; 0.333 - - - 0.750 ———; ∞ - - -.

Downloaded 03 May 2010 to 171.66.16.248. Redistribution subject to ASME license or copyright; see http://www.asme.org/terms/Terms_Use.cfm

Acknowledgment

This research was partly supported by grants from the Y. Winograd Chair in Fluid Mechanics, the Louis Edelstein Endowment Fund (to M.U.), and the Fund for Promotion of Research at Technion (to A.S.).

References

Bird, R. B., Stewart, W. E., and Lightfoot, E. N., 1960, *Transport Phenomena*, John Wiley and Sons, New York.

Hudson, J. L., 1968, "Convection Near a Cooled Disk Rotating with its Environment," *Int. J. Heat Mass. Transfer*, Vol. 11, pp. 407–414.

Levich, V. G., 1962, *Physicochemical Hydrodynamics*, Prentice-Hall, Englewood Cliffs, N.J., p. 60.

Riley, N., 1964, "The Heat Transfer from a Rotating Disk," *Quart. J. Mech. Appl. Math.*, Vol. 17, pp. 331–349.

Riley, N., 1967, "Thermally Induced Boundary-layer Flows in a Rotating Environment," *J. Fluid Mech.*, Vol. 29, No. 2, pp. 241–257.

Riley, N., and Sweet, D. A., 1979, "Effects of Rotation on Czochralski Growth," *J. Crystal Growth*, Vol. 47, pp. 557–567.

Solan, A., Olek, S., and Toren, M., 1983, "Rotating Compressible Flow Over an Infinite Disk," ASME JOURNAL OF APPLIED MECHANICS, Vol. 50, pp. 511–516.

APPENDIX

Matching the Inner and Outer Layers

The asymptotic behavior of the inner layer, as $\zeta \to \infty$ is derived from equations (23) under the assumption $\overline{R}_i \to 0$. The resulting form is

$$\overline{U}_i \sim A_i\zeta + B_i; \quad \overline{W}_i \sim A_i\zeta^2 + 2B_i\zeta + C_i; \quad \overline{V}_i = F_i\zeta + G_i. \tag{A1}$$

Here, A_i, B_i, C_i . . . are constants $O(1)$. The solution for $\overline{V}_i$ is actually the exact solution for the whole inner layer rather than an asymptotic one.

The asymptotic behavior of the outer layer for $Z \to 0$ is obtained by expanding the solution (21) in a power series:

$$\overline{U}_o \sim -A_o + (A_o + B_o)Z + \frac{1}{3}(B_o - A_o)Z^3 + \ldots$$

$$\overline{V}_o \sim B_o + (A_o - B_o)Z - A_oZ^2 + \frac{1}{3}(B_o + A_o)Z^3 + \ldots$$

$$\overline{W}_o \sim (B_o - A_o + \overline{W}_\infty) + 2A_oZ - (A_o + B_o)Z^2 + \frac{2}{3}Z^3 - \ldots. \tag{A2}$$

Recalling that $\zeta = (\sigma\epsilon)^{1/4}Z$, $(\sigma\epsilon) \to \infty$ and matching (A1) with (A2), term by term, we obtain:

$$A_o = -(\sigma\epsilon)^{-1/2}B_i \;;\; F_i = -B_i \;;\; \overline{W}_\infty = A_o$$
$$B_o = 0 \;;\; A_i = 0 \;;\; C_i = 0 \;;\; G_i = 0. \tag{A3}$$

The outer boundary condition of the inner layer is:

$$\zeta \to \infty \;:\; \frac{d\overline{U}_i}{d\zeta} \to 0, \tag{A4}$$

and B_i is given by

$$\zeta \to \infty \;:\; \overline{U}_i \to B_i \quad \text{i.e.,} \quad B_i = \overline{U}_i(\infty).$$

Downloaded 03 May 2010 to 171.66.16.248. Redistribution subject to ASME license or copyright; see http://www.asme.org/terms/Terms_Use.cfm

On Damping of the Normal Component of Fluctuations in the Wall Region of Turbulent Flow

Wlodzimierz Kozlowski
Polish Academy of Sciences,
Institute of Fundamental Technological Research,
Department of Fluid Mechanics,
00-049 Warsaw, Poland

Effective model representation of the normal component of ordered motions in the wall region of a turbulent flow is proposed. Analysis of this model enables us to express the value given by the Van Driest damping function at a point with coordinate y *(distance to the wall) as a relationship between intensities of the normal component of pulsations which are defined at points* 2y, y, *and* y/2. *The novel formula has no empirical coefficients and can successfully replace the Van Driest function in computations. It appears to take account of the damping effect which results locally from distinct classes of ordered motions directed wallwards or outwards within the wall region of a turbulent flow.*

1 Introduction

The damping function proposed by Van Driest (1956) is

$$F = 1 - \exp(-y_+/A) \tag{1}$$

employed to diminish the value of the Prandtl mixing length within the near-wall region of a turbulent shear flow. Here, $A = 26$ is the dimensionless constant; $y_+ = yu_t/\nu$, where y is the distance to the wall, ν denotes a kinematic molecular viscosity coefficient, and u_t is the friction velocity. The mixing length (Prandtl, 1925) is the average distance traveled by a distinct fluid particle in the normal direction before loss of individuality of the particle due to mixing (Rotta, 1972). As each individual fluid particle can move outwards or wallwards, one may regard an average net effect of these motions as the result of fluctuations of a virtual particle around a center point, y. In putting forward this assumption we proceeded from the method of estimating the mixing lengths which is recommended for wall-bounded flows in Minski (1940), and Derbunovitsh, Repik, and Sosedko (1978). This method exploits the idea proposed by Keller and Friedmann (1925) for correlating velocities at points located symmetrically with respect to a centerpoint, y. The $F(y)$ may be tentatively considered, under the assumption made above, as a factor that represents effective damping of the aforementioned fluctuations.

Futhermore, one may consider those fluctuations as a model source of the effects corresponding to those resulting from the mixing processes that manifest themselves in the normal direction. On the other hand, however, a number of available experimental reports reveals that classes of ordered motions directed wallwards or outwards are inherent to the bursting phenomenon occurring within the near-wall region of a turbulent flow and, generally, they are not independent (eg., Offen and Kline, 1975; Utami and Ueno, 1987). Those motions are the actual cause of the mixing. This suggested the idea for constructing the effective model representation of the normal component of the ordered motions which utilizes the concept of virtual fluid particles fluctuating along an axis normal to the wall around their center points.

That model has been constructed and analyzed in the present work (Section 2). This analysis enables us to express the $F(y)$ as a factor representing a relative decrease in the total intensity of the normal component of turbulent pulsations. That total intensity, referred to a point with the coordinate y, results from intensities $\sqrt{\langle v^2\rangle}/U$, $\sqrt{\langle v^2\rangle}/u_t$ and $\langle v^2\rangle/\langle v^2\rangle_{mx}$ defined at points with coordinates, $2y$, $y/2$, and y, respectively. The novel relationship expressing $F(y)$ is verified by employing it, instead of the formula (1), to modify phenomenological formulae, after which the kinematic eddy viscosity coefficient $\nu_t(y)$ and the Reynolds shear stress $-\rho\langle uv\rangle$ are estimated. Here, $u = u_1$ or $v = u_2$ is the streamwise or normal component of the turbulent fluctuation of velocity; ρ is the fluid density, the brackets $\langle\,\rangle$ denote conventional averaging, U is the average streamwise velocity, and the subscript mx indicates the maximal value of a quantity varying along axis of coordinates that is normal to the wall. The phenomenological model constructed on the basis of the equation for the mean turbulent energy (MTE) with application of those formulae modified is employed to compute characteristics of the fully developed turbulent flow through a stright circular pipe. Results of those computations show sufficiently good agreement with the available experimental data (Section 3). Discussion presented in

Contributed by the Applied Mechanics Division of THE AMERICAN SOCIETY OF MECHANICAL ENGINEERS for presentation at the Joint Applied Mechanics/Bioengineering Conference, Ohio State University, Columbus, OH, June 16-19, 1991.

Discussion on this paper should be addressed to the Technical Editor, Leon M. Keer, The Technological Institute, Northwestern University, Evanston, IL 60208, and will be accepted until two months after final publication of the paper itself in the JOURNAL OF APPLIED MECHANICS. Manuscript received by the ASME Applied Mechanics Division, Feb. 2, 1989; final revision, May 30, 1990.

Paper No. 91-APM-33.

Copyright © 1991 by ASME
Downloaded 03 May 2010 to 171.66.16.248. Redistribution subject to ASME license or copyright; see http://www.asme.org/terms/Terms_Use.cfm

Section 4 leads to the conclusion that the character of the damping represented by the profile $F(y)$ may be regarded as result of variation of the relation between average efficiency of ordered wallward motions and average efficiency of ordered motions directed outwards.

2 Assumptions and Analysis

Let us consider the simplest system composed of two virtual fluid particles denoted as A and B. They fluctuate around respective center points $y_A > 0$ and $y_B > 0$. Then each particle $i = A$ or B can achieve its extreme positions with the coordinates $y(i) = y_i \pm a_i$, where $a_i > 0$ is the amplitude of the fluctuation of the particle. Presence of the wall restricts each amplitude a_i to the respective limit $y_i > a_i$. Therefore, a particle i can approach the upper limits of its extreme positions at points with the coordinates 0 and $2y_i$. The particle i can also approach the lower limits of its extreme positions at a point with the coordinate y_i. The coordinate corresponding to any limit of the extreme positions of the particle i will be denoted hereafter as $Y(i) \in \{0, y_i, 2y_i\}$. Proceeding from the concept outlined briefly in the previous section one may conclude that certain criterion of identification of a virtual fluid particle in the pair (A, B) is necessary to afford the possibility for taking account of differences between effects resulting from the class of ordered wallward motions and the class of ordered motions directed outwards. With the purpose of developing that criterion we formulate the following idea of characterizing the intensity of the normal component of turbulent pulsations. That characteristic, called hereafter the total intensity, is referred to a point with the coordinate y and it may be expressed, generally, as a sum of a number of nondimensional values defined individually at the respective number of points correlated in certain way with the reference point y. Let us name those values contributing to the total intensity, "intensity components." The coordinate $Y(i)$ of the extreme position of the virtual particle i and the intensity component defined at the $Y(i)$, appropriate to the situation of the $Y(i)$ in respect to the reference point y, constitute the sole and complete information identifying a member i of a pair of the virtual particles (A, B). Thus, that information defines a virtual particle so that the virtual particles are considered only within the frame of the model being developed and they cannot be identified literally with actual fluid particles. Therefore, the contribution of a pair of the intensity components to the total intensity may be considered as the result of displacement of the virtual particles of the pair (A, B) from their extreme positions $(Y(A), Y(B))$ to the reference point y where both the particles coalesce. Then the intensity components are computed with the help of Reynolds averaged quantities characterizing the flow field at the extreme positions. Certain rules governing the foregoing displacements are assumed hereafter with the purpose of enabling us to determinate the set of pairs of the virtual particles $\{(A, B)\}$ such that displacements of the particles of each pair (A, B) belonging to this set result in the contribution to the total intensity. Accordingly, the total intensity at a point y is computed by summing the contributions resulting from displacements of the virtual particles associated in pairs $\{(A, B)\}$ from all the allowable combinations of the extreme positions $\{(Y(A), Y(B))\}$ to the reference point y.

It is assumed that particles A and B are distinguishable until they coalesce. Therefore, their order on the coordinate axis normal to the wall is unchangeable. Let us situate the particle B between the particle A and the wall. Then the latter inference will imply the inequality

$$Y(A) > Y(B) \tag{2}$$

if both the fluctuating particles approach limits of their extreme positions (this case will solely be considered hereafter). The condition (2) reduces a number of the possible combinations $(Y(A), Y(B))$ to six pairs, $(y_A, 0)$, (y_A, y_B), $(y_A, 2y_B)$, $(2y_A, 0)$, $(2y_A, y_B)$ and $(2y_A, 2y_B)$. Hence, it is easy to see that the condition (2) implies the inequality $y_A > y_B$. Consequently, $y_A = y$ is optional and y_B depends on y_A. The condition (2) implies that the lower bound of the set of distances from the position $Y(A)$ to $Y(B)$ is zero. Therefore, the relationship between y_B, and y_A can be determined from the boundary condition

$$\min\{(Y(A) - Y(B))\} = 0 \tag{3}$$

where min denotes the minimal element of the set of values $\{(Y(A) - Y(B))\}$ corresponding one-to-one to elements of the set of all the pairs $\{(Y(A), Y(B))\}$ allowed by the condition (2). As $\min\{(Y(A) - Y(B))\} = y_A - 2y_B$ we get $y_B = y_A/2 = y/2$. Consequently, the condition (2) excludes the pair $(y_A, 2y_B)$ from further consideration. Let us note that the displacements of the virtual particles associated in a pair (A, B) will take place if not more than one element $Y(i)$ of the corresponding pair $(Y(A), Y(B))$ coincides with the coordinate of the respective center point y_i; i.e., $Y(A) \neq y_A$ or $Y(B) \neq y_B$. This condition excludes the pair (y_A, y_B) from the summation. The intensity components determined at points $2y$ or $y/2$ and contributing to the total intensity at the reference point y may be naturally defined by the ratios $(\sqrt{\langle v^2 \rangle}/U)_{|2y}$ or $(\sqrt{\langle v^2 \rangle}/u_t)_{|y/2}$, respectively. Here, the denotation $(.)_{|x}$ indicated that the value in the parentheses is taken at a point with the coordinate x. The particle whose extreme position coincides with the coordinate y does not need to displace because it is already situated at the reference point. Therefore, the ratio $\langle v^2 \rangle/(\langle v^2 \rangle)_{mx}$ may be regarded as most natural definition of the intensity component at a point y. It is natural to assume that only the nonzero value of the intensity component may identify individuality of a virtual particle in the pair (A, B). Therefore, a pair $(Y(A), Y(B))$ will be excluded from the summation if intensity of the normal component of turbulent pulsations is zero at not less than one point of the pair. That is the reason for which the equality $\langle v^2 \rangle = 0$ satisfied at the wall excludes both the pairs $(y_A, 0)$ and $(2y_A, 0)$ from the summation. Eventually, the summation of the intensity components contributing to the total intensity is carried out after two pairs, $(2y_A, y_B) = (2y, y/2)$ and $(2y_A, 2y_B) = (2y, y)$. Therefore, the total intensity, denoted as $f(y)$, is expressed in the form

$$f(y) = f_1(y) + f_2(y)$$

where

$$f_1(y) := \left(\sqrt{\langle v^2 \rangle}/U\right)_{|2y} + \left(\sqrt{\langle v^2 \rangle}/u_t\right)_{|y/2},$$

$$f_2(y) := \left(\sqrt{\langle v^2 \rangle}/U\right)_{|2y} + \left(\langle v^2 \rangle/\langle v^2 \rangle_{mx}\right)_{|y}. \tag{4}$$

The model presented above enables us to specify, more accurately, the effective damping of vertical fluctuations which, on assumption made in the previous section, is represented by $F(y)$. The effective damping referred to a point with the coordinate y will be identified hereafter with the relative decrease in the total intensity of the normal component of turbulent fluctuations. As the range of variation of the $F(y)$ is $0 \leq F \leq 1$, we express this value in the form

$$F(y) = f(y)/(f(y))_{mx}. \tag{5}$$

The equation (5), with the $f(y)$ computed after equations (4) was examined tentatively in the way of comparison between the distribution $F(y)$ obtained with the help of these equations, and the plot of the Van Driest damping function (1). The values $\sqrt{\langle v^2 \rangle}/U$, $\sqrt{\langle v^2 \rangle}/u_t$, and $\langle v^2 \rangle/\langle v^2 \rangle_{mx}$ that are necessary to compute the $f(y)$ by using equations (4) were taken at the

Downloaded 03 May 2010 to 171.66.16.248. Redistribution subject to ASME license or copyright; see http://www.asme.org/terms/Terms_Use.cfm

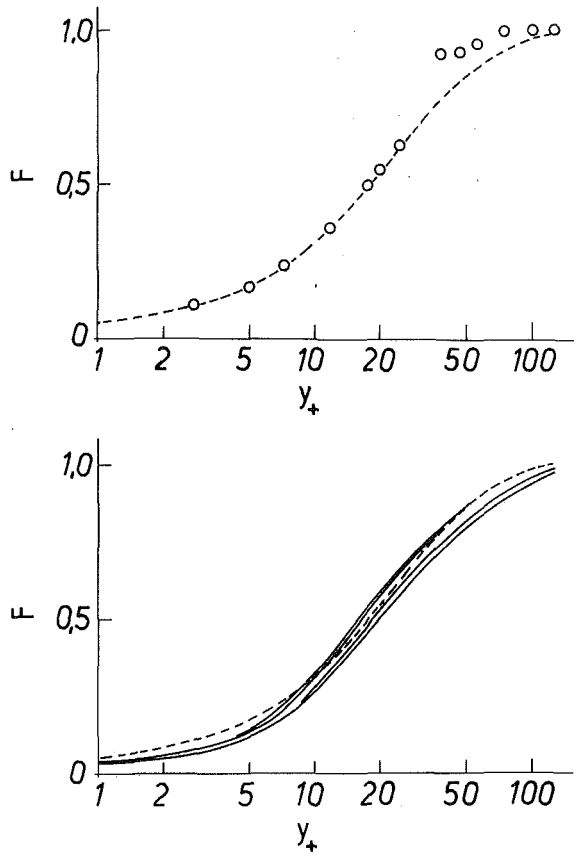

Fig. 1 The profiles of the damping factor $F(y)$ given by equations (4) and (5); circles in upper graph represent the $F(y)$ calculated from the experimental data (Kreplin and Eckelmann, 1979); solid lines in the lower graph represent the $F(y)$ obtained from the main series of computations for r_{w+} = 8750, 3700, 1150, 650 (from the lower curve to the upper one, respectively); dashed line indicates the Van Driest function (1) (it overlaps $F(y)$ for $r_{w+} \approx 650$, 1150 if $y_+ > 50$)

appropriate points from the experimental distributions obtained by Kreplin and Eckelmann (1979). The aforementioned comparison is presented in Fig. 1 and shows that values $F(y)$ determined in the new way agree rather well with those given by the formula (1). The positive result of this tentative examination is necessary but not sufficient to conclude that equations (4) and (5) represent the same flow characteristic as that whose distribution is given by equation (1). The sufficient grounds for that conclusion may be given if verification of equations (4) and (5) shows that the novel relationship can successfully replace the formula (1) in computations of turbulent flow characteristics.

3 Verification

The distributions of turbulent flow characteristics obtained with the help of a model of turbulence including the factor F, determined only by equations (4) and (5), will be compared hereafter to the respective experimental distributions and also to those computed by using the same model with the value F given by the formula (1) only. It is worth noting, therefore, that relations between the main components of the turbulent kinetic energy balance vary relatively strongly along the normal axis within the wall region where the $F(y)$ varies from zero to unity. Therefore, a turbulence model which takes account of that effect would be desirable. The version of the MTE model (abbreviation used in Section 1) which appears to satisfy that requirement was proposed for turbulent flows through pipes and channels (Kozlowski, 1987). Hereafter, we will restrict our considerations to the fully developed turbulent flow through a straight circular pipe or through a flat channel. For those flows the equations of the model previously cited are reduced to the form

$$0 = -\frac{1}{\rho}\cdot\frac{dp}{dx} + \frac{1}{r^j}\cdot\frac{d}{dr}\left(r^j\cdot(\nu+\nu_t)\cdot\frac{dU}{dr}\right),$$

$$0 = \nu_t\cdot\left(\frac{dU}{dr}\right)^2 + \frac{d}{dr}\left(\frac{\nu}{3\cdot C_K^2}\cdot\frac{dk}{dr}\right) + \frac{1}{r^j}\cdot\frac{d}{dr}\left(r^j\cdot c_5\cdot\nu_t\cdot\frac{dk}{dr}\right) - \epsilon,$$

$$\nu_t = L^{4/3}\cdot\left(\epsilon + c_4\cdot k\cdot\left|\frac{dU}{dr}\right|\right)^{1/3}\cdot F,$$

$$\epsilon = \left((c_3 + c_2\cdot N_t)\cdot\frac{k^{3/2}}{L} + c_1\cdot\nu\cdot\frac{k}{L^2}\right) - c_4\cdot k\cdot\left|\frac{dU}{dr}\right|,$$

$$L = L_0\cdot(L_{pn}/L_{pn0})\cdot(1+F_1),$$

$$L_{pn} = r_w\cdot(0.14 - 0.08\cdot R^2 - 0.06\cdot R^4),$$

$$F_1 = 0.25\cdot(8-3\cdot j)\cdot\exp(-1.163\ T)\cdot\cos(\pi\cdot T/1.1) \qquad (6)$$

where $T = \ln(0.1\cdot y_+ + 1.6)$; $j = 1$ or 0 for pipe or channel flow, respectively; r is a distance to the pipe axis or channel center line; the subscripts 0 or w indicate values taken at the axis or at the wall, respectively; $R = r/r_w$, $N_t = \nu_t/(u_t\cdot r_w)$. The mean turbulent kinetic energy is denoted as $k = \langle u_i u_i\rangle/2$ (summation with respect to repeated indices $i = 1, 2, 3$); p is the mean pressure; L_{pn} denotes the Prandtl-Nikuradse mixing length, L is the model turbulent length, $L_0/r_w = 0.106$ for $j = 1$ and 0.100 for $j = 0$. The first member of the MTE equation represents generation, the two subsequent ones constitute the diffusion term, and ϵ is the dissipation rate. The equation for $\langle v^2\rangle$ has been constructed as a supplemental member of the MTE model (6) which is necessary for us to compute the value F with the help of equations (4) and (5). This equation has been written in the form

$$0 = -c_6\left(\frac{\nu_t}{L^2}\right)\cdot\left(\langle v^2\rangle - \frac{2}{3}\cdot k\right) - \left(c_8\cdot\nu\cdot\frac{\langle v^2\rangle}{L^2} + c_7\cdot\left(\epsilon - c_1\cdot\nu\cdot\frac{k}{L^2}\right)\right) + \frac{d}{dr}\left(\nu\cdot\frac{d\langle v^2\rangle}{dr}\right) + \frac{1}{r^j}\cdot\frac{d}{dr}\left(r^j\cdot c_5\cdot\nu_t\cdot\left(\frac{d\langle v^2\rangle}{dr} + \frac{dk}{dr}\right)\right) \qquad (7)$$

which is consistent with peculiarities of the MTE model (6). The equations (6) and (7) have the following coefficients

$$c_1 = 2/3,\ c_2 = (4/3)\cdot\sqrt{2/3},\ c_3 = (1/3)\cdot\sqrt{2/3}\cdot((1-j)\cdot R + j),$$

$$c_4 = (8/15)((3/2)\cdot(1-j)\cdot R + j),\ c_5 = (2j+1)/2,$$

$$c_6 = 1/4,\ c_7 = 1/3,\ c_8 = 1.9,\ C_K = 0.4 \qquad (8)$$

where C_K is the von Karman constant. The system of equations (6) and (7) was solved when the factor F was given by equations (4) and (5) only (main series of computations). Then the F was computed for $y < y_1$ where $F(y_1) = 1$ but for $y > y_1$ we put $F = 1$. For $Y = y/r_w > 0.5$ the term $(\sqrt{\langle v^2\rangle}/U)_{|2y}$ was taken as a constant equal to its value at a $Y = 0.5$. This latter was made for numerical reasons only, because the value $Y_1 = y_1/r_w$ is obtained as result of computations. If the inequality $Y_1 > 0.5$ is satisfied, the results of computations have not clear physical relevance. Therefore, the results of computations can be accepted only if the inequality, $Y_1 < 0.5$ is satisfied. Additionally, equations (6) and (7) were solved in the separate series of computations when the factor F was given by the formula (1) only. The equations were solved numerically and following boundary conditions were satisfied

$$r = 0:\ \frac{dU}{dr} = \frac{dk}{dr} = \frac{d\langle v^2\rangle}{dr} = 0$$

$$r = r_w:\ U = k = \langle v^2\rangle = 0. \qquad (9)$$

Downloaded 03 May 2010 to 171.66.16.248. Redistribution subject to ASME license or copyright; see http://www.asme.org/terms/Terms_Use.cfm

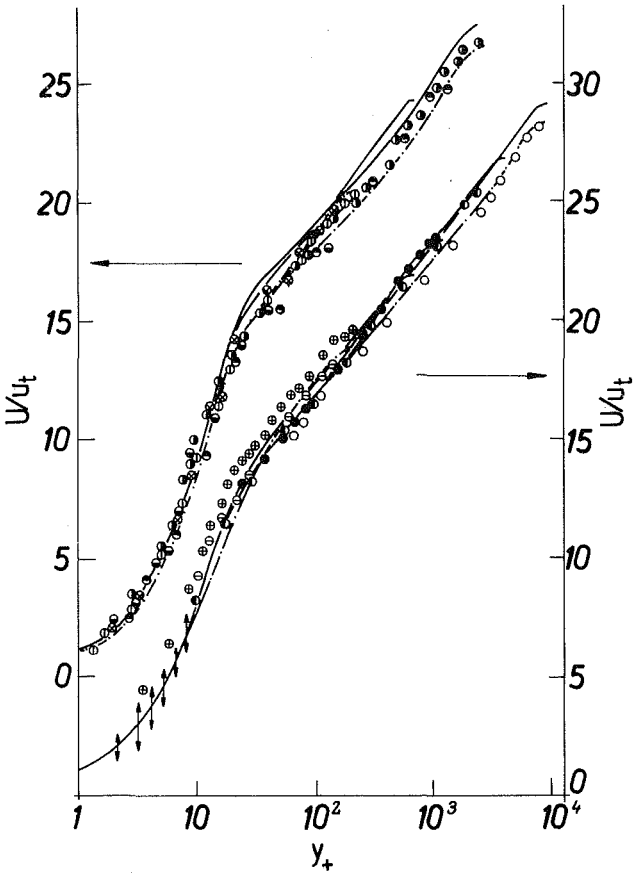

Fig. 2 The profiles of the average streamwise velocity in channel (upper curves) and pipe (lower curves); experiments for a channel flow ◒ – r_{w+} = 200 (Kreplin and Eckelmann, 1979), ⊗ – r_{w+} = 140, ◫ – r_{w+} = 210 (Eckelmann, 1974), ◓ – r_{w+} = 1250 (Clark, 1968), ◑ – r_{w+} = 2300 (Comte-Bellot, 1965) and for a pipe flow ⊖ – r_{w+} = 160 (Nikuradse, 1932), ⊕ – r_{w+} = 200 (Kudva and Sesonke, 1972), ⊙ – r_{w+} = 1200, ◐ – r_{w+} = 2300, ○ – r_{w+} = 8400 (Millionshtshikoff, Subbotin, Ibragimoff, Taranoff and Kobzar, 1973), ↕ —velocity variations at different Reynolds numbers (Millionshtshikoff, 1969)

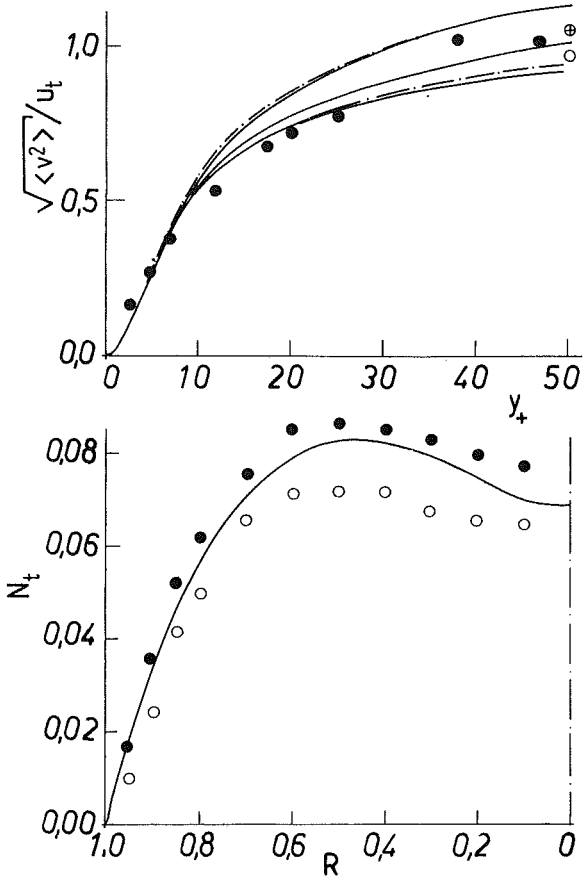

Fig. 3 The root mean square value of the normal component of pulsation in the wall region of a pipe flow for r_{w+} = 650, 1150, 8750 (from the lower curve to the upper one, respectively); experiment ● – r_{w+} = 200 channel flow (Kreplin and Eckelmann, 1979), ⊕ – r_{w+} = 3700, ○ – r_{w+} = 1000 pipe flow (Lawn, 1971); the profile of the eddy viscosity coefficient in the core of a pipe flow for r_{w+} = 1150 ÷ 8750 (lower graph), experiment ● – r_{w+} = 1180 ÷ 3500, ○ – r_{w+} = 500 ÷ 900 (Quarmby and Anad, 1969)

Let us remark, herein, where the F given by the equations (4) and (5) enters the computation. The F is the multiplier in the formula for the ν_t (see (6) what may be denoted, $\nu_t = \nu_{tc} \cdot F$. The system of equations (6) and (7) is solved by using a successive iteration procedure (then the dissipation term is written explicitly in the MTE equation). The eddy viscosity $(\nu_t)_n = (\nu_{tc})_n \cdot (F)_n$ is regarded as the variable coefficient that has been obtained at the previous iteration, n, and enters the computation of the equations for the U and k at the present iteration, $n+1$. The approximate solutions $(U)_{n+1}$, $(k)_{n+1}$ to those equations at the present iteration, and the value $(N_t)_n$ are used to compute the $(\nu_{tc})_{n+1}$ that is necessary to obtain the value $(\nu_t)_{(n+1)'} = (\nu_{tc})_{n+1} \cdot (F)_n$ which, together with $(U)_{n+1}$ and $(k)_{n+1}$, enters computation of equation (7). The solution $(\langle v^2 \rangle)_{n+1}$ to equation (7) and the $(U)_{n+1}$ enable us to compute the $(F)_{n+1}$ after equations (4) and (5). Eventually the value $(\nu_t)_{n+1} = (\nu_{tc})_{n+1} \cdot (F)_{n+1}$ is obtained, and this is utilized at the next iteration $n+2$. As the $(F)_n$ has relatively strong effect on the results of the present iteration, $n+1$ (particularly for small n), the self-consistent first approximations to the ν_t and k are desired to start the iteration procedure. The roughly approximate solution to the system (6) obtained for the F given by the formula (1) can provide such first approximations to the ν_t and k.

The results of computations are presented in the series of figures from Fig. 1 to Fig. 6 (the long chain indicates distributions obtained from additional computations carried out with the Van Driest function, whereas solid lines correspond to the main series of computations). We will consider the results of the main series of computations only. There is a good agreement between theoretical and experimental distributions of characteristics of the flow through the circular pipe at Reynolds numbers $r_{w+} = r_w \cdot u_t/\nu$ greater than 600 although there is remarkable disagreement in other cases considered (observe overestimation of the U/u_t for a channel flow shown by the upper curves in Fig. 2). For the channel flow that discrepancy may be attributed mainly to a cumulative effect resulting from approximations assumed in the equation for $\langle v^2 \rangle$ and simplicity of the formulae employed to approximate the variable coefficients c_3 and c_4 in the MTE equations. Let us note, thereby, that solutions of equations (6) and (7) obtained with the help of equations (4) and (5) for the factor F appear to be much more sensitive to the approximations alluded to previously than those obtained when the F is given by formula (1) only. Moreover, the coefficients occurring in equations (6) and (7) were chosen when $F(y)$ was given by formula (1) with the coefficient $A = 26$, which had been chosen for medium Reynolds numbers. The value of this coefficient appears to be the cause of the discrepancy seen in Fig. 1 (upper graph) between the profile of the Van Driest function and the points indicating values $F(y)$ calculated by using equations (4) and (5) from the data obtained by Kreplin and Eckelmann (1979) for $r_{w+} = 200$. The upper graph in Fig. 1 shows that the coordinate y_{1+} is smaller for the lower Reynolds number. This tendency is preserved also in results of the main series of computations (see lower graph in Fig. 1) although the differences between the

Downloaded 03 May 2010 to 171.66.16.248. Redistribution subject to ASME license or copyright; see http://www.asme.org/terms/Terms_Use.cfm

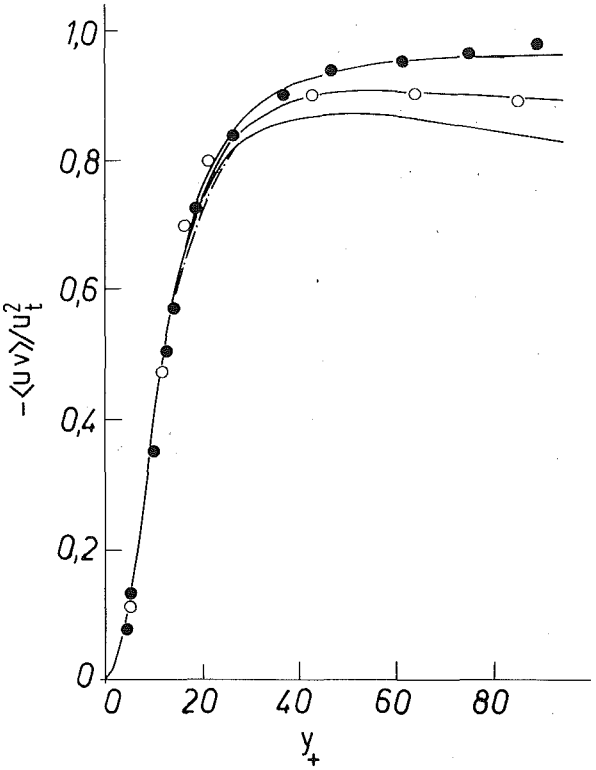

Fig. 4 The profiles of the Reynolds shear stress in the wall region of a pipe flow for r_{w+} = 650, 1150, 8750 (from the lower curve of the upper one, respectively); experiment ● – r_{w+} = 8750, ○ – r_{w+} = 1150 (Laufer, 1954)

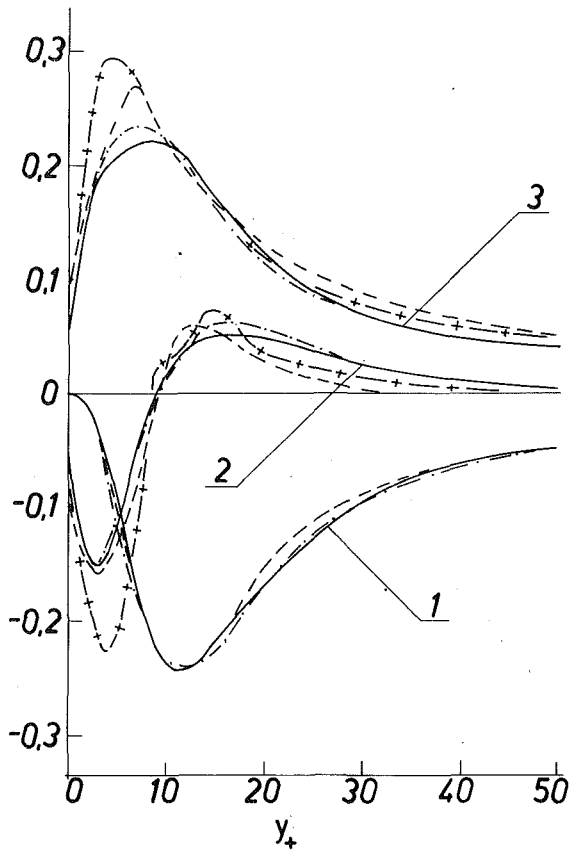

Fig. 6 The budget of the turbulent kinetic energy in the wall region of a pipe flow (r_{w+} = 1150), 1 – generation, 2 – diffusion term, 3 – dissipation rate; experimental distributions obtained by Laufer (1954) (dashed line) and by Krishnamoorthy and Antonia (1988) (curve with crosses)

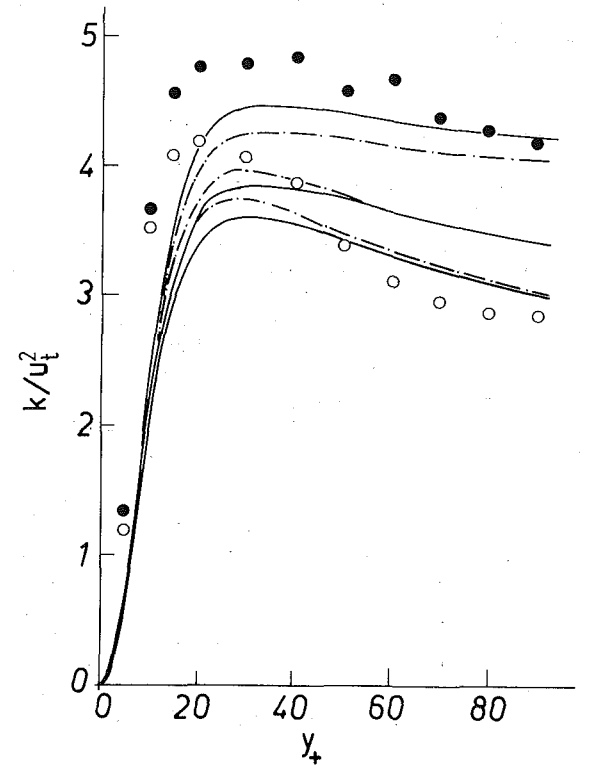

Fig. 5 The profiles of the mean turbulent kinetic energy in the wall region of a pipe flow for r_{w+} = 650, 1150, 8750 (from the lower curve to the upper one, respectively); experiment ● – r_{w+} = 8750, ○ – r_{w+} = 1150 (Laufer, 1954)

results for various Reynolds numbers appear to be augmented due to the approximations concerning equation (7) and choice of coefficients in the system (6) and (7) appropriately to the value $A = 26$. Those are the reasons for which the model constituted by equations (6) and (7) with $F(y)$ given by equations (4) and (5) affords no possibility for obtaining satisfactory results for the pipe flow at $r_{w+} < 600$. The explanations presented above enable us to conclude that, despite the discrepancy mentioned previously, the novel relationship for F can replace formula (1) in computations of turbulent flow characteristics.

4 Discussion

The satisfactory results of the computations carried out for the pipe flow have tempted us to discuss the relevance which the pattern of effects represented by our model has to an effective average pattern of ordered motions obtained in the experimental way for the wall region of a turbulent flow. That experimental pattern was reported by Brodkey, Wallace, and Eckelmann (1974) who obtained distributions of the classified Reynolds stresses $-\rho\langle uv_c\rangle$ relevant to four types of ordered motions; i.e., sweep ($c = s$: $u > 0$, $v < 0$), ejection ($c = e$: $u < 0$, $v > 0$), wallward interaction ($c = iw$: $u < 0$, $v < 0$), and outward interaction ($c = io$: $u > 0$, $v > 0$). Only the members $s_n(y)$: $= 2 \cdot \left(\sqrt{\langle v^2\rangle}/U\right)_{|2y}$ and $s_p(y)$: $= \left(\left(\sqrt{\langle v^2\rangle}/u_t\right)\right)_{|y/2}$ contributing to the value $f(y)$ appear to be source of information comparable with that experimental pattern because only they may be regarded as the members relevant to ordered motions directed wallwards (subscript n) or outwards (subscript p). The curves representing distributions of the values $S_n = s_n/f$ and

Downloaded 03 May 2010 to 171.66.16.248. Redistribution subject to ASME license or copyright; see http://www.asme.org/terms/Terms_Use.cfm

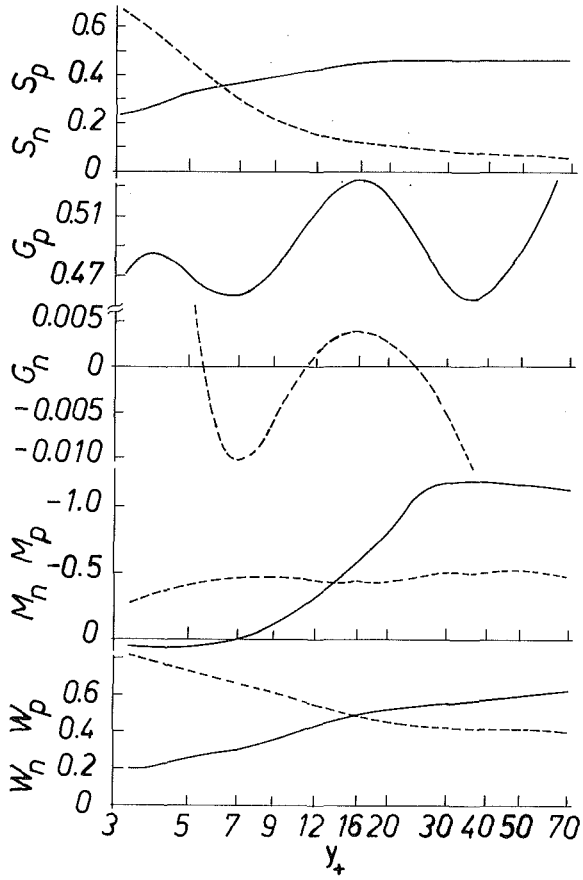

Fig. 7 Effects resulting from distinct classes of motions; dashed lines indicate wallward motions (*n*), solid lines indicate outward motions (*p*); S_n, S_p, G_n, G_p—results of computations for pipe flow at $r_{w+} = 1150$ (upper graphs), W_n, W_p, M_n, M_p—graphs drawn after plots presented by Brodkey et al. (1974)

$S_p = s_p/f$ cross each other at a point with the coordinate y_+ of about 7, as it is seen in Fig. 7. This coordinate detects the upper boundary of the layer within which the intensity components s_n have a dominant contribution to the total intensity. Moreover, the distributions of ratios, $G_n = \text{grad } s_n/\text{grad } f$ and $G_p = \text{grad } s_p/\text{grad } f$ show that both these characteristics have their extremums at a y_+ of about 7 and 16. These coordinates may be identified as situations of both the edges of the intermediate layer within which both the characteristics G_n and G_p grow with y; the outer layer extends above the $y_+ = 16$ (possible interpretation is presented further in this section). The values $y_+ = 7$ and $y_+ = 16$ remain unchanged (or change slightly) in all the cases accepted; i.e., for the pipe flow at $r_{w+} \geq 650$; the types of the extremums and signs of the values G_n, G_p at the extremums are the same in these cases. Since the characteristics S_n, S_p, G_n, and G_p are relevant only to the normal component of the motions, the experimental distributions of two pairs of values

$$W_n = (-\rho\langle uv_s\rangle - \rho\langle uv_{iw}\rangle)/(-\rho\langle uv\rangle),$$

$$W_p = (-\rho\langle uv_e\rangle - \rho\langle uv_{io}\rangle)/(-\rho\langle uv\rangle),$$

and

$$M_n = (-\rho\langle uv\rangle_s - \rho\langle uv\rangle_{iw})/u_t^2,$$

$$M_p = (-\rho\langle uv\rangle_e - \rho\langle uv\rangle_{io})/u_t^2 \qquad (10)$$

are samples from those possible to plot after experimental graphs (Brodkey et al., 1974) are made for comparison with the distributions obtained from computations. Note that only the distributions of the values W_n, W_p, M_n, and M_p may be considered as a sufficiently rich source of the available experimental information comparable with that obtained from the computations. Here, the value $-\rho\langle uv\rangle_c = -\rho\langle uv_c\rangle/(\text{fraction of total time when the flow is in the category } c)$ is equivalent to that obtained by the averaging of the uv signal with the sum of durations of events of type c. The distributions of the pairs of values (M_n, M_p) and (W_n, W_p), which are presented in Fig. 7, also show three layers within the near-wall region and the edges of the intermediate layer may be identified at a y_+ of about 7 and 16; i.e., their situation is the same as that recognized in graphs of the S_n, S_p and G_n, G_p. Having given fair warning about overinterpreting this coincidence we do feel that it does not appear fortuitously. Both the experimental and theoretical distributions M_n, M_p and S_n, S_p plotted in Fig. 7 show that the effective preponderance of wallward motions over those directed outwards appears to be inherent to the inner layer ($y_+ < 7$). This seems to testify on behalf of the following implication written for either point $y_+^x = 7$ or 16 where G_i has its extremum for each type of relevant motion $i = n$ or p whose direction is denoted as sign $(n) = -1$ or sign $(p) = 1$. If $G_i \cdot \text{sign } (i)$ has its maximum at a y^x then the effective preponderance of ordered motions of the type i is peculiar to the region where $y < y^x$ when sign $(i) < 0$ or $y > y^x$ when sign $(i) > 0$. Agreeing with this implication is the effective preponderance of outward motions over those directed wallwards peculiar to the region located above $y_+^x = 16$ (see distributions of the G_n and G_p in Fig. 7). This inference agrees with that drawn immediately from the experimental distributions of the values W_n and W_p presented also in Fig. 7. The agreement between experimental and theoretical results discussed above seems to suggest that equations (4) and (5), for the factor F, take account of the local relation between ability of the class of ordered wallward motions to produce effects inherent to turbulent flow and such efficiency of the class of ordered motions directed outwards. Accordingly, the character of damping (i.e., the relative decrease in the total intensity of the normal component of fluctuations), which is represented by the profile of the $F(y)$ may be regarded as result of variation of that relation along the axis normal to the wall.

References

Brodkey, R. S., Wallace, J. M., and Eckelmann, H., 1974, 'Some Properties of Truncated Turbulence Signals in Bounded Shear Flows," *Journal of Fluid Mechanics,* Vol. 63, Part 2, pp. 209–224.

Clark, J. A., 1968, "A Study of Incompressible Turbulent Boundary Layers in Channel Flow," *ASME Journal of Basic Engineering,* Vol. 90, pp. 455–468.

Comte-Bellot, G., 1965, "Turbulent Flow through Channel with Parallel Walls," (in French), Service de Documentation Scientifique et Technique de L'armement, Paris.

Derbunovitsh, G. I., Repik, E. U., and Sosedko, Y. P., 1978, "On Experimental Determination of Integral Scale of Turbulence in Boundary Layer," (in Russian), Izvestyia, Siberian Branch of Academy of Sciences USSR, Technical Sciences, No. 3, Part 1, pp. 3–8.

Eckelmann, H., 1974, "The Structure of Viscous Sublayer and the Adjacent Wall Region in a Turbulent Channel Flow," *Journal of Fluid Mechanics,* Vol. 65, pp. 439–459.

Keller, L. V., and Friedmann, A. A., 1925, "Differential Equations of Turbulent Motion of Compressible Fluid," *Proceedings of First International Congress of Applied Mechanics,* (in German), Delft, pp. 395–405, (also in A. A. Friedmann, 1966, Selected Papers (in Russian), L. S. Polak, ed., Nauka, Moscow, pp. 45–57.

Kozlowski, W., 1987, "Generalized Phenomenological Hypotheses for Estimating the Turbulent Energy Dissipation Rate and the Turbulent Viscosity Coefficient in Turbulent Shear Flows," *Archives of Mechanics,* Vol. 39, No. 3, pp. 123–155.

Kreplin, H. P., and Eckelmann, H., 1979, "Behaviour of the Three Fluctuating Velocity Components in the Wall Region of a Turbulent Channel Flow," *The Physics of Fluids,* Vol. 22, pp. 1233–1239.

Krishnamoorthy, L. V., and Antonia, R. A., 1988, "Turbulent Kinetic Energy Budget in the Near-Wall Region," *AIAA Journal,* Vol. 26, pp. 300–302.

Kudva, A. K., and Sesonke, A., 1972, "Structure of Turbulent Velocity and Temperature Fields in Ethylene Glicol Pipe Flow at Low Reynolds Number," *International Journal of Heat and Mass Transfer,* Vol. 15, pp. 127–145.

Laufer, J., 1954, "The Structure of Turbulence in Fully Developed Pipe Flow," NACA Report 1174, pp. 1–18.

Lawn, C. J., 1971, "The Determination of the Rate of Dissipation in Turbulent Pipe Flow," *Journal of Fluid Mechanics,* Vol. 48, Part 3, pp. 477–505.

Downloaded 03 May 2010 to 171.66.16.248. Redistribution subject to ASME license or copyright; see http://www.asme.org/terms/Terms_Use.cfm

Millionshtshikoff, M. D., 1969, *Turbulent Flows in Boundary Layer and Pipes* (in Russian), Nauka, Moscow.

Millionshtshikoff, M. D., Subbotin, V. J., Ibragimoff, M. H., Taranoff, G. S., and Kobzar, L. L., 1973, "Hydraulic Resistance and Distribution of Velocity in Pipes with Artifical Wall Roughness," (in Russian), *Atomnayia Energyia,* Vol. 34, pp. 235–245.

Minski, E. M., 1940, "Statistical Determination of Mixing Length in Turbulent Flow," (in Russian), *Doklady,* Academy of Sciences USSR, Vol. 28, No. 8, pp. 685–688.

Nikuradse, J., 1932, "Regularities of Turbulent Flow in Smooth Pipes," (in German), *Forshungsarbeiten auf dem Gebiete des Ingenieurwesens,* No. 356.

Offen, G. R., and Kline, S. J., 1975, "A Proposed Model of the Bursting Process in Turbulent Boundary Layers," *Journal of Fluid Mechanics,* Vol. 70, Part 2, pp. 209–228.

Prandtl, L., 1925, "On Fully Developed Turbulence," (in German), *Zeitschrift fur Angewandte Mathematik und Mechanik,* Vol. 5, No. 2, pp. 136–139.

Quarmby, A., and Anand, R. K., 1969, "Axisymmetric Turbulent Mass Transfer in a Circular Tube," *Journal of Fluid Mechanics,* Vol. 38, pp. 433–455.

Rotta, J. Ch., 1972, *Turbulent Flows* (in German), B. G. Teubner, Stuttgart.

Utami, T., and Ueno, T., 1987, "Experimental Study on the Coherent Structure of Turbulent Open-Channel Flow Using Visualization and Picture Processing," *Journal of Fluid Mechanics,* Vol. 174, pp. 399–440.

Van Driest, E. R., 1956, "On the Turbulent Flow Near the Wall," *Journal of the Aeronautical Sciences,* No. 9, pp. 1007–1011, 1036.

Downloaded 03 May 2010 to 171.66.16.248. Redistribution subject to ASME license or copyright; see http://www.asme.org/terms/Terms_Use.cfm

Journal of Applied Mechanics

Brief Notes

A Brief Note is a short paper that presents a specific solution of technical interest in mechanics but which does not necessarily contain new general methods or results. A Brief Note should not exceed 1500 words *or equivalent* (a typical one-column figure or table is equivalent to 250 words; a one line equation to 30 words). Brief Notes will be subject to the usual review procedures prior to publication. After approval such Notes will be published as soon as possible. The Notes should be submitted to the Technical Editor of the JOURNAL OF APPLIED MECHANICS. Discussions on the Brief Notes should be addressed to the Editorial Department, ASME, United Engineering Center, 345 East 47th Street, New York, N. Y. 10017, or to the Technical Editor of the JOURNAL OF APPLIED MECHANICS. Discussions on Brief Notes appearing in this issue will be accepted until two months after publication. Readers who need more time to prepare a Discussion should request an extension of the deadline from the Editorial Department.

Flow Across a Stretching Surface

C. Y. Wang[1]

Introduction

The fluid motion due to a stretching surface is important in extrusion processes. Crane (1970) found the exact solution of the flow due to a stretching surface in an otherwise still fluid. However, in many instances, due to free or forced convection, the fluid may be moving relative to the surface. Danberg (1976) solved the case of a uniform flow along the stretching direction. The present note considers the case of a uniform flow across a stretching surface in an arbitrary direction. Heat transfer is also discussed.

Formulation

Figure 1 shows a surface at $z=0$ stretching with velocity ax in the x direction. A uniform, forced parallel flow exists at large z. Its velocity may be decomposed into U and V in the x, y directions, respectively. Assuming no lateral pressure gradients and all variables are independent of y, the Navier-Stokes equations reduce to

$$uu_x + wu_z = \nu(u_{xx} + u_{zz}) \tag{1}$$

$$uv_x + wv_z = \nu(v_{xx} + v_{zz}) \tag{2}$$

$$uw_x + ww_z = -\frac{1}{\rho} p_z + \nu(w_{xx} + w_{zz}) \tag{3}$$

$$u_x + w_z = 0 \tag{4}$$

where (u, v, w) are velocities in the (x, y, z) directions, ν is the kinematic viscosity, p is the pressure and ρ is the density. The boundary conditions are

$$\text{at } z=0 \quad u=ax, \quad v=w=0 \tag{5}$$

$$\text{at } z\to\infty \quad u=U, \quad v=V. \tag{6}$$

The Solution

Guided by the boundary conditions we use the transform

$$u = axf'(\eta) + Ug(\eta) \tag{7}$$

$$v = Vh(\eta) \tag{8}$$

$$w = -\sqrt{a\nu} f(\eta) \tag{9}$$

where $\eta \equiv \sqrt{a/\nu}\, z$. The governing equations become

$$(f')^2 - ff'' = f''', \quad f'(0)=1, \quad f(0)=0, \quad f'(\infty)=0 \tag{10}$$

$$gf' - fg' = g'', \quad g(0)=0, \quad g(\infty)=1 \tag{11}$$

$$-fh' = h'', \quad h(0)=0, \quad h(\infty)=1. \tag{12}$$

Equation (10) is exactly Crane's (1970) problem. The solution is

$$f = 1 - e^{-\eta}. \tag{13}$$

The solution to equation (11), representing the flow along the stretching direction, was found by Danberg (1976)

$$g = \exp(-e^{-\eta}) + \left[E_1(1) - \frac{1}{e}\right] e^{-\eta} - e^{-\eta} E_1(e^{-\eta}) \tag{14}$$

where E_1 is the exponential function (e.g., Abramowitz and Stegun, 1965). The solution to equation (12) is as follows. Let $h(\eta) \equiv H(s)$, where $s \equiv \exp(-\eta)$. Equation (12) yields

$$H'' + H' = 0, \quad H(0)=1, \quad H(1)=0. \tag{15}$$

The solution is

$$h = \frac{e^{1-s}-1}{e-1} = \frac{e}{e-1}\left[\exp(-e^{-\eta}) - \frac{1}{e}\right]. \tag{16}$$

The above results represent rare, closed-form exact solutions of the Navier-Stokes equations.

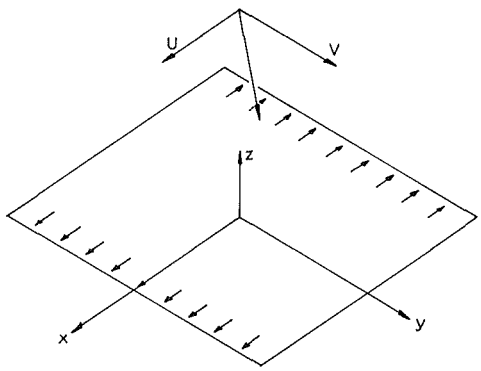

Fig. 1 The coordinate system. Uniform flow at large z is decomposed into U, V components.

[1]Department of Mathematics, Michigan State University, East Lansing, MI 48824-1027. Mem. ASME.

Manuscript received by the ASME Applied Mechanics Division, May 9, 1989; final revision, Mar. 20, 1990.

Copyright © 1991 by ASME
Downloaded 03 May 2010 to 171.66.16.248. Redistribution subject to ASME license or copyright; see http://www.asme.org/terms/Terms_Use.cfm

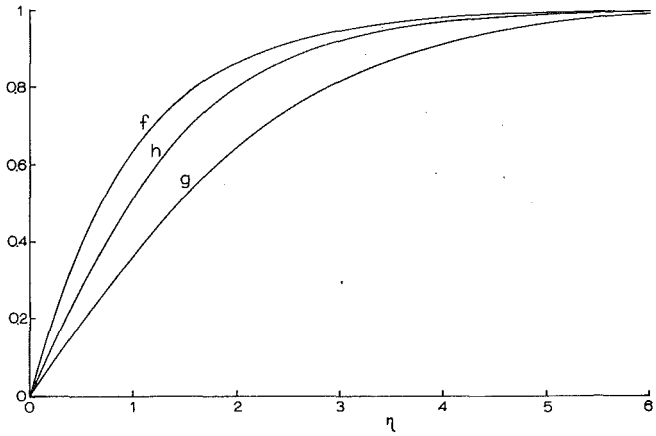

Fig. 2 The universal functions $f(\eta)$, $g(\eta)$, $h(\eta)$

Shear Stress and Heat Transfer

The universal functions f, g, h are plotted in Fig. 2. We see that all three functions increase from zero to unity, but with different rates. The shear stresses on the surface are

$$\tau_{(x)} = \mu u_z \mid_0 = \rho\sqrt{\nu a}[axf''(0) + Ug'(0)] = \rho\sqrt{\nu a}(-ax + U/e) \tag{17}$$

$$\tau_{(y)} = \mu v_z \mid_0 = \rho\sqrt{\nu a} Vh'(0) = \rho\sqrt{\nu a} V/(e-1). \tag{18}$$

The heat transfer equation is

$$uT_x + wT_z = \frac{\nu}{P}(T_{xx} + T_{zz}) \tag{19}$$

where P is the Prandtl number. If the temperature on the surface is constant at T_w, we set

$$T = T_\infty + (T_w - T_\infty)M(s) \tag{20}$$

Equation (19) becomes

$$sM'' + (1 - P + Ps)M' = 0,\ M(0) = 0,\ M(1) = 1. \tag{21}$$

The solution is

$$M = \frac{\gamma(P, Ps)}{\gamma(P, P)} \tag{22}$$

where γ is the incomplete gamma function (Abramowitz and Stegun, 1965)

$$\gamma(P, Ps) \equiv \int_0^{Ps} t^{P-1} e^{-t} dt \tag{23}$$

For integer values of P, equation (22) becomes the finite sum through integration by parts.

$$M = \left[1 - e^{-Ps} \sum_{k=0}^{P-1} \frac{(Ps)^k}{k!}\right] \Big/ \left[1 - e^{-P} \sum_{k=0}^{P-1} \frac{P^k}{k!}\right] \tag{24}$$

For $P = 1$, equation (24) reduces further to that found by Crane (1970).

$$M = \frac{e}{e-1}(1 - e^{-s}) \tag{25}$$

The local heat transfer rate is

$$q_w = -\kappa \frac{\partial T}{\partial z} \mid_W = \kappa\sqrt{\frac{a}{\nu}}(T_w - T_\infty)M'(1) \tag{26}$$

where κ is the thermal conductivity and

$$M'(1) = \frac{P^P e^{-P}}{\gamma(P, P)}. \tag{27}$$

Discussion

Because of indefinite boundary layer growth, steady, parallel flow across an infinite plate does not exist. However, if the boundary layer is contained by some means, then steady uniform flow may be approached asymptotically at large distances from the surface. Noted examples are the asymptotic suction profile and the Ekman flow in a rotating system.

It is interesting to note that Crane's solution, equation (13), was obtained earlier by Stuart (1966). Stuart studied the acoustic streaming due to oscillatory viscous flows and equation (13) is the zeroth-order steady flow. This steady flow is driven by a similar nonzero tangential velocity. Thus, the solutions of the present note can also be applied to oscillating bodies in a steady stream, provided the Stokes layer is thin.

References

Abramowitz, M., and Stegun, I. A., 1965, *Handbook of Mathematical Functions*, Dover, New York.

Crane, L. J., 1970, "Flow Past a Stretching Plate," *Zeit. fur Zngew. Math. Mech.*, Vol. 21, pp. 645–647.

Danberg, J. E., 1976, "A Nonsimilar Moving-Wall Boundary-Layer Problem," *Quart. Appl. Math.*, Vol. 34, pp. 305–309.

Stuart, J. T., 1966, "Double Boundary Layers in Oscillatory Viscous Flow," *J. Fluid Mech.*, Vol. 24, pp. 673–687.

Kinematic Hardening for Nonproportional Loading

C. S. White[2]

Introduction

This note reports on the comparison of Prager-Ziegler kinematic hardening with a series of critical experiments reported by Budiansky, Dow, Peters, and Shepherd (1951). These nonproportional experiments were fundamental in early comparisons between deformation theory, isotropic hardening flow theory, or slip theory of plasticity. Here we compare kinematic hardening flow theory with the experiments.

Background

Nonproportional loading experiments on thin-walled, aluminum tubes were conducted by Budiansky et al. (1951) by axially compressing the tubes to 0.5 percent strain then abruptly changing the loading path and continuing at a fixed ratio of axial stress increment to shear stress increment, $\frac{d\sigma}{d\tau}$. The plastic response following this change of loading direction differs significantly between the various theories. Corner theories (slip theory) and deformation theory predict immediate accumulation of plastic shear strain but flow theories having smooth yield surfaces predict initially elastic shear response.

The experiments showed initially elastic shear response but for continued loading, the plastic shear strain accumulated slower than predicted by either the slip or deformation theories but faster than predicted by isotropic hardening. Pan and Rice (1983) showed that introducing rate dependence into slip theory could greatly improve the agreement with experiment.

[2]U.S. Army Materials Technology Laboratory, Watertown, MA 02172. Assoc. Mem. ASME.

Manuscript received and accepted by the ASME Applied Mechanics Division, July 6, 1989.

Downloaded 03 May 2010 to 171.66.16.248. Redistribution subject to ASME license or copyright; see http://www.asme.org/terms/Terms_Use.cfm

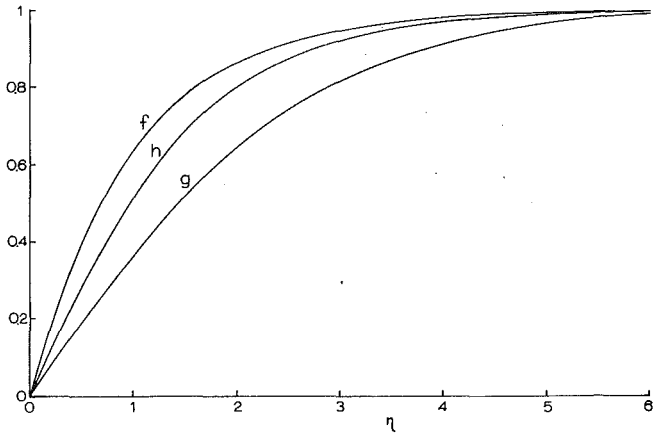

Fig. 2 The universal functions $f(\eta)$, $g(\eta)$, $h(\eta)$

Shear Stress and Heat Transfer

The universal functions f, g, h are plotted in Fig. 2. We see that all three functions increase from zero to unity, but with different rates. The shear stresses on the surface are

$$\tau_{(x)} = \mu u_z \mid_0 = \rho\sqrt{\nu a}[axf''(0) + Ug'(0)] = \rho\sqrt{\nu a}(-ax + U/e) \tag{17}$$

$$\tau_{(y)} = \mu v_z \mid_0 = \rho\sqrt{\nu a} Vh'(0) = \rho\sqrt{\nu a} V/(e-1). \tag{18}$$

The heat transfer equation is

$$uT_x + wT_z = \frac{\nu}{P}(T_{xx} + T_{zz}) \tag{19}$$

where P is the Prandtl number. If the temperature on the surface is constant at T_w, we set

$$T = T_\infty + (T_w - T_\infty)M(s) \tag{20}$$

Equation (19) becomes

$$sM'' + (1 - P + Ps)M' = 0,\ M(0) = 0,\ M(1) = 1. \tag{21}$$

The solution is

$$M = \frac{\gamma(P, Ps)}{\gamma(P, P)} \tag{22}$$

where γ is the incomplete gamma function (Abramowitz and Stegun, 1965)

$$\gamma(P, Ps) \equiv \int_0^{Ps} t^{P-1} e^{-t} dt \tag{23}$$

For integer values of P, equation (22) becomes the finite sum through integration by parts.

$$M = \left[1 - e^{-Ps} \sum_{k=0}^{P-1} \frac{(Ps)^k}{k!}\right] \Big/ \left[1 - e^{-P} \sum_{k=0}^{P-1} \frac{P^k}{k!}\right] \tag{24}$$

For $P = 1$, equation (24) reduces further to that found by Crane (1970).

$$M = \frac{e}{e-1}(1 - e^{-s}) \tag{25}$$

The local heat transfer rate is

$$q_w = -\kappa \frac{\partial T}{\partial z} \mid_W = \kappa\sqrt{\frac{a}{\nu}}(T_w - T_\infty)M'(1) \tag{26}$$

where κ is the thermal conductivity and

$$M'(1) = \frac{P^P e^{-P}}{\gamma(P, P)}. \tag{27}$$

Discussion

Because of indefinite boundary layer growth, steady, parallel flow across an infinite plate does not exist. However, if the boundary layer is contained by some means, then steady uniform flow may be approached asymptotically at large distances from the surface. Noted examples are the asymptotic suction profile and the Ekman flow in a rotating system.

It is interesting to note that Crane's solution, equation (13), was obtained earlier by Stuart (1966). Stuart studied the acoustic streaming due to oscillatory viscous flows and equation (13) is the zeroth-order steady flow. This steady flow is driven by a similar nonzero tangential velocity. Thus, the solutions of the present note can also be applied to oscillating bodies in a steady stream, provided the Stokes layer is thin.

References

Abramowitz, M., and Stegun, I. A., 1965, *Handbook of Mathematical Functions*, Dover, New York.

Crane, L. J., 1970, "Flow Past a Stretching Plate," *Zeit. fur Zngew. Math. Mech.*, Vol. 21, pp. 645–647.

Danberg, J. E., 1976, "A Nonsimilar Moving-Wall Boundary-Layer Problem," *Quart. Appl. Math.*, Vol. 34, pp. 305–309.

Stuart, J. T., 1966, "Double Boundary Layers in Oscillatory Viscous Flow," *J. Fluid Mech.*, Vol. 24, pp. 673–687.

Kinematic Hardening for Nonproportional Loading

C. S. White[2]

Introduction

This note reports on the comparison of Prager-Ziegler kinematic hardening with a series of critical experiments reported by Budiansky, Dow, Peters, and Shepherd (1951). These nonproportional experiments were fundamental in early comparisons between deformation theory, isotropic hardening flow theory, or slip theory of plasticity. Here we compare kinematic hardening flow theory with the experiments.

Background

Nonproportional loading experiments on thin-walled, aluminum tubes were conducted by Budiansky et al. (1951) by axially compressing the tubes to 0.5 percent strain then abruptly changing the loading path and continuing at a fixed ratio of axial stress increment to shear stress increment, $\frac{d\sigma}{d\tau}$. The plastic response following this change of loading direction differs significantly between the various theories. Corner theories (slip theory) and deformation theory predict immediate accumulation of plastic shear strain but flow theories having smooth yield surfaces predict initially elastic shear response.

The experiments showed initially elastic shear response but for continued loading, the plastic shear strain accumulated slower than predicted by either the slip or deformation theories but faster than predicted by isotropic hardening. Pan and Rice (1983) showed that introducing rate dependence into slip theory could greatly improve the agreement with experiment.

[2]U.S. Army Materials Technology Laboratory, Watertown, MA 02172. Assoc. Mem. ASME.

Manuscript received and accepted by the ASME Applied Mechanics Division, July 6, 1989.

Copyright © 1991 by ASME
Downloaded 03 May 2010 to 171.66.16.248. Redistribution subject to ASME license or copyright; see http://www.asme.org/terms/Terms_Use.cfm

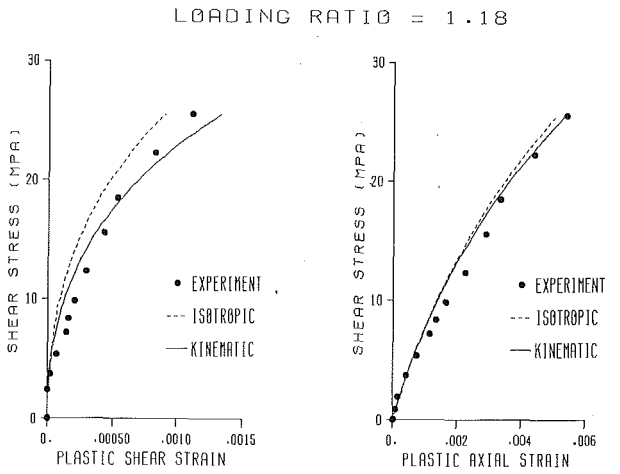

Fig. 1 Shear stress versus plastic shear strain and versus additional plastic axial strain for continued loading at $\frac{d\sigma}{d\tau} = 1.18$

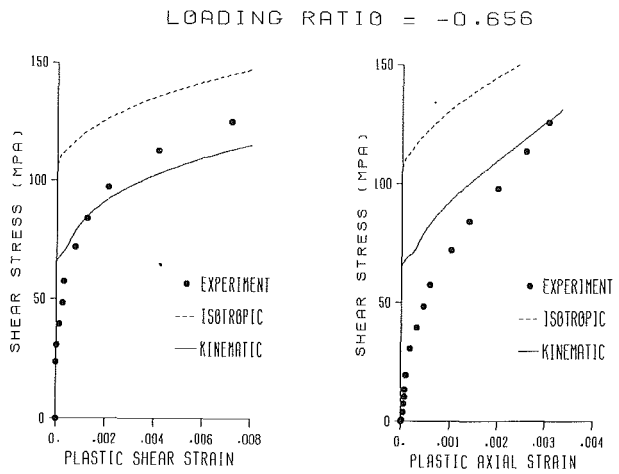

Fig. 3 Shear stress versus plastic shear strain and versus additional plastic axial strain for continued loading at $\frac{d\sigma}{d\tau} = -0.656$

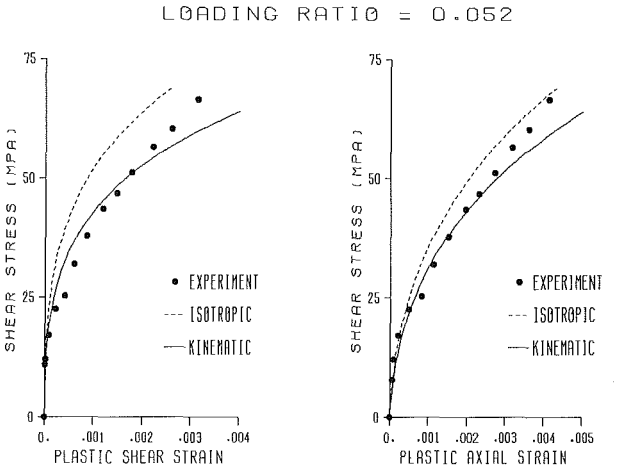

Fig. 2 Shear stress versus plastic shear strain and versus additional plastic axial strain for continued loading at $\frac{d\sigma}{d\tau} = 0.052$

Application of Kinematic Hardening

Budiansky et al. (1951) remarked that their data might be best correlated by a linear flow theory whose loading function gives a higher curvature to the loading surface at the prestress point than does isotropic hardening. The simple kinematic hardening model proposed by Prager (1956) and modified by Ziegler (1959) satisfies just such a set of conditions, the curvature being given by that of the initial yield surface. Prager introduced the concept of a translating yield surface in 1956 so the model was not available to Budiansky et al. at the time they analyzed these experiments.

We consider an initial yield surface of the von Mises type which retains its size and shape but translates without rotation during plastic straining. The flow rule is associative and the evolution law for the position, in stress space, of the yield surface center, α, is given by

$$\dot{\alpha} = \mu(\mathbf{S} - \alpha), \tag{1}$$

where $\mathbf{S}$ is the stress deviator and μ is the scalar function, derivable from the consistency condition, which describes the hardening behavior. A power-law form for the tangent modulus was applied to match the uniaxial stress strain curves in compression.

Results

The loading histories tested by Budiansky et al. (1951) were simulated. The ratios of $\frac{d\sigma}{d\tau}$ for continued loading varied from $+1.91$ to -1.13. This covered the range from total loading to elastic unloading.

Figures 1 to 3 show the results for the isotropic and kinematic models compared to the experimental data. Shear stress versus plastic shear strain and versus the increase in plastic axial strain are plotted. The kinematic hardening model matches the shear strain response very well. The initial shear response is elastic and the kinematic model accurately predicts the softer response for shear following axial extension. An interesting point is that the kinematic model predicts when plastic flow will recommence for the cases when the loading trajectories go back through the elastic zone. This is seen in Fig. 3 where the shear stress levels for the intersection of the loading path with the yield surface is much different for the two models. The kinematic model yields results much closer to experimental observation. This is an example of how nonproportional loading tests are valuable and necessary in constructing a flow rule. The kinematic hardening model provides a good overall match with experiments.

Conclusions

The calculations presented here demonstrate that although most plasticity theories yield identical results when applied to proportional load histories, the change in loading direction can greatly affect the predicted material response. In particular, simple kinematic hardening was shown to provide much better agreement with experiment than isotropic hardening.

References

Budiansky, B., Dow, N., Peters, R., and Shephard, R., 1951, "Experimental Studies of Polyaxial Stress-Strain Laws of Plasticity," *Proc. 1st U.S. National Congress of Applied Mechanics*, pp. 503–512.

Pan, J., and Rice, J., 1983, "Rate Sensitivity of Plastic Flow and Implications for Yield-Surface Vertices," *International Journal of Solids and Structures*, Vol. 19, pp. 973–987.

Prager, W., 1956, "A New Method of Analyzing Stresses and Strains on Work-Hardening Plastic Solids," ASME Journal of Applied Mechanics, Vol. 23, pp. 493–496.

Ziegler, H., 1959, "A Modification of Prager's Hardening Rule," *Quarterly of Applied Mathematics*, Vol. 17, pp. 55–65.

Downloaded 03 May 2010 to 171.66.16.248. Redistribution subject to ASME license or copyright; see http://www.asme.org/terms/Terms_Use.cfm

Asymptotic Solution for Extrusion of Sintered Powder Metals

D. Durban[3] and M. E. Mear[4]

Introduction

Structural components made from powder metals by compaction and sintering usually contain residual porosity and, as a consequence, their mechanical properties are not as good as those of chemically similar wrought or cast materials. Improvements in these properties can be achieved by reducing the residual porosity, and an effective means of doing this is to form the sintered compact with techniques such as forging, rolling, or extrusion (Avitzur and Blum, 1984; Furguson, 1984; Lenel, 1980).

An investigation of the forming of sintered powder compacts by drawing and extrusion has recently been performed by Mear and Durban (1989). In their study, friction between the die and the billet was neglected, and it was assumed that the dies were sufficiently long and tapered so that the flow field could be reasonably approximated as radial. Gurson's (1977a,b) constitutive relation was used to model the behavior of the porous metal and, by adopting an Eulerian frame of reference, the problem was reduced to the solution of a coupled set of first order ordinary differential equations. Results for the exit porosity and the processing loads were presented as functions of area reduction for an elastically rigid, power-hardening plastic matrix material.

In this Note, we readdress the problem for the case of a perfectly plastic matrix material, and we extract a simple closed-form approximation to the solution. This approximation is accurate to first order in the inlet void volume fraction, and in the limit of zero porosity it reduces to the exact solution for the radial flow of an elastically rigid, perfectly plastic material obeying the Von-Mises yield criterion. Our attention is focused on extrusion since this process is much more effective than drawing for reducing porosity, but the analysis can be easily extended to cases of drawing.

Problem Formulation

We examine the extrusion of porous metals through wedge-shaped dies (plane strain) and through conical dies (axisymmetric flow). The matrix material comprising the porous solid is assumed to be rigid-perfectly plastic with yield stress σ_y, and the mechanical behavior of the aggregate is modeled using Gurson's (1977a,b) constitutive theory which will be outlined below. In our analysis, friction between the billet and the work piece is neglected, and the dies are considered to be sufficiently long and of small enough taper so that the stream lines can be accurately assumed to be radially directed towards the virtual apex O (Fig. 1).

For the plane strain analysis, a cylindrical coordinate system with base vectors $(\mathbf{e}_r, \mathbf{e}_\theta, \mathbf{e}_z)$ is employed, while for the axisymmetric analysis, a spherical coordinate system with base vectors $(\mathbf{e}_r, \mathbf{e}_\theta, \mathbf{e}_\phi)$ is adopted. For the assumed flow field, only the radial component of the velocity vector, $-V(r)$, is nonzero, and the components of the Eulerian strain rate are

$$D_r = -\frac{dV}{dr}, \quad D_\theta = -\frac{1}{r}V \qquad (1a,b)$$

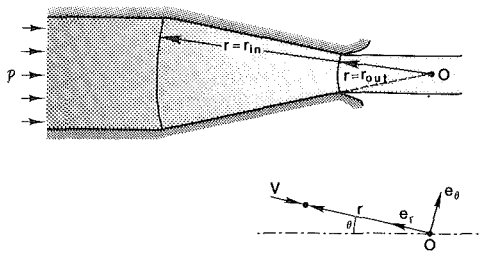

Fig. 1 Schematic showing extrusion of porous metal through a rigid die. Entry to reducing part of die is at $r = r_{in}$, and die is uniformly tapered up to die exit at $r = r_{out}$. Point O is virtual apex located by extending die walls to their point of intersection.

and D_3, where $D_3 = D_z = 0$ for plane strain and $D_3 = D_\phi = D_\theta$ for axisymmetric flow.

The only nonzero components of the macroscopic stress tensor are $(\Sigma_r, \Sigma_\theta, \Sigma_3)$, where $\Sigma_3 = \Sigma_z$ for plane strain and $\Sigma_3 = \Sigma_\phi = \Sigma_\theta$ for axisymmetric flow. It is convenient for the approximate analysis which follows to introduce the nondimensional stress variables

$$X = \frac{\Sigma_3}{\sigma_y} - \frac{1}{2\sigma_y}(\Sigma_r + \Sigma_\theta) \qquad (2a)$$

$$Y = \frac{\sqrt{3}}{2\sigma_y}(\Sigma_r - \Sigma_\theta) \qquad (2b)$$

and

$$Z = \frac{1}{2\sigma_y}(\Sigma_r + \Sigma_\theta + \Sigma_3). \qquad (2c)$$

In terms of these quantities, Gurson's yield function for the porous metal is

$$\Phi(\Sigma/\sigma_y, f) = X^2 + Y^2 + 2f_{in}F\cosh Z - (1 + f_{in}^2F^2) = 0 \qquad (3)$$

where Σ is the macroscopic stress tensor, f is the void volume fraction, $f_{in} = f(r_{in})$ is the inlet value of the void volume fraction and $F = f/f_{in}$. The relation specifying the evolution of the void volume fraction is obtained by noting that all of the dilatation results from void growth, and is

$$\dot{f} = (1 - f)(D_r + D_\theta + D_3). \qquad (4)$$

To analyze the steady-state extrusion process, it is advantageous to adopt an Eulerian frame of reference; in this reference frame

$$\dot{f} = -V\frac{df}{dr}. \qquad (5)$$

Using this relation, the fact that

$$D_r/D_\theta = \frac{\partial\Phi}{\partial\Sigma_r}\Big/\frac{\partial\Phi}{\partial\Sigma_\theta}, \qquad (6)$$

which is a consequence of normality of plastic flow, and (1a, b), the void growth relation (4) can be re-expressed as

$$\frac{f_{in}F'}{(1 - f_{in}F)} = a + \frac{X - \sqrt{3}Y - f_{in}F\sinh Z}{X + \sqrt{3}Y - f_{in}F\sinh Z}. \qquad (7)$$

Here, $(\,)' \equiv d/dx$ denotes differentiation with respect to the nondimensional variable $x = \ln(r/r_{out})$, and a is a constant with values

$$a = \begin{cases} 1 & \text{plane strain} \\ 2 & \text{axisymmetry} \end{cases} \qquad (8)$$

which has been introduced to distinguish cases of plane strain from cases of axisymmetric flow.

[3]Faculty of Aerospace Engineering, Technion, Haifa 32000, Israel.
[4]Department of Aerospace Engineering and Engineering Mechanics, The University of Texas at Austin, Austin, TX 78712.

Manuscript received by the ASME Applied Mechanics Division, Apr. 21, 1989; final revision, June 20, 1990.

Copyright © 1991 by ASME
Downloaded 03 May 2010 to 171.66.16.248. Redistribution subject to ASME license or copyright; see http://www.asme.org/terms/Terms_Use.cfm

Additional relations between the dependent variables are provided by the statement of equilibrium

$$\Sigma_r' = -\frac{2a}{\sqrt{3}}\sigma_y Y \tag{9}$$

and the constraint between the stress variables given by

$$X = -Y/\sqrt{3} \tag{10a}$$

for axisymmetric flow (since $\Sigma_3 = \Sigma_\phi = \Sigma_\theta$) and

$$X = -\frac{1}{2} f_{\text{in}} F \sinh Z \tag{10b}$$

for plane strain (which follows from the condition that $D_z = 0$).

Now, the solution to the problem of extrusion of perfectly plastic porous metals can be obtained by solving the system of equations given by (3), (7), (9), and (10*a*) or (10*b*). The inlet (or initial) values of f and Σ_r are f_{in} and $-\mathcal{P}$, respectively, where $\mathcal{P}$ is the extrusion pressure. The inlet values for the other stress components are obtained from the yield condition (3) and the relation (10*a*) or (10*b*). The condition to be met at the die exit is that $\Sigma_r = \Sigma_r(r_{\text{out}}) = 0$ (assuming that there is no front tension).

A complete closed-form solution to this system of equations cannot be found, but it is relatively straightforward to obtain accurate numerical results. To perform these calculations, the system can be cast in the form of coupled first-order ordinary differential equations, and then integrated using standard Runga-Kutta algorithms (see Mear and Durban, 1989). Results of such calculations will be presented, after a simple approximate solution to the extrusion problem is developed.

First-Order Approximation

To obtain an approximate solution for the system of equations discussed previously, we now assume that the stress variables (X, Y, Z) possess regular expansions in f_{in} (and hence also that the stresses themselves and the extrusion pressure $\mathcal{P}$ possess such expansions). That is, if W represents one of these quantities, then we write

$$W = W_0 + f_{\text{in}} W_1 + f_{\text{in}}^2 W_2 + \ldots \tag{11}$$

where W_0, W_1, W_2, ... are functions of the area reduction

$$R = 1 - \left(\frac{r_{\text{out}}}{r_{\text{in}}}\right)^a \tag{12}$$

and also depend on whether the deformation is plane strain or axisymmetric. The quantities (X_0, Y_0, Z_0, $\mathcal{P}_0$) correspond to the solution for the void-free solid, and while they can be obtained as a natural part of this analysis, we simply state them from the outset (see Durban and Budiansky, 1979; Durban, 1979; Durban, 1983). They are

$$X_0 = -(a-1)/2 \tag{13a}$$

$$Y_0 = \frac{\sqrt{3}}{2} b \tag{13b}$$

$$Z_0 = -\frac{1}{b}[1 + (1+a)x] \tag{13c}$$

and

$$\mathcal{P}_0 = -b\sigma_y \ln(1-R) \tag{13d}$$

where

$$b = \begin{cases} 2/\sqrt{3} & \text{plane strain} \\ 1 & \text{axisymmetry} \end{cases} \tag{14}$$

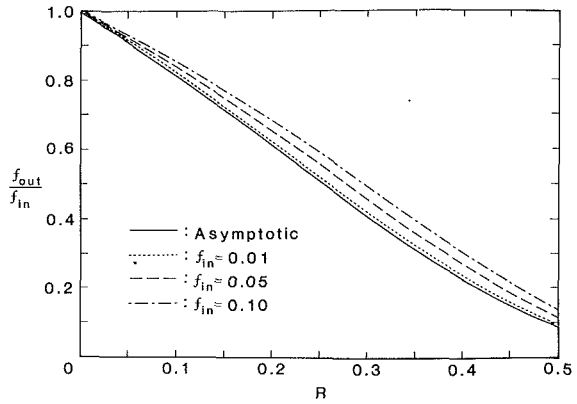

Fig. 2 Ratio of exit void volume fraction to inlet void volume fraction, $f_{\text{out}}/f_{\text{in}}$, as a function of the area reduction R

is another constant introduced to allow cases of plane strain and cases of axisymmetric flow to be treated simultaneously.

What we seek are the first-order corrections to the solution for the void-free solid. In particular, we are interested in obtaining approximate relations for the exit void volume fraction and the pressure necessary to extrude the material to a given reduction.

To obtain these relations, we insert the expansions for (X, Y, Z) into equations (3), (7), (9), (10*a*), and (10*b*), and, after simplifying, retain only the dominate terms. This gives rise to the following system of equations:

$$X_0 X_1 + Y_0 Y_1 + F\cosh Z_0 = 0 \tag{15}$$

$$\frac{F'}{F} = -\sqrt{3^a}\sinh Z_0 \tag{16}$$

$$\Sigma_{r1}' = -\frac{2a}{\sqrt{3}}\sigma_y Y_1 \tag{17}$$

and

$$X_1 = -Y_1/\sqrt{3} \tag{18a}$$

for axisymmetry while

$$X_1 = -\frac{1}{2} F \sinh Z_0 \tag{18b}$$

for plane strain.

Recalling the relation for Z_0 given in (13*c*), equation (16) can be easily integrated to obtain an expression for the void volume fraction at each location within the die. Of primary interest is the void volume fraction of the material as it exits the die, and this is given by

$$\ln(f_{\text{out}}/f_{\text{in}}) = \cosh(1/b) - \cosh[1/b - (3b/2)\ln(1-R)]. \tag{19}$$

This approximate relation is contrasted with the full (numerical) solution in Fig. 2 for cases of axisymmetric flow with three different inlet void volume fractions. The first-order solution agrees quite closely with the exact solution for the case of $f_{\text{in}} = 0.01$ and, as expected, the agreement between the approximate solution and the exact solution diminishes as the inlet void volume fraction is increased. The agreement remains reasonable, however, even for the moderate inlet void volume fraction of $f_{\text{in}} = 0.10$. Comparisons between the exact and approximate solutions have also been made for cases of plane strain, and the approximate solution compares with the exact solution in the same qualitative ways as for the corresponding cases of axisymmetric flow.

The other quantity of interest is the extrusion pressure required to process the material to a given reduction. The first-order approximation of the extrusion pressure is given by $\mathcal{P} \approx \mathcal{P}_0 + f_{\text{in}}\mathcal{P}_1$ where $\mathcal{P}_1 = -\Sigma_{r1}(r_{\text{out}})$. To obtain an expres-

Downloaded 03 May 2010 to 171.66.16.248. Redistribution subject to ASME license or copyright; see http://www.asme.org/terms/Terms_Use.cfm

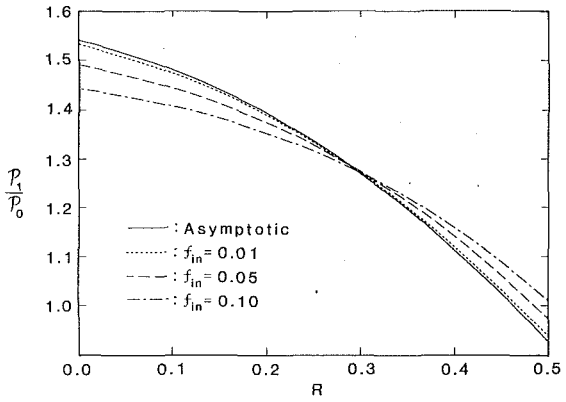

Fig. 3 Ratio of $\mathcal{P}_1$, given by equation (21), to the zeroth-order approximation of the extrusion pressure, $\mathcal{P}_0$, as a function of the area reduction R. The first-order approximation of the extrusion pressure is given by $\mathcal{P} \approx \mathcal{P}_0 + f_{in}\mathcal{P}_1$.

sion for $\mathcal{P}_1$, we first eliminate Y_1 from equation (17) using equations (15) and (18*a*) or (18*b*); the relation which results is

$$\Sigma'_{r1} = ab\sigma_y F \cosh Z_0. \tag{20}$$

Upon inserting the expression for F obtained from equation (16) into this relation and integrating, we find

$$\mathcal{P}_1 = \frac{2}{3}\sigma_y e^{-\beta} \int_\alpha^\beta \frac{e^w w}{\sqrt{w^2-1}}\, dw \tag{21}$$

where $\alpha = \cosh(1/b)$ and

$$\beta = \cosh[1/b - (3b/2)\ln(1-R)]. \tag{22}$$

In Fig. 3, the extrusion pressures predicted by the first-order approximation are compared with the exact solution for cases corresponding to those in Fig. 2. The agreement is excellent for $f_{in} = 0.01$, and remains good even for the larger inlet void volume fractions. Note that in this figure it is $\mathcal{P}_1/\mathcal{P}_0$ which is plotted, so that even for the largest void volume fraction presented, the actual error in the approximate extrusion pressure is very small (about one percent).

Finally, we remark that the present analysis can be extended to include strain hardening of the matrix material. In particular, equation (16) generalizes to

$$\frac{F'}{F} = -\sqrt{3^a}\sinh\left(\frac{Z_0}{X_0^2 + Y_0^2}\right) \tag{23}$$

where $\{X_0, Y_0, Z_0\}$ are known from the corresponding radial flow solutions for void-free strain-hardening solids. For particular matrix-hardening characterizations (e.g., a pure power-law), the integration of equation (23) can be performed analytically.

Acknowledgments

A portion of this study has been supported by the L. Kraus Fund, Technion, Haifa, and by a grant from the ALCOA Foundation.

References

Avitzur, B., and Blum, P., 1984, "Forging and Extrusion of P/M Preforms," *Mod. Dev. in Powder Metallurgy*, Vol. 8, H. H. Hausner and W. E. Smith, eds., Princeton, p. 73.

Durban, D., 1979, "Axially Symmetric Radial Flow of Rigid/Linear-Hardening Materials," ASME JOURNAL OF APPLIED MECHANICS, Vol. 46, p. 322.

Durban, D., 1983, "Radial Flow Simulation of Rigid/Hardening Materials," *Int. J. Mech. Sci.*, Vol. 25, p. 27.

Durban, D., and Budiansky, B., 1979, "Plane Strain Radial Flow of Plastic Materials," *J. Mech. Phys. Solids*, Vol. 26, p. 303.

Ferguson, B. L., 1984, "Forging and Rolling of P/M Billets," *Metals Handbook*, 9th ed., Vol. 7, p. 522.

Gurson, A. L., 1977a, "Continuum Theory of Ductile Rupture by Void Nucleation and Growth—Part 1. Yield Criteria and Flow Rules for Porous Ductile Media," *J. Engrg. Mater. Techol.*, Vol. 99, p. 2.

Gurson, A. L., 1977b, "Porous Rigid-Plastic Materials Containing Rigid Inclusions—Yield Function, Plastic Potential, and Void Nucleation," *Fracture 1977*, Vol. 2, ICF4, Waterloo, Canada.

Lenel, F. V., 1980, *Powder Metallurgy: Principles and Applications*, Metal Powder Industries Federation, Princeton, N.J., pp. 324–329; 456–464.

Mear, M. E., and Durban, D., 1989, "Radial Flow of Sintered Powder Metals," *Int. J. Mech. Sci.*, Vol. 31, p. 37–49.

The Branched Crack Problem Revisited

Anna Dollar[5] and Paul S. Steif[5,6]

Introduction

In ceramic-matrix composites, preferential cracking of the matrix first occurs during monotonic loading. When the loading consists of tension applied parallel to the fibers, the resulting matrix cracks impinge upon the fiber-matrix interface. If the interface is sufficiently weak, as is often the case, debonding of the interface will occur prior to failure of the fibers. One is interested in the response of this branched crack under futher increases in the load.

Since the branch-crack faces are just two sides of the fiber-matrix interface, it is clear that overlapping of these faces—material interpenetration—cannot be permitted. Yet, such interpenetration is a common feature of most solutions to branch-crack problems in homogeneous materials (see, for example, Vitek, 1977; Kitagawa and Yuuki, 1977; Lo, 1978), as evidenced by the negative mode I stress intensity factor at the tip of the branch crack. In this Note, we focus on the nature of branch-crack solutions when interpenetration is properly prohibited. This is done for the admittedly idealized problem of a doubly-symmetric branch crack in a homogeneous plane. Application of the notions developed here to the composite problem will be taken up in the near future.

Problem Statement and Analysis

A doubly-symmetrical branched crack subjected to remote tension σ_∞ is shown schematically in Fig. 1. The main crack faces are assumed to be free of tractions. Since each branch is essentially identical for this loading, we will henceforth refer only to the branch along $x=0$, $0<y<L$; analogous statements apply to the other branches. We assume that the branch-crack faces are fully lubricated so that the interface conditions along the branch crack are:

$$\sigma_{xy} = 0 \tag{1}$$

and

$$\sigma_{xx} = 0 \quad \text{if } h>0 \tag{2a}$$

$$h = 0 \quad \text{if } \sigma_{xx}<0 \tag{2b}$$

where h is the opening along the branch crack. It turns out that the interface will be open and will satisfy equation (2*a*) over a portion of the interface, $0<y<d$, while the interface will be closed and will satisfy (2*b*) over $d<y<L$.

We employed a method of solution which is essentially identical to that of Lo (1978). The solution is expressed as a superposition of a single crack in an infinite plane plus a suitable

[5]Department of Mechanical Engineering, Carnegie-Mellon University, Pittsburgh, PA 15213.

[6]Assoc. Mem. ASME.

Manuscript received by the ASME Applied Mechanics Division, Oct. 11, 1989, final revision, Apr. 26, 1990.

Downloaded 03 May 2010 to 171.66.16.248. Redistribution subject to ASME license or copyright; see http://www.asme.org/terms/Terms_Use.cfm

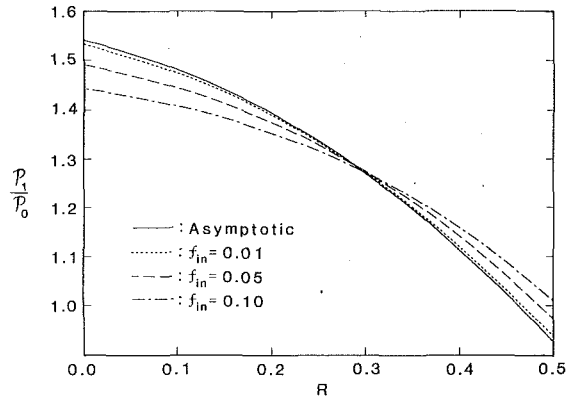

Fig. 3 Ratio of $\mathcal{P}_1$, given by equation (21), to the zeroth-order approximation of the extrusion pressure, $\mathcal{P}_0$, as a function of the area reduction R. The first-order approximation of the extrusion pressure is given by $\mathcal{P} \approx \mathcal{P}_0 + f_{in}\mathcal{P}_1$.

sion for $\mathcal{P}_1$, we first eliminate Y_1 from equation (17) using equations (15) and (18*a*) or (18*b*); the relation which results is

$$\Sigma'_{r1} = ab\sigma_y F \cosh Z_0. \tag{20}$$

Upon inserting the expression for F obtained from equation (16) into this relation and integrating, we find

$$\mathcal{P}_1 = \frac{2}{3}\sigma_y e^{-\beta} \int_\alpha^\beta \frac{e^w w}{\sqrt{w^2-1}}\, dw \tag{21}$$

where $\alpha = \cosh(1/b)$ and

$$\beta = \cosh[1/b - (3b/2)\ln(1-R)]. \tag{22}$$

In Fig. 3, the extrusion pressures predicted by the first-order approximation are compared with the exact solution for cases corresponding to those in Fig. 2. The agreement is excellent for $f_{in} = 0.01$, and remains good even for the larger inlet void volume fractions. Note that in this figure it is $\mathcal{P}_1/\mathcal{P}_0$ which is plotted, so that even for the largest void volume fraction presented, the actual error in the approximate extrusion pressure is very small (about one percent).

Finally, we remark that the present analysis can be extended to include strain hardening of the matrix material. In particular, equation (16) generalizes to

$$\frac{F'}{F} = -\sqrt{3^a}\sinh\left(\frac{Z_0}{X_0^2 + Y_0^2}\right) \tag{23}$$

where $\{X_0, Y_0, Z_0\}$ are known from the corresponding radial flow solutions for void-free strain-hardening solids. For particular matrix-hardening characterizations (e.g., a pure power-law), the integration of equation (23) can be performed analytically.

Acknowledgments

A portion of this study has been supported by the L. Kraus Fund, Technion, Haifa, and by a grant from the ALCOA Foundation.

References

Avitzur, B., and Blum, P., 1984, "Forging and Extrusion of P/M Preforms," *Mod. Dev. in Powder Metallurgy*, Vol. 8, H. H. Hausner and W. E. Smith, eds., Princeton, p. 73.

Durban, D., 1979, "Axially Symmetric Radial Flow of Rigid/Linear-Hardening Materials," ASME JOURNAL OF APPLIED MECHANICS, Vol. 46, p. 322.

Durban, D., 1983, "Radial Flow Simulation of Rigid/Hardening Materials," *Int. J. Mech. Sci.*, Vol. 25, p. 27.

Durban, D., and Budiansky, B., 1979, "Plane Strain Radial Flow of Plastic Materials," *J. Mech. Phys. Solids*, Vol. 26, p. 303.

Ferguson, B. L., 1984, "Forging and Rolling of P/M Billets," *Metals Handbook*, 9th ed., Vol. 7, p. 522.

Gurson, A. L., 1977a, "Continuum Theory of Ductile Rupture by Void Nucleation and Growth—Part 1. Yield Criteria and Flow Rules for Porous Ductile Media," *J. Engrg. Mater. Techol.*, Vol. 99, p. 2.

Gurson, A. L., 1977b, "Porous Rigid-Plastic Materials Containing Rigid Inclusions—Yield Function, Plastic Potential, and Void Nucleation," *Fracture 1977*, Vol. 2, ICF4, Waterloo, Canada.

Lenel, F. V., 1980, *Powder Metallurgy: Principles and Applications*, Metal Powder Industries Federation, Princeton, N.J., pp. 324–329; 456–464.

Mear, M. E., and Durban, D., 1989, "Radial Flow of Sintered Powder Metals," *Int. J. Mech. Sci.*, Vol. 31, p. 37–49.

The Branched Crack Problem Revisited

Anna Dollar[5] and Paul S. Steif[5,6]

Introduction

In ceramic-matrix composites, preferential cracking of the matrix first occurs during monotonic loading. When the loading consists of tension applied parallel to the fibers, the resulting matrix cracks impinge upon the fiber-matrix interface. If the interface is sufficiently weak, as is often the case, debonding of the interface will occur prior to failure of the fibers. One is interested in the response of this branched crack under futher increases in the load.

Since the branch-crack faces are just two sides of the fiber-matrix interface, it is clear that overlapping of these faces—material interpenetration—cannot be permitted. Yet, such interpenetration is a common feature of most solutions to branch-crack problems in homogeneous materials (see, for example, Vitek, 1977; Kitagawa and Yuuki, 1977; Lo, 1978), as evidenced by the negative mode I stress intensity factor at the tip of the branch crack. In this Note, we focus on the nature of branch-crack solutions when interpenetration is properly prohibited. This is done for the admittedly idealized problem of a doubly-symmetric branch crack in a homogeneous plane. Application of the notions developed here to the composite problem will be taken up in the near future.

Problem Statement and Analysis

A doubly-symmetrical branched crack subjected to remote tension σ_∞ is shown schematically in Fig. 1. The main crack faces are assumed to be free of tractions. Since each branch is essentially identical for this loading, we will henceforth refer only to the branch along $x=0$, $0<y<L$; analogous statements apply to the other branches. We assume that the branch-crack faces are fully lubricated so that the interface conditions along the branch crack are:

$$\sigma_{xy} = 0 \tag{1}$$

and

$$\sigma_{xx} = 0 \quad \text{if } h>0 \tag{2a}$$

$$h = 0 \quad \text{if } \sigma_{xx}<0 \tag{2b}$$

where h is the opening along the branch crack. It turns out that the interface will be open and will satisfy equation (2*a*) over a portion of the interface, $0<y<d$, while the interface will be closed and will satisfy (2*b*) over $d<y<L$.

We employed a method of solution which is essentially identical to that of Lo (1978). The solution is expressed as a superposition of a single crack in an infinite plane plus a suitable

[5]Department of Mechanical Engineering, Carnegie-Mellon University, Pittsburgh, PA 15213.

[6]Assoc. Mem. ASME.

Manuscript received by the ASME Applied Mechanics Division, Oct. 11, 1989, final revision, Apr. 26, 1990.

Copyright © 1991 by ASME
Downloaded 03 May 2010 to 171.66.16.248. Redistribution subject to ASME license or copyright; see http://www.asme.org/terms/Terms_Use.cfm

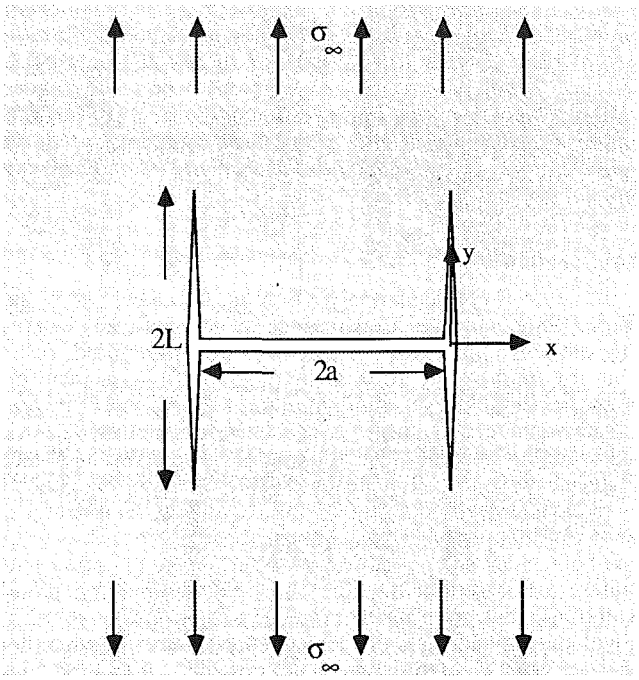

Fig. 1 Schematic of doubly-symmetrical branched crack

distribution of dislocations to represent the branch cracks. One needs to ensure that the main crack faces remain free of tractions. This is accomplished automatically by having *each* dislocation in the distribution leave the main crack faces traction-free. Thus, the appropriate kernel solution is the solution to a single dislocation in an infinite plane containing a traction-free crack lying along $-2a<x<0$. This procedure yields a pair of singular integral equations for the dislocation densities $b_x(y)$ and $b_y(y)$, which we write in abbreviated form as

$$\int_0^L b_y(y')\left[\frac{1}{y'-y}+A(y',y)\right]dy' + \int_0^d b_x(y')B(y',y)dy' + f(y)=0 \quad (0<y<L) \qquad (3a)$$

$$\int_0^L b_y(y')C(y',y)dy' + \int_0^d b_x(y')\left[\frac{1}{y'-y} + D(y',y)\right]dy' + g(y)=0 \quad (0<y<d). \qquad (3b)$$

The kernels $A\ (y', y)$, $B\ (y', y)$, $C\ (y', y)$, $D\ (y', y)$, and the functions $f(y)$ and $g(y)$ can be derived from expressions given by Lo (1978).

For a given branch crack length L, the unknowns are the densities $b_x(y)$ and $b_y(y)$ and the extent of opening d. (The density $b_x(y)$ is nonzero only on $0<y<d$.) Whenever $0<d<L$, that is, when there is opening over some, but not all, of the interface, then the contact condition $b_x(d)=0$ must be satisfied (Dundurs and Comninou, 1979). A standard numerical method of solving the singular integral equations via discretization was used (Erdogan, Gupta, and Cook, 1973), with the expected singularity $1/\sqrt{(L-y)}$ built into $b_y(y)$ (and into $b_x(y)$ if $d=L$).

Results and Discussion

In Figs. 2 and 3 the stress intensity factors at the branch-crack tip are plotted as a function of ratio L/a. Stress intensity factors based on a proper accounting of contact at the branch crack faces are plotted as the solid curves. The dashed curves correspond to the forced imposition of the traction-free condition $\sigma_{xx}=\sigma_{xy}=0$ along the branch crack (as has been generally used in the study of branch cracks), irrespective of possible crack-face overlap. It can be seen that K_I is nonzero for only

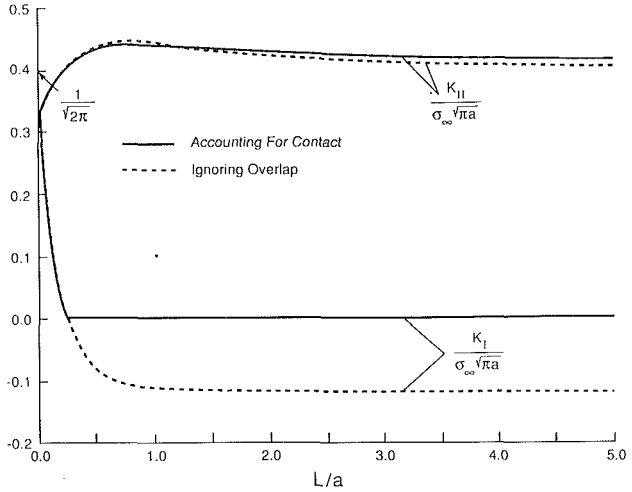

Fig. 2 Branch-crack stress intensity factors for short and moderately long branch cracks

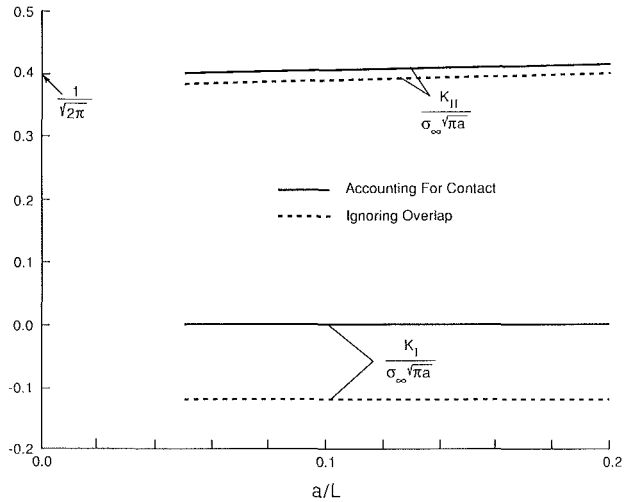

Fig. 3 Branch-crack stress intensity factors for the long branch cracks

a small range of L/a ($0<L/a<0.24$), as might be discerned from the work of others in which K_I is found to be negative when L/a is in excess of, roughly, 0.24. There is a somewhat larger range of L/a ($0<L/a<0.71$) in which there is some opening of the interface. This means that for $0<L/a<0.24$, the branch crack is fully open ($d=L$); for $0.24<L/a<0.71$, the branch crack is partially open ($0<d<L$); and, for $L/a>0.71$, the branch crack is completely closed ($d=0$).

It is potentially of great significance that the mode I stress intensity factor becomes zero as L/a increases, whereas an analysis based on a debond which is vanishingly small compared with the main crack would lead one to think that the stress intensity factors are comparable. This significance derives from experimental observations (e.g., Cao and Evans, 1989) that much less energy is required to drive a crack in mode I than in mode II. Hence, much less debonding might be predicted for a given remote loading once it is appreciated that the mode I stress intensity factor is zero.

In general, we find that our results for both stress intensity factors (corresponding to forced imposition of $\sigma_{xx}=\sigma_{xy}=0$ on the interface) are within 2.5 percent to 6 percent of the tabulated results of Vitek (1977). Kitagawa and Yuuki (1977) presented results only in graphical form. It appears that our results for K_I are within several percent of their results. In the case of K_{II}, however, not only do their results differ by as much as 10 percent from ours and Vitek's, but their K_{II} reaches

Downloaded 03 May 2010 to 171.66.16.248. Redistribution subject to ASME license or copyright; see http://www.asme.org/terms/Terms_Use.cfm

a maximum value for L/a being approximately 0.2; by contrast, our K_{II} is maximum for $L/a = 0.71$, and Vitek's K_{II} is maximum for L/a between 0.5 and 1.0.)

Neglecting branch-crack contact has an influence on the computed value of K_{II}, though, at approximately 5 percent for large L/a, this is not a substantial effect. With proper accounting for branch-crack contact, one can use an energy release argument to calculate exactly the asymptotic value of K_{II} for the limit as $L/a \to \infty$. The energy released with a unit extension of the branch cracks is precisely equal to the strain energy of a block of material (of width $2a$) under uniaxial, plane-strain tension σ_∞. This energy goes to two branch crack tips and is entirely taken up by K_{II}, since $K_I = 0$; the result is

$$\lim_{L/a \to \infty} K_{II} = \sigma_\infty \sqrt{\frac{a}{2}} = \sqrt{\frac{1}{2\pi}} \sigma_\infty \sqrt{\pi a} = 0.3989 \ \sigma_\infty \sqrt{\pi a}.$$

Our computed values for $K_{II}/\sigma_\infty\sqrt{\pi a}$ at $L/a = 10$ and $L/a = 20$ are 0.4062 and 0.4013, respectively. Extrapolating linearly to $a/L = 0$, we find $K_{II}/\sigma_\infty\sqrt{\pi a}$ approaches 0.3963, a difference of 0.65 percent.

Acknowledgments

This work has been supported in part by the National Science Foundation under grant MSM-8451080, by the General Electric Engine Business Group, and by the Department of Mechanical Engineering, Carnegie Mellon University.

References

Cao, H. C., and Evans, A. G., 1989, "An Experimental Study of the Fracture Resistance of Bimaterial Interfaces," *Mech. Materials*, Vol. 7, p. 295-304.

Dundurs, J., and Comninou, M., 1979, "Some Consequences of the Inequality Conditions in Contact and Crack Problems," *J. Elasticity*, Vol. 9, pp. 71-82.

Erdogan, F., Gupta, G. D., and Cook, T. S., 1973, "Numerical Solution of Singular Integral Equations," *Mechanics of Fracture 1. Methods of Analysis and Solutions of Crack Problems*, G. C. Sih ed., Noordhoff, The Netherlands.

Kitagawa, H., and Yuuki, R., 1977, "Analysis of Branched Cracks Under Biaxial Stresses," *Fracture 1977*, Vol. 3, D. M. R. Taplin, ed., University of Waterloo, Waterloo, Canada, pp. 201-211.

Lo, K. K., 1978, "Analysis of Branched Cracks," ASME JOURNAL OF APPLIED MECHANICS, Vol. 45, pp. 797-802.

Vitek, V., 1977, "Plane Strain Stress-Intensity Factors for Branched Cracks," *Int. J. Fract.*, Vol. 13, No. 4, pp. 481-501.

Singularities in *p*-Type Finite Element Computations: Numerical Experiments on the Locality of Pollution Effects

G. Becker,[7] P. Carnevali,[7] B. Chayapathy,[7] W. Imaino,[7] R. B. Morris,[7] Y. Tsuji,[7] and B. Yendler[7]

Using a recently developed code for three-dimensional p-type finite element computations in elasticity, we have studied, with a series of numerical experiments, the behavior of the solution in the presence of singularities. Worst-cast theoretical estimates predict a global pollution of the solution, unless optimally graded meshes are used. On the other hand, we observe that except in an immediate neighborhood of a singularity, and even using uniform meshes, the quality of the solution is not degraded to any practically relevant extent. This has important practical consequences because it allows modelers to introduce artifical singularities for the purpose of simplifying models. The size of the area around a singularity where the solution is appreciably degraded can be estimated in terms of the minimum effective wavelength of the basis functions used; the latter, in turn, can be related to the element size and the polynomial order used.

Introduction

In *p*-type finite element methods (e.g., Babuska, Szabo, and Katz, 1981), convergence is reached by systematically increasing the polynomial order of the basis functions used, rather than by mesh refinements as in standard finite element approaches (*h*-type). An abundant literature has concentrated on error estimates for the *h* and *p*-type finite element methods: Babuska (1986), Dorr (1984), Gui and Babuska (1986), Babuska and Suri (1987), Szabo (1986), Tong and Pian (1973), and Zienkiewicz and Craig (1986) are only a small subset of relevant references. The general conclusions are: that the *p*-method achieves better convergence rates (energy norm versus number of degrees-of-freedom) than the *h*-method for smooth solutions; that, even in the presence of nonsmooth solutions involving singularities, the convergence rate of the *p*-method is never worse than the convergence rate of the *h*-method; and, that optimal convergence rates are achieved, in the presence of singularities, by a combination of the *h* and *p*-methods, in which optimally graded meshes around singularities are used.

Although it is often expected (e.g, Schatz and Wahlbin, 1979) that the local accuracy becomes progressively better as the distance from the singularities increases, thus is not guaranteed in general. This situation is often referred to as a "pollution effect" (Babuska and Rosenzweig, 1972; Blum and Rannacher, 1988). Thus, conventional wisdom requires that graded meshes be used in the presence of singularities.

In this work, rather than focusing on how to find optimal meshing strategies, we emphasize some of the practical aspects of using a *p*-type finite element code for elasticity problems. In particular, one often wants to trade optimal meshes for simplified geometries, and it then becomes important to assess the practical consequences of this trade-off from the point of view of achievable accuracy.

In cases where a good description of the singularity is needed (e.g., to estimate stress intensity factors in crack problems, Johnson, 1981), an appropriate grading of the mesh is definitely needed. On the other hand, in models of elastic problems "artificial" singularities (typically due to sharp reentrant corners) are often introduced in order to simplify the model from the geometrical point of view. For example, a mechanical piece might have a reentrant "corner" with a small but finite radius of curvature, and the modeler might not necessarily be interested in computing the stress distribution correctly in the neighborhood of the "corner" because it is known in advance that there is no stress problem in that area. However, this can be done safely only if no practically significant error is introduced by this procedure, except in the neighborhood of the singularity. Functional analytical error estimates cannot be used directly to estimate actual error distributions in realistic problems, and numerical computations are needed.

Using a recently developed *p*-type finite element code (Carnevali, Morris, and Tsuji, 1990), we have performed a sequence of numerical calculations which address precisely this question. The conclusions of this study are reassuring and indicate that significant errors are only present in the immediate neighborhood of the singularity.

Outside this area no noticeable pollution occurs. The size of this area—like in the familiar situation of a Gibbs phenomenon (e.g., Stakgold, 1979)—is comparable to the minimum wavelength of the basis functions used and can be readily

[7]IBM Research Division, Almaden Research Center, San Jose, CA 95120-6099.

Manuscript received by the ASME Applied Mechanics Division, Nov. 17, 1989; final revision, Apr. 15, 1990.

Downloaded 03 May 2010 to 171.66.16.248. Redistribution subject to ASME license or copyright; see http://www.asme.org/terms/Terms_Use.cfm

a maximum value for L/a being approximately 0.2; by contrast, our K_{II} is maximum for $L/a = 0.71$, and Vitek's K_{II} is maximum for L/a between 0.5 and 1.0.)

Neglecting branch-crack contact has an influence on the computed value of K_{II}, though, at approximately 5 percent for large L/a, this is not a substantial effect. With proper accounting for branch-crack contact, one can use an energy release argument to calculate exactly the asymptotic value of K_{II} for the limit as $L/a \to \infty$. The energy released with a unit extension of the branch cracks is precisely equal to the strain energy of a block of material (of width $2a$) under uniaxial, plane-strain tension σ_∞. This energy goes to two branch crack tips and is entirely taken up by K_{II}, since $K_I = 0$; the result is

$$\lim_{L/a \to \infty} K_{II} = \sigma_\infty \sqrt{\frac{a}{2}} = \sqrt{\frac{1}{2\pi}} \sigma_\infty \sqrt{\pi a} = 0.3989\ \sigma_\infty \sqrt{\pi a}.$$

Our computed values for $K_{II}/\sigma_\infty \sqrt{\pi a}$ at $L/a = 10$ and $L/a = 20$ are 0.4062 and 0.4013, respectively. Extrapolating linearly to $a/L = 0$, we find $K_{II}/\sigma_\infty \sqrt{\pi a}$ approaches 0.3963, a difference of 0.65 percent.

Acknowledgments

This work has been supported in part by the National Science Foundation under grant MSM-8451080, by the General Electric Engine Business Group, and by the Department of Mechanical Engineering, Carnegie Mellon University.

References

Cao, H. C., and Evans, A. G., 1989, "An Experimental Study of the Fracture Resistance of Bimaterial Interfaces," *Mech. Materials*, Vol. 7, p. 295-304.

Dundurs, J., and Comninou, M., 1979, "Some Consequences of the Inequality Conditions in Contact and Crack Problems," *J. Elasticity*, Vol. 9, pp. 71-82.

Erdogan, F., Gupta, G. D., and Cook, T. S., 1973, "Numerical Solution of Singular Integral Equations," *Mechanics of Fracture 1. Methods of Analysis and Solutions of Crack Problems*, G. C. Sih ed., Noordhoff, The Netherlands.

Kitagawa, H., and Yuuki, R., 1977, "Analysis of Branched Cracks Under Biaxial Stresses," *Fracture 1977*, Vol. 3, D. M. R. Taplin, ed., University of Waterloo, Waterloo, Canada, pp. 201-211.

Lo, K. K., 1978, "Analysis of Branched Cracks," ASME JOURNAL OF APPLIED MECHANICS, Vol. 45, pp. 797-802.

Vitek, V., 1977, "Plane Strain Stress-Intensity Factors for Branched Cracks," *Int. J. Fract.*, Vol. 13, No. 4, pp. 481-501.

Singularities in *p*-Type Finite Element Computations: Numerical Experiments on the Locality of Pollution Effects

G. Becker,[7] P. Carnevali,[7] B. Chayapathy,[7] W. Imaino,[7] R. B. Morris,[7] Y. Tsuji,[7] and B. Yendler[7]

Using a recently developed code for three-dimensional p-type finite element computations in elasticity, we have studied, with a series of numerical experiments, the behavior of the solution in the presence of singularities. Worst-cast theoretical estimates predict a global pollution of the solution, unless optimally graded meshes are used. On the other hand, we observe that except in an immediate neighborhood of a singularity, and even using uniform meshes, the quality of the solution is not degraded to any practically relevant extent. This has important practical consequences because it allows modelers to introduce artifical singularities for the purpose of simplifying models. The size of the area around a singularity where the solution is appreciably degraded can be estimated in terms of the minimum effective wavelength of the basis functions used; the latter, in turn, can be related to the element size and the polynomial order used.

Introduction

In *p*-type finite element methods (e.g., Babuska, Szabo, and Katz, 1981), convergence is reached by systematically increasing the polynomial order of the basis functions used, rather than by mesh refinements as in standard finite element approaches (*h*-type). An abundant literature has concentrated on error estimates for the *h* and *p*-type finite element methods: Babuska (1986), Dorr (1984), Gui and Babuska (1986), Babuska and Suri (1987), Szabo (1986), Tong and Pian (1973), and Zienkiewicz and Craig (1986) are only a small subset of relevant references. The general conclusions are: that the *p*-method achieves better convergence rates (energy norm versus number of degrees-of-freedom) than the *h*-method for smooth solutions; that, even in the presence of nonsmooth solutions involving singularities, the convergence rate of the *p*-method is never worse than the convergence rate of the *h*-method; and, that optimal convergence rates are achieved, in the presence of singularities, by a combination of the *h* and *p*-methods, in which optimally graded meshes around singularities are used.

Although it is often expected (e.g, Schatz and Wahlbin, 1979) that the local accuracy becomes progressively better as the distance from the singularities increases, thus is not guaranteed in general. This situation is often referred to as a "pollution effect" (Babuska and Rosenzweig, 1972; Blum and Rannacher, 1988). Thus, conventional wisdom requires that graded meshes be used in the presence of singularities.

In this work, rather than focusing on how to find optimal meshing strategies, we emphasize some of the practical aspects of using a *p*-type finite element code for elasticity problems. In particular, one often wants to trade optimal meshes for simplified geometries, and it then becomes important to assess the practical consequences of this trade-off from the point of view of achievable accuracy.

In cases where a good description of the singularity is needed (e.g., to estimate stress intensity factors in crack problems, Johnson, 1981), an appropriate grading of the mesh is definitely needed. On the other hand, in models of elastic problems "artificial" singularities (typically due to sharp reentrant corners) are often introduced in order to simplify the model from the geometrical point of view. For example, a mechanical piece might have a reentrant "corner" with a small but finite radius of curvature, and the modeler might not necessarily be interested in computing the stress distribution correctly in the neighborhood of the "corner" because it is known in advance that there is no stress problem in that area. However, this can be done safely only if no practically significant error is introduced by this procedure, except in the neighborhood of the singularity. Functional analytical error estimates cannot be used directly to estimate actual error distributions in realistic problems, and numerical computations are needed.

Using a recently developed *p*-type finite element code (Carnevali, Morris, and Tsuji, 1990), we have performed a sequence of numerical calculations which address precisely this question. The conclusions of this study are reassuring and indicate that significant errors are only present in the immediate neighborhood of the singularity.

Outside this area no noticeable pollution occurs. The size of this area—like in the familiar situation of a Gibbs phenomenon (e.g., Stakgold, 1979)—is comparable to the minimum wavelength of the basis functions used and can be readily

[7]IBM Research Division, Almaden Research Center, San Jose, CA 95120-6099.

Manuscript received by the ASME Applied Mechanics Division, Nov. 17, 1989; final revision, Apr. 15, 1990.

Copyright © 1991 by ASME
Downloaded 03 May 2010 to 171.66.16.248. Redistribution subject to ASME license or copyright; see http://www.asme.org/terms/Terms_Use.cfm

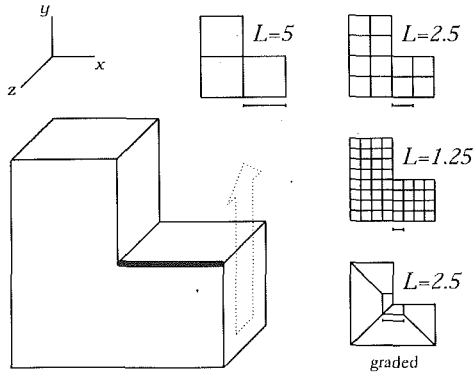

Fig. 1 Three-dimensional *L*-plate with a stress singularity at the reentrant edge. The shaded face is constrained to zero displacement, while a uniform tangential load, as indicated by the arrow, is applied. This causes a stress singularity at the reentrant edge (obviously, displacements remain finite). The edge drawn on a thicker line is the one on which stress errors (as in Fig. 2) have been computed and analyzed. Some of the different meshes used, with local element size *L*, are sketched. The *L*-plate thickness in the *z* direction is five length units. No mesh refinement in the *z* direction has been used.

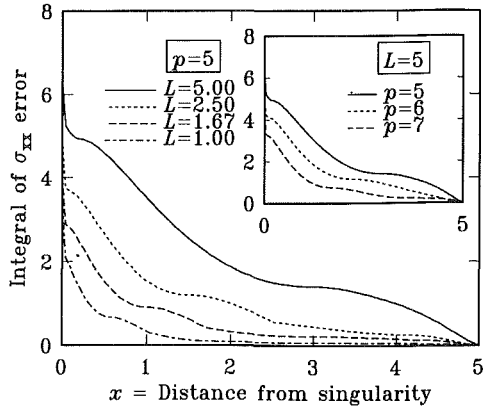

Fig. 2 Integral of stress error versus position for the *L*-plate problem. Results for various uniform meshes and different polynomial orders. We plot the integral of the absolute value of the error on the σ_{xx} stress component as a function of the distance from the singularity, measured along the edge highlighted in Fig. 1. The limits of integration are such that the integral is zero at the point furthest from the singularity. The various curves refer to some of the uniform meshes used (as sketched in Fig. 1) at different polynomial orders. *L* is the element size of each mesh, some of which are sketched in Fig. 1. Main figure: results for different meshes at polynomial order $p=5$. Inset: results for the minimal mesh, with three elements, at various polynomial orders *p*.

estimated when the element size and the polynomial order of the approximation are known.

Results and Discussion

We will not describe here the *p*-type finite element code used in the present calculations (Carnevali, Morris, and Tsuji, 1990). This code can perform static and dynamic analysis for three-dimensional elasticity problems. The code supports various types of elements, but hexahedral (brick) elements have been used for the calculations presented here. For such brick elements the code uses the hierarchical basis functions (Szabo and Peano, 1987), based on integrals of Legendre polynomials.

In a series of calculations we considered the problem, shown in Fig. 1, of a three-dimensional *L*-plate constrained at one end and with a load applied at the other end. This causes a stress singularity along the entire reentrant edge. Displacement and stress fields have been calculated for a variety of different meshes, including uniform and quasi-uniform meshes, and various types of graded meshes. An "overkill" highly refined (in all three-directions) and graded mesh has been used to produce a reliable solution which is very well converged except in a negligibly small neighborhood of the singularity. This converged solution has been used as a reference to calculate stress errors for the solutions obtained with the remaining meshes.

In Fig. 2 we plot the integral of the absolute value of the error on the σ_{xx} stress component as a function of the distance from the singularity, measured along the edge highlighted in Fig. 1. The limits of integration are such that the integral is zero at the point furthest from the singularity. The various curves refer to some of the uniform meshes used (as sketched in Fig. 1) at different polynomial orders. It is clear from the figure that, as expected, the largest stress errors are always localized in a neighborhood of the singularity. In fact, the polynomial basis functions used cannot model the singular behavior, but they try to do their best; this tends to result in an oscillating behavior. This situation is reminiscent of Gibbs phenomena for Fourier series, where a series mimics the singular function it is supposed to reproduce, but it can do so at the price of oscillations in the neighborhood of the singularity. In the case of Fourier series, one can easily characterize this behavior in the terms of the minimum wavelength λ used in the series: The behavior of the series will be inaccurate and oscillatory in a region of size $l \sim \lambda$ (the exact relation between l and λ depends on the details of how l is defined, i.e., on how much error one is willing to accept in an area of size l).

In finite element calculations the situation is more complex than in the case of a one-dimensional Fourier series; the two situations are, however, entirely similar qualitatively and, to a certain extent, quantitatively. We find that the size of the neighborhood where the error is localized, l, depends on the mesh used and on the polynomial order. It is possible to extract l from the stress error distributions $e(x)$, (Fig. 2). For example, we can define l such that

$$\int_0^l dx\,|e(x)| = \alpha.$$

In other words we accept a "total error" α within distance l of the singularity.

In order to test the hypothesis that the behavior here is analogous to that of the Fourier series, we need to check if the "size of the singularity," l obtained in this way, correlates with the minimum wavelength λ of the basis functions used. The latter quantity, unfortunately, is not well defined for polynomial basis functions. However, a typical basis function of polynomial order p (in particular, the basis functions used here) has p zeros over the size L of the element where it is defined. Consequently, we can define an effective wavelength satisfying $\lambda/2 = L/p$ or $\lambda = 2L/p$.

In this way we have calculated, for each mesh used and for each different polynomial order, the "size of the singularity" l and the effective minimum wavelength $\lambda = 2L/p$, where L is a local element size around the singularity. The resulting scatter plot (Fig. 3) shows that l and λ are well correlated, and, on the average, one can estimate $l \sim c\lambda$, where the constant c is in this case about 1.3. We expect that this number would in general depend on various factors, including the strength of the singularity, the details of the geometry, and the precise definition of l.

A similar procedure has been used in the case of the static analysis of a cantilevered beam. In this analysis we have studied the problem of a beam with an aspect ratio of 1:1:20 constrained to zero displacement at one end and subject to a bending load at the opposite end. The bending stress has a singularity at the point where the beam is constrained. The bending stress has been calculated using different meshes and

Downloaded 03 May 2010 to 171.66.16.248. Redistribution subject to ASME license or copyright; see http://www.asme.org/terms/Terms_Use.cfm

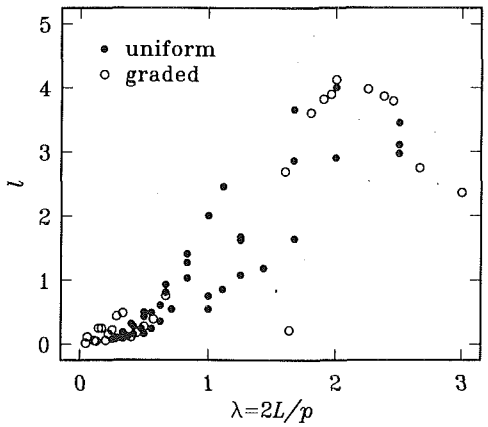

Fig. 3 Size of the singularity versus effective minimum wavelength for the *L*-plate problem. The size of the singularity in the *L*-plate problem, *l*, is plotted versus the effective minimum wavelength, $\lambda = 2L/p$, for a variety of uniform and graded meshes and different polynomial orders. *L* is the local element size around the singularity, *p* is the polynomial order used. The size of the singularity, *l*, has been defined as explained in the text.

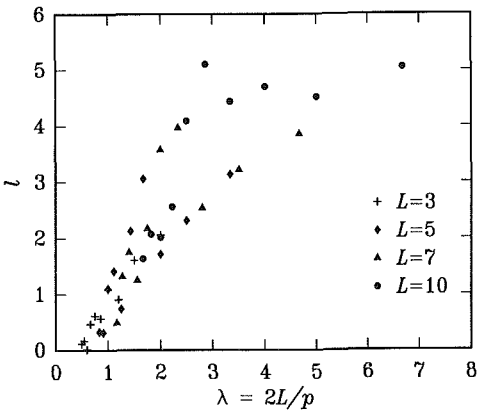

Fig. 4 Size of the singularity versus effective minimum wavelength for the beam problem. The size of the singularity in the beam problem, *l*, is plotted versus the effective minimum wavelength, λ, for a variety of different meshes and polynomial orders.

polynomial orders. The resulting correlation between λ and *l* shown in Fig. 4, is still good and in this case $c \sim 1$. This value of *c* is different from that of the *L*-plate case due to the combination of different geometry, singularity strength, and the value of α chosen in defining *l*.

The two examples described here are only a small subset of a large number of cases where we have observed the same behavior. The errors are found to be localized in a neighborhood of the singularity of size comparable to the minimum wavelength of the basis functions used: In other words, in all other cases tried, a similarly good correlation between *l* and λ was observed. Thus we are confident that this behavior has some generality, if not from a strict mathematical point of view at least from a practical perspective. This permits an important heuristic for the use of *p*-type finite element codes in the presence of singularities; i.e., the solution is essentially correct outside an area, around the singularity, of size *l*. Furthermore, the size *l* of this area can be estimated given the element size and polynomial order used. Such a rule of thumb usefully complements the error and convergence rate estimates available from functional analysis studies and, in many practical cases, can greatly simplify the meshing process by eliminating the requirement for optimal meshes. This is especially significant because ease of meshing is one of the key practical advantages of the *p*-type finite element method.

References

Babuska, I., 1986, "Feedback, Adaptivity, and a posteriori Estimates in Finite Elements: Aims, Theory, and Experience," *Accuracy estimates and adaptive refinements in finite element computations,* I. Babuska, O. C. Zienkiewicz, J. Cago, and E. R. de A. Oliveira, eds., John Wiley and Sons, New York, p. 3.

Babuska, I. and Rosenweig, M. A., 1972, A Finite Element Scheme for Domains with Corners," *Numer. Math,* Vol. 20, p.1.

Babuska, I., and Suri, M., 1987, "The Optimal Convergence Rate of the p-Version of the Finite Element Method," *SIAM J. Num. Anal.,* Vol. 24, p. 4.

Babsuka, I., Szabo, B. A., and Katz, I. N., 1981, "The p-Version of the Finite Element Method," *SIAM J. Num. Anal.,* Vol. 18, p. 515.

Blum, H., and Rannacher, R., 1988, "Extrapolation Techniques for Reducing the Pollution Effect of Reentrant Corners in the Finite Element Method," *Numer. Math.,* Vol. 52, p. 539.

Carnevali, P., Morris, R. B., and Tsuji, Y., 1990, manuscript in preparation.

Dorr, M. R., 1984, "The Approximation Theory for the p-Version of the Finite Element Method," *SIAM J. Num. Anal.,* Vol. 21, p. 1180.

Gui, W., and Babuska, I., 1986, "The h, p, and h-p versions of the Finite Element Method in One Dimension, Part 1: The Error Analysis of the p-Version; Part 2: The Error Analysis of the h and h-p Versions: Part 3: The Adaptive h-p Version," *Numer. Math.,* Vol. 49, pp. 577, 613, 659.

Johnson, A. R., 1981, "On the Accuracy of Polynomial Finite Elements for Crack Problems," *Int. J. Num. Meth. Engng,* Vol. 17, p. 1835.

Schatz, A. H., and Wahlbin, L. B., 1978, "Maximum Norm Estimates in the Finite Element Method on Plane Polygonal Domains, Part 1," *Math. Comp.,* Vol. 32, p. 73.

Schatz, A. H., and Wahlbin, L. B., 1979, "Maximum Norm Estimates in the Finite Element Method on Plane Polygonal Domains, Part 2, Refinements," *Math. Comp.* Vol. 33, p. 465.

Stakgold, I., 1979, *Green's Functions and Boundary Value Problems,* John Wiley and Sons, New York.

Szabo, B. A., 1986, "Estimation and Control of Error Bases on p-Convergence," *Accuracy estimates and adaptive refinements in finite element computations,* I. Babuska, O. C. Zienkiewicz, J. Cago, and E. R. de A. Oliveira, eds., John Wiley and Sons, New York, p. 25.

Szabo, B. A., and Peano, A. G., 1987, "Hierarchic Finite Elements," *Finite Element Handbook,* H. Kardestuncer, ed., McGraw-Hill, New York.

Tong, P., and Pian, T. H. H., 1973, "On the Convergence of the Finite Element Method for Problems with Singularity," *Int. J. Solid Structures,* Vol. 9, p. 313.

Zienkiewicz, O. C., and Craig, A., 1986, "Adaptive Refinement, Error Estimates, Multigrid Solution, and Hierarchic Finite Element Method Concepts," *Accuracy Estimates and Adaptive Refinements in Finite Element Computations,* I. Babuska, O. C. Zienkiewicz, J. Cago, and E. R. de A. Oliveira, eds., John Wiley and Sons, New York, p. 25.

An Integral Formulation for Dynamic Poroelasticity

José Dominguez[8]

A boundary integral equation formulation for dynamic poroelasticity in the frequency domain is presented. The formulation is accomplished using the solid displacements and the fluid stress as independent variables. The integral representation of the fluid stress is obtained using a fundamental solution corresponding to a combination of body forces applied in the solid and in the fluid.

Introduction

To the author's knowledge, the integral equation formulation of the dynamic poroelastic problem has not been successfully obtained in a way that permits an easy discretization and implementation in a numerical code. In a recent paper, Manolis and Beskos (1989) presented an integral formulation in the Laplace transformed domain. Their formulation is ex-

[8]Professor, Escuela Tecnica Superior de Ingenieros Industriales, Universidad de Sevilla, 41012-Sevilla, Spain.

Manuscript received by the ASME Applied Mechanics Division, Jan. 18, 1990; final revision, Apr. 24, 1990.

Downloaded 03 May 2010 to 171.66.16.248. Redistribution subject to ASME license or copyright; see http://www.asme.org/terms/Terms_Use.cfm

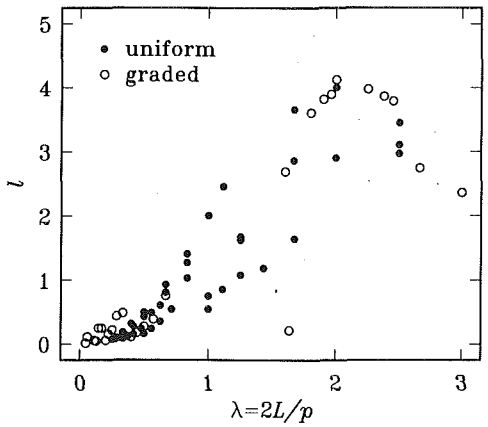

Fig. 3 Size of the singularity versus effective minimum wavelength for the *L*-plate problem. The size of the singularity in the *L*-plate problem, *l*, is plotted versus the effective minimum wavelength, $\lambda = 2L/p$, for a variety of uniform and graded meshes and different polynomial orders. *L* is the local element size around the singularity, *p* is the polynomial order used. The size of the singularity, *l*, has been defined as explained in the text.

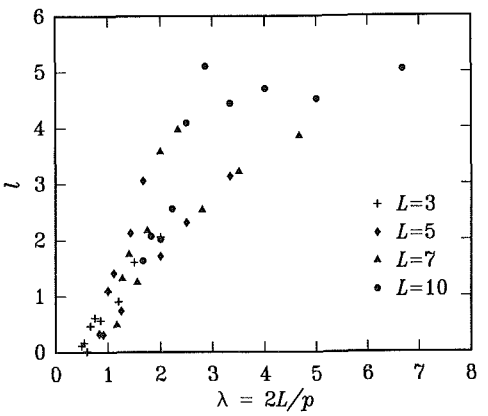

Fig. 4 Size of the singularity versus effective minimum wavelength for the beam problem. The size of the singularity in the beam problem, *l*, is plotted versus the effective minimum wavelength, λ, for a variety of different meshes and polynomial orders.

polynomial orders. The resulting correlation between λ and *l* shown in Fig. 4, is still good and in this case $c \sim 1$. This value of *c* is different from that of the *L*-plate case due to the combination of different geometry, singularity strength, and the value of α chosen in defining *l*.

The two examples described here are only a small subset of a large number of cases where we have observed the same behavior. The errors are found to be localized in a neighborhood of the singularity of size comparable to the minimum wavelength of the basis functions used: In other words, in all other cases tried, a similarly good correlation between *l* and λ was observed. Thus we are confident that this behavior has some generality, if not from a strict mathematical point of view at least from a practical perspective. This permits an important heuristic for the use of *p*-type finite element codes in the presence of singularities; i.e., the solution is essentially correct outside an area, around the singularity, of size *l*. Furthermore, the size *l* of this area can be estimated given the element size and polynomial order used. Such a rule of thumb usefully complements the error and convergence rate estimates available from functional analysis studies and, in many practical cases, can greatly simplify the meshing process by eliminating the requirement for optimal meshes. This is especially significant because ease of meshing is one of the key practical advantages of the *p*-type finite element method.

References

Babuska, I., 1986, "Feedback, Adaptivity, and a posteriori Estimates in Finite Elements: Aims, Theory, and Experience," *Accuracy estimates and adaptive refinements in finite element computations,* I. Babuska, O. C. Zienkiewicz, J. Cago, and E. R. de A. Oliveira, eds., John Wiley and Sons, New York, p. 3.

Babuska, I. and Rosenweig, M. A., 1972, A Finite Element Scheme for Domains with Corners," *Numer. Math,* Vol. 20, p.1.

Babuska, I., and Suri, M., 1987, "The Optimal Convergence Rate of the p-Version of the Finite Element Method," *SIAM J. Num. Anal.,* Vol. 24, p. 4.

Babsuka, I., Szabo, B. A., and Katz, I. N., 1981, "The p-Version of the Finite Element Method," *SIAM J. Num. Anal.,* Vol. 18, p. 515.

Blum, H., and Rannacher, R., 1988, "Extrapolation Techniques for Reducing the Pollution Effect of Reentrant Corners in the Finite Element Method," *Numer. Math.,* Vol. 52, p. 539.

Carnevali, P., Morris, R. B., and Tsuji, Y., 1990, manuscript in preparation.

Dorr, M. R., 1984, "The Approximation Theory for the p-Version of the Finite Element Method," *SIAM J. Num. Anal.,* Vol. 21, p. 1180.

Gui, W., and Babuska, I., 1986, "The h, p, and h-p versions of the Finite Element Method in One Dimension, Part 1: The Error Analysis of the p-Version; Part 2: The Error Analysis of the h and h-p Versions: Part 3: The Adaptive h-p Version," *Numer. Math.,* Vol. 49, pp. 577, 613, 659.

Johnson, A. R., 1981, "On the Accuracy of Polynomial Finite Elements for Crack Problems," *Int. J. Num. Meth. Engng,* Vol. 17, p. 1835.

Schatz, A. H., and Wahlbin, L. B., 1978, "Maximum Norm Estimates in the Finite Element Method on Plane Polygonal Domains, Part 1," *Math. Comp.,* Vol. 32, p. 73.

Schatz, A. H., and Wahlbin, L. B., 1979, "Maximum Norm Estimates in the Finite Element Method on Plane Polygonal Domains, Part 2, Refinements," *Math. Comp.* Vol. 33, p. 465.

Stakgold, I., 1979, *Green's Functions and Boundary Value Problems,* John Wiley and Sons, New York.

Szabo, B. A., 1986, "Estimation and Control of Error Bases on p-Convergence," *Accuracy estimates and adaptive refinements in finite element computations,* I. Babuska, O. C. Zienkiewicz, J. Cago, and E. R. de A. Oliveira, eds., John Wiley and Sons, New York, p. 25.

Szabo, B. A., and Peano, A. G., 1987, "Hierarchic Finite Elements," *Finite Element Handbook,* H. Kardestuncer, ed., McGraw-Hill, New York.

Tong, P., and Pian, T. H. H., 1973, "On the Convergence of the Finite Element Method for Problems with Singularity," *Int. J. Solid Structures,* Vol. 9, p. 313.

Zienkiewicz, O. C., and Craig, A., 1986, "Adaptive Refinement, Error Estimates, Multigrid Solution, and Hierarchic Finite Element Method Concepts," *Accuracy Estimates and Adaptive Refinements in Finite Element Computations,* I. Babuska, O. C. Zienkiewicz, J. Cago, and E. R. de A. Oliveira, eds., John Wiley and Sons, New York, p. 25.

An Integral Formulation for Dynamic Poroelasticity

José Dominguez[8]

A boundary integral equation formulation for dynamic poroelasticity in the frequency domain is presented. The formulation is accomplished using the solid displacements and the fluid stress as independent variables. The integral representation of the fluid stress is obtained using a fundamental solution corresponding to a combination of body forces applied in the solid and in the fluid.

Introduction

To the author's knowledge, the integral equation formulation of the dynamic poroelastic problem has not been successfully obtained in a way that permits an easy discretization and implementation in a numerical code. In a recent paper, Manolis and Beskos (1989) presented an integral formulation in the Laplace transformed domain. Their formulation is ex-

[8]Professor, Escuela Tecnica Superior de Ingenieros Industriales, Universidad de Sevilla, 41012-Sevilla, Spain.

Manuscript received by the ASME Applied Mechanics Division, Jan. 18, 1990; final revision, Apr. 24, 1990.

Copyright © 1991 by ASME
Downloaded 03 May 2010 to 171.66.16.248. Redistribution subject to ASME license or copyright; see http://www.asme.org/terms/Terms_Use.cfm

pressed in terms of solid and fluid displacements, i.e., six or four unknowns for three or two-dimensional problems, respectively. It can be shown (Bonnet, 1987) that in the poroelastic problem only the solid displacements and one additional variable, the fluid pressure, are independent since the fluid displacement is irrotational. Formulations in terms of six independent variables that use fundamental solutions with six independent sources are not adequate.

Cheng and Liggett (1984) presented the quasi-static poroelastic integral equation formulation in terms of the independent variables, i.e., solid displacement and fluid stress. The present paper gives an integral equation formulation of the dynamic poroelastic problem in the frequency domain in terms of solid displacements and fluid stress.

The fundamental solution can be obtained with the help of the analogy between poroelasticity and thermoelasticity, which is well known for the quasi-static case, and can be extended to dynamics as shown by Bonnet (1987). This analogy allowed Bonnet (1987) to present Kupradze et al. (1979) fundamental solution for three-dimensional time-harmonic thermoelastic problems as the fundamental solution for the poroelastic problem. Following the same approach as Kupradze et al., Bonnet obtained a fundamental solution for two dimensions. It should be mentioned, however, that in Bonnet's paper there is some inconsistency regarding the sign of the time variation assumed for the harmonic variables which differs in the poroelastic equations from that of the thermoelastic ones. Consequently, some errors exist in the equivalence of variables between poroelasticity and thermoelasticity.

Governing Equations

The governing equations for linear dynamic poroelasticity as given by Biot (1956) can be written as follows for a harmonic motion with a time-dependence exp $(-i\omega t)$

$$\mu\Delta u_i+\left(\lambda+\mu+\frac{Q^2}{R}\right)e_{,i}+Q\epsilon_{,i}+X_i=-\omega^2(\rho_{11}u_i+\rho_{12}U_i)-i\omega b(u_i-U_i) \quad (1a)$$

$$(Qe+R\epsilon)_{,i}+X'_i=-\omega^2(\rho_{12}u_i+\rho_{22}U_i)+i\omega b(u_i-U_i) \quad (1b)$$

where u_i and U_i are the solid and fluid displacements, respectively, b is a dissipation constant, ρ_{11}, ρ_{12}, and ρ_{22} are mass densities, and finally, X_i and X'_i are body forces acting in the solid and the fluid, respectively.

The constitutive equations are:

$$\tau_{ij}=\left(\lambda+\frac{Q^2}{R}\right)\delta_{ij}\,e+2\,\mu\,e_{ij}+Q\,\delta_{ij}\,\epsilon \quad (2a)$$

$$\tau=Q\,e+R\,\epsilon \quad (2b)$$

where τ_{ij} are the stresses in the solid, τ is the stress in the fluid related to the porosity β and the fluid pressure p according to $\tau=-\beta p$, δ_{ij} is the Kronecker delta function, $e_{ij}=0.5\,(u_{i,j}+u_{j,i})$ are the solid strains, $\epsilon=U_{i,i}$ and $e=u_{i,i}$ are the fluid and solid dilation, respectively; and λ, μ, Q, and R are elastic constants.

Pressure-Displacements relations. The six displacements in equations (1) are not independent and can be written in terms of only four variables, namely the solid displacements u_i and the fluid stress τ.

Using equations (1*b*) and (2*b*), the displacements in the fluid are written as

$$U_i=\frac{-\tau_{,i}-X'_i+(i\omega b-\omega^2\rho_{12})u_i}{i\omega b+\omega^2\rho_{22}}. \quad (3)$$

By substituting equations (2*b*) and (3) in equation (1*a*) the following is obtained:

$$\mu\Delta u_i+(\lambda+\mu)e_{,i}+\tau_{,i}\left(\frac{Q}{R}+\frac{i\omega b-\rho_{12}\omega^2}{i\omega b+\omega^2\rho_{22}}\right)+u_i\omega^2\left(\frac{\omega^2(\rho_{11}\rho_{22}-\rho_{12}^2)+i\omega b(\rho_{11}+\rho_{22}+2\rho_{12})}{i\omega b+\omega^2\rho_{22}}\right)+X_i+\frac{i\omega b-\rho_{12}\omega^2}{i\omega b+\omega^2\rho_{22}}X'_i=0. \quad (4)$$

Equation (4) only depends on the three components of the solid displacement and on the fluid stress. This equation can be written for $i=1,2$, and 3.

The fourth equation, which completes the system, is obtained by taking divergence of equation (1*b*) and substituting equation (2*b*).

$$\Delta\tau+\frac{\tau}{R}(i\omega b+\omega^2\rho_{22})+e\left[-i\omega b\left(1+\frac{Q}{R}\right)+\omega^2\left(\rho_{12}-\rho_{22}\frac{Q}{R}\right)\right]+X'_{i,i}=0 \quad (5)$$

Reciprocal Relations

Biot (1956) gives equilibrium equations for time harmonic behavior as follows:

$$\tau_{ij,j}+X_i=-\omega^2(\rho_{11}u_i+\rho_{12}U_i)-i\omega b(u_i-U_i) \quad (6a)$$

$$\tau_{,i}+X'_i=-\omega^2(\rho_{12}u_i+\rho_{22}U_i)+i\omega b(u_i-U_i). \quad (6b)$$

Weighting equation (6*a*) with u_i^* and (6*b*) with U_i^*, where u_i^* and U_i^* are displacement-type functions, adding the two equations, integrating over the body Ω, and using integration by parts twice yields the following reciprocal relation:

$$\int_\Gamma(t_iu_i^*+\tau U_n^*)d\Gamma+\int_\Omega(X_iu_i^*+X'_iU_i^*)d\Omega=\int_\Gamma(t_i^*u_i+\tau^*U_n)d\Gamma+\int_\Omega(X_i^*u_i+X'^*_iU_i)d\Omega \quad (7)$$

where Γ is the boundary of the body Ω, $t_i=\sigma_{ij}\,n_j$ and $U_n=U_i\,n_i$; n being the unit normal to the boundary. The variables denoted by superscript * are those associated with the weighting displacement fields.

Boundary Integral Representation

In order to obtain an integral representation for the solid displacements u_i, the quantities with superscript * in equation (7) will be replaced by the fundamental solution of the governing equations (4) and (5). This solution is derived by using the following body forces.

$$X_i^*=\delta(\mathbf{x})\delta_{ij}$$
$$X'^*_i=0 \quad (8)$$

in which $\delta(\mathbf{x})$ is the Dirac delta function and $\mathbf{x}$ indicates the point of application of the delta function.

The reciprocal relation gives:

$$c_{ij}u_i+\int_\Gamma t_{ij}^*u_i\,d\Gamma+\int_\Gamma\tau_j^*U_n\,d\Gamma=\int_\Gamma u_{ij}^*t_i\,d\Gamma+\int_\Gamma\tau U_{nj}^*\,d\Gamma+\int_\Omega(X_iu_{ij}^*+X'_iU_{ij}^*)d\Omega. \quad (9)$$

Equations (8) and (9) contain three (two for plane problems) individual substitutions, i.e., $j=1$, 2, and 3. The j subindex in equation (9) is used to indicate the jth set of the fundamental solution. The coefficient c_{ij} has a value δ_{ij} for points inside Ω and zero outside Ω. The value of c_{ij} for points on the boundary Γ is determined from the Cauchy's principal value of the integrals.

Downloaded 03 May 2010 to 171.66.16.248. Redistribution subject to ASME license or copyright; see http://www.asme.org/terms/Terms_Use.cfm

In order to obtain the integral representation of the fluid stress, the fundamental solution corresponding to the following body forces is used:

$$X'^{*}_{i} = \left(\frac{1}{2\pi}\ln r\right)_{,i} \qquad \text{for 2-}D$$

$$X'^{*}_{i} = \left(\frac{-1}{4\pi r}\right)_{,i} \qquad \text{for 3-}D \tag{10}$$

$$X^{*}_{i} = -\frac{i\omega b-\omega^2\rho_{12}}{i\omega b+\omega^2\rho_{22}}X'^{*}_{i}$$

where r is the distance to the point $\mathbf{x}$ at which the fluid stress is going to be represented. Notice that in this case forces in all directions exist in the two phases, simultaneously. Using these body forces and equation (3), the last integral in equation (7) may be written as follows:

$$\int_{\Omega}(X^{*}_{i}u_{i}+X'^{*}_{i}U_{i})d\Omega = -\int_{\Omega}X'^{*}_{i}\frac{\tau_{,i}+X'_{i}}{i\omega b+\omega^2\rho_{22}}d\Omega =$$

$$-\int_{\Gamma}X'^{*}_{i}\frac{\tau n_i}{i\omega b+\omega^2\rho_{22}}d\Gamma+\int_{\Omega}X'^{*}_{i,i}\frac{\tau}{i\omega b+\omega^2\rho_{22}}d\Omega$$

$$-\int_{\Omega}\frac{X'^{*}_{i}X'_{i}}{i\omega b+\omega^2\rho_{22}}d\Omega \tag{11}$$

and taking into account that $X'^{*}_{i,i}=\delta(\mathbf{x})$,

$$\int_{\Omega}(X^{*}_{i}u_{i}+X'^{*}_{i}U_{i})d\Omega = \frac{c\tau}{i\omega b+\omega^2\rho_{22}}$$

$$-\int_{\Gamma}\tau\frac{X'^{*}_{i}n_i}{i\omega b+\omega^2\rho_{22}}d\Gamma-\int_{\Omega}\frac{X'^{*}_{i}X'_{i}}{i\omega b+\omega^2\rho_{22}}d\Omega \tag{12}$$

where $c=1$ for points inside Ω and $c=0$ for points outside Ω. The value of c for points on the boundary Γ is computed from the Cauchy's principal value of the integrals.

The integral representation for the fluid stress is obtained by substitution of equation (12) in equation (7)

$$\frac{c\tau}{i\omega b+\omega^2\rho_{22}}+\int_{\Gamma}(t^{*}_{i0}u_i+\tau^{*}_{0}U_n)d\Gamma$$

$$=\int_{\Gamma}\left[t_i u^{*}_{i0}+\tau\left(U^{*}_{n0}+\frac{X'^{*}_{i}n_i}{i\omega b+\omega^2\rho_{22}}\right)\right]d\Gamma$$

$$+\int_{\Omega}\left[X_i u^{*}_{i0}+X'_{i}\left(U^{*}_{i0}+\frac{X'^{*}_{i}}{i\omega b+\omega^2\rho_{22}}\right)\right]d\Omega \tag{13}$$

where the 0 subindex is used instead of j to indicate the fundamental solution due to the second type of body forces.

It is worth noticing that the body forces used to obtain the fluid stress integral representation correspond to a point source of pressure, as can be seen from equation (5), and body forces X_i^{*} applied to the solid phase in such a way that the direct action of the fluid body forces transmitted to the solid by inertia and viscosity effects is counterpoise.

Equations (9) and (13) are the boundary integral equations for time-harmonic poroelasticity. The volume integrals included in those equations involve only body forces and fundamental solution values, which are given. If the collocation point is moved to the boundary, the integral equations can be written in terms of the boundary unknowns. An appropriate discretization of the boundary variables (Boundary Element Method) permits the solution of any well-posed dynamic poroelastic problem in terms of boundary unknowns only.

Thermoelastic Analogy and Fundamental Solutions

The governing equations for the thermoelastic oscillations

Table 1 Equivalence between thermoelasticity and poroelasticity for time-harmonic range

Thermoelasticity	Poroelasticity
u_i	u_i
ϑ	τ
μ	μ
λ	λ
γ	$-\frac{Q}{R}-\frac{i\omega b-\omega^2\rho_{12}}{i\omega b+\omega^2\rho_{22}}$
ρ	$\frac{\omega^2(\rho_{11}\rho_{22}-\rho_{12}^2)+i\omega b(\rho_{11}+\rho_{22}+2\rho_{12})}{i\omega b+\omega^2\rho_{22}}$
K	$\frac{R}{b-i\omega\rho_{22}}$
η	$-b\left(1+\frac{Q}{R}\right)-i\omega\left(\rho_{12}-\rho_{22}\frac{Q}{R}\right)$
F_i	$X_i+\frac{i\omega b-\omega^2\rho_{12}}{i\omega b+\omega^2\rho_{22}}X'_i$
$\frac{S}{K}$	$X'_{i,i}$

can be written, in accordance with Kupradze et al. (1979), as follows:

$$\mu\Delta u_i+(\lambda+\mu)e_{,i}-\gamma\vartheta_{,i}+\rho\omega^2u_i+F_i=0$$

$$\Delta\vartheta+\frac{i\omega}{K}\vartheta+i\omega\eta e+\frac{S}{K}=0 \tag{14}$$

where $\gamma=(2\mu+3\lambda)\alpha$, α is the coefficient of thermal expansion, $\eta=\gamma T/\kappa$, T is the absolute temperature, κ the heat conduction coefficient, $K=\kappa/\delta$ and δ is the specific heat. Finally, F_i and S are body forces and a heat source, respectively.

The examination of equations (4), (5), and (14) shows an analogy between time-harmonic thermoelasticity and poroelasticity. The equivalence between the variables is defined in Table 1. This equivalence differs from that given by Bonnet (1987). Apparently, a time variation of the type $\exp(i\omega t)$ is assumed in that paper in order to obtain the poroelasticity relations which are compared with thermoelasticity equations that were derived for a time variation of the type $\exp(-i\omega t)$.

The integral equations (9) and (13) have been obtained from the poroelasticity equations (4) and (5) by using two sets of fundamental solutions corresponding to the body forces given by equations (8) and (10), respectively. The fundamental solutions are analogous to those of the thermoelasticity equations (14) obtained for $F_i=\delta(\mathbf{x})\,\delta_{ij}$, $S/K=0$ and for $F_i=0$, $S/K=\delta(\mathbf{x})$.

The fundamental solution for three-dimensional frequency domain thermoelasticity is given by Kupradze et al. (1979). Bonnet (1987) followed a similar procedure to obtain his two-dimensional fundamental solution. This fundamental solution can be used for the present formulation after the Hankel function of second kind and zero order is substituted by the Hankel function of first kind and zero order which corresponds to the assumed time variation $\exp(-i\omega t)$.

Conclusion

In the preceeding sections a boundary integral equation formulation for dynamic poroelasticity in the frequency domain has been presented. Integral representations are obtained for the solid displacements and the fluid stress, which are the only independent variables. The fundamental solution resulting from a particular combination of solid and fluid body forces has given rise to the fluid stress integral representation.

Downloaded 03 May 2010 to 171.66.16.248. Redistribution subject to ASME license or copyright; see http://www.asme.org/terms/Terms_Use.cfm

References

Biot, M. A., 1956, "Theory of Propagation of Elastic Waves in a Fluid-Saturated Porous Solid," *J. Acoust. Soc. Am.*, Vol. 28, pp. 168–178.

Bonnet, G., 1987, "Basic Singular Solutions for a Poroelastic Medium in the Dynamic Range," *J. Acoust. Soc. Am.*, Vol. 82, pp. 1758–1762.

Cheng, A. H. D., and Liggett, J. A., 1984, "Boundary Integral Equation Method for Linear Porous Elasticity with Applications to Soil Consolidation," *Int. J. Numer. Meth. Engng.*, Vol. 20, pp. 255–278.

Kupradze, V. D., Gegelia, T. G., Basheleishvili, M. O., and Burchuladze, T. V., 1979, *Three-Dimensional Problems of the Mathematical Theory of Elasticity and Thermoelasticity*, North-Holland, Amsterdam, The Netherlands.

Manolis, G. D., and Beskos, D. E., 1989, "Integral Formulation and Fundamental Solutions of Dynamic Poroelasticity and Thermoelasticity," *Acta Mech.*, Vol. 76, pp. 89–104.

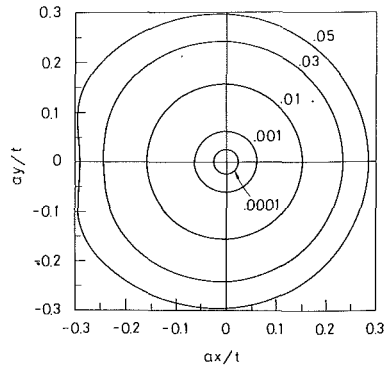

Fig. 1 Theoretical prediction of the initial curves from the dynamic transient stress field

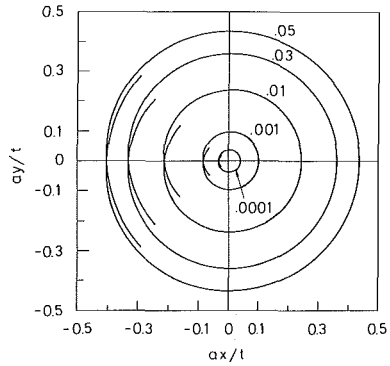

Fig. 2 Caustic curves from reflected light rays of the respective initial curves in Fig. 1

Analysis of the Caustic Method for the Transient Stress Field of Stationary Cracks

Chien-Ching Ma[9]

1 Introduction

In deriving the formula for the method of caustic, several assumptions are made: (a) the specimen is in a plane-stress state; (b) the deformation slope is small; (c) small-scale yielding prevails; (d) the measurements are made within the region of the dominant singular field. These assumptions have been made in most of the subsequent applications of caustics. These restrictions have only recently been investigated and the findings have resulted in the improvement of the validity and accuracy of this method (Rosakis and Ravi-Chandar, 1986; Rosakis and Freund, 1981; Rosakis and Zehnder, 1985).

By analogy with quasi-static fracture, the singular field is expected to dominate the crack-tip stress field at least in the immediate vicinity of the crack tip. The extent of this region of K dominance, however, is not well established particularly under transient conditions. The dynamic stress intensity factor is determined by caustic method from measurements covering a finite region around the crack tip. One must be assured that the K-field does indeed dominate within this region to get good results. In this paper, the validity of the stress singular field is investigated so that measurements of the stress intensity factor using the caustic method are made in the appropriate region with acceptable accuracy. The error in the experimental measurement of the caustics to evaluate the stress intensity factor by assuming that the singular field dominance is investigated. The experimental results of Ravi-Chandar and Knauss (1984) are also discussed in light of this theoretical analysis.

2 Caustic and Initial Curves Due to the Exact Transient Field

The instantaneous value of the dynamic stress intensity factor can be expressed as a function of the maximum transverse diameter $D_{\max}$ of the caustic curve as

$$K(t)=\frac{E}{10.708 z_0 d\nu}\,(D_{\max})^{5/2}. \tag{1}$$

where ν is the Poisson's ratio, E is the elastic modulus, d is the thickness and z_0 is the screen distance.

The dynamic stress intensity factor of a stationary crack subjected to uniform step loading σ_0 on crack faces is

$$K(t)=2\sqrt{\frac{2}{\pi}}\sigma_0\omega_0 t^{1/2}\ , \tag{2}$$

and

$$\omega_0=\frac{\sqrt{a}}{cS_+(0)}=\frac{\sqrt{2a(b^2-a^2)}}{b^2},$$

$$S_+(0)=\exp\left(-\frac{1}{\pi}\int_a^b \tan^{-1}\left[\frac{4y^2(y^2-a^2)^{1/2}(b^2-y^2)^{1/2}}{(b^2-2y^2)^2}\right]\frac{dy}{y}\right),$$

$$a=\sqrt{\frac{\rho}{\gamma+2\mu}}=\frac{1}{v_l},\quad b=\sqrt{\frac{\rho}{\mu}}=\frac{1}{v_s},$$

where μ and ρ are the shear modulus and the mass density of the material, γ is the Lamé elastic constant, a and b are the slowness of longitudinal and shear waves, respectively, and $c=1/v_R$ is the slowness of Rayleigh wave.

The validity of the caustic scheme which can be used with acceptable accuracy is discussed by using the exact transient field of uniform impulse leading σ_0 in crack faces. The shapes of the initial curves and caustic curves in the transient field are determined numerically and are shown in Figs. 1 and 2. The values of parameter $\alpha(=\sigma_0 d\nu\omega_0 z_0 t^{1/2}/E)$ equal to 0.0001, 0.001, 0.01, 0.03, and 0.05 were chosen for the numerical calculation. For small values of α, the initial curve is close to the crack-tip region so that the deformation can be described by the singular field. The initial curves derived from the singular field should be circles with radii $r_i=[3\sigma_0\omega_0 z_0 d\nu t^{1/2}/\pi E]^{2/5}$. As α becomes larger, the initial curve is distorted and is no longer circular. It is shown that, if the radius of the initial curve is about 0.1 ($\alpha\simeq 0.01$) of the longitudinal wavefront ($ar/t=1$), the initial curves are nearly circular.

The analysis of caustics is based on the assumption that the

[9]Professor, Department of Mechanical Engineering, National Taiwan University, Taipai 10764, Taiwan.

Manuscript received by the ASME Applied Mechanics Division, Oct. 4, 1988; final revision, Apr. 3, 1990.

Downloaded 03 May 2010 to 171.66.16.248. Redistribution subject to ASME license or copyright; see http://www.asme.org/terms/Terms_Use.cfm

References

Biot, M. A., 1956, "Theory of Propagation of Elastic Waves in a Fluid-Saturated Porous Solid," *J. Acoust. Soc. Am.*, Vol. 28, pp. 168–178.

Bonnet, G., 1987, "Basic Singular Solutions for a Poroelastic Medium in the Dynamic Range," *J. Acoust. Soc. Am.*, Vol. 82, pp. 1758–1762.

Cheng, A. H. D., and Liggett, J. A., 1984, "Boundary Integral Equation Method for Linear Porous Elasticity with Applications to Soil Consolidation," *Int. J. Numer. Meth. Engng.*, Vol. 20, pp. 255–278.

Kupradze, V. D., Gegelia, T. G., Basheleishvili, M. O., and Burchuladze, T. V., 1979, *Three-Dimensional Problems of the Mathematical Theory of Elasticity and Thermoelasticity*, North-Holland, Amsterdam, The Netherlands.

Manolis, G. D., and Beskos, D. E., 1989, "Integral Formulation and Fundamental Solutions of Dynamic Poroelasticity and Thermoelasticity," *Acta Mech.*, Vol. 76, pp. 89–104.

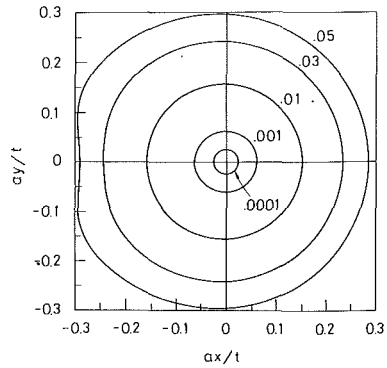

Fig. 1 Theoretical prediction of the initial curves from the dynamic transient stress field

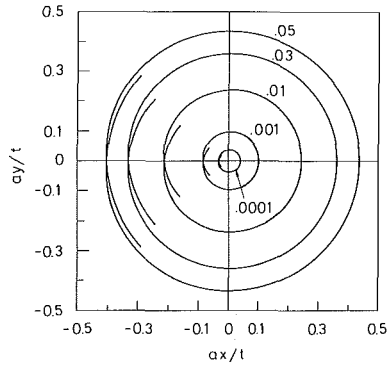

Fig. 2 Caustic curves from reflected light rays of the respective initial curves in Fig. 1

Analysis of the Caustic Method for the Transient Stress Field of Stationary Cracks

Chien-Ching Ma[9]

1 Introduction

In deriving the formula for the method of caustic, several assumptions are made: (a) the specimen is in a plane-stress state; (b) the deformation slope is small; (c) small-scale yielding prevails; (d) the measurements are made within the region of the dominant singular field. These assumptions have been made in most of the subsequent applications of caustics. These restrictions have only recently been investigated and the findings have resulted in the improvement of the validity and accuracy of this method (Rosakis and Ravi-Chandar, 1986; Rosakis and Freund, 1981; Rosakis and Zehnder, 1985).

By analogy with quasi-static fracture, the singular field is expected to dominate the crack-tip stress field at least in the immediate vicinity of the crack tip. The extent of this region of K dominance, however, is not well established particularly under transient conditions. The dynamic stress intensity factor is determined by caustic method from measurements covering a finite region around the crack tip. One must be assured that the K-field does indeed dominate within this region to get good results. In this paper, the validity of the stress singular field is investigated so that measurements of the stress intensity factor using the caustic method are made in the appropriate region with acceptable accuracy. The error in the experimental measurement of the caustics to evaluate the stress intensity factor by assuming that the singular field dominance is investigated. The experimental results of Ravi-Chandar and Knauss (1984) are also discussed in light of this theoretical analysis.

2 Caustic and Initial Curves Due to the Exact Transient Field

The instantaneous value of the dynamic stress intensity factor can be expressed as a function of the maximum transverse diameter $D_{\max}$ of the caustic curve as

$$K(t)=\frac{E}{10.708 z_0 d\nu}\,(D_{\max})^{5/2}. \tag{1}$$

where ν is the Poisson's ratio, E is the elastic modulus, d is the thickness and z_0 is the screen distance.

The dynamic stress intensity factor of a stationary crack subjected to uniform step loading σ_0 on crack faces is

$$K(t)=2\sqrt{\frac{2}{\pi}}\sigma_0\omega_0 t^{1/2}\ , \tag{2}$$

and

$$\omega_0=\frac{\sqrt{a}}{cS_+(0)}=\frac{\sqrt{2a(b^2-a^2)}}{b^2},$$

$$S_+(0)=\exp\left(-\frac{1}{\pi}\int_a^b \tan^{-1}\left[\frac{4y^2(y^2-a^2)^{1/2}(b^2-y^2)^{1/2}}{(b^2-2y^2)^2}\right]\frac{dy}{y}\right),$$

$$a=\sqrt{\frac{\rho}{\gamma+2\mu}}=\frac{1}{v_l},\quad b=\sqrt{\frac{\rho}{\mu}}=\frac{1}{v_s},$$

where μ and ρ are the shear modulus and the mass density of the material, γ is the Lamé elastic constant, a and b are the slowness of longitudinal and shear waves, respectively, and $c=1/v_R$ is the slowness of Rayleigh wave.

The validity of the caustic scheme which can be used with acceptable accuracy is discussed by using the exact transient field of uniform impulse leading σ_0 in crack faces. The shapes of the initial curves and caustic curves in the transient field are determined numerically and are shown in Figs. 1 and 2. The values of parameter $\alpha(=\sigma_0 d\nu\omega_0 z_0 t^{1/2}/E)$ equal to 0.0001, 0.001, 0.01, 0.03, and 0.05 were chosen for the numerical calculation. For small values of α, the initial curve is close to the crack-tip region so that the deformation can be described by the singular field. The initial curves derived from the singular field should be circles with radii $r_i=[3\sigma_0\omega_0 z_0 d\nu t^{1/2}/\pi E]^{2/5}$. As α becomes larger, the initial curve is distorted and is no longer circular. It is shown that, if the radius of the initial curve is about 0.1 ($\alpha\simeq 0.01$) of the longitudinal wavefront ($ar/t=1$), the initial curves are nearly circular.

The analysis of caustics is based on the assumption that the

[9]Professor, Department of Mechanical Engineering, National Taiwan University, Taipai 10764, Taiwan.

Manuscript received by the ASME Applied Mechanics Division, Oct. 4, 1988; final revision, Apr. 3, 1990.

Copyright © 1991 by ASME
Downloaded 03 May 2010 to 171.66.16.248. Redistribution subject to ASME license or copyright; see http://www.asme.org/terms/Terms_Use.cfm

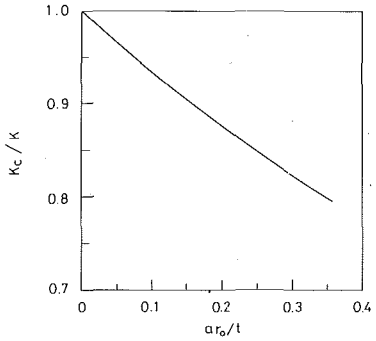

Fig. 3 Error in evaluation of the stress intensity factor by the method of caustics

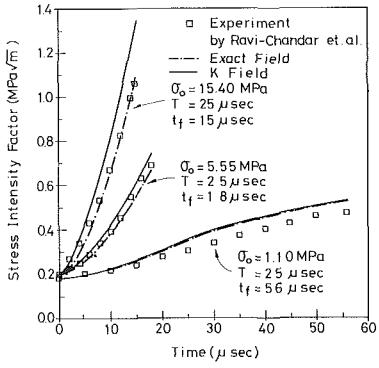

Fig. 4 The stress intensity factor history (solid lines) of the stationary crack from the loading observed in the experiments by Ravi-Chandar and Knauss (1984). Also shown is the stress intensity factor history inferred form the experimental results (data points) and the theoretical predictions (dash-dot lines) by means of the method of caustics.

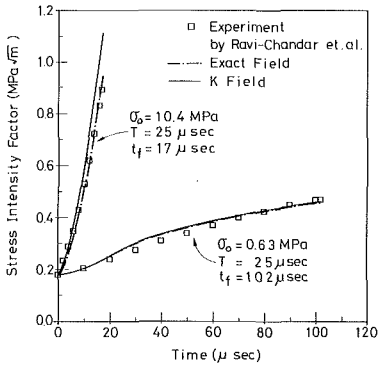

Fig. 5 Same as Fig. 4, but for data shown

stress singular field dominates in the region near the crack tip. Thus, it is important to estimate the resulting errors in evaluating the stress intensity factor by the caustic method under this assumption. A numerical simulation of the experimental observation is made by using the exact transient field for caustic mapping. By measuring the maximum transverse diameter of the caustic curve, the stress intensity factor K_c that would be calculated in an experiment on the basis of the observed caustic curve was evaluated through equation (1).

The theoretical value of the stress intensity factor K due to the uniform loading is given in (2). The ratio of the stress intensity factor K_c calculated from the caustic and K from the theoretical value is plotted as a function of the dimensionless parameter ar_0/t in Fig. 3. The initial curve radius r_0 is defined as the distance from the crack tip to the point of initial curve in $x-$axis. The deviation of K_c/K form unity indicates the error from using the singular field instead of the transient field to evaluate the stress intensity factors. Figure 3 shows that this error will be less than seven percent if the initial curve is within ten percent of the longitudinal wavefront.

3 Comparison With Experimental Results

In the work reported by Ravi-Chandar and Knauss (1984), a long edge crack was cut into a large rectangular sheet of Homalite-100 along a symmetrical line. The dimensions of the specimen were such that the waves generated by the loading device would not be reflected back onto the crack tip for about 150 μsec after application of the pressure. Therefore, for all practical purposes, the situation is that of semi-infinite crack in an unbounded body subjected to spatially uniform pressure over the crack faces during the early part of the experiment. For the material of Homalite-100 as reported by Ravi-Chandar and Knauss (1984), only one caustic is observed in experiment, and thus it can be considered as a non-birefringent material. In this case, the formula for the reflected and transmission caustics are similar and are different only by a constant.

The theoretical analysis by Ma and Freund (1986) of the exact stress intensity factor for the experiment from the measured fracture time t_f, pressure magnitude σ_0, crack propagation speed v and preload, was compared to the results reported by Ravi-Chandar and Knauss (1984). In all cases, the agreement between the theoretical and experimental results was found to be quite good for $t<t_f$ (the time for crack growth), with the general feature that the experimental data always fell below the theoretical prediction before the crack growth. With the available results discussed in the previous section, we are able to analyze in more detail for the time before crack propagation.

Up to this point in the theoretical analysis, it has been assumed that the time dependence of the loading pressure is a simple step in time. All of the results, however, can be generalized to the case of arbitrary stress profiles $g(t)$. Suppose that at time $t=0$, the crack pressure is applied, and that the magnitude of the pressure increases linearly. After some finite rise time T, the magnitude of the applied pressure reaches its maximum value σ_0 so that $g(T) = \sigma_0$. The magnitude of the pressure is held constant for $t>T$. The dynamic stress intensity factor of the stationary crack for $T<t_f$ is given by

$$K(t)=\frac{4\sqrt{2}\sigma_0\omega_0}{3\sqrt{\pi}T}[t^{3/2}-(t-T)^{3/2}H(t-T)],\ 0<t<t_f. \quad (3)$$

When $t_f<T$, we have

$$K(t)=\frac{4\sqrt{2}\sigma_0\omega_0}{3\sqrt{\pi}T}t^{3/2},\ 0<t<t_f. \quad (4)$$

The size of the initial curve depends on the reference distance z_0 and also on the stress intensity factor. If the stress intensity factor were constant, the initial curve could be adjusted by changing the distance z_0. However, if the stress intensity factor varies as in a dynamic experiment, one does not have close control over the radius of the initial curve, aside from limiting its variation through a judicious choice of the screen distance z_0. One of the screen distances z_0 used by Ravi-Chandar and Knauss (1984), 168 cm, is adopted for numerical simulation.

We have compared experimental measurements obtained by using shadow spots with analytical results in Figs. 4 and 5. The analytically predicted variation of the stress intensity factor is presented by the solid and dash-dot lines. The solid lines are the theoretical prediction for the stress intensity factor history as presented in equations (3) and (4). The dash-dot lines were calculated by numerical simulation for the experimental observation of the caustic method by using the exact transient solutions. The transmission caustic formula is used for the numerical simulation in order to be consistent with the experimental measurement. Within the error of experimental measurement, the agreement between the theoretical prediction by using the transient solutions (dash-dot line) and the exper-

Downloaded 03 May 2010 to 171.66.16.248. Redistribution subject to ASME license or copyright; see http://www.asme.org/terms/Terms_Use.cfm

imental determination of the stress intensity factor is seen to be good. The dash-dot lines are always below the solid lines and more close to the experimental results. The results indicate that the method of caustic used in the experiment might underestimate the true stress intensity factor as the K-field is not developed at the measurement points. For the low magnitude of applied load, the dash-dot lines are very close to the solid line, which means that the initial curve for these cases are within the K-field and the difference from the theoretical value (solid-lines) is very small. For the high magnitude of loading, the situation is quite different, the initial curve is relatively large, the material points of initial curve are far away from the K-field, and hence the large difference from the theoretical prediction for the stress intensity factor is expected.

Another factor that might influence the accuracy of the method of caustic is that the theoretical results are within the framework of linear elastodynamics, while there must always be a zone of nonlinear and inelastic material response near the crack tip. One is not able to make meaningful measurements at very small distances from the crack tip where the stress field is significantly altered by the process zone for the determination of the dynamic stress intensity factor. Hence, the stress singular field possibly exists near the crack tip as an annular zone. The size of the process zone increases with increasing loading, resulting in a decrease of the annular region of the singular field. For higher load levels, this process zone may extend outward from the crack tip for a greater distance on the order of the initial curve size, in which case the assumption of linear elasticity would no longer be valid.

Acknowledgment

The research support of the National Science Council, Republic of China through Grant NSC78-0401-E002-28 at National Taiwan University is gratefully acknowledged.

References

Ma, C.-C., and Freund, L. B., 1986, "The Extent of the Stress Intensity Factor Field During Crack Growth under Dynamic Loading Conditions," ASME JOURNAL OF APPLIED MECHANICS, Vol. 53, pp. 303–310.

Ravi-Chandar, K., and Knauss, W. G., 1984, "An Experimental Investigation into the Mechanics of Dynamic Fracture: I. Crack Initiation and Arrest," *International Journal of Fracture*, Vol. 25, pp. 247–262; "II. Microstructural Branching," Vol. 26, pp. 141–154; "IV. On the Interaction of Stress Waves with Propagating Cracks," Vol. 26, pp. 189–200.

Rosakis, A. J., and Freund, L. B., 1981, "The Effect of Crack Tip Plasticity on the Determination of Dynamic Stress Intensity Factors by the Optical Method of Caustics," ASME JOURNAL OF APPLIED MECHANICS, Vol. 48, pp. 302–308.

Rosakis, A. J., and Zehnder, A. T., 1985, "On the Method of Caustics: An Exact Analysis Based on Geometrical Optics," *Journal of Elasticity*, Vol. 15, pp. 347–367.

Rosakis, A. J., and Ravi-Chandar, K., 1986, "On Crack-Tip Stress State: An Experimental Evaluation of Three-Dimensional Effects," *Int. J. Solids Structures*, Vol. 22, pp. 121-134.

An Alternative Approach to the Symmetrical Top and Slender Member Analysis[10]

Nels Madsen[11]

This Note considers the problem of a symmetrical top under the action of gravity, or analogously the problem of a long, slender, initially straight linearly elastic, circular cross-section member loaded only at its ends. A nonbody fixed coordinate system is used. The standard results are obtained without any explicit reference to a space-fixed coordinate system.

Introduction

The conventional analysis of a symmetrical top under the action of gravity uses a coordinate system fixed in the top (Scarborough, 1958). The standard analysis of a long, slender, initially straight, linearly elastic, circular cross-section member loaded only at its ends also uses a body-fixed coordinate system and leads to the same equations (Love, 1944). The typical approach to the resulting equations involves the use of Euler angles to relate the body fixed coordinate system to a system fixed in space. These angles and their derivatives can be expressed in terms of elliptic functions. The objective of this note is to show that these elliptic expressions for the top angular velocity, or equivalently, the curvature of the slender member, can be developed without the introduction of Euler angles by using a nonbody fixed coordinate system. This coordinate system is commonly used in the description of space curves (Willmore, 1959), but is less familiar in the dynamics arena. The conventional approach to the problem of the symmetrical top uses a body-fixed axis system with one axis parallel to the body axis of symmetry. The analogous coordinate system for the slender member has one axis tangent to the member centerline and the other two axes fixed in the member cross-section. The approach discussed here will use what are known as path or natural coordinates. Relative to the slender member problem this system shares the tangent axis with the conventional approach but the cross-sectional axes are not body fixed. The cross-sectional axes are in the directions of the local normal and binormal associated with the member center line. The corresponding axes in the symmetrical top problem are the top axis of symmetry, an axis perpendicular to both the axis of symmetry and the instantaneous angular velocity vector, and the third axis necessary to complete the right-handed orthogonal triad. Using this coordinate system the top angular velocity, or equivalently, the centerline curvature, can be derived directly from the kinetic equations without the introduction of supplementary geometrical information. In particular the results can be obtained working solely in the local coordinate system without any explicit reference to the space-fixed coordinate system. While this alternative derivation is primarily of academic interest, it is possible that the alternative coordinate systems used have utility in other dynamics and slender member problems. The remainder of the Note provides the development for the symmetrical top problem. An analogous development for the slender member problem is possible with appropriate reidentifications of the variables. These revised identifications are introduced during the development.

Equation Development

The objective of the analysis of the symmetrical top is the determination of the time variation of the top angular velocity. In this case that angular velocity vector will be expressed relative to a rotating coordinate system so one must also determine the angular velocity of this rotating reference system. The angular velocity vector of a symmetrical top can be broken into two components, one parallel to the top axis of symmetry, and the other perpendicular to that axis. Equation (1) expresses this relationship where $\mathbf{k}$ represents the top axis of symmetry.

$$\omega = \omega_t \mathbf{k} + \omega_p \mathbf{j} \tag{1}$$

In slender member theory, $\mathbf{k}$ would represent the local tangent, $\mathbf{j}$ the local binormal, ω_p the centerline curvature, and ω_t the member twist per unit length. The orthogonal triad defined by equation (1) is not body fixed; however, a body-fixed system

[10]Work supported by SCI Systems, Inc., under SCI Contract No. 93155, dated Nov. 30, 1989.

[11]Associate Professor, Mechanical Engineering Department, Auburn University, Auburn University, AL 36849-3501.

Manuscript received by the ASME Applied Mechanics Division, Dec. 8, 1988; final revision, May 1, 1990.

Downloaded 03 May 2010 to 171.66.16.248. Redistribution subject to ASME license or copyright; see http://www.asme.org/terms/Terms_Use.cfm

imental determination of the stress intensity factor is seen to be good. The dash-dot lines are always below the solid lines and more close to the experimental results. The results indicate that the method of caustic used in the experiment might underestimate the true stress intensity factor as the K-field is not developed at the measurement points. For the low magnitude of applied load, the dash-dot lines are very close to the solid line, which means that the initial curve for these cases are within the K-field and the difference from the theoretical value (solid-lines) is very small. For the high magnitude of loading, the situation is quite different, the initial curve is relatively large, the material points of initial curve are far away from the K-field, and hence the large difference from the theoretical prediction for the stress intensity factor is expected.

Another factor that might influence the accuracy of the method of caustic is that the theoretical results are within the framework of linear elastodynamics, while there must always be a zone of nonlinear and inelastic material response near the crack tip. One is not able to make meaningful measurements at very small distances from the crack tip where the stress field is significantly altered by the process zone for the determination of the dynamic stress intensity factor. Hence, the stress singular field possibly exists near the crack tip as an annular zone. The size of the process zone increases with increasing loading, resulting in a decrease of the annular region of the singular field. For higher load levels, this process zone may extend outward from the crack tip for a greater distance on the order of the initial curve size, in which case the assumption of linear elasticity would no longer be valid.

Acknowledgment

The research support of the National Science Council, Republic of China through Grant NSC78-0401-E002-28 at National Taiwan University is gratefully acknowledged.

References

Ma, C.-C., and Freund, L. B., 1986, "The Extent of the Stress Intensity Factor Field During Crack Growth under Dynamic Loading Conditions," ASME JOURNAL OF APPLIED MECHANICS, Vol. 53, pp. 303–310.

Ravi-Chandar, K., and Knauss, W. G., 1984, "An Experimental Investigation into the Mechanics of Dynamic Fracture: I. Crack Initiation and Arrest," *International Journal of Fracture*, Vol. 25, pp. 247–262; "II. Microstructural Branching," Vol. 26, pp. 141–154; "IV. On the Interaction of Stress Waves with Propagating Cracks," Vol. 26, pp. 189–200.

Rosakis, A. J., and Freund, L. B., 1981, "The Effect of Crack Tip Plasticity on the Determination of Dynamic Stress Intensity Factors by the Optical Method of Caustics," ASME JOURNAL OF APPLIED MECHANICS, Vol. 48, pp. 302–308.

Rosakis, A. J., and Zehnder, A. T., 1985, "On the Method of Caustics: An Exact Analysis Based on Geometrical Optics," *Journal of Elasticity*, Vol. 15, pp. 347–367.

Rosakis, A. J., and Ravi-Chandar, K., 1986, "On Crack-Tip Stress State: An Experimental Evaluation of Three-Dimensional Effects," *Int. J. Solids Structures*, Vol. 22, pp. 121-134.

An Alternative Approach to the Symmetrical Top and Slender Member Analysis[10]

Nels Madsen[11]

This Note considers the problem of a symmetrical top under the action of gravity, or analogously the problem of a long, slender, initially straight linearly elastic, circular cross-section member loaded only at its ends. A nonbody fixed coordinate system is used. The standard results are obtained without any explicit reference to a space-fixed coordinate system.

Introduction

The conventional analysis of a symmetrical top under the action of gravity uses a coordinate system fixed in the top (Scarborough, 1958). The standard analysis of a long, slender, initially straight, linearly elastic, circular cross-section member loaded only at its ends also uses a body-fixed coordinate system and leads to the same equations (Love, 1944). The typical approach to the resulting equations involves the use of Euler angles to relate the body fixed coordinate system to a system fixed in space. These angles and their derivatives can be expressed in terms of elliptic functions. The objective of this note is to show that these elliptic expressions for the top angular velocity, or equivalently, the curvature of the slender member, can be developed without the introduction of Euler angles by using a nonbody fixed coordinate system. This coordinate system is commonly used in the description of space curves (Willmore, 1959), but is less familiar in the dynamics arena. The conventional approach to the problem of the symmetrical top uses a body-fixed axis system with one axis parallel to the body axis of symmetry. The analogous coordinate system for the slender member has one axis tangent to the member centerline and the other two axes fixed in the member cross-section. The approach discussed here will use what are known as path or natural coordinates. Relative to the slender member problem this system shares the tangent axis with the conventional approach but the cross-sectional axes are not body fixed. The cross-sectional axes are in the directions of the local normal and binormal associated with the member center line. The corresponding axes in the symmetrical top problem are the top axis of symmetry, an axis perpendicular to both the axis of symmetry and the instantaneous angular velocity vector, and the third axis necessary to complete the right-handed orthogonal triad. Using this coordinate system the top angular velocity, or equivalently, the centerline curvature, can be derived directly from the kinetic equations without the introduction of supplementary geometrical information. In particular the results can be obtained working solely in the local coordinate system without any explicit reference to the space-fixed coordinate system. While this alternative derivation is primarily of academic interest, it is possible that the alternative coordinate systems used have utility in other dynamics and slender member problems. The remainder of the Note provides the development for the symmetrical top problem. An analogous development for the slender member problem is possible with appropriate reidentifications of the variables. These revised identifications are introduced during the development.

Equation Development

The objective of the analysis of the symmetrical top is the determination of the time variation of the top angular velocity. In this case that angular velocity vector will be expressed relative to a rotating coordinate system so one must also determine the angular velocity of this rotating reference system. The angular velocity vector of a symmetrical top can be broken into two components, one parallel to the top axis of symmetry, and the other perpendicular to that axis. Equation (1) expresses this relationship where $\mathbf{k}$ represents the top axis of symmetry.

$$\omega = \omega_t \mathbf{k} + \omega_p \mathbf{j} \tag{1}$$

In slender member theory, $\mathbf{k}$ would represent the local tangent, $\mathbf{j}$ the local binormal, ω_p the centerline curvature, and ω_t the member twist per unit length. The orthogonal triad defined by equation (1) is not body fixed; however, a body-fixed system

[10]Work supported by SCI Systems, Inc., under SCI Contract No. 93155, dated Nov. 30, 1989.

[11]Associate Professor, Mechanical Engineering Department, Auburn University, Auburn University, AL 36849-3501.

Manuscript received by the ASME Applied Mechanics Division, Dec. 8, 1988; final revision, May 1, 1990.

Copyright © 1991 by ASME
Downloaded 03 May 2010 to 171.66.16.248. Redistribution subject to ASME license or copyright; see http://www.asme.org/terms/Terms_Use.cfm

can be obtained from this triad by a rotation about the **k**-axis. The angular velocity of this rotating reference system must thus differ from the body angular velocity only in its **k**-component. Equation (2) provides the angular velocity of the triad.

$$\boldsymbol{\Omega} = \Omega_t \mathbf{k} + \omega_p \mathbf{j} \tag{2}$$

In slender member theory, Ω_t would represent the path torsion of the member centerline. The problem has been reduced to the determination of the three angular velocity unknowns; ω_p, ω_t, and Ω_t. Three equations for these unknowns can be derived from the equality of the time rate of change of the angular momentum with the applied moment. The angular momentum of the top is expressed in equation (3) in terms of the angular velocity and the two distinct principal moments of inertia of the top about its fixed point.

$$H = I_1 \omega_t \mathbf{k} + I_2 \omega_p \mathbf{j} \tag{3}$$

In slender member theory, I_1 and I_2 would represent the torsional and bending stiffnesses, respectively. The time derivative of the angular momentum can be readily derived using equations (2) and (3). Equation (4) provides the result.

$$\frac{d\mathbf{H}}{dt} = I_2 \frac{d\omega_t}{dt} \mathbf{k} + I_2 \frac{d\omega_p}{dt} \mathbf{j} + \omega_p (I_1 \omega_t - I_2 \Omega_t)\mathbf{j} \tag{4}$$

In slender member theory, **j** would represent the local normal direction and the time derivative would be replaced by a derivative with respect to arc length. The net moment about the fixed point can be expressed in terms of a cross product of the vector from the fixed point to the mass center with the applied force vector (weight). The position vector is along the top axis of symmetry and will be assigned an arbitrary magnitude denoted l. Equations (5) and (6) express the required moment. Unfortunately, they necessitate the introduction of three new unknowns. These unknowns, T, V_x, and V_y, represent the components of the weight force along the rotating axes, **i**, **j**, and **k**. This requires three additional equations to eliminate these quantities. A second vector equation can be developed from the observation that the weight force is constant in time, thus its time derivative must vanish. Differentiating the force vector using the angular velocity of the rotating reference system yields equation (7).

$$\mathbf{M} = l \mathbf{k} \times (T \mathbf{k} + V_x \mathbf{i} + V_y j) \tag{5}$$

$$= -l V_y \mathbf{i} + l V_x \mathbf{j} \tag{6}$$

$$\left(\frac{dT}{dt} - \omega_p V_x\right) \mathbf{k} + \left(\frac{dV_x}{dt} + \omega_p T - \Omega_t V_y\right)\mathbf{j} + \left(\frac{dV_y}{dt} + \Omega_t V_x\right)\mathbf{j} = \mathbf{0} \tag{7}$$

In slender member theory, T represents the member tension, while V_x and V_y represent the local shear forces. Expressions for V_x and V_y in terms of the fundamental angular velocity unknowns can be easily extracted from the moment equation. These expressions can be used to eliminate V_x and V_y from equation (7). The third component of the moment equation reveals that ω_t must be a constant. Thus, we are left with equation (7) to determine the three unknowns ω_p, Ω_t, and T. The k-component of the modified equation (7) can be easily integrated to yield equation (8).

$$T - \frac{1}{2} I_2 \omega_p^2 / l = T_0 = \text{constant} \tag{8}$$

The **j** component of the modified equation (7) can also be readily integrated by multiplying through by ω_p. This integration yields equation (9) for Ω_t.

$$\Omega_t = \frac{I_1}{I_2} \frac{\omega_t}{2} - \frac{C}{\omega_p^2} \tag{9}$$

Using the results obtained for Ω_t and T and multiplying by $d\omega_p/dt$, the **i** component of equation (7) leads to equation (10).

$$\left(\frac{d\omega_p}{dt}\right)^2 = D - \left(\frac{T_0 l}{I_2} + \frac{I_1^2 \omega_t^2}{4 I_2^2}\right) \omega_p^2 - \frac{1}{4} \omega_p^4 - \frac{C_2}{\omega_p^2} \tag{10}$$

Equation (10) can be integrated to yield an expression for ω_p in terms of elliptic functions. Equations (11) to (13) provide the desired results. The standard expression for the varying portion of the angular velocity, or analogously the member curvature, has been obtained without the use of Euler angles relating coordinate systems to a fixed frame.

$$\omega_p^2 = g_2 + (g_1 - g_2)\, cn^2 \left(\frac{(g_1 - g_3)^{1/2}}{2} (t - t_0) \,\middle|\, \frac{g_1 - g_2}{g_1 - g_3} \right) \tag{11}$$

$$g_1 \geq g_2 \geq 0 \geq g_3 \text{ are real roots of equation (13)} \tag{12}$$

$$-4C^2 + 4Dg - \left(\frac{4T_0 l}{I_2} + \frac{I_1^2 \omega_t^2}{I_2^2}\right) g^2 - g^3 = 0. \tag{13}$$

At this point the time variation of the fundamental angular velocity unknowns, ω_p, Ω_t, and ω_t, as well as of the supplemental variables, T, V_x, and V_y, has been determined. The expressions developed involve various constants that can be evaluated from the initial conditions or as system characteristics.

Conclusions

An alternative development for the analysis of the symmetrical top under the action of gravity has been presented. With the use of Kirchoff's analogy the procedure is also applicable to the analysis of long, slender, intially straight linearly elastic, circular cross-section members loaded only at their ends. The alternative approach does not use body-fixed axes, rather it uses axes defined by the motion, or analogously the member shape. The alternative approach facilitates the integration of the equations of motion without the need for the explicit introduction of a space-fixed coordinate system. The modified approach may be of use in other dynamics and slender member problems.

References

Love, A. E. H., 1944, *A Treatise on the Mathematical Theory of Elasticity*, 4th ed., Dover Publications, New York, pp. 381–88, 399–400, 413.

Scarborough, James B., 1958, *The Gyroscope, Theory and Applications*, Interscience Publication, New York, pp. 65, 68–70.

Willmore, T. J., 1959, *An Introduction to Differential Geometry*, Clarendon Press, Oxford, U.K., pp. 1–26.

Response of Subsurface Rigid Strips to Plane Harmonic Shear Waves

R. L. Ryan[12] and S. Mall[13]

1 Introduction

In a recent study (Ryan and Mall, 1989) we analyzed the interaction of plane harmonic SV-waves with an array of rigid strips embedded in an infinite elastic medium or matrix. High

[12]Naval Research Laboratory, Department of the Navy, Washington, DC 20375-5000.

[13]Air Force Institute of Technology, Wright Patterson A.F.B., Dayton, OH 45433.

Manuscript received by the ASME Applied Mechanics Division, Mar. 20, 1989; final revision, June 8, 1990.

Downloaded 03 May 2010 to 171.66.16.248. Redistribution subject to ASME license or copyright; see http://www.asme.org/terms/Terms_Use.cfm

can be obtained from this triad by a rotation about the **k**-axis. The angular velocity of this rotating reference system must thus differ from the body angular velocity only in its **k**-component. Equation (2) provides the angular velocity of the triad.

$$\boldsymbol{\Omega} = \Omega_t \mathbf{k} + \omega_p \mathbf{j} \tag{2}$$

In slender member theory, Ω_t would represent the path torsion of the member centerline. The problem has been reduced to the determination of the three angular velocity unknowns; ω_p, ω_t, and Ω_t. Three equations for these unknowns can be derived from the equality of the time rate of change of the angular momentum with the applied moment. The angular momentum of the top is expressed in equation (3) in terms of the angular velocity and the two distinct principal moments of inertia of the top about its fixed point.

$$H = I_1 \omega_t \mathbf{k} + I_2 \omega_p \mathbf{j} \tag{3}$$

In slender member theory, I_1 and I_2 would represent the torsional and bending stiffnesses, respectively. The time derivative of the angular momentum can be readily derived using equations (2) and (3). Equation (4) provides the result.

$$\frac{d\mathbf{H}}{dt} = I_2 \frac{d\omega_t}{dt} \mathbf{k} + I_2 \frac{d\omega_p}{dt} \mathbf{j} + \omega_p (I_1 \omega_t - I_2 \Omega_t)\mathbf{j} \tag{4}$$

In slender member theory, **j** would represent the local normal direction and the time derivative would be replaced by a derivative with respect to arc length. The net moment about the fixed point can be expressed in terms of a cross product of the vector from the fixed point to the mass center with the applied force vector (weight). The position vector is along the top axis of symmetry and will be assigned an arbitrary magnitude denoted l. Equations (5) and (6) express the required moment. Unfortunately, they necessitate the introduction of three new unknowns. These unknowns, T, V_x, and V_y, represent the components of the weight force along the rotating axes, **i**, **j**, and **k**. This requires three additional equations to eliminate these quantities. A second vector equation can be developed from the observation that the weight force is constant in time, thus its time derivative must vanish. Differentiating the force vector using the angular velocity of the rotating reference system yields equation (7).

$$\mathbf{M} = l\mathbf{k} \times (T\mathbf{k} + V_x \mathbf{i} + V_y j) \tag{5}$$

$$= -lV_y \mathbf{i} + lV_x \mathbf{j} \tag{6}$$

$$\left(\frac{dT}{dt} - \omega_p V_x\right) \mathbf{k} + \left(\frac{dV_x}{dt} + \omega_p T - \Omega_t V_y\right)\mathbf{j} + \left(\frac{dV_y}{dt} + \Omega_t V_x\right)\mathbf{j} = \mathbf{0} \tag{7}$$

In slender member theory, T represents the member tension, while V_x and V_y represent the local shear forces. Expressions for V_x and V_y in terms of the fundamental angular velocity unknowns can be easily extracted from the moment equation. These expressions can be used to eliminate V_x and V_y from equation (7). The third component of the moment equation reveals that ω_t must be a constant. Thus, we are left with equation (7) to determine the three unknowns ω_p, Ω_t, and T. The k-component of the modified equation (7) can be easily integrated to yield equation (8).

$$T - \frac{1}{2} I_2 \omega_p^2 / l = T_0 = \text{constant} \tag{8}$$

The **j** component of the modified equation (7) can also be readily integrated by multiplying through by ω_p. This integration yields equation (9) for Ω_t.

$$\Omega_t = \frac{I_1}{I_2} \frac{\omega_t}{2} - \frac{C}{\omega_p^2} \tag{9}$$

Using the results obtained for Ω_t and T and multiplying by $d\omega_p/dt$, the **i** component of equation (7) leads to equation (10).

$$\left(\frac{d\omega_p}{dt}\right)^2 = D - \left(\frac{T_0 l}{I_2} + \frac{I_1^2 \omega_t^2}{4I_2^2}\right) \omega_p^2 - \frac{1}{4}\omega_p^4 - \frac{C_2}{\omega_p^2} \tag{10}$$

Equation (10) can be integrated to yield an expression for ω_p in terms of elliptic functions. Equations (11) to (13) provide the desired results. The standard expression for the varying portion of the angular velocity, or analogously the member curvature, has been obtained without the use of Euler angles relating coordinate systems to a fixed frame.

$$\omega_p^2 = g_2 + (g_1 - g_2)\, cn^2 \left(\frac{(g_1 - g_3)^{1/2}}{2} (t - t_0) \,\middle|\, \frac{g_1 - g_2}{g_1 - g_3} \right) \tag{11}$$

$$g_1 \geq g_2 \geq 0 \geq g_3 \text{ are real roots of equation (13)} \tag{12}$$

$$-4C^2 + 4Dg - \left(\frac{4T_0 l}{I_2} + \frac{I_1^2 \omega_t^2}{I_2^2}\right) g^2 - g^3 = 0. \tag{13}$$

At this point the time variation of the fundamental angular velocity unknowns, ω_p, Ω_t, and ω_t, as well as of the supplemental variables, T, V_x, and V_y, has been determined. The expressions developed involve various constants that can be evaluated from the initial conditions or as system characteristics.

Conclusions

An alternative development for the analysis of the symmetrical top under the action of gravity has been presented. With the use of Kirchoff's analogy the procedure is also applicable to the analysis of long, slender, intially straight linearly elastic, circular cross-section members loaded only at their ends. The alternative approach does not use body-fixed axes, rather it uses axes defined by the motion, or analogously the member shape. The alternative approach facilitates the integration of the equations of motion without the need for the explicit introduction of a space-fixed coordinate system. The modified approach may be of use in other dynamics and slender member problems.

References

Love, A. E. H., 1944, *A Treatise on the Mathematical Theory of Elasticity*, 4th ed., Dover Publications, New York, pp. 381–88, 399–400, 413.

Scarborough, James B., 1958, *The Gyroscope, Theory and Applications*, Interscience Publication, New York, pp. 65, 68–70.

Willmore, T. J., 1959, *An Introduction to Differential Geometry*, Clarendon Press, Oxford, U.K., pp. 1–26.

Response of Subsurface Rigid Strips to Plane Harmonic Shear Waves

R. L. Ryan[12] and S. Mall[13]

1 Introduction

In a recent study (Ryan and Mall, 1989) we analyzed the interaction of plane harmonic SV-waves with an array of rigid strips embedded in an infinite elastic medium or matrix. High

[12]Naval Research Laboratory, Department of the Navy, Washington, DC 20375-5000.

[13]Air Force Institute of Technology, Wright Patterson A.F.B., Dayton, OH 45433.

Manuscript received by the ASME Applied Mechanics Division, Mar. 20, 1989; final revision, June 8, 1990.

Copyright © 1991 by ASME
Downloaded 03 May 2010 to 171.66.16.248. Redistribution subject to ASME license or copyright; see http://www.asme.org/terms/Terms_Use.cfm

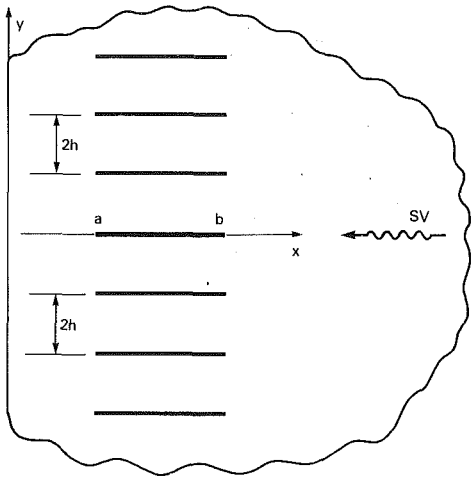

Fig. 1 Geometry of subsurface strips

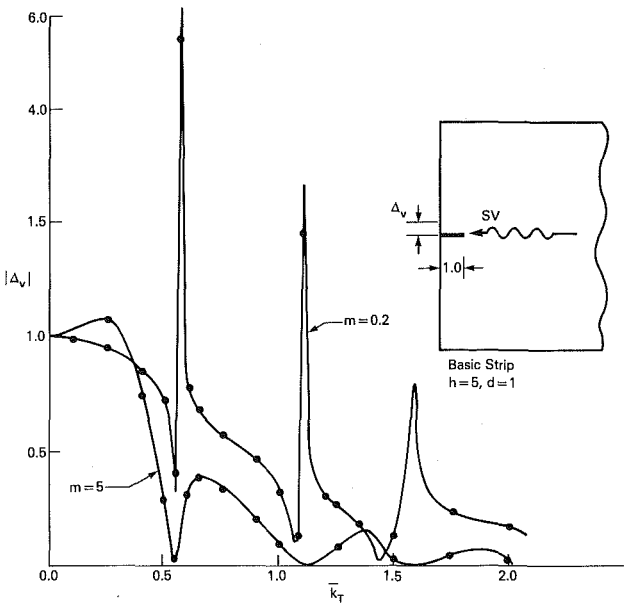

Fig. 2 Displacement $|\Delta_v|$ versus dimensionless wave number $\bar{k}_T$: d = 1, h = 5

amplifications in the strip response were found to occur at particular ("resonant") frequencies, and the effect of strip spacing-to-length ratios and strip-to-matrix mass ratios on these amplifications was examined. Compared to Ryan and Mall (1989), the present study contains an additional length parameter, namely, the subsurface depth of the strips. This parameter, of course, reflects the influence of the free surface on the strip response. The effect of this parameter was evaluated and found to be significant for the cases considered.

2 Formulation

The geometry of the subsurface array of rigid strips is shown in Fig. 1. It is assumed that the strips are bonded completely to the surrounding medium, and a state of plane strain persists. The elastic constants and mass density of the medium are denoted as (λ, μ) and ρ, respectively, and the mass per unit length of a strip is denoted as ρ^*. The array of strips is excited by a plane harmonic SV-wave of the form

$$u_i = 0,\ v_i = 2\cos k_T x\, e^{-i\omega t}, \tag{1}$$

where $k_T = \omega\sqrt{\rho/\mu}$ is the wave number of transverse waves. Henceforth, the time factor $e^{-i\omega t}$ is discarded.

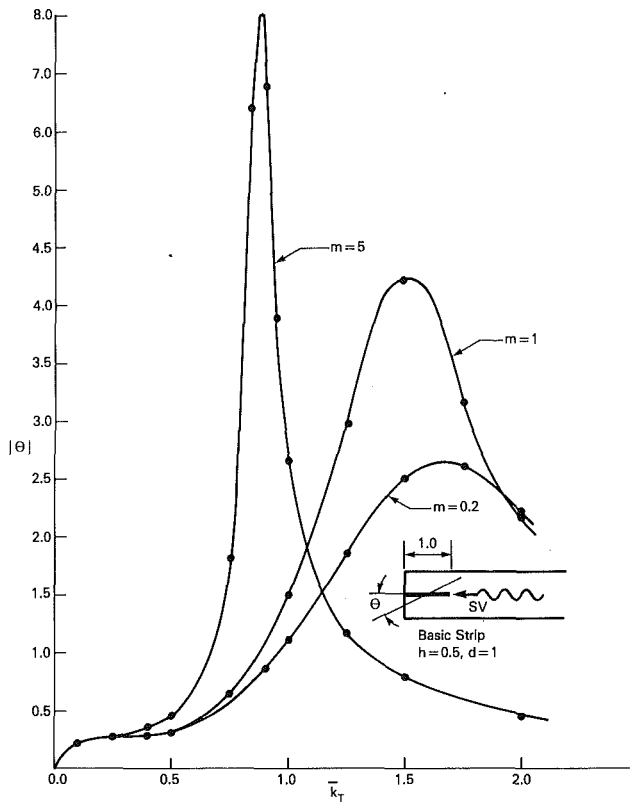

Fig. 3 Rotation $|\theta|$ versus dimensionless wave number $\bar{k}_T$: d = 1, h = 0.5

As shown in Ryan and Mall (1989), the response of the array of strips follows from the solution of an integral equation relating the vertical displacement $v(x, 0)$ and the jump in normal stress $[\sigma_y]$ across the rigid strip at $y = 0$. Taking account of the stress-free conditions on $x = 0$, the integral equation for the present case is found to be

$$4k_T^2 v(x) = \int_a^b [p(s)]\{K(|w|) + K(w') + S(s,x)\}ds,\ a<x<b, \tag{2}$$

in which $[p(s)] = \mu^{-1}[\sigma_y(s)]$, $w = s - x$, and $w' = s + x$. Aside from a factor π, kernel K is identical to that given in Ryan and Mall (1989). Kernel S, which represents the effect of the free surface, is given by

$$S(s,x) = 4/h \sum_1^\infty \delta_n^2 S_n(s) S_n(x)/\zeta_{nL} R_n, \tag{3}$$

in which $\delta_n = n\pi/h$, $k_L = k_T\sqrt{\mu/(\lambda+2\mu)}$,

$$\zeta_{nT,L} = \begin{cases} \sqrt{\delta_n^2 - k_{T,L}^2}, & \delta_n > k_{T,L} \\ -i\sqrt{k_{T,L}^2 - \delta_n^2}, & \delta_n < k_{T,L} \end{cases} \tag{4}$$

$$S_n(x) = (\delta_n^2 + \zeta_{nT}^2)e^{-\zeta_{nL}x} - 2\zeta_{nL}\zeta_{nT}e^{-\zeta_{nT}x}, \tag{5}$$

$$R_n = (\zeta_{nT}^2 + \delta_n^2)^2 - 4\zeta_{nL}\zeta_{nT}\delta_n^2. \tag{6}$$

As in Ryan and Mall (1989), the scattering of the incident wave (1) is treated as a superposition of diffracted and radiated waves. Accordingly, in the left side of equation (2) $v(x) = -2\cos k_T x$ for the diffraction case and $v(x) = \Delta_v + [x - (a + b)/2]\theta$ for the radiation case, where Δ_v and θ are the (unknown) translation and rotation, respectively, of the rigid strip on $y = 0$. Δ_v and θ are connected to the resultant force F and torque T acting on the strip, as follows:

Downloaded 03 May 2010 to 171.66.16.248. Redistribution subject to ASME license or copyright; see http://www.asme.org/terms/Terms_Use.cfm

$$F=\mu\int_a^b [p(s)]ds, \quad T=\mu\int_a^b s[p(s)]ds, \quad (7a, 7b)$$

$$\Delta_v=-F/2\mu\, m\, c\, k_T^2, \quad \theta=-3T/4\mu\, m\, c^2\, \bar{k}_T^2, \quad (8a, 8b)$$

where $m = \rho^*/\rho$, $\bar{k}_T = ck_T$, and $c = (b - a)/2$.

Results

Equation (2) was solved numerically by the Gauss-Chebyshev method, and the strip response was obtained by inserting the solution into equations (7*a*, *b*) and (8*a*, *b*). Figures (2) and (3) depict selected results for the case when the rigid strip just reaches the surface. This case was found to give the greatest peaks compared to fully submerged cases. The results correspond to a strip of unit length ($c = 0.5$) and Poisson's ratio $\nu = 0.25$ ($\lambda = \mu$). Moreover, the depth parameter d is defined as $d = (b + a)/(b - a)$. Thus, $d = 1$, $c = 0.5$ corresponds to $a = 0$, $b = 1$. A comparison with the corresponding results of Ryan and Mall (1989), Figs. 4, 6, 7, and 8, indicates the effect of the depth parameter. The results of Ryan and Mall (1989), of course, correspond to $d = \infty$. In particular, it is seen that the peak displacement and rotation are greater by about 22 percent and 43 percent, respectively, compared to those of Ryan and Mall (1989).

References

Ryan, R. L., and Mall, S., 1989, "Interaction of Shear Waves with a Periodic Array of Rigid Strips," *Int. J. Solids, Structs.*, Vol. 25, pp. 553–561.

Nonlinear Transient Analysis of Large Rotordynamic Systems

T. N. Shiau[14,16] and A. N. Jean[15,16]

A solution technique based on implicit numerical integration combined with a condensation technique is presented to predict the transient response of large flexible rotor systems with nonlinear characteristics. The analysis directly tackles the nonlinear second-order differential equations which describe the system motion. The condensation technique can lead to a reduced model in which only the coordinates associated with nonlinear components of the system are considered. Thus, a substantial reduction of computation can be expected if the nonlinear components of system are sparse. A flexible rotor system is studied to illustrate the merits of the procedures. The results show that, if the system is of a small number of coordinates associated with nonlinear components compared to that of entire system degrees-of-freedom, the computational time can be considerably reduced using this technique.

Introduction

Two most popular methods for the transient analysis of rotordynamic systems are the modal method (Adams, 1980; Nelson et al., 1981) and the direct numerical integration (Barrett and Gunter, 1975; Kascak, 1979; Nelson et al., 1983; Padovan, 1984; Rao and Sarma, 1986). The modal method can be further sorted into undamped and damped modal methods. The former approximates the system motion in terms of the undamped symmetric modes and treats the damping, gyroscopic, and nonlinear terms as pseudo-external forces. The later uses damped modes to decouple the system equations of motion.

The accuracy and the efficiency of various direct numerical integration schemes applied to rotordynamic systems have been discussed by the authors (Barrett and Gunter, 1975; Kascak, 1979; Padovan et al., 1984). Their conclusions are summarized as follows: (1) the suitability of the methods depends on the studied case, and (2) the accuracy and the efficiency of the methods are related to the system order.

Recently, the discrete time-transfer matrix method has been proposed by Kumar and Sankar (1986) for the transient analysis of large dynamic systems. Subbiah and Rieger (1988a) applied this method in conjunction with the lumped mass approach to the transient analysis of flexible rotor systems. Moreover, Subbiah et al. (1988b) utilized the finite element method for the analysis.

In the present study, the condensation technique used in the steady-state periodic response analysis (Shiau and Jean, 1989; Jean and Nelson, 1989) is employed to link implicit numerical integration schemes for the transient analysis of flexible mechanical systems with nonlinear characteristics. The analysis of rotordynamic systems is particularly emphasized. By this technique, the system degrees-of-freedom will be reduced to the number of the physical coordinates only associated with the nonlinear components of the system. A flexible rotor system modeled as 52 degrees-of-freedom with four of those directly coupled to the nonlinear components is used to demonstrate the accuracy and the efficiency of the present method.

Mathematical Development

Consider the system of N degrees-of-freedom and the equations of motion of the form

$$[M]\{\ddot{q}\}+[D]\{\dot{q}\}+[K]\{q\}=\{Q\}+\{F\} \quad (1)$$

where the $N\times N$ matrices $[M]$, $[D]$, and $[K]$ describe the system generalized mass, damping, and stiffness, respectively. The vector $\{q\}$ is associated with generalized coordinates and $\{Q\}$ is a specified time-dependent force vector. The $N \times 1$ vector $\{F\}$ is the nonlinear force vector related to the nonlinear components of the system and can be expressed as nonlinear function of the displacement, velocity, and acceleration at positions associated with nonlinear components. If $\{F\}$ is sparse, equation (1) can be rearranged into the partitioned form:

$$\begin{bmatrix}[M^{11}] & [M^{12}]\\ [M^{21}] & [M^{22}]\end{bmatrix}\begin{Bmatrix}\{\ddot{q}\}_1\\ \{\ddot{q}\}_2\end{Bmatrix}+\begin{bmatrix}[D^{11}] & [D^{12}]\\ [D^{21}] & [D^{22}]\end{bmatrix}\begin{Bmatrix}\{\dot{q}\}_1\\ \{\dot{q}\}_2\end{Bmatrix}$$
$$+\begin{bmatrix}[K^{11}] & [K^{12}]\\ [K^{21}] & [K^{22}]\end{bmatrix}\begin{Bmatrix}\{q\}_1\\ \{q\}_2\end{Bmatrix}=\begin{Bmatrix}\{Q\}_1\\ \{Q\}_2\end{Bmatrix}+\begin{Bmatrix}\{O\}\\ \{F\}_2\end{Bmatrix}. \quad (2)$$

The vector $\{q\}_2$ is referred to as those coordinates associated with the nonlinear components and $\{q\}_1$ is its complement. ($\{q\}_1$, $\{q\}_2$) are of orders (n_1, n_2) with $N=n_1+n_2$ and will be referred to as the "linear" and "nonlinear" coordinates, respectively, in this paper.

The numerical method used in this study assumes that the acceleration and velocity can be expressed as a linear function of the displacement. The expressions are given by

$$\{\ddot{q}(t_i)\}=A\{q(t_i)\}+\{B(t_i)\} \quad (3)$$

$$\{\dot{q}(t_i)\}=C\{q(t_i)\}+\{E(t_i)\} \quad (4)$$

where the quantities A, C, $\{B(t_i)\}$, and $\{E(t_i)\}$ can be determined using various numerical integration methods (Kumar and Sankar, 1986). Note that the coefficients A and C depend on the selected time step. In addition, $\{B(t_i)\}$ and $\{E(t_i)\}$ are functions of $\{\ddot{q}\}$, $\{\dot{q}\}$ and $\{q\}$ at previous time instant

[14]Professor, Mem. ASME.
[15]Graduate Student.
[16]Institute of Aeronautics and Astronautics, National Cheng-Kung University, Tainan, Taiwan 70101.

Manuscript received by the ASME Applied Mechanics Division, May 9, 1989; final revision, Feb. 27, 1990.

Downloaded 03 May 2010 to 171.66.16.248. Redistribution subject to ASME license or copyright; see http://www.asme.org/terms/Terms_Use.cfm

$$F=\mu\int_a^b [p(s)]ds, \quad T=\mu\int_a^b s[p(s)]ds, \quad (7a, 7b)$$

$$\Delta_v=-F/2\mu\, m\, c\, k_T^2, \quad \theta=-3T/4\mu\, m\, c^2\, \bar{k}_T^2, \quad (8a, 8b)$$

where $m = \rho^*/\rho$, $\bar{k}_T = ck_T$, and $c = (b - a)/2$.

Results

Equation (2) was solved numerically by the Gauss-Chebyshev method, and the strip response was obtained by inserting the solution into equations (7*a*, *b*) and (8*a*, *b*). Figures (2) and (3) depict selected results for the case when the rigid strip just reaches the surface. This case was found to give the greatest peaks compared to fully submerged cases. The results correspond to a strip of unit length ($c = 0.5$) and Poisson's ratio $\nu = 0.25$ ($\lambda = \mu$). Moreover, the depth parameter d is defined as $d = (b + a)/(b - a)$. Thus, $d = 1$, $c = 0.5$ corresponds to $a = 0$, $b = 1$. A comparison with the corresponding results of Ryan and Mall (1989), Figs. 4, 6, 7, and 8, indicates the effect of the depth parameter. The results of Ryan and Mall (1989), of course, correspond to $d = \infty$. In particular, it is seen that the peak displacement and rotation are greater by about 22 percent and 43 percent, respectively, compared to those of Ryan and Mall (1989).

References

Ryan, R. L., and Mall, S., 1989, "Interaction of Shear Waves with a Periodic Array of Rigid Strips," *Int. J. Solids, Structs.*, Vol. 25, pp. 553–561.

Nonlinear Transient Analysis of Large Rotordynamic Systems

T. N. Shiau[14,16] and A. N. Jean[15,16]

A solution technique based on implicit numerical integration combined with a condensation technique is presented to predict the transient response of large flexible rotor systems with nonlinear characteristics. The analysis directly tackles the nonlinear second-order differential equations which describe the system motion. The condensation technique can lead to a reduced model in which only the coordinates associated with nonlinear components of the system are considered. Thus, a substantial reduction of computation can be expected if the nonlinear components of system are sparse. A flexible rotor system is studied to illustrate the merits of the procedures. The results show that, if the system is of a small number of coordinates associated with nonlinear components compared to that of entire system degrees-of-freedom, the computational time can be considerably reduced using this technique.

Introduction

Two most popular methods for the transient analysis of rotordynamic systems are the modal method (Adams, 1980; Nelson et al., 1981) and the direct numerical integration (Barrett and Gunter, 1975; Kascak, 1979; Nelson et al., 1983; Padovan, 1984; Rao and Sarma, 1986). The modal method can be further sorted into undamped and damped modal methods. The former approximates the system motion in terms of the undamped symmetric modes and treats the damping, gyroscopic, and nonlinear terms as pseudo-external forces. The later uses damped modes to decouple the system equations of motion.

The accuracy and the efficiency of various direct numerical integration schemes applied to rotordynamic systems have been discussed by the authors (Barrett and Gunter, 1975; Kascak, 1979; Padovan et al., 1984). Their conclusions are summarized as follows: (1) the suitability of the methods depends on the studied case, and (2) the accuracy and the efficiency of the methods are related to the system order.

Recently, the discrete time-transfer matrix method has been proposed by Kumar and Sankar (1986) for the transient analysis of large dynamic systems. Subbiah and Rieger (1988a) applied this method in conjunction with the lumped mass approach to the transient analysis of flexible rotor systems. Moreover, Subbiah et al. (1988b) utilized the finite element method for the analysis.

In the present study, the condensation technique used in the steady-state periodic response analysis (Shiau and Jean, 1989; Jean and Nelson, 1989) is employed to link implicit numerical integration schemes for the transient analysis of flexible mechanical systems with nonlinear characteristics. The analysis of rotordynamic systems is particularly emphasized. By this technique, the system degrees-of-freedom will be reduced to the number of the physical coordinates only associated with the nonlinear components of the system. A flexible rotor system modeled as 52 degrees-of-freedom with four of those directly coupled to the nonlinear components is used to demonstrate the accuracy and the efficiency of the present method.

Mathematical Development

Consider the system of N degrees-of-freedom and the equations of motion of the form

$$[M]\{\ddot{q}\}+[D]\{\dot{q}\}+[K]\{q\}=\{Q\}+\{F\} \quad (1)$$

where the $N\times N$ matrices $[M]$, $[D]$, and $[K]$ describe the system generalized mass, damping, and stiffness, respectively. The vector $\{q\}$ is associated with generalized coordinates and $\{Q\}$ is a specified time-dependent force vector. The $N \times 1$ vector $\{F\}$ is the nonlinear force vector related to the nonlinear components of the system and can be expressed as nonlinear function of the displacement, velocity, and acceleration at positions associated with nonlinear components. If $\{F\}$ is sparse, equation (1) can be rearranged into the partitioned form:

$$\begin{bmatrix}[M^{11}] & [M^{12}]\\ [M^{21}] & [M^{22}]\end{bmatrix}\begin{Bmatrix}\{\ddot{q}\}_1\\ \{\ddot{q}\}_2\end{Bmatrix}+\begin{bmatrix}[D^{11}] & [D^{12}]\\ [D^{21}] & [D^{22}]\end{bmatrix}\begin{Bmatrix}\{\dot{q}\}_1\\ \{\dot{q}\}_2\end{Bmatrix}$$
$$+\begin{bmatrix}[K^{11}] & [K^{12}]\\ [K^{21}] & [K^{22}]\end{bmatrix}\begin{Bmatrix}\{q\}_1\\ \{q\}_2\end{Bmatrix}=\begin{Bmatrix}\{Q\}_1\\ \{Q\}_2\end{Bmatrix}+\begin{Bmatrix}\{O\}\\ \{F\}_2\end{Bmatrix}. \quad (2)$$

The vector $\{q\}_2$ is referred to as those coordinates associated with the nonlinear components and $\{q\}_1$ is its complement. ($\{q\}_1$, $\{q\}_2$) are of orders (n_1, n_2) with $N=n_1+n_2$ and will be referred to as the "linear" and "nonlinear" coordinates, respectively, in this paper.

The numerical method used in this study assumes that the acceleration and velocity can be expressed as a linear function of the displacement. The expressions are given by

$$\{\ddot{q}(t_i)\}=A\{q(t_i)\}+\{B(t_i)\} \quad (3)$$

$$\{\dot{q}(t_i)\}=C\{q(t_i)\}+\{E(t_i)\} \quad (4)$$

where the quantities A, C, $\{B(t_i)\}$, and $\{E(t_i)\}$ can be determined using various numerical integration methods (Kumar and Sankar, 1986). Note that the coefficients A and C depend on the selected time step. In addition, $\{B(t_i)\}$ and $\{E(t_i)\}$ are functions of $\{\ddot{q}\}$, $\{\dot{q}\}$ and $\{q\}$ at previous time instant

[14]Professor, Mem. ASME.
[15]Graduate Student.
[16]Institute of Aeronautics and Astronautics, National Cheng-Kung University, Tainan, Taiwan 70101.

Manuscript received by the ASME Applied Mechanics Division, May 9, 1989; final revision, Feb. 27, 1990.

Copyright © 1991 by ASME
Downloaded 03 May 2010 to 171.66.16.248. Redistribution subject to ASME license or copyright; see http://www.asme.org/terms/Terms_Use.cfm

t_{i-1}, which are known at time t_i for initial value problems. Therefore, the transient response of equation (1) or (2) can be solved by making use of equations (3) and (4).

First, consider the system equations of motion at any given time instant, t_i

$$[M]\ddot{q}(t_i)\} + [D]\{\dot{q}(t_i)\} = \{Q(t_i)\} + \{F(t_i)\}. \quad (5)$$

The substitution of equations (3) and (4) into equation (5) results in equations as follows:

$$(A[M] + C[D] + [K])\{q(t_i)\} + [M]\{B(t_i)\} + [D]\{E(t_i)\} = \{Q(t_i)\} + \{F(t_i)\} \quad (6)$$

or

$$\begin{bmatrix} [S^{11}] & [S^{12}] \\ [S^{21}] & [S^{22}] \end{bmatrix} \begin{Bmatrix} \{q(t_i)\}_1 \\ \{q(t_i)\}_2 \end{Bmatrix} + \begin{Bmatrix} \{v(t_i)\}_1 \\ \{v(t_i)\}_2 \end{Bmatrix} = \begin{Bmatrix} \{Q(t_i)\}_1 \\ \{Q(t_i)\}_2 \end{Bmatrix} + \begin{Bmatrix} \{O\} \\ \{F(t_i)\}_2 \end{Bmatrix} \quad (7)$$

where

$$[S^{\alpha\beta}] = A[M^{\alpha\beta}] + C[D^{\alpha\beta}] + [K^{\alpha\beta}], \ \alpha, \beta = 1, 2 \quad (8)$$

$$\begin{Bmatrix} \{v(t_i)\}_1 \\ \{v(t_i)\}_2 \end{Bmatrix} = [M]\{B(t_i)\} + [D]\{E(t_i)\} \quad (9)$$

Equation (6) or (7) is a set of N nonlinear algebraic equations in terms of N unknowns $q_n(t_i)$, $n = 1, 2, \ldots, N$. The system response can be obtained by directly solving the set of nonlinear algebraic equations for each time instant. However, if the system motion is governed by a large number of equations, it will be inefficient. For a large system with sparse nonlinearities, it will be more efficient if the number of nonlinear algebraic equations can be reduced.

Since the upper part of equation (7) is a set of linear equations, one can solve the linear coordinates $\{q(t_i)\}_1$ in terms of the nonlinear coordinates $\{q(t_i)\}_2$. It yields

$$\{q(t_i)\}_1 = [S^{11}]^{-1}(\{Q(t_i)\}_1 - \{v(t_i)\}_1 - [S^{12}]\{q(t_i)\}_2). \quad (10)$$

The substitution of equation (10) into the lower part of equation (7) with rearrangement results in

$$([S^{22}] - [S^{21}][S^{11}]^{-1}[S^{12}])\{q(t_i)\}_2 + [S^{21}][S^{11}]^{-1}(\{Q(t_i)\}_1 - \{v(t_i)\}_1) + \{v(t_i)\}_2 - \{Q(t_i)\}_2 - \{F(t_i)\}_2 = \{0\}. \quad (11)$$

Equation (11) only consists of n_2 nonlinear algebraic equations with n_2 unknowns, $\{q(t_i)\}_2$. If the number of nonlinear coordinates n_2 is small in comparison with the system degrees-of-freedom N, this condensation technique will lead to a substantial reduction of the computational time and an increase of the probability of locating solutions. It should be noted that the vectors $\{v(t_i)\}_1$ and $\{v(t_i)\}_2$ of equation (11) are functions of the motion at previous time and the coefficient matrices $[S^{\alpha\beta}]$, $\alpha, \beta, = 1, 2$, are functions of system parameters and the time step chosen. With knowing the motion at previous time $\{q(t_{i-1})\}$, $\{\dot{q}(t_{i-1})\}$, and $\{\ddot{q}(t_{i-1})\}$, the response of the linear coordinates can be computed from equation (10). Similarly, the displacement of the system at time instant t_{i+1} can be obtained by the same procedures.

Numerical Examples

A flexible rotor system analyzed by Chen et al. (1988) is utilized to illustrate the accuracy and the efficiency of the present method. In the example, A, C, $\{B(t_i)\}$, and $\{E(t_i)\}$ are derived by using the second-order Taylor method with the assumption of constant acceleration over each time interval (t_{i-1}, t_i) for the test of the solution technique. A computer code has been developed on a VAX-8600 computer.

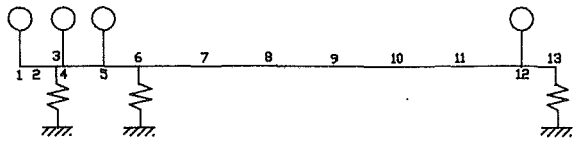

Fig. 1 Rotor schematic plot

Table 1 Rotor configuration data

Element Number	Element Length (cm)	Inner Radius (cm)	Outer Radius (cm)
1	4.27	1.42	2.95
2	4.62	1.42	2.95
3	1.60	1.42	2.95
4	9.68	1.42	2.95
5	7.47	1.96	2.95
6	16.51	2.69	2.95
7	15.24	2.69	2.95
8	15.24	2.69	2.95
9	15.24	2.69	2.95
10	15.24	2.26	2.95
11	14.94	1.42	2.95
12	7.92	2.31	2.95
$E = 20.68 \times 10^{10} N/m^2$, $\rho = 8193 kg/m^3$			

Table 2 Concentrated disk data

Station Number	Mass (kg)	Diametral Inertia ($kg \cdot m^2$)	Polar Inertia ($kg \cdot m^2$)
1	11.38	0.0982	0.1953
4	7.88	0.0835	0.1671
5	7.70	0.0880	0.1761
12	21.71	0.2224	0.4448

Table 3 Isotropic bearing properties

Station Number	Stiffness (N/cm)	Damping ($N \cdot s/cm$)
3	17510	0
6	769500	0
13	133680	0

The rotor configuration is schematically shown in Fig. 1. The detail rotor configurations and material properties are listed in Table 1. The rotor includes four rigid discs with mass properties shown in Table 2. The system is supported on a rigid foundation by isotropic undamped bearings with properties listed in Table 3. Two identical squeeze film dampers are located at stations 3 and 13 and each acts in parallel with

Downloaded 03 May 2010 to 171.66.16.248. Redistribution subject to ASME license or copyright; see http://www.asme.org/terms/Terms_Use.cfm

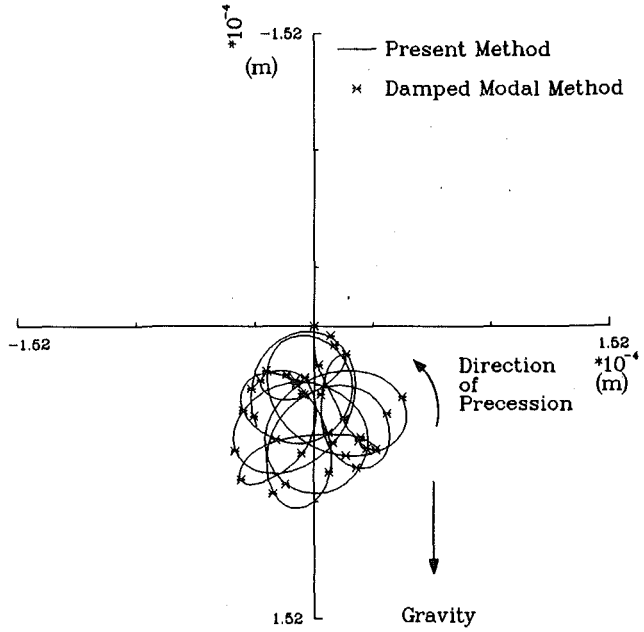

Fig. 2 The nonlinear transient response of the journal in the damper at station 3, $\omega = 700$ rad/s

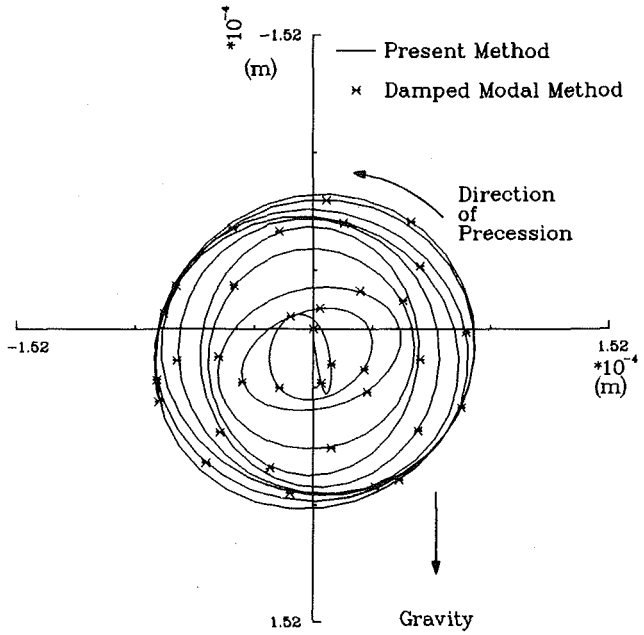

Fig. 3 The nonlinear transient response of the journal in the damper at station 13, $\omega = 700$ rad/s

the support stiffnesses. The short bearing theory with π-films for cavitation (Mohan and Hahn, 1974) is assumed for the damper. The journal in the damper is of radius = 50.8 mm and length = 25.4 mm. The radial clearance of the damper is 152 μm. The lubricant viscosity is 0.00266 N·s/m^2. The rotor is modeled as a 52 degrees-of-freedom system with 48 linear and 4 nonlinear coordinates using finite element method (Nelson and McVaugh, 1976). The system is subjected to the gravity load and an unbalance excitation due to the C. G. eccentricity of 10.16 μm in the disk at station 12.

The dynamic response of the system at the spin speed of ω = 700 rad/s is calculated using time step $T/30$, $T = 2\pi/\omega$. Figures 2 and 3 display the typical transient orbits of the journals in the dampers at stations 3 and 13, respectively. The results show a good agreement with those using the damped modal method.

The computing time on the VAX-8600 computer is 18.40 and 432.85 CPU seconds for the present method with and without condensation; 38.39 and 192.97 CPU seconds for the undamped and damped modal methods, respectively; 71.09 CPU seconds for the Transient Property Transfer Approach (Subbiah et al., 1988b). The results show that the present method can significantly reduce the computing time for the large-order systems with small number of nonlinear coordinates compared to that of system degrees-of-freedom.

Conclusions

An efficient solution technique based on the implicit time marching algorithm combined with a condensation technique has been developed to study the dynamic behaviors of large flexible nonlinear mechanical systems, especially for the systems with small number of nonlinear coordinates compared to that of the system degrees-of-freedom. A rotor system is used to demonstrate the accuracy and the efficiency of the present method. The results show that the condensation technique can greatly reduce the problem dimensionality and significantly save the computing time without losing accuracy. Moreover, no restrictions are made on the system matrices and force vectors for the present method, except the nonlinear force vector $\{F\}$ has to be sparse. The algorithm presented in this study can also be applied to the transient analysis of general flexible mechanical systems.

References

Adams, M. L., 1980, "Non-linear Dynamics of Flexible Multi-Bearing Rotors," *Journal of Sound and Vibration*, Vol. 71, No. 1, pp. 129–144.

Barrett, L. E., and Gunter, E. J., 1975, "Steady-State and Transient Analysis of a Squeeze Film Bearing for Rotor Stability," NASA CR-2548, Washington, D.C.

Chen, W. J., Rajan, M., Rajan, S. D., and Nelson, H. D., 1988, "The Optimal Design of Squeeze Film Dampers for Flexible Rotor Systems," *ASME Journal of Mechanisms, Transmissions, and Automation in Design*, Vol. 110, pp. 166–174.

Jean, A. N., and Nelson, H. D., 1989, "Periodic Response Investigation of Large Order Nonlinear Rotordynamic Systems Using Collocation," The 12th Biennial ASME Conference on Mechanical Vibration and Noise, Montreal, Canada, Sept. 17–20, 1989.

Kascak, A. F., 1979, "Direct Integration of Transient Rotor Dynamics," *Proceedings of the Conference on the Stability and Dynamic Response of Rotors with Squeeze Film Bearings*, May 8–10, 1979, pp. 231–250.

Kumar, A. S., and Sankar, T. S., 1986, "A New Transfer Matrix Method for Response Analysis of Large Dynamic Systems," *Computers and Structures*, Vol. 23, No. 4, pp. 545–552.

Mohan, S., and Hahn, E. J., 1974, "Design of Squeeze Film Damper Supports for Rigid Rotors," *ASME Journal of Engineering for Industry*, pp. 976–982.

Nelson, H. D., and McVaugh, J. M., 1976, "The Dynamics of Rotor-Bearing Systems Using Finite Elements," *ASME Journal of Engineering for Industry*, Vol. 98, No. 2, pp. 593–600.

Nelson, H. D., and Meacham, W. L., 1981, "Transient Analysis of Rotor-Bearing Systems Using Component Mode Synthesis, " ASME Paper 81-GT-110.

Nelson, H. D., Meacham, W. L., Fleming, D. P., and Kascak, A. F., 1983, "Non-Linear Analysis of Rotor-Bearing Systems Using Component Mode Synthesis," *ASME Journal of Engineering for Power*, Vol. 105, pp. 606–616.

Padovan, J., Adams, M. L., Fertis, D., Zeid, I., and Lam, P., 1984, "Nonlinear Transient Finite Element Analysis of Rotor-Bearing-Stator Systems," *Computers and Structures*, Vol. 18, No. 4, pp. 629–639.

Rao, J. S., and Sarma, K. V. B., 1986, "On Transient Dynamics of Rotors with Asymmetric Cross-Section Supported on Fluid Film Bearings," *Proceedings of 4th International Modal Analysis Conference*, pp. 1110–1116.

Shiau, T. N., and Jean, A. N., 1989, "Prediction of Steady State Response of Flexible Rotor Systems with Nonlinear Supports," The 12th Biennial ASME Conference on Mechanical Vibration and Noise, Montreal, Canada, Sept. 17–20, 1989.

Subbiah, R., and Rieger, N. F., 1988a, "On the Transient Analysis of Rotor-Bearing Systems," *ASME Journal of Vibration, Acoustics, Stress, and Reliability in Design*, Vol. 110, pp. 515–520.

Subbiah, R., Kumar, A. S., and Sankar, T. S., 1988b, "Transient Dynamic Analysis of Rotors Using the Combined Methodologies of Finite Elements and Transfer Matrix," ASME JOURNAL OF APPLIED MECHANICS, Vol. 55, pp. 448–452.

Downloaded 03 May 2010 to 171.66.16.248. Redistribution subject to ASME license or copyright; see http://www.asme.org/terms/Terms_Use.cfm

On the Response of a Partially Embedded Rod to Axial Load

Ronald Y. S. Pak[17,19] **and Jean-Daniel M. Saphores**[18,19]

Introduction

The response of a partially embedded rod in an elastic half-space under axial load is a subject of considerable interest in engineering and applied mechanics. An important approach to this class of problems is furnished in Muki and Sternberg (1970) wherein the rod is treated as a one-dimensional structure immersed in a three-dimensional elastic continuum. Under their particular formulation which adopts the axial force in the rod as the primary unknown, however, solutions are limited to relatively short embedments and low rod-to-medium stiffness ratios, no result is provided on the deformation of the rod nor the axial compliance of the system, both of which are quantities of practical interest. Owing to the importance of this class of problems, various authors have attempted to reformulate the problem within similar frameworks. For instance, on the basis of an energy principle and the Muki-Sternberg approach, Rajapakse and Shah (1987) present an approximate treatment of this problem through a discretization of the rod-medium interfacial tractions. Notwithstanding the versatility of the resulting numerical method, the analysis is not equipped to deal with the singular nature of the solution near the ends of the embedment, and is apt to suffer some numerical instability as a result (Rajapakse, 1990).

In this paper, a displacement formulation is presented for the interaction problem of an embedded rod under axial loading. Owing to its simple mathematical form and the inherent regularity of the solution variable, the governing integral equation, which features a closed-form kernel, is found to be well behaved for all parameters of practical interest.

Mathematical Formulation

Consider a circular cylindrical rod B of length L and radius a, which is embedded in a homogeneous, isotropic, linearly elastic solid and loaded axially at the top terminal section (see Fig. 1). As in Muki and Sternberg (1970), the embedding medium is extended throughout the half-space and an elastic solid S with the same material parameters as the original material is assumed to occupy the extended region. To account for the stiffening effects of the embedded rod, a fictitious embedment B_* with a Young's modulus $E_* = E_e - E_s > 0$ is introduced in D so that the axial stiffness of the resulting composite cylindrical region can be regarded as *equivalent* to that of the actual embedment. Here, the subscripts e and s denote the corresponding quantities of the embedment and the half-space, respectively. In what follows, the embedment B_* is considered as a one-dimensional elastic body subject to the equilibrium equation

$$\frac{dp_*(z)}{dz} = -q_*(z) \tag{1}$$

and the constitutive law

$$E_* A \frac{dw_*(z)}{dz} = -p_*(z) \tag{2}$$

where p_*, q_*, w_*, and A stand for the internal axial force, the lineal density of the distributed bond force acting on D, the displacement, and the cross-sectional area of B_*, respectively (see Fig. 2). For the extended medium, there are the distributed bond force q_* acting in D, and the possible concentrated load transfers $p_0 - p_*(0^+)$ and $p_*(L)$ to occur at Π_0 and Π_L, respectively. To describe the response of the extended medium to these loadings, it is convenient to employ an influence field $\hat{u}(\mathbf{x};s) = (\hat{u}_r, 0, \hat{u}_z)$ which is defined as the displacement field at a point $\mathbf{x} \in S$ due to a suitably distributed axisymmetric body-force field in Π_s acting in the z-direction with a unit resultant. As the cross-section of the rod usually remains planar in many applications, the body-force field distribution corresponding to a vertically loaded rigid disk embedded in an elastic medium is adopted. With the aid of the foregoing influence field, the displacement of the half-space can written as

$$\mathbf{u}(\mathbf{x}) = [p_0 - p_*(0^+)]\hat{u}(\mathbf{x};0) + p_*(L)\hat{u}(\mathbf{x};L) + \int_0^L \hat{u}(\mathbf{x};s) q_*(s)\, ds, \quad \mathbf{x} \in S. \tag{3}$$

In particular, the vertical displacement can be expressed as

$$u_z(z,r) = [p_0 - p_*(0^+)]\hat{u}_z(z,r;0) + p_*(L)\hat{u}_z(z,r;L) + \int_0^L \hat{u}_z(z,r;s) q_*(s) ds, \quad 0 \le z. \tag{4}$$

To ensure the deformation of B_* is compatible with that of S, the imposition of a suitable bond condition is necessary. In view of the possible deviation of the vertical displacement over Π_z from a uniform pattern despite the use of the proposed Green's function, it is deemed appropriate to require that the average of the vertical displacement of the half-space over Π_z be equal to that of the rod over the length of embedment. With the aid of equation (1), this bond condition can be written as

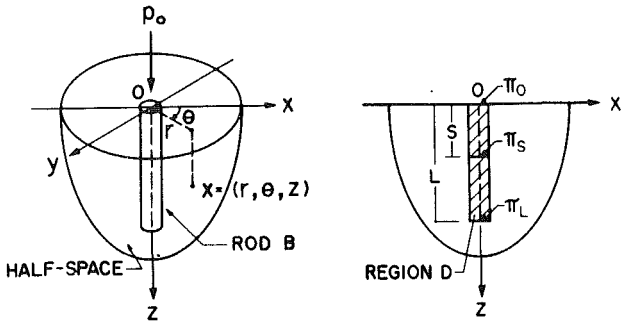

Fig. 1 Rod and medium configurations

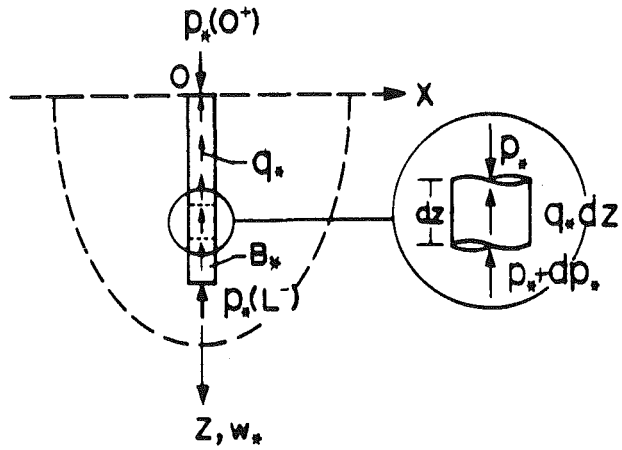

Fig. 2 Forces on B_* and sign conventions

[17]Assistant Professor of Civil Engineering, Assoc. Mem. ASME.
[18]Graduate Research Assistant.
[19]University of Colorado, Boulder, CO 80309-0428.

Manuscript received by the ASME Applied Mechanics Division, Oct. 16, 1989; final revision, Mar. 12, 1990.

Copyright © 1991 by ASME
Downloaded 03 May 2010 to 171.66.16.248. Redistribution subject to ASME license or copyright; see http://www.asme.org/terms/Terms_Use.cfm

$$w_*(z) = [p_0 - p_*(0^+)]\hat{U}_z(z;0) + p_*(L)\hat{U}_z(z;L) - \int_0^L \hat{U}_z(z;s)\frac{dp_*(s)}{ds}\,ds,\ 0 \le z \le L \quad (5)$$

where

$$\hat{U}_z(z;s) = \frac{2}{a^2}\int_0^a \hat{u}_z(z,r;s)\,r\,dr. \quad (6)$$

On an integration by parts, one can show that equation (5) yields

$$w_*(z) = p_0\hat{U}_z(z;0) + \int_0^L \frac{\partial \hat{U}_z}{\partial s}(z;s)p_*(s)\,ds,\ 0 \le z \le L. \quad (7)$$

In the above, there are two functions w_* and p_*, one of which can be eliminated by means of the constitutive relation of the rod. By differentiating equation (7) with respect to z, for instance, one arrives at a Fredholm integral equation of the second kind

$$\left(\frac{1}{E_*A} - \left[\frac{\partial \hat{U}_z}{\partial s}(z;s)\right]_{z^-}^{z^+}\right)p_*(z) + \int_0^L \frac{\partial^2 \hat{U}_z}{\partial s\,\partial z}(z;s)p_*(s)\,ds = -p_0\frac{\partial \hat{U}_z}{\partial s}(z;0),\ 0 \le z \le L \quad (8)$$

which is analogous to the one derived by Muki and Sternberg (1970). However, in the limiting case of the rod being rigid and the embedding medium being incompressible, the foregoing integral equation can be shown to degenerate into one of Fredholm's first kind, with its accompanying analytical and numerical difficulties. On the other hand, through a proper integration by parts with the adoption of the displacement as the pivotal unknown, equation (7) can be reduced to

$$A(\bar{z})\bar{w}(z) + B(\bar{z})\bar{w}(0) + C(\bar{z})\bar{w}(\bar{L}) + \int_0^{\bar{L}} K(\bar{z};\bar{s})\bar{w}(\bar{s})\,d\bar{s} = -\bar{P}_0 F(\bar{z}),\ 0 \le \bar{z} \le \bar{L} \quad (9)$$

where

$$A(\bar{z}) = \left[\frac{\partial U}{\partial \bar{s}}(\bar{z};\bar{s})\right]_{\bar{z}^-}^{\bar{z}^+} - \frac{1}{\kappa_*},\ B(\bar{z}) = \frac{\partial U}{\partial \bar{s}}(\bar{z};0),$$

$$C(\bar{z}) = -\frac{\partial U}{\partial \bar{s}}(\bar{z};\bar{L}),$$

$$K(\bar{z};\bar{s}) = \frac{\partial^2 U}{\partial \bar{s}^2}(\bar{z};\bar{s}),\ F(\bar{z}) = \frac{U(\bar{z};0)}{\kappa_*},$$

$$U(\bar{z};\bar{s}) = 2\pi\mu_s a\bar{U}_z(z;s),$$

$$\bar{P}_0 = \frac{p_0}{2\pi\mu_s a^2},\ \kappa_* = \kappa - (1+\nu_s),\ \kappa = \frac{E_e}{2\mu_s},$$

$$\bar{z} = \frac{z}{a},\ \bar{s} = \frac{s}{a},\ \bar{L} = \frac{L}{a},\ \bar{w} = \frac{w_*}{a}. \quad (10)$$

In equation (10), μ_s and ν_s are the shear modulus and the Poisson's ratio of the embedding medium, respectively; κ describes the relative magnitude of the axial stiffness of the rod to the shearing stiffness of the medium. With a form similar to the one in Pak (1989), the dimensionless integral equation (9) is one of Fredholm's second kind, whose solution furnishes the displacement of the rod. As will be illustrated, the present formulation is capable of dealing with the full spectrum of physical parameters for the interaction problem.

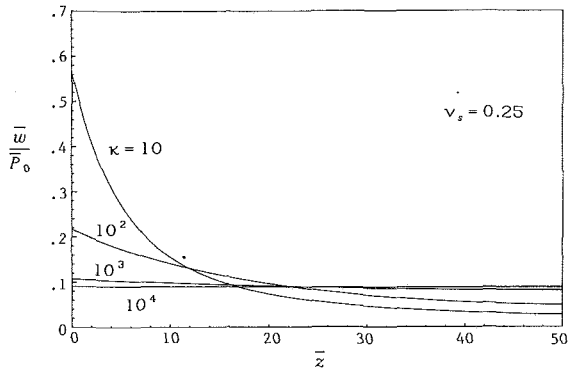

Fig. 3(*a*)

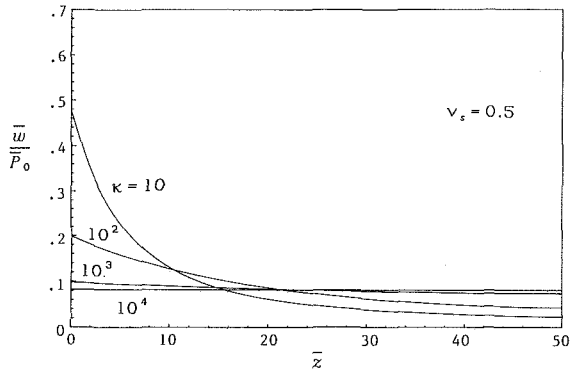

Fig. 3(*b*)

Fig. 3 Displacement of rod for $\bar{L} = 50$

Influence Field

For torsionless and rotationally symmetric problems such as the one under consideration, equilibrium solutions in the linear theory of elasticity can be represented, without loss of completeness, as

$$\mathbf{u}(r,z) = \mathbf{e}_z\nabla^2\Phi - \frac{1}{2(1-\nu_s)}\nabla(\mathbf{e}_z\cdot\nabla\Phi) \quad (11)$$

where

$$\nabla^4\Phi(r,z) = 0, \quad (12)$$

in cylindrical coordinates (Love, 1944). For the determination of the influence field $\hat{u}(\mathbf{x};s)$, equation (12) must be appended by the traction-free boundary conditions at $z = 0$,

$$\hat{\sigma}_{zz}(r,0) = \hat{\sigma}_{rz}(r,0) = 0,\ r \in [0,\infty), \quad (13)$$

the regularity conditions at infinity,

$$\hat{\sigma} \to 0,\ \sqrt{r^2+z^2} \to \infty, \quad (14)$$

and the stress discontinuity condition

$$R_0(r) = \hat{\sigma}_{zz}(r,s^-) - \hat{\sigma}_{zz}(r,s^+) = \frac{1}{2\pi a\sqrt{a^2-r^2}},\ r < a \quad (15)$$

as induced by the prescribed body-force field on Π_s (Pak and Gobert, 1990). Together with the requirement that the stresses and displacements are continuous throughout the medium except as noted in (15), it can be shown, with the aid of Hankel transforms, that the requisite dimensionless influence function can be expressed as

Downloaded 03 May 2010 to 171.66.16.248. Redistribution subject to ASME license or copyright; see http://www.asme.org/terms/Terms_Use.cfm

$$U(\bar{z};\bar{s}) = \frac{1}{4(1-\nu_s)} \left\{ \begin{array}{c} (3-4\nu_s)S(d_1;-2,1) + d_1 S(d_1;-1,1) \\ +(5-12\nu_s+8\nu_s^2)S(d_2;-2,1) + (3-4\nu_s)d_2 S(d_2;-1,1) \\ +2\bar{z}\,\bar{s}\,S(d_2;0,1) \end{array} \right\} \quad (16)$$

where

$$d_1 = |\bar{z}-\bar{s}|, \; d_2 = (\bar{z}+\bar{s}). \quad (17)$$

$$S(d;n,p) = \int_0^\infty \xi^n e^{-\xi d} \sin(\xi) J_p(\xi) d\xi, \quad (18)$$

and J_p is the Bessel function of the first kind of order p. As the integrals in (16) can all be evaluated in closed form, the various derivatives of $U(\bar{z};\bar{s})$ required in equation (10) can be computed in a straightward manner. However, it should be noted that $\partial^2 U/\partial\bar{s}^2(\bar{z},\bar{s})$, which constitutes the kernel of the integral equation, has an inverse square-root type singularity at $\bar{z}=\bar{s}$.

Numerical Results and Discussion

For the solution of the weakly singular Fredholm integral equation (9), the method of singularity subtraction together with a closed Clenshaw-Curtis scheme is found to be the most efficient. Typical results are shown in Fig. 3. As expected, the maximum displacement always occurs at the top of the rod with its value decreases as the Poisson's ratio tends to 0.5. As the stiffness of the rod increases, it can be seen that the displacement profile gradually approaches a constant, signifying that the rod can eventually be regarded as rigid. The specific value of the rod-to-medium stiffness ratio for such a delineation, however, depends on the length of the embedment as well as the Poisson's ratio of the medium.

The foregoing observation is brought out more clearly in Fig. 4 where the axial compliance C_{AA} of the system as a function of the stiffness ratio κ, the dimensionless length, and the Poisson's ratio is presented. As $\kappa \to \infty$, the compliance, which is defined as

$$C_{AA} = \frac{\bar{w}(0)}{\bar{P}_0}, \quad (19)$$

evidently has a lower bound which depends on the values of ν_s and L. On the other hand, it is clear that as the stiffness of the rod tends to that of the medium, solutions for different lengths converge to the same curve, which is in accord with physical intuition. Furthermore, as the length and stiffness of the rod both tend to infinity, it can be seen that the effect of the Poisson's ratio on the compliance diminishes. This is consistent with the observation that the problem would approach one of pure shear in such a limit. In this connection, it is relevant to contrast some existing work on the subject such as the one by Mattes and Poulos (1969) with the present solution. From Fig. 5 where the comparison is shown, it is apparent that there is a departure of the former result from the current solution at low stiffness ratios. In particular, it could be noted that there is a divergence of Mattes and Poulos' results for rods of different lengths as the elastic properties of the rod degenerate to those of the medium. Nevertheless, as $\kappa \to \infty$, the comparison becomes more favorable with their solutions being only slightly on the low side of the current result.

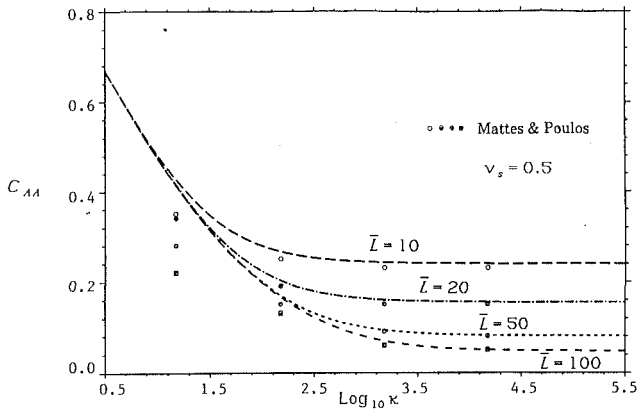

Fig. 5 Comparison with existing results

Acknowledgment

This paper is based upon studies supported by the National Science Foundation through Grant No. MSM-8611267.

References

Clenshaw, C. W., and Curtis, A. R., 1960, "A Method for Numerical Integration on an Automatic Computer," *Numerical Mathematics*, Vol. 2, pp. 197–205.

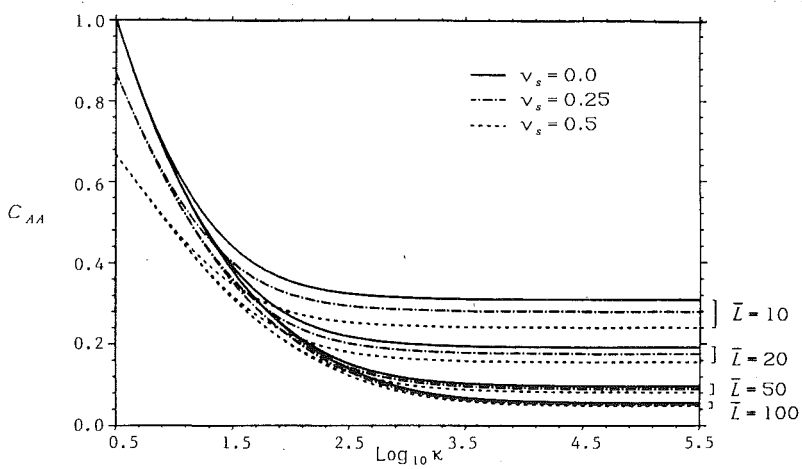

Fig. 4 Axial compliance function C_{AA}

Downloaded 03 May 2010 to 171.66.16.248. Redistribution subject to ASME license or copyright; see http://www.asme.org/terms/Terms_Use.cfm

Love, A. E. K., 1944, *A Treatise on the Mathematical Theory of Elasticity*, 4th ed., Dover, New York.

Mattes, N. S., and Poulos, H. G., 1969, "The Settlement of a Single Compressible Pile," *Journal of Soil Mechanics and Foundation Division*, ASCE, New York, Vol. 95, SM1, pp. 189–207.

Muki, R., and Sternberg, E., 1970, "Elastostatic Load-Transfer to a Half-Space from a Partially Embedded Axially Loaded Rod," *International Journal of Solids and Structures*, Vol. 6, pp. 69–90.

Pak, R. Y. S., 1989, "On the Flexure of a Partially Embedded Bar Under Lateral Loads," ASME JOURNAL OF APPLIED MECHANICS, Vol. 56, pp. 263–269.

Pak, R. Y. S., and Gobert, A. T., 1990, "On the Axisymmetric Interaction of a Rigid Disc with a Semi-Infinite Solid," *Zeitschrift für angewandte Mathematik und Physik*, Vol. 41, pp. 684–700.

Rajapakse, R. K. N. D., and Shah, A. H., 1987, "On the Longitudinal Harmonic Motion of an Elastic Bar Embedded in an Elastic Half-Space," *International Journal of Solids and Structures*, Vol. 23, pp. 287–303.

Rajapakse, R. K. N. D., 1990, "Rigid Inclusion in Nonhomogeneous Incompressible Elastic Half-Space," *Journal of Engineering Mechanics*, ASCE, New York, Vol. 116, No. 2, pp. 399–410.

APPENDIX

Notation:

$$S(d;n,p)=\int_0^\infty \xi^n e^{-\xi d}\sin(\xi)J_p(\xi)\,d\xi.$$

Results:

$$S(d;-2,1)=\frac{1}{2}\left\{\mathrm{Im}\left[\frac{(\sqrt{\alpha^2+1}-\alpha)^2}{2}\right]+\sin^{-1}\left[\frac{2}{\sqrt{d^2+4}+d}\right]\right\},$$

$$S(d;-1,1)=\mathrm{Im}[\sqrt{\alpha^2+1}-\alpha],\ S(d;0,1)=\mathrm{Im}\left[\frac{-\alpha}{\sqrt{\alpha^2+1}}\right],$$

subject to $|\alpha+\sqrt{\alpha^2+1}|>1$, $\alpha=d-i$.

Downloaded 03 May 2010 to 171.66.16.248. Redistribution subject to ASME license or copyright; see http://www.asme.org/terms/Terms_Use.cfm

Journal of Applied Mechanics

Book Reviews

Electrodynamics of Continua I: Foundations and Solid Media, by A. Cemal Eringen and Gérard A. Maugin. Springer-Verlag, New York, 1990. 436 pages, Price: $98.00.

REVIEWED BY Y. E. PAK[1]

We are entering an era of interdisciplinary research, not only between analysts and designers but also among the practitioners from traditionally separate disciplines, such as mechanics and electromagnetics. One example is a newly emerging technology, coined "intelligent" or "adaptive" materials and structures. The aim of this technology is to design and fabricate materials and structures that can sense the environment and actively adapt themselves so as to maximize their utility. This technology alone would require the use of piezoelectric, electrostrictive, magnetostrictive, electrorheological, fiber-optic, and shape memory materials. There are other numerous applications for which the material presented in this book would be of fundamental importance: technologies such as superconductivity, electromagetic sensors and actuators, electromagnetic levitation of vehicles, magnetic fusion, liquid crystals, and micromachines, to name just a few. In order to engineer such materials, one needs a basic understanding of how these electromagnetic materials behave under external mechanical and electrical stimuli.

This is the first volume of a two-volume set on continuum mechanics of electromagnetic media. The authors have successfully accomplished their goal of laying the rigorous foundation for the basic principles involved in analyzing material behavior under mechanical and/or electromagnetic loads.

The book starts out with a brief review of the mechanics of nonlinear, purely elastic continua.

The microscopic electromagnetic theory is introduced in Chapter 2, and through the statistical averaging method the classical macroscopic Maxwell's equations are derived in Chapter 3. The balance laws of electrodynamics of deformable media are then derived.

The physical theory of many interesting electromagnetic phenomena such as polarization, electrostriction, piezoelectricity, and magnetization are explained in Chapter 4, which provides invaluable insight into deriving phenomenological models for macroscopic behavior.

The axiomatic development of the constitutive equations is presented in Chapter 5 to describe phenomenologically the electromagnetic interactions in deformable media.

In Chapter 6, general governing equations and boundary conditions are simplified for a special case of rigid dielectrics, which renders possible the solving of some boundary value problems. Classical potential theory also is introduced.

Chapter 7 treats the elastic dielectrics that undergo infinitesimal and finite deformation with electro-elastic, electro-optic, and magneto-optic coupling. As a special case, technologically mature piezoelectricity is discussed in detail, covering vibration and wave propagation.

In Chapter 8, magnetoelasticity is discussed, with specific examples of stress concentration at a circular hole, plane waves, torsion of bars, and bending and buckling of plates.

In addition to eight chapters, there are five appendices on group thoeretic treatment of crystallography and one on Maxwell's equations in various systems of units. Excellent references on most of the significant work done in the field are listed at the end of the book. The problems at the end of each chapter can be very useful for course work or self-study. The typesetting is excellent, with a minimum of errors.

Most of the solved problems presented in Chapters 6 to 8 are pedagogical in nature, and there is very little discussion of the experimental verification of the phenomenological theories proposed. The book is full of complicated equations that may not be unique in describing the physical phenomena we are trying to understand. This may be somewhat discouraging to readers.

The material treated in this book is fundamental in its theoretical development and its application to boundary value problems. Since this book is a compilation of advances made over the years by both the authors (who themselves are prominent researchers) and others, it would make a good reference book for researchers in the field. It also is systematically developed and well organized by topic, so that it can be used as a textbook. However, the reviewer feels that a reader should be familiar with nonlinear continuum mechanics and classical electrodynamics, which are traditionally taught separately in engineering and physics departments, respectively. This excellent, comprehensive book on continuum mechanical aspects of electromagnetic interactions in solids is very timely. Perhaps it will aid in inspiring a new, interdisciplinary academic curriculum that will better prepare tomorrow's engineers to face new challenges in the mechanics of novel electromagnetic materials.

Tribology and Mechanics of Magnetic Storage Devices, by Bharat Bhushan. Springer-Verlag, New York, 1990. 1018 pages. Price: $148.00.

REVIEWED BY Y. W. CHUNG[2]

This is an impressive volume addressing basic issues and problems confronting modern magnetic recording industries. As the technology moves towards higher recording densities

[1]Senior Research Scientist, Grumman Corporate Research Center, Bethpage, NY 11714.

[2]Department of Material Science, Northwestern University, Evanston, IL 60208.

Copyright © 1991 by ASME
Downloaded 03 May 2010 to 171.66.16.248. Redistribution subject to ASME license or copyright; see http://www.asme.org/terms/Terms_Use.cfm